The 13th International Conference on the Electronic Properties of Two-Dimensional Systems

La 13e Conférence internationale sur les propriétés électroniques des systèmes bidimensionnels

Workbook / Livre de travail

August 1 – 6 août 1999
Ottawa, Canada

REPORT DOCUMENTATION PAGE

Form Approved
OMB No. 0704-0188

1. REPORT DATE *(DD-MM-YYYY)*	2. REPORT DATE	3. DATES COVERED *(From - To)*
04-08-1999	04-08-1999	3-01-99 To 28-02-2000

4. TITLE AND SUBTITLE
13th International Conference on Electronic Properties of Two Dimensional Systems (EP2DS-13)

5a. CONTRACT NUMBER
N/A

5b. GRANT NUMBER
N0014-99-1-0437

5c. PROGRAM ELEMENT NUMBER
N/A

6. AUTHOR(S)
HAWRYLAK, Pawel

5d. PROJECT NUMBER
N/A

5e. TASK NUMBER
N/A

5f. WORK UNIT NUMBER
N/A

7. PERFORMING ORGANIZATION NAME(S) AND ADDRESS(ES)
Institute for Microstructural Sciences
National Research Council
Ottawa, Ontario
K1A 0R6

8. PERFORMING ORGANIZATION REPORT NUMBER
N/A

9. SPONSORING/MONITORING AGENCY NAME(S) AND ADDRESS(ES)
Office of Naval Research
(ONR)

10. SPONSOR/MONITOR'S ACRONYM(S)
ONR

11. SPONSORING/MONITORING AGENCY REPORT NUMBER
N/A

12. DISTRIBUTION AVAILABILITY STATEMENT
Unlimited

13. SUPPLEMENTARY NOTES

14. ABSTRACT
13th International Conference on the Electronic Properties of 2D systems devoted to basic physics of semiconductor systems of reduced dimension. Subject areas covered include electronic properties of semiconductor heterostructures, quantum wires, quantum dots, the integer and fractional quantum Hall effect, novel probes, techniques and applications.

15. SUBJECT TERMS
ELECTRONIC PROPERTIES, LOW DIMENSIONAL STRUCTURES, FRACTIONAL QUANTUM HALL EFFECT, NANOSTRUCTURES

16. SECURITY CLASSIFICATION OF:			17. LIMITATION OF ABSTRACT	18. NUMBER OF PAGES	19a. NAME OF RESPONSIBLE PERSON
a. REPORT	b. ABSTRACT	c. THIS PAGE			HAWRYLAK, Pawel
			N/A	N/A	19b. TELEPONE NUMBER *(Include area code)* 613-993-9389

PREFACE

This volume contains unrefereed manuscripts of papers scheduled for presentation at the 13th International Conference on the Electronic Properties of Two-Dimensional Systems (EP2DS-13) to be held at The Westin Hotel, Ottawa, Canada August 1-6, 1999. Abstracts have been inserted in place of those papers not received at the time of publication. Refereed manuscripts will be published in a special issue of *Physica E* in the year 2000.

SPONSORS

We are grateful to the following organizations and companies for their generous financial support and sponsorship of this meeting. The list of sponsors as of the date of publication of this workbook is:

Elsevier Science B.V.
International Union of Pure and Applied Physics
Leybold Canada Inc.
Nortel Networks
Office of Naval Research, USA

COMMITTEES

Organizing Committee (IMS)

S. Charbonneau
P. Coleridge (*Treasurer*)
M. D'Iorio
P. Hawrylak (*Chair*)
H.C. Liu
D.J. Lockwood (*Publications*)
A. Sachrajda (*Program*)
R. Williams

International Program Committee

H. Aoki (*Tokyo*)
L. Eaves (*Nottingham*)
P. Hawrylak (*Ottawa*)
A. MacDonald (*Bloomington*)
B. McCombe (*Buffalo*)
M. Potemski (*Grenoble*)
A. Sachrajda – *Chair* (*Ottawa*)
H. Stormer (*Murray Hill*)
K. von Klitzing (*Stuttgart*)

International Advisory Committee

G. Abstreiter (*Garching*)
J. Allen (*Santa Barbara*)
T. Ando (*Tokyo*)
G. Bastard (*Paris*)
J. A. Brum (*Campinas*)
A. Chaplik (*Novosybirsk*)
L.L. Chang (*Hong Kong*)
R. Clark (*Sydney*)
T. Dietl (*Warsaw*)
R. Fletcher (*Kingston*)
A. Forchel (*Wuerzburg*)
C. Ford (*Cambridge*)
C. Glattli (*Saclay*)
B. Halperin (*Cambridge*)
M. Heiblum (*Rehovot*)
D. Heitmann (*Hamburg*)
G. Kirczenow (*Burnaby*)
S. Komiyama (*Tokyo*)
J. Kotthaus (*Munich*)
F. Kuchar (*Leoben*)
V.D. Kulakovskii (*Chernogolovka*)
J. C. Maan (*Nijmegen*)
P. McEuen (*Berkeley*)
L. Molenkamp (*Aachen*)
E. Molinari (*Modena*)
R. Nicholas (*Oxford*)
A. Pinczuk (*Murray Hill*)
J.J. Quinn (*Knoxville*)
L.J. Sham (*San Diego*)
B. Shanabrook (*Washington*)
M. Skolnick (*Sheffield*)
P. Streda (*Prague*)
C. Tejedor (*Madrid*)
J. Worlock (*Salt Lake City*)
D. Yoshioka (*Tokyo*)

CONTENTS

Withdrawals
PA.07, PA.26, PA.28
PB.10, PB.21, PB.30
PC.08, PC.09, PC.36, PC.49

MA.1

New Physics in High Landau Levels

J.P. Eisenstein[1], M.P. Lilly[1], K.B. Cooper[1], L.N. Pfeiffer[2] and K.W. West[2]

[1]*California Institute of Technology, Pasadena, CA 91125*
[2]*Bell Laboratories, Lucent Technologies, Murray Hill, NJ 07974*

Abstract

Recent magneto-transport experiments on ultra-high mobility 2D electron systems in GaAs/AlGaAs heterostructures have revealed the existence of whole new classes of correlated many-electron states in highly excited Landau levels. These new states, which appear only at extremely low temperatures, are distinctly different from the familiar fractional quantum Hall liquids of the lowest Landau level. Prominent among the recent findings are the discoveries of giant anisotropies in the resistivity near half filling of the third and higher Landau levels and the observation of re-entrant integer quantum Hall states in the flanks of these same levels. This contribution will survey the present status of this emerging field.

PACS numbers: 73.20Dx, 73.40Kp, 73.50.Jt

Introduction

The discovery and study of the fractional quantum Hall effect (FQHE) has dominated the discussion of strong correlation physics in two-dimensional electron systems for over 15 years[1]. The existence of a diverse family of incompressible quantum liquids as well as novel "composite fermion" compressible states makes the early predictions[2] of charge density wave ground states a striking example of the failure of Hartree-Fock theory. On the other hand, essentially all of this physics concerns the behavior of many-electron systems in the lowest (N=0) Landau level. Until recently, remarkably little research has been done on the problem of electron-electron correlations in the excited Landau levels.

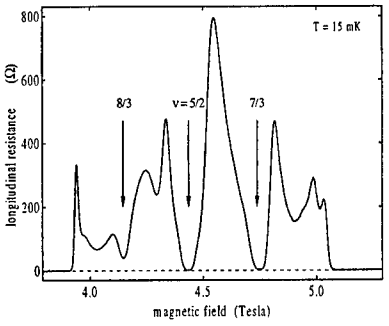

Fig. 1. Resistivity data from the N=1 Landau level taken at T=15mK. The 5/2, 7/3, and 8/3 FQHE states are indicated.

That the situation in these higher levels is not merely a replica of lowest Landau level physics has actually been evident for quite some time. In 1987 the first FQHE state having an even-denominator was discovered[3] at filling factor ν=5/2 in the N=1 second Landau

level (LL). Since then, in spite of great improvements in sample quality, the only other even-denominator FQHE known is the ν=7/2 state[4]. This state, which is also in the N=1 LL, is presumably the particle-hole conjugate of the 5/2 state. Figure 1 shows resistivity data in the vicinity of ν=5/2 taken at T=15mK using a high quality GaAs/AlGaAs heterostructure having a mobility of $11\times10^6 cm^2/Vs$. Although the 5/2 state is quite well developed in this sample, it is accompanied by *only two* odd-denominator FQHE states, at ν=7/3 and 8/3. This near-absence of the FQHE in the N=1 level contrasts sharply with the plethora of states seen in the N=0 level.

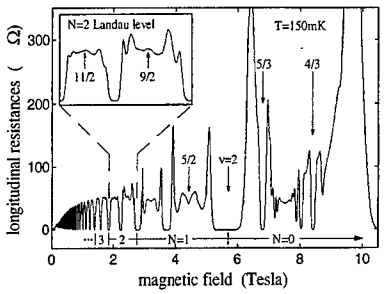

Fig. 2. Overview of the longitudinal resistivity at T=150mK in an $11\times10^6 cm^2/Vs$ mobility 2D electron gas. Data from the N=2 Landau level is expanded in the inset.

In the *third* and higher LLs (N≥2 and $\nu\geq4$) the situation changes again. Little attention has been paid to this low magnetic field regime owing to the expectation that subtle correlation effects would be overwhelmed by disorder. Nonetheless, as early as 1988 there were hints from transport experiments that interesting things might be going on[5]. Figure 2 shows longitudinal resistivity data obtained at T=150mK from the same sample as used for Fig.1. Above B=2.7T, the Fermi level is in either the N=1 or N=0 LL. Familiar odd-denominator fractional quantum Hall states are seen in the N=0 level and the emerging ν=5/2 and 7/2 states in the N=1 level are also evident. In the inset the data from the N=2 LL (filling factors between $6>\nu>4$) are magnified and substantial structure in the resistivity is apparent. This structure is not consistent with a disorder-driven transition between integer quantized Hall states and is instead clear evidence for electron correlations. To determine the nature of these correlations obviously requires lower temperatures.

The remainder of this paper will survey, in outline form, the prominent findings of recent transport measurements on high mobility 2D electron gases in at high Landau level filling factors. While the first conclusive reports of dramatic transport anomalies were those of the Caltech/Bell group[6,7], essentially identical findings have been reported by the Utah/Columbia/Princeton/NHMFL/Bell collaboration[8,9]. Most recently, related findings have also been reported for 2D *hole* systems by Shayegan and Manoharan[10].

II. Anisotropic Transport

Figure 3 shows the temperature development of the resistance in the vicinity of ν=9/2. Two traces are shown at each temperature: these correspond to two different current flow configurations in the 5x5mm square sample. In both cases the current is driven between two ohmic contacts placed at the midpoints of opposite sides of the sample and the voltage is detected using two contacts at the corners along one side of the current flow axis. For the dashed trace the average current flow direction is along the <1-10> crystallographic direction; the resistance measured thusly is denoted R_{xx}. For the solid trace the current is along the orthogonal <110> direction and the resistance is R_{yy}.

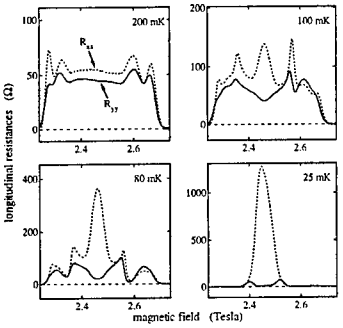

Fig. 3. Temperature development of resistance features around ν=9/2.

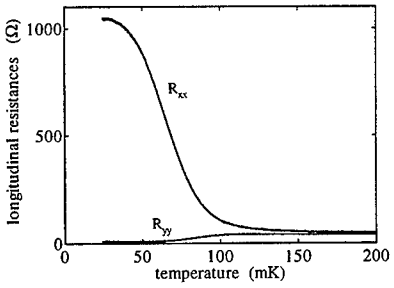

Fig. 4. Resistances at exactly ν=9/2.

(Note that the R_{yy} trace has been multiplied by 0.6.) At high temperatures the two traces are very similar but below about 150mK a clear difference develops around half-filling. A maximum develops in R_{xx} while a minimum forms in R_{yy}. Note that the peak in R_{xx} does not narrow as the temperature is reduced. By T=25mK the difference between the two measurements has become enormous (about 100x) and dwarfs the factor of 0.6 originally applied to facilitate the comparison. The development of this giant anisotropy in the resistance is perhaps the most striking aspect of transport in high Landau levels in clean 2D electron systems. Figure 4 shows the rapid way in which the anisotropy at ν=9/2 develops as the temperature is reduced below 100mK. Notice that below about 40-50mK both R_{xx} and R_{yy} have apparently saturated at finite values. This saturation seems to be genuine and not simply a heating effect.

Figure 5 shows an overview of the resistances R_{xx} and R_{yy} at T=25mK. The insets clarify the two measurement configurations. It is clear that the anisotropy seen around ν=9/2 is also present at ν=11/2, 13/2, 15/2, and with decreasing strength at still higher half-odd integer fillings. Most importantly, however, the anisotropy is *absent* at ν=7/2 and 5/2 in the N=1 LL and (though not shown) in the N=0 lowest LL. This simple observation is perhaps the clearest indication that correlation phenomena in the N≥2 levels are quite different from those in the lower two Landau levels.

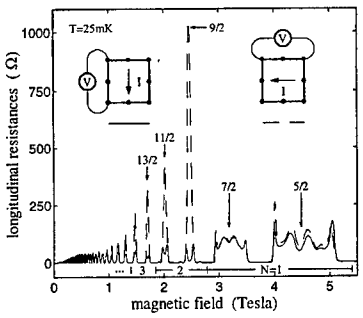

Fig. 5. Overview of transport anisotropy in high Landau levels.

III. Re-entrant Integers

Away from half-filling of the N≥2 levels, the resistance again becomes essentially isotropic. Figure 6 shows data from a sample having low temperature mobility of $\mu=15.6\times10^6 cm^2/Vs$. For this sample, the observed resistances R_{xx} and R_{yy} differ by about a *factor or 3500* at

ν=9/2[11]. In contrast, in the flanks of the Landau level the two resistances return to approximate equality (at the factor-of-two level). Furthermore, both resistances drop to essentially zero[6,8] near B=1.9 and 2.1T (ν≈4.25 and 4.75), suggesting the existence of new fractional quantized Hall states. Figure 6 reveals that while the Hall resistance *is* quantized in these regions, it is at the value of the nearby *integer* quantum Hall states. (The apparent plateaus in ρ_{xy} elsewhere in Fig. 6 are not stable and disappear at very low temperatures. We believe they are artifacts arising from mixing of the longitudinal and Hall resistances.) These observations therefore suggest that at these filling factors the electrons in the N=2 Landau level have assumed an *insulating* configuration. The fact that these new phases are well separated from the conventional integer QHE states suggests that the origin of the insulating behavior is not simply single particle localization; electron correlations are clearly playing an essential role. We emphasize that this re-entrant integer QHE is not found in the N=1 or N=0 Landau levels but is apparently present in several LLs with N≥2. This effect represents another of the surprising new results from high Landau levels.

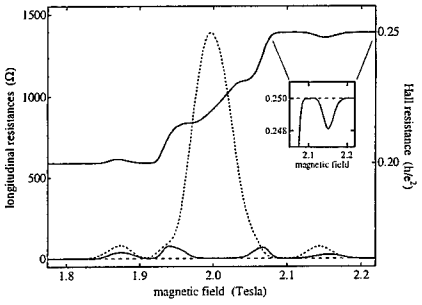

Fig. 6. Hall and longitudinal resistance in the range 4<ν<5. Inset shows the re-entrant ν=4 integer QHE.

IV. Stripes and Bubbles?

At the qualitative level, these observations overlap strongly with the recent theoretical suggestions of charge density wave (CDW) states in high Landau levels. The early work of Koulakov, Fogler and Shklovskii[12] and Moessner and Chalker[13] has been supplemented recently by several additional contributions[14-18]. Unlike the situation in the lowest Landau level, these theoretical works conclude that Hartree-Fock CDW states are in fact good starting points for understanding the many-electron ground state in the N≥2 LLs. Near half-filling of the LLs, the CDW is predicted to be a unidirectional stripe phase in which the filling factor ν_N of the uppermost LL jumps between ν_N=0 and 1. The wavelength of this stripe pattern is expected to be a few times the classical cyclotron radius, or about 1000-1500Å under typical experimental conditions. It is certainly plausible that if such a phase were coherently oriented over macroscopic dimensions it could produce a highly anisotropic resistivity. At the same time, the theories also predict that in the flanks of the LL there is a transition from the stripe phase to "bubble" phases and eventually a Wigner crystal. Such phases would likely be isotropic and probably pinned by disorder. This too is broadly consistent with the experimental observations.

Beyond these qualitative comparisons however, there are many important unanswered questions. How and why the stripes are pinned coherently across the sample is only the most obvious one. At a deeper level, the basic nature of transport in stripe or bubble phases is not understood. Should the resistances R_{xx} and R_{yy} measured at half-

filling saturate at low temperatures? Should the width of the resistance peak remain finite as T→0? Can the existence of the re-entrant integer QHE state in the flanks of the LL be incorporated into a scenario of bubble or Wigner crystal phases? What about interaction effects beyond Hartree-Fock? Are the stripes themselves stable against a Peierls-type instability[15]? Do quantum fluctuations produce liquid crystalline behavior?[14] Obviously, much remains to be understood.

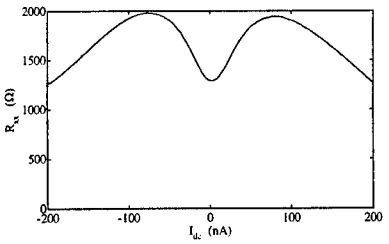

Fig. 7. Non-linearity at T=25mK in the resistance R_{xx} at ν=9/2.

V. Non-linearities

Less heralded, but nonetheless intriguing, are the substantial non-linearities of the resistivity observed around half filling of high LLs by Lilly, *et al.*[6]. Figure 7 shows the effect on the peak resistance R_{xx} of a dc current added to the small ac current used for the measurement. (The resistance R_{xx} is really dV_{xx}/dI). For small dc currents, the resistance R_{xx} *rises*. Since R_{xx} falls rapidly with increasing temperature, the observed non-linearity at small dc current is inconsistent with simple electron heating. As the figure shows, larger dc current do indeed drive R_{xx} down and this could well be a heating effect. It is interesting to consider what the enhancement of R_{xx} at small dc current implies for the conductivity of the system. Inversion of the resistivity tensor of an anisotropic system yields $\sigma_{yy} = \rho_{xx}/(\rho_{xx}\rho_{yy}+\rho_{xy}^2)$. Since the Hall resistance ρ_{xy} is much larger (about 6kΩ at ν=9/2) than both R_{xx} and R_{yy}, we have approximately $\sigma_{yy} \approx \rho_{xx}/\rho_{xy}^2$. Thus, a large *resistance* R_{xx} in the <1-10> direction is equivalent to a large *conductance* in the <110> direction. Hence, within the stripe model, the enhancement of R_{xx} at small dc current implies enhancement of the conductivity along the stripes. The data in Fig. 7 show that this enhancement turns on continuously rather than exhibiting a sharp threshold as expected for the depinning of a charge density wave. On the other hand, Fertig[15] has recently suggested that the non-linearity we observe is consistent with a model of a quantum melted modulated stripe phase. In Fertig's model the Hall electric field along the stripes produced by the dc current increases the population of charged soliton-antisoliton pairs and thereby increases the conductance.

VI. Tilted Fields

To further examine the anisotropic phases near half filling, tilted magnetic field studies have been performed[7,9]. The in-plane magnetic field $B_{\|}$ created by tilting the sample couples to the system through the spin Zeeman energy and the finite thickness of the electronic wavefunction in the direction perpendicular to the 2D plane. Beyond this, however, the in-plane field also breaks the rotational symmetry of the system. It is important to see how this symmetry breaking interacts with the internal symmetry breaking field which macroscopically orients the intrinsic transport anisotropy of half-filled high Landau levels in the first place.

Figure 8 shows the $B_{\|}$-dependence of the resistances R_{xx} (dashed curves) and R_{yy} (solid curves) at T=50mK at ν=9/2 and 11/2 in the N=2 LL. In the left two panels $B_{\|}$ is

directed along the <110> crystal direction while in the right two it is along <1-10>. Recall that (at $B_{||}$=0) transport along the <110> direction yields the minimum in R_{yy} while transport along <1-10> gives the tall peak in R_{xx}. It is clear from the figure that theses resistances are quite sensitive to both the magnitude and direction of the in-plane magnetic field.

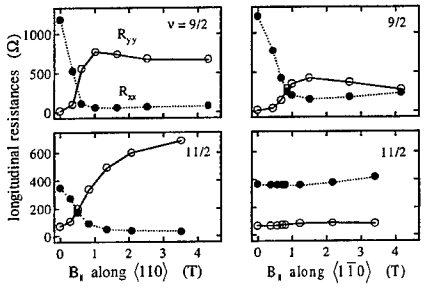

Fig. 8. Left two panels: Interchange of "hard" and "easy" transport directions induced by an in-plane magnetic field along <110>. Right panels: Effect of an in-plane field along <1-10>.

With $B_{||}$ oriented along <110> the large anisotropy (R_{xx}>>R_{yy}) at $B_{||}$=0 gives way to the opposite condition at large in-plane field. This remarkable "interchange effect" is also seen at ν=13/2 and 15/2 in the N=3 LL and in several higher half-filled levels as well. It appears that the in-plane magnetic field rotates the anisotropy axes by 90° in the 2D plane. Interestingly, the interchange seems to always to occur at $B_{||}$≈0.5T. If one adopts a stripe model, and assumes that transport transverse to the stripes produces higher resistance than transport along them, then these data suggest the stripes want to orient themselves perpendicular to $B_{||}$. Recent theoretical calculations[17,18] have shown that the preferred orientation of stripes is sensitive to numerous quantitative details. Nonetheless, the most realistic of such calculations[18] are in agreement with the experiment. These calculations also provide a useful estimate of the built-in symmetry breaking field: 10mK/electron is typical.

The data for $B_{||}$ along <1-10> (right-hand panels of Fig. 8) shows that the situation is not quite so simple. The above discussion leads to the prediction that if the stripes are already perpendicular to $B_{||}$, the in-plane field should have little effect. At ν=11/2 this is indeed the case: there is essentially no dependence of R_{xx} and R_{yy} on $B_{||}$. At ν=9/2, however, there is a substantial effect[19]. The resistances become roughly equal as the in-plane field increases. This is a particularly puzzling result, especially since ν=9/2 and 11/2 are in the *same* N=2 orbital LL. Similar dependences on the spin sub-level are seen in essentially every aspect of these new anisotropic correlated phases in high Landau levels. We remind the reader, however, that breakdowns of particle-hole symmetry are seen in the lowest and first excited LLs as well.

VII. The N=1 Landau Level

The even-denominator fractional quantum Hall state at ν=5/2 in the N=1 LL has been one of the enduring mysteries of the 2D electron field. Early tilted field studies[20] showing the collapse of the 5/2 state were widely interpreted as indicating the existence substantial spin reversal in the ground state, but that conclusion has been brought into question, especially by recent numerical studies[21]. The early tilt experiments, however, missed an important point. In addition to suppressing the 5/2 (and 7/2) FQHE state, the tilting leaves the transport in the N=1 LL highly anisotropic. Figure 9 shows data at zero and large tilt angle demonstrating both of these effects. For the data shown,

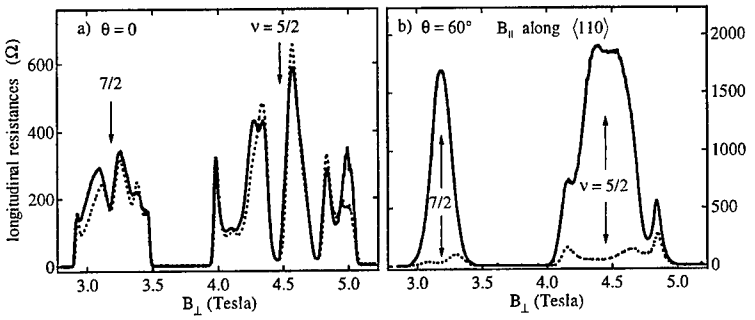

Fig. 9. Effect of an in-plane magnetic field on R_{xx} (dotted) and R_{yy} (solid) in the N=1 LL. In addition to destroying the ν=5/2 and 7/2 FQHE states, the in-plane field leaves the transport highly anisotropic.

$B_{\|}$ is along <110>, but very similar results are found for $B_{\|}$ along <1-10>. As in the case of the N≥2 Landau levels, at large tilt angle higher resistance is found for transport along the direction of the in-plane magnetic field[22].

These results do not explain the mechanism for the destruction of the 5/2 FQHE state itself. However, they do suggest that the 5/2 state is close in energy to an anisotropic correlated phase similar to those found at half filling of the higher Landau levels. This is an interesting finding since one might have expected the 5/2 FQHE state to be replaced, at large tilt angle, by a composite fermion liquid phase like that observed at ν=1/2 in the N=0 lowest Landau level. These qualitative ideas have found support in recent numerical calculations.[23]

VIII. Summary and Outlook

The recent transport experiments on ultra-clean 2D electron systems at high Landau level filling have yielded a number of fascinating discoveries. Highly anisotropic correlated electron phases near half filling and intriguing new insulators in the wings of the Landau levels have been found. These new phenomena appear in several adjacent Landau levels, provided N≥2. This suggests a generic mechanism and heightens the overall significance of the results. The absence of the fractional quantum Hall effect (so far, at least) in these same Landau levels is also remarkable. In the N=1 Landau level new tilted field experiments show that the 2D electron system is somehow at a boundary between fractional quantum physics and the new, possibly striped, world of high Landau levels.

Obviously, much remains to be done. The bulk transport measurements discussed here offer no direct way to determine whether a charge density modulation on the scale of 1000Å exists or not. Other techniques are needed to probe the system on this length scale. Surface acoustic waves and inelastic light scattering are obvious candidates. Application of scanned probes, though still in the dark ages from the standpoint of QHE physics, offers another multi-year funding opportunity. What is clear at this point is that a new class of 2D electron correlated states has been uncovered. Rumors of the death of the 2D electron field have, once again, been exaggerated.

REFERENCES

1. For a review of the field, see *Perspectives in Quantum Hall Effects*, edited by S. Das Sarma and A. Pinczuk, John Wiley, 1996.
2. H. Fukuyama, P.M. Platzman, and P.W. Anderson, Phys. Rev. B**19**, 5211 (1979)
3. R.L. Willett, *et al.*, Phys. Rev. Lett. **59**, 1776 (1987).
4. There are, of course, even denominator FQHE states in *double layer* 2D systems.
5. R.L. Willett and J.P. Eisenstein, 1988, unpublished; H.L. Stormer, *et al.* Bull. Am. Phys. Soc. **38**, 235 (1993).
6. M.P. Lilly, *et al.*, Phys. Rev. Lett. **82**, 394 (1999).
7. M.P. Lilly, *et al.*, cond-mat/9903196, accepted for publication in Phys. Rev. Lett.
8. R.R. Du, *et al.*, Solid State Commun. **109**, 389 (1999).
9. W. Pan, *et. al.*, cond-mat/9903160.
10. M. Shayegan and H.C. Manoharan, cond-mat/9903405.
11. M.P. Lilly, *et al.*, cond-mat/9903153
12. A.A. Koulakov, M.M Fogler, and B.I. Shklovskii, Phys. Rev. Lett. **76**, 499 (1996) and Phys. Rev. B**54**, 1853 (1996); M.M. Fogler and A.A. Koulakov, Phys. Rev. B**55**, 9326 (1997).
13. R. Moessner and J. Chalker, Phys. Rev. B**54**, 5006 (1996).
14. E. Fradkin and S. Kivelson, Phys. Rev. B**59**, 8065 (1999).
15. H. Fertig, Phys. Rev. Lett. **82**, 3693 (1999).
16. E.H. Rezayi, F.D.M. Haldane, and K.Yang, cond-mat/9903258.
17. T. Stanescu, I. Martin and P. Philips, cond-mat/9905116.
18. T. Jungwirth, A.H. MacDonald, L. Smrcka, and S.M. Girvin, cond-mat/9905353.
19. The data in Fig. 8 show that the R_{xx} and R_{yy} actually cross briefly at $\nu=9/2$ when $B_{\|}$ is along <1-10>. At the highest $B_{\|}$ they appear to be about to re-cross. Pan, *et al.*[9] did not observe this crossing but found instead that the resistance at first became very nearly equal and then at very large $B_{\|}$ separated again. We believe there is no significance to this minor difference in the two findings.
20. J.P. Eisenstein, *et al.*, Phys. Rev. Lett. **61**, 997 (1988).
21. R. Morf, Phys. Rev. Lett. **80**, 1505 (1998); E.H. Rezayi and F.D.M. Haldane, unpublished.
22. Similar findings are reported in Ref. 9.
23. F.D.M. Haldane and E.H. Rezayi, unpublished.

Strongly Anisotropic Electronic Transport in Higher Landau Levels

R. R. Du [a,b], W. Pan[a, c], H. L. Stormer [d,e], D. C. Tsui [a],
L. N. Pfeiffer [d], K. W. Baldwin [d], and K. W. West [d]

a) Princeton University, Princeton, NJ
b) University of Utah, Salt Lake City, UT
c) NHMFL, Tallahassee, FL
d) Bell Labs, Lucent Technologies, Murray Hill, NJ
e) Columbia University, New York, NY

Abstract

Low-temperature, electronic transport in higher Landau levels (N>1) in a two-dimensional electron system is strongly anisotropic. At half-filling of either spin level of such Landau levels (ν=9/2, 11/2, 13/2, 15/2, ...) the magnetoresistance either collapses to form a deep minimum or is peaked in a sharp maximum, depending on the in-plane current direction. The anisotropic axis can be *reoriented* by applying an in-plane magnetic field of ~ 1 -2 T strength. The magnetoresistance at ν =5/2 and ν = 7/2 (N=1) is initially isotropic but an in-plane field *induces* a strong anisotropy. Our observations are strong evidence for a new many-electron phase in higher Landau levels, which forms spontaneously or can be induced by an in-plane field.

1. Introduction

Two-dimensional electron systems (2DES) in high magnetic field exhibit a multitude of novel electronic phases [1]. The electronic states of the fractional quantum Hall effect (FQHE) are the most abundant and probably also the best known. Most of the transport studies have been performed on the lowest Landau level, N=0. Magnetotransport on higher Landau levels had been limited to the still enigmatic even-denominator FQHE state at filling factor ν=5/2 and features in its immediate vicinity in the N=1 Landau level [2, 3]. Only recently have experiments on N>1 Landau levels been reported [4-7], indicating novel electronic phases.

We report magnetotransport measurements [5,6] in higher Landau levels (filling factor $\nu > 2$, *i.e.*, N >1) from high-mobility 2DES in modulation-doped GaAs/AlGaAs heterostructures. Electronic transport in higher Landau levels, $\nu > 4$, differs remarkably from the usual electronic transport in Landau levels $\nu \leq 4$. Low-temperature (T < 100 mK) electronic transport at half-filling of either spin level $\nu > 4$ (ν=9/2, 11/2, 13/2, 15/2, ...) is strongly anisotropy. At these half-fillings the magnetoresistance either collapses to form a deep minimum or is peaked in a sharp maximum, depending on the in-plane current direction. Such anisotropies are absent in the $\nu < 4$ Landau level, which are dominated by the states of the FQHE. In the vicinity of quarter-fillings in the $\nu > 4$ levels satellite minima (not unlike those from the FQHE), which do not show such anisotropy, are observed. However, these satellite minima forgo FQHE plateau formation in the Hall resistance, approaching instead integer values for their concomitant plateaus.

The transport anisotropies may be indicative of a new many-electron state, which forms exclusively in higher Landau levels [8-10]. While the origin of these states remains unclear, they are believed to arise from the formation of a striped electronic phase or an electronic phase akin to a liquid crystal phase. The satellite minima, and their associated integer Hall plateaus may be manifestations of novel phase not unlike a charge density wave.

We have further investigated the influence of an in-plane magnetic field on these states under tilted magnetic field. In the electrically anisotropic phase at ν=9/2 and 11/2 an in-plane magnetic field of ~ 1-2 T overcomes its initial pinning to the crystal lattice and *reorients* this phase. In the initially isotropic phase at ν=5/2 and 7/2 an in-plane magnetic field *induces* a strong anisotropy. In

all cases, for high in-plane fields, the high resistance axis is parallel to the direction of the in-plane field.

2. Experiment

The magnetotransport coefficients were measured in a square specimen cleaved along the *[110]* and *[$\bar{1}$10]* directions from a MBE wafer. Eight indium contacts were diffused symmetrically around the edges of the sample, permitting the measurements of the R_{xx} and the R_{yy} from the same specimen. The only difference between the two cases (R_{xx} and R_{yy}) is the configuration of the current and voltage probes, which have been rotated by 90^0 (see schematics in Fig. 1). Experiments were performed in a dilution refrigerator immersed into a superconducting solenoid.

In tilted field experiments the sample is placed on a precision rotator inside the mixing chamber of the dilution refrigerator. The sample can be rotated *in-situ* around an axis perpendicular to the field. An in-plane magnetic field, $B_{ip} = B \times sin\theta$, is introduced when the magnetic field, B, is tilted away (tilt angle θ) from the sample normal. As usual, the perpendicular field is determined by $B_{perp} = B \times cos\theta$.

3. Results and discussion

The data for $\theta = 0^o$ were measured from a sample having an electron density of $n = 2.3 \times 10^{11}/cm^2$ and a mobility of $\mu = 1.2 \times 10^7 cm^2/Vs$. Fig. 1 shows R_{xx} and R_{yy} traces recorded at T = 60 mK between Landau level filling factor ν = 2 and ν = 12, *i.e.*, for N=1 through 6. In the N=1 Landau level (between ν=2 and 4) the previously observed characteristic features of the FQHE are well developed. In particular, sharp minima of the even-denominator FQHE states at ν=5/2 and ν=7/2 are clearly visible, in both traces.

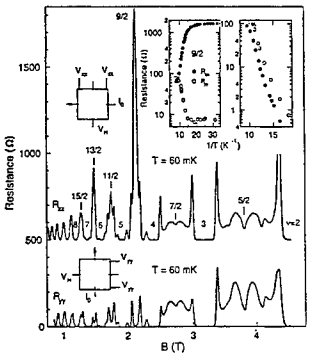

Fig.1. Magnetoresistance along two perpendicular in-plane directions of a two-dimensional electron system at 60mK. Insert: (Left) Temperature dependence of the 9/2 resistance maximum and 9/2 resistance minimum at ν=9/2 versus inverse temperature. (Right) Temperature dependence of the magnetoresistance minimum around ν ~4+1/4 for both R_{xx} and R_{yy}.

The most striking discrepancy between the N>1 and N = 1 data lies in their extraordinary dependence on the in-plane current direction. While the N = 1 FQHE features are essentially independent of the in-plane current direction, the *minima* at half-filling in N >1 Landau levels turn into a set of sharp *peaks* when the current is being rotated by 90^0. In particular the spikes at ν=9/2 exceeds all other features of the spectrum by almost a factor of two. The data in R_{xx} seem to be a superposition of R_{yy} and the sharp spikes at half-fillings. We have observed the anisotropy

seen for N > 1 in several other samples of electron densities 1.1 to 2.9 x 10^{11}/cm^2 and mobilities 6.8 to 12.8 x 10^6 cm^2/Vs.

Beyond the strong minima at half-filling, additional satellite minima are visible in the N=2 Landau level. Their positions do not seem to follow the sequence observed in the N = 1 level. It is difficult to associate these structures with a particular rational filling factor, but they are located in the vicinity of 1/4 and 3/4 filling. Comparison between the R_{xx} and the R_{yy} traces indicates that transport at these minima is isotropic.

The temperatures dependence of the ν=9/2 resistance is shown in the insert (left panel) in FIG. 1. Resistance is essentially isotropic above T = 100 mK but bifurcates into a rapid rise and rapid drop, depending on the in-plane current direction. In the range between T ~ 100 mK and T ~ 60 mK, the behavior of both the R_{xx} and the R_{yy} can be described by an exponential $R \propto exp(\pm E/kT)$, with an energy scale of E ~ 0.55K.

The temperature dependence of the satellite minima is not unlike that of the FQHE. The right panel quantifies the temperature dependence of one of the satellite minima (close to 1/4 filling) in a standard Arrhenius plot for both R_{xx} and R_{yy}. Both show the same exponential *drop* in resistance with an activation energy of $\Delta = 1.7 \pm 0.2K$, where $R \propto exp(-\Delta/2kT)$. However, its associated Hall resistance, R_H, is unusual [5]. The concomitant R_H value converges towards the nearest *integer* (*i.e.*, $i = 4$), rather than the usual fractional, quantum Hall plateau.

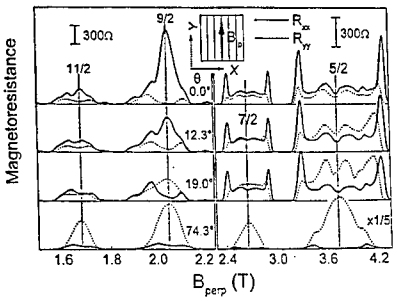

Fig. 2. Dependence of the magnetoresistance R_{xx} and R_{yy} around filling factor 9/2 and 11/2 as well as around 5/2 and 7/2 on angle, θ, in a tlted field where an in-plane field is pointing the easy direction. Temperature T ~ 40 mK.

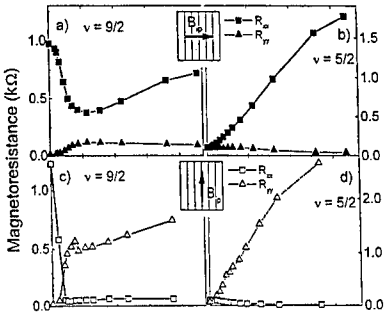

Fig. 3. Amplitudes of R_{xx} and R_{yy} at ν =9/2 and ν = 5/2 as a function of in-plane magnetic field B_{ip}.

The tilted field experiments were performed using a similar specimen, having a yet higher mobility of $\mu = 1.7 \times 10^7 cm^2/Vs$. The sample was mounted in two different configurations onto the rotator, either placing the B_{ip} along the x -axis ("hard direction"), or along the y -axis ("easy direction").

As an example, Fig. 3 shows R_{xx} and R_{yy} data taken for B_{ip} along the *easy* direction, y, of the anisotropic state. The inserts depicts the geometry. With an increasing B_{ip}, R_{xx} collapses and develops into a minimum, while R_{yy} rises and becomes a maximum at the highest tilt, $\theta = 74.3^o$. This can be viewed as if the anisotropic axis has been rotated by 90^0.

For ν=5/2 and 7/2, in the absence of tilt, the data show practically no anisotropy. However, tilting of the sample and the associated increase of B_{ip} drastically alters the data and introduces a strong anisotropy between R_{xx} and R_{yy}. As shown in Fig. 3, as B_{ip} increases along the *easy* direction, R_{xx} decreases, while R_{yy} increases.

In the situation where the B_{ip} is along the *hard* direction, the in-plane field *preserves* the 9/2 and 11/2 anisotropies while the 5/2 and 7/2 develop anisotropies in a similar fashion as the previous case. Fig. 4 summarizes the anisotropies for the strongest of states at ν=9/2 and ν=5/2 for both B_{ip} directions. In all cases, for high in-plane fields, the high resistance axis is parallel to the direction of the in-plane field.

In summary, electronic transport in the higher Landau levels, N>1, differs in several ways from the usual electronic transport in Landau levels N≤1. Whereas in the lowest Landau levels the standard features of the FQHE dominate, transport around half-filling in N>1 Landau levels is extremely anisotropic, developing large maxima or deep minima depending on the in-plane current direction. Satellite minima in the vicinity of quarter-filling do not show this anisotropy, but the concomitant Hall resistance converges to nearest integer Hall plateau.

The nature of the state at $\nu = 5/2$ is believed to be quite distinct from the state at $\nu = 9/2$. For one, the former is a true FQHE state [1-3] with plateau formation in R_H, whereas such a plateau seems to be absent for the latter. And secondly, dramatic anisotropies in electronic transport in purely perpendicular magnetic field have only been observed for the states at $\nu = 9/2$ and equivalent, whereas they are absent in the $\nu = 5/2$ state. It is remarkable that anisotropies not unlike those of the $\nu = 9/2$ state can be induced in the $\nu = 5/2$ state at sufficiently high in-plane magnetic field. This result is being viewed as consistent with a phase transition from a quantum Hall liquid to a strongly anisotropic phase [11,12].

Acknowledgments

All transport experiments were performed at the Francis Bitter Magnet Lab in Cambridge, Massachusetts, and National High Magnetic Field Lab in Tallahassee, Florida. RRD, PW, and DCT are supported by AFOSR, NSF, and DOE.

References

[1] Perspectives in Quantum Hall Effects, edited by S. DasSarma and A. Pinczuk,Wiley and Sons, 1997.
[2] R. L. Willett, J. P. Eisenstein, H. L. Stormer, D. C. Tsui, A. C. Gossard, and J. H. English, Phys. Rev. Lett. **59**, 1776 (1987).
[3] J. P. Eisenstein, R. L. Willett, H. L. Stormer, D. C. Tsui, A. C. Gossard, and J. H. English, Phys. Rev. Lett. **66**, 997 (1988).
[4] M. P. Lilly, K. B. Cooper, J. P. Eisenstein, L. N. Pfeiffer, and K. W. West, Phys. Rev. Lett. **82**, 394 (1999).
[5] R. R. Du, D. C. Tsui, H. L. Stormer, L.N. Pfeiffer, K. W. Baldwin, and K. W. West, Solid State Commun. **109**, 389 (1999).
[6] W. Pan, R. R. Du, H. L. Stormer, D. C. Tsui, L.N. Pfeiffer, K. W. Baldwin, and K. W. West, preprint (cond-mat/9903160).
[7] M. P. Lilly, K. B. Cooper, J. P. Eisenstein, L. N. Pfeiffer, and K. W. West, preprint (cond-mat/9903196).
[8] A. A. Koulakov, M. M. Fogler, and B. I. Shklovskii, Phys. Rev. Lett. **76**, 499 (1996).
[9] R. Moessner and J. T. Chalker, Phys. Rev. **B54**, 5006 (1996).
[10] E. Fradkin and S. A. Kivelson, Phys. Rev. **B59**, 8065 (1999).
[11] T. Jungwirth, A. H. MacDonald, L. Smrcka, and S. M. Girvin, preprint (cond-mat/9905353).
[12] E. H. Rezayi and F. D. M. Haldane, preprint (cond-mat/9906137).

MA.3

Anisotropic Transport of Two-Dimensional Holes in High Landau Levels

M. Shayegan, H. C. Manoharan,[1], S. J. Papadakis, and E. P. De Poortere
Department of Electrical Engineering, Princeton University, Princeton, New Jersey 08544

Magnetoresistance data taken along [$\bar{2}33$] and [$01\bar{1}$] directions in a GaAs/AlGaAs two-dimensional hole sample with van der Pauw geometry exhibit significant anisotropy at half-integer filling factors. The anisotropy appears to depend on both the density and symmetry of the hole charge distribution.

Keywords: Quantum Hall Effect, Anisotropy

PACS: 73.20.Dx, 73.40.Kp, 73.50.Jt

A remarkable magnetotransport anisotropy at half-integer fillings was recently reported in high-mobility GaAs/AlGaAs two-dimensional electron systems (2DESs) [2,3]. In particular, at half fillings in the third and higher Landau levels ($\nu \geq \frac{9}{2}$), the in-plane longitudinal magnetoresistance (R_{xx}) in one direction was observed to be much larger than in the perpendicular direction. We present here qualitatively similar anomalies in a high-mobility GaAs/AlGaAs 2D *hole* system (2DHS). The 2DHS data, however, provide an intriguing twist to this problem as they exhibit the anomaly at fillings as small as $\nu = \frac{5}{2}$.

Figure 1 highlights our data which were taken with the magnetic field B perpendicular to the 2DHS. The sample is a GaAs quantum well flanked by AlGaAs barriers, grown on a GaAs (311)A substrate, and modulation-doped with Si. The van der Pauw geometry of the sample and the measurement configurations are shown as insets to the main figure. The anisotropy of R_{xx} at half filling $\nu = \frac{5}{2}$ is most pronounced: the resistance along the [$01\bar{1}$] direction (solid trace) exhibits a *maximum* which is about 15 times larger than the resistance *minimum* observed along [$\bar{2}33$] (dashed trace). Note in Fig. 1 that, as B decreases, the strength of the anisotropy diminishes in an alternating fashion: larger anisotropies are observed at $\nu = \frac{5}{2}$, $\frac{9}{2}$, and $\frac{13}{2}$ compared to $\frac{7}{2}$, $\frac{11}{2}$, and $\frac{15}{2}$. This is similar to the case of 2DESs [2,3].

In Fig. 1, the transport anisotropy persists down to $B = 0$, implying a higher mobility (by a factor of about two) along [$\bar{2}33$] compared to [$01\bar{1}$]. This is typical of 2DHSs grown on GaAs (311)A substrates [4]. The origin of this mobility anisotropy can be traced to corrugations, aligned along [$\bar{2}33$], which are present at the GaAs/AlGaAs (311)A interface [5]. Such interface morphology anisotropy, however, cannot by itself explain the much larger *and* alternating transport anisotropy observed at high B.

Both Refs. [2] and [3] suggest that the anisotropy observed at half fillings is intrinsic to very high mobility 2DESs and may signal the formation of a new, correlated, striped phase of the 2D electrons. They also conclude that, in the absence of a parallel B, such a state forms exclusively in the higher Landau levels (LLs), namely $N = 2$ and higher, since they observe the transport anisotropy only at half-fillings $\nu \geq \frac{9}{2}$. If so, why does the 2DHS exhibit the anisotropy at ν as small as $\frac{5}{2}$? The origin of this difference is not obvious. We propose here three possibilities: (i) The (311)A interface corrugations may help stabilize the anisotropic state in 2DHSs. (ii) It may be related to the nonlinear LL fan diagram for 2D holes and, in particular to the mixing and crossings of the spin-split LLs [6]. The exact sequence and spin-character of the 2DHS LLs, however, depend on the 2D density as well as the shape and symmetry of the confinement potential and the hole wavefunction, so that a quantitative assesment of this hypothesis requires further work. (iii) The larger effective mass of GaAs holes renders the 2DHS effectively more dilute [7]. At a given filling, such diluteness favors crystalline states of the 2D system over the fractional quantum Hall (FQH) liquid states [7,8]. It is therefore possible that a striped phase is favored in the 2DHS at $\nu = \frac{5}{2}$ while in the 2DESs the ground state is a FQH liquid. Such a scenario is consistent with the very recent data in 2DESs [9,10] which reveal that applying an in-plane B-field destroys the $\nu = \frac{5}{2}$ FQH state and stabilizes an anisotropic state.

Figure 2 illustrates the evolution with density of R_{xx} for the 2DHS of Fig. 1. The density obtained by cooling the sample in the dark, $p_0 = 2.17 \times 10^{11}$ cm^{-2} was lowered via successive illumination at low temperature by a red light-emitting diode. At all densities the transport is highly anisotropic at half-integer fillings. At the highest density however, R_{xx} along [$01\bar{1}$] exhibits a clear minimum along $\nu = \frac{5}{2}$. The minimum is accompanied by a weak feature in the Hall resistance [11], suggestive of a developing FQH state. As the density is lowered, this minimum vanishes and is replaced by a maximum. This evolution with decreasing density has some resemblance to the 2DES data where increasing the in-plane B leads to the destruction of the $\nu = \frac{5}{2}$ FQH state [9,10]. It is also consistent with the above interpretation (iii) that diluteness (lower density) favors the anisotropic state over the FQH state.

Finally, in Fig. 3 we show data taken on an L-shaped Hall bar sample from a different wafer [12]. The two arms of the Hall bar are aligned along the [$\bar{2}33$] and [$01\bar{1}$] directions, and the sample has front and back gates which are used to tune the symmetry of the hole wavefunction while keeping the density fixed [13]. The data overall exhibit much less

transport anisotropy, confirming that the van der Pauw geometry exagerates anisotropy because of the non-uniform current distribution [14]. Moreover, only the data of Fig 3b, taken with an asymmetric charge distribution, show significant anisotropy at half-integer fillings for $\nu \geq \frac{9}{2}$; note also that the magnitude of the anisotropy alternates with decreasing B. The data for the symmetric charge distribution (Fig. 3a), on the other hand, exhibit a smaller size anisotropy which appears to be monotonic with B. While we do not understand the origin of these differences, we mention that the LL fan diagrams for the two charge distributions are likely to be different and also the 2DHS becomes more sensitive to interface corrugations when the charge distribution is made asymmetric.

This work was supported by the National Science Foundation.

[1] Current address: IBM Research Division, Almaden Research Center, 650 Harry Road, San Jose, CA 95120.

[2] M. P. Lilly *et al.*, Phys. Rev. Lett. **82**, 394 (1999).
[3] R. R. Du *et al.*, Solid State Commun. **109**, 389 (1999).
[4] J. J. Heremans, M. B. Santos, K. Hirakawa, and M. Shayegan, J. Appl. Phys. **76**, 1980 (1994).
[5] M. Wassermeier *et al.*, Phys. Rev. B **51**, 14721 (1995).
[6] See, *e.g.*, U. Ekenberg and M. Altarelli, Phys. Rev. B **32**, 3712 (1985).
[7] M. B. Santos *et al.*, Phys. Rev. Lett. **68**, 1188 (1992).
[8] For a review, see M. Shayegan in "Perspectives in QHEs", edited by A. Pinczuk and S. Das Sarma (Wiley, New York, 1997, p.).
[9] W. Pan *et al.*, cond-mat/9903160.
[10] M. P. Lilly *et al.*, cond-mat/9903196.
[11] H. C. Manoharan and M. Shayegan, Phys. Rev. B **50**, 17662 (1994).
[12] Data taken at $p = 2.3 \times 10^{11}$ cm^{-2} in a Hall bar sample fabricated from the same wafer as in the sample of Figs. 1 and 2 also show very little anisotropy.
[13] S. J. Papadakis *et al.*, Science **283**, 2056 (1999).
[14] S. H. Simon, cond-mat/9903086.

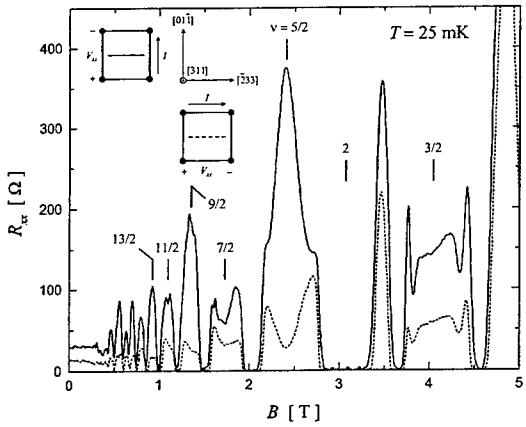

FIG. 1. Longitudinal magnetoresistance of a 2DHS measured along perpendicular directions (see insets for van der Pauw measurement geometry). The sample is cooled to 25 mK and has an areal hole density of 1.5×10^{11} cm^{-2}.

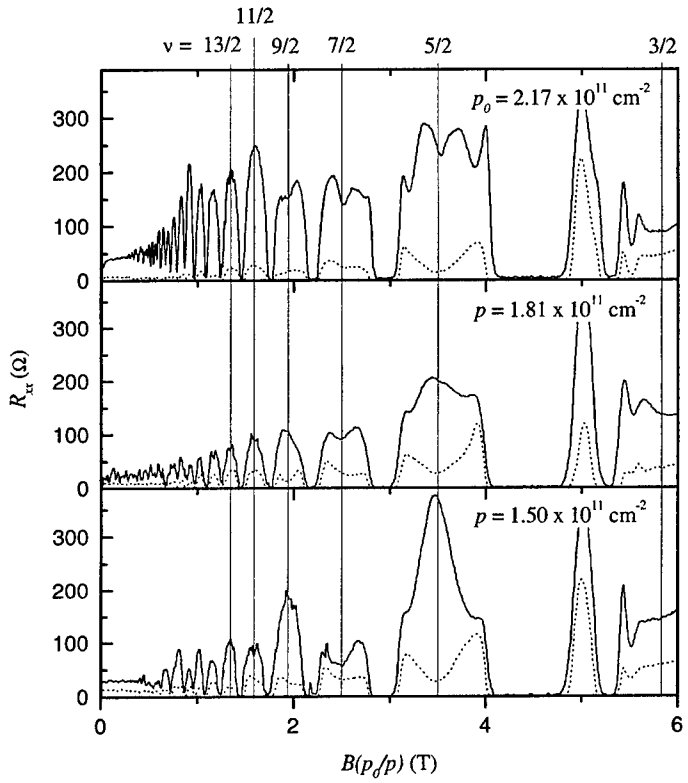

FIG. 2. Evolution with denisty of R_{xx} in the 2DHS of Fig. 1.

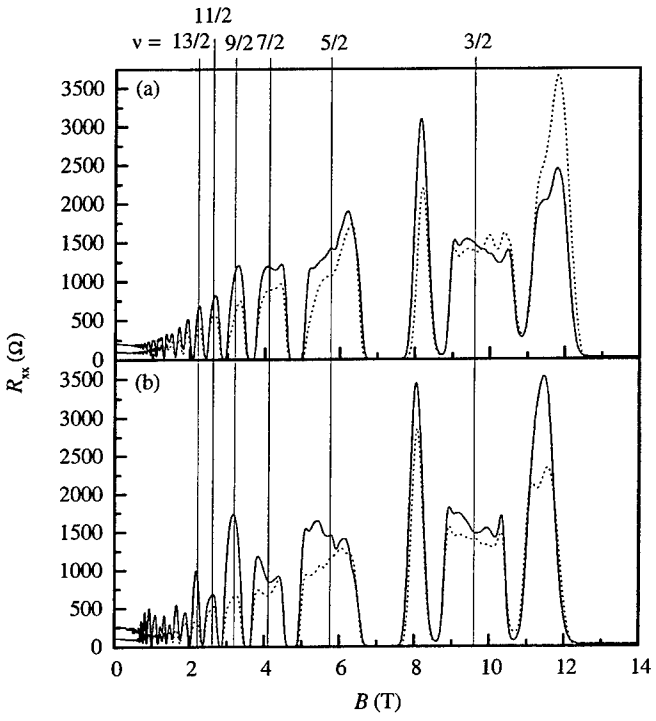

FIG. 3. R_{xx} for a 2DHS sample with an L-shaped Hall bar revealing much less anisotropy than the van der Pauw sample of Figs. 1 and 2. The density of the sample is fixed at 3.3×10^{11} cm^{-2} while the confinement potential for the holes is varied: in (a) the potential is symmetric but in (b) it is made asymmetric by applying a perpendicular electric field of about 6000 V/cm.

In-plane Magnetic Field Induced Anisotropy and Orientation Energy of Stripe Phases at Half-Filled High Landau Levels

T. Jungwirth[1,2], A. H. MacDonald[1], L. Smrčka[2], and S. M. Girvin[1]

[1] Department of Physics, Indiana University, Bloomington, Indiana 47405
[2]Institute of Physics ASCR, Cukrovarnická 10, 162 00 Praha 6, Czech Republic

Abstract

We report on detailed Hartree-Fock calculations of the unidirectional charge density wave orientation energy induced by a tilted magnetic field. We find that for current experimental samples stripes are oriented perpendicular to the in-plane field, consistent with experiment. For wider two-dimensional electron systems we predict tilt-induced stripe states with variable anisotropy energy sign.

Recently several groups have reported [1]-[4] the observation of strong anisotropies in the longitudinal resistivity of a 2D electron system with valence Landau level (LL) index $N \geq 2$. Although the origin of these anomalies has not been firmly established, the anisotropy is probably associated with the unidirectional charge density wave (UCDW) states which have been predicted to occur under precisely these circumstances [5]. In this paper we evaluate the UCDW state's energy for the magnetic field tilted away from the 2D electron system normal. Theoretical studies along similar lines have recently been carried out by two other groups [6]. Using a realistic model for the sample of Lilly *et al.* (a single GaAs/Al_xGa_{1-x}As heterojunction with density $N_e = 2.67 \times 10^{11}$ cm^{-2}) we quantitatively determine the anisotropy energy as a function of field-tilt angle and LL filling factor. To explore the dependence of UCDW anisotropy energy on system geometry we have repeated these calculations for a parabolic confinement quantum well models with variable subband separation.

In our calculation we choose the in-plane component $B_\parallel$ of the magnetic field to be in the $\hat{x}$-direction and use the following Landau gauge for the vector potential, $\vec{A} = (0, B_\perp x - B_\parallel z, 0)$. The one-particle orbitals for any z-dependent single-particle confining potential can then be written as

$$< \vec{r}|k, i, \sigma >= \frac{e^{iky}}{\sqrt{L_y}} \varphi_{i,\sigma}(x - \ell^2 k, z) \, , \tag{1}$$

where k is the wave vector which labels states within LL i, σ is the spin index, and $\ell^2 = \hbar c/eB_\perp$. The translational symmetry responsible for LL degeneracy leads to a 2D wavefunction $\varphi_{i,\sigma}(x, z)$ which is independent of the state label k, except for the rigid shift by $\ell^2 k$ along x-axis. This in turn leads to two-particle matrix elements of the Coulomb interactions with a dependence on state labels which is identical to that for the lowest LL of a zero-thickness 2D electron system provided the 2D Coulomb interaction is replaced by the following effective interaction:

$$V(\vec{q}) = \frac{4\pi e^2}{\epsilon_0} e^{q^2\ell^2/2} \int_{-\infty}^{\infty} \frac{dq_z}{2\pi} \frac{|M_\sigma^{i,i}(\vec{q})|^2}{q^2 + q_z^2} \tag{2}$$

where $\vec{q} = (q_x, q_y)$, ϵ_0 is the semiconductor dielectric function and

$$M_\sigma^{i,i}(\vec{q}) = \int_{-\infty}^{\infty} dx \int_{-\infty}^{\infty} dz e^{iq_x x} e^{iq_z z} \varphi_{i,\sigma}(x + \ell^2 q_y/2, z) \varphi_{i,\sigma}(x - \ell^2 q_y/2, z) \, . \tag{3}$$

Since the stripe states are found at relatively weak magnetic fields, the valence LL will not be widely separated from remote LL's. We include remote LL degrees of freedom in our calculation by modifying the dielectric function, using the RPA approximation [7]. The wavefunctions and single-particle eigenvalues used to define the effective interactions were obtained from local-spin-density self-consistent-field calculations which include the solution of the two-dimensional single-particle Schrödinger equation that arises at tilted magnetic fields. The effective interactions are anisotropic because $B_\parallel$ mixes the cyclotron and electric subband levels.

The energy per electron of the UCDW state at fractional filling ν^* of the valence LL is given by [8]

$$E = \frac{1}{2\nu^*} \sum_{n=-\infty}^{\infty} \Delta_n^2 U\left(\frac{2\pi n}{a}\hat{e}\right) \, , \quad \Delta_n = \nu^* \frac{\sin(n\nu^*\pi)}{n\nu^*\pi} \, , \tag{4}$$

where a is the period of the UCDW state and $\hat{e}$ is the direction of charge variation. In HF theory, the UCDW state energy depends only on a and $\hat{e}$ and the optimal UCDW is obtained by minimizing Eq.(4) with respect these parameters. In Eq.(4), $U(\vec{q})$ can be separated into direct, $H(\vec{q})$, and exchange, $X(\vec{q})$, contributions with

$$H(\vec{q}) = \frac{1}{2\pi\ell^2} e^{-q^2\ell^2/2} V(\vec{q}) \, , \quad X(\vec{q}) = -\int \frac{d^2p}{(2\pi)^2} e^{-p^2\ell^2/2} e^{i(p_x q_y - p_y q_x)\ell^2} V(\vec{p}) \, . \tag{5}$$

We now turn to evaluation for the anisotropy energy at filling factors ν=5/2, 9/2, and 13/2 in the sample of Lilly *et al.* [1]. The self-consistent-field separation between lowest spin-up electrical subbands is 9.8 meV so that the valence LL's at perpendicular field for these filling factors are the spin-up N=1, 2, and 3 LL's of the first electrical subband, respectively. The in-plane magnetic field has only a weak effect on the LL spacing even at field-tilt angles as high as $\theta = 60^o$. We represent the effective interaction anisotropy by performing a Fourier expansion in the angle ϕ between $\hat{e}$ and the in-plane field:

$$H(q,\phi) = \sum_n H_{2n}(q)\cos(2n\phi) \, , \quad X(q,\phi) = \sum_n X_{2n}(q)\cos(2n\phi) \, , \tag{6}$$

where

$$X_{2n}(q) = -\int_0^\infty dp \, p H_{2n}(p) J_{2n}(pq) \tag{7}$$

and $J_m(x)$ is the Bessel function. Even at large $B_\parallel$ the anisotropy of the effective interaction is relatively weak and is accurately proportional to $\cos(2\phi)$. This property of $H(\vec{q})$ is shared by $U(\vec{q})$ and greatly simplifies the UCDW energy (4) minimization procedure. For a given a the extrema of E lies either at $\phi = 0$ or at $\phi = \pi/2$. We define the anisotropy energy per electron E_A as the minimum of $E(\phi = \pi/2)$ minus the minimum of $E(\phi = 0)$.

Details of the anisotropy energy calculation are summarized in Table II. We first discuss the results obtained when RPA screening is neglected. Most qualitative features are already captured in a simple theory which retains only the $n = 1$ leading harmonic in the UCDW

	NO SCREENING			SCREENING			
θ	$E^H_{A,0}$	$E^X_{A,0}$	E_A	$E^H_{A,0}$	$E^X_{A,0}$	E_A	a^*/ℓ
			$\nu = 5/2$				
20°	-32.79	36.16	1.16	-17.65	28.94	2.80	5.15
40°	-45.70	78.73	8.85	-21.26	70.63	12.38	5.24
60°	-127.32	174.73	10.73	-75.64	164.19	21.25	5.15
			$\nu = 9/2$				
20°	-13.52	6.17	-1.40	-5.58	7.59	0.67	6.41
40°	-43.84	18.17	-4.44	-10.83	19.51	2.23	6.41
60°	-101.57	39.78	-9.59	-15.00	47.00	8.07	6.68
			$\nu = 13/2$				
20°	-3.76	0.06	-0.77	-0.81	0.91	0.04	7.66
40°	-18.49	2.75	-3.48	-1.93	6.20	0.87	7.66
60°	-70.55	6.33	-12.49	-2.54	16.03	2.68	7.85

Table 1: Field-tilt anisotropy energy components for Lilly's *et al.* sample. Energies are per electron and in units of $10^{-4}\ e^2/\epsilon_0\ell \sim k_B 10\text{mK}$.

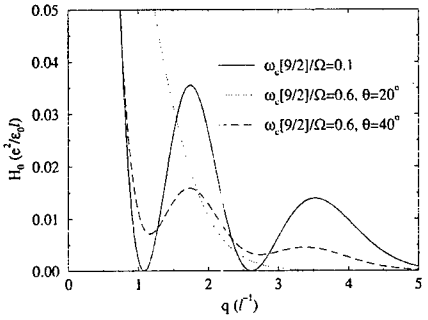

Fig. 2. Wavevector dependent Hartree energies for parabolic quantum well model and $\nu = 9/2$.

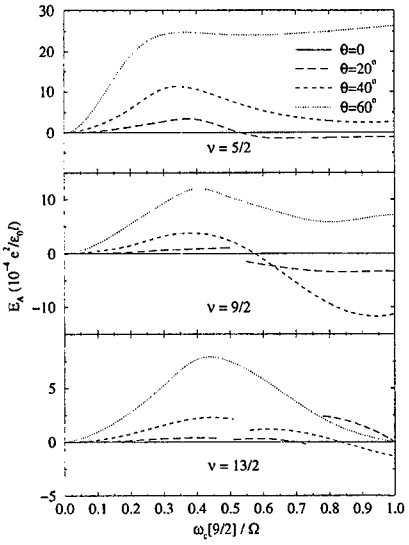

Fig. 1. Field-tilt anisotropy energy as a function of parabolic confining potential strength. Data for the valence LL close to degeneracy with another LL are not plotted as the theory fails to describe this circumstance.

energy expression and finds the optimal UCDW period a_0^* by minimizing $H_0(2\pi/a)+X_0(2\pi/a)$. The Hartree anisotropy energy $E^H_{A,0} = -2H_2(2\pi/a_0^*)$ is consistently negative (stripes along in-plane field) but is countered by the exchange energy $E^X_{A,0} = -2X_2(2\pi/a_0^*)$. For $\nu = 9/2$ and 13/2, the Hartree term dominates when screening is neglected but exchange dominates when screening is accounted for. Our finding that the stripes prefer to be aligned perpendicular to the $B_\parallel$ direction is consistent with the experimental finding [1, 3] that this is the easy transport direction. Including all harmonics in the UCDW energy expression and reoptimizing the lattice constant $a = a^*$, reduces numerical value of anisotropy energy but does not change its sign. We can use the values for E_A to estimate the temperature below which anisotropy will be observed in the transport properties of these systems. Current experimental samples have a native anisotropy which can be overcome by the application

of an in-plane field, reorienting the stripes and changing the easy transport direction. Since $\theta < 20^0$ can reorient the stripes for $N = 2$ and $N = 3$, we estimate from Table II that the native anisotropy energy is less than $10^{-4}(e^2/\epsilon_0\ell) \sim k_B 10\text{mK}$ per electron. We can also use E_A to estimate the temperature below which anisotropy will be observed in transport measurements. Based on an experimental onset temperature $T^* \sim 100\text{mK}$ with native anisotropy we estimate that $k_B T^* \sim 10E_A$. According to our calculations the largest anisotropies occur for $N = 1$ for which we predict an onset temperature exceeding 1K at large θ.

Finally, we discuss UCDW energy for parabolic quantum wells with different electric subband splittings $\hbar\Omega$. The results are summarized in Fig. 1; $B_\perp$ was chosen to correspond to the 2D density in the experiments of Lilly *et al.* [1], *i.e.* the cyclotron frequency at $\nu = 9/2$ is $\hbar\omega_c[9/2] = 4.24$ meV. For $\omega_c[9/2]/\Omega < 0.5$, only the lowest electrical subband is occupied at $\theta = 0$, the stripes orient perpendicular to $B_\parallel$, and the magnitude of E_A increases with θ and decreases with N. Lilly's *et al.* [1] and Pan's *et al.* [3] samples fall into this regime. In wider quantum wells the perpendicular field valence LL can belong to a higher electrical subband, and more complex behavior occurs. The solid curve in Fig. 2 shows H_0 for $\nu = 9/2$ and a narrow parabolic quantum well. It has a structure characteristic of the $N = 2$ LL effective interaction. (θ is not indicated as the field-tilt has a negligible effect on this $H_0(q)$ curve.) The dotted and dashed curves correspond to the case where the perpendicular field valence LL is the lowest LL of the second electrical subbands. For $\theta = 20^o$, $H_0(q)$ decreases monotonically with q, as for $\theta = 0$; the UCDW is not [5, 7] the likely ground state for the system in this circumstance. However, at $\theta = 40^o$, $H_0(q)$ is more akin the perpendicular field $N = 2$ LL effective interaction which favors the UCDW state. Our calculations indicate that both perpendicular and parallel orientations of the stripes with respect to $B_\parallel$ can be realized for these tilt-induced UCDW states. The competition between isotropic and anisotropic states, and the anisotropy energy of UCDW states, will both have a complicated dependence on ν and θ in this regime.

The authors acknowledge stimulating interactions with J. P. Eisenstein, M. Fogler, and R. Moessner. This work was supported by NSF grant DMR-9714055 by the Grant Agency of the Czech Republic under grant 202/98/0085.

References

[1] M. P. Lilly *et al.*, Phys. Rev. Lett. **82**, 394 (1999); M. P. Lilly *et al.*, preprint (cond-mat/9903196).

[2] R. R. Du *et al.*, Solid State Comm. **109**, 389 (1999).

[3] W. Pan et al., preprint (cond-mat/9903160).

[4] M. Shayegan and H. C. Manoharan, preprint (cond-mat/9903405).

[5] A. A. Koulakov *et al.*, Phys. Rev. Lett. **76**, 499 (1996); R. Moessner and J. T. Chalker, Phys. Rev. B **54**, 5006 (1996).

[6] T. Stanescu, I. Martin, and P. Phillips, preprint (cond-mat/9905116); M. Fogler, unpublished.

[7] T. Jungwirth *et al*, preprint (cond-mat/9905353).

[8] A. H. MacDonald, Phys. Rev. B **30**, 4392 (1984).

MA.5

A Phase Diagram for the Breakdown of the odd integer Quantum Hall Effect

L. B. Rigal, D. K. Maude, M. Potemski and J.C.Portal
Grenoble High Magnetic Field Laboratory, MPI-CNRS, 38042 Grenoble, France.

L. Eaves,
Department of Physics, University of Nottingham, Nottingham, NG7 2RG, U.K.

Z. R. Wasilewski,
Institute for Microstructural Sciences, NRC, Ottawa, Canada, K1A 0R6.

G. Hill, M.A.Pate
Dept. of Electronic and Electrical Engineering, University of Sheffield, S1 4DU, U.K.

A.I.Toropov
Institute of Semiconductor Physics, Novossibirsk 630090, Russia.

Abstract

The breakdown of the dissipationless conductance in the integer quantum Hall effect regime has been investigated for odd filling factors. The temperature dependence of the critical current and of the critical magnetic field at breakdown is presented and the scaling between filling factors discussed.

At integer filling factors and under quantum Hall conditions the resistance of a 2-dimensional electron gas (2-DEG) is vanishingly small. This 'dissipationless' conductance can be destroyed by either applying a sufficiently large current or changing the magnetic field so as to move away from integer filling factor. The so called breakdown of the integer quantum Hall effect (IQHE) has been extensively investigated [1-5] with emphasis on the sample width and magnetic field (filling factor) dependence of the critical current required to destroy the dissipationless conductance. While a number of models have been proposed [6-11] the exact mechanism for the breakdown remains controversial. What is clear, is that the breakdown is driven by the largest electric field present in the system, namely the electric field resulting from the Hall voltage $V_H = I\,h/ve^2$ for a current I at integer filling factor v. In addition, for the rather high critical currents typically observed, current flows through both edge states and the bulk of the sample [5,12].

We have previously shown [13] that for even filling factors it is possible to map out a phase diagram (critical current or critical magnetic field versus temperature) for the breakdown of the IQHE. The measured phase diagram bears a striking resemblance to the phase diagram for the coercive field in a superconductor. In addition, the phase diagrams for different filling factors are all related by a remarkably simple scaling law. The samples investigated all had a rather high electron density ($>7 \times 10^{11}$ cm^{-2}) which permitted to investigate a wide range of even filling factors (ν = 4-12) in the high magnetic field limit in which Landau level mixing can be neglected. It is important to have data for a large number of filling factors in order to determine unambiguously the scaling law. This is particularly true for the complex behaviour of the critical magnetic field whose temperature dependence resembles the phase diagram for a HTc superconductor. The relatively low mobility (≤ 10 $m^2V^{-1}s^{-1}$) prevented a systematic investigation of odd filling factors as only filling factors ν = 3,5 were in magnetic field range and dissipationless.

Here we present preliminary measurements on heterojunction sample which has filling factors ν = 1,3,5 dissipationless at low temperatures. The number of filling factors which are dissipationless is limited due to the critical collapse of spin splitting [14,15]. The scaling for odd filling factors is complicated by the many body nature of the spin gap which is in general dominated by the exchange energy [16,17]. Theoretically it is difficult to correctly predict the size of the gap or its evolution with filling factor. The phase diagram for odd filling factors turns out to be similar to that for even filling factors with a scaling law modified to take into account the many body nature of the spin gap [16,17]. However, due to the limited number of odd filling factors investigated (ν = 1,3,5) an unambiguous determination of the scaling law is not possible.

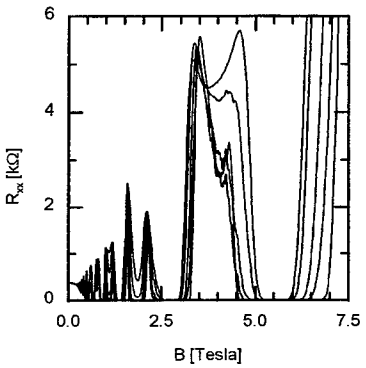

Fig 1. Typical magnetoresistance traces measured for temperatures 0.05-1.1 K.

For the measurements a 50 $m^2V^{-1}s^{-1}$ mobility heterojunction sample with a carrier density of 1.3×10^{11} cm^{-2} was processed into standard Hall bars with a width d = 250μm and with 750μm between voltage probes. The sample was mounted in the mixing chamber of a dilution refrigerator. Typical magnetoresistance traces measured for temperatures between 50mK and 1.1 K are shown in Fig.1. The phase diagrams for the breakdown are determined as described in reference [13]. The critical current I_c was determined by measuring four terminal I-V characteristics at each filling factor. I_c has been defined as the current for which the measured voltage between the voltage probes exceeds 50μV. The critical magnetic field B_c is defined as the half width of the dissipationless region. In order to determine the width of the dissipationless region we define a critical sample resistance $R_c \approx 5\Omega$ which is approximately 5% of the zero field resistance. We have verified that, although choosing different critical voltages or critical resistance changes the absolute value of I_c or B_c it does not in anyway modify the form of the temperature dependence or the scaling between different filling factors.

The temperature dependence of I_c is shown in Fig. 2(a) for filling factors ν = 1,3,5. For a given filling factor I_c has a constant value at low temperatures before decreasing rapidly and then vanishing at a critical temperature T_c. In contrast to the case for even filling factors it is not possible to fit this dependence with the phenomenological Gorter-Casimir [18] two fluid model for superconductivity. Instead a modified form with a T^4 power dependence is required to correctly fit the rapid decrease just below T_c.

$$I_c(T,\nu) = \left(\frac{I_{co}}{\sqrt{\nu}} - \frac{I_{co}}{\sqrt{\nu_o}}\right)\left(1 - \left(\frac{T}{T_{co}/\sqrt{\nu}}\right)^4\right) \qquad (1)$$

where I_{co} =49.2μA and ν_o = 5.1 are obtained from the straight line fit to $I_c(T \approx 0)$ versus $1/\sqrt{\nu}$ shown in Fig. 2(b). As for the even filling factors [13] the value of ν_o has the physical significance that filling factors larger than ν_o are not expected to be dissipationless at zero temperature. The scaling ($1/\sqrt{\nu}$) between different filling factors in Equation (1) has also been modified to take into account the many body nature of the spin gap. For even filling factors [13] the critical current and critical temperature scales as the cyclotron gap i.e $1/\nu$. Assuming that the spin gap is dominated by the exchange energy the spin gap should scale roughly as the Coulomb energy $e^2/\varepsilon\,\ell_B \propto 1/\sqrt{\nu}$ (here $\ell_B = \sqrt{\hbar/eB}$ is the magnetic length). The remaining parameter T_{co} = 1.43 K is found by fitting Eq. (1) to the temperature dependence of I_c for the

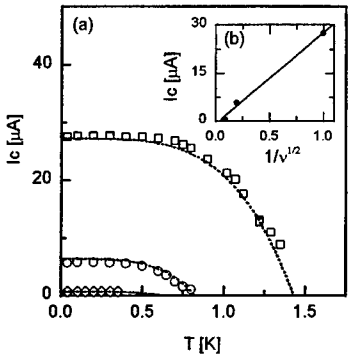

Fig. 2(a) Critical current I_c as a function of temperature for filling factors ν=1,3,5. The dotted lines are fits generated using Eq.(1) as described in the text. (b) $I_c(T \approx 0)$ versus $1/\sqrt{\nu}$, the solid line is a least squares fit to the data points.

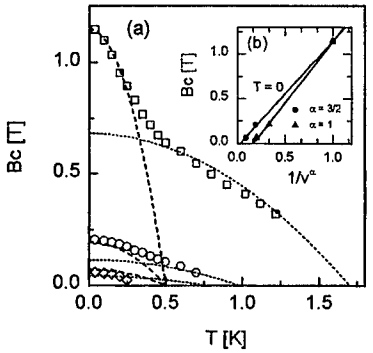

Fig 3(a). Critical magnetic field B_c as a function temperature. The dotted and dashed lines are fits generated using Eq.(2) and Eq.(3) as described in the text. (b) $B_c(T \approx 0)$ versus $1/\nu^{\alpha}$, the solid lines are a least squares fit to the data points plotted with $\alpha=3/2$ and $\alpha=1$.

filling factor ν =1. The temperature dependence of I_c can then be generated using Eq. (1) for the other filling factors with no adjustable parameters (dotted lines Fig.2(a)). The agreement between the data and the model for all filling factors is reasonably good. While it is possible to obtain a reasonable fit to $I_c(T \approx 0)$ assuming a $1/\nu$ dependence of the gap the critical temperature can only be fitted by assuming a $1/\sqrt{\nu}$ behaviour.

The reason for the T^4 dependence is less evident. In the QUILLS model [8] for the breakdown of the IQHE breakdown occurs when the Hall voltage is sufficiently large to energetically align states of the full and empty Landau levels in the vicinity of the Fermi energy over a spatial distance for which there is significant overlap of the wave-functions. Breakdown then occurs via quasi-inelastic scattering processes between Landau levels. The Hall voltage is proportional to the current and thus the critical current is expected to scale as the gap. We therefore suggest that the rapid decrease of I_c (T^4 dependence) is due to a collapse of the exchange enhanced spin gap with increasing temperature. While this interpretation is speculative, we stress that all samples studied show the same T^4 behaviour for the critical current at odd filling factors.

We now turn our attention to the temperature dependence of the width ($2B_c$) of the dissipationless regions in the magnetoresistance traces. The measurements (Fig. 1) were performed with a small current ≈10-100nA using low frequency (10.7Hz) phase sensitive detection. The temperature dependence of B_c for odd integer filling factors is shown in Fig. 3(a). The phase diagram is very similar to that for even filling factors [13]. Two phase are observed : a high temperature (HT) phase with a critical temperature which scales as $1/\sqrt{\nu}$ and a low temperature (LT) phase which by analogy with even filling factors is expected to have a T_c which is independent of filling factor. In contrast to the critical current the temperature dependence is well fitted by a conventional $(1-(T/T_c)^2)$ Gorter-Casimir phenomenological model (dotted and dashed lines in Fig. 3(a)).

B_c is a direct measure of the number of localised states ($n_{loc}=2\nu B_c/\Phi_o$) between spin Landau levels which should be independent of the gap in the high field limit in which spin Landau level mixing can be neglected. It is not possible to unambiguously determine the correct scaling of $B_c(T \approx 0)$ as can be seen in Fig 3(b) in which $1/\nu$ and $1/\nu^{3/2}$ dependence give equally good fits. $B_c(T \approx 0) \propto 1/\nu$ would imply that n_{loc}

was independent of filling factor (or gap). On the other hand $B_c(T \approx 0) \propto 1/\nu^{3/2}$ would imply that $n_{loc} \propto 1/\sqrt{\nu}$ scales as the gap which would imply a constant (energy independent) background of localised states. For even filling factors [13] $n_{loc} \propto 1/\nu$ can be interpreted as scaling as the cyclotron energy (ie a constant background of localised states) or as scaling with the number of Landau levels (i.e. the localised states at B=0 collapse onto ν Landau levels in a magnetic field). High field measurements on high density/high mobility samples in order to have access to a large number of dissipationless odd and even filling factors are required in order to determine unambiguously the correct scaling law. The dotted and dashed lines in Figure 3(a) are generated using

$$B_c(T,\nu) = \left(\frac{B_{co}^{HT}}{\nu^{\alpha}} - \frac{B_{co}^{HT}}{\nu_o^{\alpha}}\right)\left(1 - \left(\frac{T}{T_{co}^{HT}/\sqrt{\nu}}\right)^2\right) \tag{2}$$

and

$$B_c(T,\nu) = \left(\frac{B_{co}^{LT}}{\nu^{\alpha}} - \frac{B_{co}^{LT}}{\nu_o^{\alpha}}\right)\left(1 - \left(\frac{T}{T_{co}^{LT}}\right)^2\right) \tag{3}$$

for the HT and LT phases respectively with $\alpha=3/2$.although $\alpha=1$ would give an equally good fit but with slightly different parameters.

In conclusion, we have measured the phase diagram for the breakdown if the odd integer quantum Hall effect. Further work to determine unambiguously the scaling law is required. In particular for the critical magnetic field, we believe that the comparison of the scaling law for odd and even filling factors is worth pursuing since the different scaling of the energy gaps, should allow to extract information on the density of localised states between Landau levels.

1. G. Ebert, K. von Klitzing, K. Ploog and G. Weimann, J. Phys. C: Solid State Phys. **16**, 5441 (1983).
2. S. Kawaji, Semicond. Sci. Technol. **11**, 1546 (1996) and references therein.
3. M. E. Cage, R. F. Dziuba, B. F. Field, E. R. Williams, S. M. Girvin, A. C. Gossard, D. C. Tsui and R. J. Wagner, Phys. Rev. Lett. **51**, 1374 (1983).
4. P. M. Mensz and D. C. Tsui, Phys. Rev. B **40**, 3919 (1989).
5. N. Q. Balaban, U. Meirav, H. Shtrikman and Y. Levinson, Phys. Rev. Lett. **71**, 1443 (1993). N. Q. Balaban, U. Meirav and H. Shtrikman, Phys. Rev. B **52**, R5503 (1995).
6. S. Komiyama, T. Takamasu, S. Hiyamizu and S. Sasa, Solid State Commun. **54**, 479 (1985).
7. O. Heinonen, P. L. Taylor and S. Girvin, Phys. Rev. B **30**, 3016 (1984).
8. L. Eaves and F. W. Sheard, Semicond. Sci. Technol. **1**, L346 (1986).
9. S. A. Trugman, Phys. Rev. B **27**, 7539 (1983).
10. K. Ishikawa, N. Maeda and K. Tadaki, Phys. Rev. B **54**, 17819 (1996)
11. V. Tsemekhman, K. Tsemekham, C. Wexler, J. H. Han and D. J. Thouless, Phys. Rev. B **55**, R10201.
12. K. von Klitzing, Physica B **184**, 1 (1993).
13. L.B.Rigal, et al., Phys. Rev. Lett. **82**,1249 (1999).
14. M. M. Fogler and B. I. Shklovski, Phys. Rev. B **52**, 17366 (1995).
15. D. R. Leadley, R. J. Nicholas, J.J. Harris and C.T. Foxon, Phys. Rev. B **58**, 13036 (1998).
16. T. Ando and Y. Uemura, J. Phys. Soc. Japan, **37**, 1044 (1974).
17. C. Callin and B.I. Halperin, Phys. Rev. B **31**, 3635 (1985) and Phys. Rev. B **30**, 5655 (1984).
18. C. J. Gorter and H. B. G. Casimir, Physica **1**, 306.

Internal Transitions of Two-Dimensional Charged Magneto-Excitons X^-: Theory and Experiment

A. B. Dzyubenko*
Institut für Theoretische Physik, J.W. Goethe-Universität, 60054 Frankfurt, Germany

A. Yu. Sivachenko
The Weizmann Institute of Science, Rehovot 76100, Israel

H. A. Nickel, T. M. Yeo, G. Kioseoglou, B. D. McCombe, and A. Petrou
Department of Physics and Center for Advanced Photonic and Electronic Materials, SUNY Buffalo, Buffalo, NY 14260, USA

(June 28, 1999)

Internal spin-singlet and spin-triplet transitions of charged excitons X^- in magnetic fields in quantum wells have been studied experimentally and theoretically. The allowed X^- transitions are photoionizing and exhibit a characteristic double-peak structure, which reflects the rich structure of the magnetoexciton continua in higher Landau levels (LL's). We discuss a novel exact selection rule, a hidden manifestation of translational invariance, that governs transitions of charged mobile complexes in a magnetic field.

73.20.Dx, 71.70.Di, 76.40.+b, 78.90.+t

Recently there has been considerable interest in charged excitonic complexes, X^- and X^+, commonly referred to as trions. The X^- complex, which can be observed in photoluminescence- and reflectance spectra of low-density, quasi-2D electron gases (2DEGs), has been the subject of extensive experimental and theoretical work since its observation in 1993 [1]. The bulk of this work to date has been concerned with *inter*-band transitions only. *Intra*-band, or internal, transitions of X^-, which lie in the far-infrared (FIR), can provide additional important insight into the properties of the ground and excited states of this complex.

The X^--complex, consisting of an exciton binding an additional electron, is superficially similar to its close relative, the negatively charged donor ion, D^- [2]. Both complexes are often considered to be the semiconductor analogs of the hydrogen ion, H^-. When the H^- ion is treated in the infinite proton mass approximation, such analogy is exact for the D^- complex — a localized positive charge binding two electrons. This analogy fails, however, in certain very important aspects for the *mobile* X^- complex. In particular, we show here that the magnetic translations for the X^- imply the existence of an exact selection rule that *prohibits* certain bound-to-bound internal X^- transitions, the analogs of which are very strong for the D^-. In an arbitrary uniform B this selection rule is applicable to charged electron-hole, as well as to one-component electron systems. In the latter case Kohn's theorem [3] based on translational invariance also works. Due to the center-of-mass separation for electron systems in B, both theorems — though based on different operator algebras — give in this case equivalent predictions. To understand the main qualitative features, we first consider the strictly-2D electron-hole (e–h) system in high magnetic fields. In this limit, $\hbar\omega_{ce}, \hbar\omega_{ch} \gg E_0 = \sqrt{\pi/2}\, e^2/\epsilon l_B$, where E_0 is the binding energy of the 2D magnetoexciton (MX) in zero LL's [4] and $l_B = (\hbar c/eB)^{1/2}$. The mixing between different LL's can then be neglected, and the X^- states can be classified by total electron and hole LL numbers, $(N_e N_h)$. The corresponding basis for X^- is of the form [5] $\phi^{(e)}_{n_1 m_1}(\mathbf{r})\, \phi^{(e)}_{n_2 m_2}(\mathbf{R})\, \phi^{(h)}_{N_h M_h}(\mathbf{r}_h)$, and includes different three-particle $2e$–h states such that the total angular momentum projection $M_z = N_e - N_h - m_1 - m_2 + M_h$ (and $N_e = n_1 + n_2$, N_h) are fixed. Here $\phi^{(e,h)}_{nm}$ are the e- and h- single-particle factored wave functions in B: n is the LL quantum number; and m is the oscillator quantum number $[m_{z e(h)} = {}^{+}_{(-)}(n-m)]$. We use the electron relative and center-of-mass coordinates: $\mathbf{r} = (\mathbf{r}_{e1} - \mathbf{r}_{e2})/\sqrt{2}$ and $\mathbf{R} = (\mathbf{r}_{e1} + \mathbf{r}_{e2})/\sqrt{2}$. Permutational symmetry requires that for electrons in the spin-singlet s (triplet t) state the relative motion angular momentum $n_1 - m_1$ should be even (odd). This basis complies with the axial symmetry about the z-axis and the permutational symmetry. The symmetry associated with magnetic translations (e.g., [6]) and its consequences are still hidden at this point.

The calculated three-particle $2e$-h eigenspectra (electrons in the triplet state) in the two lowest LL's are shown in Fig. 1.

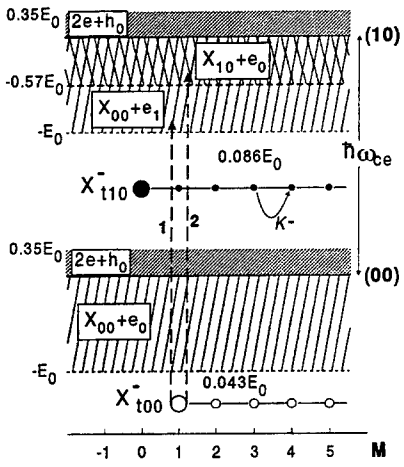

FIG. 1. Schematic drawing of bound and scattering electron triplet $2e$-h states in the lowest LL's (N_eN_h)=(00), (10). The quantum number $M = -M_z$ for the (N_eN_h)=(00) states and $M = 1 - M_z$ for the (N_eN_h)=(10) states; allowed transitions must satisfy $\Delta N_e = 1$; $\Delta M_z = 1$; $\Delta k = 0$. The energy $E_0 = \sqrt{\pi/2}\, e^2/\epsilon l_B$ parametrizes the 2D system in the limit of high B. Large (small) dots correspond to the bound parent (daughter) X^- states; see text for further explanations.

Generally, the eigenspectra associated with each LL consist of bands of *finite* width $\sim E_0$. The states within each such band form a *continuum* corresponding to the extended motion of a neutral magnetoexciton (MX) as a whole with the second electron in a scattering state. As an example, the continuum in the lowest (N_eN_h)=(00) LL consists of the MX band of width E_0 extending down in energy from the free (00) LL. This corresponds to the $1s$ exciton ($N_e = N_h = 0$) plus a scattered electron in the zero LL, labeled $X_{00} + e_0$. The structure of the continuum in the (N_eN_h)=(10) LL is more complicated: in addition to the $X_{00}+e_1$ band of the width E_0, there is another MX band of width $0.574E_0$ also extending down in energy from the free (N_eN_h)=(10) LL. This corresponds to the $2p^-$ exciton ($N_e = 1$, $N_h = 0$) [4] plus a scattered electron in the $N_e = 0$ LL, labeled $X_{10}+e_0$. Moreover, there is a band above each free LL originating from the bound internal motion of two electrons with the hole in a scattering state (labeled $2e + h_0$) [7].

Bound X^- states (finite internal motions of all three particles) lie *outside* the continua (Fig. 1). In the limit of high B the only bound X^- state in the zeroth LL (N_eN_h)=(00) is the X^--triplet. There are no bound X^--singlet states [8,9] in contrast to the $B = 0$ case. The X^--triplet binding energy in zero LL's (N_eN_h)=(00) is $0.043E_0$ [8,9]. In the next electron LL (N_eN_h)=(10) there are no bound X^--singlets, and only one bound triplet state X^-_{t10}, lying below the lower edge of the MX band [7]. The X^-_{t10} binding energy is $0.086E_0$, twice that of the X^-_{t00}, and similar to the stronger binding of the D^--triplet in the $N_e = 1$ LL [5].

We focus here on internal transitions in the σ^+ polarization governed by the usual selection rules: spin conserved, $\Delta M_z = 1$. In this case the e-CR–like inter-LL ($\Delta N_e = 1$) transitions are strong and gain strength with B. Both bound-to-bound $X^-_{t00} \to X^-_{t10}$ and photoionizing X^- transitions are possible. For the latter the final three-particle states in the (10) LL belong to the continuum (Fig. 1), and calculations show that the FIR absorption spectra reflect its rich structure [7]. Transitions to the $X_{00}+e_1$ continuum are dominated by a sharp onset at the edge (transition 1) at an energy $\hbar\omega_{ce}$ plus the X^-_{t00} binding energy. In addition, there is a broader and weaker peak corresponding to the transition to the $X_{01}+e_0$ MX band, transition 2. The latter may be thought of as the $1s \to 2p^+$ internal transition of the MX [10,11], which is shifted and broadened by the presence of the second electron. Photoionizing transitions to the $2e+h_0$ band have extremely small oscillator strengths and are not considered further.

The inter-LL bound-to-bound transition, $X^-_{t00} \to X^-_{t10}$, lies *below* the e-CR energy $\hbar\omega_{ce}$. In contrast to the analogous, strong triplet T^- transition for D^- [5,12,13] this transition for X^- has exactly *zero* oscillator strength, a hidden manifestation of the magnetic translational invariance [7]. Consider the operator $\hat{\mathbf{K}} = \sum_j(\boldsymbol{\pi}_j - \frac{e_j}{c}\mathbf{r}_j \times \mathbf{B})$, which commutes with the Hamiltonian of interacting charged particles in a uniform $\mathbf{B}$; here $\boldsymbol{\pi}_j = -i\hbar\boldsymbol{\nabla}_j - \frac{e_j}{c}\mathbf{A}(\mathbf{r}_j)$ is the kinematic momentum of the j-th particle. The components of $\hat{\mathbf{K}} = (\hat{K}_x, \hat{K}_y)$ are the generators of magnetic translations ([6] and references therein)

and commute as canonically conjugate operators: $[\hat{K}_x, \hat{K}_y] = i\frac{l_B}{c}\sum_j e_j$. For the X^-, therefore, the operators $\hat{k}_\pm = (\hat{K}_x \pm i\hat{K}_y)l_B/\sqrt{2}\hbar$ are the intra-LL lowering and raising operators. Thus $(\hbar/l_B)^2\hat{\mathbf{K}}^2$ has the oscillator eigenvalues $2k+1$ ($k = 0, 1, \ldots$). There is the macroscopic Landau degeneracy in the discrete quantum number k, and k can be used, together with M_z, to label the exact eigenstates. The additional selection rule is conservation of k for dipole-allowed transitions [14].

As a result of the macroscopic degeneracy of k, there exist *families* of bound, degenerate X^- states in B. One family of X^- bound states is associated with the (00) and (10) LL's. Each i-th family starts with its *Parent State* (PS) $|\Psi^{(P_i)}_{M_z}\rangle$, which has the maximal possible value of M_z in the family, (Fig. 1). The daughter states in the i-th family, $|\Psi^{(D_i)}_{M_z-l}\rangle = \hat{k}^l_-|\Psi^{(P_i)}_{M_z}\rangle/\sqrt{l!}$ are constructed out of the PS with the help of the raising operator $\hat{k}_-$ [7]. Any PS carries the exact quantum number $k = 0$ (while a daughter state in the l-th generation carries $k = l$). The additional requirement of conservation of k for allowed electric-dipole transitions means that *parent states*, $|\Psi^{(P_i)}_{M_z}\rangle$ and $|\Psi^{(P_j)}_{M'_z}\rangle$ in the two families, must satisfy $M'_z = M_z \pm 1$ for there to be allowed FIR transitions. The PS's in the (00) and (10) LL's have $M_z = -1$ and $M'_z = +1$, and do not satisfy this requirement. Therefore, the family of X^-_{i10} bound states is *dark*, i.e., is not accessible by internal transitions from the ground X^-_{i00} bound states. Breaking of translational invariance (by impurities, disorder etc.) would make the $X^-_{i00} \rightarrow X^-_{i10}$ transition allowed.

Most qualitative features discussed above are preserved at finite fields and confinement where both triplet and singlet bound X^- states exist, as shown by calculations for a representative case (200 Å GaAs/$Ga_{0.7}Al_{0.3}As$ QW at $B > 9$ T). We obtain eigenstates of X^- using an expansion [12,9] in e and h LL's and size-quantization levels in a QW: we assume a simple valence band for holes with in-plane $m_{h\|} = 0.24$ and perpendicular $m_{hz} = 0.34$ effective masses ($m_e = 0.067$ is isotropic, the GaAs dielectric constant $\epsilon = 12.5$). For the singlet and triplet binding energies of X^- in the zeroth LL we obtain results equivalent to the high-accuracy calculations of [9]. Both singlet and triplet transitions exhibit a characteristic double-peak structure, but the singlet transitions are broader, and the peak at higher energies has a larger oscillator strength. Results for the singlet transitions at 9 Tesla are shown in Fig. 2(a). For comparison with the theoretical calculations we have studied two 20 nm wide GaAs/$Al_{0.3}Ga_{0.7}As$ multiple quantum well (MQW) structures, one undoped and one modulation-doped in the barrier with silicon donors at 2×10^{10} cm^{-2}, by optically detected resonance (ODR) spectroscopy [15]. Both samples show the X^--photoluminescence (PL) line. The experiment confirms the theoretical predictions discussed above. In Fig. 2(b) a series of ODR scans for the undoped sample is shown at several FIR laser wavelengths. During the magnetic field sweep the spectrometer was stepped to remain centered on the peak of the X^-recombination line. The recorded changes in the PL intensity ($\Delta I_{\rm PL}$) of the X^--PL line correspond to a decrease in the PL intensity of X^-. Tracking the PL peak of X instead of X^-yields ODR scans which are inverted (increase in PL strength), but otherwise very similar. The spectra in Fig. 2(b) are displaced in magnetic field such as to align the position of the sharp, negative going electron cyclotron resonance (e-CR) present in all scans at the position of the e-CR at 118.8 μm, 6.23 Tesla. In this way, the behavior of features occurring at lower magnetic fields, and with an amplitude approximately one order of magnitude smaller than e-CR, are more easily seen.

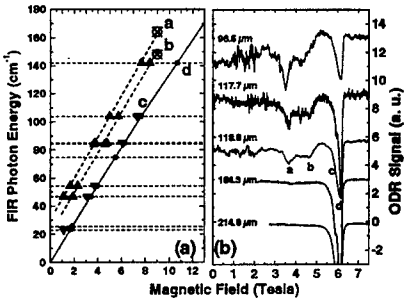

FIG. 2. (a) Summary plot of the observed internal transitions of X^-as a function of magnetic field. Dashed lines are guides to the eye, the solid line represents a fit through the measured positions of electron cyclotron resonance. The crossed out circles at 9T are the results of the calculation described in the text. (b) ODR scans as a function of magnetic field for several FIR laser wavelengths. The horizontal (B) scale corresponds to the scan taken at 118.8 μm. (a) and (b) denote the X^--singlet transitions and (c) marks the X^--triplet transition.

These ODR scans show several resonances at magnetic fields below that of e-CR. For instance, the

ODR scan recorded at a FIR wavelength of $118.8\,\mu m$ has features at 4.08 Tesla (a) and 4.60 Tesla (b), in addition to a shoulder roughly 0.1 Tesla (c) below e-CR (d). Resonances of similar shape are observed in all ODR scans recorded with FIR wavelengths shorter than $393.6\,\mu m$. At $393.6\,\mu m$ and $432.6\,\mu m$ no resonances were observed at magnetic fields below e-CR. The qualitative behavior of the modulation-doped sample is very similar: however, the strength of features (a) and (c) at lower magnetic fields is greatly enhanced with respect to e-CR. In this sample the intensity of the X^--PL line is much larger than in the undoped structure, so X^--features are expected to be stronger.

The observed resonances are summarized in Fig. 2(a), where the peak positions in the ODR scans for the undoped sample are plotted as a function of magnetic field for all measured FIR laser lines. Features labeled (a) and (b) in Fig. 2(b) are shown by upright triangles, feature (c) is represented by an inverted triangle, and e-CR is marked by solid circles. Features (a) and (c) occur in the modulation-doped sample approximately 0.1 Tesla lower than the data points in this figure. Feature (b) is observed at elevated temperature. Two points from the numerical calculation for the singlet transitions at 9 Tesla are plotted as crossed-out circles at the end of the two dashed lines, which are guides to the eye. The predicted double-peak structure for the X^-singlet transition is clearly observed and in good agreement with the calculations.

Based on the discussion above and the good qualitative as well as quantitative agreement of the experiment with theory, we assign features (a) and (b) to the internal X^--singlet transition, and feature (c) to the internal X^--triplet transition. No evidence was found for any features on the high-field size of e-CR corresponding to the localized-to-localized state transitions (*e.g.* the X^--triplet) that are dominant in magneto-spectroscopy of D^-. In conclusion, photoionizing spin-singlet and spin-triplet transitions of X^- have been observed experimentally. The experimental findings are in good agreement with theoretical predictions, which show that due to an additional exact selection rule resulting from a hidden symmetry, the bound-to-bound X^- singlet- and triplet-transitions to the next electron LL are forbidden. The appearance of a corresponding triplet feature *below* the e-CR energy should be a characteristic feature associated with breaking of translational invariance. This may be used as a tool for studying the extent of X^- localization.

ABD is grateful to the Department of Physics, University at Buffalo, where part of this work was performed, and to the Humboldt Stiftung for financial support. The work at SUNY at Buffalo was supported by NSF grant DMR 9722625.

---

* on leave from General Physics Institute, RAS, Moscow 117942, Russia.

[1] K. Kheng, R.T. Cox, Merle Y. d'Aubigné *et al.* Phys. Rev. Lett. **71**, 1752 (1993).

[2] Z.X. Jiang, B.D. McCombe, J.-L. Zhu *et al.*, Phys. Rev. B **56**, R1692 (1997), and references therein.

[3] W. Kohn, Phys. Rev. **123**, 1242 (1961).

[4] I.V. Lerner and Yu.E. Lozovik, Sov. Phys. JETP **51**, 588 (1980).

[5] A.B. Dzyubenko, Phys. Lett. A **165**, 357 (1992); **173**, 311 (1993).

[6] J.E. Avron, I.W. Herbst, and B. Simon, Annals of Phys. **114**, 431 (1978).

[7] A.B. Dzyubenko and A.Yu. Sivachenko, cond-mat/9902086.

[8] J.J. Palacios, D. Yoshioka, and A.H. MacDonald, Phys. Rev. B **54**, R2296 (1996).

[9] D.M. Whittaker and A.J. Shields, Phys. Rev. B **56**, 15 185 (1997).

[10] J. Cerne, J. Kono, M.S. Sherwin *et al.* Phys. Rev. Lett. **77**, 1131 (1996); M. Salib, H.A. Nickel, G.S. Herold *et al.* Phys. Rev. Lett. **77**, 1135 (1996).

[11] A.B. Dzyubenko, Pis'ma ZhETF, **66**, 588 (1997) [JETP Lett. **66**, 617 (1997)].

[12] A.B. Dzyubenko and A.Yu. Sivachenko, Phys. Rev. B **48**, 14 690 (1993).

[13] R.S. Ryu, Z.X. Jiang, W.J. Li *et al.* Phys. Rev. B **54**, R11 086 (1996).

[14] The Hamiltonian of the interaction with the FIR radiation of polarization $\sigma^\pm$ is of the form $\hat{V}^\pm \sim \sum_j e_j \pi_j^\pm / m_j$, where $\pi_j^\pm = \pi_{jx} \pm i\pi_{jy}$, and commutes with $\hat{\mathbf{K}}$ (and $\hat{\mathbf{K}}^2$).

[15] see *e.g.*: H.A. Nickel, G.S. Herold, M.S. Salib *et al.*, Physica B **249-251**, 598 (1998), and references therein.

Absorption and emission in n type II-VI quantum wells

V. Huard, R.T. Cox, K. Saminadayar
Département de Recherche Fondamentale sur la Matière Condensée/SP2M,
CEA-Grenoble, 17 rue des Martyrs, 38054 Grenoble Cedex 9, France

C. Bourgognon, A. Arnoult, J. Cibert, S. Tatarenko
Laboratoire de Spectrométrie Physique, CNRS-Université Joseph Fourier
BP 87, 38042 Saint Martin d'Hères Cedex, France

Abstract

The evolution of the optical properties as a function of 2D electron concentration n_e is studied using CdTe quantum wells. The trion absorption peak evolves to the Fermi Edge Singularity (FES) as the exciton peak progressively disappears. The splitting between these two peaks is linear in n_e. This is explained in the framework of Hawrylak's theory of the many-body optical response of free carriers. The emission spectra show a transformation similar to that observed for gated electron gases and previously attributed to a metal-insulator transition. There is however a contradiction with the absorption results which can be explained in terms of a Fermi sea of electrons over the whole range of densities.

PACs : 78.66.-w, 71.35.Cc, 73.20.Dx, 71.10.Ca
keywords : quantum wells, excitons, optical spectroscopy
email : vhuard@cea.fr phone +33 476883677 fax +33 476885097

Optical properties of a semiconductor quantum well containing a two dimensional electron gas (2DEG) depend strongly on the electron density n_e. For low n_e (10^{10} cm^{-2}) and strong coulomb interaction one sees, in both absorption and emission spectra, two sharp peaks corresponding to creation of the negatively charged exciton or trion X^- and the neutral exciton X, the latter at higher energy [1,2,3].

For high n_e, the absorption spectrum evolves to become an asymmetrically broadened Fermi Edge Singularity (FES). The FES is known to result from multiple scattering processes involving many electrons near the Fermi level. The emission spectrum then exhibits a broadened peak with a width of roughly the Fermi energy shifted towards lower energy. It is no longer appropriate to think of interaction between an optically injected hole and one or two electrons : a proper understanding needs many body theory involving interactions between all carriers.

The evolution of the spectrum as peaks X^- and X transform into the FES has been studied, mainly in emission, for the 2DEG in gated GaAs quantum wells [3]. The main conclusions were that as n_e increases the excitons are screened, that the spectrum evolves to a "free carrier-like" behavior and that this can be linked to a insulator to metal transition. In this viewpoint, trion and exciton species occur only as a result of the localization of carriers, which makes them ineffective for screening the excitonic interaction and the potential of the remote donors.

We present 2K measurements of absorption and emission of 100Å, modulation-doped CdTe quantum wells between CdZnMgTe barriers with n_e ranging up to 4.10^{11} cm^{-2}. The structures were grown by MBE on $Cd_{0.88}Zn_{0.12}Te$ substrates. The strain induced in the CdTe quantum well by lattice mismatch shifts light hole excitations 40 meV above heavy hole excitations. Also, with 12% Zn, the substrate is transparent at the energy of the CdTe quantum well heavy-hole bandgap, so optical absorption measurements can be done easily. The barriers are doped with indium or aluminium donors at a spacer distance 200 Å or greater from the edge of the well. For Al doping, the total electron density can be reduced by blue laser light. The values of n_e can be

deduced from the field dependence of the Landau level filling factor for $n_e > 10^{11}$ cm^{-2}. Values of n_e below 10^{11} cm^{-2} were taken to be the MBE design values.

Absorption (dotted line) and emission (full line) spectra are given in Fig. 1 for various electron densities. For an undoped quantum well, the exciton peak X dominates the absorption spectrum (Fig. 1(a)), but the presence of a few electrons is shown by a very weak, low energy shoulder corresponding to the trion peak X^-. As n_e is increased (Fig. 1(b-f)), the X^- absorption peak gains in intensity compared to the X peak. The important new feature seen for these samples is that the X absorption peak moves away rapidly from X^- as n_e increases. The X peak loses amplitude until it is no longer detectable and the X^- peak evolves into the FES absorption.

The evolution of the photoluminescence (PL) is shown in Figs 1, 2 and 3. For very low n_e, the emission spectrum consists of two sharp peaks corresponding to recombination of the trion X^- and of the neutral exciton X (Fig. 1(a)). They show only a small, disorder-related Stokes shift with respect to the X^- and X absorption peaks. As n_e increases, the X peak weakens very fast. Initially, the X^- peak remains quite sharp and intense, with a constant Stokes shift (top of Fig.2). For a density which exceeds 10^{11} cm^{-2}, the emission spectrum broadens drastically and redshifts (Fig. 2). The change occurs over a very small range of densities. The main intensity is now at the lower energy edge, and the linewidth between the main peak and a weak, high energy shoulder (arrows 1,2 in Fig. 3) is about equal to the Fermi energy. This shoulder is shifted below the absorption peak by a gap which increases as n_e increases. Also there is an even weaker emission shoulder (arrow 3 in Fig. 3) slightly Stokes shifted below the absorption peak.

To get an insight into the evolution of the properties of the 2DEG, we first discuss absorption results for low n_e where trion and exciton peaks are still visible. We measure the splitting between the two absorption peaks as a function of the Fermi energy E_F and we find a linear dependence on E_F. A least squares fit to our measurements gives:

$$E(X) - E(X^-) = E_{b1} + aE_F \qquad \text{(eq.1)}$$

with E_{b1}=2.1 meV and with a=1.07, close to 1. This dependence on E_F of the X, X^- splitting shows that a proper many-body description of excited states in an electron gas is needed.

The presence of two peaks in absorption is clearly in contrast with early theories of the optical response of a 2DEG including many-body effects because they predicted only one absorption peak[4]. More recently, Hawrylak adapted the original theory of the FES in 3D [5] to the 2D case including different channels for the two spin states and emphasizing that the injection of a hole into a 2DEG always gives a bound state, no matter how high n_e is [6]. This bound state, created by an optical transition with threshold $\hbar\omega_1$, is occupied by two electrons with opposite spins. For vanishing n_e, it corresponds to the trion X^- described by Stebe [1]. The bound state can be "ionized" to give a singly occupied configuration that corresponds to the exciton X in an undoped sample. The latter state is created by an optical transition with threshold $\hbar\omega_2$. The splitting between the two thresholds corresponds to the energy for removing one of the two electrons from the bound state. Since all the states below the Fermi level are occupied, one must add the Fermi energy E_F to the binding energy E_{b1} of the bound state. Thus this model of a bound state in a gas of free carriers results in eq. 1 with a=1.

Hawrylak's theory initially considered a localized hole. Developed further, it found two important effects of a finite valence hole mass in absorption spectra. First the excitonic enhancement at the absorption threshold should be suppressed for high n_e [6] and second the threshold should shift toward higher energies with increasing electron density [7].

The disappearance of the excitonic enhancement at the absorption threshold at high n_e is observed clearly in our absorption spectra (Fig. 1). Besides, we see a blueshift as we vary n_e in a given sample. These two results can only be explained in terms of a finite valence hole mass. So we conclude that mobile valence holes are a valid concept in our samples.

These absorption results seem clear and are discussed in more detail elsewhere [8]. We now consider our emission results keeping the above findings in mind. A main feature is that, for high n_e, most of the intensity is at the lower energy edge. This is in contradiction with theoretical [6,9]

and experimental [10] results for the case of *localized* valence holes where most of the intensity is at the upper energy edge. But it agrees with experimental spectra for clean GaAs quantum wells [11] and with theoretically calculated spectra for free electrons recombining with mobile valence holes [12,13]. Although a theory including binding in the initial state is not yet available, the increasing shift of emission shoulder 2 (Fig. 3) below the absorption threshold $\hbar\omega_1$ as n_e increases is surely linked to a finite valence-band dispersion, with emission involving a hole at the top of the valence band while absorption involves a hole with the Fermi wave vector. The third, very weak shoulder, distinguished at the same energy as the absorption threshold (Fig. 3) implies that the hole with Fermi wave vector does not always thermalize before recombination.

But for low n_e, there is no mark of a valence band dispersion: the emission lines are just disorder-shifted below the corresponding absorption lines. The most interesting feature is the sudden transformation of the spectrum shape as n_e increases. For gated structures, this kind of transformation has been attributed to an insulator-metal transition, from comparison of emission and transport measurements [3]. But our absorption spectra correspond to the concept of a Fermi sea of free carriers, fitting eq.1 even at very low n_e, a few 10^{10} cm^{-2}.

The sudden transformation of the emission spectrum at a critical density n_{ec} recalls the spectroscopic effects of the exciton unbinding transition predicted by Bauer [14]. But, in Hawrylak's model [6,7], no such effect can exist : the bound state always exists in 2D even for finite hole mass. Moreover if unbinding did occur, n_{ec} should be roughly the same in all samples, linked only to the value of the hole mass. Whereas we find that n_{ec} is linked to the spacer width S, since $n_{ec}=1.2\ 10^{11}$ cm^{-2} for S=400Å and $n_{ec}=1.9\ 10^{11}$ cm^{-2} for S=250Å. So we tend to agree that this transformation of the spectrum is related to the electrostatic disorder. Nevertheless, it is not at all clear whether the behaviour at low n_e is due to the system being in an insulator state. Localized holes in a Fermi sea give rise to an exciton-like spectrum at low E_F in ref. [6].

To conclude, our absorption spectra are coherent, in the framework of Hawrylak's theory, with the concept of a Fermi sea of free carriers over the whole range of densities studied. The fundamental excitation must now be considered as a doubly-occupied bound state. We must also conclude that we have mobile valence holes. The explanation for the evolution of the emission is much less obvious. If, for high n_e, emission and absorption results are coherent (finite hole mass, free carriers), the low n_e range is difficult to understand.

Spectra 1(a), (b), (c) were provided by K. Kheng. This work was part of the CEA-CNRS joint research programme "Microstructures de Semiconducteurs II-VI".

References

[1] B. Stébé and A. Ainane, Superlattices Microstruct. **5**, 545 (1989)
[2] K. Kheng, R.T. Cox, Y. Merle-d'Aubigné, Franck Bassani, K. Saminadayar, and S. Tatarenko, Phys. Rev. Lett. **71**, 1752 (1993)
[3] G. Finkelstein, H. Shtrikman, and I. Bar-Joseph, Phys. Rev. Lett. **74**, 976 (1995)
[4] S. Schmitt-Rink, D.S. Chemla, and D.A.B. Miller, Advances in Physics **38**, 89 (1989)
[5] M. Combescot and P. Nozières, J. Phys. (Paris) **32**, 913 (1971)
[6] P. Hawrylak, Phys. Rev. B **44**, 3821 (1991)
[7] J.A. Brum and P. Hawrylak, Comments on Condensed Matter Physics **18**, 135 (1997)
[8] V. Huard *et al.*, (to be published)
[9] I. Perakis and Yia-Chung Chang, Phys. Rev. B **43**, 12556 (1991)
[10] M.S. Skolnick *et al.*, Phys. Rev. Lett. **58**, 2130 (1987)
[11] M.C. Smith *et al.*, Proc. 17th Int. Conf. Physics of Semiconductors, Eds J.D. Chadi and W.A. Harrison, Springer-Verlag (1984), p. 547
[12] S.K. Lyo and E.D. Jones, Phys. Rev. B **38**, 4113 (1988)
[13] T. Uenoyama and L.J. Sham, Phys. Rev. Lett. **65**, 1048 (1990)
[14] G.E. Bauer, Phys. Rev. B **45**, 9153 (1992)

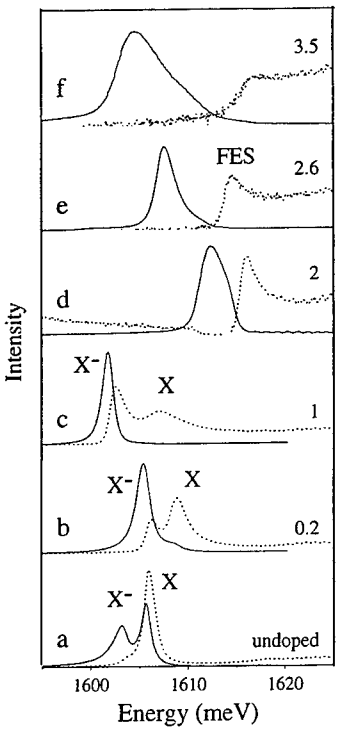

Fig. 1. Optical absorption (dotted line) and emission (full line) spectra at T=2 K for 6 samples with different doping : (a-c) are CdTe and (d-f) are CdMnTe (0.2% Mn) quantum wells. Electron concentrations n_e are expressed in 10^{11} cm^{-2} units. Sample (a) is nominally undoped. We normalized the integrated optical density (=log(1/transmission)) since the structures have different numbers of wells. Energies vary due to different well widths (nominal widths are 100 Å) and with Mn alloying.

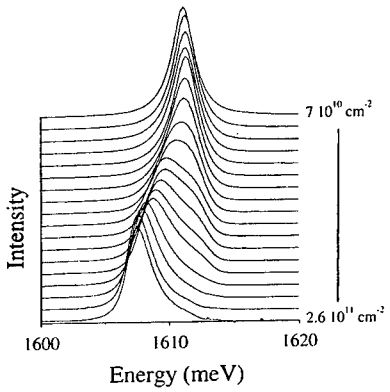

Fig. 2. Emission spectra at 2 K for a 100 Å CdMnTe (0.2% Mn) quantum well as a function of electron density n_e varied by illuminating the cap layer with blue laser light.

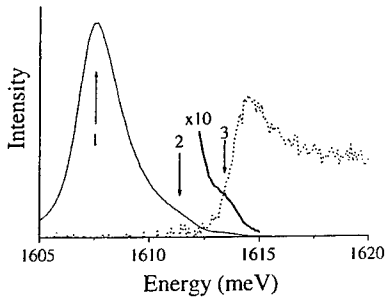

Fig. 3. Optical absorption (dotted line) and mission (full line) spectra for a 100 Å CdMnTe (0.2% Mn) quantum well with $n_e = 2.6\ 10^{11}$ cm^{-2}. Arrows 1, 2, 3 mark the main PL peak and the two PL shoulders at higher energy. Shoulder 3 is magnified 10 times (bold line).

Collective Excitations in Low Density 2D Electron Systems

M.A. Eriksson[a], A. Pinczuk[a,b,c], B.S. Dennis[a], C.F. Hirjibehedin[a,b],
S.H. Simon[a], L.N. Pfeiffer[a], and K.W. West[a]
[a]Lucent Technologies, Bell Labs, Murray Hill, NJ 07974
Depts. of [b]Physics and [c]Applied Physics, Columbia University, New York, NY 10027

Abstract

We report the observation of sharp plasmon and magnetoplasmon modes in ultra-low density 2D electron systems. Well defined dispersions for the modes are observed at densities as low as 1.1 x 10^9 cm^{-2} and with excitation wave vectors as large as 1.2 x 10^5 cm^{-1}. Interestingly, both modes are found to be more easily measured in low density systems than in high density systems. The strength of the light scattering cross-sections at low density suggests potential applications to the study of quantum phase transitions at large r_s.

1. Introduction

Low density two-dimensional electron and hole systems have been studied for decades due to interest in the effects of the Coulomb interaction at large r_s [1]. Experiments at low density have used a wide variety of techniques, including transport, surface acoustic waves, NMR, photoluminescence, inelastic light scattering, and many more. In the last several years this field of study has become even more exciting as transport experiments in particular have prompted renewed questions about the nature of metal-insulator transitions at low density in two-dimensions [2-8].

Our motivation in this work is to explore the capabilities of inelastic light scattering for the study of ultra-low density electron systems, and its applications to the study of quantum phase transitions at low temperature. We find that collective excitations of a type that are usually associated with metallic systems, namely plasmons and magnetoplasmons, can be observed using light scattering at electron densities as low as $n \sim 1.1 \times 10^9$ cm^{-2}. In fact, we find that light scattering from long wavelength plasmons and magnetoplasmons is actually stronger at low electron density than it is at high density – a surprising and promising sign for future work with this technique.

Inelastic light scattering measures the energy and wave vector dependence of collective excitations. These excitations are a high frequency ($0.05 < \omega < 1$ meV) property of electron systems. Most importantly, light scattering is a probe of electron systems at length scales on the order of several times the excitation wavelength ($\lambda \sim 1$ μm). This is in contrast to transport experiments which can probe the conductivity of electron and hole systems on length scales as large as several millimeters or more.

Our observations of sharp dispersive plasmons and magnetoplasmons are consistent with local metallic behavior at densities as low as 10^9 cm^{-2}. This is of particular interest because metal-insulator behavior has been observed at substantially larger densities [6]. An intriguing possibility is that our samples may also show a metal-insulator transition when probed at longer length scales, yet retain sharp plasmons in the apparently insulating phase.

	Sample 1	Sample 2	Sample 3
Density (cm^{-2})	5.4×10^{10}	2.7×10^{10}	1.2×10^{10}
Mobility (cm^2/Vs)	7.2×10^6	3.5×10^6	1.5×10^6

Table 1. Mobility and density at a temperature of 0.3K.

2. Samples and Experimental Technique

The 2D electron systems studied in this work are formed in single 330 Å wide GaAs quantum wells with $Al_xGa_{1-x}As$ barriers. The density of the electron system is varied by changing x in the range $0.03 \le x \le 0.066$ and the setback d between the donors and the quantum well in the range $600Å \le d \le 20{,}000Å$. Because of the low barrier heights associated with small values of x, transport measurements at our lowest experimental densities are difficult due to parallel conductivity through the donor layer. However, measurements of the zero-field mobility are available at densities as low as $n = 1.2 \times 10^{10}$ cm^{-2}. At this density we find that the mobility $\mu = 1.5 \times 10^6$ cm^2/Vs (see Table 1). In order to estimate the level of disorder in our samples we can extrapolate the data shown in Table 1 to lower electron densities. Assuming a linear dependence of the mobility on density, a good fit to the data in Table 1, we extrapolate to find $\mu \sim 138{,}000$ cm^2/Vs at our lowest density $n = 1.1 \times 10^9$ cm^{-2}. This extrapolation serves only to indicate the general level of disorder in the samples studied here, and does not reflect a measurement of the mobility at that density.

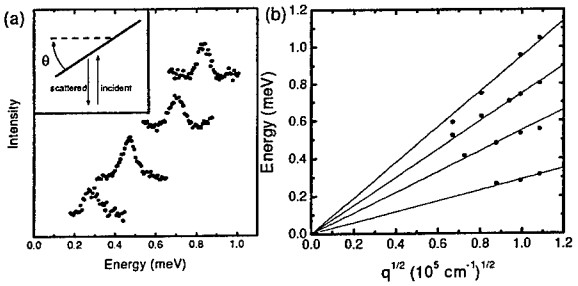

Fig. 1 (a) Light scattering spectra of plasmon excitations in four separate samples. In the two lowest energy spectra $\theta = 30°$, and in the two highest energy spectra $\theta = 35°$. The sample density increases as the peak energy increases. (b) Measured dispersions for the four samples of part (a). The solid lines correspond to Eqn. (1) with $n = 1.2 \times 10^{10}$, 7.2×10^9, 3.7×10^9, and 1.1×10^9 cm^{-2}. *Inset*: Backscattering geometry, in which the wavevector transferred in the scattering process is $q = (4\pi/\lambda)\sin\theta$.

Inelastic light scattering spectra are obtained using the backscattering geometry shown in the inset to Fig. 1. The samples are cooled in a dilution refrigerator with optical windows for laser excitation and scattered light collection. We achieve a base temperature of 40 mK. From the temperature dependence of the light scattering spectra we estimate

that the 2D electron system temperature is less than 100 mK under optimal experimental conditions.

3. Inelastic Light Scattering Observation of Plasmons and Magnetoplasmons

We highlight here the observations of inelastic light scattering from plasmon and magnetoplasmon excitations at densities as low as n = 1.1 x 10^9 cm^{-2}. Fig. 1(a) shows spectra from four samples of increasing density. The sharp peaks correspond to long wavelength plasmon excitations of energy given by

$$\hbar\omega_p(q) = \hbar\sqrt{\frac{2\pi ne^2 q}{m\kappa}}, \qquad (1)$$

where κ is the dielectric constant, and m is the band effective mass [1]. This relation is used to determine the density of each sample, as shown in Fig. 1(b). The typical line width for the excitations plotted in Fig. 1 is about 0.1 meV. The observation of such sharp peaks indicates long scattering times $\tau > 1/\omega_p$. In the case of the sample with a density of 1.1 x 10^9 cm^{-2}, $\hbar\omega_p \sim 0.3meV$, implying a scattering time $\tau >> 1/\omega_p \sim$ 2 ps. This is consistent with the extrapolation of the transport mobilities discussed above. From our light scattering observations we conclude that at electron densities of order 10^9 cm^{-2} the 2D electron system in our samples displays metallic behavior on length scales of several wavelengths of the collective excitations.

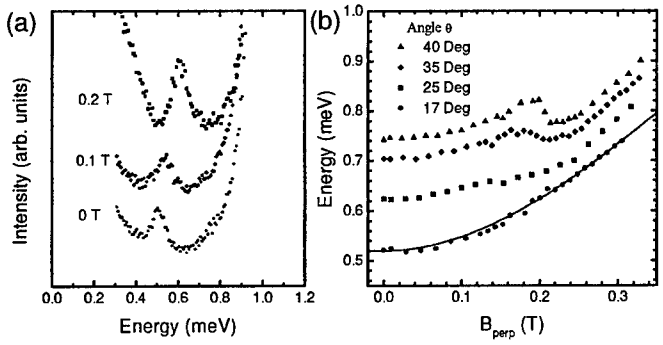

Fig. 2 (a) Inelastic light scattering spectra from a sample of density $n \sim 7.2$ x 10^9 cm^{-2}. The sample temperature $T \leq 200mK$, the incident power density was less than $3\times10^{-4}W/cm^2$, and θ = 17°, corresponding to $q \approx 4.5\times10^4 cm^{-1}$. (b) Peak energy as a function of perpendicular field for the sample of part (a). The solid line is from the classical equation for the magnetoplasmon energy (see text).

Figure 2 (a) shows the evolution of the plasmon peak in a sample with a density of 7.2 x 10^9 cm^{-2} as the magnetic field is increased. The peaks clearly shift to higher energy with increasing field. The same behavior is found in all measured samples with $n \leq 1.2\times10^{10} cm^{-2}$. At higher electron densities, light scattering from magnetoplasmons is dominated by peaks at energies where there are critical points in the density of states for

the magnetoplasmon dispersion [9-11]. In such samples the light scattering spectra do not depend on angle θ. The transition from this high density behavior to the low density behavior shown in Figs. 1 and 2 was described in detail in ref. [9]. Very recent data indicate that this transition is indeed tied to density n rather than a different parameter like the setback d of the doping layer [12].

Figure 1(b) shows the magnetoplasmon energy as a function of the perpendicular field B. The data shown extend from $B = 0$ up to a value of $B = 0.33$T, where the Landau level filling factor $\nu \sim 1$. The solid line in the figure corresponds to the "classical" magnetoplasmon energy, $\hbar\omega_{mp} = \hbar\sqrt{\omega_p^2(q) + \omega_c^2}$. The nonmonotonic behavior at higher angles is likely due to avoided crossings in the inter-Landau level (magnetoplasmon) excitation [9].

4. Conclusions

We have reported data which indicate the existence of strong cross-sections for inelastic light scattering from plasmon and magnetoplasmon excitations in ultra-low density 2D electron systems. Several features of the data point to local metallic behavior of the electron system at densities as low as 10^9 cm^{-2}. These include the narrow width of the plasmon peaks, the observation of well defined dispersion curves, and the clean evolution of the plasmon into a magnetoplasmon mode. The strength of these light scattering peaks at such low density suggests potential applications to the study of quantum phase transitions at large r_s

Acknowledgements

The authors would like to acknowledge helpful discussions with A.P. Ramirez and A.P. Mills.

References

[1] T. Ando, A.B. Fowler, and F. Stern, Rev. Mod. Phys. **54**, 437 (1982) and ref. therein.
[2] S.V. Kravchenko et al., Phys. Rev. B **51**, 7038 (1995)
[3] S.V. Kravchenko et al., Phys. Rev. Lett. **77**, 4938 (1996).
[4] Y. Hanein, et al., Phys. Rev. Lett. **80**, 1288 (1998).
[5] M.Y. Simmons et al., Phys. Rev. Lett. **80**, 1292 (1998).
[6] Y. Hanein et al., Phys. Rev. B **58**, R13338 (1998).
[7] S.J. Papadakis et al., Science **283**, 2056 (1999).
[8] A.P. Mills, et al., cond-mat/9905176.
[9] M.A. Eriksson, et al., Phys. Rev. Lett. **82**, 2163 (1999).
[10] A. Pinczuk *et al.*, Phys. Rev. Lett. **61**, 2701 (1988).
[11] A. Pinczuk *et al.*, Phys. Rev. Lett. **68**, 3623 (1992).
[12] M.A. Eriksson, A. Pinczuk, B.S. Dennis, et al., to be published.

Direct Observation of Hole Edge Channels in a Two Dimensional Electron Gas

A. Zrenner, J. Frankenberger, A. Paassen, A. L. Efros*, M. Stopa,
M. Bichler, and W. Wegscheider
Walter Schottky Institut, Technische Universität München,
Am Coulombwall, 85748 Garching, Germany

Abstract

In spatially resolved magneto-optical experiments we observe hole confinement at the edge of a two-dimensional electron gas and hole transport in edge channels. In a theoretical analysis we show that a repulsive edge potential for holes at the boundary of a two dimensional electron gas is caused by a polaron effect.

PACS: 73.61. r, 73.50.Pz, 72.20.Fr, 72.20.Ht, 73.40.Hm

Since almost 10 years the concept of edge state transport has been successfully applied in the quantum Hall regime [1]. Classically such edge states can be described as skipping orbits. In our current contribution we investigate the properties of optically excited minority holes in a 2DEG [2, 3]. We study the confinement and transport of these holes within the sea of two dimensional electrons in the presence of boundaries. In these studies we use spatially resolved optical techniques to image the spatial distribution of minority holes in the presence of finite electric and magnetic fields. Our experiments show, that minority holes are confined to the 2DEG by a new and unexpected edge potential. In the presence of magnetic fields this edge potential leads to the formation of hole edge states.

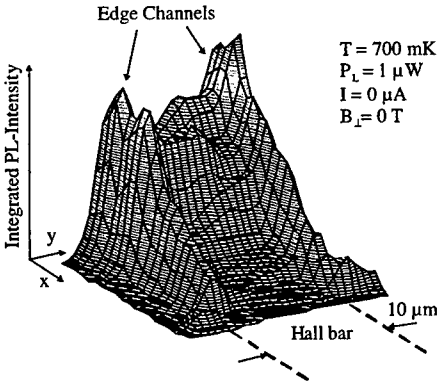

FIG. 1. 3D PL-image of the QW PL from a section of a 10 μm wide Hall bar for zero electric and magnetic field. Optical excitation is via a defocussed Ar^+-Laser.

For our experiments we use a high mobility remotely doped GaAs QW structure grown by molecular beam epitaxy. The layer sequence consists of a 3000 nm thick GaAs/$Al_{0.32}Ga_{0.68}As$ superlattice followed by a 15 nm thick GaAs QW, which is the active layer in our structure. After the QW a 20 nm wide $Al_{0.32}Ga_{0.68}As$ spacer layer was grown, followed by a Si delta-doped 1.5 nm GaAs QW, a 30 nm $Al_{0.32}Ga_{0.68}As$ layer, and a 8.5 nm GaAs cap-layer. The 2DEG in the 15 nm GaAs QW has a density of 4×10^{11} cm^{-2} and a low-field mobility of 4×10^{5} cm^2/Vs at T=700 mK. The 10 μm wide Hall bars (etch depth 40 nm) were mounted in a cryogenic confocal microscope setup (1μm spatial resolution), which is operated in a He3-

system. The sample was optically excited with an Ar^+-Laser at λ=514 nm or a HeNe-Laser at λ=632.8 nm. Detection was performed with a cooled CCD camera in the image plane of the confocal setup. Filters were introduced to obtain PL images only in the spectral range of the 15 nm GaAs QW.

A PL image of a section of a 10 μm wide Hall bar is shown in Fig. 1. Optical excitation was done by a defocused Ar^+-Laser at λ=514 nm centered in the upper left part of the displayed area. Clearly the edge of the 2DEG shows an enhanced PL intensity compared to the inner part of the Hall bar. In the mesa structure under investigation the band bending at the edges assures in a simple picture electron confinement to the Hall bar and hole repulsion from the Hall bar. Photo-generated holes would therefore be subjected to a drift field at the edge of the Hall bar which would result in hole depletion rather than enhancement. Changes in the PL intensity can have different reasons, such as variations in carrier densities or in the radiative and non-radiative recombination rates. In a charged electron-hole plasma a major contribution certainly comes from the product of the local electron and hole densities. Since the electron density is decreasing towards the edges of the Hall bar, the observed PL image is consistent with an enhancement of the hole density at the edge of the Hall bar.

A proof for the existence of an additional edge potential for holes can be provided by experiments in crossed electric and magnetic fields. The general arrangement of such experiments is explained in Fig. 2. The 2DEG in the Hall bar is subjected to a longitudinal electric field E_X and a perpendicular magnetic field $B_\perp$. This in turn leads to the formation of a Hall field E_{Hall} caused by the drift motion of the 2DEG. For the magnetic fields and the sample considered in this work E_{Hall} is always larger than E_X ($\mu B_\perp > 1$).

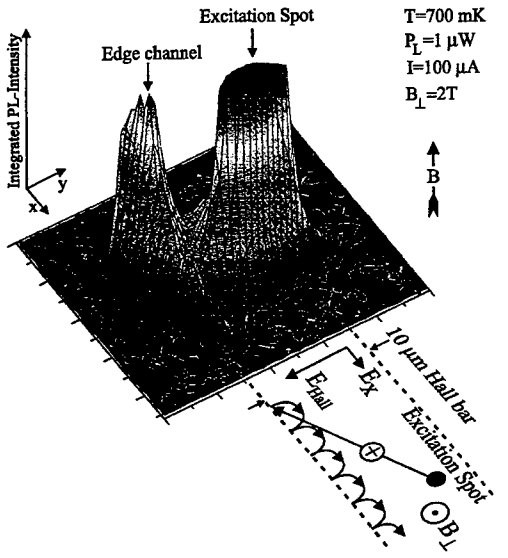

FIG. 2. PL intensity for local optical excitation (excitation spot). By $E \times B$ drift the left edge channel is occupied. Subsequent hole propagation along the edge is in positive x-direction.

In this experiment electron hole pairs are locally excited at the right edge of the Hall bar (excitation spot). Whereas the excess electrons can be neglected, the excess holes are subjected to the total electric field $E_X + E_{Hall}$ and the magnetic field $B_\perp$. Consequently the holes are expected to perform an $E \times B$ drift in the indicated direction. In the central part of the Hall bar the holes undergo therefore a drift motion which is mainly collinear with the electron motion, however with an additional component oriented towards the left edge of the Hall bar. If there is an effective potential barrier, which prevents holes from escaping the 2DEG, we expect the formation of skipping orbits at the edges of the Hall bar. With the given orientation of $B_\perp$ the propagation of this hole edge state will be opposite to the initial direction of hole motion.

Experimental data for the above described situation is shown for B=2 T in Fig. 2. The data has been recorded for a base temperature of T=700 mK, excitation with a HeNe laser at P_L=1 μW, and a drift current of I=100 μA. Under this condition the intensity of the left edge of the Hall bar is found to be selectively enhanced. While the direction of hole propagation inside the Hall bar is apparently from the excitation spot to the upper left side (negative *x*-direction), the direction of propagation along the left edge is opposite. This can be easily shown by shifting the optical excitation directly onto the lower edge of the Hall bar. Under this condition we find hole edge transport in the positive *x*-direction.

Since the hole velocity should be constant in the hole edge channel for a given edge potential and magnetic field, the space coordinate along the edge should be directly proportional to time. With an exponential decay law for holes in the edge channel we would therefore expect an exponential decay of the QW PL along the direction of propagation at the edge. The observed decay of the edge PL along the positive x-direction in this linear scaled contour-plot shown in Fig. 2 in fact nicely follows the expected exponential law.

In the following we discuss the origin of this effective edge potential for holes. The depletion region adjacent to the Hall bar is inaccessible to conduction band electrons but attracts holes. However, single holes in an electron gas are bound to the screening charge which they induce, an essentially polaronic effect. This binding increases with the polarizability, and hence with density of the electron gas. The competition between these „bare band" and polaronic effects determines the effective potential contour for holes near the edge of an electron gas.

We have calculated, within the local density approximation (LDA) to density functional theory, and within a single band, effective mass approximation, the self-consistent electronic structure for the Hall bar near the edge of the depletion region.

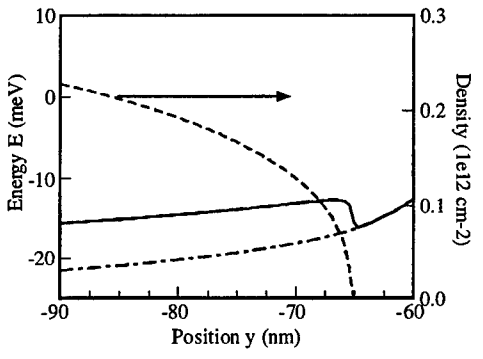

FIG. 3. Valence (dash-dot) subband energies as a function of position. Fermi energy is energy zero, valence band shifted upward by ~ 1.5 eV. The valence subband energy with polaronic energy correction (solid) shows that holes are repelled from the center of the Hall bar but are trapped at the edge where the electron density (dash) vanishes.

Treating the direction of current flow *x* as translationally invariant, we employ the nominal growth profile in the *z*-direction for the conduction band edge offset $V_B(z)$. For the shallow etched depletion region we maintain the *same growth profile* as in the 2DEG region, but we artificially terminate the positive donor layer, specifically we take $N_d(y,z) = N_0\,\delta(z-z_0)\theta(-y)$, where $N_0 = 2\times10^{12}$ cm^{-2} and z_0 is the position of the donor layer. The exposed GaAs surface has an interface charge [4] which can be modeled by pinning the Fermi level at 0.8 eV below the conduction band edge. The value of N_0 is chosen so that the 2DEG density far from the edge is approximately equal to the experimental value of 4×10^{11} cm^{-2}. Neumann boundary conditions for Poisson's Eq. are taken at large |y| and at large *z* the chemical potential is taken to be pinned in the shallow donor layer at 1 *Ry** below

the conduction band, i.e. we employ Dirichlet boundary conditions on the electrostatic potential, setting it 1 *Ry**.

The energy of the lowest electron subband $E_0^e(y)$ is used in a *2D* Thomas-Fermi approximation for the electron density [5]. The lowest hole subband, $E_0^h(y)$ is calculated from the self-consistently computed electrostatic potential $\Phi(y,z)$, but the charge of the hole itself is not treated self-consistently. Note that 2DEG depletion occurs before the edge of the donor layer (i.e. at $y<0$) due to the electric field created by the surface charge layer. By contrast, the hole subband energy, which is unaffected by the XC potential, decreases monotonically with y, suggesting that a positive test charge would escape from the 2DEG into the depletion region.

The density functional calculation for the hole subband energy does not include the polarizing effect of the hole on the electron gas. The interaction energy between a positive point charge and an *homogeneous* 2DEG of density n is :

$$K(n) = -\frac{e^2}{\kappa}\int dq\left[\frac{1}{\varepsilon(q)} - 1\right] \qquad (1)$$

where κ is the background dielectric constant for *GaAs* (κ= 12.5). Within the static screening approximation, the *T*=0, *2D* Linhard-Stern dielectric function [6]:

$$\varepsilon(q) = 1 + \frac{q_s}{q} \qquad q \le 2k_F \qquad (2)$$

$$\varepsilon(q) = 1 + \frac{q_s}{q}\left[1 - \sqrt{1-(2k_F/q)^2}\right] \qquad q > 2k_F \qquad (3)$$

where the Fermi momentum is $k_F = 2\pi\sqrt{n}$ and $q_s \equiv 2/a_0$, a_0 being the effective Bohr radius. Using the density $n(y)$ from the self-consistent calculation and an adiabatic approximation (i.e. $K(y)=K[n(y)]$) we thereby obtain the effective *2D* hole energy corrected for the polaronic effect $E_0^h(y) + K(y)$, plotted as the solid line in Fig. 3. The sharp falloff of $n(y)$ results in a sudden vanishing of the polaronic effect at the edge of the 2DEG and a local energy "minimum" (seen in Fig. 3 as a local maximum at $y \approx -65$ nm). The corrected subband curve shows that holes generated at the Hall bar center will be drawn toward the edge but will be bound at the edge by their image charge in the 2DEG, in striking agreement with experiment.

The authors would like to thank Professor G. Abstreiter for his continuous support and Frank Stern for helpful discussions. A. L. Efros likes to thank the Humbold foundation for financial support. This work has been supported financially by the Deutsche Forschungsgemeinschaft (SFB 348).

*Permanent Address: Department of Physics, University of Utah, Salt Lake City, UT 84112, USA

[1] M. Büttiker, Phys. Rev. B **38**, 9375 (1988)
[2] R. A. Höpfel, J. Shah, P. A. Wolff, and A. C. Gossard, Phys. Rev. B **37**, 6941 (1988)
[3] A. Zrenner et al., Physica B **256-258**, 300-307 (1998)
[4] For a discussion of the treatment of surface states see: J. H. Davies and I. A. Larkin, Phys. Rev. B **49**, 4800 (1994);
J. H. Davies, Semicond. Sci. Technol. **3**, 995 (1988).
[5] M. Stopa, Phys. Rev. B, **54**, 13767 (1996).
[6] F. Stern, Phys. Rev. Lett. **21**, 546 (1967).

IMAGING ELECTRON AND CONDUCTION-BAND-HOLE TRAJECTORIES THROUGH ONE AND TWO SERIES CONSTRICTIONS

R. Crook, C. G. Smith, C. H. W. Barnes, M. Y. Simmons and D. A. Ritchie
Cavendish Laboratory, Madingley Road, Cambridge CB3 0HE, United Kingdom

A charged scanning probe has been used to investigate electron transport in a two-dimensional electron gas (2DEG) patterned with 1D constrictions in a GaAs/AlGaAs heterojunction at 4.2 K. The probe creates a local perturbation in the 2DEG electrostatic potential capable of scattering transport electrons. A highly collimated hot-electron beam emanating from a single constriction is imaged by backscattering from the probe perturbation. Images of electron and conduction-band-hole cyclotron orbits and small angle scattering sites between two series constrictions are also presented. Conduction-band-holes are positively charged quasi-particles existing below the Fermi energy, which are equivalent to unoccupied electron states.

Low temperature scanning probe technology has recently been developed to explore quantum phenomena of subsurface semiconductor nanostructures. For example, images of electron compressibility in the quantum Hall regime [1] and images of static electronic charge [2] have been produced. In this letter experiments are reported that use an invasive probe which perturbs the two-dimensional electron gas (2DEG) electrostatic potential to scatter transport electrons [3,4] and conduction-band-holes. Conduction-band-holes or cb-holes are the positively charged quasi-particles existing below the Fermi energy, which are equivalent to unoccupied electron states.

The device has a 2DEG at 98 nm beneath its surface created at a GaAs/AlGaAs heterojunction. After illumination the high-mobility modulation-doped 2DEG was found to have a carrier concentration of 2.4×10^{11} cm^{-2} and a mean free path of 20 μm. Negatively biased surface electrodes locally deplete electrons from the underlying 2DEG, and are arranged in split-gate configurations to define 1D constrictions. The lithographic constriction width is 700 nm and the electrodes extend 30 nm above the GaAs surface. The scanning probe is a modified atomic force microscope with a conductive boron-doped silicon tip fabricated on a piezoresistive cantilever, [5] and operates to 1.8 K in magnetic fields of up to 3 T.

When the tip scans over the device surface on the drain side of a single constriction, the resulting perturbation scatters electrons back through the constriction to modify the constriction's conductance. [4] Figure 1 (a) shows an image where the contrast is proportional to the constriction ac drain current. A -2 mV dc bias was applied to 2DEG on the source side of the constriction, with a low frequency 0.5 V_{rms} ac signal applied to the tip. The surface electrodes, which are outside the image, were biased to define a constriction with 5 transmissive subbands. A wide cone diverging at $\pm 34°$ is observed in agreement with the established semiclassical collimation theory. [6] A highly collimated beam which diverges at $\pm 3°$ is also observed emanating from the constriction. This beam is interpreted as a beam

of hot-electrons, being restricted to those electrons which retain adiabatic transport from the constriction to the backscattering event and back to the constriction. The minimum beam divergence is limited by quantum mechanical diffraction derived from the uncertainty principle $|\Delta y \Delta k_y| \geq 1$ applied in the constriction. For this device $\Delta y = W \approx 200$ nm giving $\Delta k_y \geq 5 \times 10^6$ m^{-1}. The Fermi energy for this device $E_F = 8.5$ meV is approximately equal to the electron energy at the constriction. Using the dispersion relation $k_x^2 + k_y^2 = 2m^* E_F/\hbar^2$, quantum mechanical diffraction therefore limits the collimation to an approximate minimum of $\pm 2.3°$, in good agreement with the $\pm 3°$ divergence of Fig. 1 (a). When a +2 mV bias is applied to the source, the wide cone and the highly collimated beam are still observed to an equal intensity, and are attributed to cb-holes being injected from the constriction. Figure 1 (b) shows schematically the generation of a cb-hole with a hot-electron at a 1D constriction, and injected in opposite directions into the neighbouring 2DEG regions. The hot-electron energy E_e is larger than the cb-hole energy $E_{\rm cbh}$, and charge is transported equally between the electrons and cb-holes.

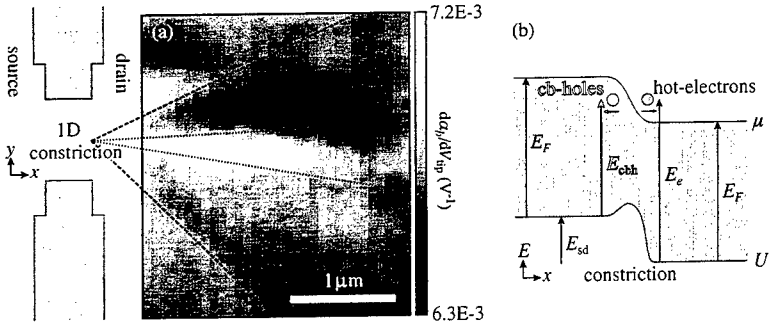

FIG. 1. (a) Image made by scanning the tip 60 nm off the device surface with a 0.5 $V_{\rm rms}$ ac tip bias. The scanned region is on the drain side of a single constriction where the surface electrodes are outlined, with a source bias of -2 mV to inject electrons, at $B = 0$ T and $T = 4.2$ K. Backscattered ratio $\alpha_b = I_{\rm backscattered}/I_{\rm transmitted}$. Dashed lines enclose the $\pm 34°$ semiclassical collimation cone, while the dotted lines enclose the $\pm 3°$ quantum mechanical diffraction limited cone. (b) Schematic band diagram of occupied electron states on both sides of the constriction in the absence of the tip perturbation. Where U is the electrostatic potential, μ is the electron chemical potential, E_F is the Fermi energy, $E_{\rm sd}/e$ is the source-drain bias, and E_e and $E_{\rm cbh}$ are the energies of injected hot-electrons and cb-holes respectively.

Figure 2 (a) illustrates the gate layout of a different device fabricated from the same wafer. Two series constrictions are defined to separate three 2DEG regions, referred to as the source, the drain, and the central 2DEG region. A -1 mV dc + 0.5 $V_{\rm rms}$ ac bias was applied to the source side of the device, and the central 2DEG region held at 0 V. In the absence of the tip, the magnetic field was swept to steer the injected electron beam over the collection constriction. [7] The ac drain current was recorded to produce the plot of Fig. 2 (b) where the central peak is due to those electrons transmitted directly between the two constrictions. In a different experiment using the same device, a 0.5 $V_{\rm rms}$ ac signal was applied to the scanning

tip with the central 2DEG region again held at 0 V. Figure 2 (c) to (f) present images where the ac drain current was recorded to determine the image contrast. These images were made in magnetic fields of either -15 mT or $+15$ mT with a source bias of either -1 mV to inject electrons or $+1$ mV to inject cb-holes. The tip perturbation reduces the electron transfer from the injection to the collection constrictions when it scatters those electrons which would have been transmitted through both constrictions in the absence of the tip. Such electrons are ballistic as the constrictions are separated by 4 μm and the mean free path is 20 μm. The images therefore reveal the possible trajectories that travel through both constrictions. In a weak magnetic field the images show an arc of the cyclotron orbit, originating from electrons or cb-holes at the edge of the semiclassical injection cone. A least squares fit to the peak transfer of the images in Fig. 2 gives cyclotron radii of 6.1 ± 0.1 μm and 5.9 ± 0.1 μm for electrons and cb-holes respectively. The calculated energies are $E_e = 11.1 \pm 0.3$ meV and $E_{\mathrm{cbh}} = 10.3 \pm 0.3$ meV which are positioned 0.4 meV to the expected sides of the measured Fermi energy for this device $E_F = 10.7$ meV. The cb-holes are magnetically steered in the same direction as the hot-electrons because the cb-holes have a negative effective mass as well as positive charge. Enhanced transfer is observed in the borders of the paths where the tip scatters additional electrons from the injection constriction through the collection constriction. The enhanced transfer seen at both ends of the paths is due to the tip directly modifying the constriction's conductance.

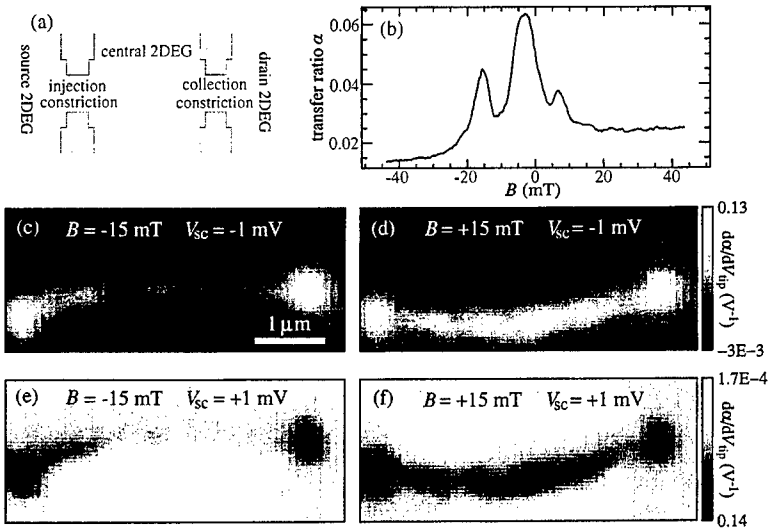

FIG. 2. (a) Schematic layout of the surface electrodes to define two series constrictions. (b) Plot of transfer ratio $\alpha = I_{\mathrm{centre,drain}}/I_{\mathrm{source,centre}}$ against perpendicular magnetic field B, at $T = 4.2$ K. (c) to (f) Images made by scanning the tip 60 nm off the surface with a 0.5 V_{rms} ac tip bias. In (c) and (d) the source bias is -1 mV dc to inject electrons while in (e) and (f) the bias is $+1$ mV dc to inject cb-holes. In (c) and (e) $B = -15$ mT while in (d) and (f) $B = +15$ mT.

Upon closer inspection, finer structure is seen in the images of Fig. 2. The paths bend slightly and the contrast varies along their length. The image shown in Fig. 3 (a) was generated by vibrating the tip at 22 Hz with a +0.5 V dc tip bias, which was found to enhance such structure. In Fig. 3 (b) the minima of image Fig. 3 (a) are plotted to the same spatial scale. The path is seen to bend and sometimes split, and such behaviour is believed to be due to disorder originating in the donor layer. Previous experiments [8] have suggested that the transport mean free path is typically ten times longer than the quantum mean free path which is determined by small angle scattering events. This 2DEG was measured to have a transport mean free path of 20 μm so there are predicted to be on average two small angle scattering events between the constrictions, in good agreement with Fig. 3. The large side peaks observed in Fig. 1 (b) are also interpreted as the result of small angle scattering events.

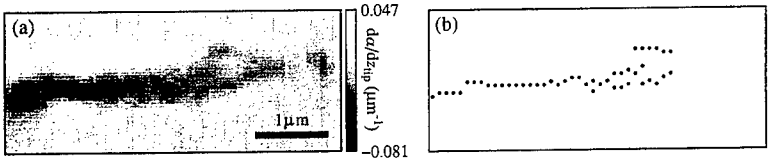

FIG. 3. (a) Experimental image made by vibrating the tip at 10 nm off the surface with a −0.5 V dc tip bias, at $T = 4.2$ K. (b) Image minima spatially corresponding to (a).

In conclusion, images of electron and conduction-band-hole trajectories backscattered from a single constriction, and scattered between between two series constrictions have been presented. A scanning probe technique has been demonstrated that is capable of imaging transport phenomena in subsurface devices. A backscattered highly collimated beam has been observed emanating from a single constriction, with a divergence limited by quantum mechanical diffraction. Between two series constrictions the cyclotron trajectories of electrons and conduction-band-holes have been imaged, enabling a measure of their energies. Small angle scattering sites originating from donor disorder have been directly imaged.

We thank C. J. B. Ford and J. T. Nicholls for helpful discussions. We acknowledge financial support from the EPSRC and from the RW Paul Instrument Fund, and DAR also acknowledges Toshiba Research Europe Limited.

[1] S. H. Tessmer *et al.*, Nature **392**, 51 (1998).
[2] M. J. Yoo *et al.*, Science **276**, 579 (1997).
[3] M. A. Eriksson *et al.*, Appl. Phys. Lett. **20**, 435 (1996).
[4] R. Crook *et al.*, in *Proceedings of the 24th International Conference on the Physics of Semiconductors* (to be published by World Scientific Publishing, Singapore, 1998).
[5] Park Scientific Instruments, Sunnyvale, CA 94089, U. S. A.
[6] C. W. J. Beenakker and H. van Houten, Phys. Rev. B **39**, 10445 (1989).
[7] L. W. Molenkamp *et al.*, Phys. Rev. B **41**, 1274 (1990).
[8] P. T. Coleridge, Phys Rev. B **44**, 3793 (1991).

MB.6

Scanned potential microscopy of edge states in a quantum Hall liquid

Michael T. Woodside[a], Chris Vale[a], Kent L. McCormick[a], Paul L. McEuen[a], C. Kadow[b], K.D. Maranowski[b], A.C. Gossard[b]

[a] *University of California and Lawrence Berkeley National Laboratory, MS 2-200, Berkeley, California, 94720, USA*
[b] *University of California at Santa Barbara, Santa Barbara, California 93106, USA*

Using a low-temperature atomic force microscope as a local voltmeter, we measure the Hall voltage profile in a quantum Hall conductor in the presence of a gate-induced non-equilibrium edge state population at ν=3. We observe sharp voltage drops at the sample edges which are suppressed by re-equilibrating the edge states.

Since the discovery of the quantum Hall effect [1], two-dimensional electron systems (2DES) at low temperatures and high magnetic fields have been found to have a number of unusual properties. One of these is the important role played by the electronic states at the boundary of the 2DES, the edge states of the quantum Hall liquid [2-4]. These quasi-1D extended states form at the edge of the 2DES where the confinement potential causes the energy of filled Landau levels (LLs) to intersect the Fermi level E_F. When the effects of electrostatic screening are considered, the picture that emerges is one of compressible strips of partially-filled LLs (variable electron density), occurring where the bulk LLs cross E_F along the 2DES edges, separated by incompressible strips of filled LLs (fixed electron density) [5,6] . Numerous experiments have shown that the properties of the edge states decisively influence transport in a quantum Hall conductor [7,8]. A variety of techniques, including transport measurements [7,8], magnetocapacitance studies [9], photovoltage measurements [10], edge magnetoplasmon studies [11], inductive probes[12], and in-situ single electron transistor electrometers [13], have been used to study the properties of the edge states. Only recently, however, has it been possible to investigate directly the local properties of the quantum Hall liquid, using novel scanned probe techniques [14-16]. We report here measurements of the electrostatic potential at the edge of the quantum Hall liquid made using a cryogenic atomic force microscope.

The system we study is a GaAs/AlGaAs heterostructure grown by molecular beam epitaxy with a 2DES lying 90 nm below the surface [17]. The device is patterned into 10 μm-wide Hall bars by wet chemical etching of the heterostructure. The 2DES has a density of 2.4×10^{15} m^{-2} and a mobility of 19 m^2/Vs. The device was characterised by standard transport measurements. All measurements were performed at temperatures between 0.7 and 1 K.

Our scanned probe measurements employ a low-temperature atomic force microscope (AFM) [18] operating in non-contact mode which measures the local electrostatic potential in the sample. As shown schematically in Fig. 1, an AC potential V_0 at the resonant frequency of the AFM cantilever (30 kHz) is applied to the contacts of the sample, establishing in the sample the AC potential V(x,y) whose distribution is to be measured. This local sample potential V(x,y) interacts electrostatically with the sharp, metallised AFM tip positioned about 50 nm above the sample, causing a deflection of the AFM cantilever. The force on the tip, and hence the deflection of the cantilever, is directly proportional to V(x,y), the local electrostatic potential in the sample. This cantilever deflection is detected with a piezoresistive sensor [19]. A self-resonant positive feedback loop maintains the frequency of the driving voltage V_0 at the resonant frequency of the AFM cantilever in order to enhance the force sensitivity, resulting in a

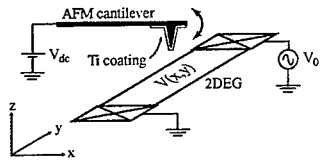

Fig. 1. Schematic diagram of measurement technique. Applying V_0 to the sample creates a potential V(x,y) inside the sample which interacts electrostatically with the metallised AFM tip, causing the AFM cantilever to vibrate by an amount proportional to V(x,y).

sensitivity of about 10 $\mu V/Hz^{1/2}$. The spatial resolution is approximately 0.2-0.3 μm, limited by the size of the AFM tip (~100 nm diameter) and the distance from the 2DES to the tip. Note that height and contact potential fluctuations [20] cause local variations in the signal strength. We account for these by normalising the measured signal with a simultaneously-measured reference signal whereby a uniform voltage is applied to all contacts on the sample. Further details of the design and operation of the AFM are discussed elsewhere [15,21].

Previous studies of the local Hall voltage distribution in a quantum Hall conductor underlined the influence of the edge states on the Hall voltage profile [15]. Sharp voltage gradients at the sample edges were observed when transport measurements indicated the presence of edge states out of equilibrium with the bulk. In the current measurements, we focus more closely on the behaviour at the sample edges by controlling the edge state population using gates on the sample. By changing the electron density beneath the gates, we selectively backscatter some of the edge states and establish a non-equilibrium population downstream of the gates (see Fig. 2) [8]. Standard transport measurements (not shown) confirm the presence of a non-equilibrium edge state population, although there is significant inter-edge scattering due to the low sample mobility. In order to maximise the equilibration length, all measurements are taken at a bulk filling factor of $\nu=3$, which is known to support disequilibrated states over long distances [8].

The results of scanning the AFM tip at $\nu=3$ across the Hall bar about 5-10 μm downstream of the gate are shown in Fig. 3 for three different gate voltages. When the gate is open, all of the Hall voltage drops in the bulk of the sample with a slightly non-uniform distribution (Fig. 3a). When the gate voltage is set to backscatter the $\nu=3$ edge state, the potential in the bulk flattens out somewhat and a sharp voltage gradient develops at one edge of the Hall bar, the edge where the backscattered state flows (Fig. 3b). Approximately half of the Hall voltage drop occurs at this edge; the rest occurs in the bulk. When the gate is entirely closed off, the Hall voltage profile is flat (Fig. 3c). The effect of the gate voltage on the Hall voltage profile at the edge of the 2DES can be seen more clearly in an expanded view of the edge (Fig. 3e,f). The voltage gradient arising from the backscattering of the $\nu=3$ edge channel drops over a distance of 0.3 μm, about 0.2 μm from the edge.

These observations can be readily understood in terms of standard theories of a quantum Hall conductor. When the gate is open and all edge states pass through, the edge states are all at the same potential, and there is no voltage drop at the edges (Fig. 3d). Instead, the Hall voltage drops in the bulk of the sample (Fig. 3a), where the Hall voltage distribution is determined by the local conductivity of the states at E_F [15]. When the gate is fully pinched off, all of the edge states are reflected and hence no Hall voltage is observed (Fig 3c). When the gate reflects only the $\nu=3$ edge state, however, the outer edge states downstream of the gate are at potential V_0

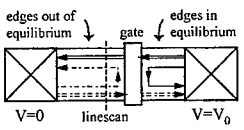

Fig. 2. Measurement configuration. Applying a voltage to the gate reduces the electron density locally, backscattering the innermost edge state (the bulk filling factor shown here is $\nu=3$). The AFM scans across the Hall bar downstream of the gate, where a non-equilibrium edge state population is established.

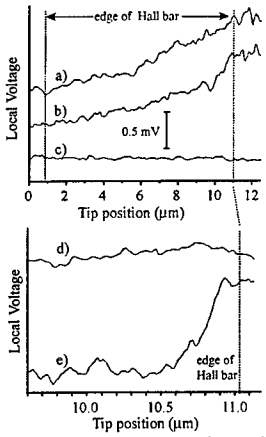

Fig. 3. Hall voltage profiles across 10 μm wide Hall bar at ν=3 (traces offset for clarity). (a) With the gate open, V_H drops in the bulk of the sample. Voltage gradients in the bulk are due to non-uniform local conductivity in the states at E_F. (b) With the gate at ν=2, a sharp voltage gradient develops at the edge of the Hall bar where the non-equilibrium edge states flow. Only half of V_H drops at the edge, due to inter-edge scattering. (c) When the gate is pinched off entirely so that all edge states are reflected, the Hall voltage disappears. (d), (e) Close up of the Hall voltage profile at the edge of the sample. There is no gradient at the edge when the gate is open (d). When the gate is at ν=2, the Hall voltage drops over ~ 300 nm, about 200 nm from the edge of the Hall bar.

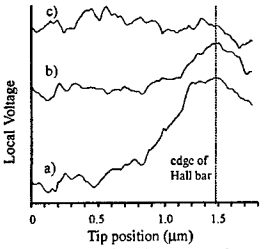

Fig. 4. Effect of DC Hall voltage on voltage profile near edge of Hall bar at ν=3 (traces offset for clarity). (a) The disequilibrated edge states are clearly seen with 0 DC bias. (b) At 5 mV DC bias, little of the voltage gradient is left and the edge states are mostly equilibrated. (c) At 8 mV DC Hall voltage, the edge states are completely equilibrated and no gradient is observed at the sample edge.

while the innermost state is at potential 0, as in Fig. 2. This gives rise to a sharp voltage drop across the incompressible strip separating the ν=2 and ν=3 edge states (Fig. 3e). The length over which the voltage drops suggests that the incompressible strip is at most ~300 nm wide. This result agrees well with other measurements [13], but it is close to the resolution limit of the measurement and hence should be viewed as an upper bound on the width of the incompressible strip [22]. Note also that not all the Hall voltage drops across the incompressible strip (Fig 3b), because of inter-edge scattering that occurs between the gate and the measurement location. Transport measurements indicate that the edge states are mostly equilibrated after travelling 40 μm. Hence noticeable equilibration is expected over the 5-10 μm distances in the AFM measurements.

Having established edge states out of equilibrium, the edge state population can be re-equilibrated by applying a DC Hall voltage of the order of the LL splitting, $\hbar\omega_c$ [23]. The voltage near the sample edge in the presence of a DC Hall voltage is shown in Fig. 4. All linetraces have the gate reflecting the ν = 3 edge state. As the DC bias is increased from 0 (Fig. 4a) to 5 mV (Fig. 4b), just below $\hbar\omega_c$ = 5.5 meV, the voltage drop due to the disequilibrated edge states is reduced substantially, indicating significant re-equilibation. At 8 mV DC bias, well above $\hbar\omega_c$, there is no voltage drop at the sample edge (Fig. 4c), and the edge states are completely equilibrated.

Finally, we studied the perturbation of the sample induced by the measurement technique. The DC voltage applied to the AFM tip in order to detect the local potential in the sample changes the density of the 2DES by ≤ 10% at typical operating conditions [15, 21]. Studies of the effect of the tip voltage, however, show no qualitative change in the measured Hall voltage profile

for perturbations of the 2DES ranging from 5% to 20%. In particular, there seems to be little or no equilibration of the edge states induced by the AFM tip, even at tip voltages twice those in the measurements above. We are thus confident that our measurement is not qualitatively affecting the non-equilibrium edge state population we are studying.

In conclusion, we have measured the local Hall voltage across a quantum Hall conductor in the presence of gate-induced disequilibrated edge states at $\nu = 3$. We observe a sharp voltage drop at the edge of the sample along which flow the non-equilibrium edge states. This voltage gradient can be suppressed by equilibrating the edge states, either with the gate or with a DC Hall voltage of order $\hbar\omega_c$. Future work will include more detailed studies of inter-edge channel equilibration and measurements of the local compressibility of the edge of the quantum Hall liquid.

This work was supported by the NSF, NSERC, the AT&T Foundation, and the Packard Foundation. We acknowledge the Berkeley Microlab for sample fabrication.

References:

[1] K. von Klitzing, G. Dorda, and M. Pepper, Phys. Rev. Lett. **45**, 494 (1980).

[2] B. I. Halperin, Phys. Rev. B **25**, 2185 (1982).

[3] A. H. MacDonald and P. Streda, Phys. Rev. B **29**, 1616 (1984).

[4] M. Buttiker, Phys. Rev. B **38**, 9375 (1988).

[5] D. B. Chklovskii, B. I. Shlovskii, and L. I. Glazman, Phys. Rev. B **46**, 4026 (1992).

[6] I. A. Larkin and J. D. Davies, Phys. Rev. B **52**, 5535 (1995).

[7] B. E. Kane *et al.*, Phys. Rev. Lett. **59**, 1353 (1987); Komiyama *et al.*, Phys. Rev. B **40**, 12566 (1989); B. J. van Wees *et al.*, Phys. Rev. Lett. **62**, 1181 (1989); B. W. Alphenaar *et al.*, Phys. Rev. Lett. **64**, 677 (1990); P. L. McEuen *et al.*, Phys. Rev. Lett. **64**, 2062 (1990).

[8] B. J. van Wees *et al.*, Phys. Rev. B **39**, 8066 (1989).

[9] S. Takaoka *et al.*, Phys. Rev. Lett. **72**, 3080 (1994).

[10] R. J. F. van Haren, F. A. P. Blom, and J. H. Wolter, Phys. Rev. Lett. **74**, 1198 (1995); A. A. Shashkin *et al.*, Phys. Rev. Lett. **79**, 5114 (1997).

[11] N. B. Zhitenev *et al.*, Phys. Rev. B **49**, 7809 (1994).

[12] E. Yahel *et al.*, Phys. Rev. Lett. **76**, 2149 (1996).

[13] Y. Y. Wei *et al.*, Phys. Rev. Lett. **79**, 1674 (1998).

[14] S. H. Tessmer *et al.*, Nature **392**, 51 (1998).

[15] McCormick *et al.*, Phys. Rev. B **59**, 4654 (1999).

[16] A. Yacoby *et al.*, Solid State Comm., to be published.

[17] K. D. Maranowski *et al.*, Appl. Phys. Lett. **66**, 3459 (1995).

[18] G. Binnig, C. F. Quate, and C. Gerber, Phys. Rev. Lett. 56, 930 (1986).

[19] M. Tortonese, R. C. Barrett, and C. F. Quate, Appl. Phys. Lett. **62**, 834 (1993).

[20] M. J. Yoo *et al.*, Science **276**, 579 (1997).

[21] K. L. McCormick *et al.*, Physica B **249-251**, 79 (1998); K. L. McCormick , Ph. D. thesis, University of California, Berkeley (1998).

[22] The fact that we do not observe any change in the width of the voltage drop with changing magnetic field, from ν=2.5 to ν=4, suggests that the incompressible strip is indeed narrower than the resolution of the AFM.

[23] Komiyama *et al.*, Phys. Rev. B **45**, 11085 (1992).

Metal-insulator transition in two dimensions*

S. V. Kravchenko
Physics Department, Northeastern University, Boston, MA 02115, U.S.A.

Recent experiments (see, *e.g.,* Refs.[1-6]) on a number of two-dimensional electron and hole systems suggest that there exists a metal-insulator transition in two dimensions at zero magnetic field, contrary to conventional wisdom [7]. The "metallic" state is characterized by a strong decrease in the resistance with decreasing temperature, while the opposite is found for the "insulating" state. At the critical electron (hole) density, the resistivity is essentially temperature-independent and close to h/e^2, the quantum of resistivity. An external magnetic field, applied either parallel or perpendicular to the 2D plane, suppresses the metallic temperature dependence and eliminates the metal-insulator transition [8]. I will review the main experimental facts and suggested explanations of this unexpected phenomenon. In particular, I will discuss similarities between the zero magnetic field metal-insulator transition and the quantum-Hall-effect-insulator transition [9].

* Work done in collaboration with M. D'Iorio, J. E. Furneaux, G. V. Kravchenko, Whitney Mason, M. P. Sarachik, D. Simonian, and V. M. Pudalov.

[1] S. V. Kravchenko et.al., Phys. Rev. B **50**, 8039 (1994); Phys. Rev. B **51**, 7038 (1995); Phys. Rev. Lett. **77**, 4938 (1996).
[2] D. Popovic, A. B. Fowler, and S. Washburn, Phys. Rev. Lett. **79**, 1543 (1997).
[3] P. M. Coleridge, R. L. Williams, Y. Feng, and P. Zawadzki, Phys. Rev. B **56**, R12764 (1997).
[4] Y. Hanein et.al., Phys. Rev. Lett. **80**, 1288 (1998).
[5] M. Y. Simmons et.al., Phys. Rev. Lett. **80**, 1292 (1998).
[6] S. J. Papadakis and M. Shayegan, Phys. Rev. B **57**, R15068 (1998).
[7] E. Abrahams, P. W. Anderson, D. C. Licciardello, and T. V. Ramakrishnan, Phys. Rev.\ Lett. **42**, 673 (1979).
[8] D. Simonian, S. V. Kravchenko, M. P. Sarachik, and V. M. Pudalov, Phys. Rev. Lett. **79**, 2304 (1997); V. M. Pudalov, G. Brunthaler, A. Prinz, and G. Bauer, JETP Lett. **65**, 932(1997).
[9] Y. Hanein et.al., preprint cond-mat/9901186 (1999) (Nature,in press).

MC.2

UNEXPECTED BEHAVIOR OF THE LOCAL COMPRESSIBILITY NEAR THE METAL-INSULATOR TRANSITION OF A TWO-DIMENSIONAL HOLE GAS

S. Ilani, A. Yacoby, D. Mahalu, and Hadas Shtrikman
Weizmann Institute of Science, Rehovot 76100, Israel.

We present, for the first time, measurements of the electronic compressibility of a two-dimensional hole gas (2DHG) as it crosses the zero magnetic field Metal-Insulator-Transition. The compressibility is found to behave qualitatively different on the metallic and insulating sides of the transition, where on each side a unique oscillatory structure is observed. Our results suggest that the system experience a thermodynamic change as it crosses the transition.

The recent discovery of a Two-Dimensional (2D) Metal-Insulator-Transition (MIT) has raised the fundamental question concerning the existence of metallic 2D systems. In contrast to the scaling theory of localization that predicts only an insulating phase in 2D, there is a growing amount of evidence for metallic-like behavior in many 2D systems. To date, the vast majority of this evidence comes from transport measurements.

If a true zero-temperature phase transition exists, it is expected to reveal itself also in thermodynamic properties of the 2D gas such as the magnetization or the electronic compressibility, $\kappa = n^{-2}\,\partial n/\partial\mu$ (where μ is the chemical potential and n is the carrier density). Moreover, the behavior of the compressibility at the critical point can further clarify the type of the transition: For example, a cross-over to a Mott insulator would result in a vanishing compressibility at the transition, whereas a cross-over to an Anderson insulator would involve a continuous evolution of the compressibility across the transition.

Macroscopic compressibility measurements of low-density 2D electron/hole gases were carried out in the past[1]. These measurements demonstrated a quantitative agreement with the theory of this interacting regime. The main observation was that μ *increases* monotonically with decreasing n (negative compressibility), contrary to the non-interacting case. These measurements however, could not be extended to sufficiently low densities where the metal insulator transition occurs.

In this work we have measured the density dependence of the *local* chemical potential, μ, across the MIT. The measurements utilize several Single Electron Transistors, situated directly above a 2DHG. This technique allows us not only to determine the local behavior of the chemical potential but also to study its spatial variations. Simultaneous transport measurements were conducted to ensure precise determination of the critical density within the same sample. The samples have a wide density range extending from high densities ($1\cdot10^{11}cm^{-2}$) to very low densities ($2\cdot10^{9}cm^{-2}$) around the critical density $n_C = 2\cdot10^{10}cm^{-2}$.

Our major findings are:

1) The measured *local* μ shows unexpected reproducible oscillatory structure. This structure stands in contrast to previous *macroscopic* measurements and to theoretical predictions.

2) Qualitatively different behaviors are seen on the metallic and on the insulating side, with a crossover that takes place at close proximity to the transport measured critical density.
3) On the metallic side, μ exhibits periodic oscillatory behavior as a function of density, with a characteristic scale of $(1-2)\cdot 10^{10} cm^{-2}$.
4) On the insulating side $\mu(n)$ has rapid saw-tooth-like oscillations, with a characteristic scale of $(1-2)\cdot 10^{9} cm^{-2}$. The number of peaks observed between critical and zero density roughly corresponds to the number of holes clearing out from the effective area of the detector at this density range.
5) Qualitatively similar behavior is found in several samples and at different points within a single sample. The details of the oscillatory behavior is however different, suggesting that it is of mesoscopic origin.

The behavior in the metallic phase cannot be explained within the framework of current macroscopic theories. We may however speculate, that the oscillatory structure in the insulating phase results from single-electron charging of isolated metallic islands that form once the system becomes insulating. Though currently unexplained, we believe that the observed structure holds an important clue for understanding the microscopic origin of the zero magnetic field metal-insulator transition.

[1] J. P. Eisenstein *et. al.*, Phys. Rev. Lett. **77**, 674 (1992); S. Shapira *et. al.*, Phys. Rev. Lett. **77**, 3181 (1996).

MC.3

Metal-Insulator Transition and Spin Degree of Freedom in Silicon 2D Electron Systems

T. Okamoto,[1] K. Hosoya,[1] S. Kawaji,[1] A. Yagi,[2] A. Yutani[3] and Y. Shiraki[3]
[1]*Department of Physics, Gakushuin University, Mejiro, Toshima-ku, Tokyo 171-8588, Japan*
[2]*NPC Ltd., Shiobara-cho, Tochigi 329-2811, Japan*
[3]*RCAST, The University of Tokyo, Komaba, Meguro-ku, Tokyo 153-0041, Japan*

Abstract

Magnetotransport in 2DES's formed in Si-MOSFET's and Si/SiGe quantum wells at low temperatures is reported. Metallic temperature dependence of resistivity is observed for the *n*-Si/SiGe sample even in a parallel magnetic field of 9 T, where the spins of electrons are expected to be polarized completely. Correlation between the spin polarization and minima in the diagonal resistivity observed by rotating the samples for various total strength of the magnetic field is also investigated.

Metallic temperature dependence of resistivity at a zero magnetic field has been observed in two-dimensional electron systems (2DES's) in Si-MOSFET's [1,2] and other 2D systems [3–8] characterized by strong Coulomb interaction between electrons (or holes) [7]. In experiments on Si-MOSFET's, it was found that a magnetic field applied parallel to the 2D plane can suppress the metallic behavior [9–11]. This result indicates that the spins of electrons play an important role in the metallic region as well as in the insulating region [12,13].

The parallel magnetic field $B_\parallel$ does not couple the orbital motion of electrons within the 2D plane, but it changes the spin polarization of the 2DES. The spin polarization can be defined as $p = (N_\uparrow - N_\downarrow)/N_s$, where $N_\uparrow$ and $N_\downarrow$ are the concentrations of electrons having an up spin and a down spin, respectively, and N_s is the total electron concentration ($N_s = N_\uparrow + N_\downarrow$). p is expected to increase linearly with the total strength $B_{\rm tot}$ ($= B_\parallel$) of the magnetic field. We have $p = B_{\rm tot}/B_c$ for $p < 1$ and $B_c = 2\pi\hbar^2 N_s/\mu_B g_v g_{\rm FL} m_{\rm FL}$ if the system can be considered as Fermi liquid. Here, $\mu_B (= \hbar e/2m_e)$ is the Bohr magneton and the valley degeneracy g_v is 2 on the (001) surface of silicon. The strong e-e interaction is expected to change the effective g-factor $g_{\rm FL}$ and the effective mass $m_{\rm FL}$ from $g^* = 2.0$ and $m^* = 0.19m_e$ in the non-interacting 2DES in a (001) silicon surface.

In the present work, we use two n-type silicon samples. A Si-MOSFET sample denoted Si-M has a peak electron mobility of $\mu_{\rm peak} = 2.4$ m^2/V s at $N_s = 4 \times 10^{15}$m^{-2} and $T = 0.3$ K. The estimated SiO_2 layer thickness is 98 nm. A Si/SiGe sample denoted Si-G was grown by combining gas-source MBE and solid-source MBE. Details of the growth and characterization have been reported elsewhere [14,15]. The thickness of the strained silicon channel layer is 20 nm. It is sandwiched between relaxed $Si_{0.8}Ge_{0.2}$ layers and separated from a Sb-δ-doped layer by a 20 nm spacer. The electron concentration N_s can be controlled by varying the substrate bias voltage above 20 K. It has a high mobility of $\mu = 66$ m^2/V s at $N_s = 2.2 \times 10^{15}$m^{-2} (at zero substrate bias volt-

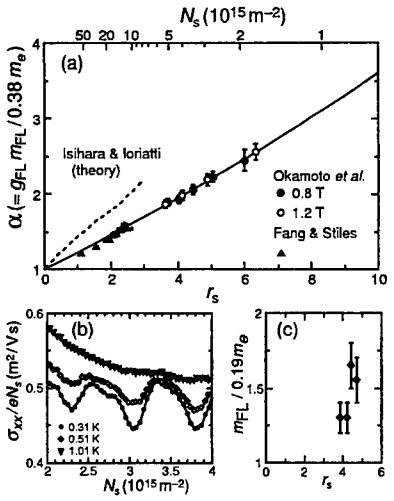

FIG. 1. (a) The enhancement factor $\alpha = (g_{FL}/g^*)/(m_{FL}/m^*)$. (b) Temperature dependence of the Shubnikov-de Haas oscillation at $B_{tot} = B_\perp = 0.8$ T. (c) The enhancement factor for the effective mass ($= m_{FL}/m^*$).

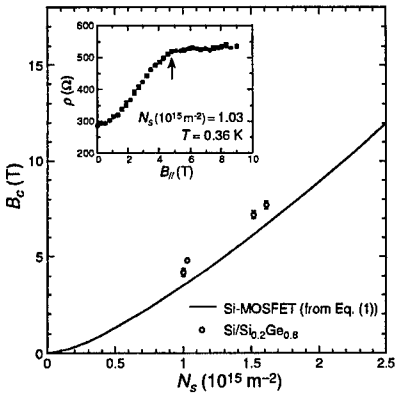

FIG. 2. Solid line represents B_c for Si-MOSFET's calculated using (1) (see text). Open circles are determined from the kink that appears in the ρ vs $B_\parallel$ curve for Si-G as shown in the inset.

age) and $T = 0.36$ K. The samples were mounted on a rotatory thermal stage in a pumped ^{3}He refrigerator or in a ^{3}He-^{4}He dilution refrigerator together with a GaAs Hall generator and resistance thermometers calibrated in magnetic fields.

In Ref. [11], some of the present authors have determined the product of g_{FL} and m_{FL} in Si-M from the low-temperature Shubnikov-de Haas oscillations in tilted magnetic field based on work of Fang and Styles [16]. The obtained enhancement factor $\alpha = g_{FL}m_{FL}/0.38m_e$ is shown in Fig. 1(a) as a function of $r_s = \pi^{1/2}(e/h)^2(m^*/\kappa\varepsilon_0)N_s^{-1/2}$. r_s is a dimensionless parameter indicating the ratio of the Coulomb energy to the Fermi energy. Here, $m^* = 0.19m_e$ and the relative dielectric constant $\kappa = 7.7$ are used. The dashed line represents calculation based on Ref. [17]. The previous experiment could not determine α for the low-N_s region, while the metallic behavior was clearly observed in this sample for $1 \le N_s(10^{15}\mathrm{m}^{-2}) \lesssim 2$ [11]. We assume a simple extrapolation function

$$\alpha - 1 = 0.2212r_s + 0.003973{r_s}^2. \qquad (1)$$

represented by the solid line in Fig. 1(a).

Fig. 1(b) shows typical temperature dependence of the Shubnikov-de Haas oscillation in a perpendicular field of 0.8 T. The effective mass roughly estimated is plotted in Fig. 1(c). The effective g-factor is expected to be also enhanced by the e-e interaction since $\alpha = (g_{FL}/g^*)/(m_{FL}/m^*)$ in Fig. 1(a) is larger than m_{FL}/m^*.

The critical magnetic field $B_c = 2\pi\hbar^2 N_s/\mu_B g_v g_{FL} m_{FL}$ for the complete spin polarization is calculated using (1) and shown as the solid line in Fig. 2. It was found that the low-temperature resistivity

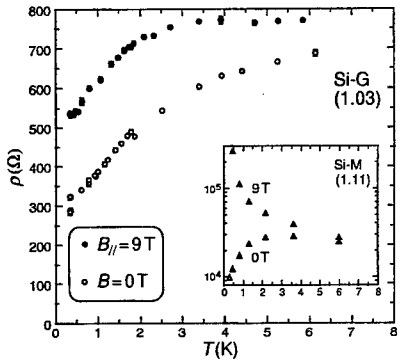

FIG. 3. Temperature dependence of resistivity of Si-G at $N_s = 1.03 \times 10^{15}\mathrm{m}^{-2}$ in a zero magnetic field and a parallel magnetic field of 9 T. The inset shows the data for Si-M at $N_s = 1.11 \times 10^{15}\mathrm{m}^{-2}$.

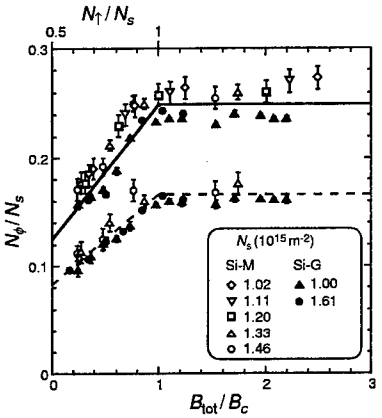

FIG. 4. Positions of the ρ_{xx} minima for different values of N_s in Si-M (Ref. [11]) and Si-G are plotted. Solid line represents $N_\uparrow/N_\phi = 4$. Dashed line represents $N_\uparrow/N_\phi = 6$.

of Si-MOSFET's increases with the parallel magnetic field and it saturates at high fields [9,10,12,13]. The saturation has been related with the complete spin polarization at B_c [11]. Similar magnetoresistance is also observed in Si-G, while the $B = 0$ resistivity is much smaller than that reported for Si-MOSFET's. Typical data are shown in the inset to Fig. 2. A sharp kink is observed at 4.8 T. The critical magnetic field in Si-G determined from the kink (open circles) is slightly higher than the solid line for Si-MOSFET's. We consider that the deviation arises from the difference in the effective dielectric constant in the proximity to the interface.

Figure 3 shows temperature dependence of the resistivity. The metallic temperature dependence ($d\rho/dT > 0$) in a zero magnetic field is observed in Si-G as well as in Si-M. The temperature dependence of ρ in Si-M changes to insulating in a parallel magnetic field (see the inset) as reported on other Si-MOSFET's [9,10]. On the other hand, the metallic temperature dependence is observed for Si-G even at $B_{||} = 9$ T, where the spins of electrons are expected to be polarized completely. The result indicates that the metallic behavior can appear even if the spin degree of freedom is limited.

Tilting the 2DES samples from the plane parallel to the magnetic field, one can apply the perpendicular component $B_\perp$ of the magnetic field independently of the total strength B_{tot}. Measurements on ρ_{xx} in the low-$B_\perp$ region for various fixed values of B_{tot} using Si-M have been reported in Ref. [11]. Unlike ordinary Shubnikov-de Haas oscillations which show ρ_{xx} minima at fixed points with $N_\phi/N_s = \mathrm{integer}^{-1}$ ($N_\phi = eB_\perp/h$), the N_ϕ/N_s values at the ρ_{xx} minima depend on the total strength B_{tot}.

Similar behavior was also observed for Si-G [18]. In Fig. 4, the positions of the ρ_{xx} minima for Si-M and Si-G are shown. B_{tot} is normalized by B_c presented in Fig. 2. All the data are distributed along the solid line

or the dashed line. The value of N_ϕ/N_s increases linearly with $B_{\rm tot}/B_c$ for $B_{\rm tot}/B_c < 1$, but saturates for $B_{\rm tot}/B_c \geq 1$ where the spin polarization is expected to be completed.

We link this behavior to the concentration $N_\uparrow$ of electrons having an up spin. Assuming that a change in p by N_ϕ/N_s is negligible in the low-N_ϕ/N_s region, we have $N_\uparrow/N_s = (1 + B_{\rm tot}/B_c)/2$ for $B_{\rm tot}/B_c < 1$ and $N_\uparrow/N_s = 1$ for $B_{\rm tot}/B_c \geq 1$. The number of "spin-up" electron per flux quantum takes constant value of $N_\uparrow/N_\phi = 4$ on the solid line or $N_\uparrow/N_\phi = 6$ on the dashed line.

The data plotted in Fig. 4 have been obtained in the metallic region and the insulating region. The resistivity at $B_\perp = 0$ ranges from 10^2 Ω to 10^6 Ω [11,18]. An interpretation based on the Shubnikov-de Haas oscillation seems to be hard to apply for the high resistivity region since the Landau level separation is considered to be entirely smeared out by the level broadening [11]. We believe that the ρ_{xx} minima linked with $N_\uparrow$ is inherent in the strongly correlated electron systems which show the metal-insulator transition.

In summary, we have studied the magnetotransport in 2DES's formed in silicon inversion layers using two samples having quite different electron mobilities. Positive temperature dependence of the resistivity was observed for a $Si/Si_{0.8}Ge_{0.2}$ quantum well even in a parallel magnetic field of 9 T, while the strong parallel magnetic field eliminates the metallic behavior in Si-MOSFET's. We also investigated the ρ_{xx} minima observed in the $B_\perp$-dependence. It was related to the concentrations of "spin-up" electrons.

This work is supported in part by Grants-in-Aid for Scientific Research from the Ministry of Education, Science, Sports and Culture, Japan, and High-Tech-Research Center in Gakushuin University.

References

[1] S. V. Kravchenko *et al.*, Phys. Rev. B **50** (1994) 8039.
[2] S. V. Kravchenko *et al.*, Phys. Rev. B **51** (1995) 7038.
[3] J. Lam *et al.*, Phys. Rev. B **56** (1997) 12741.
[4] P. T. Coleridge *et al.*, Phys. Rev. B **56** (1997) 12764.
[5] Y. Hanein *et al.*, Phys. Rev. Lett. **80** (1998) 1288.
[6] M. Y. Simmons *et al.*, Phys. Rev. Lett. **80** (1998) 1292.
[7] S. J. Papadakis and M. Shayegan, Phys. Rev. B **57** (1998) 15068.
[8] Y. Hanein *et al.*, Phys. Rev. B **58** (1998) 13338.
[9] D. Simonian *et al.*, Phys. Rev. Lett. **79** (1997) 2304.
[10] V. M. Pudalov *et al.*, Pis'ma Zh. Éksp. Teor. Fiz. **65** (1997) 887 [JETP Lett. **65** (1997) 932].
[11] T. Okamoto *et al.*, Phys. Rev. Lett. **82** (1999) 3875.
[12] T. Okamoto and S. Kawaji, J. Phys. Soc. Jpn. **65** (1996) 3716.
[13] T. Okamoto and S. Kawaji, Phys. Rev. B **57** (1998) 9097.
[14] A. Yutani and Y. Shiraki, Semicond. Sci. Technol. **11** (1996) 1009.
[15] A. Yutani and Y. Shiraki, J. Crys. Growth **175/176** (1997) 504.
[16] F. F. Fang and P. J. Stiles, Phys. Rev. **174** (1968) 823.
[17] A. Isihara and L. Ioriatti, Physica **113B** (1982) 42.
[18] T. Okamoto *et al.*, to be published elsewhere.

MC.4

Magnetic Field Dependence of the Metal-Insulator Transition in Ga[Al]As-Heterostructures

R. D. Jäggi,[1] M. von Waldkirch, T. Heinzel, E. Ribeiro*, K. Ensslin
Solid State Physics Laboratory, ETH Zürich, 8093 Zürich, Switzerland
G. Medeiros-Ribeiro, and P. M. Petroff
Materials Department, University of California, Santa Barbara, Ca 93106, USA

Abstract. A metal-insulator transition at zero magnetic field is observed in Ga[Al]As-heterostructures where a high density of self-assembled InAs-quantum dots is located in the region of the two-dimensional electron gas (2DEG). This transition occurs only in samples with high dot densities. In contrast to other two-dimensional systems showing a metallic phase the Coulomb energy is comparable to the kinetic energy in our systems.
Measurements in perpendicular fields reveal that the resistivity at B=0 is composed of several contributions. In the metallic regime a weak localization peak is superposed on top of a broad negative magnetoresistivity. In the insulating regime, the weak localization peak at B=0 develops into a very pronounced negative magnetoresistivity with decreasing electron density. Pronounced, almost B-periodic oscillations in the magnetoresistivity are observed in addition to universal conductance fluctuations.
PACS: 71.30.+h, 73.40.Kp

Introduction. Metal-insulator transitions (MIT) at zero magnetic field ($B = 0$) have been observed in various two-dimensional systems after the discovery in Si-MOSFETs [1]. The transition point is characterized by a critical charge carrier density, for which the resistivity becomes temperature independent at a value consistent with $k_F\ell \sim 1$ where k_F is the Fermi wave vector and ℓ is the elastic scattering length. At lower (higher) densities the resistivity displays a negative (positive) temperature gradient. Scaling theory [2] neglecting interactions does not predict the occurrence of a metallic phase in two-dimensional systems. To achieve theoretical understanding of the MIT various approaches have been considered, based on charge- or spin-dependent interactions.

We have observed a MIT at B=0 in Ga[Al]As-heterostructures where a high density of self-assembled InAs-quantum dots is incorporated within the region of the two-dimensional electron envelope wave function [3]. The MIT in our samples differs from other systems that show a metallic phase in two respects:

1) The electron-electron interaction energy E_{ee} is comparable to the kinetic energy E_F with $r_s = E_{ee}/E_F = (e^2\sqrt{\pi}/\varepsilon\varepsilon_0 h^2) \times (m^*/\sqrt{n_s}) = 1.6$ using the effective mass and permittivity of GaAs. In other systems r_s takes a value of the order of 10. Furthermore, the elastic scattering rate is $1/\tau_e \approx 30 \times 10^{11}\mathrm{s}^{-1}$ where τ_e is the scattering time. This is a factor 5 to 250 larger than in other systems [4].

2) The metallic phase in our system is not destroyed by in-plane magnetic fields up to 12T (data shown in [3]) in contrast to other systems [5].

Metal-insulator transition. The two-dimensional electron system is formed in a Ga[Al]As-heterostructure. Self-assembled InAs-dots have been incorporated 3nm below the heterointerface, near the maximum of the 2D-electronic wave function [6]. The GaAs wafer has not been rotated during the deposition of InAs. Hence, the density of InAs-dots varies gradually across the wafer from 0 to $\approx 5 \times 10^{14}\mathrm{m}^{-2}$ as determined from transmission electron

[1] Corresponding author: Tel. +41-1-6333908, Fax. +41-1-6331146, email: jaeggi@solid.phys.ethz.ch

microscopy and transport measurements. Details of the sample growth and characterization can be found in [6]. The wafer has been cut to yield samples with different dot densities which have been structured into Hall-bars. About two electrons are confined to each InAs dot. It was shown [6] that the quantum dots act as repulsive scattering centers located within the region of the 2D electron wave envelope. They are the relevant scattering centers in our system: the higher the density of dots, the lower the mobility of the 2DES.

In Fig. 1 the temperature dependent resistivity ρ_{xx} is plotted versus electron density n_s at zero magnetic field for two samples (denoted as sample A and B, respectively) from the high dot density region of the wafer. Note that the measurements for the two samples have been obtained at different temperature ranges. The transition from insulating to metallic behavior occurs at an electron density of $(1.21 \pm 0.08) \times 10^{15}\mathrm{m}^{-2}$ for sample A and $(1.25 \pm 0.2) \times 10^{15}\mathrm{m}^{-2}$ for sample B. The traces cross each other at $\rho_{xx} = (0.93 \pm 0.04) \times h/e^2$ (sample A) and $\rho_{xx} = 0.77(\pm 0.08) \times h/e^2$ (sample B). This is consistent with $k_F \ell \sim 1$. A high InAs-dot density of about $5 \times 10^{14}\mathrm{m}^{-2}$ is needed to produce a metallic phase. Samples with a lower dot density have a higher mobility but show insulating behavior in their temperature dependence only.

Perpendicular magnetic fields. Magnetoresistivity measurements in perpendicular magnetic fields $B_\perp$ are shown in Fig. 2 and Fig. 3. In the metallic phase, a weak localization peak is superposed on top of a broad negative magnetoresistivity background going up to 3T (Fig. 2). Pronounced, almost B-periodic oscillations in resistivity besides universal conductance fluctuations are superposed on top of this background in the magnetic field range between 0T and the Shubnikov-de Haas regime. The positions of the minima and maxima do not change with varying electron density, i. e. they even persist in the insulating phase (Fig. 3). The oscillation period is $\Delta B \approx 0.4$T for sample A and $\Delta B \approx 0.68$T for sample B. The oscillation amplitude is decreasing with increasing temperature (Fig. 2).

We tentatively attribute these oscillations to a modified type of Aharonov-Bohm effect described by Al'tshuler et. al [7]. The dephasing time in our systems increases with decreasing temperature to a value of $\tau_\phi \approx 17$ps at 300mK (data not shown) as determined from weak localization and universal conductance fluctuations. At temperatures below 300mK the dephasing time saturates. The phase coherence length is larger than 300nm below 300mK. We speculate that the electrons might perform closed trajectories, presumably around the InAs-dots, without loosing their phase and that they constructively interfere with the time-reversed wave functions. However, a phase shift is aquired proportional to the magnetic flux Φ_B enclosed in the trajectory of an electron. Therefore, as a function of perpendicular magnetic field, constructive and destructive interference of the time-reversed wave functions is obtained. This results in an oscillatory behavior of the resistivity. The oscillation period ΔB is proportional to the flux Φ_B through the area S enclosed in the trajectory: $\Delta B = (h/2e) \times 1/S$. Assuming that the trajectories around the dots are circles the radii corresponding to S would be 40nm and 31nm for sample A and B, respectively. This is in accordance with the situation in our samples where the distances between the centers of the dots is $\approx$ 44nm and the dot diameter is $\approx$ 20nm. The circumference of such a path is 250nm and 207nm, respectively. With increasing temperature, the phase coherence length is decreasing from $>$ 300nm below 300mK to $\sim$ 170nm at 800mK. As observed in our data (Fig. 2) the oscillating behavior has to disappear with increasing temperature because the phase coherence is lost on the path corresponding to the circumference.

Because the electrons interfere with their time-reversed trajectories after a full trip around the dots, this effect is insensitive to changes of the path length around the dots of the order of $\lambda_F \approx 14$ to 50nm. Presumably, the ordinary Aharonov-Bohm effect is not relevant for the observed oscillations in magnetoresistivity, since it is drastically averaged out if the

fluxes enclosed in the trajectories around the dots are not identical for each dot.

In the following, the behavior of the magnetoresistivity in the metallic phase is compared to the insulating phase. As mentioned above, in the metallic regime a weak localization peak is superposed on top of a broad negative magnetoresistivity background going up to 3T. At higher magnetic fields, Shubnikov-de Haas (SdH) oscillations are observed. Note that the resistivity displays metallic behavior up to and within the SdH-regime without showing the typical crossing point corresponding to quantum-Hall insulator-to-metal phase transitions [8] (Fig. 2). In the insulating regime, the weak localization peak at $B = 0$ develops into a pronounced negative magnetoresistivity with decreasing electron density (Fig. 3). The resistivity at $B = 0$ decays exponentially with increasing temperature, indicating hopping transport in the insulating phase (fit not shown). Apparently several mechanisms with different temperature dependences contribute to the resistivity at $B = 0$. In the metallic regime (Fig. 2) the increase in resistivity with increasing temperature (i. e. metallic behavior) is due to the mechanism which shows the broad negative magnetoresistivity background. This delocalizing mechanism is stronger than weak localization, because the reduction of the weak localization peak height with temperature is not sufficient to result in an overall insulating behavior. With decreasing electron density the peak at $B = 0$ becomes the dominant mechanism resulting in an insulating temperature dependence.

In conclusion, we have observed a metal-insulator transition at $B = 0$ in a 2D system in Ga[Al]As with InAs-quantum dots as the relevant scattering centers. A metallic phase can only be observed for samples with a high density of InAs dots. Apparently, the MIT is due to interactions between electrons and quantum dots. The detailed potential landscape around the dots and the spin configuration of the confined electrons remains to be understood in detail, but presumably is an important key to the understanding of the MIT in our systems. The behavior of the resistivity in perpendicular magnetic fields is discussed with regard to the MIT. Oscillations in longitudinal magnetoresistivity observed at low magnetic fields are attributed to a modified Aharonov- Bohm effect.

We are grateful to T. Ihn and V. Senz for helpful discussions. This work was supported by the Schweizerische Nationalfonds and by QUEST. E. R. acknowledges financial support from Fundação de Amparo à Pesquisa do Estado de São Paulo.

References

* Present address: Instituto de Física "Gleb Wataghin", UNICAMP, 13081-970 Campinas, SP, Brazil.

[1] S. V. Kravchenko, G. V. Kravchenko, J. E. Furneaux, V. M. Pudalov, and M. D'Iorio, Phys. Rev. B **50**, 8039 (1994)

[2] E. Abrahams, P. W. Anderson, D. C. Licciardello, and T. V. Ramakrishnan, Phys. Rev. Lett. **42**, 673 (1979)

[3] E. Ribeiro, R. D. Jäggi, T. Heinzel, K. Ensslin, G. Medeiros-Ribeiro, and P. M. Petroff, Phys. Rev. Lett. **82**, 996 (1999)

[4] J. Yoon, C. C. Li, D. Shahar, D. C. Tsui, and M. Shayegan, Phys. Rev. Lett. **82**, 1744 (1999)

[5] D. Simonian, S. V. Kravchenko, M. P. Sarachik, and V. M. Pudalov, Phys. Rev. Lett. **79**, 2304 (1997)

[6] E. Ribeiro, E. Müller, T. Heinzel, H. Auderset, K. Ensslin, G. Medeiros-Ribeiro, and P. M. Petroff, Phys. Rev. B **58**, 51506 (1998)

[7] B. L. Al'tshuler, A. G. Aronov, and B. Z. Spivak, JETP Lett. **33**,94 (1981)

[8] Y. Hanein, D. Shahar, H. Shtrikman, J. Yoon, C. C. Li, and D. C. Tsui, cond-mat/9901186

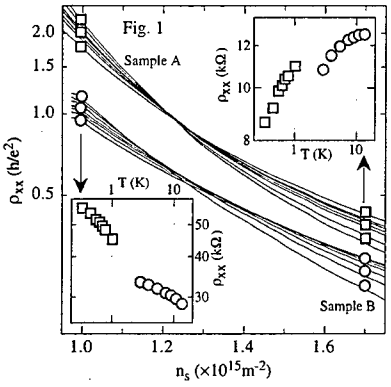

Fig. 1. ρ_{xx} as a function of electron density n_s for a set of temperatures ranging from 0.33K to 1.02K for sample A (squares) and from 2.9K to 13.6K for sample B (circles). These two samples have a high InAs-dot density of $\approx 5 \times 10^{14}\mathrm{m}^{-2}$. The curves from sample B have been offset by $-0.2 \times h/e^2$. Insets: temperature dependence of the resistivity at fixed electron densities illustrating metallic ($d\rho/dT > 0$) and insulating ($d\rho/dT < 0$) behavior. Upper inset: $n_s = 1.7 \times 10^{15}\mathrm{m}^{-2}$ (metallic phase). Lower inset: $n_s = 1.0 \times 10^{15}\mathrm{m}^{-2}$ (insulating phase).

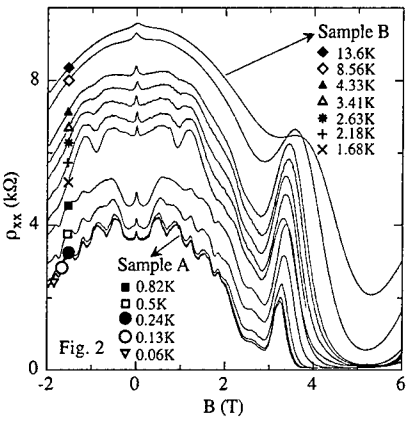

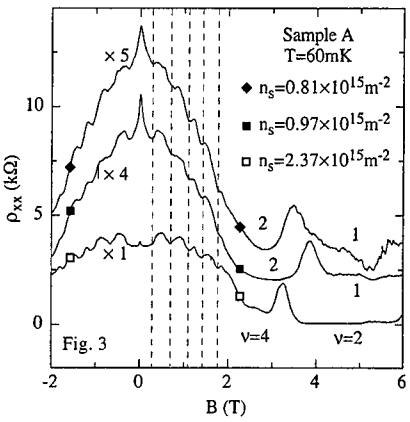

Fig. 2. Resistivity vs. perpendicular magnetic field B in the metallic phase at comparable electron densities of 2.24 (sample A) and $2.37 \times 10^{15}\mathrm{m}^{-2}$ (sample B), respectively; corresponding temperatures are referenced by symbols. B-periodic oscillations in resistivity are visible in the magnetic field range below 3T with periods $\Delta B \approx 0.4T$ (sample A) and $\Delta B \approx 0.68T$ (sample B). At $B > 3$T Shubnikov-de Haas oscillations are observed.

Fig. 3. Magnetoresistivity for three fixed electron densities in sample A. Corresponding electron densities are referenced by symbols; $n_s < 1.2 \times 10^{15}\mathrm{m}^{-2}$ belong to the insulating phase, $n_s > 1.2 \times 10^{15}\mathrm{m}^{-2}$ belongs to the metallic phase. The plots are scaled down by the factors indicated and offset for clarity. The minima of the B-periodic oscillations are connected by dashed lines to illustrate that the oscillation period $\Delta B \approx 0.4T$ (sample A) is independent of electron density. Note that the peak at $B = 0$ is growing with decreasing electron density. To the right, the filling factors ν corresponding to fully occupied Landau levels are indicated.

MC.5

Universal Behaviour of Metal-Insulator Transitions in the p-SiGe System

P.T. Coleridge, P. Zawadzki, A.S. Sachrajda, R.L. Williams and Y. Feng
Institute for Microstructural Sciences, National Research Council of Canada, Ottawa, Ontario, K1A 0R6, Canada

Magnetoresistance measurements are presented for a strained p-SiGe quantum well sample where the density is varied through the B=0 metal-insulator transition. The close relationship between this transition, the high field Hall insulator transition and the filling factor ν=3/2 insulating state is demonstrated.

The strained p-type SiGe system exhibits, in addition to the normal integer quantum Hall effect (IQHE) transitions, an insulating phase near filling factor $\nu = 3/2$ [1,2] and a B=0 metal-insulator transition of the kind observed in high mobility Si-MOSFETs [3]. Results are presented here that show the close relationship between these various transitions.

Samples were grown by a UHV chemical vapour deposition process. An intrinsic Si layer is followed by a 40nm $Si_{.88}$ $Ge_{.12}$ quantum well, a spacer layer of variable thickness and a boron doped silicon layer. The quantum well is sufficiently narrow that the lattice constant difference between the alloy and the pure Si is all taken up by strain which means the heavy hole band, characterised by a $|M_J| = 3/2$ symmetry, is well separated from other bands. The g-factor is large (of order 6) and depends only on the perpendicular component of magnetic field [4,5]. At high fields the spin splitting is further enhanced by exchange resulting in a fully polarised "ferromagnetic" spin system at $\nu = 2$. The ratio of the transport and quantum lifetimes, determined from the Shubnikov-de Haas oscillations, is about one [6] showing that the disorder is dominated by a short-ranged scattering potential.

Transitions between the N_L and N_{L+1} integer quantum Hall states are well described (in units of e^2/h) by [7]

$$\sigma_{xx} = s/(1+s^2), \qquad \sigma_{xy} = N_L + 1/(1+s^2). \tag{1}$$

with a scattering parameter s, (which can be identified with the Chern-Simons boson conductivity $\sigma_{xx}^{(b)}$ [8]) given by

$$s = \exp[(\nu_c - \nu)(T_0/T)^{\kappa}]. \tag{2}$$

Here ν_c is the critical filling factor and the exponent κ is close to 3/7 at low temperatures. For N_L =0, ie at the termination of the Quantum Hall sequence, this gives

$$\rho_{xx} = s, \qquad \rho_{xy} = 1 \tag{3}$$

corresponding to a quantised Hall insulator.

Near $\nu = 1.5$ another insulating phase is observed in many samples. The presence of this phase depends on density, disorder and on magnetic field tilt [1,2]. An activation analysis [2] correlates insulating behaviour with the existence of degenerate spin states at the Fermi level: that is it is suppressed when the ferromagnetic polarisation of the spins at $\nu = 2$

persists through $\nu = 1.5$ as the field is increased. This can be demonstrated to be a re-entrant transition, growing out of the $\nu = 1$ IQHE state although, but when it is very strongly developed it appears to grow directly out of the $\nu = 2$ or 3 states.

Figure 1a shows the ν=3/2 and high field Hall insulating transitions measured using a two terminal technique in a sample with a density of 1.4 $\times 10^{11}$cm^{-2}. A scaling plot of this data (fig.1b) shows ρ_{xx} plotted against $(\nu_c - \nu)/T^{\kappa}$ with $\kappa = 3/7$. There is good agreement with eqn.2 in both cases with slightly different values of T_0. The scaling deteriorates in the $\nu = 3/2$ insulating phase because of the close proximity of the two critical points.

For the B=0 metal-insulator transition the temperature dependence of ρ_{xx} in the insulating phase is well described over several orders of magnitude, by $\rho_c \exp[(T_0/T)^n]$ with $\rho_c \sim 0.5 h/e^2$ and n $\sim$ 0.4 [6]. In the metallic phase, at low T, it is of the general form

$$\rho_{xx}(T) = \rho_0 + \rho_1 \exp[-(T_1/T)^p]. \quad (4)$$

As is commonly observed in these systems [9,10], for densities near the critical value the resistance does not always increase monotonically and often has a maximum and a tilted separatrix between the metallic and insulating phases. This makes it difficult to independently determine the prefactor ρ_1 and the exponent p by fitting to eqn.4. Choices of p=1 (and ρ_1 small) or alternatively p $\approx$ 0.4 (with ρ_1 then of order 0.5 h/e^2) are equally successful. In each case, however, the parameter T_1 varies with density and there is a general similarity to eqn. 2.

Although the temperature dependence in the "metallic" phase is dominated by activated behaviour there is also evidence of weak localisation [11]. Within experimental error, a ln(T) term cannot be detected directly, but the negative magnetoresistance around B = 0 and positive behaviour at higher fields, can be consistently interpreted in terms of a sum of weak localisation and Zeeman contributions. The value of F* [12] extracted in this way is large (2.45). Combined with the cancellation between the two terms it leads to a coefficient for the ln(T) behaviour which is close to zero, consistent with the experimental data.

Figure 2 shows magnetoresistance data for a sample where the density was varied, by exploiting a persistent photoconductivity effect, through the B=0 critical value. The zero field resistivities (figure 3) show the critical density is 7.8 $\times$ 10^{10}cm^{-2} . For the highest density trace (figure 2a) there are three fixed points corresponding respectively to transitions into the $\nu = 3/2$ insulating phase, into the $\nu = 1$ QHE state and into the high field Hall insulating phase. As the density is reduced the first transition disappears (or moves to a much lower field); this is followed, in the next trace by the simultaneous disappearance of the two higher field fixed points so, at the lowest density, the temperature dependence over the whole field range is insulating. The low field Hall resistance is well defined through the whole range of densities. This indicates a Hall insulator with σ_{xx} and σ_{xy} both diverging but with the ratio $\rho_{xy} = \sigma_{xy}/\sigma_{xx}^2$ taking the classical value (B/pe, where p is the density). At higher fields it retains this classical behaviour until it becomes quantised near ν=1 and approximate quantisation then continues well into the high field insulating state, consistent with eqn.3.

The critical resistivities for all three transitions: the B=0 transition, the $\nu = 3/2$ transition, and the high field Hall insulator transition are approximately 0.5 h/e^2. In contrast to the situation in p-GaAs[[10]] the resistivity at the high field transition point (and also for

the $\nu = 1.5$ transition) is almost independent of density. Furthermore, the B = 0 transition is unchanged by magnetic field. Again, this is in contrast to the situation in p-GaAs where the B=0 transition transforms smoothing into the IQH effect transition. This difference in behaviour is probably a consequence of the strong spin-coupling in p-SiGe which quenches the independent degree of freedom of the spins.

The behaviour is summarised in a phase diagram (figure 4) which is to some extent schematic. At high densities a well defined Landau level structure is observed with the re-entrant $\nu = 3/2$ insulating phase. At lower densities this is washed out in a region where Γ (the Landau level broadening) is larger than $\hbar\omega_c$ (the Landau level spacing), but the high field and $\nu = 3/2$ insulating phases persist. At the lowest density the behaviour is insulating, over the whole field range, with no clear distinction between the three types of insulating behaviour. The well-known "floating-up" of the lowest Landau level is shown. In this case the condition $\Gamma = \hbar\omega_c$ is the same as the criterion for the appearance of the insulating behaviour $k_F l = 1$ (where l is the mean free path). For higher Landau levels, however, this is not the case and the disappearance of the Landau levels must be associated more with the dominance of the disorder than with "floating-up".

In all cases spin plays an important role. For the B = 0 transition, in the insulating phase, this is demonstrated by the insensitivity to magnetic field; in the metallic regime it is presumeably is the cause of the large value of F^*. The high field quantised Hall insulating state is, by definition, spin polarised and spins also seem to play a role in the formation of the $\nu = 3/2$ insulating state.

REFERENCES

[1] R.B. Dunford *et al*, Surface Science **361/362**, 550 (1996); S.I. Dorozhkin *et al*, Surface Science **361/362**, 933 (1996)

[2] P.T. Coleridge *et al*, Sol. St. Comm. **102**, 755 (1997)

[3] S.V. Kravchenko *et al*, Phys. Rev. B **51**,7038 (1995); S.V. Kravchenko *et al*, Phys. Rev. Lett. **77**, 4938 (1996)

[4] F. Fang *et al*, Surface Science **263**, 175 (1992)

[5] P.T. Coleridge *et al*, Phys. Rev. B **54**, 14518 (1996)

[6] P.T. Coleridge, R.L. Williams, Y. Feng and P. Zawadzki, Phys. Rev. B **56** , R12764 (1997)

[7] P.T. Coleridge, Phys. Rev. B (accepted); see also preprint cond-mat/9902103.

[8] S. Kivelson, D.-H. Lee and S.-C. Zhang, Phys. Rev. B **46**, 2223 (1992)

[9] A.P. Mills *et al*, preprint cond-mat/9905176

[10] Y. Hanein *et al* preprint cond-mat/9901186

[11] P.T. Coleridge, Proc. XXXIV Rencontres de Moriand, (1999)

[12] P.A. Lee and T.V. Ramakrishnan, Reviews of Modern Physics **57**, 287 (1985)

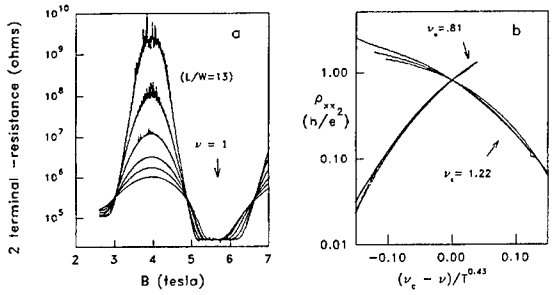

FIG. 1. (a) Two terminal resistance showing the $\nu = 3/2$ insulating phase with a critical point at ν_c=1.22 and the high field Hall insulating transition (with ν_c=.81) at T = 75, 120, 220, 400, 600 and 900mK. (b) Scaling plot for the 120,220 and 400mK data from (a).

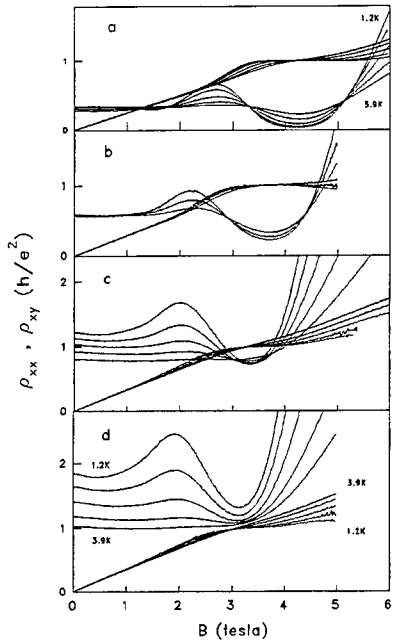

FIG. 2. Magnetoresistance at temperatures of 1.2, 1.55, 2.15, 3.0 and 3.9K for densities (in units of 10^{10}cm^{-2}) of:(a) 9.7, (b) 8.1 (1.2 - 2.15K data only) , (c) 7.0, (d) 6.6.

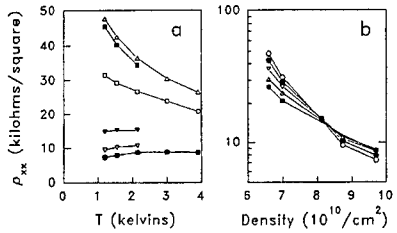

FIG. 3. Zero field resistivity (a) as a function of T; (b) as a function of density.

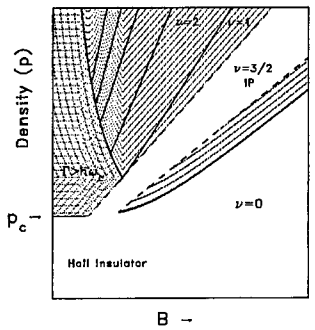

FIG. 4. Schematic phase diagram showing Landau levels, the re-entrant insulating phase at ν=3/2 and the high field insulating phase. p_c is the B=0 critical density. Note also the region where the Landau level broadening is larger than the spacing.

PA.1

The thermopower of a high-mobility Si-MOSFET around the metal-insulator transition

R. Fletcher, Physics Dept., Queen's University, Kingston, Ontario, Canada K7L 3N6.
V. M. Pudalov, Solid State Physics, P. N. Lebedev Institute, 117924 Moscow, Russia.
M. Tsaousidou and P. N. Butcher, Physics. Dept., University of Warwick, Coventry, UK, CV4 7AL.

The thermopower of a high mobility Si-MOSFET sample has been measured as a function of electron density around the metal-insulator transition over the temperature range of about 0.5-4 K. Both diffusion and phonon drag effects are clearly seen, the latter for the first time in an insulator. Each contribution appears to vary smoothly through the MIT with neither reflecting the strong variation observed in the conductivity.

High mobility Si-MOSFETs show a metal-insulator transition (MIT) as the carrier density, n, is decreased, the origin of which is not yet understood. All previous work has focussed on the resistivity, ρ, e.g., see [1]. In contrast the present experiments investigate the thermopower, S. There are two additive, but essentially independent, contributions to S, diffusion, S^d, and phonon drag, S^g. The latter arises from momentum transferred to the electrons from the non-equilibrium distribution of phonons and, in normal metallic systems, it is a direct measure of the phonon limited electron mobility and electron-phonon interaction [2]. At low temperatures it is insensitive to impurity scattering, and recently it was shown to be independent of the presence of weak localization [2]. The temperature variation of S^g is rapid, perhaps $\sim T^3$, in the temperature range examined here. In Si-MOSFETs, conduction on the insulator side of the MIT is believed to be due to Mott VRH, or Efros-Shklovskii VRH with a Coulomb gap at the Fermi level ε_F [1]. For VRH $\rho = \rho_o \exp(T_o/T)^r$ where T_o is a constant and $r = 1/3$ or $1/2$ for the two cases respectively. Zvyagin [3] and Pollack and Friedman [4] predict S^g to be zero for VRH but there seems to be almost no previous experimental information pertaining to this problem. Andreev *et al.* [5] have claimed that their data on transmutation-doped Ge:Ga are in agreement with the prediction, but the evidence is not convincing.

In normal metallic samples S^d is given by the Mott relation $S^d = (\pi^2 k_B^2 T/3e)(\partial \ln \rho/\partial \varepsilon)_{\varepsilon_F}$ where ε is the electron energy. When the electron relaxation time varies as τ^p, this becomes $S^d = -(\pi^2 k_B^2 T/3e\varepsilon_F)(p+1)$. For Efros-Shklovskii VRH, Burns and Chaikin [6] (see also Zvyagin [3]) predict S^d to be a constant given by $S^d = -(k_B/e)(k_B T_o/C)(\partial \ln N/\partial \varepsilon)_{\varepsilon_F}$ where N is the density of states. In this case $k_B T_o = Ce^2/4\pi\epsilon_o \kappa a$, with a the localization length, κ the dielectric constant, ϵ_o the permittivity of free space and C a constant estimated to be about 6.2. As far as we are aware, such behaviour has never been seen experimentally in either 2D or 3D.

The present experiments were carried out at zero magnetic field over the temperature range 0.5-4.2K on a Si-MOSFET with peak mobility of about 1.7 m^2/Vs at 1.1K. The low T limit for thermopower measurements on the insulating side of the MIT was determined by the difficulty of resolving μV signals with high sample resistances. Fig. 1 shows $\log \rho$ at various fixed n as a function of $1/\sqrt{T}$. The MIT occurs at $n \approx 1.01 \times 10^{15} m^{-2}$ for this sample. We expect straight lines for Efros-Shklovskii VRH on the insulating side. The data show only approximate straight lines which is perhaps due the fact that T_o is only 8K and 2.4K at the lowest and next lowest densities shown. Data at lower densities (not shown) do give good straight lines.

Fig. 2 shows S, mostly for the same n as in Fig. 1. We identify the rapid falloff as T is lowered with phonon drag, and the weaker low T dependence with diffusion. There are no strong features immediately visible that indicate the presence of the MIT. In all cases S does not exhibit saturation to a constant at low T, as expected with S^d for Efros-Shklovskii VRH. An estimate of S^d for this case requires $(\partial \ln N/\partial \varepsilon)_{\varepsilon_F}$, which is zero for clean 2D systems. With $(\partial \ln N/\partial \varepsilon)_{\varepsilon_F} \sim 1/\varepsilon_F$ we find $S^d \sim 19 \mu V/K$ and $5 \mu V/K$ for the lowest and next lowest n shown, which are too small to resolve at the present time. Mott VRH may be more appropriate near the MIT, which gives $S^d \propto T^{1/3}$ [3,6] with magnitudes similar to the Efros-Shklovskii model, but this T dependence is also too weak to explain the data. Instead S appears to tend to a linear dependence at low T typical of S^d in normal metals, and the dashed lines are our best estimates of S^d assuming they are given by the Mott relation quoted above. The lines are actually curved because the degeneracy temperatures are low in these samples. The inset of Fig. 2 gives the variation of p with n, which shows no obvious evidence of the MIT. We note that current theories [7] for an Anderson disorder-induced MIT predict $S^d \propto k_B T/(\varepsilon_F - \varepsilon_c)$ (providing this ratio is $\ll 1$, except very close to the MIT where one obtains a constant) on the metal side with ε_c being the energy of the mobility edge; on the insulator side S^d diverges as T is lowered. We see no such behaviour here.

Fig. 3 shows S^g evaluated from $S^g = S - S^d$. The magnitude of S^g again shows no discontinuities nor any other prominent feature at the MIT. There is no evidence favouring the prediction $S^g = 0$ on the insulating side as mentioned above [3,4]. This is a surprise because this prediction is based on the fact that phonon drag requires the conservation of crystal momentum, which should not be satisfied for phonon mediated transitions between localized states in the VRH regime.

In the absence of a more appropriate theoretical framework for this problem, we have attempted to describe our S^g data using the standard Boltzmann formalism which we have successfully used recently for the same Si-MOSFET at $n = 8.5 \times 10^{15} m^{-2}$, well away from the MIT [8]; full details for the S^g expression and the values for the material parameters are given in that paper. Fig. 4 shows the results for two different values of n: 1.24×10^{15} m^{-2} (metallic) and 0.79×10^{15} m^{-2} (insulating). The symbols are the experimental values and the dashed lines are the theoretical results using screening of the electron-phonon interaction as described by the static dielectric function given in [8]. The results are not in good agreement with experiment. Clearly this description is not adequate near the MIT and the role of dynamical screening should be examined. Inspection of the resistivity data shows that the product of the electron mean free path l and the in-plane phonon wave number q is < 1

at all T, especially on the insulator side. In this case the screening dielectric function should be evaluated in the dirty limit [9]. The crucial quantity here is the polarization $\Pi(\omega, q) = \nu_F Dq^2/(i\omega + Dq^2)$, where $\nu_F = m^{*2}/\pi\hbar^2$ and $D = v_F l/2$ is the diffusion coefficient with v_F the electron velocity at the Fermi level [9]. We calculate l from the resistivity data and substitute it in the expression for $\Pi(\omega, q)$. The values of S^g calculated in this manner are shown by the dot-dash lines in Fig. 4, but again agreement is not good. We also show calculations without screening (dotted) but these too are not very successful in describing the data. The most interesting results are obtained by multiplying the frequency in denominator of $\Pi(\omega, q)$ with a scaling factor Z [10]. The best fits to the data, the solid lines, result from using $Z = (\rho_f/\rho)(1 + T_f^{-1}T)$, where $\rho_f = 39\ k\Omega$, $T_f = 1$ K and ρ is the measured resistivity in $k\Omega$ as function of T. This empirical form for Z gives very good agreement with the S^g data for all n between $0.79 - 1.24 \times 10^{15}\,\mathrm{m}^{-2}$.

In conclusion, we are unable to qualitatively detect the MIT from the behaviour of the thermopower. However, this is the first time that S^g has been unambiguously observed on the insulating side of a MIT, either in 2D or 3D; our results imply, surprisingly, that electron-phonon scattering varies smoothly through the MIT.

[1] S. V. Kravchenko, W. E. Mason, G. E. Bowker, J. E. Furneaux, V. M. Pudalov and M. D'Iorio, Phys. Rev. B**51**, 7038 (1995).
[2] A. Miele, R. Fletcher, E. Zaremba, J. J. Harris, C. T. Foxon and Y. Feng, Phys. Rev. B**58**, 13181 (1998).
[3] I. P. Zvyagin in *Hopping transport in solids* edited by M. Pollak and B. Shklovskii, (North-Holland, Amsterdam) p143. (1991).
[4] M. Pollack and L. Friedman in *Localization and Metal-Insulator Transitions* edited by H. Fritzsche and D. Adler, (Plenum, N. Y.) p347 (1995).
[5] A. G. Andreev, A. G. Zabrodskii, S. V. Egorov and I. P. Zvyagin, phys. stat. sol. (b) **205**, 381 (1998).
[6] M. J. Burns and P. M. Chaikin, J. Phys. C: Solid State Phys., **18** L743 (1985).
[7] C. Villagonzalo, R. A. Romer and M. Schrieber, Cond-mat/9904362.
[8] R. Fletcher, V. M. Pudalov, Y. Feng, M. Tsaousidou and P. N. Butcher, Phys. Rev. B**56**, 12422 (1997).
[9] D. V. Khveshchenko and M. Yu. Reizer, Phys. Rev. Lett.**78**, 3531 (1997).
[10] C. Castellani, C. Di Castro and P. A. Lee, Phys. Rev. B**57**, R9381 (1998).

Figure Captions

Fig.1 Resistivity ρ (on a logarithmic scale) as a function $1/\sqrt{T}$ at various n (in units of $10^{15}\,\mathrm{m}^{-2}$).
Fig.2 Experimental S versus T at various n. The dashed lines are the estimated S^d. The inset shows p versus n.
Fig.3 Experimental S^g versus T at various fixed n.
Fig.4 Calculated results for S^g versus T at $n = 0.79 \times 10^{15}\,\mathrm{m}^{-2}$ and $1.24 \times 10^{15}\,\mathrm{m}^{-2}$ for various screening functions. The text gives the details.

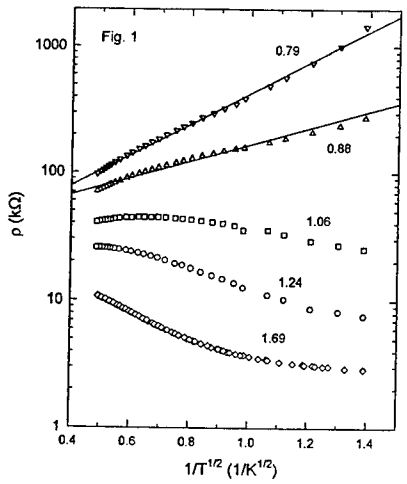
Fig. 1
0.79
0.88
1.06
1.24
1.69
ρ (kΩ)
1/T^1/2 (1/K^1/2)

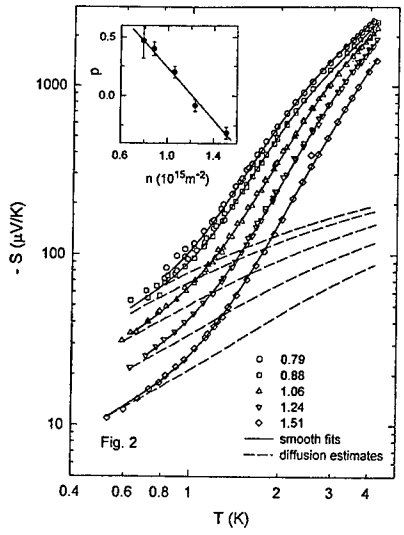
ρ
n (10^15 m^-2)
- S (μV/K)
0.79
0.88
1.06
1.24
1.51
smooth fits
diffusion estimates
Fig. 2
T (K)

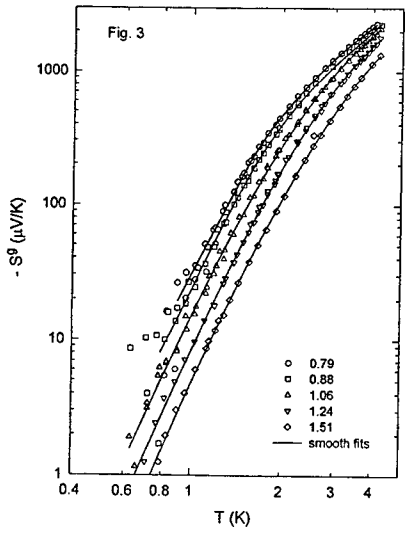
Fig. 3
- S^g (μV/K)
0.79
0.88
1.06
1.24
1.51
smooth fits
T (K)

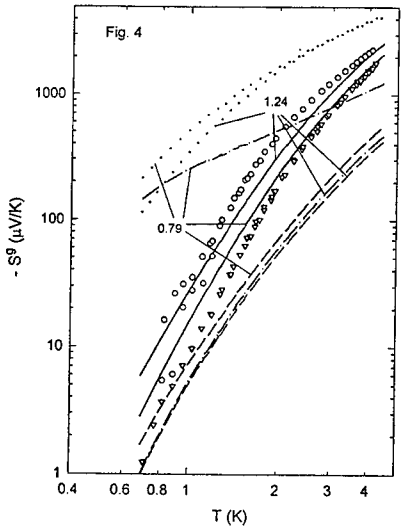
Fig. 4
1.24
0.79
- S^g (μV/K)
T (K)

PA.2

NOVEL EFFECTS PRODUCED ON A TWO DIMENSIONAL ELECTRON GAS BY INTRODUCING InAs DOTS IN THE PLANE OF THE QUANTUM WELL

S. Cina'[$*], D.D. Arnone[$], H.P. Hughes[*], D. Whittaker[$], M. Pepper[$*], and D.A. Ritchie[*]

** Cavendish Laboratory, University of Cambridge, Madingley Road, Cambridge, UK*
\$ Toshiba Research Europe Limited, 260 Science Park, Milton Road, Cambridge, UK

We show that the presence of InAs dots embedded in a host GaAs quantum well containing a two-dimensional electron gas dramatically modifies the cyclotron resonance (CR). Far infrared CR measurements show two modes with different dispersions with applied magnetic field B. The lower frequency mode, with a sub-linear dependence on B, is identified as a CR at low B, developing into a skipping orbit around the dot perimeters at higher B. This has not been previously observed for a system with randomly distributed scatterers. The higher frequency mode is identified as a magnetoplasmon localised by the confining effect of the arrays of repulsive potentials due to the dots in the well.

Far infrared spectroscopy of a 2DEG in the absence of impurities or other potential fluctuations in or near the QW which destroy its in-plane translational invariance, produce a single CR absorption mode [1]. In the present study, self-organised InAs dots are introduced into a GaAs QW, breaking the translational invariance of the 2DEG and splitting the CR mode into two modes with different dispersions with magnetic field B. The effects observed are distinct in important respects from previous work in which charged impurities were placed close to the QW [2,3], in that one mode shows a clear sub-linear dependence on B and the two observed modes have a significantly different dependence on carrier density.

The samples were fabricated on an undoped (100) GaAs substrate by first growing 600 nm of GaAs at 580°C, followed by a 50 nm undoped AlGaAs barrier, a 30 nm GaAs QW, a 40 nm undoped AlGaAs spacing layer, a 40 nm Si-doped (1×10^{18} cm^{-3}) AlGaAs layer, and a 17 nm GaAs capping layer. A semi-transparent (7 nm) NiCr gate on top of the structure allowed control of the 2DEG carrier density N_s. Following the Stranski-Krastanov technique [4], several samples with different dot densities (N_d) and different dot radius (R_d) were studied. Since similar behaviour was observed in all the different samples, in this paper we concentrate on two samples with different R_d, produced by including respectively 2.0 (sample a) and 2.8 (sample b) monolayers of InAs in the centre of the QW. Previous studies of the structural and electrical properties of the same samples have been reported [5], and values of R_d and N_d, averaged over a large area (12 μm^2) were measured directly by using transmission electron microscopy (TEM).

Magnetotransport and FIR CR measurements (using a Fourier transform spectrometer) were performed at 3.3 K using a 4 mm^2 Hall bar on a wedged substrate (5°) to avoid interference effects. N_s at different gate biases (V_g) were estimated from Shubnikov-de Haas measurements. The relative FIR transmission ($\Delta T/T=1-T(B)/T(B=0)$) measured for a reference sample containing no InAs dots showed a single CR peak with a frequency well described by $\omega_c=eB/m^*$ (with $m^*=0.070\ m_e$, e the electronic charge and m_e the free electron mass), as expected [1]. Similar FIR measurements were made for samples a and b. Fig. 2 shows spectra for $N_s=2.6\times10^{11}$ cm^{-2} at various B for sample a, and Fig. 3 shows the CR peak position vs. B for sample b at the same N_s. A single peak is observed for $B\leq$ 2.7 T and $B>4.6$ T for sample a ($B\leq$ 4.2 T and $B>7.2$ T for b), while at intermediate fields two peaks are observed. The intensities of these peaks, proportional to the number of electrons involved in each transition, change markedly with B. For sample a the higher

frequency mode is first observed at B=3.2 T, and its intensity is ~30% that of the lower mode. The intensities become equal around B=4 T, and at B=4.6 T, when the lower mode is last observed, the intensity of the higher mode is 3 times that of the lower. Similar behaviour occurs for sample b. The frequencies of the lower modes in each sample lie below the CR line, and, as shown for sample b in Fig. 3, they also vary sub-linearly with B. Because of their lower conduction band minima, the InAs dots, coexisting with the 2DEG, must be negatively charged [6]. This results in a repulsive potential around each dot [7], and corresponding potential fluctuations in the plane of the 2DEG, for which the InAs inclusions therefore have anti-dot electrostatic characteristics. It is therefore natural to look for anti-dot like phenomena to explain our observations.

This random array of repulsive centres in the QW can give rise to two types of electron motion in the presence of B: skipping orbits around individual repulsive centres [8] and a collective motion effectively confined in ``corrals" by the surrounding repulsive centres (Fig. 1). The latter behaviour has been observed for a GaAs-AlGaAs QW with a nearby δ-doped negatively charged acceptor (Be) layer [2], and discussed theoretically by Merkt [9] (see below). These types of behaviour are in some sense similar in that the electron orbits scatter from repulsive centres, but because no comprehensive theoretical description satisfactorily covers both, we therefore separate the discussion for the lower and higher frequency modes observed.

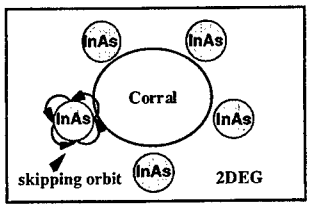

Fig. 1. Schematic of the skipping orbits, and a confining ``corral"

The lower branch can be explained in terms of anti-dot-like behaviour. At low B, when the cyclotron radius R_C is greater then the InAs dot radius R_d, a simple CR mode is observed. With increasing B, R_c becomes comparable with R_d and the mode evolves into a skipping mode around a dot (Fig. 1). As for the anti-dot systems in which such skipping orbits have been observed [10], the mode energy increases sub-linearly with B (i.e. with decreasing R_c), and decreases in intensity, until a critical value is reached beyond which the mode shows a downturn and negative dispersion with B.

This value depends on R_d as well as on N_d, and is characterised by a spatial filling factor f, the ratio between the area covered with dots and the total sample area, used in effective medium approximation (EMA) calculations of the energy dispersion (ω vs. B) [11,12]. The mode dispersions for an anti-dot system in such an EMA are obtained from [11]:

$$1-\frac{1-f}{\Omega(\Omega+\Omega_c)}-\frac{f}{\Omega(\Omega-\Omega_c)}=0 \qquad (1)$$

where $\Omega=\omega/\omega_1$ and $\Omega_c=\omega_c/\omega_1$ and

$$\omega_1=\sqrt{\frac{3\pi^2 N_s e^2}{8m^*\varepsilon_0\varepsilon_{eff}R_d}} \qquad (2)$$

Eq. 1 was used to fit the lower frequency branches, as shown in Fig. 3 for sample b, and gave R_d=25 nm and f=0.03 for sample a, and R_d=33 nm and f=0.04 for sample b. These results are consistent with the values of R_d and N_d obtained from the TEM images and reported by [5]. The validity of this anti-dot model is also confirmed by demonstrating that the lower mode follows the N_s dependence in Eq. 1 and Eq. 2. Reducing N_s to 2.0×10^{11} cm^{-2} markedly reduces the range of B over which the low frequency branch can be observed, as shown in Fig. 3. Then a fit with Eq. 1 is too imprecise, but the lower branch of Eq. 1 can be drawn by using the same values of f and R_d obtained for to 2.6×10^{11} cm^{-2}, but changing N_s in Eq. 2. Fig. 3 shows that the low frequency branch should be roughly unaffected by the change in N_s in the observed range of B, consistent with our data.

The higher frequency branch of Eq. 1 corresponds at high B to CR motion between the anti-dots [8] and at lower B shows a negative dispersion with B.

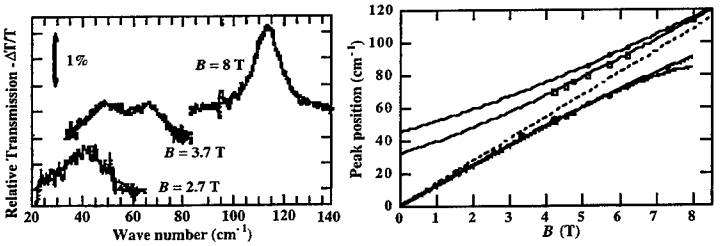

Fig.2. (left) Relative transmission measured for sample a at different B. Dotted lines are Lorentzian fits. Fig.3. (right) Measured peak positions vs. B for sample b. The data dot size reflects the energy error bar. The continuous lines are fits with the solutions of Eq. 1 for the low frequency branches, and with ω_c from Eq. 3 for the high frequency branches. Dots correspond to N_s=2.6×10^{11}cm^{-2} and squares to N_s=2.6×10^{11}cm^{-2}. The dashed line shows the CR measured on the reference sample. The lower frequency modes have clear sub-linear dependencies on B.

This mode has been observed in square arrays of anti-dots, and attributed [8] to a one-dimensional (1D) edge magnetoplasmon propagating along the regular rows. This picture obviously cannot be applied to our devices, where the InAs dots are irregularly distributed. Our experimental high frequency branches cannot be realistically fitted with the higher frequency modes from Eq. 1. However, since the low frequency branch corresponds to electrons skipping around individual anti-dots, it is relatively unaffected by the irregularity of the anti-dot distribution and can be fitted quite well with Eq. 1.

To explain the higher frequency branch we note that the CR resonance was split by ~20 cm^{-1} for a GaAs-AlGaAs QW with a δ-doped (Be) acceptor layer nearby [2]. These acted as repulsive centres, and the potential fluctuations in the QW constrained the 2DEG in ``puddles" to produce a confined collective mode. This picture is supported by the theoretical discussions of Merkt [9], who noted that the new CR modes mark a departure from Kohn's theorem and have a B-dispersion of the same form as for a 2DEG confined in zero dimension [13].

A similar interpretation can be applied to the repulsive centres in the InAs/GaAs system here. TEM images [5] show that the distribution of InAs dots is not completely random, but regions of the 2DEG, corrals, are loosely enclosed by more closely spaced dots. The high frequency data can then be fitted using the upper branch (+) of the dispersion relation for the collective modes of a 2DEG confined in all three dimensions [13], which is also valid for confinement by randomly distributed centres [9]

$$\omega_{\pm} = \pm\frac{\omega_c}{2} + \sqrt{\frac{\omega_c^2}{4} + \omega_0^2} \qquad (3)$$

where ω_0 is the magnetoplasmon frequency at B=0, given by [13]:

$$\omega_0 = \sqrt{\frac{0.81 N_s e^2}{2m^* \varepsilon_0 \varepsilon_{eff} R}} \qquad (4)$$

where $2R$ is the overall size of the corral and ε_{eff}(=12.5) is the effective dielectric constant. Fitting the higher frequency mode data with Eq. 3 ω_0=35 cm^{-1} for sample a, and 45 cm^{-1} for sample b, yields confinement dimensions $2R$=180nm and 140nm respectively, in good agreement with the average corral dimensions measured in the TEM images. Measurements were also made for various N_s, modified by V_g. Fitting the high frequency branches with Eq. 3 gave values of ω_0 which decreased with decreasing N_s as shown in Fig. 3 and consistent with Eq. 4. It is important to note that, although two modes have previously been observed in samples with embedded negatively charged impurities [2,3], our measurements of the sub-linear dispersion of the low frequency mode, and the different N_s dependence, allow a clear identification of the two modes.

In conclusion, GaAs QWs with embedded InAs quantum dots of different dimensions and densities show two FIR absorption modes with different energy dispersions vs. B. The higher frequency mode behaves like a magnetoplasmon, localised by the potential fluctuations introduced by the InAs dots. The lower frequency mode is a CR mode at low B, and evolves into a skipping orbit around the dots for increasing B, as previously observed in anti-dot systems. It appears that InAs dots in an n-type QW act as repulsive centres for the host 2DEG, and that, for these large diameter (~30 nm) scatterers, electron trajectories corresponding to both dot and anti-dot behaviour have been simultaneously observed.

References

1. W. Kohn, Phys. Rev. 123, 1242 (1961).
2. J. Richter, H. Sigg, K. von Klitzing, and K. Ploog, Phys. Rev. *B* 39, 6268 (1989).
3. H. Sigg, D. Weiss and K. von Klitzing, Surf. Sci. 196, 293 (1988).
4. J.M. Gerard, in Confined Electrons and Photons, edited by E. Burstein and C. Weisbuch, (Plenum Press, New York, 1995), p. 357.
5. G. H. Kim et al., Appl. Phys. Lett. 73, 2468 {1998}.
6. M. Sato and Y. Horikoshi, Appl. Phys. Lett. 56, 1555 (1990).
7. E. Ribeiro et al., Phys. Rev. *B* 58, 1506 (1998).
8. D.Heitmann and J.P Kotthaus, Physics Today June 1993, p56.
9. U. Merkt, Phys. Rev. Lett. 76,1134 (1996).
10. K. Kern et al., Phys. Rev. Lett. 66, 1618 (1991).
11. S.A. Mikhailov and V.A. Volvov, Phys. Rev. *B* 52, 17260 (1995).
12. D.S. Kainth, private communication.
13. D. Heitmann et al., Surf.Sci. 267, 245 (1992).

PA.3

A new metallic state in two dimensions

X. G. Feng[1], Dragana Popović[1,*], S. Washburn[2], V. Dobrosavljević[1]

[1] *National High Magnetic Field Laboratory, Florida State University, Tallahassee, FL 32310, USA*
[2] *Dept. of Physics and Astronomy, University of North Carolina at Chapel Hill, Chapel Hill, NC 27599, USA*

Abstract

We report the discovery of a new and unexpected kind of metal in two dimensions (2D), which exists in the presence of scattering by local magnetic moments. The experiment was carried out on a 2D electron system in silicon, where the local magnetic moments have been induced by disorder and their number was varied using substrate bias. In the new metal, the conductivity *decreases* with a power law $\sigma \propto T^2$ to a *non-zero* value as temperature $T \to 0$. In three dimensions, this T^2 dependence is well known, and results from Kondo scattering by local magnetic moments. In two dimensions, however, the existence of a metal with $d\sigma/dT > 0$ is very surprising. As the number of local moments is reduced, the range of temperatures where they dominate transport becomes smaller. In the absence of local moments, we observe the usual 2D metallic behavior with $d\sigma/dT < 0$.

Keywords: Metal-insulator transition; Kondo effect; Correlated electrons

1. Introduction

The metallic phase observed in 2D systems has been characterized by an increase of conductivity σ as temperature $T \to 0$ (*i. e.* $d\sigma/dT < 0$). Both magnetic field [1] and an arbitrarily small amount of spin flip scattering by local magnetic moments [2] suppress such a metallic phase, and lead to a decrease of conductivity as $T \to 0$. Here we show that, in the presence of local moments, this behavior describes a new and unexpected kind of metal, where σ decreases but *does not go to zero* (as expected for an insulator) when $T \to 0$. While unambiguously established by our data, this behavior is in a striking contradiction with any theoretical description available to date.

2. Experimental results

The measurements were carried out on a 2D electron system realized in standard Si metal-oxide-semiconductor field-effect transistors (MOSFETs) with a peak mobility of ~ 1 m^2/Vs at 4.2 K. The details of the sample structure have been given elsewhere [3]. The local magnetic moments in our samples arise from a relatively large number of singly occupied (due to a strong on-site Coulomb repulsion) localized states associated with the upper subband. For a fixed electron density n_s, the negative

*Corresponding author. Tel: (850) 644-3913, fax: (850) 644-5038, e-mail: dragana@magnet.fsu.edu.

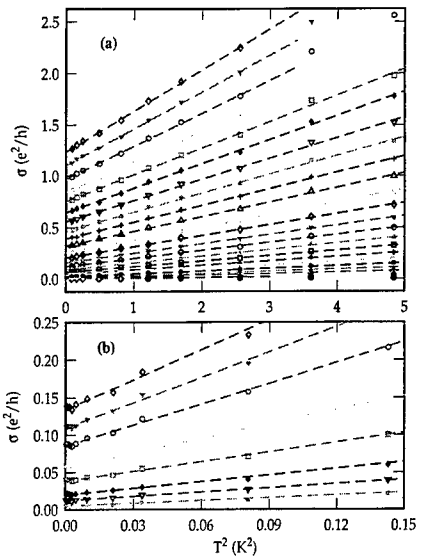

FIG. 1. Temperature dependence of the conductivity plotted *vs.* T^2 for different carrier densities. The dashed lines are fits. (a) Sample 12: σ is shown for n_s from $3.0 \times 10^{15}\mathrm{m}^{-2}$ (top) down to $0.7 \times 10^{15}\mathrm{m}^{-2}$ (bottom) in steps of $0.1 \times 10^{15}\mathrm{m}^{-2}$ and $0.3 \leq T \leq 4.5$ K. (b) Sample 11: σ is shown for (top to bottom) $n_s = 3.7, 3.6 \times 10^{15}\mathrm{m}^{-2}$, and $3.5 \times 10^{15}\mathrm{m}^{-2}$ to $2.5 \times 10^{15}\mathrm{m}^{-2}$ in steps of $0.2 \times 10^{15}\mathrm{m}^{-2}$. $0.022 \leq T < 0.4$ K.

substrate bias V_{sub} increases the subband splitting and decreases the number of local moments by depopulating the upper subband. In addition, there are also some local moments associated with the ground subband but they can not be removed by applying V_{sub} [2]. A systematic study of the change in $\sigma(T)$ with V_{sub} for a given n_s has been reported elsewhere [2,4]. The local moments were observed to dominate transport at the lowest temperatures. In this experiment, however, we keep V_{sub} constant at +1 V, which leads to a large number of local moments, and hence to the observation of the novel behavior of σ in the entire temperature range studied (up to 4.5 K) for all n_s. For a fixed V_{sub}, n_s is controlled by the gate voltage V_g [5].

Fig. 1(a) shows $\sigma(T)$ for different values of n_s. An excellent fit (dashed lines) to the data is obtained with

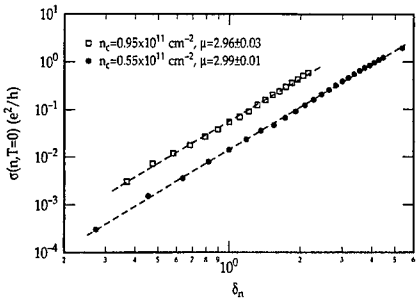

FIG. 2. Zero-temperature conductivity *vs.* the distance from the metal-insulator transition for samples 9 (squares) and 12 (dots). The dashed lines are fits with the slopes equal to the critical exponent μ.

$$\sigma(n_s, T) = \sigma(n_s, T = 0) + A(n_s)\, T^2 \qquad (1)$$

over a wide range of n_s as shown, where σ measured at the lowest T (0.3 K) varies over three orders of magnitude below e^2/h (e^2/h – quantum unit of conductance). The data obtained on another sample [Fig. 1(b)] show that the T^2 dependence continues unchanged down to 0.022 K. Such $\sigma(T)$ is often considered to be a signature of local magnetic moments, and results from the Kondo effect [6]. In general, one expects the T^2 behavior for a magnetic impurity embedded in a Fermi liquid metal in any dimension. On the other hand, it has been suggested [7] that the metallic state in 2D may not have a Fermi liquid character, but this interesting question requires further theoretical and experimental work.

The high quality of the fits allows a reliable extrapolation of the zero-temperature conductivities $\sigma(n_s, T = 0)$, whose non-zero values mean that, in spite of the decrease of $\sigma(n_s, T)$ with decreasing T, *the 2D system is in the metallic state.* $\sigma(n_s, T = 0)$ obtained from the fits to Eq. (1) is shown in Fig. 2 as a function of $\delta_n = (n_s - n_c)/n_c$, the distance from the metal-insulator transition (n_c – critical density). We find the power-law behavior $\sigma(n_s, T = 0) \sim \delta_n^{\mu}$, as expected in the vicinity of a quantum critical point [8] such as the metal-insulator transition (MIT). In addition, even though the MIT occurs at different critical densities in different samples, the critical exponents μ are the same in both samples (Fig. 2), as expected from general arguments [8]. A detailed scaling analysis of the transition between this new metallic state and an insulator has been presented elsewhere [9].

Another interesting question is the effect of the number of local moments on the properties of this

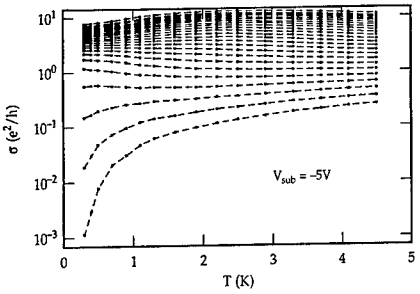

FIG. 3. Temperature dependence of the conductivity σ for sample 12 with $V_{sub} = -5$ V. n_s ranges from $3.0 \times 10^{15}\mathrm{m}^{-2}$ (top curve) to $0.7 \times 10^{15}\mathrm{m}^{-2}$ (bottom curve) in steps of $0.1 \times 10^{15}\mathrm{m}^{-2}$.

new metallic phase. We have established earlier [2] that, for a fixed n_s, the low-temperature regime (where local moments dominate) becomes smaller as their number is reduced by increasing negative V_{sub}. Fig. 3 shows $\sigma(T)$ for different n_s and $V_{sub} = -5$ V, for which the local moments are still present in the sample at an intermediate range of n_s ($\sim 2 - 7 \times 10^{15}\mathrm{m}^{-2}$) [2,4]. Indeed, the T^2 behavior is observed at the highest n_s shown in Fig. 3 albeit in a smaller temperature range ($\lesssim$ 1.4 K). As n_s is reduced, $d\sigma/dT$ changes sign from positive, reflecting $\sigma(T)$ of the new metal, to negative, characteristic of the 2D metal observed in absence of local magnetic moments. It is important to note here that decreasing V_g (*i. e.* n_s) both lowers the Fermi energy E_F and decreases the subband splitting [10]. Smaller E_F tends to decrease the number of local moments, but smaller subband splitting increases their number by populating the upper subband. Our data suggest that, in this range of n_s, the first effect dominates – the number of local moments decreases as n_s is lowered. It is interesting that this is the opposite of what is observed [4] at the highest densities ($\sim 10^{16}\mathrm{m}^{-2}$), where the change in the subband splitting is dominant and, as a result, the number of local moments increases as n_s is lowered. It would be also interesting to compare our conclusions to the subband structure calculations for Si MOSFETs but, to the best of our knowledge, there are none available for the low n_s ($\sim 10^{15}\mathrm{m}^{-2}$) range. The metal-insulator transition between the 2D metal with $d\sigma/dT < 0$ observed at low n_s in the absence of local moments, and an insulating state at lower n_s has been studied in detail elsewhere [3,2], and found to be in good agreement with results obtained in other, higher peak mobility Si MOSFETs [11].

In order to investigate the effect of a smaller number of local moments on the properties of the new metal, all the (high n_s) data with $d\sigma/dT > 0$ shown in Fig. 3 were fitted successfully to Eq. (1). The same analysis has been also done on the data obtained with smaller (negative) values of V_{sub} (*e. g.* $-0.5, -1, -2$ V). Even though, for each V_{sub}, the zero-temperature conductivities still seem to obey the power law $\sigma(n_s, T = 0) \sim \delta n_s^{\mu}$, the exponent μ decreases with increasing (negative) V_{sub}, whereas n_c appears to increase. We attribute the apparent change in the critical exponent μ to a change in the number of local moments with n_s, as discussed above. The fact that such corrections to scaling can give rise to parameter-dependent effective exponents is well known near other phase transitions [8].

3. Conclusion

We have discovered a new and unexpected type of metal in two dimensions, such that $d\sigma/dT > 0$. This metal exists in the presence of scattering by local magnetic moments. The observed temperature dependence is well established for three-dimensional metals containing magnetic impurities, and is believed to result from the Kondo effect. In 2D, however, the existence of such a metal still awaits theoretical understanding.

Acknowledgements

This work was supported by NSF Grant No. DMR-9796339, NHMFL, an NHMFL In-House Research Program grant, and Alfred P. Sloan Foundation (V. D.).

References

[1] D. Simonian, S. V. Kravchenko, M. P. Sarachik, and V. M. Pudalov, Phys. Rev. Lett. 79 (1997) 2304; V. M. Pudalov, G. Brunthaler, A. Prinz, G. Bauer, JETP Lett. 65 (1997) 932.

[2] X. G. Feng, D. Popović, S. Washburn, Phys. Rev. Lett. (in press); preprint cond-mat/9902036 (1999).

[3] D. Popović, A. B. Fowler, and S. Washburn, Phys. Rev. Lett. 79 (1997) 1543.

[4] D. Popović, X. G. Feng, S. Washburn, Proc. XXXIVth Rencontres de Moriond (Editions Frontieres, 1999); preprint cond-mat/9905141 (1999).

[5] At very high n_s ($\gtrsim 7\times10^{15}\mathrm{m}^{-2}$), the novel metallic behavior disappears as the upper subband is depopulated by an increase in V_g [4].
[6] See, for example, A. C. Hewson, *The Kondo Problem to Heavy Fermions* (Cambridge University Press, Cambridge, England, 1993).
[7] V. Dobrosavljević, E. Abrahams, E. Miranda, and S. Chakravarty, Phys. Rev. Lett. 79 (1997) 455.
[8] N. Goldenfeld, *Lectures on Phase Transitions and the Renormalization Group* (Addison-Wesley, 1992).
[9] X. G. Feng, D. Popović, S. Washburn, and V. Dobrosavljević, preprint cond-mat/9903236 (1999).
[10] See T. Ando, A. B. Fowler, and F. Stern, Rev. Mod. Phys. 54 (1982) 437.
[11] S. V. Kravchenko, *et al.*, Phys. Rev. B 50 (1994) 8039; S. V. Kravchenko, *et al.*, Phys. Rev. B 51 (1995) 7038.

PA.4

CRITICAL VIEW OF THE "METALLIC" REGIME IN TWO DIMENSIONS

Y. Yaish[a], O. Prus[a], E. Buchstab[a], U. Sivan[a], and A. Stern[b]
[a]Physics dep. and Solid State Institute, Technion-IIT, Haifa 32000, Israel
[b]Dep. of Condensed Matter Physics, Weizmann Inst. of Science, Rehovot 76100, Israel.

The magnetotransport of holes in a GaAs/AlGaAs heterostructures is studied experimentally as a function of density and temperature in the regime where a "metal-insulator transition" is observed. It is shown that in the "metallic" phase, namely, at the higher densities and lower temperatures where the sheet resistance grows with temperature, conduction proceeds through two singly degenerate bands with very different masses[1] and mobilities. Using Landau fan diagrams and the classical positive magnetoresistance characteristic to two-band transport, the carrier densities in the two bands, their corresponding mobilities and the interband scattering rates are mapped as a function of the various parameters.

It is found that the Arrhenius increase in resistance with temperature, $\rho = \rho_0 + \alpha \exp(-T_0/T)$, observed here as well as in other systems, can be fully accounted for by two bands physics and Drude type considerations with no need to invoke a metallic phase. Two band physics is also consistent with other features common to many experimental systems, like the existence of a certain density for which the resistance is practically independent of temperature (commonly interpreted as a metal-insulator transition) and the positive magnetoresistance at magnetic fields parallel to the layer.

The interpretation of the experimental results rests on the observation that the thermodynamics of two bands with very different masses is analogous to that of a liquid-gas system along its coexistence curve. In a way analogous to the Arrhenius increase of vapor pressure with temperature in the gas-liquid case, carriers are transferred from the light band to the heavy one with similar temperature dependence of the densities. The analogy is formulated by writing the corresponding Clausius-Clapeyron equation and identifying the latent heat with the Coulomb correlation energy involved in transferring one hole from the light to the heavy band.

Since holes in the heavy band are hardly mobile, this carrier transfer results in a resistance increase. Our experimental measurements yield the interband scattering rate as well. We find that the latter follows the same Arrhenius temperature dependence and hence contribute again to the Arrhenius resistance increase with temperature.

The positive magnetoresistance in parallel fields is traced to the increased energy spacing between the bands due to the Zeeman effect.

[1] The very existence of two hole bands in GaAs/AlGaAs heterostructures is well documented in both the theoretical and experimental literature.

PA.5

LIMITS FOR THE SCALING BEHAVIOR FOR THE *B*=0 CONDUCTIVITY TRANSITION IN Si MOSFETS

J. E. Furneaux
Laboratory for the Electronic Properties of Materials,
Department of Physics and Astronomy,
University of Oklahoma, Norman, OK 73019-6021, USA

Daniel Lilliehöök
Department of Physics, Stockholm University
S-113 85 Stockholm, Sweden

Since the original report of a conductivity transition in ultra-high mobility Si MOSFETs at $B = 0$[1], there has been considerable further work and interest. In particular the work on newly prepared MOSFETs by Heemskerk and Klapwijk[2] and the quantum non-scaling in the QHE regime reported by Shahar[3] have generated considerable discussion. In particular, a consensus built within the community indicating that a collaborative, careful analysis of the considerable data, both previously published and unpublished, from the University of Oklahoma could be fruitful[4]. We have proceeded with such a program including, in particular, a careful and consistent consideration of experimental errors and their propagation. Our goal is not only to place rigorous error-bars on the parameters extracted from the analysis such as critical exponents, critical densities and critical resistivities, but also to determine confidence limits on the applicability of such an analysis. Our first preliminary and somewhat unexpected result is for the case of *E*-field scaling. Here we find different scaling exponents for the two sides of the transition. Further results will be presented at the meeting.

We acknowledge support from the Swedish Government and NSF via OKEPSCoR and DMR96-24699, and numerous fruitful discussions with Anders Karlhede, Sankar Das Sarma, T. Klapwijk, Kieran Mullen, Bruce Mason, Sheena Murphy, and Xincheng Xie. The data used in this analysis was taken over a number of years at OU with the assistance of S. Kravchenko, Whitney Mason, S. Murphy, G. Kravchenko, G. Bowker, B. Nelson, J. Frese, and A. Ogsten.

1. S. V. Kravchenko, *et al., Phys. Rev. B* **50**, 8039 (1994); *Phys. Rev. B* **51**, 7038 (1995)
2. R. Heemskerk and T. M. Klapwijk, *Phys. Rev. B* **58**, R1754 (1998)
3. D. Shahar, *et al., Solid State Commun.* **107**, 19 (1998)
4. Institute of Theoretical Physics *Program on Disorder and Interactions in Quan-tum Hall and Mesoscopic Systems* (http://www.itp.ucsb.edu/online/qhall98/)

PA.6

Tunable $B = 0$ Spin-Splitting and its Effect on the Metallic Behavior of GaAs Two-Dimensional Holes

S. J. Papadakis, E. P. De Poortere, H. C. Manoharan,[1] M. Shayegan
Department of Electrical Engineering, Princeton University, Princeton, New Jersey 08544, USA.

R. Winkler
Institut für Technische Physik III, Universität Erlangen-Nürnberg, Staudtstr. 7, D-91058 Erlangen, Germany.
(June 13, 1999)

Experiments on a constant-density two-dimensional hole system in a GaAs quantum well reveal that the metallic behavior observed in the zero-magnetic-field temperature dependence of the resistivity depends on the symmetry of the confinement potential and the resulting spin-splitting of the valence band.

Keywords: Spin-Splitting, 2D holes, 2D Metal-Insulator transition

71.30.+h, 73.20.Dx, 73.50.h

For many years, it was widely accepted that there can be no metallic phase in a disordered two-dimensional (2D) carrier system [2,3]. However, recent experiments on high quality 2D systems in Si have provided us with reason to re-visit this belief [4]. Since these experiments, the metallic behavior has been observed in Si MOSFETs [4,5], SiGe quantum wells [6,7], GaAs/AlGaAs heterostructures [8,9], and AlAs quantum wells [10]. Multiple mechanisms [11–13] have been proposed to explain the metallic behavior, but no clear model has emerged which fully describes this sizeable body of experimental data.

Our experiments demonstrate a correlation between the zero-magnetic-field spin-splitting and the metallic behavior. Spin-splitting of carriers at zero magnetic field in a 2D system is caused by spin-orbit interaction and by an inversion asymmetry of the confinement potential [14]. The energy bands are split into two spin-subbands whose existence has been well established both experimentally and theoretically [14–20]. In GaAs, the spin-splitting arises from the inversion asymmetries of the zincblende crystal structure and of the potential which confines the carriers to two dimensions. The asymmetry of the crystal structure is fixed, but the asymmetry of the confining potential, and therefore the spin-splitting, can be changed by applying an electric field perpendicular to the 2D plane ($E_\perp$) using gates [19]. We demonstrate that the spin-splitting can be tuned while the density is kept constant, and show that the metallic behavior of the 2D holes appears to be related to the size of spin-splitting observed.

Our samples are p-type, 200 Å-wide QWs grown by molecular beam epitaxy on undoped (311)A GaAs substrates. They are patterned with an L-shaped Hall bar aligned along the low- and high- mobility directions ($[01\bar{1}]$ and $[\bar{2}33]$ respectively, see [21,22] and references therein), and have metal front and back gates (for more details see Ref [23]). Measurements are done in a dilution refrigerator at temperatures from 0.8 K to 25 mK and in perpendicular magnetic fields (B) up to 16 T. We use the low-frequency lock-in technique to measure the longitudinal (ρ) and Hall resistivities. Experiments are done on samples from three different wafers at four different hole densities: 3.3×10^{11} cm^{-2} ($r_s = 5.7$), 2.3×10^{11} cm^{-2} ($r_s = 6.8$), 1.2×10^{11} cm^{-2} ($r_s = 9.5$), and 7.0×10^{10} cm^{-2} ($r_s = 12$) [24]. These densities place the samples well into the metallic regime [8,9]. The 25 mK mobilities vary from 83 to 31 m^2/Vs for the various samples and mobility directions. We will present data from the low mobility direction (the high-mobility-direction data is qualitatively similar) and we will focus on the highest and lowest density data, as the intermediate density data behaves predictably between these.

To measure the spin-splitting of the two higher density samples, the low-B Shubnikov-de Haas (SdH) oscillations are examined [18–20]. The frequencies of these oscillations are a measure of the zero-B spin-splitting. We tune the spin-splitting by changing the front gate and back gate voltages in opposite directions, in a manner that keeps the density constant (to within 1%) but changes $E_\perp$ [23].

Examples of the low-B ρ data are shown in Fig. 1A at a density of 3.3×10^{11} cm^{-2} for different values of $E_\perp$. The top trace was taken with the sample at a large positive $E_\perp$ (roughly 5 kV/cm pointing towards the front gate). $E_\perp$ is reduced for the second trace, nearly zero in the middle trace, and increasingly negative in the next two traces (it is about -6 kV/cm in the bottom trace). The Fourier transforms of the low-mobility data, in the range below 0.9 T, (Fig. 1B), reveal how the spin-splitting changes as $E_\perp$ is changed from positive, through zero, to negative.

The next part of the experiment involves measuring the T dependence of ρ at $B = 0$ from 25 mK to about 0.8 K. The data are shown in Fig. 1C, with the traces separated vertically and aligned with their corresponding Fourier

transforms in Fig. 1B. Their ρ values at 25 mK and $B = 0$ (ρ_0) are shown on the y-axis. The most striking feature is that the T dependence of the $B = 0$ resistivity is larger when the two Fourier transform peaks are well separated and smaller when there is no separation. The magnitude of the T dependence appears to be correlated with that of the spin-splitting.

The above procedure is repeated for the three lower densities. At the density of 2.3×10^{11} cm^{-2}, the quality is still good enough that the SdH oscillations show two frequencies. At the lower two densities, 1.2×10^{11} cm^{-2} and 7.0×10^{10} cm^{-2}, we can no longer resolve two frequencies in the SdH oscillations, and must estimate the gate voltages corresponding to $E_\perp = 0$. However, we can calculate very accurately the changes in $E_\perp$ as we change the gate voltages, and we know that spin-splitting increases with increasing $E_\perp$. In these samples, once again, the T dependence increases as $E_\perp$, and therefore the spin-splitting, is increased.

For a density of 7.0×10^{10} cm^{-2}, some examples of magnetoresistance data are shown in Fig. 2A and temperature dependences in Fig. 2B, from bottom to top in order of increasing $E_\perp$ (from near 0 to 14 kV/cm). Note that at this density, $E_\perp$ is varied to one side of zero, while at the highest density (Fig. 1), $E_\perp$ is varied symmetrically around zero (roughly -6 kV/cm to 5kV/cm). Figs. 1 and 2 illustrate that the spin-splitting has qualitatively the same effect on the metallic behavior at both densities. The temperature dependence is larger for the lower density, consistent with previous experiments on the metallic behavior [8,9]

The data show clearly that the magnitude of the temperature dependence increases with the magnitude of $E_\perp$, which directly affects the amount of spin-splitting. Another parameter that is affected by $E_\perp$ is the mobility, but for different samples and different mobility directions we do not observe a simple dependence of mobility on $E_\perp$. Thus, while it may have an effect, it is unlikely that the mobility variation causes the changes in the temperature dependence.

The fact that magnitude of the temperature dependence of the resistivity increases with the magnitude of the spin-splitting is surprising given that a parallel B field, which increases the spin-splitting, quenches the metallic state [9,25]. We surmise that in relation to the metallic behavior there is some fundamental difference between the $B = 0$ spin-splitting, which is caused by the GaAs band structure and the confinment potential, and the non-zero-B spin-splitting, which is the difference in energy between carriers with spins parallel and anti-parallel to the applied B field. Futhermore, our results point out a complication in experiments that have examined the dependence of the metallic behavior on the carrier density: they varied the spin-splitting as they changed the density [4–10]. Recognition of the fact that the zero-B spin-splitting is on its own important for the metallic behavior will help untangle the causes of this unexpected phenomenon.

This work was supported by the NSF and the ARO.

---

[1] current address: IBM Research Division, Almaden Research Center, 650 Harry Rd., San Jose, CA 95120.

[2] E. Abrahams, P. W. Anderson, D. C. Licciardello, and T. V. Ramakrishnan, Phys. Rev. Lett. **42**, 673 (1979).
[3] D. J. Bishop, D. C. Tsui, and R. C. Dynes, Phys. Rev. Lett. **44**, 5737 (1980).
[4] S. V. Kravchenko, G. V. Kravchenko, and J. E. Furneaux, Phys. Rev. B **50**, 8039 (1994); S. V. Kravchenko *et al.*, Phys. Rev. B **51**, 7038 (1995); S. V. Kravchenko, D. Simonian, M. P. Sarachik, W. Mason, and J. E. Furneaux, Phys. Rev. Lett. **77**, 4938 (1996).
[5] D. Popović, A. B. Fowler, and S. Washburn, Phys. Rev. Lett. **79**, 1543 (1997).
[6] P. T. Coleridge, R. L. Williams, Y. Feng, and P. Zawadzki, Phys. Rev. B **56**, R12764 (1997).
[7] J. Lam, M. D'Iorio, D. Brown, and H. Lafontaine, Phys. Rev. B **56**, R12741 (1997).
[8] Y. Hanein *et al.*, Phys. Rev. Lett. **80**, 1288 (1998).
[9] M. Y. Simmons *et al.*, Phys. Rev. Lett. **80**, 1292 (1998).
[10] S. J. Papadakis and M. Shayegan, Phys. Rev. B **57**, R15068 (1998).
[11] V. Dobrosavljević, E. Abrahams, E. Miranda, and S. Chakravarty, Phys. Rev. Lett. **79**, 455 (1997).
[12] V. M. Pudalov, Pis'ma Zh. Éksp. Teor. Fiz. **66**, 168 (1997) [JETP Lett. **66**, 175 (1997)].
[13] B. L. Altshuler and D. Maslov, Phys. Rev. Lett. **82**, 145 (1999).
[14] Yu. A. Bychkov and E. I. Rashba, Pisma Zh. Eksp. Teor. Fiz. **39**, 66 (1984) [JETP Lett. **39**, 78 (1984)]. For a review, see U. Rössler, F. Malcher, and G. Lommer, in High Magnetic Fields in Semiconductor Physics II, edited by G. Landwehr (Springer, Berlin, 1989) [Springer Series in Solid State Sciences, **87**] p. 376.
[15] E. I. Rashba and E. Y. Sherman, Phys. Lett. A **129**, 175 (1988).
[16] B. Jusserand *et al.*, Phys. Rev. B **51**, 4707 (1995).
[17] P. D. Dresselhaus, C. M. A. Papavassiliou, R. G. Wheeler, and R. N. Sacks, Phys. Rev. Lett. **68**, 106 (1992).

[18] J. P. Eisenstein, H. L. Stormer, V. Narayanamurti, A. C. Gossard, W. Wiegmann, Phys. Rev. Lett. **53**, 2579 (1984); B. Das *et al.*, Phys. Rev. B **39**, 1411 (1989); M. Schultz *et al.*, Semicon. Sci. Technol. **11**, 1168 (1996); J. Nitta, T. Akazaki, H. Takayanaga, and T. Enoki, Phys. Rev. Lett. **78**, 1335 (1997).
[19] J. P. Lu *et al.*, Phys. Rev. Lett. **81**, 1282 (1998).
[20] K. Muraki and Y. Hirayama, Physica B **249**, 65 (1998).
[21] J. J. Heremans, M. B. Santos, K. Hirakawa, and M. Shayegan, J. Appl. Phys. **76**, 1980 (1994).
[22] M. Wassermeier *et al.*, Phys. Rev. B **51**, 14721 (1995).
[23] S. J. Papadakis *et al.*, Science **283**, 2056 (1999).
[24] r_s is a parameter used to characterize the importance of carrier interaction. It is the average inter-carrier separation in units of the effective Bohr radius. We use a GaAs dielectric constant of 13 and an effective hole mass of $0.4m_e$, deduced from cyclotron resonance measurements on similar samples [K. Hirakawa *et al.*, Phys. Rev. B **47**, 4076 (1993)].
[25] V. M. Pudalov, G. Brunthaler, A. Prinz, and G. Bauer, Pis'ma Zh. Éksp. Teor. Fiz. **65**, 168 (1997) [JETP Lett. **65**, 932 (1997)]; D. Simonian, S. V. Kravchenko, M. P. Sarachik, and V. M. Pudalov, Phys. Rev. Lett. **79**, 2304 (1997); S. V. Kravchenko, D. Simonian, M. P. Sarachik, A. D. Kent, and V. M. Pudalov, Phys. Rev. B **58**, 3553 (1998); J. Yoon *et al.*, Phys. Rev. Lett. **82**, 1744 (1999).

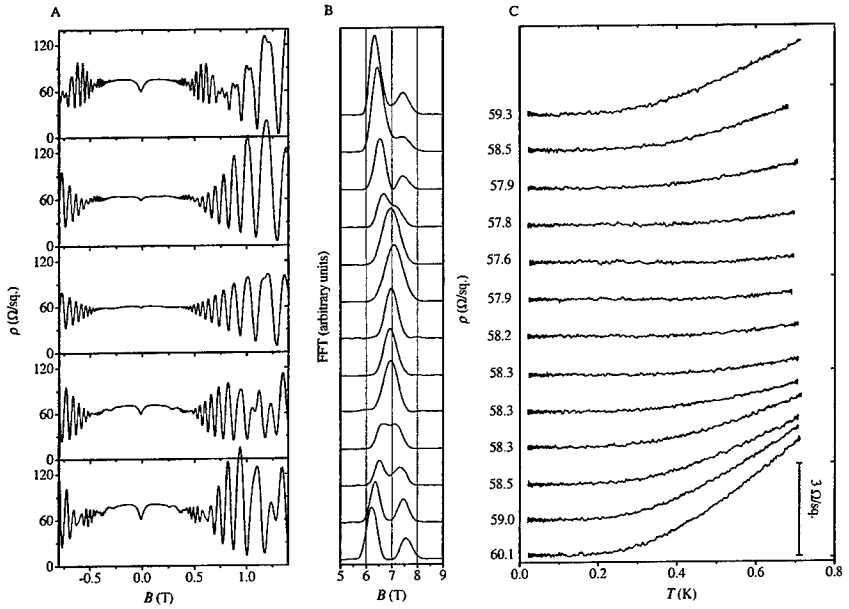

FIG. 1. A: Magnetoresistance traces, all at a density of 3.3×10^{11} cm^{-2}, but at different values of $E_\perp$. The data shown are from the low-mobility [01$\bar{1}$] direction. B: Fourier transforms of the Shubnikov-de Haas oscillations, showing that the spin-splitting is being tuned through a minimum. C: Temperature dependence of ρ for the low-mobility direction. The traces are shifted vertically for clarity, with the value of ρ at 25 mK listed along the y-axis for each trace. Each ρ vs. T trace is aligned with its corresponding Fourier transform. B and C together show that the magnitudes of the spin-splitting and the temperature dependence are related.

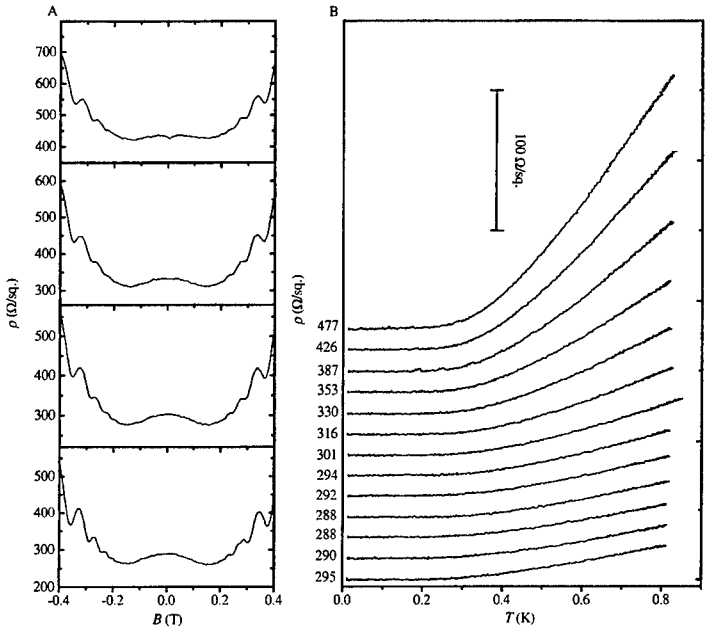

FIG. 2. A: Magnetoresistance traces, and B: Temperature dependence of ρ; for the low-mobility direction at a density of 7.0×10^{10} cm^{-2}. The temperature dependence traces are shifted vertically for clarity, with the value of ρ at 25 mK listed along the y-axis for each trace.

PA.8

Exchange Interaction Effects in the Crossing of Spin Polarized Landau Levels in a Silicon-Germanium Heterostructure: Transition into a Ferromagnetic State

U. Zeitler[a], H.W. Schumacher[a], J. Regul[a], R.J. Haug[a],
P. Weitz[b], A.G.M. Jansen[c], F. Schäffler[d]

[a] *Institut für Festkörperphysik, Universität Hannover, Appelstraße 2, 30167 Hannover, Germany.*
[b] *Max-Planck-Institut für Festkörperforschung, Heisenbergstr. 1, 70569 Stuttgart, Germany.*
[c] *Grenoble High Magnetic Field Laboratory, MPIF-CNRS, 38042 Grenoble Cedex 09, France.*
[d] *Institut für Halbleiterphysik, Universität Linz, 4040 Linz, Austria.*

The crossing of spin-split Landau levels in a Si/SiGe heterostructure is investigated by means of magneto-transport experiments in tilted magnetic fields. We observe a transition from a paramagnetic into a fully-spin polarized state. During the transition strongly enhanced maxima in the transverse resistivity ρ_{xx} appear when the parallel field component is oriented along the Hall bar. We assign this effect to an energy level structure strongly modified by exchange interaction effects between different Landau levels. Surprisingly the maximum in ρ_{xx} totally disappears when the parallel field component is perpendicular to the Hall bar.

The interplay of Landau quantization and Zeeman splitting in the level structure of a two-dimensional electron system (2DES) can be accessed by means of magneto-transport experiments in tilted magnetic fields [1]. Such coincidence measurements are used to investigate the spin splitting in various 2DESs in heterostructures based on GaAs/GaAlAs [2], Si/SiGe [3, 4, 5, 6] and InAs/AlSb [7].

The density of states (DOS) of a 2DES in a magnetic field with a component perpendicular to the 2DES, $B_\perp$, is quantized into discrete Landau levels N. Each Landau level (LL) splits into two spin-levels $s = \pm 1/2$. The LL splitting, $\Delta E_L = \hbar\omega_c$, is governed by $B_\perp$. Here $\omega_c = eB_\perp/m^*$ denotes the cyclotron frequency of electrons with effective mass $m^* = 0.19m_e$ for Si. In contrast, the spin splitting, $\Delta E_Z = g^*\mu_B B_{tot}$ ($g^* \approx 3.15$ [6] is the effective Landé factor of the electrons), depends on the *total* magnetic field, B_{tot}. In Si/SiGe heterostructures an additional splitting into two valley states is present in the level structure with a valley splitting, $\Delta E_V = \varphi\hbar\omega_c$. Here we assume ΔE_V to be governed by $B \perp$ [4, 5].

The principle of coincidence experiments is based on the fact that the ratio $\Delta E_Z/\Delta E_L$ can be increased drastically by tilting the magnetic field. The general quantization energies in a magnetic field tilted by an angle ϑ away from the direction normal to the 2DES can be written as:

$$E_{N,s} = \hbar\omega_c(N + \frac{1}{2}) + sg^*\mu_B B_{tot} \pm \frac{1}{2}\Delta E_V = \hbar\omega_c \left[N + \frac{1}{2} + s\,\frac{g^*m^*}{2m_e}\sqrt{1+\tan^2\vartheta} \pm \frac{\varphi}{2}\right].$$

In the following we will always consider energy levels in units of the LL splitting, i.e we define their relative energies $\epsilon_{N,s} = E_{N,s}/\hbar\omega_c$.

The evolution of the lowest LLs as a function of $\tan\vartheta$ is illustrated in Fig. 1 for $g^* = 3.15$ [6] and $\varphi = 0.1$. On the left panel, the relative energy $\epsilon_{N,s}(\vartheta)$ is shown, the right panel sketches the DOS for three exemplary tilt angles. In a perpendicular field ($\vartheta = 0^o$) ΔE_Z

is about 0.3 $\hbar\omega_c$, each spin-level contains two valley states. When increasing the tilt angle, the $\uparrow$-levels move to a higher relative energy whereas the $\downarrow$-levels move downwards. ΔE_Z reaches about 0.7 $\hbar\omega_c$ at $\vartheta = 65^o$ and as a consequence the splitting between the states $(N,\downarrow)$ and $(N,\uparrow)$ of one given Landau level is more than two times larger than the splitting between two neighboring Landau levels with opposite spin. At $\vartheta = 72.5^0$ the spin splitting equals the LL splitting, $\epsilon_{N,\uparrow}$ coincides with $\epsilon_{N+1,\downarrow}$, see positions (A1), (B1), and (C1) in Fig. 1. Increasing ϑ further, the $(N,\uparrow)$-level moves further upwards. The $(N+1,\downarrow)$-level keeps moving downwards. Finally $\epsilon_{N+1,\downarrow}$ is situated below $\epsilon_{N,\uparrow}$, see $\vartheta = 76^o$. Increasing the tilt angle further leads to higher order coincidences when the Zeeman splitting equals an integer multiple m of the LL splitting, see positions (Am) and (Bm) in Fig. 1. This simple picture is modified by the fact that due to exchange interaction effects g^* also depends on ϑ and the LL filling [6]. The positions of the coincidences are shifted, however, the global picture remains similar.

To access the level structure experimentally we have performed magneto-transport experiments in the 2DES defined in a Si channel of a Si/SiGe heterostructure (sheet density $n = 7.2 \times 10^{15}$ m^{-2}, electron mobility $\mu = 20$ m^2/Vs, patterned into a 100-μm wide Hall bar) in tilted magnetic fields up to 30 T at temperatures down to 400 mK. The experimental consequences of the first coincidence is displayed in Fig. 2 where the magneto-resistivity ρ_{xx} and the Hall resistivity ρ_{xy} at $T = 0.4$ K are shown as a function of $B_\perp$ for three different tilt angles ϑ. In a perpendicular magnetic field ρ_{xx} displays Shubnikov-de Haas oscillations and quantized Hall plateaus show up in ρ_{xy}. The strongest minima (broad plateaus) occur at filling factors $\nu = 4N$ corresponding to the situation when the Fermi energy lies between two LLs, $N-1$ and N. Additional minima occur at $\nu = 4N-2$ where the Fermi energy is situated between the two spin-levels of the same Landau level. Even the valley splitting can be resolved for the lower Landau levels, $\nu = 5, 7, 9$.

For $\vartheta = 68.7^o$ the situation is essentially similar. However, the strengths of the $\nu = 4N$ minima have decreased. The dominant minima are now related to the spin-splitting. This corresponds to the above illustrated situation ($\vartheta = 65^o$) where the splitting between the two spin-states $(N,\downarrow)$ and $(N,\uparrow)$ exceeds the splitting between the $(N,\uparrow)$-level and the next higher Landau level with opposite spin.

In the first series of coincidence ($\vartheta = 72.4^o$) the minima for $\nu = 8, 12, 16, ..$ turn into maxima. Now the Fermi energy lies in the middle of two degenerate levels with opposite spin, namely $(N,\downarrow)$ and $(N+1,\uparrow)$. Due to the presence of valley splitting the maximum around $\nu = 8$ displays an additional structure, for higher filling factors the valley splitting is no more resolved. The expected maximum for $\nu = 4$ (position (A1) in Figs. 1 and 2) only occurs in a very narrow range of tilt angles $\vartheta = 69^o..70^o$, see below. The behaviour of this coincidence peak strongly deviates from that expected from the naive level structure as sketched above.

In the following we will concentrate on the coincidences (A1), (A2), and (A3). Their particular interest lies in the fact that these coincidences transform the 2DES into a ferromagnetic state. Evidences for such a phase transition were already reported using coincidence experiments at $\nu = 2$ in the 2DES of a GaInAs/InP heterostructure [8].

In Si this transition happens at $\nu = 4$ when crossing the (A1) coincidence. Initially $(0,\downarrow)$ and $(0,\uparrow)$ are situated below the Fermi energy. Leaving ν constant and increasing the tilt angle ϑ redistributes electrons from the $(0,\uparrow)$-state into the $(1,\downarrow)$-level when moving through

the coincidence (A1). Finally the $(0,\uparrow)$-level is totally depopulated and the $(1,\downarrow)$-level has moved below the Fermi energy, see illustration for $\vartheta = 75^o$ in Fig. 1. The electrons are now totally spin polarized. For higher tilt angles a totally spin polarized state can also be obtained for $\nu = 6$ when only the spin-down polarizations of the three lowest Landau levels remain occupied after having crossed the coincidence (A2). Finally crossing (A3) at $\nu = 8$ leaves the 2DES with four spin-down polarized Landau levels occupied.

The development of ρ_{xx} during the crossing of the (A1) coincidence is shown in Fig. 3. Strongly enhanced maxima occur in ρ_{xx} when the parallel field component is oriented along the current direction. They are more than an order larger than the SdH-peaks in the untilted case. We assign this effect to a modified energy level structure in the system due to exchange interaction which becomes important when the energy levels start coinciding. Temperature dependent experiments give another insight into the nature of this new correlated state. From 0.4 K to 0.8 K the height of ρ_{xx} in the maximum of the coincidence remains unaffected by temperature and breaks down drastically between 1 K and 1.3 K. Here it recovers a value comparable to the SdH-peaks outside the coincidence. The energy related to this level correlation can be estimated to $\Delta E_C \approx 1$ K.

Also for $\nu = 6$ and $\nu = 8$ (Sketched (A2) and (A3) in Fig. 1) we observed similar extremely enhanced peaks in ρ_{xx}, again more than an order of magnitude larger than SdH-peaks outside the coincidences. This observation supports the above model that the enhancement of ρ_{xx} can be in fact related to a correlated state formed during the transition into the ferromagnetic 2DES. The anomalous enhancement of ρ_{xx} is absent for all other coincidences which do not result into a spin-polarized state.

Very surprisingly the ρ_{xx}-enhancement as a signature of the spin-correlated state is also absent when the parallel field component is turned by 90^o with respect to the orientation of the Hall bar, see right panel of Fig. 3. This may be due to a domain structure introduced by an anisotropic 2DES. An alternative explanation might lie in the fact that for this field orientation an additional Hall voltage is induced perpendicular to the 2DES which might quench the correlation effects.

Another hint for a level redistribution can be gained from Hall-effect measurements. For a tilt angle $\vartheta = 69.4^o$, slightly below the angle where the broad maximum in ρ_{xx} occurs, the $\nu = 4$ plateau is still present. When changing the filling factor by increasing the magnetic field ρ_{xy} strongly overshoots the value for $\nu = 3$ nearly approaching its expected value for $\nu = 2$, see Fig. 3. This means that a level with a two-fold degeneracy is depopulated simultaneously. Only when the magnetic field is increased further the naive level structure is recovered. Now one valley state of the $(0,\uparrow)$ level and the far below situated two valley states of $(0,\downarrow)$ are occupied.

In conclusion we have measured extremely enhanced coincidence peaks in the SdH oscillations of 2DES in a Si/SiGe heterostucture which we assign to the formation of a new correlated state formed during the transition into a fully spin-polarized 2DES. This work has been supported by the TMR Programme of the European Union under contract no. ERBFMGECT950077.

References

[1] F. Fang, P.J. Stiles, Phys. Rev. 174 (1968) 823.
[2] R. Nicholas *et al*, Phys. Rev. B 37 (1988), 1294.

[3] S. J. Koester, K. Ismail, J.O. Cho, Semicond. Sci. Technol. 12 (1996) 348.
[4] P. Weitz *et al*, Surf. Sci. 361/362 (1996) 542 and to be published.
[5] F. F. Fang *et al*, in D. Heimann (Ed.), High Magnetic Fields in the Physics of Semiconductors, World Scientific, Singapore, 1995, pp. 620-623
[6] H. W. Schumacher *et al.*, Physica B 256-258 (1998) 260.
[7] S. Brosig *et al.*, Physica B 256-258 (1998) 239.
[8] S. Koch *et al.*, Phys. Rev. B 47 (1993) 4048.

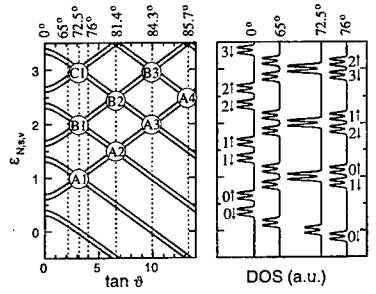

Figure 1:
(a) Energy levels $\epsilon_{N,s}$ of a 2DES in a Si (in units of $\hbar\omega_c$) as a function of the tilt angle. The circles mark positions of coincidences where ΔE_Z equals an integer multiple m of $\hbar\omega_c$. (b) Schematic DOS of the Landau levels for different tilt angles.

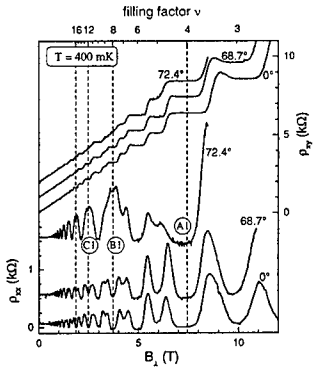

Figure 2: *Transverse resistivity ρ_{xx} and Hall resistivity ρ_{xy} as a function of the magnetic field perpendicular to the 2DES for different tilt angles.*

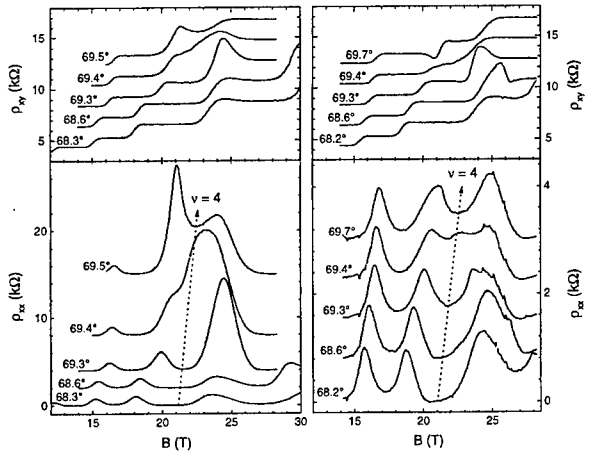

Figure 3:
ρ_{xx} and ρ_{xy} at 400 mK around the (A1) coincidence. On the left panel the parallel field component $B_{||}$ is oriented along the direction of the Hall bar, on the right $B_{||}$ is perpendicular to the Hall bar. Note the different scales for ρ_{xx}.

PA.9

Studies of the Quantum Hall to Quantum Hall Insulator Transition in InSb based 2DESs

S.Q. Murphy, J.L. Hicks, W.K. Liu, S.J. Chung,
K.J. Goldammer and M.B. Santos
Department of Physics and Astronomy, University of Oklahoma
Norman, OK 73019, USA

Abstract

The temperature dependence of ρ_{xx} is studied in the vicinity of the quantum Hall to quantum Hall insulator transition ($\nu = 1 \rightarrow 0$) in InSb/InAlSb based 2DESs. ρ_{xx} displays a symmetric temperature dependence about the transition with $\rho_{xx} \propto e^{-\sqrt{T_0/T}}$ on the QH side and $\rho_{xx} \propto e^{+\sqrt{T_0/T}}$ on the insulating side. A plot of $1/T_0$ for successive ν displays power-law divergence with $1/T_0 \propto |\nu - \nu_c|^{-\gamma}$, [1] with $\gamma = 2.2 \pm 0.3$. This critical behavior in addition to the $\rho_{xx} \propto e^{-\sqrt{1/T}}$ behavior expected of the quantum transport regime confirms that the QH/QHI transition is indeed a good quantum phase transition.

The classification of the integer quantum Hall (QH) to quantum Hall insulator (QHI) transition ($\nu = 1 \rightarrow 0$) as a quantum phase transition has been called into question as the result of recent transport and microwave experiments.[2] The inference from these GaAs and InAs 2DES transport studies where $\rho_{xx} \propto e^{-1/(\alpha T+\beta)}$, is that the critical region of the transition stays of finite width as $T \rightarrow 0$, hence the transition cannot be a true quantum phase transition. Disturbingly, the demonstrated similarity between the QH/QHI transition and the localization/delocalization transitions between quantum Hall (QH) plateaus [3] would suggest that these latter, well-understood transitions are not quantum phase transitions either.

Motivated by these experiments, we have undertaken a study of the QH/QHI transition in InSb/InAlSb based 2DESs grown via molecular beam epitaxy.[4] InSb is unique amongst the III-V family of semiconductors with the smallest energy gap ($236meV$ at $4.2K$), the smallest electron effective mass ($m^* = 0.0139m_o$) and the largest Lande g-factor (-51). These extreme parameters make the InSb/InAlSb system an interesting alternative to those systems in which the quantum Hall effect has previously been studied. The small effective mass and large g factor translate to extremely large cyclotron ($\omega_C \propto 1/m^*$) and spin gaps ($\Delta_s \propto g$); not unexpectedly, this results in an integer QHE which persists at high temperature ($> 25K$) and high excitation currents ($> 200\mu A$). More subtly, these large gaps affect the nature of the quantum Hall transport itself. Whereas in most 2DESs the quantum Hall transport displays Arrhenius behavior $\rho_{xx} \propto e^{-(\Delta/T)}$, where 2Δ is the cyclotron or spin gap, in our samples $\rho_{xx} \propto e^{-\sqrt{T_0/T}}$ at all but the highest temperatures. This $\sqrt{T_0/T}$ behavior is the signature of the Coulomb gap (GG) [5] and has been observed in all of our InSb samples. Because the spin and cyclotron gaps in InSb based 2DESs are so large ($> 100K$), Arrhenius behavior is highly suppressed and the transport at integer ν is dominated by CG behavior over virtually our entire experimental temperature range (0.5 to $20K$). Since CG behavior is inherently an interaction effect, the parameter T_0 conveniently provides an effective temperature proportional to the scale of the electron-electron interaction, $k_B T_0 \propto e^2/\varepsilon\xi$, where ε is the dielectric constant of InSb ($\varepsilon = 17.7\varepsilon_0$), and ξ is the electronic localization length. Due to this connection, we have made extensive use of CG behavior to study various localization/delocalization transitions in our InSb samples.

As a measure of the method's usefulness, we have tracked the CG behavior of ρ_{xx} as a function of ν, sweeping through the localization/delocalization transition between QH states ($\nu = 1 \rightarrow \frac{3}{2}$ and $\nu = 2 \rightarrow \frac{5}{2}$) for a number of InSb samples. While the assignment of CG behavior at integer ν is unambiguous, we can only assume this temperature dependence closer to the transition where T_0 should vanish. Reassuringly, it is observed that $1/T_0$ diverges as ν is swept towards ν_c, the critical filling factor of the interleaving delocalized states, with characteristic power-law behavior, $|\nu - \nu_c|^{-\gamma}$. This confirms that $1/T_0 \propto \xi$, as the correlation length should diverge as the delocalized states are approached. Indeed, our resultant measurements of γ in several samples (γ ranges from 2.1 to 2.5 with an uncertainty of ± 0.3 [6]) are in excellent agreement with theoretical predictions ($\gamma = 7/3$)[7] and previous experimental measurements.[8]

The method continues to be useful at the QH/QHI transition. Figure 1a displays ρ_{xx} *vs.* T for a series of applied magnetic fields spanning the $\nu = 1 \rightarrow 0$ transition for a sample with $n_s = 7.25\text{x}10^{10}/cm^2$ and a $\mu = 6300 cm^2/Vs$ [9]. The transition is close to a magnetic field of 5.06T ($\nu_c = 0.595$) where ρ_{xx} should intersect the $T = 0$ axis with zero slope. Figure 1b displays the same data *vs.* $\sqrt{1/T}$. As can be seen, $\sqrt{1/T}$ behavior can be extrapolated across the transition, persisting with a sign change on the QH insulator side. Surprisingly such a symmetry has also been observed at the $B = 0$ metal/insulator transition in low mobilty 2DESs such as SiMOSFETs and SiGe heterostructures[10] where $\rho \propto e^{-\sqrt{T_0/T}}$ is observed in the metallic phase and $\rho \propto e^{+\sqrt{T_0/T}}$ is observed in the insulating phase. The extracted $1/T_0 s$ from both sides of the transition are displayed in Figure 2a with the solid and open squares representing data from the QH and QHI sides of the transition respectively. The $1/T_0 s$ from both sides of the transition fall on the same divergent power-law with the same exponent ($\gamma = 2.2 \pm 0.3$) as observed in the higher filling factor transitions, in good agreement with the view that the QH/QHI transition is in the same universality class as the localization/delocalization transitions.[3]

Traditionally scaling exponents have also been extracted in a number of studies which scale the data by sliding sets at fixed ν (or n_s in the case of $B = 0$) to form a common scaling function. This is done in Figure 2b for our data for all 16 magnetic fields with $0.5 < T < 2K$ where the value of γ which results in the best fit is closer to 3. The scaling function method can be problematic since the scaling function is unknown. It is easy to weight higher temperature points which are outside the critical region too heavily and hence extract an erroneous value of the scaling exponent.

While the power-law behavior of $1/T_0$ and the strong scaling behavior are suggestive, they are not sufficient evidence that this is a good quantum phase transition; even the data which suggests a finite size critical region as $T \rightarrow 0$ collapses onto a common scaling function.[11] Rather the evidence that we have a good quantum phase transition lies in the temperature dependence of ρ_{xx}. A recent preprint by Shimshoni[12] examines the crossover from classical to quantum transport at the QH/QHI transition. This paper explains the $1/(\alpha T + \beta)$ behavior observed in the finite sized critical regime experiments[2] as a high temperature transport regime which is dominated by hopping between nearest neighbor QH puddles. According to Shimshoni, the quantum regime is indicated by variable range hopping (i.e. $1/\sqrt{T}$ behavior) which occurs when the size of the QH puddles becomes smaller than the dephasing length. Hence our observation that $\rho_{xx} \propto e^{-\sqrt{1/T}}$ implies that we are in the the requisite low temperature limit to see quantum behavior. In the model the crossover between the classical and quantum regimes moves to lower temperatures as the critical point is approached. While we do not see a clear crossover to classical behavior, we do observe that the temperature range over which we can credibly assign $1/\sqrt{T}$ behavior shrinks towards lower temperatures as we approach the transition. Suggestions of such a crossover can be seen in a recent preprint reporting QH transitions studies in p-SiGe 2DESs by Coleridge *et. al*[13].

In conclusion, the observation of strong scaling behavior in the *low temperature limit* (i.e. the

quantum regime) suggests that the QH/QHI transition is indeed a good quantum phase transition. And the symmetry in the temperature dependence is a tantalizing suggestion that the transition has a commonality with the transition at $B = 0$ for low mobility samples.

Acknowledgments

We acknowledge the support of the Sloan Foundation (SQM),and the NSF through grants DMR-9624699 and DMR-9631709.

References

[1] We use the γ to represent the exponent more commonly known as νz to avoid confusion with the filling factor.

[2] D. Shahar, M. Hilke, C.C. Li, D.C. Tsui, S.L. Sondhi, J.E. Cunningham and M. Razeghi, *Sol. State Comm.* **107**, 19 (1998); N.Q. Balaban, U. Meirav and I. Bar-Joseph, *Phys. Rev. Lett.* **81**, 4967 (1998).

[3] D. Shahar, D.C. Tsui, M. Shayegan, E. Shimshoni, and S.L. Sondhi, *Phys. Rev. Lett.* **79**, 479 (1997).

[4] K.J. Goldammer, W.K. Liu, G.A. Khodaparast, S.C. Lindstrom, M.B. Johnson, R.E. Doezema and M.B. Santos, *J. Vac. Sci. Technol.* **B16**, 1367 (1998).

[5] A.L. Efros and B.I. Shklovskii, *J. Phys. C* **8** L49 (1975).

[6] S.Q. Murphy, J.L. Hicks, S. Raymond, E. Waters, W.K. Liu, S. Chung, K.J. Goldammer and M.B. Santos, *in preparation.*

[7] G.V. Mil'nikov and I.M. Sokolov, *JETP Lett.* **48**, 536 (1988); J. T. Chalker and P.D. Coddington, *J. Phys. C* **21**, 2655 (1988); Bodo Huckestein and Bernhard Kramer, *Phys. Rev. Lett.* **64**, 1437 (1990); Y. Huo and R.N. Bhatt, *Phys. Rev. Lett.* **68**, 1375 (1992); Dung-Hai Lee, Ziqiang Wang, and Steven Kivelson, *Phys. Rev. Lett.* **70**, 4130 (1993); Hui Lin Zhao and Shechao Feng, *Phys. Rev. Lett.* **70**, 4134 (1993).

[8] H.P. Wei, D.C. Tsui, M.A. Paalanen and A.M.M. Pruisken, *Phys. Rev. Lett.* **61**, 1294 (1988); S. Koch, R.J. Haug, K. v. Klitzing and K. Ploog, *Phys. Rev. Lett.* **67**, 883 (1991).

[9] While samples with moblities as high as $300,000 cm^2/Vs$ are available, we have focussed our studies on low mobility samples.

[10] S.V. Kravchenko, Whitney Mason, G.E. Bowker, J.E. Furneaux, V.M. Pudalov and M. D'Iorio, *Phys. Rev. B* **51**, 7038 (1995); Dragana Popovic, A.B. Fowler and S. Washburn, *Phys. Rev. Lett.* **59**, 1543 (1997); P.T. Coleridge, R.L.Williams, Y. Feng and P. Zawadzki, *Phys. Rev. B* **56**, R12764 (1997).

[11] Ref. [19] of our Ref. [2] Shahar *et.al*

[12] Efrat Shimshoni, cond-mat/9904145

[13] P.T. Coleridge and P. Zawaszki, cond-mat/9903246.

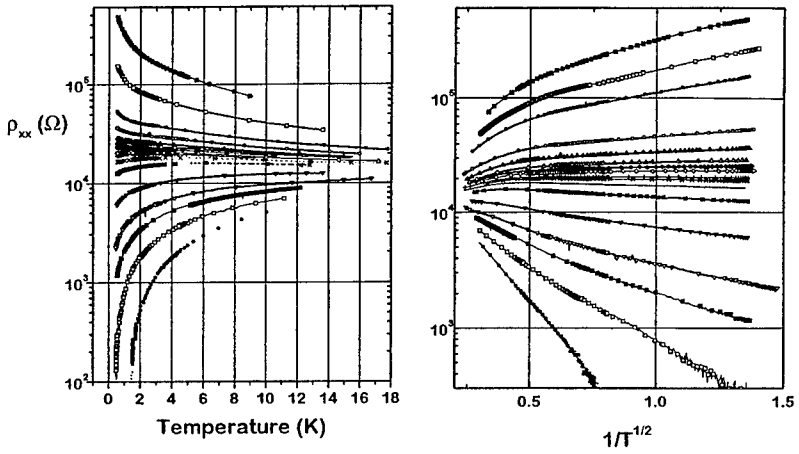

Figure 1: Figure 1a displays ρ_{xx} *vs.* T on a log-linear scale for 16 magnetic fields (3.97, 4.17, 4.43, 4.47, 4.67, 4.88, 4.97, 5.01, 5.04, 5.09, 5.12, 5.17, 5.26, 5.43, 5.97, and 6.78T) in the vicinity of the QH/QHI transition (the transition field is close to 5.06T). The sample has an $n_s = 0.725x10^{11}/cm^2$ and a $\mu = 6300cm^2/Vs$. Figure 1b displays the same data *vs.* $1/\sqrt{T}$. The Coulomb gap behavior seen on the QH side of the transition at low fields can be extrapolated through the transition to the insulating side with a change of sign.

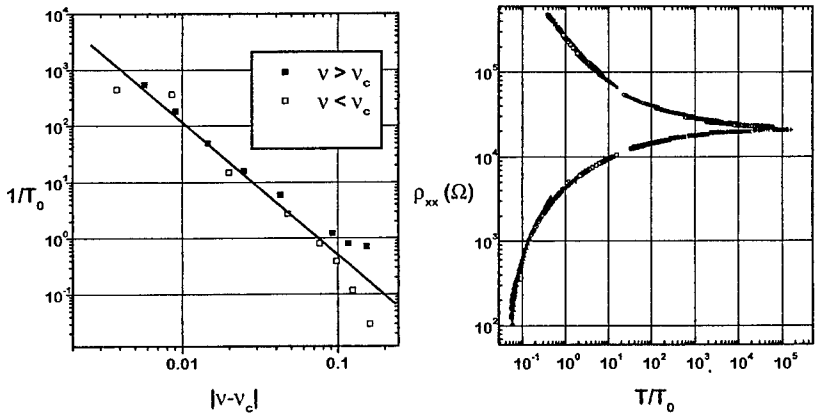

Figure 2: Figure 2a displays the values of $1/T_0 s$ extracted from the fits to Fig. 1b vs. $|\nu - \nu_c|$ on a log-log scale. The solid symbols represent data from the QH side of the transition and the open symbols that from the insulating side. The graph on the right displays the magnetic field sweeps for $T < 2K$ scaled onto a common scaling function. The exponent which results in the best data reduction is $\gamma = 3$.

PA.10

UNIVERSALITY AT A QUANTUM HALL - HALL INSULATOR TRANSITION IN A $Si/Si_{0.87}Ge_{0.13}$ 2D HOLE SYSTEM

R.B. Dunford[1]*, N. Griffin[1]‡, M. Pepper[1], C.J. Emeleus[2#], P.J. Phillips[2] and T.E. Whall[2]

[1]*Cavendish Laboratory, University of Cambridge, Madingley Rd, Cambridge CB3 OHE, UK*

[2]*Department of Physics, University of Warwick, Coventry, CV4 7AL, UK*

The temperature dependence of the magnetoresistivity of a $Si/Si_{0.87}Ge_{0.13}$ 2D hole system with $n=2.2\times10^{11}cm^{-2}$ and $\mu=16\,900\ cm^2/Vs$ (at 50mK) has been studied. An insulating phase is observed for $\nu<1$, with ρ_{xy} remaining finite and close to h/e^2, indicating a possible quantised Hall insulator state. The data on either side of the $\nu=1$ to Hall insulator transition can be scaled to a single pair of curves with a scaling exponent of $\kappa=0.68\pm0.05$. Temperature-independent conductivities close to $\nu=0.69$ and $\nu=1.5$ are found to appear at values of $\sigma_{xx}=0.5e^2/h$ ($\sigma_{xy}=0.5e^2/h$) and $\sigma_{xx}=0.5e^2/h$ ($\sigma_{xy}=1.5e^2/h$) respectively, in agreement with theory.

The 2D hole system (2DHS) in a compressive biaxially stressed $Si_{0.87}Ge_{0.13}$ channel is an unusual system because of the complex valence band structure, high effective mass and large, anisotropic g*-factor. This makes it an interesting system to study universalities in conduction at the B=0 metal-insulator transition [1,2], the quantum Hall effect and the Hall insulator regimes. New phenomena have been observed in this system such as an unanticipated insulating phase at $\nu=1.5$ which has been attributed to the unusual Landau level degeneracy [3-9].

We report on the magnetic field driven integer quantum Hall effect (QHE) to insulator transitions in a high mobility, low density 2DHS $Si/Si_{0.87}Ge_{0.13}$ heterostructure. At zero magnetic field, the sample is on the metallic side close to the B=0 metal-insulator transition [1,2].

The sample was grown by MBE on a bonded silicon-on-insulator substrate [10]. Firstly a 200nm Si buffer layer was grown, followed by a 25nm compressive biaxially stressed $Si_{0.87}Ge_{0.13}$ channel, a 20nm Si spacer layer, a 50nm doped Si supply layer (B: $N_A=2\times10^{18}cm^{-3}$) and a 30nm Si cap. The sample mobility of $\mu=16\,900\ cm^2/Vs$ at a hole density of $n=2.2\times10^{11}cm^{-2}$ (at 50mK) is one of the highest ever reported for 2D holes in a Si-based system. The ratio of the transport relaxation time to the quantum lifetime ($\tau_q=2.12ps$) is $\alpha=1.4$, suggesting that large-angle scattering is not completely dominant in this sample. In this strained system, the heavy hole band has the lowest energy for holes. An in-plane effective mass of $m^*=0.325\pm0.004m_e$ was obtained from the temperature-dependence of the low field Shubnikov-de Haas oscillations. The sample was mounted in a dilution refrigerator and magnetoresistivity measurements were performed using four-terminal, low-frequency ac techniques with a sample current of 2nA.

The longitudinal (ρ_{xx}) and Hall (ρ_{xy}) resistivity at 50mK are shown in Fig. 1. At intermediate fields, the integer QHE is only observed at odd-integer filling factors, due to the large g*-factor which causes the spin-splitting ($g^*\mu_B B$) to be comparable to the Landau level (LL) splitting ($heB/(2\pi m^*)$) [11]. Even-integer filling factor states only appear at $\nu=2$ [3-8,11] and, at the lowest temperatures, at $\nu=4$ [7]. The anomalous overshoot in ρ_{xy} just before the $\nu=3$ plateau is much smaller than in previously published results [3,7,9], possibly due to the higher sample mobility.

At high magnetic fields, for $\nu<1$, ρ_{xx} increases rapidly to at least $\sim10h/e^2$ at 50mK. This divergence is quenched upon increasing the temperature (Fig. 2a, 1.7K data). The $\nu<1$ insulating phase has been observed previously for p-type $Si/Si_{1-x}Ge_x$ [3,7] but no ρ_{xy} data has been presented. In the insulating region where ρ_{xx} is large, the ρ_{xy} data has to be averaged over both magnetic field

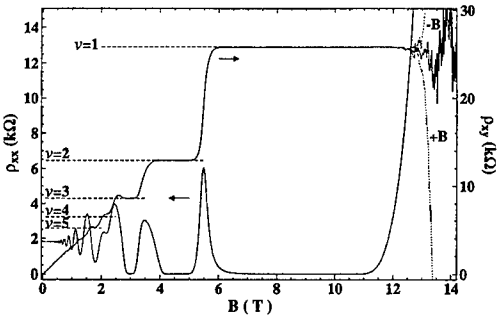

Fig. 1. Longitudinal and Hall magnetoresistivity at 50mK. The Hall data has been average over both field directions (+B, -B data at high field are shown by the dotted lines).

directions (+B, -B) to remove ρ_{xx} admixture effects due to slight asymmetries in the Hall bar geometry. The averaged ρ_{xy} data remains finite and close to the classical Hall slope, indicating a Hall insulator (HI) state [12]. In fact ρ_{xy} stays close to $1h/e^2$, the quantised value of the $\nu=1$ Hall plateau, suggesting a possible quantised Hall insulator state [13] which has recently been observed in a Ge channel device [14]. Measurements to higher fields are required.

The crossover from the $\nu=1$ to the HI state occurs at a temperature-independent point where both $\rho_{xx}=\rho_{xy}=1h/e^2$ (or $\sigma_{xx}=\sigma_{xy}=0.5e^2/h$, by matrix inversion) at a critical value of ν, $\nu_c=0.69$. (Fig. 2a). This is in agreement with a numerical calculation that found that both σ_{xx} and σ_{xy} should equal $0.5e^2/h$ at the transition for non-interacting electrons in the lowest LL [15]. It has been predicted that the resistivity between integer QHE states should exhibit universal temperature scaling behaviour with a T^{κ} dependence. The scaling exponent is given by $\kappa=p/2D$ where p is the inelastic scattering exponent and D is the localisation length exponent [16]. In Fig. 2b $\log(\rho_{xx})$ has been plotted against the scaling variable $|\nu - \nu_c|/T^{-\kappa}$. The temperature data on either side of the $\nu=1$ to HI transition can be scaled to a single pair of curves for a scaling exponent of $\kappa=0.68\pm0.05$. The theoretical prediction of $\kappa=0.43$ [17] assumes that p=1, and has been observed experimentally for the $\nu=2$ to HI [18] and $\nu=1/3$ to HI [18,19] transitions in $Al_xGa_{1-x}As/GaAs$ heterostructures. It has also been found that κ increases with decreasing mobility [20]. In our sample we find that p=1.5 [21] (from the low field weak localisation behaviour), which would increase the theoretical universal scaling exponent to 0.65, in agreement with our experimental value.

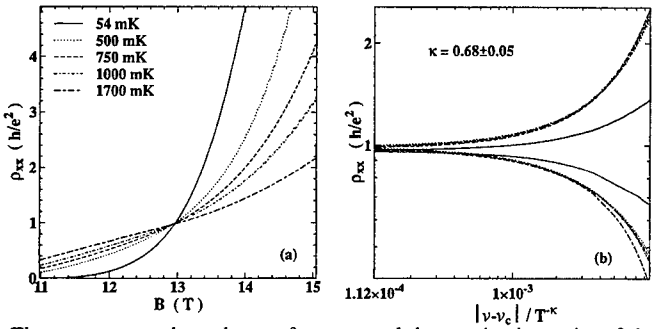

Fig. 2. (a) The temperature-dependence of ρ_{xx} around the termination point of the $\nu=1$ QHE state. (b) The temperature-scaling behaviour of ρ_{xx} around the $\nu=1$ to Hall insulator transition. Most of the temperatures scale to a single pair of curves for a scaling exponent $\kappa=0.68\pm0.05$. The deviation of the 54mK data is due to carrier heating.

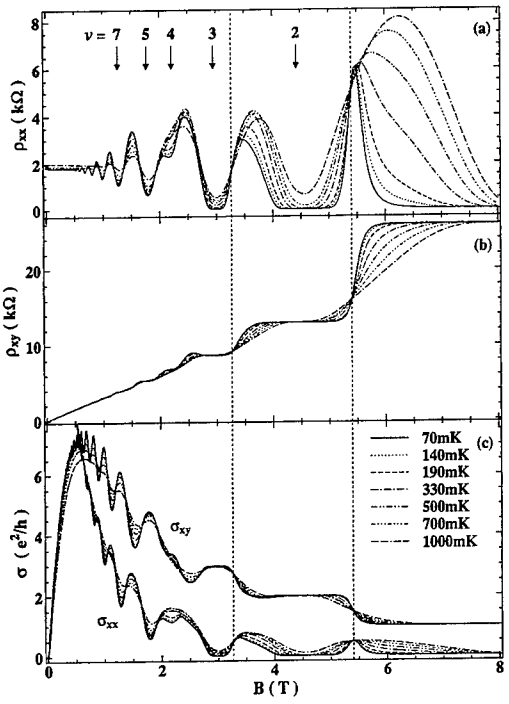

Fig. 3. Temperature-dependence of (a) longitudinal and (b) Hall magnetoresistivity. In (c), the conductivity components calculated by matrix inversion are shown. The positions of the temperature-independent points at the ν=3 to 2 and ν=2 to 1 transitions are shown by vertical dashed lines.

The detailed temperature dependence of ρ_{xx} and ρ_{xy} in the integer QHE region is shown in Fig. 3. At zero magnetic field, there is a small decrease in ρ_{xx} as the temperature is lowered, characteristic of the metallic phase close to the metal-insulator transition [1,2]. At the ρ_{xx} maxima close to ν=1.5, ρ_{xx} also decreases with decreasing temperature, in contrast to many previous results [3-9] where an insulating phase close to ν=1.5 has been attributed to an unusual LL degeneracy. It is not clear if this is due to the higher mobility or the high m* which reduces the LL degeneracy in our sample.

An interesting feature of Fig. 3a,b is that there are two points which are temperature-independent for both ρ_{xx} and ρ_{xy} between adjacent integer QHE states at the ν=3 to 2 and ν=2 to 1 transitions (marked by vertical dashed lines in Fig. 3). The ρ_{xx} maxima are not centred around a particular field value but become increasingly displaced to higher field as the temperature is increased. By converting the data to conductances using matrix inversion, the maxima become much more symmetrical (Fig. 3c) [22]. The temperature-independent conductivity close to ν=1.5 is at the maxima of σ_{xx} at $\sigma_{xx}=0.5e^2/h$ and halfway between the σ_{xy} QHE plateau at $\sigma_{xy}=1.5e^2/h$. The results are again in agreement with the theory of Huo *et al.*, [15] when it is considered that σ_{xy} gains a contribution of $1e^2/h$ for each LL below the Fermi energy.

In conclusion, the parallels between the universal conductivities at the ν=2 to 1 and ν=1 to HI transitions suggests that these transitions are similar in nature. It will be shown elsewhere that by removing the effect of the lowest Landau level [22], the temperature-independent point at ν=1.5 can also be considered a QHE to HI transition, which can be roughly scaled using κ=0.70±0.06 [21]. The similarity of the scaling exponents demonstrates the similarity of the two transitions in our $Si/Si_{0.87}Ge_{0.13}$ 2DHS and is confirmation of the universality of the conclusion of Shahar *et al.* that in $Al_xGa_{1-x}As/GaAs$ heterostructures [22] a inter-QHE transition is equivalent to a QHE to HI transition in the highest-energy Landau level.

This work was funded by the EPSRC. We thank D.J. Paul for useful discussions on sample preparation.

* Corresponding author: tel: 44 1223 337469, fax: 44 1223 337271, email:rd225@cam.ac.uk.
‡ Currently at National Microelectronics Research Centre, Lee Maltings, Prospect Row, Cork, Ireland.
# Currently at Department of Physics & Astronomy, The University of Glasgow, University Avenue, Glasgow, G12 8QQ, UK.

[1] J. Lam, M. D'Iorio, D. Brown and H. Lafontaine, Phys. Rev. B 56 (1997) 12741.
[2] P.T. Coleridge, R.L. Williams, Y. Feng and P. Zawadzki, Phys. Rev. B 56 (1997) 12764.
[3] F.F. Fang , R.B. Dunford, R. Newbury, R.P Starrett, A.V. Skougarevsky, R.G. Clark, J.O. Chu and B.S. Meyerson, in: D. Heiman (Ed.), High Magnetic Fields in the Physics of Semiconductors, World Scientific, Singapore, 1995 620.
[4] S.I. Dorozhkin, C.J. Emeleus, O.A. Mironov, T.E. Whall and G. Landwehr, Phys. Rev. B 52 (1995) R11 638.
[5] S.I. Dorozhkin, C.J. Emeleus, O.A. Mironov, T.E. Whall, G. Landwehr, Surf. Sci. 362 (1996) 933.
[6] M. D'Iorio, D. Stewart, S. Deblois, D. Brown and J.-P. Noël, Surf. Sci. 362 (1996) 937.
[7] R.B. Dunford, E.E. Mitchell, R.G. Clark, V.A. Stadnik, F.F. Fang, R. Newbury, R.H. McKenzie, R.P. Starrett, P.J. Wang and B. S. Meyerson, J.Phys.: Condens. Matter 9 (1997) 1565.
[8] P.T. Coleridge, A.S. Sachrajda, and P. Zawadzki, R.L. Williams, Y. Feng, and H. Lafontaine, Solid State Commun. 102 (1997) 755.
[9] T.Y. Lin, M.S. Tsai, Y.F. Chen and F.F. Fang, J.Phys.: Condens. Matter 10 (1998) 9691.
[10] D.J. Paul, N. Griffin, D.D. Arnone, M. Pepper, C.J. Emeleus, P.J. Phillips and T.E. Whall, Appl. Phys. Lett. 69 (1996) 2704.
[11] F.F. Fang , P.J. Wang, B.S. Meyerson, J.J. Nocera and K.E. Ismail, Surf. Sci. 263 (1992) 175.
[12] S. Kivelson, D. -H. Lee and S. -C. Zhang, Phys. Rev. B 46 (1992) 2223.
[13] E. Shimshoni and A. Auerbach, Phys. Rev. B 55 (1997) 9817.
[14] M. Hilke, D. Shahar, S.H. Song, D.C. Tsui, Y.H. Xie and D. Monroe, Nature 395 (1998) 675.
[15] Y. Huo, R.E. Hetzel and R.N. Blatt, Phys. Rev. Lett. 70 (1993) 481.
[16] A.M.M. Pruisken, Phys. Rev. Lett. 61 (1988) 1297.
[17] H.L. Zhao and S. Feng, Phys. Rev. Lett. 70 (1993) 4134.
[18] R.J.F. Hughes, J.T. Nicholls, J.E.F. Frost, E.H. Linefield, M. Pepper, C.J.B Ford, D.A. Ritchie, G.A.C. Jones, E. Kogan and M. Kaveh, J.Phys.: Condens. Matter 6 (1994) 4763.
[19] L.W. Wong, H.W. Jiang, N. Trivedi and E. Palm, Phys. Rev. B 51(1995) 18033.
[20] S. Koch, R.J. Haug, K. v. Klitzing and K. Ploog, Phys. Rev. B 43(1991) 6828.
[21] R.B. Dunford, N. Griffin, C.J. Emeleus, P.J. Phillips and T.E. Whall, to be published.
[22] D. Shahar, D.C. Tsui, M. Shayegan, E. Shimshoni and S.L. Sondhi, Phys. Rev. Lett. 79 (1997) 479.

PA.11

Single-Electron States in the Quantum Hall Effect.

N.B. Zhitenev, T.A. Fulton, A. Yacoby*, H. Hess†, L.N. Pfeiffer, K.W. West
Bell Labs., Lucent Technologies, Murray Hill, NJ 07974
* Weizmann Institute of Science, Rehovot, Israel
† Phasemetrics Inc., San Diego, CA 92121

Spatially localized electronic states in a two-dimensional electron gas in the quantum Hall regime are imaged using a scanning single-electron-transistor probe. Two different regimes of localization are identified depending on the strength of the built-in long-range density fluctuations. In the smoother regions localized states merge into dielectric-like blobs a few μm in extent. In the places with a stronger density gradient complex patterns occur which change markedly with an addition of a single electron. The simplest appearance of the latter is a ring collapsing toward the center as an electron is added to the area.

It is accepted that in the quantum Hall (QH) regime electronic states at the Fermi level in the interior of two-dimensional electron gas (2DEG) are localized [1,2]. To advance the physics of localization further, new microscopic characterization tools are desirable. By definition, localization means a confinement of the electron wavefunction within a restricted area, which may result in an inhomogeneous charge and potential distribution. Recently, several scanning probe experiments [3-6] have demonstrated the capability to image electrical properties in a two-dimensional electron system. In addition to micrometer-scale features showing the Hall potential distribution and edge-state contours [5,6], finer structures in compressibility and resistance were seen [4] down to the scale of 100 nm. Here, we look for localized states in the QH regime near filling factor ν=2, employing the technique of Ref. 6 with higher resolution in position and density. The behavior observed is complex, but contains systematic features. In particular, individual objects are seen which are evidently single-electron localized states.

To measure the local electrostatic potential we employ a single electron transistor fabricated on a tip of a tapered glass fiber as described in [3,6,7]. The tip is scanned just above the surface of a GaAs/AlGaAs heterostructure having the 2DEG buried 100 nm below the surface. The average density n_0 of the 2DEG is $1.5*10^{11}$ cm^{-2}. Additionally, a bias V_{bg} on the backgate, located 5.4 μm under 2DEG, allows us to vary the density of electrons (V_{bg}=-1 V reduces the density by $1.3x10^{10}$ cm^{-2}). The SET is operated in a feedback loop maintaining constant potential on the SET's central island. The feedback voltage V_{fb}, applied to the 2DEG and backgate, directly reflects the local potential seen by the SET. In addition, we modulate the 2DEG density at a frequency above the roll-off of the feedback loop and record the "transparency", the ac potential seen by the SET. With all other charges being immobile at low temperature, the contrast in the ac signal is determined solely by charges in the 2DEG layer. Transparency is only seen near integer filling factors, and denotes low electron compressibility and/or high resistivity. All measurements shown are carried out at temperature of 0.8 K.

In the experiments, the magnetic field is set at ~3.1 T, nominally corresponding to ν=2, although the local densities vary by a few percent. At a variety of arbitrary locations we then record either the V_{bg} (density) dependence of the dc ($-V_{fb}$) and ac (transparency) signals at fixed locations, or spatial images of these at a set of fixed V_{bg}.

For the density dependence, the SET tip is fixed in place and the 2DEG density is swept so that the local filling factor passes through the integer value. Broadly, the behavior tends to be of one of two types. Typical records of these responses are shown in Fig.1a. In both, the dc potentials ($-V_{fb}$) display the same characteristic step of $\sim\hbar\omega_c/2\pi$ associated with the Fermi level passing between the third and second Landau levels [6,8], but the accompanying ac signal amplitude differs by up to x10. Quantitatively, the smaller signals in the right panel in Fig.1a

correspond to the derivative of the dc step, as expected at equilibrium (the structure in the signal is discussed below). The larger size of the signal in the leftmost ac curve shows that a significant resistance is impeding charge transport to the particular location at the frequency of 70 Hz. Correspondingly, an out-of-phase component of the ac signal appears at the condition where the charging rate of the location is comparable with the ac modulation rate. In the following, we examine some typical spatial structures of regions first without and then with ac equilibrium charging.

A set of in-phase ac transparency data taken in an area with incomplete charging is shown in Fig.1b. A region of ~1x1 μm^2 is sampled on a 3x3 square grid. The maximum shift of the peaks across the area is ~100 mV of V_{bg} , for an typical local density gradient of $<1x10^{13}$ cm^{-3}. Such a gradient is representative for the smoother areas in the sample, and is generally associated with non-equilibrium charging. As seen from Fig.1b, a typical ac curve is not smooth but rather appears to be a superposition of smaller peaks centered at different V_{bg} voltages. The characteristic spatial correlation length is in the micrometer range. As the strength of a particular peak changes with spatial position, the overall maximum changes its shape and slides across the V_{bg} scale. Apparently, each such peak is an event centered around a distinct location and density.

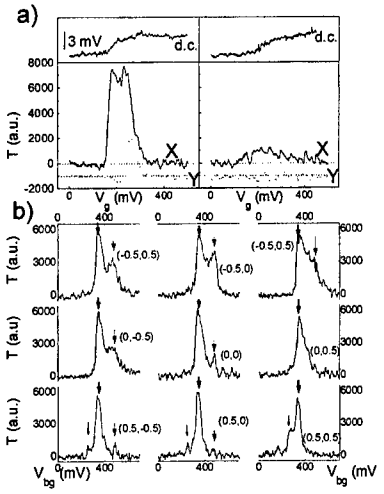

Fig.1 a) Two typical sets (left and right panels) of data acquired by SET as the electron density (~V_g) is swept through ν=2 at different spatial locations. On each panel: top - dc signal displaying the characteristic step of the chemical potential as the Fermi level moves from second to third Landau level; bottom in-phase (X) and out-of-phase component (Y) (shifted down by 1000) of ac transparency signal. b) In-phase ac transparency signals as a function of V_g measured at 9 spatial locations arranged in 3x3 grid over an area of strong transparency of 1x1 μm^2. Different types of arrows mark the equivalent peaks detected at distinct spatial locations.

Typically, the evolution of strong transparency passes through two stages. First, as the density is changed toward the local integer ν, a number of neighboring spots with typical individual diameters of ~0.5 μm become slightly transparent at close but separate values of V_{bg}. Then, as some area becomes filled up by the latest emerging spots, the area as a whole becomes strongly transparent, giving rise to a transparency peak like those in Fig.1b. The reverse sequence describes the falling edge of the strong transparency peak. An example of an area becoming strongly transparent as the last spot completes the merging is shown on a gray scale in Fig. 2. The transparency signal, acquired over an area of 5x5 μm^2, is shown for three V_{bg} voltages, a total electron density change of 2.5 electron/μm^{-2}. The only significant change to the shape of the transparent regions is the addition of a transparent (darker) spot centered at around (35,25) and subtraction of the spot at (30,2), which is not adjoining the main transparent area. However, the whole area becomes significantly more transparent, while mostly preserving its shape.

The tendency of larger blobs to display a stronger transparency can be understood on the following model. We assume that the blob is made up of multiple isolated (at 70 Hz.) islands. The potential modulation induced on an island is proportional to C_{bg}/C_{Σ} where C_{bg} is the island-

backgate capacitance and C_Σ is the total capacitance of the island. C_Σ is determined mainly by the distance between the island and the compressible regions. The maximal potential amplitude and, therefore, the maximal transparency occur farthest from the compressible area. The larger the blob, the stronger the transparency signal in its center. The amplitude of ac potential drops toward the edges of the blobs as the screening compressible area becomes closer. All this is in agreement with the experimental observations (Fig. 2).

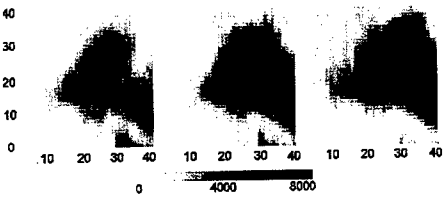

Fig.2 Spatial images of in-phase ac signal over 5x5 μm^2 area of strong transparency taken at three different densities. V_{bg} is changed by 10 mV between images.

Quite different patterns of transparency are observed in regions with significantly larger built-in potential gradients. Representative transparency curves are shown in Fig.3a. There is no out-of-phase signal exceeding the noise floor all over the range, indicating that the charging is in equilibrium at 70 Hz. The typical local density gradient in this region is ~$1x10^{14}$ cm^{-3}, 10x steeper than for the region shown in Fig.1b. The transparency signal, which is ~5x weaker than in the previous example, displays multiple oscillations with peaks separated by 30-40 mV in V_{bg}. The oscillation pattern is generally reproducible as illustrated by the traces (3) and (4) but can slowly vary with time. In places, the transparency oscillations reach definite, reproducible negative values. The dc signals show corresponding step structure, but these are more often obscured by noise.

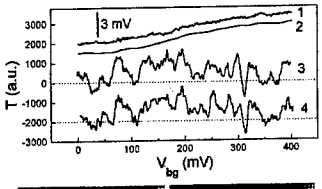

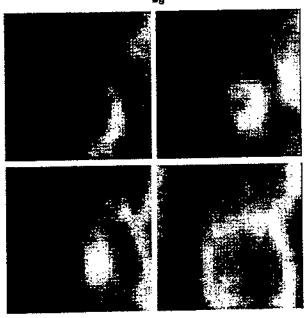

The corresponding spatial maps are complex. However, when the oscillations with density are well-defined, we generally find relatively simple patterns whose features move about with density, giving rise to the oscillations. An example of such maps is shown in Fig.3b. The scanned area of 0.45x0.45 μm^2 is shown for four values of V_{bg} changed by 15 mV between the panels, nominally an addition of 0.4 electrons over the panel area. There are clearly-seen ring-like structures contracting to a common center. The transparency signals on the rings are comparatively small, and sometimes negative, while those in the center of the rings (dark regions) are larger and positive. For this particular place we observed two full periods of rings oscillation as the density is swept. In the general case, the patterns are much more complicated. We often observe several circular objects placed close one to another. As the objects expand and collide, the overall pattern evolves rapidly, losing self-similarity quickly as a function of density. We do not see

Fig.3 a) dc (1) and ac in-phase (3,4) signals as a function of V_g measured at arbitrary location in a region of weak transparency at ν=2. Curves (3) and (4) are taken sweeping V_{bg} forth and back to illustrate the reproducibility. The integrated ac signal (2) closely reproduces the measured dc signal (1). b) Spatial images of the in-phase ac signal over 0.45x0.45 μm^2 area of weak transparency taken at four different densities. V_{bg} is changed by 15 mV between images which adds on average ~0.4 electrons to the total area of the frame. White denotes zero or slightly negative transparency.

any correlation between the extrema of the surface potential and the centers of the rings.

The multiple oscillations of the transparency are reminiscent of single electron charging effects in quantum dots [9]. There the analogous Coulomb-blockade charging behavior in quantum dots would be saw-tooth changes of dc potential. Other experimental facts also parallel the single electron blockade behavior. First, the quasi-period of the rings against the density increment approximately corresponds to the addition of a single electron charge over the maximal correlated area of the structure. Second, as noted above, the peaks often overshoot the level of zero yielding negative transparency, as is seen in the capacitance measurements under Coulomb blockade conditions [10].

In some manner the contraction of a ring through one cycle adds one electron to the immediate area, but just how is not clear. A model in which the electron is being transferred into a fixed potential energy minimum created by disorder does not provide the observed continuous spatial variation of electrical potential. Also, the screening is weak. It is broadly accepted that the density of the carriers able to move freely and to participate in the screening is determined by the deviation from the integral filling [11]. This density is less than $3x10^9$ cm^{-2} yielding the average distance between the free carriers of >200 nm. This distance is comparable to the typical sizes of the ring patterns. It is not clear how the continuous variation of the potential of the ring evolution can be provided by so few screening carriers.

In analogy with the oscillating regions, we believe that the strongly transparent regions with incomplete charging are built up from single localized electron states. The formation of the blobs by merging small, slightly transparent spots supports this idea. But unlike the weak transparency case, the electron states inside blobs are localized far apart and do not overlap with each other or with the extended (compressible) states.

The distinction of the regions with either strong or weak transparency with respect to the built-in potential gradient can be understood qualitatively. It is predicted [12] and observed experimentally [6] that the contour lines with integer filling factors widen into strips. This depletes the number of carriers able to screen the disorder potential within the strip. The macroscopic electrostatic model yields the strip width of ~1.2 μm for the gradient of $\sim 1x10^{13}$ cm^{-3} typical for the regions occupied by the strongly transparent blobs. The screening of the disorder potential by the compressible states 1 μm apart is not very efficient and electrons are strongly localized. With the gradient of $\sim 1x10^{14}$ cm^{-3}, the strip width is ~400 nm, improving the screening. This reduces effective disorder strength allowing for significant correlation effects.

In summary, the experiment described here has shown strong evidence for single-electron localized states in the QH regime with the image contrast originating either from the local resistance or from the local charging blockade.

1. R.E. Prange and S.M. Girvin, ed. *The Quantum Hall Effect*. 1990, Springer-Verlag.
2. R.B. Laughlin, Phys. Rev. B **23**, 5632 (1981).
3. M.J. Yoo *et al.*, Science **276**, 579 (1997).
4. S.H. Tessmer *et al.*, Nature **392**, 51 (1998).
5. K.L. McCormick *et al.*, Phys. Rev. B, **59**, 4654 (1999).
6. A. Yacoby *et al.*, Solid State Comm. **111**, 1 (1999).
7. T.A. Fulton and G.J. Dolan, Phys. Rev. Lett. **59**, 109 (1987).
8. T.P. Smith *et al.*, Phys. Rev. B **32**, 2696 (1985).
9. M.A. Kastner, Physics Today **46**, 24(1993).
10. D. Berman *et al.*, Phys. Rev. Lett. **82**, 161 (1999).
11. A.L. Efros, Solid State Comm. **67**, 1019 (1988).
12. D.B. Chklovskii, B.I. Shklovskii, and L.I. Glazman, Phys. Rev. B **46**, 4026 (1992).

PA.12

Hall-potential investigations under quantum Hall conditions using scanning force microscopy

P. Weitz, E. Ahlswede, J. Weis, K. v. Klitzing, and K. Eberl
Max-Planck-Institut für Festkörperforschung,
Heisenbergstrasse 1, D-70569 Stuttgart, Germany

Hall-potential profiles of a two-dimensional electron system (2DES) under quantum Hall (QH) conditions have been investigated at $T = 1.4$ K with submicron resolution using a scanning force microscope sensitive to electrostatics. At an even integer Landau level filling factor a rather nonlinear Hall-potential profile across the Hall-bar is observed. But at reduced magnetic field values corresponding to filling factors slightly above this even integer value almost no Hall-potential drop across the bulk region is found. Instead, the potential clearly drops across prominent areas associated with the positions of incompressible strips that just had emerged at that filling factor at both edges. This shows that the dominant incompressible strips of locally even integer filling factor can decouple the bulk from the edge, hence demonstrating the importance of the edge region for the Hall-field distribution even at non-integer filling factors.

Introduction

The spatial potential distribution in two-dimensional electron systems (2DES) under quantum Hall (QH) conditions [1] is still controversially discussed. Theoretical models favor either that a current applied to the sample flows at the edge regions of the 2DES [2–4], or that the current distribution extends throughout the bulk of the 2DES [5–7].

In the presence of a magnetic field, the existence of so-called compressible and incompressible strips within the depletion region of the edge of the 2DES has been predicted [8,9]. These strips behave either metal- or insulator-like, influencing the current distribution and hence the Hall-potential profile within the 2DES. Several experimental studies could affirm the principle importance of the edge region (for a review see [10]). Spatially resolved investigations of the potential distribution were carried out by using e. g. electro-optical effects [11–14] or more recently by scanning probe methods [15–17], although only [17] studied a conventional Hall-bar geometry so far. Most of the data indicate that around integer filling factors the observed Hall-potential profile is nonlinear with the major potential drop located in the inner part of the sample, while the reported results are not so clear for non-integer filling factors. In order to investigate this issue in more detail we have developed a low-temperature scanning force microscope (SFM) sensitive to electrostatics.

Experimental details

The sample studied consists of a modulation-doped $GaAs/Al_{0.33}Ga_{0.67}As$ heterostructure grown by molecular beam epitaxy with the 2DES formed at the heterojunction 40 nm beneath the surface [18]. The electron concentration is $n_s = 4.3 \times 10^{15}$ m^{-2} and the electron mobility is 50 m^2/Vs at the temperature $T = 4.2$ K. A Hall-bar mesa with two ohmic contacts and a central width of 10 μm (see Fig.1(a)) was defined into the heterostructure. All measurements were performed at $T = 1.4$ K in a 13 T superconducting magnet. The home-made SFM [19] has been designed for a 3-inch piezoelectric tube, allow-

ing a scan range of about 20 μm $\times$ 20 μm at $T = 1.4$ K, while coarse positioning of the sample is managed by means of a moving stage driven by slip-stick technique. Scanning and data acquisition is accomplished by a commercial Omicron SCALA system. As force sensitive probes we used Ir-coated piezoresistive Si-cantilevers [20]. The SFM is used in dynamic force mode at a constant height typically 30 nm above the surface.

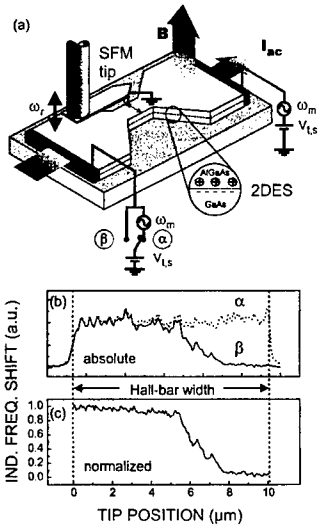

FIG. 1. (a) Sketch of the experimental setup. (b) Absolute and (c) normalized induced shift of the cantilever's resonance frequency for 9.1 T ($\nu = 1.98$). The modulation is applied at only one contact (curve β) or at both contacts simultaneously, giving the calibration curve α.

The cantilever is mechanically driven at its resonance frequency ω_r ($\approx 2\pi \times 37$ kHz), which is continuously adjusted by a slow feedback loop. A uniform *dc* bias $V_{t,s}$ is applied between sample and tip in order to diminish the contact potential $\Delta\mu^{ch}_{t,s}/e$ (≈ 0.35 V) between tip and sample to an effective bias of $(V_{t,s} + \Delta\mu^{ch}_{t,s}/e) \approx 0.1$ V [21]. An *ac* current modulation through the 2DES, driven by an additional small *ac* modulation $\hat{V}^m_{t,s} \sin\omega_m t$ ($\hat{V}^m_{t,s} = 0.02$ V (RMS), $\omega_m = 2\pi \times 3.4$ Hz [22]) applied at one contact while the other is grounded, builds up the Hall-voltage, which in turn induces a shift of the resonance frequency $\Delta\omega_r(x,y)$ proportional to the modulation of the local potential with $0 \le \hat{V}^m_{t,s}(x,y) \le \hat{V}^m_{t,s}$:

$$\Delta\omega_r(x,y) \propto \Big\{ \partial_d^2 Q(x,y) + \partial_d^2 C(x,y) \cdot \Big[V_{t,s} + \Delta\mu^{ch}_{t,s}(x,y)/e \Big] \Big\} \cdot \hat{V}^m_{t,s}(x,y) \quad (1)$$

The quantity $\partial_d^2 C(x,y)$ is related to the second derivative of the tip-sample capacitance with respect to the tip-sample distance d, and $\partial_d^2 Q(x,y)$ is related to the second derivative of the amount of image charges induced on the tip by the donor charge layer between 2DES and tip [23]. Serving as the measured signal, this frequency shift $\Delta\omega_r$ is recorded during single-line scans in the Hall-bar center by means of lock-in technique (an example is shown in Fig.1b, curve β, corresponding to switch position β in Fig.1a). We account for the dependence of $\partial_d^2 Q$ and $\partial_d^2 C$ on the tip position (x,y), which effects $\Delta\omega_r(x,y)$ according to (1), by calibrating the signal with reference data obtained by applying a uniform modulation to all sample contacts simultaneously, so that $\hat{V}^m_{t,s}(x,y) \equiv \hat{V}^m_{t,s}$ (curve α in Fig. 1b, corresponding to switch position α in Fig. 1a). The position dependent proportionality factor in (1) is hence eliminated in the normalized potential profile obtained by dividing curve β by curve α (see Fig.1c) [24].

Since we are measuring the induced frequency shift $\Delta\omega_r$ caused by the *change* of the force on the cantilever with distance, the contribution from the tip-sample interaction is enhanced but capacitive background signals are reduced so that a high spatial resolution of about 0.1 μm is achieved. Furthermore this

technique allows the investigation of poorly conducting areas such as those present under QH conditions, since only *ac* voltage excitations of a few Hertz are required and hence high-frequency charging effects are avoided.

Results

Fig.2 shows the development of the Hall-potential profiles with magnetic field B at filling factors $\nu \equiv hn_s/eB$ in the range $1.67 < \nu < 2.73$. Coming from the high field side towards the QH plateau, the potential drops linearly across the whole sample width. Then starting at $B = 9.6$ T ($\nu = 1.96$) the profile flattens at the edges but drops now rather arbitrarily in the inner region. This behavior develops throughout the QH plateau until finally at 8.4 T ($\nu = 2.14$) a new situation occurs. Here the Hall-potential profile runs nearly horizontally in the inner region of the sample, but shows relatively sharp potential steps at the Hall-bar edges. The slope of the potential drop in this inner region increases if the magnetic field is further reduced, indicating that the inner region couples more and more to the edge regions until finally slightly below $\nu = 3$ the potential drop takes place across the whole width again. This evolution is repeated across $\nu = 3$ only in outlines, but is clearly traceable again for even $4 \leq \nu \leq 8$ (not shown).

These findings can be associated with the existence of compressible and incompressible strips in the 2DES. Bulk-edge equilibration at non-integer filling factors is related to the capability of the innermost incompressible strip of isolating the compressible inner region (i.e. the bulk) from the outer compressible strips. As incompressible strips related to odd ν are rather narrow due to the small spin splitting of the related Landau levels, bulk-edge equilibration is only slightly suppressed and a linear potential drop across the whole Hall-bar width is observed for $1 < \nu < 2$. When the magnetic field is reduced, it is not before the incompressible strip due to the local filling factor $\nu_l = 2$ has emerged that a decoupling of the bulk from the edges occurs and the Hall-voltage drops mainly across the incompressible strip.

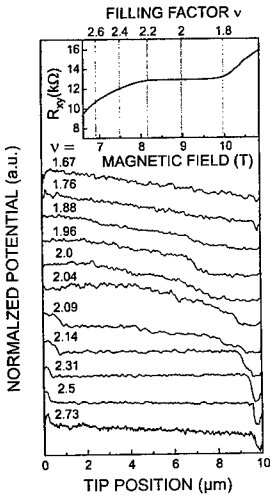

FIG. 2. Normalized Hall-potential profiles across the Hall-bar for different magnetic fields around filling factor $\nu = 2$ ($B = 9.0$ T) [25].

As this strip width decreases with decreasing magnetic field, the coupling rises again, resulting in a linear potential drop throughout the bulk region. Well within a QH plateau the entire bulk region is no longer metal-like and the Hall-potential profile is affected by the local distribution of impurities and inhomogenities in this area, leading to a rather unpredictable potential drop across the bulk. The results reported in [17] are similar in the case of integer ν, but do not show this strong decoupling between the bulk and the outer edge region for non-integer ν.

In summary, we have investigated the Hall-potential profiles of a 2DES using a low-temperature scanning probe microscope. At

integer filling factors the potential drop takes place preferably in the bulk of the sample. Slightly above integer filling factors the innermost incompressible strip at the edge region of the sample decouples the outer edge region from the bulk. The grade of decoupling is related to the width of this incompressible strip. These results indicate the importance of the edge strips for the Hall-potential distribution even at non-integer filling factors.

Acknowlegdments

The authors thank M. Hauser, M. Riek, T. Reindl and M. Schmid for technical support, and R. Gerhardts, G. Nachtwei and J. Smet for discussions. This work has been supported by the Bundesministerium für Bildung und Forschung (BMBF) under the grant 01 BM 624/7.

[1] K.v. Klitzing, G. Dorda, M. Pepper, Phys. Rev. Lett. 45 (1980) 494.

[2] B.I. Halperin, Phys. Rev. B 25 (1982) 2185.

[3] M. Büttiker, Phys. Rev. B 38 (1988) 9375.

[4] J.K. Wang, V.J. Goldman, Phys. Rev. B 45 (1992) 13479.

[5] R. Woltjer, R. Eppenga, J. Mooren, C.E. Timmering, Europhys. Lett. 2 (1986) 149.

[6] D.J. Thouless, Phys. Rev. Lett. 71 (1993) 1879.

[7] K. Tsemekhman, V. Tsemekhman, C. Wexler, D.J. Thouless, Solid State Comm. 101 (1997) 549.

[8] D.B. Chklovskii, B.I. Shklovskii, L.I. Glazman, Phys. Rev. B 46 (1992) 4026; D.B. Chklovskii, K.A. Matveev, B.I. Shklovskii, Phys. Rev. B 47 (1993) 12605.

[9] K. Lier, R.R. Gerhardts, Phys. Rev. B 50 (1994) 7757; J.H. Oh, R.R. Gerhardts, Phys. Rev. B 56 (1997)13519.

[10] R.J. Haug, Semicond. Sci. Tech. 8 (1993) 8.

[11] P.F. Fontein, J.A. Kleinen, P. Hendriks, F.A. Blom, J.H. Wolter, H.G.M. Lochs, F.A.J.M. Driessen, L.J. Giling, C.W.J. Beenaker, Phys. Rev. B 43 (1991)12090.

[12] R. Knott, W. Dietsche, K.v. Klitzing, K. Eberl, K. Ploog, Semicond. Sci. Technol. 10 (1995) 117.

[13] R.J.F. van Haren, W. de Lange, F.A.P. Blom, J.H. Wolter, Phys. Rev. B 52 (1995) 5760.

[14] A.A. Shaskin, A.J. Kent, J.R. Owers-Bradley, A.J. Cross, P. Hawker, M. Henini, Phys. Rev. Lett. 79 (1997) 5114.

[15] A. Yacoby, H.F. Hess, T.A. Fulton, L.N. Pfeiffer, K.W. West, Solid State Comm., in print.

[16] S.H. Tessmer, P.I. Glicofridis, R.C. Ashoori, L.S. Levitov, M.R. Melloch, Nature 392 (1998) 51.

[17] K.L. McCormick, M.T. Woodside, M. Huang, M. Wu, P.L. McEuen, C. Duruoz, J.S. Harris, Phys. Rev. B 59 (1999) 4654.

[18] The donor layer providing the electrons for the 2DES is located between the 2DES and the surface.

[19] P. Weitz, PhD thesis, University of Hamburg, Germany (1999).

[20] M. Tortonese, R.C. Barret, C.F. Quate, Appl. Phys. Lett. 62 (1993) 834.

[21] Although the tip acts at that effective bias in principle as a scanning gate electrode, its influence on the carrier density is less than 2 % as estimated from separate gate measurements.

[22] The resulting ac current of ≈ 1.5 μA near $\nu = 2$ is still small enough to ensure QH conditions.

[23] To be published.

[24] Similar to what was done in [17].

[25] The influences of the contact and longitudinal resistance have been eliminated for clarity so that the total Hall-potential drop always corresponds to 100 %. A constant offset has been added to all curves. The values for ν are within 5 %.

PA.13

Imaging the Low Compressibility Strips Formed by the Quantum Hall Liquid in a Smooth Potential Gradient

G. Finkelstein[1], P.I. Glicofridis[1], S.H. Tessmer[1,2], R.C. Ashoori[1] and M. R. Melloch[3]
[1]Department of Physics, Massachusetts Institute of Technology, Cambridge, MA 02139.
[2]Department of Physics, Michigan State University, East Lansing, MI 48824.
[3]Department of Electrical Engineering, Purdue University, West Lafayette, IN 37907.

Abstract

We locally image the low compressibility strip corresponding to integer Quantum Hall filling factor ν=2 and find that its width appears significantly larger than that predicted by theory. We explain this result by a disorder-induced finite density of states in the cyclotron gap.

Introduction

It was predicted that narrow strips with precisely integer Landau level filling factor should be formed in a 2DEG subject to a smooth potential gradient, in particular near the sample edges [1,2]. The strips arise due to the cyclotron gap in the electron density of states between two Landau levels. As a result of the gap, the 2DEG in the strip should have zero compressibility, $dn/d\mu=0$. The recently-developed technique of Subsurface Charge Accumulation (SCA) imaging measures the local charge accumulation in a 2D system underneath a sharp scanning probe [3]. In this work we use the SCA microscopy to image low compressibility strips formed in the presence of a smooth potential gradient at different Landau level filling factors. The widths of the strips appear a few times wider than that predicted by theory [2]. We describe how our results may be explained if we take into account the disorder-induced final density of states in the cyclotron gap.

Experimental results

We study a standard 2DEG formed at the GaAs/AlGaAs interface *90 nm* below the sample surface. It has an electron density of $\sim 3.5\times10^{11}/cm^2$ and mobility $\sim 4\times10^5\ cm^2/Vsec$. To create a density gradient in the 2DEG, we locally perturb the charge distribution in the sample by applying a voltage of *+2* to *+3.5 V* between the scanning probe and the sample for *~30 sec*. We find that the injected tunneling current increases the 2DEG density in a region of a few microns. The electron density in the center of the perturbation is about *20%* higher than the bulk value. After the current is switched off, this density profile does not change with time. We speculate that the local modification of the electron density is a result of electron transfer from the sample surface or the donor layer to the 2DEG, similar to the persistent photoconductivity effect.

In SCA imaging we apply a small AC excitation (typically *3mV RMS*) at a frequency of *100 kHz* to an Ohmic contact at the edge of the 2DEG. Due to the self-capacitance of the sample, a resulting electric charge flows in and out from the 2DEG. We monitor this charging of the 2DEG locally by placing a sharp scanning probe at a small distance (*~10 nm*) from the sample

surface. The charge induced on the scanning probe is proportional to the change in the 2DEG density. We measure the charge using a sensitive cryogenic charge amplifier. The contrast in the SCA images indicates that different regions of the 2DEG charge differently, due to variations in either local compressibility or resistivity. Below, we discuss both situations.

The SCA measurement performed at zero magnetic field does not show any structure in the region of study, despite the induced perturbation. Indeed, the 2DEG fully charges according to its self-capacitance and the applied voltage, because its resistivity is low and the 2D density of states does not depend on the electron density. The situation changes when we apply large magnetic fields. In magnetic fields around $B=8\ T$ ($\nu = 2$ in the bulk of the sample is reached at $B=7\ T$) a ring feature appears in the SCA image. The magnitude of the SCA signal is higher inside and outside the ring than on the ring itself. The SCA signals measured on a single line ($y=0$) across the center of the perturbation at several magnetic fields are shown in Fig. 1. In these cross sections the rings appear as two minima located symetrically around $x=0$ (the features marked by arrows, upper curves of Fig. 1a). As the field increases, the ring shrinks, moving toward the center of the perturbed area. At even higher magnetic fields the charging signal in the interior of the ring drops, forming a circular depression in the SCA signal (Fig. 1a, lowest curve).

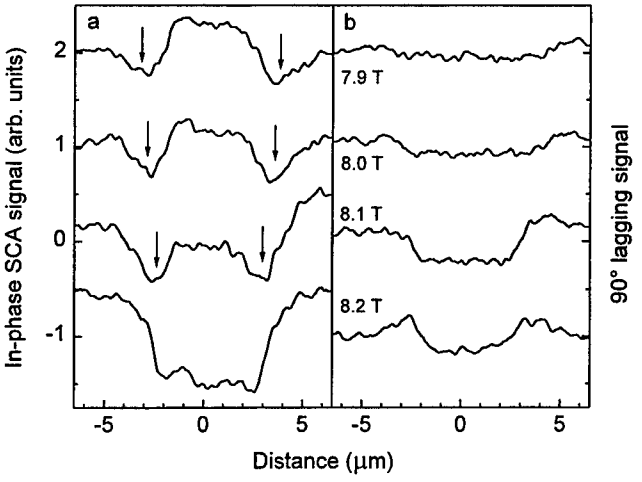

Figure 1. a) In-phase and b) 90° lagging SCA signals across the perturbed region close to $\nu=2$ at magnetic fields from 7.9 T to 8.2 T. Individual curves are shifted for clarity. The vertical scale is the same for a) and b).

We attribute the SCA minima at $B=7.9\text{-}8.1\ T$ (Fig. 1) to a low compressibility strip formed in the region of filling factor $\nu = 2$. When the scanning probe is located just above a low

compressibility region, the 2DEG below does not charge efficiently with the weak AC excitation. At higher field $\nu = 2$ corresponds to a higher electron density causing the ring to move up the density gradient and shrink toward the center. The position of the $\nu = 2$ strip shifts by *~500 nm* as we step magnetic field by *0.1 T. At* $\nu = 2$, this change in magnetic field corresponds to a $5 \times 10^9/cm^2$ change in the electron density. Therefore, we estimate the magnitude of the electron density gradient $dn/dx \approx 5 \times 10^9/cm^2/500\ nm = 1 \times 10^{10}/cm^2 \mu m$. The value of the density gradient depends on the specific realization of the density perturbation. The low compressibility strip discussed above for the filling factor $\nu = 2$ reappears at filling factors $\nu = 4$ and *6*.

A suppression of the high frequency SCA signal at a certain region might be a result of either lower compressibility at this region or low conductivity. In the latter case, there is insufficient time to charge the region during the period of excitation. As the 2DEG longitudinal conductivity is very low in the vicinity of integer filling factors, this possibility must be examined carefully. To distinguish between the two mechanisms we study both the in-phase and out of phase SCA signals.

A negligible out of phase signal was observed at *B=7.9 T*. We therefore conclude that the observed feature reflects a suppressed 2DEG compressibility at integer filling factor. However in other situations we do observe a phase shifted signal. Typically, at higher magnetic fields the SCA features appear both in phase and 90° lagging from the excitation, which demonstrates that the 2DEG does not have enough time to fully charge during the excitation cycle. Under conditions giving rise to a phase shift, a ring-shaped feature in the 90° lagging signal accompanies the circular-shaped region of the suppressed in-phase SCA signal (Fig. 1, *B=8.2 T*). We interpret this pattern as resulting from inefficient charging of the interior of the circle through a poorly conducting integer $\nu = 2$ strip around it. This situation resembles an *RC* circuit with a variable *R*. Moving the scanning probe toward the regions in the interior of the strip steadily increases the effective resistance. This causes the measured in-phase signal to steadily decrease to zero, while the 90° lagging signal first increases from zero and then decreases back to zero level. In such circumstances, it is difficult to extract separately the conductivity and compressibility information from the signal. We have performed extensive numerical modeling allowing us to reproduce qualitatively the major features observed in Fig. 1. The results of this modeling will be published elsewhere.

Discussion

We may use the lowest curve of Fig. 1a to estimate the sensitivity of the SCA measurement. At this magnetic field the resistive strip at $\nu = 2$ prevents charging of the interior region, while the exterior region charges fully. This difference in signal levels between the fully charging and non-charging regions may be taken as the measure of the degree of charging. We observe that the contrast in the low compressibility strip (Fig. 1a, upper curves) reaches only about *50%* of this value. We conclude that the 2DEG in the $\nu = 2$ strip still has a sufficiently high compressibility, and the large geometric capacitance causes charge to enter this region.

The strips at *B = 7.9 - 8.1 T* are *~2 μm* wide, which is significantly larger than predicted by the theory.[2] Indeed, taking $dn/dx \approx 1 \times 10^{10}/cm^2 \mu m$ from Fig. 1 we obtain from Eq. 20 of Ref. [2] a width of *~0.5 μm*. This situation is typical for other realizations of the density perturbation

with different density gradients. We proceed now to show how this discrepancy may be qualitatively explained by considering a random potential, which renders a finite density of states D localized between Landau levels.

Theory predicts that the magnetic field should modify the electron distribution, so that within the incompressible strip the electron density clamps at a level corresponding to an integer Landau level filling factor [2]. This picture strongly relies on the zero density of states in the cyclotron gap. It should be altered if we take into account the finite density of states between the Landau levels. The resulting screening should smear the region of $dn/dx=0$. Nevertheless, even in this case a low compressibility strip should be formed in the regions where the Fermi energy lies between the Landau levels and the density of states is low. If the average density of states between the Landau levels is D, then the areal density of these states is $\sim\hbar\omega_c D$. This quantity should be equal to the span of the electron density across the strip wdn/dx. We estimate the average density of states between the Landau levels from $\hbar\omega_c D \sim wdn/dx$. Taking $w=2\ \mu m$ and $dn/dx \approx 1\times10^{10}/cm^2\mu m$ from the experiment, we obtain that D equals to approximately *5%* of the zero field density of states. The result of this rough estimate agrees reasonably well with the values from the bulk measurements of the 2DEG density of states between Landau levels [4]. The corresponding screening length *~100 nm* is much smaller than the width of the strip, both measured and calculated. This indeed confirms that the basic assumption of reference [2] should be violated in our case.

Conclusion

We have studied the 2DEG in the Quantum Hall regime close to integer filling factors. In a smooth potential gradient, we have observed low compressibility strips corresponding to integer Landau level filling factors. These strips turn out to be significantly wider than predicted by theory, which does not include the disorder potential [2]. We conclude that in our case the width of the strip is determined by a low, but finite density of states between the Landau levels.

Recently, widening of the low compressibility strips as a result of the finite density of states in the cyclotron gap was discussed theoretically [5,6].

The authors thank L.S. Levitov for numerous discussions.

References

1. A.L. Efros, Solid State Commun. **67**, 1019 (1988); A.M. Chang, Solid State Commun. **74**, 871 (1990); C.W.J. Beenakker, Phys. Rev. Lett. **64**, 216 (1990).
2. D.B Chklovskii, B.I. Shklovskii and L.I. Glazman, Phys. Rev. **B46**, 4025 (1992).
3. S.H. Tessmer, P.I. Glicofridis, L.S. Levitov, R.C. Ashoori and M. R. Melloch, Nature **392**, 51 (1998).
4. See *e.g.* V.T. Dolgopolov, A.A. Shashkin, A.V. Aristov, D. Schmerek, H. Drexler, W. Hansen, J.P. Kotthaus and M. Holland, Phys. Low-Dim. Struct. **6**, 1 (1996) and references therein.
5. A.L. Efros, preprint cond-mat/9905368.
6. I.A. Larkin and L.S. Levitov, preprint.

PA.14

Imaging of Carrier Dynamics in Semiconductor Heterostructures by Surface Acoustic Waves

M. Streibl, A. Wixforth and J.P. Kotthaus
Sektion Physik and CeNS der LMU München, Geschwister-Scholl-Platz 1, D-80539 München, Germany

C. Kadow, A. C. Gossard
Materials Departement and QUEST, University of California, Santa Barbara, California 93106
(June 7, 1999)

Surface acoustic waves (SAW) are an ideal tool for the noninvasive detection of conductivity and carrier distributions in otherwise unstructured semiconductor systems. Here we demonstrate a technique that allows for spatially resolved experiments with a resolution of a few acoustic wavelengths. Extremely narrow acoustic paths, excited by tapered intergitital transducers, are employed to probe conductivity profiles. The method is used to resolve the spatial form of a photogenerated electron hole plasma and allows for the direct observation of room-temperature drag and transport of electrons and holes in the coherent phonon wind of an intense SAW beam. By application of a tomographic technique we are able to reconstruct 2D charge distributions.

On piezoelectric substrates like most of the III/V materials are, surface acoustic waves are accompanied by strong piezoelectric fields. On GaAs heterostructures vertical and lateral fields on the order of 10^4 to $10^5 V/cm$ are achievable. Just as these fields modulate the electrical and optical properties of a quantum well system, free carriers in the wells influence the waves propagation by dynamic screening. The interaction of carriers and the waves fields leads to a decrease of the wave velocity. In general for a conducting sheet near the surface with conductivity σ the change in velocity is given by [1]

$$\frac{\Delta v}{v} = \frac{K_{eff}^2}{2} \frac{1}{1+(\sigma/\sigma_m)^2} \qquad (1)$$

where K_{eff}^2 is the electromechanical coupling constant ($6.4 \cdot 10^{-4}$ for GaAs) and σ_m gives the crititical conductivity where the energy transfer from the SAW to the electron system is maximum, i.e. the screening currents are dissipative. The energy loss by screening currents leads to a damping of the acoustic waves which is characterized by the damping constant

$$\Gamma = \frac{K_{eff}}{2} k_{SAW} \frac{\sigma/\sigma_m}{1+(\sigma/\sigma_m)^2} \qquad (2)$$

The measurement of the SAW intensity and the propagation velocity respectively provides a simple and extremely sensitive method for the determination of the dynamic conductivity $\sigma(\omega, k)$ of carriers in a semiconductor structure. It has been extensively used for the investigation of properties of a two-dimensional electron system in the quantum hall regime [2] and in the fractional quantum hall regime [3] where it played an important role in the experimental verification of the composite fermion picture. In this paper we present a modification of the SAW scanning of charge distributions by introducing an additional spatial resolution of a few acoustic wavelengths, i.e. usually a few micrometers. Its high sensitivity even at room temperature enables us to study the shape and dynamics of photogenerated carrier profiles in detail.

Surface acoustic waves are usually generated by interdigitated transducers (IDT). When a high frequency voltage signal is applied to the interdigitated gate structure on the semiconductors surface the piezoelectric crystal is periodically deformed. The propagating derformations superpose constructively if the resonance condition $d \cdot f_0 = v_{SAW}$ is met, where f_0 is the resonance frequency, d is the periodicity of the IDT and v_{SAW} is the speed of sound. On the weakly piezoelectric GaAs many transducer periods are necessary to achieve high SAW amplitudes. However an increased number of periods simultaneously reduces the bandwidth of the IDTs resonance which is expressed by

$$P_{SAW} \propto N^2 \frac{sin^2 f'}{f'^2} \qquad (3)$$

where P_{SAW} is the acoustic power, $f' = N\pi(f - f_0)/f_0$ and N is the number of transducer periods. Typical values in our experiments are $N = 100$ and $f_0 = 1GHz$ so the bandpass Δf is approximately $\Delta f_0 = f_0/N = 10MHz$. In fact, because of internal reflections of the SAW within the transducer the effective bandpass is reduced even more to only a few MHz.

Our experiments are based on this high selectivity in frequency space. When the periodicity of the transducer is varied linearly on its length as shown in

Fig. 1 also the resonance condition is spatially modulated. This leads to a correlation between the frequency f of the applied voltage signal and the position in the transducer where resonance occurs and the SAW is launched.

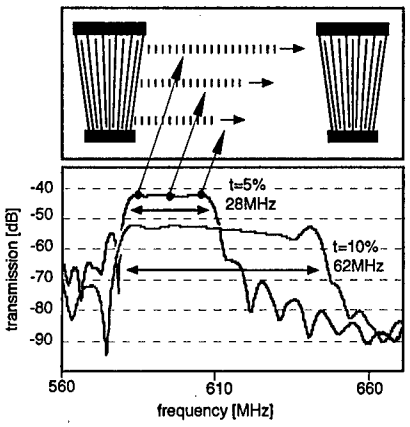

FIG. 1. SAW transmission of tapered IDTs with variation of the transducer periodicity of 5% and 10%. The usually sharp transmission is broadend to a bandpass of 28MHz and 64MHz respectively. The upper half indicates the correspondence between a point in frequency space and the origin of the SAW beam in real space.

The so-called tapered IDTs enable us to adjust the vertical position of the SAW beam by variing f. Moreover the fan shape of the transducer results in a band-spread of the sharp transmission corresponding to the relative variation $t = \Delta d/d$ of the IDT period. Fig. 1 shows the resulting bandpasses for $N = 100$ and tapering factors of $t = 5\%$ and $t = 10\%$ respectively. The upper panel indicates the correspondence between frequency space and real space. Each point of the bandpass corresponds to a single point of resonance in the IDT, where the narrow SAW beam is launched. The width of the beam is approximately $w = L/Nt$ where L is the IDT aperture. For our 560MHz IDT with $t = 10\%$ and aperture $L = 400\mu m$ we expect $w = 40\mu m$. In fact most of the SAWs energy is found within a much smaller core region. In X-ray topography experiments at the ESRF in Grenoble as described by Sauer et al. [4] the generation of such an adjustable narrow SAW beam could directly be confirmed. Like a radar beam the narrow SAW path can be used to scan the charge distribution between the two IDTs. This is economically done by a network analyzer which automatically does the frequency sweep and records phase and amplitude of the transmitted SAW.

The simplest object to test the imaging technique is an electron-hole plasma (EHP) generated by a μm laser spot. In our experiments we used a Ti-sapphire laser to excite carriers selectively only in the quantum wells of an InGaAs heterostructure midway between the IDTs. Typical laser intensities were $100\mu W$. The IDTs were fabricated by e-beam lithography and had an electrical period of $d = 4\mu m$ and a center frequency of 750MHz corresponding to a SAW velocity $v_{SAW} = 2865m/s$ for GaAs.

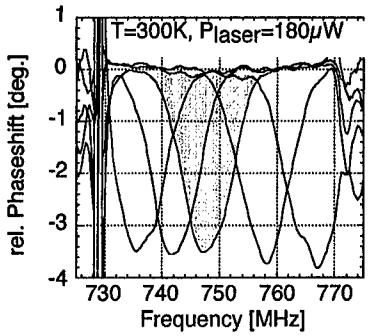

FIG. 2. Phase shift signal induced by a photogenerated electron hole plasma within the SAW path. The different traces correspond to different positions of the laser spot on the sample.

We measured the phase shift of the transmitted acoustic wave as a function of the exciting frequency as shown in Fig. 2. Different traces for different laser spot positions were taken. A maximum phase shift is observed at the frequency where the scanning SAW beam hits the core of the EHP. To evaluate the data we calculate the expected shape of the phase shift signal. For simplicity a gaussian conductivity profile $\sigma(x, y) = \sigma_0 \cdot \sigma_m \exp(-(x^2 + y^2)/r^2)$ for the EHP is assumed. The constant σ_0 here gives the peak conductivity in units of the critical conductivity σ_m. From the reduction of SAW velocity given by Eq. 1 the phase shift is calculated and integrated along each acoustic path crossing the gaussian distribution. Numerical fitting of the theory trace to the data nicely reproduces the shape of the peaks and allows for the extraction of the width r and the maximum conductivity σ of the EHP. For the phase shift

mesurements in Fig. 2 we get a width of $r = 66\mu m$ and $\sigma = 1.46\sigma_m$. What width would be expected? The diffusive expansion of the EHP is described by $r^2(t) = r_0^2 + 4Dt$ where D is the diffusion constant and r_0 the initial radius. From electron hole lifetime measurements on the same quantum well structure we know that the average lifetime is $\tau = 20ns$ at room temperature. So we can estimate the diffusion constant to be $D \approx 540cm^2/s$.

A series of publications demonstrated that the dynamics of a EHP is at least at low tempertures governed by a phonon wind mechanism [5] [6]. The thermalization of photoexcited carriers in the laser spot leads to a so-called phonon hot spot which emits ballistic phonons. Electrons and holes follow the phonon wind with the speed of sound so that the width of the charge distribution is determined by $\tau \cdot v_s$ where v_s is the sound velocity.

Surface acoustic waves provide a coherent phonon wind and so demonstrate the interaction of carriers and phonons in its purest form. At sufficient amplitudes they can be used to capture and transport carriers in their traveling piezoelectric potential superlattice [7]. On hybrid systems, i.e. the combination of strong piezoelectic materials like $LiNbO_3$ with the excellent electronic properties of AlGaAs heterostructures the rending of a two dimensional electron system into propagating stripes of carriers could be achieved with high efficiency by Rotter et al. [8]. The SAW imaging technique presented here can be applied for the direct observation of carrier localization in the SAWs propagating potential pattern. For this experiment a sample with an additional SAW path, orthogonal to the probing SAW path was fabricated. This second SAW beam was designed to provide high SAW aplitudes and in fact converted more than 10% of the electrical signal into acoustic power. Fig. 3 shows a typical measurement. The inset schematically depicts the two SAW paths. The vertical SAW beam provides the phonon wind to pump carriers away from the laser spot. The horizontal probing SAW beam generated by tapered IDTs measures the conductivity profile in and around the laser spot. Fig. 3 shows two scans of the EHP. The solid line was taken with and the broken line without orthogonal phonon wind, which yields two effects: First the reduction of the EHP density in the laser spot and a shift of the plasma core along with the phonon wind; Secondly a charge transport tail which indicates the effective trapping of carriers in the coherent phonon wind of the pump SAW beam. The captured electrons and holes are transported over macroscopic distances, on the order of millimeters as shown in the experiment.

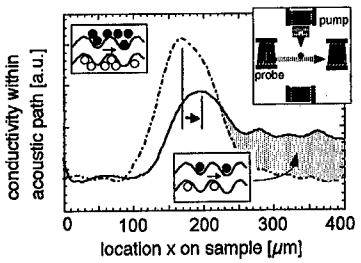

FIG. 3. Phase shift induced by a laserspot in the SAW path. The inset shows the experimental setup. The broken line is taken without and the solid line with an additional vertical pump SAW. Carrier drag of the EHP core and carrier trapping and transport in the coherent phonon wind of the intense pump beam is observed.

In the core region of the EHP the piezoelectric fields of the pump SAW are dynamically screened. The residual fields are not sufficient for charge separation and trapping. However momentum is still transfered from the SAW to the EHP which results in the observed peak shift. In the transport regime electrons and holes find their respective potential minimum half a wavelength apart from each other, resulting in an effective suppression of their radiative decay. Compared to the experiments by Rocke et al. [7] the sensitivity of our method is high even at room temperature and allows for a direct comparision of the number of injected and transported carriers. Rocke et al. found a transport efficiency of about 20% at $T = 4.2K$. From the ratio of the conductivity within the EHP core and the transport tail we can extract an even higher transport efficiency of up to 50% at room temperature for our InGaAs quantum well system. When repeated for various SAW amplitudes and laser intensities the presented experiments outline the dependence of the transport efficiency on SAW amplitude and carrier density and provide guidelines for the application of charge conveyance in optoelectronic devices. A detailed discussion however is beyond the scope of this paper and will be given elsewhere [9].

Up to now we only concentrated on 1D scans of charge distributions. When complex 2D carrier profiles should be scanned as might be interesting for imaging applications we can borrow basic principles of computer tomography to reconstruct 2D pictures from a series of 1D scans. In our case this would mean to roentgenize a 2D charge profile by probing SAW beams from various angles. To keep the ex-

periment simple, we went the other way round and rotated the 2D charge profile on a fixed SAW path. Experimentally this is achieved by exchanging the laser of our previous experiments by a white light source which projects a slide onto the sample. The slide defines the desired shape of the photogenerated EHP. The rotation of the charge distribution is achieved by rotating the slide. A 1D scan of the carrier profile is taken at angles between 0° and 180°. For the experiment in Fig. 4 the picture of a double slit aperture was projected and rotated on the SAW path.

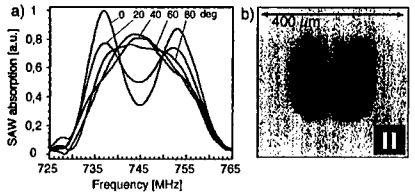

FIG. 4. a) Scans of the charge distribution induced by the optical projection of a double slit aperture at various angles. b) Reconstruction of the 2D charge distribution by standard tomography backprojection techniques.

Fig. 4a shows scans for various angles. Using standard tomography backprojection techniques [10] we reconstructed the 2D charge distribution as shown in Fig. 4b and find the shape of the double slit aperture well reproduced. From the sharpness of the edges we get a spatial resolution of about $20\mu m$. Future work will be concentrated on the improvement of the spatial resolution and sensitivity. Moving to higher frequencies, i.e. shorter SAW wavelengths will improve both. Extremely high sensitivities can be achieved when hybrid materials are used and conventional semiconductor systems are combined with strong piezoelectric substrates.

To conclude, we demonstrated the imaging of carrier density profiles by surface acoustic waves with a resolution of a few acoustic wavelengths. Extremely narrow SAW paths were excited by tapered transducers and used to scan photogenerated charge distributions. The drag and transport of electrons and holes by the coherent phonon wind of a high amplitude SAW could directly be observed at room temperature. The transition between the weak momentum transfer of the drag-effect and the complete trapping of carriers in the transport regime is detected at the fringe of a photogenerated electron hole plasma. The sensitivity of the method allows for the comparision of room temperature dynamics with low temperature experiments. By use of a tomographic technique we were able to record and reconstruct 2D charge distributions.

We gratefully acknowledge the financial support by the Bayerische Forschungsstiftung BayFor (294d/98) and the Deutsche Forschungsgemeinschaft DFG. The work at UCSB has been supported through AFOSR (grant No F49620-94-1-0158) and the center for quantized electronic structures (QUEST).

[1] A. Wixforth, J.P. Kotthaus and G. Weimann, Phys. Rev. Lett **56**, 2104 (1986)
[2] A. Wixforth, J. Scriba, M. Wassermeier, J.P. Kotthaus, G. Weimann and W. Schlapp, Phys. Rev. B **40**, 7874 (1989)
[3] R.L. Willet, R.R. Ruel, W. West and L.N. Pfeiffer, Phys. Rev. Lett. **71**, 3846 (1993)
[4] W. Sauer et al., submitted to Appl. Phys. Lett.
[5] L.M. Smith, J.S. Preston, J.P. Wolfe, D.R. Wake, J. Klem, T. Henderson and H. Morkoc, Phys. Rev. B **39**, 1862 (1989)
[6] A.E. Bulatov and S.G. Tikhodeev, Phys. Rev. B **46**, 15058 (1992)
[7] C. Rocke, S.Zimmermann, A. Wixforth, J.P. Kotthaus, G. Böhm and G. Weimann, Phys. Rev. Lett. **78**, 4099 (1997)
[8] M. Rotter, A.V. Kalameitsev, A.O. Govorov, W. Ruile and A. Wixforth, Phys. Rev. Lett. **82**, 2171 (1999)
[9] M. Streibl et al., submitted to Appl. Phys. Lett.
[10] John C. Russ, *The Image Processing Handbook*, Second Edition. Boca Raton, FL: CRC Press, 674 pp. (1995)

PA.15

Fine Structure in the Local Chemical Potential of a Two-Dimensional-Electron System at Filling Factor $\nu = 2/3$

J. Hüls, J. Weis, K. v. Klitzing, and K. Eberl
Max-Planck-Institut für Festkörperforschung, Heisenbergstraße 1, D-70569 Stuttgart, Germany

For investigating the compressible and incompressible strips in the depletion region near the edge of a two-dimensional electron system (2DES) in the integer and fractional quantum Hall regime at $T < 0.1$ K, a metal single-electron transistor (SET) used as a local potential probe is directly fabricated on top of a GaAs/AlGaAs heterostructure containing the 2DES. A negative voltage applied to a sidegate electrode at 0.9 μm distance to the SET allows to shift the edge towards the SET island. Within the integer quantum Hall regime, due to charge fluctuations vs. time, strips of different screening properties are clearly resolved as a function of the sidegate voltage and the applied magnetic field -- in agreement with previous results of Wei *et al.* (Phys. Rev. Lett. **81**, 1674 (1998)). Measurements reflecting the chemical potential variations of the 2DES vs. magnetic field show wiggles in the fractional quantum Hall regime around bulk filling factor $\nu = 2/3$, which still lack a good explanation.

Keywords: Quantum Hall Effect; Single-Electron Transistor; Electrical Compressiblity.
PACS: 73.40.Hm;71.30.+h;07.50.Ls

I. INTRODUCTION

The integer quantum Hall effect (IQHE) [1] has been related to the existence of one-dimensional channels at the edge of a two-dimensional electron system (2DES) [2]. According to theoretical models, these edge channels carry the current within the integer quantum-Hall regime (IQHR) [3,4]. The concept of edge channels has also been extended from the integer to the fractional quantum Hall regime (FQHR) [5] in several papers [6-8].

Calculations [9,10] have shown that within the depletion region of a 2DES in the IQHR two types of strips are formed - called compressible and incompressible strips - which show metal-like and insulator-like screening properties, respectively. Electro-optical [11-13] and scanning force techniques [14,15] have been used to measure the electrostatic potential profile of the 2DES under quantum Hall conditions. In another approach, a single-electron transistor (SET) has been used as a scanning probe for imaging the current-induced Hall potential profile and for visualizing compressible and incompressible regions within the 2DES [16]. The edge structure within the depletion region has recently been investigated by using a metal SET as a potential probe, but directly deposited on top of a GaAs/AlGaAs heterostructure containing the 2DES [17]. In this approach, a negative voltage applied to a sidegate electrode allows to shift the edge towards the SET. That way, compressible and incompressible strips in the depletion region of the 2DES have been mapped out [17-19]. In this experiment, the results of Wei *et al.* are reproduced using a similar GaAs/AlGaAs heterostructure. In addition, the investigations are further extended to the FQHR.

II. EXPERIMENTAL SETUP

The sample used in this experiment is based on a GaAs/$Al_{0.33}Ga_{0.67}$As heterostructure. The 2DES is located 90 nm below the surface and has a sheet electron concentration of $n_s^{bulk} = 2.2 \times 10^{15}$ m^{-2} with an electron mobility of 1.3×10^6 cm^2/Vs at a temperature of $T = 4.2$ K. In the first step, a standard Hall-bar mesa is etched and ohmic contacts are alloyed to the 2DES. In a second step, a metal SET used as a highly sensitive electrometer is fabricated on top of the Hall-bar mesa by using a shadow-evaporation technique [21] with aluminum. During the same evaporation process a sidegate electrode is deposited at a distance of 0.9 μm from the SET island.

Fig. 1 shows the measurement setup and a scanning-electron-microscope (SEM) image of the SET and the sidegate. The SET island has a size of 0.9 μm $\times$ 0.1 μm and is connected by tunnel junctions of about 0.1 μm $\times$ 0.1 μm size to aluminum source and drain contacts. The Coulomb energy $e^2/2C_\Sigma$ which is required for charging an additional electron to the SET island is measured to be 0.05 meV, where C_Σ is the total capacitance of the island. Since the presence of the SET on the surface of the heterostructure induces an inhomogeneity in the electron concentration of the 2DES, a bias voltage V_{bias} is applied to the 2DES in order to adjust the electron concentration below the SET to n_s^{bulk}. To determine the correct V_{bias} the methods described in Ref. [17] are used. All measurements were done in a ^{3}He-^{4}He dilution refrigerator at the base temperature of $T = 30$ mK in a magnetic field up to $B = 16$ T applied perpendicular to the plane of the 2DES.

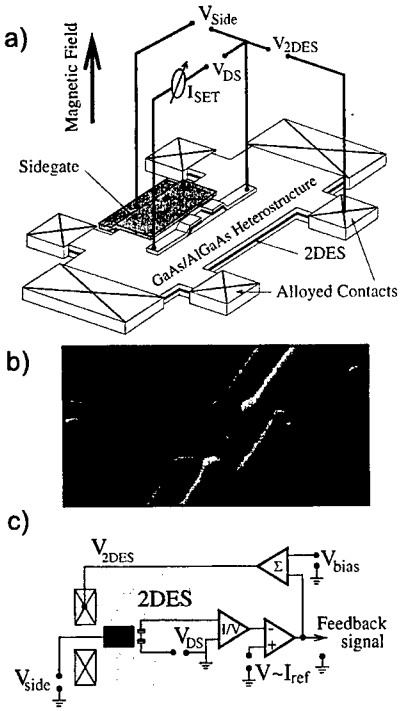

FIG. 1. (a) Sketch of the experimental setup and sample (not on scale): A SET is fabricated on top of a Hall bar which has been etched into a GaAs/AlGaAs heterostructure containing a 2DES. Alloyed ohmic contacts give electrical connections to the 2DES. (b) SEM picture of the SET and the sidegate.(c) Feedback circuit which keeps I_{SET} constant.

III. RESULTS

The Coulomb blockade characteristic of the SET [20] is sensitive to the electrostatic potential of the 2DES region under the SET island. Variations in the chemical potential μ_{ch}^{2DES} of the 2DES due to the applied magnetic field B are reflected in a change of the electrostatic potential of the 2DES. It allows the direct measurement of the chemical potential variations of the 2DES versus magnetic field [22]. This is done in an elegant way by using the feedback circuit shown in Fig. 1c: The current I_{SET} through the SET is kept constant by adjusting the voltage V_{2DES} applied to one of the ohmic contacts to the 2DES, assuring that the electrostatic potential difference between SET and 2DES is kept constant. Therefore, the feedback voltage reflects directly the change of μ_{ch}^{2DES} with magnetic field B. Using this method the Landau level depopulation with increasing B has been observed [22].

Like it was done in [17], the magnetic field is kept constant and the voltage V_{side} applied to the sidegate electrode is varied. At $V_{side} = -0.37$ V, the 2DES below the sidegate is depleted and the edge of the 2DES is now defined below the edge of the sidegate at 0.9 μm distance to the SET island. With more negative V_{side}, the edge of the 2DES is shifted closer to the SET island. At about $V_{side} = -4$ V, the edge of the 2DES has reached the position of the SET island. By monitoring the feedback signal versus V_{side}, the electrostatic potential profile of the depletion region is mapped out for different magnetic fields [19]. Regions of flat and varying electrostatic potential are observed indicating a strip-like structure at the edge. Low-frequency fluctuations in the feedback signal versus time are observed in the regimes where the electrostatic potential drop occurs as described in [19]. These fluctuations indicate low-frequency charge fluctuations versus time within the 2DES under the SET island. The occurrence of charge fluctuations within the 2DES has been related [17] to the presence of an incompressible strip under the SET, which has weak screening properties. The map of feedback signal fluctuations versus V_{side} for the present sample is shown in greyscale in Fig. 2 for the magnetic field range of $B = 1.5$ T to $B = 15.5$ T in steps of 0.1 T [23]. By converting V_{side} into a spatial shift of the edge profile [17], the evolution of these fluctuation regimes in the range of $B = 1.5$ T to $B = 10$ T – i.e. for Landau level filling factor $\nu = hn_s^{bulk}/eB > 1$ – is qualitatively in agreement with the evolution of the incompressible strips in the IQHR [9,10].

But the measurements shown in Fig. 2 extend into the FQHR $\nu < 1$. Instead of the noisy pattern observed along incompressible strips in the IQHR, a characteristic pattern appears in the range of $B = 10$ T to $B = 15.5$ T, following the local filling factor $\nu_1 = 2/3$. This fluctuation pattern seems to be static and has a typical variation amplitude of about 0.1 mV. A similar pattern comes in from high magnetic field values at highly negative V_{side}. This pattern might be related to the local filling factor $\nu_1 = 1/3$. Inverting the argumentation chain from before, that by tuning V_{side} spatial information about the electrostatic potential profile at the edge is obtained, these electrostatic potential wiggles

should be superimposed on the overall potential profile expected from the calculations [9,10]. The wiggles occur with a typical distance of several 10 nm with an amplitude of 0.1 meV. It is not clear whether this behaviour is an intrinsic property of the FQHE regime with the dominating electron-electron interaction.

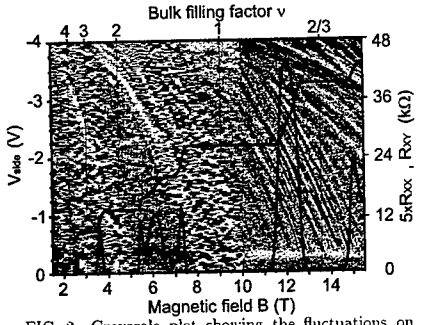

FIG. 2. Greyscale plot showing the fluctuations on the measured signal which indicate the incompressible strips. Regions of smooth signal represent a metal-like behaviour of the 2DES. Around filling factor $\nu = 2/3$ a bunch of fluctuations on the signal is resolved. The Hall- and longitudinal resistance as well as the bulk filling factors are provided for orientation. For better visibility, the contrast is enhanced for $B > 10$ T.

Looking at the boundaries of the incompressible strips of integer filling factors in Fig. 2, a similar pattern can be observed indicating that they have the same origin as the pattern in the FQHR.

In Fig. 3, measurements of the local electrostatic potential versus magnetic field are shown where the sidegate voltage is changed as the parameter. With this approach, the variation of the electrostatic potential along the B axis is maintained, which has been cancelled out in the preparation of Fig. 2 [23]. The data are obtained after substracting a smooth, increasing background due to the increase in the chemical potential of the 2DES at these filling factors. Clearly, the wiggles are already observed when the edge is still far away from the SET island ($V_{side} > -0.37$ V). At $V_{side} = -0.37$ V, the pattern starts to shift with V_{side} which marks the voltage value, where the 2DES below the gate is just depleted and the edge gets closer to the SET. The appearance of the pattern at $V_{side} = 0$ V shows that the pattern is a characteristic of the bulk as well and does not inevitably belong to the edge of the 2DES. What else can be the reason for this pattern mimicing wiggles in the chemical potential vs. B on a scale of about 30 mT? The presence of the SET? As mentioned before, a local inhomogeneity in the electron concentration of the 2DES deriving from the presence of the SET on top of the heterostructure is adjusted by a bias voltage V_{bias} (see Fig. 1c). But the metal SET on the surface of the sample might disturb the 2DES due to mechanical strain resulting in electron puddles below the SET, which might show single-electron charging effects themselves. Instead or in addition, electron puddles below the SET island might be created by the statistical donor distribution within the heterostructure. The amount of charge on each puddle - and therefore its electrostatic potential - depends on the magnetic field as well as on the sidegate voltage V_{side} and might cause the pattern visible in Fig. 2, although a conclusive picture cannot be given up to now.

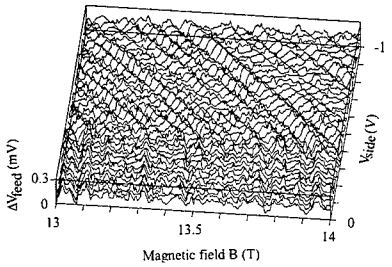

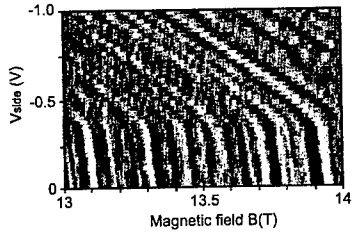

FIG. 3. 3d-plot and greyscale plot of the fluctuations on the measured local electrostatic potential versus magnetic field. The sidegate voltage is changed as a parameter. A smooth, increasing background is substracted from the data.

IV. CONCLUSIONS

A metal SET is fabricated on top of a 2DES together with a sidegate electrode close to the SET

island. By applying a negative voltage to the sidegate, the edge is shifted closer to the SET. In certain regimes given by the sidegate voltage and magnetic field, the SET detects charge fluctuations which we relate to the occurrence of incompressible strips under the SET island. That way, the results of Wei *et al.* are reproduced. Furthermore, the measurements are extended to the FQHR. Around filling factor $\nu = 2/3$, a bunch of small fluctuations superimposes the measured potential. Either these fluctuations belong to the potential profile of the edge, or they result from single-electron charging effects of one or more puddles below the SET island. They might be induced by the presence of the SET on the surface or caused by the statistical distribution of the donors within the heterostructure. The origin of these small static fluctuations – which appear also along incompressible strips of integer filling factor – still remains to be clarified.

V. ACKNOWLEDGEMENT

The authors thank M. Hauser for growing the heterostructure, M. Riek, F. Schartner and U. Waizmann for technical support, C. Albrecht for bonding the sample and J. Schmid for reading the manuscript. This work has been supported by the Bundesministerium für Bildung und Forschung (BMBF) under the Grant No. 01 BM 624/7.

[1] K. v. Klitzing, G. Dorda, and M. Pepper, Phys. Rev. Lett. **45**, 494 (1980).
[2] See the reviews: R. J. Haug, Semicond. Sci. Technol. **8**, 131 (1993); K. v. Klitzing, Physica B **184**, 1 (1993); K. v. Klitzing, Physica B **204**, 111 (1995).
[3] B. I. Halperin, Phys. Rev. B **25**, 2185 (1982).
[4] M. Büttiker, Phys. Rev. B **38**, 9375 (1988).
[5] D. C. Tsui, H. L. Stormer, and A. C. Gossard, Phys. Rev. Lett. **48**, 1559 (1982).
[6] C. W. J. Beenakker, Phys. Rev. Lett. **64**, 216 (1990).
[7] A. H. MacDonald, Phys. Rev. Lett. **64**, 220 (1990).
[8] A. M. Chang, Solid State Comm. **74**, 871 (1990).
[9] D. B. Chklovskii, B. I. Shklovskii, and L. I. Glazman, Phys. Rev. B **46**, 4026 (1992); D. B. Chklovskii, K. A. Matveev, and B. I. Shklovskii, Phys. Rev. B **47**, 12605 (1993).
[10] K. Lier and R. R. Gerhardts, Phys. Rev. B **50**, 7757 (1994).
[11] R. J. F. Haren, F. A. P. Blom, and J. H. Wolters, Phys. Rev. Lett. **74**, 1198 (1995).
[12] R. Knott, W. Dietsche, K. von Klitzing, and K. Ploog, Semicond. Sci. Technol. **10**, 117 (1995).
[13] A. J. Kent, D. J. McKitterick, L. J. Challis, P. Hawker, C. J. Mellor, and M. Henini, Phys. Rev. Lett. **69**, 1684 (1992); D. J. McKitterick, A. Shik, A. J. Kent, and M. Henini, Phys. Rev. B **49**, 2585 (1994); A. A. Shashkin, A. J. Kent, J. R. Owers-Bradley, A. J. Cross, P. Hawker, and M. Henini, Phys. Rev. Lett. **79**, 5114 (1997).
[14] K. L. McCormick, M. T. Woodside, M. Huang, M. Wu, P. L. McEuen, C. I. Duruoz, J. S. Harris Jr., Phys. Rev. B **59**, 4654 (1999).
[15] P. Weitz, E. Ahlswede, J. Weis, K. v. Klitzing, K. Eberl, in same issue.
[16] A. Yacoby, H. F. Hess, T. A. Fulton, L. N. Pfeiffer, K. W. West, Solid State Comm., in press.
[17] Y. Y. Wei, J. Weis, K. v. Klitzing, and K. Eberl, Phys. Rev. Lett. **81**, 1674 (1998).
[18] J. Weis, Y. Y. Wei, K. v. Klitzing, Physica E **3**, 23 (1998).
[19] J. Weis, Y. Y. Wei, K. v. Klitzing, Physica B **256-258**, 1 (1998).
[20] See for example *Single Charge Tunneling - Coulomb Blockade Phenomena in Nanostructures*, NATO ASI series B 294, edited by H. Grabert and M. H. Devoret, (Plenum Press, New York, 1992).
[21] G. J. Dolan and J. H. Dunsmuir, Physica **B 152**,7 (1988).
[22] Y. Y. Wei, J. Weis, K. v. Klitzing, and K. Eberl, Appl. Phys. Lett. **71**, 2514 (1997).
[23] To relate the data of different B, the curves – measured versus V_{side} – are all set at $V_{\text{side}} = 0$ to the same greyscale value.

PA.16

Electron-Electron Scattering and the Propagation of Electron Beams in a Two-Dimensional Electron Gas

H. Buhmann, H. Predel, and L.W. Molenkamp
Physikalisches Institut, Universität Würzburg, Am Hubland, 97074 Würzburg, Germany

R.N. Gurzhi, A.I. Kopeliovich, A.N. Kalinenko, and A.V. Yansovski
Low-Temperature Physics and Engineering Institute, Kharkov, Ukraine
(June 14, 1999)

Experimental studies of electron-beam propagation in a degenerate 2DEG in a GaAs-(Al,Ga)As heterostructure are presented for a wide range of injection energies, $0 < E \leq E_F$. The electron beam is injected and detected in the 2DEG via electrostatically defined quantum point-contacts with typical distances of 3.4 μm. Energy-dependent beam injection is used to reveal the characteristics of the electron-beam propagation. Considering the specific character for electron-electron scattering events in 2D systems linearized Boltzmann equations could be used to model the experimental observations.

Electron-electron collisions are the main factor responsible for the attenuation of ballistic electron beams in metals at low temperature ($T < 4$ K) [1]. Because of the differences in the density-of-states, decisively different characteristics are expected for electron-electron scattering processes in three- and two-dimensions [2]. As shown theoretically in Ref. [2], the signal of an electron beam in a two-dimensional electron gas (2DEG) is determined by a small group of "quasi-ballistic" electrons which either do not experience any collision or, have only been scattered over small angles.

Here, we present experimental studies of electron-beam propagation in a degenerate 2DEG in a GaAs-(Al,Ga)As heterostructure for a wide range of injection energies, $0 < E \leq E_F$. The electron collimation effect of quantum point-contacts is used to inject and detect narrow electron beams in the 2DEG. Energy-dependent beam injection is used to reveal the characteristics of the electron-beam propagation. Non-linear effects related to the specific character of a 2D system have been observed and interpreted in terms of a one-collision approximation.

The experiments were performed on gate-defined nanostructures in conventional Si modulation doped GaAs-(Al,Ga)As heterojunctions. Typical values for the carrier density and mobility are $n_e = 2.45 \times 10^{11}$ cm^{-2} and $\mu \approx 1 \times 10^6$ cm^2(Vs)$^{-1}$, corresponding to an impurity mean-free-path of $l_{\mathrm{imp}} \approx 10$ μm. A schematic topview of the sample gate-structure is given in Fig. 1. Schottky gates (grey areas) form two opposite quantum point-contact, i and d, at a lithographical distance of $W = 3.4$ μm.

In experiments the electron beam was injected through the injector quantum point-contact i by applying a dc voltage $V_i = V_{12}$ and detected as the non-local voltage $V_d = V_{34}$ the across detector point-contact d. The numbers 1, 2, 3, and 4 denote the Ohmic contacts to the 2DEG of the sample (Fig. 1, crossed squares). We find

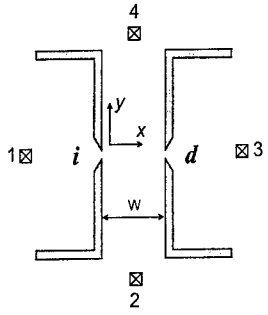

FIG. 1. Schematic top view of the device structure showing the injector, i, and detector, d, quantum point-contact and the Ohmic contacts (crossed squares), labeled 1, 2, 3, and 4. Schottky gate are represented by grey areas.

that the use of all-dc techniques is very important for a proper interpretation of the observed signals. Both injector and detector point-contacts are adjusted at the $n = 1$ plateau i.e., both contain one transverse mode, and tnus remain in the metallic regime or, in other words, they do not act as tunnel barriers. Thus, electrons of all possible energies, $0 < E < eV_i$, are present in the injected beam.

In Fig. 2 the experimental results prensented for $B = 0$ T at a sample temperatures of $T_0 = 1.6$ K. On increasing the accelerating potential difference across the injector, V_i (corresponding to an excess energy up to eV_i for injected electrons), the resulting signal at the detector, V_d,

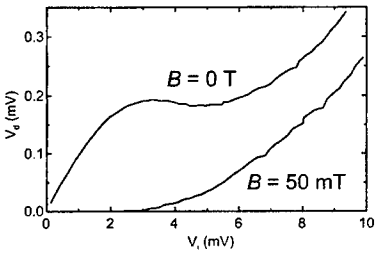

FIG. 2. Measured $V_d(V_i)$-dependence for $B = 0$ T and $B = 50$ mT at $T = 1.6$ K.

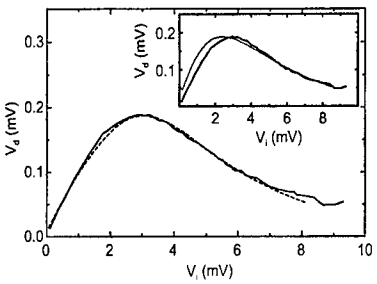

FIG. 3. Experimental quasiballistic detector signal (after correctrion for the thermopower contribution) (solid line) and modified one-collision approximation (dashed line). Inset: Experimental quasiballistic detector signal (solid line) in comparison with the ordinairy one-collision approximation which neglects 2-dimensional density-of-states effects.

first increases linearly, but then tends to saturate. This implies that with increasing intensity of the injected beam, the fraction of the electrons arriving at detector decreases. A further increase of V_i yields a curve with a distinct maximum and minimum (cf. Fig. 2). This experimental result can be understood from the following qualitative considerations: Let us assume, for simplicity, that the sample temperature (the primary temperature of the system) is equal to zero. Then, for a nonequilibrium electron with an excess energy E above the Fermi energy E_F, the mean-free-path for collisions with equilibrium electrons decreases with increasing E, roughly speaking as $l_{ee}(E) \sim E^{-2} \ln E^{-1}$, $E \ll E_F$ [3]. Therefore, at sufficiently small V_i all injected electrons will reach the detector, whose readout then is proportional to the number of injected electrons, $V_d \propto V_i$. (Electrons of all energies $0 \leq E \leq eV_i$ are present in the beam, with equal weight). This linear increase of V_d with V_i saturates for energies $E \geq E_0$ when the electron-electron scattering mean-free-path length becomes comparable to W, the distance between injector and detector: $eV_i = E_0$ for $l_{ee}(E_0) = W$. Electrons with larger energies, $E_0 < E < eV_i$, will scatter and not reach the detector. Thus, the signal V_d is determined by a *quasiballistic* group of electrons which is completely present at $eV_i \sim E_0$ and should not change on a further increase of V_i. However, as it is evident in Fig. 2, on reaching a maximum, the signal starts to decrease slightly (despite the growth of the beam intensity!). In our opinion, the only possible mechanism leading to such behaviour is heating of the 2DEG in between injector and detector point-contact by the electron beam. The heated 2DEG then leads to damping of the quasiballistic group due to enhanced electron-electron scattering. At even higher V_i V_d again increases. This, we believe, is due to the additional build-up of a thermovoltage across the detector point-contact, which is driven by the temperature difference between the heated 2DEG in between injector and detector and the still cold 2DEG behind the detector.

In order to extract the thermopower effect we performed the same experiment in the presence of small magnetic field, $B = 50$ mT, (Fig. 2). In this case the electron beam is deflected and electrons do not reach the detector directly hence, the detector signal $V_d(V_i)$ represents the isotropic background signal due to the thermopower of the detector quantum point-contact caused by electron-heating in the channel. Subtracting this thermovoltage signal at 50 mT from the data at zero magnetic field one obtains the response due to quasiballistic electrons reaching the detector, Fig. 3 (solid line). Thus, having corrected for the thermovoltage, we are in a position to analyze quasiballistic and heating effects separtely.

The detected signal V_d is determined by the distribution function of nonequilibrium electrons f in the vicinity of detector point-contact. For small V_i, we may neglect nonlinearities due to heating of the 2DEG in between injector and detector. The linearized Boltzmann equation, describing the behaviour of the distribution function f, then has the form

$$v_x \frac{\partial f}{\partial x} + v_y \frac{\partial f}{\partial y} = \widehat{J} f, \qquad f(x = 0, y, \mathbf{p}) = f_0(y, \mathbf{p}) \quad (1)$$

Here, $f_0(y, \mathbf{p})$ is the beam profile at the exit from the injector, and the axis x is directed from injector to detector (cf. Fig. 1). $\widehat{J} f$ is the linearized integral of electron-electron collisions. It is convenient to write it as

$$\widehat{J} f = -\nu f + \int d\mathbf{p}' \nu_{\mathbf{pp}'} f_{\mathbf{p}'}, \qquad \nu = \int d\mathbf{p}' \nu_{\mathbf{p}'\mathbf{p}}. \quad (2)$$

Here, the collision-integral kernel $\nu_{\mathbf{p}'\mathbf{p}}$ determines the probability of the appearance of a nonequilibrium electron ($\nu_{\mathbf{p}'\mathbf{p}} > 0$) or hole ($\nu_{\mathbf{p}'\mathbf{p}} < 0$) in state $\mathbf{p}'$ after the

nonequilibrium electron has disappeared from state $\mathbf{p}$ (i.e., has been scattered into another state). The kernel has a complex structure and in the general case can not be presented in elementary functions [2].

For the general case, Eq. 1 can not be solved. However, under conditions where the probability of multiple collisions is small in comparison with the time of passing from injector to detector, i.e. $l_{ee} = v(E)\nu^{-1}(E) > W$, or $E < E_0$, we can use perturbation theory for the collision integral. In the first order or one-collision approximation (OCA) we then have

$$f(x, y, \mathbf{p}) \equiv \left(1 - \frac{x\nu}{v_x}\right) f_0 + \widehat{Q} f_0. \qquad (3)$$

The first term in the r.h.s of Eq. 3 describes the number of nonscattered particles reaching into the vicinity of a point (x, y). The second (integral) term $\widehat{Q} f_0$ describes particles that reach the same spacial region, after having been scattered once.

Note that for high-energy beams ($E \gg k_B T$), the probability of undergoing a second collision is approximately one order of magnitude lower than of the first collision [5]. This is connected with the fact that after collision with equilibrium (Fermi sea) electrons, the excess energy of a nonequilibrium electron (ε) must be redistributed between three partners i.e., $\bar{E} \approx E/3$, $l_{ee}(\bar{E}) \approx 3^2 l_{ee}(E)$, $k_B T \ll E \ll E_F$, where $\bar{E}$ is the characteristic energy of the scattered electrons. Therefore, the one-collision approximation is valid for a wide range of energies as long as $l_{ee}(\bar{E}) \geq W$. On observing this and taking into account the fact that $\widehat{Q}\,\nu\, f_0 \sim \nu(E)\widehat{Q}\, f_0 \gg \nu\,\widehat{Q}\, f_0 \sim \nu\,(\bar{E})\;\widehat{Q}\, f_0$ it is straightforward to build a new "modified" one-collision approximation which takes the anisotropic scattering in the 2-dimensional system [2] fully into account. After partial summation of the terms of the iteration series on the parameter $x/l_{ee}(E)$ of Eq. 1 one obtains a zero-eth order approximation for the parameter $x/l_{ee}\,(\bar{E})$. This is valid when $E < 3\ E_0$. In this regime 2d density-of-states effects are expected to dominate the detector signal.

In addition, we have to model the attenuation of the beam due to enhanced electron-electron scattering with the current-heated electron gas in between the injector and detector ($V_i > 3$ meV). We use the following quasi-linear approach: First, we find the electron gas heating $\Delta T(V_i)$ from thermovoltage measurements and then, using the temperature T thus obtained, we calculate the signal of the quasiballistic part. For example, we have in the relaxation-time approximation

$$f = e^{-\frac{L}{v_x \tau_{ee}(E,T)}} f_0\left(y - L\frac{v_y}{v_x}, \mathbf{p}\right), \qquad (4)$$

where $T = T_0 + \Delta T(V_i)$. We now are able to calculate the entire detector signal:

$$V_d = e \int dE \int d\varphi\ \rho(\varphi)\, v_x\ f(x = W, y = 0, \mathbf{p})\ . \qquad (5)$$

Here, $\rho(\varphi)$ is the function characterizing the angular acceptance of the detector point-contact, which is positioned at $(W, 0)$. The results are plotted in Fig. 3 (dashed line), where we used the modified OCA for V_i up to the maximum of $V_d(V_i)$ and the ordinairy OCA for high injection energies. The inset of Fig. 3 shows that the ordinary OCA, which implicitly assumes the isotropic scattering associated with a 3-dimensional electron gas, is not able to explaine the low energy part of the beam signal i.e., the part where 2d-effects dominate the detector signal. The only free parameter in these curves was fitting the maximum amplitude.

In conclusion, we have used electron-beam experiments to investigate electron-electron scattering in reduced dimensions. Energy dependent measurements reveal the importance of small angular scattering for low injection energies while for 'high' energies the electron-electron scattering is isotropic and the detector signal is well describes by the ordinary one-collision approximation.

ACKNOWLEDGMENTS

Part of this work were supported by the Volkswagen-Stiftung (Grant No. I/72 531), and by the DFG MO 771/1-1.

[1] L.W. Molenkamp, M.J. Brugmans, H. van Houten and C.T. Foxon, Semicond. Sci. Technol. **7**, B228 (1992).

[2] H. Buhmann, R. N. Gurzhi, A. N. Kalinenko, A. I. Kopeliovich, L. W. Molenkamp, A. V. Yanovsky, Fiz. Nizk. Temp. **24**, 978 (1998) [Low Temp. Phys. **24** 737, (1998)].

[3] A. V. Chaplik, Zh. Eksp. Teor. Fiz. **60**, 1845 (1971) [Sov. Phys.-JETP **33**, 997 (1971)].

[4] L.W. Molenkamp, H. van Houten, C.W.J. Beenakker, R. Eppenga and C.T. Foxon, Phys. Rev. Lett. **65**, 1052 (1990).

[5] R.N. Gurzhi, A.N. Kalinenko, A.N. Kopeliovich, Surface Science **361/362**, 497 (1995).

The Hanbury Brown and Twiss Experiment with Fermions

S. Oberholzer[1, a], M. Henny[a], C. Strunk[a], C. Schönenberger[a], T. Heinzel[b], K. Ensslin[b], and M. Holland[c]

[a] *Institut für Physik, Universität Basel, Klingelbergstr. 82, CH-4056 Basel, Switzerland*
[b] *Solid State Physics Laboratory, ETHZ, CH-8093 Zürich, Switzerland*
[c] *Department of Electronics, University of Glasgow, Glasgow G12 8QQ, United Kingdom*

Abstract

We realized an equivalent Hanbury Brown and Twiss experiment for a beam of electrons in a two dimensional electron gas in the quantum Hall regime. A metallic split gate serves as a tunable beam splitter which is used to partition the incident beam into transmitted and reflected partial beams. The current fluctuations in the reflected and transmitted beam are fully anticorrelated demonstrating that fermions tend to exclude each other (antibunching). If the occupation probability of the incident beam is lowered by an additional gate, the anticorrelation is reduced and disappears in the classical limit of a highly diluted beam.

Keywords: quantum statistics; noise; correlation

The first quantum statistical measurements were carried out with photons by Hanbury Brown and Twiss (HBT) in the 1950s. In a pioneering experiment HBT determined the size of astronomical radio sources by measuring the spatial coherence of the emitted radiation from *intensitiy* correlations at two different locations [1]. In a subsequent optical table-top experiment, they tested their idea by measuring intensity correlations for visible light: the light beam of a Hg vapor lamp (IN) was split into a transmitted (T) and a reflected beam (R) (see Fig. 1). The equal-time intensity correlations between the two separated photon streams was found to be positive (bunching) [2,3]. This is a generic property of particles obeying Bose-Einstein statistics. In contrast to bosons, a negative correlation or 'antibunching' is expected for fermions, because fermions have to exclude each other due to the Pauli principle.

In general, the time dependent number of particles $n(t)$ detected during a certain time interval exhibits fluctuations $\Delta n(t) = n(t) - \langle n \rangle$ around the average $\langle n \rangle$, called shot noise. Shot noise in the electrical current is caused by the discreteness of the electron charge and has been extensively studied in submicrometer-sized nanostructures [4,5]. In a HBT type experiment, not the fluctuations in a single beam are measured, but the correlation between fluctuations in the transmitted (T) and reflected (R) beam originating from a beam splitter (see Fig. 1). If the incident beam (IN) is not prepared at a single-particle level, but shows intensity

[1] To whom correspondence should be addressed: E-mail: Oberholzers@ubaclu.unibas.ch

fluctuations Δn around the mean value $\langle n \rangle$, the correlator $\langle \Delta n_t \Delta n_r \rangle$ between the fluctuations in the transmitted Δn_t and the reflected Δn_r beam is given by:

$$\langle \Delta n_t \Delta n_r \rangle = t(1-t) \cdot \Big\{ \langle (\Delta n)^2 \rangle - \langle n \rangle \Big\}, \quad (1)$$

where t is the transmission probability of the beam splitter. The cross-correlation in Eq. 1 is a sum of a term proportional to $\langle (\Delta n)^2 \rangle$, which depends on the particle statistics in the incident beam, and a term proportional to $\langle n \rangle$, which is caused by the probabilistic partitioning of single particles at the beam splitter. This second term always gives a negative contribution to the cross-correlation independent of whether the particles are bosons or fermions. The auto-correlation of the transmitted (or reflected) beam is given by

$$\langle (\Delta n_t)^2 \rangle = t(1-t) \cdot \Big\{ \frac{t}{1-t} \langle (\Delta n)^2 \rangle + \langle n \rangle \Big\}. \quad (2)$$

Here, the sign of the second term is positive in contrast to the cross-correlation in Eq. 1. For an incident beam of particles obeying *Poisson* statistics with $\langle (\Delta n)^2 \rangle = \langle n \rangle$ the cross-correlation is zero (see Eq. 1). For *super-Poisson* statistics, $\langle (\Delta n)^2 \rangle > \langle n \rangle$, the cross-correlation is positive (HBT result for thermal light). In contrast, anticorrelation results if the noise in the incident beam is *sub-Poissonian* $\langle (\Delta n)^2 \rangle < \langle n \rangle$. Maximal anticorrelation is obtained if the incident beam carries no fluctuations ($\langle (\Delta n)^2 \rangle = 0$), which is the case for a completely degenerated electron beam at zero temperature. Noise suppression in a single beam according to the Pauli principle has recently been found in electrical measurements on quantum-point contacts and nanowires [6].

A HBT-type intensity correlation experiment for particles with non classical Fermi-Dirac statistics has not yet been carried out. Attempts to measure the expected negative correlation in a beam of free electrons have not been successful yet, mainly because of the low particle density in such a beam. The HBT experiment for fermions has recently been carried out in two independent experiments based on semiconductor devices [7]. Theoretically,

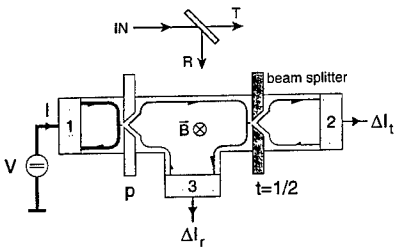

Fig. 1. Intensity correlation experiment for a degenerated beam of electrons realized in a Hall bar connected to four electron reservoirs (shaded). A metallic split gate serves as tunable beam splitter. The incident current can be depleted by an additional gate p. Electrons escaping from contact 1 travel along the upper edge until reaching the beam splitter, where they are either reflected into contact 3 or transmitted to contact 2.

these experiments and other multiterminal correlation experiments have been considered before [4,8–10].

One way to realize a HBT experiment with electrons has been proposed by Büttiker [4]: In a two dimensional electron gas (2 DEG) in the quantum Hall regime the current flows in one-dimensional channels along the edges of the device (see Fig. 1). These edge channels can be used to separate the incident from the reflected beam. If there would be no magnetic field the current would also flow in the bulk and incident and reflected beam could not be distinguished. The beam splitter is a lithographically patterned metallic split gate, which can be tuned by an applied voltage. In addition, there is a second gate with transmission probability p before the beam splitter which is used to dilute the occupation in the incident beam. Applying a constant voltage V to contact 1 the charge current I is injected into the Hall bar. The magnetic field perpendicular to the 2 DEG is adjusted to filling factor $\nu = 2$, so that the current flows in one spin-degenerated edge state. Let us first consider the case, where the additional gate p is not used: the electrons escaping from contact 1 travel along the upper edge until reaching the beam splitter, where

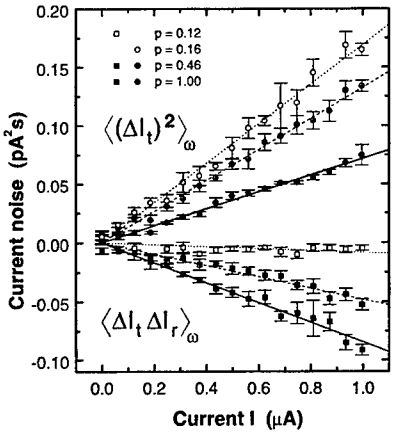

Fig. 2. Measured spectral densities of correlations between current-fluctuations as a function of the current I of the incident beam at $T = 2.5$ K. $\langle\Delta I_t \Delta I_r\rangle_\omega$ denotes the cross-correlation between the transmitted and reflected beams and $\langle(\Delta I_t)^2\rangle_\omega$ the auto-correlation in the transmitted beam. The offset noise arising from thermal fluctuations and residual amplifier noise has been subtracted. The absolute slopes are $0.23 \cdot 2e$ and $0.26 \cdot 2e$ for the auto-correlation and cross-correlation, respectively, in agreement with the expected prefactor $t(1-t) = 1/4$. If the incident beam is diluted by lowering the transmission probability p, the cross-correlation gets smaller and disappears for p close to zero. The auto-correlation itself increases, because the incident beam is noisy.

they are either transmitted with probability t to leave the device at contact 2, or reflected with probability $r = 1 - t$ leaving at contact 3. Provided $eV \gg kT$, the theory predicts for the spectral densities of the auto- and cross-correlation according to Eq. 1 and 2 [9]

$$\langle\Delta I_\alpha \Delta I_\beta\rangle_\omega = \pm 2e|I|t(1-t) \qquad (3)$$

with e the electron charge and α, β either t or r. The positive sign corresponds to the auto-correlation, where $\alpha = \beta$, and the negative one to the cross-correlation with $\alpha \neq \beta$. Because the cross-/auto-correlation is largest for $t = 1/2$ the beam splitter is adjusted to transmit and reflect electrons with 50 % probability.

Figure 2 shows the cross-correlation $\langle\Delta I_t \Delta I_r\rangle_\omega$ (solid squares) of the fluctuations ΔI_t and ΔI_r versus bias current I at $T = 2.5$ K. A nearly linear dependence with a negative slope is found showing that the fluctuations are indeed anticorrelated. The auto-correlation (solid circles) of the transmitted current $\langle(\Delta I_t)^2\rangle_\omega$ (or reflected current, not shown) has a positive slope. The negative cross-correlation and the positive auto-correlation are equal in magnitude confirming that the partial beams are fully anticorrelated. We can therefore conclude that there is no uncertainty in the occupation of the incident beam, that is $\langle(\Delta n)^2\rangle = 0$ in Eq. 1 and 2. All states in the incident beam are occupied with probability one and hence are noiseless by virtue of the Pauli principle. Formally, this follows also from $\langle(\Delta n)^2\rangle = \langle(\Delta n_t + \Delta n_r)^2\rangle = \langle(\Delta n_t)^2\rangle + 2\langle\Delta n_t \Delta n_t\rangle + \langle(\Delta n_r)^2\rangle = 0$ within experimental accuracy. The fact that the current I of the incident beam is noiseless demonstrates that the constant voltage applied to reservoir 1 is converted into a *constant* current e^2V/h (per accessible mode) according to the fundamental requirement of the Landauer-Büttiker formalism.

In an extension of our experiment we have changed the statistics in the incident beam using the additional gate with transmission $p \in [0,1]$. If $\langle n\rangle$ is the mean particle number of the beam incident to the beam splitter, the particle number behind the first gate p is given by $\langle\tilde{n}\rangle = p\langle n\rangle$ with noise $\langle(\Delta\tilde{n})^2\rangle = p(1-p)\langle n\rangle$. Using Eq. 1 and 2 the normalized auto- and cross-correlation depend on the transmission probability p as

$$\frac{\langle(\Delta I_t)^2\rangle_\omega}{2eI} = t(1-pt) = \frac{2-p}{4} \qquad (4)$$

$$\frac{\langle\Delta I_t \Delta I_r\rangle_\omega}{2eI} = -t(1-t)p = -\frac{p}{4}, \qquad (5)$$

for $t = 1/2$. If p decreases from 1 to 0 the states in the incident beam are diluted and the anticorrelation (Eq. 5) becomes smaller ('+-centered' and open squares in Fig. 2). In case of very low transmission p the statistics in the incident beam is Poissonian and the anticorrelation disappears as dis-

cussed above. The auto-correlation itself increases ('+-centered' and open circles in Fig. 2), because of the noise in the incident beam (see Eq. 2). The dependence of the auto- and cross-correlation on the probability p is shown in Fig. 3. The measured slopes of the data in Fig. 2 are in good agreement with the predictions of Eq. 4 and 5 within experimental accuracy.

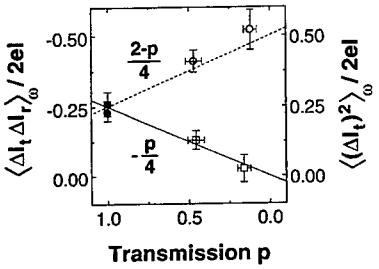

Fig. 3. Dependence of the auto- and cross-correlation on the transmission probability p of the additional gate for $t = 1/2$. If p is lowered from 1 to 0 the statistics in the incident beam are changed from Fermi-Dirac to Poisson statistics. The normalized auto-correlation $\langle(\Delta I_t)^2\rangle_\omega/2eI$ increases from 1/4 to 1/2 and the normalized cross-correlation $\langle(\Delta I_t)^2\rangle_\omega/2eI$ from $-1/4$ to 0 in good agreement with the prediction of Eq. 4 and 5.

In conclusion, a HBT type experiment with electrons has been realized in a solid state device. We demonstrate that current correlations are sensitive to the particle statistics in the incident beam. Full anticorrelation is observed for electrons obeying Fermi-Dirac statistics, whereas the anticorrelation is gradually suppressed if the incident beam is diluted. It would be interesting to extend this kind of experiments to electronic states obeying different statistics like the fractional quantum Hall state [11]. The observation of bunching of electrons might be possible by preparing electronic states with fluctations larger than the classical Poisson value, which have recently been observed in resonant tunneling devices and in superconducting weak links [12].

The authors would like to thank M. Büttiker, D. C. Glattli, and T. Gramespacher for valuable comments. This work was supported by the Swiss National Science Foundation.

References

[1] R. Hanbury Brown and R. Q. Twiss, *Philos. Mag. Ser. 7* **45**, 663 (1954).

[2] R. Hanbury Brown and R. Q. Twiss, *Nature* **177**, 27 (1956); R. Hanbury Brown and R. Q. Twiss, *Nature* **178**, 1046 (1956); E. Purcell, *Nature* **178**, 1449 (1956).

[3] B. L. Morgan and L. Mandel, Phys. Rev. Lett. **16**, 1012 (1966).

[4] M. Büttiker, Phys. Rev. Lett. **65**, 2901 (1990).

[5] For recent reviews, see: M. J. M. de Jong and C. W. J. Beenakker in *Mesoscopic Electron Transport*, L. P. Kouwenhoven, G. Schön, L. L. Sohn eds., NATO ASI Series E, Vol. 345 (Kluwer Academic, Dordrecht 1996).

[6] M. Reznikov, M. Heiblum, H. Shtrikman, D. Mahalu, Phys. Rev. Lett. **75**, 3340 (1995); A. Kumar, L. Saminadayar, D. C. Glattli, Phys. Rev. Lett. 76, 2778 (1996); R. C. Liu, B. Odom, Y. Yamamoto, S. Tarucha, Nature **391**, 263 (1998); A. Steinbach, J. M. Martinis, M. H. Devoret, Phys. Rev. Lett. **76**, 2778 (1996); R. J. Schoelkopf, P. J. Burke, A. A. Kozhevnikov, D. E. Prober, Phys. Rev. Lett. **78**, 3370 (1997); M. Henny, S. Oberholzer, C. Strunk, C. Schönenberger, Phys. Rev. B. **59**, 2871 (1999).

[7] M. Henny, S. Oberholzer, C. Strunk, T. Heinzel, K. Ensslin, M. Holland, C. Schönenberger, *Science* **284**, 296 (1999); W. D. Oliver, J. Kim, R. C. Liu, Y. Yamamoto, *ibid.*, p. 299.

[8] Th. Martin and R. Landauer, Phys. Rev. B **45**, 1742 (1992).

[9] M. Büttiker, Phys. Rev. B **46**, 12485 (1992).

[10] R. C. Liu and Y. Yamamoto, Phys. Rev. B **49**, 10520 (1994); Ya. M. Blanter and M. Büttiker, Phys. Rev. B **56**, 2127 (1997); E. V. Sukhorukov and D. Loss, Phys. Rev. Lett. **80**, 4959 (1998); T. Gramespacher and M. Büttiker, Phys. Rev. Lett. **81**, 2763 (1998).

[11] L. Saminadayar, D. C. Glattli, Y. Jin, B. Etienne, Phys. Rev. Lett. **79**, 2526 (1997); R. de-Picciotto *et al.*, *Nature* **389**, 162 (1997).

[12] G. Torres and T. Martin, cond-mat/9906012; G. Burkard *et al.*, cond-mat/9906071; G. Innacone, G. Lombardi, M. Macucci, B. Pellegrini, Phys. Rev. Lett. **80**, 1054 (1998); T. Hoss *et al.*, cond-mat/9901129.

Magnetotransport spectroscopy of a quantum dot: effects of lead opening and phase coherence

D. P. Pivin, Jr., A. Andresen, J. P. Bird, R. Akis, and D. K. Ferry

Center for Solid State Electronics Research, Arizona State University
Tempe, Arizona 85287-6206

Abstract

We compare open quantum dot magnetoconductance spectra from experiment and theory in the presence of environmental coupling and attributed broadening. Estimates of the phase-breaking time in experiment, and effective broadening in simulation, are determined independently. In a larger, more open dot, with a significantly shorter phase-breaking time, the observed spectrum is broadened, most noticeably about $B = 0$. The required broadening in simulation is characterized by effective temperatures higher than estimates from experiment; however, without accounting for disorder, which will further broaden the spectrum, the agreement is reasonable.

Keywords: quantum dot, phase breaking, magnetoresistance, spectroscopy

1. Introduction

At suitably low temperatures, magnetoconductance fluctuations in ballistic quantum dots are a manifestation of the underlying level spectrum as it is swept through the Fermi surface [1-4]. Open quantum dots are necessarily coupled to the electrical environment via quantum point contact leads. These leads provide a means of 'probing' the level spectrum and in turn modify the closed Darwin-Fock spectrum in a magnetic field. This process may be interpreted as selection, or mode-matching, of the bare dot states [5,6]. In addition, the thermal and electromagnetic conditions couple to the system to further modify the observed spectrum. One common measure of the effect of the intrinsic environment on the electron wavefunction is the phase-breaking time. At temperatures well below 1 K, this time can be relatively long, allowing for the observation of magnetoconductance fluctuations which are characteristic of the unaveraged quantum mechanical density of states.

In this paper we present a comparison of measurement and simulation which reveals the underlying spectrum of the dot. We describe the effects of a variation of the dot size and the phase-breaking time on the observed spectrum.

2. Experiment and Results

The device we employ has a self-aligned gate, which masks a shallow etch of high mobility $Al_{0.3}Ga_{0.7}As/GaAs$ heterojunction material [7,8]. The gated dot is defined lithographically (without depletion) to be 0.8 μm square with ~150 nm quantum point contact leads positioned at either side. The bulk material has a carrier density of 3.8×10^{15} m^{-2} (E_F = 13.7 meV) and a mobility of 30 m^2/Vs, as determined by *in situ* Shubnikov-de Haas measurements. The device was mounted in good thermal contact to the sample post of a dilution refrigerator with a base temperature of 10 mK. Measurements were taken in a four-probe configuration, using standard lock-in amplification techniques. The source-drain excitation was kept well below kT.

In this structure, the gate may have two effects. By applying negative voltages, the density may be decreased by vertical depletion of the 2DEG. At positive voltages, however, the density of the 2DEG saturates. With further increases of the (positive) gate voltage, the equilibrium surface depletion at the sides of the dot (brought about by the etching) is decreased. In this way, the size of the dot, including the width of the quantum point contacts, can be uniformly varied without a change in electron sheet density. The magnetoresistance of the dot is measured as a function of the gate voltage, and thus, the size of the dot and the width of the quantum point contact leads can be estimated. The dot size dependence on gate voltage is determined from the Aharonov-Bohm-like oscillations at high magnetic fields. The width of the leads may be inferred from the estimated dot size (assuming uniform depletion) and the observed linear change in conductance with gate voltage. In this experiment, the dot conductance at zero magnetic field could be varied from less than e^2/h to about $3e^2/h$. Successive illuminations of the device, with a red LED in the dilution refrigerator, remove progressively more equilibrium sidewall depletion. After each illumination, the density remains constant under

positive gate voltages, while a new range of dot size is available due to the decreased sidewall depletion.

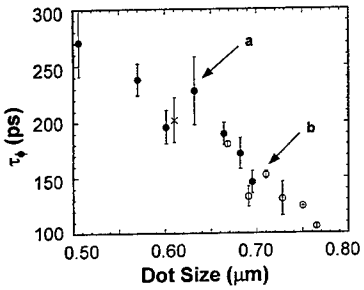

Fig. 1. Variation of the phase-breaking time with square dot size (side dimension) at base temperature for three different illuminations of the dot (corresponding to the three symbols). There is a clear trend of decreasing phase-breaking time with increasing size. Symbols (a) and (b) indicate the estimates for the corresponding spectra shown in Figs. 2 and 3.

Magnetoconductance traces were taken after several illuminations and over many ranges of positive gate voltage at base temperature (<100 mK). The phase-breaking time τ_ϕ as a function of gate voltage was estimated from magnetoconductance traces by the increase in correlation field of the fluctuations as the transition to edge state dominated transport is reached [9]. The resulting relationship between the dot size and phase-breaking time estimates is shown in Fig. 1. At low temperatures, τ_ϕ exhibits the saturation behavior which has now been observed in several mesoscopic systems, including quasi-2D films, 1D wires, and quantum dots. In this system, as the dot becomes uniformly *smaller* at lower gate bias, a *higher saturated* τ_ϕ is observed [7]. Thus, we may observe the combined effects of a significant variation in dot size and phase-breaking time on the results.

Several magnetoconductance traces for a series of gate voltages are assembled to form spectroscopic images of the dot. A small increase in positive gate voltage brings about a corresponding small linear increase in dot size, causing the dot states to sweep through the Fermi surface. Spectroscopic images for median dot sizes of approximately 0.65 and 0.71 μm are shown in Fig. 2. The relatively smaller dot (0.65 μm) has a larger estimated phase-breaking time and lower overall conductance. The two spectra differ qualitatively with regard to the apparent amount of broadening of the bare dot spectrum. This effect is noticeable in the 'streaked' appearance of the broadened features at higher magnetic field. The broadening is particularly evident near $B = 0$ when individual traces are plotted offset to each other as in Fig. 3. For the same range of gate voltage variation, the larger dot exhibits a wide, non-monotonic variation in the structure near $B = 0$, while there is practically no variation for the smaller dot. These features have been previously associated with the weak localization effect [10], however in the absence of ensemble averaging, there is no clear lineshape [11]. In the larger dot, greater broadening of the underlying spectrum due to environmental coupling causes the structure near $B = 0$ to take a universal Lorentzian-like shape, indicative of significant averaging.

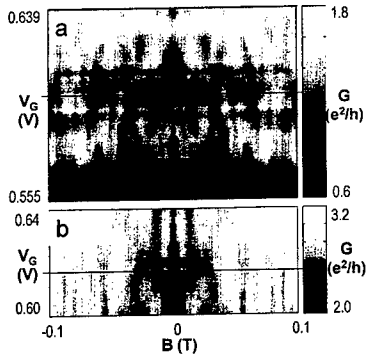

Fig. 2. Magnetoconductance spectra for median dot sizes of 0.65 μm (a) and 0.71 μm (b). The horizontal lines through each spectrum intersect prominent similar features and indicate the center trace for the offset traces in Fig. 3.

Broadening of the dot spectrum may be expressed as an effective temperature T^* via:

$$kT^* = kT + \frac{h}{\tau_\phi} + \Gamma, \qquad (1)$$

where T is the temperature of the device, τ_ϕ is the phase-breaking time, and Γ is the level broadening due to disorder. In the experiment, T is held fixed at base temperature ($kT < 9$ μeV), therefore level broadening is attributed to the latter two terms of Eq. 1. The effective broadening in experiment, due only to phase breaking, is 28 μeV for the larger dot and 19 μeV for the smaller. While disorder may play an important variable role here (especially after repeated illuminations), its effect is difficult to quantify and we consider the major trend in broadening to be associated with the significant variation in estimated phase-breaking time. It should also be noted that wider

lead opening (and hence higher overall conductance), modifies somewhat the selection of dot states for transport, giving the qualitative result of a reduction in the fine structure of the observed spectrum [12].

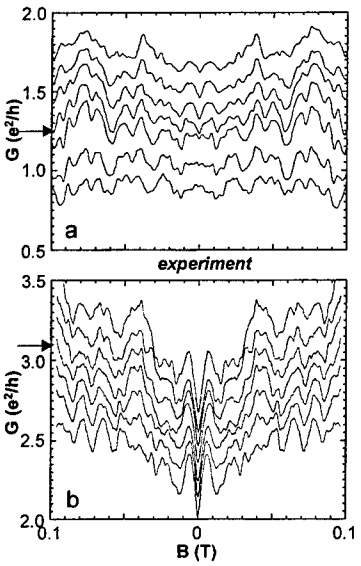

Fig. 3. Offset magnetoconductance traces from the spectra of Fig. 2. The center trace in each plot (indicated by the arrow and corresponding to the horizontal line of Fig. 2) is *not* offset in G. Traces above and below the center trace are for successive +2 mV and –2 mV changes in gate voltage. Traces are offset by 0.15 e^2/h.

Quantum mechanical simulations of the experimental conditions reveal similar spectra (shown in Fig. 4) for the two dot sizes. The details of the simulation can be found in Ref. 13. These spectra were obtained by varying the Fermi energy for separate fixed dot profiles. Effective temperature averaging has been accounted for by simply integrating the $T = 0$ result with the derivative of the Fermi-Dirac distribution function at the effective temperature T^*, resulting in an averaged conductance:

$$G_{av}(B, E_F) = \int G(E)\left[-\frac{df(E-E_F)}{dE}\right]dE. \quad (2)$$

To obtain qualitative agreement with the experimental results, it was necessary to use $T^* = 1.0$ and 0.7 K for the large and small dot respectively (corresponding to 86 and 60 μeV). A comparison of the offset traces of experiment and simulation in Figs. 3 and 5 illustrates the qualitative agreement in the behavior about $B = 0$. The key feature is the variation in the lineshape modified by the degree of broadening.

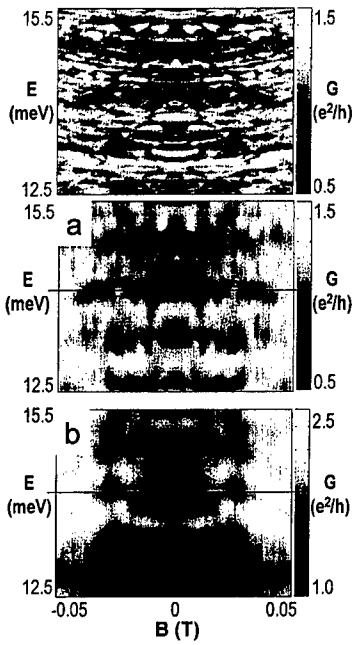

Fig. 4. Simulated magnetoconductance spectra for comparison to experimental results shown in Fig. 2. The spectrum shown at the top is the $T = 0$, unaveraged situation of (a) for reference. Spectra (a) and (b) have been created to correspond to the experimental results of Fig. 2(a) and 2(b) respectively. The effective temperatures (T^*) are 0.7 in (a) and 1.0 in (b). (Note that the magnetic field scale is different than that of Fig. 2.) The horizontal lines through each spectrum intersect prominent similar features and indicate the center trace for the offset traces in Fig. 5.

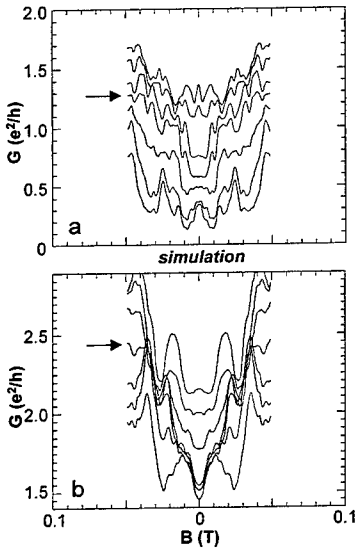

Fig. 5. Offset simulated magnetoconductance traces from the spectra of Fig. 4. The center trace in each plot (indicated by the arrow and corresponding to the horizontal line of Fig. 2) is *not* offset in G. Traces above and below the center trace are for successive +0.1 meV and –0.1 meV changes in Fermi energy. Traces are offset by 0.15 e^2/h. (For reference, the Fermi energy from experiment is 13.7 meV.)

The aim here is not perfect agreement between experiment and simulation. In experiment, the spectrum is obtained by varying gate voltage, which slightly varies the size of the dot. Without detailed self-consistent simulations of the dependence of the dot profile on gate voltage, the correspondence is inexact. (In simulations, the dot profile is approximated by infinite square-well potentials.) The agreement found is nonetheless meaningful. The main spectral features are similar and evident in both experiment and simulation. Ranges of gate voltage and Fermi energy variation have been chosen to reveal roughly the same spectral content. For example, the lines across the spectra of Figs. 2 and 4 intersect one of the most prominent features of the spectrum, common to all. The offset traces in Figs. 3 and 5 represent a sample about these points.

3. Conclusions

In conclusion, we have demonstrated a meaningful comparison of open quantum dot magnetoconductance spectra from experiment and theory in the presence of environmental coupling and attributed broadening. Estimates of the phase-breaking time in experiment, and effective broadening in simulation, are determined independently. In a larger dot, with a significantly shorter phase-breaking time, the observed spectrum is broadened, most noticeably about $B = 0$. By comparison, the broadening in simulation is characterized by effective temperatures higher than estimates from experiment; however, without accounting for disorder, which will further broaden the spectrum, the agreement is reasonable.

This work is supported by the Office of Naval Research.

References

1. P. L. McEuen, E. B. Foxman, U. Meirav, M. A. Kastner, Y. Meir, N. S. Wingreen, and S. J. Wind, Phys. Rev. Lett. **66**, 1926 (1991).
2. M. Persson, J. Petersson, B. von Sydow, P. E. Lindelof, A. Kristensen, and K. F. Berggren, Phys. Rev. B **52**, 8921 (1995).
3. S. Tarucha, D. G. Austing, T. Honda, R. J. van der Hage, and L. P. Kouwenhoven, Phys. Rev. Lett. **77**, 3613 (1996).
4. J. P. Bird, R. Akis, and D. K. Ferry, submitted to Phys. Rev. B.
5. R. Akis, D. K. Ferry, and J. P. Bird, Phys. Rev. B **54**, 17705 (1996).
6. I. V. Zozoulenko, R. Schuster, K. F. Berggren, and K. Ensslin, Phys. Rev. B **55** 10209 (1997).
7. D. P. Pivin, Jr., A. Andresen, J. P. Bird, and D. K. Ferry, Phys. Rev. Lett. **82**, 4687 (1999).
8. M. W. Keller, A. Mittal, J. W. Sleight, R. G. Wheeler, D. E. Prober, R. N. Sacks, and H. Shtrikmann, Phys. Rev. B **53**, 1693 (1996).
9. J. P. Bird, K. Ishibashi, D. K. Ferry, Y. Ochiai, Y. Aoyagi, and T. Sugano, Phys. Rev. B **51**, 18037 (1995).
10. H. U. Baranger, R. A. Jalabert, and A. D. Stone, Phys. Rev. Lett. **70**, 3786 (1993).
11. R. Akis, D. K. Ferry, J. P. Bird, and D. Vasileska, Phys. Rev. B, *in press*.
12. R. Akis and D. K. Ferry, Semicon. Sci. Technol. **13**, A18 (1998).
13. R. Akis, D.K. Ferry, and J. P. Bird, Phys. Rev. B **54**, 17705 (1996).

PA.19

Gate Voltage Dependent Aharanov-Bohm Experiment in the Presence of Rashba Spin-orbit Interaction

J. Nitta, F. Meijer, Y. Narita, and H. Takayanagi
NTT Basic Research Laboratories,
3-1 Wakamiya Morinosato Atsugi-shi, Kanagawa 243-0198 Japan

Abstract

We measured gate voltage dependent Aharonov-Bohm oscillations in an InGaAs-based two-dimensional electron gas ring with a gate on top of one of the branches. After ensemble averaging, the h/e oscillation spectrum showed smooth oscillatory behavior as a function of the gate voltage. This could be a manifestation of the spin-orbit interaction induced interference.

Introduction

Mesoscopic transport affected by spin-orbit interaction is currently of growing interest. It is pointed out that the effect of spin-orbit interaction in disordered conductors is a manifestation of the Aharanov-Casher (AC) effect in the same sense as the effect of weak magnetic fields is a manifestation of the Aharanov-Bohm (AB) effect [1]. The spin-orbit interaction affects the transport through the effective spin vector-potential which causes a phase shift in AB-oscillations and a periodic intensity of the Fourier spectrum as a function of the spin-orbit interaction [2]. A recent experiment [3] on AB-rings using an AlSb/InAs quantum well showed a splitting in the *ensemble averaged* Fourier spectrum as expected for the presence of the Berry phase [4]. From a different perspective, the spin-orbit interaction plays a crucial role in the so-called spin-polarized field effect transistor proposed by Datta and Das [5]. These effects in mesoscopic transport depend on the strength of the spin-orbit interaction.

Recently, it is experimentally shown that the spin-orbit interaction can be controlled by the gate voltage in InGaAs-based two-dimensional electron gas (2DEG) [6], [7] and GaAs two-dimensional hole gas (2DHG) [8] systems. These results show that the Rashba spin-orbit interaction [9], [10] is a dominant mechanism in these semiconductor systems. For the purpose of studying the interference effect induced by the spin-orbit interaction, we measured AB-oscillations in an InGaAs-based 2DEG ring with a gate on top of one of the branches. The gate voltage dependence of h/e oscillations could be attributed to the phase shift due to the effective spin vector-potential which is controlled by the gate voltage.

Sample Fabrication

The AB-ring was fabricated by electron beam lithography and electron cyclotron resonance (ECR) dry etching. The fabricated structure is shown in Fig. 1. The outer radius and

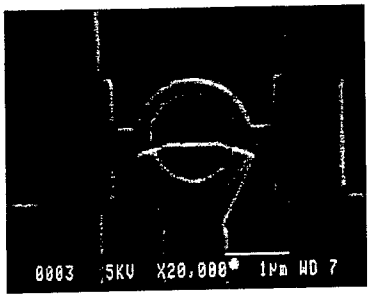

Fig. 1 SEM picture of the fabricated AB-ring

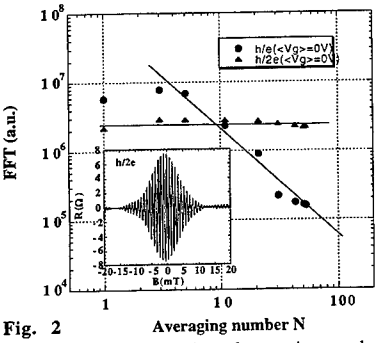

Fig. 2 FFT spectrum as a function of averaging number. Inset shows h/2e oscillations after averaging 52 R(B) data and filtering.

the channel-width were 0.92 μm and 0.25 μm, respectively. The heterostructure used in the present experiment was an InAs-inserted InGaAs/InAlAs heterostructure. The carrier concentration *Ns* at *Vg*= 0.3V and -0.3V can be determined to be 2.15 x 10^{12} cm^{-2} and 1.65 x 10^{12} cm^{-2}, respectively. The electron mean free path after fabrication was estimated to be about 0.5 μm.

Experiment and Discussion

The magnetoresistance *R(B)* curves up to 30 mT were measured as a function of the gate voltage *Vg* from –0.26V to 0.26V in 0.01V steps. The expected h/e AB oscillations and the h/2e oscillations around *B*= 0 were visible. A fundamental distinction between these two periods is that the phase of the h/e oscillations is sample-specific, whereas the h/2e oscillations contain a contribution from time-reversed trajectories that has a sample-independent phase. To eliminate the sample specific feature, we averaged *R(B)* by summing different sequences *Vg* data, and then obtained the Fourier spectrum. If the ensemble averaging range is much smaller than the phase change of a 2π, this averaging does not wash out the phase information. For example, the dynamical phase of electron $\Delta k_F(Vg)L$ can easily be washed out by averaging of different *Vg* data. However, the phase shift $\Delta\alpha(Vg)Lm^*/\hbar^2$ in the channel covered with the gate due to the spin vector-potential [2] is not so much sensitive to the gate voltage, and can still survive after averaging. Here *L* is the channel length covered with the gate

Figure 2 shows the averaging number *N* dependence of the spectrum. By ensemble averaging, the spectrum decreases in proportional to $N^{1/2}$. This has been experimentally confirmed by using series of arrays of AB-rings [11]. Strikingly, the spectrum of AB h/e oscillations decreased in proportional to N^{-1} ~N^{-2} as increasing the averaging number *N*. This can be explained in terms of the two-terminal measuring configuration which requires *R(B)*= *R(-B)* and restricts the phase of AB oscillation to either 0 or π. The experimental data can be reproduced by the model proposed by Büttiker *et al.* [12].

On the other hand, the h/2e spectrum was almost constant because the time reversal symmetric interference ensures a fixed phase at *B*= 0. Clear Altshuler-Aronov-Spivak (AAS) oscillations in the inset of Fig. 2 can be obtained by averaging 52 *R(B)* data and filtering. Note

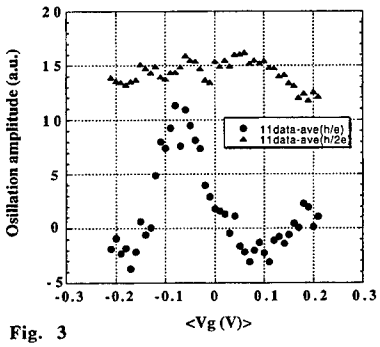

Fig. 3 Oscillation amplitude of h/e and h/2e as a function of gate voltage

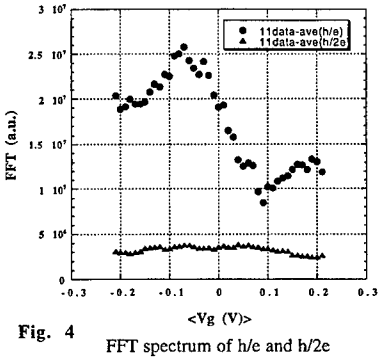

Fig. 4 FFT spectrum of h/e and h/2e as a function of gate voltage

that the AAS oscillations showed the minimum in the resistance at B= 0, whereas it was reported that the resistance maximum was observed in an AB-ring using 2DEG GaAs [13].

Figure 3 shows the mean gate voltage dependence of the h/e and h/2e oscillation amplitudes at B= 0 after averaging 11 $R(B)$ data and filtering. *Before averaging*, the spectrum of h/e and h/2e showed a random variation as a function of Vg. The sudden changes in the spectrum are due to the change in the trajectory and the wavelength of the electrons underneath the gate. Averaging over 11 data is enough to wash out the effect of $\Delta k_F(Vg)L$ but not enough to smear out the effect of $\Delta\alpha(Vg)Lm^*/\hbar^2$. *After averaging*, the amplitude of h/e oscillations showed smooth change, and the oscillation phase flipped by the gate voltage. The amplitude of the h/2e oscillations showed a small oscillatory behavior while the phase of h/2e did not flip. A similar mean gate voltage dependence was obtained in the *ensemble averaged* FFT spectrum shown in Fig. 4 when we first performed the Fourier analysis of each $R(B)$ data separately and averaged 11 Fourier spectra by summing different sequences of Vg data. In Fig. 4, the plotted spectrum corresponds to the integrated Fourier spectrum including a few peaks because the spectrum was not always a single peak but it showed a few peaks.

The constant amplitude and spectrum of h/2e oscillations as a function of Vg can be explained by the weak anti-localization effect. The spectrum of h/2e oscillation is not dependent of the averaging number N. The h/2e oscillation phase was fixed, and did not show a phase flip and showed the minimum in the resistance at B= 0 which was not affected by the gate voltage in this experiment. These results mean that the observed h/2e is not due to the higher harmonic of h/e oscillation but mainly due to the AAS oscillation. When the circumference $2\pi r$~ 5.0 μm of the ring is much longer than the spin-orbit scattering length [1] $L_{SO} = \hbar^2/\alpha m^*$ = 0.5~ 0.8 μm in our gate voltage range, spins of electrons lost their memory of their original orientations, and the orientations of the final spin states are statistical. Then, the phase of the AAS h/2e oscillations should be fixed and show the minimum at B= 0. The observed small oscillatory behavior as a function of Vg is maybe due to the fact that the spin does not completely lost its phase memory and partially spin interference effect survives.

A possible explanation for the gradual change in the h/e spectrum and amplitude by the

gate voltage could be attributed to the phase shift due to the effective spin vector-potential which is controlled by the gate voltage. According to the carrier concentration dependence of the spin-orbit interaction α [6] , we can evaluate the spin-orbit interaction α= 0.74x 10^{-11} eVm at Vg= 0.3V and α= 1.05 x10^{-11} eVm at Vg= -0.3V. The phase shift $\Delta\phi = \Delta\alpha(Vg)m^*L/\hbar^2$ gives about a 3π shift. Recent theory [14] predicts that the peak intensity of the h/e oscillations in the Fourier spectrum oscillates with a period of $2\pi[1+(r\alpha m^*/\hbar^2)^2]^{1/2}$ where r is a radius of the AB-ring. This theory also supports the experimental result.

Conclusion

A gate voltage dependent AB experiment was performed in the presence of Rashba spin-orbit interaction. Ensemble averaging washed out the sample specific feature and revealed a spin-dependent interference effect. The averaging number dependence of the h/e spectrum can be explained in terms of the two-terminal measuring configuration. The h/2e oscillations are due to the AAS oscillations influenced by the strong spin-orbit scattering. The gate voltage dependence of h/e oscillations could be attributed to the phase shift due to the effective spin vector-potential which is controlled by the gate voltage.

We thank Michel Devoret, Can-Ming Hu and Jan Willem Berghuis for their fruitful discussion. We are also indebted to Sunao Ishihara for his encouragement. This work has been partially supported by the Core Research for Evolutional Science and Technology (CREST) of the Japanese Science and Technology Corporation (JST).

References

[1] H. Mathur and A. D. Stone, Phys. Rev. Lett. 68 (1992) 2964
[2] Y. B. Lyanda-Geller, Surface Science 361/362 (1996) 692
[3] A. F. Morpurgo, J. P. Heida, T. M. Klapwijk, B. J. van Wees, and G. Borghs, Phys. Rev. Lett. 80 (1998) 1050
[4] A. G. Aronov and Y. B. Lyanda-Geller, Phys. Rev. Lett. 70 (1993) 343
[5] S. Datta and B. Das, Appl. Phys. Lett. 56 (1990) 665
[6] J. Nitta, T. Akazaki, H. Takayanagi, and T. Enoki, Phys. Rev. Lett. 78 (1997) 1335; Physica E2 (1998) 527
[7] G. Engels, J. Lange, Th. Schäpers, and H. Lüth, Phys. Rev. B55 (1997) R1958
[8] J. P. Lu, J. B. Yau, S. P. Shukla, M. Shayegan, L. Wissinger, U. Rössler, and R. Winkler, Phys. Rev. Lett. 81 (1998) 1282
[9] E. I. Rashba, Sov. Phys. Solid State 2 (1960) 1109
[10] Y. A. Bychkov and E. I. Rashba, J. Phys. C17 (1984) 6039
[11] C. P. Umbach, C. van Haesendonck, R. B. Laibowitz, S. Washburn, and R. A. Webb, Phys. Rev. Lett. 56 (1986) 386
[12] M. Büttiker, Y. Imry, and M. Ya Azbel, Phys. Rev B30 (1984) 1982
[13] C. J. B. Ford, T. J. Thoronton, R. Newbury, M. Pepper, H. Ahmed, D. C. Peacock, D. A. Ritchie, J. E. F. Frost, and G. A. C. Jones, Appl. Phys. Lett. 54 (1989) 21
[14] A. G. Mal'shukov, V.V. Shlyapin, and K. A. Chao, cond-mat/9902122

PA.20

Symmetric, Gated, Ballistic Rings as Tunable Electron Interferometers

E.B. Olshanetsky[a,c], M. Cassé[a,b], Z.D. Kvon[c], G.M. Gusev[d], L.V. Litvin[c], A.V. Plotnikov[c], D.K. Maude[a], J.C. Portal[a,b,e]

[a]*Grenoble High Magnetic Field Laboratory MPI-FKF/CNRS. BP 166, F-38042, Grenoble Cedex 9, France.*
[b]*INSA-Toulouse, Complexe Scientifque de Rangueil F-31077, France*
[c]*Institute of Semiconductor Physics, Russian Academy of Sciences. Novosibirsk 630090, Russia*
[d]*Instituto de Fisica da Universidade de São Paulo, CP 66318, CEP 05315-970, São Paulo, SP, Brazil*
[e]*Institut Universitaire de France*

Abstract

In the present work we investigate the coherent electron transport in a symmetrically designed ballistic ring uniformly covered by a top metal gate. We find that as the Fermi energy is varied, the phase of Aharonov-Bohm (AB) oscillations near zero magnetic field switches between 0 and π. It seems unlikely that this behaviour can be explained by some accidental asymmetry in the structures. We give a qualitative explanation of our results using a model where the ring is considered to be weakly coupled to the leads and the conductance is calculated on the basis of an exact energy spectrum of an ideal ring. This model predicts that a variation of the phase of AB oscillations with gate voltage may be observed in a symmetrical ring.

Ever since the start of the mesoscopic physics, the properties of quantum ring interferometers have been intensively studied [1-4]. In the present work we investigate the effect of the gate voltage on electron interference in a symmetric ring interferometer uniformly covered by a top metal gate. The problem is closely related to the concept of the quantum interference device [5], in which the electron wave is split into two and then recombines again after a phase difference has been added between the two partial waves. If the waves are in phase, they interfere constructively to give a large amplitude (low resistance). When out of phase, destructive interference yields a high resistance. In a real interferometer it is necessary to sum over the amplitudes of all the possible trajectories circling the ring and so the situation is more complicated. However in any case there exist only two principal ways in which a controllable variation of the transmission of the device can be accomplished. The first is the use of a variable external magnetic field normal to the ring which gives rise to AB oscillations. The other is changing the Fermi wave vector in the ring conducting channels by means of an electrostatic gate. It has been generally assumed so far that the latter can only be possible in an asymmetric structure [6-8]. In the present work we study the effect of the variation of gate voltage on AB oscillations in uniformly gated rings of symmetrical design. As the gate voltage is varied, the phase of the h/e oscillations in magnetic field switches between 0 and π. We find that the asymmetry factor that would be needed to explain this variation of phase within conventional approach is too big to be considered realistic. We, therefore, use a different model that gives a qualitative explanation of our results and shows that the variation of the phase of AB oscillations with gate voltage doesn't necessarily require asymmetry and should be observable in any symmetrical ring uniformly covered by gate.

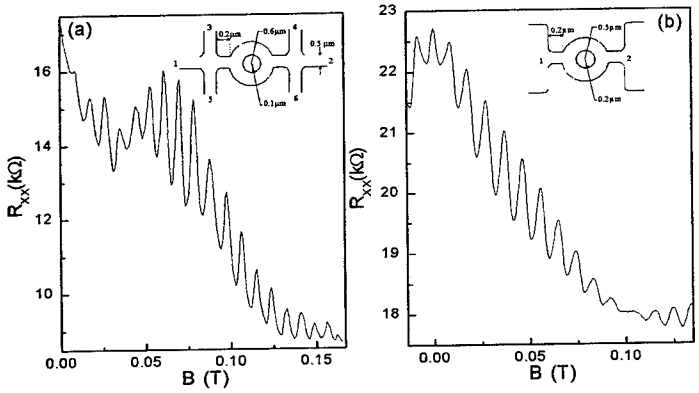

Fig. 1. Typical magnetoresistance curves and the schematic top view of the ring interferometer (a-type 1, b-type 2).

The samples (see the inserts to Fig.1) were four- and two-terminal ring interferometers fabricated from AlGaAs/GaAs heterolayers with the 2D electron density $n_s=(1.5\text{-}6)\times10^{11}$ cm^{-2} and mobility $\mu\approx(0.5\text{-}1)\times10^6$ cm^2/Vs. The average radius of the rings was $r_0=0.35$ μm, the lithographical width of the channels $W_{lith}=(0.5\text{-}0.3)$ μm. The structures were entirely covered by Au/Ti gate. The measurements were performed at T≈100 mK by a conventional lock-in technique with an ac current 1 nA at a frequency 13 Hz.

The typical magnetoresistance of our devices is presented in Fig. 1. As expected the magnetoresistance is dominated by AB-h/e oscillations, whose regularity and beating indicate that the the devices are in a single or a few-mode regime. Fig. 2a,b show the modification of AB oscillations with gate voltage in a four terminal and a two terminal structure. A qualitatively similar behaviour has been observed in all our structures. The oscillations are symmetrical with respect to B=0 indicating that the phase coherence length is smaller than the distance between the probes used to measure the voltage drop across the ring. The symmetry of the oscillations also means that no other phase except 0 and π should be possible at B=0 As the gate voltage is varied, the phase of the h/e oscillations switches irregularly between 0 and π. Because of the condition of symmetry imposed on the oscillations near B=0, oscillations with $\varphi=0$ can evolve continuously into oscillations with $\varphi=\pi$ via an intermediate state with h/2e oscillations [8], which is observed experimentally. The experimental structures, although symmetrical in design, can still have some individual accidental asymmetry. This asymmetry will result in a variation of the phase of AB oscillations if the integral $\int \vec{k}_F \cdot d\vec{l}$ in the two channels of the ring changes unequally when the gate voltage is varied. Using the approach developed in [9] we have estimated the degree of asymmetry needed to account for the change of phase in Fig. 2a and found it to be about 100%, which we believe unrealistic in our case. In the present work we attempt to give a qualitative explaination of the observed behaviour using the model proposed recently by W.C. Tan and J.C. Inkson [10] which is based on the exact energy spectrum of an isolated ring in magnetic field. The spectrum (Fig. 3a) consists of subbands originating from the quantization of the

radial motion of electron. The energy levels in each subband correspond to the clockwise and unticlockwise motion along the channel of the ring.

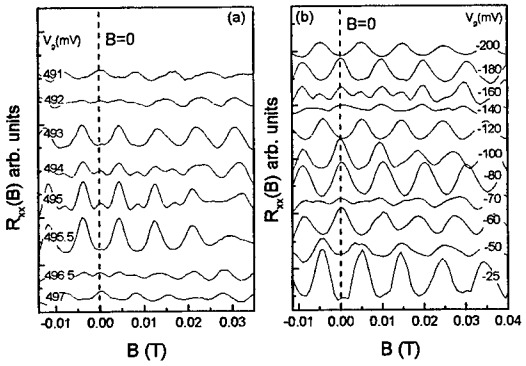

Fig. 2. The variation of the phase of the Aharonov-Bohm oscillations with gate voltage in symmetrical ballistic rings uniformly covered by gate (a-type 1; b-type 2).

The ring is considered to be weakly coupled to two leads. An electron can reach from one lead to the other by tunneling though the quasibound states in the ring which are approximated by broadened energy levels of an isolated ring. Let us consider the situation where only the first subband in the ring is occupied. The oscillations in the conductance arise when the the Fermi level is aligned with one of the energy levels of the quasibound states in the ring. As can be seen from Fig. 3b, the phase of the AB oscillations in magnetic field depends on the position of the Fermi level relative to the energy levels in the ring. Shifting the Fermi level by $\Delta=hv_F/(2\pi r_0)$ (the distance between the energy levels in the ring in zero magnetic field) changes the phase of the AB oscillations by 2π. Whenever the Fermi level lies between the positions corresponding to the states with $\varphi=0$ and $\varphi=\pi$ one observes h/2e oscillations. It is also interesting to note that when the Fermi energy is varied, each time the phase of AB oscillations changes by π the number of occupied energy levels in the ring changes by one. That leads to a quite universal conclusion that in a single mode ring the addition or removal of only two electrons would be sufficient to change the phase of AB oscillations by π. We get a surprisingly close result $\Delta N\approx 3$ from our estimates based on the data presented in Fig. 2a.

Although all the main features of the behaviour discussed above are present in the experimental results, there is also a certain difference. The phase of AB oscillations is not a simple periodical function of the gate voltage as one would expect it to be in the case of a single mode ring for relatively small variations of the Fermi energy. A possible explanation of this fact can be that the characteristics of the ring necessarily undergo certain modifications as the gate voltage is varied. That means that at each new gate voltage we have a slightly different ring and this might account for the lack of the expected periodicity in the variation of the phase. One can also consider a situation when two radial subbands in the ring are occupied instead of one. In that case the energy spectrum is more complicated as the energy levels of the two subbands are intermixed. We have checked that under these circumstances the modification of AB oscillations with gate voltage can look very similar to what we find in the experiment.

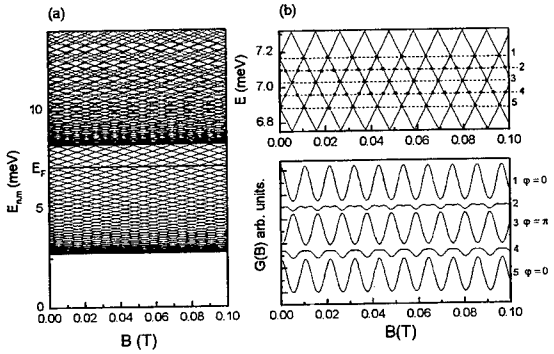

Fig. 3. (a) The energy spectrum in the 4-leads ring calculated after [10]; the energy levels of the first two radial energy subbands are shown. (b) The phase of Aharonov-Bohm oscillations (below) for different positions of the Fermi energy with respect to the energy levels in the ring (above).

To conclude, in the present work we report the modification of phase of the Aharonov-Bohm oscillations in a symmetrical ballistic ring interferometer uniformly covered by top metal gate. As the Fermi energy is varied the phase of the AB oscillations near zero magnetic field switches between 0 and π. We show that these results can be qualitatively explained using a model where the conductance of the interferomtere is calculated on the basis of an exact energy spectrum in an ideal ring which is considered to be weakly coupled to the leads.

Acknowledgements

This work has been supported by NATO Linkage grant HTECH.LG 971304 and grant N 97-1078 "Physics of solid state nanostructures", and CNRS-RFBR through grant PICS 628-RFBR98-22008. G.M.G. acknowledges support from CNPq.

References

[1] S.Washburn, C.P.Umbach, R.B. Leibowitz, R.A.Webb, Phys.Rev.B32, 4789 (1985).
[2] R.A. Webb, S.Washburn, C.P. Umbach, R.B. Leibowitz, Phys.Rev.Lett. 54, 2696 (1985).
[3] K.Ismail, S.Washburn, K.Y. Lee, Appl.Phys.Lett. 59, 1998 (1991).
[4] A.A.Bykov, Z.D.Kvon, E.B.Olshanetsky, L.V.Litvin, Yu.V.Nastaushev, V.G.Mansurov, V.P.Migal, S.P.Moschenko, V.G.Plyukhin, JETP Lett. 57, 613 (1993).
[5] S.Datta, M.R.Melloch, S.Bandyopadhyay, M.S.Lundstrom, Appl.Phys.Lett.48, 487 (1986).
[6] C.J.B.Ford, A.B.Fowler, J.M.Hong, C.M.Knoedler, S.E.Laux, J.J.Wainer, S.Washburn, Surf.Science 229, 307 (1990).
[7] S.Washburn, H.Schmid, D.Kern, R.A.Webb, Phys.Rev.Lett.59, 1791 (1987).
[8] A.Yakoby, R.Schuster, M.Heiblum, Phys.Rev.B57, 9583 (1996).
[9] Gefen Y., Imry Y., Azbel M.Y., Phys.Rev.Lett.52, 129 (1984); Surf. Science 142, 203 (1984).
[10] W.C.Tan, J.C.Inkson, Phys.Rev.B53, 6947 (1996).

Magnetoconductance of a few-electron open quantum dot.

I. V. Zozoulenko*, A. S. Sachrajda†, C.Gould†‡, K.-F. Berggren*, P. Zawadzki†, Y. Feng†, and Z. Wasilewski†

*Department of Physics (IFM), Linköping University, S-581 83 Linköping, Sweden.
†Institute for Microstructural Science, National Research Council, Ottawa K1A 0R6, Canada
‡ Département de Physique and CRPS, Université de Sherbrooke, Sherbrooke J1K 2R1, Canada

(June 11, 1999)

Abstract

Magnetoconductance of a small open lateral dot is studied both theoretically and experimentally for the conditions when the dot contains down to ~ 15 electrons. We confirm the existence of a new regime for open dots in which the transport through the structure occurs through individual eigenstates of the corresponding closed dot. In particular, at low magnetic fields the characteristic features in the conductance are related to the underlying eigenspectrum shells. When the number of modes in the leads is reduced more detailed structures within the shells due to single eigenlevels becomes discernible.

Keywords: quantum dots, electron billiards, magnetoconductance

The present state-of-the-art of the semiconductor technology allows one to fabricate routinely small quantum dots where electron motion can be confined in all spatial dimensions and the phase coherence is preserved over the whole device [1–9]. In transport measurements on such structures, two different regimes can be clearly distinguished. One of them is commonly referred to as a Coulomb blocade regime [1–4]. It takes place when the dot is weakly coupled to electron reservoirs by means of tunneling barriers. In the Coulomb blocade regime the broadening of the energy levels Γ is much smaller than the mean level spacing separation Δ. However, a direct assesment of the level energy spectrum in transport measrements is rather ambigouse because of the single-elecron charging which dominates the spacing between Coulomb blockade peaks.

The second regime, "an open dot regime", corresponds to the case when the coupling to the reservoirs is realized via quantum point contacts accomodating at least one propagating mode [5–9]. In this regime the charging term is proved to be unimportant. This is because the charge quantization in the dot, – a necessary condition for the Coulomb blockade to occur, – no longer holds as electrons can easily leave/enter the dot through the quantum point contacts which support propagating modes. As a result the conductance of the dot is dominated by typically random but reproducible fluctuations due to interference of the electron waves inside the dot. It has been demonstrated by explicit analysis of the scattering wave functions that transport through an open dot is effectively mediated by the eigenstates of the corresponding closed structure [10,9,11]. Moreover, under conditions in which only a few propagating modes in the leads exist the lifetime broadening of the level associated with the open leads is sufficiently small ($\Gamma < \Delta$) that observed features in the conductance are found to be related to individual levels of the underlying dot level spectrum [11]. Therefore under these conditions, one can in principle perform spectroscopic measurements of a closed dot by measuring the conductance of an open dot with the same geometry. However, for the quantum dot of a moderate size ($\sim 1\mu$m; $\Delta \sim 100$mK) the features in the conductance associated with the underlying discrete spectrum can be easily hindered by temperature smearing,

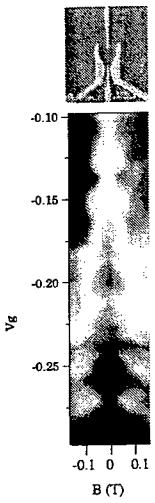

FIG. 1. A gray scale of the conductance G vs magnetic field B and gate voltage V_g at 50 mK. The inset is an SEM micrograph of a device similar to the one used in these experiments.

inelastic scattering etc. Therefore in this paper we use a small lateral dot where $\Delta < 2$K. This enables us for the first time to resolve single energy levels in the transport measurements on the *open* dot.

The inset in Fig. 1 is a SEM micrograph of a device identical to one of the two used in these measurements. The dot is electrostatically defined by four gates above a GaAs/AlGaAs heterostructure. The lithographic width and height of the triangular dots was aproximatelly 0.45μm. The bulk density (mobility) of the AlGaAs/GaAs wafer used were $1.7\times10^{11}\text{cm}^{-2}(2 \times 10^{6}\text{cm}^{2}\text{V}^{-1}\ \text{S}^{-1})$. The density inside the dot is shown to be much lower $\sim 0.6 \times 10^{11}\text{cm}^{-2}$ [8]. As an indication of how small the defined dots are we note that by using single electron tunnelling measurements [4] we were able to control the number of electrons in this dot under Coulomb blockade conditions to lie between 5 and 15 electrons. While for the experiments in this paper the dot is slightly larger (because of the less negative voltages applied to the finger gates) it is still expected to contain far fewer electrons than any previously measured open dot.

Figure 1 shows the magnetoconductance of the dot from -0.1T to 0.1T as a grey scale. It is composed of many individual gate voltage sweeps. All the gates were swept uniformily to preserve the triangular shape of the dot. As can be seen the conductance in this region breaks up into characteristic triangle (T) and diamond (D) patterns centered at B=0. The internal structure of these T and D structures becomes more highly resolved as the number of modes in the leads is reduced, see Fig 2 (a). At higher magnetic fields (not shown here) the Aharonov-Bohm (AB) oscillations become clearly visible. Note that for both devices qualitatively similar plots were obtained either by sweeping a single gate or by sweeping all of the gates.

The regions of interest for this paper lies in the regime of low fields (T and D structures) as well as in the regime when the number of modes in the leads is reduced to one. We argue below that the features seen in the dot conductance under these conditions can be directly traced to the underlying dot eigenspectrum. To understand these results theoretically we have calculated the spectrum of closed triangular dots and also performed numerical conductance calculations.

Fully quantum-mechnical transport calculations are performed within the Landauer formalism which relates the zero-temperature two terminal conductance of the device, G and the transmission coefficient T by the formula $G = (2e^2/h)T$ [12]. A modified version of a standard recursive Greens function technique [13] is used to compute T. The eigenspectrum of an isolated, equilateral triangular dot is calculated variationally by expanding the eigenstates in the set of exact analytical solution for $B = 0$. We use a model of the hard-wall confinement which is certainly an oversimplification of the actual dot potential. However, the main

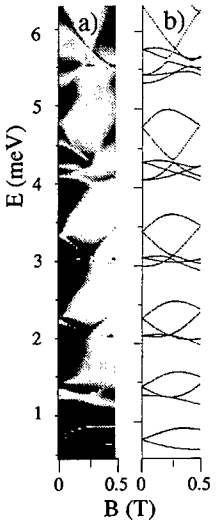

FIG. 2. a) A gray scale of the calculated conductance vs magnetic field and the Fermi energy of an equilateral triangular dot of the size $L = 300$nm with the lead geometry corresponding to the experimental dot; the lead openings are 75 nm. b) Eigenspectrum of an equilateral triangular dot of the same size.

purpose of the present calculations is to underline the relationships between the calculated conductance and the eigenspectrum of the dot, rather than to achieve a detailed one-to-one correspondence between the calculated and observed magnetoconductance.

Figure 2 (b) shows an eigenspectrum of the equilateral triangular dot at low magnetic magnetic field B. In the chosen energy interval the dot contains up to 60 electrons (including a factor of two which accounts for the spin degeneracy). Although this system is not separable, it is integrable at $B = 0$ with energy levels [14]

$$E_{nm} = \frac{\hbar^2 k_{mn}^2}{2m^*}, \qquad (1)$$

where $k_{mn}L = (4\pi/3)\sqrt{n^2 + m^2 - mn}$; m, n are positive integers with $m \geq 2n$ and m^* being the effective mass and L the side of triangle. Levels are doubly degenerate except for $m = 2n$. The eigenspectrum exhibits the characteristic "shell structure" with quantum number $m - 1$ giving the shell number. At high magnetic fields the energy spectrum exhibits the "Landau Level condensation" where the eigenlevels coalesce to the bulk Landau Levels (LL) [15], see Fig. 3 (c).

Figure 2 (a) shows the calculated magnetoconductance of the open equilateral triangular dot whose lead geometry corresponds to the experimental device (see also Fig. 3 (b)). Most of the features in the conductance can be easily traced to those of the eigenspectrum. In particular, the characteristic D and T features centered at $B = 0$ represent the shell structure of the eigenspectrum at $B = 0$ and its evolution as the magnetic field is raised. However, the above correspondence is not perfect: Some energy levels are not seen in the conductance. Besides, many closely lying energy levels are apparently merged because the life-time broadening in this case exceeds the level separation.

Let us now turn to the comparison of the theory and the experiment. The most striking similarity between these two are the T and D structures at low magnetic fields. To demonstrate that experimentally observable features can be explained within the eigenspectrum picture outlined above, one has to relate the variation of the experimental gate voltage to the energy (or $k-$) scale. We perform this calibration on the basis of the high-field Aharonov-Bohm oscillations observed as a function of the gate voltage (details will be reported elsewhere). Then, the typical interval between neighboring triangles, $\Delta V_g \approx 0.025$V translates into a difference in the dot size, $\Delta L_{exp} \approx 36$nm. On the other hand, we can use scaling arguments in (1) to estimate the difference in the triangle side dimension for a fixed k corresponding to the two neighboring shells. This gives a typical distance between neighboring shells $\Delta L_{theor} \approx 65$nm. Because of the uncertainty in the dot size, potential shape etc., one cannot expect the two estimated values, ΔL_{theor} and ΔL_{exp} to be identical. However, the fact that they are in a good quantitative agre-

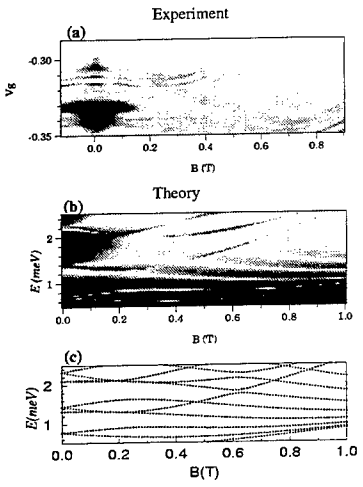

FIG. 3. A close up of (a) the lower part of Fig. 1; (b), (c) the lower part of Fig. 2 (a), (b).

ement strongly supports our conclusion that the observed T and D features correspond to the shell structures of the isolated dot.

Both theory and experiment agree that as the number of modes in the leads is reduced more detailed structures within the shells becomes discernible. This is illustrated in Fig. 3(a) where there exists one mode in the leads. Figure 3(b,c) shows the conductance calculation for the 2nd through 4th shell and the corresponding eigenspectrum. Many of the theoretical features can be observed in the experimental data. The broad resonances moving down as the magnetic field is raised are the levels collapsing to the lowest Landau level at high fields. This is a clear manifestation of the Landau level condensation mentioned above. The resonances are broad because the wavefunctions are largely close to the boundaries of the dot and hence the coupling to them is strong. Consider the top shell in the experimental data of Fig. 3 (a). The top line is largely due to a single level, whilst the bottom two contain several levels each. The sharp amplitude modulation along the levels seen both experimentally and theoretically is due to the interplay of these levels. At slightly higher fields the resonances sharply turn up again both experimentally and theoretically going to the next Landau level. They apparently cross with the levels collapsing to the lowest Landau level. Thus, the level crossings seen in the eigenspectrum clearly translates into the theoretical as well as experimental conductances.

[1] R. Ashhori, Nature **379**, 413 (1996).
[2] P. L. McEuen *et al.*, Phys.Rev **B45**, 11419 (1992).
[3] S. Tarucha *et al.*, Phys. Rev. Lett. **77**, 3613 (1996).
[4] P. Hawrylak *et al.*, Phys.Rev **B59**, 2801 (1999).
[5] C. M. Marcus *et al.*, Phys. Rev. Lett. **69** 506 (1992).
[6] M. Persson *et al.*, Phys. Rev. B **52**, 8921 (1995).
[7] A. S. Sachrajda *et al.*, Phys. Rev. Lett. **80** 1948 (1998).
[8] I. V. Zozoulenko *et al.*, Phys. Rev. B **58** 10597 (1998).
[9] I. V. Zozoulenko *et al.*, Phys. Rev. B **55** R10209 (1997).
[10] K.-F. Berggren, Z.-J. Ji, and T. Lundberg, Phys. Rev. B **54**, 11612 (1996).
[11] I. V. Zozoulenko and K.-F. Berggren, Phys. Rev. B **56**, 6931 (1997).
[12] see, e.g., A. D. Stone and A. Szafer, IBM J. Res. Dev. **32** 384 (1988) and references therein.
[13] I. V. Zozoulenko, F. A. Maaø and E. H. Hauge, Phys. Rev B **53**, 7975 (1996); ibid. B **53**, 7987 (1996).
[14] M. Brack and R. K. Bhaduri, *Semiclassical Physics*, (Addison-Wesley, Reading, Mass., 1997).
[15] V. Fock, Z. Phys. **47**, 446 (1928); C. G. Darwin, Proc. Cambridge Philos. Soc. **27**, 86 (1930).

Resonance Behaviour of the Hall-like Effect Induced by Spin-Orbit Interaction in a Four-Terminal Junction

K.N. Pichugin, P. Středa, P. Šeba, A.F. Sadreev*
Institute of Physics, Acad. of Sci. of the Czech Republic, Cukrovarnická 10, 162 53 Praha
*) Kirensky Institute of Physics, 660036, Krasnoyarsk, Russia

Abstract

Spin dependent anisotropy of the electron transmission coefficients is studied for a four terminal device, a quantum dot coupled to current and potential probes by point contacts. It is shown that injection of polarized electrons induces voltage drop perpendicularly to the direct current flow between source and drain. Model calculation predicts that at resonances the Hall-like resistance can reach values of the order of h/e^2.

Introduction

The spin-orbit interaction is responsible for azimuthal asymmetry of scattering coefficients describing scattering of a polarized particle beam on a spin-less nuclei [1]. Similar effect is expected in microstructures which might be viewed as electron waveguides. It has already be shown [2] that in the simple cross-junction device transmission probabilities between perpendicular arms differ for spin-up and spin-down states of incident electrons. Consequently, polarized incident electron beam leads to Hall-like effect, i.e. there appears voltage drop perpendicularly to the direct current flow between source and drain. The resulting Hall-like resistance have been estimated to be of the order of 10^{-3}-10^{-2} h/e^2 for technologically available structures.

Proper device geometry for which appearance of pronounced circulating currents is expected could strengthen the above described effect. Natural candidate is a quantum dot with symmetrically placed quantum point contacts to current and voltage probes. Spin-orbit interaction removes spin degeneracy of quantum-dot eigenstates. Due to easier matching of incident polarized electron beam with eigenstates of the same spin orientation strong resonance behaviour of the Hall-like resistance is expected.

Four-terminal quantum-dot device

Quantum devices are usually fabricated from $A_{III}B_V$ semiconductor heterostructures with a two-dimensional electron gas. The model Hamiltonian of such systems is assumed to be of the following form [3, 4]

$$H = \frac{p_x^2 + p_y^2}{2m^*} + \hbar\beta\left[\sigma_x p_y - \sigma_y p_x\right] + V(x,y)\,, \qquad (1)$$

where σ_μ denotes Pauli matrices. The spin-orbit coupling term is linear in momentum $\vec{p}$ and its strength β has meaning of an effective electric field along $\hat{z}$ direction given by the

form of the confining potential and including effect of the absence of an inversion centre [5]. In available structures the coupling constant $\hbar^2\beta$ is of the order of few mV·nm [6, 7].

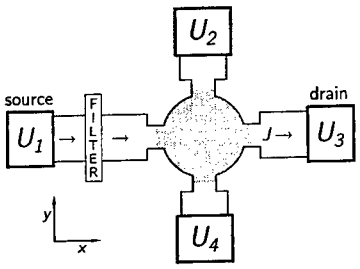

Fig. 1. The four-terminal quantum-dot device. Spin-orbit coupling is supposed to be non-zero in shadowed area only.

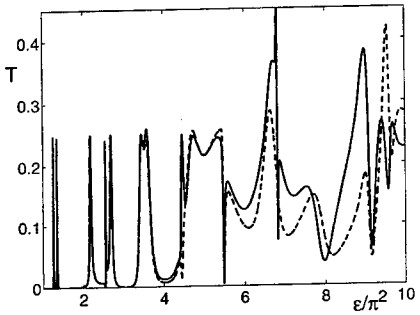

Fig. 2. Energy dependence of the transmission coefficients $\mathcal{T}_{12}$ (full line) and $\mathcal{T}_{14}$ (dashed line). Filter is supposed to be transparent for spin-up electrons and the width of point contacts is $0.5w$.

The considered device geometry is sketched in Fig. 1. The potential $V(x,y)$ entering Eq.(1) represents hard-wall conditions at the device boundary, i.e. it is zero inside and infinite outside the device area. We assume that spin-orbit interaction has much weaker effect in current and voltage probes than within dot. It allows us to neglect spin-orbit coupling outside the dot region. The ideal leads placed between probes and point contacts allow simplify scattering boundary conditions. In these asymptotic regions electron wavefunctions can be expressed as linear combination of eigenfunctions of the straight infinite lead at given energy E. For each subband n they have form of a plane wave, e.g. for ideal leads parallel to $\hat{x}$ direction we have

$$\psi(x,y) = \sqrt{\frac{1}{\pi w}}\, e^{\pm ik_n x} \sin\frac{\pi n y}{w}\, \chi(s) \quad ; \quad \chi(s_z) = \begin{pmatrix} 1 \\ 0 \end{pmatrix} \text{or} \begin{pmatrix} 0 \\ 1 \end{pmatrix} \tag{2}$$

where w denotes the width of leads and $k_n^2 = (\epsilon - \pi^2 n^2)/w^2$, $\epsilon = 2m^* E w^2/\hbar^2$. Each spin state $s_z = \pm\frac{1}{2}$ is forming its own quantum channel.

It is natural to suppose that reservoirs representing current and voltage probes act as black bodies, i.e. they are emitting and absorbing electrons independently on their spin orientation. To model injection of polarized electrons from the source we have placed a filter between source and dot. Filter is assumed to be fully transparent for spin-up electrons, $s_z = \frac{1}{2}$. Spin-down electrons are supposed to be reflected. For simplicity we have assumed that there is no spin-flip process associated with reflections at the filter boundary. We have also neglected any interference effects due to multiple scattering processes in the region between filter and dot assuming an inelastic equilibration processes in the filter vicinity leading to equal occupation of spin-down channels.

Scattering coefficients and Hall-like resistance

Electron transport properties of a quantum device allowing elastic scattering only are fully determined by transmission and reflection coefficients, $\mathcal{T}_{ij}$ and $\mathcal{R}_{ii}$, representing electron transition from the reservoir i to a reservoir j. To obtain these coefficients the eigenfunctions of the Hamiltonian, Eq.(1), subjected to the scattering boundary conditions discussed above, have to be solved. The value $2m^*\beta w = 1$ has been chosen for numerical calculation. It represents e.g. an InAs structure ($m^* = 0.023m_0$) of the lead width $w \approx 0.2$ μm and with the spin-orbit coupling constant $\hbar^2\beta \sim 6 \times 10^{-3}\text{eV} \cdot \text{nm}$ [4]. Numerical results have been obtained by using similar procedure as that already described by Ando [8].

Energy dependence of transmission coefficients $\mathcal{T}_{12}$ and $\mathcal{T}_{14}$ for the case of injection of spin-up electrons is shown in Fig. 2. It is clearly seen that due to the spin-orbit coupling transmission to the right differs from that to the left. Note, that for injection of spin-down electrons into the dot region (filter transparent for spin-down electrons) transmission to the right is just equal to $\mathcal{T}_{12}$ and transmission to the left equals to $\mathcal{T}_{14}$. This is due to symmetry properties of the model Hamiltonian, Eq.(1), described in detail elsewhere [2].

Current flow J applied along $\hat{x}$ direction, i.e. from the source to the drain, induces not only a voltage drop along the current path, $U_{\parallel} \equiv U_1 - U_3$, but there also appears a voltage drop in perpendicular direction, $U_{\perp} \equiv U_2 - U_4$. Their relation can be expressed with the help of scattering coefficients by solving following set of equations [9]

$$\begin{aligned} -\frac{h}{e^2}J &= (-2N + \mathcal{R}_{11})U_1 + \mathcal{T}_{21}U_2 + \mathcal{T}_{31}U_3 + \mathcal{T}_{41}U_4 \\ 0 &= \mathcal{T}_{12}U_1 + (-2N + \mathcal{R}_{22})U_2 + \mathcal{T}_{32}U_3 + \mathcal{T}_{42}U_4 \\ \frac{h}{e^2}J &= \mathcal{T}_{13}U_1 + \mathcal{T}_{23}U_2 + (-2N + \mathcal{R}_{33})U_3 + \mathcal{T}_{43}U_4 \\ 0 &= \mathcal{T}_{14}U_1 + \mathcal{T}_{24}U_2 + \mathcal{T}_{34}U_3 + (-2N + \mathcal{R}_{44})U_4 \end{aligned} \tag{3}$$

where N denotes number of subbands at given energy. Making use of symmetry properties, $\mathcal{T}_{34} \equiv \mathcal{T}_{23}$ and $\mathcal{T}_{32} \equiv \mathcal{T}_{43}$, we get

$$U_{\perp} = \frac{\mathcal{T}_{12}\mathcal{T}_{23} - \mathcal{T}_{14}\mathcal{T}_{43}}{(2N - \mathcal{R}_{22})(2N - \mathcal{R}_{44}) - \mathcal{T}_{24}\mathcal{T}_{42}} U_{\parallel} \ . \tag{4}$$

The structure of this formula is similar to that for Hall resistance [9]. The nominator is proportional to the difference between currents flowing along upper and lower parts of the device. Without spin-orbit coupling no perpendicular voltage drop appears.

Results of the numerical calculation are presented in Fig. 3 and Fig. 4. Conductance maxima appear at energies of quasi-bound states formed within dot region. Pronounced maxima of the Hall-like resistance $R_{\perp} \equiv U_{\perp}/J$ are located at their vicinity where conductance is strongly suppressed. In these cases resistance $R_{\perp}$ reaches values of the order of h/e^2. Detail structure of its energy dependence originates in a non-trivial mixing of bound and transport states in the presence of the spin-orbit coupling. Narrowing point contacts the Hall-like effect becomes stronger. The only effect of the injection of spin-down polarized electrons is that the Hall-like resistance $R_{\perp}$ changes its sign.

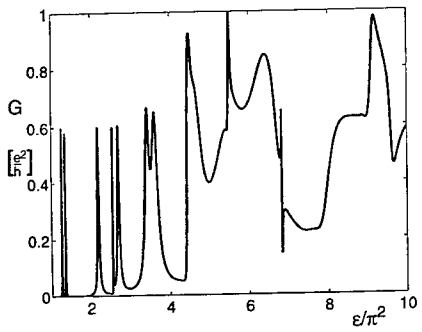

Fig. 3. Conductance $G \equiv J/U_{\|}$ as function of the energy ε for the width of point contacts $0.5w$.

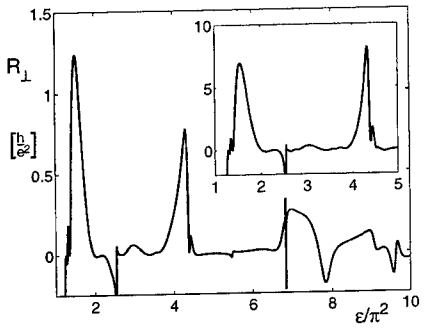

Fig. 4. Hall-like resistance $R_{\perp}$ as function of the energy ε for two values of the point contact width: $0.5w$ and $0.4w$ (inset).

Conclusion

The obtained values of the Hall-like resistance induced by spin-orbit coupling are much higher than those already reported for the simple cross-junction [2]. Chosen device geometry supports formation of bound states with large orbital momentum responsible for strong resonances. To model real quantum dots electron-electron interactions have to be taken into account. Although resulting resonance structure will be different, it can be expected that peak values will be of the same order. Considered four-terminal device seems to be appropriate candidate for experimental verification of the Hall-like resistance which might be a useful tool to study spin-orbit coupling in quantum dots.

Acknowledgement

This work has been supported by the Grant Agency of the Czech Republic under Grant 202/98/0085, INTAS-RFBR Grant 95-IN-RU-657 and by the Theoretical Physics Foundation in Slemeno.

References

1. A.S. Davydov, Quantum Mechanics, Pergamon Press, Oxford, 1965.
2. E.N. Bugakov, K.N. Pichugin, A.F. Sadreev, P. Středa, P. Šeba, will appear in Phys. Rev. Lett.
3. A.G. Aronov, Y.B. Lyanda-Geller, Phys. Rev. Lett. 70 (1993) 343.
4. Y.B. Lyanda-Geller, Phys. Rev. Lett. 71 (1993) 657.
5. E.I. Rashba and E.Ya. Sherman, Phys. Lett. A 129 (1988) 175.
6. B. Das, D.C. Miller, S. Datta, R. Reifenberger, W.P. Hong, P.K. Bhattacharya, J. Singh. M. Jaffe, Phys. Rev. B 39 (1989) 1411.
7. J. Nitta, T. Akazaki, H. Takayanagi, Phys. Rev. Lett. 78 (1997) 1335.
8. T. Ando, Phys. Rev. B 44 (1991) 8017.
9. M. Büttiker, Phys. Rev. Lett. 57 (1986) 317.

ZERO-FIELD PEAKS IN THE MAGNETO-RESISTANCE OF OPEN QUANTUM DOTS: A MEASURE OF THE ENERGY AVERAGED SPECTRUM*

R. Akis, J. P. Bird, and D. K. Ferry
Center for Solid State Electronics Research & Department of Electrical Engineering, Arizona State University, Tempe AZ 85287-5706, USA

The magneto-resistance of open quantum dots may exhibit a pronounced peak at zero magnetic field that is attributed to the ballistic analog of weak localization. The lineshape of this peak is predicted to show a Lorentzian behavior when the motion of electrons in the dot is chaotic [1]. Recent studies of electron interference in open dots suggest, however, that the wavefunctions are strongly *scarred* by the remnants of a small number of semi-classical orbits [2,3]. The scarring implies a non-uniform sampling of the dot geometry and thus indicates that *electron motion in open dots is intrinsically non-chaotic in nature.* The zero-field peak is found to constitute a unique signature of the energy spectrum of the open dot [4]. At temperatures where experiments are performed, this spectrum is broadened by thermal smearing and electron dephasing, and by the introduction of coupling between the dot and its external environment. Transport measurements provide a probe of this broadening; in particular, the lineshape of the zero-field peak is determined by the specific energy range over which the broadening is performed [4,5]. Here, we present experimental evidence in support of the above interpretation. We measure the low temperature magneto-resistance of a number of different split-gate quantum dots and compare the form of the magneto-resistance with the results of realistic numerical simulations that account for both dephasing and the non-zero temperature of experiment. The figure below shows a comparison of experiment (left) and theory (right). In the former case, magneto-resistance curves for a number of different gate voltages are shown, while in the latter the variation of the magneto-resistance with Fermi energy is plotted. The basic trends apparent in the experimental figure are reproduced by theory, which also shows the non-monotonic variation of peak height characteristic of most experiments. The details of the zero field peak are related to the existence of highly degenerate crossing points in the density of states, which occur both at zero and non-zero magnetic field. Lorentzian and/or linear lineshapes are obtained for the zero-field peak, depending upon whether or not such crossings are included in the energy window over which broadening is effective (e.g. depending upon the Fermi energy at which the average is performed). We conclude that the zero-field peaks may *not* be used as a *reliable* indicator of chaos in quantum dots.

* Supported in part by ONR and DARPA.

[1] H. U. Baranger *et al.*, Phys. Rev. Lett. **70**, 3876 (1993).
[2] J. P. Bird *et al.*, Chaos Solitons and Fractals **8**, 1299 (1997).
[3] R. Akis *et al.*, Phys. Rev. Lett. **79**, 123 (1997).
[4] R. Akis *et al.*, J. Phys. Condens. Matter, *in press.*
[5] J. P. Bird *et al.*, Phys. Rev. B **52**, R14336 (1995).

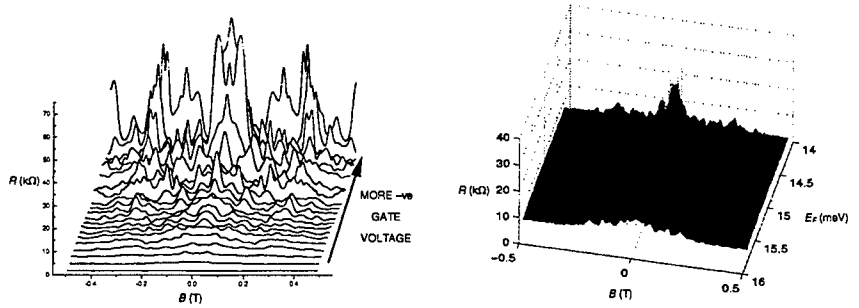

PA.24

The Role of Intersubband Mixing in Single-Electron Charging of Open Quantum Dot

D. G. Baksheyev,[1] O. A. Tkachenko,[1,2] V. A. Tkachenko[1]
[1]Institute of Semiconductor Physics, Novosibirsk, 630090 Russia
[2]Novosibirsk State University, Novosibirsk, 630090 Russia

We compare the electrostatics and electron transmission through the quantum dots that have the inlet/outlet constrictions made by (i) split finger gates and (ii) overlaying finger gates. It has been found numerically that the intermode mixing is large in the former case while almost absent in the latter. We believe this difference is responsible for single-electron charging of the open quantum dot of new type (ii) observed in [1]. Our calculations show that the measured periods of conductance oscillations agree well with the change of the total charge of the dot by one elemental charge as the gate voltages change. Conventionally single-electron charging does not show up in the transport through open quantum dots due to high transition probability from localized states to fully open channels.

Recently Liang *et al.* [1] reported striking survival of Coulomb oscillations of the conductance G of quantum dot in zero magnetic field in the region $G > 2e^2/h$. The effect was observed on the quantum dot fabricated on basis of high mobility 2DEG in a novel way: the metal split gate formed a channel, and three ultrathin (60 nm) continuous overlaying finger gates (fingers) were placed across the channel (Fig. 1), isolated from the split gate by a PMMA layer. With some depletion voltage V_F at the outermost fingers, quasiperiodic oscillations of conductance $G(V_{SG})$ in wide range $0 < G < 6e^2/h$ were observed, superimposed on quantized conductance steps. The authors of Ref. [1] clearly demonstrated continuous transition of these oscillations with increasing V_F from region $G > 2e^2/h$ to $G < e^2/h$ with conservation of the period. Since the orthodox theory of Coulomb blockade [2] works well in the region $G < e^2/h$ and gives conductance oscillations, the conclusion is made in Ref. [1] that the single-electron charging was observed in the presence of up to three fully transmitted 1D-subbands. However in contrast to orthodox theory [2] and to experimental works [3–5] no peak narrowing with increase of resistance were observed in [1]. The oscillations remained smoothed and disappeared quickly when the background conductance was suppressed. Besides, the peak spacing fluctuated by several tens percent. Thus no pronounced narrow equidistant Coulomb peaks were observed.

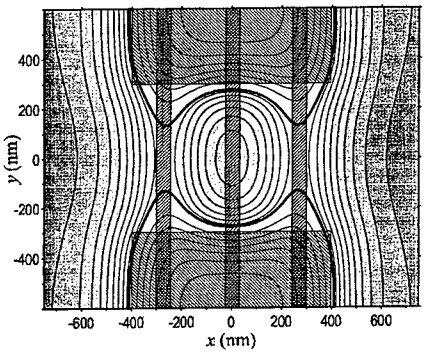

Fig. 1. Calculated potential for the open quantum dot from Ref. [1], $V_{F1,3} = -1.4$ V, $V_{F2} = 0$, $V_{SG} = -0.5$ V. Split gates and overlaying finger gates are shown by hatched rectangles.

The present work is aimed on modeling electrostatic potential of the structure from Ref. [1] and multiple-mode electron transmission through quantum dots. Calculation of the capacitance of the dot with

respect to contacts, fingers, and split gates is necessary to check the correspondence between the observed oscillation period and the change of the dot charge by one electron, and to obtain a correct estimate of the charging energy. The analysis of the transverse subband contributions into total transmission for the calculated potential, both for split and continuous fingers, will help to understand why in the latter case the charging of the quantum dot takes place in the presence of fully transmitted 1D-subbands.

The electrostatic potential profile in the device [1, 6] was determined by solution of 3D Poisson equation with local 2DEG density given by 2D Thomas-Fermi approximation and boundary condition of frozen charge at the surface states and impurities. We have found that the number of electrons in the dot changes from 80 to 140 as $V_{SG} = -0.7$ to -0.5 V, in concord with estimates of Ref. [1]. Calculated capacitances of the dot to the gates are also close to the experimentally estimated and lay within measured period fluctuations ($\Delta V_{SG} = 2.8 \div 4.5$ mV for experimental 3.6 ± 1 mV, and $\Delta V_F = 13.2 \div 22$ mV for $\Delta V_{F1} = 23.8$ mV and $\Delta V_{F3} = 25.9$ mV). The capacitances obtained demonstrate the same systematic drift with V_{SG} and V_F as observed. Thus, the conclusion that each oscillation of the conductance reflects the change of the dot charge by one electron is confirmed. However, the calculated capacitance of the dot with respect to 2DEG reservoirs is $340 \div 370$ aF for almost closed quantum dot and is doubled when three 1D-subbands are transmitted. Thus, this capacitance is almost an order higher than that to the gates and it cannot be neglected, so the charging energy is $e^2/2C = 0.1 \div 0.2$ meV.

Some modeling details. The Fermi level in 2DEG is $E_{Fl} = 5$ meV (carrier density $n = 1.6 \cdot 10^{-11}$ cm^{-2}). At $V_F = 0$ the channel pinches off when $V_{SG} = -1.8$ V (the same as in the experiment). When $V_{SG} = -0.7$ V the finger gates raise the potential barriers in the constrictions above the Fermi level at $V_F = -1.4$ V (experimental pinch-off voltages are $V_{F1} = -1.9$ V and $V_{F3} = -1.7$ V). We calculated potential profile, total charge of the dot, and the capacitances in range $V_{SG} = -0.7 \div -0.5$ V and $V_F = -1.2 \div -1.4$ V, which is considered to correspond to the experiment. The quantum dot width across the channel changed from 350 to 560 nm, and the depth at the center from 2.5 to 3.1 meV (counting from E_F). Practically, the width and depth of the quantum dot were found to depend on V_{SG} only. It worth interest that the presence of zero-biased central finger makes the dot 0.5 meV deeper and stabilizes the depth at ~ 3 meV. Along the channel axis the top of the barrier in the constriction is 0.5 meV below E_F and higher, as controlled by V_F. At high finger gate voltages $V_F = -1.3 \div -1.4$ V the transverse potential profile of the constriction resembles rectangular well with the width at Fermi level ranging from 100 to 280 nm (Fig. 1, Fermi level marked by thick line).

In numerical modeling of multiple-mode electron transmission through the quantum dot we used 2D-potential obtained from the calculations of electrostatics for the case when (i) the outermost 160 nm wide finger gates were broken with a 260 nm gap and (ii) 60 nm wide fingers were continuous (i.e. overlaying, as in [1]).

By solution of 2D Schrödinger equation it was found that when $2 \div 3$ transverse modes in the constrictions become open the transmission through type (ii) quantum dot via each of the first three 1D-subbands is independent, i.e. no mode mixing occurs. The transmission coefficient dependence $T(E_F)$ for different subbands is the same as for transmission through 1D system with two smooth barriers (Fig. 2a, notice that only Fabry–Pérot resonances present). Contrarily, in case (i) the intermode mixing is very intensive and shows up in $T(E_F)$ dependence as sharp Fano resonances due to electron scattering on the levels of the dot (Fig. 2d).

The difference is due to transverse crossection of the potential in the constrictions. For type

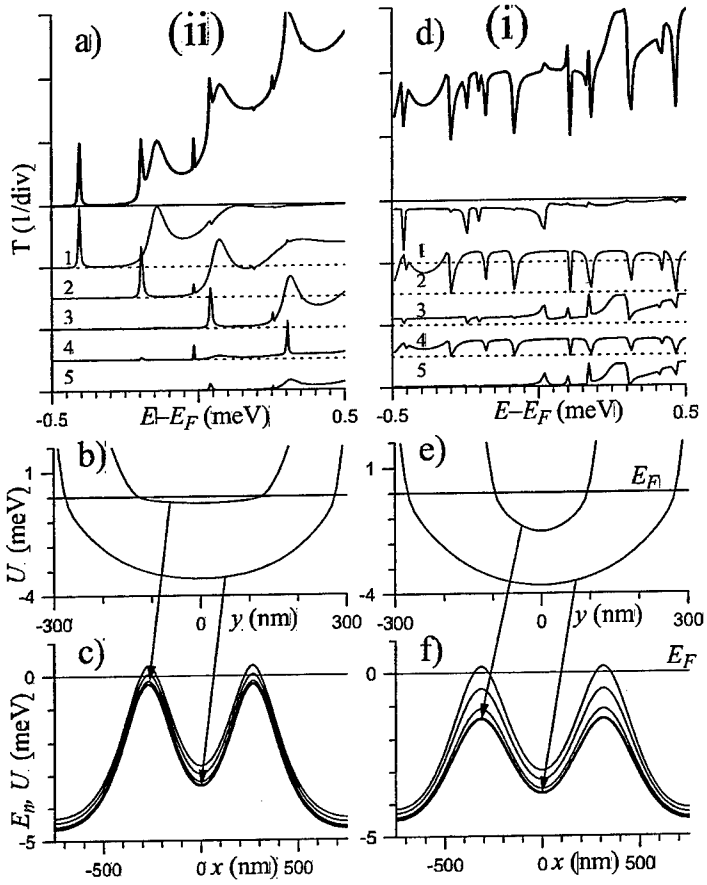

Fig. 2. Characteristics of open quantum dots of types (ii)—overlaying finger gates and (i)—split finger gates. (a,d)—total transmission coefficient and contributions of 1–5 1D-subbands. (b,e)—transverse crossections of the channel in the central parts of the dots and in the constrictions. (c,f)—potential profiles along the channels and energies $E_n(x)$ of $n = 1$–3 1D-subbands. The gate voltages are (ii)—the same as in Fig. 1, and (i)—$V_P = -1.6$ V, $V_{1G} = -0.5$ V.

(ii) quantum dot [1] it is not parabolic, rather flat and wide (Fig. 2b), and 1D-subband spacing is significantly less than in the case when the constrictions (i) are created by split fingers, when the parabola is always narrow and deep (Fig. 2e). As a consequence, in case (ii) the lowest transverse subbands run practically in parallel to each other in both dot and constrictions (Fig. 2c), while in usual quantum dots in the constrictions the distance between 1D-subbands in the constrictions is 2–3 times larger than that inside the dot (Fig. 2f), even when the dot is open. So the transmission through dot (ii) may be considered one-dimensional in contrast with substantially two-dimensional transport in dot (ii). Notice that the tunneling via closed subbands in dots (ii) is much larger than in dots (i) due to small subband spacing, though transverse subbands do not mix.

We argue that in the absence of intersubband mixing the transport in the low-transparency subbands is due to sequential tunneling with single-electron charging of the dot, resulting in the Coulomb oscillations observed in Ref. [1]. The open subbands transmit the electrons coherently and provide for parallel background current and quantization steps in the conductance. With each new step the single-electron charging in the opening subband ceases while it still takes place in a higher low-transparency subband, since the intersubband transition probability in the considered dot at low temperature is very small. With increasing temperature this probability grows and Coulomb oscillations disapper first in higher subbands, as seen in Ref. [1], Fig. 2. For the lowest subband the oscillations survive up to 0.5 K that corresponds to the condition of observation of Coulomb oscillations $kT \ll e^2/2C = 0.2$ meV.

Usual quantum dot of type (i) in the open state do not allow observing the effects of single-electron charging even at low temperatures because of strong intersubband mixing, but they demonstrate strong interference Fano resonances [4, 5].

In summary, we have numerically confirmed that the conductance oscillations observed in Ref. [1] are caused by single-electron change of the dot's charge. The conclusion is made that the effects of single-electron charging can be observed in the open dots provided that no intersubband mixing takes place.

We are grateful to Chi-Te Liang for the data, and Kvon Ze Don, M. V. Éntin, and A. G. Pogosov for discussions. The work is supported by programs of Ministry of Science of Russian Federation "Physics of Solid-State Nanostructures" (grant No. 98-1102) and "Prospective Technologies and Devices for Micro- and Nanoelectronics" (No. 02.04.5.1), and by program "Universities of Russia—Fundamental Research" (No. 1994).

1. C.-T. Liang, M. Y. Simmons, C. G. Smith, G. H. Kim, D. A. Ritchie, M. Pepper, Phys. Rev. Lett. **81**, 3507 (1998).
2. K. K. Likharev, IBM J. Res. Develop. **32**, 144 (1988).
3. E. B. Foxman, P. L. McEuen, U. Meirav, N. S. Wingreen, Y. Meir, P. A. Belk, N. R. Belk, M. A. Kastner, Phys. Rev. B **47**, 10020 (1993).
4. T. Heinzel, S. Manus, D. A. Wharam, J. P. Kotthaus, G. Böhm, W. Klein, G. Tränkle, G. Weimann, Europhys. Lett. **26**, 689 (1994).
5. M. Persson, J. Pettersson, B. von Sydow, P. E. Lindelof, A. Kristensen, K. F. Berggren, Phys. Rev. B **52**, 8921 (1995).
6. C.-T. Liang, private communication, 1999.

PA.25

Evidence for charging effects in an open dot at zero magnetic field

C.-T. Liang, M. Y. Simmons, C. G. Smith, G. H. Kim,* D. A. Ritchie and M. Pepper
Cavendish Laboratory, Madingley Road, Cambridge CB3 0HE, United Kingdom

Abstract

We have measured the low-temperature transport properties of an open quantum dot formed in a clean one-dimensional channel. At zero magnetic field, continuous and periodic oscillations superimposed upon ballistic conductance steps are observed when the conductance through the dot G exceeds $2e^2/h$. We ascribe the observed conductance oscillations to evidence for charging effects in an open dot. This is supported by the evolution of the oscillating features for $G > 2e^2/h$ as a function of both temperature and barrier transparency.

Electrostatically-shaped semiconductor quantum dots with discrete zero-dimensional (0D) electronic states [1], have been attracting much theoretical and experimental interest. In particular, the Coulomb blockade of single electron tunnelling through quantum dots [2] has been extensively investigated. It has been shown that transport through a small quantum dot is determined by charging effects as well as quantum confinement effects [3].

At present it is widely accepted that at zero magnetic field, the conductance $2e^2/h$ is the upper limit for which Coulomb charging effects can occur in a quantum dot [4,5], though existing results had questioned this concept [6–9]. In this paper, we report low-temperature conductance measurements of an open quantum dot device in which impurity scattering is negligible. Due to the unique design of our devices fabricated on an ultra high-quality HEMT, we find clear evidence of Coulomb charging effects in an open quantum dot at zero magnetic field. This is supported by the temperature and barrier transparency dependence of the observed periodic conductance oscillations when the conductance through the dot G is greater than $2e^2/h$.

The two-layered Schottky gate pattern shown in the inset to Fig. 1 (a) was defined by electron beam lithography, 157 nm above a two dimensional electron gas (2DEG). There is a 30 nm-thick layer of Polymethylmethacrylate (PMMA) which has been cross-linked with a high dose from an electron beam, to act as a dielectric [10,11] between the split-gate (SG) and three gate fingers (F1, F2, and F3) so that all gates can be independently controlled. The carrier concentration of the 2DEG was 1.6×10^{15} m^{-2} with a mobility of 250 m^2/Vs after brief illumination by a red LED. The corresponding transport mean free path is 16.5 μm, much longer than the effective 1D channel length. In all cases, a zero-split-gate-voltage series resistance ($\approx$ 900 Ω) due to the bluk 2DEG is subtracted.

Trace 1 in Fig. 1 (a) shows the conductance measurements $G(V_{SG})$ as a function of split-gate voltage V_{SG} when all finger gate voltages V_{F1}, V_{F2}, and V_{F3} are zero. We observe conductance plateaux at multiples of $2e^2/h$, as expected for a clean 1D channel, with no resonant features superimposed on top. When the channel is defined at $V_{SG} = -1.132$ V, five quantised conductance steps are observed when each one of the finger gates is swept while the others are earthed to the 2DEG as shown in traces 2-4 (Fig. 1 (a)). These experimental results demonstrate that we have a clean 1D channel in which impurity scattering is negligible.

We can define a lateral quantum dot by applying voltages on SG, F1, and F3 while keeping F2 grounded to the 2DEG. Trace 1 in Fig. 1 (b) shows the gate characteristics $G(V_{SG})$ for $V_{F1} = -1.941$ V and $V_{F3} = -1.776$ V at $T = 50$ mK. Striking periodic and continuous con-

ductance oscillations superimposed on ballistic conductance steps are observed. We ascribe the observed conductance oscillations for $G < 2e^2/h$ to Coulomb charging effects [4]. The observed periodic conductance oscillations for $G > 2e^2/h$ are the main subject of this paper. Unlike conventional lateral quantum dots whose tunnel barriers are defined by two pairs of split-gates, in our system, the tunnel barriers arise from depletion from overlying finger gates. This causes a large barrier thickness so that we do not observe well-isolated single-electron tunnelling peaks beyond pinch-off in our case. In contrast to the well-quantised conductance plateaux shown in trace 1 in Fig. 1 (a), applying voltages to F1 and F3 results in conductance steps that are not as flat or well quantized. With the finger gates grounded to the 2DEG, the channel pinches off at $V_{SG} = -1.8$ V compared with $V_{SG} = -0.7$ V when $V_{F1} = -1.941$ V and $V_{F3} = -1.776$ V. Thus as voltages are applied to F1 and F3, the lateral confinement weakens and the conductance steps become less pronounced. The conductance steps also deviate from their quantized values. The most likely reason for this effect is the introduction of two tunnel barriers which enhances back-scattering in the channel, thereby reducing the transmission probability of 1D channels [12] to be less than 1.

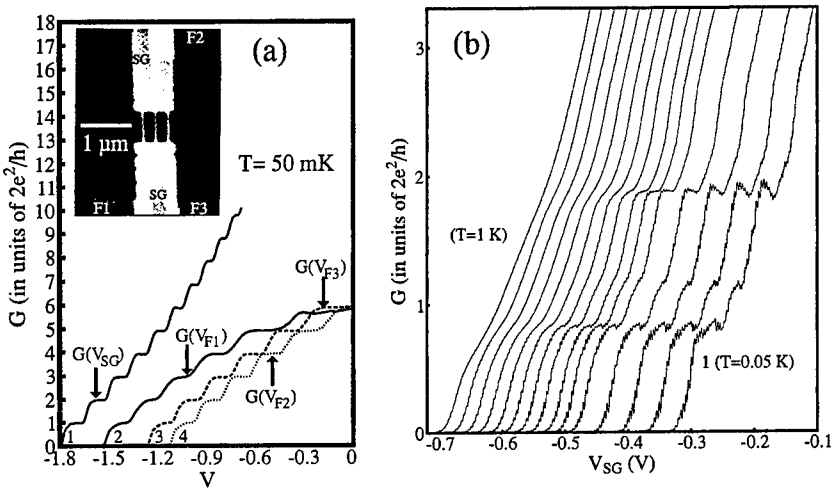

FIG. 1. (a) Trace 1: $G(V_{SG})$ for all finger gates at 0 V. Trace 2 to 4: $G(V_{F1})$ (in solid line), $G(V_{F3})$ (in dashed line) and $G(V_{F2})$ (in dotted line) for $V_{SG} = -1.132$ V. The inset shows an scanning electron micrograph of a typical device. The brightest regions correspond to finger gates with joining pads, labelled as F1, F2, and F3 lying above the split-gate (labelled as SG), with an insulating layer of crosslinked PMMA in between. (b) $G(V_{SG})$ for $V_{F1} = -1.941$ V, $V_{F2} = 0$ V, and $V_{F3} = -1.776$ V at various temperatures T. From left to right: T =1, 0.5, 0.45, 0.41, 0.35, 0.3, 0.26, 0.2, 0.18, 0.17, 0.15, 0.11, 0.09, 0.065 and 0.05 K. Curves are successively displaced by a horizontal offset of 0.02 V for clarity.

Having defined a quantum dot, we now calculate the dot size and the number of electrons it contains following the method described in Ref. 13. From this we estimate the dot area to

be 2.81×10^{-13} m^2 and the number of electrons in the dot to be ≈ 126. In our system, the estimated 0D quantum confinement energy is at most 12.4 μeV, comparable to the thermal smearing at 50 mK. Therefore electron transport through our quantum dot can be described in terms of a classical Coulomb charging picture where the 0D quantum confinement energy is much smaller than the Coulomb charging energy, similar to the case of a metal.

As shown in Fig 1 (b), for $G < 2e^2/h$, the conductance oscillations persist up to $T = 1$ K. The oscillations for $G > 2e^2/h$ have a strong temperature dependence and become unresolvable above $T = 410$ mK. Note that the thermal broadening k_BT at this temperature is still much larger than the estimated 0D quantum confinement energy, excluding an interpretation that conductance oscillations for $G > 2e^2/h$ are due to tunnelling through 0D states in the quantum dot. To determine the total capacitance between the dot and the gates of the sample, we measured the conductance oscillations by varying the voltage on the different gates, while keeping the voltages on the remaining gates fixed. From this the total gate-dot capacitance C_g is estimated to be 7.58×10^{-17} F. Neglecting the capacitance between the dot and the 2DEG reservoirs, we calculate the Coulomb charging energy e^2/C_g to be 0.21 meV, comparable to the thermal broadening at $T \approx 2$ K.

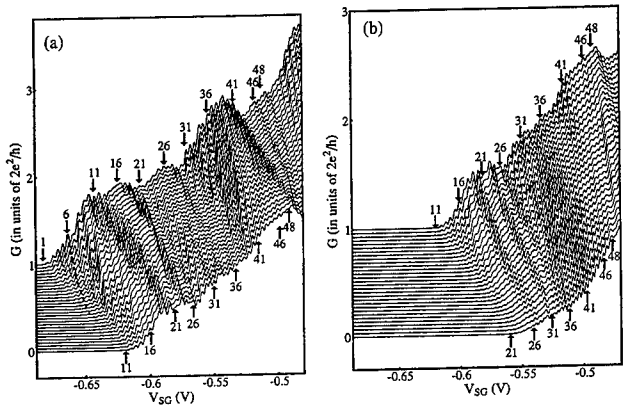

FIG. 2. (a) $G(V_{SG})$ at various voltages applied on F1 and F3 at zero magnetic field. From top to bottom: $V_{F1} = -1.907$ V to -1.965 V in 2 mV steps ($V_{F3} = -1.733$ V to -1.805 V in 2.5 mV steps) (b) Continuation of figure 2 (a). From top to bottom: $V_{F1} = -1.965$ V to -2.023 V in 2 mV steps ($V_{F3} = -1.805$ V to -1.8775 V in 2.5 mV steps) Curves are successively offset by $(0.0344)(2e^2/h)$ for clarity. Conductance tunnelling peaks are numbered to serve a guide to the eye for the evolution of oscillating structures in $G(V_{SG})$. The dashed line in Fig. 2 (a) serves as a guide to the eye for the evolution of peak 6.

To study the presence of periodic conductance oscillations for $G > 2e^2/h$ in more detail, we have measured their dependence on barrier transparency. Figure 2 (a) shows $G(V_{SG})$ as V_{F1} and V_{F3} are simultaneously decreased, thus increasing barrier height (decreasing barrier transparency) at zero magnetic field. Figure 2 (b) is a continuation of Fig. 2 (a) at

even more negative finger-gate voltages. We number peaks in $G(V_{SG})$ counted from pinch-off. Note that at pinch-off, we estimate that there are still ≈ 70 electrons within the dot. Consider the sixth single-electron tunnelling peak counted from pinch-off. It is evident that as the barrier heights are raised by making the gate finger voltages more negative, the peak height decreases, and the peak occurs at a more positive V_{SG}, i.e., where the channel is wider, as indicated by the dashed line. We note that the first ten tunnelling peaks counted from pinch-off in Fig. 2 (a) gradually disappear as the finger-gate voltages are made more negative. This is due to the increasing barrier thickness such that tunnelling conductance becomes immeasurably small [13]. Over the whole measurement range, we can follow 48 conductance tunnelling peaks at various $V_{F1}(V_{F3})$ and are thus able to study their barrier transparency dependence. Note that the observed conductance oscillations for $G > 2e^2/h$ have the *same* period as that of the oscillating features for $G < 2e^2/h$. Most importantly, as shown in Fig. 2 (a) and (b) peaks 31-48, where $G > 2e^2/h$ (shown in the uppermost curve), all gradually evolve into conductance oscillations for $G < 2e^2/h$ due to Coulomb charging [4] as the barrier heights and thickness increase. This result strongly suggests that the conductance oscillations (for peaks 31-48 in the uppermost curve shown in Fig. 2 (a)) and the oscillations shown in the lowermost curves (Fig 2 (b)) are of the *same* physical origin – Coulomb charging. This is compelling experimental evidence for charging effects in the presence of a transmitted 1D subband at *zero* magnetic field.

In conclusion, we have presented low-temperature experimental results on an open quantum dot. Periodic and continuous oscillations superimposed upon ballistic conductance steps are observed even when the conductance through the quantum dot is greater than $2e^2/h$. At zero magnetic field, a direct transition of conductance oscillations for $G > 2e^2/h$ to those for $G < 2e^2/h$ due to Coulomb charging effects is observed with decreasing barrier transparencies. The temperature dependence of the observed oscillating features for $G > 2e^2/h$ excludes the interpretation that they are due to tunnelling through single-particle states within the dot. Both results suggest that charging effects can occur in the presence of a transmitted one-dimensional channel at zero magnetic field.

This work was funded by the UK EPSRC, and in part, by the US Army Research Office.

References

1. C.G. Smith *et al.*, J. Phys. C **21**, L893 (1988).
2. U. Meirav, M.A. Kastner, and S.J. Wind, Phys. Rev. Lett. **65**, 771 (1990).
3. P.L. McEuen *et al.*, Phys. Rev. Lett. **66**, 1926 (1991).
4. L.P. Kouwenhoven *et al.*, Z. Phys. B **85**, 367 (1991).
5. L.W. Molenkamp, K. Flensberg and M. Kemerink, Phys. Rev. Lett. 75, 4282 (1995).
6. C. Pasquier *et al.*, Phys. Rev. Lett. **70**, 69 (1993).
7. I.L. Aleiner and L.I. Glazman, Phys. Rev. B **57**, 9608 (1998).
8. C.-T. Liang, Ph.D. thesis, Cambridge University (1995).
9. C.-T. Liang *et al.*, Phys. Rev. B **55**, 6723 (1997).
10. I. Zailer *et al.*, Semicond. Sci. Technol. **11**, 1235 (1996).
11. C.-T. Liang *et al.*, Phys. Rev. Lett. **81**, 3507 (1998).
12. M. Büttiker, Phys. Rev. B **41**, 7906 (1990).
13. M. Field *et al.*, Phys. Rev. Lett. **70**, 1311 (1993).

*Present address: Telecommunication Basic Research Laboratory, Electronics and Telecommunications Research Institute, Yusong P. O. Box 106, Taejon 305-600, Korea

PA.27

DETECTION OF COULOMB CHARGING AROUND AN ANTIDOT

M. Kataoka,[1] C. J. B. Ford,[1] G. Faini,[2] D. Mailly,[2] M. Y. Simmons,[1] D. R. Mace,[1] C.-T. Liang,[1] and D. A. Ritchie[1]

[1] *Cavendish Laboratory, Madingley Road, Cambridge CB3 0HE, United Kingdom*

[2] *Laboratoire de Microstructures et de Microelectronique - CNRS, 196, Avenue Henri Ravera, 92220 Bagneux, France*

We have detected oscillations of the charge around a potential hill (antidot) in a two-dimensional electron gas as a function of a perpendicular magnetic field B. The field confines electrons around the antidot in closed orbits, the areas of which are quantised through the Aharonov-Bohm effect. Increasing B reduces each state's area, pushing electrons closer to the centre, until enough charge builds up for an electron to tunnel out. This is a new form of the Coulomb blockade seen in electrostatically confined dots. We have also studied $h/2e$ oscillations and found evidence for coupling of opposite spin states of the lowest Landau level.

Coulomb blockade (CB) in an open system sounds paradoxical. CB arises from the discrete charge of an electron. For charging to happen, it has been generally believed that electrons must be electrostatically confined in a small cavity. Although it has recently been reported that "open" dots can also show charging effects [1–3], they are not completely open systems, still having some degree of electrostatic confinement.

In contrast, an antidot, which is a potential hill in a two-dimensional electron gas (2DEG), is in a completely open system. Thus it has often been assumed that CB does not occur when an electron tunnels through a state bound around an antidot by a large perpendicular magnetic field B (> 0.2 T). Here, electron waves travel phase-coherently around the antidot with quantised orbits, each enclosing an integer number of magnetic flux quanta h/e through the Aharonov-Bohm (AB) effect. Where the potential is sloping, these single-particle (SP) states have distinct energies. Conductance oscillations observed as a function of B or gate voltage have been attributed to resonant tunnelling through such discrete states from one edge of the sample to the other. This causes resonant backscattering or transmission depending on the tunnelling direction [4]. Up until now, no charging effect has been taken into account in the system [5,6]. However, Ford *et al.* [7] proposed that antidot charging should be present to explain double-frequency AB oscillations, where two sets of resonances through the two spin states of the lowest Landau level (LL) were found to lock exactly in antiphase, giving $h/2e$ periodicity, and to have the same amplitudes in spite of different tunnelling probabilities [7,8]. There is as yet no full explanation for these phenomena.

The aim of this paper is to demonstrate that magnetic confinement causes charging in antidot systems, although there is no electrostatic confinement. We have conducted non-invasive detector experiments [9] and obtained clear evidence of charge oscillations around an antidot as a function of B [10]. We have also investigated $h/2e$ AB conductance oscillations. The data show that the resonance only occurs through states of one spin, explaining the matched amplitudes.

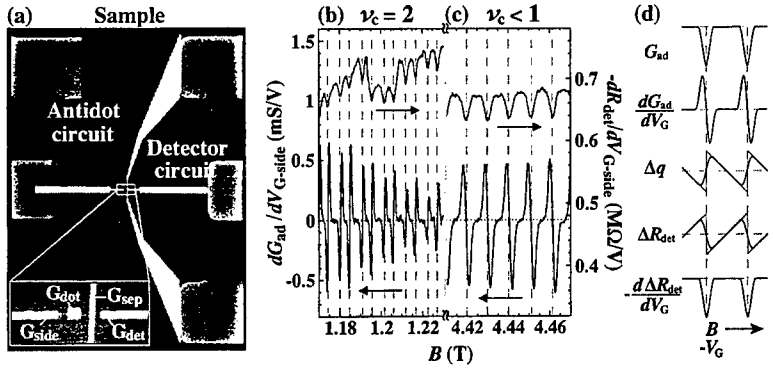

FIG. 1. (a) SEM micrograph of a device prior to second metallisation. (b) and (c) dG_{ad}/dV_{G-side} of the antidot circuit and $-dR_{det}/dV_{G-side}$ of the detector circuit with the gate voltage on G_{side} modulated in two different regimes: (b) $\nu_c = 2$ and (c) $\nu_c < 1$. Vertical dashed lines show the alignment of the dips in the detector signal with zeros in the transconductance oscillations. (d) Illustration of the relation between various lineshapes. Grey lines in Δq and ΔR_{det} are the ideal case, and black curves represent broadened lineshapes.

The samples were fabricated from a GaAs/AlGaAs heterostructure containing a 2DEG of sheet carrier density 2.2×10^{15} m^{-2} with mobility 370 m^2/Vs. An SEM micrograph of a device is shown in Fig. 1(a). A square dot gate (G_{dot}), 0.3 μm on a side, was contacted by a second metal layer evaporated on top of an insulator (not shown) to allow independent control of gate voltages. The lithographic widths of the antidot and detector constrictions were 0.45 and 0.3 μm, respectively. All constrictions showed good 1D ballistic quantisation at $B = 0$. A voltage of -4.5 V on the separation gate (G_{sep}), of width 0.1 μm, divided the 2DEG into separate antidot and detector circuits. The detector gate (G_{det}) squeezed the detector constriction to a high resistance to make it very sensitive to nearby charge. To maximise the sensitivity, transresistance measurements were made by modulating the dot-gate voltage (or the voltage on the side-gate G_{side}) at 10 Hz with 0.5 mV rms and applying a 1 nA DC current through the detector constriction. Simultaneously, the transconductance of the antidot circuit was measured with a 10 μV DC source-drain bias, when necessary. The experiments were performed at temperatures down to 50 mK.

Figures 1(b) and (c) show the transresistance $-dR_{det}/dV_{G-side}$ (transconductance dG_{ad}/dV_{G-side}) vs B of the detector (antidot) circuit in two different field regions: (b) $\nu_c = 2$ and (c) $\nu_c < 1$, where ν_c is the filling factor in both antidot constrictions, which were determined from the conductance G_{ad}. The filling factors in the bulk 2DEG were $\nu_b = 7$ and 2, respectively. The oscillations in G_{ad} occur as SP states around the antidot rise up through the Fermi energy E_F. The AB effect causes the overall period ΔB to be h/eS, where S is the area enclosed by the state at E_F. The curve in (b) has pairs of spin-split peaks, whereas in (c) only one spin of the lowest LL is present. The dips in $-dR_{det}/dV_{G-side}$ correspond to

a saw-tooth oscillation in the change $\Delta R_{\rm det}$ from the background resistance (see Fig. 1(d)). Thus the net charge Δq nearby suddenly becomes more positive (making the effective gate voltage less negative) whenever the antidot comes on to resonance (since the dips line up with the zeros in $dG_{\rm ad}/dV_{\rm G-side}$). The charging signals are not dependent on the presence of conductance oscillations in the antidot circuit. It is still possible to observe the signal with no applied bias in the antidot circuit, or when the side-gate voltage is set to zero so that there is no tunnelling between that edge and the antidot. Hence we conclude that this charge oscillation is associated with states near the antidot, and interpret it as CB.

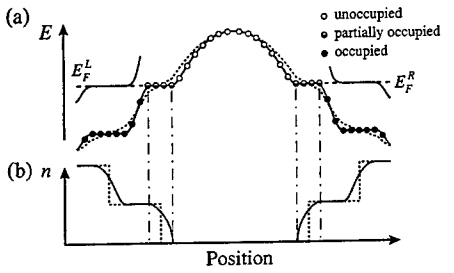

FIG. 2. Cross-section through the antidot: (a) energy of the lowest LL near the antidot and (b) carrier density distribution. The conventional and self-consistent pictures are shown as dotted and solid lines, respectively. A bulk LL, which is reflected from the constrictions, is also shown. The vertical dash-dotted lines indicate the edges of a compressible region.

Before showing how the charging occurs, it is worth reconsidering the shape of the antidot potential. The conventional picture is a potential hill smoothly increasing towards the centre as shown dotted in Fig. 2(a). However, for $B > 0$, such a potential would require abrupt changes in the carrier density where LL intersect $E_{\rm F}$, which is not electrostatically favourable. Chklovskii *et al.* [11] treated such a problem along the edge of a 2D system and introduced alternating compressible and incompressible strips. Compressible strips require flat regions in the self-consistent potential as depicted by a solid line in the figure. It has always been considered that the potential should not be completely flat in antidot systems [6], since the presence of several SP states at $E_{\rm F}$ makes AB conductance oscillations impossible in the simple non-interacting picture. However, if CB of tunnelling into the compressible region occurs, conductance oscillations with periodicity h/e can still occur for such a self-consistent potential.

We explain the charging as follows. As B increases, each SP state encircling the antidot moves inwards, reducing its area to keep the flux enclosed constant. This results in a shift of the electron distribution towards the antidot centre. One may think such a shift should not occur due to screening in the compressible region. However, since each state is discrete and is trapped around the antidot, and the incompressible regions obviously have one electron per state, the total number of electrons in the compressible regions must be an integer. Hence the compressible region also moves inwards with the states. As a result, a net charge Δq builds up in the region. When it reaches $-e/2$, one electron can leave the region and Δq becomes $+e/2$. This is when resonance occurs, as for CB in a dot. At the same time, the compressible region, by losing the innermost state and acquiring one at its outer edge, shifts back to its original position just after the previous resonance. The same argument also applies, of course, even if there is no compressible region, as the states are still discrete.

As in quantum dot systems, the SP energy spacing ΔE_{sp} and the charging energy e^2/C together determine when resonance occurs (C is the capacitance of the antidot). We have deduced these energy scales from the temperature dependence of the charging signals and the antidot conductance oscillations, and the DC-bias measurements of the differential antidot conductance. The detailed analysis is given in Ref. [10]. We found that ΔE_{sp} decreases as $1/B$, as expected. In contrast, Maasilta and Goldman [6] found an almost constant energy gap, which we interpret as the interplay of ΔE_{sp} and a charging energy which is small at low B and saturates at high B.

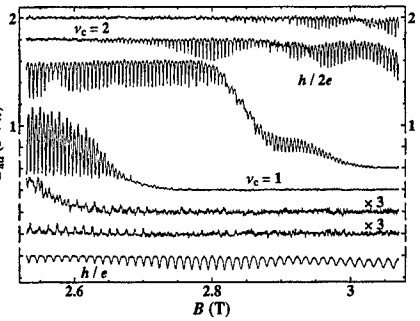

FIG. 3. AB conductance oscillations: the two constrictions were squeezed symmetrically between traces, which are offset by $0.2e^2/h$ down the page for clarity. Around $B = 2.6$ T the pure $h/2e$ oscillations are not completely established.

The presence of charging should help to explain the $h/2e$ AB oscillations. Fig. 3 shows AB conductance oscillations as both constrictions are narrowed keeping the symmetry. On the $\nu_c = 1$ plateau the outer spin state is excluded from the constrictions. Peaks up from this plateau for $B < 2.7$ T are due to inter-LL resonant transmission [4]. This is only noticeable when resonant backscattering is absent, i.e., on the plateau. The flat plateau implies that there is no tunnelling into the inner spin state. Hence, at higher ν_c *at the same field*, where the constrictions are wider, there can also be no such tunnelling, despite the presence of $h/2e$ oscillations.

In conclusion, we have used a non-invasive charge detector to show that tunnelling into antidot states is Coulomb blockaded. When states of both spins are occupied, $h/2e$ oscillations are seen but tunnelling is only via states of one spin, showing that there is a strong coupling with states of the other spin.

This work was funded by the UK EPSRC. We thank C. H. W. Barnes and C. G. Smith for useful discussions. M. K. acknowledges financial support from Cambridge Overseas Trust.

References

[1] C. Pasquier *et al.*, Phys. Rev. Lett. **70**, 69 (1993).
[2] S. M. Cronenwett *et al.*, Phys. Rev. Lett **81**, 5904 (1998).
[3] C. T. Liang *et al.*, Phys. Rev. Lett. **81**, 3507 (1998).
[4] D. R. Mace *et al.*, Phys. Rev. B **52**, R8672 (1995).
[5] V. J. Goldman and B. Su, Science **267**, 1010 (1995).
[6] I. J. Maasilta and V. J. Goldman, Phys. Rev. B **57**, R4273 (1998).
[7] C. J. B. Ford *et al.*, Phys. Rev. B **49**, 17456 (1994).
[8] A. S. Sachrajda *et al.*, Phys. Rev. B **50**, 10856 (1994).
[9] M. Field *et al.*, Phys. Rev. Lett. **70**, 1311 (1993).
[10] M. Kataoka *et al.*, Phys. Rev. Lett. (to be published in July 1999).
[11] D. B. Chklovskii *et al.*, Phys. Rev. B **46**, 4026 (1992).

PA.29

Electron Magnetotransport in a Honeycomb Lattice of Antidots

A.G.Pogosov[a], M.V.Budantsev[a], A.Pouydebasque[b,c],
D.K.Maude[b], J.C.Portal[b,c,d], A.E.Plotnikov[a], A.I.Toropov[a], A.K.Bakarov[a]

[a]*Institute of Semiconductor Physics, Siberian Branch of RAS, 630090 Novosibirsk, Russia.*
[b]*Grenoble High Magnetic Field Laboratory, MPI-FKF and CNRS,*
B.P. 166, F-38042 Grenoble Cedex 09, France
[c]*INSA, F-31077 Toulouse Cedex 4, France*
[d]*Institut Universitaire de France*

Abstract

Magnetotransport properties of a honeycomb lattice of antidots were experimentally investigated. The features of magnetoresistance and magnetoconductivity tensor were attributed to special stable electron orbits. The presence of both delocalized and pinned orbits was illustrated by numerical calculations of the Poincaré sections of the system for the magnetic fields corresponding to the anomalies observed experimentally.

Transport properties of a two-dimensional electron gas with antidot lattices has been widely investigated [1-5]. It was established that the main features of magnetotransport, observed at liquid helium temperatures, can be described in the framework of classical chaotic dynamics of an electron in the lattice. Numerical simulations of electron motion usually applied to describe the observed anomalies of magnetoresistance averaged over all possible electron trajectories and thus failed to point out special electron orbits responsible for the observed features. In this regard the study of different types of lattices is meaningful, because electron trajectories essential for one type of the lattice may be less important or completely absent in the lattice of another type. At the present time square [1-3], rectangular [4] and hexagonal [5] periodical lattices have been studied. In this paper we investigate the magnetotransport properties of a honeycomb lattice of antidots. This lattice has the symmetry similar to the hexagonal lattice already studied in [5]. Nonetheless, in contrast to the hexagonal lattice the honeycomb lattice is more open and like a square lattice can contain delocalized electron trajectories in magnetic fields corresponding to a commensurability between the cyclotron diameter and the lattice period [3]. In the hexagonal lattice these trajectories cannot exist due to the shading. On the other hand, the trajectories skipping along arrays of antidots, which are the main delocalized trajectories for the square lattice with large period, are absent in the honeycomb lattice due to its special symmetry. The aim of the present work is to investigate the magnetotransport features of the honeycomb lattice and to attribute them to the certain regular electron trajectories.

Test samples were Hall bars fabricated from a two-dimensional electron gas formed at a GaAs/AlGaAs heterojunction with electron density $n_s = 4\times10^{11}\text{cm}^{-2}$ and initial mobility $\mu = 600\,000\ \text{cm}^2/\text{V s}$. The honeycomb lattice of antidots was introduced by means of electron beam lithography and subsequent plasma etching. The lattice constant was $d = 0.8\ \mu\text{m}$ and the Hall bar dimensions were $50\times100\ \mu\text{m}$. A schematic view of the sample is presented in Fig. 1. The components of the resistivity tensor were measured at liquid helium temperature in magnetic fields up to 2 T. Illuminating with a LED was used to increase the electron density and thus decrease the width of the depletion layer surrounding antidots which determines the actual radius a of antidots.

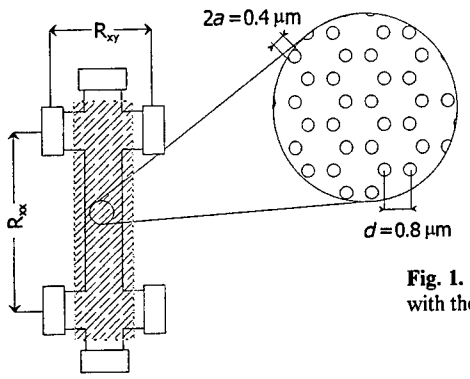

Fig. 1. A schematic view of the Hall bar with the honeycomb lattice of antidots.

Fig. 2 shows the typical magnetoresistance $\rho_{xx}(B)$ of the lattice measured after strong illumination together with diagonal σ_{xx} and nondiagonal σ_{xy} components of conductivity tensor recalculated from the measured resistivity tensors. The electron density for this case determined from the Shubnikov–de Haas oscillations (not shown) was $n_s = 4.2\times10^{11}\,\mathrm{cm}^{-2}$. The diagonal component of the resistivity tensor (ρ_{xx}) exhibits four commensurability peaks marked by the arrows in the figure. The main peak (marked by arrow 1 in Fig. 2) is at a magnetic field corresponding to the cyclotron diameter $2R_c \approx 1.1d$. The curve $\sigma_{xx}(B)$ also exhibits a peak superimposed on the background of monotonous decrease at the same value of magnetic field, as well as a second peak (2) corresponding to $2R_c \approx 1.9d$, and thus indicating the presence of delocalized electron trajectories. The peaks 1, 2 and 3 in $\rho_{xx}(B)$ are accompanied by dips in $\sigma_{xy}(B)$.

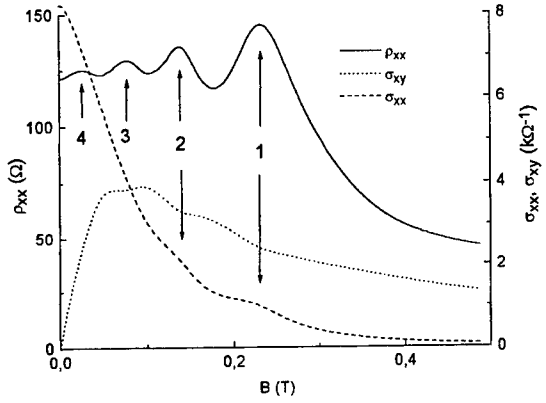

Fig. 2. The longitudinal resistivity ρ_{xx}, the longitudinal conductivity σ_{xx} and the Hall conductivity σ_{xy} of the honeycomb lattice as a function of magnetic field.

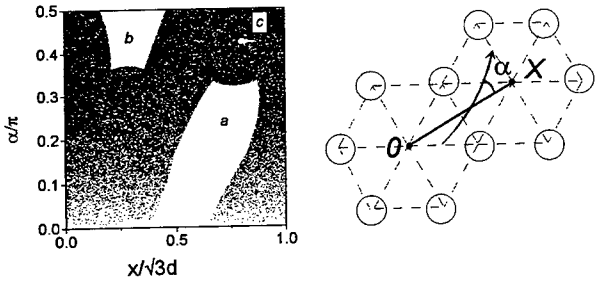

Fig. 3. Calculated Poincaré section for the honeycomb lattice in the magnetic field corresponding to the condition $2R_c \approx 1.1d$.

In order to determine possible electron trajectories responsible for the observed anomalies, the Poincaré sections of the system were calculated. For the case $2R_c \approx 1.1d$ (peak 1) the Poincaré section is presented in Fig. 3. The section was calculated for one initial condition and multiple collisions with antidots. One can see three regions that are not available for an electron with initial conditions chosen outside of them. Choosing initial conditions inside these areas enables to determine the special electron trajectories. Thus, trajectories *a*, *b* and *c* in Fig. 4 correspond to three areas of stability in Fig. 3 marked by the same letters. Orbits *a* and *b* are pinned while *c* is delocalized and may account for the peak in $\sigma_{xx}(B)$. This stable trajectory is of second order in the sense that it recurs after two collisions with antidots. Notice that under conditions of the main magnetoresistance peak in the square lattice ($2R_c = d$) stable running trajectories of first order are essential. The symmetry of the honeycomb lattice forbids the presence of trajectories of this sort.

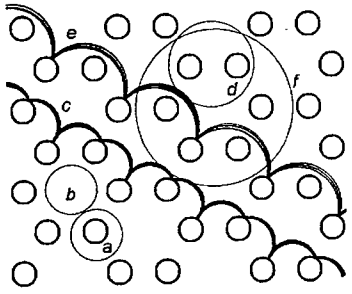

Fig. 4. Special electron trajectories in the honeycomb lattice of antidots.

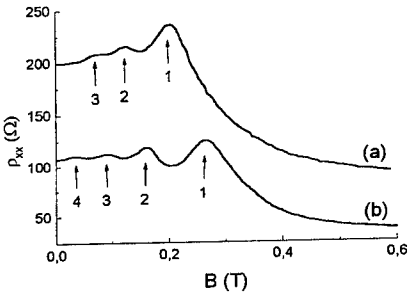

Fig. 5. Magnetoresistance traces before (a) and after (b) illumination.

The same analysis for peak 2 (Fig. 2) shows two special areas in the Poincaré section corresponding to the trajectories *d* and *e* (Fig. 4). One of them (*e*) is again delocalized and may cause the peak in $\sigma_{xx}(B)$. For peak 3 only pinned electron orbit (*f*) was found, which correlates with the absence of peak in $\sigma_{xx}(B)$ at this value of magnetic field.

No special electron trajectories were found for the magnetic field corresponding to peak 4. Another peculiarity of this peak is its high sensitivity to the antidot dimensions. Fig. 5 shows magnetoresistance of the honeycomb lattice before and after illumination. One can see that peak 4 is absent before the illumination when actual size of antidots including depletion layer is greater. The origin of this peak is connected with destruction by magnetic field of channeling electrons that move without collisions between the arrays of antidots in zero magnetic field [4,6]. The characteristic cyclotron radius can be estimated assuming that an electron starting between two adjacent antidots and moving along the channel touches the next antidot. The period of the honeycomb lattice along the widest channels (of the width d–$2a$) is $\sqrt{3}$d, which gives $R_c^* \approx 3d^2/(d-2a)$. For a=0.17 μm and d=0.8 μm this characteristic cyclotron radius $R_c^* \approx 4.2$ μm which is in agreement with experimental value of R_c for peak 4 in Fig. 5. The absence of the peak for the case of large antidot dimensions is caused by the decrease of the width of channels and thus the number of channeling electrons. An additional reason is the influence of an error in antidot positions that also decreases the width of channels and is more important for the channels of small width.

The work was supported by RFBR (99-02-16756), RFBR-CNRS (PICS628-RFBR98-22008) and NATO HTECH-LG 971304.

References

1. K. Ensslin and P. M. Petroff, Phys. Rev. B 41 (1990) 12307.
2. D. Weiss, M. L. Roukes, A. Menschig, P. Grambow, K. von Klitzing and G. Weimann, Phys. Rev. Lett. 66 (1991) 123.
3. E.M.Baskin, G.M.Gusev, Z.D.Kvon, A.G.Pogosov, M.V.Entin, JETP Lett. 55 (1992) 678.
4. S.Luthi, T.Vancura, K.Ensslin, R.Schuster, G.Bohm, W.Klein, Phys. Rev. B 55 (1997) 13088.
5. T.Yamashiro, J.Takahara, Y.Takagaki, K.Gamo, S.Namba, S.Takaoka, K.Murase, Sol. St. Commun. 79 (1991) 885.
6. E.M.Baskin, A.G.Pogosov, M.V.Entin, JETP 83 (1996) 1135.

PA.30

Aharonov-Bohm oscillation of localization in antidot lattices

Seiji URYU and Tsuneya ANDO

Institute for Solid State Physics, University of Tokyo
7-22-1 Roppongi, Minato-ku, Tokyo 106-8666, Japan

Localization length in antidot lattices subjected to uniform magnetic fields is numerically calculated based on a finite-size scaling method. It is demonstrated that the localization length oscillates with a period of flux quantum $\Phi_0 = ch/e$ as a function of flux passing through a unit cell near or higher than the critical magnetic field of an insulator–quantum Hall transition.

1. Introduction

Two kinds of quantum oscillation of resistivity were observed in hexagonal antidot lattices [1]. One is an oscillation with a period of $\Phi_0/2$ as a function of flux Φ passing through a unit cell near a zero magnetic field, where $\Phi_0 = ch/e$ is the flux quantum. The other is that with a period Φ_0 in magnetic fields near or higher than an insulator–quantum Hall transition point where the resistivity is observed to be independent of temperature. The former arises from an oscillation of the localization length [1,2]. The purpose of this paper is to study the Φ_0 oscillation of the localization length and an insulator–quantum Hall liquid transition in a hexagonal antidot lattice by a numerical finite-size scaling method.

2. Model and Method

As a model of antidot lattices, we take a two-dimensional array of quantum-wire junctions, each of which is characterized by a scattering matrix calculated in a nearest-neighbor tight-binding model [2,3]. We use the following model potential $V(\mathbf{r})$ of an antidot in a hexagonal lattice with a center at the origin [4,5]

$$V(\mathbf{r}) = U_0 \left| \cos\left(\frac{\pi \mathbf{a}_1 \cdot \mathbf{r}}{a^2}\right) \cos\left(\frac{\pi \mathbf{a}_2 \cdot \mathbf{r}}{a^2}\right) \cos\left(\frac{\pi (\mathbf{a}_1 - \mathbf{a}_2) \cdot \mathbf{r}}{a^2}\right) \right|^{4\beta/3}, \tag{2.1}$$

with U_0 being a maximum of the potential, a a potential period, $\mathbf{a}_1 = (\sqrt{3}a/2, a/2)$, $\mathbf{a}_2 = (0, a)$, and β a parameter describing the steepness of the potential.

We consider two kinds of disorders. One is the impurity potential and the other is the fluctuation in the antidot diameter d [4,5]. The former is characterized by the mean free path l_e of the two-dimensional system in the absence of the antidot potential. The latter is characterized by $d_f = \sqrt{\langle (d - \langle d \rangle)^2 \rangle}$, where $\langle \cdots \rangle$ means an average over different antidots.

We shall use a finite-size scaling method [6,7]. The inverse localization length $\alpha(L)$ is calculated for a long strip-form antidot lattice with a finite width L. We assume a scaling hypothesis for $\alpha(L)$:

$$\alpha(L)L = f(\alpha_{2D}L), \tag{2.2}$$

where α_{2D} is an inverse localization length in a two-dimensional system. It should be noted that the system in the absence of a magnetic field, i.e., $\Phi/\Phi_0 = 0$, may have to be excluded because it belongs to a different universality class (orthogonal) from that of the others (unitary).

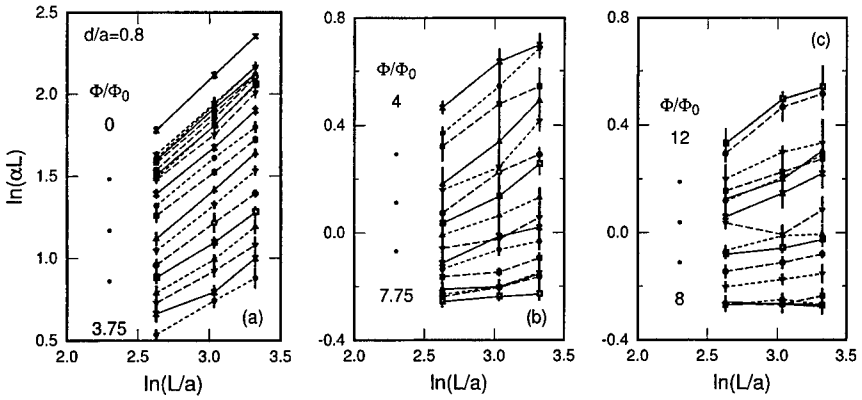

Fig. 1 System-size dependence of normalized inverse localization length αL for various magnetic fields. (a) $0 \leq \Phi/\Phi_0 \leq 3.75$, (b) $4 \leq \Phi/\Phi_0 \leq 7.75$, and (c) $8 \leq \Phi/\Phi_0 \leq 12$.

In the followings, we choose the parameters $\lambda_F/a = 0.27$ with λ_F being the Fermi wavelength, $l_e/a = 4$, $d_t/a = 0.035$, and $\beta = 1$ which are consistent with those of experiments [1,4,5] and use $d/a = 0.8$ which will later turn out to be slightly larger than that in actual systems. The width of a strip system is chosen as $L/\sqrt{3}a = 8$, 12, and 16, and periodic boundary conditions are imposed in the direction of the width.

The typical length of the strip system is 20,000 in units of a for $0 \leq \Phi/\Phi_0 \leq 6$ and $10 \leq \Phi/\Phi_0 \leq 12$ in the strong-localization regime and 120,000 for $6.25 \leq \Phi/\Phi_0 \leq 9.75$ in the weak localization regime. The typical statistical errors of resulting $\alpha(L)$ for the strong and the weak localization regimes are less than 4 % and 2.5 %, respectively.

3. Results

Figures 1 (a), (b), and (c) show the system-size dependence of normalized inverse localization length $\alpha(L)L$ at various magnetic fields lying in the range $0 \leq \Phi/\Phi_0 \leq 12$. The data with large values and the strong dependence on the size L/a indicate the strong localization regime and the data with small values and the weak dependence on the size the weak localization regime.

The qualitative feature in Fig. 1 is that the localization is strongest at a zero magnetic field, becomes weaker with increasing magnetic field, and becomes strong again after taking a minimum at $\Phi/\Phi_0 \sim 8$ where the normalized inverse localization length has almost no dependence on the system size. It is likely that states are extended and an insulator-quantum Hall transition occurs at this magnetic field as will be discussed below.

Figure 2 shows the scaling function determined by calculated normalized inverse localization length. It shows that the scaling works reasonably well and the inverse localization length at different magnetic fields is scaled into a single common curve.

Figure 3 shows the two-dimensional inverse localization length which are obtained from the above scaling. The absolute value of the inverse localization length is determined by the condition that the geometric average of the inverse localization length at different magnetic fields in the range $0 \leq \Phi/\Phi_0 \leq 1$ reproduces that of the previous results obtained

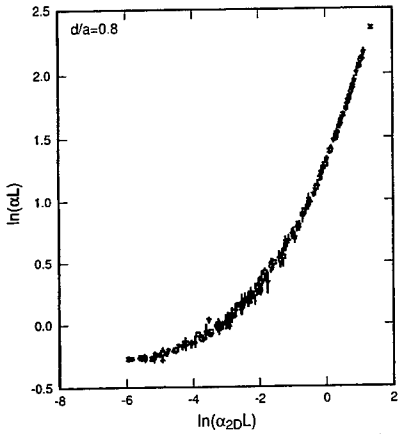

Figure 2. Scaling of data in the magnetic field where $0 \leq \Phi/\Phi_0 \leq 12$.

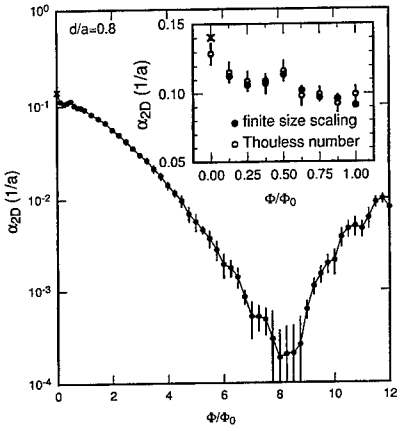

Figure 3. Magnetic-field dependence of two-dimensional inverse localization length. The inset shows the results around a zero magnetic field.

in a Thouless-number method [2]. The result of this fitting is shown in the inset where filled circles indicate the results of the finite-size scaling method and open ones with error bars those of the Thouless number method. The inverse localization length oscillates with a period $\Phi_0/2$ near a zero magnetic field $0 \leq \Phi/\Phi_0 \leq 1$ in good agreement with the results of the Thouless-number method and also with those of experiments [1].

There are two important features in higher magnetic fields. One is the presence of a minimum in the inverse localization length at $\Phi/\Phi_0 \sim 8$ as has been expected from the results in Fig. 1. The localization length at this field exceeds 5000 in units of a ($\sim$1 mm for typical $a = 2000$ Å). Although it is quite difficult to draw a definite conclusion whether states are really extended or not, we can practically regard states to be extended at this field and the corresponding field as an insulator–quantum Hall transition point. Another important feature is the oscillation with a period Φ_0 in magnetic fields close to or larger than this critical magnetic field. In this case the localization effect becomes weaker at magnetic fields where Φ/Φ_0 is exactly an integer.

The present results are qualitatively in good agreement with those of experiments [1]. In the experiments, a prominent oscillation with a period Φ_0 is observed in magnetic fields near or higher than the magnetic field corresponding to an insulator-quantum Hall transition where the resistivity is independent of temperature. In the oscillation, the diagonal conductivity takes peaks at integer Φ/Φ_0 in consistent with the decrease of the localization effect obtained here theoretically.

There seems to be some quantitative difference. The critical magnetic field of the experiments is $\Phi/\Phi_0 \sim 4$ which is smaller than our result $\Phi/\Phi_0 \sim 8$. This difference may be attributed to a difference in the value of d/a, i.e., actual d/a in experiments seems to be smaller than 0.8 adopted in the numerical calculation. Preliminary calculations for $d/a = 0.7$ currently underway seem to give a critical magnetic field close to that obtained

experimentally.

It should be noted that the scaling of data near the critical magnetic field must be carefully performed due to the presence of a possible correction to scaling [8]. More accurate analysis including such corrections requires a further reduction in statistical errors and calculations for wider systems. Such works are underway.

4. Summary and Conclusion

The localization effect in hexagonal antidot lattices has been numerically studied with the use of a finite-size scaling method. It has been shown that the inverse localization length takes a minimum at a certain critical magnetic field and oscillates with a period Φ_0 around this critical field. The localization length at the critical field exceeds 5000 in units of the array period and is therefore macroscopically large. It is likely that this field corresponds to an insulator-quantum Hall transition.

Acknowledgments

This work is supported in part by the Japan Society for the Promotion of Science ("Research for the Future" Program JSPS-RFTF96P00103). One of the authors (S.U.) has been supported by Research Fellowships of the Japan Society for the Promotion of Science for Young Scientists. Some numerical calculations were performed on FACOM VPP500 in Supercomputer Center, Institute for Solid State Physics, University of Tokyo.

References

1. F. Nihey, M. A. Kastner, and K. Nakamura, Phys. Rev. B **55**, 4085 (1997).
2. S. Uryu and T. Ando, Phys. Rev. B **58**, 10583 (1998).
3. S. Uryu and T. Ando, Phys. Rev. B **53**, 13613 (1996).
4. T. Nakanishi and T. Ando, Phys. Rev. B **54**, 8021 (1996).
5. T. Nakanishi and T. Ando, Physica B **227**, 127 (1996).
6. A. MacKinnon and B. Kramer, Phys. Rev. Lett. **47**, 1546 (1981).
7. A. MacKinnon and B. Kramer, Z. Phys. B **53**, 1 (1983).
8. B. Huckestein, Phys. Rev. Lett. **72**, 1080 (1994).

PA.31

Magnetoplasmon excitations in quantum dot arrays

B. P. van Zyl and E. Zaremba
Department of Physics, Queen's University,
Kingston, Ontario, Canada K7L 3N6

Motivated by the far-infrared transmission experiments of Demel *et al.*, we have investigated the magnetoplasmon excitations in an array of quantum dots within the Thomas-Fermi-Dirac-von Weizsäcker (TFDW) approximation. Detailed calculations of the magnetic dispersion and power absorption from a uniform radiation field unambiguously demonstrates that the noncircular symmetry of the individual dots is responsible for the anticrossing behaviour observed in the experiments. The interdot Coulomb interaction is unimportant at the interdot separation of the samples studied.

In one of the earliest studies of its kind, Demel *et al.* [1] observed the far-infrared (FIR) response of an array of quantum dots fabricated by means of the deep-mesa-etching technique. The spectrum clearly shows a resonant coupling (anticrossing) between different branches of the magnetic dispersion which is in direct contrast to the well known two-mode dipole excitation spectrum found in ideally parabolic dots. In [1], the mode anticrossings were attributed to a nonlocal dynamical response associated with the electronic compressibility which is responsible for the wavevector dispersion of plasmons in a uniform electron gas. However in subsequent work, attention shifted towards the noncircular confining potential as being the most likely explanation of the observed behaviour [2,3]; deviations from perfect parabolicity lead to additional modes becoming dipole active. In this study, we revisit the origin of these mode anticrossings, paying special attention to the role of symmetry in determining the collective mode spectrum.

The results we present here are based on the TFDW hydrodynamic theory which was first developed to study the magnetoplasmon excitations in parabolic quantum wells [4], and then later applied to quantum rings [5] and wires [6]. There are two essential ingredients in the TFDW approach [7]: (i) the defining energy functional (atomic units are used throughout)

$$E[n] = \int d^2\mathbf{r}\left[\frac{\pi}{2}n^2 + \frac{\lambda_w}{8}\frac{|\nabla n(\mathbf{r})|^2}{n(\mathbf{r})} - \frac{4}{3}\sqrt{\frac{2}{\pi}}n^{3/2}\right] + \frac{1}{2}\int d^2\mathbf{r}\int d^2\mathbf{r}'\frac{n(\mathbf{r})n(\mathbf{r}')}{|\mathbf{r}-\mathbf{r}'|} + \int d^2\mathbf{r}\, v_{\rm ext}(\mathbf{r})n(\mathbf{r})\,, \tag{1}$$

which contains Thomas-Fermi and von-Weizsäcker kinetic energies together with exchange, Hartree and external energy contributions, and (ii) the use of hydrodynamic equations to describe the dynamics of the electronic system, *viz.*,

$$\left(\frac{\partial n}{\partial t}\right) + \nabla\cdot(n\mathbf{v}) = 0\,, \qquad n\left[\frac{\partial \mathbf{v}}{\partial t} + \mathbf{v}\cdot\nabla\mathbf{v}\right] = n\mathbf{F}^{\rm tot}\,, \tag{2}$$

with

$$\mathbf{F}^{\rm tot}(\mathbf{r},t) = -\nabla\left[v_{\rm eff}(\mathbf{r},t) - \frac{\lambda_w}{2}\frac{\nabla^2\psi(\mathbf{r},t)}{\psi(\mathbf{r},t)}\right] - \left(e\mathbf{E} + \frac{e}{c}\mathbf{v}\times\mathbf{B}\right) . \qquad (3)$$

In Eq. (1), the Thomas-Fermi and exchange energies are written in a form applicable to a strictly two-dimensional electron gas. The total force $\mathbf{F}^{\rm tot}$ acting on the electrons includes both an internal force which is defined by the energy functional ($v_{\rm eff}$ is a self-consistent effective potential and $\psi(\mathbf{r},t) \equiv \sqrt{n(\mathbf{r},t)}$ is the so-called von-Weizsäcker wavefunction), as well as any external force arising from imposed electric and magnetic fields. In the following, we take the external magnetic field to be static, $\mathbf{B} = B_0\hat{\mathbf{z}}$, while the external electric field corresponds to a spatially uniform radiation field polarized in the $\hat{\mathbf{x}}$-direction.

Our main objective is to determine the collective modes which correspond to small-amplitude oscillations around the equilibrium state of the system. We must therefore first obtain the ground state density distribution $n_0(\mathbf{r})$ by solving self-consistently the Euler-Lagrange equation obtained from Eq. (1), *viz.*, $\delta E[n]/\delta n = \mu$, with μ the chemical potential. This information is then used in the linearized version of Eq. (2) to obtain either the collective modes of the system (for $\mathbf{E} = 0$), or the power absorption in the presence of an external radiation field.

In the following, we assume material parameters corresponding to the experimental situation in [1], and restrict our calculations to $N = 210$ electrons per dot. The form of the confinement potential for each dot in the square array is taken to be

$$v_{\rm ext}(r,\theta) = \frac{1}{2}kr^2 + \frac{1}{4}pr^4 + \frac{1}{4}p\varepsilon r^4\cos(4\theta) , \qquad (4)$$

where θ is the azimuthal angle in polar coordinates. For $p = 0$, we have purely parabolic confinement; setting $\varepsilon = 0$ with k, $p \neq 0$ introduces a quartic radial perturbation. If all three parameters are nonzero, the last term in (4) breaks the circular symmetry of the potential. The form of this term is consistent with the geometry of the fabricated dots [1].

In Figs. 1(a-b), we present the magnetic dispersions for two circularly symmetric cases ($\varepsilon = 0$). The parameter k in the parabolic case (a) and the parameters k and p in the radially anharmonic case (b) were chosen to reproduce the lowest experimental $B = 0$ mode frequency in both cases. The branches which disperse from this point are the two well-known center-of-mass modes. Clearly, the dispersion of these branches is very similar in both (a) and (b), indicating that it is impossible to determine the form of the radial confinement from a knowledge of the mode dispersion alone. The main difference between the calculated spectra is the blue-shift of the higher lying modes relative to the two center-of-mass modes induced by the r^4 perturbation.

As will be discussed in more detail later, the arrangement of the dots on a square lattice plays no role in determining the mode dispersions at the experimental interdot separation. In other words, the calculated spectra essentially correspond to *isolated* circularly symmetric dots. For an isolated dot with strictly $SO(2)$ symmetry, the modes belong to different irreducible representations, thereby precluding the possibility of any anticrossing behaviour. The mode frequencies, ω_l, can be labelled by an index corresponding to the angular character $e^{il\theta}$ of the density fluctuation on each dot. Fig. 1(c) shows the magnetic dispersion of an array of dots which have a noncircular perturbation ($\varepsilon \neq 0$). In this case, the local symmetry of the

dots is lowered from $SO(2)$ to C_4 by the confining potential. From a group theoretic point of view, the modes in this case must be classified according to their transformation under C_4. It can be shown that the original ω_l modes no longer transform according to different irreducible representaions under C_4, implying that the modes of the circularly symmetric situation are mixed. An example of this can be seen in Fig. 1(c) which shows an anticrossing between the ω_{+1} and ω_{-3} branches. It is this mode anticrossing which we associate with that observed in [1], rather than between the ω_{+1} and ω_{-2} branches as was originally conjectured. Furthermore, although not resolveable in the plots, we would generally expect anticrossings between any pair of modes with indices satisfying $\mid l - l' \mid = 4m$, where m is an integer.

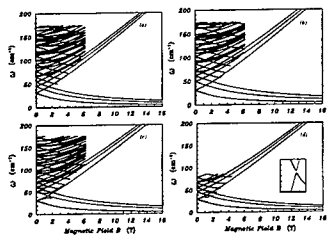

Fig. 1. The magnetic dispersions for a square array of isolated (a) parabolic dots, (b) radially anharmonic dots, (c) noncircular dots, and (d) closely spaced parabolic dots (inset: a magnification of the boxed region illustrating the lattice induced anticrossings). The solid curves are fits to the ideal two-mode spectrum corresponding to an isolated parabolic dot.

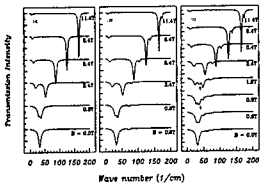

Fig. 2. Theoretical far-infrared power absoption for a square array of isolated (a) parabolic dots, (b) radially anharmonic dots, and (c) noncircular dots. In (c), the anticrossing intersection at w=40 (1/cm) is indicated by an arrow.

We next consider the effect of the interdot separation. Fig. 1(d) represents the *same* confining potential as in Fig. 1(a), but now with a lattice spacing reduced to 600 nm from 1000 nm. We observe two subtle, yet important changes. First, we note the appearance of a weak anticrossing between the ω_{+1} and ω_{-3} modes (figure inset), and second, the center-of-mass mode frequency at $B = 0$ has been slightly reduced from that of Fig. 1(a). Both of these effects can be explained in terms of the interdot Coulomb interaction. In the case of the anticrossings, it is the interdot interaction that reveals the existence of the lattice, and the local $SO(2)$ symmetry of each dot is now superposed with the C_4 symmetry of the lattice. However, it is important to realize that this lattice induced anticrossing is *too weak* to explain the data in [1]. Similarly, the reduction in the center-of-mass mode frequency can be explained within a simple model which takes into account only the dipole-dipole coupling between the dots [6].

In Figs. 2(a-c), we display the theoretical FIR power absorption for a range of magnetic fields corresponding to the experimental situation in [1]. Fig. 2(a) illustrates the well know power absorption found for parabolic dots; of all the modes in Fig. 1(a), only the center-of-mass (Kohn) modes are dipole active. The single peak at the confinement frequency splits as the magnetic field increases, with most of the oscillator strength residing in the high-frequency cyclotron mode at high fields. This behaviour is characteristic of pure parabolic confinement and demonstrates that the crystal field of the lattice is negligible in this case. The line-shapes in these figures is determined by a phenomenological viscous damping term inserted into the velocity equation of Eq. (2). As discussed elsewhere [8], one must assume a

damping parameter which is frequency-dependent in order to reproduced the observed field dependence of the resonance line widths.

In Fig. 2(b), the r^4 perturbation ($p \neq 0$, $\varepsilon = 0$) is introduced, and we see that the main effect of this anharmonic term is to allow the excitation of higher energy dipole resonances. These higher resonances have additional radial nodes in their density fluctuations. The power absorption is almost identical to that for purely parabolic dots, except for the presence of a weak satellite peak that tracks along the high energy side of the upper center-of-mass-like mode. Finally, in Fig. 2(c) we show the effects of a noncircular perturbation ($\varepsilon \neq 0$). What is most evident is the development of a tertiary peak (denoted by an arrow) at intermediate field strengths. This peak attains a maximum oscillator strength at around $B = 1.5$T, and disappears completely by $B = 5.4$T. This additional peak is of course a manifestation of the anticrossing behaviour illustrated in Fig. 1(c), and arises as a result of the transfer of oscillator strength from the $l = 1$ Kohn mode to the originally dipole inactive $l = -3$ mode. The calculated power absorption is in good agreement with the experimental FIR transmission data presented in Fig. 1 of Ref. [1]. An important lesson to be learned from Figs. 2(a-c) is that the FIR power absorption provides a much better probe of the confining potential than does the magnetic dispersion itself.

In conclusion, we have examined the magnetoplasmon excitations in both circular and noncircular dots. By considering a potential which included terms representing both radial anharmonicity and a noncircular perturbation, we were able to fully explore the effects of geometric confinement, and Coulomb-derived interdot coupling, on the magnetoplasmon excitations of the dots. In the case of circular dots, our results indicate that the addition of an r^4 radial perturbation can account for the satellite peak structure observed in the experiments [1]. We have also seen that interdot interactions, while in principle giving rise to mode couplings, are too weak to account for the observed anticrossing behaviour at the experimental interdot separation. On the other hand, the addition of a noncircular perturbation to the confining potential $\propto r^4\cos(4\theta)$ was shown to induce anticrossings in the magnetoplasmon dispersion that are entirely consistent with the observed FIR transmission data. Based on these results, we conclude that only the explicit noncircular symmetry of the confining potential can fully account for the mode anticrossings reported in [1].

[1] T. Demel, D. Heitmann, P. Grambow and K. Ploog, Phys. Rev. Lett. **64**, 788 (1990).

[2] V. Gudmundsson and R. R. Gerhardts, Phys. Rev B **43** R12098 (1991).

[3] S. Nazin, K. Tevosyan and V. Shikin, Surf. Sci. **263** 351 (1992).

[4] E. Zaremba and H. C. Tso, Phys. Rev. B **49**, 8147 (1994).

[5] E. Zaremba, Phys. Rev. B **53**, R10512 (1996).

[6] B. P. van Zyl and E. Zaremba, Phys. Rev. B **59**, 2079 (1999).

[7] For details regarding the TFDW hydrodynamic formalism, the interested reader may consult Refs. [4-6].

[8] Z.L. Ye and E. Zaremba, Phys. Rev. B **50**, 17217 (1994).

PA.32

Dynamic behavior of asymmetric quantum dot cells*

F. Rojas[a], E. Cota[a] and S. E. Ulloa [b]
[a] Centro de Ciencias de la Materia Condensada–UNAM,
Apartado Postal 2681, Ensenada, B.C. 22800, México
[b]Department of Physics and Astronomy and
Condensed Matter and Surface Sciences Program,
Ohio University, Athens, Ohio 45701-2979, USA

Abstract

We study the dynamic evolution of 4- and 5-quantum dot cells in the presence of a time-dependent driver cell. We analyze the effects of imperfections, tunneling intensity and switching times on the response of the basic cell, for linear and periodic switching of the driver polarization. We find that the effects of the imperfections have strong consequences in slowing down the response of the basic cell and that the 5 dot cell is less sensitive to these effects. Further studies show that a rapid deterioration of the response takes place as more cells are included. Effects of a time-dependent variation of the tunneling parameter as the switching takes place are also analyzed.

PACS: 73.40.Gk, 73.20.Dx, 73.50.Bk
Keywords: quantum dots, quantum computation

1 Introduction

Arrays of quantum dots, quantum cellular automata (QCA), have been proposed [1] as systems for implementing novel logical computing elements and even quantum computing [2]. Each cell in the array contains four or five quantum dots where two electrons are allowed to move within the cell, tunneling from one dot to the next, while interacting with each other, and with a positive neutralizing background. These electrons also interact with those in neighboring cells, but are not allowed to tunnel from cell to cell. Typically, the cells are arranged in a square geometry (with a quantum dot in each corner), so that the ground state of an isolated cell is doubly degenerate, with two electrons on opposite corners of the cell. Each of these ground states is characterized by a polarization number (+1 and −1, as per Ref. [1]), which would allow the encoding of binary information and quantum bits. In this paper, we study the response of such a cell arrangement to a time dependent driver cell in close proximity. The effects of such drivers have been studied recently [3], including dissipative effects [4]. We analyze the time evolution of the polarization, energy

*F.R. and E.C. acknowledge support from CONACYT (Grant 27702-E), and S.E.U. from US-DOE

expectation value and transition probability to a final "response" state, and evaluate the effects of imperfections, tunneling intensity and switching times on these quantities. The presence of an additional cell shows that a rapid deterioration of the response takes place, a feature that would be unacceptable for quantum computation. It has been suggested [4] that a time-dependent variation of the tunneling parameter as the switching takes place should correct the response for a chain of cells. We study this situation considering different forms for the time variation.

2 Model

To describe each cell, we use an extended Hubbard model composed of four terms $H = H_0 + H_t + H_V + H_D$. Here, $H_0 = \sum_j \epsilon_j \hat{n}_j$, where $\hat{n}_j$ is the number operator on dot j. In this term, possible asymmetry is introduced by changing the energy in the corner k-th QD $\epsilon_k \rightarrow \epsilon_k - \delta$, where δ is the measure of the imperfection due either to a different dot size or local environment. The tunneling between dots in a cell is given by $H_t = -\sum_{j,j'=j+1}(t_{jj'}\hat{C}_j^\dagger \hat{C}_{j'} + t_{j'j}\hat{C}_{j'}^\dagger \hat{C}_j)$; here $\hat{C}_j^\dagger/\hat{C}_j$ are the creation/annihilation operators of an electron in site j and $t_{jj'}$ is the tunneling intensity. Notice we consider a single-orbital per site, as the confinement is strong in real systems and higher orbitals are not accessed; similarly, double occupancy is improbable due to a large on-site repulsion. The interaction in a cell is described by $H_V = \sum_{j,j'>j} V_{jj'}\hat{n}_j\hat{n}_{j'}$, where $V_{jj'}$ is the inter-dot Coulomb interaction and depends on the dot separation. Finally, the last term represents the Coulomb interaction with the time-dependent driver cell, at a separation c, and has the form $H_D(t) = \sum_{i,j} W_{ij}\rho_i^d(t)\hat{n}_j$, where $\rho_i^d(t)$ is the charge density at site i in the driver cell d. We consider two cases for the time-evolution of $\rho_i^d(t)$ that correspond to two models of the driver polarization (P_d): (a) a linear switching form $P_d(t) = 1 - 2t/\tau$, for $t \leq \tau$, where τ is the switching time; and (b) a time-periodic switching of P_d. In case (a), the corresponding charge densities are $\rho_1^d(t) = \rho_3^d(t) = 1 - t/\tau$, and $\rho_2^d(t) = \rho_4^d(t) = t/\tau$ if $t \leq \tau$. In case (b), we model the densities by $\rho_1^d(t) = \rho_3^d(t) = \cos^2\omega t$, and $\rho_2^d(t) = \rho_4^d(t) = \sin^2\omega t$, so that $P_d(t) = \cos(2\omega t)$.

From the time-dependent Schrödinger equation for $\Psi(t) = \sum_i a_i|\hat{e}_i\rangle$ in the particle number representation for two electrons, we find the probability amplitudes a_i by solving the resulting coupled differential equations, using as initial conditions the eigenstates of the system with $P_{driver} = +1$. From the coefficients a_i, we determine the polarization of the target cell, defined as [1]

$$P = \frac{\rho_1 + \rho_3 - \rho_2 - \rho_4}{\sum_i \rho_i}, \tag{1}$$

where the density in each site i is $\rho_i(t) = \langle\Psi(t)|\hat{n}_i|\Psi(t)\rangle$. Moreover, we compute the energy expectation value $\langle H\rangle = \sum_{ij} a_i^*(t)H_{ij}a_j(t)$ to understand the energy transfer mechanisms taking place. Finally, we look at the probability of finding the target cell in the ideal final ground state, where $P_{driver} = -1$, and determined by the amplitude $\mathcal{P}(t) = |\langle\Psi_{-1}|\Psi(t)\rangle|^2$.

3 Results and Discussion

We present results for the effects of imperfections on polarization, energy average and the transition probability to a response state, as the driver switches from $P_d = +1$ to $P_d = -1$

in a time τ. Fig. 1 shows results for the four dot cell.

In the symmetric ideal case, $\delta = 0$, we see (Fig. 1(a)) that the target cell switches polarization from the initial state with polarization $+1$ to a response state with at best $P \approx -0.6$. The final state has oscillations that increase in amplitude as the asymmetry increases, due to the presence of tunneling. Also, in the asymmetric cells, we observe a shift in the time of switching of the target polarization. Although the oscillations decrease for longer switching times τ, they are always substantial for δ values studied. The curve for the energy (Fig. 1(b)), for $\delta = 0$, is symmetric with respect to $\tau/2$ and shows that the final energy is approximately the same as the initial energy. In the asymmetric cells, these curves show a shift of the maximum position, tracking the polarization, and the difference between initial and final energy increases linearly as δ increases. The probability functions (not shown) are not strongly affected unless the size of the imperfection is very large. Fig. 1(c) shows the results for a driver switching periodically with frequency $\omega = 2\pi/2000$, which corresponds to a change of polarization $+1$ to -1 in 500 ps (continuous curve). The polarization in the symmetric case $\delta = 0$, is a curve with small oscillations that roughly follows the driver. The target cell response presents several minima with amplitudes less than -1, instead of one minimum in a period. For the case $\delta = .05$, however, the target polarization oscillates, but its value never reaches the region of negative polarization. Clearly, the desired transition does not occur.

In Fig. 2 we describe the results for a 5-dot cell, where we can see that the transition to a final state with $P \approx -1$ occurs. Considering the case with imperfections, we observe that even in the case of $\delta = 0.1$, the transition still occurs, whereas in the 4-dot cell that transition no longer develops. Fig. 2(a) shows that the final state has smaller oscillations than for the 4-dot case. It is interesting to note, from Fig. 2(b), that the difference in energies between initial and final states is similar to that for the 4-dot cell, but in this case the transition to the response state is accomplished. We understand this result by observing that in the 5-dot cell, the four states that involve the central site still contribute to the polarization thus allowing a larger energy fluctuation and rendering this cell more stable with respect to imperfections.

Fig. 3(a) shows the polarization for two cells (5 QD) and a driver. We observe large oscillations in the polarization of the second cell (P_2) which would render the system unacceptable for quantum computation. It has been suggested [4] that a time varying tunneling at the same that the driver is being switched would correct this behavior. We have calculated the response for different functional dependencies of tunneling with respect to time. The best results are obtained (Fig. 3(b)) for a gaussian variation centered at $\tau/2$ and of width $\sigma = \tau/4$. Although cells follow the driver, P remains at ≈ -0.7 at long times.

In conclusion, we have studied the effect of imperfections and tunneling intensity on three properties: polarization P, energy expectation value $\langle H \rangle$ and transition probability to a response state $\mathcal{P}(t)$, for 4- and 5-quantum dot cells. We find that the effects of imperfections include a shift to longer response times for the polarization transition, and an increase in the amplitude of final-state oscillations. We observe that the effect is stronger for periodic switching, and that the 5-dot cell is more stable against imperfections. Adding one more cell to the system results in large oscillations of the polarization in the final state. This response is shown to be improved substantially by considering a gaussian time-dependence for the interdot tunneling amplitude.

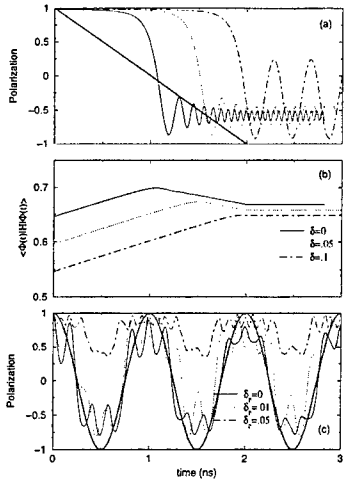

Figure 1: 4-dot cell. (a) Polarization vs time for the symmetric case ($\delta = 0$, continuous line) and different values of asymmetry. Here, $V =$ 1meV, $t = .02$meV, $c = 1.25a$, $a = 20$nm $\tau =$ 2ns. (b) Time dependence of expectation value of the total energy. (c) Polarization vs time for periodic driver cell with frequency $\omega = 2\pi/2000$. Parameters as above, but $c = 1.75a$.

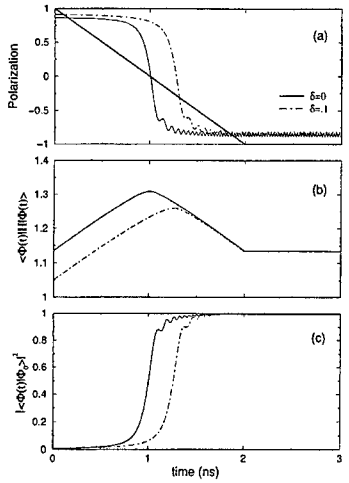

Figure 2: 5-dot cell. (a) Polarization, (b) energy and (c) transition probability to the final state, as a function of time, for the symmetric ($\delta =$ 0) and asymmetric ($\delta = .1$) cases. Parameters: $V = 2$meV, $t = .01$meV, $c = a = 20$nm.

References

[1] C.S. Lent *et al.*, J. Appl. Phys. **28**, 3558 (1993).

[2] D.P. DiVincenzo, Science **270**, 255 (1995); A. Ekert and R. Jozsa, Rev. Mod. Phys. **68**, 733 (1996).

[3] P.D. Tougaw and C.S. Lent, J. Appl. Phys. **80**, 4722 (1996).

[4] C.K. Wang *et al.*, J. Appl. Phys **84**, 2684 (1998).

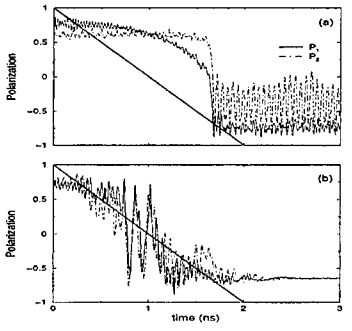

Figure 3: 5-dot cell. (a) Polarization as a function of time, for two cells (5 QD) and driver in symmetric case. Parameter values are $V =$ 1meV, $t = .01$meV, $c = a$. (b) Same as (a), but with gaussian time-variation of tunneling amplitude.

PA.33

Pillow–Shape Motion in Antidot–Arrays

M. Hochgräfe, R. Krahne, Ch. Heyn, and D. Heitmann

Institut für Angewandte Physik und Zentrum für Mikrostrukturforschung, Universität Hamburg, Jungiusstraße 11, 20355 Hamburg, Germany

Abstract

Theory predicts a rich mode spectrum for the dynamic excitations in antidot arrays. In addition to the dominating high $\omega_{1,0}^{+}$– and low ω_{EMP}^{+}–modes, there are higher frequency $\omega_{n,m}^{+}$– and in particular $\omega_{n,m}^{-}$–modes with pillow–shaped anticyclotron motions in a magnetic field B. We have prepared antidot arrays with different potentials and were able to detect these modes.

Far infrared (FIR) experiments on antidot arrays [1–6] show that the dynamic response in a perpendicular magnetic field B is dominated by a high–frequency $\omega_{1,0}^{+}$–mode and a low–frequency edge magnetoplasmon mode ω_{EMP}^{+} which are both cyclotron polarized (+). This was confirmed by theory [4,7,8]. However, Refs. [4,8] also predict additional higher frequency modes $\omega_{m,n}^{\pm}$. Some of them exhibit an anticyclotron polarization (-). We have prepared antidot arrays with different potentials in gated and etched $Ga_{0.67}Al_{0.33}As$–GaAs heterostructures and were able to detect these modes.
The theoretical mode spectrum according to the effective–medium model of [7] is given by the implicite expression

$$1 - \frac{1-f}{\frac{\omega}{\omega_0}\left(\frac{\omega}{\omega_0} \pm \frac{\omega_c}{\omega_0}\right)} - \frac{f}{\frac{\omega}{\omega_0}\left(\frac{\omega}{\omega_0} \mp \frac{\omega_c}{\omega_0}\right)} = 0. \qquad (1)$$

It is shown in Fig. 1a. In this model the antidot array is characterized by a geometrical filling factor $f = \pi R^2/a^2$, where R is the radius of the depleted area, i.e. the 'antidot' in the original two–dimensional electron system (2DES), a is the period of the array and ω_c is the cyclotron resonance frequency. The frequencies of the modes at $B = 0$ T, $\omega_{m,n}^{\pm}$, depend on the shape of the antidot potential [8]. Of particular interest is the $\omega_{1,0}^{-}$–mode, which has an anticyclotron polarization. This mode has, as shown in Fig. 1b, intrinsically a very weak oscillator strength. It exists practically only at small B and is weaker than the already weak $\omega_{1,0}^{+}$–mode at small B.

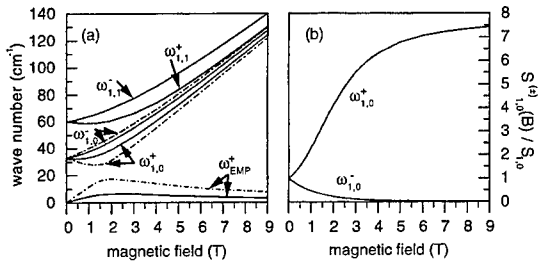

Fig. 1. (a) Theoretical dispersion of antidot modes for $f_{1,0} = 0.3$ (full lines) and $f_{1,0} = 0.05$ (dashed lines). (b) shows the normalized oscillator strength for the $\omega^{+(-)}_{1,0}$–modes.

For the sample preparation we start from a 2DES in a AlGaAs–GaAs–heterostructure with typical 2D densities of $N_S = 3 * 10^{11}$ cm^{-2}. All structures were dry etched through the original 2DES [1]. Onto some structures we evaporated an additional Ti–Gate. FIR transmission experiments where performed in superconducting magnets, which were connected to a Fourier transform spectrometer. In gated structures we evaluate the relative transmission $T(N_S)/T(N_S = 0)$ and in structures without a gate $T(B)/T(B_{\rm ref})$ where $T(B_{\rm ref})$ has a flat response in the relevant frequency regime. The temperature was 1.8 K.

The experimental dispersions for a gated structure with period $a = 600$ nm are shown in Fig. 2. Fits to the dispersions demonstrate that one can change the filling factor f with the gate voltage V_g, e.g. from $f = 0.3$ to $f = 0.46$ for the given V_g. (For these f the ω^+_{EMP}–mode is expected at such low frequencies that it is not within the spectral range of our spectrometer). However, in these gated structures the intensity of the $\omega^+_{1,0}$–mode decreases so strongly with decreasing B that it was not possible to detect the even weaker $\omega^-_{1,0}$–mode.

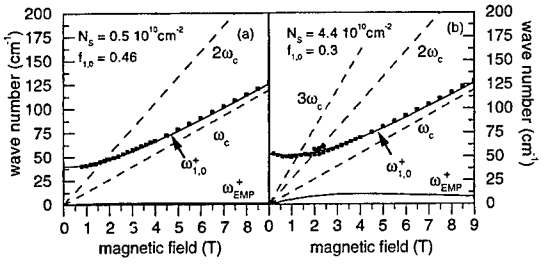

Fig. 2. Experimental dispersions of an antidot array for different gate voltages V_g. In (a) the gate voltage is $V_g = 0$ mV, in (b) $V_g = 600$ mV. The threshold voltage was $V_g = -100$ mV. The variation of the gate voltage leads to different densities N_S which are shown in the figure.

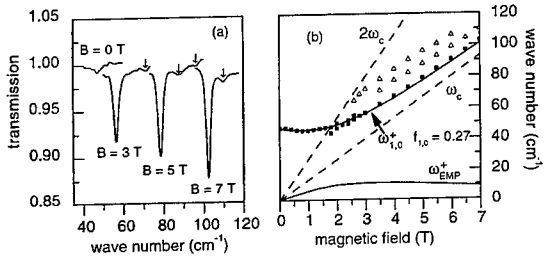

Fig. 3. (a) Experimental spectra at different magnetic fields B for another sample without gate. One can observe higher frequency modes marked by arrows. (b) shows the experimental dispersion. The full line is the calculated dispersion with $f_{1,0} = 0.27$.

In Fig. 3 we show experimental results for another antidot array with a period $a = 600$ nm and a geometrical hole diameter $d = 400$ nm. The spectra in Fig. 3a demonstrate the decreasing oscillator strength of the dominating $\omega^+_{1,0}$–mode with decreasing B, however, at higher B additional modes appear. The dispersions of the modes are depicted in Fig. 3b. The $\omega^+_{1,0}$–mode can be described by $f_{1,0} = 0.27$. Comparisons to the theoretical results in [8] lead us to identify these higher–frequency modes with the $\omega^+_{1,1}$– and the $\omega^+_{2,0}$–modes. The anticrossing of the $\omega^+_{1,0}$–mode with the dashed line $2\omega_C$ is the well known interaction with Bernstein modes [1,6,9]. The experimental results in Fig. 3b indicate that this interaction is even stronger for the higher frequency modes. Similarly as for the gated structures above, the intensity of the $\omega^+_{1,0}$–mode at $B = 0$ T is so weak (see Fig. 3a) that it is not possible to resolve the $\omega^-_{1,0}$–mode in this sample.

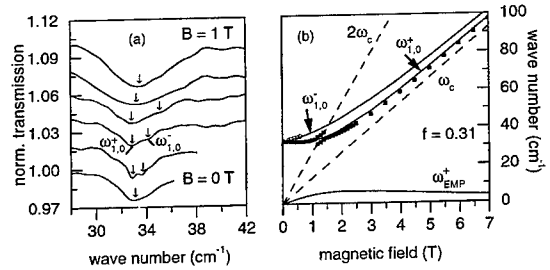

Fig. 4. (a) Experimental relative transmission of a different antidot array at various magnetic fields B. Spectra for $B > 0$ have been shifted vertically for clarity. The $\omega^-_{1,0}$–mode has an anticyclotron polarisation. (b) Experimental dispersions of the $\omega^-_{1,0}$– and the $\omega^+_{1,0}$–modes. Full lines are the theoretical dispersions according to equation (1) for $f_{1,0} = 0.31$.

In Fig. 4 we show experimental results of another etched sample without gate with $a = 1000$ nm and $d = 500$ nm. In this sample we observe, as shown in Fig. 4a, an additional resonance, labeled $\omega^-_{1,0}$, which decreases in intensity and increases in energy with increasing B. The dispersions in Fig. 4b indicate that both modes nicely follow the theoretical dispersion for $f_{1,0} = 0.31$. We have also performed experiments with circular polarization and could confirm the anticyclotron polarization of this mode. All FIR excitations are clearly collective excitations. Nevertheless, in a simple model one can visualize this $\omega^-_{1,0}$–mode by a classical single–particle motion, which is a pillow–shape trace between adjacent antidots and which indeed leads to an anticyclotron polarization.

We acknowledge financial support by the German Science Foundation through SFB 508 'Quantum Materials'.

References

[1] K. Kern *et al.*, Phys. Rev. Lett. **66**, 1618 (1991).

[2] A. Lorke, J. P. Kotthaus, and K. Ploog, Superlattices Microstruct. **9**, 103 (1991).

[3] Y. Zhao *et al.*, Appl. Phys. Lett. **60**, 1510 (1992).

[4] G. Y. Wu and Y. Zhao, Phys. Rev. Lett. **71**, 2114 (1993).

[5] K. Bollweg *et al.*, Phys. Rev. B **52**, 8379 (1995).

[6] K. Bollweg *et al.*, Phys. Rev. Lett. **76**, 2774 (1996).

[7] S. A. Mikhailov and V. A. Volkov, Phys. Rev. B **52**, 17260 (1995).

[8] S. A. Mikhailov, Phys. Rev. B **54**, R14293 (1996).

[9] V.Gudmundsson *et al.*, Physical Rev. B **51**, 17744 (1995).

PA.34

BIAS VOLTAGE DEPENDENT PHOTOLUMINESCENCE NEAR FERMI LEVEL IN N-TYPE MODULATION DOPED QUANTUM DOT ARRAYS

Shintaro Nomura,[1,2] Takuo Sugano,[2] and Yoshinobu Aoyagi[2]
[1]*Institute of Physics, University of Tsukuba*
Tennodai, Tsukuba, Ibaraki, Japan
[2]*The Institute of Physical and Chemical Research (RIKEN)*
Hirosawa, Wako-shi, Saitama, Japan.
E-mail: snomura@sakura.cc.tsukuba.ac.jp

Abstract

We report on a bias voltage dependent photoluminescence (PL) peak near the Fermi level in *n*-type modulation doped quantum dot arrays. A remarkably sharp peak with the spectral width of less than 0.1 meV is observed near the Fermi level in the PL at 0.4 K, which shows strong temperature dependence. This peak is considered to be due to the Coulomb interaction between the electron gas and a photo-generated hole.

PACS numbers: 73.20.Dx, 78.55.Cr, 78.66.-w

1. Introduction

Bias voltage controlled quantum dot (QD) arrays [1-3] are currently attracting interests of researchers. The electron gas in such systems can be controlled from 2-dimensional electron gas (2DEG) through an interconnected QD array to an isolated QD array by continuously changing the bias voltage applied to the metal electrodes. This is an interesting system to investigate the role of the Coulomb interaction between many electrons and a hole because the electron-electron and the electron-hole interaction energies are modulated through a change in a single particle energy and the spatial variation in the density of electrons.

One of the most striking features due to the interaction by many electrons and a hole is manifestation of the Fermi-edge singularity (FES) [4-7]. Photoluminescence (PL) and absorption spectra near the Fermi energy (E_F) show a power law divergence due to the Coulomb interaction between electron-gas and an optically generated hole. This enhancement in the optical transitions was shown to be modulated such as by dimensionality[8-10] or by an unoccupied higher subband state near E_F [11]. An application of a lateral confining potential is considered to change this divergence in the optical transitions. In this paper, we report on the enhancement of the PL near E_F in *n*-type modulation doped QD arrays depending on the bias voltage (V_B), the initial 2DEG density, and temperature.

2. Experimental

The samples studied were molecular-beam epitaxy grown GaAs-AlGaAs *n*-type modulation-doped quantum well (MDQW) structures on *n*-type GaAs substrates used as back contacts [12]. The electron densities of the 2DEG (n_s) were estimated to be 4 and 2.8×10^{11} cm^{-2} for sample A and B, respectively. Semi-transparent Schottkey gate structures were fabricated on the surface with a square mesh of a period of 250 nm and a width of 25 nm by the electron beam lithography.A bias voltage was applied between the surface mesh gate structure and a AuGe/Ni/Au ohmic back-contact. The samples were excited by an 488-line of an Ar ion laser at the incident power density of 1.6 meV/cm^2 or less through the metal mesh structure.

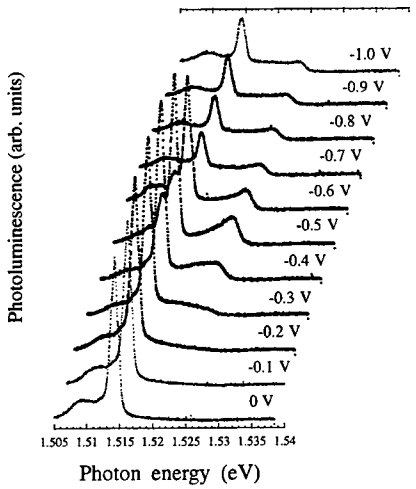

Fig. 1. The photoluminescence spectra at the bias voltage varied from 0 to –1.0 V at 4 K of a sample with $n_S = 4\text{x}10^{11}\text{cm}^{-2}$.

3. Results and discussion

Figure 1 shows the PL spectra of the higher density sample A depending on V_B at 4 K. The strong PL at 1.514 eV is the PL from a bulk exciton state in the GaAs buffer layer below the MDQW, which will not be discussed in the followings. The difference of the PL at V_B=0 and a sample without a surface mesh gate structure is small. The band-gap (E_g) and the Fermi energy (E_F) are 1.509 and 1.531 eV, respectively. At V_B=0, the PL from the 2DEG decreases monotonously between E_g and E_F. No enhancement of the PL at the Fermi level is identified, showing no FES at V_B=0. The energy difference between E_F and $n_z = 2$ exciton state is larger than 10 meV in sample A. Thus no enhancement of the FES is expected because of small mixing of the 2DEG-hole state and the higher subband exciton states [11,6]. The PL at V_B=0 also shows that there is no strong localization of a photo-generated hole which enhances the FES.

A striking feature of the PL spectra near the Fermi level is appearance of a shoulder or a peak by increasing $|V_B|$. The initially weak PL by recombination of the 2DEG with a free photo-generated hole at V_B=0 increases with increasing $|V_B|$, which develops to a bump at –0.5 V. This structure becomes smaller by changing V_B from –0.5 V to –1.0 V, and only a shoulder is identified at –1.0 V [12].

Sample B with lower n_s requires smaller $|V_B|$ and temperature to observe this structure near E_F. A remarkably sharp peak with the spectral width of less than 0.1 meV is observed at V_B = -0.2 V at 0.4 K at 1.523 eV as shown in Fig. 2 (a). It is found that this peak is very sensitive to the temperature. By increasing the temperature to 1.2 K, this sharp peak broadens and a bump similar to sample A at V_B = -0.5 V is observed. This bump disappears at 4 K to be seen as a shoulder as shown in Fig. 2 (a). No well-developed bump structure is observed near E_F at 4 K for V_B varied between +1 and -3 V. A small shoulder at V_B = -0.2 V at 1.523 eV disappears at V_B = -0.5 V at 4 K, which contrasts with the case of sample A, where a bump is observed at V_B = -0.5 V.

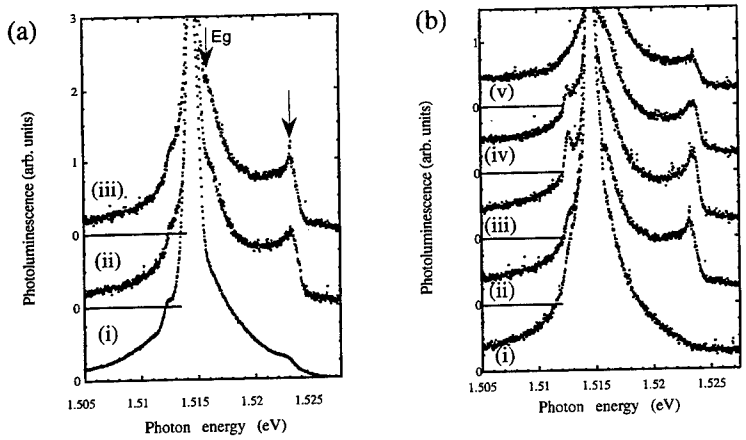

Fig. 2. The photoluminescence spectra of a sample with $n_S = 2.8\text{x}10^{11}\text{cm}^{-2}$ (a) at V_B = -0.2 V at (i) 4.2, (ii) 1.2, and (iii) 0.4 K, and.(b) at the bias voltage (V_B) varied from (i) +0.3, (ii) -0.2, (iii) -0.5, (iv) -0.7, and (v) –1.0 V at 0.4 K. A sharp peak is observed at 1.523 eV at 0.4 K as depicted by the arrow.

Figure 2 (b) shows V_B dependence of the PL of sample B at 0.4 K. The structure at 1.523 eV is most well-developed and sharpest at V_B = -0.2 V. The peak becomes smaller and broader by changing V_B from –0.2 V to –1.0 V. The PL at V_B = 0.3 V is indistinguishable to that of unbiased case, showing a weak PL at E_F.

The interconnection of the electron density of QDs correlates with the condition for the observation of the enhanced PL structure near E_F. The QDs are interconnected at V_B = -0.5 and -0.2 V for n_s = 4 and $2.8\text{x}10^{11}$ cm^{-2}, respectively, while they are isolated by stronger confining potential for larger $|V_B|$, as predicted by a realistic calculation based on a finite-difference method with a local-density-approximation [12]. The Fermi-surface is well-defined in this interconnected QD array, which is essentially important for the FES. This condition is not satisfied for an isolated array of QDs, where much smaller bump is observed.

We consider that the Coulomb interaction between a photo-generated hole and the electron-gas plays an important role to the observed PL. A remarkably sharp peak at 1.523 eV at 0.4 K and its strong temperature dependence cannot be explained within a single-particle model, although the increase of the PL for higher photon energy is partly explained by the change of the electron density of states due to the change of 2- to 0-dimensional potential confinement.

Optical transition probability between a hole and electrons near E_F with large momentum is sensitive to the localization and the position of a hole. The potential minimum for a hole is located beneath the metal mesh structure at a negative bias voltage. A hole which relaxes to this minimum is spatially separated from the potential minimum for electrons. This spatially indirect distribution of the electrons and a hole could be a possible explanation for the formation of a bump near E_F. The electrons with larger momentum may have more overlap with a hole at the potential minimum, resulting in an enhancement of the PL.

In summary, an enhancement of the PL near E_F is observed depending on the applied negative bias voltage in n-type modulation doped QD arrays. The optimum $|V_B|$ for the observation of the enhanced PL is smaller for the lower electron density sample. The strong temperature dependence and the narrow spectral width of less than 0.1 meV for the lower electron density sample show that the Coulomb interaction between the electron gas and a photo-generated hole plays an important role for the observed PL.

References

1. Heitmann, D. and Kotthaus, J.P., Phys. Today **46 (6)**, 56 (1993).
2. Heitmann, D., Physica B **212**, 201 (1995).
3. Jacak, L., Hawrylak, R., and Wojs, A., *Quantum Dots* (Springer-Verlag, 1997).
4. Mahan, G.D., *Many-Particle Physics, 2nd ed.* (Plenum, 1990).
5. Schmitt-Rink, S., Ell, C., and Haug, H., Phys. Rev. B **33**, 1183 (1986).
6. Hawrylak, P., Pulsford, N., and Ploog, K., Phys. Rev. B **46**, 15193 (1992).
7. Otani, H. and Ogawa, T., Phys. Rev. B **54**, 4540 (1996).
8. Calleja, J.M., Goni, A.R., Dennis, B.S., Weiner, J.S., Pinczuk, A., Schmitt-Rink, S., Pfeiffer, L.N., West, K.W., Müller, J.F., and Ruckenstein, A.E., Solid State Commun. **79**, 911 (1991).
9. Calleja, J.M., Goni, A.R., Pinczuk, A., Dennis, B.S., Weiner, J.S., Pfeiffer, L.N., and West, K.W., Phys. Rev. B **51**, 4285 (1995).
10. Ogawa, T., Furusaki, A., and Nagaosa, N., Phys. Rev. Lett. **68**, 3638 (1992).
11. Chen, W., Fritze, M., Walecki, W., Nurmikko, A.V., Ackley, D., Hong, J.M., and Chang, L.L., Phys. Rev. B **45**, 8464 (1992).
12. Nomura, S., Sugano, T., and Aoyagi, Y., Solid State Commun. **106**, 815 (1998).

PA.35

EXCITON g-FACTORS IN SEMICONDUCTOR NANOSTRUCTURES

Manfred Bayer and Alfred Forchel
Technische Physik, Universität Würzburg, Germany

Roza Kotlyar and Thomas L. Reinecke
Naval Research Laboratory, Washington, USA

The effects of quantum confinement on the electronic states in quantum wells, wires and dots have been a central focus of semiconductor research. Spin properties have become very important during the last few years because many new concepts such as spin transistors or solid state implementations of a quantum computer often rely on them. Thus it is important to develop a detailed understanding of g-factors in confined geometries. g-factors are particularly sensitive to band mixing and thus furnish detailed insight into the electronic band structure.

Here we give for the first time a comprehensive picture of the dependence of exciton g-factors on dimensionality and confinement. InGaAs/GaAs quantum wires and quantum dots of widely varying sizes have been studied by magneto-photoluminescence spectroscopy. For comparison, quantum wells of varying widths have also been studied. The experimental data are compared to the results of detailed calculations made using a 6-band $\mathbf{k}\cdot\mathbf{p}$ model which includes fully the coupling between valence and conduction bands and also considers the stress due to lattice mismatch at the interface.

We find, that the exciton g-factors depend strongly on the dimensionality and on the size of the quantum structure. The strong deviations of the g-factors from their values for large sizes go as D^{-2} with D being the size of the structure. These changes originate from the band mixing effects due to the quantum confinement.

The right hand figure shows as an example the variation of the exciton g-factor in cylindrical InGaAs/GaAs quantum disks with dot diameter (symbols: experiment, line: calculations). The dots were fabricated from a 5 nm wide quantum well and the magnetic field was aligned normal to the disk. For large diameters the g-factors converge to the quantum well limit of about -0.5. At small diameters the g-factor decreases drastically to a value of -11.3 for the smallest dots with a diameter of 23 nm. In quantum wires we observe a decrease down to -5.2 for 15 nm wide structures. The experimental data is in good accord with the calculations.

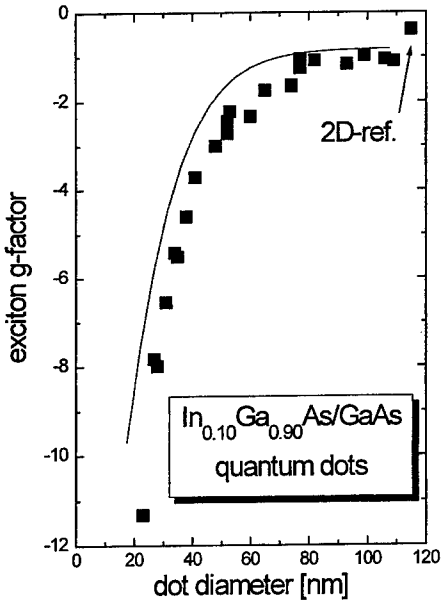

Hole coupling in stacked self-assembled InP quantum dots

M. Hayne[a], R. Provoost[a], M.K. Zundel[b], Y. Manz[b], K. Eberl[b] and V.V. Moshchalkov[a]

[a]*Laboratorium voor Vaste-Stoffysica en Magnetisme, Katholieke Universiteit Leuven, Celestijnenlaan 200D, B-3001 Leuven, Belgium.*
[b]*Max-Planck-Institut für Festkörperforschung, Heisenbergstrasse 1, 70569 Stuttgart, Germany.*

We have studied the photoluminescence of doubly-stacked layers of InP quantum dots in magnetic fields up to 50 T. We find that in contrast to the triply-stacked layers studied previously, which were strongly coupled for layer separations of 4 nm or less, the dots in the double-layers do not couple. We explain this surprising difference in behaviour by proposing a model in which the holes are confined in the GaInP layers separating the stacked dots. For triply-stacked dots two such layers exist, allowing the possibility of coupling via the holes. In doubly stacked dots, there is only such layer, thus coupling is absent. Our model is consistent with measurements of the exciton masses and radii in the dots, and with calculations of electron and hole wavefunctions in self-assembled quantum dots.

1. Introduction

Vertically-aligned stacks of coupled self-assembled quantum dots have proven very interesting for the implementation of quantum dots lasers [1]. Improvements in performance are attributed to the reduction in size fluctuations in such stacks compared to a single layer, as demonstrated by the decrease in the photoluminescence (PL) linewidth [2,3]. Stacked layers of quantum dots are also interesting for the study of quantum-mechanical coupling phenomena, and as we shall show, have the potential to reveal quite detailed information about the electron and hole confinement in such structures. We have recently reported PL measurements on triply-stacked layers of self-assembled InP quantum dots in high magnetic fields [4]. These measurements revealed that the dots become strongly coupled for layer separations ≤4 nm. Besides the reduction in PL linewidth [3], we also observed two new effects by applying the field perpendicular to the growth direction: an increase in the size of the PL shift signalling a reduction in confinement due to coupling, and a highly unconventional field dependence of the PL line. (In order to make a useful comparison with the new data, some of these results are reproduced in fig.1 and table 1.) Here, we present data on a sample which has two stacked-layers of InP dots separated by 4 nm, but is otherwise identical to its triple-layer counterpart. In stark contrast to the latter, the double-layer sample shows no evidence of coupling. We explain this rather suprising result by proposing that coupling occurs via holes confined in the GaInP matrix separating the stacked dots. The triple-layer sample has two such layers, so coupling can occur, whereas in the double-layer sample only one such layer exists, so coupling is excluded. We show that this explanation is consistent with our measurements of the

No. of layers	PL linewidth	μ (m_0)	$\sqrt{\langle \rho^2 \rangle}$
1	43 meV	-	-
2	43 meV	0.25±0.003	8.1±0.3 nm
3	28 meV	0.12±0.001	8.0±0.02 nm

Table 1: Photoluminescence linewidth, exciton masses and radii for the three samples.

exciton masses and radii in the dots, and with calculations of electron and hole wavefunctions in self-assembled quantum dots [5,6].

2. Experimental details

The sample consisted of two stacked-layers of self-assembled InP quantum dots (nominally 3.0 ML) separated by 4 nm, and embedded in a GaInP matrix. Details of the growth procedure can be found elsewhere [3]. PL spectra were taken at 4.2 K in a 50 T pulsed field magnet, using a bundle of seven 400 μm core fibres to transmit the light from a frequency-doubled solid-state laser operating at 532 nm, and to collect the PL. Magnetic field (B) discrimination of ±1% (or ±3%) was achieved by gating the intensifier of a CCD detector at the peak (or during the down sweep) of the pulse for 1.8 ms (0.3 ms). The energy of the centre of mass of the PL peak (E_{CM}) was obtained to within 1 meV by numerical analysis. A separate analysis of the PL peak showed it to be a Gaussian with a width that did not vary with B.

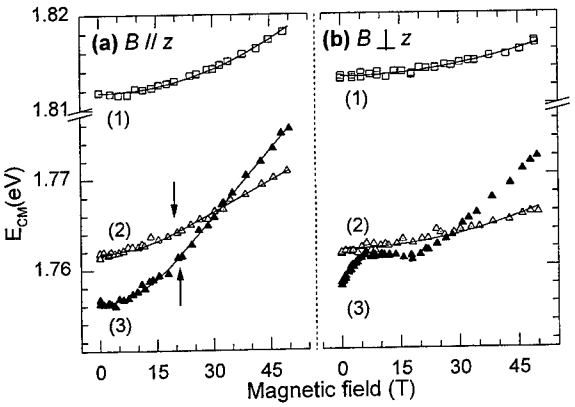

Fig. 1: E_{CM} with the field applied (a) parallel and (b) perpendicular to the growth direction (z) for the single (1), double (2) and triple-layer samples (3). The lines are fits to the data using eqn. (1).

3. Results

Fig. 1 presents the variation of E_{CM} with B applied parallel and perpendicular to the growth direction. Also shown are the data for the equivalent triple-layer and for single-layer samples studied previously [4]. The solid lines are a fit to

$$E_{CM} = E^0_{CM} + \frac{e^2\langle\rho^2\rangle}{8\mu}B^2 \qquad \text{for} \qquad B < \frac{2\hbar}{e\sqrt{\langle\rho^2\rangle}} \tag{1a}$$

$$E_{CM} = E^0_{CM} - \frac{\hbar^2}{2\mu\langle\rho^2\rangle} + \frac{\hbar eB}{2\mu} \qquad \text{for} \qquad B > \frac{2\hbar}{e\sqrt{\langle\rho^2\rangle}} \tag{1b}$$

where E^0_{CM} is E_{CM} at zero magnetic field, $\sqrt{\langle\rho^2\rangle}$ is the exciton radius and μ is the reduced mass. E^0_{CM}, $\sqrt{\langle\rho^2\rangle}$ and μ are fitting parameters. The crossover between the parabolic (low field) and linear (high field) regimes occurs when the magnetic length is equal to $1/\sqrt{2}$ times the exciton radius, and is indicated by arrows in the figure. For fits where there is no arrow the data remains parabolic at large B, i.e. the high field regime is not reached.

The effects on the PL of coupling between dots can be demonstrated by comparing the triple-layer and single-layer samples. In the first instance, there is a large decrease in the PL linewidth (table 1), which is widely attributed to the decrease in size fluctuations in coupled dots [2,3]. Secondly, we can see that the shift of E_{CM} with B applied perpendicular to the growth direction is much larger for the triple layer sample than the single layer sample (fig. 1(b)). This is a result of the decrease in the confinement in the growth direction, due to the effects of coupling [4]. Finally, the B dependence of E_{CM} in fig. 1(b) does not conform to the usual form given by eqn. (1) for the triple layer sample, which we also attribute to the effects of coupling between the dots. The same features might also be expected in the case of the double-layer sample, but this is not the case. In the first instance the PL linewidth is the same as the single-layer sample, and not the triple-layer sample (table 1). Secondly, when B is applied perpendicular to the growth direction the shift of the PL line is a factor of three smaller for the double-layer sample than for the triple-layer sample (fig. 1(b)). Finally, the shift of the PL line with the field applied in this direction shows the conventional dependence described by eqn. (1a). These facts all indicate that the dots in the double-layer sample are not coupled.

4. Discussion

In order to explain our results we propose that the coupling occurs via the holes, which are weakly confined in the GaInP matrix between the dots. The triply-stacked sample has two such regions, so coupling can occur, whereas the doubly-stacked sample has only one such layer, thus coupling via the holes is impossible. Support for this model comes from theoretical calculations of electron and hole confinement in self-assembled quantum dots [5,6], and from a closer examination of our experimental results.

We first discuss the theory. It has been shown that the hole confinement in self-assembled InP quantum dots does not come from the valence-band offset between the InP dots and the GaInP matrix, since this is negative, but is entirely due to the effects of strain [5]. For an isolated pyramidical-dot the hole wavefunction is expected to form a broken-ring structure around the edge of the dot. On the other hand, the conduction band offset for the electrons is large and positive, so they are strongly confined to the centre of the InP dot. This makes hole coupling much more likely than electron coupling. In our samples the dots are lens or disc-shaped [3] and in closely stacked layers. This is a rather different situation from that considered in the theory, but we might expect the holes to be confined in a similar way in the strained GaInP layer which separates the dots. It has to be remembered that it is the strain induced in this layer by the underlying dot which forms the nucleation zone for the next dot layer, and results in the vertical alignment of the dots in the stack. Calculations for stacks of InAs dots are in support of this conjecture [6]. These have shown that when the InAs dots are sufficiently close the holes become confined by strain in the GaAs separating the dots, despite the fact that for isolated dots they are confined in the InAs dot material by the valence-band offset.

We now turn to a detailed discussion of the measured values for the exciton masses and radii in table 1, which we shall show are also consistent with our explanation. The first piece of evidence is the exciton masses. These are $0.12m_0$ and $0.25m_0$ (m_0 is the mass of the electron) for the triply and doubly-stacked layer samples respectively. The bulk value for InP is $0.0876m_0$. Mass enhancements have also been found in studies of InAs quantum dots [7], and attributed to the effects of strain, but it seems very unlikely that this could account for the almost factor of three increase in mass in the double-layer sample. We suggest that the large masses result from

the fact that the movement of the PL line is dominated by the holes. Eqn. (1) was written in terms of the exciton mass, but it can also be separated into the electron and hole contributions [8]. For the holes to dominate (leading to a large μ) it would be necessary for them to have a large wavefunction spread, and for the electrons to be tightly bound to a small region. This is exactly what we expect from the theory, as discussed above. We believe that the difference in masses between the stacked-layer samples is due to increased hole-wavefunction penetration into the InP for the triply-stacked layers (due to the coupling), compared to the doubly-stacked sample. The effective masses for GaInP are not well understood, and are dependent on the details of ordering within the crystal structure [9], but can be much larger than for InP or InAs: for the thick GaInP waveguide layer in the double-layer sample we find an exciton mass of $0.2m_0$. Turning to the exciton radii for the dots, we find that the values for the both the triple and double-layer samples are the same, and equal to half the dot diameter as measured by TEM [4]. This is also consistent with our proposed model. We note that this result, and the small difference in E^0_{CM} for the stacked-layer samples, both imply that the difference between the samples is the coupling, and not in the dots themselves. Finally, we speculate as to why the single-layer dot sample remained in the low field limit with B applied in the growth direction. In this case the wavefunctions should be much more similar to the calculations for single InP dots discussed above, with the hole wavefunction forming a (broken) ring around the dot. For this configuration the important length scale might not be the diameter of the ring, but its thickness.

5. Conclusions

We have studied the PL of doubly-stacked layers of self-assembled InP quantum dots in fields up to 50 T. In contrast to a nominally identical sample with three layers of dots studied previously, we observe no signs of coupling. We explain this diffference in behaviour using a model in which the coupling is via the holes, which are confined to the GaInP regions separating the InP dots. This is shown to be consistent with theoretical calculations of electron and hole wavefunctions in self-assembled InP quantum dots, and with our experimentally determined masses and radii for the dots.

Acknowledgements: This work is supported by the FWO-Vlaanderen, the Flemish GOA and the Belgian IUAP programmes. M.H. would like to thank the Onderzoeksraad of the Kathlolieke Universiteit Leuven and the Flemish Institute for the Promotion of Scientific-Technological Research in Industry (IWT) for financial support.

[1] D. Bimberg *et al.*, Solid State Electronics **42**, 1433 (1998); M.K. Zundel *et al.*, Appl. Phys. Lett. **73**, 1784 (1998).
[2] G.S. Solomon *et al.*, Phys. Rev. Lett. **76**, 952 (1996); R. Heitz *et al.*, Phys. Rev. B **57**, 9050 (1998).
[3] M.K. Zundel *et al.*, Appl. Phys. Lett. **71**, 2972 (1997).
[4] R. Provoost *et al.*, submitted to Appl. Phys. Lett.
[5] C. Pryor, M-E. Pistol and L. Samuelson, Phys. Rev. B **56**, 10404 (1997).
[6] C. Pryor, Phys. Rev. Lett. **80**, 3579 (1998).
[7] R.K. Hayden *et al.*, Physica B **249-251**, 262 (1998).
[8] I.E. Itskevich *et al.*, Appl. Phys. Lett. **70**, 505 (1997).
[9] P. Ernst *et al.*, J. Appl. Phys. **81**, 2814 (1997).

Auger Processes in InAs Self-Assembled Quantum Dots

P.P. Paskov,[a] P.O. Holtz,[a] S. Wongmanerod,[a] B. Monemar,[a] J.M. Garcia,[b] W.V. Schoenfeld,[b] P.M.Petroff[b]

[a]*Department of Physics and Measurement Technology, Linköping University, S-581 83, Linköping, Sweden*

[b]*Materials Department, University of California, Santa Barbara, California 93106, USA*

Abstract

An experimental evidence of Auger-like excitation processes in InAs/GaAs quantum dots is demonstrated. Photoluminescence spectra of resonantly excited dots exhibit a rich satellite structure below the ground-state emission band. The energy position and the intensity distribution of the satellites are analyzed and an interpretation of the satellites as due to shake-up processes of the interacting carriers in the higher quantum dot states is suggested.

The potential of quantum dot (QD) structures for optoelectronic device applications has been frequently questioned due to the suppression of the carrier relaxation rate in zero-dimensional systems [1]. The discrete nature of the density-of-states dispersion in QD's prevents the effective carrier relaxation unless the electron level spacing is smaller than a few meV to favour the LA-phonon scattering or equals the typical LO-phonon energies. This effect, referred to as the "phonon bottleneck", should result in a considerable reduction of the luminescence efficiency and should also constitute a significant limitation of the performance for QD based devices. The phonon bottleneck problem could be removed or at least reduced if the carrier transfer to lower states could occur via Auger processes [2–4]. Experimentally, Auger processes can be demonstrated by means of satellite spectroscopy. In this case, the photo-excited electron-hole pair interacts with other carriers and as result an excitation of the additional carriers in higher states takes place. These shake-up processes can be monitored in photoluminescence (PL) spectra as satellites which are red-shifted relatively the principal electron-hole pair recombination. The satellite spectroscopy has been a widely used method to study Auger-like processes in semiconductor quantum wells (QW's), but the final state for the interacting carriers varies for different shake-up processes, e.g., a higher Landau level for an electron gas or a negatively charged exciton in a magnetic field [5, 6] and a higher subband for a two-particle transition [7]. The prerequisite for all these processes is the localization of the involved particles. In this respect, the situation should be even more favourable in QD's. We report here satellite spectroscopy experiments on self-assembled InAs/GaAs QD's.

The QD samples used in this study were grown by Molecular Beam Epitaxy on top of an n^+-doped GaAs (100) substrate [8]. The dots were formed by depositing 1.7 InAs monolayers at T_g = 530°C. A growth interruption of 30 s was used to narrow down the size distribution. Then the dots were overgrown at T_g = 530°C with a thin GaAs cap of a thickness adjusted between 1 and 7.5 nm followed by a second 30 s growth interruption and a final capping with GaAs. Atomic Force Microscopy (AFM) after such a growth procedure revealed

well-defined lens-shaped islands with narrow size distribution. With a decrease of the capping layer thickness, the height of the InAs islands is reduced from 10 nm to 1.5–2.5 nm, while their lateral dimensions typically range 60–80 nm [8].

The non-resonant PL spectra of the QD sample at three different excitation intensity are shown in Fig. 1. At low excitation intensity only the QD ground-state emission at 1.303 eV, is

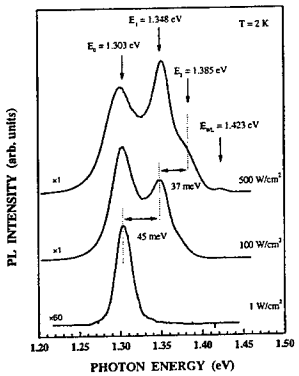

Fig.1 Intensity-dependent PL spectra of the QD sample excited with an Ar^+-laser. The arrows mark the position of the ground-state (E_0), the excited states (E_1, E_2), and the wetting layer (E_{WL}) emissions.

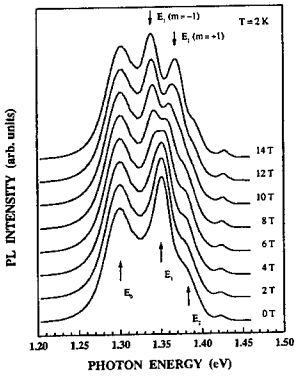

Fig.2 Magneto-PL spectra measured at an excitation intensity of 500 W/cm^2 and different magnetic fields applied parallel to the growth direction.

observed. With an increase of the laser intensity the ground-state emission saturates and two additional peaks attributed to the recombination from QD excited states appear at 1.348 and 1.385 eV. The calculations of the electronic structure of similar lens-shaped InAs/GaAs QD's predict several confined states for electrons and holes [9]. The ground states (s-like shell) have a magnetic momentum m = 0 and can be occupied by only two carriers. The next higher p-like (m = ±1) and d-like (m = 0, ±2) shells can hold up to four and six carriers, respectively. Due to the selection rules, only transitions between states with an equal magnetic momentum are possible. Then we identify the peaks at 1.348 eV and 1.385 eV as the electron-hole recombination from the p-like and d-like shells, respectively. Such an interpretation is confirmed by magneto-PL measurements shown in Fig. 2. In a magnetic field, the second PL peak splits into two bands as expected for a transition between states with p-like character, while the ground-state emission exhibits only a diamagnetic shift of $\approx 10\ \mu eV/T^2$.

The emission of our specially designed samples is at a higher energy than is observed for the standard InAs/GaAs self-assembled QD's. The blue shift of the spectrum enables us to carry out resonant PL spectroscopy by means of a tunable Ti:Sapphire laser. As long as the excitation is above the ground-state emission, the PL spectrum is dominated by the peak at 1.303 eV, but when the laser energy is further down-shifted, novel satellites are observed at lower energies. Figure 3 shows the PL spectrum with an excitation at the maximum of the ground-state emission. There are three distinguishable satellites, labelled S_1, S_1' and S_2. The two sharp lines observed at 33.8 and 36.6 meV below the laser energy correspond to the Raman modes of bulk GaAs TO and LO phonons. With a decreasing excitation energy, the satellites appear at a slightly varying energy separation from the laser energy. This is clearly

illustrated in Fig. 4, where the satellite spectra are plotted with the laser energy as a reference energy. There are several notable observations to be extracted from Fig. 4. As the excitation energy is decreased, the overall intensity level is reduced, since there will be successively fewer dots resonantly excited in this region. There is a general trend towards increasing satellite energies, defined as the energy displacement between the laser excitation and the satellite peak position, with decreasing laser excitation energy. Finally, the satellite intensity distribution is changed in such a way that high energy satellites are enhanced with decreasing excitation energy.

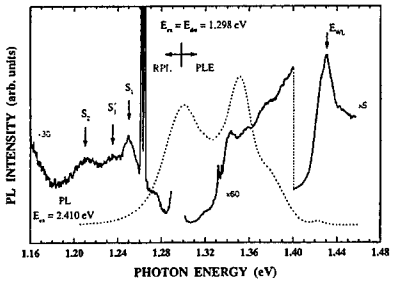

Fig.3 Resonant PL spectrum (RPL) of the QD sample excited at E_{ex} = 1.298 eV and the corresponding PLE spectrum detected at the same energy. The dashed line shows the PL spectrum with a non-resonant excitation.

As can be seen in Fig. 3 the satellite spectrum exhibits a nearly mirror-like symmetry with the corresponding PL excitation (PLE) spectrum. This fact together with the excitation energy dependence of the satellite position implies an electronic rather than phonon related origin of the satellites. The interpretation of the satellite spectra is based on an Auger-like process, in analogy with the earlier reported satellites in QW's [7]. The photo-excited electron-hole pair can interact with other carriers localized in the dot to form biexcitons, charged excitons and/or multiexciton complexes [10, 11]. At the electron-hole recombination, the additional carriers are normally left in their ground-state, however, there is non-zero probability that these carriers are excited into an empty higher state. This will result in a satellite, which is red-shifted relatively the principal electron-hole pair recombination with an energy separation corresponding to the shake-up energy (see the inset in Fig. 4). When an electron-hole pair is shaken up into the first or the second excited state, the satellite energies should be similar to the energy splitting between the emission peaks observed in the non-resonant PL. In fact, the energies of the two predominant satellites S_1 and S_2, 44–52 meV and 84–92 meV, are in a good agreement with the energy separations E_1–E_0 = 45 meV and E_2–E_0 = 82 meV. The excess in satellite energy can be attributed to the biexciton binding energy of 2–4 meV [11]. The satellites S_1' and S_2' appear at an energy of 13–15 meV higher than the satellites S_1 and S_2, respectively. This energy separation is practically independent on the excitation energy implying some kind of pairing between these satellites. Moreover, with decreasing excitation energy, the satellites S_1' and S_2' gain intensity relatively the satellites S_1 and S_2,. The difference in energies of the paired satellites is proposed to be due to the Coulomb blockade effect when the electrons are shaken up into a partly filled

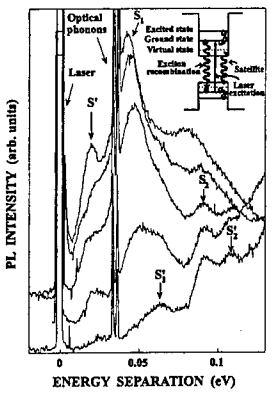

Fig.4 RPL spectra as a function of energy separation from the laser energy. The bottom spectrum corresponds to the lowest excitation energy. The inset shows a schematic description of the shake-up process.

shell. Due to the smaller interlevel spacing, the hole relaxation is much faster and an excess of electrons in the higher states can be expected. In this case, the shake-up energy should overcome the electron-electron interaction and will result in a red-shifted satellite. The estimations of the electron addition energies for p- and d-shell yield a value of 12–14 meV [12], consistent with the observed energy separation of 13–15 meV. Summarising the above consideration, we interpret the satellites S_1/S_1' and S_2/S_2' as a biexciton being the initial state and in the final state one exciton recombines as a satellite, while the second exciton is shaken up into the first or the second excited state, respectively. The origin of the weak satellite S′ is currently not fully understood, but one possible explanation is a recombination of a negatively charged exciton and a shake-up of the second electron into the p-like electron shell. The energy of S′ (21–25 meV) is very close to the electron single-particle energy of 24 meV as estimated from the simple parabolic potential model [12].

The increase of the satellite energies with decreasing excitation energy is explained in terms of a varying QD size. When the laser energy is down-shifted from the maximum of the ground-state emission, the thicker dots are excited. These dots have a smaller lateral dimension as shown by AFM [8] and consequently, a larger intersubband spacing. The trend of the satellite energies is consistent with the results from PL measurements on other QD samples from the same growth series. The PL spectrum of the samples with a capping layer of 7.5 nm is shifted towards lower energies with the ground-state emission peaking at 1.16 eV, while the spacing between the emission bands increases to about 72 meV.

In conclusion, satellite spectroscopy has been performed to study Auger-like processes in InAs/GaAs self-assembled QD's. The rich satellite structure observed with a resonant excitation of the low energy part of the PL emission is interpreted as being to shake-up processes of interacting carriers in the QD excited states.

References

1. H. Benisty, C.M. Sotomayor-Torres, C. Weisbuch, Phys. Rev. B **44**, 10945 (1991).
2. U. Bockelmann, T. Egeler, Phys. Rev. B **46**, 15574 (1992).
3. A.V. Uskov, F. Adler, H. Schweizer, M.H. Pilkuhn, J. Appl. Phys. **81**, 7895 (1997).
4. R. Ferreira, G. Bastard, Appl. Phys. Lett., **74**, 2818 (1999).
5. K.J. Nash, M.S. Skolnick, M.K. Saker, S.J. Bass , Phys. Rev. Lett. **70**, 3115 (1993).
6. G. Finkelstein, H. Shtrikman, I. Bar-Joseph, Phys. Rev. B **53**, 12593 (1996).
7. P.O. Holtz, Q.X. Zhao, B. Monemar, M. Sundaram, J.L. Merz, A.C. Gossard, Phys. Rev. B **50**, 4439 (1994).
8. J.M. Garcia, T. Mankad, P.O. Holtz, P.J.Wellman, P.M. Petroff, Appl. Phys. Lett. **72** 3172 (1998).
9. A. Wojs, P. Hawrylak, S. Fafard, L Jacak, Phys. Rev. B **54**, 5604 (1996).
10. E. Dekel, D. Gershoni, E. Ehrenfreund, D. Spektor, L. M. Garcia, P M. Petroff, Phys.Rev.Lett. **80**, 4991 (1998).
11. M. Bayer, T. Gutbrod, A. Forchel, V. D. Kulakovskii, A. Gorbunov, M. Michel, R. Steffen, K. H. Wang, Phys. Rev. B **58**, 4740 (1998).
12. R. J. Warburton, B. T. Miller, C. D. Durr, C. Bödefeld, K. Karrai, J. P. Kothaus, G. Medeiros-Ribeiro, P. M. Petroff, S. Huant, Phys. Rev. B **58**, 16221 (1998).

EXCITONS IN SELF-ASSEMBLED QUANTUM RING-LIKE STRUCTURES

H. Pettersson, R. J. Warburton, A. Lorke, K. Karrai, and J. P. Kotthaus
Center for NanoScience and Sektion Physik, Ludwig-Maximilians Universität, Geschwister-Scholl-Platz 1, 80539 Munich, Germany

J. M. Garcia and P. M. Petroff
QUEST and Materials Department, University of California, Santa Barbara, California 93106

Abstract

A remarkable morphological change of self-assembled InAs quantum dots takes place during growth if a pause is introduced after overgrowing the dots with a few nm of GaAs. Atomic force microscopy indicates that the shape of the dots changes lens-like to ring-like. We report here the results of capacitance and interband transmission experiments on such ring-like structures embedded in a GaAs matrix. In particular, we compare the electronic properties of conventional dots with those of the rings. Significant changes are found which qualitatively support a quantum ring model.

Self-assembly offers an attractive route for nano-structuring semiconductor materials. In particular, the Stranski-Krastanow growth mode can be used to produce InAs quantum dots in GaAs. The dots are typically lens shaped [1]. However, this is not the only possibility. It has been shown that a pause in the growth after the deposition of the InAs dots and a few nm of GaAs induces a remarkable transformation in the dots' shape from lens-like to ring-like [2]. This is probably driven by lateral diffusion of indium. We report here experiments to probe the electronic structure of these rings.

The samples were are all grown by solid-source molecular beam epitaxy. A nominal deposition of approximately 1.7 monolayers of InAs results in lens-shaped islands of 20 nm diameter and 6 nm height, with a typical density of about 10^{10} cm^{-2}. If a short interruption of a few minutes is introduced after a 1 nm overgrowth of GaAs, the shape of the quantum dots changes to a ring-like structure with an outer diameter of about 80 nm and an inner diameter of about 30 nm [2]. The self-organized quantum rings are subsequently completely overgrown. The rings are embedded in a MISFET-type of heterostructure where a highly doped GaAs layer serves as a back contact, and a metal layer on the surface as a Schottky contact [3,4]. The distance between the GaAs back contact and the layer with rings is small enough to allow for tunneling which makes it possible to tune the electron occupancy of the rings.

Fig. 1 shows typical capacitance traces obtained by measuring the differential capacitance between the Schottky contact and the buried back contact while sweeping the DC bias. The lower trace shows the differential capacitance spectrum of a dot sample. The observed resonances are due to tunneling of electrons from the back contact into discrete states of the dots. The twin peak at -1 V and the broad peak at -0.3 V correspond to tunneling into the two-fold degenerate s-state and the four-fold degenerate excited p-state of a parabolic confinement. The splitting of the peak corresponding to tunneling into the s-state is due to the electron-electron interaction (Coulomb charging) and amounts to about 25 meV [5]. At 0.1 V, there is a rapid rise in the capacitance which corresponds to tunneling into the wetting layer [3,4]. The upper trace is a differential capacitance spectrum of a ring sample. Comparing the two traces we observe both similarities and differences. The features corresponding to tunneling into the rings are

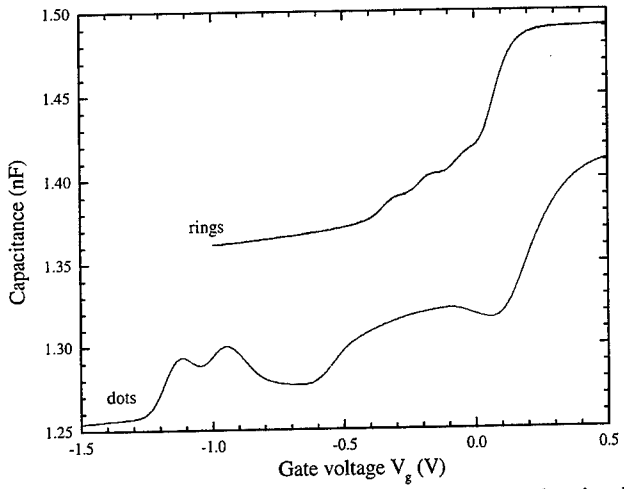

Fig. 1. The differential capacitance for a dot sample and a ring sample are plotted against gate voltage at 4.2 K. In both cases the gate was circular with a diameter of 1.5 mm. The curve for the rings is offset vertically for clarity.

all shifted to much higher voltages but the rapid increase in signal corresponding to tunneling into the wetting layer is at the same voltage. The interpretation is that the rings have a higher ground state energy than the dots, pushing the charging peaks to higher voltage. This can be understood from the AFM measurements: the rings are thinner in the vertical direction than the dots, giving larger vertical confinement energies. The rings exhibit three charging peaks. By calculating the area under each peak, and taking into account the concentration of rings estimated from AFM measurements, we can deduce that each of the peaks corresponds to loading one electron into each ring. We thus conclude that the observed splitting of ca. 20 meV between the first two peaks corresponds to the Coulomb charging energy for two ground state electrons in the ring. This energy is very similar to the charging energy of the dots despite the fact that the rings are considerably larger in diameter than the dots. This suggests that the rings have a different geometry than the dots. Furthermore, the three charging peaks for the rings are approximately equally spaced whereas there is a large gap between the second and third charging peaks for the dots. For the dots, this gap arises from the large quantization energy separating the s- and p-states. In other words, the dots are in the large quantization regime where the single-particle splittings are larger than the Coulomb interactions [6]. For the rings, the equi-distant charging peaks are reminiscent of Coulomb blockade on lithographically defined dots which are in the weak confinement regime where the Coulomb energies dominate over the quantization energies. The implication is that in the rings there are states separated by energies considerably less than the charging energy of 20 meV.

In order to get more information on the electronic structure of the rings, we have performed transmission experiments in the near infrared to detect absorption through interband transitions. Such experiments have already been reported on InAs dots and are particularly useful here because they measure not only the energies but also the oscillator strengths of the various transitions [7]. The absorption measurements on the rings were performed with a Fourier transform spectrometer and a Si p-i-n diode as detector. In Fig. 2 we show an absorption spectrum for dots together with an absorption

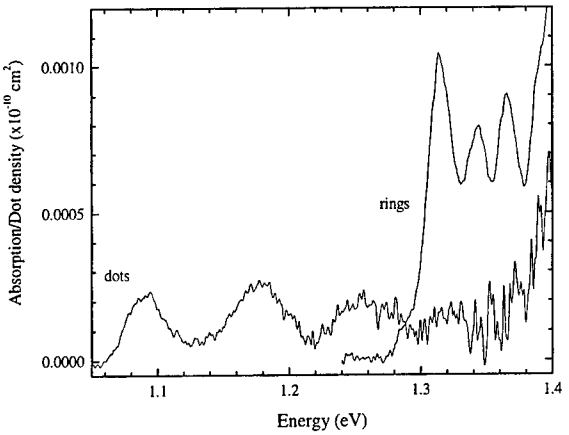

Fig. 2. Absorption per density of absorbers is plotted against photon energy for dots and rings at 4.2 K. The absorption was determined by subtracting the measured transmission from 1. The dot density and the ring density were determined from the capacitance.

spectrum for rings. In both cases, the gate voltage was more negative than the onset of electron tunneling so that we are measuring the properties of neutral rings and dots. Although the dot and ring densities were not identical, we have scaled the dot and ring absorption with the dot and ring densities, respectively, so that the intensities can be directly compared. For the dots we observe three transitions, which denote as s-s, p-p and d-d, labeling the conduction and valence band states as s, p, and d [6]. We observe also three peaks for the rings, but they have quite different properties.

We concentrate initially on the ground state transition. The most obvious effect is that the fundamental transition is at 1.31 eV for the rings, yet only 1.1 eV for the dots. This is consistent with the different onset of charging in the capacitance, and strongly supports the assertion that the vertical confinement energy is larger for the rings. Additionally, the oscillator strengths are quite different in the two cases. We integrate the area of the first charging peak in the capacitance traces to give the dot and ring densities. We then fit the absorption curves to four Gaussian curves, three for the dot or ring resonances and one for the absorption of the wetting layer at large energy. The area of each Gaussian is linearly related to the density of absorbers and the oscillator strength [6]. For the ground state transition, we find f=10.9 for the dots, yet f=31 for the rings. The result for the dots can be understood in the strong confinement picture [6]. The oscillator strength represents simply the overlap between the electron and hole wave functions. The much increased oscillator strength for the rings implies that an exciton in a ring is in the weak confinement limit [8]. This is entirely consistent with the analysis of the capacitance spectra. In terms of the relevant length scales, the conclusion is that at least one dimension of the rings is larger than the excitonic Bohr radius. The picture is that the exciton moves as a composite particle in the complex potential landscape of the ring.

The excited interband transitions also emphasize the point that the rings are quite different from the dots. First, the first excited transition has a lower oscillator strength (18) than the fundamental transition. Conversely, for the dots, the first excited transition is almost twice as intense as the fundamental transition simply because the degeneracy is a factor of two higher. Secondly, the first excited transition for the rings exhibits only a diamagnetic shift on applying a magnetic field, i.e. it has s character. For the dots, the first excited transition splits into two in magnetic field, i.e. it has p

character. Thirdly, we observe quite different behavior of the interband spectra on occupation with electrons.

It might be argued that all our data imply simply that the rings are dots with a smaller vertical dimension but a larger lateral extent. This would account for the shift to positive voltages of the charging peaks, the larger band gap, the equi-distant charging peaks in the capacitance trace and the increased oscillator strength of the exciton. However, it is difficult to account for the large charging energy and in particular the existence of the excited interband transitions in this model. These transitions have the same orbital angular momentum as the ground state transition but yet have higher energy. We propose that the states of the ring can be labeled by two quantum numbers, m and n. m is the quantum number of angular momentum projected along the growth direction and n is the quantum number describing the eigenstates in the radial confinement potential [9]. The separation of the states with different m but the same n can be estimated to be a few meV from the geometry of the rings. Conversely, we propose that the separation of states with the same m but different n is ca. 20 meV for the electrons. In the interband transmission, we see transitions between different sets of radial states. The transitions have an overall s character because various transitions with different m are admixed by the Coulomb potential between electron and hole. These conclusions are in excellent agreement with far infrared measurements of intraband transitions on these structures where a resonance was observed at 20 meV [10] which can be attributed to a transition with $\Delta m=\pm 1$ and $\Delta n=1$.

In conclusion, we have studied self-organized InAs ring-like structures embedded in GaAs using capacitance and transmission spectroscopy. We have compared the results with those from conventional InAs dots and have found significant changes. Our experimental results are consistent, at least qualitatively, with the expected properties of a quantum ring for which the confinement in the radial direction is much larger than the confinement in the orbital direction.

The authors gratefully acknowledge fruitful discussions with A. O. Govorov and R. J. Luyken. One of the authors (H. P.) would like to thank the Alexander von Humboldt foundation for financial support and the group at LMU for their hospitality. This work is supported by the Deutsche Forschungsgemeinschaft (SFB 348).

References

[1] D. Leonard, K. Pond, and P. M. Petroff, Phys. Rev. B **50**, 11687 (1994).
[2] J. M. Garcia *et al.*, Appl. Phys. Lett. **71**, 2014 (1997).
[3] H. Drexler *et al.*, Phys. Rev. Lett. **73**, 2252 (1997).
[4] G. Medeiros-Ribeiros *et al.*, Phys. Rev. B **55**, 1568 (1997).
[5] B. T. Miller *et al.*, Phys. Rev. B **56**, 6764 (1997).
[6] R. J. Warburton *et al.*, Phys. Rev. B **58**, 16221 (1998).
[7] R. J. Warburton *et al.*, Phys. Rev. Lett. **79**, 5282 (1997).
[8] W. Que, Phys. Rev. B **45**, 11036 (1992).
[9] D. Wohlleben *et al.*, Mod. Phys. Lett. B **6**, 1481 (1992).
[10] A. Lorke and R. J. Luyken, Physica B **256-258**, 424 (1998).

PA.39

Self-Assembled Quantum Dots with Well-Resolved Excited-States

S. Fafard, Z. R. Wasilewski, C. Ni. Allen, M. Spanner, J.P. McCaffrey, E.M. Griswold*, K. Hinzer, C. Gould, A. Sachrajda, P. Hawrylak, S. Raymond, J. Lapointe, Y. Fang.
Institute for Microstructural Sciences, National Research Council, Ottawa, Ontario, Canada, K1A 0R6. *Nortel Networks, Ottawa, Ontario, Canada, K1Y 4H7.

Artificial atoms with up to five well-defined electronic shells are fabricated using self-assembled quantum dots (QDs) grown by molecular beam epitaxy. A combination of detailed studies of the growth kinetics with specific growth sequences leads to an additional degree of size and shape engineering, and to tailoring of their intersublevel energy spacings. We demonstrate improved uniformity of the macroscopic ensembles of QDs, with well-resolved electronic shells. In addition to size and shape engineer the QDs in the case of single-layer samples, we demonstrate significant improvements in the uniformity of the vertically self-assembled stacked QDs. The study clearly identifies the key parameters to be controlled: a precise amount of strain material deposited with an appropriate in-plane coverage of QDs, an anneal time which together with the deposition rate allows the QDs to evolve to the desired size and uniformity, a growth temperature which yields QDs with the desired intersublevel energy spacing, and an indium-flush technique which cycles the temperature during the overgrowth of InAs/GaAs QDs. State-filling spectroscopy of the zero-dimensional transitions between confined electrons and holes demonstrates that the energy levels are readily tunable. One to five confined levels, with an inter-level energy spacing between 25 and 90 meV, are obtained by adjusting the growth temperature or with post-growth annealings. Well-defined excited-states are also obtained with stacked layers of vertically self-assembled QDs, and with QDs grown in the active region of devices such as laser diodes or detectors. For example, we demonstrate laser diodes with very low current threshold densities of 13 A/cm2 at 77K and 82 A/cm2 at 15 oC. We also demonstrate how the micro-spectroscopic properties of the single QDs can be correlated with the macroscopic properties of the QD ensemble which emits a well-defined excited-state shell structure. In this presentation, the emphasis will be on recent results obtained for the optical properties of such QDs having well-defined excited-states in an external magnetic and electric fields, or on the effects of charged carriers on the exciton recombination in modulation doped QD structures.

PA.40

INTERDOT COUPLING AND SPECTRAL DIFFUSION: CONSEQUENCES OF WETTING LAYER POTENTIAL FLUCTUATIONS IN SELF-ASSEMBLED QUANTUM DOTS

Hans D. Robinson and Bennett B. Goldberg
Boston University, Physics Dept. Boston, MA 02215

ABSTRACT

A thin quantum well called the wetting layer is created whenever self-assembled quantum dots are fabricated. The wetting layer is highly non-uniform, thereby producing potential fluctuations that influence the physics of the quantum dots. Here we report several effects that are caused by such fluctuations. In particular, light induced spectral diffusion on a very long time scale and interdot coupling are observed in a sample of InAlAs quantum dots. We show that the existence of both these phenomena is due to the wetting layer fluctuations.

PACS: 73.23.Dx, 78.66.Fd, 78.55.Cr
Keywords: quantum dot, self-assembly, wetting layer, spectral diffusion, near-field

1. Introduction

Self-assembled quantum dots (SADs) are manufactured using conventional epitaxial techniques, by growing a semiconductor on a barrier material to which it is strongly lattice mismatched [1,2]. When the thickness of the epitaxial layer reaches a certain critical level, the strain is partially relieved by spontaneous formation of islands in the layer. If the growth is interrupted soon after this transition has occurred, the islands are all dislocation free and relatively uniform in size. The sample is then capped with barrier material, transforming the islands into quantum dots (QDs) that can confine carriers in all three spatial dimensions.

After the dots have formed, some of the QD material remains distributed in a 2-dimensional wetting layer (WL) that connects all the SADs. The WL is highly non-uniform [3], which inevitably leads to potential fluctuations in the barrier separating the dots. These fluctuations can be quite large since the WL is typically quite thin (<20 Å), and occur in the immediate vicinity of the QDs. In spite of this, most studies to date neglect such effects, treating SADs as near ideal zero-dimensional (0D) systems. In this paper we describe several recent observations in a SAD sample that can only be explained by departing from the ideal model to take into account WL potential fluctuations.

The sample consists of an $In_{0.55}Al_{0.45}As$ quantum dot layer embedded in an $Al_{0.35}Ga_{0.65}As$ barrier. This sample is well characterized [4-7], with a dot density of ~200 dots/μm^2, a lateral dot size of ~18 nm, and a ground state-excited state splitting of 35-40 meV, which means that the ground state and two excited states are confined below the ~140 meV lateral energy barrier. In order to resolve the spectral lines from individual SADs, a near-field scanning optical microscope (NSOM) capable of operating at low temperatures was used to limit data acquisition to a small area containing only a few quantum dots.

2. Experimental

A typical photoluminescence (PL) spectrum taken in the optical near-field is shown in Fig. 1. The sharp lines between 1840 meV and 1940 meV are emission from the ground states of individual

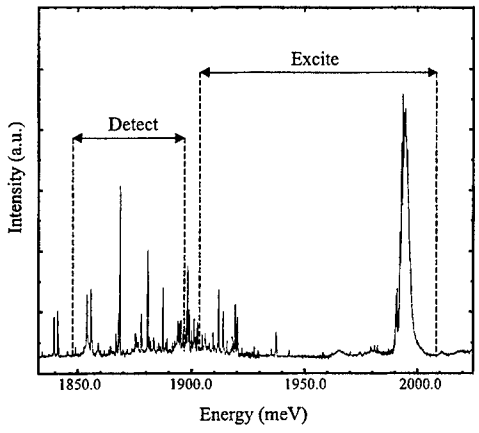

Figure 1. A typical PL spectrum of the sample taken in the near-field. The sharp lines between 1840 meV and 1940 meV are due to individual quantum dots, and the feature at 1995 meV is the WL exciton. Detection and excitation wavelengths for PLE are schematically indicated.

quantum dots, and the feature at 1995 meV is due to the WL exciton. A closer look reveals that the exciton line has significant internal structure.

2.1 Spectral Diffusion

At low optical power, the PL spectrum is stable over time. However, if the power is increased above approximately 2 μW, the energy of the emission lines begin to slowly shift as a function of time, as shown in Fig. 2. This phenomenon is known as spectral diffusion (SD). At sufficiently high powers, we observe SD at a very long timescale (minutes-hours) in virtually all QD lines.

A more extensive analysis of this experiment is published elsewhere [8], and here we only relate the main points of that discussion: Because of the very long time scale of the SD, trapping of charge near the dots is the likely cause. Since the sample is not in mechanical contact with the near-field tip, and other perturbations are unlikely to affect the structure of a hard semiconductor crystal, structural changes can be excluded. The fact that the SD is light induced leads to the same conclusion. Light can generate charges in a semiconductor through several mechanisms, such as photoionization of excitons or auger recombination of biexcitons, and with the WL providing a sufficient number of nearby traps the observations are fully explained. Since we are exciting at energies well below the AlGaAs barrier, these traps must lie in the WL or on its interface with the barrier, where we already known potential fluctuations to exist. We can then conclude that one possible effect of a non-uniform WL is light induced spectral diffusion.

2.2 Interdot coupling

Photoluminescence excitation (PLE) spectroscopy was performed on the sample in the same experimental configuration as described in the previous subsection. The laser was tuned through wavelengths below the WL exciton to

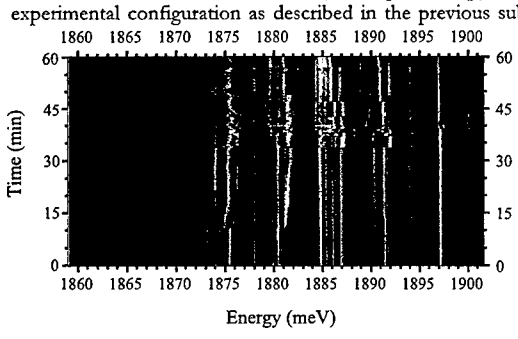

Figure 2. Near-field PL spectra as a function of time and energy of a number of SAD emission lines. The grayscale indicates signal intensity. Total tip output power was 4μW, and the tip-sample distance is 15 nm. Spectral diffusion is clearly visible.

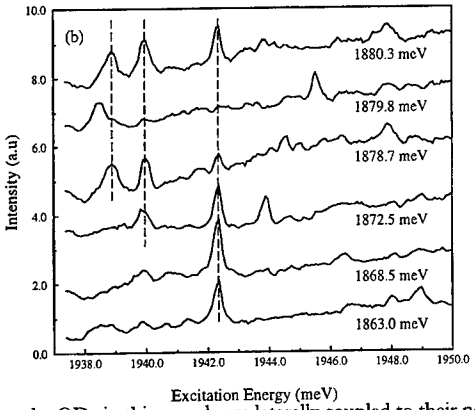

Figure 3. Six simultaneously acquired PLE spectra of different quantum dots. The label of each trace is the detection energy. The dashed lines indicate resonances occurring simultaneously in more than one dot. The traces are offset vertically for clarity.

map out the excited states of individual dots. Resonances consistent with the second excited states of the dots were indeed seen in the data, as shown in Fig. 3. However, as is also clear from Fig. 3, resonances in sets of two or more PL lines often occur at exactly the same excitation energy. It can be shown [9] that each line in such a set in general originates from a separate quantum dot. Hence, a subset of the QDs in this sample are laterally coupled to their neighbors.

There are many mechanisms that could mediate such a coupling. However, since the typical dot-to-dot separation is larger than 10 nm, only Förster [10] (dipole-dipole) interaction is sufficiently long-range to transfer excitation directly over such a distance. The Förster interaction requires overlap between the donor emission spectrum and the acceptor absorption spectrum in order to be non-zero. Since all bound states in the SADs are quite narrow (<0.4 meV) and emission typically is seen only from the ground state, this condition is in general not satisfied.

Thus the lateral interdot interaction is indirect in nature, and we must again invoke the WL potential fluctuation to produce the necessary intermediate states. The precise mechanism for the coupling remains unknown, although multistep exciton tunneling and multiple Förster type energy transfers are two good candidates.

2.3 Other effects

In addition to the phenomena listed above, which are of major importance for the physics of SADs, there are several other ways in which the non-uniformity of the WL manifests itself in our data. We have already mentioned the fact that the PL spectrum of the WL exciton has internal structure not seen in a regular quantum well. Another manifestation is a non-zero PLE signal for laser energies below the WL exciton, where the density of states should be zero for an ideal, uniform WL. This results in a broad tail on top of which we observe the excited state resonances, as is illustrated in Fig. 4a.

The localized states created by the WL fluctuations are also directly visible in PL, although with some difficulty. Examining PL spectra at energies immediately below the WL exciton, one can discern a number of very weak, easily saturable sharp lines, as shown in Fig. 4b. The properties of these states are clearly different from those of the QD states, and therefore their physical origin must be different. In other words, the WL fluctuations are not simply due to unusually small quantum dots.

Finally, we also have preliminary data that suggests that carrier diffusion in the WL in this sample is both anisotropic and inhomogeneous. More data is needed before more definite conclusions can be reached, but the phenomenon would be a natural consequence of a non-uniform distribution of WL potential fluctuations.

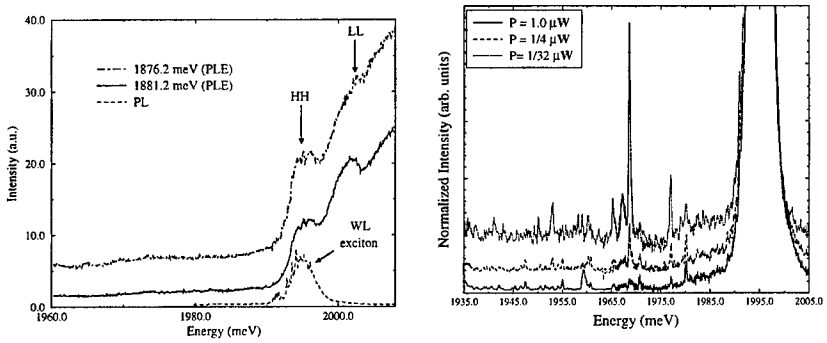

(a) (b)

Figure 4. (a) A comparison of the PLE of two quantum dot emission lines with the PL of the wetting layer exciton. There are no vertical offsets of the graphs. (b) PL with λ_{exc} = 514.5 nm. The spectra have been scaled inversely to power and offset slightly to enable mutual comparison. The heights of the WL exciton peaks at 1995~meV are about eight times the full vertical scale of the figure.

3. Conclusion

We have shown that the WL in a SAD sample contains potential fluctuations that have a strong influence on the physics of the quantum dots. Even though the severity of the fluctuations may be smaller in many other SAD samples, we believe it to be imperative to take them into account when analyzing the results of any experiment in these systems, unless they can independently be shown to be insignificant.

Acknowledgements

This work was supported by NSF Grant No. DMR-9701958. The authors gratefully acknowledge Dr. Rosa Leon, who grew the sample used for these studies, as well as Prof. James L. Merz, Dr. Pawel Hawrylak, and Dr. Richard Mirin for helpful discussions.

References

[1] P. M. Petroff and S. P. Denbaars, Superlatt. Microstruct. **15**, 15 (1994).
[2] M. Grundmann *et al.*, Phys. Status Solidi B **188**, 249 (1995).
[3] R. Heitz, T. R. Ramachandran, A. Kalburge, Q. Xie, I. Mukhametzanov, P. Chen, and A. Madhukar, Phys. Rev. Lett. **78**, 4071 (1997).
[4] S. Fafard, R. Leon, J. L. Merz, and P. M. Petroff, Phys. Rev. B **52**, 5752 (1995).
[5] R. Leon, S. Fafard, D. Leonard, J. L. Merz, and P. M. Petroff, Science **267**,1966 (1995).
[6] R. Leon, S. Fafard, D. Leonard, J. L. Merz, and P. M. Petroff, Appl. Phys. Lett. **67**, 521 (1995).
[7] P. D. Wang, J. L. Merz, S. Fafard, R. Leon, D. Leonard, G. Medeiros-Ribeiro, M. Oestrich, P. M. Petroff, K. Uchida, N. Miura, H. Akiyama, and H. Sakaki, Phys. Rev. B **53**, 16458 (1995).
[8] H. D. Robinson and B. B. Goldberg, submitted for publication (1999).
[9] H. D. Robinson, B. B. Goldberg, and J. L. Merz, submitted for publication (1999).
[10] V. M. Agranovich and M. D. Galanin, *Electronic Excitation Energy Transfer in Condensed Matter* (North-Holland, New York, 1982).

PA.41

Polaritonic coupling and spin dynamics in GaAs microcavities

M. D. Martín [a], L. Viña [a,*], J. K. Son [b], R. Ruf [b] and E. E. Mendez [b]
[a] Dpt. Física de Materiales, Universidad Autónoma de Madrid. E-28049 Madrid, Spain
[b] Dpt. of Physics and Astronomy, SUNY at Stony Brook, N.Y. 11794-3800, USA

Abstract

We have used time-resolved photoluminescence spectroscopy to study the light emission dynamics in a semiconductor microcavity as a function of excitation density and exciton-cavity coupling. We paid special attention to polariton spin relaxation by using circularly polarized excitation. We have found a striking behavior of the photoluminescence degree of polarization, which reaches its maximum value at a finite time. As the excitation density is increased and the system enters the stimulated emission regime, this maximum is followed by a negative dip, whose depth strongly depends on polariton coupling.

Keywords: microcavities; spin relaxation; time-resolved spectroscopy.

PACS numbers: 71.35.Cc, 71.36.+c, 78.45.+h, 78.47.+p

Introduction

Microcavities are designed to enhance light-matter interaction. In the last decade the optical studies on semiconductor microcavities have focused on both low and high excitation regimes. At low powers, the polariton dispersion [1], relaxation [2] and bleaching [3] have been investigated. The high excitation regime has been explored mainly in vertical cavity surface emitting lasers (VCSEL's). Only recently, the spin properties of the carriers and their influence on light emission have been considered in VCSEL's [4, 5] and in microcavities [6]. The intermediate region has not been explored in detail. In this work, we report on the dependence of polariton relaxation and spin dynamics on excitation power.

The samples are grown by molecular beam epitaxy. They include dielectric mirrors separated by an $Al_{0.25}Ga_{0.75}As$ region in which three pairs of coupled GaAs quantum wells (QWs) are placed in the antinode positions of a $3\lambda/2$ planar microcavity. The interruption of the substrate's rotation during growth originates a slight wedge in the cavity thickness, which allow tuning the cavity resonance to the transition in the QW. A detailed description of the sample can be found elsewhere [6]. Our experiments were performed under non-resonant excitation using a conventional up-conversion spectrometer with a time resolution of ~2 ps. The excitation light was circularly polarized and the photoluminescence (PL) emitted by the sample was analyzed into its σ^+ and σ^- components by means of a $\lambda/4$ plate. The time evolution of the PL and of its degree of polarization, $\wp$, were studied as a function of excitation density and exciton-photon coupling.

* Corresponding author. Fax: +(34) 91 397 8579. E-mail: luis.vina@uam.es

Polariton recombination dynamics

Under low excitation density conditions, we have resolved a Rabi splitting ~300 ps after excitation. The splitting varies between 3.5 and 7 meV moving the excitation spot across the sample. This increase is due to the change in the photon-like mode energy caused by the variation of the cavity thickness. Taking into account the results of temperature dependent cw-PL and its magnetic field dependence [7], we have attributed an excitonic character to the lower polariton branch (LPB) and a photonic character to the upper polariton branch (UPB). We have confirmed that, under non-resonant excitation, there is no influence of the coupling strength on the PL's characteristic rise and decay times, in agreement with [8]. These times are similar for both polariton branches and amount to τ_r^X ~100 ps, τ_d^X ~300 ps, τ_r^γ ~70 ps, τ_d^γ ~250 ps, where X(γ) and r(d) denote exciton-(photon-) like and rise (decay) time, respectively.

At high excitation densities the light emission dynamics changes drastically. Figure 1 depicts a time-resolved PL spectrum taken 60 ps after excitation: the LPB appears as a very narrow peak (FWHM<1 meV), together with a broader UPB (FWHM~2 meV). Changing the detuning permits a control of their relative intensities. Figure 2 shows the time evolution of the PL measured at the cavity mode energy for two different excitation densities. At low densities (~50 kW/cm^2, •) the behavior is similar to that found, under non-resonant excitation, for excitons in QWs: the emission begins at zero time delay and is characterized by slow rise- and decay-times. The evolution is markedly different for high densities (~650 kW/cm^2, o). There is an onset of the PL at ~30 ps, followed by a very fast rise and decay [9]. This finite time for the PL onset is related to the accumulation and relaxation of excitons, created above the cavity's stop band, towards energies where they can couple with the cavity.

The initial rise of the PL time evolution can be characterized by its curvature, η. The inset of Fig. 2 depicts η versus excitation density at 20 ps. A large increase is seen for excitation densities above 500 kW/cm^2. The integrated emission of the LPB presents a similar threshold density, as shown in the inset of Fig. 1. The threshold for both quantities increases as exciton-cavity coupling is reduced. All these findings lead us to identify the narrow peak as the stimulated emission of the LPB.

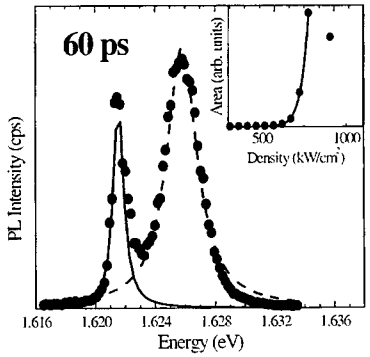

Fig. 1.- PL spectrum 60 ps after excitation with ~500kW/cm^2, E_{exc}=1.706 eV at 5 K. The inset shows the excitation density threshold of the integrated emission of the LPB.

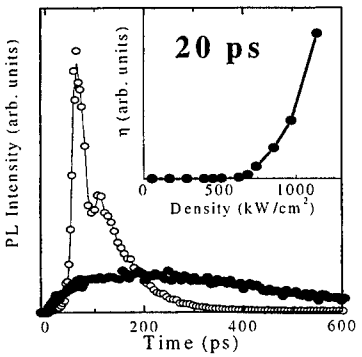

Fig. 2.- Time evolution of the cavity mode for low(•) and high (o) excitation densities. Inset: PL's initial rise curvature as a function of excitation density.

Under high excitation conditions, the LPB is photon-like, while the UPB is exciton-like. Following the temporal evolution of both polariton branches, a clear anticrossing is observed once the stimulated emission is over [6]. At long times (>500 ps) the LPB (UPB) recovers its exciton-like (photon-like) character. The stimulated emission has heavily decreased the polariton population and the emission spectra are now similar to those obtained under low excitation densities.

Polariton spin dynamics

In the following, we will call spin to the third component of the total angular momentum. An analysis of the temporal evolution of the PL's degree of polarization, $\wp$, gives direct information about the spin relaxation. Under σ^+ excitation, $\wp$ is defined as $(I^{\sigma^+} - I^{\sigma^-})/(I^{\sigma^+} + I^{\sigma^-})$ and is directly related to the difference between +1 and −1 spin populations. $I^{\sigma^\pm}$ denotes the PL emission with ±1 helicity. In a QW, a σ^+ pulse will mainly create +1 excitons with center of mass momentum $\mathbf{K}\neq 0$. During their relaxation towards $\mathbf{K}=0$ a −1 population will appear as a result of spin-flip processes. Eventually, both populations will be equal and therefore $\wp$ will vanish.

We have found that the time evolution of $\wp$ in a microcavity is very different to that typical of isolated QWs [10]. For bare excitons, $\wp$ reaches its maximum almost instantly after excitation. Then, spin relaxation processes will take $\wp$ back to zero. Let us concentrate first on the behavior of $\wp$ in microcavities at moderate excitation densities. Figure 3 shows the time evolution of $\wp$ of the cavity mode for different excitation densities: (*) and (o) below the threshold for stimulated emission and (♦) at threshold. The initial value of $\wp$ is only ~10% and $\wp_{max}$ occurs a few tenths of ps after excitation. The value of $\wp_{max}$ increases strongly with increasing excitation density, reaching values as high as 80%. The delay to reach $\wp_{max}$ increases both with exciton-cavity coupling (not shown) and with excitation density (Fig. 3). The fact that a finite time is needed to reach $\wp_{max}$ implies that the exciton-cavity field interaction favors +1 polaritons at expenses of the −1 population. This process competes with the spin-relaxation, which tends to equalize both populations.

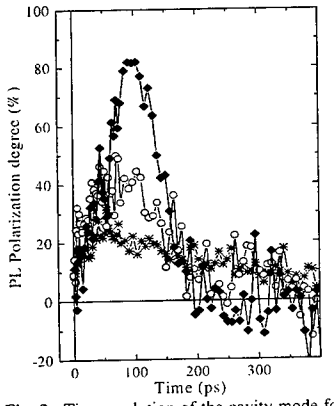

Fig. 3.- Time evolution of the cavity mode for different excitation densities: I_0 (*), 2.3 I_0 (o), 3 I_0 (♦).

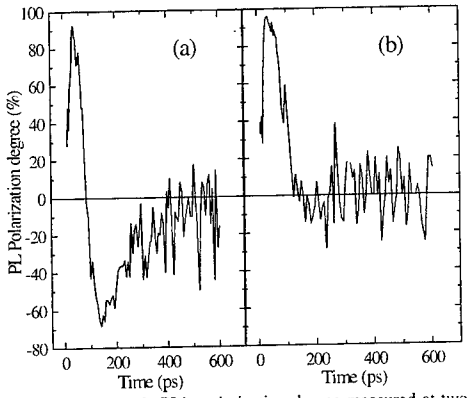

Fig. 4.- Cavity mode PL's polarization degree measured at two different points of the sample, with high (a) and low (b) exciton-cavity coupling. The experimental conditions were the same for all the measurements.

Above the threshold for stimulated emission the time evolution of $\wp$ becomes even more conspicuous. Figure 4 demonstrates that the +1 polaritons are initially 65% of the total population, i.e. $\wp$~30%, and they increase up to a 95% at ~30 ps. The value of $\wp_{max}$ does not depend on coupling strength. However, the temporal evolution of $\wp$, after the maximum is reached, is drastically modified by the detuning. For small Rabi splitting, Fig. 4a, a negative dip is observed (–60%), which is a consequence of the fast emptying of the +1 spin population due to the stimulated emission. The –1 polariton population exceeds the +1 and negative values of $\wp$ result. When the minimum value of $\wp$ is reached the stimulated emission is over, and the majority –1 polaritons will "slowly" relax their spin, bringing $\wp$ back to zero. Figure 4b shows that, for larger Rabi splittings, the negative dip disappears due to modification of the stimulated emission dynamics by the exciton-cavity coupling strength.

In summary, we have found evidence for simulated emission for the lower polariton branch in a microcavity. We have demonstrated the influence of coupling strength on the polariton dynamics. The PL degree of polarization has a maximum at finite times. This delay depends strongly on excitation density and Rabi splitting. A reversal of the polariton's spin is observed for small exciton-cavity detuning.

This work has been partially supported by "Fundación Ramón Areces", Spanish DGICYT under contract PB96-0085, the Spanish-U.S Joint Commission and the US Army Research Office.

References

1. C. Weisbuch, M. Nishioka, A. Ishikawa and Y. Arakawa, *Phys. Rev. Lett.* **69**, 3314 (1992). R. Houdré, C. Weisbuch, R. P. Stanley, U. Oesterle, P. Pellandini and M. Ilegems, *Phys. Rev. Lett* **73**, 2043 (1994).
2. T. B. Norris, J. –K. Rhee and C. –Y. Sung, *Phys. Rev.* B **50**, 14663 (1994). B. Sermage, S. Long, I. Abram, J. Y. Marzin, J. Bloch, R. Planel and V. Thierry-Mieg, *Phys. Rev.* B **53**, 16516 (1996).
3. R. Houdré, J. L. Gibernon, P. Pellandini, R. P. Stanley, U. Oesterle, C. Weisbuch, J. O'Gorman, B. Roycorft and M. Ilegems, *Phys. Rev.* B **52**, 7810 (1995).
4. J. Martín-Regalado, F. Prati, M. San Miguel and N. B. Abraham, IEEE *J. Quant. Elect.* **33**, 765 (1997).
5. H. Ando, T. Sogawa and H. Gotoh, *Appl. Phys. Lett.* **73**, 566 (1998).
6. M. D. Martín, G. Aichmayr, L. Viña, J. K. Son and E. E. Mendez, To appear in Proc. 23rd Int. Conf. on the Physics of Semicond. (1999).
7. I. W. Tao, J. K. Son, C. Pecharromán, E. E. Mendez and R. Ruf, *Physica* E **2**, 685 (1998).
8. I. Abram, B. Sermage, S. Long, J. Bloch, R. Planel and V. Thierry-Mieg in *Microcavities and Photonic Bandgaps: Physics and Applications. NATO ASI Series* E Vol. **324**, edited by J. Rarity and C. Weisbuch, 69 (Kluwer Academic Publisher, 1996).
9. The peak at 110 ps is due to spin effects.
10. T. C. Damen, L. Viña, J. E. Cunningham, J. Shah and L. J. Sham, *Phys. Rev. Lett.* **67**, 3432 (1991).
11. The same behavior is observed for the UPB, but the effect is much smaller ($\wp_{max}$~60%).

PA.42

EXCITONS IN QUANTUM DOTS: DEPENDENCE ON BARRIER HEIGHT, DOT SHAPE, AND PROFILE OF BOUNDARY DIELECTRIC MISMATCH

P. G. Bolcatto and C. R. Proetto

Centro Atómico Bariloche and Instituto Balseiro, (8400) S. C. de Bariloche, Río Negro, Argentina

The excitonic properties of semiconductor quantum dots have been theoretically analyzed, in the strong confinement approximation and within the framework of the effective mass approximation. Realistic features such as the finite barrier height, the shape of the dot, and the dielectric mismatch at the dot boundary are included in the calculations. Excellent qualitative and quantitative agreement has been found for the unscreened Coulomb energy and exchange splitting with state-of-the-art calculations. Concerning the dot shape, strong similarities have been found between spherical and cubic dots, even in the presence of strong dielectric mismatch. For the case of spherical dots with finite confining barriers, we have studied the effects of giving a finite spatial size to the transition of the dielectric mismatch, instead of the physically unrealistic and mathematically ill-behaved step function usually employed.

SPIN POLARIZATION OF A 2DEG NEAR $\nu = 1$ FROM NUCLEAR MAGNETIC RESONANCE OF Ga NUCLEI

V. Bayot and S. Melinte
Université Catholique de Louvain, B-1348 Louvain-la-Neuve, Belgium

N. Freytag, L.-P. Lévy, M. Horvatic, and C. Berthier
Grenoble High Magnetic Field Laboratory, MPI-CNRS, F-38042 Grenoble, France

M. Shayegan
Department of Electrical Engineering, Princeton University, Princeton, New Jersey 08544

We report nuclear magnetic resonance (NMR) measurements on an electron-doped GaAs/AlGaAs multiple-quantum-well heterostructure. The ^{69}Ga and ^{71}Ga NMR spectra were obtained using a standard spin-echo technique for Landau-level filling factor $\nu \leq 2$ and temperatures $0.1\ \mathrm{K} < T < 10\ \mathrm{K}$. We have determined the Knight shift K_s of Ga nuclei located in the quantum wells, which provide direct insight to the electron spin polarization of the two-dimensional electron gas (2DEG) in the fractional quantum Hall regime.

By subjecting the 2DEG *only* to a perpendicular magnetic field, at $T = 1.3$ K, we find that K_s displays a sharp maximum centered at $\nu = 1$ ($B = 5.7$ T). The peak evokes the presence of Skyrmions in the $\nu = 1$ electronic ground state [1]. Compared to results reported in Ref. [2], the measured spin depolarization away from $\nu = 1$ is substantially weaker. The data revealed a monotonous increase of electron spin polarization in the low-filling regime, without any sharp features at fractional fillings. For surveyed filling factors where the ground state is expected to be completely polarized, K_s at $T = 1.3$ K does not reach the saturation value of about 23 kHz (measured near $\nu = 1/3$ at $T \leq 0.3$ K). The Knight shift shows a marked increase when ν approaches 1/3, which is suggestive for the formation of spin-reversed charged excitations near $\nu = 1/3$ much consistent with optically pumped NMR results [2].

The Knight shift was also obtained as a function of the angle θ between B and the normal to the plane of the 2D electron layers, varying from 0° to 90°. From the angular dependence of K_s we found that the electron spin polarization goes to zero when $\nu \rightarrow 2$, as expected in the independent electron model. Particularly striking is the fact that K_s fails to exhibit a maximum near $\nu = 1$ when a strong magnetic field ($B = 14.8$ T) is applied to the sample. In fact, the theory of the $\nu = 1$ quantum Hall state [1] predicts that a transition from Skyrmions to single spin-flip excitations occurs when the ratio $\eta = |g^*|\mu_B B/(e^2/\varepsilon l_B)$ between Zeeman and Coulomb exchange energies ($|g^*| \approx 0.44$, $\varepsilon \approx 13$, $l_B = (\hbar/eB_\perp)^{1/2}$ is the magnetic length) exceeds a critical value. The results described here show compelling experimental evidence for such transition, driven by tilting the magnetic field, in our sample, for $0.022 < \eta_C < 0.037$. This value compares reasonable well with theoretical estimates for the transition at $\eta_C = 0.054$ for an *ideal* 2DEG [1].

[1] S.L. Sondhi, A. Karlhede, S.A. Kivelson, and E.H. Rezayi, *Phys. Rev. B* **47**, 16419 (1993); H.A. Fertig, L. Brey, R. Côté, A.H. MacDonald, *ibid.* **50**, 11018 (1994); E.H. Rezayi, *ibid.* **43**, 5944 (1991).
[2] S.E. Barrett *et al.*, *Phys. Rev. Lett.* **74**, 5112 (1995); R. Tycko *et al.*, *Science* **268**, 1460 (1995).

PA.44

Spin dependent exchange and correlation effects on the orbital magnetization of two–dimensional electron systems

I. Meinel [a], D. Grundler [a], T. Hengstmann [a],
Ch. Heyn [a], and D. Heitmann [a],
W. Wegscheider [b,c] and M. Bichler [b]

[a] *Institut für Angewandte Physik und Zentrum für Mikrostrukturforschung, Universität Hamburg, Jungiusstraße 11, 20355 Hamburg, Germany*

[b] *Walter Schottky Institut, Technische Universität München, Am Coulombwall, 85748 Garching, Germany*

[c] *Universität Regensburg, Universitätsstr.31, 93053 Regensburg, Germany*

Abstract

We have investigated the orbital magnetization of tunable two–dimensional electron–systems (2DES) in GaAs/AlGaAs–heterostructures in the magnetic quantum limit using a high–sensitive superconducting susceptometer. In particular we have studied the magnetization at filling factor $\nu = 1$, where the 2DES forms the quantum Hall ferromagnet. We extract from our data that the orbital magnetic moment is strongly enhanced at low temperatures T by spin–dependent exchange effects. Temperature dependent measurements show that in addition correlation effects dominate the excited states of the many–body system.

The physics of high–mobility 2DES in the extreme quantum limit is known to be ruled by many–body interactions. This leads to the formation of the fractional quantum Hall states and to spin textures (skyrmions) in the excitation spectrum near filling factor $\nu = 1$. The magnetization probes the magnetic–field dependent free energy of an electron system, thus it is an advantageous quantity in order to study the many–body effects on the electron energy spectrum. Collective spin textures have been the subject of extensive experimental studies [1,2] regarding only the bare *spin* magnetism of the 2DES. From the temperature scaling of our data at $\nu = 1$ where the 2DES forms an itinerant ferromagnet we infer a strong coupling between the *spin* and *orbital* magnetic moment.

We have investigated 2DES with an area of about $10\,\mathrm{mm}^2$ in GaAs/AlGaAs–

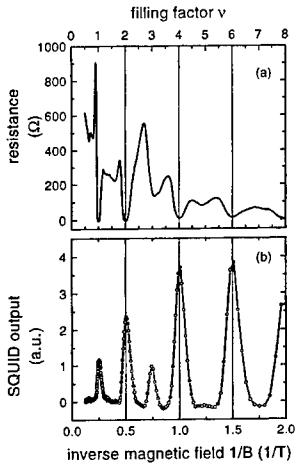

Fig. 1. Magnetoresistance and differential magnetization of sample #1 as a function of magnetic field at zero gate voltage ($T = 0.3\,\mathrm{K}$). Filling factors are indicated on the top axis.

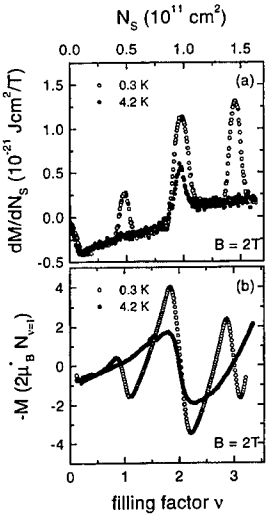

Fig. 2. Differential (a) and absolute (b) magnetization of sample #1 at $B = 2\,\mathrm{T}$, $T = 0.3\,\mathrm{K}$ and 4.2 K.

heterostructures. Via a metal front gate we were able to adjust different carrier densities via the voltage V_g. We have investigated samples from two different wafers with different transport mobilities $\mu = 7\,900\,000\,\mathrm{cm}^2/\mathrm{Vs}$ (sample #1, illuminated) and $1\,000\,000\,\mathrm{cm}^2/\mathrm{Vs}$ (sample #2) at $T = 0.3\,\mathrm{K}$ and carrier densities $n_s = 0.97$ and $2.3 \times 10^{11}\,\mathrm{cm}^{-2}$, respectively. Modulating V_g with a small amplitude we have measured the differential magnetization via a high-sensitive SQUID-susceptometer and a phase-sensitive lock-in technique [3]. This was done either at fixed magnetic field as a function of the carrier density or at fixed carrier density varying the magnetic field in small steps.

Using this technique we always get a maximum SQUID output signal whenever there is a discontinuity in the chemical potential, i. e. in the single-particle picture when the Fermi energy crosses an energy gap. This is in contrast to magnetoresistance measurements where a minimum is observed (see Fig. 1).

The absolute magnetization is obtained from the integration of the differential data with respect to the carrier density. Figure 2 shows the differential (a) and absolute (b) magnetization of sample #1 at different temperatures at fixed magnetic field $B = 2\,\mathrm{T}$. The integrated data show the saw-tooth like de Haas-van Alphen oscillations. Whereas at 0.3 K the structures at odd filling factors are very prominent they totally vanished at 4.2 K. The temperature

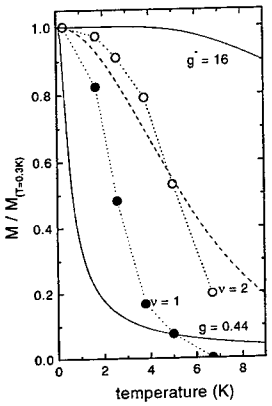

Fig. 3. Temperature dependence of the normalized signal strength at $\nu = 1$ (closed circles) and $\nu = 2$ (open circles) of sample #1. The solid lines show the dependence for $\nu = 1$ obtained from the single–particle model for $g = 0.44$ and $g^* = 16$, respectively. The dashed line shows the single–particle behavior for $\nu = 2$.

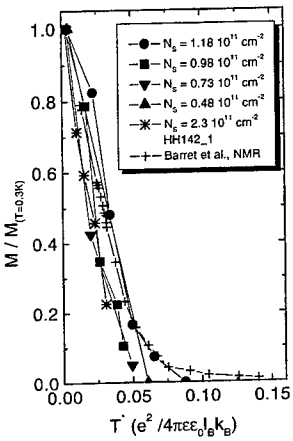

Fig. 4. Normalized signal strength at $\nu = 1$ versus the normalized temperature T^* of sample #1 (closed symbols) at different carrier densities and sample #2 (stars). The crosses are the (corrected) experimental NMR data from [1].

dependence of filling factor 2 is less distinct. From a comparison of the single–particle energy gaps at $\nu = 1$ and $\nu = 2$ one derives for the discontinuities in the chemical potential $\frac{\Delta E_{\text{Zeeman}}}{\Delta E_{\text{Landau}}} = \frac{g\mu_B B}{\hbar\omega_c} = \frac{1}{68}$, with $g = 0.44$ for an electron in GaAs. Our experimental ratio for ΔM per electron is 36 times larger. This indicates that strong electron–electron interaction has to be taken into account at $\nu = 1$. If one would express this enhancement in terms of an enhanced g–factor this leads to $g^* = 36 \cdot g = 16$. This value is significantly larger than ever observed in magnetotransport [5], demonstrating that transport measures a different quantity than magnetization.

In order to elucidate the interaction further, we have measured the temperature scaling of the $\nu = 1$ signal strength which contains information on the many–body excitation spectrum of the quantum Hall ferromagnet. Figure 3 shows the data of sample #1 for $\nu = 1$ and $\nu = 2$. The signal strength M is normalized to its saturation value $M_{(T=0.3\,\text{K})}$ at low temperatures (here at $T = 0.3\,\text{K}$). The temperature scaling of our data at the spin–unpolarized $\nu = 2$ state is approximated quite well (dashed line) by a single–particle model leading to $M(T)/M_{(T=0.3\text{K})} = (T/0.3\text{K}) \cdot \sinh\left(\frac{\pi^2 k_B \cdot 0.3\text{K}}{\mu_B^* B}\right) / \sinh\left(\frac{2\pi^2 k_B \cdot T}{\mu_B^* B}\right)$, $\mu_B^* = e\hbar/2m^*$ is the effective Bohr magneton [4]. The discrepancy is due to electron–

electron interaction causing a renormalization of the free energy also at even filling factors [6]. For $\nu = 1$ the Fermi–Dirac statistics for noninteracting electrons regarding only the low-energy $\nu = 1$ and the upper $\nu = 2$ spin-split Landau Level seperated by the Zeeman energy gap $\Delta E_{\mathrm{Zeeman}} = g\mu_B B$ lead to a temperature dependence $M(T)/M_{(T=0.3\,\mathrm{K})} = \tanh(\Delta \mathrm{E_{Zeeman}}/4\mathrm{k_B T})$. The solid line for $g = 0.44$ fails to fit the data. The experimentally observed signal is enhanced by exchange interaction effects since the degree of spin polarization is high. However, the expected behavior for an assumed factor $g^* = 16$ calculated from Fig. 2 is even worse. Therefore it is of great interest to compare the data with the temperature scaling of the spin polarization. In Fig. 4 NMR data from Barrett et al. [1] (crosses) and our data from the different samples and carrier densities are plotted versus the normalized temperature T^*. T^* accounts for the relevant interaction energy $E_{Coulomb} = e^2/4\pi\epsilon\epsilon_0 l_B$ ($l_B = \sqrt{\hbar/eB}$ is the magnetic length) which is different for different carrier densities (i. e. different magnetic fields at $\nu = 1$). The data of Barrett et al. [1] are corrected in the way that the value at $T = 1.55\,\mathrm{K}$ is supposed to be 80% of the saturation value as described in [2]. Interestingly, the temperature scaling of these *spin* polarization data and our *orbital* magnetization are very similar leading to the conclusion that the *orbital* magnetism is dominated by exchange effects which are maximum at a high degree of spin polarization. In [1] it is pointed out that correlation effects like finite-size skyrmions are the reason for the precipitous drop of the spin moment in the excitation spectrum at $\nu = 1$. In conclusion, the temperature dependence of the magnetization is governed by low lying energy states, i. e. collective spin–waves and not single–particle spin-flip transitions.

We acknowledge financial support by the Deutsche Forschungsgemeinschaft via the Sonderforschungsbereich 508 "Quantenmaterialien".

References

[1] S. E. Barrett, G. Dabbagh, L. N. Pfeiffer, K. W. West, and R. Tycko, Phys. Rev. Lett. **74**, 5112 (1995).

[2] P. Khandelwal, N. N. Kuzma, S. E. Barrett, L. N. Pfeiffer, and K. W. West, Phys. Rev. Lett. **81**, 673 (1998).

[3] I. Meinel, D. Grundler, S. Bargstädt-Franke, Ch. Heyn, D. Heitmann, and B. David Appl. Phys. Lett. **70**, 3305 (1997).

[4] D. Shoenberg, *Magnetic oscillations in metals.* Cambridge, University Press, 1984.

[5] A. Usher, R. J. Nicholas, J. J. Harris and C. T. Foxon, Phys. Rev. B **41**, 1129 (1990).

[6] A. H. MacDonald, H. C. A. Oji, and K. L. Liu, Phys. Rev. B **34**, 2681 (1986).

PA.45

Inelastic Light Scattering by Collective Excitations in the Fractional Quantum Hall Regime

Moonsoo Kang,[1,2] A. Pinczuk,[1,2] B.S. Dennis,[2] M.A. Eriksson,[2]
L.N. Pfeiffer,[2] and K.W. West[2]

[1] *Departments of Physics and Applied Physics, Columbia University, New York, NY 10027*
[2] *Bell Labs, Lucent Technologies, Murray Hill, NJ 07974*

We report an inelastic light scattering study of long wavelength collective gap excitations of fractional quantum Hall (FQH) states at $\nu = \frac{p}{2p+1}$ for $1/3 \leq \nu \leq 2/3$. The ν-dependence of the gap energy suggests a collapse of the collective excitation gap near $\nu = 1/2$. In a range of filling factors close to $\nu = 1/2$, where the FQH gap is believed to collapse, we observe a novel collective excitation that exists only at temperatures below 200 mK.

Inelastic light scattering (ILS) enables the measurement of collective excitation modes of electron liquids in the quantum Hall regimes. Light scattering measurements at $\nu = 1/3$ revealed dispersive gap excitations in the incompressible quantum liquid state [1–3]. These gap modes are understood as charge-density excitations associated with the lowest Landau level [4–6]. The initial light scattering work at $\nu = 1/3$ studied the long wavelength ($q \approx 0$) limit [1], where the modes have finite energy. In subsequent studies, another excitation mode was discovered at lower energy [2,3]. This mode was assigned to the magneto-roton at $q \approx l_o^{-1}$, where $l_o = \sqrt{\hbar c/eB}$ is the magnetic length and B is the perpendicular component of magnetic field. Light scattering by roton modes, with relatively large wave vectors, is explained by a loss of translational symmetry due to residual disorder effects in the FQH state.

Recently, several groups reported theoretical investigations of collective gap excitations. These works are based on Chern-Simons (CS) gauge field frameworks and composite fermion (CF) theory [7,8]. Light scattering studies of gap excitations could thus offer crucial insights on the physics underlying condensation of the 2D system into a FQH liquid. However, in the past, the method has been successful only at $\nu = 1/3$. To the best of our knowledge, light scattering by collective gap modes of other FQH states has not been previously reported. We report here the first inelastic light scattering study of $q \approx 0$ collective excitations in the FQH states at several filling factors within $1/3 \leq \nu \leq 2/3$. Long wavelength collective excitations from incompressible states with marked temperature and magnetic field dependences are observed at ν =1/3, 2/5, 3/7, 2/3, and 3/5. In a range of ν near $\nu = 1/2$, we observe a novel collective excitation that displays a dramatic temperature dependence at $T < 200$ mK.

We measured inelastic light scattering from the high quality 2D electron system in a GaAs single quantum well (SQW) sample of thickness $d = 300$ Å. The electron density (n) in the well is 5.4×10^{10} cm^{-2}. The low-temperature mobility is 7.2×10^6 cm^2/Vs, which is remarkably high considering the low electron density. The sample was cooled down to temperatures as low as 45 mK in a ^{3}He/^{4}He dilution refrigerator / superconducting magnet system with windows for optical access. The power density of the excitation laser was kept

below 10^{-4} W/cm^2 to prevent heating the electron gas. The laser excitation energy was tuned close to the fundamental optical gap of the GaAs SQW to resonantly enhance the light scattering cross-section. The experimental scattering geometry is shown in Fig. 1(b). In such geometry, the light scattering wave vector is $q = 4\pi/\lambda \sin\theta \approx 8 \times 10^4$ cm^{-1}, which gives $ql_o \leq 0.1$. The dynamical structure factor, the function that enters in conventional expressions for the scattering cross sections, is $S(q,\omega) \sim (ql_o)^4$ for $q \to 0$. Since $l_o \sim 1/\sqrt{n}$ for a given ν, we expect to have a larger cross section from samples with lower density. The density in our sample (5.4×10^{10} cm^{-2}) is considerably lower compared to those in the previous literature ($n > 1 \times 10^{10}$ cm^{-2}) [1–3].

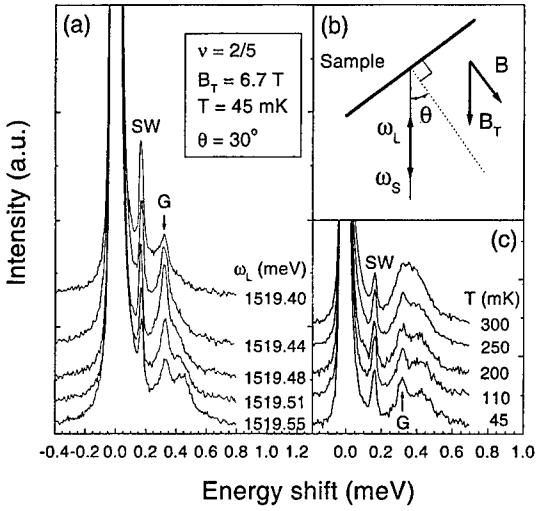

FIG. 1. (a) Resonant inelastic light scattering spectra at $\nu = 2/5$. SW and G denote the long wavelength spin wave and the collective gap excitations respectively. (b) Experimental geometry. (c) Temperature dependence of the light scattering spectra at $\nu = 2/5$.

The collective gap excitation energy at $\nu = 1/3$ is measured to be 0.93 meV (0.081 $e^2/\epsilon l_o$), as also reported elsewhere [1–3]. Fig. 1(a) shows resonant light scattering spectra measured in the FQH state at $\nu = 2/5$. The spectra shown were taken at 45 mK. Sharp features labeled SW are inelastic light scattering by the $q \approx 0$ spin wave (SW) excitation. This mode has energy E_Z, the Zeeman energy of electrons in GaAs. The peaks labeled G are assigned to the $q \approx 0$ collective gap excitation of the FQH state. The broad features under the light scattering peaks are due to photoluminescence, as revealed by the shifts in their positions as the incident photon energy is changed. The collective excitation peak at ν =2/5 is observed below 300 mK as shown in Fig. 1(c). The peak is seen only in a small range of magnetic field close to $\nu = 2/5$. Such well-defined behaviors under changes of temperature and magnetic field indicate that the observed excitation is associated with the FQH state.

The collective excitation energy assigned here to the long wavelength gap mode at $\nu = 2/5$ is 0.32 meV ($0.031e^2/\epsilon l_o$). This determination indicates a significant reduction in energy from the value measured at $\nu = 1/3$. The collective gap excitation measured at $\nu = 3/7$ is at the remarkably low energy of 0.08 meV ($0.0078\ e^2/\epsilon l_o$). Here the light scattering peak has somewhat more pronounced temperature and magnetic field dependences than the light scattering measured at $\nu = 2/5$.

At $\nu \approx 4/9$, a novel collective excitation is observed at energy 0.29 meV. Light scattering by this mode has a surprisingly strong temperature dependence (disappears above 150 mK). This peak, however, does not have a sharp magnetic field dependence. It continues to be observed over a range of filling factors around $\nu = 1/2$ from $\nu \approx 0.43(\approx 4/9)$ to $\nu \approx 0.6(\approx 3/5)$. The persistence of this light scattering peak over a broad range of filling factor may be regarded as evidence that the new excitation, that emerges close to $\nu = 1/2$, is not associated with one of the FQH states.

In the range of magnetic field of $\nu > 1/2$ we observe sharp light scattering peaks which occur at $\nu = 2/3$ and $3/5$. These light scattering features show the characteristic temperature and magnetic field dependences of FQH states. On this basis they could be assigned to $q \approx 0$ gap excitations of the FQH states. The gap excitation peak at $\nu = 2/3$ disappears above 250 mK and the peak at $\nu = 3/5$ above 200 mK. The excitation energies in both states are found to be 0.20 meV, a result that is somewhat unexpected since the gap energy at $\nu = 2/3$ is expected to be larger than the one at $\nu = 3/5$.

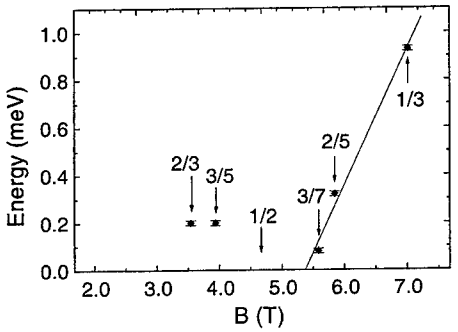

FIG. 2. The energies of long wavelength FQH state gap. The solid line is a linear fit of the gap energies at $\nu = 1/3$, 2/5, and 3/7.

The FQH gap energies at $\nu = 1/3$, 2/5, and 3/7 show almost a linear monotonic decrease as the magnetic field approaches $\nu = 1/2$ as shown in Fig. 2. The linear extrapolation of those points suggests that the FQH gap vanishes at around $\nu \approx 4/9$, well before the system reaches $\nu = 1/2$. Similar behaviors have been previously observed for thermally excited activation gaps in the FQH regime [11,12]. The collapse of the FQH gap before the 2D electron system reaches $\nu = 1/2$ was previously considered to be a consequence of either the broadening of the electronic (fermionic) states due to residual disorder [11], or to the finite

thickness of the 2D electron system [13]. This is an issue that remains to be resolved. It is remarkable that the $q \approx 0$ collective excitation gaps also show a linear behavior similar to the $q \to \infty$ gaps determined in magneto-transport experiments.

The lower limit of ν to observe the new excitation peak ($\nu \approx 0.43$) is close to the filling factor at which the gap collapses in the linear fit. Consequently, this collective excitation might be characteristic of the ground state which takes over from the FQH state at $\nu \approx 1/2$. Understanding the nature of the new excitation mode may give insights on the states near $\nu = 1/2$.

The energy of the collective excitation that emerges near $\nu = 1/2$ has a linear dependence on magnetic field. Its value is close to $1.8E_Z$. This suggests a link to a state constructed from two $q \approx 0$ spin wave excitations. However, the observed reduction in energy from $2E_Z$ and the strong temperature dependence are intriguing. One possible scenario is the presence of a significant interaction between quasiparticles (composite fermions) around $\nu = 1/2$.

In summary, we measured collective gap excitations in various FQH states. The measurements of the energy gaps suggest an instability of the FQH state in the vicinity of $\nu = 1/2$. A novel collective excitation is observed to emerge near $\nu = 1/2$, at the magnetic field close to the one where the FQH gap seems to collapse. Further light scattering studies of this collective excitation may uncover key physics of 2D electron sytem at filling factors near $\nu = 1/2$.

REFERENCES

[1] A. Pinczuk, B.S. Dennis, L.N. Pfeiffer, and K.W. West, Phys. Rev. Lett. **70**, 3983 (1993).

[2] A. Pinczuk, B.S. Dennis, L.N. Pfeiffer, and K.W. West, Physica B **249-251**, 40 (1998).

[3] H.D.M. Davies, J.C. Harris, J.F. Ryan, and A.J. Turberfield, Phys. Rev. Lett. **78**, 4095 (1997).

[4] F.D.M. Haldane and E.H. Rezayi, Phys. Rev. Lett. **54**, 237 (1985).

[5] S.M. Girvin, A.H. MacDonald, P.M. Platzman, Phys. Rev. Lett. **54**, 581 (1985); Phys. Rev. B **33**, 2481 (1986).

[6] S. He and P.M. Platzman, Surf. Sci. **361-362**, 87 (1996).

[7] A. Lopez and E. Fradkin, Phys. Rev. B **47**, 7080 (1993); S.H. Simon and B.I. Halperin, *ibid.* **48**, 17368 (1993); **50**, 1807 (1994); S. He, S.H. Simon, and B.I. Halperin, *ibid.* **50**, 1823 (1994); X.C. Xie, *ibid.* **49**, 16833 (1994); L. Zhang, *ibid.* **51**, 4645 (1995).

[8] R.K. Kamilla, X.G. Wu, and J.K. Jain, Phys. Rev. Lett. **76**, 1332 (1996); R.K. Kamilla and J.K. Jain, Phys. Rev. B **55**, 13417 (1997).

[9] W.P. Su and Y.K. Wu, Phys. Rev. B **36**, 7565 (1987).

[10] P.M. Platzman and S. He, Phys. Rev. B **49**, 13674 (1994).

[11] R.R. Du, H.L. Stormer, D.C. Tsui, L.N. Pfeiffer, and K.W. West, Phys. Rev. Lett. **70**, 2944 (1993).

[12] H.C. Manoharan, M. Shayegan, and S.J. Klepper, Phys. Rev. Lett. **73**, 3270 (1994).

[13] K. Park and J.K. Jain, Phys. Rev. Lett. **81**, 4200 (1998).

PA.46

STRONG BULK–EDGE COUPLING IN THE COMPRESSIBLE HALF–FILLED QUANTUM HALL STATE

Milica V. Milovanović[1,2] and Efrat Shimshoni[2,*]
[1] *Department of Physics, The Technion, Haifa 32000, Israel.*
[2] *Department of Mathematics-Physics, Oranim–Haifa University, Tivon 36006, Israel.*
[*] *Corresponding author*

ABSTRACT

We study bulk and edge correlations in the compressible half–filled state, using a modified version of the plasma analogy. The corresponding plasma has anomalously weak screening properties, and as a consequence we find that charge correlations along the edge do not decay algebraically as in the Laughlin (incompressible) case, while the bulk correlations decay in the same way. The results suggest that due to the strong coupling between charged modes on the edge and the neutral Fermions in the bulk, reflected by the weak screening in the plasma analogue, the (attractive) correlation hole is not well defined on the edge. Hence, the system there can be modeled as a free Fermi gas of **electrons** *(with an appropriate boundary condition).*

1. Introduction

Laughlin's theory of the fractional quantum Hall effect (QHE) [1] was given in terms of wave functions of the ground state and quasihole excitation. Using a plasma analogy to calculate the static many-body correlators, which characterize these wave functions, he was able to advance a very successful physical picture of the electron system. The wave functions, describing the incompressible states, contain the Laughlin-Jastrow factor, which leads to special, later introduced, Girvin-MacDonald (GM) correlations in the bulk [2], and Wen's correlations on the edge [3]. The Laughlin-Jastrow factor is everpresent in QHE states - it exists even in the compressible half-filled state [4], for which an explicit wave–function has been proposed by Read and Rezayi (RR) [5]. The question arises whether its manifestations, in terms of the above mentioned correlations, survive in more general quantum Hall states, and in particular in the compressible states. These correlations provide important information on the nature of charged excitations in the states.

Experimentally, these correlations are in principle accessible by tunneling measurements. Indeed, recent edge–tunneling experiments by M. Grayson et al [6] prompted the question whether the Luttinger liquid picture [3], which is characterized by Wen's correlations, is valid for general QHE systems, including the compressible states. A number of theoretical works [7],[8] have attempted to explain the puzzling results of Ref. [6], in terms of charged excitations on the edge that are effectively decoupled from the bulk [9].

To test these ideas from a microscopic point of view, we focus here on the correlators that characterize the compressible QHE system at filling factor 1/2 [10]. We assume

that the ground state is well described by the RR wave function [5]

$$\Psi_{RR} = \mathcal{P}_{LLL}\{\det_{i,j}[\exp(i\vec{k}_i\vec{R}_j)]\Psi_L\}, \tag{1}$$

where $\mathcal{P}_{LLL}$ stands for the projector to the lowest Landau level (LLL), Ψ_L is the Laughlin wave function with $m = 2$ multiplied by a Slater determinant of free waves. The physical picture underlying this state is that of a condensate of neutral dipoles (electrons bound to correlation holes) that have Fermi statistics [11]. The GM and Wen's correlations (appropriately redefined for the RR state) are then derived [10] employing the analogy with an anomalous, *weakly–screening* plasma. This implies a dramatic modification of the behavior of charged edge excitations with respect to the incompressible states. Below we sketch our derivation and the principal results.

2. Principal Results

The plasma analogy enables the calculation of correlators and expectation values in LLL quantum many–body states, by mapping them onto a classical statistical mechaniscs problem - the two–dimensional Coulomb gas, at an 'inverse temperature' $\beta = \frac{2}{m}$. Thus, for example, the GM correlator corresponding to the Laughlin state $1/m$ can be written as

$$\rho(z, z') = n|z - z'|^{-\frac{m}{2}} \exp\{V_{eff}(z - z')\}\,, \tag{2}$$

where $V_{eff}(z - z')$ is the interaction between two point–like charges (of charge $m/2$ each) immersed in a plasma of charge m particles. A diagrammatic expansion of this interaction [10] yields effectively (in q–space)

$$V_{eff}(|\vec{q}|) = \frac{-\frac{2\pi\beta m^2}{|\vec{q}|^2}}{1 + \frac{2\pi\beta m^2}{|\vec{q}|^2}n}\,, \tag{3}$$

namely, a screened Coulomb interaction. As a result, the GM correlator Eq. (2) acquires the familiar asymptotic form

$$\rho(z, z') \sim |z - z'|^{-\frac{m}{2}}\,. \tag{4}$$

We now consider the parallel of the GM correlator in the 1/2 state (Eq. (1)). The approach mentioned above yields a diagrammatic expansion, in which the vertex is modified by the Fermi correlations in the wave–function. The effective interaction in the fake plasma becomes (at small momenta)

$$V_{eff}(|\vec{q}|) = \frac{-\frac{2\pi\beta m^2}{|\vec{q}|^2}}{1 + \frac{2\pi\beta m^2}{|\vec{q}|^2}s_0(\vec{q})}\,, \quad s_0(\vec{q}) = \frac{3}{4}\frac{k_f|\vec{q}|}{\pi^2}\,. \tag{5}$$

In the coordinate space, at large distances $V_{eff} \sim 1/r$, i.e. it is still long ranged and only *partially screened*. Nevertheless, Eq. (2) implies asymptotically the same algebraic decay of the GM correlations as in the Laughlin states. This signifies the presence of

some kind of bosonic order even in the compressible state, and correspondingly the existence of (weakly localized) vortices (correlation holes) in the bulk.

The weak screening properties of the plasma analogue corresponding to the 1/2 state have a far more significant effect on the edge excitations. To see this, note that in the Laughlin $1/m$–states, within the plasma analogy the unit–charge correlator on the edge of a confined droplet can be related to the following correlator [3]

$$G_c^{(L)}(z,z') \sim \exp\{V_{im}(x)\}\,, \quad x = |z - z'|\,, \tag{6}$$

where $V_{im}(x)$ is the interaction of a confined plasma with a point–like charge m placed at a distance x from its boundary. Due to the perfect screening in the plasma, the correlator behavior is dominaed by the interaction of this external charge with its image,

$$V_{im}(x) = -m\ln(x)\,. \tag{7}$$

Thus, the resulting correlator (which in this case can be directly related to the electron propagator along the edge) exhibits the algebraic decay, $G_c^{(L)} \sim 1/x^m$, characteristic of a Luttinger liquid. In contrast, the anomalous plasma corresponding to the compressible 1/2 state is not sufficiently well screening, and the electrostatic parallel of the image charge term Eq. (7) is found to be (to leading order) independent of x [10]. As a consequence, the correlator G_c is nearly constant, indicating that charged excitations on the edge are not well–defined. This is a signature of a strong coupling between edge and bulk.

To find out the electron correlations, we note that, in the scope of our approach, the electron can be viewed as a composite of a charged object and a neutral component, associated with the Fermi statistics. The neutral component introduces the algebraic decay of free fermions in the final expression for the electron correlator,

$$G_e(x) \sim g\frac{\sin(k_x^F x)}{x}\,, \tag{8}$$

x is a distance along the edge and g is a coefficient that depends on the boundary conditions. Therefore the electron correlations on the edge appear to be as of a free (two-dimensional) Fermi gas of *electrons*.

3. Concluding Remarks

The above results suggest that due to the strong coupling between charged modes on the edge and the neutral Fermions (dipoles) in the bulk, the (attractive) correlation hole is not well defined on the edge. Hence, the system there can be modeled as a free Fermi gas of *electrons*. An experimental indication of a strong bulk–edge coupling at half–filling has been indeed observed in non–local resistance measurements [12].

Finally, while our results contradict the validity of an effective one–dimensional description of the edge excitations on the *static* level, the *dynamics*, in a certain energy range, may decouple the edge and bulk so as to recover the Laughlin–like behavior apparent in Ref. [6] (similar ideas are raised in Ref. 8 as well).

We gratefully acknowledge useful discussions with A. Auerbach, J. Feinberg, J. H. Han, A. MacDonald, R. Rajaraman, N. Read, S. Sondhi, A. Stern and X.-G. Wen. This work was partly supported by grant no. 96-00294 from the United States-Israel Binational Science Foundation (BSF), and the Israeli Academy of Sciences (M.V.M.).

References

1. R.B. Laughlin, Phys. Rev. Lett. **50**, 1395 (1983); R.B. Laughlin in *The Quantum Hall Effect*, edited by R.E. Prange and S.M. Girvin (Second edition, Springer Verlag, New York, 1990).

2. S.M. Girvin and A.H. MacDonald, Phys. Rev. Lett. **58**, 1252 (1987).

3. X.-G. Wen, Phys. Rev. B **41**, 12838 (1990); *ibid* **43** 11025 (1991); X.-G. Wen, Int. J. Mod. Phys. B **6**, 1711 (1992).

4. B. I. Halperin, P. A. Lee and N. Read, Phys. Rev. B **47**, 7312 (1993).

5. E. Rezayi and N. Read, Phys. Rev. Lett. **72**, 900 (1994); *ibid* **73**, 1052 (1994).

6. M. Grayson, D.C. Tsui, L.N. Pfeiffer, K.W. West, and A.M. Chang, Phys. Rev. Lett. **80**, 1062 (1998).

7. S. Conti and G. Vignale, J. Phys. Cond. Matt. **10**, L779 (1998); U. Zülicke and A. H. MacDonald, cond-mat/9802019.

8. D.H. Lee and X.-G. Wen, cond-mat/9809160.

9. See also C. L. Kane, M. P. A. Fisher and J. Polchinski, Phys. Rev. Lett. **72**, 4129 (1994); C. L. Kane and M. P. A. Fisher, Phys. Rev. B **51**, 13449 (1995); A. V. Shytov, L. S. Levitov and B. I. Halperin, Phys. Rev. Lett. **80**, 141 (1998).

10. For more details see M. V. Milovanović and E. Shimshoni, Phys. Rev. B **59**, 10757 (1999).

11. N. Read, Semicond. Sci. Technol. **9**, 1859 (1994); N. Read, Surface Sci. **361/362**, 7 (1996);R. Shankar and G. Murthy, Phys. Rev. Lett. **79**, 4437 (1997); cond-mat /9802244; B.I. Halperin and Ady Stern, Phys. Rev. Lett. **80**, 5457 (1998); V. Pasquier and F.D.M. Haldane, Nucl. Phys. B **516**, 719 (1998); D.H. Lee, Phys. Rev. Lett. **80**, 4745 (1998); N. Read, Phys. Rev. B **58**, 16262 (1998); A. Stern, B. I. Halperin, F. von Oppen and S. H. Simon, Phys. Rev. B **59**, 12547 (1999).

12. J. K. Wang and V. J. Goldman, Phys. Rev. Lett. **67**, 749 (1991); J. K. Wang and V. J. Goldman, Phys. Rev. B **45**, 13479 (1992).

PA.47

Singular Pair Breaking in the Fermion Chern-Simons Theory of the Half-Filled Landau Level[1]

N.E. Bonesteel

Department of Physics and NHMFL, Florida State University

Motivated by recent speculation that the $\nu = 5/2$ fractional quantum Hall state is described by the spin-polarized Read-Moore 'Pfaffian' state — a state which can be viewed, roughly, as a p-wave 'superconductor' of composite fermions — the effect of fluctuations of the Chern-Simons gauge field on the BCS pairing of composite fermions is investigated within the Halperin-Lee-Read formalism. For the case of short-range electron-electron interactions these fluctuations give rise to a $\Delta^{5/3}$ term in the condensation energy and so are sufficiently strong to (i) stabilize the composite Fermi liquid if the pairing interaction is weak enough, and (ii) drive the $T = 0$ pairing transition which eventually occurs as the pairing interaction is increased from second order to first order. For the case of Coulomb interactions the Chern-Simons gauge fluctuations are weaker and a continuous transition may be possible. Work supported by US DOE grant DE-FG0297ER45639 and the A.P. Sloan Foundation.

[1] N.E. Bonesteel, Phys. Rev. Lett. **82**, 984 (1999).

On the high–temperature expansion for a partially filled lowest Landau level

S. Sawatdiaree and W. Apel
Physikalisch-Technische Bundesanstalt, Bundesallee 100, 38116 Braunschweig, Germany.

We study the two-dimensional interacting electron gas in a strong magnetic field in the limit in which all electrons are confined to the lowest Landau level. Reconsidering the high–temperature expansion of the grand canonical thermodynamic potential performed in the work by Zheng and MacDonald, we push the exact expansion up to the seventh order in the interaction. This is done with a method known from expansions in spin systems. The equivalence of this method with the many–body perturbation treatment is explicitly checked up to the third order. We evaluate the series for the case of the short–range electron–electron interaction. As an application, we study the temperature dependent energy. It shows indications of a cusp developing, as expected, at the filling factor 1/3 as temperature is lowered. We confirm this result by extrapolating the energy to zero temperature.

PACS: 73.40.Hm, 71.10.Hf, 71.10.Pm
Keywords: Quantum Hall Effect, Non-Fermi-liquid ground states, Fermions in reduced dimensions

I. INTRODUCTION

The quantum Hall effect continues to be a fascinating topic in condensed matter physics [1,2]. The new ground state wavefunction [3] proposed shortly after the discovery of the fractional quantum Hall effect (FQHE) proved to be an extremely fruitful concept: It lead to the current picture of the FQHE – an incompressible ground state at the "magic" electron densities, separated by a gap from the quasiparticle excitations – and paved the way for many recent developments. While the overwhelming majority of studies deal with zero–temperature properties, much less work has been devoted to finite temperature properties [4,5]. In this contribution, we wish to investigate thermodynamic properties, in particular, the energy of the system as a function of temperature T and electron density. Our motivation is both conceptual and technical:

(i) Typically, the existence of a gap above the incompressible ground state is demonstrated by starting out from Laughlin's ground state [3] and by using a short–range interaction model [6–8]. However, at the other end of the temperature scale, i. e., at high temperatures, there is no preferred state in the thermodynamic ensemble. Extrapolating from high to low temperatures, then, opens a route to proving, without any prior assumption, the existence of a gap.

(ii) In calculations of properties of model systems of interacting electrons, which are confined to the lowest Landau level due to a strong magnetic field, one encounters a number of difficulties. Numerical calculations, being restricted to moderate particle numbers at selected densities, face the problem of an extrapolation to the thermodynamic limit. Analytical calculations, on the other hand, are handicapped by the lack of an expansion parameter, since the electron states of the non-interacting model are degenerate in energy. The temperature variable now provides such an expansion parameter. Moreover, the density, instead of being fixed at selected values as in numerical calculations, can be continuously varied and there is no problem with the thermodynamic limit.

A high–temperature series expansion up to the third order in the interaction has been performed before by Zheng and MacDonald [4]. Here, we wish to reconsider this expan-

sion applying a different method. We reproduce and extend the result of Ref. [4] obtaining the exact series up to the seventh order.

II. EXPANSION PROCEDURE

We study a thermodynamic system of interacting electrons moving in two dimensions in a strong magnetic field B. Considering the high field limit, we restrict the electron states to the lowest Landau level. We thus expect that our considerations are valid for temperature $k_B T < \hbar\omega_c$ where ω_c is the cyclotron frequency. Then, the Hamiltonian reads

$$H = \frac{1}{2} \sum_{k_1,k_2,k_3,k_4} W_{k_1 k_2 k_3 k_4}\, c^\dagger_{k_1} c^\dagger_{k_2} c_{k_3} c_{k_4} \,. \quad (1)$$

Here, we use the Landau gauge with N_ϕ single particle states. The notations are standard. The electron–electron interaction, $W_{k_1 k_2 k_3 k_4}$, can be parameterized by the eigenvalues of the two particle Hamiltonian, the pseudopotentials [6].

We start with expanding the grand canonical thermodynamic potential $\Omega(T, N_\phi, \mu) = -\frac{1}{\beta} \ln\left\{\mathrm{Tr}\left[e^{-\beta(H-\mu N)}\right]\right\}$ with respect to the interaction H. Here, each order in this expansion gives a finite contribution since H is bounded from above. Compared to the standard many–body perturbation approach, the direct expansion has the advantage that there is no need to use the interaction representation and, thus, no frequency sums have to be calculated. In this respect, the high–temperature expansion, presented in this work, is similar to a high–temperature expansion in spin systems [9]. However, there is an important difference. In spin systems, a diagramatic perturbation theory is performed in real space with a short range interaction, while in the present work, (momentum) sums have to be calculated, cf. Eq. (1). In the end, the calculation here is still limited to orders lower than those usually reached in spin systems.

As usual, the expansion involves cumulant averages $< H^n >_c$ taken with the unperturbed statistical operator $e^{\beta\mu N}$. These are now calculated easily by application of Wick's theorem. Consider, as an example, the second order:

$$\lim_{N_\phi\to\infty} \frac{1}{N_\phi} < H^2 >_c =$$
$$f^2\,(1-f)^2\, W_a^{(2)} + 4 f^3\,(1-f)\, W_b^{(2)} \,. \quad (2)$$

f is the Fermi function, $f = 1/(e^{-\beta\,\mu} + 1)$, and $W_{a,b}^{(2)}$ denote the momentum sums :

$$W_a^{(2)} = \lim_{N_\phi\to\infty} \frac{1}{N_\phi} \sum_{\{k_j\}} W_{k_2 k_1 k_3 k_4}\, W_{k_4 k_3 k_1 k_2},$$

$$W_b^{(2)} = \lim_{N_\phi\to\infty} \frac{1}{N_\phi} \sum_{\{k_j\}} W_{k_2 k_1 k_1 k_3}\, W_{k_4 k_3 k_2 k_4}.$$

Generally, a cumulant average $< H^n >_c$ is given by a sum of connected diagrams (as in Eq. (2)) which result from the contractions in Wick's theorem. Each diagram is given by an integer prefactor, a polynomial of the form $f^k(1-f)^{2n-k}$, and a momentum sum, as in $W_a^{(2)}$, which we denote as "pattern". We implemented Wick's theorem in a computer program. The result, for fixed order n, is a list containing prefactor, polynomial, and pattern for each connected diagram.

order n	d	cd	p	pp
1	1	1	1	1
2	3	2	2	1
3	11	8	5	2
4	50	36	14	4
5	242	176	50	10
6	1555	1202	265	42
7	11088	8920	1601	198

TABLE I. Total number diagrams(d), number of connected diagrams(cd), patterns(p) and proper patterns(pp) up to seventh order.

In Table I, we show up to $n = 7$ the number of diagrams, connected diagrams, patterns, and "proper patterns". The latter are those

patterns which do not contain any selfenergy insertion. Note that the number of patterns is about the number of connected diagrams divided by the order n, since each pattern can appear with $\sim n$ different polynomial prefactors.

In the second step of our procedure, we transform to the canonical ensemble by eliminating the chemical potential μ (i. e., f) in favour of the filling factor $\nu \equiv N/N_\phi$. This is done term by term in the expansion with a symbolic computer program. Then, selfenergy patterns, such as $W_b^{(2)}$, cancel out in all orders n and particle–hole symmetry is explicitly restored in the energy $E(T, N_\phi, \nu)$. The result is generally valid for an arbitary interaction.

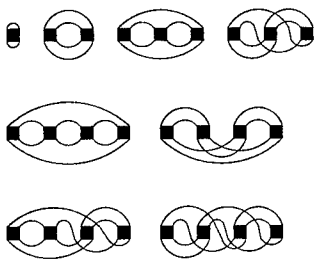

FIG. 1. Proper patterns up to the fourth order.

In the third and last step, we evaluate the momentum sums in the proper patterns for the short range interaction potential. This calculation can also be performed exactly due to the form of $W_{k_2k_1k_3k_4}$ which is Gaussian. Here, the high orders are obtained by using a symbolic computer program with a recursive method. Fig. 1 shows the proper patterns contributing to the calculation up to the fourth order; $W_a^{(2)}$ is the second order. The number of proper patterns given in Table I shows that with our method, one has to calculate only a fraction of the number of diagrams calculated in the standard perturbational approach. We checked the equivalence of both methods explicitly up to $n = 3$.

III. RESULTS AND DISCUSSION

We write the energy $E(T, N_\phi, \nu)/N_\phi = \sum_{n=0}^{\infty} \beta^n \alpha_{n+1}(\nu)$ and take the interaction constant of the short range model as scale for energy and temperature. Then, $\alpha_1(\nu) = 2\nu^2$ and for $2 \leq n \leq 7$, the functions $\alpha_n(\nu)$ are given in Table II. The coefficients result as exact fractions of large integers; for $n = 6$ and 7, we give the leading digits of the coefficients. Fig. 2 shows $e(T, \nu) \equiv E(T, N_\phi, \nu)/N$ as a function of ν for various temperatures. As T is lowered from the high–temperature result (straight line), it can be seen how a cusp develops around $\nu = 1/3$, as expected. Below $T = 0.5$, the compressibility becomes negative, which indicates that we are leaving the region of applicability of the high–temperature expansion. In the first order in ν, our result coincides with the expansion of the second virial coefficient calculated by Tevosyan and MacDonald [5].

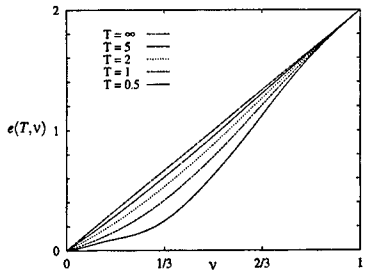

FIG. 2. Energy per particle resulting from the high–temperature expansion up to the seventh order in the interaction for various temperatures as a function of the filling factor.

We conclude by giving preliminary results of an extrapolation to zero temperature. We use the rational Padé approximants of equal degree k in numerator and denominator. From the first seven coefficients in $e(T, \nu)$, one can determine the approximants for $k = 1, 2, 3$. The $[1, 1]$–Padé approximant shown in Fig. 3 coincides with the result in Ref. [4]; note that

n \ p	0	1	2	3	4	5
3	$-\frac{32}{27}$	1				
4	$-\frac{548284}{253125}$	$\frac{352696}{253125}$	$-\frac{1}{3}$			
5	$-\frac{9543734359421915 56}{474812234640253125}$	$\frac{1260938295327852601}{379849787712202500}$	$-\frac{65491329614}{89685275625}$	$\frac{1}{12}$		
6	-5.121609632389	3.490438330504	-3.274027914006	0.186460175728	$-\frac{1}{60}$	
7	-6.234653674573	6.225558335588	-6.163032601771	2.259167774425	0.01011359315068	$\frac{1}{360}$

TABLE II. The coefficient functions $\alpha_n(\nu)$ of the high–temperature series expansion of the energy for the short range model are generally given by $\alpha_n(\nu) = \sum_{p=2-n}^{n-2} C_p^{(n)}\ \nu^{n+p}\ (1-\nu)^{n-p}$. Due to particle–hole symmetry, $C_p^{(n)} = C_{-p}^{(n)}$. The first coefficient $C_0^{(2)} = -2$ and the table shows the coefficients $C_p^{(n)}$ for $3 \le n \le 7$.

Ref. [4] extrapolates the free energy while we extrapolate the energy. The $[k,k]$–Padé approximants are characterized by k poles in the T plane. For $k = 1$, the pole is at negative T for all ν. For $k = 2$, one of the poles is located at large positive T; thus this approximant cannot be used for an extrapolation to low temperature. For $k = 3$, two poles are complex conjugates and one is negative for all ν. Thus, for $k = 3$ (as for $k = 1$) the finite temperature approximant approaches its zero–temperature limit smoothly (and uniformly in ν) as T is lowered and shows a clear indication of a cusp developing at $\nu = 1/3$ as displayed in Fig. 3.

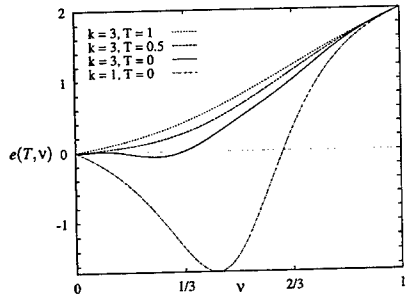

FIG. 3. Padé approximants of order $[k,k]$ for the energy per particle as a function of the filling factor.

ACKNOWLEDGMENTS

One of us (W. A.) thanks A. H. MacDonald for a valuable discussion. This work is supported by the Deutsche Forschungsgemeinschaft under grant No. Ap47/1-2.

[1] *The Quantum Hall Effect*, edited by R. E. Prange and S. M. Girvin (Springer–Verlag, New York, 1987).

[2] *Perspectives in Quantum Hall Effects : Novel Quantum Liquids in Low Dimensional Semiconductor Structures*, edited by S. Das Sarma and A. Pinczuk (John Wiley & Sons, New York, 1996).

[3] R. B. Laughlin, Phys. Rev. Lett. **50**, 1395 (1983).

[4] L. Zheng and A. H. MacDonald, Surface Science **305**, 101 (1994).

[5] K. Tevosyan and A. H. MacDonald, Phys. Rev. B **56**, 7517 (1997).

[6] F. D. M. Haldane, in Ref. [1], Chap. 8.

[7] V. L. Pokrovskii and A. L. Talapov, JETP Lett. **42**, 80 (1985).

[8] S. A. Trugman and S. Kivelson, Phys. Rev. B **31**, 5280 (1985).

[9] C. Domb and M. S. Green, *Phase Transition and Critical Phenomena* (Academic Press, New York, 1974), Vol. 3.

Skyrme liquid vs. Skyrme solid

J. J. Palacios and B. Paredes
Departamento de Física Teórica de la Materia Condensada Universidad Autónoma de Madrid, Cantoblanco, Madrid 28049, Spain.

Abstract

Based on generic sum rules for two-dimensional, isotropic electron quantum liquids in the lowest Landau level, we propose analytic pair distribution functions for spin-polarized and spin-unpolarized liquid phases at filling factors $2/3 \leq \nu \leq 1$. From the pair distribution functions we calculate the energy of such liquid phases and compare with the energy of the solid phase. The comparison suggests that the quantum melting phase transition to the Skyrme solid may lie much closer to $\nu = 1$ than ever expected.

1 Introduction

After Laughlin's proposal of a wave function for the main filling factors $\nu = 1/M$ (where M is an odd integer ≥ 3), many other wave functions have been proposed for other filling factors with notorious success[1]. For many purposes, however, a many-body wave function contains redundant information which can be compacted in a more advantageous way. For instance, the ground state energy per particle, $E/N \equiv \epsilon$, for an infinite, neutral, and isotropic liquid state can be obtained from the pair distribution function $g(r)$[1]:

$$\epsilon = \frac{\nu}{2} \int_0^\infty dr\, r[g(r) - 1]V(r), \tag{1}$$

where $V(r)$ is the interaction potential. In general, $g(r)$ can only be obtained from the wave function using the plasma analogy[1]. On occasions[2], however, one can find an analytic approximation for $g(r)$ based on the fact that it must fulfill generic sum rules. In addition to these sum rules and in order to get the desired accuracy, one must provide microscopic information specific to the quantum liquid state. Here we find $g(r)$ and calculate the energy of spin-polarized and spin-unpolarized quantum liquid phases in the range of filling factors between $\nu = 2/3$ and $\nu = 1$. Exact diagonalizations for $\nu = 2/3$, where we certainly expect liquid phases, and $\nu = 4/5$ allow us to confirm the reliability of this procedure.

Following early work by Girvin[2], we start by noting that the pair distribution function of a liquid state in the lowest Landau level (LLL) can be expanded in terms of wave functions for relative states of two particles:

$$g(r) = \frac{1}{\nu^2} e^{-r^2/2} \sum_{m=0}^{\infty} \langle n_m n_0 \rangle \frac{r^{2m}}{2^m m!}. \tag{2}$$

where the correlation factors $\langle n_m n_0 \rangle \equiv 2\langle c^\dagger_{m\uparrow} c_{m\uparrow} c^\dagger_{0\uparrow} c_{0\uparrow} \rangle + 2\langle c^\dagger_{m\uparrow} c_{m\uparrow} c^\dagger_{0\downarrow} c_{0\downarrow} \rangle$. Girvin noticed that it is convenient to recast this expansion in terms of the pair distribution function for the $\nu = 1$ liquid plus a perturbative series. When the liquid is fully polarized

$$g(r) = 1 - e^{-r^2/2} + e^{-r^2/4} \sum_{m=1}^{\infty} {}'\beta_m \frac{2}{m!} \left(\frac{r^2}{4}\right)^m, \tag{3}$$

where the prime denotes a sum restricted to odd values of m. Since $g(r) \to 1$ for $r \to \infty$ the coefficients β_m vanish for large m. The series can be safely truncated by setting to zero all the coefficients beyond a certain one. The finite set of remaining coefficients is determined by imposing generic sum rules and the short-range behavior of the pair distribution function.

The generalized $g(r)$ for fully spin-unpolarized states (i.e., with equal density of spin-up and spin-down electrons) $g(r) = [g_{\uparrow\uparrow}(r) + g_{\uparrow\downarrow}(r)]/2$, is divided into a contribution coming from equal spin electrons, $g_{\uparrow\uparrow}(r)[\equiv g_{\downarrow\downarrow}(r)]$, and a contribution from opposite spin electrons, $g_{\uparrow\downarrow}(r)[\equiv g_{\downarrow\uparrow}(r)]$. It is natural to expand $g_{\uparrow\uparrow}(r)$ in a way similar to that in (3). It is also convenient to make a similar expansion for $g_{\uparrow\downarrow}(r)$, except for the fact that the sum must run now over all possible non-negative integer values of m.

2 Spin-polarized liquids

We consider first the spin polarized liquid phase and we restrict ourselves to filling factors $\nu = 1 - 1/M$. Particle-hole symmetry allows us to assume a Laughlin state of holes at these filling factors. For these states no pair of holes exists at relative angular momentum lower than M. This restriction yields $\langle n_m n_0 \rangle = 2\nu - 1$ for $m \leq M - 1$ which determines the coefficients $\alpha_m = -(1 - \nu^{-1})^2$ for odd $m \leq M - 2$. Next, we apply the charge neutrality, perfect screening, and compressibility sum rules[2] to the expression (3). and we obtain a set of equations from which we fix the next three coefficients. The charge neutrality and perfect screening sum rules can actually be derived exactly from general considerations applicable to any isotropic liquid state in the LLL[3]. In short, they come about due to the fact that the number of particles and the total angular momentum are good quantum numbers for the Hamiltonian. The compressibility sum rule can only be invoked if there is a classical plasma analog similar to that for the Laughling states[1]. For the filling factors considered here this analog exists[4].

We have calculated the energy using the analytic $g(r)$'s so obtained for $\nu = 2/3$ (-0.518 e^2/ℓ) and $\nu = 4/5$ (-0.552 e^2/ℓ). The values obtained from exact numerical diagonalizations on the spherical geometry for the same filling factors coincide to the fourth digit. The agreement between these two values confirms the existence of a Laughlin liquid state of holes at those filling factors and, moreover, confirms the reliability of the analytic pair distribution functions.

3 Spin-unpolarized liquids

The charge neutrality and perfect screening sum rules can also be imposed to the pair distribution function of the spin-unpolarized liquid. The compressibility sum rule is not invoked this time for we are not aware of any two-species plasma analog for the filling factors considered above. Its existence cannot be discarded though. The spin-degree of freedom breaks the particle-hole duality and no liquid spin-unpolarized wave functions are known for the filling factors $\nu = 1 - 1/M$. However, the hard-core interaction model $V_0 \gg V_1 > V_2 = V_3 \ldots = 0$, where V_i are Haldane pseudopotentials, guarantees that the unpolarized ground state satisfies $\langle n_{0\uparrow} n_{0\downarrow} \rangle = \langle n_{0\downarrow} n_{0\uparrow} \rangle = 0$ for $\nu \leq 1$. It also guarantees the upper limit $\langle n_1 n_0 \rangle \equiv 2\langle n_{1\uparrow} n_{0\uparrow} \rangle + 2\langle n_{1\uparrow} n_{0\downarrow} \rangle \leq (2\nu - 1)$, which is the value associated to the fully polarized state. The inequality reflects the freedom for a pair of particles to occupy states with even

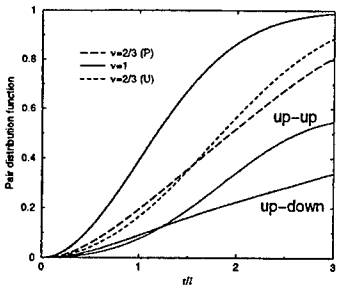

Figure 1: Spin-polarized and spin-unpolarized pair distribution functions for filling factor $\nu = 2/3$ obtained from exact diagonalizations for the maximum number of particles available (see Table I). Near the origin the spin-unpolarized $g(r)$ presents a slower increase than the spin-polarized one. The equal-spin and opposite-spin contributions to the total spin-unpolarized $g(r)$ are also shown in the figure.

relative angular momenta. This can be seen in Fig. 1 which shows the pair correlation function for both spin-polarized and spin-unpolarized states at $\nu = 2/3$ extracted from the exact diagonalizations. We propose the following factorization: $\langle n_1 n_0 \rangle = f(\nu)(2\nu - 1)$ with $f(\nu) \leq 1$. In general, $f(\nu) = \alpha + (1-\alpha)\nu$ since we do not expect terms proportional to ν^3 or higher to be relevant in a density-density correlation function and the condition $f(\nu = 1) = 1$ must be fulfilled. We set $\alpha = 0.2966$ which is consistent with our best numerical estimate of $\langle n_1 n_0 \rangle$ for $\nu = 2/3$. The energy obtained from the analytical expression of $g(r)$ for $\nu = 2/3$ (-0.528 e^2/ℓ) and $\nu = 4/5$ (-0.566 e^2/ℓ) and the exact results for the real Coulomb interaction are remarkably close (see Fig. 2). One can interpret these unpolarized states as $\nu = 1/3$ and $\nu = 1/5$ hole liquid states, each hole being "accompanied" by one and two spin flips (i.e., spin waves), respectively. Although we cannot present a rigorous argument, it is tempting to interpret this hole-spin waves association as a skyrmion[5], and call these states Skyrme liquids.

4 Liquid to solid transition

Figure 2 shows the energy per particle for $\nu = 1 - 1/M$ of both liquid phases compared to that of the solid phase proposed by Brey et al.[6] in a mean-field approximation. The solid phase energy lies clearly above the exact and estimated values for $\nu = 2/3$, $\nu = 4/5$, and even $\nu = 6/7$, which proves the existence of unpolarized liquid phases at these filling factors. However, one should keep in mind that quantum fluctuations have not been considered in the solid phase calculation and that they are bound to lower the energy of this phase. Borrowing the results from Ref. [7] we estimate the shift to be $-0.001e^2/\ell$ for $\nu = 4/5$, decreasing in absolute value as $\nu \to 1$. In our favor we must stress that partially polarized liquid phases, which have not been considered here, are expected to lower the ground state energy for typical values of the Zeeman energy. All considered, our results seem to place the quantum melting phase transition point very close to $\nu = 1$. As expected, the triangular Skyrme crystal dominates sufficiently close to $\nu = 1$, but the transition point to the square

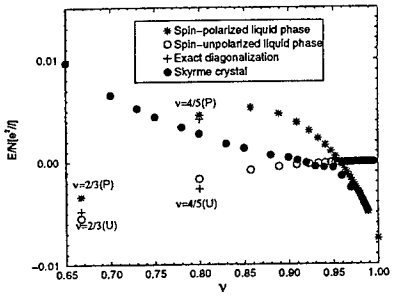

Figure 2: Energy per particle in the Hartree-Fock approximation of the solid phase or Skyrme crystal (dots) and of the polarized (stars) and unpolarized (circles) liquid phases proposed in the text. For completeness, the values obtained from the exact diagonalizations are presented by crosses for both polarized and unpolarized phases. The results for the polarized liquid phase include a Zeeman energy shift of $g\mu_B B/2 = -0.0075e^2/\ell$ and all the energies are referred to $-\frac{1+\nu}{4}\sqrt{\pi/2}$.

lattice ($\nu \approx 0.96$)[6] lies near the one where the unpolarized liquid phase begins to take over ($\nu \approx 0.92$).

5 Acknowledgments

We would like to thank Luis Brey for providing us with the data for the solid phase. We also acknowledge fruitful discussions with C. Tejedor, P. Tarazona, E. Chacón, J. Fernandez-Rossier, and L. Martín-Moreno. This work has been funded by MEC of Spain under contract No. PB96-0085.

References

1. See for instance T. Chakraborty and P. Pietiläinen, *The Quantum Hall Effects: Fractional and Integral*, Springer Series in Solid State Sciences **85**, (Springer-Verlag Berlin, Heidelberg, 1995), and references therein.
2. S. M. Girvin, Phys. Rev. B **30**, 558 (1984).
3. S. M. Girvin, A. H. MacDonald, and P. M. Platzman, Phys. Rev. B **33**, 2481 (1986).
4. See A. H. MacDonald, G. C. Aers, and M. W. C. Dharma-wardana, Phys. Rev. B **31**, 5529 (1985).
5. M. Abolfath et al., Phys. Rev. B **56**, 6795 (1997); J. J. Palacios and H. A. Fertig, Phys. Rev. Lett. **79**, 471 (1997); J. H. Oaknin, B. Paredes, and C. Tejedor, Phys. Rev. B **58**, 13028 (1998).
6. L. Brey et al., Phys. Rev. Lett. **75**, 2562 (1995).
7. H. Yi and H. Fertig, Phys. Rev. B **58**, 4019 (1998), and references therein.

Composite Fermions with a Spin Freedom

Daijiro YOSHIOKA
Department of Basic Science, The University of Tokyo
3-8-1 Komaba, Meguro-ku, Tokyo 153-8902, Japan

A set of rules for the composite fermion transformation, when the electrons are partially spin-polarized is derived. Condition for the quantum phase transition between various spin states is obtained based on the rules. These rules give foundation for the experimental determination of the mass and g-factor of the composite fermion.

73.40Hm, fractional quantum Hall effect, composite fermion, g-factor

Energy gap due to the Landau quantization or the spin Zeeman splitting is essential for the integer quantum Hall effect[1,2]. When the Landau level filling factor ν is equal to an integer N, the lowest N spin-split Landau levels are filled, and the IQHE will be observed, in principle. However, if we can change the Landau level spacing $\hbar\omega_c$ and the size of the Zeeman splitting $g^*\mu_B B$ independently, level crossings of the Landau levels belonging to the different spin states can be caused. Here ω_c is the cyclotron frequency, g^* is the g-factor of the two-dimensional electron and μ_B is the Bohr magneton. The condition for the level crossing is given as

$$j\hbar\omega_c = g^*\mu_B B, \tag{1}$$

where j is an integer.

If the level crossing occurs for the Landau levels at the Fermi energy, configuration of the electrons changes. This is a quantum phase transition, and the energy gap vanishes at the transition. As shown in Fig.1, the phase transition occurs only when $j = 1$ for $\nu = 2$, while it occurs at $j = 2$ and 4 for $\nu = 5$.

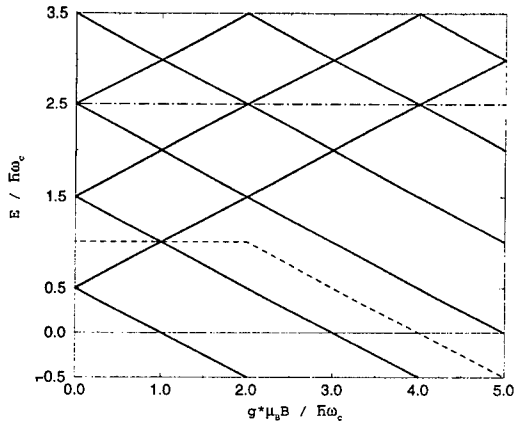

FIG. 1. Energy of the Landau levels as functions of the Zeeman splitting, $g^*\mu_B B$. The level crossing occurs when the horizontal axis takes an integer value j. The dashed line and the dash-dotted line are the Fermi level at $T = 0$ for $\nu = 2$ and 5, respectively.

Since, the fractional quantum Hall effect can be understood as an integer quantum Hall effect of the composite fermions (CF)[3,4], similar quantum phase transition between different spin polarization is expected to occur. Actually, such transitions are observed experimentally[5,6], and they have been used to deduce the effective mass m^* and g-factor of the composite fermion g^*. In these experiments tilting of the magnetic field is used to enhance the spin Zeeman splitting.

As we will see later, the interpretation of the experiment is quite simple, as long as the filling factor is expressed as $\nu = p/(mp+1)$, or its electron-hole conjugate, $\nu = 2 - p/(mp+1)$, where $p = \pm 1, \pm 2, ...$ is an integer and m is an even integer. Here $|p|$ gives the filling factor of the composite fermion and m describes the number of flux quanta attached to the electron or the hole to transform it to a composite fermion. On the other hand, for the filling factor expressed as $\nu = 1 \pm p/(mp+1)$, such as $\nu = 5/7$ or $4/5$, it is not simple. For example let us consider the situation at $\nu = 5/7$. If the Zeeman splitting is quite large, $\nu = 5/7$ can be considered as an electron-hole symmetric state of $\nu = 2/7$. This filling has the form of $\nu = p/(mp+1)$ with $p = -2$, and $m = 4$. In this case, since the filling factor of the composite fermion is 2, quantum phase transition between the spin-polarized ground state and spin-singlet ground state seems possible. However, as the true electron-hole symmetric state of $\nu = 5/7$ is not $\nu = 2/7$ but $\nu = 1 + 2/7$, we first need to establish rules to handle the situation where both spin states are occupied before we can consider the possibility of the transition.

In the experiment by Yeh *et al.*[6], they considered $\nu = 5/7$ to be equivalent to $\nu = 2/7$. However, in this treatment, they could not relate the observed collapse of excitation gap to level crossing *at the Fermi level.* Namely, they tried to determine m^* and g^* so that energy gap collapse is related to the level crossing of the Landau levels. Then they found that a unique choice of the product m^*g^* can relate every feature in the resistivity to level crossings in a consistent way. However, then the most prominent feature in the resistivity at $\nu = 5/7$ had to be connected to the condition that twice of the Landau level splitting is equal to the Zeeman splitting, i.e. it occurs at $j = 2$. At this point the filling of the lowest two CF Landau levels will not change: the level crossing occurs between the third and fourth lowest Landau levels. Therefore, $\nu = 5/7$ should not be mapped to $\nu = 2/7$, for which the CF filling factor is two. The situation was the same for other filling factors around $\nu = 3/4$: None of the prominent features in the resistivity could be related to the quantum phase transition, if states around $\nu = 3/4$ are considered as electron-hole symmetric states around $\nu = 1/4$.

I have briefly pointed out that the apparent discrepancy is resolved, if we correctly take into account both spin states of the original electrons[7]. It is pointed out that the spin freedom of the composite fermion should be understood as a result of that of the electrons. Details of the theory will be published elsewhere[8]. In the present paper, I will give an extended abstract of the paper.

We consider the filling factor related to $\nu = p/(mp+1)$. We assume that the magnetic field is so strong that the Landau level splitting can be considered to be infinitely large, while the spin Zeeman splitting is finite. Therefore in the following we retain only the lowest single Landau level for each spin polarization. Then obviously the filling factor $\nu_1 = 2 - \nu$ is equivalent to ν due to the electron-hole symmetry. As stated above the quantum phase transition at filling $\nu = p/(mp+1)$ or $\nu_1 = 2 - \nu$ is easy to understand. When the electrons or holes are dressed into composite fermions by attaching m flux quanta, the effective magnetic field perpendicular to the plane is reduced to

$$B_{\rm eff} = \frac{B_\perp}{mp+1}, \tag{2}$$

where $B_\perp$ is the component of the external magnetic field perpendicular to the 2-d plane. Then the lowest Landau level of each spin is split into $mp+1$ CF Landau levels, and CF

occupies $|p|$ Landau levels among those $2(mp+1)$ levels. The CF Landau levels of up and down spin are offset by $g^*\mu_B B_{\rm tot}$, therefore a quantum phase transition between two different spin polarization occurs when the following condition is satisfied,

$$(|p|-2k-1)\hbar\omega_c^* = g^*\mu_B B_{\rm tot}. \tag{3}$$

Here $\omega_c^* = eB_{\rm eff}/m^*$ is the CF cyclotron frequency, and $k = 0, 1, 2, ...$ is an integer.

Now we want to know a condition for the phase transition at filling factor $\nu_2 = 1 + p/(mp+1)$ or $\nu_3 = 1 - p/(mp+1)$. We claim that these states are expressed by CFs at total filling factor

$$\nu_{\rm CF} = |mp+1| + |p|, \tag{4}$$

according to the following rules: (1) All the electrons are changed into CF's by attaching m flux quanta. (2) However, each electronic states in the lower energy, down spin Landau level gives $|m|$ flux quanta with opposite sign. (3) The maximum allowed CF filling factor for each spin state is $|mp+1|$. (4) The Zeeman splitting of these levels are $g^*\mu_B B_{\rm tot}$, while the Landau level splitting is given by the effective magnetic field,

$$B_{\rm eff} = \frac{B_\perp}{mp+1}. \tag{5}$$

We can rewrite $B_{\rm eff}$ in a different way also. It is proportional to the deviation of $B_\perp$ from that at $\nu = 1 \pm 1/m$, $B_{\perp,1\pm1/m}$:

$$B_{\rm eff} = \pm(m \pm 1)(B_\perp - B_{\perp,1\pm1/m}). \tag{6}$$

The condition for the gap collapse, or the quantum phase transition point, is given by these rules as follows:

$$(|mp+1| - |p| - 2k - 1)\hbar\omega_c^* = g^*\mu_B B_{\rm tot}, \tag{7}$$

where k is a non-negative integer.

We argue the appropriateness of these rules in the following. Theoretically we can verify these rules by applying them to the filling factor $\nu_2 = 1 + p/(2p+1)$. We notice that this filling factor can also be expressed as $\nu_1 = 2 - p'/(2p'+1)$, where $p' = -p-1$. Therefore we have two choices to express the same filling by CF: In the former case, electrons are changed into CFs, and CF filling factor is $|2p+1|+|p|$. On the other hand, in the latter, the holes are changed into CFs at CF filling factor $|p'|$. Since $|2p+1| = |2p'+1|$, the effective magnetic field is the same, so is the Landau level splitting in both cases. Furthermore $|2p+1| - |p|$ and $|p'| = |p+1|$ has the same parity. Therefore the conditions for the quantum phase transition, eq.(3) and eq.(7), are the same.

Experimental verification comes from the experiment by Yeh *et al.*[6]. Comparison with the experiment shows that the present theory can correctly explain the distinct peaks of the resistance at $\nu = 8/11$ and $5/7$. These filling factors belong to negative p side of the series $\nu = 1 - p/(4p+1)$.

On the other hand, at $\nu = 4/5$ and $7/9$, namely positive p side of the series, the stronger peaks correspond to half-integer k. This discrepancy and the existence of weaker peaks are left as problems to be solved in the future. The existence of weaker peaks seems to indicate that the CF theory is too naive, even if the stronger peaks can be understood successfully. Possible origin of the discrepancy at $\nu = 4/5$ and $7/9$ could be the exchange enhancement of the Zeeman splitting or the effect of skyrmion.

The experimentally determined phase transition point gives the combination g^*m^* through the condition eq.(7). To get g^* and m^* separately, the experimentalists used the temperature dependence of the Schubnikov-de Haas data to deduce m^*. From the value of m^*, g^* of about 0.6 is obtained at $\nu = 5/7$ as well as around $\nu = 3/2$. They could not find a reason why the g-factor of the two-flux quanta CF is equal to that of the four-flux quanta CF. However, in the present simple theory, the g-factor of the CF is nothing but that of original electrons, this coincidence is not strange at all. Actually, 0.6 is close to the g-factor of electron, 0.44.

In conclusion in this paper we developed a set of rules for the CF transformation, which can explain the quantum phase transition observed experimentally. We also found that there still remain several problems to be solved in the future.

Acknowledgements

I thank Dan Tsui who showed me the experimental results prior to publication while we stayed at Aspen Center for Physics, where part of this work was done. This work is supported by Grant-in-Aid for Scientific Research (C) 10640301 from the Ministry of Education, Science, Sports and Culture.

REFERENCES

1) K. von Klitzing, G. Dorda and M. Pepper: Phys. Rev. Lett. **45** (1980) 494.
2) *The Quantum Hall Effect*, ed. R.E. Prange and S.M. Girvin (Springer, New York, 1990) 2nd ed.
3) J.K. Jain: Phys. Rev. Lett. **63** (1989) 199.
4) *Composite Fermions* ed. O. Heinonen (World Scientific, Singapore, 1998).
5) R.R. Du, A.S. Yeh, H.L. Stormer, D.C. Tsui, L.N. Pfeiffer and K. West: Phys. Rev. Lett. **75** (1995) 3926.
6) A.S. Yeh, H.L. Stormer, D.C. Tsui, L.N. Pfeiffer, K.W. Baldwin and K. West: Phys. Rev. Lett. **82** (1999) 592.
7) D. Yoshioka: to be published in Phys. Rev. Lett. (cond-mat/9811279).
8) D. Yoshioka: preprint (cond-mat/9906073).

PA.51

VORTEX DETACHMENT IN FRACTIONAL QUANTUM HALL STATES

Daniela Pfannkuche and Allan H. MacDonald

Max-Planck-Institut für Festkörperforschung, Heisenbergstr. 1, D-70569 Stuttgart, Germany
Department of Physics, Indiana University at Bloomington, Bloomington, Indiana, 47405, USA

Quasi-particles in the fractional quantum Hall regime are considered to be composites of electrons and flux quanta [1]. Their signature is a characteristic vortex structure of the many-body wave functions which exhibit vortex pinning at electron positions. In our contribution we visualize this vortex structure at different filling factors and elucidate the crossover between composite particles and simple electrons in the lowest Landau level.

One situation in which this crossover can be studied is the transition between fractional and integer quantum Hall states induced by a commensurate lateral superlattice with tunable amplitude [2]. Fractional quantum Hall states at odd-denominator filling factors $\nu = N_e / N_\Phi$ are characterized by a bunching of $1/\nu$ flux quanta at the N_e electron positions [3]. (N_Φ: number of flux quanta in the system.) This way electrons are strongly repelled from each other, thus, minimizing the Coulomb energy. Accordingly, the many-body wave function at filling factor $\nu=1/3$ exhibits a threefold vortex whenever two electrons approach each other, i.e. the wave function becomes zero and its phase changes by three times 2π when one electron encircles the other.

With a lateral superlattice applied, the three vortices spread apart from one another. Their small mutual distance at small modulation amplitude, however, indicates the strong electron correlations which still dominate the physics of the finite size system which we can treat numerically. Once the transition to the integer quantum Hall state is complete, only a single vortex remains fixed to each electron position with no obvious spatial correlation to the other free vortices. We study the spreading of the vortices at the phase transition quantitatively and determine its finite size behavior.

At filling factor $\nu = ½$ two flux quanta are supposed to be pinned close to each electron. However, Pauli's Principle forbids the two vortices to collapse at the same position. We determine the size of the composite fermion at half filling of the lowest Landau level from the distance between the two vortices.

[1] H. L. Störmer, Solid State Comm. **92**, 159 (1994).
[2] D. Pfannkuche and A. H. MacDonald, Phys. Rev. B **56**, R7100 (1997).
[3] R. B. Laughlin, Phys. Rev. Lett. **50**, 1395 (1983).

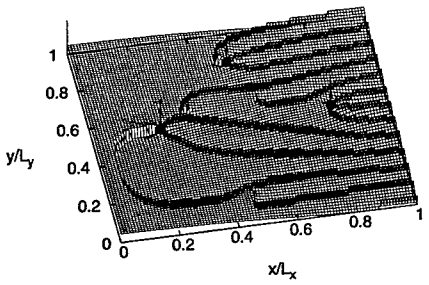

Phase of a four-electron wave function defined on a torus. The positons of three electrons have been fixed (black dots). Coordinates x and y correspond to the remaining particle. Vertical bars indicate the winding number of the wave function at the corresponding zero.

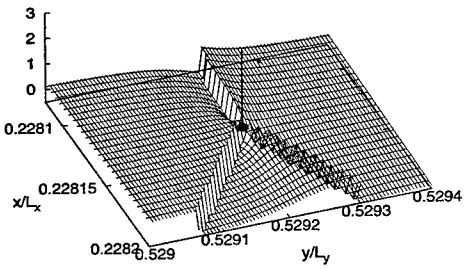

Threefold vortex at the position of one of the fixed electrons. At the discontinuity the phase jumps by 2π.

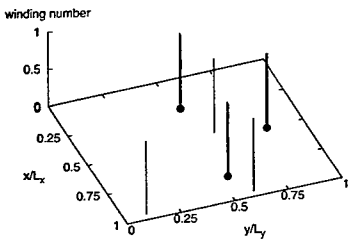

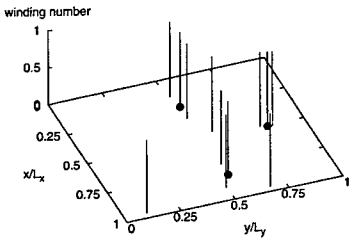

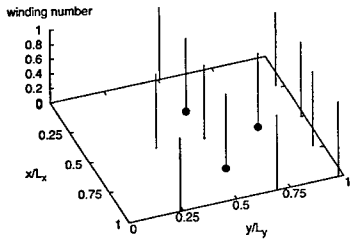

Flux detachment due to an applied lateral superlattice with tunable amplitude. For small amplitude (upper row) the three vortices are still pinned to the fixed electron position.
Beyond the transition to an integer quantum Hall state no spatial correlations between the fixed and free vortices is aparent.

PA.52

Energy dependence of the quasiparticle lifetime in a 2DES

R J A Hill, S T Stoddart, P C Main, L Eaves, K A Benedict and M Henini

School of Physics and Astronomy, University of Nottingham, Nottingham, NG7 2RD, UK.

We present a novel technique for measuring the lifetime of quasiparticle excitations of a 2DES by investigating the tunnelling into a quantum dot from a 2DES over an extended range of energy from the Fermi energy to the sub-band edge. We find that the lifetime τ_{qp}, of a quasihole excitation, caused by removing an electron from a 2DES state with energy ε below the Fermi energy, E_F, has the form $\tau_{qp} = \alpha\hbar/\varepsilon$, where α is a constant of order unity.

Key words: quasiparticle lifetime, tunnelling, quantum dot
PACS: 71.70.Di, 85.30.Vw, 73.40.Gk, 73.20.-r

Most transport experiments on two-dimensional electron systems (2DES) involve measurements of the linear conductance, which depends only on the properties of electrons within k_BT of the Fermi energy. Consequently, the effects of the quasiparticle (or quasihole) lifetime, τ_{qp}, are difficult to observe. In addition, such experiments do not provide information about excitations of the 2DES at energies well away from the Fermi energy, E_F. In fact, we are able to speak of well-defined electron or hole excitations only because, in Landau Fermi liquid theory, the lifetime is expected to become very long close to E_F, varying as ε^{-2}, where $\varepsilon = |E_F - E|$. Calculations of τ_{qp} at larger ε are difficult. Furthermore, no experimental values have been reported in this regime, although there have been optical investigations of electron-hole recombination for excitations well below E_F[1].

In this paper we describe a novel method for measuring τ_{qp}. It relies on the use of a self-assembled quantum dot as a tunnelling spectrometer of a 2DES [2]. The dot is incorporated into the barrier of a tunnelling device and electrons tunnel into its ground state from a 2D accumulation layer. The energy width of the state is very narrow, ~ 10 μeV, so the tunnel current acts as a very sensitive probe of the density of states of the 2DES. By altering the bias across the device we can vary the energy of the dot state relative to the 2DES and hence investigate the full range of electron energies. In particular, when a magnetic field, B, is applied perpendicular to the plane of the 2DES, we can resolve peaks in the density of states due to the formation of Landau levels (LLs). For energies well below E_F, we assume that Landau levels may be resolved only when $\omega_c\tau_{qp} > 1$, which enables us to obtain values for τ_{qp}.

Our devices consist of a 10 nm AlAs tunnel barrier separated from graded n-type top and bottom contacts by 100 nm undoped GaAs spacer layers. InAs quantum dots (QDs) were grown on the centre plane of the barrier using the Stranski-Krastonov growth mode, producing a dot density ~ 2×10^{15} m^{-2}, with a typical dot diameter ~ 10 nm. More details may be found in ref [2]. Under bias, a 2DES

forms in an accumulation layer on one side of the AlAs barrier (see Fig 1). Increasing the applied voltage, V, reduces the energy of the QD states relative to the 2DES. When a particular dot state is resonant with the 2DES, electrons may tunnel through the dot into the collector and a current flows. The electrons flow in the direction shown in Fig 1. Because of the finite height of the dots, the effective barrier for tunnelling into the dots is much thicker than that for tunnelling out and the current is limited by the rate at which electrons tunnel from the 2DES.

Although there are several thousand dots in the device (mesa diameter 5 μm), near the onset of current, we see the current due to electrons tunnelling through a single dot. The ability to see the current due to one dot is a feature common to many different devices; we assume the particular dot must be near the lower end of the energy distribution.

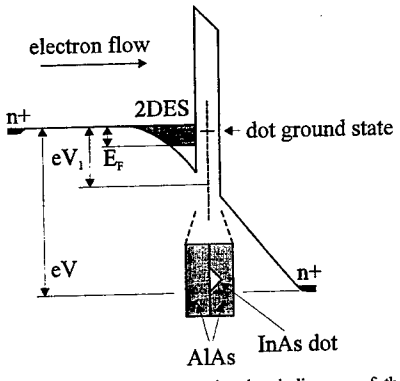

FIG. 1. Schematic conduction band diagram of the device under bias. The lower inset shows the orientation of a single dot in forward bias. The energy scale of the probe, eV_1, is related to the voltage across the device by the leverage factor, $f = (dV/dV_1) \approx 14.4$.

Typical low-temperature I(V) curves are shown in Figure 2 for several values of B applied parallel to the current direction, i.e. perpendicular to the plane of the 2DES. The sharp rise in the current around 210-215 mV occurs when the dot state is resonant with E_F. As V is increased further, the dot state falls in energy relative to the occupied 2DES states, so the current is due to electrons tunnelling at energies below E_F. Eventually, around 265 mV, the current falls close to zero as the dot state falls below the 2D band edge. The range of voltage over which a current is observed, suitably scaled by the electrostatic leverage factor of the device (see Fig 1), indicates $E_F \approx 4$ meV, corresponding to an electron density $\sim 1.2 \times 10^{15}$ m^{-2}.

At 0.36 T we resolve clearly the current peaks due to the n = 5 and n = 4 LLs, where $E_n = (n + \frac{1}{2})\hbar\omega_c$ is the energy of a LL, with ω_c the cyclotron frequency. At this field, the chemical potential lies within the n = 5 LL. The identification of the LL indices is provided by a fan diagram of the voltage positions of the various peaks as a function of

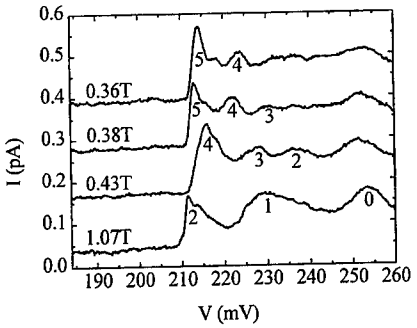

FIG. 2. I(V) characteristics in magnetic field, B, applied parallel to the current. The curves are offset for clarity. The numbers indicate the corresponding Landau index for the peaks as determined by a Landau fan diagram.

B, shown in Fig 3. The lines drawn on Fig. 3 are the expected values of E_n, taking into account the measured leverage factor, and involve no adjustable parameters. Only the $n = 4$ and $n = 5$ LLs may be resolved at 0.36 T. Lower energy levels appear when B is increased. For example, at $B = 0.38$ T, $n = 3$ is just visible but $n = 0$, 1 and 2 are not resolved. At 0.43 T, $n = 2$ is clearly visible but $n = 0$ and 1 are not resolved. There is, however, a clear, broad feature, centred around 252 mV (also visible at lower B). Eventually, both the $n = 0$ and $n = 1$ LLs emerge from this feature but at these low B values its voltage position is only very weakly dependent on B. At sufficiently high B, see for example the curve at 1.07 T, $n = 0$ and $n = 1$ are clearly resolved.

We now relate the successive emergence of LLs with decreasing index as B is increased to the effect of τ_{qp}. In a simple picture, we assume that the current peak due to a particular LL is resolved provided that $\omega_c\tau_{qp}$ is of order 1. Since we expect τ_{qp} to decrease as ε increases, the LL at lower energies will require a higher value of ω_c, and hence B, to be resolved. This idea allows us to obtain quantitative information of how τ_{qp} varies with ε. First, we identify the value of B where we can just resolve a current peak due to the n^{th} LL, which gives the critical value for ω_c. Then, we note the voltage at which the peak occurs when it is first resolved. This tells us the energy, relative to E_F, after appropriate scaling by the leverage factor. Consequently, the emergence of each LL gives a single value of τ_{qp} at a known energy. In fact, the emergence of $n = 5$ is ambiguous due to the presence of mesoscopic fluctuations at low B but we are able to obtain values for $n = 4$, 3, 2 and 1.

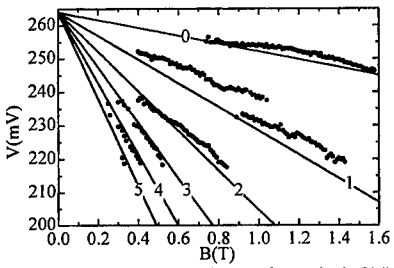

FIG. 3. Landau fan diagram for peaks in I(V). Lines are the expected variations. The numbers are the LL indices, n.

Values of τ_{qp} versus $E_F - E$ are shown in Fig 4. The straight line represents $\tau_{qp} = \alpha\hbar/\varepsilon$, where $\alpha \approx 1.6$. Since the definition of when a LL is first resolved is slightly subjective, we cannot guarantee the numerical value of α beyond saying that it is of order 1. However, the resolution criterion is applied consistently so the proportionality is not in question.

Conventional Fermi liquid ideas would lead us to expect that τ_{qp} varies quadratically with energy, i.e. $\tau_{qp}(\varepsilon) \sim \hbar/\varepsilon^2$. Such behaviour is a result of the severe restrictions on phase space for quasiparticle decay processes due to the Pauli exclusion principle. This quadratic dependence, which ensures that the energy

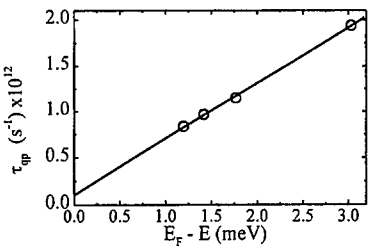

FIG. 4. τ_{qp}^{-1} plotted against (E_F - E).

width of a quasiparticle state is always much smaller than its energy, underpins our understanding of the properties of metals and semiconductors in terms of Landau's Fermi liquid theory. There are a number of possible reasons why our observations are not consistent with the conventional Fermi liquid behaviour. The most mundane explanation is that we are not probing excitations sufficiently close to E_F. The ε^{-2} behaviour is an asymptotic result in the limit $\varepsilon \to 0$; the existence of correction terms linear in ε has been predicted by Hawrylak *et al* [3] for 2D electrons confined to a quantum well using a modified random phase approximation (RPA). Deviations from conventional Fermi liquid behaviour in that calculation arise for energies of order 10–20 meV, much higher than is the case for the current experiment. However, it is clear that the energy scale depends in detail on the way in which multi-particle effects (vertex corrections) are included in the RPA.

A more interesting explanation of our data arises from the fact that the Landau treatment assumes that the quasiparticle states are plane waves. In reality, of course, electronic transport in a disordered system is generally diffusive (the mobility of our 2DES is $\mu \approx 3\ m^2V^{-1}s^{-1}$). Abrahams *et al* [4], following work by Schmid [5] and Alschuler and Aronov [6], have shown that this leads to marginal Fermi liquid behaviour where τ_{qp}^{-1} is predicted to vary linearly with ε as

$$\frac{1}{\tau_{qp}} = \frac{1}{4ma_0q_0D}\varepsilon \ ,$$

where q_0^{-1} is the screening length, a_0 and m are the Bohr radius and electron effective mass for GaAs respectively, and D is the diffusion constant appropriate for density fluctuations involving states close to the Fermi energy. Clearly, our experimental data are insufficient in themselves to distinguish between these two possibilities since we have information on τ_{qp}^{-1} at a few discrete energies below E_F.

In summary, we have used a novel technique to determine values for the quasiparticle lifetime deep in the Fermi sea. We find that the scattering rate varies linearly with the energy of the quasiparticle.

Acknowledgements

This work is supported by EPSRC (UK). LE is grateful to EPSRC for financial support.

References

1. D-S Kim, J Shah, J E Cunningham, T C Damen, S Schmitt-Rink, and W Schaefer, Phys. Rev. Lett. **68**, 2838 (1992).
2. I E Itskevich, T Ihn, A Thornton, M Henini, T J Foster, P Moriarty, A Nogaret, P H Beton, L Eaves and P C Main, Phys. Rev. **B 54**, 16401 (1996).
3. P Hawrylak, J F Young and P Brockmann, Phys. Rev. **B 49**, 13624 (1994).
4. E Abrahams, P W Anderson, P A Lee and T V Ramakrishnan, Phys. Rev. **B 24**, 6783 (1981).
5. A Schmid, Z. Phys. **271**, 251 (1974).
6. B L Altschuler and A G Aronov, JETP Lett. **30**, 482, (1979).

A Light-Induced Tunneling State In a Submicron Double Barrier Tunneling Diode With a Center-Doped Well

Y. W. Suen,[a] C. C. Young,[a] C. J. Chang,[a] J. C. Wu,[b] S. Y. Wang,[c] and C. P. Lee[c]
[a]*Dept. of Physics, National Chung Hsing University, Taichung, Taiwan*
[b]*Dept. of Physics, National Changhua University of Education, Changhua, Taiwan*
[c]*Dept. of Electronics Engineering, National Chiao Tung University, Sinchu, Taiwan*

Abstract

We will present the observation of a light-induced meta-stable impurity state in a submicron center-doped double barrier tunneling diode (DBRTD) manufactured by a novel single-step e-beam lithography process in which no further alignment for the interconnect between the bonding pad and the small active device region is required. We attribute the meta-stable tunneling state, which can be switched by light and high voltage bias, to the light- or field-induced charge redistribution in the active tunneling region.

Study on the double-barrier resonant tunneling diodes (RTDs) with intentionally doped donor impurities between the barriers has revealed additional features related to tunneling through the localized impurity levels at bias lower than that of the conventional tunneling through the quasi two dimensional (2D) states in the well [1]. Further lateral confinement of the device size down to submicron scale perpendicular to the tunneling direction allows us to investigate the electronic energy levels in the few-impurity or even single-impurity system in a quantum box [2-4]. In this paper we will present the observation of a light-induced meta-stable tunneling state in a submicron center-doped double barrier tunneling diode (DBRTD) manufactured by a novel single-step e-beam lithography process in which no further alignment for the interconnect between the bonding pad and the small active device region is required. We attribute this meta-stable state which can be switched by light and high voltage bias to the light- or field-induced charge redistribution in the active tunneling region.

The MBE layer structure of the DBRTD mainly consists of a 10 nm GaAs quantum well (QW) with a 3×10^{10} cm^{-2} Si doping layer in the center, flanked with a 4 nm AlAs barrier on both side, set back from the n^+-type emitter and collector regions by a 10 nm and a 50 nm undoped spacer layers respectively. A schematic of the device structure is shown in Fig. 1. An evaporated Au/Ti bonding pad separated from the semiconductor surface by an insulating layer (SrF_2) is first formed. The active device area, a 0.5 μm-diameter dot with a 0.2 μm-wide long tail connected to the bonding pad, is defined by a single e-beam writing process on the standard spin-on PMMA resist. The ohmic contact is formed by thermally depositing a 200 nm of Au/Ge/Ni layer followed by a lift-off, a wet mesa etching, and an annealing process consecutively. The region under the narrow long tail is completely depleted, and thus the only possible tunneling path is through the dot-shaped region. We have examined the *I-V* characteristics of the connecting wires of 0.3

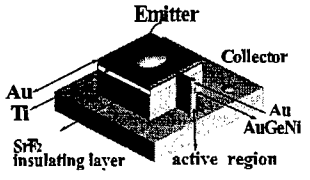

Fig.1 Schematic diagram of the device structure.

μm and 0.2 μm width without the dot. The 0.3 μm wide wire exhibits a tunneling diode behavior while the 0.2 μm one shows only a very low leakage current (≤1 pA) much lower than the tunneling current in the whole experimental bias range. The actual diameter of the device is about 0.3 μm, i.e. 0.2 μm smaller than the nominal metal size due to undercut and edge depletion. The main advantage of this single-e-beam process technique is simple and straightforward compared to other techniques [5-13]. The only drawback is the high resistance of the narrow long connecting wire (about few kΩ), which can be overcome by using multiple wires connected to the active dot. We can even arrange a metal ring around the dot to form a remote control gate to tune the diode in the same e-beam writing process. Details of the device processing will be reported elsewhere [14].

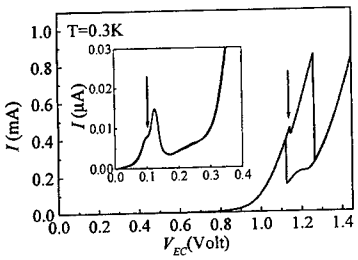

Fig.2 The *I-V* characteristics of a 0.5 μm-diameter DBRTD with 3×10^{10} cm^{-2} Si doping layer in the center of the QW.

The *I-V* characteristics in Fig. 2 for positive emitter to collector voltage (V_{EC}) at 0.3K shows the first tunneling peak at 0.12 V with a shoulder near 0.1 V, and the second peak is at about 1.26 V (on the sweeping-up curve) with a small satellite peak at 1.15 V. For such a bias condition, the electron actually tunnels from the collector to the emitter, i.e. the device operates in a reversed mode. The small peaks below the main tunneling peaks become weaker upon applying high magnetic fields (B) in the direction of tunneling current while the main peaks does not, indicating these features come from the localized impurity levels in the QW instead of extended 2D levels [1].

After illumination by a GaAs infrared LED near the sample at low temperature, we find an extra peak at the high-bias side of the first tunneling peak. More interestingly, if the applied bias exceeds 0.35 V, this light-induced peak will vanish and the *I-V* curve shape will be reset to the one before illumination as shown in

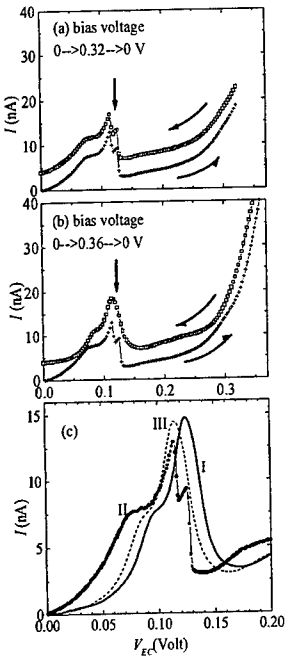

Fig. 3 The *I-V* characteristics right after LED illumination: (a) with bias applied less than 0.35 V, (b) with bias applied exceeding 0.35 V. The sweeping-down curve is offset by 4 nA for clarity. (c) The original curve I before illumination, the curve II right after illumination and the curve III obtained after applying a high bias voltage.

Figs. 3(a) and (b). However we notice a negative voltage shift of the tunneling *I-V* curve, indicating certain amount of negative charge is removed from the active tunneling region, including two AlAs barriers, QW in between and the undoped spacer next to top emitter. Figure 3(c) shows the original curve (solid line labeled I) before illumination, the one (solid circle line labeled II) right after illumination and the one (dash line labeled III) obtained after applying a high bias voltage together for comparison. The *I-V* curves II and III can be repeatedly switched back and forth by illumination and high electric fields.

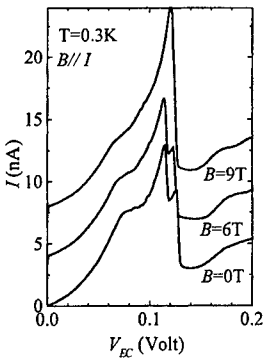

Fig. 4 The *I-V* characteristics right after illumination at low bias for B = 0, 6, and 9 T. The offset between two adjacent curves is 4 nA.

To investigate the origin of the light-induced extra features in the *I-V* curve, we also study the evolution of these peaks as a function of B parallel to tunneling current. As shown in Fig. 4, at high B the main tunneling peak survives and becomes stronger with a slightly positive shift on the peak position while the additional peak at 0.13 V disappears similar to the peak associated with impurity level near 0.85 V. The origin of the additional peak is very possible related to the impurities in the well. We have measured similar devices without the doping layer in the QW and no similar behavior was found.

The width of the QW is 10 nm, very close to the effective Bohr radius a_B^* of a hydrogen-like impurity in bulk GaAs. The average spacing between Si-impurities is about 60 nm, much larger than a_B^*. The 0.3 μm effective device area contains about 85 Si impurities in the well. The shape of the wave function and the energy level of the electron bonded to the impurity ion are very sensitive to the charged impurities in the barriers, which can cause dramatic change on the boundary conditions. A negative charge trapped in the barrier will effectively increase the barrier high, which may raise the energy level nearby and also reduce the tunneling probability. A positive charge in the barrier will have opposite effect. Not only the positions but also the shape of the *I-V* curve II in Fig. 3(c) is very different from the original curve I, indicating that the potential distribution near the tunneling barrier is seriously modified. Thus part of the electrons removed by illumination must reside originally near the AlAs tunneling barriers, probably trapped by background acceptor impurities. The shape of the tunneling curve III after applying high enough electric fields restores to its original form but with a residual negative shift which has to do with the trapped electrons removed by light but not recovered by electric field in the spacer layer. These electrons can originally be trapped by deep levels within the bandgap. The charge distribution in the spacer, contrary to the those near the tunneling barriers, will give only an energy shift to all the tunneling levels and will not effect the other tunneling properties. The origin of the tunneling state associated with the light-induced peak near 0.13 V on curve II in Fig. 3(c) is still not clear. It may relate to the anti-bonding states of two or more impurities very close to each other.

In conclusion, we have successfully used a novel single-step e-beam lithography to

manufacture submicron-sized tunneling devices. We have observed a meta-stable tunneling state which can be switched by light and high voltage bias in a DBRTD of 0.3 μm diameter with a Si doping layer between tunneling barriers and attribute them to the light- or field-induced charge redistribution in the active tunneling region.

This work was supported by the National Science Council of the Republic of China through grant No. of NSC88-2112-M-005-003.

Reference:

1. J. W. Sakai, T. M. Fromhold, P. H. Beton, L. Eaves, M. Henini, P. C. Main, F. W. Sheard, and G. Hill, Phys. Rev. B48, 5664 (1993).
2. M. W. Dellow, P. H. Beton, C. J. G. M Langerak, T. J. Foster, P. C. Main, L. Eaves, M. Henini, S. P. Beaumont, and C. D. W. Wilkinson, Phys. Rev. Lett. 68, 1754 (1992).
3. K. Nomoto, T. Suzuki, K. Taira and I. Hase, Jpn. J. Appl. Phys. 33, L1143 (1994).
4. J. W. Sakai, P. C. Main, P. H. Beton, N. La Scala, Jr., A. K. Geim, L. Eaves, and M. Henini, Appl. Phys. Lett. 64, 2563 (1994).
5. M.A. Reed, J. N. Randall, R.J. Aggarwal, R.J. Matyi, T.M. Moore, and A.E. Wetsel, Phys. Rev. Lett. 60, 535 (1988).
6. T. Tewordt, V. J. Law, M. J. Kelly, R. Newbury, M. Pepper, D. C. Peacock, J. E. F. Frost, D. A. Ritchie, and G. A. C. Jones, J. Phys.: Condens. Matter 2, 8969 (1990).
7. M. R. Deshpande, J. W. Sleight, M. A. Reed, R. G. Wheeler, and R. J. Matyi, Phys. Rev. Lett. 76, 1328 (1996).
8. P. H. Beton, M.W. Dellow, P.C. Main, T.J. Foster, L. Eaves, A.F. Jezierski, M. Henini, S. P. Beaumont, and C. D. W. Wilkinson, Appl. Phys. Lett. 60, 2508 (1992).
9. P. Gueret, N. Blanc, R. Germann, and H. Rothuizen, Semicond. Sci. Technol. 7, B462 (1992).
10. J. Wang, P. H. Beton, N. Mori, L. Eaves, H. Buhmann, L. Mansouri, P. C. Main, T. J. Foster, and M. Henini, Phys. Rev. Lett. 73, 1146 (1994).
11. J. Wang, P. H. Beton, N. Mori, L. Eaves, H. Buhmann, L. Mansouri, P. C. Main, T. J. Foster, and M. Henini, Appl. Phys. Lett. 65, 1124 (1994).
12. P. H. Beton, J. Wang, N. Mori, L. Eaves, P. C. Main, T. J. Foster, and M. Henini, Phys. Rev. Lett. 75, 1996 (1995).
13. N. Mori, P. H. Beton, J. Wang, and L. Eaves, Phys. Rev. B51, 1735 (1995).
14. J. C. Wu, Y. W. Suen, C. C. Young, S. Y. Wang, and C. P. Lee, submitted to Appl. Phys. Lett.

Corresponding author: Yuen-Wuu Suen,
e-mail: ysuen@phys.nchu.edu.tw

PA.54

ANOMALOUS RESONANT-TUNNELING EFFECT IN TYPE II HETEROSTRUCTURES

E. E. Mendez, V. V. Kuznetsov, and D. Chokin
State University of New York at Stony Brook, Stony Brook, NY 11794-3800
J. D. Bruno
Army Research Laboratory, Adelphi, MD 20783

Abstract

We have observed unusual negative differential-conductance features in the magneto-tunneling current-voltage characteristics of GaSb-AlSb-InAs-AlSb-GaSb heterostructures. These features are very narrow (~ 2 mV) and shift to higher voltage with increasing magnetic field, both properties being in sharp contrast with those of the features associated with conventional resonant tunneling through Landau levels in the InAs well. The new results are explained by a three-step sequential tunneling process, in which two Landau levels –one empty and one occupied– are involved.

Introduction

Resonant tunneling in a double-barrier semiconductor heterojunction generally occurs in a two-step process. In type I junctions, exemplified by the GaAs-GaAlAs system, an electron from a GaAs electrode tunnels through two GaAlAs barriers via the quantized state of a GaAs quantum well between the barriers. In a type II heterojunction such as GaSb-AlSb-InAs-AlSb-GaSb, first an electron tunnels out of the InAs quantum well to the valence band of the GaSb collector electrode and then an electron from the GaSb emitter's valence band tunnels into the InAs well. The essence of this two-step process remains unchanged when a magnetic field parallel to the tunneling direction is applied, although tunneling now involves magnetic quantum levels (Landau levels) formed in the quantum well [1-3].

Tunneling through Landau levels is specially noticeable experimentally in type II structures, because at moderate magnetic fields (above a few Tesla) the energy separation between Landau levels for electrons in the InAs well (~ 5 meV/T) is larger than the Fermi energy of heavy holes in the collector. At low temperatures, the current-voltage (I-V) characteristics exhibit a saw-tooth shape, with several regions of an almost linear increase in current each followed by an abrupt drop, as the collector scans down in energy through individual Landau levels [3]. With increasing field, the negative-differential-conductance (NDC) structures move to lower voltage and gradually disappear, reflecting a decrease in the number of occupied Landau levels.

This behavior is illustrated in Fig. 1, which shows the I-V characteristics of a GaSb-AlSb (30Å)-InAs (150Å)-AlSb (30Å)-GaSb heterostructure under magnetic fields between 9.5 and 10 T. For each voltage polarity three strong features are readily observable, corresponding to

tunneling through the N = 2, 1 and 0 Landau levels in the InAs well, each feature moving toward lower voltage (in absolute value) as the field increases.

Experimental Results

Recently, we have observed, in addition to these well-known results, new features in the I-V characteristics of these type II heterostructures [4]. Examples of such features are shown in Fig. 1, their positions highlighted with arrows because of their small size compared to the main NDC peaks. The heterostructures were prepared by molecular beam epitaxy on n^+ GaSb substrates and lithographically patterned in the form of circular diodes ranging in diameter from 10 μm to 100 μm. The measurements were done at temperatures between 1.6 K and 6K in a 14-T superconducting magnet with the field parallel to the tunneling current through the diodes.

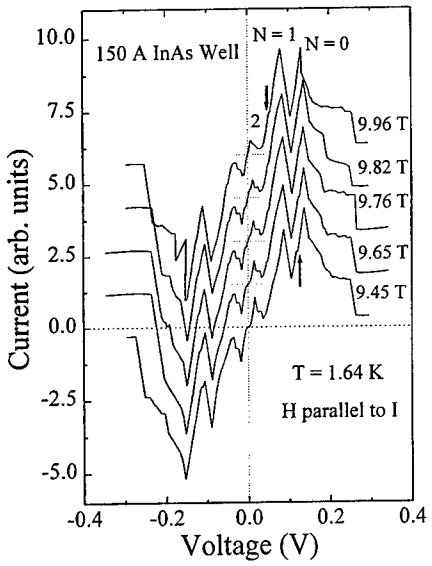

Fig. 1 Current vs-voltage characteristics of a GaSb-AlSb-InAs-AlSb-GaSb structure under a magnetic field parallel to the current. In addition to the main negative differential-conductance features, labeled with their Landau-level indices (N = 0, 1, 2), weak structures indicated by arrows are observable.

A typical example of the new features we have discovered is shown in detail in Fig. 2. Its most striking characteristic is its narrowness in voltage, just 2 mV, compared with the width of conventional NDC features in semiconductors. At certain fields, the new structures, which appear superimposed on the rising sides of the main saw-tooth pattern, exhibit clear negative differential conductance (only slightly affected by temperature in the 1.6 K ≤ T ≤ 6K range), although much weaker than the main NDC peaks. But their most striking difference is the magnetic field dependence of their voltage positions. While the main peaks shift to lower voltage monotonically with increasing field, at a rate determined by their Landau-level index N, the new structures shift in the opposite direction, that is, to higher voltage with increasing field.

Figure 3 summarizes the voltage positions of these anomalous features as a function of magnetic field, for both bias polarities. A fan-like pattern, common to phenomena that involve Landau levels, is clearly revealed. Indeed, linear least-squares fits to the various group of data in

Fig. 3 yield slopes that increase linearly with the label number N' indicated in the figure, with a rate of increase of 10.7 ± 2.3 mV/T. If we assume that the voltage between the GaSb electrodes falls entirely, and symmetrically, in the AlSb barriers, then we can convert that voltage rate of increase into an energy simply by dividing it by two. The resulting number, 5.3 ± 1. 1 meV/T, is in good agreement with the cyclotron energy of electrons in InAs (5.0 meV/T), if we use their conduction-bandedge effective mass. This agreement, although meaningful, as we show below, is somewhat fortuitous in view of the strong non-parabolicity of InAs, which makes the effective mass larger and consequently the cyclotron energy smaller. The real discrepancy of this number with the rate of increase in the slopes of Fig. 3 is reduced when one considers that only a fraction of the total voltage applied to the diode falls in its active tunneling region.

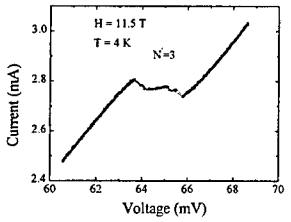

Fig. 2 Detail of a feature similar to those indicated by arrows in Fig. 1 but at a higher magnetic field.

Analysis and Interpretation

If, as it seems, the new magneto-tunneling features have their origin in InAs Landau levels, how to explain their shifts to higher voltage with increasing magnetic field? The answer lies in Fig. 4, which shows a sketch of the heterostructure's energy profile and of the Landau-level energies in the quantum well, for a field of ~9.7 T. At this field, at zero bias the N = 0, 1, and 2 levels are occupied with electrons while any level above them is unoccupied (N' = 3, 4 ...). As a negative bias is applied to the emitter, the collector scans down through each of the occupied levels (N) and whenever both are aligned in energy the tunneling current is enhanced resonantly. This is the origin of the main saw-tooth pattern in the I-V characteristics.

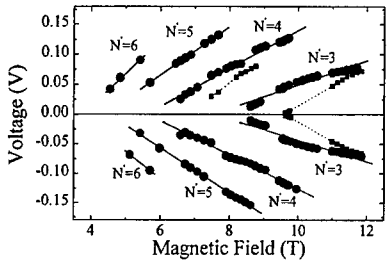

Fig. 3 Plot of the voltages at which the new features described in the text show minimum conductance. The straight lines correspond to linear least squares fits to experimental points.

But, in addition to this main tunneling mechanism, there is another one, which involves a second resonance, this time between an unoccupied Landau level (N') and the emitter electrode. When, for a fixed magnetic field, the voltage is such that an empty state, say N = 3, is aligned with the Fermi edge of the emitter an electron from the electrode can tunnel to the collector in a three-step process: first it tunnels into the well, then it relaxes to a lower, partially occupied Landau level, and finally it tunnels out to the collector.

Such a double resonance explains the limited field regions at which the features are best observed, their relative weakness, and that they are always riding on the main current structures. For instance, the feature highlighted in Fig. 1 with an arrow pointing down corresponds to the double resonant condition (N' = 3, N = 1) shown in Fig. 4, and the feature marked with an arrow pointing up corresponds to the N' = 4, N = 0 double resonance.

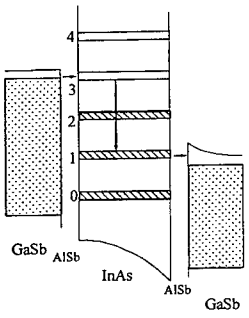

Fig. 4 Potential profile for a heterostructure in a magnetic field at which the N = 0, 1, 2 Landau levels are occupied and the N' = 3, 4 states are empty. The arrows indicate the three-step tunneling process responsible for the new features shown in Figs. 1 and 2.

With this interpretation of the anomalous features, it is easy to explain their magnetic field dependence. The crucial element is the resonance between unoccupied Landau levels and the emitter's Fermi edge: as the field increases so does the Landau level energies. Consequently, a higher voltage is required for the emitter to be aligned with an empty magnetic level and the rate of increase in the voltage is in proportion to the Landau level index N'.

In spite of this satisfactory explanation of the origin and behavior of the new features discussed here, important questions remain. One is the mechanism by which electrons lose energy between the two Landau levels. Another is how that double resonant condition leads to the observed I-V characteristics, specially the negative differential conductance

The narrowness of the negative-differential-conductance region suggests a density-of-states singularity analogous to a zero-bias singularity, but there seems to be no good theoretical justification for this analogy. A third question is whether the phenomenon depends on the dimensionality of the confined states; in other words, whether it is possible to observe similar NDC at zero magnetic field in an heterostructure configuration appropriately designed.

Acknowledgements

We thank Y. Lin for her help with the analysis of the data presented here and J. T. Pham for diode processing. We are grateful to W. I. Wang, who provided some of the heterostructures used in this study. We acknowledge DOE's and ARO's financial support for this work.

References

1. E. E. Mendez, L. Esaki, and W. I. Wang, Phys. Rev. B **33,** 2893 (1986).
2. V. J. Goldman, D. C. Tsui, and J. E. Cunningham, Phys. Rev. B **35,** 9387 (1987).
3. E. E. Mendez, H. Ohno, L. Esaki, and W. I. Wang, Phys. Rev. B **43,** 5196 (1991).
4. E. E. Mendez, V. Kuznetsov, D. Chokin, and J. D. Bruno, Bull. Am. Phys. Soc. **44**, 1471 (1999)

PA.55

MAGNETIC-FIELD-DEPENDENT ZERO-BIAS DIFFUSIVE ANOMALY

Eugene V. Sukhorukov
Department of Physics & Astronomy, University of Basel

We present the theoretical study of the strongly anisotropic magnetic field dependence of the zero-bias diffusive anomaly (ZBA) in tunnel structures with 2D and 3D electron states coexisting near the semiconductor surface. We demonstrate that the specific scenario of tunneling is realized in this structures: the electrons tunnel into 2D states and move diffusively in a 2D layer, whereas the main contribution to the screening comes from 3D electrons. This gives rise to the unusual magnetic field dependence of the ZBA. When the magnetic field **B** is perpendicular to the interface of the tunnel junction, the amplitude of the ZBA grows as B^2 in agreement with Ref. [1]. The ZBA amplitude strongly depends on the orientation of the magnetic field, in agreement with Ref. [2]. When the magnetic field lies in the plane of the junction interface, the ZBA amplitude is linear in B. The origin of the strong anisotropy is in the different characters of the charge relaxation at the semiconductor surface for different orientations of the magnetic field. This effect has been recently confirmed in the experiment [3]. We propose to use the magnetic field dependence to distinguish diffusive anomalies from other types of ZBA.

1. B.L. Altshuler and A.G. Aronov, Sov. Phys. JETP **50**, 968 (1979).
2. E.V. Sukhorukov and A.V. Khaetskii, Phys. Rev. B **56**, 1456 (1997).
3. G.M. Minkov, A.V. Germanenko, S.A. Negachev, O.E. Rut, and E.V. Sukhorukov, cond-mat/9807041

PA.56

TUNNELING TRANSVERSE TO THE MAGNETIC FIELD IN CORRELATED 2D ELECTRON SYSTEMS

T. Barabash†, M.I. Dykman†, and P.M. Platzman*
† Physics Department, Michigan State University, East Lansing, Michigan 48824, USA
* Bell Laboratories, Lucent Technologies, Murray Hill, New Jersey 07974, USA

We investigate tunneling from a 2D electron layer in the presence of a magnetic field parallel to the layer. We show that correlations in the electron system *exponentially strongly* affect the tunneling rate. This happens because the in-plane momentum **p** of the tunneling electron can be transferred to other electrons. As a result, the "magnetic barrier" for tunneling $[\mathbf{p} - e\mathbf{A}(\mathbf{r})]^2/2m$ is significantly decreased. The problem of tunneling transverse to the magnetic field is intrinsically multidimensional. The tunneling exponent may not be found from the standard analysis of motion in real space with imaginary time, and the particle no longer comes out from beneath the barrier at the turning point. We develop a general approach to tunneling in the magnetic field, which is based on the investigation of semiclassical trajectories in complex space and time, and of singularities of the set of these trajectories. Explicit results are obtained assuming that the electron which tunnels away from the surface state is additionally confined in an in-plane parabolic well created by other electrons. The tunneling exponent depends on the interrelation between the characteristic in-plane vibration frequency ω_0 and the cyclotron frequency ω_c. It sharply decreases with the increasing ω_0, for large ω_c. The results explain the experimental observations by L. Menna *et al.* (PRL **70**, 2154 (1993)) on tunneling from helium surface.

$k_{//}=0$ filtering effects in ballistic electron transport through sub-surface GaAs-AlGaAs double barrier resonant tunneling structures

J. Smoliner, R. Heer, G.Ploner, G. Strasser
Institut für Festkörperelektronik & Mikrostukturzentrum der TU-Wien
Floragasse 7, A-1040 Wien, Austria

Abstract

In Ballistic Electron Emission Microscopy on Au-GaAs double barrier resonant tunneling diodes, electrons are transferred across an interface between an area of high and low effective mass and subsequently through a low dimensional state. Experimentally, the resonant level in the double barrier structure becomes evident as clear step in the ballistic current measured as a function of sample bias. To analyze the spectrum, an extended Transfer Matrix Method, together with the commonly accepted Bell Kaiser model is used. In terms of this model we show that only electrons with zero wave vector parallel to the barriers can be transmitted resonantly.

Introduction :

Until now, only a small amount of literature treats the coupling of the longitudinal and transversal components of the electron wave vectors, which occurs, when electrons are transferred between areas of different effective mass[1,2,3,4]. A field of research, where electron transfer between areas of different effective mass plays an especially important role, is Ballistic Electron Emission Microscopy (BEEM)[5,6]. BEEM is a three terminal extension of conventional scanning tunneling microscopy (STM), where ballistic electrons are injected from a STM tip into a semiconductor (GaAs, $m^*=0.067m_0$) via a thin metal base layer ($m^*=m_0$) evaporated onto the sample. Originally, BEEM was mostly applied to measure metal-semiconductor Schottky barrier heights[7,8,9,10], but later, BEEM experiments were also used to study sub-semiconductor-surface sample properties. On a GaAs/AlGaAs double barrier structure, e.g. it was possible to investigate the resonant states[11] and on self assembled InAs quantum dots[12,13,14], the BEEM current was found to be enhanced. In our group, buried GaAs-AlGaAs superlattice structures were already studied in BEEM experiments[15,16] and we have found that due to the difference in electron mass between the Au base and the GaAs collector, parallel momentum conservation leads to electron refraction effects at the Au-GaAs interface.

In this paper, sub-surface GaAs-AlGaAs resonant tunneling diodes are investigated by BEEM. Using the commonly accepted Bell-Kaiser model[6,7,17] together with an extended Transfer Matrix Method (TMM) we show, that that due to parallel momentum and total energy conservation at the Au-AlGaAs interface, only electrons with zero wave vector parallel to the barriers can be transmitted resonantly.

Experiment :

As samples we used GaAs-AlGaAs double barrier resonant tunneling structures which were directly grown below the sample surface. The AlGaAs barriers of our sample had a thickness of 37 Å (x=0.4) and the GaAs well was 30 Å wide.
Figure 1(a) shows a schematic view of our experiment, Figure 1 (b) shows typical BEEM spectra of our sample.

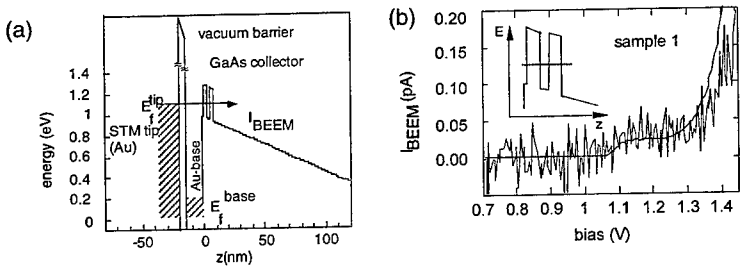

Figure 1 (a) : Schematic view of the experimental setup. (b)Typical experimental data.

As long as the Fermi level in the tip is below the resonant state, the ballistic electron current is zero. In the energy range between the resonance energy and the barrier height, a steplike feature is observed. As soon as the Fermi level in the tip exceeds the AlGaAs barrier height, the BEEM current increases approximately quadratically.

To understand this feature qualitatively, we first neglect the coupling between the longitudinal and transverse components of the electron wave vector, which occurs at interfaces between regions of different effective mass and only consider the total energy and parallel momentum conservation at the interface between Au and GaAs. In the following $E_\perp = \hbar^2 k_\perp^2 / 2m^*$ denotes the component of kinetic energy perpendicular to the interface and $E_{//} = \hbar^2 k_{//}^2 / 2m$ the component of kinetic energy parallel to the interface. For simplicity, the Fermi level in the Au base is defined to be the zero point of energy. Figure 2 (a) shows the in plane dispersion relations for electrons in the Au base at different given values of $E_\perp^{Au}$ and the dispersion relation for electrons in GaAs at the resonance energy, respectively. Due to the large difference in effective mass, the curvature of the parabolas is strongly different. The bold part of the parabola indicates the $k_{//}$ range of occupied states in the base, the resonant state below the surface is empty. By changing the voltage V_{STM}, the dispersion curves are shifted in energy. If V_{STM} is too small, the Au-dispersion curve is completely below the GaAs-dispersion and therefore, tunneling into the GaAs is not possible. If V_{STM} increases, the Au-parabola starts to intersect the GaAs parabola, which means that from the viewpoint of parallel momentum and total energy conservation, electrons are now allowed to tunnel as long as the intersection of both parabolas is in the range of occupied states.

Besides total energy and parallel momentum conservation, however, also the transmission coefficient of the resonant tunneling structure T(E) has an influence on the $k_{//}$ distribution of

transmitted electrons. For simplicity, we first assume that the transmission depends on $E_\perp$ only. As one can see from the transmission coefficient T($E_\perp$) plotted in Figure 2(b), the resonant level acts as narrow energy filter in $E_\perp$ and suppresses all tunneling processes at higher energy, although they would be in principle allowed from the viewpoint of total energy and parallel momentum conservation. Moreover, due to the strongly different curvature of the dispersion curves in Au and GaAs (see Figure 2 (a)), only electrons around $k_{//}$=0 are allowed to tunnel resonantly. This is illustrated in Figure 2(c), where the narrow bold region of the parabola around $k_{//}$=0 symbolizes the allowed $k_{//}$ range of transmitted electrons in the GaAs.

Qualitatively, this behavior explains the steplike features in the BEEM spectra: As long as the Fermi energy in the tip is below the AlGaAs barrier height, always a constant number of electrons will tunnel through the resonant level, since the allowed energy regime for resonant tunneling is always the same in $E_{//}$ and $E_\perp$, independent what the Fermi energy in the tip is.

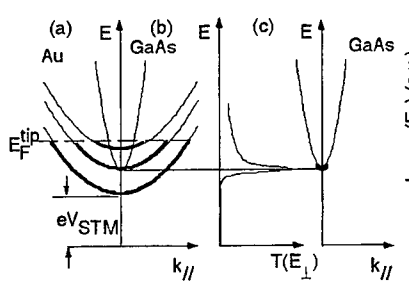

Figure 2 : (a) dispersion relations in the Au-base and inside the double barrier structure. (b) Transmission coefficient T($E_\perp$) of the resonant tunneling structure. (c): Range of allowed $k_{//}$ values around $k_{//}$=0 (indicated by the bold part of the parabola).

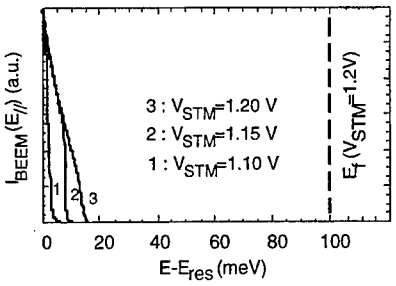

Figure 3 : Normalized BEEM current distribution as function of $E_{//}$ plotted for different values of the STM bias V_{STM}. E_{res} is the energy of the resonant level.

To investigate this feature in a quantitative way, we used the so called Bell-Kaiser model together with an extended Transfer Matrix Method[18,19],[20]. In this way, we also account for the coupling between $E_{//}$ and $E_\perp$, which occurs at each interface where the effective electron mass is changed and obtain a transmission coefficient T($E_\perp$,$E_{//}$), which both depends on $E_\perp$ and $E_{//}$. Details of the calculation will be published elsewhere.

The results of our calculation are shown in Figure 1 and Figure 3. The bold line in Figure 1(b) shows the calculated spectrum and the steplike behavior is nicely reproduced. In addition, the $k_{//}$ =0 filtering effect is explained quantitatively in terms of this model. In Figure 3, we show the BEEM current $I_{BEEM}(E_{//})$ as a function of $E_{//}$ calculated for various STM voltages. The voltages were chosen in a way that the corresponding Fermi level in the tip (E_F^{TIP}=eV_{STM}) is above the resonance energy (1.08 eV) but still below the AlGaAs barrier height. The width of the current distribution increases with increasing bias, but for V_{STM} =1.2 V, the Fermi level in the tip

(dashed line) is already ≈100 meV above the resonant level but the allowed $E_{//}$ range for the transmitted BEEM current is only 10 meV wide. This nicely demonstrates that the structure really acts as filter for electrons around $k_{//}=0$ (or $E_{//}=0$).

Summary :

In summary, we used a simple extension to the Transfer Matrix Formalism which allows a calculation of electron transmission coefficients in the case of a spatially varying effective mass. We have found that for electrons tunneling from an area of high effective mass through a resonant level into an area of low effective mass, a momentum filter is established for electrons close to $k_{//}=0$. The underlying physical principle also applies for all material systems with large difference in effective mass such as the InAs-AlSb heterostructures, e.g. and can be used to fabricate injector structures with narrow energy distribution both in $E_{\perp}$ and $E_{//}$.

Acknowledgments :

This work was sponsored by FWF project No. P12925-TPH and Gesellschaft für Mikroelektronik. The authors are grateful to E.Gornik for continuous support.

References :

1 Xue-Hua Wang, Ben-Juan Gu, Guo-Zhen Yang, Phys. Rev. **B55**, 9340 (1997)
2 J.N.Schulman, Appl. Phys. Lett. **72**, 2829 (1998)
3 V.V.Paranjape, Phys. Rev. **B52**, 10740 (1995)
4 R.Tsu, L.Esaki, Appl. Phys. Lett. **22**, 562, (1973)
5 W.J. Kaiser and L.D. Bell, Phys. Rev. Lett. **60**, 1406 (1988)
6 L.D. Bell and W.J. Kaiser, Phys. Rev. Lett. **61**, 2368 (1988)
7 W.J. Kaiser, M.H. Hecht, L.D. Bell, F.J. Grunthaner, J.J. Liu, L.C. Davis, Phys. Rev. **B48**, 18324 (1993)
8 H. Sirringhaus, E.Y. Lee and H.von Känel, Phys. Rev. Lett. **73**, 577 (1994)
9 R.Ludeke, M.Prietsch, A.Samsavar, J. Vac. Sci. Technol. **B9**, 2342, (1991)
10 M.Prietsch, R.Ludeke, Phys. Rev. Lett. **66**, 2511, (1991)
11 T. Sajoto, J.J. O'Shea, S. Bhargava, D. Leonard, M.A. Chin, V. Narayanamurti, Phys. Rev. **B74**, 3427 (1995)
12 M.E.Rubin, G.Medeiros-Ribeiro, J.J.O'Shea, M.A.Chin, E.Y.Lee, P.M.Petroff, V.Narajanamurty, Phys. Rev. Lett. **77**, 5268 (1996)
13 W.Wu, J.R.Tucker, G.S.Solomon, J.S.Harris, Jr., Appl. Phys. Lett. **71,** 1083 (1997)
14 E.Y.Lee, V.Narayanamurty, D.L.Smith, Phys. Rev. **B55**, R16033 (1997)
15 J.Smoliner, R.Heer, C.Eder, G.Strasser, Phys. Rev. **B58**, 7516 (1998)
16 R. Heer, J. Smoliner, G. Strasser, E.Gornik, Appl. Phys. Lett. **73**, 3138 (1998)
17 D. L. Smith and Sh. M.Kogan, Phys. Rev. B **54**, 10354 (1996)
18 E.O.Kane, "Tunneling Phenomena in Solids" eds.: E.Burnstein, S.Lundquist, Plenum Press, New York (1969)
19 B.Ticco, M.Y.Azbel, Phys. Rev. **B29**, 1970 (1984)
20 Xue-Hua Wang, Ben-Juan Gu, Guo-Zhen Yang, Phys. Rev. **B55**, 9340 (1997)

Observation of Large Conductance Oscillations in a Superconducting Single Electron Transistor Coupled to a Two-dimensional Electron Gas

Ç. Kurdak[a,b] R. Therrien[a], J. B. Kycia[a], J. Clarke[a], K. L. Campman[c], and A. C. Gossard[c]
a) *Department of Physics, University of California, Berkeley, CA 94720, USA and Materials Sciences Division, Lawrence Berkeley National Laboratory, Berkeley, CA 94720, USA*
b) *Department of Physics, University of Michigan, Ann Arbor, MI 48109-1120, USA*
c) *Department of Electrical and Computer Engineering, University of California, Santa Barbara CA 93106-9560, USA*

Abstract

We fabricated superconducting single electron transistors (SETs) on a GaAs/AlGaAs heterostructure with a two-dimensional electron gas (2DEG) located 1000 Å below the surface. The superconducting island is coupled to the leads by submicron tunnel junctions with a tunnel junction capacitance of 0.3 fF, and to the 2DEG by a gate capacitance of 1.5 fF. The tunnel resistances of the junctions are comparable to the quantum resistance and therefore the Coulomb blockade is suppressed by the strong Josephson coupling in these devices. In a device with a tunnel resistance of 9 kΩ, we observe large Coulomb blockade-like oscillations as a function of gate voltage with a peak-to-peak amplitude of 18 e^2/h. The dissipation of the SET is varied by changing the resistance of the 2DEG. Temperature and dissipation dependence of these large Coulomb blockade-like oscillations is explained by co-tunneling of the Cooper pairs across the SET.

There has been recent interest in studying systems of Josephson junctions coupled to a two-dimensional electron gas (2DEG) since one can vary the dissipation in these quantum systems independently of other parameters of the system [1-4]. In such a coupled system, the tunneling of Cooper pairs is accompanied by the motion of the corresponding image charges in the 2DEG. At low temperatures, the dissipation is caused by the motion of these image charges and therefore can be controlled *in situ* by varying the resistance of the 2DEG. In this letter, we report on the first measurements of superconducting single electron transistors (SETs) coupled to a 2DEG. A rich structure in the current-voltage characteristics of the superconducting SETs arising from effects such as even-odd electron number parity of the island [5,6] and the BCS singularity of the density of states of the electrodes [7,8] have been previously observed. Here, we will focus on higher order tunneling effects such as co-tunneling of two Cooper pairs – the simultaneous tunneling of pairs onto and out of an island.

A typical SET consists of two tunnel junctions in series and a gate capacitively coupled to the island between them. The physics of superconducting SETs is governed by the ratio of two energies: the Josephson coupling energy, $E_J = \Delta(h/4e^2)/(2R_T)$, where Δ is the BCS energy gap and R_T is the resistance of the tunnel junction, and the island charging energy,

$E_C = e^2/2C_\Sigma$, where C_Σ is the capacitance of the island (sum of all junction and gate capacitances). In the limit $E_C >> E_J$, at low temperatures the free motion of Cooper pairs across the tunnel junctions is inhibited, a phenomenon known as Coulomb blockade, and there would be a definite number of Cooper pairs on the superconducting island. This number N is canonically conjugate to the Josephson phase difference, ϕ, leading to the uncertainty relationship $\Delta N \Delta\phi \geq 1$. In the opposite limit $E_C << E_J$, the Josephson phase is well defined and behaves classically. The devices we have studied are in the intermediate regime, $E_C \approx E_J$, where, according to the uncertainty relationship both variables have significant quantum fluctuations. In this case, higher order tunneling processes, such as co-tunneling, become increasingly important and the orthodox approach of treating co-tunneling as a perturbation is no longer justified.

The superconducting SETs used in this work consist of two sub-micron Al/AlOx/Al tunnel junctions in series and a side gate fabricated using electron beam lithography and shadow evaporation techniques [9]. The devices are deposited on a GaAs/AlGaAs heterostructure with a 2DEG located 1000 Å below the surface. The substrate, thinned to approximately 200 μm, is placed on a metal back gate which is used to vary the resistance of the 2DEG. Shubnikov-de Haas and Hall measurements are carried out to characterize the 2DEG at different back gate voltages; from these measurements, we deduce electron sheet density, mobility, and sheet resistance of $n = 1.6\times10^{11}$ cm^{-2}, $\mu = 3.5\times10^5$ cm^2/V·s, and $R_g = 110\ \Omega$, respectively at zero back gate voltage. From the area of the tunnel junctions, the tunnel junction capacitance is estimated to be $C = 0.3$ fF. The island to 2DEG capacitance, $C_g = 1.5$ fF, is determined from the period of the Coulomb blockade oscillations measured at sufficiently high magnetic fields where the Al is normal. From these capacitance values, we estimate $C_\Sigma = (C_g + 2C) = 2.1$ fF and hence $E_C = 38\ \mu$eV. The tunnel resistance of the tunnel junctions is determined from the slope of the current-voltage (I-V) characteristics at high currents to be 9 kΩ and 25 kΩ for the two devices we studied. We present only data from the 9 kΩ sample ($E_J = 65\ \mu$eV) where the effects of co-tunneling are strongest.

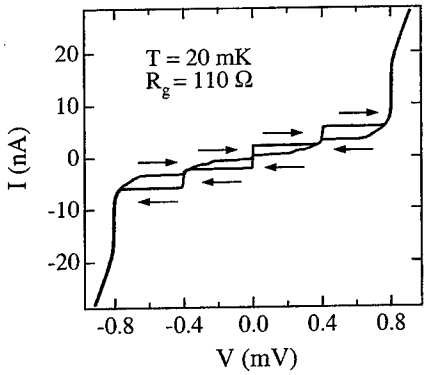

Figure 1: Current-voltage characteristics of the SET at 20 mK. The arrows indicate the sweep direction of the current. The gate voltage is adjusted to give the maximum switching current.

Electrical measurements are performed in a dilution refrigerator at temperatures down to 20 mK. The sample leads were filtered by π-filters at room temperature, microwave filters at 4.2 K, and a second set of microwave filters at the temperature of the mixing chamber. Battery operated low-noise voltage and current amplifiers in the screened room surrounding the

refrigerator were used to make four-terminal measurements. The I-V characteristics of the SET with a tunnel resistance of 9 kΩ are shown in Fig. 1. In these underdamped junctions, as the bias current is swept through the critical current we observe switching from the supercurrent branch to the quasiparticle branch. As there are two tunnel junctions in series, the switching behavior is observed at two distinct currents. The current at which the first switching occurs, I_C, depends on the gate charge as shown in Fig. 2 whereas the second switching current is found to be independent of the gate charge. The dependence of I_C on gate charge is periodic with a period e. For low bias voltages, the current is carried only by Cooper pairs as the quasiparticle gap is much larger than both charging energy and thermal energy. Therefore, we expect the periodicity with respect to the gate charge to be $2e$ [6]. However, as observed before by other groups, most devices do not show $2e$-periodicity because of the motion of background charges [10-11].

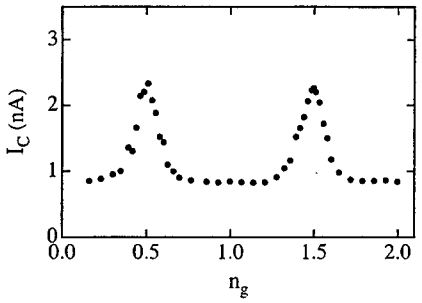

Figure 2: Switching current, I_C, versus gate charge in units of e.

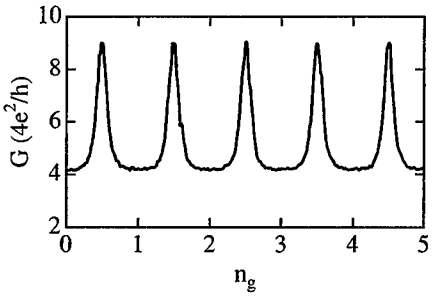

Figure 3: Zero-bias conductance versus gate charge in units of e.

For bias currents much smaller than I_C, the I-V characteristics are linear. Even though the device is in the strong tunneling limit, the zero-bias device conductance exhibits Coulomb blockade-like oscillations as a function of gate charge, as shown in Fig. 3. However, these oscillations are very different from the Coulomb blockade oscillations observed in weakly coupled SETs. First, the size of these oscillations is much larger than the quantum conductance (about 18 e^2/h at 20 mK). Second, between the conductance peaks there are flat regions of nonzero conductance. For the leading order tunneling processes, the sequential tunneling of Cooper pairs, the island charge changes after the tunneling event, and the corresponding energy difference associated with this change must be supplied from either thermal or quantum fluctuations. Therefore, the rate of such tunneling processes is expected to be strongly dependent on gate charge. On the other hand, for some of the higher order tunneling processes, such as the co-tunneling of two Cooper pairs, the charge on the island does not change, and we expect the rate of such higher order tunneling processes to be independent of gate charge. Thus, we infer that the flat conductance background observed in our device is due to co-tunneling of Cooper pairs.

Since the device was fabricated on a 2DEG, we were able to vary the dissipation of the system by changing the resistance of the 2DEG. As in the case of two- and one-dimensional Josephson junction arrays, the conductance of the device is found to decrease with increasing 2DEG resistance [1-2]. The dependence of the peak conductance on the 2DEG resistance was much stronger than the dependence of the background conductance consistent with our interpretation that the background conductance is due mainly to co-tunneling processes. We find that the height of the peak and background conductance have strong temperature dependences while the width of the conductance peaks has a weak temperature dependence. This temperature dependence is consistent with the recent theory of Wilhelm *et al.* where the coupling between the superconducting SET and the 2DEG is included [4]. The temperature and dissipation dependence of this device will be discussed in detail elsewhere [12].

In conclusion, we studied superconducting SETs coupled to a 2DEG which enabled us to vary the dissipation of the system by changing the carrier density of the 2DEG. In one of the devices we observed large Coulomb blockade-like peaks as a function of gate voltage with an amplitude of 18 e^2/h. The flat regions of nonzero conductance between the peaks can be explained by the co-tunneling of Cooper pairs. For a co-tunneling event the image charge under the island does not change. Consistent with this picture, the dependence of conductance on the 2DEG resistance is found to be much weaker for the flat regions between conductance peaks where co-tunneling is dominant, than on the peaks.

We acknowledge valuable discussions with G. Zimanyi and F. K. Wilhelm. The work at Berkeley was supported by the Office of Naval Research, Order No. N00014-95-F-0099 through the U. S. Department of Energy under Contract No. DE-AC03-76SF00098.

References

1. A. J. Rimberg, T. R. Ho, Ç. Kurdak, J. Clarke, K. L. Campman, and A. C. Gossard, Phys. Rev. Lett. 78, 2632 (1997).
2. T. R. Ho, Ph.D. Thesis, University of California, Berkeley (1997).
3. K.-H. Wagenblast, A. van Otterlo, G. Schon, and G. T. Zimanyi, Phys. Rev. Lett. 79, 2730 (1997).
4. F. K. Wilhelm, G. Schon, and G. T. Zimanyi, unpublished.
5. M. T. Tuominen, J. M. Hergenrother, T. S. Tighe, and M. Tinkham, Phys. Rev. Lett. 69, 1997 (1992).
6. K. A. Matveev, M. Gisselfalt, L. I. Glazman, M. Johnson, and R. I. Shekhtre, Phys. Rev. Lett. 70, 2940 (1993).
7. D. V. Averin, A. N. Korotkov, A. J. Manninen, and J. P. Pekola, Phys. Rev. Lett. 78, 4821 (1997).
8. Y. Nakamura, A. N. Korotkov, C. D. Chen, and J. S. Tsai, Phys. Rev. B 56, 5116 (1997).
9. G. T. Dolan, Appl. Phys. Lett. 31, 337 (1977).
10. T. M. Eilis and J. M. Martinis, Phys. Rev. B 50, 627 (1994).
11. T. M. Eilis, J. M. Martinis, and M. H. Deverot, Phys. Rev. Lett. 70, 1862 (1993).
12. Ç. Kurdak, R. Therrien, J. B. Kycia, J. Clarke, K. L. Campman, and A. C. Gossard, unpublished.

Intersubband Absorption in Nb-Clad InAs Quantum Wells

T.A. Eckhause[1], S. Tsujino[1) 2)], E.G. Gwinn[1)], M. Thomas[3)] and H. Kroemer[3)]

1) Department of Physics, University of California, Santa Barbara, CA 93106
2) Quantum Transition Project, Japan Science and Technology Corp., 4-7-3 Park. Bld. 4F, Komaba, Meguro-ku, 153 Tokyo, Japan
3) Department of Electrical and Computer Engineering, University of California, Santa Barbara, CA 93106

We use mid-infrared (MIR) spectroscopy to investigate the contact region at the Nb/InAs superconductor/semiconductor interface. We observe a remnant of the intersubband (ISB) resonance in Nb-clad InAs quantum wells, both in samples where we have grown Nb directly on InAs in situ, and samples where we have etch exposed the InAs surface before depositing the Nb. The presence of this remnant ISB indicates partial confinement of the electrons to the InAs. The similar resonance widths in the MBE grown Nb/InAs sample and the samples with Nb on etched InAs suggest that coupling of electron states in the InAs to those in Nb, rather than etch-induced damage, produces most of the resonance broadening.

InAs quantum wells (QWs) have recently been used to make superconducting weak links that exhibit novel behavior, such as Andreev bound states [1], subgap optical absorption [2], supercurrent reversal [3], and a frequency-doubled a.c. Josephson effect [4]. In these junctions, the quasi-two-dimensional electron gas in an InAs QW couples superconducting Nb electrodes. Conduction between the Nb electrodes and the electron gas in the InAs QW is typically achieved by removing the top AlSb barrier with a selective etch, and depositing Nb over the exposed InAs. The InAs layer is continuous across the region of unmodified AlSb/InAs/AlSb QW that serves as the "weak link" (Fig. 1). The critical current, I_c, of these novel Josephson junctions is sensitive to the procedure used to prepare the Nb/InAs interface, and to the properties of the QW material in the weak link. Here we describe investigations of the Nb/InAs interface using mid-infrared optical transmission spectroscopy.

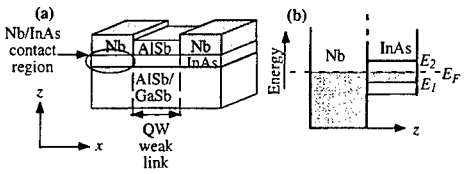

Fig 1 a) An InAs-based QW weak link, shown in greater detail. We use MIR spectroscopy to study the Nb/InAs contact region. b) Models of the proximity effect in Nb/InAs examine partial reflection of electrons at the Nb/InAs interface, which produces subbands in the InAs, indicated schematically as E_1 and E_2.

The energy of an optically excited intersubband resonance in a semiconductor quantum well is depolarization-shifted from the difference in subband energies by an amount dependent on the density of carriers in the QW [5]. When Nb, instead of an semi-insulating AlSb barrier, is placed on top of the InAs, ISB absorption features should be present, as long as electrons are partially confined in the InAs, to produce structure in the density of states. This confinement could be produced by partial reflection from an interfacial barrier (though none is expected at a clean Nb/InAs interface, due to Fermi-level pinning in the InAs conduction band) , or from the differences in the band structures and Fermi energies of Nb and InAs. Partial confinement of electrons in InAs is examined in theoretical models of proximity effects in this type of weak link [6], but has not been demonstrated experimentally.

Here we present ISB absorption data on three Nb-clad, 150Å-InAs QW samples. The first two Nb-clad InAs samples, A and B, are fabricated from unmodified, symmetrically doped, MBE-grown AlSb/InAs/AlSb quantum wells. Samples A and B have low temperature mobilities of 1.97×10^5 and $2.22 \times 10^5 cm^2/V\text{-}s$, and densities of 5.2 and 5.5 $\times 10^{12} cm^{-2}$ respectively, before we process the samples, which places the Fermi energy in the second subband. These densities and mobilities are typical of those used in InAs-based SNS junctions [1-4]. After we remove the top AlSb barrier with a $NH_4OH:H_2O$ (1:5) wet etch we move samples A and B to a deposition chamber, where, after sputter cleaning the exposed InAs with a low power rf Ar ion plasma we deposit, *in situ*, an 1800Å thick layer of Nb. The processing steps used to prepare samples A and B were nominally identical. Sample C, including the Nb overlayer, was grown in the MBE chamber. The lower barrier layers are grown with Te-dopants, followed by the 150Å-InAs layer, followed, without breaking vacuum, by a layer of MBE deposited Nb [7]. The Nb/InAs interface in sample C is, therefore, free of the etch-induced disorder present in samples A and B.

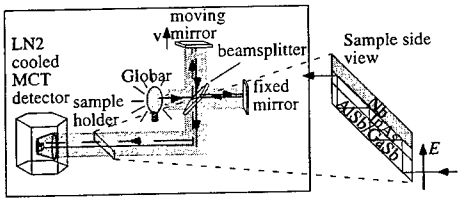

Fig 2. Transmission measurement setup using FTIR. The sample is held at a 45 degree angle to the incident light. The inset shows a magnified view of the sample from the side. Light is polarized to couple to the ISB transition.

To measure the MIR transmission spectrum, we bevel the samples' edges at 45-degrees to allow multiple passes of the light through the QW (Fig. 2). The MIR light, p-polarized to couple with the ISB transition, is incident on the beveled edge. A Bruker Fourier Transform Infrared Spectrometer (FTIR) collects the transmission spectra. To remove spurious spectral features due to the source, the optics, and due to thin-film interference from the semiconductor layers beneath the InAs, we normalize all transmission spectra to a reference. The reference for samples A and B is fabricated by selectively removing both the top AlSb barrier and the InAs from the AlSb/InAs/AlSb QW structure, and depositing a metal over the lower AlSb barrier layers. The reference for sample C is fabricated by removing the MBE grown Nb and the InAs, and again depositing a metal over the lower barrier layers.

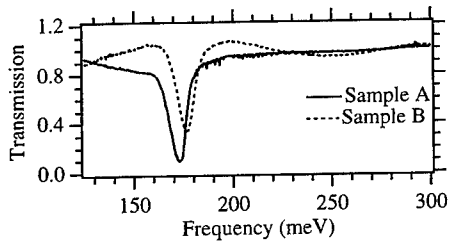

Fig 3. Transmission spectra, taken at room temperature, normalized to reference. The unmodified AlSb/InAs QWs show a large ISB absorption centered around 174 meV and 178 meV in samples A and B, respectively.

In figure 3 we show the transmission spectra of the two unmodified QWs from which we fabricated samples A and B. The QW material for sample A shows an ISB resonance narrowly centered around 174 meV, close to the 185 meV calculated for the ISB transition from the second to the third subband of this 1.35 eV-deep InAs quantum well. The unmodified QW for sample B

shows a similar narrow resonance at 178 meV. All ISB resonances are from the second to the third subband. The different peak absorption energies of the resonances are due to the depolarization shift of the resonance away from the bare subband spacing, by an amount dependent on the electron density in the QW, and the band structure non-parabolicity [5]. The strength of the absorption, however, cannot be compared quantitatively because the optical path length varies by ~15% between samples, and between the samples and the reference.

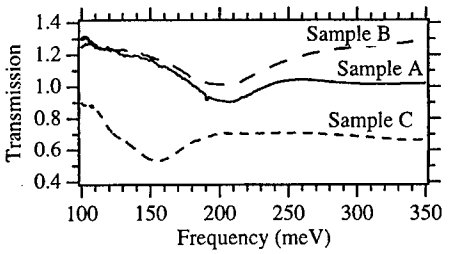

Fig 4. The Nb-clad InAs in all three samples shows remnant ISB absorption. The resonances of samples A and B are broadened and shifted up in frequency compared to the unmodified QW ISB resonances (Fig. 3). The ISB resonance of sample C is lower in energy, but has a comparable width to the resonances of samples A and B.

Figure 4 shows the normalized transmission spectra for samples A, B and C. The changes in these spectra from those of the unmodified QWs in Fig. 3 are due to changes in electron confinement in the InAs produced by replacing the AlSb barrier with Nb. As shown, Samples A and B have broader resonances than the unmodified QWs, centered at about 207 meV. This remnant ISB has been seen at varying frequencies and line widths when other metals are used in place of the Nb [8]. The presence of this remnant ISB resonance in the Nb-clad InAs indicates that some degree of confinement of carriers in the InAs persists in these structures. As reported elsewhere, we have shown that an InAs weak-link fabricated from the material of sample A has a critical current comparable to other high-quality InAs based junctions. Thus, the partial electron confinement, which we believe to be a general feature of the Nb/InAs contact region, coexists with phase coherent transport through the InAs QW-based weak-link [9].

The shift in energy of the remnant ISB, relative to the ISB in the unmodified QW, could be due to an increased carrier density in the InAs, the altered boundary conditions, or a narrowing of the well by a few monolayers which may occur during the rf Ar ion cleaning of the InAs. The lowest energy resonance is in sample C, which is not subjected to Ar cleaning, suggesting that a narrowing of the InAs may be the dominant cause of the energy shift. In sample C, where interface roughness and QW width fluctuations should be minimal, we also observe a broadened resonance of similar width to those of samples A and B. This suggests that inhomogenous broadening due to well-width fluctuations is not the dominant source of the observed broadening of the remnant ISB relative to the unmodified QW ISB resonance. While the process of replacing the top AlSb barrier with Nb induces disorder in the InAs [10] and is probably responsible for some of the broadening of the resonance, incomplete confinement of the carriers in the InAs appears to be the main source of the large resonance width.

In conclusion, we have used MIR spectroscopy to investigate the contact region near a superconductor/semiconductor interface. The remnant ISB absorption we observe in Nb-clad InAs demonstrates that partial confinement of electrons to the InAs persists after replacement of the top AlSb barrier with Nb. This partial confinement does not destroy phase coherence: we observe substantial critical currents across a 1μm InAs QW weak-link between the Nb/InAs contact regions[9]. The partial confinement most likely results from the large mismatch in materials properties across the Nb/InAs interface, rather than an interfacial barrier. In the future, one might be able to use MIR spectroscopy to calculate the reflection probability for electrons at the Nb/InAs interface and compare with superconducting transport properties across InAs-based Josephson

Junctions. The authors wish to acknowledge support for this work from the NSF under grant nos. NSF-DMR-9314899 and NSF-DMR-9700767, and from the ONR under N00014-92-J-1452, and from QUEST, an NSF Science and Technology Center.

[1] C. Nguyen, H. Kroemer, and E.L. Hu, Phys. Rev. Lett. **69**, 2847 (1992).
[2] E.L. Yuh, J.G.E. Harris, T.A. Eckhause, K. Wong, E.G. Gwinn, H. Kroemer, and E.L. Hu, Surf. Sci. **361/362**, 315 (1996).
[3] A.F. Morpurgo, B.J. van Wees, T.M. Klapwijk, and G. Borghs, Phys. Rev. Lett. **79**, 4010 (1997).
[4] K.W. Lehnert, N. Argaman, H.-R. Blank, K.C. Wong, S.J. Allen, E.L. Hu, and H. Kroemer, Phys. Rev. Lett. **82**, 1265 (1999).
[5] R.J. Warburton, C. Gauer, A. Wixforth, J.P. Kotthaus, B. Brar, and H. Kroemer,. Superlattices and Microstructures, **19**, 365 (1996). See eqns. 4 and 5.
[6] For superconductor-normal metal interfaces with reflection induced by a δ-function potential barrier see e.g. A.F. Volkov, P.H.C. Magnee, B.J. van Wees, and T.M. Klapwijk, Physica C, **242**, 261 (1995) or M. Octavio, M. Tinkham, G.E. Blonder, T.M. Klapwijk, Physical Review B, **27**, 6739 (1983).
[7] To produce a good mirror we sputtered a thicker layer of Nb on top of the MBE deposited Nb.
[8] S. Tsujino, *et. al., in preparation.*
[9] T.A. Eckhause, S. Tsujino, K.W. Lehnert, E.G. Gwinn, S.J. Allen, M. Thomas, and H. Kroemer, *in preparation.*
[10] P.H.C. Magnee, S.G. den Hartog, B.J. van Wees, T.M. Klapwijk, W. van de Graaf, and G. Borghs, Appl. Phys. Lett., **67**, 3569 (1995).

Shot noise and Luttinger like properties in the FQHE regime.

D.C. Glattli*,V. Rodriguez, H. Perrin and P. Roche.
Service de Physique de l'Etat Condensé, CEA Saclay,
F-91191 Gif-sur-Yvette, France

Y. Jin and B. Etienne
Laboratoire de Microstructures et Microélectronique, C.N.R.S.,
B.P. 107, F-92225 Bagneux, France
(June 15, 1999)

We present shot noise measurements in the Fractional Quantum Hall regime at $\nu = 1/3$ when the fractional edges are coupled by an artificial impurity, namely a Quantum Point Contact. For weak coupling and large voltage, recent experiments have established that the current noise power S_I is proportional to the *backscattered current* I_B and to the fractional charge $e/3$. For low voltage, Chiral Luttinger liquid models suggested a renormalization of the coupling strength, even with weak bare coupling, leading to strong backscattering and to a noise power proportional to the *transmitted current* I and to the bare electronic charge. We discuss here new noise measurements which confirm such an important prediction.

PACS: 73.40-Hm, Hm 71.10, Pm 72.20.My
Key words : Fractional Quantum Hall Effect; Shot noise; Luttinger liquids.

* *Corresponding author.*
E-mail : cglattl@spec.saclay.cea.fr, Fax : 33-169088786.

One of the most central question toward a deep understanding of the FQH effect is wether transport at the edges can be understood in term of Chiral Luttinger Liquid (χLL) models and, if so, how these models [1] [2] [3] [4] [5] could be refined to better describe the experiments. In order to contribute to answer this question, we present results combining non-equilibrium measurements of the differential conductance and of the current noise. We have investigated the transport between opposite fractional edges weakly coupled by the potential of a Quantum Point Contact (QPC) at $\nu = 1/3$. We find that for low temperatures and low bias voltage: - 1) the conductance goes to zero, even for extremely weak coupling, reflecting the renormalization of the coupling strength predicted by the χLL models; however we did not reach the predicted power law regime. - 2) the shot noise becomes proportional to the *transmitted current* I and to the electron charge as predicted by the χLL models for strong backscattering. This is to be compared with the large bias voltage weak backscattering regime previously investigated in [6] [7] where shot noise was proportional to the *backscattered current* $I_B = Io - I$ and to the Laughlin charge ($I_0 = (e^2/3h)V$ is the current incident on the QPC).

The measurements are made using a GaAs/Ga(Al)As heterojunction with a 100nm deep 2DEG of density 0.95 10^{11}cm^{-2} and mobility 10^6 cm^{2}V^{-1}s^{-1}. The lithographic width of the QPC is 250nm. The sample is enclosed in a metallic box and each lead is highly filtred by using low temperature lossy microcoaxial leads, giving a photon temperature as low as 100mK from 0.1GHz to 1THz [8]. Because noise measurements in the audio frequency range are highly demanding, the microphonically induced electrical fluctuations, which become very important at 12 Tesla because of residual vibrations, have been reduced to a very low level and the integrated rms unwanted voltage fluctuations over 0-10kHz never exceed 0.5μV, well below k_BT ($\simeq 1.7\mu$eV for 20 mK) . This give us unprecedented reliable conditions to study transport at $\nu = 1/3$ without which most of the low temperature non-linear transport features would not be observed.

Non linear transport at ν=1/3:

Before presenting our new results on shot noise, we describe below our observations of non-linear transport at $\nu = 1/3$.

The hallmark of transport in the fractional quantum Hall regime is *non-linear* current voltage characteristics. This can be qualitatively understood as resulting from electron *charge fractionalization*. For example if an electron is injected on a 1/3 fractional edge in the energy range $[eV, eV + d(eV)]$ above the Fermi energy, the number of ways to generate three quasiparticles, according to energy conservation, is $\sim (eV)^2 d(eV)$. This means that the differential conductance dI/dV should varies as V^2. This is indeed what predicts the standard χLL models [1] [2] [3] [4] for the tunneling of electrons from an ordinary metal to 1/3 edges. Similar temperature power law is predicted for the zero bias conductance and in general voltage and temperature are expected to give similar power laws. More generally it is found that $dI/dV \sim V^{\frac{1}{\nu}-1}$ for $\nu = 1/(2m+1)$. At $\nu = 1/3$, this has been remarkably confirmed in experiments by A. Chang et al [9] where a power law close to 2 has been found when measuring the tunneling form a metallic contact to the edge of a 2D electron gas (2DEG). Within the same χLL models, a doubled exponent: $\frac{2}{\nu} - 2$ is expected for the conductance

measured between two $\nu = 1/(2m+1)$ regions in the strong backscattering regime. Experiments using QPCs have been done at $\nu = 1/3$ to check these predictions. In [10] the predicted T^4 temperature variation of the conductance was observed in a limited range of temperature, but this was not clearly confirmed by other groups [11]. We present below differential conductance measurements that have been recorded simultaneously with noise which show that in general a power 2 rather than 4 is observed in the range of weak coupling and low temperature explored here.

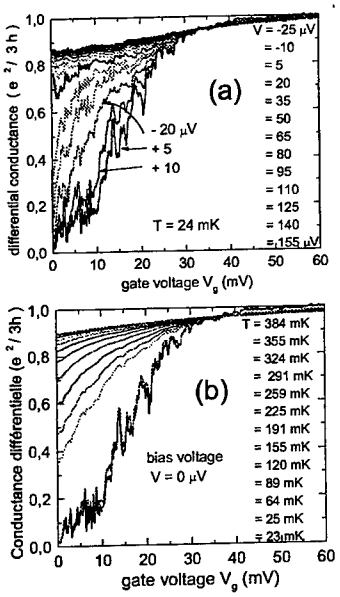

FIG. 1. (a) differential conductance versus gate voltage for different bias voltages at $\nu = 1/3$ and fixed low temperature. (b) zero bias voltage conductance versus gate voltage for different temperatures.

Fig.1(a) shows the low temperature differential conductance dI/dV versus gate voltage V_g for various bias voltage V and Fig.1(b) the zero voltage conductance versus V_g for different temperatures at bulk filling factor $\nu = 1/3$. The striking features of Fig.1 are – 1) the similarity between both graphs : finite bias voltages and finite temperatures produce similar effects on conductance; – 2) the insulating behavior at low energy (temperature or voltage). Both features qualitatively agree with the χLL prediction that the weakest impurity, here the artificial impurity realized with a QPC, leads to an insulator at low energy due to the renormalization of the strength of the potential which couples opposite edges. Similar features typical for the 1/3 state are observed when the bulk filling factor, for instance 1/2 or 2/3, is different than the filling factor at the QPC. We would like to emphasize the non-trivial origin of the non-linear conduction. Indeed, the lower is the bias voltage or the temperature, the stronger are the non-linearities. If they were merely due to a change in the strength of coupling with bias voltage they would be less pronounced at low bias. Also, the nearly zero conductance found at the low bias voltage and temperature does not correspond to the pinch-off regime which would occur for gate voltages around -400mV. Instead the high T and large V saturation of the conductance at the lowest gate voltage shown in Fig.1 (0 mV) is around 0.85-09 ($e^2/3h$). This indicates that the density at the middle of the QPC is at most 10-15% smaller than the bulk density. From this we can infer that the QPC only *weakly perturbs* the quantum Hall fluid. The insulating behavior and the non-linearities are thus *fundamental properties* of the fractional state.

In Fig.2(a) the differential conductance versus bias for a series of fixed gate voltages at $T = 24$mK is displayed. For small V_g a rapid increase of the low bias conductance followed by a cross-over to a slow variation toward an asymptotic value shows the transition from strong to weak backscattering. For larger V_g only the weak backscattering regime is observed. Again, the shape of the curves qualitatively follow the prediction of χLL models, but not in the very details. To be more quantitative we have plotted in Fig.2(b) a series of differential conductance traces normalized to the zero bias conductance versus $eV/2\pi k_B T$ and taken at different temperatures and low bias for the same $Vg = 2.07$mV. All traces merge rather well together to give a unique curve except for few departures from it at large bias. This means that $eV/2\pi k_B T$ is a good parameter to describe the conductance at fixed coupling as suggested by χLL models. In particular the conductance is doubled for $eV \simeq 2\pi k_B T$. The inset shows however a power law variation with exponent 2 in contrast with the χLL exponent 4. If we compare with the χLL prediction: $dI/dV(V,T) = dI/dV(0,T)(1+\frac{-1+2/\nu}{\Gamma(\nu)^2}\left(\frac{eV}{2\pi T}\right)^{-2+2/\nu})$ for $\nu = 1/3$, solid curve, there is clearly no good agreement although the predicted value are quantitatively not too far from the experimental data. We found that similarly all the traces of Fig.2(a) start as V^2 and a power 4 is hardly observed. More details will be given elsewhere.

To summarize this first part devoted to characterize the transport, we have found *qualitative* agreement with the χLL picture. Combining these results with previous studies [10] [11] [12], it seems that finding quantitative agreement with experiments using QPC probably requires modifications of the χLL models: – 1) long

range intra-edge interactions: for $V < 50\mu$V, using a typical 10^7cm.s^{-1} drift velocity, the χLL boson modes have wavelengths $>100\mu$m and screening by the QPC gates is inoperant [13]. This would give I-V curves intermediate between χLL and dynamic Coulomb blockade predictions [14]; - 2) χLL models consider a sharp δ potential coupling the edges, while the QPC potential is smooth and locally slightly lowers the electron density. A local variation of the Luttinger liquid parameter in the coupling region should be included; - 3) It is likely that spin is important: when moving away from 1/3, spin reversed quasi-particles may be created together with ordinary Laughlin quasi-particles. A possible spin texture at the edge may affect the χLL predictions.

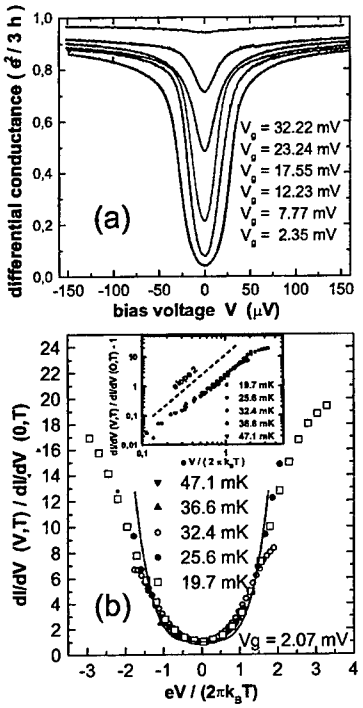

FIG. 2. (a) differential conductance versus bias voltage for different gate voltages. The curve with lower $V = 0$ conductance corresponds to $V_g = 2.35mV$. (b) differential conductance curves normalized to their zero bias conductance plotted versus the reduced variable $eV/2\pi k_B T$. The data are taken at $V_g = 2.07mV$ and for different temperatures. Inset : a log-log plot shows a dominant V^2 variation.

Finally, the small random potential fluctuations adding to that of the QPC and a possible change of coupling with bias have to be considered but they are probably not the most relevant effects.

After the characterization of the transport, we now discuss another χLL prediction about shot noise when renormalization of the coupling leads to strong backscattering regime.

Shot noise in the strong backscattering regime: χLL models predict that in the large bias voltage limit the backscattered current $I_B = I_0 - I$ vanishes and shot noise experiments would observe the Poissonian noise of fractional quasiparticles $e/3$ at $\nu = 1/3$ [15] [3] [4]. Indeed two experiments, one measuring the autocorrelation $S_I = \langle \Delta I^2 \rangle / \Delta f$ of the total current fluctuations with $\nu_{bulk} = 1/3$ [6] and the other one measuring the anticorrelated fluctuations of the total and backscattered current $S_{I,I_B} = -\langle \Delta I_B \Delta I \rangle / \Delta f$ with $\nu_{QPC} = 1/3$ and $\nu_{bulk} = 2/3$ [7], have found the predicted noise power $\simeq 2(e/3)I_B$ when $I_B \ll I_0$. Here we focus on another remarkable χLL prediction: we have checked that, even for a very weak coupling, the insulating regime occuring at sufficiently low V and T will make the quasiparticles *condense* into electrons to give a Poissonian shot noise $S_I \simeq 2eI$ when $I \ll I_0$. The result may seem trivial as it is similar to what is expected for tunneling in the pinch-off regime but we emphazise that *there is no tunnel barrier* and we are far from pinch-off as shown in the first part. Instead we are considering a weakly perturbed but fundamentally insulating fractional quantum Hall fluid.

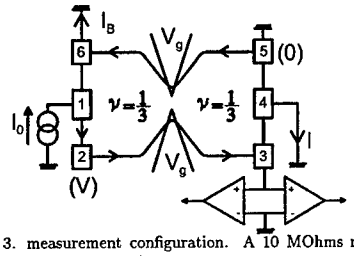

FIG. 3. measurement configuration. A 10 MOhms resistance at 4.2 K (not shown) realizes a current source to send a current I_0 through the sample. This generates a bias voltage V such that $I_0 = (e^2/3h)V$. The incident current I_0 is transmitted toward contact (3) giving the current I and is reflected toward contact (6) giving the current I_B. The average current and its fluctuations are measured through the voltage variations of contact (3) with respect to ground using $V_{(3)} = (h/3e^2)I$. Two separate amplification paths and cross-correlation measurements perform a very reliable noise detection. $V/2$ is added to V_g for symmetrization.

The noise measurement configuration used is shown in Fig.3. It has the advantage that the variation of the

measured shot noise at fixed temperature only reflects changes in the partition noise, or excess noise, S_I^{Exc}. Indeed, we have experimentally checked that the Johnson-Nyquist noise contribution measured did not depend on dI/dV. The voltage fluctuations measured at contact 3 are given by: $S_V = (3h/e^2)^2 \left(S_I^{Exc} + 4k_BTe^2/3h + S_I^N\right)$. If we were measuring the partition shot noise of uncorrelated electrons crossing a barrier of transmission t, the excess partition noise would be $S_I^{Exc} = 2eI(1-t)(\coth(eV/2k_BT) - 1)$.

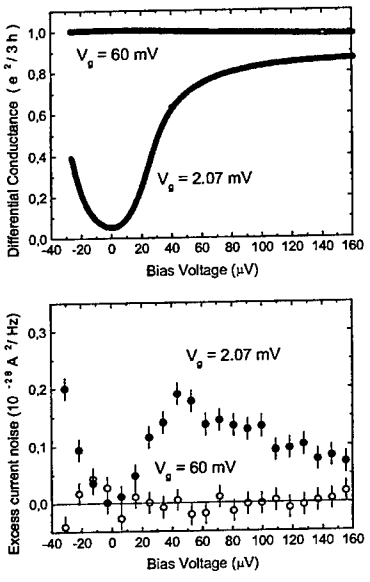

FIG. 4. (a) differential conductance versus bias voltage at 24mK for two different couplings : one at $V_g = 60mV$ corresponding to the absence of backscattering, the other one at $V_g = 2.07mV$ corresponding to a finite but weak coupling which gives rise to both strong and weak backscattering. In (b) the data correspond to shot noise measurements performed simultaneously with the conductance measurements shown in (a).

The second term in the expression of S_V corresponds to the Johnson-Nyquist voltage noise $4k_BT3h/e^2$ of contact 3 whose resistance is $3h/e^2$. This thermal contribution does not depend on dI/dV because the thermal voltage fluctuations observed in contact (3) correspond to the sum of the thermal current fluctuations emitted by contact (3) plus the thermal current fluctuations emitted by contacts (2) and (5), one with a weight equal to the transmission and the second with a weight equal to the reflection (in the case of fermions the three contributions would be respectively : $2k_BTe^2/3h$, $t2k_BTe^2/3h$ and $(1-t)2k_BTe^2/3h$ [16]). S_I^N is the current noise of the circuit. Systematic equilibrium thermal noise measurements from 20mK to 300mK at $\nu = 1/3$ allowed us to check the noise calibrations with high accuracy in the frequency range 3 to 6kHz.

Fig.4 shows in (a) the differential conductance and the noise versus bias voltage taken at $V_g = 60$mV, well on the 1/3 plateau. No appreciable noise is observed, and as already checked in [6] [7], the fractional quantum Hall fluid is noiseless. In (b) the measurements are taken at finite coupling, $V_g = 2.07$mV. We can see the cross-over from strong to weak backscattering for the conductance and the noise. At the largest voltage, the ratio I/I_0 , about 0.65, tells us that we have not reached a sufficiently large transmission to observe the Poissonian noise of the Laughlin charges as in [6] [7]. Instead we will concentrate on the strong backscattering regime at low voltage and temperature. Fig.5 shows data taken at $V_g = 2.07$mV and two temperatures, 47.8 and 36 mK, for a limited range of applied bias voltage (-25μV to +25μV).

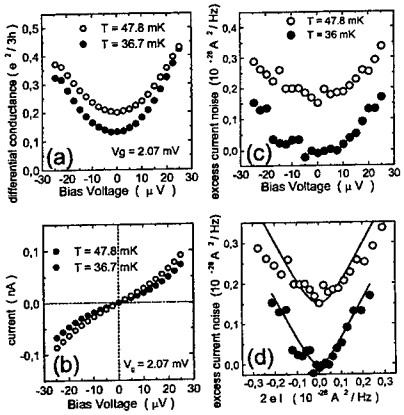

FIG. 5. differential conductance (a) and shot noise measurements (c) versus a series of bias voltages V taken at fixed $V_g = 2.07mV$ for two temperatures. In (b) is plotted the integrated I-V characteristics and in (d) the shot noise versus current in units of Poissonian shot noise of electrons. The solid line curves correspond to the finite temperature excess current noise $S_I^{Exc.} = 2eI\coth eV/2k_BT$ in the Poissonian regime. In (c) and (d) a voltage independent background has been substracted and the high temperature noise data have been shifted for clarity.

Fig.5(a) and (b) show the measured differential conductance versus V and the integrated current voltage characteristics respectively. In Fig.5(c) we have plotted the results of noise measurements taken simultaneously with conductance. Curves (a), (b), and (c) all show non-linear variations with V reflecting Luttinger like properties when the weak coupling is renormalized to give a strong backscattering regime (here dI/dV is in the range 0.15 to 0.4 $e^2/3h$). In Fig.5(d) we have plotted the excess current noise versus current in units of $2eI$. What is striking here is the linear variation of S_I^{Exc} with $|I|$ compared to the non linear variation with V. The solid curves are comparison with the excess noise expected for the Poissonian transfer of charges e through the QPC, as predicted by χLL models in this regime: $S_I^{Exc.} = 2e\,|I|\,(\coth(eV/2k_BT) - 1)$ [15] [17].The lowest temperature data compare well with this expression while the data at the larger temperature shows a slightly lower linear increase of noise with current. This may be understood as follows: the larger conductance for 47.8mK makes the noise less Poissonian and an effective reduction factor taking into account the cross-over between Poissonian and binomial noise should be included. For $V = 25\mu$V (12.5μV) the ratio I/I_0 is 0.28 (0.11) for 47.8mK and while it is 0.22 (0.077) for 36mK.

We have also performed noise measurements at much lower temperature which very accurately confirms that variation of noise is linear with the transmitted current I. However preliminary measurements at very low temperature seems to give a different regime where the noise is above the Poissonian value for electrons. This will be published elsewhere.

In conclusion, we have shown that the χLL features, i.e. non-linear conduction and appearance of a strong backscattering regime even for weak coupling, are qualitatively observed in transport experiments using QPC at bulk filling factor 1/3. Shot noise measurements have verified the prediction that at low voltage and temperature the current noise is linear with current reflecting the Poissonian transfer of integer charges trough the QPC.

We acknowledge usefull discussions with B. Kramer, Th. Martin, Y. Nazarov, V. Pasquier, H. Saleur, I. Safi, N. Sandler, M. Sassetti and K. Schoutens.

[1] X.G. Wen, Phys. Rev. Lett. **64** (1990) 2206.
[2] C.L. Kane and M.P.A. Fisher, Phys. Rev. B **46** (1992) 15233
[3] C. de C. Chamon, D.E. Freed, and X.G. Wen, Phys.Rev. B **51** (1995) 2363.
[4] P. Fendley, A.W.W. Ludwig, and H. Saleur, Phys. Rev. Lett. **75** (1995) 2196.
[5] A. Lopez and E. Fradkin, cond-mat/9810168.
[6] R. de-Picciotto *et al.*, con-mat/9707289; Nature **389** (1997) 162.
[7] L. Saminadayar, D.C. Glattli, Y. Jin, and B; Etienne, con-mat/9706307, Phys. Rev. Lett. **79** (1997) 2526.
[8] D.C. Gattli *et al.*, J. Appl. Phys. **81** (1997) 7350.
[9] A. M. Chang, L. N. Pfeiffer, K. W. West, Phys. Rev. Lett. **77** (1996) 2538.
[10] F.P. Milliken, C. P. Umbach, and R.A. Webb, Solid State Commun. **97** (1995) 309.
[11] P.J. Turley, D.P. Druist, E.G. Gwinn, K. Maranowski, K. Campmann, A.C. Gossard, Physica B **249-251**, (1998) 410.
[12] Masato Ando, Akira Endo, Shingo Katsumoto, Yasuhiro Iye, Physica B **249-251**, (1998) 427.
[13] K. Moon and S. M. Girvin, Phys. Rev. B **54** (1996) 4448.
[14] M. Sassetti and B. Kramer, Phys. Rev. B **57**, (1998) 1515.
[15] C.L. Kane and M.P.A. Fisher, Phys. Rev. Lett. **72** (1994) 724
[16] see for example : M. Büttiker, Phys. Rev. B **46** (1992) 12485; Th. Martin and R. Landauer, Phys. Rev. B **45**, (1992) 1742; Physica B **175** (1991) 167.
[17] P. Fendley and H. Saleur, Phys. Rev B **54** (1996) 10845.

TA.2

Entanglement in 2DEG systems: towards a detection loophole-free test of Bell's inequality

Xavier Maître,[1] William D. Oliver, and Yoshihisa Yamamoto
ICORP Quantum Entanglement Project
Edward L. Ginzton Laboratory, Stanford University
Stanford, California 94305-8045

We propose a continuous quiet source of position and spin-entangled electrons at the output of a non-linear beam-splitter. Featured in the quantum Hall regime of two-dimensional systems, the generated entanglement can be tested by two-particle interferometry. Preparation and detection schemes of two complete sets of Bell states are given. Such a novel source of entanglement could lead to a new test of Bell's inequality derived in terms of noise correlation measurements. The intrinsic noiseless and lossless aspects of the source are essential to exhibit a violation. This system could close the detection efficiency loophole.

PACS numbers: 03.65.Bz, 05.30.Fk, 73.40.Hm
Key words: two-dimensional electron gas, two-particle interferometry, Bell states, Bell's inequality

The indistinguishability of two identical particles is a source of entanglement in quantum mechanics. It is expressed in Bohm's formulation of the Einstein-Podolsky-Rosen problem [1]. A pair of spin-$\frac{1}{2}$particles initially in

$$|\Psi_{\text{in}}\rangle = |k_1 k_2\rangle \otimes \frac{1}{\sqrt{2}}(|\uparrow_1\downarrow_2\rangle - |\downarrow_1\uparrow_2\rangle) \,, \tag{1}$$

where 1 and 2 are the particle labels and k stands for the particle spatial mode, is split apart [2]. Delimited by Bell's inequality [3], a set of spin measurements along specific directions leads to a conflict between the predictions of quantum mechanics and the concepts of reality and locality [1]. Yet, experimental imperfection tends to erase the contradiction. The required auxiliary assumptions generally lead to the communication loophole [4] and the detection loophole [5]. In mesoscopic two-dimensional systems, current conservation is a major key to close the second loophole.

1. A two-dimensional entangled electron source. A twin edge channel in the quantum Hall regime at low magnetic field with a filling factor ν=2, can be used to generate single-mode electron pairs into the system. When the split gates in figure 1.a are not biased, the conductance through the device from k to g reaches the first plateau $2e^2/h$ and the current is noiseless. Electrons are emitted from the reservoir in the same spatial mode k and are already in $|\Psi_{\text{in}}\rangle$. If the sheet density is low in the confined region, the Coulomb interaction

[1]email: maitre@loki.stanford.edu

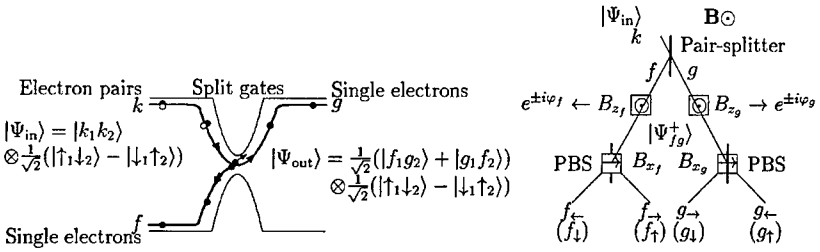

Figure 1: a. Deterministic pair-splitting by Coulombic repulsion b. Experimental scheme for a test of Bell's inequality

may be revealed (figure 1). We assume that the two electrons repel each other. If this spin-independent pair-splitting is perfect, the transmitted and reflected beams are quiet streams of single electrons in the state:

$$|\Psi^+_{fg}\rangle = \frac{1}{2}\left(|f_1 g_2\rangle + |g_1 f_2\rangle\right) \otimes \left(|\uparrow_1\downarrow_2\rangle - |\downarrow_1\uparrow_2\rangle\right) . \tag{2}$$

This is a regulated source of entangled pairs of distant electrons.

2. Two-electron interferometry. The most straightforward way to test this entanglement is to collide the two electrons at a subsequent beam-splitter. They bunch into the state:

$$|\Phi^+_{fg}\rangle = \frac{1}{2}\left(|f_1 f_2\rangle + |g_1 g_2\rangle\right) \otimes \left(|\uparrow_1\downarrow_2\rangle - |\downarrow_1\uparrow_2\rangle\right) , \tag{3}$$

where the coefficients of the beam-splitter r and t are taken with the same half square modulus and overall phase factors are omitted. The two output currents exhibit full shot noise. This bosonic behaviour is explained by the symmetric orbital wave-function [6, 7]. Following this guideline, electrons prepared in one of the symmetric triplet spin states are expected to antibunch. The shot noise is consequently suppressed in the output currents. The statement based on the symmetry of the orbital wave function fails when one cannot guarantee one electron in each arm. First, when the above collision is reversed: $|\Phi^+_{fg}\rangle \rightarrow |\Psi^+_{fg}\rangle$, electrons prepared in a symmetric orbital wave-function antibunch. Secondly, electrons prepared in a symmetric orbital wave-function given by the state:

$$|\Phi^-_{fg}\rangle = \frac{1}{2}\left(|f_1 f_2\rangle - |g_1 g_2\rangle\right) \otimes \left(|\uparrow_1\downarrow_2\rangle - |\downarrow_1\uparrow_2\rangle\right) , \tag{4}$$

bunch when colliding. Therefore, one measurement after collision at a beam-splitter is not sufficient to distinguish between the singlet spin states and the triplets. To describe the whole situation, we introduce the Bell-state notation both for spin and for position:

$$\begin{array}{l}\text{Orbital}\\ \text{triplet}\end{array} \left\{ \begin{array}{l} |\Phi^+_{fg}\rangle = |\phi^+_{fg}\rangle \otimes |\psi^-_{\uparrow\downarrow}\rangle \\ |\Phi^-_{fg}\rangle = |\phi^-_{fg}\rangle \otimes |\psi^-_{\uparrow\downarrow}\rangle \\ |\Psi^+_{fg}\rangle = |\psi^+_{fg}\rangle \otimes |\psi^-_{\uparrow\downarrow}\rangle \end{array} \right. \quad \begin{array}{l}\text{Spin}\\ \text{triplet}\end{array} \left\{ \begin{array}{l} |\Phi^+_{\uparrow\downarrow}\rangle = |\psi^-_{fg}\rangle \otimes |\phi^+_{\uparrow\downarrow}\rangle \\ |\Phi^-_{\uparrow\downarrow}\rangle = |\psi^-_{fg}\rangle \otimes |\phi^-_{\uparrow\downarrow}\rangle \\ |\Psi^+_{\uparrow\downarrow}\rangle = |\psi^-_{fg}\rangle \otimes |\psi^+_{\uparrow\downarrow}\rangle \end{array} \right. \tag{5}$$

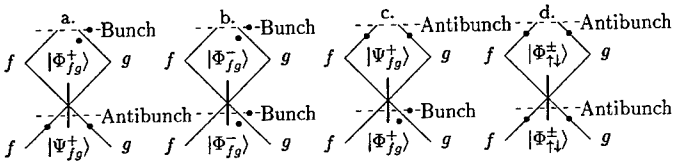

Figure 2: Differentiation schemes of the six Bell-product states (a.) $|\Phi^+_{fg}\rangle$, (c.) $|\Phi^-_{fg}\rangle$ (b.) $|\Psi^-_{fg}\rangle$, (d.) $|\Phi^\pm_{\uparrow\downarrow}\rangle$ and $|\Psi^+_{\uparrow\downarrow}\rangle$ by two series of measurements. Bunching behaviour is pictured by two dots in one arm, and antibunching by one dot in each arm

where $|\phi^\pm_{fg}\rangle=\frac{1}{\sqrt{2}}(|f_1f_2\rangle \pm |g_1g_2\rangle)$, $|\psi^\pm_{fg}\rangle=\frac{1}{\sqrt{2}}(|f_1g_2\rangle \pm |g_1f_2\rangle)$, $|\psi^\pm_{\uparrow\downarrow}\rangle=\frac{1}{\sqrt{2}}(|\uparrow_1\downarrow_2\rangle \pm |\downarrow_1\uparrow_2\rangle)$, and $|\phi^\pm_{\uparrow\downarrow}\rangle=\frac{1}{\sqrt{2}}(|\uparrow_1\uparrow_2\rangle \pm |\downarrow_1\downarrow_2\rangle)$ are the four Bell states for spin and position.
These states can be prepared from the state $|\Psi^+_{fg}\rangle$. The collision at a standard 50/50 beam-splitter prepares the state $|\Phi^+_{fg}\rangle$. If the spins are flipped in the arm f, the state $|\Phi^+_{\uparrow\downarrow}\rangle$ is prepared. If they are flipped twice, then it is $|\Phi^-_{fg}\rangle$. To do so, two polarizing beam-splitters are required to separate the two spin components in one arm and to finally recombine them so only the spin down is flipped in f (or g). A polarizing beam-splitter could be realized by the adjunction of a micromagnet designed on the top of the two-dimensional electron gas and close to a pair of split gates [8, 9]. Since the spin degeneracy is locally lifted, the transmission and reflection coefficients of the corresponding beam-splitter are spin-dependent.
The three orbital triplet states $|\Phi^\pm_{fg}\rangle$ and $|\Psi^+_{fg}\rangle$ can be distinctively detected from the three spin triplet states $|\Phi^\pm_{\uparrow\downarrow}\rangle$ and $|\Psi^+_{\uparrow\downarrow}\rangle$ with two sets of measurements before and after a beam-splitter (figure 2). To discriminate the spin triplet states $|\Phi^\pm_{\uparrow\downarrow}\rangle$ and $|\Psi^+_{\uparrow\downarrow}\rangle$, the inverse transformation required for their preparation must be applied first.

3. A new test of Bell's inequality. The most striking evidence of entanglement remains the violation of Bell's inequality. The anticorrelations between the electron spins of each entangled pair should be measured in different bases at the output of the pair-splitter while electrons fly apart. We must extract from the data a signal which is limited by any local theories but which takes greater values if the two electrons are quantum mechanically entangled. This is the essence of Bell's inequality.
When the spin degeneracy is transiently lifted, free evolution of the two spin components results in a rotation in the plane perpendicular to the magnetic field **B**. This transformation can be induced independently on each arm with two additional micromagnets (figure 1.b). The induced rotation angles φ_f and φ_g can be tuned by applying a bias voltage on two gates in order to vary the path length taken by the electrons under the micromagnets. To read out theses transformations, the local magnetic field for the polarizing beam-splitters must be generated by a second type of micromagnets in the plane of the 2DEG along the x direction. Therefore, if the global magnetic field in the z direction is negligible compared to the field in the x direction, then the spin is measured along $\{|\rightarrow\rangle, |\leftarrow\rangle\} = \{(|\uparrow\rangle+|\downarrow\rangle)/\sqrt{2}, (|\uparrow\rangle-|\downarrow\rangle)/\sqrt{2}\}$.

We now examine noise correlations between different ports which can lead to a conflict with locality. By rotating the spins we can register the noise anticorrelations and correlations as a function of the phase shifts φ_f and φ_g experienced by the electrons:

$$\langle \delta n_{f_\leftarrow} \delta n_{g_\rightarrow} \rangle = \langle \delta n_{f_\rightarrow} \delta n_{g_\leftarrow} \rangle = +\frac{1}{4} \cos(\varphi_f - \varphi_g) \tag{6}$$

$$\langle \delta n_{f_\leftarrow} \delta n_{g_\leftarrow} \rangle = \langle \delta n_{f_\rightarrow} \delta n_{g_\rightarrow} \rangle = -\frac{1}{4} \cos(\varphi_f - \varphi_g) \tag{7}$$

Following the generalization of Clauser et al. [10], we define equivalently for the spins of the electron pairs the correlation function as a function of φ_f and φ_g:

$$E(\varphi_f, \varphi_g) = \langle \delta n_{f_\uparrow} \delta n_{g_\uparrow} \rangle + \langle \delta n_{f_\downarrow} \delta n_{g_\downarrow} \rangle - \langle \delta n_{f_\uparrow} \delta n_{g_\downarrow} \rangle - \langle \delta n_{f_\downarrow} \delta n_{g_\uparrow} \rangle \, . \tag{8}$$

Any local theories must then satisfy the inequality

$$-2 \leq S(\varphi_f, \varphi_g, \varphi'_f, \varphi'_g) \leq +2 \, , \tag{9}$$

with $S(\varphi_f, \varphi_g, \varphi'_f, \varphi'_g) = E(\varphi_f, \varphi_g) - E(\varphi_f, \varphi'_g) + E(\varphi'_f, \varphi_g) + E(\varphi'_f, \varphi'_g)$.
For the set of angles $\varphi_f - \varphi_g = \varphi'_f - \varphi_g = \varphi'_g - \varphi'_f$:

$$S(\varphi_f, \varphi_g) = \cos 3(\varphi_f - \varphi_g) - 3\cos(\varphi_f - \varphi_g) \, . \tag{10}$$

A maximal violation of Bell's inequality can be reached for $\{\varphi_f, \varphi_g\} = \{\pi/8, 3\pi/8\}$, $\{3\pi/8, \pi/8\}$, $S(\varphi_f, \varphi_g) = \pm 2\sqrt{2}$.

We would like to thank Edo Waks for helpful comments.

References

[1] Albert Einstein, Boris Podolsky, and Nathan Rosen, Phys. Rev. **47**, 777 (1935).
[2] D. J. Bohm, *Quantum Theory*, Constable, London, England, 1954
[3] J. S. Bell, Physics **1**, 195 (1964).
[4] Paul G. Kwiat, Philippe H. Eberhard, Aephraim M. Steinberg, and Raymond Y. Chiao, Phys. Rev. A **49**, 3209 (1993).
[5] P. Pearle, Phys. Rev. D **2**, 1418 (1970).
[6] Markus Michler, Klaus Mattle, Harald Weinfurter and Anton Zeilinger, Phys. Rev. A **53**, R1209 (1996).
[7] Guido Burkard, Daniel Loss, and Eugene V. Sukhorukov, cond-mat/9906071 (1999).
[8] P. D. Ye, D. Weiss, R. R. Gerhardts, M. Seeger, K. von Klitzing, K. Eberl, and H. Nickel, Phys. Rev. Lett. **74**, 3013 (1995).
[9] V. Stepankin, Physica **211**, 345 (1995).
[10] J. F. Clauser, M. A. Horne, A. Shimony, and R. A. Holt, Phys. Rev. Lett. **23**, 880 (1969).

TA.3

CONTROLLED DEPHASING OF ELECTRONS BY A "PHASE SENSITIVE" *WHICH PATH* DETECTOR

D. Sprinzak, E. Buks*, Ji Yang, H. Moritz, M. Heiblum, D. Mahalu, and Hadas Shtrikman

Braun Center for Submicron research, Condensed Matter Physics,
Weizmann Institute of Science, Rehovot 76100, Israel.
*Current address: Condensed Matter Physics, California Institute of Technology, Pasadena, California 91125, USA.

We report on an intriguing and novel *which path type* experiment – where the electrons in the *which path detector* experience ONLY a quantum mechanical phase change even though the present set-up DOES NOT allow any direct extraction of *which path* information from the detector. We utilize a mesoscopic system to show that such a detector induces dephasing that agrees qualitatively with theory. Such an experiment raises fundamental questions concerning the type of *which path information* needed for dephasing.

Recently, a mesoscopic *which path type* experiment was performed by Buks *et al* [1]. A quantum point contact (QPC), in close proximity to one path of a double-path electron interferometer, served as a *which path detector*. When electrons passed in the nearby path (of the interferometer) they affected the **conductance** of the QPC, hence, affecting the current and the dissipation in the reservoirs. Even though no current, noise, or dissipation were actually measured - the more *which path information* was available (in principle), the weaker was the visibility of the interference fringes of the nearby interferometer.

In the present experiment we constructed a new kind of *which path detector* where the transmitted electrons acquired ONLY a phase change. There were no other changes in the detector's properties (conductance, noise, dimensions, etc.). Even though this phase change is not measurable in the existing setup it strongly dephased the nearby interferometer.

Our detector is composed of one or more partly transmitted edge-states at high magnetic field. Partition of the electrons is provided by a QPC (with transmission T_d) and phase is added to the transmitted electrons via Coulombic repulsion by the nearby electrons in the interferometer (which is electrically separated from the detector). Since a *double path interferometer* is difficult to realize at high magnetic fields we utilize a *double quantum dot* (DQD) device (a Fabry-Perot type interferometer) located near the transmitted edge-states but far (30 μm) from the QPC, hence, affecting only the electrons' phase (but not T_d). Such detector distinguishes between short and long trajectories within the DQD interferometer. Consequently, interference strength was tested via the line shape of the conductance resonance of the DQD. Specifically, as partitioned edge current ($T_d<1$) passed through the detector the resonances of the nearby DQD became wider and weaker. Note that we used a DQD instead of a single-QD to observe the intrinsic level width (rather than thermally broadened resonance peaks).

A relatively simple theory shows that the detector must be phase coherent with a dephasing rate proportional to $T_d(1-T_d)$, which represents the shot noise in the detector (produced by partitioning in the QPC-splitter). We found a dephasing rate proportional to $T_d(1-T_d)$ and to the electron probing rate of the detector (the applied voltage on the detector). However, when an Ohmic contact was introduced between the QPC-splitter and the DQD-interferometer, the dephasing rate of the DQD was drastically reduced – providing an experimental verification that the dtector has to be phase coherent.

[1] E. Buks et al. Nature **39**, 872-874 (1998)

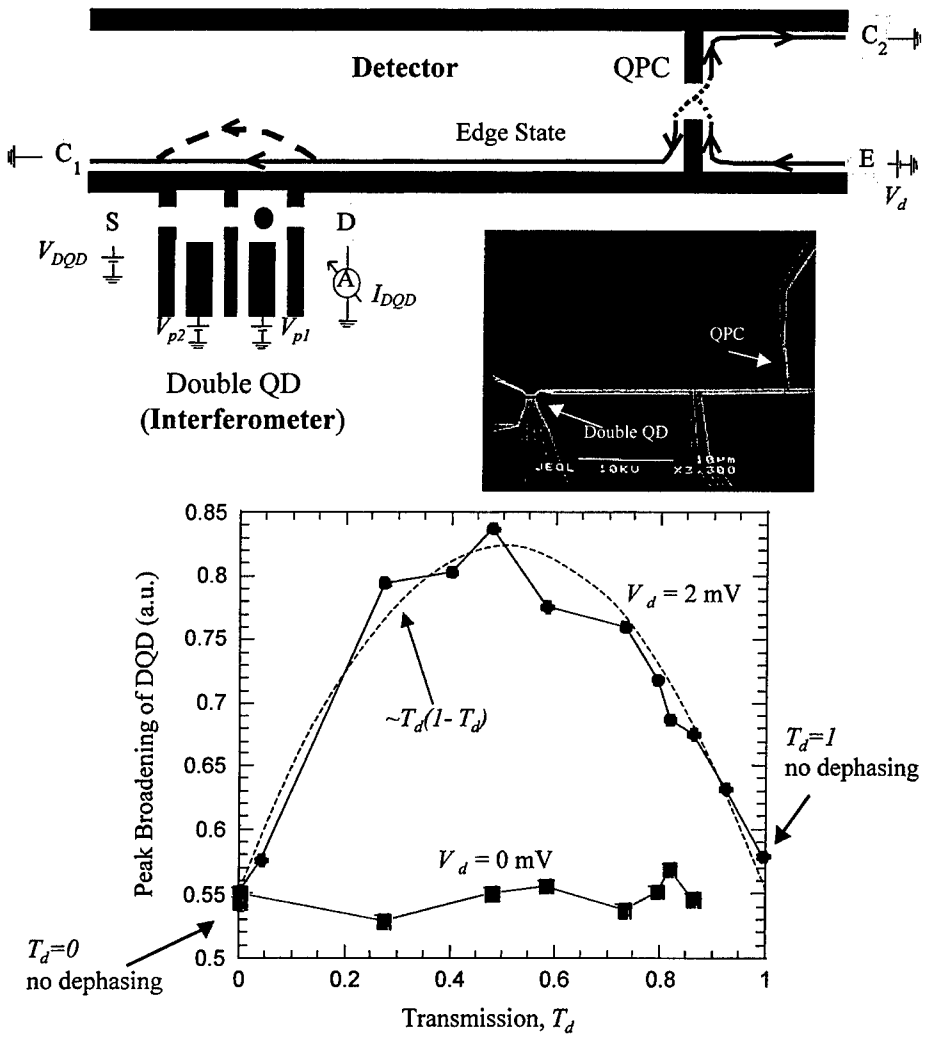

Experimental configuration with an SEM micrograph (top) and results of peak broadening of the DQD (proportional to the dephasing) as a function of T_d (bottom). The data shown is for V_d = 0 mV (squares-no probing current) and V_d = 2 mV (circles- with probing current). The dashed line is a fit to a parabola using the qualitative theory developed.

TA.4

Quantum Computing Using the Best 2-D Conductor: Electrons Floating on Liquid Helium

P. M. Platzman
Bell Labs, Lucent Technologies
700 Mountain Ave.
Murray Hill, NJ 07974 USA

M. I. Dykman
Dept. of Physics and Astronomy
Michigan State University
East Lansing, MI 48824 USA

There is a great deal of interest in constructing Analog Quantum Computing (AQC) such objects could possibly solve problems that no classical digital computer could possibly solve even if it were hundreds of orders of magnitude bigger than current computers. An AQC is made up of N interacting quantum objects which have at least two states. The problem is to find a system where N can be fairly large $N > 10^3$, where the interactions can be easily controlled, i.e. changed and where the Q bits are almost completely decoupled from the external world. All real physical systems proposed so far have almost insurmountable technological and scientific barriers which must be overcome to achieve a useful AQC.

In this talk we discuss the possibility of using a set of $1 < N < 10^9$ electrons trapped in vacuum in 1D hydrogenic levels above a micron thick film of liquid helium as large AQC. Individual electrons are laterally confined by some lithographically defined pattern of micron sized superconducting metal pads, which make up one plate of a parallel plate capacitor. Information is stored in the lowest two hydrogenic levels (subbands) and individual Q bits can be placed in an arbitrary linear superposition of states by the application of microwave fields at 100 GHZ. Interaction between Q bits are strong. They arise from well-defined Coulomb interactions having an energy scale of roughly 20 Kelvin. At temperatures of 10^{-2} K and in the presence of a modest 1.5 Tesla magnetic field we are able to prove that decoherence coupling times are of the order of 10^{-4} seconds. In addition we show that the application of time dependent electric fields created by voltages on the pads allows one to change the wave functions of groups of electrons in almost an arbitrary fashion. The many electron wave functions may be conveniently "read out" at some time when the computation is done using an inverted DC voltage. This voltage allows electrons in the excited subband to tunnel off the surface to a channel plate imaging system.

Tunneling into Ferromagnetic Quantum Hall States: Observation a Spin Bottleneck

H. B. Chan[1], R. C. Ashoori[1], L. N. Pfeiffer[2] and K. W. West[2]

1. Department of Physics, Massachusetts Institute of Technology, Cambridge, MA 02139
2. Bell Laboratories, Lucent Technologies, Murray Hill, NJ 07974

Abstract

We explore the characteristics of equilibrium tunneling of electrons from a 3D electrode into a high mobility 2D electron system. For most 2D Landau level filling factors, we find that tunneling can be characterized by a single, well-defined tunneling rate. However, for spin-polarized quantum Hall states (ν =1, 3 and 1/3) tunneling occurs at two distinct rates that differ by up to 2 orders of magnitude. The dependence of the two rates on temperature and tunnel barrier thickness suggests that slow in-plane spin relaxation creates a bottleneck for tunneling of electrons.

The interplay between Zeeman coupling of the electronic spins to an applied magnetic field and Coulomb interactions among electrons leads to remarkable spin properties of quantum Hall systems. Theorists predict that the elementary charge excitations of the $\nu = 1$ ferromagnetic quantum Hall state consist of spin textures known as Skyrmions [1]. Nuclear spin resonance and magneto-optical absorption experiments [2] have shown that the spin polarization of the 2D electrons attains a maximum at $\nu = 1$ and falls off sharply on either side. This rapid loss of spin polarization away from $\nu = 1$ provides the strongest evidence for the existence of Skyrmions. Transport and heat capacity measurements [3] offer additional support for the Skyrmion picture.

Tunneling experiments have demonstrated a capability to probe electron-electron interactions [4-6]. Given the measured and predicted richness of the spin properties of quantum Hall systems, we decided to explore whether tunneling could also prove useful for revealing effects of interactions among electronic spins [7]. Such study should be most interesting for the ferromagnetic quantum Hall states, but experimental data for tunneling in these regimes have been limited. The major obstacle is that the in-plane conductance of the 2D system drops to near zero around $\nu = 1$. As a result the tunneling charge cannot be collected and measured via conduction in the 2D plane.

In this talk, we describe measurements of tunneling from a 3D electrode into a high mobility 2D electron system in a GaAs/AlGaAs heterostructure at $\nu = 1$. A novel capacitance technique [6] enables us to measure the tunneling current in the quantum Hall regimes when the in-plane conductance is very low. While it is well-known that Coulomb interaction of electrons suppresses tunneling near the Fermi energy, we have discovered that non-equilibrium spin accumulation also leads to a reduction of tunneling rates into spin-polarized quantum Hall states. We observe that the process of electron tunneling into spin-polarized quantum Hall states differs qualitatively from tunneling into other filling fractions: electrons tunnel into ferromagnetic quantum Hall states at two distinct rates. Some electrons tunnel into the 2D system at a fast rate while the rest tunnel at a rate up to 2 orders of magnitude slower. We observe such novel double-rate tunneling only in spin polarized quantum Hall states (ν = 1, 3 and <1/3) in samples of highest mobility. Our detailed study of the dependence of the two rates on temperature, magnetic field and tunnel barrier thickness indicates that slow in-plane spin relaxation leads to a bottleneck for tunneling and gives rise to the double tunneling rate phenomenon.

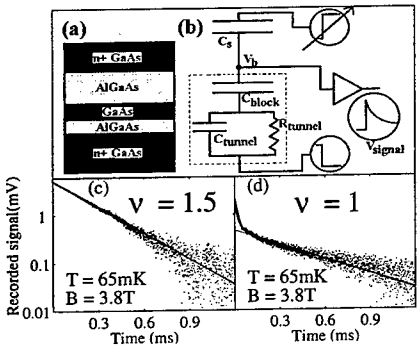

FIG. 1. (a) Structure of our samples. (b) External circuit used to measure R_{tunnel}. The sample can be modeled by linear circuit elements (box) when the excitation voltage is smaller than *kT*. (c) Recorded signal (amplification of V_b) decays exponentially at $\nu = 1.5$. (d) Recorded signal is non-exponential at $\nu = 1$.

Figure 1a shows a schematic of our samples. The following sequence of layers is grown on n+ GaAs substrate: 6000 A n+ GaAs, 300 A GaAs spacer layer, AlGaAs/GaAs tunnel barrier, 175 A GaAs quantum well, 700 A AlGaAs (undoped) blocking barrier and 1.3 μm n+ GaAs cap layer. Samples A and C have AlGaAs/GaAs superlattice tunnel barriers of thickness 193 A and 147 A respectively. For sample B, the tunnel barrier is made of 130 A AlGaAs. A major advantage of our structure is the complete absence of silicon dopants in the AlGaAs layers, eliminating the main source of disorder in the 2DEG. Electrons are attracted into the quantum well from the bottom n+ GaAs electrode by application of a positive dc bias to the cap layer. As a result, the mobility of our samples is expected to be higher than 10^6 $cm^2V^{-1}s^{-1}$, which is consistently achieved in modulation doped GaAs/AlGaAs quantum well heterostructures grown in the same MBE machine. The dc bias to the cap layer also permits variation of the 2D electron density from depletion to 3×10^{11} cm^{-2}.

We measure "zero-bias" tunneling into the 2DEG by applying excitation voltages smaller than *kT*. In this equilibrium tunneling regime [4], we model the tunnel barrier by a capacitor C_{tunnel} shunted by a resistor R_{tunnel}, while a capacitor C_{block} represents the blocking barrier (Fig.1b). Figure 1b also shows the capacitance bridge used to measure R_{tunnel}. Voltage steps of opposite polarity are applied to the top electrode of the sample and to one plate of a standard capacitor C_s. The other plate of C_s and the bottom electrode of the sample are electrically connected, and the voltage V_b at this balance point is amplified and recorded as a function of time. When the excitation voltage amplitude is smaller than *kT*, the tunneling resistance R_{tunnel} is independent of voltage across the tunnel barrier. The equivalent circuit of the bridge consists of linear circuit elements and therefore we expect V_b to decay exponentially.

Figure 1c plots on a semi-log scale the recorded voltage as a function of time at $\nu = 1.5$. The signal decays exponentially for more than 2 orders of magnitude. In general, we observe such agreement with an exponential decay when ν is close to half integer. This indicates that for filling factors at which the 2DEG is compressible, electrons tunnel into the 2DEG at a single rate and the equivalent circuit model in Fig. 1b adequately describes the sample. Figure 1d shows a drastically different recorded signal at $\nu = 1$. The decay is clearly non-exponential. We can fit it well with a sum of two exponential decays with different time constants and prefactors:

$$V(t) = A_1 \exp(-t/\tau_1) + A_2 \exp(-t/\tau_2) \quad (1)$$

In other words, at $\nu = 1$ electrons tunnel from the 3D electrode into the 2DEG at two distinct rates. Some electrons tunnel at a fast rate while the rest tunnel at a significantly slower rate.

Figure 2 shows the dependence of relaxation rates on gate voltage at a fixed magnetic field of 3.8 T. At each gate voltage in Fig. 2, we record a time trace similar to the ones in Fig. 1c and 1d. For gate voltages at which we can fit the time trace by a single exponential decay as in Fig. 1c, we plot the relaxation rate as a hollow square. When it is necessary to use a sum of two

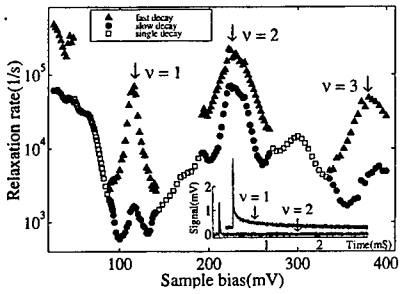

FIG. 2. Dependence of the relaxation rate on sample bias for sample B at 3.8T and 65mK. Inset: Comparison of recorded signal at ν=1 and ν=2.

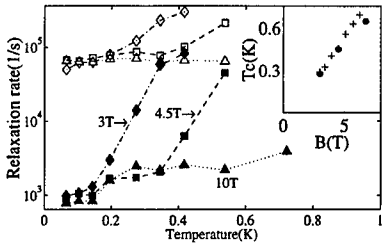

FIG. 3. Temperature dependence of the fast (hollow) and slow (filled) relaxation rates for sample B at ν = 1 for 3T (diamonds), 4.5T (squares) and 10T (triangles). Inset: Characteristic temperature T_C vs. magnetic field for sample A (crosses) and sample B (circles).

exponential decays (Eq. (1)) to fit the signal as in Fig. 1d, filled triangles and circles represent the corresponding fast and slow relaxation rates ($1/\tau_1$ and $1/\tau_2$) obtained respectively. Figure 2 indicates that tunneling occurs at two distinct rates near integer Landau level filling factors, while electrons tunnel at a single rate when the 2DEG is compressible near half integer fillings.

At integer filling factors, the in-plane conductance vanishes as the electronic states at the chemical potential become localized. Inhomogeneity, such as monolayer fluctuations in the tunnel barrier thickness, results in non-uniform tunneling rates into different lateral positions of the 2D plane. In Fig. 2, the two relaxation rates at ν = 2 differ approximately by a factor of three and can be explained well by this argument. In contrast, the fast and slow relaxation rates at ν = 1 differ by about a factor of 60. Relaxation rate differences of such magnitude cannot be explained by fluctuations in the tunnel barrier thickness. The inset of Fig. 2 illustrates the difference between a time trace at ν = 1 and ν = 2. Both traces decay at a comparable rate initially (with time constants ~10 μs), whereas only the ν = 1 signal contains an additional slower decaying component with a time constant of about 600 μs.

Figure 3 shows the temperature dependence of the two relaxation rates at ν = 1 for three magnetic field strengths. At each magnetic field, we adjust the density to maintain the filling factor at ν = 1. Both the slow and fast rates have rather weak temperature dependence at low temperature for all three magnetic fields. The weak temperature dependence of the slow relaxation rate persists up to a temperature beyond which the slow relaxation rate speeds up significantly and the double tunneling rate phenomenon recedes. This onset of strong temperature dependence shifts to a higher temperature as the magnetic field is increased. From Fig. 4, we identify the characteristic temperature T_C (as indicated by the arrows) and plot it as a function of magnetic field in the inset of Fig. 4. In this range of magnetic field, T_C (~350mK at 4.5T) sets an energy scale that is much smaller than the Coulomb energy and the cyclotron energy (106 K and 90K at 4.5T respectively). The only obvious energy scale comparable to T_C is the Zeeman energy (1.3K at 4.5T). In other words, electrons tunnel into the ν = 1 state at two rates only when the temperature is lower than the Zeeman energy. This demonstrates that spin effects are crucial in explaining why tunneling occur at two rates at ν = 1.

Possible explanations of the double tunneling rate phenomenon at ν = 1 can generally be classified into two approaches. In the first approach, electrons are assumed to tunnel into the 2D system at a fast rate. The system then undergoes certain form of relaxation, possibly spin related,

within the 2D plane at the slow rate. Through the spin relaxation, the 2D system is able to accept more electrons tunneling from the 3D electrode giving rise to a second, slower tunneling rate. Unlike the fast tunneling rate, the slow relaxation is expected to have no dependence on the thickness of the tunnel barrier. A second approach considers the $\nu = 1$ system bifurcating into separate regions into which electrons tunnel at different rates. In contrast to the first scenario, the ratio of the two tunneling rates should remain constant as the tunnel barrier thickness is varied.

In order to differentiate between these two possibilities, we measure the relaxation rates for samples grown in the same MBE machine with various tunnel barrier thickness. As the tunnel barrier becomes more transparent, the relaxation rate at $\nu = 1/2$ increases by more than 3 orders of magnitude. In contrast, the slow rate at $\nu = 1$ is relatively insensitive to the thickness of the tunnel barrier, varying by less than a factor of 10. This provides strong evidence that the slow tunneling rate at $\nu = 1$ is largely due to relaxation within the 2D plane. Since the slow tunneling rate only appears in spin polarized quantum Hall states at temperatures lower than the Zeeman energy, we describe it as arising from a "spin bottleneck" in which in-plane spin relaxation must proceed before additional electrons can tunnel into the system.

One example of in-plane relaxation that might be relevant is the formation of Skyrmions. For a perfectly uniform system precisely in the $\nu = 1$ ferromagnetic state, tunneling injects a single minority spin because the thickness of the tunnel barrier ensures that electrons tunnel as single entities. Since this is not the lowest energy excitation, over time the 2D system can lower its energy by flipping more spins to create Skyrmions. As the energy of the 2D system is lowered by Skyrmion formation, more electrons tunnel from the 3D electrode to keep the chemical potentials on the two sides of the tunnel barrier aligned. When the time scale for spin relaxation is long, the intermediate stage forms a bottleneck and temporarily prevents more electrons from tunneling. MacDonald [8] considers spin-up and spin-down electrons tunneling into the $\nu = 1$ state with equivalent tunneling rates. They must, however, be added to the system according to a certain ratio in order to form Skyrmions. For instance, creation of a Skyrmion consisting of 3 flipped spins requires the addition of 4 minority spins together with the removal of 3 majority spins. This constraint leads to non-equilibrium spin accumulation in the tunneling process, and MacDonald predicts a ratio of fast and slow relaxation rates in good agreement with our data.
This work is supported by the ONR, JSEP-DAAH04-95-1-0038, the Packard Foundation, NSF DMR-9357226 and DMR-9311825.

[1] S. L. Sondhi *et al.*, Phys. Rev. B **47**, 16419 (1993); H. A. Fertig *et al.*, Phys. Rev. B **50**, 11018 (1994).
[2] S. E. Barrett *et al.*, Phys. Rev. Lett. **74**, 5112 (1995); E. H. Aifer *et al.*, Phys. Rev. Lett. **76**, 680 (1996).
[3] A. Schmeller *et al.*, Phys. Rev. Lett. **75**, 4290 (1995); D. K. Maude *et al.*, Phys. Rev. Lett. **77**, 4604 (1996); D. R. Leadley *et al.*, Phys. Rev. Lett. **79**, 4246 (1997); V. Bayot *et al.*, Phys. Rev. Lett. **79**, 1718 (1997).
[4] R. C. Ashoori *et al.*, Phys. Rev. Lett. **64**, 681 (1990); R. C. Ashoori *et al.*, Phys. Rev. B **48**, 4616 (1993); V. T. Dolgopolov *et al.*, Phys. Rev. B **51**, 7958 (1995).
[5] J. P Eisenstein, L. N. Pfeiffer and K. W. West, Phys. Rev. Lett. **69**, 3804 (1992); K. M. Brown *et al.*, Phys. Rev. B **50**, 15465 (1994).
[6] H. B. Chan *et al.*, Phys. Rev. Lett. **79**, 2867 (1997).
[7] J. J. Palacios and H. A Fertig, Phys. Rev. Lett. **79**, 471 (1997).
[8] A. H. MacDonald, cond-mat 9906049.

TB.1

Electronic Structure of InAs-GaAs Self Assembled Quantum Dots Studied by Perturbation Spectroscopy

M S Skolnick[1], I E Itskevich[2,1], P W Fry[1], D J Mowbray[1], L R Wilson[1], J A Barker[3], E P O'Reilly[3], I A Trojan[4], S G Lyapin[4,5], M Hopkinson[6], M Al-Khafaji[6], A G Cullis[6], G Hill[6] and J C Clark[6]
[1]Department of Physics, University of Sheffield, Sheffield S3 7RH, UK
[2]Institute for Solid State Physics, RAS, Chernogolovka, Moscow district 142432, Russia
[3]Department of Physics, University of Surrey, Guildford GU2 5XH, UK
[4]Institute of High Pressure Physics, RAS, Troitsk, Moscow district, 142092, Russia
[5]Clarendon Laboratory, University of Oxford, Parks Road, Oxford OX1 3PU, UK
[6]Department of Electronic and Electrical Engineering, University of Sheffield, Sheffield S1 3JD, UK

In spite of the intense interest in the last few years in InAs-GaAs self-assembled quantum dots, relatively little direct experimental information has been available on the electronic structure and the forms of the electron-hole wavefunctions. The present paper reviews the results of recent experiments in which the external perturbations of electric field, hydrostatic pressure and magnetic fields enable key information on the electronic structure of the QDs to be obtained. Some of this information is particularly surprising and contrary to the predictions of recent theories. These findings are expected to provide important guides to future theoretical modelling of the electronic structure of InAs QDs

1. Introduction

In spite of the large amount of work on self-assembled InAs-GaAs quantum dots (QDs) relatively little experimental information is available on the nature of the electronic structure and the forms of the electron and hole wavefunctions in such structures. Such QDs provide nearly ideal examples of zero-dimensional semiconductor systems[1] and have very favourable opto-electronic properties. As a result they have generated very considerable interest for both fundamental studies and for device applications. However because of the uncertainty regarding the nature of the wavefunctions, and because precise structural information is very difficult to obtain, reliable modelling of the electronic structure is very likely still lacking.

In this paper we show that perturbation spectroscopy using external electric fields (the quantum confined Stark effect), hydrostatic pressure and magnetic fields (Zeeman effect) is able to clarify several important questions regarding the electronic structure and the nature of the electron-hole wavefunctions in QDs. Some of the findings contrast strongly with the predictions of theoretical modelling.[2,3,4,5] The results of this work have the potential to provide a reliable guide to electronic structure calculations of self-assembled InAs QDs.

The rest of the paper is organised in the following way. In section 2 the Stark effect work is described. This is followed in section 3 by a discussion of the significance of the photocurrent techniques of section 2 for the spectroscopy of QDs. Sections 4 and 5 describe the hydrostatic pressure and Zeeman spectroscopy studies. Finally in section 6 the paper is summarised.

2. The Quantum Confined Stark Effect

In this section the results of photocurrent spectroscopy experiments on InAs-GaAs self-assembled QDs are described. It is shown that such spectroscopy enables absorption spectra of the QDs to be investigated with high sensitivity and the response of the electron-hole wavefunctions to applied electric fields (F) to be investigated. We are able to deduce the vertical

extent and relative vertical alignment of the electron-hole wavefunctions, and are also able to show that the excited state splittings in the spectra arise from lateral quantisation.

Two types of dots were studied, both grown by MBE on (001) GaAs substrates at 500°C. The first type (samples A-C) was deposited at 0.01 monolayers per second (ML/s) to give a density ~1.5×10^{9}cm^{-2}, base size 18nm and height 8.5nm, as determined from transmission electron microscopy. The second type (sample D) had a higher deposition rate of 0.4 ML/s, resulting in a density ~5×10^{10}cm^{-2} and size 15nmx3.5nm. The asymmetric shaped QDs, sitting on a ~1 ML thick wetting layer, have their apex oriented along the growth direction. The samples contained single layers of dots at the centre of the intrinsic region (width d) of either p-i-n or n-i-p structures, allowing fields (F) up to 300kV/cm to be applied either parallel or anti-parallel to the growth direction. Applying a reverse bias to a p-i-n structure (p region at surface) results in F pointing from substrate to surface. For an n-i-p structure the field direction is reversed. The total electric field is given by $F=(V+V_{bi})/d$, where V is the externally applied voltage and V_{bi} is the built in voltage (≈1.5V). Monochromated white light (~3mW/cm^2, corresponding to extremely low dot carrier occupancies (<<1)) was used for excitation.

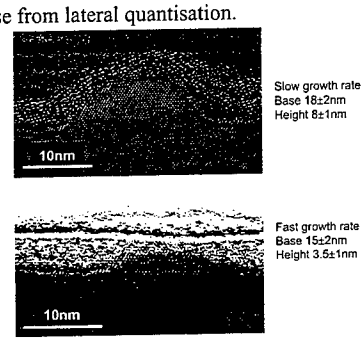

Fig. 1 TEM micrographs of slow and fast growth rate samples.

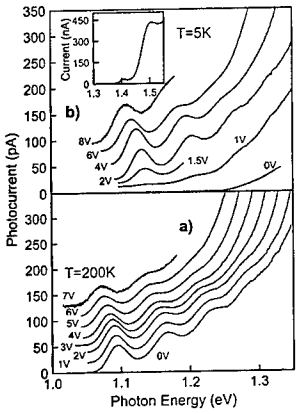

Fig. 2 Photocurrent spectra for sample A.

Photocurrent spectra, recorded as a function of reverse bias from 0 to 8V (total field F from 50 to 320kV/cm), are shown in Figs. 2a and b for sample A (p-i-n) at temperatures of 5 and 200K respectively. At 200K, four well defined features are seen in the range 1.1 to 1.3eV, arising from inter-band transitions between the confined electron and hole levels in the dots. Similar spectra are seen at 5K, though at low fields the interband transitions are quenched, and a photocurrent signal is only observed from the InAs wetting layer (1.41eV) and the GaAs barriers (1.5eV) (see inset to Fig 2b). The temperature dependence of the spectra is discussed in detail elsewhere,[6] where it is shown that the variation of the photocurrent intensities in Figs 3a, b with field and temperature reflect a transition from carrier escape by tunnelling at low temperature to thermal escape at high temperature. The most important point in Fig 2 is that with increasing field, at all temperatures, all the QD transitions shift strongly to lower energy (by 30meV at 8V (≡300kV/cm)), the signature of the quantum confined Stark effect[7], but without any qualitative change in the form of the spectra.

The ground state transition energies at 200K for all samples are plotted as a function of F, in Fig. 3. We focus attention on samples B (p-i-n) and C (n-i-p)[8]. Positive field corresponds to reverse bias for the p-i-n structure. The transition energy exhibits a marked asymmetry about F=0, with the maximum obtained for a non-zero field of -90kV/cm. This asymmetry implies that

the QDs have a permanent dipole moment (p). A non-zero Stark shift at F=0 of the ground state transition has also been observed in the PL of InAlAs-AlGaAs QDs[9] over the limited field range of ±60kV/cm since the PL is unavoidably quenched at high fields.

The field dependence of the transition energies (E) in Fig. 3 can be described to a very reasonable approximation by the expression $E = E_0 + pF + \beta F^2$ (the solid lines in Fig. 2), where E_0 is the energy at F=0, the second term arises from the non-zero dipole moment (p), and the third term from polarisation of the dots in the applied field (the quantum confined Stark effect). By fitting to the experimental data for samples B and C a value of $p=(7\pm2)\times10^{-29}$ Cm is determined, corresponding to an electron-hole separation of r=4.0±1Å (from $p=er$).

Self-assembled QDs are expected to possess a permanent dipole moment as a result of their asymmetric shape.[2] In general the lack of inversion symmetry means that the eigenfunctions of the system do not have definite parity, the dots are expected to have a permanent dipole moment and the first order perturbation due to an applied electric field will be non-zero. For the same reason asymmetric molecules such as CO are polar and possess a permanent dipole moment whereas symmetric molecules such as CO_2 have no dipole moment.[10] Thus although the existence of a permanent dipole moment for self-assembled quantum dots is not surprising, the experimentally determined direction of the observed dipole is highly unexpected. The maximum transition energy occurs for F in the direction from apex to base, corresponding to electron (hole) attraction to the apex (base) of the dots. This implies that the electron charge density distribution lies below that of the hole at F=0, with the dipole pointing from base to apex. This result, to the best of our knowledge, is in contrast to that predicted by all accurate modelling[2-5] of InAs QDs which predicts hole localisation towards the base of the dots, below the electrons. This alignment, which is predicted for pure InAs dots of *any shape* for which the lateral size decreases from base to apex (e.g. the pyramidal shape in Refs. 2-5) results from the strain-induced form of the valence band edge profile[3] which leads to hole localisation in the widest region of the dots, and from the ratio of the effective masses along the growth direction ($m^*_{hh} >> m^*_e$) which means that the electrons tend to spread out to fill the dots whereas the (heavy) holes are localised in the regions of deepest potential.

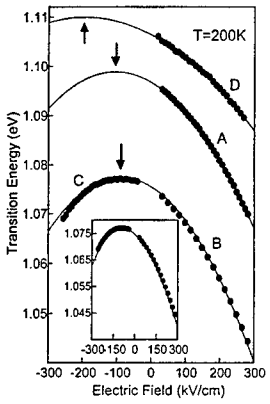

Fig. 3 Transition energies as a function of electric field. The fits are discussed in the text.

To determine dot parameters necessary to reverse the relative alignment of the electron and hole, and to fit to the experimental data, envelope function calculations, treating the electrons and holes with separate one-band Hamiltonians, have been carried out. The strain distribution for a given dot shape was calculated using a Green's function technique which provides an analytical expression in the form of a Fourier series for the strain tensor[11]. The band gaps and offsets were calculated using model solid theory, including hydrostatic strain effects; the heavy-hole Hamiltonian included the spatial variation of the biaxial strain deformation potential and the directional dependence of the heavy-hole mass. Carrier effective masses, determined using 3-band **k.p** theory, and band offsets were assumed to vary linearly with composition.

For pure InAs pyramidal dots[12] our calculations give good agreement with previous

theories[2-5], with the hole wavefunction always below that of the electron, confirming the accuracy of our approach. Reversal of this alignment is only possible for dots having a graded $In_{1-x}Ga_xAs$ composition, with x decreasing from base to apex (the holes tend to be localised in the region with the largest In composition). This tends to shift the localisation of the holes away from the base. However, in addition it is also necessary to severely truncate the pyramid to achieve a dipole of the correct sign, since strain effects continue to localise the hole strongly below the electron until the truncation factor is greater than ≈0.6.

The best fit to the experimental data for samples B and C is shown in the Fig 3 inset. This was obtained using a pyramid of base length (w) 15.5 nm, height 22 nm, of which the top 75% is truncated (see Fig 4 for the shape employed) to give an actual height (d) of 5.5 nm, and an x varying linearly from 50 % at the base to zero at the top surface. The quadratic shift is determined principally by d, the dipole by the grading and the degree of truncation, and the absolute energy mainly by d and w. Although other parameter sets can give a good fit, we emphasise that the shape employed represents a good approximation to that obtained from structural measurements (Fig. 1a). Furthermore pyramids without truncation, and any shape wider at the base than the apex but without grading, never have a dipole of the correct sign. We thus obtain new information by optical methods on the structure and composition of buried quantum dots.

Contour plots of the calculated electron and hole probability densities are presented in Fig. 4, for the parameter set that gives the best fit to the experimental Stark shift data. At zero electric field, the localisation of the electron below the hole is seen very clearly. For negative fields the hole distribution moves towards the base and the electron to the apex, with the dipole moment being zero for fields of -90kV/cm in very good agreement with the results of Fig 3. For positive fields by contrast the hole is attracted further to the apex and the electron to the base with a consequent increase of the dipole moment.

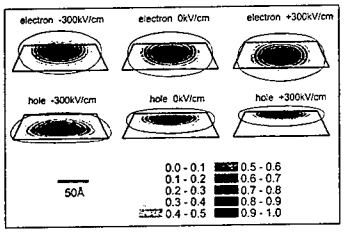

Fig. 4 Contour plots of electron-hole probability densities

Our conclusions regarding the composition of *buried* InAs dots are consistent with results of previous STM investigations on *uncapped* dots.[13,14] For the growth temperature used for the present QDs (500°C) the total dot volume was found in ref 13 to be greater than that of the deposited InAs, a finding that could only be explained by in-diffusion of Ga. The grading required to explain the sign of the observed dipole has also been observed in STM studies of $In_{0.3}Ga_{0.7}As$ QDs and attributed to In segregation during growth.[14]

Data for devices A and D (slow and fast growth rates respectively) in Fig. 3 also exhibit a maximum transition energy for a negative field, showing that a permanent dipole with hole above electron is a general property of our QDs. In addition the size of the quadratic component of the Stark shift for the slow growth rate samples (A-C) is larger than that of the faster growth rate sample D, consistent with the smaller height of the dots in these samples as seen by inspection of the TEM images in Figs 1a, b.[15] The same sign of asymmetry of the Stark effect has been reported by Raymond et al for AlInAs/AlGaAs self-assembled QDs[9] supporting the generality of our findings.

In Fig 1, the energy separations and relative intensities of the transitions are independent of field, in strong contrast to the behaviour for quantum wells[7]. In quantum wells the excited

states arise from quantisation along the growth direction and thus in applied field transitions which are symmetry forbidden at F=0 become allowed, and allowed transitions become weaker, with a resultant marked change in the form of the spectra. Our results for the QDs show that the excited state splittings arise from lateral quantisation since, to first order such lateral confinement is independent of field along z. The z-quantisation is thus common to all the states involved in the spectra. The results show that the decoupled model for the z and in-plane motions (adiabatic approximation) employed in much simplified modelling of the electronic structure of QDs has a sound foundation.

3. Significance of Photocurrent Spectroscopy for Investigation of Electronic States of Self-Assembled Quantum Dots

Absorption spectra provide the most fundamental optical probe of the electronic properties of bulk and low dimensional semiconductors. However absorption spectra of QDs are very difficult to obtain due to their very small absorption strengths. The two reports of absorption spectra in the literature previously required the use of very difficult experimental techniques. Calorimetric absorption spectroscopy[16] requires very low temperatures and resulted in broadened spectra, and direct absorption spectroscopy required the development of very sensitive detection techniques and long integration times.[17] Photoluminescence excitation spectroscopy, commonly employed to measure absorption spectra in quantum wells, is dominated by phonon related features in self assembled quantum dots.[18] Photocurrent spectroscopy by contrast suffers from none of these drawbacks permitting absorption spectra to be obtained with very good signal to noise in short experimental times (~5minutes). At sufficiently high fields all carriers escape from the dots and their absorption strength (A) can be determined directly from the magnitude of the photocurrent (I) and the relationship $I=APe/h\nu$ where P is the optical power at frequency ν. A value of A=1.3x10^{-5} is obtained, in good agreement with a previously published value after correcting for the different dot density.

One feature of the spectra of Fig 2 remains unexplained, the presence of the broad background signal underlying particularly the excited state spectra. Its origin remains uncertain at the present time, although it most likely arises from band tail absorption from either the GaAs band edge or from the InAs wetting layer, some enhancement occurring in applied electric field due to Franz-Keldysh effects.

4. Hydrostatic Pressure experiments

High hydrostatic pressures lead to a very large perturbation of the band structures of semiconductors. Of particular relevance to the present work they lead to large upshifts of the Γ point band gap by 10meV/kbar, whereas the X point conduction band Γ valence band transition shifts down at ~2meV/kbar. In bulk GaAs this leads to a crossover of the Γ and X conduction band minima at ~40kbar,[19] with typically a very large reduction in PL intensity being seen as the interband transitions are transformed from being

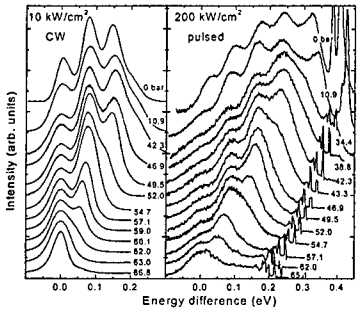

Fig 5. PL spectra as a function of hydrostatic pressure for InAs-GaAs quantum dots.

direct in k-space to indirect. In this part of the paper, we describe recent experiments we have carried out on InAs-GaAs QDs under high pressures up to 70kbar. The Γ-X crossover effect is employed to show that the features observed in interband PL spectra arise from transitions involving different electron states and that very likely strong symmetry-conserving selection rules determine the form of the spectra. A full account can be found in ref 20.

A series of PL spectra at high excitation intensity under cw (left panel) and pulsed conditions (right panel) are shown in Fig 5 as a function of pressure from 0 to 67kbar, for a sample containing a single layer of QDs prepared under fast growth conditions. The horizontal energy scale expresses the transition energies relative to the ground state transition. The absolute energies versus pressure are presented in Fig 6. We first consider the spectra at zero pressure. For pulsed excitation (200kW/cm^2) the ground state and four higher energy transitions from the dots are observed, with the two highest energy sharp lines at ~0.4eV relative energy arising from transitions in the GaAs matrix material. Under these conditions the dots are strongly loaded with carriers (>20 electron-hole pairs) and transitions involving all electron states in the dots are seen (the situation regarding the hole states is less clear since there are more hole than electron states due to the larger hole effective mass). The overall qualitative similarity to the photocurrent spectra of Fig 2 is clear, although we emphasise that the photocurrent spectra provide a direct representation of the absorption spectrum of the dots, whereas the form of the PL spectra is determined also by the level populations. It is notable however that the broad background underlying the photocurrent spectra of Fig 2 is not present in PL, supporting its suggested identification in section 3 as arising from band tail states, enhanced by Franz-Keldysh effects.

With increasing pressure very little change in the form of the spectra is seen up to 30 kbar (although the energies increase strongly, see Fig 6). However for pressures above 35-40kbar, qualitative changes occur. The lines from the GaAs matrix are first quenched (the sharp lines visible in the high energy part of the spectrum then arise from the ruby calibration lines), the signature of the Γ-X crossover. This is followed by successive quenching of the higher energy QD lines with increasing pressure. The lines disappear from the spectra in sequence; the higher the pressure, the greater the number of lines quenched.

The linear blue shift of the lines in Fig 6 over a wide range of pressure is replaced by a small red shift over a small pressure range above crossover, until the particular line is fully quenched. Each of the higher energy transitions is quenched due to the corresponding electron level in the dots crossing with an X-valley related state, as shown in the inset to Fig 6 where a schematic diagram of the energy level structure under pressure is shown. For P>65kbar, the lowest energy line is not quenched, but becomes asymmetric in shape and starts to shift to lower energy, the fingerprint of the of the Γ-X crossover for the ground electron state in the dots.[21] The sequential quenching of all other lines at different pressures indicates the sequential crossing of different electron states with the X level. We can thus conclude with certainty that each line in the PL spectrum arises from a transition involving a different electron level in the dots. This proves the existence of four excited electron levels in the ~15x3nm dots studied, consistent with the expectations of e.g. reference 22. These experiments resolve definitively much previous controversy in the literature (summarised in ref 20) concerning the number of bound electron states in InAs-GaAs QDs, and demonstrates the

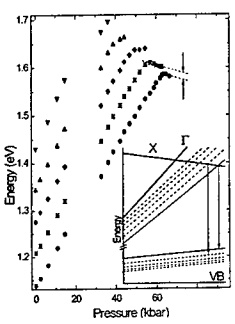

Fig 6. PL transition energies as a function of hydrostatic pressure.

power of perturbation spectroscopy in answering fundamental questions concerning the electronic structure of semiconductor systems.

The hydrostatic pressure measurements also provide additional information on the nature on the optical transitions, a subject of much previous speculation. In Fig 6 energy gaps are clearly seen between the lines above the crossover pressures (marked by vertical arrows between the two lowest energy lines on Fig 6). In the small pressure range above crossover for each line, the transition occurs from the same X-valley electron state to the corresponding hole level. The gaps therefore indicate that the transitions occur to different hole states, and correspond to the energy differences between these states. Consequently each transition below crossover corresponds to a particular pair of electron and hole states. This demonstrates that strong selection rules determine the optical transitions which are observed: the allowed transitions are furthermore very likely to be between states of the same symmetry. Combined with the Stark effect studies of section 2, we conclude that the excited state transitions arise from transitions between states of the same symmetry which in turn arise from lateral quantisation.

5. Zeeman spectroscopy

Although the Stark effect and hydrostatic pressure measurements permit much insight into the nature of the optical transitions and of the electronic states involved in spectra of InAs-GaAs QDs to be obtained, they provide no direct information into the angular momentum quantum numbers of the states involved. Further light can be shed on these questions by Zeeman spectroscopy which is able to lift orbital and spin degeneracies. The results of photoluminescence excitation (PLE) measurements will be summarised very briefly here.[23]

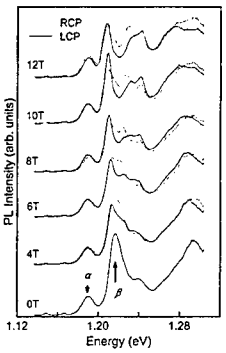

Fig 7. PLE spectra as a function of magnetic field.

Typical PLE spectra as a function of magnetic field up to 14T, parallel to the growth direction, are shown in Fig 7. At B=0 the spectra are dominated by two features, α and β, occurring at ~60 and ~85 meV above the detection energy corresponding to 2 and 3LO phonon relaxation to E_{det}. No electronic features are observed directly in the PLE spectrum at B=0 (see section 3). This arises since relaxation to E_{det} is severely restricted as a result of the discrete 0D density of states ('the phonon bottleneck'); in the presence of competing non-radiative recombination, PL is only excited for those dots within the inhomogeneous distribution whose ground and excited states are separated by an integral number of LO phonons.[24, 25]

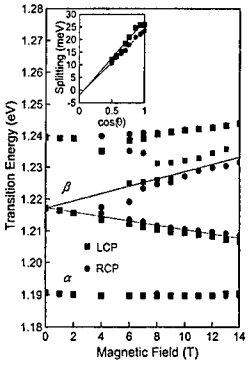

Fig. 8 PLE energies as a function of magnetic field.

In spite of the phonon-related form of the B=0 spectra, splittings in magnetic field are observed for the β feature, as seen in Fig 7, and in the plot of PLE energies versus B in Fig 8, probably due to the suppression of the competing non-radiative paths (e.g. carrier diffusion) at finite B. The β line exhibits an approximately linear splitting with B, thus demonstrating that the

first excited state transition (nearly resonant with β) involves at least one state having p-like character. Further analysis is required however to reconcile the reduced mass of $0.065m_e$ deduced from the p-like splitting with the expected electron mass in the strained InAs of $0.045m_e$.[4] Finally we mention that the diamagnetic shift of the ground state PL in ref 23 permits the lateral extent of the ground state wavefunctions to be deduced to be ~50Å,[26] in reasonable agreement with the wavefunction probability densities presented in Fig 5.

6. Conclusion

In summary, we have shown that the use of the Stark effect, hydrostatic pressure and Zeeman effect spectroscopies is able to provide a comprehensive picture of the nature of the electron and hole states, their wavefunctions and the character of the optical transitions in InAs-GaAs self-assembled quantum dots. It is hoped that these results will be able to provide a reliable guide to future theoretical modelling of the electronic structure of these systems, and the basis for the interpretation of a number of other experiments.

References

1 D Bimberg, M Grundmann and N N Ledentsov, 'Quantum Dot Heterostructures' Wiley (1998).
2 M Grundmann, O Stier and D Bimberg, Phys. Rev. B. **52,** 11969, (1995)
3 M Cusack, P R Briddon and M Jaros, Phys. Rev. B. **54,** R2300 (1996)
4 C Pryor, Phys. Rev. B. **57,** 7190 (1998) . This reference provides a summary of most earlier theoretical work.
5 J Kim, L-W Wang and A Zunger, Phys. Rev. B. **57,** R9408 (1998).
6 P W Fry, I Itskevich, D J Mowbray, M S Skolnick, J A Barker, E P O'Reilly, L R Wilson, I A Larkin, P A Maksym, M Hopkinson, M Al-Khafaji, J P R David, A G Cullis, G Hill and J C Clark, unpublished
7 D A B Miller, D S Chemla, T C Damen, A C Gossard, W Wiegmann, Phys. Rev. B. **32,** 1043 (1985).
8 A small shift of 7meV to higher energy has been applied to the results of sample C.
9 S Raymond, J P Reynolds, J L Merz, S Fafard, Y Feng and S Charbonneau, Phys. Rev. **B58,** R13415 (1998)
10 see e.g. B Bleaney and B I Bleaney, Electromagnetism (Oxford University Press, 1965), p477
11 A.D. Andreev, J R Downes, D A Faux and E.P. O'Reilly, J Appl Phys July 1999
12 S Ruvimov et al Phys. Rev. B. **51,** 14766 (1995). This paper reported pyramidal shapes for InAs quantum dots from transmission electron microscopy and provided the basis for much subsequent modelling. However other reports (e.g. D S L Mui, D Leonard, L A Coldren and P M Petroff, Appl. Phys. Lett. **66,** 1620 (1995) including our own in figure 1 of this paper, find the dots more closely approximate to lens shapes.
13 P B Joyce, T J Krzyzewski, G R Bell, B A Joyce and T S Jones, Phys. Rev. B **58,** R15981 (1998).
14 N Grandjean, J Massies and O Tottereau, Phys. Rev. B. **55,** R10189 (1997).
15 The dipole separation deduced for the fast growth sample B is 3.2Å, as opposed to 4Å for the slow growth samples, probably as expected for these samples of smaller vertical height (see Fig 1).
16 M Grundmann, J Christen, N N Ledenstov, J Bohrer, D Bimberg et al, Phys Rev Lett, **74,** 4043, 1995
17 R Warburton, C S Durr, K Karrai, J P Kotthaus, G Mideiros-Ribeiro and P M Petroff, Phys. Rev. Lett. **79,** 5282 (1997).
18 M J Steer, D J Mowbray, W R Tribe, M S Skolnick, M D Sturge, H Hopkinson, A G Cullis, C R Whitehouse and R Murray, Phys Rev **B54,** 17738, 1996, R Heitz et al, Appl Phys Lett **68,** 361, 1996
19 D J Wolford and J A Bradley, Solid State Commun **53,** 1069, 1985
20 I E Itskevich, M S Skolnick, D J Mowbray, I A Trojan, S G Lyapin, M J Steer, L R Wilson, M Hopkinson, L Eaves and P C Main, Phys Rev B, Rapid Communications, in press, July 1999.
21 I E Itskevich et al, Phys Rev **B58,** R4250, 1998
22 J N Kim, L W Wang and A Zunger, Phys Rev **B57,** R9408, 1998
23 L R Wilson, D J Mowbray, M S Skolnick, M Morifuji, M J Steer, I A Larkin and M Hopkinson, Phys Rev **B57,** R2073, 1998
24 R Heitz, M Grundmann, N N Ledontsov, L Eckey, M Veit et al, Appl Phys Lett **68,** 361, 1996
25 M J Steer, D J Mowbray, W R Tribe, M S Skolnick et al, Phys Rev **B54,** 17738, 1996
26 A similar value is found in I E Itskevich, M Henini, H A Carmona, L Eaves, P C Main, D K Maude and J C Portal, Appl Phys Lett **70,** 505, 1997

Vertical Quantum Dots at High Magnetic Fields beyond the Few-Electron Limit

D. G. Austing[1], Y. Tokura[1], S. Tarucha[1,2], T. H. Oosterkamp[3], J. W. Janssen[3], M. W. S. Danoesastro[3] and L. P. Kouwenhoven[3]

[1] NTT Basic Research Laboratories, 3-1 Wakamiya, Morinosato, Atsugi, Kanagawa 243-0198, Japan
[2] Department of Physics, University of Tokyo, 7-3-1 Hongo, Bunkyo-ku, Tokyo 113-0033, Japan
[3] Department of Applied Physics and DIMES, Delft University of Technology, PO Box 5046, 2600 GA Delft, The Netherlands

Abstract

We describe phenomena that can be studied in vertical quantum dot single electron transistors. Moving from the *few*-electron to the *several*- and *many*- electron regimes, features in the conductance peaks initially related to spin polarization evolve with magnetic field. This allows us to first probe the spin-flip region beyond the last single-particle crossing at low field, and then the formation and stability of the spin-polarized maximum density droplet at high field. According to a simple capacitance model, charge redistribution in the dot at higher magnetic fields is accompanied by abrupt changes in the area of the droplet.

Single electron phenomena in quantum dots continue to attract attention [1,2]. We have reported atomic-like properties of well-defined vertical quantum dot disks [3,4]. For a small dc source-drain voltage applied across the dot, V_{SD}, ground states have been probed in the linear response regime when the number of electrons trapped on the dot, N, is between 0 and 20 for a magnetic (B-) field up to 3.5 T by measuring the current, I, flowing through the dot as a function of voltage, V_g, applied to a single Schottky gate [3]. With a finite V_{SD}, and measuring current stripes instead of current peaks, the first few excited states can also be accessed in the non-linear response regime in the *few*-electron limit (N<6) for B-fields up to 16 T [4].

We expand our recent studies to probe features, which show up strikingly in a B-N phase diagram beyond the *few*-electron regime [5,6]. Because of the reduction of the lateral confinement and the increase in screening as N increases, a two-dimensional limit is approached for large N. In the presence of a B-field, which strengthens electron interactions, we see features related to those familiar in the quantum Hall regime for a two-dimensional electron gas (2DEG), and the concept of a filling factor, ν, becomes useful. Features which can be fully explained by many-body calculations up to N=5 in the *few*-electron regime [4], extend in to the *several*- and *many*-electron regimes and reflect a larger dot with a more 2D character. As the B-field is increased beyond that required to achieve ν=2, from 'cusps' and 'steps' in the position of the conductance peaks, we

identify the spin-flip regime before the formation at ν=1 of a maximum density droplet (MDD)- so called because it is the densest spin-polarized electron configuration allowed by the available quantum states [7]. Until now, only two-terminal *capacitance-voltage* measurements have permitted access to the interesting physics at high B-fields in a **vertical** quantum dot [1].

The material is a specially designed double barrier structure with an $In_{0.05}Ga_{0.95}As$ well, $Al_{0.22}Ga_{0.78}As$ barriers, and *n*-doped GaAs contacts [3], which is processed to form circular mesas by a special etching technique, and a gate is placed around each dot-mesa [8,9]. We discuss two devices A and B which both have a geometrical diameter of 0.54 μm. Measurements on device A and B are performed in a dilution refrigerator and in a ^{3}He cryostat respectively. The B-field is applied parallel to the current. N typically varies from several tens at V_g= 0 V to zero at the 'pinch-off' voltage (≈ -2 V).

Figure 1 shows the current peaks versus B for device A for N from 0 to 18 up to 14 T. On making V_g more positive, peaks are measured for every extra electron that enters the dot. At 0 T, a shell structure for a 2D harmonic potential is observed in the addition energy (large peak spacings for N=2, 6, 12), and Hund's first rule explains the relatively large peak spacing for N=4. Peaks evolve in pairs for B<2 T, implying that each single-particle state is filled with two electrons of opposite spin [3]. "Wiggles" indicate crossings between single-particle states. For N>4, the last "wiggle" identifies when all electrons occupy spin-degenerate states belonging to the lowest orbital Landau level which corresponds to ν=2 in a 2DEG. This means that for even-N, the ground state is spin-unpolarized (total spin, S, is 0), and the total angular momentum, M, is N(N-2)/4.

In the constant interaction model, no transitions in the ground states beyond ν=2 are expected if the weak Zeeman effect is neglected. However, in the presence of many-body effects, transitions in the N-electron ground states occur in such a way that M is increased, and S is maximized. The former is favored by the direct Coulomb energy and influenced by the kinetic energy, whilst the latter is favored by exchange and Zeeman energies, and modified by correlation effects [10-12]. Beyond ν=2, according to a simple self-consistent model introduced for planar-dots containing *several*-electrons [13], it is energetically favorable for minority spin-down electrons at the compressible dot center to sequentially tunnel through an incompressible 'ring' to the compressible dot edge so becoming majority spin-up electrons. Spin-flip processes have been studied experimentally in planar dots [13-16], and theoretically [16,17].

For N<6, we have measured current peaks and stripes to track the transitions beyond ν=2 [4]. Our spectra compare well with those calculated incorporating many-body effects, so we can confidently identify the configurations of the ground and first few excited states. In Fig. 1, ▼ locates the position of the singlet-triplet (S-T) transition for N=2 [10,11]. In a single spin-flip process, both S and M simultaneously change from 0 to 1, and the 2-electron system becomes spin-polarized. For N>2 the process of spin-polarization occurs over a finite B-field range. Weak features mark where this process occurs. At B-fields marked by ▼ and ●, the N-electron system has become completely spin-polarized. S is N/2 and M is N(N-1)/2. Not all the predicted

transitions can readily be observed, and not all transitions actually involve a spin-flip (although one naively expects for even-N and odd-N respectively, N/2 and (N-1)/2 spin-flips) [5].

For device B, there seem to be just one or two weak features in the spin-flip regime for N from 5 to about 10 [5], and their number does not clearly increase with N, so not all the expected transitions for $2>\nu>1$ can yet be readily distinguished. Crucially, N may not be sufficiently large that compressible and incompressible regions can meaningfully be defined in the still quite small dot. Many-body states are still expected to be important, and B-field induced transitions are presumably responsible for the weak features, although the states cannot be labeled at present. Increasing N, into the *several*-electron regime, N is sufficiently large that the simple self-consistent model should be helpful [13]. Figure 2 (a) shows the B-N phase diagram for $N\approx25$. Beyond $\nu=2$, there is a sequence of six or seven features (solid squares) before the final feature at ≈ 6.2 T marking $\nu=1$. The shape of the features changes from 'cusp'-like at low field to 'step'-like and even 'peak'-like at high field. The number of features still does not obviously increase with N for consecutive peaks. Compressible and incompressible regions within the dot should have formed, and the MDD should be clear, but still we can expect a small but finite excitation energy in the single-particle picture, and many-body states are probably not yet negligible. Increasing N further, we move into the *many*-electron regime. Figure 2 (b) shows the B-N phase diagram for $N\approx45$. Beyond $\nu=2$, there is a string of about nine or ten features (solid ovals) before the last feature at ≈6.2 T marking $\nu=1$. Compressible and incompressible regions inside the dot, and the MDD should now be very well established. Many-body states are now not expected to be important. The features in Fig. 2 (b) are similar to those in Fig. 2 (a), but yet again the number of features does not really increase with N for successive peaks, and their number is certainly a lot less than N/2.

Naively, one expects the simple self-consistent model [13] to be applicable, and yet based on our observations, and the *capacitance-voltage* data of Ashoori [1], the appearance of the spin-flips, and their number are very different in vertical dots compared to planar dots. i.e. geometry is important. The influence of the emitter in the former is not well understood. It is probable that at low B-fields ($\nu\approx2$) there are incomplete edge states in the emitter, so the complex nature of these states and how they couple to dot states across the emitter barrier could strongly influence the spin-flips. In contrast, N/2 oscillations in the position of each peak for planar dots are well resolved [13-16], because the edge states in the emitter are well defined, and the current is carried principally by the strong coupling of these states to nearby edge states in the dot. We note that in subsequent work on planar dots, the self-consistent model was superceded by other more advanced models [15,16] to explain important experimental observations [13-16].

Returning to Fig. 1, after the last spin-flip, for $N>2$, solid circles mark the beginning of the spin-polarized MDD (which for N=2 is the S-T transition identified by ▼), and open circles seem to mark the end of the MDD. Solid circles actually identify $\nu=1$, and the beginning of a distinct MDD phase in which all N-electrons are in the lowest Landau level, and all successive single-

particle states (n, ℓ)= (0, 0), (0, 1), ..., (0, N-1) are occupied by one spin-up electron (n and ℓ respectively are the radial and angular momentum quantum numbers for a 2D harmonic potential) [7]. The stability of the MDD as the B-field is further increased is set by the balance of forces acting on this finite electron system [7,18,19]; namely the inward force of the confining potential, the repulsive force of the direct Coulomb interaction between electrons, and a binding force due to the exchange interaction. In addition, Zeeman energy and correlation effects are important. As the B-field and the electron number are changed, the relative strength of these forces is tuned, which induces transitions between the MDD and other states [1,15,16].

As N increases, the start of the MDD first moves to larger B and then becomes roughly independent of N. As the B-field is increased further, the angular momentum states shrink in size such that the density of the MDD increases. At some threshold (identified by O), the direct Coulomb interaction becomes so large that the MDD breaks apart into a larger lower density droplet (LDD). Assuming the LDD remains spin-polarized, successive angular momentum states are no longer occupied, i.e. M>N(N-1)/2. Whether the unoccupied states are in the center [7], or at the edge [19], depends critically on the relative strengths of the confinement, exchange, and direct Coulomb interactions, as well as the Zeeman energy and correlation effects. It has been suggested, especially when the Zeeman energy is small, that the MDD may even become unstable towards the formation of spin-texture [20,21]. The stability conditions for the MDD (i.e. the B-range between ● and O) has been calculated by several different theoretical approaches with different assumptions [7,18,19]. One recent spin-density functional calculation predicts left and right boundaries for the MDD that are strikingly similar to those in Fig. 1 [22]. It is nonetheless challenging to make good quantitative comparisons, since the phase diagrams are very sensitive to the finite thickness of the dot and to screening effects from electrons in the contacts.

Figure 3 (a) shows the peak positions versus B-field for device A for N>11. Between the boundaries marked by ● and O a new transition seems to develop for N>15, and indicates a new electronic configuration inside this region (see dotted line). We believe the MDD continues on the right of this new transition but, since we cannot identify the new state on the left, this is debatable. At this moment no calculations exist for our specific sample. Intriguingly, kinks in the peak evolution marking the boundaries of the MDD for small N turn into abrupt steps for N≥10. This is also true for the new unidentified transition as N is increased, and also at higher B-fields, e.g. in region marked by the dotted oval, additional steps can be discerned in Fig. 3 (a). We argue that at all these steps, the charge distribution of the droplet changes abruptly. Figures 3 (b) and 3 (c) show I versus V_g (N=27 to 31) in greyscale for B-values around the steps marked by O. The step width is about 50 mT. For V_{SD}=100 μV, the peaks are much narrower than their spacings. An increased source-drain voltage V_{SD}=300 μV broadens these peaks. The important point is that the peak width, ΔV_g, increases by about 10% after crossing the step as indicated by the arrows. At low temperature $\alpha \Delta V_g = eV_{SD}$, where according to a simple capacitance model $\alpha = eC_g/C_\Sigma$. As the total capacitance, C_Σ, in our geometry is roughly proportional to the dot area, and since the gate

capacitance C_g increases only slowly with the dot area, the change in peak width implies that the dot area changes abruptly by about 10 %. However, it is not clear how well the MDD state can be modeled by capacitances. It is also evident in Figs. 3 (b) and 3 (c) that the peak width *during* the step is about twice the width outside the step region. All steps show similar behavior.

To study the nature of these unusual steps we have measured excitation spectra. Figure 4 shows dI/dV_{SD} in the V_{SD}-V_g plane for ten B-values around a particular step that separates two different LDD states in the B-field regime within the dotted oval in Fig. 3 (a). We again stress that the same behaviour is found at all steps. At the lowest and highest B-fields the Coulomb blockade regions have the expected diamond shape, but the diamond at B=7.48 T is about 10% smaller in the V_{SD} direction, indicating that the energy to overcome the Coulomb gap has decreased by $\approx$10%. This is again consistent with a $\approx$10% larger dot area after the charge redistribution. Strikingly, the shape of the diamonds measured inside the step region is severely distorted, where the size of the Coulomb blockade region collapses to as little as $\approx$40% of its value outside the step region. This agrees with the peak broadening by about a factor of 2 during the steps in Figs. 3 (b) and 3 (c). We are not aware of such a collapse of the Coulomb gap in metallic or semiconducting systems. Elsewhere, we outline how the distorted and collapsing Coulomb blockade regions can be obtained within a simple phenomenological model in which a set of parabolas representing one charge configuration (e.g. the MDD) is gradually displaced relative to another set of parabolas representing a different charge configuration (e.g. the LDD) [6]. From this we again conclude that the instability of the MDD and the instability of LDD states at higher B-fields is accompanied by a redistribution of charge. It remains a challenge, however, to calculate the microscopic origin of the difference in offset charge between two states with different charge distributions.

We gratefully acknowledge the considerable assistance of T. Honda in the fabrication of the devices. We also thank G. Bauer, S. Cronenwett, M. Devoret, L. Glazman, R. van der Hage, J. Mooij, K. Muraki, Yu. Nazarov, and S.J. Tans for experimental help and discussions. The work was supported by the Dutch Foundation for Fundamental Research on Matter (FOM), and by the NEDO joint research program (NTDP-98).

References:

[1] R. C. Ashoori, Nature **379** (1996) 413; R. C. Ashoori et al., Phys. Rev. Lett. **71** (1993) 613.
[2] U. Meirav, E. B. Foxman, Semicond. Sci. Technol. **11** (1996) 255.
[3] S. Tarucha et al., Phys. Rev. Lett. **77** (1996) 3613.
[4] L. P. Kouwenhoven et al., Science **278**, (1997) 1788.
[5] D. G. Austing et al., Jpn. J. Appl. Phys. **38** (1999) 372.
[6] T. H. Oosterkamp et al., Phys. Rev. Lett. **82** (1999) 2931.
[7] A.H. MacDonald et al., Aust. J. Phys. **46** (1993) 345.
[8] D. G. Austing et al., Jpn. J. Appl. Phys. **34** (1995) 1320.
[9] D. G. Austing et al., Semicond. Sci. Technol. **11** (1996) 388.

[10] M. Wagner et al., Phys. Rev. B **45** (1992) 1951.
[11] D. Pfannkuche et al., Phys. Rev. B **47** (1993) 2244.
[12] P. A. Maksym, T. Chakraborty, Phys. Rev. Lett. **65** (1990) 108; P. A. Maksym, T. Chakraborty, Phys. Rev. B **45** (1992) 1947; P. Hawrylak, Phys. Rev. Lett. **71** (1993) 3347; S. -R. E. Yang et al., Phys. Rev. Lett. **71** (1993) 3194; M. Ferconi, G. Vignale, Phys. Rev. B **50** (1994) 14722; J. J. Palacios et al., Phys. Rev. B **50** (1994) 5760; M. Eto, Jpn. J. Appl. Phys. **36** (1997) 3924; A. Harju et al., Phys. Rev. B **59** (1999) 5622.
[13] P. L. McEuen et al., Phys. Rev. B **45** (1992) 11419; ibid, Physica B **189** (1993) 70.
[14] N. C. van der Vaart et al., Phys. Rev. Lett. **73** (1994) 320.
[15] O. Klein et al., Phys. Rev. Lett. **74** (1995) 785; ibid, Phys. Rev. B **53** (1995) R4221.
[16] P. Hawrylak et al., Phys. Rev. B **59** (1999) 2801.
[17] A. K. Evans et al., Phys. Rev. B **48** (1993) 11120; J. H. Oaknin et al., Phys. Rev. B **49** (1994) 5718; T. H. Stoof, G. E. W. Bauer, Phys. Rev. B **52** (1995) 12143.
[18] J. H. Oaknin et al., Phys. Rev. Lett. **74** (1995) 5120; K-H. Ahn et al., Phys. Rev. B **52** (1995) 13757; M. Ferconi, G. Vignale, Phys. Rev. B **56** (1997) 12108; A. Wojs, P. Hawrylak, Phys. Rev. B **56** (1997) 13227; M. Eto, Jap. J. Appl. Phys **38** (1999) 376.
[19] C. de C. Chamon, X. G. Wen, Phys. Rev. B **49** (1994) 8227.
[20] A. Karlhede et al., Phys. Rev. Lett. **77** (1996) 2061.
[21] J. H. Oaknin et al., Phys. Rev. B **54** (1996) 16850.
[22] S. M. Reimann et al., submitted to Phys. Rev. Lett. (1998): also see cond-mat/9904067.

Figure Captions:

Fig. 1: B-N phase diagram for device A. V_{SD} is ≈100 μV. The positions of the conductance peaks reflecting the N-electron ground states is built-up of many current traces versus V_g (from -2.1 to -0.8 V) that have been offset by a value proportional to B. The solid (open) dots mark the beginning (end) of the MDD. The singlet-triplet (S-T) transition for N=2 is identified by ▼.

Fig. 2: B-N phase diagram for device B in the spin-flip regime between ν=2 and ν=1 in the region of (a) N≈25 and (b) N≈45. V_{SD} is ≈30 μV.

Fig. 3: (a) Peak positions versus B for device A for N=12 to 39 extracted from many current traces (V_g is from -0.9 to -0.1 V). ● and O mark the same transitions as in Fig. 1. Additional transitions beyond the open circles are indicated (see Fig. 4). Greyscale plots, (b) and (c), of I versus V_g for B-values in a small interval around steps marked by O. V_{SD} is 100 μV in (b) and 300 μV in (c).

Fig. 4: Greyscale plots of dI/dV_{SD} in the V_g-V_{SD} plane (-1 mV $<V_{SD}<$+1 mV and -0.42 V $<V_g<$-0.32 V) for device A for ten B-values before, during, and after a sequence steps beyond the open circles as indicated in Fig. 1. N=31 is marked by ◆. The regular Coulomb blockade regions at the lowest and highest B-field have the familiar shapes, but in between, they are severely distorted.

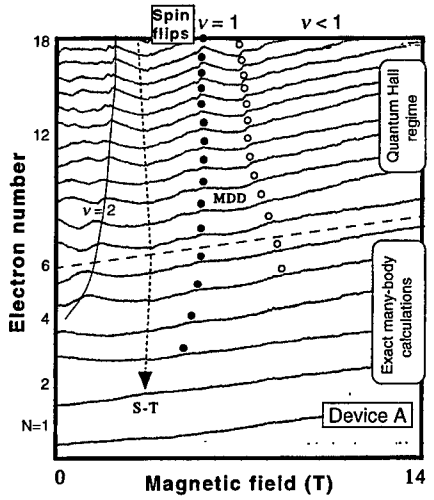

Fig. 1 Austing et al.

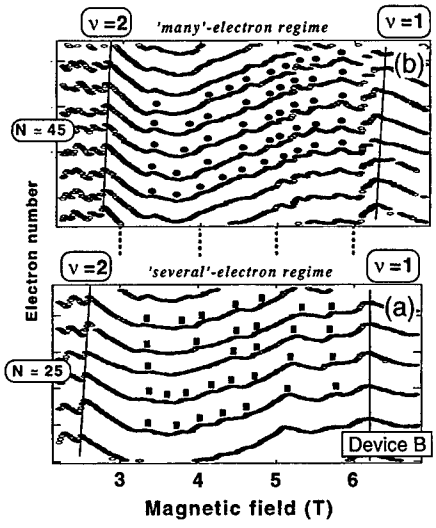

Fig. 2 Austing et al.

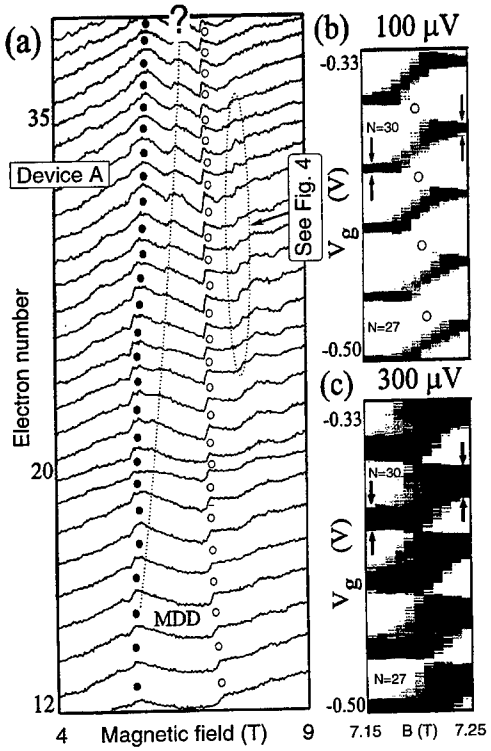

Fig. 3 Austing et al.

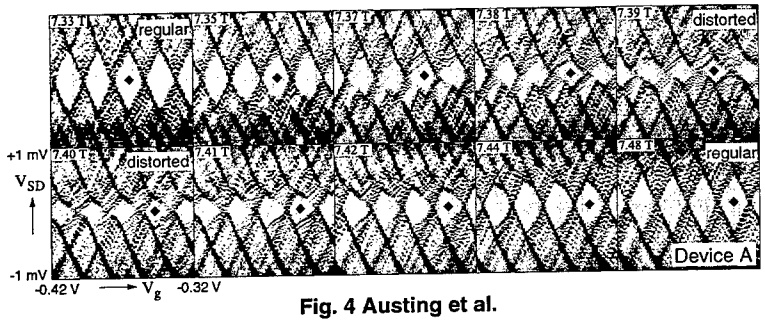

Fig. 4 Austing et al.

TB.3

Coulomb-Interaction Induced Crossover from Confined to Bulk Quantum-Dot States in a Magnetic Field

E. Ulrichs [a], C. Steinebach [a], C. Schüller [a,b], C. Heyn [a], and D. Heitmann [a]

[a] *Institut für Angewandte Physik und Zentrum für Mikrostrukturforschung, Universität Hamburg, Jungiusstraße 11, 20355 Hamburg, Germany*

[b] *Lawrence Berkeley National Laboratory, One Cyclotron Road MS 2-346, Berkeley Ca. 94720*

Abstract

We have employed inelastic light scattering to investigate electronic excitations of quantum dots in a magnetic field. For small magnetic fields the dispersion of the single-particle excitations (SPE's) follows the Fock-Darwin behavior. But already at moderate fields of $B \geq 0.6$ T the SPE's deviate from that dispersion and follow directly the cyclotron resonance. That finding is explained by Coulomb-interaction induced formation of bulk states in the center of the dot. Self-consistent ground-state calculations within the local-density approximation reproduce this result.

Quantum dots (QD's) probed by inelastic light scattering have attracted a lot of interest in the past few years. The measurements reveal that different kinds of electronic excitations can be detected in the dots [1,2], such as single-particle (SPE's), charge-density (CDE's), and spin-density excitations. Polarization selection rules allow to distinguish between these excitations: CDE's can be observed in polarized geometry, SDE's in depolarized geometry, whereas SPE's occur in both polarizations. The parabolic confinement in 0D systems gives rise to discrete, equidistant energy levels of the non-interacting system. The atomic-like shell-structure of such QD's has been detected by transport and optical experiments [3–5].

Our GaAs/AlGaAs QD's were prepared starting from a modulation-doped single-quantum-well structure with a well width of 15 nm and a carrier density of $n_s = 6.5 \times 10^{11}$ cm^{-2}. An array of QD's was produced using holographic lithography followed by a reactive ion-etching process. The diameter $2R$ of the dots was half of the period. Taking into account the depletion length, the array periods between 600 nm and 800 nm lead to electronic radii of 100–150 nm. The Raman spectra were measured at $T = 2$ K in a grazing-incidence geometry at magnetic fields of $B = 0 - 8$ T. The wavevector transfer q was

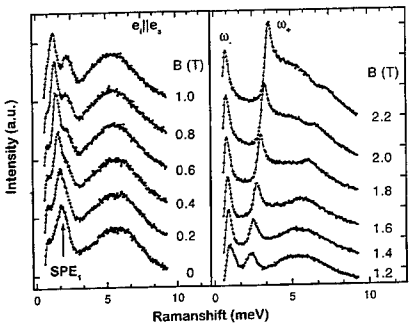

Fig. 1. Polarized Raman spectra from 300 nm QD's ($\vec{e}_i \| \vec{e}_s$). The SPE_1 at $E = 1.8$ meV splits with increasing magnetic field into the two branches ω_- and ω_+.

limited to fixed values of either 0 or $q = 0.8 \times 10^5$ cm^{-1}. We have also performed far-infrared transmission experiments in order to obtain information on the electron number per dot ($N \approx 170$) and the confinement potential which is, to a good approximation, parabolic with a confinement energy of $\hbar\omega_0 = 3$ meV.

In this paper we concentrate on the SPE's of the QD's. The energies of non-interacting electrons confined in a two-dimensional parabolic potential are described by the well known Fock-Darwin levels. In the presence of a magnetic field and in the case of $\Delta m = \pm 1$ (m is the angular-momentum quantum number), the dipole-allowed modes are

$$\omega_\pm = \sqrt{\omega(0)^2 + (\omega_c/2)^2} \pm \omega_c/2, \qquad \text{with} \quad \omega_c = \frac{eB}{m^*}. \tag{1}$$

Figure 1 shows Raman spectra taken from dots with $2R = 300$ nm in polarized geometry with a wavevector transfer of $q = 0.8 \times 10^5$ cm^{-1} and magnetic fields ranging from $B = 0 - 3$ T. The mode labeled by SPE_1 is present in both scattering geometries which shows that it is indeed an SPE. This picture is confirmed by the sharpening of the lineshape with increasing magnetic field. One clearly sees the splitting of the low-energy SPE with increasing magnetic field. From the magnitude of the splitting, which is given by $\omega_+ - \omega_- \approx \omega_c$, we conclude that these excitations correspond to a change in the angular momentum of $\Delta m = \pm 1$. Figure 2 displays the magnetic-field dispersion of the SPE_1. Also shown as straight lines are the dispersions of the cyclotron resonance frequency ω_c and the two branches ω_+ and ω_-. It is clearly seen that the two branches of the SPE_1 follow nearly perfectly ω_+ and ω_- up to a magnetic field of 0.6 T. At higher fields of $B \geq 0.6$ T the ω_+ branch deviates from the Fock-Darwin behavior and immediately follows ω_c.

In the following we will explain this experimental result by the formation of bulk states in center of the dot. These bulk states emerge with increasing

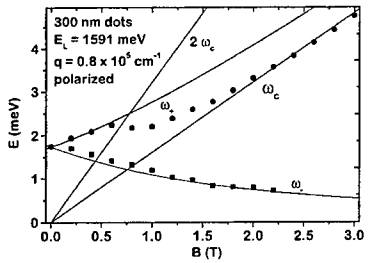

Fig. 2. Magnetic-field dispersion of the ω_- and ω_+ modes of the SPE_1. At fields of $B \geq 0.6$ T the ω_+ branch decreases and follows ω_c.

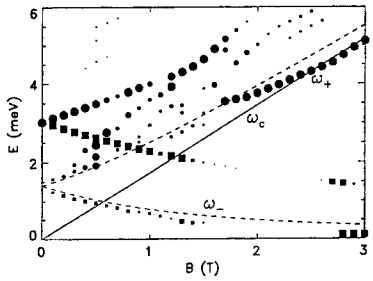

Fig. 3. Calculated peak positions as a function of the magnetic field B. Circles (squares) indicate resonances with $\Delta m = 1$ ($\Delta m = -1$), the solid, straight line is the cyclotron energy, and the dotted lines are calculated from Eq. (1). The size of the symbols is a measure for the excitation strength.

magnetic field B and are therefore a signature of the crossover from 0D dot states to the Landau levels in a high magnetic field. The formation of these Landau-level like states is strongly enhanced by the electrostatic screening of the electron system. In order to demonstrate the effect of screening on the SPE's, we have calculated the resonant Raman cross section of a QD with $N = 30$ and $\hbar\omega_0 = 3\,\text{meV}$. The spectra are obtained within the same scheme as described in Ref. [6], where the ground state was calculated with the local-density approximation. It was shown that, under the condition of extreme resonance, SPE's are expected to become visible in the Raman cross section of QD's [6]. The large excitation strength of the SPE's is due to the **pA** term in the Hamiltonian that describes the coupling of the external field with vector potential **A** to the electronic system [7].

Figure 3 shows the calculated peak positions as a function of the magnetic field. Two pairs of branches are found, i.e., the SPE's ω_+ and ω_-, starting with an energy of $\hbar\omega_\pm = 1.4$ meV at $B = 0$ T and the two magnetoplasmon modes starting at 3 meV. Due to the generalized Kohn's theorem, the dispersions

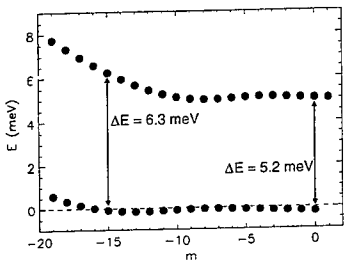

Fig. 4. Kohn-Sham energies of a 30-electron QD with $\hbar\omega_0 = 3$ meV at $B = 3$ T as a function of m. The dashed line represents the chemical potential.

of the latter are exactly described by Eq. (1) with $\omega(0) = \omega_0$. The relative strengths of the different branches depend sensitively on the resonance condition. In contrast to the experiment, the calculation shows, for the selected parameters, both CDE's and SPE's.

The most interesting result of the calculation is the behavior of the ω_+ branch at magnetic fields $B > 1.5$ T. In this region ω_+ falls below the value predicted by Eq. (1) and quickly approaches the cyclotron frequency ω_c. This behavior is a result of the filling-factor-dependent screening in the QD. Figure 4 shows the single-particle Kohn-Sham energies at $B = 3$ T. For this magnetic field, the chemical potential lies within the lowest Landau band. The good screening properties of the electron system lead to a level spacing of $\Delta E \approx 5.2$ meV $\approx \hbar\omega_c$ for small values of $|m|$. These m values can be identified with states in the center of the QD. We conclude that the cyclotron-like excitation ω_+ originates from this region of the QD.

In summary we have presented Raman spectra of SPE's in QD's. We observed strong deviations from the Fock-Darwin energies which are explained by an interaction-induced crossover from 0D dot states to a bulk region in the center of the QD. Our observations are confirmed by self-consistent calculations of the resonant Raman cross section.

We acknowledge financial support by the DFG under grants No. He1938/6, He1938/7, the Graduiertenkolleg "Physik nanostrukturierter Festkörper", and the Sonderforschungsbereich 508 "Quantenmaterialien".

References

[1] R. Strenz *et al.*, Phys. Rev. Lett. **73**, 22 (1994).
[2] P. D. Wang *et al.*, Superlatt. Microstruct. **15**, 1 (1994).
[3] S. Tarucha *et al.*, Phys. Rev. Lett. **77**, 3613 (1996).
[4] D. J. Lockwood *et al.*, Phys. Rev. Lett. **77**, 2 (1996).
[5] C. Schüller *et al.*, Phys. Rev. Lett. **80**, 12 (1998).
[6] C. Steinebach, C. Schüller, and D. Heitmann, Phys. Rev. B **59**, 10240 (1999).
[7] F. A. Blum, Phys. Rev. B **1**, 1125 (1970).

SINGLE FIR-PHOTON DETECTION USING A QUANTUM-DOT

V.Antonov[1,2], O.Astafiev[1,2], T.Kutsuwa[2], H.Hirai[2], S.Komiyama[1,2]
[1]*CREST, Japan Science and Technology Corporation (JST)*
[2]*Department of Basic Science, University of Tokyo*

Abstarct

We study single-electron-transistor (*SET*) operation of the quantum dot (*QD*) in a strong magnetic field under weak illumination of far-infrared (*FIR*) radiation, which causes cyclotron resonance (*CR*) excitation inside the *QD*. We find that the *SET* conductance resonance is exceedingly sensitive to the *FIR*: It switches *on* (*off*) upon the excitation of just one electron to a higher Landau level inside the *QD*, whereby enabling us to detect individual events of *FIR*-photon ($h\nu \cong$ 6meV) absorption.

Keywords: quantum dot, cyclotron resonance, Coulomb blockade, edge states

Introduction

The electron energy profile of relatively large quantum dots in strong magnetic fields B is well described by discrete Landau levels (*LL*). This gives way to use the *QD* for sensitive detection of the *FIR* radiation [1]. The *QD* absorbs radiation close to the cyclotron frequency, ω_C, so that an electron-hole pair is excited on two consecutive Landau levels. This gives rise to an internal charge polarization inside the *QD*, which in turn strongly affects the Coulomb conductance oscillations. Each event of the photon absorption can thus be recorded as a dramatic change of the conductance.

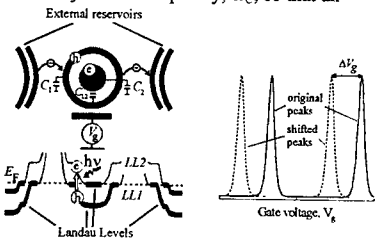

Fig. 1 Schematic picture of the *QD* in magnetic field. Two edge states, "inner-core" and "outer-ring", are formed from *LL2* and *LL1* respectively. An electron-hole pair is excited in the *QD* via absorption of a *FIR* photon, $h\nu$. The electron and the hole relax to the "inner-core" and the "outer-ring" making the *QD* to be polarized. C_i denotes the mutual capacitance. Right part: conductance of the *QD* as a function of V_g; conductance has the Coulomb resonance peaks when the electrochemical potential of the reservoirs lines up with that of the *QD*. The peak pattern shifts to the left by ΔV_g when the electron-hole pair is excited in the *QD*.

A simplified picture of the processes is shown in Fig. 1. We limit our discussion to the case when two Landau levels are effective in the *QD*: the first Landau level, *LL1*, is completely filled, while the second Landau level, *LL2*, is only slightly occupied. The Landau levels are bent by the electrostatic confining potential, whereby *LL1* amd *LL2* form an "outer-ring" and an "inner-core", respectively, at the Fermi level [2]. The two edge states corresponding to the *LL1* with opposite spin polarization are represented as one "outer-ring" in Fig. 1. Conductance through the *QD* takes place predominantly via the tunneling through the "outer-ring", which has a stronger coupling to the external reservoirs. The tunneling is affected by the Coulomb blockade effect, and, when the gate voltage V_g is scanned, the conductance has a resonance peak every time when an electrochemical potential of the "outer-ring" lines up with that of the external reservoirs.

The presence of the "inner- core" becomes important when a *FIR* photon is absorbed to excite an electron in the higher *LL2*. The excited electron and the hole in the lower *LL1* rapidly release their excess energy to the lattice and, eventually, relax into the spatially separated "inner-core" and "outer-ring". This makes the *QD* charge polarized. As a result electrochemical potential of the "outer-ring" shifts by $\Delta\mu=-eC_2/(C_2C_1+C_{12}C_1+C_2C_{12})$, where C_i and C_{ij} are capacitances denoted in Fig. 1. Correspondingly each Coulomb peak is expected to shift towards a position of a more negative V_g-value by $\Delta V_g=\alpha\Delta\mu$, $\alpha>0$. A simple estimation shows that the shift can be as large as 20% of the spacing between the original Coulomb peaks. The shift of the Coulomb peak is maintained until the excited electron-hole pair vanishes due to recombination. Importantly, this lifetime can be extremely long due to the space separation between the "inner-core" and the "outer-ring". When a second electron-hole pair is excited inside the *QD*, while the initially excited electron-hole pair is still present without recombination, the induced polarization will be doubled, yielding the Coulomb peak at a doubly shifted position $2\Delta V_g$.

We report here the observation of single photon detection due to mechanism described in the above: The wavelength range is 170-220 μm. The lifetime of the excited electron-hole pair is discussed in relation to the electronic structure of the *QD* in high magnetic field.

Experimental results and discussion

Samples are 0.7μm-size *QD*'s fabricated on a GaAs/AlGaAs heterostructure (μ=80m^2/Vs and n_s=2.4x10^{-11}cm^{-2} at 4.2K). The two dimensional electron gas (*2DEG*) is confined to form the *QD* by negatively biasing the metal gates on top of the heterostructure. We estimate ~300 electrons are trapped in the *QD*. The electrical leads to the metal gates of 100 μm length serve as a dipole antenna for the *FIR* radiation. The *QD* sample is placed in a mixing chamber of a dilution refrigerator with the base temperature of 0.05K. To study photo-response of the *QD* we install a calibrated source of the *FIR* radiation in the same mixing chamber. The *FIR* source is a 200 μm long and 10 μm wide *2DEG* Hall-bar fabricated on a *GaAs*

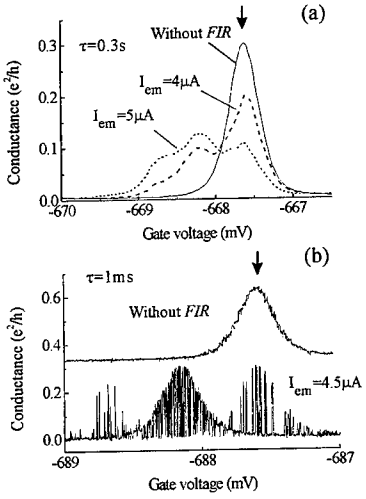

Fig. 2 Conductance of the *QD* as a function of the gate voltage V_g at B=3.67 T and T=0.05 K. (a) Time constant of the measurement set up is 0.3 s. Single Coulomb resonance peak (solid line) is splat to two peaks (dashed line) or three peaks (dotted line), when the *QD* is illuminated by the *FIR* radiation. The new peaks are shifted by by –0.6 mV and –1.2 mV from the position of the original peak. The spacing between the original Coulomb peaks is 3.5 mV. (b) Time constant of the measurement set up is 3 ms. Under the *FIR* radiation the switches between original Coulomb peak (indicated by the arrow) and two shifted peaks occur. The new peaks correspond to the excitation of one and two electron-hole pairs inside the *QD*.

heterostructure crystal [3]. The Hall-bar emits narrow-band radiation centered at the cyclotron frequency $\omega_C = eB/m^*c$, when a current I_{em} is passed through the device

(m^*=0.068 m_0 is the effective electron mass). To match the plasma-shift of the resonance frequency of the *QD* [4], we place the emitter in a stronger magnetic field than that for the *QD*. The radiation is guided from the emitter to the *QD* using a silicon rod. The *FIR* power incident on the effective antenna area (~100x100 μm^2) does not exceed ~0.01 fW in the experiment.

Striking photo-response is observed in the magnetic field range B=3.4~4.2 T, where the second Landau level (*LL2*) is slightly occupied. In the absence of *FIR*-illumination, the conductance shows regular Coulomb peaks when V_g is scanned (Fig. 2a). Under the *FIR*-illumination, each peak of conductance resonance is suppressed while two new peaks appear at the positions shifted from the original one by –0.6 mV and –1.2 mV (Fig. 2a). Time averaging with τ=0.3s is effective in this measurement. The sum of the amplitudes of these three peaks is equal to the amplitude of the original peak measured without *FIR* irradiation. Faster measurements with τ=1ms reveal that the photo-response comes from switches between the original peak and the two shifted peaks (Fig. 2b). The rate of the switches increases with increasing the I_{em}. If V_g is fixed at the position of the original Coulomb peak, then the switches are seen as telegraph type transitions between two conductance states. The switching behavior is clearly discerned up to T=0.4 K, although the amplitude of the switches decreases.

The observations are consistent with the model discussed above. The first shifted peak in Fig. 2 corresponds to the excited state with one electron-hole pair inside the *QD*, while the second shifted peak to the state with two electron-hole pairs. A strong support of this interpretation is shown by Fig. 3, which displays the peak positions of the conductance resonance in V_g-B coordinates. The data are taken without *FIR* illumination. As magnetic field increases the electrochemical potential of the "outer-ring" decreases causing a continuos downward shift of the Coulomb peak position. This process continues until it becomes energetically

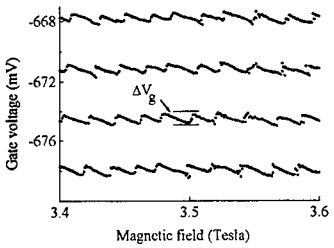

Fig. 3 Position of the Coulomb peaks in the V_g – B co-ordinates. The Coulomb peaks shift upward by ΔV_g, when one electron moves from the "inner-core" to the "outer-ring".

favorable for one electron to move from the "inner-core" to the "outer-ring", which is seen as an upward jump of the peak position. The process repeats every time when extra magnetic flux quantum is added to the *QD*. The observed jump in the peak position, ΔV_g=+0.6mV (Fig. 3), is equal in amplitude and opposite in direction to the peak shift caused by the *FIR* illumination (Fig. 2) assuring our interpretation above. We thus conclude that the switches in Fig. 2 represent the events of single *FIR* photon absorption.

The lifetime of the excited electron-hole pair, τ_{ex}, derived from the statistical analysis of the switching spectrum, exhibits a remarkable behavior. τ_{ex} varies between 1 ms and 20 minutes in the magnetic field range 3.4- 4.2 T, as shown in Fig. 4. Outside this range, τ_{ex} is smaller than the present instrumental time constant τ=1 ms. On an average τ_{ex} strongly increases as B increases up to about 4.0T, above which it rapidly drops to a level smaller than 3 ms. In addition to this overall behavior, the curve of τ_{ex} versus B exhibits an evident saw-tooth structure. As it is seen in Fig. 4, the saw-tooth structure accurately correlates with the jumps of the

conductance peak occurring without *FIR* illumination.

When magnetic field increases the electrons move from the "inner-core" to the "outer-ring", reducing the size of the "inner-core". This increases spatial separation

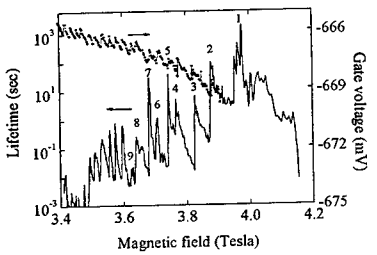

Fig. 4 The lifetime of an excited electron-hole pair in the *QD* (solid line) and the position of the Coulomb peak in B-V_g-coordinates without *FIR* illumination (solid line with the circles). The number of electrons residing at the "inner-core" are marked.

between the "inner-core" and the "outer ring", so that the probability of the recombination of the excited electron- hole pair decreases. The number of electrons in the "inner-core" are marked in Fig. 4 [5]. The longest τ_{ex} is achieved when only one electron remains at the "inner-core". The lifetime decreases sharply when the last electron leaves the "inner-core".

Right after the transition of one electron from the "inner-core" to the "outer-ring" the excited *QD* state (N_C+1, N_R-1) and the ground *QD* state (N_C, N_R) have almost the same energy (N_C is the number of the electrons at the "inner-core" and N_R is the number of the electrons at the "outer-ring"). This makes the excited state (N_C+1, N_R-1) to be long living. Away from the transition point the energy of the excited state (N_C+1, N_R-1) becomes larger compared to the energy of the ground state (N_C, N_R), therefore the rate of the electron-hole recombination increases. The largest rate, and, correspondingly, the shortest lifetime happens at the magnetic field just before the transition of the next electron from the "inner-core" to the "outer-ring".

Summarizing the results we study the effects in the *QD* caused by the absorption of the individual *FIR* photons of 170-210 μm wavelength. Each event of *FIR* photon absorption is seen as the dramatic change of the conductance due to internal charge polarization induced by the excitation of the electron-hole pair in the *QD*. The lifetime of the induced charge polarization reaches as large a value as 20 min. We show that remarkable dependence of the lifetime on B is closely linked to evolution of the edge states in the *QD*.

Acknowledgments

The work has been supported by Core Research for Evolutional Science and Technology (CREST) of Japan Science and Technology Corporation.

References

1. H. Hirai, et al. Proc. 4th Int. Symp. *On Advanced Physical Fields:* Tsukuba, Japan, p. 13 (1999).
2. N. C. van der Vaart, L. P. Kowenhowen, M. P. de Rueter van Stereninck, Y. V. Nazarov, C. J. P. M. Harmans, C. T. Foxon, Phys. Rev. B **55**, 9746 (1997)
3. Y. Kawano, Y. Hisanaga, and S. Komiyama, Phys. Rev. B **59**, 12537 (1999)
4. K. Bollweg, T. Kurth, D. Heitmann, V. Gudmundsson, E. Vasiliadow, P. Grambow, and K. Eberl, Phys. Rev. Lett. **76**, 2774 (1996).
5. The numbers are derived analyzing the graphs analogous to that shown in Fig. 3 over a wide B-range.

Charge Detection with Nanomechanical Resonators

R.H. Blick*, A. Erbe, H. Krömmer, A. Kraus, and J.P. Kotthaus
Center for NanoScience and Sektion Physik, Ludwig-Maximilians-Universität, Geschwister-Scholl-Platz 1, 80539 München, Germany.
T: +49 89 2180 3733, F: +49 89 2180 3182, Electronic address: robert.blick@physik.uni-muenchen.de.
(June 11, 1999)

*Corresponding author

We report on our recent work on nanomachined electromechanical resonators applied as mechanically flexible beams and tunneling contacts operating in the radio frequency regime. We will discuss how to build Au/Si beams of lengths varying from 1-4 μm and width down to only 80 nm. We will show how to apply them as charge detectors and how to drive the freely suspended beams into nonlinear response. This not only enables extremely sensitive charge detection, but also allows investigations of nonlinear dynamics in mechancial systems close to the quantum limit. Furthermore, we demonstrate how these nanometer devices can be used to mechanically transfer only a few electrons in each cycle of operation.

07.10.Cm - Micromechanical devices, 77.65.Fs - Electromechanical resonance, 73.40.Gk - Electron tunneling

Measuring charge nowadays is commonly performed with electronic solid state devices, like field-effect transistors. However, the classical approach developed by Coulomb in the 18th century [1] is based on a mechanical electrometer. In the present work we want to demonstrate how nanomechanical devices can be applied for charge detection. The advantages of these systems are clearly given by their speed of operation in the radio frequency (rf) range and, as will be discussed, their sensitivity.

As everyone knows, the audible sounds of a guitar are generated by the clamped strings. Halving such a string the eigenfrequencies are increased by an octave. Scaling down the string to only some 100 nm yields frequencies in the rf range. Recent work on such nanomechanical resonators [2-4] demonstrated their versatility, although not for musicians, but for applications in metrology. Integrating mechanically flexible structures with single electron devices or two-dimensional electron gases [5] on the nanometer scale offers not only high speed of operation but also broad tunability of the tunneling contacts. This is of great interest regarding electrometry with single electron devices, which are currently limited to operating frequencies of 10 MHz and extremely low temperatures (< 10 mK). Applications of mechanical resonators in nonlinear oscillators [6] or parametric amplifiers [7] are of great importance for scanning probe measurements and accurate frequency counters or clocks in general.

In this first part, we want to demonstrate how to observe nonlinear response of such nanomechanical resonators and how to apply these devices for charge detection. The resonators are operated in the rf regime with typical dimensions of only a few 100 nm in width and height. Applying a sufficiently large excitation amplitude the suspended beam shows a highly nonlinear response, which in turn allows extremely sensitive charge detection. Moreover, the device represents a model to studying phenomena such as stochastic resonance and deterministic chaos in a mechanical system on the nanometer scale.

The samples were machined out of single-crystal silicon-on-insulator (SOI) substrates by a combined dry- and wet-etch process. The SOI-substrate consists out of a 190 nm thick silicon layer, a 390 nm SiO_2 sacrificial layer and the semi-insulating Si wafer material. In a first step optical lithography was performed defining metallic gates and pads capable of supporting radio and microwave frequencies. In a second step we used electron-beam lithography to define the metallic nanostructure. The metal layers deposited on Si during lithography are a thin adhesion layer of Ni/Cr (1.5 nm), a covering Au-layer (~50 nm), and an Al-etch mask (30 nm). A reactive-ion etch was then applied to mill down the silicon by 600 nm not covered with metal. Finally, the sample was etched in diluted HF, defining the suspended silicon layer with a thickness of 190 nm. One of the suspended resonators is shown in Fig. 1: The beam has a length of almost 3μm, a width of $w = 200$ nm and a height of $h = 250$ nm and is clamped on both sides. The gate contact couples capacitively to the resonator.

All measurements shown in this case were conducted at 4.2 K in a sample holder with a residual ^{4}He-gas pressure of about 10^{-2} bar. The sample was mounted between interconnecting microstrip lines, designed to feed the circuit with frequencies up to 10 GHz, and then aligned in parallel with the externally applied magnetic field. The absolute resistance of the metal wire on top of the resonator was found to be 30 Ω, which results in a fairly well

defined impedance matching of the whole circuit. In contrast to the electrostatic excitation of motion in case of the quantum bell discussed later on, the beam is now set into motion by applying a high frequency electromagnetic excitation and ramping the magnetic field in plane. This results in an effective Lorentz force generated perpendicular to the sample surface. The response of the beam is finally probed with a spectrum analyzer, showing directly the electromagnetic power absorbed by the motion of the beam. The preamplifier employed is a low-noise broad-band (UHF- to L-band) JS amplifier with a specified noise figure of $NF = 0.6$ dB and a gain of $G = 30$ dB.

FIG. 1. Micrograph of a nanomechanical resonator, machined out of Si with a 100 nm evaporated Au-layer. The center gates couple capacitively to the resonator. Inset shows a close-up the suspended beam.

The onset of the resonance in dependence of the magnetic field is depicted in Fig. 2(a): With increasing magnetic field the peak is more pronounced, it varies according to $\propto B^2$. The driving amplitude in this case is -66 dBm – the quality factor obtained is $Q = f/\delta f = 2.3 \times 10^3$. In order to estimate effective attenuation by the ^{4}He-coupling gas, we varied the residual pressure. We found that the maximum resonance amplitude is sensitively reduced already, by small amounts of gas. Liquid ^{4}He can damp out the mechanical motion comletely [8].

The capacitive coupling between beam and gate is determined by numerical evaluation, as noted before. From these calculations we obtain a capacitive coupling between gate and beam in the linear regime of $C_{gb} \cong 220$ aF. The frequency shift δf of the mechanical resonance is found to be

$$\delta f = \sqrt{f^2 - \frac{C''(0)}{2m_{eff}}V^2} - f \cong -\frac{C''(0)}{4m_{eff}f^2}V^2, \quad (1)$$

where m_{eff} is the beam's effective mass (in our case $\sim 4.3 \times 10^{-16}$ kg), V the applied gate voltage, and C'' represents the second derivative of the capacitance with respect to the spatial coordinate. It has to be noted that for an absolute charge measurement the necessary charging of all the metallic contacts, e.g. bond pads and leads have to be taken into account. For one of the bond pads for example we estimate a capacitance of $C_{bp} = \epsilon A/d \cong 2.11$ fF. However, it is still possible to determine the relative charge δq on the closely connected gate with a high accuracy [9].

The nonlinearity found in the beam response (see Fig. 2(b)) is caused by the variation of the restoring force at the clamping points [3] and can be modelled by adding a cubic term in the equation of motion of the beam [6]. Comparing the model derived by Greywall and Yurke [10] with our data we find excellent agreement. In a more detailed study of the nonlinear properties we found that it can even be used for the generation of 'mechanical' harmonics [11].

The best operating conditions for electrometry are obtained by adjusting the amplitude at the critical point, as indicated in Fig. 3. The excitation power is levelled at -52.8 dBm and the magnetic field at 12 T. As seen in the inset the peak position varies as the square of the gate voltage applied. We achieve a sensitivity of $\Delta V/\sqrt{\Delta f} \cong 4.1 \times 10^{-2}$ V/$\sqrt{\text{Hz}}$. The slope at the critical point $dA/df|_{f=f_c} \to \infty$ diverges resulting in extremely sensitive amplification. In the measurements presented we obtain a charge resolution at a finite bias on the gate ($V = \pm 4$ V) of $\sim 0.7 \times 10^2$ e/$\sqrt{\text{Hz}}$ limited by electronic noise. It is important to note the enhancement of sensitivity with increasing gate voltage (see inset of Fig. 3).

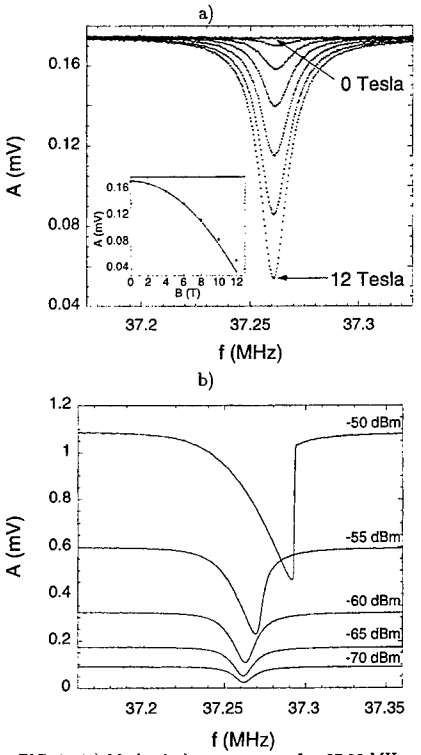

FIG. 2. (a) Mechanical resonance at $f = 37.26$ MHz: The excitation level is fixed at $P_{exc} = -66$ dBm with peak maximum increasing as B^2 (inset). (b) Beam response driven into the nonlinear regime at $B = 12$ T with power levels as indicated.

The accuracy of the measurement can even be more enhanced by determining the phase shift the mechanical resonance causes within the whole electrical circuit. For this measurement we modified our setup according to Ref. [2], i.e. including a mixer and a phase shifter. With this setup it was possible to obtain a sensitivity of $\sim 1.0 \times 10^{-1}$ e/$\sqrt{\text{Hz}}$. As before the operating point is adjusted in the transistion region at the critical point, as seen in Fig. 4. The phase shift itself is proportional to $V \propto \delta\phi$, where V denotes the voltage applied on the gate contact.

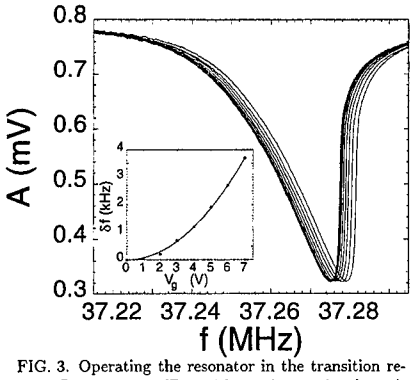

FIG. 3. Operating the resonator in the transition region at $P_{exc} = -52.8$ dBm with maximum signal sensitivity. Resonance traces are shifted by an applied gate voltage. Note the shifting of the critical point when the gate voltage is varied (inset).

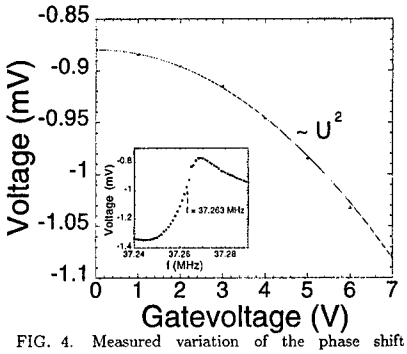

FIG. 4. Measured variation of the phase shift ($V \propto \delta\phi$) of the nanomechanical resonator in the transition region at $f = 37.263$ MHz. Inset: Measured phase shift when resonance is passed.

As a second approach towards building electromechanical devices on the nanometer scale, we started off from a sample similiar to the one shown in Fig. 1, but disconnected one of the clamping points. Hence, we ended up with a structure similar to a clapper in between two electrodes. At a certain voltage the mechanical clapper is pulled towards one of the electrodes and charge can flow onto the metallic link.

The clapper itself is then pulled back by the mechanical restoring force and delivers the acquired charge to the grounded electrode. This process is periodically repeated and the clapper resonates or 'rings' much like a classical bell. Since the electron's charge is quantized the configuration shown can in principle be used to count single electrons, much in the same way as in Millikan's famous experiment with oil drops [12] or by using single-electron transistors [13], [14].

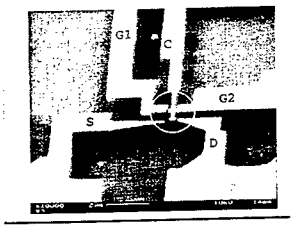

FIG. 5. Shown is a scanning electron beam micrograph of the suspended silicon structure covered by an evaporated metallic layer. The clapper in the center is undercut up to the second joint. The inset shows an electrical circuit diagram of the bell with drain (D), source (S). clapper (C) and gate contacts (#1 and #2). The clapper is biased and current flows through the drain contact. Radio frequencies are applied at gate contacts #1 and #2, while the source contact is grounded. The rf-signal on gate #1 is phase shifted by $\phi = \pi$ to gate #2.

Here, we demonstrate a new technique for counting electrons with a mechanical resonator, which is based on a mechanically flexible tunneling contact. In the case of macroscopic bells the granularity of the charge carriers is not observed, due to the large currents applied. In the present case the underlying idea is to scale down a classical bell in order to build a 'quantum bell' with which single electrons can be transferred. Naturally, there are some differences between a classical bell and our resonator: We rely on radio frequency electrostatic excitation of the clapper and not on a small magnet. Moreover, the clapper shown in the scanning electron microscope (SEM) micrograph of Fig. 5 has a size of only 1000 nm × 150 nm × 190 nm (length × width × thickness), leading to eigenfrequencies up to 400 MHz. However, regarding the fundamental similarities we find that electrons are transferred by a mechanically flexible contact. Besides reducing the size of the resonator, a quantum bell requires tunneling contacts in order to achieve tunneling of only a few electrons in each cycle of motion onto and off the clapper. In Fig 5 the contacts are marked as follows: drain (D) and source (S) tips function as tunneling contacts for the metallized Si-clapper (C) in the center. The clapper can be adjusted by dc-biasing the additional gate contacts #1 (G1) or #2 (G2). These two gate contacts (#1 and #2) allow effective capacitive radio frequency (rf)-coupling, leading to an in-plane motion of the clapper between drain and source.

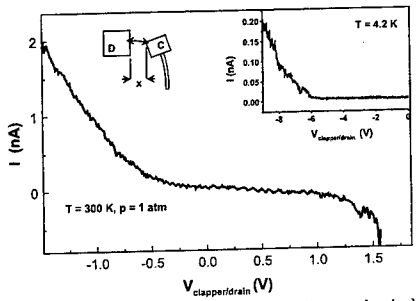

FIG. 6. Static IV-characteristic of the mechanical clapper without radio frequency applied. Plotted is the dc-current as a function of bias voltage across the clapper/drain contact at $T = 300$ K. Inset shows the IV-characteristic at 4.2 K.

In the present measurements the rf-modulation is applied to gates #1 and #2, while the source contact is grounded – the signal on gate #1 is phase shifted by $\phi = \pi$. We operate at frequencies up to some 100 MHz across the clapper electrode. Current then flows from the clapper to the drain contact and the dc-current is finally amplified. The sample is mounted in a standard sample holder allowing measurements in vacuum and at low temperatures. The obtained dc-IV-characteristic is shown in Fig. 6: At 300 K we find an exponential increase of the current with $V_{clapper/drain}$ when the clapper is pulled towards the drain contact around $V_{clapper/drain} \cong -1$ V. Electrons are then tunneling across the gap. Further biasing of the clapper finally leads to a metallic contact. The upper right inset shows the same characteristic measured at 4.2 K: Clearly the onset of the tunneling current occurs at larger bias voltage. The temperature dependence of

the IV-characteristics can be explained by the enhanced Brownian motion and the reduced stiffness of the clapper at room temperature (no hysteresis is observed at 300 K).

At low temperatures we find a hysterisis from which we estimate the contact force to be on the order of $\sim$ 330 nN (here we calibrated the displacement of the clapper with respect to drain-voltage applied and used the spring constant for Si). The dc-IV-response is not symmetrical when the current preamplifier is connected to the source contact. The measurements at low temperatures were performed after the sample holder was evacuated and a small amount of ^{4}He-gas was introduced in order to enhance cooling. The pressure in the sample holder was thus around some 10 mbar. Interestingly this results in an increased noise presumeably caused by ionization of the gas in between the clapper and drain contact tips where the electric field gradient is maximum ($E_{tip} \sim 10^7 - 10^8$ V/m). Under ambient gas pressure this discharging at the contact tip is strongly reduced.

We have seen that the resistance of the contact (clapper/drain) depends exponentially on the tip displacement and hence on the distance to drain/source by $R(x(t)) = R_0 \exp(x(t)/\lambda)$. This can be adjusted by electrostatic tuning; λ is a material constant of the metallic electrodes defined by $\lambda^{-1} = \sqrt{(2m_e\Phi)}/\hbar$, with Φ being the work function and m_e the electron mass. This allows a mechanical variation of the RC-constant and hence the tunneling characteristics of the junction, which is not possible for common single electron transistor (SET) devices. By applying radio frequencies up to 100 MHz across gate #1 and the source contact, we finally realize the nanomechanical resonator. We estimate the capacitance of the clapper tip to drain contact to be on the order of $C \approx 25$ aF. This estimation is based on calculations with electromagnetic problem solvers (MAFIA, ver.3.20, 1993). Combining the capacitance and the tunneling resistance found in dc-measurements, we obtain an RC-constant of $\tau \sim 25$ aF $\times$ 1 GΩ = 25 nsec. Hence, the electrons are transferred one by one with a rate which can be approximated by the RC-constant. The values of 25 nsec corresponds to 40 MHz, which is the range of operation of our mechanical resonator. Hence, the mechanical motion leads to a modulation or 'chopping' of the electron tunneling rate. Electron tunneling is a discrete process, as exemplified by shot noise [15]. Since we are able to modulate the resonator at this rate, we transfer only a small discrete number of electrons in each cycle of operation. In other words, the average current is given by $< I >=< q > f =< n > ef$, where $< n >$ is the average number of electrons being transferred at frequency f in each cycle.

A ceratin drawback of this mechanical resonator is the discrete set of eigenfrequencies in comparison to the simple beam shown in Fig. 1. Accordingly, only a limited number of frequencies are available for electron transfer. On the other hand this gives the flexibility to design a resonator with a specific mode spectrum in the radio frequency range only, which in turn minimizes 'leakage' currents in the low-frequency regime and the influence of $1/f$-noise. A simulation of the mechanical properties of our resonator is performed with a software package (MCS PATRAN, ver. 6.2), allowing us to test the influence of shape and clamping points on the eigenmodes of the device. Since the Au-layer has almost the same thickness as the silicon supporting structure it is necessary to model a hybrid Au/Si-system. This is done by simply assuming two rigidly coupled bars with different spring constants ($\kappa_{Au} = 0.38$ N/m, $\kappa_{Si} = 46$ N/m – these values include geometrical factors). The resulting eigenfrequency spectrum shows a strong resonant response between $f = 10$ and 100 MHz. It is obvious that the mass of the metallic layer on top reduces the attainable maximum frequency and the quality factor Q of our resonator ($Q = f/\delta f$). As expected, maximum strain is found at the clamping points, which further limits the performance (data not shown).

The rf-response of the resonator is presented in Fig. 7 and 8 – it is obtained at 300 K under He^4-gas pressure of 1 bar and an excitation amplitude of $V_{rf}^{pp} = \pm 5$ V: The different traces in Fig. 8 correspond to various dc-bias voltages on the clapper. As seen, we find a number of mechanical resonances with small quality factor Q of 100, 30, and15 where the complex resonance structure is a result of the geometry of the clapper. Applying the relation for the average dc-current $< I >=< n > ef$ (see inset in Fig. 7). In the low-frequency resonances up to 10^4 electrons are transferred in each cycle, while at 73 MHz we find a transfer rate of $\sim$ 130 electrons at this amplitude of the driving voltage. The peak currents and the noise increase at larger bias voltages (0.1 V – 0.5 V). It can also be seen that the background conductance increases. The peak values themselves show an exponential increase of the current with $V_{clapper/drain}$, which is shown in detail in the inset for the peak at $f = 73$ MHz. Here the solid line is an exponential fit to the data points. From this exponential behavior of the peak current at 73 MHz shown in the inset of Fig. 8, we can estimate x, which gives a value for the distance between

clapper and drain contacts at the maximum applied dc-voltage – we obtain $x_{max} \approx 5$ nm.

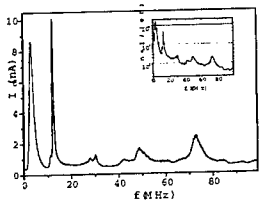

FIG. 7. Tunneling current through the clapper/drain contact plotted vs. applied frequency (applied at gate contacts #1 and #2). Several mechanical resonances up to 73 MHz with a quality factor of $Q \sim 100, 30$, and 15 are found (from left to rqight. Inset: Log-plot of electron number vs. frequency (see text). In the high-frequency peaks about 130 electrons are transferred in each cycle, which can be easily reduced to only 5 electrons/cycle at a reasonable S/N-ratio.

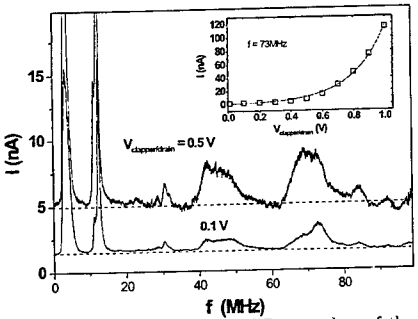

FIG. 8. Resonance curves at different values of the dc-voltage bias across clapper/drain contact. The variation of the voltage bias results in an exponential increase of peak and background current. Inset: exponential increase of peak current at 30.5 MHz – the solid line is an exponential fit to the data points (open boxes).

In conclusion we demonstrated the operation of a variety of nanomechanical resonators. Our main focus is the accurate detection of single electron charges with the help of these mechanical devices. The main features are the high speed of operation and the increased sensitivity, due to the operation in the nonlinear regime. Furthermore, by scaling down a classical bell in size we have shown that a quantum bell can be built which rings in the ultrasonic frequency range. The essential requirement is a nanometer scale clapper resonating at radio frequencies and the ability to tune the RC-constant of the tunneling contact. So far, we have obtained an accuracy of about ± 2 electrons, which can be transferred in a single revolution of the clapper. In the newly developed setup of the experiment we included a metallic island on the tip of the clapper, forming a metallic SET, in order to realize an electron shuttle mechanism, as proposed by Gorelik *et al.* [16]. A detailed theoretical description of this approach is already given by Weiss and Zwerger [17], indicating that such a mechanical single electron shuttle should operate up to temperatures of 1 K. The Coulomb repulsion in this case functions as an additional energy barrier for electrons to tunnel onto the island.

We like to thank Ch. Weiss, W. Zwerger, and U. Sivan for valuable discussions. This work was funded in part by the Bundesministerium für Bildung, Wissenschaft, Forschung und Technologie (BMBF) and the Deutsche Forschungsgemeinschaft (DFG). The SOI-wafers used to machine the quantum bell were donated by Siemens Corp., Germany.

[1] C.A. Coulomb, Memoires de l'Academie Royale des Sciences, 229, *Academie royale des sciences*, Paris (1784).
[2] A.N. Cleland and M.L. Roukes, Nature **392**, 160 (1998).
[3] A.N. Cleland and M.L. Roukes, Appl. Phys. Lett. **69**, 2653 (1996).
[4] A. Erbe, R.H. Blick, A. Tilke, A. Kriele, J.P. Kotthaus, Appl. Phys. Lett. **73**, 3751 (1998).
[5] R.H. Blick, M. L. Roukes, W. Wegscheider, M. Bichler, Physica A **249-251**, 784 (1998).
[6] D.S. Greywall, B. Yurke, P.A. Busch, A.N. Pargellis, and R.L. Willett, Phys. Rev. Lett. **72**, 2992 (1994).
[7] D. Rugar and P. Grütter, Phys. Rev. Lett. **67**, 699 (1991).
[8] A. Kraus, A. Erbe, R.H. Blick, submitted to Appl. Phys. Lett. (1999).

[9] H. Krömmer, A. Erbe, A. Tilke, S. Manus, and R.H. Blick, submitted to Phys. Rev. Lett. (1999); H. Krömmer, Diploma Thesis, Ludwig-Maxmilians Universität München (1999).
[10] B. Yurke, D.S. Greywall, A.N. Paragellis, P.A. Busch, Phys. Rev. A **51**, 4211 (1995).
[11] A. Erbe, H. Krömmer, A. Kraus, R.H. Blick, G. Corso, K. Richter, submitted to Europhys. Lett. (1999).
[12] R.A. Millikan, Phys. Rev. **32**, 349 (1911).
[13] T.A. Fulton and G.J. Dolan, Phys. Rev. Lett. **59**, 109 (1987); D.V. Averin and K.K. Likharev, J. Low Temp. Phys. **62**, 345 (1986); P. Lafarge, H. Pothier, E.R. Williams, D. Esteve, C. Urbina, and M.H. Devoret Z. Phys. B **85**, 327 (1991); M.W. Keller, J.M. Martinis, N.M. Zimmerman, and A.H. Steinbach, Appl. Phys. Lett. **69**, 1804 (1996).
[14] R.J. Schoelkopf, P. Wahlgren, A.A. Kozhevnikov, P. Delsing, D.E. Prober, Science **280**, 1238 (1998).
[15] H. Birk, M.J.M. de Jong, and C. Schönenberger, Phys. Rev. Lett. **75**, 1610 (1995).
[16] L.Y. Gorelik. A. Isacsson, M.V. Voinova, B. Kasemo, R.I. Shekhter, and M. Jonson, Phys. Rev. Lett. **80**, 4526 (1998).
[17] Ch. Weiss and W. Zwerger, Europhys. Lett., in press (1999); cond-mat/9904149.

TC.2

Free-standing and overgrown InGaAs/GaAs nanotubes, nanohelices and their arrays

V.Ya. Prinz, V.A.Seleznev, A.K.Gutakovsky, A.V.Chehovskiy
V.V.Preobrazenskii, M.A.Putyato, T.A.Gavrilova

Institute of Semiconductor Physics, Lavrent'eva ave.13,
630090, Novosibirsk, Russia, e-mail: prinz@isp.nsc.ru

Abstract

The paper is devoted to further development of new approach in nanostructure fabrication. The possibility is shown of self-scrolling of initially flat (2D) strained GaAs/InGaAs bilayers in tubes, helices, scrolls and more complex objects. MBE overgrown structures with embedded nanotubes arrays have been obtained. Using an ultra-thin film (1 ML GaAs: 1 ML InAs), nanotubes with an inside diameter of ~2 nm have been obtained, which constitutes the limiting size for this system.

Introduction

Nano-objects of ultra-small dimensions, to which carbon nanotubes with the diameter of 1 to 20 nm can be assigned, have attracted widespread attention of researchers. Disadvantage of carbon nanotubes is their technological incompatibility with solid state device processing.

Recently, self-formed semiconductor micro- and nanotubes have been fabricated, and the possibility of precise control of their parameters has been shown [1]. The present work continues our previous studies aimed at further development of this new approach to fabrication of nano-objects.

The possibility is shown for self-scrolling of initially flat (2D) strained GaAs/InGaAs structures in radially symmetrical 3D structures: tubes, helices, scrolls and more complex objects. MBE overgrown structures with embedded nanotubes and nanohelices arrays have been obtained.

Basic principles, fabrication process and results

Figure 1 schematically illustrates the essence of the method of nanotube formation based on the use of strained InAs/GaAs bilayerd films. The lattice parameters of InAs and GaAs layers differ significantly (lattice mismatch $\Delta a/a$=7.2%). After accommodation of the two monolayers (ML), a highly strained heterostructure forms containing 2ML films of InAs and GaAs being compressed and in tension, respectively. After the freeing of the bilayer by using selective etching of sacrificial AlAs layer in HF based etchant [2], the interatomic forces will act to increase the interatomic distance in the compressed InAs layer and to decrease it in the tensile-stressed GaAs layer (Fig.1,a). The forces F_1 and F_2 are oppositely directed, and they give rise to a moment of forces M, which tends to bend the bilayer. Under the action of the moment, the initially two-dimensional (2D) (flat) bilayer is rolling up into a tube. It has been shown that the rolled up layers get close together, thus forming perfectly bonded tube walls. The tube diameter D is determined by the bilayer thickness d and by the mismatch of lattice parameters $\Delta a/a$ (i.e., by the composition of the InGaAs solution used): $D \approx d \cdot a/\Delta a$. It was shown that InAs/GaAs nanotubes with the tube diameter D as small as 4 nm and longer then 1 mm can be produced. The described ML technology makes it possible to obtain free-standing MLs. Possibilities of making nanoobjects have been demonstrated on a series of epitaxial structures grown on GaAs and InP substrates.

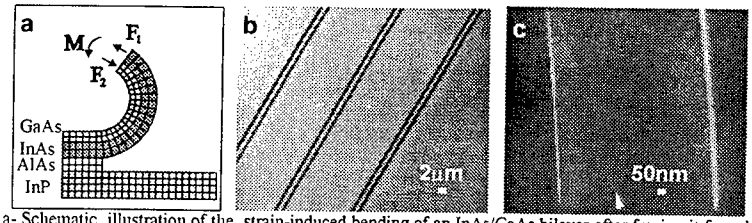

Fig.1 a- Schematic illustration of the strain-induced bending of an InAs/GaAs bilayer after freeing it from bonding with substrate (removal of sacrificial AlAs layer). b- array of identical tubes (tube diameter - 2 μm, tube wall thickness - 10 nm, typical tube length - 1-2 cm). c- SEM image of nanotubes with different outer diameters formed from a 2ML GaAs+1ML InAs film. The arrow shows the place from which the tube rolling started. The right and left tubes have 25 and 12 turns, respectively. Typical tube length - 1-2 mm, inner tubes diameter <10nm.

The technology allows to fabricate a highly ordered array of long tubes with a predetermined geometry, namely, length L, position on the substrate surface and orientation along a desirable crystal direction. Figure 1 (b, c) exemplifies arrays of long tubes (L>>D). Position, length and orientation of the tubes on substrate were determined by initial narrow slits fabricated using either electron lithography or crack-assisted lithography [3]. These slits open up windows for penetrating etchant towards the buried-in sacrificial AlAs layer. In this paper we illustrate the possibilities of controllable fabrication of arrays of tubes with different outer diameters (Fig.1.c)

The fabricated tubes were studies by high-resolution transmission electron microscopy (HRTEM). Figure 2 exemplifies HRTEM images of three nanotubes, which were just parts of

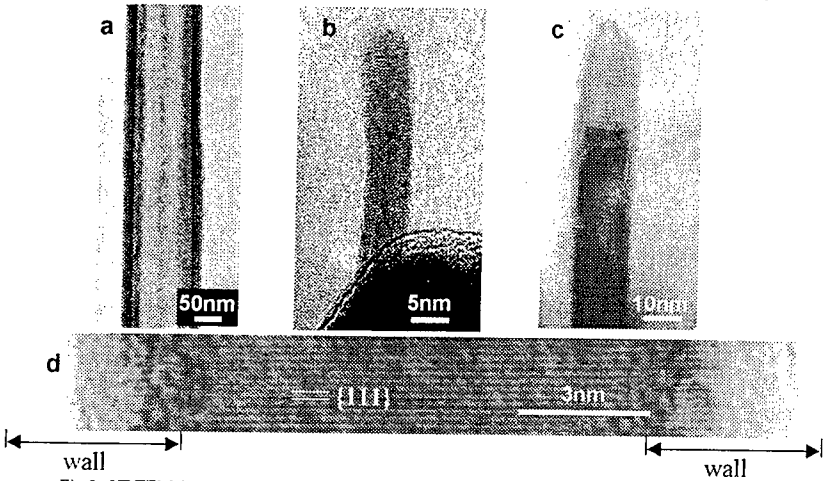

Fig.2. HRTEM images of multi-coil InGaAs/GaAs nanotubes: the thickness of self-scrolled bilayer: a - 4ML GaAs+4ML $In_xGa_{1-x}As(x=0.6)$: b - 2ML GaAs+1ML InAs; c-2ML GaAs+1ML$In_xGa_{1-x}As(x=0.8)$; d- magnified image of a part of the tube shown in fig.2.c. Atomic planes normal to the tube axis are clearly seen (the atomic planes are observed along the entire tube length).

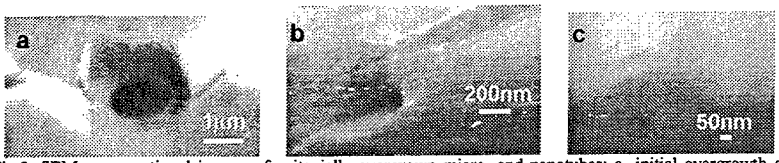

Fig.3. SEM cross-sectional images of epitaxially overgrown micro- and nanotubes: a- initial overgrowth stage of tubes of large diameter (1μm); b- fully overgrown tube of 200 nm diameter, the tube is inclined at an angle to the cleavage; c- an overgrown tube of a ~10 nm inner diameter, outside diameter ~60 nm (tube was self-scrolled from a 2ML GaAs+1ML InGaAs film and consisted of 20 turns).

tubes extended from the substrate (full length of tubes on substrate may be as large as 1 cm). The inner diameters (D) of the tubes were 120 nm (Fig.2.a), 3 nm (Fig.2.b) and 10nm (Fig.2.c). A nearly equal spacing between tube's coils was observed in the multicoil (five coils) tubes (Fig.2.a) made from a relatively thick bilayer (4ML+4ML). The interwall spacing in the tubes of small diameter (Fig.2.b, c) is seen to vanish with the formation of a single tube wall, i.e. the scroll-shaped tube really turns into a hollow cylinder. Figure 2.d presents a magnified view of the tube (four coils) shown in Fig.2.c. Atomic planes normal to the tube axis are clearly seen (these planes observed along the entire tube length). So, we can conclude that the wall in a multi-coil tube formed by layers forced together, is monocristalline throughout its entire thickness.

The tubes of minimal inner diameter (3 nm) were found to form from bilayers consisting of only 3MLs. Using an ultra-thin film (1 ML GaAs: 1 ML InAs), nanotubes with an inside diameter of ~2 nm have been obtained, which constitutes the limiting size for this system. The fabricated tubes were stable at room temperature and the exposure to atmospheric conditions did not cause any noticeable oxidation of tube walls.

The action of surface tension forces results in a decreased tube diameter as compared to the value which formula mentioned above predicts.

For the first time, MBE overgrown structures with embedded arrays of nanotubes and nanohelices have been obtained. Hollow tubes with diameter ranging from 1 μm to ~10 nm embedded into a GaAs matrix are shown in Fig.3.

After the formation of array of tubes fixed to the substrate, the sample was rinsed with isopropilen alcohol and loaded into a vacuum chamber. The removal of oxidized layer from the substrate and tubes was carried out in a As_4 flow at 580°C. Subsequently, Reflection High Energy Electron Diffraction (RHEED) was used to observe reconstruction (2×4) formed on the substrate surface. The overgrowth rate was 1μm/h at 530°C under condition of sample rotation. The thickness of the additionally deposited GaAs layer was 0.5 to 1μm. Microwave conductivity measurements confirm high anisotropy (>10) of the obtained new materials. Conducting wires (including organic metal ones) were obtained with using capillarity-induced filling of nanotubes.

Fabrication of 3D nanoobjects, discussion

So far, only the fabrication of free-standing and overgrown GaAs/InGaAs nanotubes has been described. The proposed approach can be successfully applied not only to semiconductor structures but also to strained metal, dielectric or hybrid structures. As an example, nanotubes from a more complex structure, In/Al/GaAs/InAs, with the tube diameter of ~50 nm have been obtained.

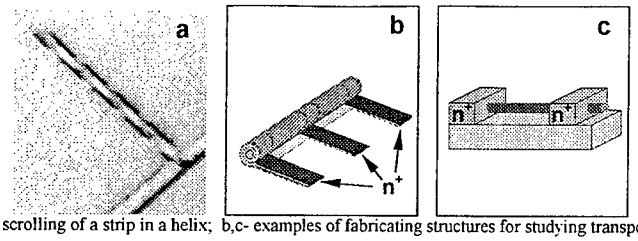

Fig.4.a- scrolling of a strip in a helix; b,c- examples of fabricating structures for studying transport phenomena.

In this work, not only free-standing and overgrown nanotubes, but also a wide variety of other 3D nanostructures was obtained. To produce them, we applied the self-scrolling process to initial mesa-structures of various (e.g., rectangular, triangular, squared, circular, etc.) geometries. As an sample, Fig.4.a shows a narrow strip of a (100) bilayer misoriented from the [010] direction, which was scrolled up in a helical coil. The rolling of strip is clearly influenced by anisotropy of Young's modulus in A^3B^5 crystals [4]. A narrow strip of a (100) plane bilayer oriented along the [010] direction will be rolled up in a ring-shaped tube. The spacing between spirals in the coil is determined by the value of misorientation angle. Helical coils with minimal diameter 7nm were obtained using 6ML bilayers.

Moreover, we scrolled not only laterally uniform 2D systems, but also systems with laterally modulated properties, e.g. lateral superlattices. To obtain contacts to the tubes with electron gas we propose here two methods. First methods include fabrication of conductive strips on structure surface followed by self-scrolling for making tubes with external contacts (see Fig.4 b). The alternative way is overgrowing the tubes by high-doped wide band gap material followed by local selective etching and opening some fraction of buried-in tubes (see Fig.4.c). In both cases, we suspect to obtain almost ohmic contacts to the tubes. We believe that fabricated conducting nanostructures with two-dimensional electrons on a cylindrical surface are prominent for study of ballistic transport, spin-orbital interaction [5] and interference Aharonov-Bohm type effects.

Acknowledgments

We thank Dr. A.I.Toropov for supplying us with MBE-grown multilayer structures. This work was supported by the Russian Foundation for Basic Research (Grants № 97-02-18479, №99-02-16689), Russian State Science Programme "Promising Technologies and Devices for Micro- and Nanoelectronics" (Project № 42) and Russian National Program "Physics of Solid State Nanostructures" (Project № 98-2030)

References

[1] V.Ya. Prinz, V.A. Seleznev and A.K. Gutakovsky, The 24 th Int. Conf. on the Phys. of Semicond. (ICPS 24), Israel, 1998, p. Th3-D5. and in The Physic of Semiconductors 1999 .

[2] E.Yablonovitch, T.Gmitter, T.Harbison and J.Bhat Appl. Phys. Lett. **51** (1987) p.2222.

[3] V.Ya.Prinz, V.A.Seleznev, V.A.Samoylov and A.K.Gutakovsky Microelectronic Engineering **30** (1996) pp.439-442.

[4] R.I.Cottam and G.A.Saunders, J. Phys. C: Solid State Phys. **6** (1973) p.2105

[5]L.I.Magarill, D.A.Romanov and A.V.Chaplik, JETP **86** (1998) pp.771-779

TC.3

DISSOCIATION OF INDIRECT EXCITONS: DISCONTINUITY AND BISTABILITY IN THE TUNNEL CURRENT OF 2D ELECTRON-HOLE LAYERS

A. Parlangeli, P.C.M. Christianen, A.K. Geim, J.C. Maan
Research Institute for Materials, High Field Magnet Laboratory, University of Nijmegen, Toernooiveld, NL-6525 ED, Nijmegen, The Netherlands
T.M. Fromhold, F.W. Sheard, L. Eaves, P.C. Main, M. Henini
Department of Physics, University of Nottingham NG7 2RD, U.K.

We studied a novel bistability and discontinuity in the tunnel current of a 12 nm single barrier GaAs/AlAs p-i-n heterostructure where a system of spatially separated electron and hole (*e-h*) layers is realized. Both features appear at T<300 mK and when the in-plane *e-e* (*h-h*) distance is comparable to the inter-layer (*e-h*) one. Whereas the High Current State (HCS) behaves normally and can be identified with the uncoupled *e-h* gases, the Low Current State (LCS) shows some peculiarities: it has low current, a density 10% lower than the HCS at the same bias, a marked phase shift in the current magneto-oscillations (MO), and - contrary to the HCS - does not show any fractional feature. We identify the LCS with a gas of indirect excitons, the binding energy of which we estimate to be ~0.5 meV and ~5 meV at B=0 and 10 T respectively. We explain the bistability and the discontinuity as a first order phase transition between a gas of excitons and the uncoupled 2D *e-h* gases.

PACS codes: 73.20.Dx, 73.40.Gk, 71.35.-y
Keywords: electron-hole correlations, excitons, tunneling, QHE

Tel.: ++31 24 3653052
Fax : ++31 24 3652440
E-mail: andrea@sci.kun.nl

Two dimensional (2D) electron-hole (*e-h*) layers of equal density, separated by a distance comparable to the effective Bohr radius, are particularly interesting physical systems [1-5]. On the one hand, in a magnetic field, the two *e-h* layers can separately condense into *Laughlin* states, giving rise to the fractional quantum Hall effect (FQHE) [6]. On the other hand, electron and holes from the adjacent layers can form bound states called indirect excitons, which are widely considered as good candidates for undergoing Bose-Einstein condensation because of their long recombination time.

The transition between these two regimes has not been reported to date, because of the difficulties in engineering systems with tunable parameters such as density or inter-layer distance. Tunable density can be achieved in optically pumped Quantum Wells [2,3], but at the prize of perturbing the thermodynamic equilibrium. Another possibility is to use p-i-n single barrier heterostructures (SBH) under forward bias. If the barrier is sufficiently thick (~10 nm) the tunneling and optical recombination times are sufficiently low to allow quasi-equilibrium; the electron and hole chemical potentials separately align to the respective ones in the doping regions. Two limits are known in these structures: spatially indirect excitons have been observed by Neves *et al.* [4] in 12 nm thick SBH in the low density regime (~10^{10} cm^{-2} for both *e* and *h*); at high densities (~10^{12} cm^{-2}), Teisser *et al.* studied the tunneling properties of uncoupled *e-h* layers [7].

We studied a 12 nm GaAs/AlAs p-i-n SBH, grown in the <311> direction (high in-plane hole mobility), in the intermediate regime n~10^{11} cm^{-2}, i.e. when the in-plane *e-e* (*h-h*) distance is comparable to the inter-layer (*e-h*) one. The density was tuned by the applied voltage, and the chemical potential of the *e-h* system, defined as the energy required to add an electron-hole pair, was directly proportional to the applied voltage: $\mu_{e\text{-}h} = eV$, where *e* is the electron charge.

We observed a discontinuity of a factor of two, with bistable behavior, in the *I(V)* curves of the tunnel current at B=0 and T=70 mK (Fig.1). The temperature T* that suppresses both the features is ~300 mK (~0.05 meV). As shown in Fig.1, only a kink remains in the *I(V)* at T=4.2 K (~0.5 meV), and a single exponential dependence remains at temperatures of ~50 K. In general, as the temperature increases, the feature shifts to higher currents and lower voltages, and it eventually disappears. In the inset of Fig.1, we show in an Arrhenius plot the temperature dependence of the current difference ΔI between the HCS and the LCS, measured at the center of the transition. The voltage position of the feature shows very similar properties, which cannot be described by a simple thermal activation. Such a behavior probably arises because of a difference between the bath and the electron temperatures at T<1 K, but could be also due to an intrinsic saturation of the process.

The bistability width, the current discontinuity, and T* increase by an order of magnitude under a magnetic field B=10 T perpendicular to the layers, as shown in Fig.2. In this case, T* exceeds 4.2 K, pointing to an energy scale ~20 times larger than at B=0. It is remarkable that also the ratio of the widths gives the same value.

In order to characterize the LCS and the HCS, we measured the magneto-oscillations (MO) of the tunneling current as a magnetic field perpendicular to the layers was swept at constant applied bias, i.e. at fixed chemical potential. Such measurements reveal the Density of States (DOS) of the 2D Electron Gas (2DEG) in a magnetic field. In first approximation, the DOS quantizes in Landau Levels (LLs) with degeneracy *eB/h*. The physical properties are determined by the number of occupied LLs, the filling factor $\nu = nh/eB$, where *n* is the density. The Fermi Energy E_F of the 2DEG is pinned to the last occupied LL and to the chemical potential (fixed by the applied voltage) in the doped region. When *B* is swept, this condition induces a self-consistent rearrangement of the band profile, which modulates the tunnel current with periodicity *1/B* [8]. The minima occur approximately at integer filling factor (we resolve spin-splitting), at fields $B_\nu = nh/e\nu$.

The magneto-oscillations that we measured at T=70 mK are shown in fig.3 at three different regimes: in the LCS (-1.642 V), in the HCS (-1.660 V and T=1.2 K), and at the transition (-1.645 V). It is clear from the picture that the LCS and the HCS have different qualitative behaviors and that the transition between the two is discontinuous. For example, the position of the maxima are different in the two regimes, which shows a difference in the DOS. This observation is confirmed by a change of periodicity: whereas the minima positions are proportional to $\nu = 1/B$ in the HCS, they are proportional to $\nu' = \nu - \alpha$ ($0.2 < \alpha < 0.25$, corresponding to a phase shift $\varphi = \alpha * 360°$) in the LCS [Fig.4].

We discussed this phase shift in detail in [5], and we focus here on another interesting property of Fig.3: the presence of small dips in the HCS MO at $\nu = 2/3$. These minima are not visible in the LCS and disappear at T=1.2 K; moreover, they allow the determination of the HCS density at the transition. The results, shown in Fig.4, naturally extend the values deduced from the analysis of the full *1/B* periodicity at T=1.2 K [5] and agree with calculations (line in Fig.4). Our data show that in the region of bistability (~-1.650 V) the system can be stable in two configurations of different density; more precisely the density of the HCS is, at the same applied voltage, ~10% bigger than the one in the LCS. This conclusion agrees with the analysis of the bistability in the MO under a sweep of magnetic field [5].

We can identify the HCS with the uncoupled 2D *e-h* layers, since it behaves normally under all conditions [7] and shows the fractional minimum ν=2/3 at T=70 mK (corresponding to the condensation into states that minimize the in-plane interactions among carriers of the same charge [6]).

We believe that the LCS is a (dense) gas of indirect excitons. This interpretation is supported by the observation of a phase-shift in the MO, since a similar behavior has been recently observed in the optical properties of 2D excitons [9] and directly witnesses a change in the DOS, as confirmed by the general behavior of the MO [5]. In the same picture, we explain the LCS low current as a consequence of the reduced tunneling probability of indirect excitons with respect to free-carriers. This suppression occurs because, in the exciton state, the electron is confined in the plane of the layer by the Coulomb attraction caused by accompanying hole and has, therefore, a small overlap with the plane-wave states in the collector. In addition, the absence of any fractional feature in the MO is naturally explained by the fact that inter-layer attraction leads to exciton binding rather than to the incompressible *Laughlin* fluids.

Our data suggests that the transition is discontinuous because it is driven by a strong non-linearity in the chemical potential: it is a first-order phase transition. The bistability arises because an energy difference, the exciton binding energy, must be overcome in going from one state to the other. The system has a memory which arises from the competition between in-plane (repulsive: screening) and inter-plane (attractive: exciton binding) interactions. Remarkably, the temperature dependence, in particular T*, suggests that the bistability width is directly related to the binding energy. With this assumption, the binding energy at B=0 and 10 T can be estimated to be, respectively ~0.3 meV and ~5 meV, at T=70 mK.

In conclusion, we observed a new discontinuity and bistability in the tunnel current of SBH, in the presence of strongly interacting *e-h* layers. We interpret our results as a first order phase transition between a gas of indirect excitons and the uncoupled *e-h* gases.

This work is part of a research program of the Stichting voor Fundamenteel Onderzoek der Materie (FOM) financially supported by NWO (The Netherlands).

REFERENCES

[1] Yu.E.Lozovik and O.L.Berman, JEPT **84**, 1027 (1997); Yu.E.Lozovik, O.L.Berman, and V.G.Tsvetus, JEPT Lett. **66**, 355 (1997).
[2] T.Fukuzawa, E.E.Mendez, and J.M.Hong, Phys. Rev. Lett. **66**, 3066 (1990); J.A. Kash *et al.*, Phys. Rev. Lett. **66** 2247 (1991).
[3] L.V. Butov *et al.*, Phys. Rev. Lett. **73**, 304 (1994); L.V.Butov and A.I.Filin, Phys Rev. B **58**, 1980 (1998).
[4] B.R.A. Neves *et al.*, in *Proceedings of the 23rd International Conference on Physics of Semiconductors, Berlin, 1996,* edited by M.Scheffler and R.Zimmermann (World Scientific, Singapore), p.2275.
[5] A.Parlangeli *et al.*, Physica B **256-258**, 531 (1998).
[6] *The Quantum Hall Effects, Second Edition,* T.Chakraborty and P.Pietilainen (Springer-Verlag, Berlin, 1995).
[7] R.Teisser *et al.*, Phys. Rev. B **51**, 5562 (1995).
[8] K.S.Chan *et al.*, Phys. Rev. B **56**, 1447 (1997).
[9] O.V. Volkov *et al.*, JEPT Lett. **64**, 774 (1996).

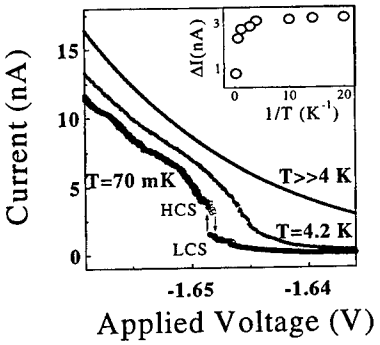

Fig.1 I(V) curves at T=70 mK, 4.2 K, and ~50 K (B=0). At T=70 mK, the sweep up and down are indicated by filled and open circles respectively. In the inset, we show the Arrhenius plot of the current difference ΔI between HCS and LCS at the center of the transition.

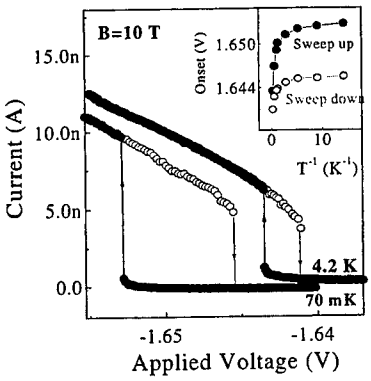

Fig. 2 I(V) curves at T=70 mK and 4.2 K, under a magnetic field B=10 T perpendicular to the layers. The sweeps up and down are shown with filled and open circles respectively. The Arrhenius plot of the discontinuity positions is shown in the inset.

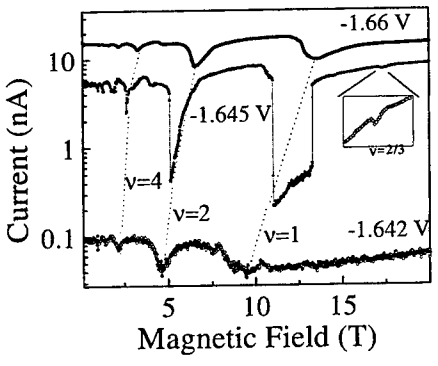

Fig.3 Magneto-oscillations, at T=70 mK, of the tunnel current at fixed bias -1.642 V (LCS), -1.645 V (LCS+HCS), -1.66 V (HCS, taken at T=1.2 K [6]). The feature at ν = 2/3 is observed only in the HCS and at T=70 mK.

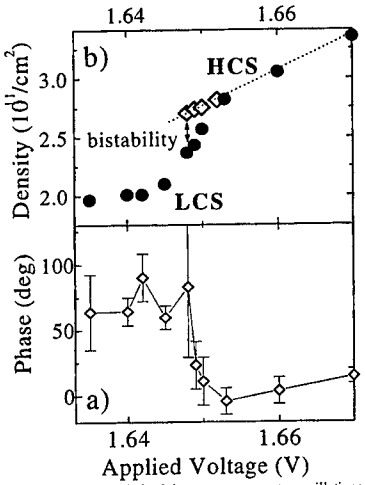

Fig.4 a) Phase shift of the current magneto-oscillations. b) Density of the 2D e-h layers as a function of bias. The filled dots are deduced from the 1/B periodicity at T=1.2 K [5]; open triangles are obtained from the ν = 2/3 minima. The line shows the calculated behavior of the uncoupled e-h layers.

TC.4

A Digital Quantum Hall Effect

R.J. Nicholas[a], M. Lakrimi[a], B. Kardynal[a], S. Khym[a], N.J. Mason[a], J. Rehman[a], K. Takashina[a], P.J. Walker[a], D.M. Symons[b], D.K. Maude[b], and J.C. Portal[b]

a: Department of Physics, Clarendon Laboratory, Oxford University, Parks Road, Oxford OX1 3PU, U.K.

b: L.M.C.I.-C.N.R.S., Grenoble, B.P.166X, Grenoble, France

Abstract

Quantum Hall effect and magnetoresistance have been studied in a bipolar InAs/GaSb system and are shown to give new behaviour where the resistivity oscillates from insulating to metallic behaviour and the quantum Hall effect shows a digital character oscillating from 0 to 1 conductance quantum e^2/h. This behaviour is attributed to the formation of a total energy gap in the system.

InAs/GaSb heterojunctions form bipolar 2-D layers due to the overlapping conduction and valence bands. Such systems have generated considerable interest recently due to the possibilities of gap formation by both excitonic and single particle interactions. We have studied the quantum Hall effect in this system at very high fields (up to 50T) and low temperatures when both the electrons and holes contribute to the quantized Hall conductance. It is found that the Hall conductance shows a digital sequence oscillating from 0 - 1 - 0 conductance quanta and the diagonal resistivity, ρ_{xx}, shows oscillatory insulating behaviour due to the formation of a total gap in the energy spectrum. The quantum Hall effect has become well known since its first observation by von Klitzing et al [1] but still raises a number of fundamental questions, including the role of edge states in its interpretation. The electron-hole system demonstrates completely different behaviour in which the edge states of the electron and hole systems interact forming closed and localised states.

The first observation of quantum Hall plateaux in an electron-hole system was made by Mendez et al, [2] who found that plateaux were formed at quantum numbers corresponding to the difference in the occupancies of the electron and hole Landau levels. Subsequently Daly et al [3] found that in superlattices with closely matched electron and hole densities the special case of zero Hall resistance could be observed. Here we examine this behaviour for the case of a structure containing one layer each of electrons and holes which interact via interband mixing. As a result of the mixing which occurs between the electron and hole edge states the system can display re-entrant insulating behaviour in certain regions of magnetic field.

The samples studied consisted of a single layer of InAs sandwiched between thick layers of GaSb. This conduction band edge of the InAs lies 150meV below the valence band edge of the GaSb. The samples are grown by Metal Organic Vapour Phase Epitaxy (MOVPE) and are known to possess a relatively low level of extrinsic doping so that the majority of charge carriers are created by intrinsic charge transfer from the GaSb layers to the InAs layer. Typical structures are grown onto semi-insulating GaAs followed by 2μm of GaSb to achieve lattice relaxation. The active layer of InAs is typically 30nm thick, followed by a 90nm GaSb capping

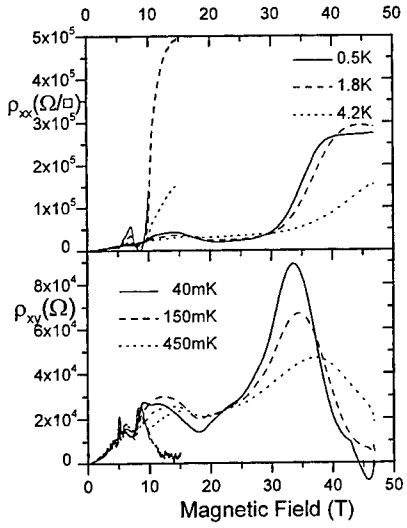

Figure 1 Plots of the resistivity and Hall resistance for an InAs/GaSb Double Heterostructure measured using steady fields at 40, 150 and 400mK and pulsed fields at 0.5K, 1.6K and 4.2K.

layer. Fitting the low field magnetoresistance and Hall effect to classical two carrier formulae indicate that the carrier densities of the electrons and holes are of order 6.5×10^{15} m^{-2} and 4.5×10^{15} m^{-2} respectively. Evidence suggests that the structure is asymmetric due to surface state pinning and all of the holes are on one side of the structure. Determination of the carrier mobilities is less straightforward due to the presence of the minigap formed due to electron-hole interaction, however the use of a large parallel magnetic field which is known to decouple the electrons and holes suggests that the mobilities for the two carriers are approximately 20 and 1 $m^2V^{-1}s^{-1}$ when minigap effects are removed [4]. Magnetotransport measurements were made using a dilution refrigerator and 15T superconducting magnet, and a He^3 cryostat and 50T pulsed field magnet system on wide Hall bars of width 0.5 mm.

Fig. 1 shows a typical series of plots of the magnetoresistance and Hall resistivity as a function of temperature from 1K to 40mK using both pulsed and steady fields. The traces show a number of striking features which are characteristic of two carrier systems [5,6]. Firstly there is a very large positive magnetoresistance with, relatively weak oscillatory features at low field. At higher fields there is a strong minimum at 8.5T and a large resistivity peak above 10T which diverges to several thousand times its zero field value. By contrast the Hall resistivity shows stronger oscillations at low fields, but has only one feature which can be attributed to the formation of a quantum Hall plateaux at 8.5T which only appears at the lowest temperatures. At higher fields a minimum occurs in the Hall resistance which is difficult to measure precisely due to the simultaneous divergence of ρ_{xx} which requires careful measurements with reversed field in order to eliminate any small components mixed in from ρ_{xx}. Extending the measurements to 50T at He^3 temperatures shows that this behaviour is repeated, with a further divergence of the resistivity and minimum in the Hall voltage around 45T. The origins of this behaviour become clearer when the resistivity components are converted to conductivity as shown in fig. 2, where σ_{xy} shows a low temperature zero at fields above 40T and in the region 10 - 15T, and has values which approach zero around 7T. Between these fields a quantum value is observed of e^2/h at the lowest temperatures in the steady field data, and a peak which is moving towards this value with falling temperature at around 20T in the pulsed field data.

The particular characteristic of broken gap systems is that the electron Landau levels start at a lower energy than the hole levels, and as a function of magnetic field the two sets of levels

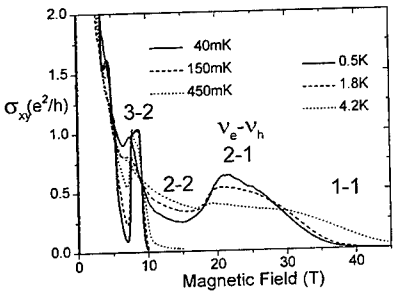

Figure 2: The Hall conductivity deduced from the magnetoresistivity components shown in fig. 1.

must cross each other. Due to the finite interband mixing which occurs between the valence and conduction bands the levels in fact show an anticrossing behaviour leading to the formation of a miniband gap, shown schematically in fig. 3i [4,6-10]. The movement of the levels through each other leads to oscillatory carrier densities due to the varying total density of states, but the position of the Fermi energy varies much less than in single carrier systems due to the possibility of charge transfer between the bands. For structures with a small but finite net doping level the Fermi energy can lie in the extended states close to the centre of either electron or hole Landau levels or within the minigap where most states are probably localised. For the majority of the field range the Fermi level lies closer to one of the hole levels due to the more rapid variation with energy of the electron levels compared with the hole levels. In the simplified schematic Fig. 3i the Fermi level is shown as constant. Under these circumstances the net occupancy of levels oscillates between zero at fields indicated as positions a (where ν_e - ν_h = 0 - 0) and c (where ν_e - ν_h = 1 - 1) and 1 for b (where ν_e - ν_h = 1 - 0) and d (where ν_e - ν_h = 2 - 1). The particularly unusual features of the conduction process occur when the Fermi level lies in between equal numbers of electron and hole Landau levels. In this case the system is able to show a complete energy gap which leads to the appearance of oscillatory insulating behaviour as a function of magnetic field.

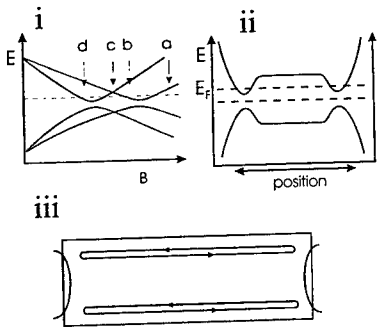

Figure 3: (i) A schematic picture of the Landau levels of a broken gap heterostructure (ii) A plot of the Landau levels as a function of position for a system with one electron and one hole level. Two values of the Fermi energy are shown which lie in the bulk and the edge state gap. (iii) a plot of the possible edge currents flowing in the region of the zero Hall resistance state.

In single carrier systems the quantum Hall condition also corresponds to a situation where the Fermi level lies within a mobility gap between Landau levels. As the levels approach the sample edges they move upwards in energy and form conducting edge states which generate zeroes in the resistivity and quantum Hall plateaux. This picture is quite different in interacting electron-hole systems. Considering a spatial plot of the energy levels as shown in fig. 3ii we expect that as we approach the edges of the structure the electron levels will move upwards due to the edge confinement, while in contrast the hole levels will move downwards. As a result the electron and hole levels will always approach each other but due to the interband coupling the levels will anticross, leading to the formation of an energy gap. When the position of the Fermi level in the bulk lies between an equal number of electron and hole levels then the structure will always show insulating behaviour. This conclusion is obvious

when the Fermi level in the bulk also corresponds to the anticrossing gap at the edges. It also holds when it crosses the interacting electron and hole edge states since the number of these states is equal leading to zero net current flow. At contacts to the structure, where separate electron and hole conduction paths would cross, we might expect that these states would connect due to the anticrossing. This would lead to the formation of isolated conducting loops which are no longer continuous through the sample, with one possible arrangement shown schematically in fig. 3iii. In both cases the system would develop insulating behaviour due to the lack of any conducting channel connecting the ends of the structure. Further evidence of a strong distortion of the current paths comes from the large mixing of the diagonal and Hall components which occurs specifically at the points where the system becomes insulating. By contrast when there is population within the bulk of an unequal number of Landau levels there is population of a finite net number of edge states and consequently the appearance of compensated quantum Hall plateaux in the Hall resistance and a zero in the resistivity. For a structure with a small net n-type doping and broadened energy levels the position of the Fermi level moves through regions where the level lies just above or below the central (extended state) region of both hole and electron levels as shown in fig. 3i. When a substantial part of the density of states of each level is localized the net total of occupied electron and hole Landau levels can be either 0 or 1. The system oscillates between insulating behaviour with a resistivity which increases rapidly with falling temperature as seen in fig. 1 in the field range 10-15T and above 40T, and a conducting region where the resistivity falls with falling temperature at around 25T and 8.5T.

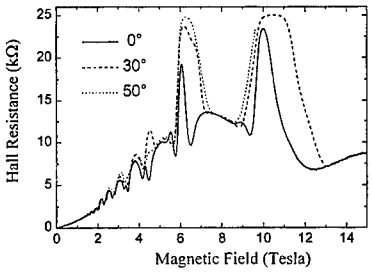

Figure 4: The effect of tilting on the Hall resistance measured at 100 mK, showing the enhanced quantum Hall plateaux as a function of the perpendicular component of magnetic field.

One further surprising feature of the behaviour is that the appearance of the quantum Hall pleateaux for unequal balance is found to be strongly enhanced when the sample is tilted relative to the magnetic field direction, as shown in fig. 4. This is probably due to a change in the magnitude of the electron-hole coupling, which is usually decreased by the presence of any parallel field component caused by the tilted field. The decreased mixing of the two bands may then increase the probability of localisation.

References

[1] K. von Klitzing, G. Dorda and M. Pepper, Phys. Rev. Lett. **45** (1980) 494
[2] E.E. Mendez, L. Esaki and L.L. Chang, Phys. Rev. Lett. **55** (1985) 2216
[3] M.S. Daly, et al, Phys. Rev. **B53** (1996) R10524
[4] M. Lakrimi et al, Phys. Rev. Lett. **79** (1997) 3034
[5] R.J. Nicholas et al, Physica B **201** (1994) 271
[6] K.S.H. Dalton et al, Surf. Sci. **156** (1994) 305
[7] M.Altarelli, Phys. Rev. B28 **842** (1983)
[8] Jin-Chen Chiang, Shiow-Fon Tsay, Z.M. Chau and Ikai Lo, Phys. Rev. Lett. **77** (1996) 2053
[9] M.J. Yang, C.H. Yang, B.R. Bennett and B.V. Shanabrook, Phys. Rev. Lett. **78** (1997) 4613
[10] L.J. Cooper et al., Phys. Rev. B **57** (1998) 11915

TC.5

A New Principle for Electronic Cooling of Mesoscopic Systems

Luis G. C. Rego and George Kirczenow*
Department of Physics, Simon Fraser University, Burnaby, BC, Canada V5A 1S6
*email: kirczeno@sfu.ca

Abstract

We introduce the concepts of a new form of cooling of semiconductor mesoscopic samples. The cooling process is the result of work performed quasi-statically on the quasi-2D subbands of a quantum well or multiple-quantum-well array by an external electric field applied perpendicularly to their planes. Under ideal conditions the final temperature is half of the original and the dynamics of the process is universal and reversible. The feasibility of the process is investigated by self-consistent calculations at temperatures below 1K.

In many mesoscopic devices the electrons behave like a low dimensional system which exhibits new properties susceptible to control by an external parameter. In this work we introduce the concepts and possible applications of a mechanism capable of cooling mesoscopic samples which are adiabatically isolated. The cooling effect is a consequence of the quasi-static expansion of a two dimensional electron gas (2DEG) and the process is controllable by an external electric field perpendicular to the plane of the quantum well (QW).

The cooling occurs when an empty subband moves below the Fermi level and charges are transferred from the lowest degenerate subbands into the empty one, while keeping the total areal density of the 2DEG constant. The process is illustrated schematically in Fig. 1, where diagrams (a) and (b) represent the initial and final states of the process, respectively. As a realistic implementation of this mechanism, consider the quantum well depicted in Fig. 1(c). It is doped in the barrier region to its left, and is designed so that the chemical potential lies below the second subband. By applying an electric field perpendicularly to the QW plane, the effective thickness of the well can be changed and, as a result, the subband edges move, producing the desired effect. This is represented by Figures 1 (c) and (d), where the field is used to increase the effective thickness of the well and thus bring the second subband below the chemical potential.

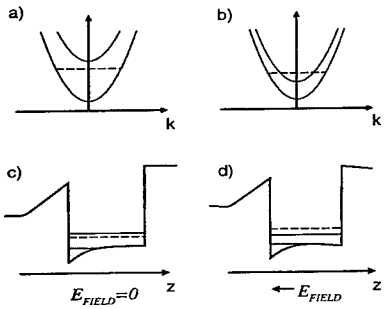

Figure 1: (a) and (b): schematic representation of the energy of 2D subbands as a function of the in-plane wave vector $\vec{k}$. The dashed line indicates the chemical potential. (c) and (d): conduction band profiles of a doped QW along the growth direction ($\hat{z}$). The horizontal solid lines indicate the two lowest subbands.

Zawadzki and Lassnig [1] predicted a related effect in which the specific heat and temperature of a 2DEG oscillate as a function of the strength of a magnetic field applied perpendicularly to its plane. This behavior was subsequently observed by Görnick et al. [2] in an adiabatically isolated multiple-QW heterostructure. However, major differences exist between that mechanism and the one we propose here: The high magnetic fields, necessary to produce the magneto-thermal oscillations, are replaced by moderate electric fields, which can be applied individually to each element of a multiple-QW array. In addition, the magnetically driven oscillations are very sensitive to the precise details of the Landau level density of states, whereas the present effect can be described analytically in terms of an universal expression, independent of material parameters.

We begin by showing that the process can be represented exactly by a simple model, which is treated analytically. Self-consistent calculations for realistic systems are presented towards the end of the paper.

Consider the two lowest subbands of a QW. The internal energy of (non-interacting) electrons in subband i is $U_i = \sum_{\vec{k}}(\varepsilon_{\vec{k}} + E_i) f_{\vec{k}}(T_i, \mu_i, E_i)$ and the number of particles $N_i = \sum_{\vec{k}} f_{\vec{k}}(T_i, \mu_i, E_i)$, with i =1 or 2 for the lowest (first) or second subband. Here $\vec{k}$ is the in-plane electron wave vector, $f_{\vec{k}}$ the Fermi-Dirac distribution, T_i the electronic temperature, μ_i the chemical potential and E_i the band edge energy which is controlled by the width of the well. $\varepsilon_{\vec{k}} = \hbar^2 k^2/2m^*$ where m^* is the effective mass. Summations over spin are understood. We also consider the energy of the phonon system $U_p(T_p, V)$, a function of the phonon temperature T_p and the volume of the sample. Putting these systems in thermal contact and allowing work to be exchanged adiabatically with the external electric field we obtain

$$\sum_{i=1}^{2} \frac{d}{dt} U_i(T, \mu, E_i) + \frac{d}{dt} U_p(T) = \dot{W}_1 + \dot{W}_2 \,, \qquad (1)$$

with the extra condition that the total number of particles is conserved during the process

$$\frac{d}{dt} N_1(T, \mu, E_1) + \frac{d}{dt} N_2(T, \mu, E_2) = 0 \,. \qquad (2)$$

Equations (1) and (2) are equivalent to $\delta S_1 + \delta S_2 + \delta S_p = 0$, where S is the entropy. To understand the process, we analyze, initially, a simplified model in which the phonons are not present; they will be included towards the end when we consider realistic systems. For analytic simplicity let us assume that the lowest subband contains a degenerate population and that the electric field does not perform any work in it. In this case E_1 is a constant which we set equal to zero. The results that we obtain using this simplification are found to be in perfect agreement with our self-consistent calculations (presented below) in which both E_1 and E_2 are free to vary. For this model we can write $\delta S_1 + \delta S_2 = 0$,

$$\sum_{i=1}^{2} \left(\frac{\partial S_i}{\partial T} dT + \frac{\partial S_i}{\partial \mu} d\mu \right) + \frac{\partial S_2}{\partial E_2} dE_2 \;=\; 0 \qquad (3)$$

The work δW_2 is done quasi-statically by rigidly changing the energy of subband 2. Therefore $\delta W_2 = N_2 dE_2$. Expansion of the 2DEG occurs when $dE_2 < 0$, and compression otherwise. Because the lowest subband is degenerate throughout the process, i.e., $(\mu - E_1)/k_B T \gg 1$,

we have $\partial S_1/\partial T = \frac{\pi^2}{3} C k_B^2$ and $\partial S_1/\partial \mu = 0$, where $C = m^* A/(\hbar^2 \pi)$ is the 2D density of states which is *constant* for a parabolic subband. A is the area of the QW. Substituting these results into Eq. (3) and using the relation $\partial S_2/\partial E_2 = -\partial S_2/\partial \mu$, we obtain

$$\left[C\frac{\pi^2}{3}k_B^2 + \frac{\partial S_2}{\partial T}\right] = \frac{\partial S_2}{\partial \mu} d(E_2 - \mu) \; . \tag{4}$$

A new independent variable $\alpha \equiv (E_2 - \mu)/(k_B T)$ can then be defined, in terms of which we rewrite Eq.(4) in the form

$$\frac{d}{d\alpha} \ln\left[\frac{T(\alpha)}{T_0}\right] = -\frac{d}{d\alpha} \ln\left[\frac{\pi^2}{3} - 2D(1+e^{-\alpha}) + \alpha \ln(1+e^{-\alpha})\right] \; , \tag{5}$$

where $D(x)$ is the dilogarithm function [3]. Explicit use of the definition of $S = -(\frac{\partial \Omega}{\partial T})_{A,\mu}$, with $\Omega = -k_B T \sum_{\vec{k}} \ln[1 + \exp((\mu - \varepsilon_{\vec{k}})\beta)]$, was made to obtain (5). From Eq. (5) it follows immediately that

$$T(\alpha) = \frac{\pi^2}{3} T_0 \left\{\frac{1}{\frac{\pi^2}{3} - 2D(1+e^{-\alpha}) + \alpha \ln(1+e^{-\alpha})}\right\} = \left(\frac{S_1}{S_1 + S_2}\right) T_0 \; , \tag{6}$$

where T_0 is the initial temperature of the system when $E_2 - \mu \gg k_B T$.

We emphasize the generality of the result (6), which is completely free from material and geometric parameters, such as the effective mass and quantum well thickness, and independent of thermodynamic parameters like the electron density and internal energy. Under the above conditions, i.e., without thermal contact with the phonons, the final temperature of all the electrons is $T_f = T_0/2$, which is reached when the second subband becomes degenerate. This is illustrated by the dashed line in Fig.2, where we show $T(\alpha)/T_0$ as a function of $\alpha = (E_2 - \mu)/(k_B T)$. Notice that T_0 is arbitrary as long as the conditions assumed for the derivation of (6) are satisfied.

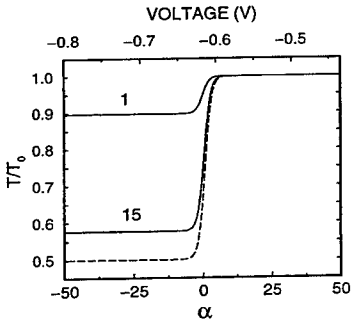

Figure 2: The relative temperature T/T_0 as a function of $\alpha \equiv (E_2 - \mu)/(k_B T)$. The dashed line represents the cooling process without phonons, in which case T_0 is arbitrary. The solid line describes the process with the phonons taken into account. For this case $T_0 = 100mK$ and $L = 1\mu m$. The numbers 1 and 15 indicate the number of quantum wells. Results of self-consistent calculations for 1QW show perfect agreement with model results and are shown as a function of the voltage applied across the sample.

Our self-consistent calculations, within the Hartree approximation, show that the cooling process can be controlled by an external electric field applied along the growth direction ($\hat{z}$) as depicted in Fig.1(d). The results coincide with the dashed line curve of Fig. 2. In this simulation we considered a single $Al_{0.3}Ga_{0.7}As/GaAs$ quantum well of thickness 300Å,

density of carriers $N_e = 4.2 \times 10^{11} cm^{-2}$ and donor concentration in the barrier $N_d = 1.5 \times 10^{17} cm^{-3}$. The energies of the lowest subbands and the chemical potential are $E_1 = 156.4$ meV, $E_2 = 172.9$ meV and $\mu = 170.7$ meV, in the absence of the external electric field.

We now consider the effects caused by the presence of the acoustic phonons. Their influence will manifest in terms of the lattice specific heat [4]

$$C_V = \left(\frac{\partial U_p}{\partial T}\right)_V \simeq \frac{2\pi^2}{5} \frac{V}{\hbar^3 v^3} k_B^4 T^3 \,, \tag{7}$$

which is implicit in Eq.(1). In the above expression $3/v^3 =< 1/v_l^3 + 2/v_t^3 >$, where v_l and v_t are the longitudinal and transverse phonon velocities and $< ... >$ denotes angular averaging. Note that C_V is proportional to the volume of the sample $V = LA$, whereas the electronic extensive quantities are proportional to the area. At temperatures $T \gg 1$ K the energy and specific heat of the phonons dominate the system and the acoustic phonons behave as a true thermal bath, keeping the temperature of the electrons fixed despite of the work done. However, for $T < 1$ K the phonon specific heat ($\propto T^3$) decreases much faster than the electronic specific heat ($\propto T$) eventually reaching the point, at low enough temperatures, when the temperature of the phonons just follows the electron temperature. Between these two limiting cases cooling occurs at an intermediate efficiency. The condition for efficient cooling is determined primarily by the initial temperature T_0, but other parameters also influence the process, such as the thickness of the sample, phonon velocities and the carrier effective mass (efficiency increases with m^*). The solid curve 1 in Fig.2 illustrates the effect of the phonons for a sample of thickness $L = 1\mu m$, initial temperature $T_0 = 100mK$ and carrier effective mass $m^* = 0.07m_0$. The efficiency of the cooling process decreases due to the presence of phonons, nonetheless the 2DEG is responsible for cooling the entire sample which is orders of magnitude thicker than the quantum well. In fact, as we showed above the thickness of the quantum well itself is not relevant to this mechanism.

To conclude, we stress that the cooling mechanism we have proposed is very general and could be used as a basis for other device configurations capable of extending the efficiency of the process to higher temperatures and larger samples. As an example, the efficiency of the process is improved substantially in samples with an array of independent quantum wells where the transfer of charge from one well to another is prevented by sufficiently thick barriers. The cooling approaches the ideal case as the number of quantum wells increases for fixed sample thickness. For this purpose we considered the cooling due to an array of 15 quantum wells, grown in a layer of thickness $L = 1\mu m$. The final temperature is much closer to the ideal in this case; this result is shown as curve 15 in Fig. 2.

The authors would like to thank M. Hayden for calling our attention to this problem and for very stimulating discussions. This work was supported by NSERC.

REFERENCES

[1] W. Zawadzki and R. Lassnig, Sol. Stat. Commun. **50**, 537 (1984).

[2] E. Gornik, R. Lassnig, G. Streasser, H.L. Störmer, A.C. Gossard, and W. Wiegmann, Phys. Rev. Lett. **54**, 1820 (1985).

[3] The dilogarithm function is defined by the identity $D(x) = -\int_1^x ln(t)/(t-1)dt$.

[4] Statistical Physics, L.D. Landau and E.M. Lifshitz, vol. 5 (Pergamon,Oxford,1975).

TD.1

Multi-terminal ballistic transport in one-dimensional wires

R. de Picciotto[a], H. L. Stormer[a,b], A. Yacoby[a,c], K. W. Baldwin[a], L. N. Pfeiffer[a] and K. W. West[a]

a) Bell-Labs, Lucent Technologies, Murray Hill, NJ, 07974, US

b) Dept. Phys. and Dept. Appl. Phys. Columbia University, New York, NY 10003

c) Braun Center for Submicron Research, Dept of Cond. Matter Physics, Weizmann Institute of Science, Rehovot 76100, Israel

Abstract

In contrast to theoretical predictions of the Luttinger model, recent experiments [1-3] have shown *non-universal* conductance quantization in one-dimensional wires that are fabricated using the cleaved edge overgrowth technique [4]. In one of the papers [1], it was speculated that the origin of the reduced conductance lies in the interface between the one-dimensional wire and the two dimensional electron gas regions, which serve as ohmic contacts and thermal reservoirs.

Here we report the results of a systematic study of such 2D-1D interfaces. By embedding a 2D-1D interaction region of controllable length inside an otherwise isolated wire, we were able to study the properties of the coupling between these two subsystems. Our results show that 2D-1D interface is in fact the origin of the non-universal conductance.

One-dimensional electronic systems, so-called Luttinger-liquids, are expected to show unique transport properties as a consequence of the Coulomb interaction between carriers [5-11]. In contrast to Fermi liquid theory [12-16], the Luttinger model predicts that even the weakest impurity embedded in an otherwise perfectly clean 1D wire will completely suppress its conductance at zero temperature. Furthermore, the tunneling conductance into such a perfect wire will also be completely suppressed at zero temperature.

One of the fingerprints of a clean non-interacting 1D conductor is its quantized conductance in multiples of the universal value $g_0=2e^2/h$. This quantization results from an exact cancellation of the increasing electron velocity and the decreasing density of states as the carrier density increases [17-19]. Therefore, as subsequent 1D electronic sub bands are filled with electrons the conductance increases in a series of plateaus (or steps) with values equal to g_0 multiplied by the number of occupied wire modes. Surprisingly, the inclusion of interactions does *not* alter this prediction. Early papers [8-11], considering infinitely long wires, did in fact predict quantization of conductance with a renormalized, non-universal, value of $g=\nu \cdot g_0$, where $\nu=(1+U/E_F)^{-1/2}$. Here, U is the strength of the Coulomb interaction between neighboring electrons and E_F is the Fermi energy. Later works [20-22], however, considered a more realistic wire of finite length that is connected to large, Fermi-liquid like, reservoirs at both ends. In the clean limit, the contact resistance to the reservoirs dominates the conductance and the universal value, g_0, is restored. Oreg and Finkelstein [23] have further demonstrated that if one calculates the conductance due to the self consistent electric field in the wire rather than the external electric field, the universal value is restored even for the infinite wire case. In contrast to these theoretical predictions, recent papers [1-3], using wires that were fabricated by the cleaved edge overgrowth method showed that the contribution of each one-dimensional channel to the overall conductance is not universal and smaller than the conductance quantum. In these two-terminal measurements, the combined contribution of the one-dimensional channel

and the unavoidable interfaces between this channel and the 2D reservoirs at its two ends was determined. Here we present results of measurements designed to address the origin of this puzzling observation. We embedded a 2D-1D Interaction Region (IR) of controllable length within an otherwise isolated 1D wire in order to study the properties of the coupling between these two subsystems.

The geometry of the devices under study is illustrated in figure 1. A substrate, containing a two-dimensional electron gas (2DEG) in a single side doped GaAs quantum well is epitaxially grown on a [100] GaAs surface. The 2DEG has a carrier density $n_s \sim 2.5\times10^{11}$ cm^{-2}, and mobility $\sim 4\times10^{6}$ cm^2/Vs. The substrate is then cleaved in situ and a 2nd modulation doping sequence is overgrown on the [011] cleaved edge. This procedure results in high quality one-dimensional (1D) electronic channels propagating along the cleaved edge. These channels, existing throughout the cleaved edge of the 2D plane, are coupled to the adjacent 2DEG (see Fig. 1b).

The length of a Cleaved Edge Overgrowth wire (CEO-W) that is *measured* is defined by a gate which is pre-patterned on the top surface of the structure prior to the cleave and overgrowth steps (see Fig. 1a). A negative voltage applied to this gate depletes the 2DEG from underneath it, leaving only the wire to connect the two 2DEG sections. Thus, the width of the gate defines a length, L, over which the 1D wire is isolated from the adjacent 2DEG. By increasing the voltage beyond depletion of the 2DEG one can control the number of occupied 1D modes in this region.

To study the interaction of current carriers in a wire with the adjacent 2DEG we split the gate in two (gates A and B in Fig. 1a.), creating a 2D-1D overlap region of controllable length, W, between the wire and a 2DEG. With this device, there are 3 distinct regions along the wire: In the two long sections $|x|>W/2+L$ the wire is coupled to the adjacent 2DEGs. These regions are the source and drain. The two regions $W/2<|x|<W/2+L$ are isolated wires. The number of channels in each wire is controlled independently by gates A and B. The region $|x|<W/2$ is the interaction region (IR). Here 1D modes are coupled to the 2DEG between the two gates. Current is injected from the source into an isolated wire of length L, electrons are then allowed to interact with an adjacent, floating, 2DEG in the IR for a length W before proceeding into another wire and finally into the drain. Since the gates have an electrostatic influence on the wire, the potential along the wire is lower in the IR - where the gate is absent. The electrons thus also interact with the smooth resultant static 1D potential dip of length W. While this trough is estimated to be deep enough to change the number of 1D channels in the IR, it has a smooth shape (due to a large distance of ~0.5μm between the gates and the wire). The overall influence of this electrostatic potential on back scattering in our device is thus minor.

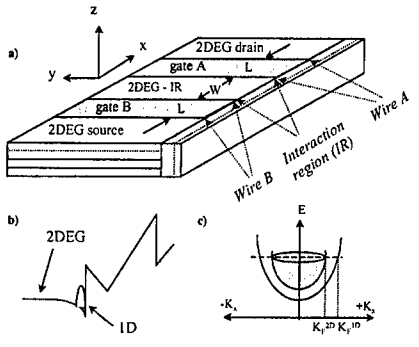

Figure 1: a). The geometry of the device under study (see text) **b).** Conduction band profile in the Y direction at the quantum well level and in a non-gated region. The 2DEG and the first 1D mode are also shown. **c).** Dispersion relation for electrons in the 2DEG and 1D wire. The Fermi wavevector of the two systems is indicated.

The behavior of such a device is shown in figure 2. The conductance of each individual L~2μm long wire, g_1, when the other gate is not activated, exhibits clear

conductance plateaus as a function of gate voltage with a plateau height of $g_1 \sim 0.8g_0$, as shown by the solid line in this figure. With both gates activated, we measure the overall conductance, g_2, of the two single mode isolated wires plus the IR. For a relatively long IR, W~10μm, g_2 equals half the conductance of each individual wire; $g_2 \sim 0.4g_0 \sim \frac{1}{2}g_1$ (not shown). This indicates complete thermalization in the IR, leading to ohmic combination of the two resistors in series, resulting in half the conductance for the combined system.

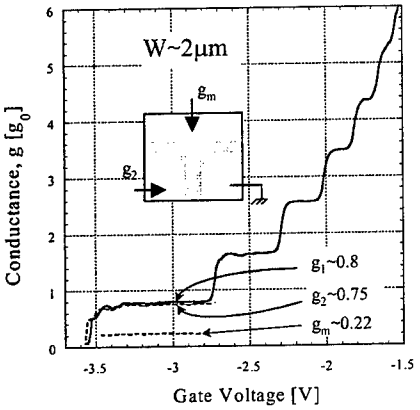

Figure 2: Conductance, in units of the conductance quantum $2e^2/h$, of an isolated 2μm long wire, g_1 (solid line) and the conductance of two isolated single mode wires combined in series with a W~2μm long interaction region, g_2, (dashed line) plotted against the applied gate voltage. The conductance from the interaction reagion into both single mode wires, g_m, is also shown (dashed line). **Inset:** Graphical illustration of the measurement scheme.

The same measurement with a shorter IR, W~2μm, renders a very different result, as shown in figure 2. Under the same conditions, namely when both isolated wires support a single mode, the overall conductance nearly *equals* the conductance of each isolated wire in spite of the presence of the IR ($g_2 \sim 0.75g_0 \sim 0.94g_1$ at a temperature, θ=300 mK). This clearly demonstrates ballistic 1D transport through a 2μm long IR where the wire overlaps with a 2DEG. For an intermediate IR length of W~6μm we find $g_2 \sim 0.6g_0 \sim 0.75g_1$ (not shown) - indicating partial back scattering.

The conductance from the 2DEG of the IR into the single mode wires on both sides, g_m, equals $2g_1$ for W~10μm (not shown). This result is again the ohmic combination of the two wires – now in parallel – resulting in twice the conductance. For W~2μm, the value of the measured conductance, g_m, (again when both wires support only one mode) is much smaller; $g_m \sim 0.22g_1$ (see Fig. 1).

We model the behavior of our device within a Buttiker-Landauer scattering approach. The coupling of the 2DEG to the wire at the drain and source regions, $|x|>L+W/2$, is modeled by assuming a maximal emissivity $\alpha=g_1/g_0 \sim 0.8$. The shorter length of the IR is modeled by a smaller emissivity - $T_1\alpha$. Here $T_1(W)$ is the transmission probability from the 2DEG into each branch of the 1D dispersion of the first channel ($\pm K_F^{1D}$). Assuming symmetric coupling of the 2DEG to both sides, the scattering matrix of the junction may be written in terms of α and T_1. One finds for the measured quantities; $g_2=\alpha(1-\frac{1}{2}T_1)g_0$ and $g_m=2T_1\alpha g_0$. The two *measured* values are both in excellent agreement with this model using $T_1 \sim 0.13$ for W~2μm. The value of α is deduced from g_1, which is measured independently.

The reduction of g_2 compared to g_1 is a consequence of 1D backscattering that is mediated by the 2DEG in the IR. An electron in the wire that was scattered into the 2DEG has an equal probability to scatter back into either direction in the 1D ($\pm K_F^{1D}$) therefore loses on average half its momentum (assuming fast relaxation in the 2DEG). At first glance it would seem that 1D backscattering might be modified by the presence of the 2DEG even *without* charge transfer between the two subsystems. However, e-e scattering that

involves momentum exchange without charge transfer can *not* occur because the 2D Fermi momentum, k_F^{2D}, is smaller than the one in the 1D wire (see Fig. 1.b and c). This excludes this scattering mechanism to first order. The smallness of k_F^{2D} also leads to poor screening of the disorder potential at wave vectors relevant to 1D back scattering. Therefore, the additional back scattering induced by the IR is mostly due to charge transfer between the two subsystems. Our results thus indicates a mean free path for scattering between the 2DEG and the 1D $l_{2D\leftrightarrow 1D}$~6μm (for W~6μm T_1~½).

Since this new length scale is smaller than, but comparable to, the backscattering length inside a CEO-W, an analysis of the 2D-1D interface is called for - as was suggested in previous work [1]. Using a Boltzman equation approach, the authors derived an expression for the conductance of an ideal, single channel, wire which is coupled to 2DEGs at its ends; $g_1=g_0(1+2l_{2D\leftrightarrow 1D}/l_B)^{-1/2}$, where l_B is the 1D back scattering length at the two ends, namely in the 2D-1D *overlaps* regions [1]. In view of the above discussion, we assume that l_B is not very different from the back scattering length inside an *isolated* CEO-W, which was previously found to be ~20μm [1]. One finds an expected conductance of g_1~$0.79g_0$ - in excellent agreement with the observed value.

In conclusion, we have shown results of a systematic study of CEO-W 2D-1D interface. By embedding a 2D-1D overlap section of controllable length inside an isolated wire, we were able to study the properties of the coupling between the two. We find a scattering mean free path of ~6μm. Our results show that the origin of the non universal conductance [1] lies in the 2D-1D interface.

References:

1. A. Yacoby *et al*, Phys. Rev. Lett. **77**, 4612 (1996).
2. A. Yacoby *et al*, Solid State Comm., **101**, 77 (1997).
3. M. Rother *et al*, ICPS-24, Th-P137.
4. L. N. Pfeiffer *et al*, Microelectronics J., **28**, 817 (1997).
5. e.g. Highly Conducting One Dimensional Solids, J. T. Devreese edt, (Plenum Press, New York 1979).
6. D. C. Mattis, in 'The Many Body Problem', World Scientific Publishing Co., 1992.
7. F. D. M. Haldane, J. Phys. **C 14**, 2585 (1981).
8. W. Apel and T. M. Rice, Phys. Rev. **B 26**, 7063 (1992).
9. C. L. Kane and M. P. A. Fisher, Phys. Rev. Lett. **68**, 1220 (1992)
10. D. Yue *et al*, Phys. Rev. **B 49**, 1966 (1994).
11. M. Ogata and H. Fukuyama, Phys. Rev. Lett. **73**, 468 (1994).
12. A. V. Chaplik, Zh. Exsp. Teor. Fiz. **60**, 1845 (1971).
13. H. F. Fukuyama and E. Abrahams, Phys. Rev. **B 27**, 5976 (1983).
14. G. F. Guliani and J. J. Quinn, Phys. Rev. **B 26**, 4421 (1982).
15. T. Jungwirth and A. M. Macdonald, Phys. Rev. **B 53**, 7403 (1996).
16. B. L. Altshuler, A. G. Aronov in: Electron-Electron Interactions in Disordered Systems, Edited by A. L. Efros and M. Pollak.
17. R. Landauer, IBM J. Res. Dev. **32**, 306 (1988). M. Buttiker, Phys. Rev. Lett. **57**, 1761 (1996).
18. C. W. J. Beenakker and H. von Houten, in Solid State Physics, Semiconductor Heterostructures and Nanostructures, H. Ehrenreich and D. Turnbull edts, (Academic Press, New York 1991).
19. Y. Imry, in 'Introduction to Mesoscopic Physics', Oxford university Press, 1997.
20. I. Safi and H. J. Schulz, Phys. Rev. **B 52**, R17040 (1995).
21. V. V. Ponomarenko, Phys. Rev. **B 52**, R8666 (1995).
22. D. L. Maslov, Phys. Rev. **B 52**, R14368 (1995).
23. Y. Oreg and A. M. Finkel'stein, Phys. Rev. **B 54**, 14255 (1996).

TD.2

From the Kondo Regime to the Mixed-Valence Regime in a Single-Electron Transistor

D. Goldhaber-Gordon*, J. Göres, and M.A. Kastner
Department of Physics, Massachusetts Institute of Technology
Cambridge, MA 02139

Hadas Shtrikman, D. Mahalu, and U. Meirav
Braun Center for Submicron Research
Weizmann Institute of Science
Rehovot, Israel 76100
(June 18, 1999)

We demonstrate that the conductance through a single-electron transistor at low temperature is in quantitative agreement with predictions of the equilibrium Anderson model. When an unpaired electron is localized within the transistor, the Kondo effect is observed. Tuning the unpaired electron's energy toward the Fermi level in nearby leads produces a cross-over between the Kondo and mixed-valence regimes of the Anderson model.

PACS 75.20.Hr, 73.23.Hk, 72.15.Qm, 73.23.-b; Kondo effect, Anderson model, Quantum Dot, Single-Electron Transistor

The following paper appeared with only slight differences in *Phys. Rev. Lett.* **81**, 5225 (1998). I include it here as a concise description of recent advances in the study of the Kondo effect in a Single-Electron Transistor (SET). In my talk at EP2DS, I will introduce the concept of the Kondo effect (and its manifestation in an SET) in a more gradual and extended manner. After the introduction, my central focus will be the striking match between experiments and a range of theoretical predictions, but I also hope to delve into some of the puzzles and complexities which have emerged recently. In particular, the quantized level structure of the localized electrons in an SET changes the Kondo effect in ways that are still incompletely understood [19].

The effect of magnetic impurities on metals — the Kondo effect — has been studied for half a century, and enjoys continued relevance today in attempts to understand heavy-fermion materials and high-T_c superconductors. Yet it has not been possible to experimentally test the richly varied behavior predicted theoretically. The theory depends on several parameters whose values are not independently tunable for impurities in a metal, and are often not even *a priori* known. On the other hand, it has been predicted [1–5] that a single-electron transistor (SET) should be described by the Anderson impurity model, and hence should also exhibit the Kondo effect. An SET contains a very small droplet of localized electrons, analogous to an impurity, strongly coupled to conducting leads, analogous to the host metal. We have recently shown that when the number of electrons in the droplet is odd, and hence one electron is unpaired, the SET exhibits the Kondo effect [6] in electronic transport. This observation has since been confirmed [7,8] with additional quantitative detail. As we show in this Letter, in SET experiments one can tune the important parameters and test predictions of the Anderson model that cannot be tested in bulk metals.

In our SET, a droplet of about 50 electrons is separated from two conducting leads by tunnel barriers. A set of electrodes (Fig. 1(a)), on the surface of a GaAs/AlGaAs heterostructure which contains a two-dimensional electron gas (2DEG), is used to confine the electrons and create the tunnel barriers. The 2DEG is depleted beneath the electrodes, and the narrow constrictions between electrodes form the tunnel barriers. Details of the device fabrication and structure are given elsewhere [6].

In the Anderson model, the SET is approximated as a single localized state, coupled by tunneling to two electron reservoirs. The state can be occupied by $n_d = 0, 1$, or 2 electrons with opposite spin; couplings to all other filled and empty states of the droplet are neglected. Adding the first electron takes an energy ϵ_0 referenced to the Fermi level in the leads, but the second electron requires $\epsilon_0 + U$, where the extra charging energy U (1.9 ± 0.05 meV in our SET) results from Coulomb repulsion. In the diagram of Fig. 1(b), $\epsilon_0 < 0$, but $\epsilon_0 + U > 0$, so there is one electron in the orbital. However, this electron can tunnel into the leads, with rate Γ/h, leading to Lorentzian broadening of the localized-state energies with full width at half maximum (FWHM) Γ. The energy ϵ_0 can be raised by increasing the negative voltage V_g on a nearby electrode (the middle left "plunger gate" electrode in Fig. 1(a)) and Γ can be tuned

*davidg@mit.edu. Tel: (617) 354-3935, Fax: (617) 258-6883. Room 13-2134, 77 Massachusetts Ave., Cambridge MA 02139. Also at Weizmann Institute.

by adjusting the voltages on the gates that form the constrictions. Two other important energies (not shown) are the spacing between quantized single-particle levels $\Delta\epsilon \approx 400\,\mu$eV, and the thermal broadening of the Fermi level in the leads $kT = 8 - 350\,\mu$eV. The Kondo temperature T_K is a new, many-body energy scale that emerges for a singly-occupied Anderson impurity [9]. It is essentially the binding energy of the spin singlet formed between the localized, unpaired electron and electrons in the surrounding reservoirs; $kT_K \approx 4 - 250\,\mu$eV in our SET, depending on the other tunable parameters.

The conductance G of an SET is analogous to the resistivity ρ of a bulk Kondo system. Although one thinks of the increase in resistivity at low T as the hallmark of the Kondo effect, transport properties have proven more difficult to calculate than thermodynamic properties. For $T \ll T_K$, ρ is theoretically and experimentally known to equal $\rho_0 - cT^2$ (Fermi liquid behavior) [10] and for $T_K < T < 10\,T_K$, ρ is roughly logarithmic in T [11,12], but the crossover region has only recently been successfully treated [13].

Furthermore, the Anderson model has several interesting regimes parametrized by $\tilde{\epsilon}_0 \equiv \epsilon_0/\Gamma$: the Kondo regime $\tilde{\epsilon}_0 \ll -0.5$, the mixed-valence regime $-0.5 \lesssim \tilde{\epsilon}_0 \lesssim 0$, and the empty orbital regime $\tilde{\epsilon}_0 \gtrsim 0$, each of which has different transport properties. The Kondo regime describes many systems of dilute magnetic impurities in metals, while the mixed-valence regime provides some understanding of heavy-fermion compounds [14–16]. We know of no material described by the empty orbital regime. Though conductance through an SET normalized to its zero-temperature value $\tilde{G}(\tilde{T}) \equiv G(T/T_K)/G_0$ is expected to be universal in the Kondo regime, where the only small energy scale is T_K, it should change as $\tilde{\epsilon}_0 \to 0$ (the mixed-valence regime), where T_K and Γ become comparable [13]. The great advantage of the SET is that ϵ_0 can be tuned by varying V_g to test the predictions for all regimes in one and the same system.

As V_g is varied, the conductance of an SET undergoes oscillations caused by what is usually called the Coulomb blockade. Current flow is possible in this picture only when two charge states of the droplet are degenerate, i.e. $\epsilon_0 = 0$ or $\epsilon_0 + U = 0$, marked by vertical dashed lines in Fig. 2 as determined by the analysis of Fig. 5. The conductance between these dashed lines is expected to be very small. However, in this range the charge state of the site is odd, as portrayed in Fig. 1, and the Kondo effect allows additional current flow. Strikingly, at low temperature (dots, 100 mK and triangles, 800 mK), the conductance maxima do not even occur at $\epsilon_0 = 0$ and $\epsilon_0 + U = 0$ — the Kondo effect makes the off-resonant conductance even larger than the conductance at the charge-degeneracy point [4]. Raising the temperature suppresses the Kondo effect, causing the peaks to approach the positions of the bare resonances.

The inset of Fig. 2 shows how Γ is determined: For $T \geq \Gamma/2$, the conductance peak is well-described by the convolution of a Lorentzian of FWHM Γ with the derivative of a Fermi-Dirac function (FWHM $3.52kT$). This convolution has a FWHM $0.78\Gamma + 3.52kT$, so extrapolating the experimentally-measured linear dependence back to $T = 0$ gives $\Gamma = 295 \pm 20\,\mu$eV.

When the energy of the localized state is far below the Fermi level ($\tilde{\epsilon}_0 \ll -1$), scaling theory predicts that T_K depends exponentially on the depth of that level [17]:

$$T_K = \frac{\sqrt{\Gamma U}}{2} e^{\pi\epsilon_0(\epsilon_0+U)/\Gamma U}. \qquad (1)$$

Note that, because U is finite, $\log T_K$ is quadratic in ϵ_0. This strong dependence on ϵ_0 causes the Kondo-enhanced conductance to persist to higher temperatures near $\epsilon_0 = 0$ (and near $\epsilon_0 = -U$, by particle-hole symmetry) than in-between. In fact, at $T = 0$ the conductance should sustain its maximum value all the way between the two observed peaks in Fig. 2 [1,2,6] (see Fig. 5(b) for expected $G(\tilde{\epsilon}_0)$ at $T = 0$), but in the valley even our $T_{base} \simeq 100$ mK $> T_K \approx 40$ mK.

Figure 3(a) shows that, for fixed $\tilde{\epsilon}_0$ in the Kondo regime, $G \sim -\log(T)$ over as much as an order of magnitude in temperature, beginning at T_{base}. Thermal fluctuations in localized state occupancy cut off the $\log(T)$ conductance for $kT \gtrsim |\epsilon_0|/4$, consistent with simulations of thermally-broadened Lorentzian resonances. As $\tilde{\epsilon}_0 \to 0$ (Fig. 3(b)), T_K increases, as evinced by the saturation of the conductance at low temperature.

To fit the experimental data for each ϵ_0 we use the empirical form

$$G(T) = G_0\Big(\frac{T_K'^2}{T^2 + T_K'^2}\Big)^s, \qquad (2)$$

where T_K' is taken to equal $T_K/\sqrt{2^{1/s} - 1}$ so that $G(T_K) = G_0/2$. For the appropriate choice of s, which determines the steepness of the conductance drop with increasing temperature, this form provides a good fit to numerical renormalization group results [13] for the Kondo, mixed-valence, and empty orbital regimes, giving the correct Kondo temperature in each case. The parameter s is left unconstrained in the fit to our data, but its fit value is nearly constant at 0.20 ± 0.01 in the Kondo regime, while as expected it varies rapidly as we approach the mixed-valence regime (Figure 3(b)). The expected value of s in the Kondo regime depends on the spin of the impurity: $s = 0.22 \pm 0.01$ for $\sigma = 1/2$.

Using the values of G_0 and T_K extracted in this way we confirm that $\tilde{G}$ is universal in the Kondo regime. Figure 4 shows $\tilde{G}(\tilde{T})$ for data like those of Figure 3 for various values of $\tilde{\epsilon}_0 \sim -1$ (on the left peaks of Fig. 2). We have also included data from the same SET, but with Γ reduced by 25% by adjusting the point-contact voltages. The data agree well with numerical renormalization group calculations by Costi and Hewson (solid line) [13]. In the

mixed-valence regime it is difficult to make a quantitative comparison between theoretical predictions and our experiment. Qualitatively, in both calculation and experiment, $\tilde{G}(\tilde{T})$ exhibits a sharper crossover between constant conductance at low temperature and logarithmic dependence at higher temperature in the mixed-valence regime than in the Kondo regime (see Fig. 4) [13].

In Figure 5(a), we plot $T_K(\tilde{\epsilon}_0)$ extracted from our fits, along with the theoretical prediction (Eq. 1) for the Kondo regime. The value of $\Gamma = 280 \pm 10\,\mu$eV extracted is in good agreement with the value $\Gamma = 295 \pm 20\,\mu$eV determined as illustrated in Fig. 2 (inset). The prefactor is approximately three times larger than $\sqrt{\Gamma U}/2$, which must be considered good agreement given the simplifying assumptions in the calculations and the sensitivity to the value of the exponent [19].

G_0 is predicted to vary with the site occupancy n_d, and hence also with $\tilde{\epsilon}_0$, according to the Friedel sum rule

$$G_0(n_d) = G_{max} \sin^2\left(\frac{\pi}{2} n_d\right), \qquad (3)$$

where G_{max} is the unitary limit of transmission: $2e^2/h$ if the two barriers are symmetric, less if they are asymmetric. For small $|\tilde{\epsilon}_0|$, $T_K \gg T_{base}$, so we can directly measure the value of G_0. Even when T_K is not $\gg T_{base}$, we can still extract the value of G_0 from our fit. In Figure 5(b), we compare the combined results of both these methods with $G_0(\tilde{\epsilon}_0)$ inferred from a non-crossing approximation (NCA) calculation [4] of $n_d(\tilde{\epsilon}_0)$ according to Equation 3. The agreement is excellent except outside the left peak, where experimentally the conductance does not go to zero even at zero temperature (see Fig. 2) [21].

We have demonstrated quantitative agreement between transport measurements on an SET and calculations for a spin-1/2 Anderson impurity. The SET allows us to both accurately measure and vary Γ and ϵ_0, and to observe their effect on T_K and G_0. We have also observed the cross-over between the Kondo and mixed-valence regimes.

We acknowledge fruitful discussions with David Abusch-Magder, Igor Aleiner, Ray Ashoori, Gene Bickers, Daniel Cox, Leonid Glazman, Selman Hershfield, Wataru Izumida, Steven Kivelson, Leo Kouwenhoven, Patrick Lee, Leonid Levitov, Avraham Schiller, Chandra Varma, and especially Ned Wingreen, Yigal Meir, and Theo Costi. Theo Costi, Wataru Izumida, and Ned Wingreen generously provided data from their prior calculations. D. G.-G. thanks the Hertz Foundation, and J. G. thanks NEC, for graduate fellowship support. This work was supported by the US Army Research Office Joint Services Electronics Program under contract DAAG 55-98-1-0080, by the US Army Research Office under contract DAAG 55-98-1-0138, and by the MRSEC Program of the National Science Foundation under Award No. DMR94-00334.

[1] T. K. Ng and P. A. Lee, Physical Review Letters **61**, 1768 (1988).
[2] L. I. Glazman and M. E. Raikh, JETP Letters **47**, 452 (1988).
[3] Y. Meir, N. S. Wingreen, and P. A. Lee, Physical Review Letters **70**, 2601 (1993).
[4] N. S. Wingreen and Y. Meir, Physical Review B **49**, 11040 (1994).
[5] W. Izumida, O. Sakai, and Y. Shimizu, J. Phys. Soc. Jap. **67** 2444 (1998).
[6] D. Goldhaber-Gordon *et al.*, Nature **391**, 156 (1998).
[7] S. M. Cronenwett, T. H. Oosterkamp, and L. P. Kouwenhoven, Science **281** 540 (1998).
[8] We have now observed the Kondo effect in six SETs. All the data presented in this Letter are from a single SET nominally identical to, but distinct from, that discussed in [6].
[9] A. C. Hewson, *The Kondo problem to heavy fermions*, *Cambridge Studies in Magnetism* (Cambridge University Press, Cambridge, 1993).
[10] P. Nozières, Journal of Low Temperature Physics **17**, 31 (1974).
[11] J. Kondo, in *Solid State Physics*, edited by H. Ehrenreich and D. Turnbull (Academic Press, New York, 1964), Vol. 23, p. 183.
[12] D. R. Hamann, Physical Review **158**, 570 (1967).
[13] T. A. Costi and A. C. Hewson, Journal of Physics: Cond. Mat. **6**, 2519 (1994).
[14] In the latter case, a single-impurity picture is incomplete: inter-impurity interactions must also play a major role.
[15] C. M. Varma, Rev. Mod. Phys. **48**, 219 (1976).
[16] N. E. Bickers, Physical Review Letters **54**, 230 (1985).
[17] F. D. M. Haldane, Physical Review Letters **40**, 416 (1978).
[18] E. B. Foxman *et al.*, Physical Review B **50**, 14193 (1994).
[19] Inoshita *et al.* [20] have proposed that Kondo temperatures in quantum dots should be enhanced by orders of magnitude if the quantized level spacing is small enough for several levels to participate in equilibrium transport. We do not see such a large enhancement, however we do observe satellites of the Kondo peak in differential conductance at bias $V_{ds} \approx \pm\Delta\epsilon/2$, as predicted for multilevel transport [20]. These results will be discussed in detail elsewhere.
[20] T. Inoshita, Y. Kuramoto, and H. Sakaki, Superlattices and Microstructures **22**, 75 (1997).
[21] There is no zero-bias peak in differential conductance in this region, demonstrating that the extra conductance is *not* caused by the Kondo effect here.
[22] When $-\tilde{\epsilon}_0 \gtrsim 2$ or $-\tilde{\epsilon}_0 \lesssim 5.5$, the measured T_K and G_0 sharply decrease below their predicted values. This could be caused by an unintentional ac bias V_{ac} applied across the SET. Such a bias has often been known to raise the effective temperature of small electron systems. Here, it could have an even more drastic effect on the Kondo resonance, and hence on the conductance, at these values of $\tilde{\epsilon}$, for which $V_{ac} \gtrsim T_K$.

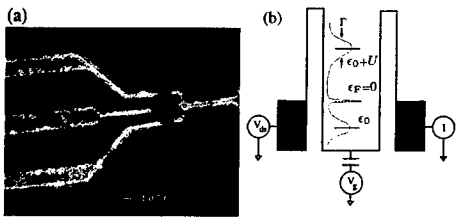

FIG. 1. (a) Electron micrograph of the SET. The lithographic diameter of the gate-enclosed central region is 150 nm. (b) Schematic energy diagram of the SET, showing an electron droplet separated by tunnel barriers from conducting leads. Since the number of electrons in the droplet is odd, the (inset) local density of states exhibits a sharp Kondo resonance at the Fermi level. The broad resonance at energy ϵ_0 represents a transition from $n_d = 0$ to $n_d = 1$, while the one at $\epsilon_0 + U$ corresponds to a transition from $n_d = 1$ to $n_d = 2$.

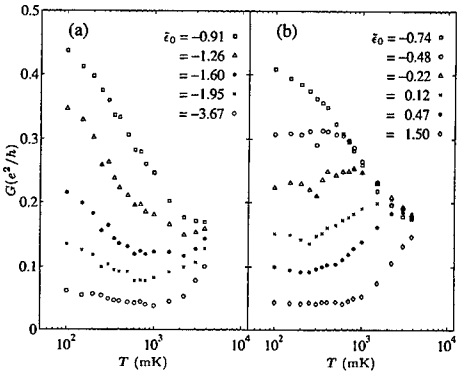

FIG. 3. Conductance versus temperature for various values of ϵ_0 on the right side (a) and left side (b) of the left-hand peak in Fig. 2.

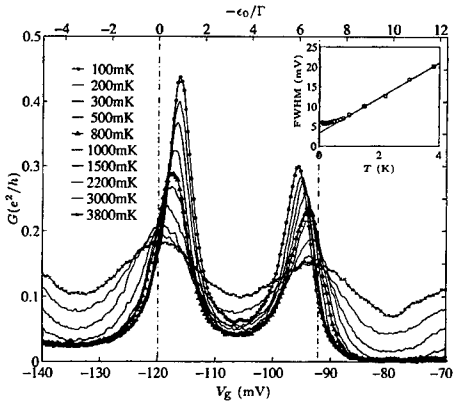

FIG. 2. Conductance versus plunger gate voltage V_g at various temperatures. The localized-state energy $\epsilon_0 = \alpha V_g +$ constant. The vertical dashed lines mark gate voltages at which two charge states are degenerate (i.e. $\epsilon_0 = 0$ or $\epsilon_0 + U = 0$) based on the analysis in Figs. 5 (a),(b). Between the dashed lines the charge state of the site is odd, as portrayed in Fig. 1, and the Kondo effect enhances conductance. Inset: Linear temperature dependence of peak width extrapolated back to $T = 0$ to extract $\Gamma = 295 \pm 20\,\mu$eV. The slope of the same temperature-dependence gives the constant of proportionality $\alpha = 0.069 \pm 0.0015$ between ϵ_0 and V_g [18].

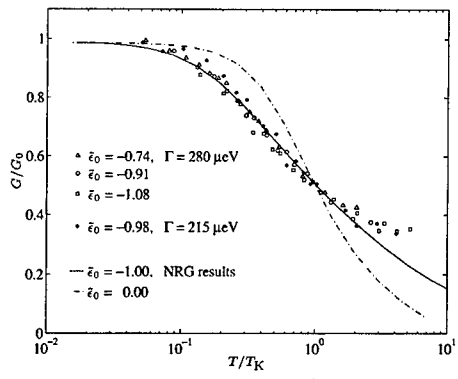

FIG. 4. The normalized conductance $\tilde{G} \equiv G/G_0$ is a universal function of $\tilde{T} \equiv T/T_K$, independent of both $\tilde{\epsilon}_0$ and Γ, in the Kondo regime, but depends on $\tilde{\epsilon}_0$ in the mixed-valence regime. Scaled conductance data for $\tilde{\epsilon}_0 \approx -1$ are compared with NRG calculations [13] for Kondo (solid line) and mixed-valence (dashed line) regimes. The stronger temperature dependence in the mixed-valence regime is qualitatively similar to the behavior for $\tilde{\epsilon}_0 = -0.48$ in Fig. 3b.

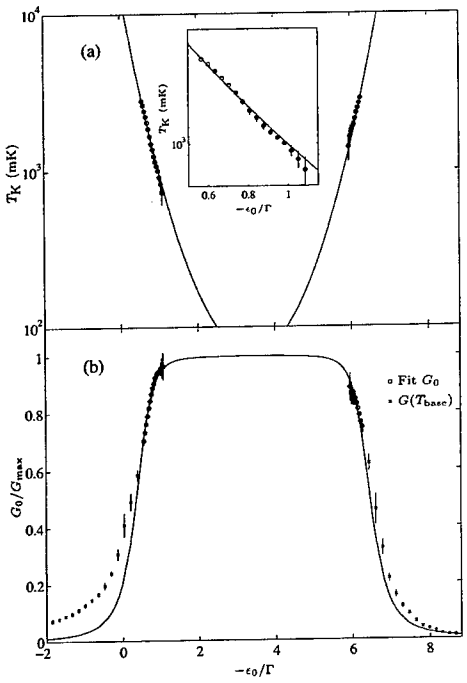

FIG. 5. (a) Fit values of T_K for data like those in Fig. 3 for a range of values of ϵ_0 [22]. The dependence of T_K on ϵ_0 is well-described by Eq. 1 (solid line). Inset: Expanded view of the left side of the figure, showing the quality of the fit. (b) Values of G_0 extracted from data like those in Fig. 3 at a range of ϵ_0. Solid line: $G_0(\epsilon_0)$ predicted by Wingreen and Meir [4]. $G_{\max} = 0.49e^2/h$ for the left peak, and $0.37e^2/h$ for the right peak.

Quantum fluctuations and the Kondo effect in small quantum dots

Jürgen König[a], Teemu Pohjola[b,c], Herbert Schoeller[d], and Gerd Schön[b]
[a]*Department of Physics, Indiana University, Bloomington, Indiana 47405, USA*
[b]*Institut für Theoretische Festkörperphysik, Universität Karlsruhe, 76128 Karlsruhe, Germany*
[c]*Materials Physics Laboratory, Helsinki University of Technology, 02150 Espoo, Finland*
[d]*Institut für Nanotechnologie, Forschungszentrum Karlsruhe, 76021 Karlsruhe, Germany*

We consider electron transport through quantum dots with large level spacing and charging energy. At low temperature and strong coupling to the leads, quantum fluctuations and the Kondo effect become important. They show up, e.g., as zero-bias anomalies in the current-voltage characteristics. We use a recently developed diagrammatic technique as well as a new real-time renormalization-group approach to describe charge and spin fluctuations. The latter gives rise to a Kondo-assisted enhancement of the current through the dot as seen in experiments.

PACS: 73.40.Gk, 72.15.Qm, 73.20.Dx, 73.50.Fq
Keywords: Quantum dots, Coulomb blockade, Kondo physics, renormalization group

Introduction. Electronic transport through single levels in small quantum dots is strongly affected by Coulomb interaction between the dot electrons. At temperatures lower than the charging energy Coulomb blockade phenomena arise. Due to the coupling to leads the dot states have a finite life time and both the charge and the spin of the dot fluctuate.

In recent experiments [1,2] on quantum dots with both strong Coulomb interaction and strong coupling to the leads the Kondo effect has been observed as an enhacement of the conductance with lowering the temperature or bias voltage. For the Kondo effect to occur the combination of both, charging effects *and* quantum fluctuations, is important.

We describe this interplay of charging effects and quantum fluctuations in terms of a recently developed diagrammatic technique as well as a new renormalization-group (RG) method. Both formulations cover the linear and non-linear response regime. We find zero-bias anomalies in the current-voltage characteristics and discuss their dependence on temperature, an applied gate voltage and an external magnetic field.

Model Hamiltonian. The extreme limit of a quantum dot containing only one spin-degenerate level is equivalent to the single-impurity Anderson model, $H = H_0 + H_T$,

$$H_0 = \sum_{k\sigma r} \epsilon_{k\sigma r} a^\dagger_{k\sigma r} a_{k\sigma r} + \sum_\sigma \epsilon_\sigma c^\dagger_\sigma c_\sigma + U n_\uparrow n_\downarrow$$

$$H_T = \sum_{k\sigma r} \left(T^r_k a^\dagger_{k\sigma r} c_\sigma + h.c. \right) .$$

The first term describes noninteracting electrons in state k with spin σ in the left or right lead, $r = L/R$, and the second one the dot electrons characterized by spin $\sigma = \uparrow, \downarrow$. The position of the dot levels can be tuned by an applied gate voltage. The spin degeneracy may be lifted by a finite Zemann energy due to an external magnetic field B. The charging energy U is accounted for in the third term, and the coupling of the dot states to the leads is modeled by the standard tunnel term. The spin σ is conserved during a tunnel process. The tunnel coupling H_T leads to a finite lifetime τ of the dot states and, therefore, to an intrinsic level broadening $\Gamma = \hbar/\tau$. The latter is related to the classical tunnel rates $2\pi\gamma^+_r(\omega) = \Gamma_r f_r(\omega)$ into and $2\pi\gamma^-_r(\omega) = \Gamma_r(1 - f_r(\omega))$ out of the dot through barrier r, obtained from simple golden-rule arguments, by $\Gamma = \sum_r \Gamma_r$ and $\Gamma_r = (2\pi/\hbar) \sum_k |T^r_k|^2 \, \delta(\omega - \epsilon_{k\sigma r})$. Here, $f_r(\omega)$ is the Fermi distribution of reservoir r.

Real-Time Transport Theory. In general, a quantum-statistical expectation value of an operator A at time t can be written as

$$\langle A(t)\rangle = \mathrm{tr}\left[\rho_0 T_K \exp\left(-i\int_K dt' H_T(t')_I\right) A(t)_I\right] \quad (1)$$

where the index I denotes the interaction picture with respect to H_0 and T_K is the time-ordering operator on the Keldysh contour going from $-\infty$ to t and then back to $-\infty$. We expand the exponential in powers of H_T and perform the trace of each term of the expansion. Since the Hamiltonian H_0 is bilinear in the lead electron operators, Wick's theorem holds for these degrees of freedom and the lead operators are contracted in pairs representing equilibrium distribution functions $\gamma_r^{\pm}(\omega)$. For the dot electrons Wick's theorem does not hold since the Coulomb interaction is expressed by a quartic term. A product of those operators has to be treated explicitly.

The tunneling current $I = I_L = -I_R$ is

$$I(t) = -ie\sum_{k\sigma}\left\{T_k^L\langle(a_{k\sigma L}^{\dagger}c_\sigma)(t)\rangle - H.c.\right\} \quad (2)$$

or, using the spectral density $A_\sigma(\omega)$ of the dot level $I = e\Gamma_L\Gamma_R/\Gamma\sum_\sigma\int_{-\infty}^{\infty}d\omega\, A_\sigma(\omega)[f_R(\omega) - f_L(\omega)]$.

In the following we concentrate on the limit of strong Coulomb repulsion such that double occupancy is forbidden. In order to describe the Kondo regime, we need a nonperturbative treatment of the tunneling, where quantum fluctuations yield finite lifetime broadening and renormalization effects of the dot levels.

Relation to the Kondo Model. For a low-lying level ϵ the quantum dot is always filled with one electron, either with up or down spin, and the Anderson model can be mapped onto the Kondo model. Spin flip occurs via a virtual empty dot. At low temperature, the spin of the dot electron is screened by the reservoir electrons, and the Kondo effect shows up as an increase of the transmittivity through the dot, expressed by a spectral density with a sharp resonance near the Fermi level of the leads. As a result the current is increased. At zero temperature and bias voltage Friedel's sum rule yields Langreth's formula

$$G|_{T,V=0} = 2\frac{e^2}{h}\frac{4\Gamma_L\Gamma_R}{\Gamma^2}\sin^2(\pi\langle n_\sigma\rangle) \quad (3)$$

for the linear conductance $G = \partial I/\partial V$. The maximal conductance is achieved for $\langle n_\sigma\rangle = 1/2$, which is realized in the Kondo regime.

By varying the gate voltage the level position can be shifted near the Fermi level of the leads. In this regime (mixed-valance) the dot can be either empty or singly occupied. While in the Kondo regime spin fluctuations are important, in the mixed-valence regime charge fluctuations dominate. Finally for the level being well above the Fermi levels the dot is always empty (empty-orbital regime).

Resonant-Tunneling Approximation: Zero-bias Anomalies and Magnetic-Field Dependence. In Refs. [3,4] we developed a diagrammatic technique to evaluate Eq. (2). Within the "resonant-tunneling approximation" we take into account non-diagonal matrix elements of the total density matrix up to the difference of one electron-hole pair excitation in the leads.

For a low-lying level Kondo resonances arise at the Fermi levels of the leads, and at zero bias a peak in the conductance evolve (zero-bias maximum; Fig. 1).

An external magnetic field shifts the Kondo resonances in the spectral density $A_\sigma(\omega)$ by the level splitting $\Delta\epsilon = \epsilon_\uparrow - \epsilon_\downarrow$. For this reason, there is no Kondo-assisted tunneling at low transport voltage but sets on if transport voltage and level splitting are equal. Therefore, the conductance peak at zero bias splits up into two peaks separated

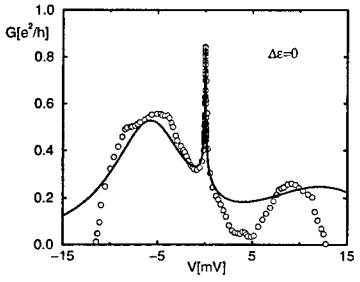

FIG. 1. The differential conductance vs. bias voltage for $T = 4.3\mu$eV, $\epsilon_\sigma(B = 0) = -5.2$meV, $\Gamma = 3.4$meV, $a_c = 0.33$, and $U = 30$meV. The circles are experimental data from Ref. [2] in which Kondo-assisted tunneling via a single charge trap of a point contact tunnel barrier has been measured.

by twice the level splitting (see Fig. 2) in agreement with experiments.

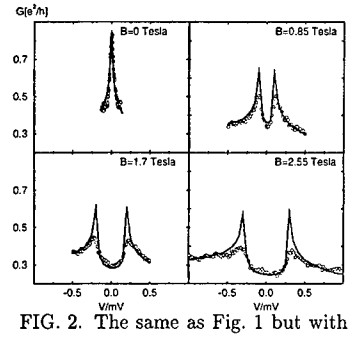

FIG. 2. The same as Fig. 1 but with a finite magnetic field. The zero-bias anomaly splits due to a finite magnetic field.

Two-Level Quantum Dot. The resonant-tunneling approximation can be extended to more complex systems [4]. In Fig. 3 we show an example for a quantum dot with two levels (each level is spin degenerate). We expect Kondo resonances in the spectral density at the Fermi level as well as at energies shifted by the level splitting. This leads to a triple-peak structure near zero-bias for low-lying levels.

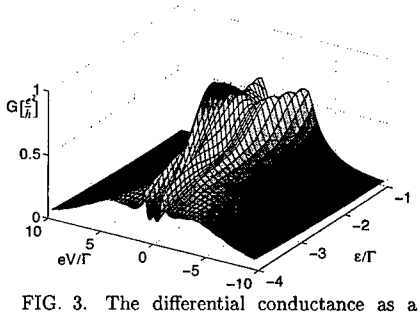

FIG. 3. The differential conductance as a function of the bias voltage and the level position ϵ of the lower level. The level splitting is fixed to $\Delta\epsilon = 0.8\Gamma$, and the temperature is $k_BT = 0.04\Gamma$.

Real-Time Renormalization-Group Approach. For a more quantitative analysis we formulate an RG approach working in Liouville space with $L = [H, \cdot] = L_0 + L_T$. We continously integrate out all contractions with time difference t_c from 0 to ∞. The result can be interpreted as a renormalization of L_0, L_T or as a generation of double (and higher) vertex terms (see Ref. [5] for details), symbolically written as

$$\frac{dL_0}{dt_c} = -i\gamma(t_c)e^{iL_0t_c}Ge^{-iL_0t_c}G \qquad (4)$$

$$\frac{dG}{dt_c} = -\gamma(t_c)\int_0^{t_c} dt[G(t), G]_+G(t-t_c) \qquad (5)$$

where we have neglected double and higher vertex generation, and G represents the tunnel coupling vertex. As an essential difference to conventional poor man scaling and operator product expansion methods (besides the fact that we work in Liouville space), we have not expanded the propagation $\exp(\pm iL_0t_c)$ of the dot in t_c. This is why we can send the final cutoff t_c to infinity, i.e., we can integrate out

all time scales. Furthermore, the renormalized Liouville operator of the dot is no longer represented as the commutator with a renormalized Hamiltonian $L_0 \neq [H_0, \cdot]$. This non-Hamiltonian dynamics describes the physics of dissipation and finite life times.

In the mixed valence and empty-orbital regime, $\epsilon > -1.5\Gamma$, we find that propagator and single vertex renormalization are sufficient within the real-time RG described above. At $T = V = 0$, we obtain Friedel sum rule within $2-3\%$. Furthermore we find excellent agreement with the Bethe ansatz solution for the spin and charge susceptibility. Fig. 4 shows the temperature dependence of the linear conductance for various values of the dot level. For a low-lying level we find a

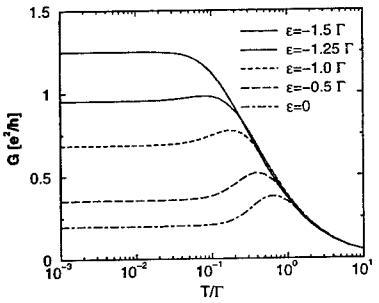

FIG. 4. Linear conductance as function of temperature; band-width $D = 10^4\Gamma$.

logarithmic increase of conductance with decreasing temperature and finally a saturation. We note that in this region the Kondo effect is not important but nevertheless we find pronounced zero-bias maxima for the nonlinear conductance, see Fig. 5. On the other hand, for a level close to the Fermi levels of the reservoirs, the linear conductance shows a local maximum as function of temperature. Here, the renormalized level is above the Fermi levels of the reservoirs, and therefore the conductance increases with increasing temperature due to thermal occupation of the local level. In this region one obtains zero-bias minima for the nonlinear conductance.

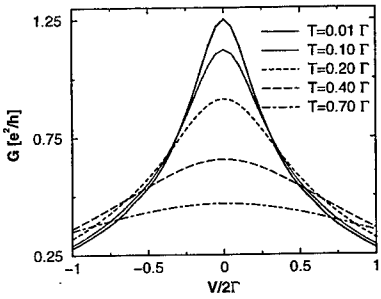

FIG. 5. Nonlinear conductance as function of bias voltage for $\epsilon = -1.5\Gamma$.

[1] D. Goldhaber-Gordon *et al.*, Nature (London), **391**, 156 (1998); D. Goldhaber-Gordon *et al.*, Phys. Rev. Lett. **81**, 5225 (1998); S.M. Cronenwett *et al.*, Science **281**, 540 (1998); J. Schmid *et al.*, Physica B**256-258**, 182 (1998); F. Simmel *et al.*, cond-mat/9812153.

[2] D.C. Ralph and R.A. Buhrman, Phys. Rev. Lett. **72**, 3401 (1994).

[3] H. Schoeller, in *'Mesoscopic Electron Transport'*, eds. L.L. Sohn *et al.* (Kluwer 1997), p. 291; J. König, *Quantum Fluctuations in the Single-Electron Transistor*, Shaker, Aachen (1999).

[4] H. Schoeller and G. Schön, Phys. Rev. **B50**, 18436 (1994); J. König *et al.* Europhys. Lett. **31**, 31 (1995); Phys. Rev. Lett. **76**, 1715 (1996); J. König *et al.*, Phys. Rev. **B54**, 16820 (1996); T. Pohjola *et al.*, Europhys. Lett. **40**, 189 (1997).

[5] J. König and H. Schoeller, Phys. Rev. Lett. **81**, 3511 (1998); H. Schoeller and J. König, submitted to Phys. Rev. Lett..

Kondo resonances in split-gate quantum dots

Jörg Schmid, Jürgen Weis and Karl Eberl

Max-Planck-Institut für Festkörperforschung, Heisenbergstraße 1, 70569 Stuttgart, Germany
e-mail: jschmid@klizix.mpi-stuttgart.mpg.de

Abstract

The Kondo resonances observed in quantum dots are studied as a function of the tunnel coupling to the leads. It is observed that a Kondo resonance develops in one Coulomb blockade region as the coupling is increased. This is taken as an indication that there is a degeneracy on the dot for this electron number, which is a prerequisite of the Anderson impurity model predicting the Kondo resonances. The nature of this degeneracy is studied in tilted magnetic fields and the picture, that a spin degeneracy is responsible for the Kondo resonance, is confirmed.

Key words: Kondo resonance, Quantum dot, Anderson model, Spin splitting
PACS: 75.20.Hr 73.20.Dx 73.23.Hk

The Anderson impurity model has been introduced [1] in 1961 to describe the effect of localized impurity states in bulk metals. It has been calculated [2,3] that the degenerate localized states coupled to the electron reservoir of the host metal display a unique behavior at low temperatures – the so-called Kondo effect. Recently it has become possible to study single such impurities in metallic point contacts [4] or realize them in quantum dots [5–7] as suggested in [8,9] and worked out further in [10] and [11].

In our experiments we use quantum dots that are electrostatically defined in a two-dimensional electron system (2DES) in a $GaAs/Al_{0.33}Ga_{0.67}As$ heterostructure (electron density $3.2 \times 10^{15}\mathrm{m}^{-2}$, mobility $30m^2/Vs$) at 4.2 K at the hetero-junction 50 nm below the surface. Fig. 1(a) is a SEM picture of the metallic top gates: In the free area surrounded by gates a dot forms when a voltage of approximately -0.6 V is applied to these gates. The geometrical "diameter" of the dot is 180 nm, the corresponding area multiplied with the electron density gives an upper limit of 80 for the number of electrons on the dot. The actual area will be smaller and the electron number lower due to depletion from the negative gate voltages. This number changes with the voltages applied to the top gates and also with the voltage of an electrode on the back side of the 0.5 mm thick substrate (back gate).

Electron transport through the dot is measured via ohmic contacts to the 2DES regions on either side of the dot as indicated in Fig. 1. The measurements are done at the base temperature of a dilution refrigerator (30 mK). In this paper, we will concentrate on the differential conductance, which is obtained by adding a small modulation ($4\ \mu V_{\mathrm{rms}}$) to the drain-source voltage V_{DS}

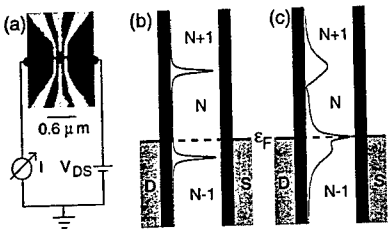

Fig. 1. (a) Top view of the metallic split-gate structure and sketch of the experimental setup. (b) Energy scheme of the quantum dot for weak tunnel coupling. The light grey stands for the reservoirs, the dark grey for the barriers, the curve is a calculated spectral density of a dot [12]. (c) Same as (b) for strong tunnel coupling; the other parameters are chosen as in (b).

and measuring the corresponding current change by a lock-in technique. This quantity corresponds closely to the spectral density of the dot broadened by the Fermi distribution of the leads [13]. Two spectral densities calculated for the Anderson impurity model [12] are given in Fig. 1(b) and (c) – for weak and strong coupling respectively. In the case of weak tunnel coupling the two peaks – slightly broadened by the tunnel coupling – correspond to the transition energies between the N electron state and the $N+1$ and $N-1$ states, respectively. Their position relative to the Fermi energies of the leads depends on the gate voltage. For the case of strong tunnel coupling an additional peak, the Kondo resonance, develops. Its position is fixed to the Fermi levels ϵ_F of the leads and independent of the gate voltage.

In Fig. 2 we study the differential conductance as a function of V_{DS} and V_{BG} in a parameter range, where an occupation number of N electrons on the dot is relevant for transport. The tunnel coupling is varied by changing the voltages applied to the outer gates. To keep the electron number fixed, the resulting shift of the electrostatic potential of the quantum dot is compensated by adjusting the voltages applied to the middle gate fingers and the back gate. Horizontal cuts through these plots correspond to transport spectra. We observe qualitative agreement between Fig. 1(b) and Fig. 2(a) as well as Fig. 1(c) and Fig. 2(b) and (c): The maximum in the Spectral density (Kondo resonance), that appears in in Fig. 1(c) at the Fermi energy corresponds to the maximum in the differential conductance in Fig. 2(b) and (c) at $V_{DS} = 0$.

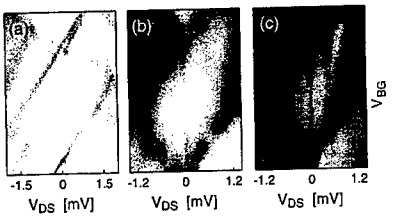

Fig. 2. Differential conductance dI/dV_{DS} (0 corresponds to white, e^2/h corresponds to black) as a function of the back-gate voltage V_{BG} and the drain-source voltage V_{DS}. Tunnel coupling increases from (a) to (c). The V_{BG} range in all plots is 30 V, the absolute values are shifted so that the number of electrons in the central Coulomb blockade region in (a)-(c) is identical.

The nature of the degeneracy responsible for the Kondo resonance has been studied by applying a magnetic field. A value of the Kondo resonance splitting close to the spin splitting in bulk GaAs has been found in [6,7] where the magnetic field was applied in the plane of the 2DES. A deviation from this value was reported in [5] where the magnetic field was applied perpendicular to the 2DES. Here we study the splitting of the Kondo resonance with magnetic fields using a gate voltage and the angle between the plane of the 2DES and the magnetic field direction as parameters (on a different sample). The measurement presented in Fig. 3(a) corresponds to the situation in Fig. 2(b) or (c): A Kondo reso-

nance is visible across one Coulomb-blockade region at $V_{DS} = 0$. When a magnetic field of $B = 2$ T is applied in the plane of the 2DES, this resonance splits into two resonances (Fig. 3(b)) parallel to the V_G-axis across this Coulomb-blockade region. The parallel field direction was chosen because a parallel field will lift a spin degeneracy without having a large influence on the wave function which has an extension of approximately 5 nm perpendicular to the plane of the 2DES.

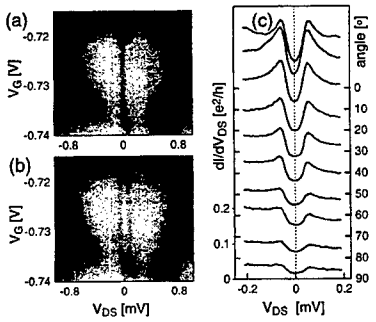

Fig. 3. Splitting of the Kondo resonance with magnetic field. (a) and (b) differential conductance, 0 corresponds to white, $e^2/2h$ corresponds to black. A magnetic field B is applied in the plane of the 2DES; (a) $B = 0$ T and (b) $B = 2$ T. The voltage V_G applied to the middle gate fingers is the parameter. (c) Differential conductance for a fixed gate voltage of $V_G = 0.73$ V and fixed field of 2 T as a function of the angle between 2DES and field; the curves are offset for clarity.

The field component perpendicular to the plane has a significant effect on the wave functions. This means that the energies of the levels on the dot and the tunnel coupling changes As long as one considers a single spin degenerate level, the splitting of the Kondo resonance should still be given by the spin splitting, i.e. the absolute magnetic field. If the origin of the degeneracy is not spin, the splitting would most likely depend on the direction of the magnetic field. As can be seen in Fig. 3(c), the value of the Kondo-resonance splitting does not change with the angle of the magnetic field indicating a spin splitting. The amplitude changes, corresponding to a decrease in tunnel coupling with increasing magnetic field.

The Kondo resonance is linked to a spin degeneracy of the N electron system on the dot, the effect of the Zeeman splitting being the split Kondo resonance described above. The perpendicular magnetic field will also cause changes in the N electron system on the dot that are not related to the Zeeman splitting. The split Kondo resonance will disappear when the state responsible for the Kondo resonance is replaced by a lower energy non Kondo-type state. On the sample from which the data in Fig. 3 were taken, the Kondo resonances are observable up to a perpendicular field of 2.5 T which is consistent with the data in [5], where the split Kondo resonance was observed at even higher perpendicular magnetic fields. This field value is unexpectedly high since the energy scale of the perpendicular magnetic field is the cyclotron energy $\hbar\omega_C = \hbar eB/m^*$ (= 1.7 meV at 1 T) while we obtain a typical level spacing [14] of approximately 0.2 meV from the data of the weakly tunnel coupled dot in Fig. 2(a). This means that the typical level spacing of the dot is not the scale to which the degeneracy leading to the Kondo resonance is sensitive.

In conclusion, we have demonstrated that a Kondo resonance is linked to a certain electron number on the dot indicating, that there is a degeneracy present for this electron number and that it is robust against significantly changing the gate voltages defining the dot. The nature of this degeneracy has been confirmed to be a spin degeneracy. The Kondo

resonances are less sensitive to perpendicular magnetic fields than would be expected from comparing cyclotron energy and typical level spacing.

The authors thank M. Riek, T. Reindl, M. Schmid and U. Waizmann for technical support and D. Pfannkuche and U. Wilhelm for helpful discussions. We gratefully acknowledge the support by the Bundesministerium for Bildung and Forschung (BMBF) under grant No. 01BM624/7.

References

[1] P. W. Anderson, Phys. Rev. **124** (1961) 41.

[2] H. R. Krishna-murty, J. W. Wilkins, K. G. Wilson, Phys. Rev. B **21** (1980) 1003.

[3] N. E. Bickers, Rev. Mod. Phys. **59** (1987) 845; F. D. M. Haldane, Phys. Rev. Lett. **40** (1978) 416.

[4] D. C. Ralph, R. A. Buhrman, Phys. Rev. Lett. **72** (1994) 3401.

[5] D. Goldhaber-Gordon, H. Shtrikman, D. Mahalu, D. Abusch-Maggder, U. Meirav, M. A. Kastner, Nature **391** (1998) 156.

[6] S. M. Cronenwett, T. H. Oosterkamp, L. P. Kouwenhoven, Science **281** (1998) 540.

[7] J. Schmid, J. Weis, K. Eberl, K. v. Klitzing, Physica B **256-258** (1998), 182.

[8] L. I. Glazman, M. É. Raĭkh, JEPT Lett. **47** (1988) 452.

[9] T. K. Ng, P. A. Lee, Phys. Rev. Lett. **61** (1988) 1768.

[10] Y. Meir, N. S. Wingreen, P. A. Lee, Phys. Rev. Lett. **70** (1993) 2601; N. S. Wingreen, Y. Meir, Phys. Rev. B **49** (1994) 11040.

[11] J. König, J. Schmid, H. Schoeller, G. Schön, Phys. Rev. B **54** (1996) 16820.

[12] J. Schmid, J. König, H. Schoeller, G. Schön, Physica E **1**, 241.

[13] For instance, the spectral density is not independent of the position of the Fermi energies, see [10,11] i.e. the drain-source Voltage.

[14] J. Weis, R. J. Haug, K. v. Klitzing, and K. Ploog, Phys. Rev. Lett. **71** (1993) 4019.

AC transport through a quantum dot: from Kondo to Coulomb-Blockade behaviour

Rosa López[1], Ramón Aguado[1,2], Gloria Platero[1] and Carlos Tejedor[3]

[1] Instituto de Ciencia de Materiales (CSIC), Cantoblanco,28049 Madrid, Spain.

[2] Rutgers University, 136 Frelinghuysen Road Piscataway,New Jersey 08854-8019

[3] Universidad Autónoma de Madrid, Cantoblanco,28049 Madrid, Spain.

Abstract

We analyze the conductance of a quantum dot in an ac potential at finite temperature. The Friedel-Langreth sum rule (FLSR) is generalized to include the effect of an ac potential and finite T. We have solved the Anderson hamiltonian by means of a selfconsistent procedure which fulfills the generalized FLSR. New features are found in the DOS and in the conductance when an ac voltage is applied. Our model describes the effect of an ac potential on the transition from Kondo regime to a Coulomb blockade behaviour as T increases.
PACS numbers: 73.40.Gk, 72.15Qm, 85.30Vw, 73.50.Mx

Bulk Kondo phenomena are caused by the interaction among de-localized electrons in a host metal and the localized electrons of magnetic impurities. Technological advances allow to test all theoretical predictions in quantum dots (QDs) [1]. The contacts in a QD play the role of the host metal and the confined electrons in the QDs are analogous to those localized in the impurity. In a QD it is possible to vary all the parameters which control the Kondo physics using a combination of dc and ac voltages. The aim of this work is to investigate ac transport in the Kondo and Mixed Valence regime and the transition to Coulomb blockade (CB) behaviour. The time dependent Anderson Hamiltonian reads:

$$\begin{aligned} H &= \sum_{k\in\{L,R\},\sigma} \epsilon_k c^\dagger_{k,\sigma} c_{k,\sigma} + \sum_\sigma \epsilon_\sigma d^\dagger_\sigma d_\sigma + \sum_{k\in\{L,R\},\sigma} V_k (c^\dagger_{k,\sigma} d_\sigma + d^\dagger_\sigma c_{k,\sigma}) \\ &+ U d^\dagger_\uparrow d_\uparrow d^\dagger_\downarrow d_\downarrow + \sum_\sigma V_{AC} cos\omega_0 t d^\dagger_\sigma d_\sigma \end{aligned} \quad (1)$$

The AC voltage has an intensity V_{ac} and a frequency ω_0 ($\beta = V_{AC}/\omega_0$). We derive an effective selfenergy within the framework of finite U perturbation theory which gives the correct behaviour in the atomic and high energy limits and which fullfils the FLSR, i.e., the charge conservation [2]. Thus, this model is an extension for the time dependent case of those developed in the static one [3]. The FLSR is a statement of charge neutrality which relates the displaced charge to the phase shift of the electronic wave function. Our first aim is to define a generalized FLSR for finite T. The displaced charge is defined as: $\langle \delta n_\sigma \rangle = \langle n^{(0)}_{kk,\sigma} \rangle - \langle n_{kk,\sigma} \rangle + \langle n_\sigma \rangle$ where time-average is performed. Here, $\langle n^{(0)}_{kk,\sigma} \rangle$ and $\langle n_{kk,\sigma} \rangle$ is the leads occupation without and with coupling to the QD respectively. Finally $\langle n_{d,\sigma} \rangle$ is the QD occupation. The formal expression for the QD Green functions in presence of an ac voltage is: $G^{r,a,<}_{d,\sigma}(t,t') = e^{i\frac{V_{AC}}{\omega_0} sen\omega_0 t} e^{-i\frac{V_{AC}}{\omega_0} sen\omega_0 t'} \times G^{r,a,<}_{d,\sigma}(t-t')$. After some algebra we obtain for the displaced charge [4]:

$$N = -Im \sum_{m=-\infty}^{\infty} J_m^2(\beta) \int_{-\infty}^{-\infty} d\epsilon \, G^r_\sigma(\epsilon - m\hbar\omega_0) f(\epsilon)$$
$$\times \left(1 - \sum_{s=-\infty}^{\infty} J_s^2(\beta) \sum_k \frac{|V_k|^2}{[\epsilon - \epsilon_k - (m-s)\hbar\omega_0]^2} \right) \qquad (2)$$

The next step is to obtain the phase shift. In presence of scattering the electronic wave function suffers a phase shift which changes in π in each resonant event and it is related to the time average S matrix. The phase shift can be written as [2]: $2i\pi\delta(\epsilon) = ln(1 - i\Gamma(\epsilon) \sum_{n=-\infty}^{\infty} J_n^2(\beta) G_{d\sigma}(\epsilon - n\omega_0)) \approx Im ln(\sum_{n=-\infty}^{\infty} J_n^2(\beta) G_{d\sigma}(\epsilon - n\omega_0))$. Finally the FLSR establishes that the phase shift must be equal to N. Thus, the generalized FLSR in presence of ac fields at finite T is: $N = \int_{-\infty}^{\infty} d\epsilon \frac{df(\epsilon)}{d\epsilon} \times \delta(\epsilon)$. Once the selfenergy is obtained selfconsistently, we evaluate the DOS and the conductance $\mathcal{G}$.
At zero T, in the absence of ac , $\mathcal{G}$ has a broad peak of width U centered around $\epsilon_0 = -U/2$ and it reaches the maximum value of $2e^2/h$. As T increases the singularity in the DOS at ϵ_F is suppressed due to inelastic processes, and $\mathcal{G}$ decreases in the Kondo region. Fig.1a shows the QD conductance in the presence of an ac potential at zero T. The ac produces a reduction of the central peak and the appearance of novel structures at $\epsilon_0 \approx -4\pi\Gamma$ and $\epsilon_0 \approx 1.5\pi\Gamma$. For these values of ϵ_0 the DOS has a peak at E_F giving a large contribution to $\mathcal{G}$. The separation of these new satellites is $U(1 - \langle n_{d,\sigma} \rangle) + 2\hbar\omega_0$ [5]. This behavior is different from the one predicted by a mean field theory, where instead, satellites at $-\hbar\omega_0$ and $\hbar\omega_0 - U$ appear. At finite T the $\mathcal{G}$ shows a deep Kondo valley due to the suppression of the Kondo peak. However within this region one observes a maximum produced by the ac (fig. 1.a). This structure comes from the satellites of the mean field peaks ϵ_0 and $\epsilon_0 + U$, in the DOS, which give a contribution at ϵ_F. We observe a maximum since they overlap. Moreover the satellites of $\mathcal{G}$ at $\epsilon_0 \approx -4\pi\Gamma$ and $\epsilon_0 \approx 1.5\pi\Gamma$ continue present in the $\mathcal{G}$. For higher T all these structures are not well defined since T yields a broadening of the peaks. In order to see clearly the satellites

of the mean field peaks we increase the interaction U (Fig.1b). When U increases T_K decreases and CB behaviour is achieved at lower T. In Fig. 1.b, the system has reached a CB behaviour (the MF peaks are located at the degeneration points) and it is possible to resolve the structure within the Kondo valley. We analyze as well the behavior of $\mathcal{G}$ as a function of T for a fixed ϵ_0. In the Kondo region $\mathcal{G}$ decreases as $-T^2$ and, at higher T, in a logarithmic way. In the presence of ac, $\mathcal{G}$ is globally reduced as β increases (fig. 2.a) the ac provokes the appareance of satellites in the DOS, the Kondo peak is reduced and $\mathcal{G}$ decreases. Increasing β further ($\beta = 2$) $\mathcal{G}$ increases at a certain T and it presents a maximum. At β=2 the Kondo peak suffers a strong reduction but as T increases the ac satellites start to contribute to $\mathcal{G}$,i.e., start to give a contribution at EF in the DOS due to the smearing of the peaks. These contributions provoke an anomalous behaviour of $\mathcal{G}$ as a function of T. In the Mixed valence regime (Fig.2.b) we do not observe a significant modification of $\mathcal{G}$ as a function of T for small frequencies. However, for higher frequencies (Fig. 2.b) it has the same behavior than in the previous case for low frequencies. The reason is that in the Mixed valence regime the width of the peak at ϵ_F, in the DOS is larger than in the Kondo regime and the effect of a low frequencysignal is not observed.

Work is supported in part by the MEC of Spain under contracts PB96-0875 and PB96-0085 and by the EU via contract FMRX-CT98-0180.

References

(1) S. M. Cronenwett, *et al*, Science, **281**, 540, (1998); D. Goldhaber-Gordon, *et al*, Nature, **391**, 156 (1998); J.Schmid et al.Physica B,**256-258**,182 (1998).

(2) D. C. Langreth, phys. Rev. **150**, 516 (1966).

(3) H. Kajueter and G. Kotliar, Phys. Rev. Lett., **77**, 131 (1996).

(4) R. López, R. Aguado, G. Platero, C. Tejedor, Phys.Rev. Lett., **81**, 4688, (1998).

(5) R. López, R. Aguado, G. Platero, C. Tejedor, to be published.

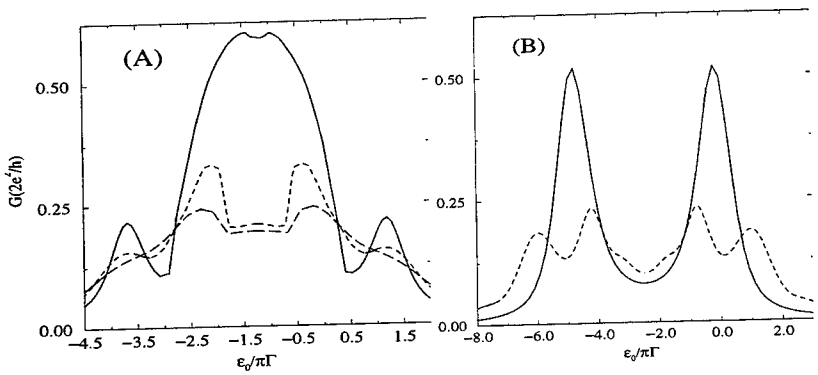

Figure 1: $\mathcal{G}/\frac{\epsilon_0}{\pi\Gamma}$, Γ is the imaginary part of the hybridyzation selfenergy. (A) $u = \frac{U}{\pi\Gamma} = 2.5$, $\beta = \frac{V_{AC}}{\omega_0} = 1$ and $\omega_0 = 1.5\pi\Gamma$, solid line $T = 0$, dashed line $T = 0.6\Gamma$ and long-dashed $T = \Gamma$ (B) $u = \frac{U}{\pi\Gamma} = 5$: solid line $V_{ac} = 0$ and $T = \Gamma$, dashed lined $\beta = \frac{V_{AC}}{\omega_0} = 1$ and $\omega_0 = 1.5\pi\Gamma$ at $T = \Gamma$

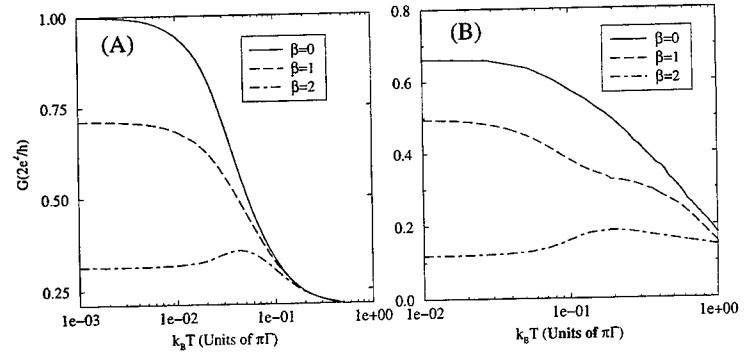

Figure 2: $\mathcal{G}/T$, $u = \frac{U}{\pi\Gamma} = 2.5$, (A) $\epsilon_0 = -1.1\pi\Gamma$, $\omega_0 = 0.25\pi\Gamma$, (B) $\epsilon_0 = -\Gamma$, $\omega_0 = \pi\Gamma$

Electron-Electron Scattering in Two-Dimensional Electron Gas under a Controllable Spatially Modulated Magnetic Field

Mayumi Kato[1], Makoto Sakairi, Akira Endo, Shingo Katsumoto[2] and Yasuhiro Iye[2]

Institute for Solid State Physics, University of Tokyo,
7-22-1 Roppongi, Minato-ku, Tokyo 106-8666, Japan

Abstract

Two-dimensional electron gas at GaAs/AlGaAs heterointerface subjected to a lateral magnetic superlattice exhibits a T^2-dependent excess resistivity, which is attributed to electron-electron Umklapp scattering. This has been corroborated by the effect of increased electron temperature. In a sample with an oblique lateral superlattice, the same process gives rise to a transverse component of resistivity.

Keywords: magnetic Weiss oscillation; GaAs/AlGaAs; lateral magnetic superlattice; electron-electron scattering; hot electron

1. Introduction

Electron-electron (e-e) scattering is known to give rise to a T^2-term of resistivity. The T^2-term is observed in various systems such as heavy fermion metals, organic conductors and transition metal oxides, but not in two-dimensional electron gas(2DEG) at semiconductor heterointerface. This is because, in order to contribute to the resistivity, the e-e scattering has to involve the Umklapp process (otherwise the total momentum of two colliding electrons is unchanged) [1]. Since the Fermi circle of a typical 2DEG is much smaller than the Brillouin zone, the Umklapp process cannot occur. When a superlattice with a length scale comparable to the Fermi wave length is imposed on an otherwise plain 2DEG, the e-e Umklapp process does occur [2].

In the present study, we investigated in 2DEG under the influence of a magnetic lateral superlattice, *i.e.* a periodic magnetic field modulation [3,4]. We studied the anisotropy of the effect with respect to the direction of modulation wavevector relative to the transport current. We also studied the effect of increased bias current.

[1] Corresponding author. Tel: +81 3 3478 6811(Ext. 5602); Fax: +81 3 3401 5169; e-mail: mayumi@kodama.issp.u-tokyo.ac.jp.
[2] also at CREST, Japan Science and Technology Corporation (JST)

2. Experimental

Samples used in the present study were fabricated from a molecular beam epitaxy (MBE) grown GaAs/AlGaAs single hetero junction wafer with electron density n_e=2.4× $10^{15}m^{-2}$ and mobility μ=60$m^2V^{-1}s^{-1}$ at 4.2K. The 2DEG plane was at a depth 75nm from the surface. Samples were patterned in a standard Hall-bar shape by photolithography. A ferromagnetic metal grating with periodicity a=500nm was fabricated on top of the current channel by electron beam lithography, thermal evaporation and lift-off. The grating was so aligned that the modulation wavevector was parallel to the [100] direction, in order to minimize the effect of strain induced piezoelectric potential modulation [5]. Transport measurements were carried out by the standard low frequency AC technique. The ferromagnetic grating was magnetized by an external magnetic field applied parallel to the sample surface. The fringing field creates a sinusoidal magnetic field pattern at the 2DEG plane as shown in the inset of Fig. 1. By changing the azimuthal angle φ of the parallel magnetic field, we can control the modulation amplitude.

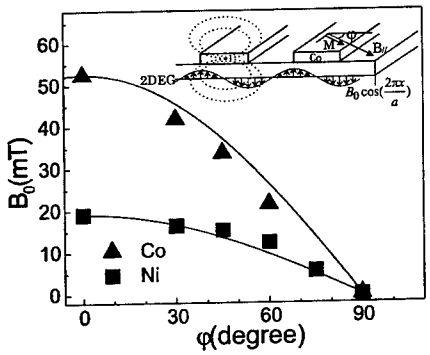

Fig. 1 *Inset:* Schematic illustration of the device. *Main Panel:* φ-dependence of B_0.

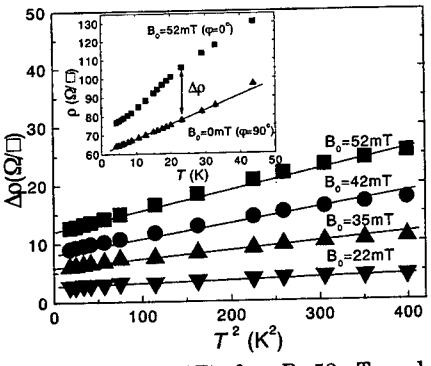

Fig. 2 *Inset:* ρ(T) for B_0=52mT and B_0=0mT. *Main Panel:* Δρ plotted against T^2 for different B_0.

3. Results and Discussion

The magnetic field modulation amplitude B_0 at the 2DEG plane was estimated from the analysis of the commensurability oscillation of magnetoresistance (magnetic Weiss oscillation).

Figure 1 shows the φ-dependence of B_0 for two samples with different grating materials (Co and Ni). The cosφ-dependence comes from the fact that only the magnetization component parallel to the modulation wave vector is effective in

producing the magnetic field modulation. This enables us to vary the modulation amplitude in a single sample. An advantage of using the magnetic field modulation rather than an electrostatic one is that the modulation amplitude can be changed without affecting the electron density. In the present work, we systematically study the resistivity under a modulated magnetic field with zero uniform component.

The temperature dependences of the resistivity for B_0=0 and B_0=52 mT are shown in the inset of Fig. 2. The data for B_0=0 shows a T linear resistivity due to the electron-phonon scattering. The difference between the resistivities with and without magnetic field modulation defines the excess resistivity $\Delta\rho$, which represents the extra scattering caused by the spatial modulation. The excess resistivity $\Delta\rho$ is proportional to $\cos^2\varphi$, and hence to B_0^2 [3]. The main panel of Fig. 2 shows the excess resistivity $\Delta\rho$ for different values of B_0 plotted against T^2. The T^2-term is attributed to e-e Umklapp scattering. In the following, we show experiments that reinforce this conclusion.

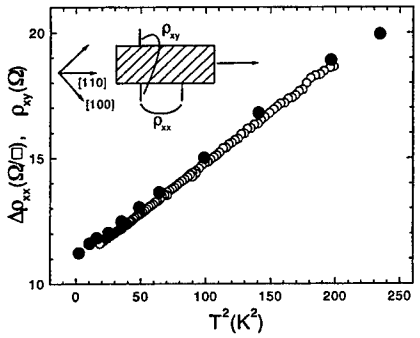

Fig. 3 *Inset:* Schematic illustration of the device. *Main panel:* $\Delta\rho_{xx}$ (solid circles) and the transverse resistivity ρ_{xy} (open circles) plotted against T^2.

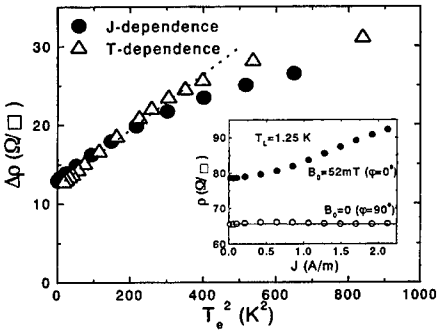

Fig. 4 *Inset:* J-dependence of ρ for B_0=52mT and B_0=0mT. *Main panel:* $\Delta\rho$ plotted against T_e^2 (solid circles) compared with T_L^2 (open triangles)-dependence at low current bias.

We fabricated a sample in which the modulation wavevector was at 45 degree with respect to the current direction, as depicted in the inset of Fig. 3. Solid circles in Fig. 3 show the excess longitudinal resistivity $\Delta\rho_{xx}$ for B_0=52 mT plotted against T^2. In this oblique superlattice, the e-e Umklapp scattering which gives rise to $\Delta\rho_{xx}$ also does a transverse resistivity ρ_{xy}. It is seen that the relation $|\rho_{xy}(T)|=\Delta\rho_{xx}(T)$, which is expected for the Umklapp backscattering by a 45 degree oblique superlattice, holds well. Another sample in which the modulation wavevector was set perpendicular to the current direction showed no excess resistivity [3]. These results establish firmly that the extra scattering is caused by the Umklapp process.

We investigate the hot electron effect at higher current bias. The inset of Fig. 4

shows the resistivity as a function of the current bias J for B_0=0 and 52 mT at the lattice temperature T_L =1.25K. The fact that the resistivity for B_0=0 does not change with J guarantees that T_L remains unchanged. The electron temperature T_e was determined from analysis of the Shubnikov-de Haas amplitude. The main panel of Fig. 4 shows $\Delta\rho$ plotted against T_e^2 (solid circles). It agrees well with the T_L^2-dependence at the lowest current bias (open triangles). This result proves that the effect is governed by the electron temperature, and supports the picture of e-e scattering. We also note that the present result provides a basis for a new method for measuring the electron temperature.

4. Summary

To summarize, we have measured the resistivity of 2DEG samples subjected to magnetic lateral superlattice. The excess resistivity shows T^2-dependence characteristic of e-e scattering. The occurrence of transverse resistivity in an oblique superlattice and behavior at higher current densities are consistent with the e-e Umklapp scattering picture.

We thank Prof. H. Fukuyama for helpful conversations.

References

[1] J.M. Ziman, *Electrons and Phonons* (Clarendon Press, Oxford, 1960)
[2] A. Messica, A. Soibel, U. Meirav, A. Stern, H. Shtrikman, V. Umansky, and D. Mahalu, Phys. Rev. Lett. 78 (1997) 705.
[3] M. Kato, A. Endo, S. Katsumoto and Y. Iye: Phys. Rev. B58(1998) 4876; M. Kato, A. Endo, S. Katsumoto and Y. Iye: J. Phys. Soc. Jpn. 68(1999) 1492
[4] N. Overend, A. Nogaret, B.L. Gallagher, P.C. Main, R. Wirtz, R. Newbury, M.A. Howson, and S.P. Beaumont: Physica B 249-251(1998) 326.
[5] E.Skuras, A.R.Long, I.A.Larkin, J.H.Davies and M.C.Holland, Appl. Phys. Lett. 70 (1997)871; A.Nogaret, S.Carlton, B.L.Gallagher, P.C.Main, M.Henini, R.Wirtz, R.Newbury, M.A.Howson and S.P.Beaumont, Phys. Rev. B55(1997)16037.

FAR-INFRARED SPECTROSCOPY OF A TWO DIMENSIONAL ELECTRON GAS IN A TUNEABLE, PERIODICALLY MODULATED MAGNETIC FIELD

S. Cina'*$, D. Whittaker$, D.D. Arnone$, T. Burke*, H.P. Hughes*, M. Leadbeater$, M. Pepper*$, and D.A. Ritchie*

* Cavendish Laboratory, University of Cambridge, Madingley Road, Cambridge, UK
$ Toshiba Research Europe Limited, 260 Science Park, Milton Road, Cambridge, UK

We report the first infrared optical measurements of a two dimensional electron gas (2DEG) in the presence of an external periodically modulated perpendicular magnetic field, realised using epitaxial regrowth to produce a corrugated quantum well (QW). Two active modes are observed, with relative intensities and resonance frequencies depending on the amplitude of the magnetic field modulation as well as on the total external magnetic field. The two modes are interpreted as being magnetoplasmons coupled by the presence of the magnetic field modulation. A magnetoplasmon band structure calculation has been used to describe the experimental data. The agreement between theory and experiment is excellent.

There has been recently increasing interest, theoretically [1-4] and experimentally [5-7] in studying the effects produced by a new kind of periodic potential, produced by the presence of a periodically modulated magnetic field (B) in a two dimensional electron gas (2DEG). While the effects produced by the presence of a periodic electrostatic potential have been extensively studied in the last twenty years, most of the theoretical predictions of the periodic magnetic modulation effects produced on a 2DEG still have to be discovered. The experimental evidence produced so far just refers to transport measurements of the effects produced by the modulating field, but experimental observation of the optical properties of a 2DEG in presence of a periodically modulated magnetic field (PMMF) have so far eluded experimental observation.

In this paper we report on the first optical measurements of a 2DEG in presence of a PMMF. Two active modes are observed, with relative intensities and resonance frequencies depending on the amplitude of the magnetic field modulation as well as on the total external magnetic field. The two modes are interpreted as being a magnetoplasmon (MP) coupled to the cyclotron resonance (CR) mode by the magnetic field modulation. We also present a calculation of the MP band structure produced by the PMMF, and successfully describe all the experimental data.

The devices were fabricated on a (100) GaAs substrate, and optical lithography was used to produce an array of equally spaced stripes of photoresist. Devices with various periods d have been produced (d=2-3μm). Since similar behaviour was observed in all samples, in this letter we concentrate on the data relating to the sample with d=2 μm. A flat QW was also grown as a reference sample.

An anisotropic buffered hydrofluoric etch was used to expose (331)B facets at a 25° angle to the (100) substrate after a vertical etch of 95 nm. After a hydrogen radical surface cleaning [8], a superlattice structure was regrown using molecular beam epitaxy (MBE) on top of the corrugated surface. 3 nm of GaAs were first grown, followed by 20 multilayers of 1nm AlAs and 1nm GaAs. The QW was then realised by growing 7nm AlGaAs, 15nm GaAs, 20nm AlGaAs, a 40nm Si-doped 2×10^{18} cm^{-3} AlGaAs and finally a 100 nm GaAs layer. Since (331)B and (100) planes are known to support electron gases [9,10], after the epitaxial regrowth the 2DEG should be continuous and periodically corrugated in one direction. Figure 1(a) shows the atomic force microscope (AFM) image of the 2 μm period sample. An angle α=13° was measured after the epitaxial regrowth. In an external B, the 2DEG embedded in the

QW experiences a unidirectional periodically modulated perpendicular magnetic field B_{perp}. The intensity of the field modulation can also be tuned by changing the angle β between B and the perpendicular to the sample's substrate, as shown in Fig.1(b).
To verify the continuity of the 2DEG along the corrugation, the longitudinal resistance was cross measured along the modulation and perpendicular to the modulation.

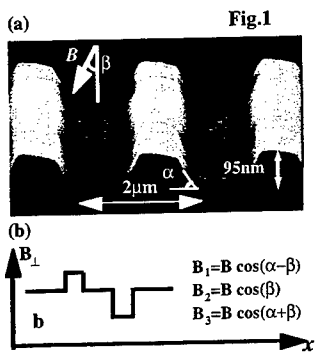

Fig.1

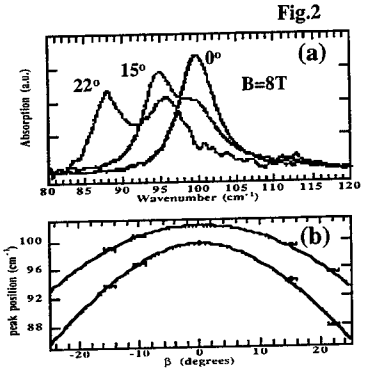

Fig.2

Fig.1 (a) AFM image of the d=2μm sample taken after the epitaxial regrowth. (b) Perpendicular component of the external magnetic field. Fig.2 Absorption spectra measured at various β. Continuous line, dashed line and dotted line show spectra measured respectively at β=0°, 15° and 22°. (b) Peaks position vs. β; dots are experimental points, while continuous lines are the first two lowest modes obtained by calculating the eigenvalues of H given in Eq.3 at various β.

The optical measurements were performed at 3.3K by using a Fourier transform infrared (FTIR) spectrometer and unpolarised radiation. The relative transmission ($-\Delta T/T$), or absorption, was recorded at various B and, in order to change the magnitude of the field modulation, the spectra have also been recorded at various angles β.
The reference sample shows a single CR absorption peak, at frequency $\omega_c=eB\cos\beta/m^*$, corresponding to $m^*=0.071\ m_e$, e being the electronic charge and m_e the free electron mass, as expected for transitions between adjacent Landau levels and in accord with Kohn's theorem [11]. Changing β only produces a shift down in the energy of the absorption peak, confirming that introducing an in plane component of B does not affect the observed CR.
After illumination with band-gap light, Shubnikov de Haas measurements have been recorded by varying B from 0 up to 8T, giving a carrier density of $N_s=4.5\times10^{11}cm^{-2}$. Figure 2(a) shows the absorption measured at B=8T and various β. A single absorption peak is observed at β=0°, at about 100 cm^{-1}. By increasing β, the peak shifts down in energy, and a second peak evolves on its high energy shoulder. The intensity of the high energy peak increases with β and so does the energy separation between the two observed peaks. β=22° is the maximum angle we can use without strongly affecting the quality of the absorption spectra.
Fixing β and decreasing B the relative intensity of the two peaks changes, and, at B<4T, just the low frequency peak is observed, showing that the two modes are coupled together. The separation between the two peaks also decreases with B as shown in Fig.3 (a) for β=15° and in Fig. 3(b) for β=22°.

The coupling between the two peaks clearly shows that they are not simply related to different CR modes on the different facets, but that something more intriguing is going on. In particular, the high energy branch clearly shows a non zero intercept, indicating that it might be related to a MP mode. Indeed, a MP mode could be excited because of the presence of the PMMF shown in Fig. 1(b). In this case, not only is its origin related to the presence of the PMMF, but also its intensity should increase with the strength of the PMMF and so should its degree of coupling to the CR mode.

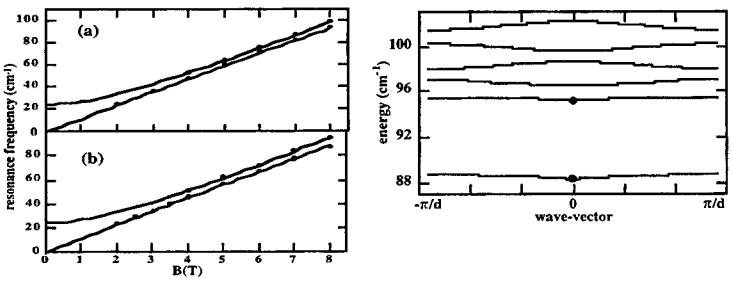

Fig.3 (left) (a) Peak position measured at various B and β=15° and (b) at β=22°. Continuous lines are the first two lowest modes obtained by calculating the eigenvalues of H given in Eq.3 at various B.
Fig.4 (right) Magnetoplasmon band structure at B=8T and β=22°. Dots indicate the two lowest active modes (G=0 and $G=2\pi/d$) observed in the experiments.

To model the MP bandstructure produced by the PMMF we ``flatten" the 2DEG, i.e. we treat the 2DEG as if it were flat, and consider instead the presence of an external periodic magnetic field. In this way we neglect the effect produced by the presence of the in-plane B component in the real measurement, which we know from the flat reference sample does not affect the infrared spectra; we also neglect the contribution from the small regions at the junction between the (100) and the (311)B planes, where B_{perp} changes, and consider $\omega_c(x)=eB_{perp}(x)/m^*$.
In this approximation we can calculate the MP bandstructure by assuming that the PMMF couples together MP modes with wavevectors (q) differing by reciprocal lattice vectors $G_n=n2\pi/d$, n=0,1,2..., shown in Fig. 4. The MP dispersion is given by:

$$\omega_{mp} = \sqrt{\omega_c^2 + \omega_p^2(q)} = \sqrt{\omega_c^2 + \frac{N_s e^2 q}{2\varepsilon\varepsilon_0 m^*}} \qquad (1)$$

where ω_p is the plasma frequency, and ε_0, ε=12.5 are respectively the vacuum and the average dielectric constant of the system embedding the 2DEG. The bandstructure in Fig.4, calculated at β=22°, shows the generation of energy gaps at the edges of the Brillouin zone, and the dots show the two main active mode observed in the infrared spectra. The coupling terms between modes with different q can be determined by considering the Fourier components of the magnetic field modulation at $G=G_i-G_j$, i.e:

$$\Delta_{ij} = \frac{1}{d}\int_d \omega_{mod}(x) e^{i(G_i - G_j)x} dx \qquad (2)$$

where $\omega_{mod}(x)=\omega_c(x)-\omega_{avg}$, $\omega_{avg}=eB_{avg}/m^*$, B_{avg} being the average perpendicular magnetic field. The Hamiltonian (H) of the system, considering all the MP modes coupled together, can be written as:

$$H_{ij} = \omega_{nm}(G_i)\delta_{ij} + \Delta_{ij} \qquad (3)$$

The energy dispersion of the coupled modes are determined by calculating the eigenvalues of H. The continuous lines in Fig. 3(a) and Fig. 3(b) show the ω vs. B dispersion for the lowest two modes, calculated by including the coupling with the MP modes up to $|n|=4$ in Eq.3; inclusion of higher orders modes produces a negligible effect.
We only show the dispersion of the lowest two active MP modes because the intensities of the higher modes are very small, and the only effect they produce is to add a tail on the high frequency side of the absorption spectrum, as clearly showed in Fig.2(a) (see $\beta=22^o$), but without affecting its peak position.
The dependence of the two peaks on the field modulation can also be determined in the same way, by calculating Eq. 3 at various β. Figure 2(b) shows the peaks position vs. β, while the continuous lines are the lowest two modes of Eq. 3 calculated at various β.
It is important to observe that the continuous lines in Fig. 2(b), Fig. 3(a) and Fig. 3(b) do not contain any fit parameter, but rather, all the physical quantities used in the calculation have been determined experimentally (N_s, d, $B_{mod}(x)$, m^*), and the agreement between the calculated curves and the experimental data is excellent.
Energy dispersion calculated at various β and different d also have the same quality of agreement with the experimental data measured at various β and on various samples.
In conclusion, we have reported the first optical measurements of a 2DEG in the presence of an external periodically modulated magnetic field. The absorption spectra show two modes, with relative intensities and separation depending on the intensity of the magnetic modulation, as well as on the total external magnetic field. The two modes have been interpreted as due to MP bandstructure effects--the coupling of MP spatial harmonics in the presence of the magnetic field modulation, with excitation via coupling with the CR-like mode. A MP band structure calculation models all the experimental results, with an excellent degree of agreement.

References

1. S.M. Stewart and C. Zhang, J. Phys. C 8, 6019 (1996).
2. U.J. Gossmann, A. Manolescu and R.R. Gerhardts, Phys. Rev. B 57,1680 (1998).
3. F.M. Peeters and P. Vasilopoulos, Phys. Rev. B 47, 1466 (1993).
4. S. Ibrahim and F.M. Peeters, Phys. Rev. B 52,17321 (1995).
5. M. Leadbeater *et al*, Phys. Rev. B 52, 8629 (1995).
6. P.D. Ye *et al*, Phys. Rev. Lett. 74, 3013 (1995).
7. Q.W. Shi and K.Y. Szeto, Phys. Rev. B 55, 4558 (1997).
8. T.M. Burke *et al*, J. Cryst. Growth, 175/176, 416 (1997).
9. W.I. Wang, E.E. Mendez, T.S. Kuan, L. Esaki, Appl. Phys. Lett., 47, 826 (1985).
10. S.Cina *et al*, Physica B, 249-251} 286 (1998).
11. W. Kohn, Phys. Rev. 123, 1242 (1961).

Semiclassical Transport in a Random Magnetic Field

F.Evers [a,1], A. D. Mirlin [a,2], J. Wilke [b] D. G. Polyakov [b,3] P. Wölfle [b]

[a] *Institut für Theorie der kondensierten Materie, Universität Karlsruhe, 76128 Karlsruhe, Germany*

[b] *Institut für Nanotechnologie, Forschungszentrum Karlsruhe, 76021 Karlsruhe, Germany*

Abstract

We present a theoretical description of the semiclassical kinetics of two-dimensional fermions in a smoothly varying random magnetic field (RMF), with emphasis on the composite-fermion (CF) approach to the half-filled Landau level. We demonstrate that the Drude picture of the CF kinetics is only marginally valid at $\nu = 1/2$ and becomes totally inadequate already at a small deviation from half filling. We show that the non-Markovian character of the transport leads to a strong positive magnetoresistance ρ_{xx} at small $\nu - 1/2$. At larger deviations from $\nu = 1/2$, the positive magnetoresistance is followed by a sharp falloff of ρ_{xx} ("adiabatic localization"). We show that the *ac* conductivity $\sigma_{xx}(\omega)$ in the long-range RMF exhibits distinct non-Drude features. In particular, it has a sharp kink $[\sigma_{xx}(\omega) - \sigma_{xx}(0) \propto |\omega|]$ at zero ω and falls off exponentially at higher ω.

Keywords: Quantum Hall effect, Composite fermions, Localization

There has been much recent interest in the transport properties of two-dimensional (2D) particles moving in a spatially random magnetic field (RMF) $\mathbf{B}(\mathbf{r})$. This interest has been largely motivated by the fractional quantum Hall experiments near half-filling—these probe a disordered composite-fermion (CF) metal [2] subject to a fictituos RMF—and also by experiments with real RMFs in semiconductor heterostructures with superconducting or ferromagnetic overlayers [3–6]. The case of a long-range RMF is particularly interesting since the compressible state in a half-filled Landau level is observed in high-mobility samples where the correlation length of disorder is of the order of the large spacer width d ($k_F d \sim 10$, where k_F is the Fermi wave vector).

The purpose of this paper is to give a brief account of our recent results [9–11] on the semiclassical ($k_F d \gg 1$) kinetics of 2D fermions in a RMF, with particular emphasis on the resistivity in an external (homogeneous) magnetic field $\overline{B} = \langle B(\mathbf{r}) \rangle$ and/or at finite frequency ω. Note that in the CF model a finite $\overline{B} \propto \nu - 1/2$ corresponds to a deviation from half filling $\nu = 1/2$. Our study has found a variety of regimes with very different transport properties, depending on the relative strength B_0 of the random component of $B(\mathbf{r})$ and $\overline{B}$.

At zero $\overline{B}$, the governing parameter is $\alpha = d/R_0$, where R_0 is the Larmor radius in the field B_0. In

[1] Corresponding author. E-mail: fevers@tkm.physik.uni-karlsruhe.de

[2] Also at Petersburg Nuclear Physics Institute, 188350 St. Petersburg, Russia

[3] Also at A. F. Ioffe Physico/Technical Institute, 194021 St. Petersburg, Russia

the weak-scattering limit $\alpha \ll 1$, the conductivity $\sigma_{xx} \propto \alpha^{-2}$ is correctly given by the conventional Drude theory. We have shown, however, that the *ac* conductivity $\sigma_{xx}(\omega)$ exhibits a zero-ω anomaly. By solving a semiclassical Boltzmann equation we find a nonanalytic correction

$$\Delta\sigma_{xx}(\omega) = -\sigma_0 \frac{\pi}{2} \frac{d}{l} |\omega| \tau \,, \qquad (1)$$

where σ_0, l, and τ denote the Drude conductivity, the mean free path, and the scattering time, respectively. Moreover, we have generalized the standard diagramatic method to scattering at impurities with finite range and recover $\sigma_{xx} \propto |\omega|$ also within this method. The nonanalytic frequency structure reflects long time tails in the velocity autocorrelation function $\langle v(t)v(0)\rangle \propto -v_F^2(\tau/t)^2$ familiar from the Lorentz model. As in this case, their physical origin is related to repeated scattering at a single scatterer after an intermediate diffusive motion. In addition to the analytical methods we have employed computer simulations. Here, the dip related to nonanalyticity is seen most clearly in the presence of small magnetic fields and also at larger α (Fig. 1).

Let us emphasize that in the smooth RMF ($k_F d \gg 1$) the anomalous ω-dependent correction (1) exceeds the quantum corrections $\sim (e^2/h) \ln|\omega|\tau$ in a wide range of ω. A similar effect in $\sigma_{xx}(\omega)$ exists in the case of a random potential, but the effect is then weaker by a factor of $(d/l)^2$ as compared to the RMF case. Also the sign is different, so that we find a "tip" rather than the "dip" of RMFs (Fig. 1). We expect that the quasiclassical zero-ω anomaly should be observable experimentally in the CF system.

In the opposite limit of strong scattering ($\alpha \gg 1$) the particle dynamics is no longer chaotic: most particles drift adiabatically along closed contours and are localized in the adiabatic approximation. The conductivity at $\overline{B} = 0$ is determined by a special class of trajectories, the "snake states", which move adibatically along the $B(\mathbf{r}) = 0$ lines and percolate by scattering at saddle points of the RMF (where the adiabaticity of their motion breaks down). The snake-state percolation yields $\sigma_{xx} \propto \alpha^{-1/2} \ln^{1/4} \alpha$.

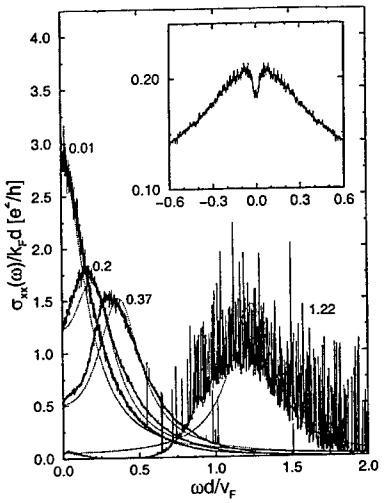

Fig. 1. main: *ac* conductivity at four values of the average magnetic field $\overline{B}$ and $\alpha = 0.2$, which is the value relevant to the case of composite fermions. The dashed lines indicate the conductivity according to Drude. inset: *ac* conductivity at $\overline{B} = 0$ and $\alpha = 4.04$.

We have calculated the magnetoresistivity $\rho_{xx}(\overline{B})$ in the external field $\overline{B}$, by using the Boltzmann-equation approach in the limit $\alpha \ll 1$ and also by means of a computer simulation (Fig. 2). We have found that in a broad range of $\overline{B}$ the non-Markovian character of the transport leads to a strong positive magnetoresistance. Again, this effect is related to returns that can occur in disorder with long range correlations and exists in the case of a smooth random potential as well: in the regime where the guiding center moves less than the distance d within a cyclotron period the magnetic field forces the particle to return back to the same scatterer. It is worth emphasizing that this type of return effect is quite different from the earlier one that leads to the long time tails.

Previously, the real space motion of the particle inbetween two correlated scattering events was diffusive whereas in the present case the corresponding trajectory is close to a cyclotron orbit. The effect is especially pronounced in the case of RMF, where $\rho_{xx}(B)$ with increasing $\overline{B}$ becomes parametrically much larger than its $\overline{B} = 0$ value ρ_0:

$$\rho_{xx}/\rho_0 = 1/2 + [1/4 + (\overline{B}/B_0)^2]^{1/2} . \qquad (2)$$

At $\overline{B}/B_0 \sim \alpha^{-1/3}$ the resistivity reaches its maximum $\rho_{xx} \sim \alpha^{-1/3}\rho_0$; in still higher fields, ρ_{xx} drops rapidly due to the adiabatic character of motion to be discussed below. The numerically found MR (Fig. 2) shows good agreement with the theoretical expectations at $\alpha \ll 0.1$. At $\alpha = 0.2$ it also agrees well with experiment in the regime of $\overline{B}$ where quantum oscillations can be ignored (Fig. 2). Therefore, we believe that our findings explain the positive MR of composite fermions observed experimentally around $\nu = 1/2$.

A strong enough $\overline{B}$ suppresses the diffusive motion by creating a percolation network of drifting cyclotron orbits. This kind of percolation is due only to a weak violation of the adiabaticity of the cyclotron rotation, yielding an exponentially fast drop of the conductivity,

$$-\ln \sigma_{xx} \propto \overline{B}^2 . \qquad (3)$$

Likewise, the positive magnetoresistance at weak field changes sign with increasing $\overline{B}$ and shows a sharp falloff in this regime $\omega_c\tau \gg (l/d)^{2/3}$ [7–9].

At $\alpha \gg 1$, the crossover between the snake-state percolation and the percolation of the drift orbits with increasing $\overline{B}$ has the character of a phase transition (localization of the snake states) smeared exponentially weakly by nonadiabatic effects. The *ac* conductivity also reflects the dynamical properties of particles moving on the fractal percolation network. In particular, it has a sharp kink at zero frequency and a nonanalytic structure

$$\sigma_{xx}(\omega)/\sigma_{xx}(0) \sim \left(\frac{|\omega|L}{v_d}\right)^{3/7} , \qquad (4)$$

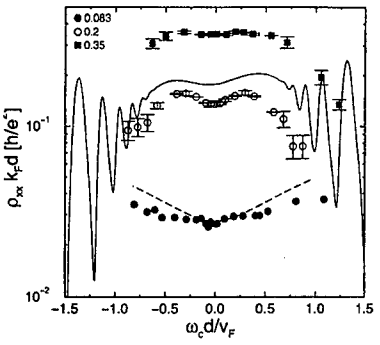

Fig. 2. Magnetoresistivity in a random magnetic field from computer simulations for three different values of the scattering strength α in comparison with experimental data by J. Smet [12]. The x-values of the lowermost data curve have been multiplied by a factor of 10 and the error bars are slightly larger than the symbol size. The dashed line indicates the analytical result valid at $\alpha \ll 1$.

in an intermediate regime (L is the size of a characteristic cell of the percolation network and v_d is the drift velocity along its links). The "fractal" behavior of $\sigma_{xx}(\omega)$ [Eq. (4)] is related to long-time correlations of the percolating dynamics. At higher frequencies, $\sigma_{xx}(\omega)$ starts to drop exponentially (which is a signature of the "ballistic" dynamics of the snake states or drifting orbits on short spatial scales), until it reaches the low-frequency wing of the disorder-broadened cyclotron resonance peak.

We have demonstrated that the quantum magnetooscillations of the conductivity start to develop in the range of $\overline{B}$ where the dimensionless conductivity $g = \sigma_{xx}/(e^2/h)$ drops to a value ~ 1, in agreement with experiment [13]. In contrast to the conventional approach, the magnetooscillations in the case of long-range disorder have nothing to do with those of the total density of states (which are damped by disorder much more strongly), but are determined by the oscillations of the density of states of a small fraction of particles moving along extended trajectories, as well as by the quantum localization effects.

In conclusion, we have demonstrated that the 2D fermion gas shows for weak long-range correlated disorder pronounced deviations from Drude behavior. At moderately strong magnetic fields $1 \ll \omega_c\tau < (l/d)^{2/3}$ it has a strong positive magnetoresistance, due to the non-Markovian character of transport brought about by multiple returns to the same impurity. The effect is especially pronounced in the case of the RMF. Our findings explain, in particular, the positive MR of composite fermions observed experimentally around $\nu = 1/2$. A different kind of return process, leads to a nonanalytic frequency correction to the Drude value even at $\overline{B} = 0$ that we expect to be observable in experiments as well.

Acknowledgement

This work was supported by the SFB 195 der Deutschen Forschungsgemeinschaft and by the INTAS grant No. 97-1342.

References

[1] See, e.g., P.A. Lee and T.V. Ramakrishnan, Rev. Mod. Phys. **57**, 287 (1985); B.L. Altshuler and A.G. Aronov, in *Electron-Electron Interactions in Disordered Systems*, edited by A.L. Efros and M. Pollak, (North-Holland, Amsterdam, 1985).

[2] B.I. Halperin, P.A. Lee, and N. Read, Phys. Rev. B **47**, 7312 (1993).

[3] S.J. Bending, K. von Klitzing, and K. Ploog, Phys. Rev. Lett. **65**, 1060 (1990).

[4] A. Geim, S. Bending, and I. Grigorieva, Phys. Rev. Lett. **69**, 2252 (1992); A. Geim, S. Bending, I. Grigorieva, and M.G. Blamire, Phys. Rev. B **49**, 5749 (1994).

[5] P.D. Ye, D. Weiss, G. Lütjering, R.R. Gerhardts, K. von Klitzing, K. Eberl, H. Nickel, and G. Weimann, in Proc. of the 23rd Int. Conf. on *The Physics of Semiconductors* (World Scientific, Singapore, 1996), p. 1529.

[6] F.B. Mancoff, R.M. Clarke, C.M. Marcus, S.C. Zhang, K. Campman, and A.C. Gossard, Phys. Rev. B **51**, 13269 (1995); L. Zielinski, K. Chaltikian, K. Birnbaum, C.M. Marcus, K. Campman, and A.C. Gossard, Europhys. Lett. **42**, 73 (1998).

[7] M. M. Fogler, A. Yu. Dobin, V. I. Perel, and B. I. Shklovskii, Phys. Rev. B **56**, 6823 (1997).

[8] A.D. Mirlin, D.G. Polyakov, and P. Wölfle, Phys. Rev. Lett. **80**, 2429 (1998).

[9] F. Evers, A.D. Mirlin, D.G. Polyakov, and P. Wölfle, cond-mat/9901070, submitted to Phys. Rev. B.

[10] A.D. Mirlin, J. Wilke, F. Evers, D. G. Polyakov, P. Wölfle, cond-mat/9905364, submitted to Phys. Rev. Lett.

[11] A.D. Mirlin, J. Wilke, F. Evers, D. G. Polyakov, P. Wölfle to be published.

[12] J. H. Smet, V. Umansky (unpublished)

[13] P. T. Coleridge, Z. W. Wasilewski, P. Zawadzki, A. S. Sachrajda, H. A. Carmona, Phys. Rev. B **52**, 11603 (1995).

Scattering of Ballistic Electrons at a Strong Magnetic Protuberance of Submicron Size

S.V. Dubonos[†*], A.K. Geim[†], K.S. Novoselov[†*], J.G.S. Lok[†], J.C. Maan[†] and M. Henini[°]
[†]University of Nijmegen, Toernooiveld 1, 6525 ED Nijmegen, The Netherlands
[*] Institute for Microelectronics Technology, 142432 Chernogolovka, Russia
[°]School of Physics, University of Nottingham, Nottingham NG7 2RD, UK

We have studied ballistic transport of 2D electrons through individual magnetic inhomogeneities of the height up to 1 Tesla and the size down to 100 nm. Such magnetic fields were created by placing dysprosium microtablets on top of a near-surface 2D electron gas (2DEG). The cyclotron orbit for such inhomogeneities becomes smaller than their size and incident electrons are strongly deflected. We report an inversion of the sign of the Hall effect: a positively magnetised micromagnet on top of a 2DEG gives rise to a Hall signal which corresponds to a negative field applied to the 2DEG. This dramatic anomaly is attributed to the fact that 2D electrons are not able to reach the central, strongest part of the magnetic field and, therefore, the dominant contribution to the Hall effect comes from a stray field having the opposite sign.

Electron transport in micro-inhomogeneous magnetic fields continues to attract significant attention that is driven by both the fundamental interest and possible applications for various micro-magnetic sensors and devices. Among a large number of reports on the subject (more than 300 papers during the last decade, according to the ISI database), commensurability oscillations in a periodic magnetic potential have arguably been the highlight of this research [1-3]. Current experimental efforts start to concentrate on the understanding of transport through individual magnetic barriers [4,5]. In this paper, we report an anomalous transport in a 2DEG pierced locally, on a submicron scale, by a magnetic field of about 1 Tesla. The magnetic energy of 2D electrons in such a magnetic protuberance reaches a tenth of their Fermi energy. Semiclassically, incident electrons are turned away before they reach the centre of the magnetic disturbance. This leads to a pronounced suppression of the contribution from the central region to electron transport, which has been clearly observed in our experiment.

We have measured Hall resistance in small ballistic crosses with submicron magnets placed in the cross centre. A micrograph of one of our devices is shown in Figure 1. This is a set of Hall probes with the wire width w of about 1.5 μm. A shallow 2DEG with concentration $n \approx 5 \cdot 10^{15} m^{-2}$ is embedded at a

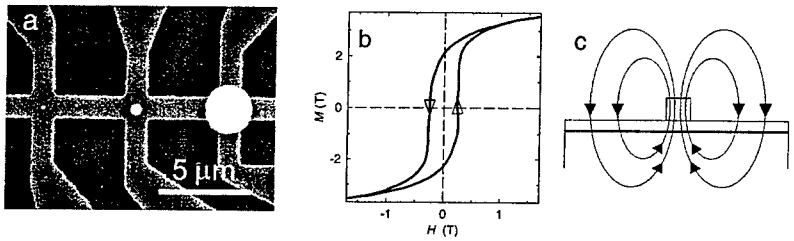

Figure 1. Experimental devices. (a) Micrograph of our ballistic Hall probes with Dy micromagnets deposited in the centre of the crosses; (b) magnetisation loop for the material of our Dy films; (c) schematic view of the distribution of the magnetic flux induced by a micromagnet in a 2DEG.

GaAlAs/GaAs interface located 50 nm below the surface. The initial mobility of the 2DEG heterostructure was ≈100 m^2/Vs. For the final devices, measurements of the nonlocal bend resistance at various separations between the crosses yield the electron mean free path ≈5 μm. Magnetic tablets of

various diameters, D, from 5 μm down to 70 nm and of thickness d of about 0.15 μm were deposited in the centre of Hall crosses. Regarding the magnetic material, we used dysprosium and nickel as well as various superconductors. In this paper, we concentrate on the results obtained for Dy micromagnets. Dy is a material with the highest known saturation magnetisation (≈3.7 T at low temperatures) while Ni and, especially, superconductors create much weaker magnetic disturbances in a 2DEG. Another advantage of Dy is its negligibly small effect on the electrostatics of the 2DEG: we did not notice any difference in electron concentration between the Hall crosses covered with Dy and the empty ones, while in the case of Ni the difference could reach a few per cent. The previously reported Hall measurements on ballistic crosses with Ni and superconducting disks [6,7] serve as a good reference, which allows comparison of the present results with the case of relatively weak magnetic inhomogeneity. In the latter case, the Hall response is simply given by the average magnetic field in the central area of a ballistic cross [6, 8]. As we show below, this is no longer valid for the case of strong inhomogeneities.

Examples of the Hall resistance measured in our devices are plotted in Figure 2. The empty probe exhibits the conventional behaviour for a ballistic Hall cross with slightly rounded corners [9]. The geometry leads to an enhanced Hall coefficient in low magnetic fields which, in our case, is approximately 20% larger than its normal (high-field) value of $1/ne$. The rapid change in the slope occurs at 0.1 T where the cyclotron orbit matches the probe width ($w = 2^{1/2}R_c$, yielding $w \approx 1.6$ μm in our case) [8,9]. Further, the Hall cross totally covered by a 3.4 μm disk also shows the expected behaviour. There is a large anti-clockwise hysteresis due to sweeping of the field between plus and minus 4T. The swaying feature in fields below 0.5T is related to the enhanced Hall coefficient. The Hall cross with a 1.0 μm tablet on top, however, exhibits an astonishing behaviour: the magnetic hysteresis becomes inverted. In low magnetic fields, the hysteresis has the normal anti-clockwise rotation, i.e. the measured field is delayed relative to the external field B due to pinning in the magnetic material (cf. hysteresis for the 3.4 um disk and Fig. 1c). However, in high fields the hysteresis rotation changes to clockwise and, there, the Hall response seemingly leads the external magnetic field. This inversion becomes progressively more pronounced for smaller Dy tablets and, for $D < 0.1$μm, the hysteresis is inverted in all magnetic fields. Note that a magnet itself can never have a clockwise hysteresis as this would mean that the energy can be gained from nowhere by cycling the field.

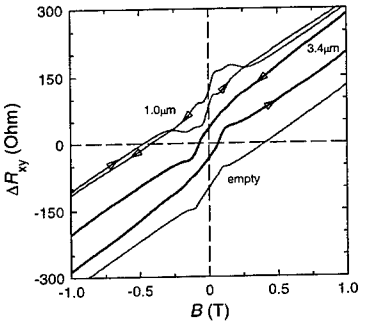

Figure 2. Hall resistance measured in the presence of Dy micromagnets by sweeping external magnetic field B between plus and minus 4 Tesla. In order to resolve fine features in small fields, only a part of the full hysteresis loop is plotted and a linear slope of 1 kOhm/T is subtracted from all the curves. The data for the 1.0 μm disk and the empty device (thin curves) are shifted for clarity by 100 Ohms.

For small micromagnets, the hysteresis in R_{xy} is practically indiscernible on the scale of Fig. 2 and we therefore choose an alternative way to present the corresponding results. Figure 3 plots the difference between Hall resistances for sweeps in different directions, $\delta R_{hyst} = 0.5*[R_{xy}(\text{down}) - R_{xy}(\text{up})]$. This value can be measured very accurately and carries a rather simple physical meaning. It presents the additional Hall signal induced in a 2DEG by a positively magnetised micromagnet, for which the value of the magnetic moment is given by the delay in magnetisation due to hysteresis in the magnet's material. In addition, we have found the same δR_{hyst} by taking the difference between R_{xy} measured for the cases when the micromagnets are magnetised and completely demagnetised. The demagnetised situation is reached by cycling B between its progressively lower absolute values. For demagnetised Dy tablets, R_{xy}

follows exactly the middle line between R_{xy}(down) and R_{xy}(up) curves and the hysteresis remains negligible in applied fields up to 0.4 T.

As a reference, Fig. 3 also shows δR_{hyst} for a Dy micromagnet on top of a diffusive Hall probe, in which case the area under the δR_{hyst} curve is proportional to the energy dissipated during a sweep. For ballistic probes and micromagnets smaller than the probe width, δR_{hyst} is no longer positive. A negative δR_{hyst} explicitly means that, in a particular field, a positively magnetised Dy tablet is somehow seen by the Hall probe as negatively magnetised.

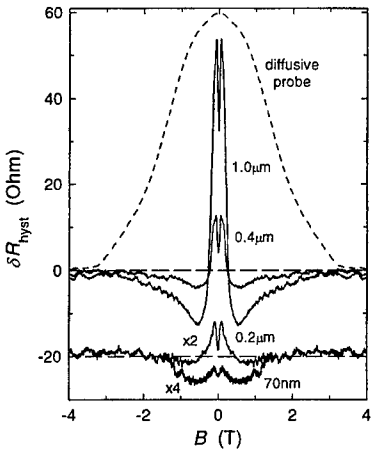

Figure 3. Additional Hall resistivity induced by the presence of a micromagnet. Negative sign of δR_{hyst} means that a clockwise hysteresis is detected in a particular applied field B and that the 2DEG senses the magnetisation direction opposite to the actual one. The curves for the two smallest tablets are shifted and magnified for clarity.

In order to explain the observed behaviour, it is important to understand first how the field distribution and, particularly, its strength change with the size of micromagnets. Figure 1b shows the magnetisation loop for our Dy films. The curve was obtained by measuring Hall response from a small diffusive cross totally covered by a Dy film. Note that the magnetisation curve refers to the internal magnetisation M and the internal field H which are the material's properties and do not depend on geometry. The magnetic field induced in a 2DEG by a magnet made from such a material can be directly calculated from the M-H dependence by taking into account demagnetisation effects and, for the smallest magnets, the finite distance h to the 2DEG. The magnetic field at the disk surface B_D is $B + M^*(1\text{-}N_z)$, and $\mu_0 H = B - M^* N_z$, where B is the applied field and N_z is the demagnetisation factor along the field [10]. Demagnetisation factors for disks and cylinders are extensively tabulated but, for simplicity, one can use $N_z \approx (1\text{-}\pi d/2D)$ if $d << D$, and approximate the smallest disks ($d \approx D$) by a sphere with $N_z = 1/3$. We have verified that B_D under our large disks ($D > 2$ μm) is well described by the M-H dependence of Fig. 1. Furthermore, even for the smallest tablets, we do not observe movements of individual magnetic domains, which indicates that their size in Dy is extremely small [7]. This justifies the use of the macroscopic description for calculations of the field distribution even around submicron Dy magnets. Because of demagnetisation effects, the field induced in the 2DEG by our micromagnets rapidly decreases with increasing their size. For example, from the M-H dependence, we find that, in zero B, the field in the 2DEG underneath micromagnets is ≈0.1 T for a 1.0 μm disk and 0.7 to 0.9 T for the smallest tablets.

Now we can turn to the discussion of the observed reversal of the Hall effect. For magnets with D down to 0.2 μm, δR_{hyst} changes its sign at approximately 0.25 T, i.e. beyond the region of the ballistic transfer, $|B| < 0.1$T, which is marked by the pronounced minimum on the curves of Fig. 3. The origin of the inverted hysteresis in high fields can be explained by considering the field distribution around a micromagnet (Fig. 1c). The field is positive underneath the magnet but negative further away, close to the edges of the 2DEG. In high applied fields, electrons start moving along skipping orbits (and, eventually, along edge states) and the central part of the wire - the one below the micromagnet - may no longer be expected to contribute to electron transport. At the edges, the stray field is negative, which explains the observed sign reversal of δR_{hyst} and, consequently, the clockwise hysteresis in high B. This

explanation agrees with numerical simulations for our experimental geometry [8]. The theory shows that in sufficiently high fields the Hall signal may be insensitive to the absence of magnetic field in the centre of a ballistic cross. The high-field limit is reached when the skipping orbits do not reach the zero-field region [8]. In our samples, the skipping orbits cannot probe underneath the disk centres for $B > 0.2$ T where R_c becomes smaller than $w/2^{3/2}$. This value nicely agrees with the field values in Fig. 3 where the sign reversal tends to start for relatively large disks.

For our smallest Dy tablets, the above explanation does not hold any more. Here, the situation reaches its extreme: even in zero applied field (no skipping orbits), the Hall signal induced by a micromagnet has the sign opposite to the expected one. Nevertheless, the origin of the zero-field reversal is somewhat similar to the one discussed above: the field induced by the smallest magnets is so strong that, also in this situation, electron trajectories are not able to sample the region underneath the magnets. Indeed, for small D, the demagnetisation effects diminish and the field induced in the 2DEG approaches ≈1 Tesla. This corresponds to $R_c \approx 0.1$ μm, i.e. incident electrons turn away before they reach the field centre. Qualitatively, the non-accessibility requires R_c to be smaller than the size of the field protuberance. The latter can be estimated as $D + h$, if D is not smaller than the distance h to the 2DEG. The above non-accessibility condition is met for our micromagnets with $D \leq 0.1$ μm.

The non-accessibility effect also follows from numerical simulations of Peeters *et al* [8] who found the inverted Hall effect for the case of a strong magnetic dipole above a 2DEG. Extrapolating their results to the range of dipole strengths in our experiment, we find a good agreement with the theory: according to the extrapolation, the sign reversal at $B = 0$ can be expected to occur for $D \approx 0.1$ μm. Furthermore, according to the theory, the sampling of the central region under a dipole should be suppressed already for smaller dipole strengths than those required for the sign reversal. Therefore, we attribute the pronounced minima at $|B| < 0.1$T to such initial suppression. Note that the enhanced Hall factor leads to a maximum rather than a minimum in δR_{hyst}, as indeed observed for the ballistic Hall crosses completely covered with Dy.

In conclusion, we find that a strong micromagnet placed on top of a shallow 2DEG can modify electron trajectories so strongly that they no longer reach the region underneath the magnet. In this case, the Hall effect measures the opposite (false) direction for magnetisation of the magnet. In addition, our experiment nicely shows that, in high fields, transport coefficients are determined by the skipping orbits and the bulk contribution to the Hall effect becomes unimportant, in agreement with the edge-state picture for the quantum Hall effect.

Discussions with F. Peeters are gratefully acknowledged.

1. H.A. Carmona *et al*, *Phys. Rev. Lett.* **74**, 3009 (1995).
2. P.D. Ye *et al*, *Phys. Rev. Lett.* **74**, 3013 (1995).
3. A. Nogaret *et al*, *Phys. Rev. B* **55**, R16037 (1997).
4. V. Kubrak *et al*, *Physica B* **258**, 380 (1998).
5. K. Tsubaki, *Physica B* **258**, 392 (1998).
6. A.K. Geim *et al*, *Appl. Rev. Lett.* **71**, 2379 (1997).
7. J.G.S. Lok *et al*, *Phys. Rev. B* **58**, 12201 (1998).
8. F.M. Peeters and X.Q. Li, *Appl. Rev. Lett.* **72**, 572 (1998).
9. C.W.J. Beenakker and H. van Houten in *Semiconductor Heterostructures and Nanostructures, ed.* H. Ehrenreich and D. Turnbull (Academic Press, 1991).
10. W.F. Brown, *Magnetostatic Principles in Ferromagnetism* (North-Holland, Amsterdam 1962).

TRANSPORT PROPERTIES OF A TWO DIMENSIONAL ELECTRON GAS DUE TO A SPATIALLY RANDOM MAGNETIC FIELD.

A.W. Rushforth[a*], B.L. Gallagher[a], P.C. Main[a], A.C. Neumann[a], C.H. Marrows[b], I. Zoller[b], M.A. Howson[b], B.J. Hickey[b], M. Henini[a].

[a]*School of Physics and Astronomy, University of Nottingham, University Park, Nottingham NG7 2RD, UK.*
[b]*Department of Physics, University of Leeds, Leeds LS2 9JT, UK.*

Abstract

We have studied the magnetoresistance of a near-surface two dimensional electron gas (2DEG) in the presence of a random magnetic field produced by CoPd multilayers deposited onto the surface of the heterostructure. This novel method allows us to switch the random field on and off by applying an external magnetic field and also to control the amplitude and correlation length of the random field by varying the growth parameters of the multilayers. The presence of the random field is confirmed by quenching of the Shubnikov de Haas oscillations and we see an enhanced magnetoresistance which can be interpreted semi-classically. We also observe other unusual features which may be quantum in origin.

Keywords: Random magnetic field, CoPd multilayers, Hybrid devices, Magnetoresistance.
PACS: 72.20.My, 73.50.Jt, 75.70-i

The properties of a two dimensional electron gas (2DEG) in the presence of a spatially random magnetic field has attracted great theoretical interest and has relevance for the study of composite fermions [1]. Recently there have been several experimental realisations of a random magnetic field at the site of a 2DEG [2-6].

We present here a new method for producing a large amplitude random magnetic field with a correlation length much smaller than the electron mean free path. This method involves depositing CoPd multilayers onto the surface of a heterostructure containing a high mobility, near-surface 2DEG. These multilayers have the property that, at certain points in the magnetization loops, maze-like domain patterns form, magnetized perpendicular to the plane of the multilayers (Figure 1a). The domains, which are of the order of 100-500nm in size, produce a random magnetic field at the plane of the 2DEG. By varying the growth parameters during deposition of the multilayers, we are able to control the size of the domains and the part of the magnetization loop where the random pattern forms. We therefore have control over the correlation length of the random magnetic field and we can turn the random field on or off by the application of an external magnetic field.

Our samples consist of a $GaAs/Al_xGa_{1-x}As$ heterostructure containing a 2DEG 35nm below the surface. At 4.2K the electron density, $n=4 \times 10^{15} m^{-2}$ and the mobility, $\mu=70 m^2V^{-1}s^{-1}$ corresponding to a mean free path, $\Lambda=7\mu m$. The device geometry is a modified Van der Pauw arrangement with a 1mm square of the metal multilayers deposited over the central region (Figure 1b). This ensures that the voltage probes are a long way inside the area covered by

* Corresponding author. Fax +44 115 9515180: e-mail: ppxawr@hermes.nottingham.ac.uk

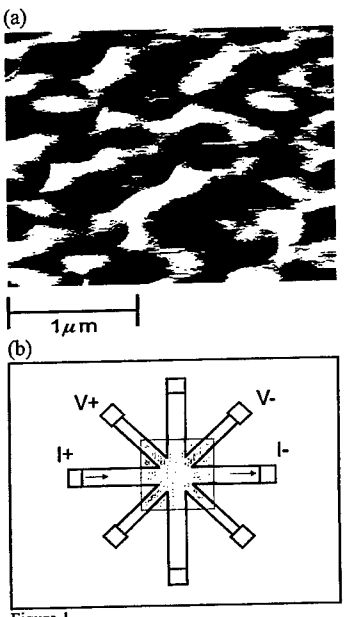

Figure 1.
(a) Magnetic force microscope image of the CoPd multilayers from sample S2 in zero external field.
(b) Device geometry. The shaded region represents the CoPd multilayer film. The arrows represent the direction of the current.

the multilayers so that we are only measuring the properties of electrons which are influenced by the random magnetic field. We measure the resistance of the device with the external field applied perpendicular to the plane of the 2DEG and the multilayers. The CoPd multilayers are deposited using dc magnetron sputtering. We present here results for two devices (S1&S2). S1 consists of 15 bilayers with a Co layer thickness of 1.7Å and a Pd layer thickness of 5Å deposited at an argon pressure of 15mTorr. S2 consists of 200 bilayers with a Co layer thickness of 4.75Å and a Pd layer thickness of 14.25Å

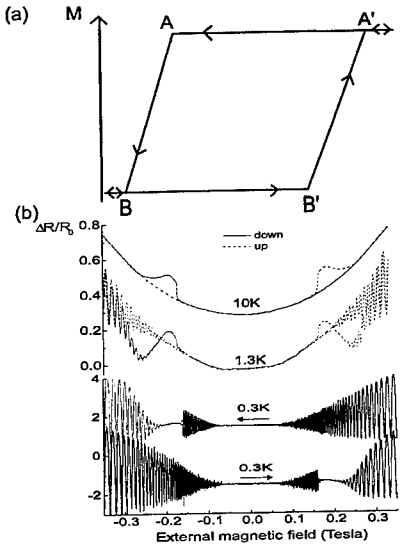

Figure 2 :
(a) Schematic diagram of the square hysteresis loop of sample S1. The random domain configuration is present between B' and A' on the up sweep and A and B on the down sweep.
(b) Observed magnetoresistance of sample S1 at 10K, 1.3K and 0.3K. Curves are offset for clarity. ΔR is the change in resistance from R_0, where R_0 is the resistance at zero external field. The magnetoresistance features between 0.15T and 0.3T (sweep up) and -0.15T and -0.3T (sweep down) are correlated with the region where the random domain configuration is present.

deposited at an argon pressure of 3mTorr.

Figure 2a shows a schematic diagram of the hysteresis loop for the multilayers in S1. These multilayers are known to have a large area hysteresis loop [7]. As the external magnetic field is swept up from a large negative field the magnetization remains constant past point B until the random domain configuration starts to form at point B'. The random field persists until the magnetization is saturated at point A' at which point the magnetization is again

uniform and the random field is turned off [8]. The same behaviour is observed as the external field is swept down from a large positive field with the random field existing between points A and B. Figure 2b shows the longitudinal resistance measured at several temperatures as the external field is cycled through the full hysteresis loop of the multilayers. The bottom curve shows the resistance at 0.3K as the field is swept from -0.35T to +0.35T (through points BB'A' in Figure 2a). Between -0.35T and +0.17T the Shubnikov de Haas oscillations are as expected for a 2DEG in the presence of a uniform magnetic field. This is consistent with the magnetization of the multilayers being saturated between B and B'. At +0.17T we see a dramatic quenching of the Shubnikov de Haas oscillations as the random field forms at B'. This occurs because the random magnetic field causes smearing of the Landau levels. The Shubnikov de Haas oscillations slowly recover as the field is increased between +0.2T and +0.3T until the magnetization of the multilayers saturates again at point A'. The same features are seen as the field is swept from +0.35T to -0.35T (through points A'AB in Figure 2a). The Shubnikov de Haas oscillations at 0.3K hide certain features which are seen more clearly at higher temperatures. The curves at 1.3K and 10K both show an enhanced resistance at the point where the random magnetic field forms followed by a return to lower resistance as the multilayers return to a uniform magnetization. At 1.3K we observe a negative magnetoresistance following the initial increase in resistance. This feature is not observed at 10K indicating that it may be quantum in origin. We have confirmed that the temperature dependence of the magnetoresistance feature is due to the electrons and not the multilayers by performing the experiment at 1.3K and increasing the current through the 2DEG. The feature disappears when the current reaches 30μA and the corresponding electron temperature is above 10K.

Figure 3a shows a schematic hysteresis loop for the multilayers of sample S2. This narrow hysteresis loop is known to exist for multilayers sputtered at a low argon pressure [9,10]. The random domain configuration forms at point B as the field is swept up from a large negative field. The random configuration persists until the magnetization of the multilayers is saturated at A' when the magnetization is again uniform. Magnetic Force Microscopy images at zero external field confirm that the domain sizes are approximately 500nm (Figure 1a). Figure 3b shows the longitudinal resistance measured at 4.2K as the external field is cycled through a full hysteresis loop of the multilayers. As the external field is swept up from -0.5T we observe a sharp increase in resistance at -0.33T which correlates with the random field switching on at point B. This increase in resistance is larger than that seen in sample S1, which is reasonable since the multilayers in S1 are thinner and so will produce a smaller amplitude random magnetic field. As the external field is swept from B to A' the magnetoresistance decreases as the multilayers return to a uniform magnetization. An additional resistance peak is observed at +0.38T just before the magnetization of the multilayers saturates. The origin of this feature is not clear, but we note that it occurs at a point where the cyclotron diameter is roughly commensurate with the domain size measured at zero external field. We observe identical features as the external field is swept down from +0.5T (through points A'AB' in Figure 3a). We have carried out computer simulations in an

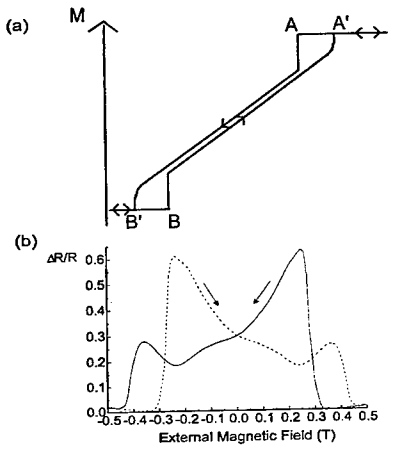

Figure 3 :
(a) Schematic diagram of the narrow hysteresis loop of sample S2. The random domain configuration is present between B and A' on the up sweep and A and B' on the down sweep.
(b) Magnetoresistance measurements at 4.2K. ΔR is the change in resistance from R, where R is the lowest resistance point measured when the domains have a uniform configuration. Solid line is for the external field sweeping down. Dashed line is for the field sweeping up. The observed increase in resistance is correlated with the formation of the random domain pattern.

attempt to interpret the enhanced resistance seen in S2 when the random field is switched on. To do this we calculated the field profile which would be seen at the 2DEG due to a random pattern of square slabs of side 500nm and thickness equal to that of the multilayers. This pattern had an rms field amplitude of 0.122T. We then calculated the trajectories of electrons at the Fermi energy in this field pattern and used the Kubo formalism to calculate the magnetoresistance. Our calculations yield $\Delta R/R=117\%$ which compares with the experimental value of 60% when the random field switches on. This indicates that the enhanced magnetoresistance in the presence of a random field is consistent with a semi-classical reduction of the electron diffusivities.

In summary, we have used CoPd multilayers as a novel method for producing a large amplitude, small correlation length random magnetic field at the level of a 2DEG. This method enables us to control the correlation length of the random field and we can switch the random field on and off by applying an external magnetic field. The random magnetic field leads to a quenching of the Shubnikov de Haas oscillations and causes an enhanced magnetoresistance which we interpret semi-classically. We also observe additional features which may be quantum in origin.

Acknowledgements

We gratefully acknowledge funding by the EPSRC (UK) and the ESPRIT SPIDER programme (EU).

References

[1] A.D. Mirlin, D.G. Polyakov, and P. Wölfe, Phys. Rev. Lett. 80, 2429 (1998).
[2] F.B. Mancoff et al, Phys. Rev. B. 51, 13269 (1995).
[3] A. Smith et al, Phys. Rev. B. 50, 14726 (1994)
[4] P.D. Ye et al, Proceedings of the 23rd International Conference on the Physics of Semiconductors, eds Scheffer & Zimmermann (World Scientific Publishing) p 1537.
[5] A.K. Geim, S.J. Bending, and I.V. Grigorieva, Phys. Rev. Lett. 69, 2252 (1992)
[6] G.M. Gusev et al, Phys. Rev. B. 59, 5711 (1999)
[7] S.N. Piramanayagam et al, IEEE Transactions on Magnetics, 33, 3247 (1997).
[8] Sug-Bong Choe and Sung-Chul Shin, Phys. Rev. B. 57, 1085 (1998).
[9] S. Hashimoto, Y. Ochiai, and K. Aso, J. Appl. Phys. 66, 4909 (1989).
[10] J.R. Barnes et al, J. Appl. Phys. 76, 2974 (1994)

PB.6

Longitudinal and Hall resistance induced by large-amplitude magnetic barriers

V. Kubrak [a], A. C. Neumann [a], B. L. Gallagher [a], P. C. Main [a], M. Henini [a], C. H. Marrows [b] and M. A. Howson [b]

[a] *School of Physics and Astronomy, University of Nottingham, Nottingham NG7 2RD, UK*

[b] *Department of Physics and Astronomy, University of Leeds, Leeds LS2 9JT, UK*

Abstract

We study the longitudinal and Hall resistances of a two-dimensional electron gas subjected to a magnetic barrier generated by a ferromagnetic element on the surface of the device. The barrier amplitude is varied by applying an in-plane external field, allowing us to investigate the two regimes in which the transmission through the magnetic barrier is either classically allowed or forbidden in the absence of scattering. We compare how the longitudinal and the Hall resistance depend on the barrier amplitude. The temperature dependence of the longitudinal resistance is qualitatively different in the allowed and forbidden regimes, indicating a change-over from ballistic to scattering-assisted transmission through the barrier.

Hybrid ferromagnet-semiconductor devices have potential applications as magnetic field sensors, magnetic memory elements and magnetometers. One class of devices consists of a ferromagnetic element on the surface of a semiconductor heterostructure with a near-surface two-dimensional electron gas (2DEG). We have recently shown that the stray field from a single sub-micron cobalt line acts as a barrier to the electrons in the 2DEG and can cause an increase in the longitudinal resistance R_{xx} [1]. This effect was used to infer the magnetic hysteresis loop of the line, which cannot be measured by conventional magnetometry because the total magnetic moment is too small. Here, we investigate a magnetic barrier device of the same type as ref. [2] in which a thin, rectangular magnetic element is placed on a standard Hall bar such that one edge of the element coincides with a pair of voltage probes (fig. 1a). The stray field of the element induces a Hall resistance R_{xy} for this lead pair, the polarity of which depends on whether the element's magnetization is parallel or antiparallel to the x axis. The device can therefore be used as a Hall magnetometer or magnetic memory element[2]. In this paper, we investigate the effect of the stray field on R_{xx} as well as R_{xy} and extend the previous studies [1,2] from the regime in which transmission through the magnetic barrier is classically allowed to the regime in which transmission is classically forbidden in the absence of scattering. In the latter regime, an electron can only traverse the barrier if it undergoes scattering within the barrier, tunnels through the barrier, or skips along the

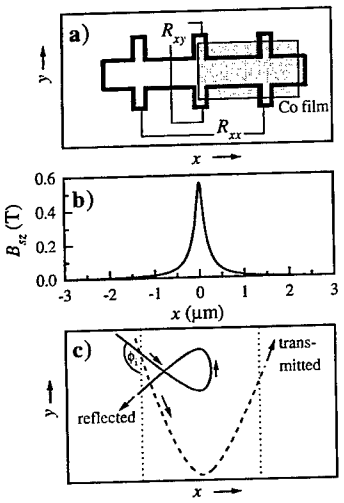

Fig. 1. (a) Schematic sketch of the device, (b) field profile at the 2DEG due to the stray field of the Co element, and (c) schematic sketch of transmitted and reflected orbits.

device edge.

Our devices are made by depositing a 300 nm thick Co element of length 135 μm in the current direction and width 200 μm on top of a Hall bar with a 2DEG formed at a GaAs-AlAs hetero-junction 50 nm below the surface. The 2DEG has an electron density of 4.2×10^{15} m^{-2}, a mobility of 60 m^{2}V^{-1}s^{-1} and a mean free path of 6.4 μm at $T = 1.3$ K. The Hall bar is 15 μm wide, and the separation between pairs of voltage probes is 40 μm. In sample A, one edge of the Co element is aligned with a pair of voltage probes (fig. 1a). Sample B has the Co element shifted along x so that the edge is between two pairs of voltage probes. The magnetization M of the element lies in the x-y plane, but the stray field from the magnet can result in a large-amplitude (up to 0.55 T), peak-shaped perpendicular magnetic field $B_{sz}(x)$ at the 2DEG. This field profile is maximum underneath the edge of the element and decays rapidly over a distance of a few hundred nanometres. The height of the peak is proportional to the x-component of M. By sweeping an external magnetic field applied in the x direction, it is possible to change M_x continuously between $+M_{\rm sat}$ and $-M_{\rm sat}$, where $M_{\rm sat}$ is the saturation magnetization, and thereby vary the amplitude and the sign of the inhomogeneous field profile that the 2DEG experiences. Figure 1b shows $B_{sz}(x)$ for $M_x = M_{\rm sat}$.

The inhomogeneous magnetic field changes the electron trajectories and effectively acts as a barrier. A ballistic electron entering the barrier region from the left hand side at angle ϕ_i ($0 < \phi_i < \pi$) to the y axis will be deflected by the Lorentz force and either exit the barrier on the right hand side at angle $0 < \phi_f < \phi_i$ if ϕ_i exceeds the critical angle ϕ_c, or be reflected by the barrier with $\phi_f = -\phi_i$ if $\phi_i < \phi_c$ (see fig. 1c). The critical angle is given by $\phi_c = \arccos(1 - e\Phi m^{-1} v^{-1})$, where v is the electron velocity and Φ is the integrated magnetic flux of the barrier, $\Phi = \int B_{sz}(x)\,dx$. If $\phi_c < \pi$, ballistic transmission is allowed, below referred to as the "transparent" regime. The conductance through the barrier decreases with increasing amplitude of the barrier as fewer and fewer electrons are transmitted. If the argument of the arccos becomes smaller than -1, all electrons are reflected and the semiclassical ballistic conductance equals zero, referred to as the "opaque" regime. The measured conductance, however, may remain finite due to scattering-aided trasmission, tunneling, or edge-channel transmission. To our knowledge, opaque magnetic barriers have so far been investigated only for barrier widths comparable to the electron mean free

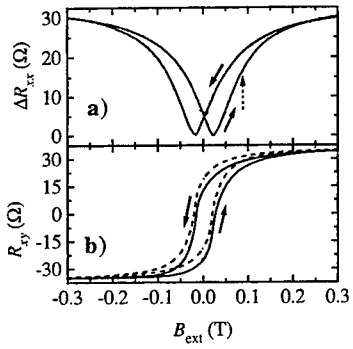

Fig. 2. Longitudinal resistance R_{xx} (a) and Hall resistance R_{xy} (b) hysteresis loops versus applied field. In (b), the full line shows the data shifted by -11Ω and the broken line shows the symmetrized curve. The dotted arrow is explained in the text.

path[3]. In contrast, our barrier width (260 nm FWHM) is much smaller than the mean free path and ballistic transmission is possible when the barrier amplitude is small.

Figure 2 shows the measured longitudinal and Hall resistance of sample A at $T = 1.3$ K for a full sweep through the hysteresis loop of the magnetic element. Sweeping the external field B_{ext} from -0.4 T to $+0.4$ T, the longitudinal resistance R_{xx} reduces from its maximum value (for $M_x = -M_{\text{sat}}$) to its minimum at the coercive field of the Co element ($M_x = 0$) and then rises back to the maximum value when M_x reaches $+M_{\text{sat}}$. The same behaviour is found for sample B. Although the change in R_{xx} may not seem large compared to the resistance per square of the 2DEG ($R_\square = 25\Omega$), the relative resistance change in the barrier region is greater than 10 since the barrier is much narrower than the width of the Hall bar. For the same sweep of B_{ext} from -0.4 to $+0.4$ T, the Hall resistance R_{xy} (fig. 2b) changes from a negative to a positive value, its total change being of similar magnitude to that of R_{xx}. Note that R_{xy} is noticeably asymmetric about $B_{\text{ext}} = 0$ and consequently does *not* represent accurately the hysteresis curve $M_x(B_{\text{ext}})$ of the Co element. This arises because, in this sample, R_{xy} has a considerable amount of the longitudinal resistance change ΔR_{xx} mixed in, which is symmetric rather than antisymmetric in M_x. However, it is possible to symmetrize the R_{xy} hysteresis loop under the assumption that $M_x(B_{\text{ext}})$ has the usual symmetry property, $M_x(B_{\text{ext}})|_{\text{sweep up}} = -M_x(-B_{\text{ext}})|_{\text{sweep down}}$. The symmetrized R_{xy} curve is also shown in figure 2b. The difference between this curve and the raw data shows that care must be taken if the Hall resistance is to be used as a magnetometer for an element on the surface of the device.

It is often assumed that R_{xy} is proportional to the *average* magnetic field in the Hall cross[2]. Whilst this is believed to be valid in the ballistic case if most electrons are transmitted, theory suggests it is not a good approximation if the transport is diffusive[4]. If we make this assumption and calculate the value of M_x at which the cross-over between the transparent and the opaque regime occurs ($\phi_c = \pi$), we obtain a cross-over at $R_{xy} \approx 29\Omega$ and $B_{\text{ext}} \approx 90$ mT for the sweep in positive field direction. This cross-over point is indicated by dotted arrows in figures 2 to 4.

A comparison of the changes in R_{xx} and R_{xy} just before they saturate at large B_{ext} reveals that the longitudinal resistance is much more sensitive to small changes in the integrated barrier flux Φ than the Hall resistance in this range. This can be seen more clearly if the symmetrized ΔR_{xx} is plotted versus the symmetrized R_{xy} (fig. 3). In the transparent regime (at small B_{ext}), ΔR_{xx} increases approximately quadratically with

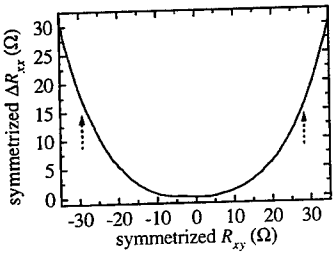

Fig. 3. Longitudinal resistance change ΔR_{xx} versus R_{xy} of sample A after both have been symmetrized (see text).

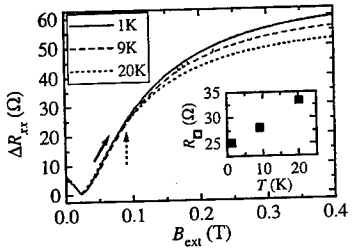

Fig. 4. Longitudinal resistance change versus applied field for different temperatures. The inset shows the temperature dependence of the resistance per square.

R_{xy}, which itself is proportional to Φ. In the opaque regime, ΔR_{xx} has a stronger dependence on R_{xy}. We believe that this is mainly due to a rapid additional increase of ΔR_{xx} in the opaque regime, but a change in the relationship between R_{xy} and Φ could also contribute.

Clear evidence for a qualitative difference in the behaviour of the longitudinal resistance between the transparent and the opaque regime is observed in its temperature dependence. Figure 4 shows a section of the $\Delta R_{xx}(B_{\rm ext})$ hysteresis loop of sample B for three temperatures between 1 and 20 K. In the transparent regime at low $B_{\rm ext}$, $\Delta R_{xx}(B_{\rm ext})$ is temperature independent although the total resistance increases significantly with temperature (see inset). This shows that the transmission through the barrier is ballistic in the transparent regime. However, ΔR_{xx} decreases with increasing temperature at large $B_{\rm ext}$. This is what we expect in the opaque regime if the transmission through the barrier is accomplished by scattering within the barrier, as the scattering rate increases with temperature. For much higher temperatures, the mean free path of the electrons eventually becomes shorter than the barrier width, and ΔR_{xx} is significantly reduced for any applied field.

In summary, we have shown that a large-amplitude magnetic barrier generated by the stray field from a ferromagnetic element on the surface of a GaAS-AlAs Hall bar induces a Hall resistance and a longitudinal resistance change of similar magnitudes in the 2DEG. At low temperatures, the transmission through the barrier is ballistic when the barrier is transparent and scattering-assisted when the barrier is opaque.

We gratefully acknowledge financial support by the EPSRC (UK) and the ESPRIT MEL/ARI SPIDER programme (EU).

References

[1] V. Kubrak et al., Appl. Phys. Lett. **74**, 2507 (1999).

[2] M. Johnson et al., Appl. Phys. Lett. **71**, 974 (1997).

[3] M. L. Leadbeater et al., Phys. Rev. B **52**, 8629 (1995).

[4] J. Reijniers, F. M. Peeters, Appl. Phys. Lett. **73**, 357 (1998).

PB.7

The Hall resistivity of a two-dimensional electron gas in the presence of magnetic clusters with perpendicular magnetization

J. Reijniers [a], F. M. Peeters [a], and A. Matulis [b]

[a] *Departement Natuurkunde, Universiteit Antwerpen (UIA), B-2610 Antwerpen*

[b] *Semiconductor Physics Institute, Goštauto 11, 2600 Vilnius, Lithuania*

Abstract

The Hall and longitudinal resistivity of a two-dimensional electron gas (2DEG) situated a small distance from a random distribution of identical perpendicular magnetized ferromagnetic clusters is studied. The magnetic clusters are modelled by thin magnetic disks. The electrons in the 2DEG are scattered by the magnetic field profiles as created by the magnetic clusters. Although the average magnetic field is zero, we find a nonzero Hall resistivity, which increases with k_F, for small Fermi energies, but which tends to zero for higher energies. We find resonances in both the Hall and the longitudinal resistivity as function of the Fermi wave vector, which can be assigned to quasi-bound states under the disks.

Key words: Hall resistivity, magnetic clusters, two-dimensional electron gas

1 Introduction

Over the last decade the two-dimensional electron gas (2DEG) has been exposed to a wide range of physical experiments, in which the electrons have been perturbed by different configurations of electrostatic potentials, with or without a homogeneous perpendicular magnetic field. More recently, there has been increasing interest in systems where the 2DEG is subjected to an inhomogeneous perpendicular magnetic field. In such systems the inhomogeneities in the magnetic field act as scattering centers for the 2DEG. Smith *et al.* [1] studied the transport properties of a 2DEG subjected to the random magnetic field profile created by depositing superconducting grains on top of a heterojunction. Another way of creating a random inhomogeneous magnetic field is by growing a superconducting type II film on top of a heterostructure [2]. Brey *et al.*,[3] and also Nielsen and Hedegård [4] studied the scattering on

vortices, the magnetic inhomogeneities that arise when an external magnetic field is applied. We consider a system in which electrons are scattered by a random array of identical circular magnetic field profiles, which are created by means of magnetic clusters located a distance z from the 2DEG.[5] Such a system was realized by Ye *et al.*,[6] who deposited Dy micromagnets on top of a GaAs/AlGaAs heterostructure. This problem is essentially different from the earlier problems, since in the present case the average magnetic field strength is zero.

2 Theoretical approach

We rely on a semi-classical theory where we assume the average distance between the clusters sufficiently large, so we can neglect interference from multiple scattering events. We solved the (classical) Boltzmann equation, linearized in the external electric field

$$e\mathbf{E}\frac{\partial f_0}{\partial \mathbf{k}} = e\frac{\partial f_0}{\partial \epsilon}\mathbf{k}\cdot\mathbf{E} = n_0\frac{\hbar^2}{ma^3}\frac{L^2}{(2\pi)^2}\int d^2\mathbf{k}'\left[w(\mathbf{k}',\mathbf{k})f(\mathbf{k}') - w(\mathbf{k},\mathbf{k}')f(\mathbf{k})\right],$$

with $w(\mathbf{k},\mathbf{k}')$ the scattering probability for scattering on the stray field of a single magnetic cluster, which is calculated quantum mechanically. n_0 is the density of disks, f_0 is the equilibrium electron distribution function, and $f(\mathbf{k})$ is the perturbation on this distribution due to the presence of the magnetic clusters. For cylindrical symmetric scatterers this results in the following longitudinal (R_{xx}) and Hall resistivity (R_H)

$$R_{xx} = \frac{n_0}{n_e}\frac{\hbar}{e^2}\sum_{m=-\infty}^{\infty} 2\sin^2\left(\delta_m - \delta_{m+1}\right), \tag{1}$$

$$R_H = \frac{n_0}{n_e}\frac{\hbar}{e^2}\sum_{m=-\infty}^{\infty} \sin[2(\delta_m - \delta_{m+1})], \tag{2}$$

where δ_m are the phase shifts of the partial wave with angular momentum $\hbar m$. The phase shifts are calculated by solving the Schrödinger equation numerically, where the inhomogeneous magnetic field profile enters the problem as the nontrivial vector potential $V_m(r) = \left[m/r - \gamma a(r)\right]^2/2$ in the Hamiltonian. $a(r)$ is the dimensionless vectorpotential and $\gamma = eM_0/\hbar cR$ is the dimensionless parameter which characterizes the magnetic strength, where M_0 is the magnetization of the cluster and R is the radius of the magnetic disk. Magnetic field strength, energy and resistivity are expressed in $B_0 = c\hbar/eR^2$, $E_0 = V_0 = \hbar^2/mR^2$, and $R_0 = (n_0/n_e)(\hbar/e^2)$, respectively. The magnetic field profile resulting from a magnetic disk (see inset of Fig. 1) is shown in

Fig. 1 for various z, the distance from the disks to the 2DEG. The effective potential is shown in Fig. 2.

3 Results and discussion

The Schrödinger equation with the scattering potentials depicted in Fig. 2 was solved numerically from which we obtain the phase shifts δ_m as function of the energy of the scattered electron. This result was inserted into Eqs. (1) and (2). In the latter equations, the sum over the angular momentum m converged very slowly. By calculating this sum as function of m_{max}, we found that for large values of m_{max} (typically $m_{max} > 150$) it can be very accurately fitted to $\alpha + \beta/m_{max}^2$, from which we determined the $m_{max} \to \infty$ result.

Although the average magnetic field is zero, we find a nonzero Hall resistivity, which increases with k_F, for small Fermi energies ($E_F = \hbar^2 k_F^2/2m$), but which tends to zero for higher energies. The magnitude of the longitudinal and Hall resistivity strongly depends on the magnetic strength γ and z, the distance from the clusters to the 2DEG as is apparent from Figs. 3 and 4. We also find resonances in both the Hall and the longitudinal resistivity as function of the Fermi wave vector, which are more pronounced for decreasing z. These resonances in R_H and R_{xx} are a consequence of quasi-bound electron states which are formed in the non-homogeneous magnetic field profiles, and so electrons are trapped underneath the magnetic disk. The magnetic field produced by the magnetic disks in the 2DEG have an inner (outer) core where the perpendicular B component is directed upward (downward). For small k_F-values

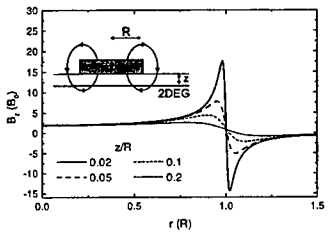

Fig. 1. The perpendicular magnetic field component of the strayfield of a magnetic disk with perpendicular magnetization as funtion of the radial distance to the center, for various distances z to the 2DEG. The inset shows the side-view of the configuration.

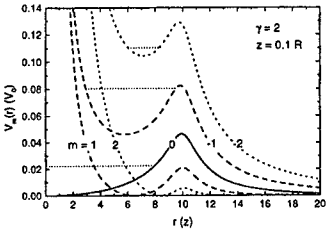

Fig. 2. The partial effective potential $V_m(r)$ of a magnetic disk with $\gamma = 2$ at a distance $z = 0.1R$ from the 2DEG for different values of m. The thin dotted lines correspond to the positions of the quasi-bound states.

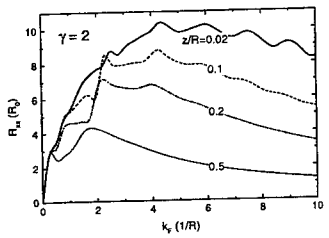

Fig. 3. Longitudinal resistivity of a 2DEG subjected to the stray field of a random array of magnetic disks with $\gamma = 2$ for various z.

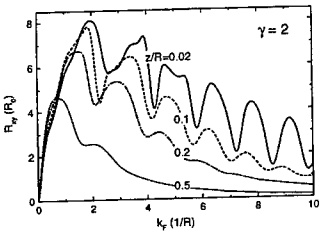

Fig. 4. The same as Fig. 3, but now for the Hall resistivity.

only the outer region is sampled by the electrons and the average magnetic field felt by the electrons is nonzero. With increasing k_F the electrons will also start to feel the inner region, which reduces the average magnetic field felt by the electrons and consequently reduces R_H. At resonance the electrons spend a longer time in the inner core, thus R_{xx} increases, which is visible as local maxima in Fig. 3. These quasi-bound states tend to localize the electrons, so they inhibit piling up of a Hall voltage, and consequently R_H reduces strongly, leading to the dips in the curves of Fig. 4. Experimentally, the predicted oscillatory behavior in R_H and R_{xx} can be measured by e.g. changing the strength of the magnetization of the disks at zero external magnetic field.

Acknowledgments: Part of this work is supported by IMEC, FWO-Vl, and IUAP. J. R. is supported by IWT and F.M.P. is a research director with the FWO-Vl.

References

[1] A. Smith, R. Taboryski, L. T. Hansen, C. B. Sørensen, P. Hedegård, and P. E. Lindelof, Phys. Rev. B **50**, 14726 (1994).

[2] A. K. Geim, JETP Lett. **50**, 389 (1989).

[3] L. Brey and H. A. Fertig, Phys. Rev. B **47**,15961 (1993).

[4] M. Nielsen and P. Hedegård, Phys. Rev. B **51**, 7679 (1995).

[5] F. M. Peeters, A. Matulis, and I. S. Ibrahim, Physica B **227**, 131 (1996).

[6] P. D. Ye, D. Weiss, G. Luthering, R. R. Gerhardts, K. Von Klitzing, K. Eberl, H. Nickel and G. Weimann, 23rd Int. Conf. on the Physics of Semiconductors (World Scientific, Singapore, 1997), p. 1529.

Composite Fermions in a weakly density modulated 2DEG: Direct evidence of a periodic magnetic field around $\nu = ½$

S. Jobst[1], S. Zwerschke[2], J.H. Smet[2], R.R. Gerhardts[2], D. Weiss[1], K. v. Klitzing[2], V. Umansky[3]

[1]Universität Regensburg, D-93040 Regensburg, Germany
[2]Max-Planck-Institut für Festkörperforschung, Heisenbergstraße 1, D-70569 Stuttgart, Germany
[3]Braun Center for Submicron Research, Weizmann Institute of Science, Rehovot 76100, Israel

We investigate the magnetoresistance of a weakly density modulated high mobility two-dimensional electron system around filling factor $\nu = ½$. The density modulation with periods a between 300 nm and 500 nm was generated by in-situ interferometric illumination. At low B we found commensurability oscillations of the magnetoresistance characteristic for transport in *weak electrostatic* potentials with minima positions on the magnetic field axis given by $2R_C = (\lambda\text{-}1/4)a$. Here $2R_C$ is the electron cyclotron diameter at the Fermi-energy and λ an integer. In contrast we find clear *magnetic commensurability* features around filling factor $\nu = ½$ with a pronounced minimum for a Composite Fermion cyclotron radius $R_{C,CF}$ matching $1.25a$. This gives direct evidence that the density modulation results in a modulated effective magnetic field for Composite Fermions. The experimental ρ_{xx}-traces around $\nu = ½$ are well described by novel model calculations, based on a semiclassical solution of the Boltzmann equation, taking into account anisotropic scattering.

Composite Fermions (CF), consisting of an electron with two flux quanta attached, provide a different approach to the fractional quantum Hall effect (FQHE) [1]. At filling factor $\nu = ½$ the attached flux quanta are 'compensated' by externally applied magnetic flux such that the CF move in a vanishing effective magnetic field. Away from $\nu = ½$ the effective magnetic field increases, the CF move on circles with radius $R_{C,CF}$ and the Landau quantization of the circular motion of the new particles is the origin of the FQHE. The radius $R_{C,CF}$ is given by $\hbar\sqrt{4\pi n_s}\,/eB_{eff}$ with the electron density n_s, the effective magnetic field $B_{eff} = B - B_{1/2}$, and $B_{1/2}$ the magnetic field at $\nu = ½$. Experimental evidence for the existence of CF mainly stems from commensurability experiments where the Fermi wave vector $k_{F,CF}$ of the novel quasi-particles is probed by a periodic external perturbation [2-4].

Here we describe the application of in-situ interferometric illumination inside a ^{3}He-sample holder to generate a weak density modulation employing the persistent photoconductivity effect in our high-mobility GaAs/AlGaAs heterojunctions. The amplitude of the density modulation with submicron periods of the two-dimensional electron gas (2DEG) is typically of order 2%. At low magnetic fields the weak periodic potential gives rise to commensurability oscillations with minima appearing for commensurate ratios of cyclotron radius R_C and the period a of the modulation: $2R_C = (\lambda\text{-}1/4)a$, with $\lambda = 1,2,...$[5]. Similar oscillations can be found if the 2DEG is subjected to a laterally modulated magnetic field which can be generated, e.g., by a periodic array

of ferromagnetic strips. For a periodic magnetic field the phase of the commensurability oscillations is shifted and minima appear whenever $2R_C = (\lambda+1/4)a$ holds [6]. A weak density modulation should result in a modulation of the effective magnetic field for the CF as the external magnetic flux at $\nu = ½$ is no longer compensated locally by the flux carrying CF. For a density modulation of $\Delta n_s / \overline{n_s}$ we expect a periodic effective magnetic field of amplitude $\Delta B_{eff} = B_{1/2} \cdot \Delta n_s / \overline{n_s}$. Since the CF move in a periodic (effective) magnetic field we expect to observe features in the magnetoresistance characteristic for *electrons* in a periodic magnetic field.

The samples used in our experiment are MBE-grown GaAs/AlGaAs heterostructures. The 2DEG is located 114 nm below the surface separated from the Si-doped layer by a 80 nm undoped AlGaAs-buffer. Hall-bars were fabricated by using standard lithographic methods. The measurements were carried out on two different Hall-bars. After interferometric illumination the sheet densities n_s were $1.54 \cdot 10^{11}$ cm^{-2} and $1.57 \cdot 10^{11}$ cm^{-2} and the mobilites $2.9 \cdot 10^6$ cm^2/Vs and $1.5 \cdot 10^6$ cm^2/Vs, respectively. The measurements were carried out using standard lock-in measurement techniques.

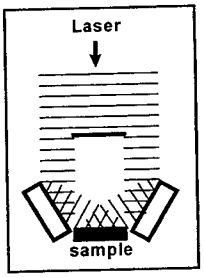

Fig. 1: Principle of interferometric illumination

We used the interferometric illumination technique to impose a weak periodic potential upon the 2DEG. For the exposure we used an expanded and spatially filtered beam of a HeNe laser (λ = 632,8 nm) coupled into a ^{3}He-sample holder, kept at about 4 K. Just above the sample the beam is split into two parts. Two mirrors beneath the sample deflect the beams which interfere on the surface of the heterojunction. The period a of the interference grating is controlled by the angle of incidence θ with respect to the surface normal: $a = \lambda/2\sin\theta$. The angles used in the experiments were 70°, 50° and 40°. The illumination times range between 30 ms and 100 ms depending on the period of the grating. Due to the persistent photoconductivity effect in AlGaAs-based heterojunctions the light-grating generates persistently (as long as the sample is kept cold) a weak density modulation in the 2DEG. The advantage of the technique is (i) the defect free generation of a periodic potential with submicron periodicity, (ii) that the same device can be measured for several modulation periods (after thermal cycling) and (iii) that a weak sinusoidal modulation can be maintained also for larger periods. The latter turned out to be critical for etched samples. A sufficiently weak periodic potential is necessary to ensure a sufficently small amplitude of the periodic effective magnetic field to get magnetic commensurability effects clearly resolved [7]. Interferometric illumination is a simple technique complementary to the method of shallow etching which allows to generate smaller periods. Combining both methods weak periodic potentials with periods between 280 and 490 nm have been realized experimentally [8].

The low-B data for weakly modulated 2DEGs with periods between 337 and 492 nm are displayed in Fig. 2. The sample shows a striking negative magnetoresistance around $B = 0$ whose origin is not yet understood. At higher B clear commensurability oscillations appear in the resistivity which are characteristic for weak *electrostatic* periodic potentials. Minima (marked by arrows) appear whenever the condition $2R_C = (\lambda-1/4)a$ holds. From the amplitude of the ρ_{xx}-oscillations we

estimate the amplitude of the density modulation as 1.5% to 3% of the Fermi-energy. For this estimate we used Beenakker's model [9] and ignored the effect of anistropic scattering [10,11], which is known to lead to a stronger damping at smaller B.

Fig. 3 shows the data of the same modulated devices around filling factor $\nu = ½$ which were taken after cooling the interference sample holder down to 0.3 K. While ρ_{xx} for unmodulated samples is essentially flat around $\nu = ½$ the modulated devices show striking features. These features are: (i) a pronounced V shaped minimum near $B_{1/2}$, (ii) a clear minimum corresponding to the fundamental minimum (λ=1) of the magnetic commensurability oscillations characterized by $2R_{C,CF} = (\lambda+1/4)a$ and (iii) the steep increase of ρ_{xx} for effective magnetic field values beyond the commensurability minimum. The small dip in the immediate vicinity of $\nu = ½$ can be ascribed to open orbits of CF. This is in analogy to electron motion in a periodic magnetic field where electrons on snake orbits (along lines of vanishing magnetic field) give rise to a positive magnetoresistance [6]. Composite Fermions moving along lines of vanishing *effective magnetic* field (open orbits) are responsible for an increasing ρ_{xx} at low effective fields around $\nu = ½$. The positive magnetoresistance saturates once the B_{eff}-value exceeds the modulation amplitude ΔB_{eff} and the CF's are forced to move on cyclotron orbits. From saturation fields ranging from 200 mT to 250 mT we estimate the amplitude of the density modulation to be between 1.5 % and 2 % which agrees with the estimates of $\Delta n_s / \overline{n_s}$ from the amplitude of the *electric* commensurability oscillations. At higher fields pronounced minima appear, marked by filled arrows in Fig. 3. These positions are given by the *magnetic* commensurability condition $2R_{C,CF} = 1.25a$. The position of the magnetic

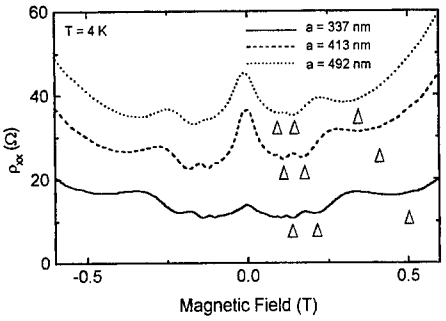

Fig. 2: Low-field electric commensurability oscillations. Arrows mark the commensurability conditions $2R_C = (\lambda\text{-}1/4)a$. The upper traces are shifted by 10 Ω (413 nm) and 20 Ω (492nm).

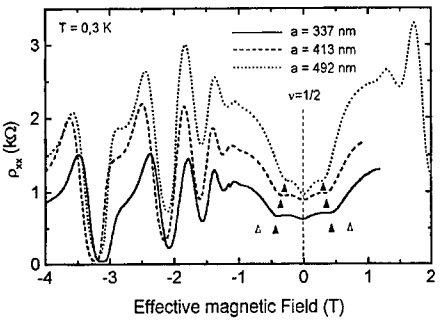

Fig. 3: Commensurability features around $\nu = ½$. The filled arrows mark the fundamental minimum of the magnetic commensurability oscillations, $2R_{C,CF} = 1.25a$, the open arrows the electric one. $B_{1/2}$ is between 12.8 and 13.1 T for the three traces shown.

commensurability condition can be clearly distinguished from the electric one ($2R_{C,CF}$ = 0.75a) marked by open arrows in the bottom trace. Our experiment demonstrates that CF moving in a weak periodic potential behave like electrons (apart from the rescaled fields) moving in a periodic magnetic field.

We compared our experimental results with calculations based on the linearized Boltzmann equation which are described in more detail in Ref [12]. The model which goes beyond the Beenakker-type approximation [9] takes into account both channeled orbits, which have been omitted in previous calculations [13], and anisotropic scattering [10]. The essential features observed in the experiments are well described by these calculations. Even the slight asymmetry around ν = ½, which is ascribed to the residual effect of an electrostatic modulation, can be reproduced (Fig. 4).

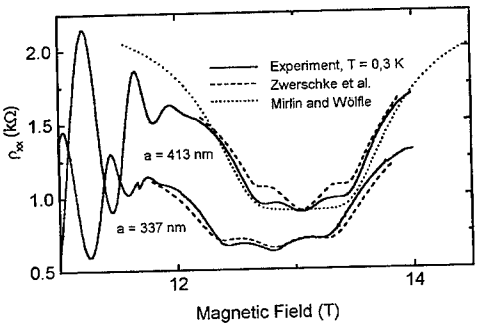

Fig. 4: Comparison of model calculations with experimental data. The dotted line corresponds to calculations of Mirlin and Wölfle [13] ignoring open orbits, the dashed ones to the model of Zwerschke and Gerhardts [12].

In summary we have shown that by means of interferometric illumination weak periodic potentials can be generated which allow to study commensurability effects in the FQHE regime. Our experiments show clearly that a weak density modulation results in a modulation of the effective magnetic field experienced by Composite Fermions.

Acknowledgements: Work was supported by BMBF grant No. 01BM622/5.

[1] J. K. Jain, Phys. Rev. Lett. **63**, 199 (1989)
[2] R. L. Willet, R. R. Ruel, K. W. West, L. N. Pfeiffer, Phys. Rev. Lett. **71**, 3846 (1993)
[3] W. Kang et al., Phys. Rev. Lett. **71**, 3850 (1993)
[4] *Composite Fermions: A unified view of the Quantum Hall Regime*, ed. O. Heinonen (World Scientific, Singapore 1998) and references therein
[5] D. Weiss, K. von Klitzing, K. Ploog, G. Weimann, Europhys. Lett. **8**, 179 (1989)
[6] P. D. Ye et al., Phys. Rev. Lett. **74**, 3013 (1995)
[7] J. H. Smet, K. von Klitzing, D. Weiss, W. Wegscheider, Phys. Rev. Lett. **80**, 4538 (1998)
[8] J. H. Smet et al., submitted to Phys. Rev. Lett.
[9] C. W. J. Beenakker, Phys. Rev. Lett. **62**, 2020 (1989)
[10] R. Menne and R. R. Gerhardts, Phys. Rev. B **57**, 1707 (1998)
[11] A. D. Mirlin and P. Wölfle, Phys. Rev. B **58**,12986 (1998)
[12] S. D. M. Zwerschke and R. R. Gerhardts, submitted to Phys. Rev. Lett.
[13] A. D. Mirlin, P.Wölfle, Y. Levinson, O. Entin-Wohlman, Phys. Rev Lett. **81**, 1070 (1998)

Ballistic Weak Localization in Classically Chaotic Antidot Arrays: Influence of Geometric Factors

Klaus Richter[1], Ralf Hennig[2], Michael Suhrke[2], and Oleg Yevtushenko[1,2]
[1]*Max-Planck-Institut für Physik komplexer Systeme, D-01187, Dresden, Germany*
[2]*Universität Regensburg, D-93040, Regensburg, Germany*
(June 15, 1999)

We address weak localization (WL) of electrons in a two-dimensional ballistic classically chaotic billiard of antidots. According to a recent proposal ballistic WL is sensitive to the transport relaxation and phase-coherence times as well as to the Ehrenfest time t_E and to the Lyapunov exponent λ of the classical system. This results in a non-trivial effect of the geometrical parameters of the antidots on the quantum WL correction to the classical magnetoconductivity. We analyze this phenomenon in detail and discuss how t_E and λ can in principle be determined from conductivity measurements.

PACS: 72.15.Rn; 73.23.-b; 05.45.Mt

During the past decade many theoretical and experimental investigations were devoted to quantum interference effects in small phase-coherent conductors. *Weak localization* (WL) – a decrease of the conductivity in disordered samples with respect to the classical one – is a prominent example of such a phenomenon. WL in diffusive systems results from the constructive interference of time-reversed trajectories which are backscattered from impurities [1]. WL in ballistic conductors has been studied mainly for small coherent cavities where the elastic mean free path considerably exceeds the relevant device dimensions [2]. Hence backscattering arises predominantly from specular reflections at the boundaries of the cavity and WL should carry features of the underlying ballistic classical dynamics, namely, whether it is chaotic or regular.

Here we address another ballistic counterpart to impurity scattering: billiards consisting of arrays of large antidots, which have recently been prepared from a high-mobility two-dimensional (2D) electron gas [3,4]. It has been shown [3] that the standard WL theory for disordered systems loses its validity in the case of antidot billiards. It is well suited to describe coherent backscattering from point-like impurities [1] which provide a *quantum* mechanism for the "splitting" of scattered classical trajectories allowing the formation of pairs of time-reversed paths. In this case the electronic motion can be regarded as a delta-correlated (diffusive) process. The standard WL theory for diffusive systems predicts the following quantum correction to the classical conductivity in the 2D case [1,5]:

$$\Delta\sigma = -\mathcal{G}\,\ln(\tau_\phi/\tau)\,; \quad \mathcal{G} \equiv e^2/\pi h\,. \tag{1}$$

Here, τ_ϕ is the phase coherence time and τ denotes the transport relaxation time.

Antidots with a diameter a considerably larger than the Fermi wavelength λ_F act as *classical* scatterers. Therefore, WL in ballistic antidot structures requires an approach beyond the diffusion approximation accounting for the correlations in the classical dynamics. According to suggestions by Argaman [6] and Aleiner and Larkin [7], the exponential separation of initially close orbits in a chaotic system with classical scatterers provides a mechanism for

a minimal wave packet of size λ_F to split into two parts which then follow time-reversed paths before they interfere constructively upon return. This approach introduces a new relevant time scale for WL in a chaotic system, namely the Ehrenfest time [8] which characterizes the spreading of the wave packet over a distance of the size a of the antidots,

$$t_E = \frac{1}{\lambda} \ln(a/\lambda_F). \tag{2}$$

Here λ is the Lyapunov exponent of the classical system. Aleiner and Larkin's approach accounts for correlations in the chaotic ballistic dynamics in the "Lyapunov region" for time scales up to t_E by replacing the diffusion operator through the regularized Liouville operator, the Frobenius-Perron operator [7]. For times larger than t_E the dynamics is assumed to be uncorrelated and treated as diffusive again. The result for ballistic WL in 2D then reads [7]

$$\Delta\sigma = -\mathcal{G}\ \mathcal{W} \ln(\tau_\phi/\tau); \quad \mathcal{W} \equiv \exp\left\{-(t_E/\tau_\phi) \cdot \left[1 - \lambda_2/(\lambda^2 \tau_\phi)\right]\right\}. \tag{3}$$

Here, $\lambda_2 \sim \langle \delta\lambda(t_1)\, \delta\lambda(t_2) \rangle$ characterizes fluctuations in λ. Correlations in the chaotic dynamics are incorporated in Eq. (3) in the exponential prefactor, while the diffusive motion on longer time scales is reflected in the logarithm.

In a previous paper [3] we have analyzed the temperature dependence $\Delta\sigma(T)$ for antidot structures which were prepared from high-mobility GaAs/AlGaAs heterostructures. Based on simplified models for the dependence of the Lyapunov exponent and transport relaxation time on the geometry of the structure (distance d and diameter a of the antidots) it has been shown that WL shows clear signatures of dynamical chaos. This opens up the principle possibility to extract the Ehrenfest time and the *classical* Lyapunov exponent of the electronic antidot billiard from the *quantum* WL correction.

In the present paper we investigate this possibility in more detail based on a direct numerical study of λ. As the Lyapunov exponent is determined by the geometry of the underlying chaotic billiard, it is natural to study the dependence of $\Delta\sigma$ upon geometric factors, such as the ratio $\mathcal{R} = d/a$. Of course, $\mathcal{R}$ affects $\Delta\sigma$ in Eq. (1) via the relaxation times τ_ϕ/τ. However, in Eq. (3) this influence is tangled by the dependence $\lambda(\mathcal{R})$ leading to the discrepancy between the results of Eqs. (1) and (3) at finite λ or non-vanishing t_E.

During the simulations we restrict ourselves to a regular lattice of antidots. The reason for this is the absence of essential differences between WL in periodic and disordered antidot billiards if the other geometrical parameters remain the same [3]. The calculations are done for GaAs/AlGaAs heterostructures (effective mass $m^* = 0.065\, m_0$) with an electron mobility $\mu \simeq 11\,\mathrm{m^2/Vs}$ and a charge carrier density of $n_s \simeq 4.9 \cdot 10^{15}\,\mathrm{m^{-2}}$. For the parameters of the antidot lattice we choose typical experimental values. While the antidot diameter is fixed at $a = 200\,\mathrm{nm}$, the lattice period d varies between 250 nm and 400 nm. Both are significantly larger than the Fermi-wavelength $\lambda_F \simeq 36\,\mathrm{nm}$. Hence the antidots can be considered as classical scatterers. On the other hand $d \ll l_{tr}$ where l_{tr} is the mean free path in the unpatterned sample. Thus the classical dynamics in the antidot lattice can be considered to be ballistic. The antidot potential is taken to be relatively steep dropping by an order of magnitude on a length of 10 nm.

We calculate the Lyapunov exponents for a mesh of initial conditions in the three-dimensional phase space at a given Fermi energy [9]. Results for the average value $\langle\lambda\rangle$

are presented in Fig. 1 together with a typical histogramm of the distribution in phase space. $\langle\lambda\rangle$ decreases with increasing lattice period for fixed antidot diameter as the regular parts of the phase space increase. The variance of the distribution is always smaller than the mean value. Consequently the part containing λ_2 in the exponent of Eq. (3) is a small correction as $\lambda\tau_\phi \gg 1$. The estimate from a model including scattering from three and four disks [10], $\lambda \simeq (v_F/d)\ln(4.276\,\mathcal{R})$, which has been used in Ref. [3], assumes that corrections to λ from (multiple) scattering at more distant antidots are small. It yields roughly the same magnitude and dependence of λ on the lattice period and corresponds to a length scale for the Lyapunov region of $v_F t_E \sim d$ (v_F is the Fermi velocity).

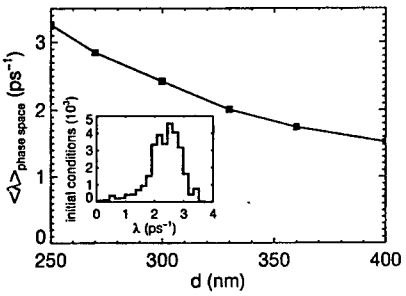

FIG. 1. Average Lyapunov exponent of an antidot lattice with antidot diameter $a = 200\,\mathrm{nm}$ as a function of the lattice period d. The inset shows the histogram of a typical distribution of Lyapunov exponents for trajectories with different initial conditions for $d = 300\mathrm{nm}$.

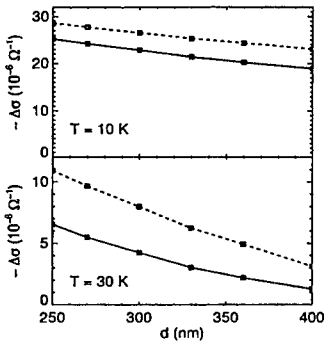

FIG. 2. Weak localization correction to the classical conductivity for the antidot lattice from Fig. (1) as a function of the lattice period for $T = 10\,\mathrm{K}$ (a) and $T = 30\,\mathrm{K}$ (b). The ballistic case, Eq. (3) (full lines), is compared to the diffusive case, Eq. (1) (dashed lines).

For the phase-coherence time we use the same model as in Ref. [3]. Two main mechanisms are responsible for the decay of phase correlation, prevailing at different temperatures: *electron-electron* (e-e) interactions ($T < 10\,\mathrm{K}$) and *electron-phonon* (e-ph) interactions ($T > 10\,\mathrm{K}$), giving an overall dephasing rate $\tau_\phi^{-1} = \tau_{e\text{-}e}^{-1} + \tau_{e\text{-}ph}^{-1}$. The value of $\tau_{e\text{-}e} \sim T^{-1}$ [K] is estimated in the framework of the Altshuler-Aronov theory on dephasing in 2D dirty systems [5]. For the electron-phonon interactions we use a "T^2"-model [11]: $\tau_{e\text{-}ph}(T) = C/T^2$ with the interaction constant $C \simeq 2.3\,\mathrm{ns\,K^2}$ extracted from the experimental data [3]. The transport relaxation time τ in Eq. (3) is obtained from a calculation of the classical conductivity of the antidot lattice using the Kubo formula [9,12].

In Fig. (2) we compare the influence of the geometric parameter $\mathcal{R}$ on WL in diffusive, Eq. (1), and ballistic systems, Eq. (3), for two different temperatures. At relatively low temperature ($T < 10\mathrm{K}$) both theories almost coincide because the ratio t_E/τ_ϕ is small in this temperature regime and we find $W(t_E/\tau_\phi) \to 1$ in Eq. (3). On the other hand, at $T \sim 30\,\mathrm{K}$ the theories for WL in diffusive and ballistic systems deviate substantially. Such high temperatures are rather unusual for WL experiments. Fortunately, due to the

suppression of the electron-phonon interaction by the antidots and due to the small τ, WL is still observable even at $T \simeq 30-40\,\mathrm{K}$ in antidot arrays [3]. Due to the decreasing Lyapunov exponent, t_E grows always faster with increasing lattice period than τ_ϕ. This is especially true at higher temperatures when electron-phonon scattering dominates τ_ϕ. At the same time the logarithm in Eq. (1) decreases with increasing lattice period since the transport relaxation time τ rises more strongly with d than τ_ϕ. This leads to the drop of $\Delta\sigma$ with increasing lattice period which has, however, different magnitudes for diffusive and ballistic structures, respectively. The influence of classical chaos is most pronounced if the relation $t_\mathrm{E} > \tau_\phi > \tau$ holds between the characteristic times. This means that there exists a certain temperature window for the observation of deviations from the diffusive picture for each $t_\mathrm{E} > \tau$. The latter relation is fulfilled for not to weak scattering by impurities.

Experimentally, the classical conductivity can be obtained for a small finite magnetic field where the weak localization correction is negligible. This allows one to extract the transport relaxation time τ and, at least within the model used above, the phase-coherence time. If the geometry of the antidot lattice and the Fermi wavelength are known, the only free parameter, to be determined via Eq. (3), is the Lyapunov exponent.

To summarize, we have studied the weak localization correction $\Delta\sigma$ to the classical conductivity of ballistic arrays of large antidots. We have paid special attention to the influence of the geometry of the antidot billiard on $\Delta\sigma$. Our results suggest that WL measurements can be used as an experimental mean to extract information on the underlying dynamical system in terms of the Ehrenfest time t_E and the Lyapunov exponent λ. For instance measurements of $\Delta\sigma$ at constant temperature $T \geq 15\,\mathrm{K}$ for a set of antidot samples, which differ only in the lattice constant, should allow one to determine the Lyapunov exponent λ and thereby the Ehrenfest time as a function of $\mathcal{R}$.

This work has been partially supported by the Deutsche Forschungsgemeinschaft (GRK 176 at University of Regensburg).

[1] G. Bergmann, Phys. Rep. **107**, 1 (1984); S. Chakravarty and A. Schmid, *ibid.* **140**, 194 (1986).
[2] For reviews see, e. g., contributions to the special issue: Chaos **3**(4) (1993), or H. U. Baranger in *Nano-Science and Technology*, edited by G. Timp, (Springer, 1997).
[3] O. Yevtushenko, G. Lütjering, D. Weiss, and K. Richter, preprint mpi-pks/9902004.
[4] D. Weiss, in *Festkörperprobleme* **31**, 341 (1991); R. Schuster and K. Ensslin, ibid **34**, 195 (1994); D. Weiss, *et. al.*, Phys. Rev. Lett. **70**, 4118 (1993); F. Nihey and K. Nakamura, Physica B **184**, 398 (1993); R. Schuster, *et. al.*, Phys. Rev. B **47**, 6843 (1993).
[5] B. L. Altshuler and A. G. Aronov in *Electron-electron interactions in Disordered Systems*, eds. A. L. Efros and M. Pollak (North Holland, Amsterdam, 1985).
[6] N. Argaman, Phys. Rev. Lett. **75**, 2750 (1995); Phys. Rev. B **53**, 7035 (1996).
[7] I. L. Aleiner and A. I. Larkin, Phys. Rev. B **54**, 14423 (1996); Chaos, Solitons & Fractals **8**, 1179 (1997).
[8] B. V. Chirikov, F. M. Izrailev, and D. L. Shepelyanskii, Sov. Sci. Rev. C **2**, 209 (1981).
[9] R. Hennig and M. Suhrke, submitted to Phys. Rev. B.
[10] P. Gaspard, *Chaos, Scattering and Statistical Mechanics* (Cambridge University Press, 1998).
[11] N. G. Ptitsina, *et. al.*, Phys. Rev. B **56**, 10089 (1997).
[12] R. Fleischmann, T. Geisel, and R. Ketzmerick, Phys. Rev. Lett. **68**, 1367 (1992).

PB.11

TESTING THE LIMITS OF COMPOSITE FERMIONS

T. J. Gramila, S. Zelackiewicz, H. Noh
Department of Physics, The Pennsylvania State University, University Park, PA 16802

L. N. Pfeiffer, and K. W. West
Bell Labs, Lucent Technologies, Murray Hill, NJ 07974

We describe new experimental tests of composite Fermions (CF) which appear in the 2D electron system at high magnetic fields. Experiments have clearly supported both the existence of the particles and a number of their remarkable properties: behaviors very similar to electrons at zero magnetic field. However, whether CF's can support large wavevector scattering events is not well established, either experimentally or theoretically. We report measurements which directly explore this question. The measurements exploit electron drag to provide direct access to phonon exchange between two CF layers. Detection of the resultant momentum transfer probes CF scattering with a tunable wavevector, since the characteristic phonon wavevector is varied by changing temperature. While phonon exchange for ordinary 2-D electrons is dominated by scattering across their Fermi surface, the temperature dependence observed for CF's indicates such scattering is missing. Measurements varying both magnetic field and density will be presented, as will the implications that such measurements have for the large wavevector behavior and internal structure of Composite Fermions. New measurements, which compare the response at nu = 1/2 to that of nu = 1/4, will also be discussed.

PB.12

Spatial evolution of the generation and relaxation of excited carriers near the breakdown of the quantum Hall effect

I.I. Kaya, G. Nachtwei, B.E. Sagol, K. v. Klitzing, and K. Eberl

Max-Planck-Institut für Festkörperforschung, Heisenbergstr. 1, D-70569 Stuttgart;Germany

We have measured the generation and relaxation of excited carriers along their drift direction near the breakdown of the quantum Hall effect (QHE). The dissipative resistivity $\rho_{xx}(x)$ at current densities close to the critical value for the QHE breakdown was measured as a function of the distance x from the electron injection at $x = 0$. By injecting „cold" electrons into constrictions at supercritical current levels, the evolution of the breakdown along the drift direction was monitored. After a smooth increase of the resistivity with the drifting distance, an avalanche-like rise towards a saturation value occurs. Drastic changes of the resistivity profiles with the applied current were found in a narrow range around the critical current. The observed behaviour is attributed to impurity-assisted tunneling between Landau levels. By injecting hot electrons (excited in a periodic set of constrictions) into a region with subcritical current density, the relaxation process was analyzed. Inelastic relaxation lengths with typical values in the range from 0.3 to 4 μm were found, which agree within 10% with the elastic mean free path determined from the Hall mobility at zero magnetic field. We conclude that the energy relaxation process is triggered by scattering at impurity potentials.

Keywords: quantum Hall effect, breakdown, hot-electron generation and relaxation.

PACS Numbers: 73.50.Fq, 73.40.Hm, 72.10.Fk

In 1990, just one decade after the discovery of the quantum Hall effect (QHE) [1], all metrological institutes agreed to realize the unit of the electric resistance on the basis of the QHE. To achieve large output signals for high precision measurements of the QHE, high currents (some 100 μA) are necessary. This accounts for the requirement of a detailed understanding of the QH transport mechanism at high currents close to the current-induced breakdown of the QHE. Although a lot of studies have been done on this field (for a review, see [2]), there is no complete microscopic model of the breakdown available yet. A good phenomenological description of the physics near the QHE breakdown can be given by the model of avalanche heating of electrons [3,4]. This model agrees with the observation that it takes macroscopic drifting distances for the electrons at supercritical current densities to complete the breakdown with a stationary value of the resistivity ρ_{xx} [4,5]. However, to gain a more detailed microscopic understanding of the breakdown, knowledge of the typical length- and time scales of the generation and relaxation of the excited electrons is necessary.

In this paper, we present recent results of space-resolved measurements near the breakdown. Typical parameters of the hot-electron generation and relaxation (e.g. relaxation lengths) could be determined. From this we conclude that the generation is dominated by impurity-enforced inter-Landau-level tunneling, and that the relaxation is triggered by Coulomb scattering at impurities.

The spatial evolution of the generation and relaxation of hot electrons was monitored by resistance measurements on multiprobe samples. To study the generation, the

potential probes were attached to a constricted region of the sample, where the electrons are heated (see inset of Fig. 1). The relaxation process was monitored in samples, where the electrons are excited in an array of parallel constrictions before they are injected into a Hall bar region (with 19 pairs of potential probes, see inset of Fig. 3) under subcritical conditions. For the interpretation of the experiments, the resistivity $\rho_{xx}(x)$ at filling factor $\nu = 2$ was taken as a measure of the electron temperature [3], equivalent to a certain occupancy of the Landau level above the Fermi energy [5]. All samples have identical geometries and comparable electron densities from 2 to 3×10^{11}cm^{-2}, but quite different mobilities in the range from 0.04 to 1×10^{6}cm^2/Vs. This allowed us to investigate systematically the influence of the density of scatterers on the evolution of the QHE.

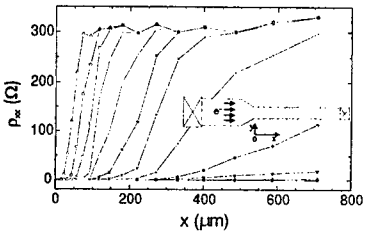

Fig. 1: Dependence of the resistivity minima ($\nu = 2$) on the distance from the constriction for a sample with $n_s = 3.0\times10^{11}$cm^{-2} and $\mu_H = 1.6\times10^{5}$cm^2/Vs. Current values are between I = 44.5 μA and 50.5 μA in 0.5 μA steps (lines are only guides to eyes connecting data points). Inset: scheme of the sample geometry.

In Fig. 1, we present a typical set of curves, showing the spatial evolution of the resistivity $\rho_{xx}=(U/I)(w/L)$ at $\nu = 2$ (at B = 5.8 T) in a constriction (width w = 50 μm) for various currents. After a smooth growth of ρ_{xx} over rather long distances, an avalanche-like rise of the resistivity towards a saturation value occurs. The shape of the $\rho_{xx}(x)$ plots changes drastically within a rather narrow range of currents near the QHE breakdown. With increasing current, the position of the sudden resistivity increase moves to smaller x-values. Further, the slope of the ρ_{xx} vs. x plots in the smooth region, $\Gamma=d\rho_{xx}/dx$, changes exponentially with current (see Fig. 2). This behaviour is common for all samples. However, the range of currents, within which the hot-electron avalanche moves from $x \approx 500\mu$m to $x \approx 20\mu$m, depends strongly on the mobility. From μ_H = 4×10^{4} cm^2/Vs to 1.6×10^{5}cm^2/Vs, the current range $\Delta I/I_c$, within which the avalanche is observable, increases from 4 to 10%. In other words, the QHE breakdown is the more abrupt, the higher the density of scatterers is.

The exponential increase of Γ with current is consistent with inter-Landau level tunneling in the presence of disorder or strong potential fluctuations [5]. With decreasing mobility, the function $\Gamma(I)$ becomes steeper, reflecting again the strong dependence of the hot-electron generation on the density of scatterers.

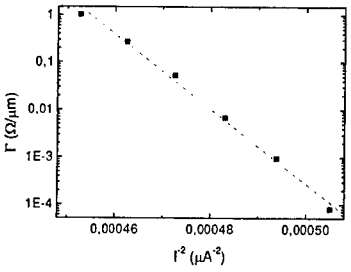

Fig. 2: Maximum slope Γ of the smooth parts of ρ_{xx} vs x curves shown in Fig. 1 with respect to $1/I_{SD}^2$. The continuous line shows the fit to the relation $1/\tau \propto \exp\{-\alpha\Delta y^2\}$ for the tunneling rate (Δy - effective tunneling distance).

In addition to the heating of electrons as a function of x, we also investigated the relaxation of hot electrons back to the $\nu = 2$ QH state in samples as shown in Fig 3 (inset). To achieve a homogeneous front of the electron temperature, the electrons are excited in a periodic array of constrictions before the injection into the wider channel at $x = 0$ [6]. The current is adjusted such that the breakdown is complete in the constricted region, but below the critical value in the wider channel for $x > 0$. This results in distinct differences of the resistivity profiles $\rho_{xx}(x)$ for the two current directions. For electrons injected *from* the array of constrictions, the resistivity falls almost exponentially from a saturation value, with a decreasing slope while approaching the critical current I_c (see Fig. 3). At I_c, $\rho_{xx}(x)$ remains at the saturation value throughout the sample. For currents $I < I_c$ of the opposite direction (current *towards* the array of constrictions), the QHE persists throughout the sample.

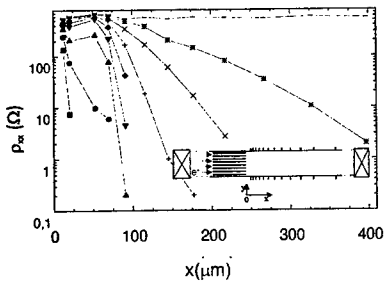

Fig. 3: Dependence of the ρ_{xx} minimum ($\nu = 2$) on the distance x of the probing contacts from the end of the wire array at different currents for a sample with low mobility ($\mu_H = 4\times10^4$ cm^2/Vs), currents from $I = 34.0$ μA (square) to 35.6 μA (dash) in 0.2 μA steps. Inset: scheme of the sample geometry.

The observed resistivity profiles $\rho_{xx}(x)$ can be approximated by the exponential dependence

$$\rho_{xx}(x) = \rho_{xx}^{0} \exp\left\{-\frac{x - x_0}{L_0}\right\} \qquad (1)$$

in the region with $x > x_0$, where ρ_{xx} is smaller than a certain saturation value ρ_{xx}^{0}. L_0 is the characteristic decay length of the resistivity at a given current $I < I_c$. To deduce L_0 as a function of the current I, we have considered a simple two-level-model [6]. Here, the resistivity ρ_{xx} is assumed proportional to the number N of electrons activated to the upper level. The change in time of the population of the upper level, dN/dt, depends on the balance between the generation rate due to Joule heating and the relaxation due to energy loss processes. As a result, we obtain

$$L_0 = \ell_D/(1 - (I/I_c)^2) \qquad (2)$$

with $\ell_D = v_D\, \tau_0$ as the average drifting length of the electrons between two inelastic scattering events [6]. From a fit of the experimental resistivity profiles to Eq.(1), the relaxation lengths ℓ_D could be determined. A remarkable coincidence of the relaxation lengths ℓ_D with the mean free path ℓ_{mfp} was observed for samples with mobilities from 4.0×10^4 to 5.3×10^5cm^2/Vs (see Fig. 4). The mean free path is mainly determined by *elastic* Coulomb scattering at ionized donors. Consequently, the relation $\ell_D \approx \ell_{mfp}$ indicates that the *inelastic* scattering (responsible for the dissipation near the QHE breakdown) is also related to Coulomb scattering. The current range, within which the relaxation near the breakdown could be observed, increases with mobility (from $\Delta I/I_C \approx 5$ to 25 % for μ_H from 4.0×10^4 to 5.3×10^5cm^2/Vs).

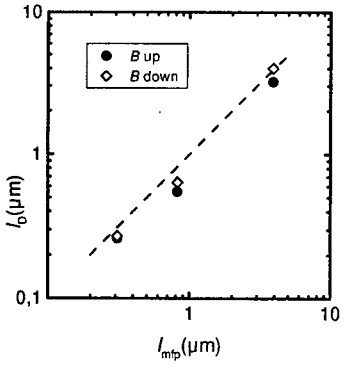

Fig. 4: Relaxation lengths ℓ_D determined from plots as in Fig. 3 as a function of the mean free path ℓ_{mfp}, deduced for samples with different mobilities (from 4.0×10^4 to $5.3\times10^5 cm^2/Vs$). Open and closed symbols: opposite directions of the magnetic field. Dotted line: $\ell_D = \ell_{mfp}$.

In summary, we have demonstrated that the QHE breakdown evolves over drift distances of typically some 100 μm at current densities close to the critical values. We measured either the *increase* of the resistivity $\rho_{xx}(x)$ along the current path at *supercritical* current densities, or the *decay* of $\rho_{xx}(x)$ if the current density becomes *subcritical* after the injection of electrons at $x = 0$. We attribute the generation process at supercritical currents to impurity-assisted inter-Landau-level tunneling. The decay of the resistivity corresponds to a cooling of hot electrons via inelastic scattering processes with a characteristic inelastic relaxation length ℓ_D in the range of $0.3\mu m < \ell_D < 4\mu m$. We found an unexpected agreement of ℓ_D with the elastic mean free path ℓ_{mfp}, which is determined by the Coulomb scattering at ionized impurities.

References:

[1] K. von Klitzing, G. Dorda, and M. Pepper, Phys. Rev. Lett. **45** (1980) 449
[2] G. Nachtwei, Physica E **4** (1999) 79
[3] G. Ebert, K. von Klitzing, K. Ploog, and G. Weimann, J. Phys. C **16** (1983) 5441
[4] S. Komiyama, Y. Kawaguchi, T. Osada, and Y. Shiraki, Phys. Rev. Lett. **77** (1996) 558
[5] I.I. Kaya, G. Nachtwei, K. von Klitzing, and K. Eberl, Europhys. Lett. **46** (1999) 62
[6] I.I. Kaya, G. Nachtwei, K. von Klitzing, and K. Eberl, Phys. Rev. B **58** (1998) R7536

PB.13

Collapse of Quantized Hall Resistance and Breakdown of Dissipationless State in The Integer Quantum Hall Effect:Filling Factor Dependence

H. Iizuka, S. Kawaji and T. Okamoto
Department of Physics, Gakushuin University
Mejiro, Toshima-ku, Tokyo 171-8588, Japan

Abstract

Magnetic field dependence of critical current for collapse of quantized Hall resistance I_{cr}(collapse) and critical current for breakdown of dissipationless state I_{cr}(breakdown) have been measured near the filling factor $\nu = 4$ of Landau levels in a GaAs/AlGaAs heterostructure Hall bar. The difference I_{cr}(breakdown) - I_{cr}(collapse) decreases against the increase and the decrease in ν from 4 and the critical behavior disappears outside of the region $3.85 < \nu < 4.15$.

Since 1990 the international standard of electrical resistance has been based on the quantum Hall effect (QHE) in two-dimensional electron systems (2DES) in strong magnetic fields.[1,2] Metrologists in standards laboratories have made clear that the quantized Hall resistance (QHR) is closely given by $R_H(i) = h/ie^2$ (i: an integer) and universal. [3 - 5] However, problems still remain unsolved in electric conduction in the QHE. Theories for the quantization relation are based on an assumption of the linear response of the system for electric field. [6-9] However, metrological applications of the QHE are carried out outside of the linear response assumption. The theories also require non-dissipation of the 2DES for complete quantization. [6-9] However the metrological applications do not necessarily satisfy the necessary condition of non-dissipation, although they are made using low currents at which dissipation is not clearly appreciable.

Recently Kawaji et al. observed the quantization of the Hall resistance is possible even when the dissipation is appreciable at high currents. [10] Moreover, they observed that collapse of the QHR (steep deviation of Hall resistance from the quantized value) occurs at a critical current I_{cr}(collapse) where no appreciable change appears in the dissipation. They found also that the collapse occurs at the same average Hall elctric field in Hall bars fabricated from the same GaAs/AlGaAs heterostructure wafer. They observed also that breakdown of the dissipationless state in the QHE (abrupt increase in dissipation) appeared at a critical current I_{cr}(breakdown) higher than I_{cr}(collapse). Therefore, the collapse they observed is a different phenomenon from the breakdown of the QHE so far studied.[11-14]

In Kawaji et al.'s experiments [10,14], they used specially designed Hall bars (butterfly-type Hall bars) to observe appreciable diagonal resistance R_{xx} passing a high current avoiding effects of high electric fields at two corners in the current electrodes.

Quite recently, Kawaji et al. [15] proposed a phenomenological model for the electronic structure of a Hall bar in the quantum Hall state

which explains the behavior of R_H and R_{xx} against the Hall electric field where the breakdown of the dissipationless state in QHE follows after the collapse of QHR. The model clearly shows that the breakdown of the QHE so far studied (breakdown of the dissipationless state in the QHE) is a high Hall electric field phenomenon in a 2DES in a strong magnetic field where the quantization of the Hall resistance disappears.

The present paper will report a new finding on the Hall resistance and the diagonal resistance against the source-drain current in a butterfly-type Hall bar at various filling factors of Landau levels ν between 3.8 and 4.2 observed at 0.35 K. The sample is the same Hall bar with the width of w=35 μm used by Kawaji et al.[15] The difference between I_{cr}(breakdown) and I_{cr}(collapse) decreases with the increase and the decrease in the filling factor from 4.0. The difference changes the sign from positive to negative at the filling factors of 4.12 and 3.88. In the outside of this filling factor region, the critical behavior disappears in both R_H and R_{xx}. The results will be discussed based on the electronic model proposed by Kawaji et al.[15]

In the higher magnetic field side of the plateau center with the filling factor of 4, the diagonal resistivity ρ_{xx} and the deviation of the Hall resistance from the quantized value $\Delta R_H/R_H$ at filling factors of ν= 4.00, 3.94, 3.89 and 3.86 as functions of the source-drain current I are shown in Fig. 1. The collapse of the QHR and the breakdown of the dissipationless state can be clearly observed in $\Delta R_H/R_H$ and ρ_{xx}, respectively, at each filling factor of 4.00 and 3.94. At the filling factor ν = 3.89, the deviation $\Delta R_H/R_H$ shows a small positive deflection prior to the clear collapse. At the filling factor ν = 3.86, the deviation $\Delta R_H/R_H$ becomes positive and very slowly changes against the change in the current and ρ_{xx} does not show any abrupt increase (breakdown of dissipationless state) against the current.

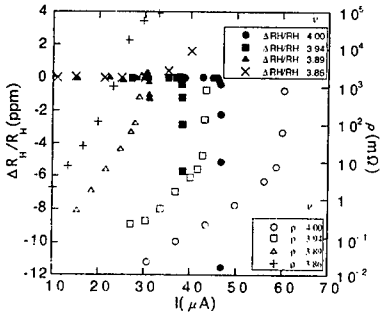

Fig. 1. Deviation of the Hall resistance from the quantized value $R_H(4)$ given by $\Delta R_H/R_H$ and the diagonal resistivity ρ against the current I at filling factors ν equal to and smaller than 4.

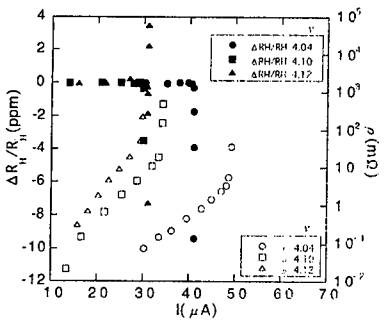

Fig. 2. Deviation of the Hall resistance from the quantized value $R_H(4)$ given by $\Delta R_H/R_H$ and the diagonal resistivity ρ against the current I at filling factors ν larger than 4.

In the lower magnetic field side of the plateau center, changes in $\Delta R_H/R_H$ and ρ_{xx} against the current are shown in Fig. 2. At the filling factor $\nu = 4.12$, $\Delta R_H/R_H$ shows a complex change against the current while ρ_{xx} shows a breakdown behavior.

Outside of the filling factor regions shown in Fig. 1 and Fig. 2, the Hall resistance does not show any steep deviation from the quantized value and the diagonal resistivity also does not show any breakdown behavior against the current. Fig. 3 shows those behavior of $\Delta R_H/R_H$ and ρ_{xx} at two filling factors of ν=4.15 and 4.17 compared with the critical behavior of the ρ_{xx} at $\nu = 4.12$.

We note here that the observed values $\Delta R_H/R_H$ are much smaller than those expected from the difference between the classical Hall resistance and the quantized value.

The model proposed by Kawaji et al.[15] assumes an electronic structure of a Hall bar which

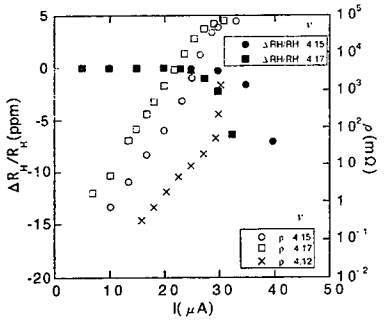

Fig. 3. Deviation of the Hall resistance from the quantized value $R_H(4)$ given by $\Delta R_H/R_H$ and the diagonal resistivity ρ against the current I at filling factors ν=4.15 and 4.17 do not show critical behavior. The critical behavior of the diagonal resistivity at $\nu = 4.12$ is shown for comparison.

consists of a one-dimensional superlattice of alternating ideal quantum Hall phase Q and dissipative quasi-quantum Hall phase D along the current. Here, the length of the phase Q along the current decreases and the length of the phase D along the current increases with the increase in the Hall electric field F_H . The collapse of the QHR occurs when the phase Q which connects opposite metallic Hall voltage electrodes disappears. The breakdown of the dissipationless state occurs in the phase D between two resistance probes when F_H reaches a critical value for abrupt increase in dissipation. Here, the dissipative phase D can contain many isolated islands of the phase Q.

At the magnetic field for the plateau center or $\nu = 4$, the Fermi level lies at the farthest energy from the adjacent two centers of Landau levels. At the collapse of the QHR, the whole Hall bar is covered by phase D, but a farther increase in F_H is necessary for abrupt increase in dissipation between resistance probes.

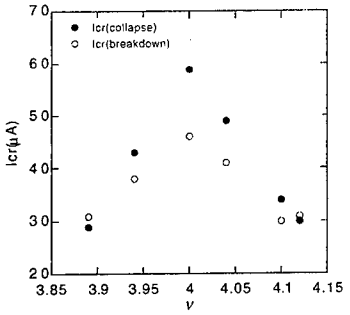

Fig. 4. Filling factor dependence of the critical current for the collapse of the quantized Hall resistance I_{cr}(collapse) and the breakdown the dissipationless state I_{cr}(breakdown) around $\nu = 4$.

For precise quantization of the Hall resistance, extended states near the center of the Landau level and localized states at the Fermi level are necessary electronic states in the phase Q which connects opposite Hall electrodes. At the current I_c(collapse). Hall electric field causes to generate electrons in the empty extended states, or to generate holes in the filled extended states, in the Q phase connecting opposite Hall electrodes to produce the collapse of the QHR. At the filling factor shifted far from the integer value and enter the region outside of $3.85< \nu < 4.15$, the Fermi level approaches to the extended states where thermal excitation of electrons and holes into extended states from the localized states is possible. Then, a steep deviation of the Hall resistance from $R_H(i)$ with the increase in current may disappear as shown in Fig. 3. At the same filling factor, the relation between the Fermi level and the extended states in islands of the phase Q in the channel between resistance probes is nearly the same as that in the phase Q which connects the Hall electrodes. Therefore, as shown in Fig. 3, an abrupt increase in dissipation cannot be observed against the increase in the current.

The picture described above to explain the filling factor dependence of the collapse of the QHR and the breakdown of the dissipationless state in the QHE is consistent with the observation of a parallel dependence of the critical current for the breakdown and the activation energy in ρ_{xx} on the filling factorν reported by Ebert et al. [12]. Observations of the decrease in the activation energy with the increase in the Hall electric field reported by Komiyama et al.[13] and Shimada et al.[16] also support the present picture.

The authors thank T. Kuga for assistance in experiments. Support from the Ministry of Education, Science and Culture in Japan and High-Tech-Research Center in Gakushuin University is also acknowledged.

References

[1] T. J. Quinn, Metrologia **26** (1989) 69.
[2] F. Delahaye, Metrologia **26**(1989) 63.
[3] A. Hartland et al., Phys. Rev. Lett. **66** (1991) 969.
[4] B.Jeckelmann et al., IEEE Trans. Instrum & Meas. **IM-44**(1995) 269.
[5] B Jeanneret et al., IEEE Trans. Instrum & Meas. **IM-44**(1995)254.
[6] T. Ando et al., J. Phys.Soc.Jpn.**39** (1975) 279.
[7] H. Aoki and T. Ando,,Solid State Commun. **38**(1981)1079.
[8] R.B. Laughlin, Phys. Rev. B **23**(1981) 5632.
[9] M. Buttiker, Phys. Rev. B **38**(1988) 9375.
[10] S. Kawaji et al., J. Phys. Soc. Jpn. **67** (1998) 1110.
[11] M. E. Cage et al., Phys. Rev. Lett. **51** (1983) 1347 .
[12] G. Ebert et al., J. Phys. C. Solid State Phys. **16**(1983) 5441.
[13] S. Komiyama et al., Solid State Commun. **54**(1985) 479.
[14] S. Kawaji, Semicond. Sci. Technol. **11** (11S) (1996) 1546.
[15] S. Kawaji et al., Physica B **256-258** (1998) 56.
[16] T. Shimada et al., Physica B **249-251** (1998) 107.

PB.14

Quantum Hall Effect Breakdown in Two-Dimensional Hole Gases

L. Eaves, S. T. Stoddart, R. Wirtz, A. C. Neumann, B. L. Gallagher, P. C. Main and M. Henini

School of Physics & Astronomy, University of Nottingham, Nottingham NG7 2RD, UK

The breakdown of dissipationless current flow in the quantum Hall effect is studied for a two-dimensional hole gas at filling factors i = 1 and 2. At high currents, the magnetoresistance curves at breakdown exhibit a series of steps accompanied by hysteresis and intermittent noise. These are compared with similar data for electron systems and are discussed in terms of a hydrodynamic model involving inter-Landau level scattering at the sample edge.

Despite the importance of the quantum Hall effect (QHE) [1] in metrology and a wealth of experimental data [2-8], the mechanism for QHE breakdown remains controversial [9]. In certain Hall bars used to define the US resistance standard, the breakdown of the dissipationless state takes the form of a series of up to 20 steps in the longitudinal magnetoresistance [7].

Mechanisms proposed for breakdown include bootstrap electron heating [10], percolation due to an increased number of delocalised states [11], quasi-elastic inter-Landau level scattering (QUILLS) [5,12-14], emission of acoustic phonons due to intra-Landau level scattering [15] and the formation of compressible metallic filaments at high Hall fields [16]. Recently it has been suggested that, in some samples characterised by high values of breakdown current [6,7], breakdown can occur when the Lorentz force is large enough to push conducting electrons close to the hard wall potential at the physical edge of the Hall bar [17]. Here the current-carrying extended states correspond classically to electrons undergoing skipping orbits along the boundary wall. These states have a large velocity gradient, i.e. vorticity $\Omega \sim \omega_c$, where ω_c is the cyclotron frequency. In addition, the skipping states of the lowest Landau level (n=0) overlap spatially with bulk states of the unfilled n=1 level so that QUILLS processes can lead to a dissipative current flow out of the skipping states. A phenomenological similarity between QHE breakdown and breakdown of laminar flow in classical fluids has also been noted [17].

Experimental work on QHE breakdown has focussed on n-doped structures and, to our knowledge, there has been no detailed study of breakdown in two-dimensional hole gases (2DHG) [18]. This is surprising since the hole system has properties which differ significantly from the 2D electron gas (2DEG). In particular, the lowest energy 2D hole subband has heavy hole character [19] and hence a cyclotron energy, $\hbar\omega_{ch}$, several times smaller than for electrons. In addition, the hole coupling to phonons differs markedly from that of electrons. Since these differences could provide new insights into breakdown, we have investigated the effect for a 2DHG heterostructure. The Hall bar

sample (width w = 200 μm) was prepared from an MBE-grown GaAs/(AlGa)As heterostructure on a (311)A GaAs substrate with Si (acceptor) doping. It has a mobility of 13.4 $m^2 V^{-1} s^{-1}$ at 300 mK and sheet density of 1.0×10^{15} m^{-2}.

Figure 1 shows typical magnetoresistance curves of the 2DHG (plotted as $V_x(B)$) at high current values in the region of the i = 1 QH plateau. By sweeping the magnetic field, B (or current I) into and out of the dissipationless state, hysteresis is observed together with clearly defined step-like structure in $V_x(B)$ on the low magnetic field side of the i = 1 minimum in $V_x(B)$. On the high B side of i = 1 there is a smooth increase of V_x with B. The inset of the figure shows a detailed plot of the series of small steps observed as B is increased to a value sufficient to bring the current flow back to a quasi-dissipationless state. Here the step height $\Delta V_x \simeq 1$ mV. On the B-downsweep, only larger step heights (~6 mV) are observed, indicating a large and sharp transition into a state of dissipative current flow. On the B downsweeps it is impossible to stabilise the device in the region of the $\Delta V_x \sim 1$ mV steps observed on the upsweeps. The data are also displayed logarithmically in Figure 2 to show the large variation of V_x over the steps. Although the field positions of the steps varies slightly in successive sweeps, they are qualitatively similar in all sweeps. If the current and magnetic field are kept constant at certain values, intermittent switching noise is observed between high and low voltage values, as has been observed previously for 2DEGs [6,7]. The step-like breakdown is destroyed when the 2DHG is illuminated with light pulses.

Figure 3 shows the breakdown curves near i = 2. Hysteresis is again observed, but in this case the steps occur on the high magnetic field side of the minimum. The steps and hysteresis become more pronounced at higher currents and the height $\Delta V_x \simeq 1$ mV of the first step increases slightly with increasing I from 7 to 8.5 μA. At 9 μA, dissipation occurs at all B around i = 2. The values of the Hall voltage at breakdown are $V_H = 0.24$ V (i = 1) and $V_H = 0.11$ V (i = 2).

The hysteresis steps observed in both upsweep and downsweep breakdown curves for our 2DHGs at i = 1 are qualitatively similar to previously published data for 2DEG systems at v = 2 [7]. For 2DEGs, the measured voltage height ΔV_x of each breakdown step on the B-upsweeps is typically 6 meV, or equivalently 0.3 $\hbar\omega_{ce}/e$, where $\hbar\omega_{ce}$ is the electron cyclotron energy. For our 2DHG the B-upsweep step height is smaller, typically 1 mV. However, given the large effective mass ratio (~0.3) for holes and the low sheet density (lower B-values at i = 1 and 2) for our sample, the step heights in units of $\hbar\omega_{ch}/e$ are 0.5-1, i.e. similar to those for 2DEGs. The similarity of our data and those in reference [7] suggests a common physical process for breakdown in both electron and hole gases.

Breakdown due to QUILLS transitions between sidewall skipping Landau states (n = 0) and bulk Landau states (n = 1) causes a flow of current down the velocity gradient and leads to a dissipative effect which, in a hydrodynamic model, is analogous to viscous drag in classical fluids [17]. QUILLS can be characterised by a kinematic viscosity $\sim\omega_c \ell_B^2 \sim \hbar/m$, which combined with the large velocity gradient, ($\sim\omega_c$), associated with skipping states leads to a dissipative drag which scales as $\hbar\omega_c$. This gives qualitatively the observed scaling of the heights of the voltage steps for 2DHGs and 2DEGs.

Prior to breakdown the ratio V_H/V_x is a large number, around 10^6 at 4.22 T. As can be seen in Figure 2, it jumps from ~24000 to 30 on the step at ~4.16 T between the

dissipative and almost dissipationless states on the B-downsweeps. A similar large jump is observed for breakdown in 2DEGs [10]. For the smallest dissipative step on the B-upsweeps (see Figure 1 inset at B $\simeq$ 4.196 T), $\Delta V_x \sim 1$ mV, giving $V_H/V_x \sim 240$. We can write V_H/V_x as wv_{av}/α, where $v_{av} = E_{Hav}/B$ is the average drift velocity of the current-carrying states and $E_{Hav} = V_H/w$ is the average Hall field. The parameter α therefore takes on the value V_x/B and is analogous to the kinematic viscosity of a classical fluid. On the dissipative side of the first B-upsweep step, $V_x \simeq \hbar\omega_c/e \simeq 1$ mV, so that $\alpha \simeq \hbar/m^* \simeq 3 \times 10^{-4}$ m^2 s^{-1} for the hole gas at i = 1; α has a value about three orders of magnitude smaller in the almost dissipationless state around 4.2 T at the bottom of the step. With the fluid dynamical analogy we can regard $V_H/V_x = wv_{av}/\alpha$ as a parameter related to the Reynolds number, which takes on very high values in the dissipationless region. As B is decreased away from 4.2 T, α increases gradually to a critical value of 3×10^{-6} m^2 s^{-1} and then jumps by several orders of magnitude to its dissipative value.

Since our breakdown curves on the B-downsweeps are qualitatively similar to those reported by Komiyama and coworkers [10], the bootstrap carrier heating model that they have proposed for 2DEGs is also a plausible description for the dissipative transition observed in the B-downsweeps for our 2DHG. However, the bootstrap model cannot easily explain the large number of steps (up to 20 in all) on the B-upsweeps which have been observed by Cage and coworkers [3] in the breakdown of the QHE of 2DEGs and the multiple steps observed here for 2DHGs on the B-upsweeps. A development of the edge breakdown model may explain the origin of the steps [20]. A better understanding of the hysteresis and intermittent noise with strange attractor behaviour observed at breakdown [20] may be achieved by further development of the hydrodynamic analogy.

This work and LE were supported by the EPSRC (UK).

References

[1] K. von Klitzing, G. Dorda and M. Pepper, Phys. Rev. Lett. **45** (1980) 494-497.
[2] G. Ebert *et al.*, J. Phys. C: Solid State Phys. **16** (1983) 5441-5448.
[3] M.E. Cage *et al.*, Phys. Rev. Lett. **51** (1983) 1374-1377.
[4] F. Kuchar *et al.*, Surf. Sci. **142** (1984) 196-202.
[5] H.L. Störmer *et al.*, Proc. 17th Int. Conf. on Physics of Semiconductors, eds. J.D. Chadi and W.A. Harrison. Springer-Verlag, 267-270 (1985).
[6] Mokerov, V. G. *et al.*, JETP Lett. **47** (1988) 71-73.
[7] M.E. Cage, J. Res. Natl. Inst. Stand. Technol. **98** (1993) 361-373; **99** (1994) 757-764; **101** (1996) 175-180.
[8] L. Bliek *et al.*, Surf. Sci. **196** (1988) 156-164.
[9] For a recent review see G. Nachtwei, Physica E 4, (1999) 79-101.
[10] S. Komiyama *et al.*, Solid State Comm. **54** (1985) 479-484 and Phys. Rev. Lett. **77** (1996) 558-561.
[11] S.A. Trugman, Phys. Rev. B **27** (1983) 7539-7546.
[12] L. Eaves *et al.*, Phys. Rev. Lett. **53** (1984) 608-11 and J. Phys. C: Solid State Phys. **17** (1984) 6177-90.

[13] O. Heinonen, P.L. Taylor and S.M. Girvin, Phys. Rev. **30** (1984) 3016-3019.
[14] L. Eaves and F.W. Sheard, Semicond. Sci. Technol. **1** (1986) 346-349.
[15] P. Streda and K. von Klitzing, J. Phys. C: Solid State Phys. **17** (1986) L483-L486.
[16] V. Tsemekhman *et al.*, Phys. Rev. B **55** (1997) R10201-R10204.
[17] L. Eaves, Physica B **256-258** (1998) 47-51
[18] M. Henini *et al.*, Appl. Phys. Lett. **65** (1994) 2054-2056.
[19] S. Hill *et al.*, Physica B **211** (1995) 440-443.
[20] L. Eaves, submitted for publication.
[21] G. Boella et al., Phys. Rev. B **50** (1994) 7608-7614.

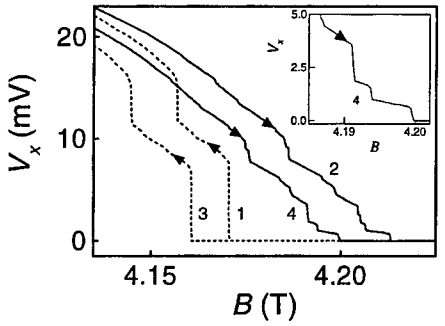

Figure 1 (left) Breakdown of the dissipationless QH state at i = 1 for a 2DHG, showing hysteresis (I = 9.2 μA, T = 300 mK). Arrows indicate the direction of the field sweep and the numbers refer to chronological order of sweeps. The inset shows in higher resolution the steps observed in the B-upsweep plots.

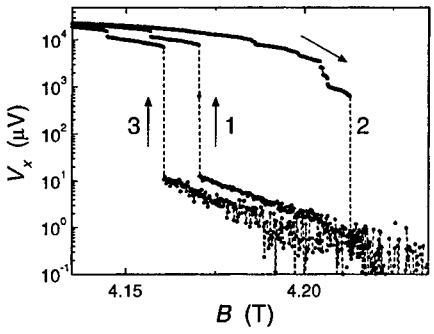

Figure 2 (left) Logarithmic plot of some of the data in Figure 1, showing the wide variation of V_x in the breakdown region.

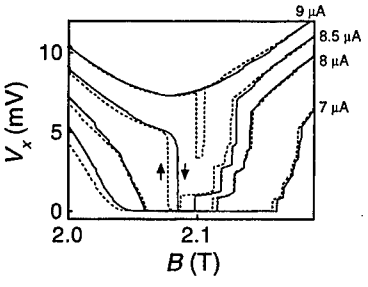

Figure 3 (right) Hysteretic breakdown of the dissipationless QH state at i = 2 for a 2DHG at various constant currents. Solid (dotted) lines are sweep up (down).

PB.15

Current breakdown of the integer and fractional quantum Hall effects detected by torque magnetometry

A.J. Matthews[1], J.P. Watts[1], M. Zhu[1], A. Usher[1], M. Elliott[2], W.G. Herrenden-Harker[2], P.R. Morris[2], M.Y. Simmons[3] and D.A. Ritchie[3]

Anthony J Matthews (A.J.Matthews@ex.ac.uk)
Tel: +44 (0)1392 264173 Fax: +44 (0)1392 264111

[1]School of Physics, University of Exeter, Stocker Road, Exeter, EX4 4QL, UK
[2]Department of Physics and Astronomy, University of Wales College of Cardiff, PO Box 913, Cardiff, CF1 9HQ, UK
[3]Cavendish Laboratory, University of Cambridge, Madingley Road, Cambridge, CB3 0HE, UK

We have developed a novel technique that enables measurements of the breakdown of both the integer and fractional quantum Hall effects in a two-dimensional electron gas without the need to contact the sample. The critical Hall electric fields that we measure are significantly higher than those reported by other workers, and support the quasi-elastic inter-Landau-level tunnelling model of breakdown. Comparison of the fractional quantum Hall effect results with those obtained on the integer quantum Hall effect allows the fractional quantum Hall effect energy gap to be determined and provides a test of the composite-fermion theory. The temperature dependence of the critical current gives an insight into the mechanism by which momentum may be conserved during the breakdown process.

PACS codes: **73.40.Hm** **73.20.Dx**
Keywords: Quantum Hall effect, fractional quantum Hall effect, magnetisation.

The mechanism of the breakdown of the integer quantum Hall effect (IQHE) at high currents is a matter of great debate.

Conventional techniques for measurements of breakdown rely on passing current through the two-dimensional electron gas (2DEG) using ohmic contacts; this has two important consequences. First, the metallic contacts provide equipotential surfaces for the 2DEG and result in focusing of any electric field. Hence any process in a 2DEG which relies on the electric field will be strongly affected by the presence of contacts. Second, the focusing of the equipotentials results in "hot-spots" at diagonally opposite corners of a Hall bar. Recent experiments [1] have shown that these may raise the local (electron) temperature up to ~ 20 K. Any processes in the 2DEG which have a temperature dependence will also be strongly influenced by contacts. Breakdown of the IQHE will be strongly influenced by both of these effects, and consequently a contactless sample geometry is highly desirable for these measurements.

In our experiments current is not driven through the 2DEG but instead it is induced to flow around it by a time-varying magnetic field. The induced current becomes large as ρ_{xx} tends to zero at integer, and some fractional, values of the Landau level (LL) filling factor, ν. We detect the induced currents, *via* their associated magnetic moments, using a milli-kelvin torque magnetometer which has been described elsewhere [2]. The induced currents are distinguishable from the equilibrium magnetisation (de Haas – van Alphen effect) as the former reverse polarity when the direction of the magnetic-field sweep is reversed (Figure 1: inset).

Early measurements on high-current breakdown of the IQHE reported critical current densities between 0.5 and 2 A m^{-1} [3,4,5]. These corresponded to critical electric fields of the order of 10^4 V m^{-1} assuming a uniform current distribution. Later work on constricted Hall bars [6] gave a much larger value for the critical field of 4.6×10^5 V m^{-1}. The variation of the critical field with width indicated that neither the current density nor Hall field is uniform across the Hall bar. MacDonald *et al.* [7] derived a self-consistent equation relating the charge, current and Hall field distribution in a 2DEG and showed that the current is strongly weighted towards the sample boundarys. Balaban *et al.* [8] refined this analysis and produced an expression relating the critical current, I_c, to the critical Hall electric field, E_c:

$$I_c = \frac{2d_n E_c}{R_H} \ln\left(\frac{W}{W_0}\right), \qquad \{1\}$$

where $d_n = (n+1)^{1/2} l_B$ represents the width of the electron's wavefunction in the n^{th} LL, $l_B = (\hbar/eB)^{1/2}$ is the magnetic length, W the sample width, W_0 a normalisation width related to l_B and the effective Bohr radius and R_H is the Hall resistance of the sample. The measurements of Balaban *et al.* confirmed the logarithmic dependence on the sample width.

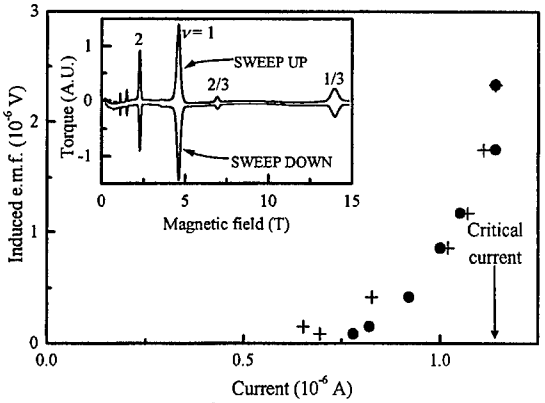

Figure 1. An example of an *I-V* curve for a 2DEG showing the breakdown of the FQHE at both ν = $^1/_3$ (•) and ν = $^2/_3$ (+) with the critical current indicated and, inset, a typical magnetic field sweep showing induced currents, as their resultant torque, as a function of magnetic field. A smooth background, resulting from the magnetisation of the magnetometer rotor, has been subtracted from these data.

Using our contactless technique critical fields of 3.7×10^5 V m^{-1} for ν = 4 and 3.1×10^6 V m^{-1} for ν = 2 were reported [9]. These results were obtained by sweeping the magnetic field at different rates, hence supplying a different electromotive force (e.m.f.) to the 2DEG, and measuring the size of the induced currents. This enables plots of induced current against e.m.f to be produced. These *I-V* curves are markedly non-linear, indicative of the breakdown of the quantum Hall effects (Figure 1). These critical fields are significantly larger than those obtained conventionally. Their size, and magnetic field dependence, supports the QUasi –elastic Inter-Landau-Level Scattering (QUILLS) model of breakdown [10], other models of breakdown predict smaller critical fields [4,11]. In the QUILLS model electrons tunnel from the highest occupied, to the lowest empty LL, conserving energy due to the Hall electric field. If tunnelling between LLs of opposite spin is prohibited then the energy separation of the levels in the absence of a Hall field is just $\hbar\omega_c$ where ω_c is the cyclotron frequency. The distance over which the electron may tunnel is constrained by the need for wavefunction overlap between the initial and final states. Thus the Hall field must provide an energy difference of $\hbar\omega_c$ in this distance. The critical field is, therefore, given by,

$$E_c = \frac{\hbar\omega_c}{el_B\left(\left[2n+1\right]^{1/2} + \left[2n+3\right]^{1/2}\right)}$$

Here the radius of the semi-classical cyclotron orbit approximates the size of the wavefunction. Momentum may be conserved during a QUILLS process either by scattering from an impurity or by interaction with the phonon system. Breakdown *via* a QUILLS process would be very sensitive to any local increase in the electric field and any breakdown measurements made with contacts are likely to measure breakdown in the region of the focused field. Conventional experiments also supply a constant current to the 2DEG through the contacts, rather than the constant e.m.f. in our technique, this allows other secondary breakdown processes, such as the electron heating model [4], to come into play. We would, therefore, expect our contactless measurements to yield higher critical fields than more conventional experiments.

Recently [12] we have measured the breakdown of both the integer and fractional quantum Hall effects in a very high mobility, modulation-doped GaAs–(Al,Ga)As heterojunction designated T320. This sample has an electron density of 1.05×10^{15} m^{-2} and a mobility of 250 m^2 V^{-1} s^{-1} as measured on a contacted portion of the same wafer. The magnetic field positions of the eddy current peaks confirm this electron

concentration. By using the IQHE results as a calibration of the FQHE ones we were able to extract a value of the FQHE gap energy Δ, which is taken to scale as:

$$\Delta = \frac{Ke^2}{4\pi\varepsilon l_B}.$$

Theoretical predictions for the value of K [13] give values ~ 0.070 for $\nu = {}^1/_3$. Our measured value of K = 0.066 is in good agreement with theory and is considerably better than other measurements of K based on activation studies which typically underestimate by as much as an order of magnitude. We believe that the good agreement with theory in our experiments is due to the fact that the tunnelling process, on which breakdown relies, is a 'local' process on the scale of the disorder present in the sample. The energy gap, when measured in this way, is therefore unaffected by disorder in the sample.

An alternate analysis of these data in which the QUILLS model for breakdown is applied to composite-fermions, subjected to an effective field $B^* = |B\text{-}B_{1/2}|$, constitute a measurement of the composite-fermion effective mass. We obtain a value of $m_{CF}^* = 0.32m_e$ which is significantly smaller than results obtained in transport experiments by fitting Shubnikov – de Haas oscillations with a modified Lifshitz – Kosevitch formula [14].

In order to examine the mechanisms for momentum conservation during QUILLS breakdown we have measured the temperature dependence of I_c in samples of different mobility. Figure 2.a shows the data for two high mobility samples, μ = 250 (♦) and 100 (•) m^2 V^{-1} s^{-1}. A rapid reduction in the critical current with temperature is apparent over the whole temperature range measured. The data for both samples, which has been normalised, follow the same trend, at ν = 1 and 2, and can be fitted fairly well with a simple exponential decay,

$$I_c(T) = I_0 e^{-\frac{T}{T_0}}$$

where T_0 has a value of 235 mK. The data for the lower mobility sample, μ = 27 m^2 V^{-1} s^{-1}, does not show the same behaviour (Figure 2.b). Instead there is a region below 300 mK where the critical current does not depend on temperature, and a region above 300 mK where the critical current becomes temperature dependent. This behaviour is the same for the two filling factors 1 and 4.

We interpret these results in the following way. In the QUILLS model, momentum is conserved during the tunnelling process either by impurity or phonon scattering. Very high mobility samples will have a low probability for impurity scattering. When the temperature is very low the phonon density will be low, and so scattering from phonons is also unlikely. Momentum conservation is therefore difficult, and so the probability of tunnelling is low hence the critical current is high. When the temperature is raised the phonon density is increased and the probability of phonon scattering is consequently raised. This will make tunnelling easier and reduce the critical current. The lower mobility sample will have a higher impurity density and, therefore at low temperatures, the role of phonons is not as significant since momentum may still be conserved by impurity scattering; the critical current will not then depend on temperature. However, at T > 300 mK the phonon density has increased sufficiently for phonon scattering to dominate over impurity scattering and the critical current becomes temperature dependent.

Rigal *et al.* [15] have measured the temperature dependence of I_c using a standard four terminal technique. This produced a power law relating I_c to T and ν:

$$I_c(T,\nu) = \left(\frac{I_{c0}}{\nu} - \frac{I_{c0}}{\nu_0}\right)\left[1 - \left(\frac{T}{T_{c0}/\nu}\right)^2\right].$$

Their data showed a constant I_c for T < 1 K which then fell off quickly with temperature above this. This is in agreement with our results; the mobility of the samples used in Rigal *et al.* experiments were low, between 3 and 22 m^2 V^{-1} s^{-1}, and so we would expect impurity scattering to dominate up to temperatures ~ 1 K. However, the power law fitted to their data gives a temperature dependence of I_c very different from the exponential behaviour observed in our experiments. We believe that the reason for this disagreement is the presence of contacts on their samples. The presence of contacts will result in the production of hot spots near the contacts and in ohmic heating of the contacts themselves, this means that the breakdown in their experiments is unlikely to be intrinsic QUILLS breakdown; but rather breakdown due to local heating or intra-Landau level scattering

[4,11]. The phenomenological similarity with the two-fluid model of superconductivity reported in their letter is not observed in the intrinsic current breakdown of the IQHE.

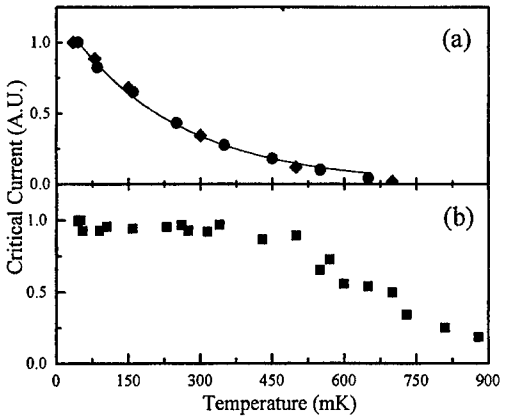

Figure 2.a The temperature dependence of I_c for both the high mobility samples (μ = 250 (♦) & 100 (•) $m^2 V^{-1} s^{-1}$) at ν = 1 showing a rapid reduction in the required current for breakdown with temperature, the solid line is an exponential decay with a characteristic temperature of 235 mK. 2.(b) shows the data for the lower mobility sample, $\mu = 27\ m^2 V^{-1} s^{-1}$. The critical current is independent of temperature below 300 mK but becomes dependent on temperature above this.

We have also managed to measure the temperature dependence of the critical current in the FQHE regime. The size of the induced currents drops much more rapidly with temperature over the measured range than the IQHE results and, as a result, for T > 150 mK no induced currents were observed. The functional form of the temperature dependence of breakdown in the FQHE regime could not, therefore, be determined.

In conclusion, we have presented a novel method for measuring the breakdown characteristics of the quantum Hall effects in 2DEGs without the need to contact the sample. This allows measurements to be made on the intrinsic properties of the 2DEG unperturbed by contacts. We have reported critical currents and fields for both the IQHE and FQHE, which are much higher than other authors but consistent with the QUILLS theory. Analysis of our data has provided direct measurements of both the FQHE gap energy, which is in close agreement with theory, and of the composite-fermion effective mass. The temperature dependence of the critical current in the IQHE has been measured, and is found to scale approximately exponentially with temperature, provided phonon scattering is the dominant mechanism for momentum conservation during the breakdown process. The critical current is independent of temperature when impurity scattering is the principal method of momentum conservation. The critical current in the FQHE regime was found to fall with temperature much more rapidly than in the IQHE.

By combining our techniques to measure *I-V* curves and $I_c(T)$ we hope to produce a complete *I-V-T* phase diagram for the IQHE, and possibly the FQHE.

1. S. Roshko, W. Dietsche and L.J. Challis, Phys. Rev. Lett. **80**, 3835 (1998).
2. C.L. Jones *et al.*, Surf. Sci. **229**, 25 (1990).
3. G. Ebert *et al.*, J. Phys. C **16**, 5441 (1983).
4. S. Komiyama *et al.*, Solid State Commun. **54**, 47 (1986).
5. M.E. Cage *et al.*, Phys. Rev. Lett. **51**, 1374 (1983).
6. L. Bliek *et al.*, Surf. Sci. **196**, 156 (1988).
7. A.H. MacDonald, T.M. Rice and W.F. Brinkman, Phys. Rev. B **28**, 3648 (1983).
8. N.Q. Balaban *et al.*, Phys. Rev. Lett. **71**, 1443 (1993).
9. C.L. Jones *et al.*, Soild State Commun. **97**, 763 (1996).
10. L. Eaves and F.W. Sheard, Semicond. Sci. Technol. **1**, 346 (1986).
11. P. Streda and K. von Klitzing, J. Phys. C **17**, L483 (1984).
12. J.P. Watts *et al.*, Phys. Rev. Lett. **81**, 4220 (1998).
13. For a review, see T. Chakraborty and P. Pietilainen, *The Fractional Quantum Hall Effect* (Springer-Verlag, Berlin, 1988).
14. D.R. Leadley *et al.*, Phys. Rev. Lett. **72**, 1906 (1994).
15. L.B. Rigal *et al.*, Phys. Rev. Lett. **82**, 1249 (1999).

PB.16

Optical Detection of the Breakdown Phenomena of Integer and Fractional Quantum Hall Effects in GaAs/AlGaAs Heterostructures

T. Takamasu, Y. Imanaka and G. Kido

National Research Institute for Metals, 3-13 Sakura, Tsukuba, 305 Ibaraki, Japan

We have studied photoluminescence (PL) signals from GaAs/AlGaAs heterostructure devices in strong magnetic fields with finite current flowing in the Hall-bar samples. An additional PL peak was found when the current density exceeds the critical value of current-induced breakdown of the quantum Hall effect. This phenomena gives us the information of heating property of electrons.

Introduction

Recently, many researchers have performed measurements of photoluminescence from two-dimensional electron gas in the interface of a GaAs/AlGaAs in quantizing strong magnetic fields[1-3]. Detailed study of these PL spectra can reveal various aspects of quantum Hall effect. However, only a few studies were dedicated to the non-equilibrium states of electrons such as finite current state[3]. Up to now, we have studied many aspects of the nonlinear transport properties of quantum Hall effect[4]. Detailed optical studies may be very useful to get information of the energy distribution of electrons in such non-equillibrium states. Here, we report the result of current dependence of PL spectra measured with GaAs/AlGaAs heterostructure devices in strong magnetic fields.

Experimental

Samples used are GaAs/AlGaAs single heterostructure devices grown by MBE method and shaped with photolithography method into Hall-bar geometry with 20μm width. Samples were placed in the ^{3}He cryostat with optical fiber, which can be used to illuminate sample with Ar-laser and detect PL light. To avoid the sample heating, we limited the laser power below 200μW. PL spectra were measured with CCD detector cooled by Pertier devices. Current can be applied during the optical measurements using two current contacts. For the evaluation of carrier densities, we measured two terminal resistance while the optical measurements were performed. Electron density of the sample is 5.3×10^{11} cm^{-2}. High magnetic field was applied to the sample using superconducting magnet and water-cooled magnet up to 25T. Current dependence of PL spectra measured at several different filling factors including fractional quantum Hall states.

Results and Discussion

Figure 1 shows magnetic field dependence of PL peak measured at T=0.5K. In the absence of magnetic field, mainly three peaks can be seen in PL spectrum. The main peak around 1.515eV can be assigned to the recombination from first excited state of electron to the hole state E_1. In addition to this peak, we have observed two acceptor related peaks at 1.47 and 1.49eV. At magnetic fields lower than ν=2, we could not observe a PL peak from the recombination between electron ground state to hole E_0. This is mainly due to difference of penetration of wave function between n=0 and n=1 [5,6]. In the single heterostructure devices, photoexcited hole

should move away from the hetero-interface. On the other hand, wave function of electronic states are confined near the interface. Because n=0 subband should be confined much strongly to the interface than n=1 state, overlap of the wave function between n=0 electronic state and hole state may be very small. So, the recombination probability of electrons and holes becomes very small for E_0 PL.

With increasing magnetic field, main peak (E_1) shifts to higher energy, however, no striking change can be observed. We have measured current dependence of the PL spectra with fixed magnetic field at ν=6 Hall plateau as shown in Fig. 2. With increasing current, an additional PL peak appears and increasing its intensity. This peak may be due to the recombination between the lowest subband of electronic state and hole state (E_0) from the energy. This peak can not be seen at zero or small magnetic fields. Similar current dependence of the additional peak can be seen with slightly different filling factor ν=6.18, however, no such peak can be seen in the transition region of two quantum Hall states. Peak intensity of the peak is not proportional to the current. In the inset of Fig.2, we show current dependence of PL intensity at ν=6. PL intensity increases drasitically at around I=6μA. At the same time of the appearance of the new peak, the intensity of the E_1 peak also increases slightly with current.

For the explanation of this additional peak, we considered current-driven breakdown phenomena of the quantum Hall effect. It is well known that finite current larger than a critical value breaks down the non-dissipative state of the quantum Hall effect [7]. This effect is explained as a super heating of electron system. Previously, we have estimated that electron temperature after the breakdown of the quantum Hall effect becomes larger than the Landau

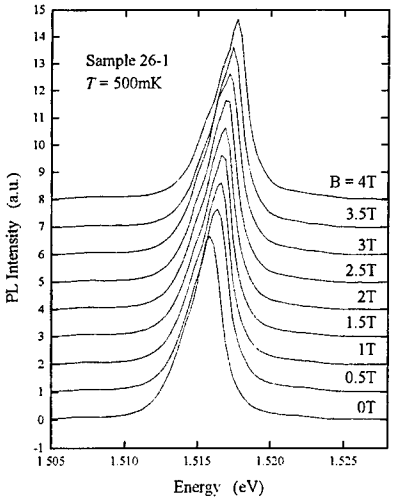

Fig. 1 Magnetic field dependence of photoluminescence measured with sample 1 at T=0.5K.

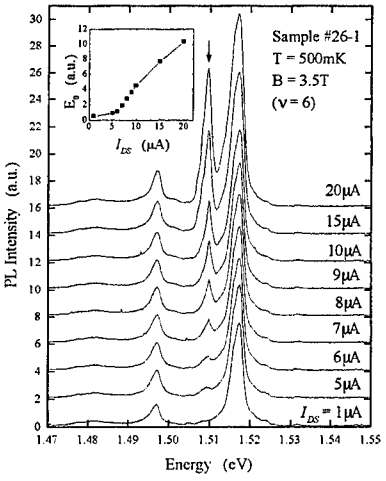

Fig. 2 Current dependence of PL signal measured at n=6 quantum Hall state. Peak intensity of arrowed PL peak is shown as a function of current in the inset.

level [7]. In such states, photoexcited electrons can recombine with holes placed far from the interface using finite wave vector of the acoustic phonon scatterings. Measured additional PL peak suggests that suppression of the E_0 PL peak appears due to this increase of acoustic phonon scatterings. With the four terminal measurements using the same sample, we confirmed that the critical current of the breakdown is around 6μA at several integer fillings. This value coincides with current value where the steep increase of PL intensity was observed. This fact means that electrons heated to the upper Landau levels of n=0 subband recombine with holes.

We have confirmed that the similar peak can be seen in different samples, however, strength and sharpness of the appearance of this peak have strong sample dependence. In the breakdown of the quantum Hall effect, electron temperature is considered to be highly inhomogeneous. Namely, electrons near the current contacts may be highly dissipative. Furthermore, energy dissipation in edge and bulk states may be different. This sample dependence can be explained by the phonon distribution in the sample. For the detailed analysis of the PL peak, it is needed that the position sensitive detection of PL measurements.
The increase of E_1 peak can be also explained when the above phonon assisted PL is correct. Recombination from n=1 subband should be also suppressed by the small overlap of wave function to the hole state. This suppression can be also released by the above phonon assisted process. However, the difference exists in that the E_1 peak needs only phonons of much higher temperature.

Current dependence of PL spectra can be also seen at the fractional quantum Hall effect.

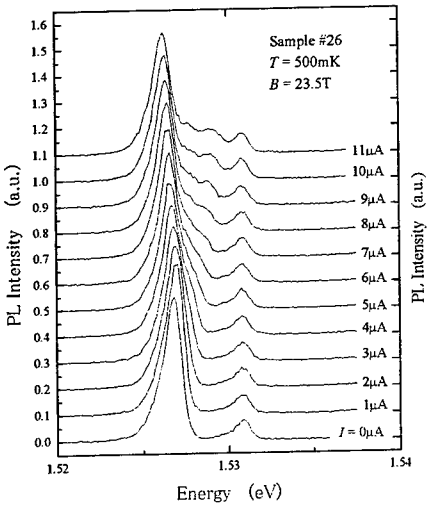

Fig. 3 PL spectra measured with sample 2 at ν=2/3 integer quantum Hall state.

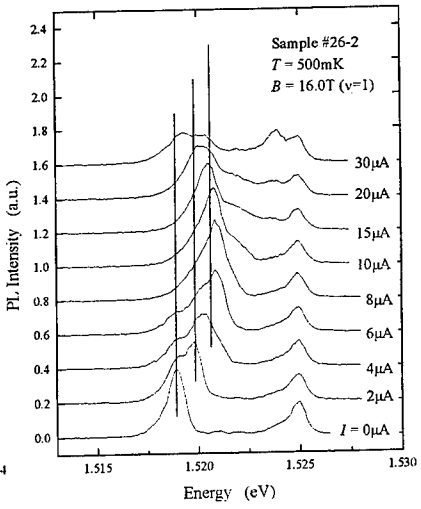

Fig. 4 The same plot measured at ν=1 fractional quantum Hall state.

Figure 3 shows PL spectra measured at ν=2/3. Here, no additional PL peak can be seen, however, main peak at 1.527eV shows obvious red-shift above 3μA. In the case of ν<2, instead of E_1 peak, E0 peak becomes dominant. For example at ν=1, with increasing current, E0 peak shows splitting which may be explained as PL peaks from higher Landau subbands. As shown in Fig. 4, average position of these splitting peaks shifts to higher energy corresponding to the raise of electron temperature due to the breakdown. On the other hand, at ν=2/3, such splitting of E_0 peak was not observed. Furthermore, the red-shift of the main peak suggests that averaged electron energy concerning to the PL decreases with increasing current. This fact strongly demonstrates the difference of electronic states between integer and fractional quantum Hall effect. At present, we have no clear explanation for the difference of PL spectra, however, it may include very important information about density of states of fractional quantum Hall effect such as higher Landau levels of composite Fermions.

In summary, we have measured current dependence of PL spectra in a wide range of current where the current-driven breakdown of the quantum Hall effect occurs and found that additional PL peak appears at integer quantum Hall states with filling factors ν<2. From the energy of the peak, we can assigned it as a E_0 which should be suppressed in this sample. Appearance of the peak is explained as a acoustic phonon assisted PL due to the super heating of the electrons in the breakdown phenomena. Furthermore, we found difference between current dependent PL spectra of integer and fractional quantum Hall states.

References

[1] I.V. Kukushkin, N.J. Pulsford, K. von Klitzing, K. Ploog, R.J. Haug, S. Koch and V.B. Timofeev, Phys. Rev. **B45** 4532 (1992).
[2] D. Heiman, B.B. Goldberg, A. Pinczuk, C.W. Tu, A.C. Gossard and J.H. English, Phys. Rev. Lett. **61,** 605(1988).
[3] N.N. Zinov'ev, A.V. Andrianov, L.J. Challis, C.T. Foxon and J.J. Harris, Physical Review **B53**, 7945 (1996).
[4] T. Takamasu, H. Dodo, M. Ohno, N. Miura, Surf. Sci. vol.361-362, 95(1996).
[5] A.J. Turberfield, S.R. Haynes, P.A. Wright, R.A. Ford, R.G. Clark, J.F. Ryan, J.J. Harris and C.T. Foxon, Phys. Rev. Lett. **65**, 637 (1990).
[6] T. Tsuchiya, S. Katayama and T. Ando, Surf. Sci. 361-362, 376(1996).
[7] S. Komiyama, T. Takamasu, S. Hiyamizu and S. Sasa, Solid State Commun. **54**, 479(1985).

PB.17

Current distribution in Hall bars and breakdown of the quantum Hall effect

K. Shizuya

Yukawa Institute for Theoretical Physics
Kyoto University, Kyoto 606-8502, Japan

Abstract

A numerical study is made of current distribution in small Hall bars with disorder. It is observed, in particular, that in the Hall-plateau regime the Hall current tends to concentrate near the sample edges while it diminishes on average in the sample interior as a consequence of localization. Also reported is another numerical experiment on a related, but rather independent topic, the breakdown of the quantum Hall effect. It is pointed out that the competition of the Hall field with disorder in the sample interior, an *intra*subband process, can account for both the magnitude and magnetic-field dependence $\propto B^{3/2}$ of the critical breakdown fields observed experimentally.

Keywords: Quantum Hall effect; Current distribution; Breakdown of quantum Hall effect

1. Introduction

The current distribution in a Hall sample is a subject of interest pertaining to the foundation of the quantum Hall effect (QHE). In spite of various studies, both experimental [1] and theoretical [2-4], it is still a focus of attention and controversy whether the Hall current flows in the sample interior or along the sample edges.

In this paper we first report on a numerical study of current distribution in small Hall samples with disorder and verify some theoretical observations [5]. In particular, we demonstrate an important physics of redistribution of the Hall current via disorder.

A by-product of the numerical analysis is a hint as to a rather independent subject, the breakdown of the quantum Hall effect [6-9]. We report on a numerical analysis [10] to verify that the competition of the Hall field with disorder in the sample interior, an *intra*subband process, can account for both the magnitude and magnetic-field dependence $\propto B^{3/2}$ of the critical breakdown fields $E^{\rm cr}$ observed in a series of experiments by Kawaji *et al.* [9].

2. Method of calculation

Consider a Hall bar bent into a loop of circumference L_x and width L_y, with a uniform magnetic field B normal to the plane. We distribute short-range impurities over it through an impurity potential $U(x,y)=\sum_i \lambda_i\,\delta(x-x_i)\delta(y-y_i)$, and detect the current j_x flowing in response to a uniform Hall field E_y. We take the $y=0$ edge to be a sharp edge where the wave function is bound to vanish and leave the other edge $y=L_y$ as a gentle edge.

For numerical calculations it is advantageous to work with the basis $\{|n,y_0\rangle\}$ of the eigenstates of the $U=E_y=0$ case, labeled by $n=0,1,2,\cdots$, and $y_0=\ell^2 p_x$, with $\ell\equiv 1/\sqrt{eB}$. Diagonalizing the Hamiltonian with respect to Landau labels n by a unitary transformation W, one obtains the Hamiltonian governing each impurity-broadened Landau subband:

$$\begin{aligned} H_n^{W}(y_0,y_0') &= h(y_0)\,\delta_{y_0y_0'} + U_{nn}(y_0,y_0') + \cdots, \\ h(y_0) &= \omega\{\nu_n(y_0)+\tfrac{1}{2}\} + eE_y\{y_0-\ell^2\nu_n{}'(y_0)\}, \end{aligned} \tag{1}$$

where the confining potentials $\omega\nu_n(y_0)$ relevant around $y_0\sim 0$ derive from the sharp edge.

Numerically diagonalizing $H_n^{\rm II'}$, one obtains eigenstates $|\alpha\rangle$ forming the nth subband and can calculate the associated current density $j_x^{(\alpha)}(x,y)$. We shall distinguish between $j_x^{(\alpha)}(x,y)$ present even in equilibrium and its response to a Hall field, the Hall-current component $j_{\rm Hall}^{(\alpha)}(x,y) = j_x^{(\alpha)}(x,y|E_y+\delta E_y) - j_x^{(\alpha)}(x,y|E_y)$, calculated with $\delta E_y = E_y/100$.

There are three competing effects to be considered. (i) Impurities capture electrons and make them localized. In contrast, (ii) a Hall field makes them drift with velocity $v_x \sim E_y/B$. A simple estimate of energy cost reveals how these two effects compete: An electron state localized around an isolated impurity of strength λ acquires an energy shift $\Delta\epsilon \approx \lambda/(2\pi\ell^2) \equiv s\,\omega$, where we have introduced a dimensionless strength s. When a Hall field is turned on, it will perceive over its spatial extent of $O(\ell)$ an energy variation of magnitude $\sim \ell E_y$. Accordingly, if the field becomes so strong that the field-to-disorder ratio

$$R \equiv e\ell\,|E_y|/(|s|\,\omega) \gtrsim 1, \tag{2}$$

the electron state would be delocalized. The numerical experiment given below reveals that $R^{\rm cr} \sim O(0.1)$ is the critical value for delocalization. Finally, (iii) the sharp edge $y = 0$ drives electrons along it by an "effective field" as strong as $e\ell E_y^{\rm eff} \sim \omega\ell\,\nu_n' \sim \omega$.

3. Hall-current distribution

We have examined current distributions for a number of samples. Here we mainly quote the case of a sample of length $\sqrt{2\pi}\ell \times 28 \approx 70\ell$ and width $\sqrt{2\pi}\ell \times 8 \approx 20\ell$, supporting $28 \times 8 = 224$ electron states in the $n = 0$ subband. 180 impurities of varying strength $|s_i| \le s_{\rm max} \sim 0.1$ are randomly distributed on it. We choose $E_y < 0$ so that the $y = 0$ edge is the "upper" edge, and in most cases take it very weak, $R = e\ell|E_y|/(s_{\rm max}\,\omega) \sim 1/10^4$.

We first summarize the observations drawn from our numerical analysis:
(i) The equilibrium current j_x and the Hall current $j_{\rm Hall}$ are substantially different in distribution. (ii) In the Hall-plateau regime the edge states (of the uppermost subband) are vacant and scarcely contribute to the current distribution. This indicates that the edge states are in no sense the principal carriers of the Hall current. (iii) In the plateau regime the Hall current $j_{\rm Hall}$ tends to diminish on average in the sample bulk and concentrate near the sample edges. (iv) The sharp edge and disorder combine to efficiently delocalize electrons near the edge. (v) The Hall field competes with disorder to delocalize electrons in the sample bulk.

Evidence for (i) and (ii) is seen from Fig. 1(a), where the total currents J_x and $J_{\rm Hall}$ carried by the $n = 0$ subband are plotted as a function of vacancies $N_{\rm v}$. There the edge states, carrying a large amount of current per state, are readily identified through a rapid decrease of J_x for $0 \le N_{\rm v} \lesssim 15$. They, however, have little effect on $J_{\rm Hall}$.

Note the contrast between the upper and lower plateaus in Fig. 1(a). This suggests observation (iv).

See next the (x-averaged) Hall-current distribution across the sample width in Fig. 1(b), which clearly demonstrates (iii). The density distribution in Fig. 1(c) also shows that in the plateau regime more electrons survive near the sample edge than in the interior. This gives evidence for the expulsion of the Hall current out of the disordered sample bulk, expected theoretically [5]. The decrease of the current in the sample bulk is correlated with the dominance of localized states there. This is confirmed by increasing a Hall field or R gradually: Drastic changes arise around $R \sim 0.1$; there the Hall plateaus disappear and a sizable amount of Hall current is seen to flow in the bulk. This leads to observation (v).

Figure 2 shows another demonstration of current redistribution via disorder. There it is clearly seen that electron states residing on the edges of the disordered region ("bulk edges")

support a considerable amount of Hall current per state and that a small number of states in the inner bulk carry an even larger amount.

Observation (v) suggests a possible mechanism for the breakdown of the QHE. We study the competition of the Hall field with disorder in detail in the next section.

4. Field-induced breakdown of the QHE

To simulate electrons in the bulk of a realistic sample we have considered electron states residing over a disordered domain of size $\approx 70\ell \times 30\ell$, where 360 random impurities with $|s_i| \leq s_{\max}$ are distributed. The main observation drawn from our numerical experiment is that, in the regime of dense impurities $N_{\rm imp}/N_{\rm state} > 1$ (which presumably applies to realistic samples), the number of localized states, $N^{\rm loc}$, decreases exponentially with $|E_y|$ and obeys an approximate scaling law written in terms of

$$R \equiv e\ell\,|E_y|/(s_{\max}\,\omega) \propto |E_y|/(s_{\max}\,B^{3/2}). \tag{3}$$

See the $N^{\rm loc} - R$ plots for the uppermost subband in Fig. 3(b); they stay approximately the same for a wide variation in magnetic field $B = B_0/\kappa$ with $\kappa = 1 \sim 4$. See also the $J_x^{\rm Hall} - N_{\rm v}$ plots in Fig. 3(a) for various choices of R. Actually the data refer to the $n = 0$ subband, but the way the plateaus shrink with increasing R turns out virtually the same for higher $n = 1, 2, 3$ subbands as well. This shows that the field-to-disorder ratio R is a good measure to express field-induced delocalization of electron states.

The underlying physical picture revealed by this scaling behavior of $N^{\rm loc}$ is that the electron states remaining localized in the near-breakdown regime are always governed by the same set of impurities of large strength $|s_i| \sim |s|_{\max}$; that is, one always encounters the same set of localized states prior to breakdown. We have confirmed this by observing that suppressing weaker impurities (e.g., $|s_i| < 0.5\,s_{\max}$) entails no essential change in the behavior of $N^{\rm loc}$ for large R.

This picture offers a simple explanation for the observed $E_y^{\rm cr} \propto B^{3/2}$ law of the critical breakdown field. (The fact that this scaling law is observed for samples differing in carrier density and mobility [9] would be attributed to relatively small variations in disorder-strength $|s|_{\max} \sim O(0.1)$ for a variety of samples.) It is also consistent with the observation of Cage *et al.* [7] that the breakdown of the dissipationless current is spatially inhomogeneous. Finally, it is a natural consequence of the present *intra*subband process that the magnitude of $E_y^{\rm cr}$ falls within the observed range of a few hundred V/cm, one order of magnitude smaller than what intersubband processes, such as Zener tunneling [8], typically predict.

5. Concluding remark

As for current redistribution via disorder, discussed in Sec. 3, it is essential to separate the (slow) Hall-current component $j_{\rm Hall}$ from the (fast) equilibrium current j_x. A way to achieve such separation in experiment is to use an alternating injected current. Information on the Hall-current distribution would then be obtained by detecting the alternating component in the Hall-potential distribution responding to it.

Acknowledgments

This work is supported in part by a Grant-in-Aid for Scientific Research from the Ministry of Education of Japan, Science and Culture (No. 10640265).

References

[1] P. F. Fontein *et al.*, Phys. Rev. B 43 (1991) 12 090, and earlier references cited therein.
[2] A. H. MacDonald, T. M. Rice, and W. F. Brinkman, Phys. Rev. B 28 (1983) 3648; O. Heinonen and P. L. Taylor, Phys. Rev. B 32 (1985) 633.
[3] T. Otsuki and Y. Ono, J. Phys. Soc. Jpn. 58 (1989) 2482.
[4] D. J. Thouless, Phys. Rev. Lett. 71 (1993) 1879; T. Ando, Phys. Rev. B 49 (1994) 4679.
[5] K. Shizuya, Phys. Rev. B 59 (1999) 2142; Phys. Rev. Lett. 73 (1994) 2907.
[6] G. Ebert, K. von Klitzing, K. Ploog, and G. Weimann, J. Phys. C 16 (1983) 5441.
[7] M. E. Cage *et al.*, Phys. Rev. Lett. 51 (1983) 1374.
[8] H. L. Stormer *et al.*, Proc. 17th Int. Conf. Physics of Semiconductors, San Francisco, 1984, ed. J. D. Chadi and W. A. Harrison (Springer Verlag, New York,1985) p. 267.
[9] S. Kawaji *et al.*, J. Phys. Soc. Jpn. 63 (1994) 2303; T. Okuno *et al.*, *ibid.* 64 (1995) 1881; T. Shimizu, T. Okamoto, and S. Kawaji, Physica B 249-251 (1998) 107.
[10] K. Shizuya, preprint YITP-99-38, submitted for publication.

Figures

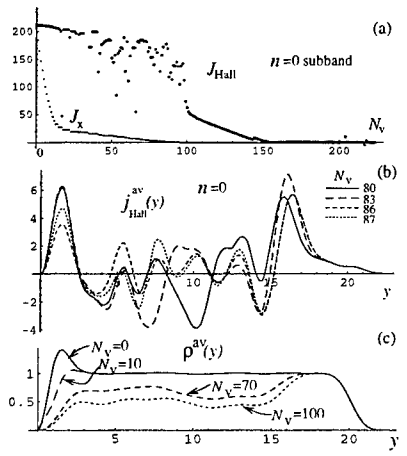

FIG. 1. (a) Total currents $J_{\rm Hall}$ and J_x (on different scales) vs vacancies N_v. (b) Hall-current distribution $j^{\rm av}_{\rm Hall}(y)$ [in units of $-(e^2/2\pi\hbar)\,\delta E_y$] in the plateau regime. (c) Density distribution.

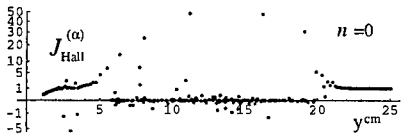

FIG. 2. Net amount of Hall current per state [on a square-root scale] as a function of center-of-mass position $y^{\rm cm}$ for each state. Impurities lie over $5\ell \le y \le 20\ell$.

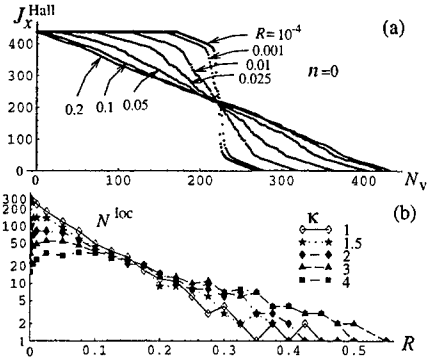

FIG. 3. (a) $J_x^{\rm Hall}$ vs N_v for $R = 0.0001 \sim 0.2$. (b) $\log N^{\rm loc}$ vs R for $B = B_0/\kappa$ with $\kappa = 1 \sim 4$.

PB.18

Relaxation of Inter-Landau-level excitations in the Quatised Hall Regime

S. Dickmann[1] and Y. Levinson[2]
[1]*Institute for Solid State Physics of Russian Academy of Sciences, 142432 Chernogolovka, Moscow District, Russia*
[2]*Department of Condensed Matter Physics, The Weizmann Institute of Science, 76100 Rehovot, Israel*

Relaxation of collective plasmon inter-Landau-level excitation is determined by emission of LO-phonons or by Auger-like processes when this emission is suppressed off the magneto-phonon resonance conditions. The decay of "one-cyclotron" magneto-plasmons with wave-vectors near the roton minimum is studied under the condition of filling $\nu = 1$. Some features of this relaxation should be helpful for the experimental detection of the magneto-rotons in a strongly correlated 2D electron gas.

In recent two decades considerable interest has been focused on the collective excitations in a strongly correlated two-dimensional electron gas (2DEG) under the quantum Hall regime conditions. For integer filling ν the calculation of the exciton-like spectra (which are in fact of Bose type) in the limit of high magnetic fields reduces to an exactly solvable problem [1-4]. At the same time the direct experimental discovery of such excitons (spin-flip waves, magneto-plasmons (MPs) without and with spin flip) presents certain difficulties. The inter-Landau-level MPs were observed in the works [5-7] by means of inelastic light-scattering. However, a massive breakdown in wave-vector conservation implied for this detection is not understood as yet.

The presented paper is devoted to the features of MP relaxation (MPR) which might help indirectly to reveal the presence of MP excitations in 2DEG. We concern only the MPs without spin flip, i.e. with the energies

$$\epsilon_{ab}(q) = \hbar\omega_c(n_b - n_a) + \mathcal{E}_{ab}(q) \qquad (n_b > n_a), \tag{1}$$

where ω_c is the cyclotron frequency, n_a and n_b are the numbers of initially (in the ground state) occupied and unoccupied Landau levels respectively. Having a Coulomb origin the energy $\mathcal{E}_{ab}$ is of the order of or smaller than $E_C = e^2/\kappa_0 l_B$ which is a characteristic energy of electron-electron interaction in 2DEG (l_B is the magnetic length, κ_0 is the dielectric constant). We should especially pay attention for MPs in such portions of their spectrum where the density of states becomes infinite (i.e. where $d\epsilon_{ab}/dq = 0$) or/and the wave-vector q is equal to zero. When so doing we take into account the definitive role of an experimental test. Indeed, the features in light-scattering spectra [5-7] attributed to the one-level excitations (where $n_b - n_a = 1$) are only detected in the vicinity of $q = 0$ (therewith $\mathcal{E}_{ab} = 0$ but $d\mathcal{E}_{ab}/dq \neq 0$) or near their roton minimum. In the latter case the interaction energy is

$$\mathcal{E}_{01} \approx \varepsilon_0 + (q - q_0)^2/2M, \quad |q - q_0| \ll q_0 \tag{2}$$

(the index ab is specified by replacing it with $n_a n_b$, since the spin state does not change in our consideration). We consider the case where $n_a = 0$ and $n_b = 1$ with filling $\nu = 1$; then in this equation $q_0 \approx 1.92/l_B$, $M^{-1} \approx 0.28\, E_C l_B^2$ and $\varepsilon_0 \approx 0.15\, E_C$ in the strict 2D limit (namely if 2DEG thickness d satisfies the condition $d \ll l_B$). Actually the MP spectra depend on d but their shape do not change qualitatively.

A. We first consider the magnetophonon resonance conditions when the energy ϵ_{01} defined by Eq. (1) is equal to the LO-phonon energy $\hbar\omega_{LO} = 35\,\text{meV}$ [8]. The resonance with $q = 0$ when $\omega_c = \omega_{LO}$ is just a consequence of the Kohn theorem and does not demonstrate the presence of MP excitations in the system. Therefore, we consider the case of magneto-roton relaxation when MP energy is transferred to the emitted optic phonon. Then in the vicinity

of $q \approx q_0$ we should expect the resonance if $\hbar(\omega_{LO} - \omega_c) \approx \mathcal{E}_{01}(q_0) = \varepsilon_0$. In the strict 2D limit this condition leads to the resonant magnetic field 19 T instead of 21 T corresponding to the case of $\omega_c = \omega_{LO}$.

We calculate now the rate of this relaxation. Describing the states of the system in terms of the Excitonic Representation which means the transition from electron annihilation and creation operators to the excitonic ones $Q_{ab\mathbf{q}}$ and $Q^+_{ab\mathbf{q}}$ (see Refs. [9-12]), we should therefore study the transition between electron states $|i\rangle = Q^+_{ab\mathbf{q}}|0\rangle$ and $\langle f| = \langle 0|$ ($\langle 0|$ is the ground state). The relevant matrix element calculation

$$\mathcal{M}_{ab\mathbf{q}} = \langle 0|\mathcal{H}_{e,ph}|Q^+_{ab\mathbf{q}}|0\rangle \tag{3}$$

assumes the Excitonic Representation for Hamiltonian of electron-phonon interaction,

$$\mathcal{H}_{e,ph} = \frac{1}{L}\left(\frac{\hbar}{L_z}\right)^{1/2} \sum_{\mathbf{k}} \tilde{U}^*_{opt}(\mathbf{k}) H_{e,ph}(\mathbf{q})\,, \tag{4}$$

where $L \times L \times L_z$ are the sample sizes, $\mathbf{k} = (\mathbf{q}, k_z)$ is the phonon wave-vector, $\tilde{U}_{opt}(\mathbf{k}) = \gamma(k_z)U_s(\mathbf{k})$ is the renormalized Fröhlich vertex (γ is the size-quantised form-factor [10]), namely: $|U_{opt}|^2 = 2\pi e^2\omega_{LO}/\overline{\kappa}k^2$ (the standard notation for the reduced dielectric constant $\overline{\kappa}^{-1} = \kappa_\infty^{-1} - \kappa_0^{-1}$ is used). The relevant representation for $H_{e,ph}$ operating on the electron states can be obtained similar to the case of exciton-acoustic-phonon interaction [10]:

$$H_{e,ph} = \frac{L}{l_B\sqrt{2\pi}}\left[h_{n_an_b}(\mathbf{q})Q_{ab\mathbf{q}} + h^*_{n_an_b}(-\mathbf{q})Q^+_{ab-\mathbf{q}}\right]. \tag{5}$$

Here $n_b \geq n_a$, and

$$h_{n_an_b}(\mathbf{q}) = (n_a!/n_b!)^{1/2}(q_+l_B)^{n_b-n_a}e^{-q^2l_B^2/4}L^{n_b-n_a}_{n_a}(q^2l_B^2/2)\,, \tag{6}$$

where L^j_n is Laguerre polynomial, $q_\pm = \mp i2^{-1/2}(q_x \pm iq_y)$. Now exploiting the relevant commutaion rules for the excitonic operators (see Refs. [10],[12]) we can find the matrix element (3) appropriate in our case,

$$\mathcal{M}_{01\mathbf{q}} = (\hbar/2\pi L_z)^{1/2}U^*_{opt}(\mathbf{k})h_{01}(\mathbf{q})/l_B, \tag{7}$$

and then the MPR rate

$$R_{ph} = \sum_{\mathbf{q}',k_z}\frac{2\pi}{\hbar}|\mathcal{M}_{01\mathbf{q}'}|^2\delta(\epsilon_{01} - \hbar\omega_{LO}) = \frac{e^2L^2\omega_{LO}}{4\overline{\kappa}|d\mathcal{E}_{01}/dq|}q^2e^{-q^2l_B^2/2}\overline{n}(q). \tag{8}$$

In the last expression q is the root of equation $\epsilon_{01}(q) = \hbar\omega_{LO}$, and $\overline{n}(\boldsymbol{q})$ is the occupation number of 01MPs.

Formally the result (8) becomes infinite when $q = q_0$. However, the real magnitude of R_{ph} in the vicinity of q_0 can be found from the analysis of the homogeneity breakdown due random impurity potential $U(\mathbf{r})$. Assuming $U(\mathbf{r})$ to be smooth (its correlation length $\Lambda \gg l_B$) one can find that the energy correction for any abMP is in the dipole approximation $\delta\mathcal{E} = -\hbar\mathbf{q}\mathbf{v}_d$, where $\mathbf{v}_d = (\hat{z} \times \nabla U(\mathbf{r}))l_B^2/\hbar$ is the drift velocity (see Refs. [3] and [12]). This energy is an inhomogeneous broadening of the MP energy and has to be added to $\mathcal{E}_{ab}$. The random potential correction plays no significant role if $|d\mathcal{E}_{ab}/dq| \gg l_B^2\,|\nabla U|$, which means that the electron-hole Coulomb interaction is stronger than the force the electron and the

hole are subjected to in the random potential. In other words, the derivative $|d\mathcal{E}_{ab}/dq|$ in Eq. (8) is limited from below by $l_B^2\,|\nabla U| \sim l_B^2\Delta/\Lambda$, where Δ is the random potential amplitude. Thus we obtain the rate near q_0 per unit area:

$$\left[R_{ph}/L^2\right]_{\max} \sim \frac{e^2\Lambda\omega_{LO}}{4\overline{\kappa}l_B^2\Delta}q_0^2 e^{-q_0^2l_B^2/2}\overline{n}(q_0). \tag{9}$$

The roton minima broadening due to inhomogeneity is $|\mathbf{q}-\mathbf{q}_0| \sim (2M\delta\mathcal{E})^{1/2}$. Estimating magneto-roton density as $N \simeq \overline{n}q_0(2M\delta\mathcal{E})^{1/2}$ and setting dN/dt equal to decay rate (9) we find the characteristic relaxation time $\tau_{ph} = \overline{n}dt/d\overline{n}$ which turns out to be of the order of

$$\tau_{ph} \sim 4\exp\left(q_0^2l_B^2/2\right)\left(\frac{\Delta}{\Lambda}\right)^{3/2}\left(\frac{2M}{q_0}\right)^{1/2}\frac{\overline{\kappa}l_B^3}{e^2\omega_{LO}} \sim 0.1 \div 0.01 \text{ ps}. \tag{10}$$

(we assume that $B = 10\,\text{T}$, $\Delta \simeq 1\,\text{meV}$, $\Lambda \simeq 50\,\text{nm}$).

B. Naturally, the above results should be compared with the analogous ones in the case when emission of LO-phonons is suppressed off the resonance conditions. Generally, the MPR mechanism seems to be determined by many-phonon emission. However, a certain additional relaxation channel exists precisely for the considered magneto-rotons. A coalescence of two of them with their conversion into a single MP of the "two-cyclotron" plasmon mode (with $n_a = 0$, $n_b = 2$) turns out to be energetically allowed because "by chance" the difference $\delta = \mathcal{E}_{02}(0) - 2\varepsilon_0$ is numerically very small. Namely, in the strict 2D limit $\delta \approx 0.019\,E_C \simeq 3 \div 4$ K for $B = 10 \div 20$ T. This coalescence leads to an Auger-like MPR process because as a result the total number of excited electrons decreases as well as the total number of MP excitations. The dependence $\mathcal{E}_{02}(q)$ is nonmonotonous, but in the range $0 < ql_B < 2.5$ does not change by more than $0.07\,E_c$. Nevertheless, it would be preferable observe the generated "two-cyclotron" MP in the state with small 2D wave-vector, because in this case the generated MP could be detected by anti-Stokes Raman scattering similar to the experiments of Refs. [5-7].

We calculate the decay rate due to such an Auger-like process,

$$\mathcal{R} = \frac{1}{2}\sum_{\mathbf{q}_1,\mathbf{q}_2}\frac{2\pi}{\hbar}\left|\mathcal{M}(\mathbf{q}_1,\mathbf{q}_2)\right|^2\overline{n}(\mathbf{q}_1)\overline{n}(\mathbf{q}_2)\delta\left[\mathcal{E}_{01}(\mathbf{q}_1)+\mathcal{E}_{01}(\mathbf{q}_2)-\mathcal{E}_{02}(\mathbf{q}_1+\mathbf{q}_2)\right], \tag{11}$$

where the required matrix element of the considered conversion is

$$\mathcal{M}(\mathbf{q}_1,\mathbf{q}_2) = \left\langle 0\left|Q_{02\,\mathbf{q}_1+\mathbf{q}_2}\left|H_{int}\right|Q^+_{01\mathbf{q}_1}Q^+_{01\mathbf{q}_2}\right|0\right\rangle. \tag{12}$$

Here bra and ket states are orthogonal, and H_{int} is the Coulomb interaction Hamiltonian of 2DEG. Rewriting H_{int} in the Excitonic Representation we should take into account that within the framework of the exploited high magnetic field approximation it is sufficient to keep in H_{int} only the terms which commute with the Hamiltonian of noninteracting electrons and therefore conserve cyclotron part of the 2DEG energy. When so doing we find that the only term which gives the contribution to the matrix element (12) is

$$H'_{int} = \frac{1}{2\pi l_B^2}\sum_{\mathbf{q}}V(q)h_{10}(\mathbf{q})h^*_{21}(\mathbf{q})Q^+_{12\mathbf{q}}Q_{01\mathbf{q}}, \tag{13}$$

where $V(q)$ is the 2D Fourier component of the Coulomb potential averaged with the wave function in the $\hat{z}$ direction (so that in the strict 2D limit: $V(q) = 2\pi l_B E_C/q$). Substituting the operator (13) for H_{int} into Eq. (12) and employing the special commutation rules for the

excitonic operators (see Refs. [10] and [12]) one can calculate the matrix element (12) for arbitrary $\mathbf{q}_1$ and $\mathbf{q}_2$. We will later need this quantity only when $\mathbf{q}_1 \approx -\mathbf{q}_2$ and $q_1 \approx q_2 \approx q_0$. In this case $\mathcal{M}(\mathbf{q}_0, -\mathbf{q}_0) = -2(2\pi)^{1/2}\mu l_B/L$, where in the strict 2D limit $\mu \approx 0.062 E_C$.

To calculate the depopulation rate of 01MPs (11) one has additionally to know the $\overline{n}(\mathbf{q}_1)$ distribution and the appropriate phase area A for the relevant final wave-vectors of 02MPs $\mathbf{q} = \mathbf{q}_1 + \mathbf{q}_2$. When this area is sufficiently small, namely if $\pi q^2 \leq A \ll 4\pi^3 M\delta$, the result is

$$\mathcal{R}/L^2 = \frac{\overline{n}^2(q_0)\mu^2 l_B^2 q_0}{2\pi\hbar}\left(\frac{M}{\delta}\right)^{1/2} A\,. \tag{14}$$

This is just the case for the rate (11) when 02MP creation occurs in the phase area relevant for anti-Stokes inelastic backscattering. Then the role of the random potential in determining the value of A is crucial. Indeed, if $ql_B < 1$, one can get an estimate $d\mathcal{E}_{02}/dq \sim E_C q^2 l_B^3$ (see Ref. [2]), and the uncertainty in q due to disorder turns out to be $\tilde{q} \sim (\Delta/E_c)^{1/2}(\Lambda l_B)^{-1/2}$ (for the adopted numerical parameters we find $\tilde{q} \sim 10^5\,\mathrm{cm}^{-1}$). The quantity $\pi\tilde{q}^2$ should be substituted into Eq. (14) for A.

If we wish to obtain the total rate of the Auger-like MP relaxation, then with the help of Eq. (11) a more complicated summation has to be fulfilled. Nevertheless, in this case Eq. (15) may be also employed for the approximate estimation if we substitute there $A \sim \pi l_B^{-2}$. Then estimating the 01MP density near their roton minima as $N \simeq \overline{n}(q_0)q_0(2M\delta\mathcal{E})^{1/2}$ and setting dN/dt equal to the relevant total rate of the coalescing 01MPs we find

$$\tau_{Aug} = \overline{n}dt/d\overline{n} \sim \frac{2\hbar}{\overline{n}\mu^2}\left(\frac{2\delta\Delta l_B}{\Lambda}\right)^{1/2} \sim 1/\overline{n}\,\mathrm{ps}\,. \tag{15}$$

This time is by about a factor of 100 is longer than that given by Eq. (10). On the other hand, the considered Auger-like process is certainly the dominant relaxation channel in the case of 01-magneto-rotons, if the magneto-phonon resonant conditions are not met.

It is very significant that the studied type of MP relaxation can reveal an additional possibility for the indirect experimental detection of the magneto-rotons. Indeed, if one somehow excites 01MPs near their roton minima, then one could simultaneously observe the 02MPs (and therefore electrons at the 2-nd Landau level). It seems such an observation might be performed by means of anti-Stokes Raman scattering or by means of hot luminescence from the 2-nd Landau level.

The work is supported by the MINERVA Foundation and by the Russian Fund for Basic Research.

References

1. Yu. A. Bychkov, S. V. Iordanskii, and G. M. Éliashberg, JETP Lett. **33**, 143 (1981).
2. C. Kallin, and B. I. Halperin, Phys. Rev. B **30**, 5655 (1984).
3. C. Kallin, and B. I. Halperin, Phys. Rev. B **31**, 3635 (1985).
4. J. P. Longo, and C. Kallin, Phys. Rev. B **47**, 4429.
5. A. Pinczuk, *et al.*, Phys. Rev. Lett. **68**, 3623 (1992).
6. A. Pinczuk *et al.*, Phys. Rev. Lett. **70**, 3983 (1993).
7. A. Pinczuk, *et al.*, Semicond. Sci. Technol. **9**, 1865 (1994).
8. We restrict ourselves to the bulk optic-phonon modes in GaAs. In this case only the longitudinal phonons interact with of the conduction band electrons.
9. A. B. Dzyubenko, and Yu. E. Lozovik, Sov. Phys. Solid State **26**, 938 (1984).
10. S. Dickmann, and S. V. Iordanskii, JETP **83**, 128 (1996).
11. S. Dickmann, Physica B **263-264**, 202 (1999).
12. S. Dickmann, and Y. Levinson, http://publish.aps.org/eprint/gateway/eplist/aps1999feb01_001 .

PB.19

Resistance fluctuations in integer quantum-Hall transitions

T. Machida [A,B], S. Ishizuka [A], K. Muraki [C], Y. Hirayama [C], and S. Komiyama [A]

[A] *Department of Basic Sciences, University of Tokyo, Komaba 3-8-1-16-622, Meguro-ku, Tokyo 153-8902, Japan*

[B] *CREST, Japan Science and Technology Corporation, Kawaguchi, Saitama 332-0012, Japan*

[C] *NTT Basic Research Laboratories, 3-1 Morinosato-Wakamiya, Atsugi, Kanagawa 243-0198, Japan*

Abstract

We study experimentally the resistance fluctuations (RF) in integer quantum-Hall transitions for high-mobility two-dimensional electron gas systems. In order to examine the role of coherence in RF, conductance through two scattering regions, that are spatially separated but interfere with each other quantum-mechanically, is studied. The experiments strongly suggest that the phase coherence does not play a substantial role in determining the pattern of RF, whereas it affects the amplitude of RF.

1. Introduction

Mesoscopic fluctuations have been intensively studied for more than a decade [1]. It has been well established that electron systems in zero magnetic field show sample specific conductance fluctuations if they are in a coherent regime. Recently, interest has been extended to the fluctuations in integer quantum-Hall (IQH) transitions [2-11]. At present, two possibilities are discussed as for the mechanism of fluctuations in high magnetic fields: (i) the interference among many different electron trajectories, analogous to the universal conductance fluctuations in low magnetic fields [4-7]; and (ii) resonant back-scattering caused by a small number of localized states [8-11]. The coherence of electron systems is the prerequisite of the fluctuations for both interpretations. In the existing experiments, however, it remains unclear whether the fluctuations are indeed attributed to a coherent process only.

In this work, in order to examine the role of coherence in the mesoscopic fluctuations in a rigorous manner, we study conductance through two scattering regions that are spatially separated but interfere quantum-mechanically with each other [12].

2. Samples and measurements

Samples are $Al_{0.3}Ga_{0.7}As/GaAs$ heterostructure Hall bars with two Schottky cross-gates separately placed in series at a distance of L_D = 10 μm as shown in the inset of Fig. 1. The samples are fabricated on three different wafers, I, II, and III, which are of the electron mobilities μ_H and the sheet carrier densities n_s at 4.2 K such that (μ_H, n_s) = (60, 2.4), (70, 3.5), and (100, 1.7) in units of m^2/Vs and 10^{15} m^{-2}. Samples with different gate lengths L_G and different widths W_G of the two-dimensional electron gas (2DEG) channel, (L_G, W_G) = (0.4, 4), (0.6, 4), (1, 4), and (3, 3) in a unit of μm, are studied. Measurements are carried out in a ^{3}He-^{4}He dilution refrigerator. Low-pass filters inside the mixing chamber and outside the cryostat efficiently eliminate the noise heating. The resistance values are studied with a standard lock-in technique, and the differential resistance values are studied by modulating the gate-bias voltage V_G with an amplitude of 250 μV at a given dc-bias current ranging from I = 125 pA to 64 nA.

3. Experimental results

When the gate-bias voltage is V_G = 0, the four-terminal longitudinal resistance R_{4t} shows standard Shubnikov-de Haas oscillations in a sweep of perpendicular magnetic field B. Resistance fluctuations (RF) are observed in all the samples in the sweep of V_G at a fixed B.

Figure 1 shows an example of R_{4t} in one sample (L_G = 3 μm, W_G =3 μm, wafer I). A magnetic field of B = 2.5 T is applied to the sample so that the 2DEG regions outside the gates are in the IQH-state with the Landau level filling factor ν = 4. In this condition, the 2DEG regions underneath and outside the gates act as scattering regions and perfect leads, respectively. By negatively biasing one of the gates (G_L or G_R), the 2DEG region underneath the gate undergoes a transition from the ν = 4 to the ν = 3 IQH-state and exhibits distinct RF. In all the samples studied, we found that the RF is reproducible and characteristic of the respective regions. Fourier transform of the RF is shown in the inset of Fig. 1.

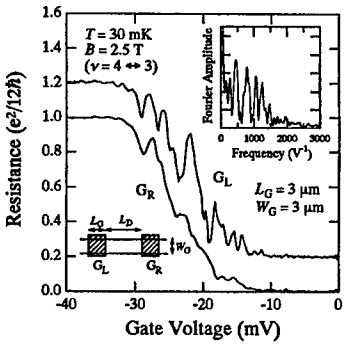

Fig. 1 IQH-transitions for G_L (upper) and G_R (lower). The line for G_L is offset for clarity. Fourier transform of the data for G_L (upper-right inset). Schematic representation of the sample (lower-left inset).

Figure 2(a) shows the differential longitudinal resistance $\partial R_{4t}/\partial V_G$ in the IQH-transition for G_L in the same sample at different I. In a lower current range (I < 2 nA), the transition spectrum is kept almost unchanged. Beyond I = 2 nA, however, the RF structure is smoothed out while the transition width ΔV_G starts increasing remarkably. Figure 2(b) elucidates the I-dependence of the average amplitude of the fluctuation, $A_{RF} = [\overline{(\partial R_{4t}/\partial V_G)^2} - \overline{(\partial R_{4t}/\partial V_G)}^2]^{1/2}$, and that of ΔV_G. The I-dependence of ΔV_G can be described as $\Delta V_G \propto I^{0.2}$ (dotted line) in the larger-current range [13]. The T-dependence of A_{RF} and that of ΔV_G are also studied and found to be similar to the I-dependence, viz. A_{RF} starts diminishing when ΔV_G starts increasing with increasing T. Similar measurements in different B (different IQH-transitions) show that the critical current I_C and the critical temperature T_C for the RF in a given sample are almost independent of B. We note here that the inelastic-scattering length L_{in} is much larger than the size of the scattering regions studied here at T < 100 mK [14]. Hence, the increase of ΔV_G in the present experiments indicates that the L_{in} becomes smaller than the size of the scattering region. Thus, the experimental results suggest that the RF structure observed here is distinct only in the condition where the electron system is coherent.

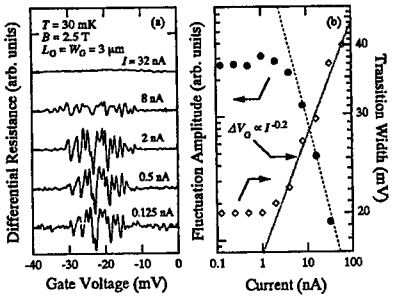

Fig. 2 (a) RF for G_L at different current levels. The lines are offset for clarity. (b) The amplitude of RF (closed circle) and the transition width ΔV_G of the IQH-transition (open square). The dotted line is a fit to ΔV_G in the higher-current range. The dashed line is a guide to eyes.

In order to examine the role of coherence in more detail, we apply the gate-bias voltage to the two gates simultaneously. Since the phase coherence length of edge states is larger [12] than the length L_D = 10 μm of edge channels connecting the two scattering regions, the electron states underneath the two gates are expected to interfere coherently.

Surprisingly, the pattern of RF structure has proven to remain substantially unchanged despite the interference. This is a general feature found in all the samples with different gate sizes as well as in the samples fabricated on the different heterostructures. The solid line in Fig.

3 shows an example of the IQH-transition taken on a sample (L_G = 0.6 μm, W_G =4 μm, wafer II) by simultaneously biasing the two gates G_L and G_R. The dashed line in Fig. 3 shows a numerical sum of the respective single-gate spectra for G_L and G_R, which are taken by biasing G_L and G_R separately. When the two gates are simultaneously biased (solid line), the IQH-transition shows a RF pattern different from either one of the single-gate spectra for G_L and G_R. However, it is important that the pattern of RF (solid line) closely resembles the one obtained by simply adding the resistance of each region (dashed line). It should be also noted, however, that the average amplitude of the RF (solid line) is distinctly larger than the one obtained by the numerical addition (dashed line) on the higher-energy side in the transition, while the feature is reversed on the lower-energy side. These features are found to be true also for different IQH-transitions as well as in all the samples studied.

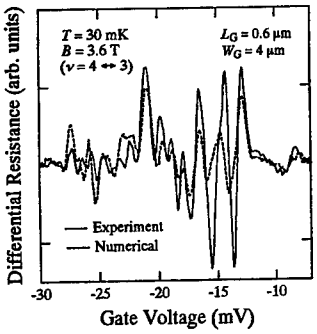

Fig. 3 The double-gate spectrum of RF for G_L and G_R (solid line). The numerical sum of the single-gate spectra for G_L and G_R (dashed line).

Figure 4 shows $\partial R_{4v}/\partial V_G$ in the same sample as a function of B. Both G_L and G_R are biased at V_G = -15.7 mV (corresponding to one peak in the RF structure). Characteristic periods of the fluctuations are on the order of δB = 10 mT. A similar pattern of the B-induced fluctuation is obtained when either one of the gates is biased. A similar feature is also found in all the samples with characteristic period of δB = 4-25 mT, corresponding to a magnetic flux quantum threading the region of S = 0.16-1 (μm)^2.

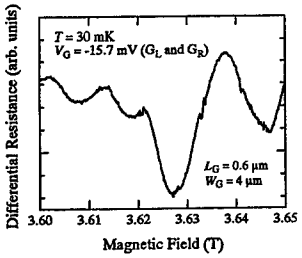

Fig. 4 Magnetic-field-induced fluctuations for the total system (G_L and G_R).

4. Discussion

The pattern of RF for the total system consisting of two scattering regions closely resembles the one obtained by classically adding the resistance of each region. This result strongly suggests that the RF observed here is of a classical origin. This view is supported further by the fact that the characteristic period in V_G of RF is relatively large, about $\delta V_G \simeq 2$ mV. This value is substantially independent of the size of the gates and the mobility of the wafers. The period of $\delta V_G \simeq 2$ mV corresponds to the number of electron states $N_e \simeq$ 50-120. Also, the characteristic period in B of B-induced RF, $\delta B \simeq$ 4-25 mT, corresponds to the number of magnetic flux quantum $N_\phi \simeq$ 6-60 threading the area of the scattering regions. Thus, all these results strongly suggest that the RF observed here is, unlike the conventional interpretation of RF [4-11], not a signature of individual electron levels.

We do not have a clear explanation of the phenomenon but can suggest two mechanisms that might be relevant: (i) Strongly localized states may be relevant to the transport through the scattering region at high magnetic fields. The charging effect at the localized states may give rise to conductance fluctuations in analogy to irregular Coulomb conductance oscillations expected for a random network of quantum dots. Polyakov and Samokhin discuss IQH-transitions in terms of the Coulomb blockade of

localized states [15]. For the relevant conductive islands, the size of S = 0.16-1 $(\mu m)^2$ may not be unreasonable in the present experiments. The charging effect is also consistent with the fact that I_C and T_C of smoothing out of the RF are almost independent of B. (ii) As electrons underneath the gate are depleted by negatively biasing V_G, the profile of the electrostatic potential is expected to vary irregularly because the screening effect due to electrons occupying the highest Landau level changes. This may cause the conductance to fluctuate as V_G is scanned. The same is also true when B is scanned.

Finally we emphasize that the total electron system is coherent in the present experiments. This is suggested not only from the fact that the inelastic-scattering length well exceeds the size of scattering region [14], but also from the present finding that the amplitude of the RF is distinctly enhanced in the higher-energy side of the IQH-transition and suppressed in the lower-energy side.

5. Summary

We study experimentally the RF in integer quantum-Hall transitions to examine the role of coherence in RF. The experiments suggest that the phase coherence does not play a substantial role in determining the pattern of RF, whereas the phase coherence affects the amplitude of RF. The charging effect of localized states and/or the screening effect of electrons may be relevant to the mesoscopic fluctuations in high magnetic fields.

Acknowledgment

The work has been supported by Core Research for Evolutional Science and Technology (CREST) of Japan Science and Technology Corporation.

References

[1] Y. Imry, *Introduction to mesoscopic physics*, Oxford univ. press, New York (1997).

[2] D. H. Cobden and E. Kogan, Phys. Rev. B **54**, 17316 (1996).

[3] S. Cho and M. P. A. Fisher, Phys. Rev. B **55**, 1637 (1997).

[4] Z. Wang, B. Jovanovic, and D-H Lee, Phys. Rev. Lett. **77**, 4426 (1996).

[5] S. Xiong and A. D. Stone, Phys. Rev. Lett. **68**, 3757 (1992).

[6] D. L. Maslov and D. Loss, Phys. Rev. Lett. **71**, 4222 (1993).

[7] A. G. Galstyan and M. E. Raikh, Phys. Rev. B **56**, 1422 (1997).

[8] J.A. Simmons, H. P. Wei, L. W. Engel, D. C. Tsui, and M. Syayegan, Phys. Rev. Lett. **63**, 1731 (1989).

[9] P. C. Main, A. K. Geim, H. A. Carmona, C. V. Brown, T. J. Foster, R. Taboryski, and P. E. Lindelof, Phys. Rev. B **50**, 4450 (1994).

[10] J. K. Jain and S. A. Kivelson, Phys. Rev. Lett. **60**, 1542 (1988).

[11] M Büttiker, Phys. Rev. B **38**, 12724 (1988).

[12] T. Machida, H. Hirai, S. Komiyama, T. Osada, and Y. Shiraki, Solid State Commun. **103**, 441 (1997).

[13] H. P. Wei, L. W. Engel, and D. C. Tsui, Phys. Rev. B **50**, 14609 (1994).

[14] T. Machida, H. Hirai, S. Komiyama, and Y. Shiraki, Phys. Rev. B **54**, 16860 (1996).

[15] D. G. Polyakov and K. V. Samokhin, Phys. Rev. Lett. **80**, 1509 (1998).

PB.20

Spatial structure of an incompressible Quantum Hall strip

Ivan A. Larkin† and L.S. Levitov‡
†*Department of Physics and Astronomy, University of Sheffield, Sheffield S3 7RH, UK*
‡*Center for Materials Science & Engineering, Physics Department, MIT, Cambridge, MA-02139*

Abstract

The incompressible Quantum Hall strip is sensitive to charging of localized states in the cyclotron gap. We study the effect of localized states by a density functional approach and find the charge density and the strip width as a function of the density of states in the gap. Another important effect is electron exchange. By using the Wiener–Hopf technique, we obtain an analytic solution for a model density functional. Both effects, localized states and exchange, lead to a substantial increase of the strip width.

Theory of the QHE predicts that near integer filling the system divides into compressible regions separated by incompressible strips [1]. Potential distribution within a QHE sample was recently imaged by using capacitance probes [2,3], atomic force microscope [4] and single electron transistor [5]. High resolution images of the incompressible strip [2,3] give the strip width several times larger than the theoretical prediction [1]. To bridge between theory and experiment one has to extend the analysis [1] to include

- the effect of disorder producing finite density of states in the cyclotron gap;
- electron exchange correlations which affect compressibility of the QHE state.

Below we study these effects using a Density Functional approach, taking special care of the effect of a large dielectric constant ($\epsilon_{GaAs} = 12.1$). Because of relatively small depth of the 2DEG beneath the semiconductor surface, the interparticle interaction within the 2DEG is affected by image charges. This changes electrostatics of the strip, and modifies potential induced on the exposed surface.

Finite density of states in the QHE gap gives rise to a finite screening length. For an incompressible strip of width exceeding this screening length, we find a large departure from the model [1], in agreement with [8]. The results compare well with the experiment [3].

The effect of electron exchange is important in determining the structure of compressible regions adjacent to the strip. Exchange correlation gives rise to negative compressibility [7] of the 2DEG. We consider negative compressibility by using a model density functional, and show that it strongly alters the distribution of electric charge, even to the extent that the potential and the charge density profiles can become nonmonotonic.

The effect of finite density of states in the cyclotron gap. Incompressible strips are formed in the regions of nonuniform 2DEG density, at nearly integer filling, created either by perturbing the exposed surface by an STM probe [2] or by gating the 2DEG [3]. The strips are aligned normal to the average 2DEG density gradient. Charge distribution around the strip is controlled by electrostatics [1,6].

Density $n(r)$ in the 2DEG buried at a distance d beneath semiconductor surface can be found by minimizing a density functional:

$$-U_{\rm ext}(r) = \int V(r-r')n(r')d^2r' + \mu(n)\,, \qquad V(r) = \frac{e^2}{\epsilon|r|} + \frac{(\epsilon-1)e^2}{\epsilon(\epsilon+1)\sqrt{r^2+4d^2}} \qquad (1)$$

Here $U_{\rm ext}(r)$ is external potential due to donors or gates, the Hartree interaction $V(r-r')$ takes into account image charges, and the chemical potential μ includes various non–Hartree contributions: finite density of states, QHE gap, exchange effects, etc.

Since the scale of the observed structures [2,3] is always larger than the 2DEG depth d, we replace the Hartree interaction in (1) by $V(r) = 2e^2/((\epsilon+1)|r|)$, assuming $|r| \gg d$.

In this section we consider a free electron model for $\mu(n)$ which includes degenerate (*i.e.*, infinitely compressible) Landau level states and localized states in the QH gap:

$$dn/d\mu = (n_{\rm LL} - n_{\rm gap}) \sum_{m>0} \delta(\mu - m\hbar\omega_c) \; + \; n_{\rm gap}/\hbar\omega_c \; , \qquad n_{\rm LL} = eB/hc \; . \tag{2}$$

In the simplest model Eq.(2) the density of localized states is constant.

Below we focus on the $m = 1$ QHE plateau. To introduce the 2DEG density gradient into the problem, we express $U_{\rm ext}$ in terms of fictitious positive charge density within the 2DEG plane:

$$U_{\rm ext}(r) = \int V(r-r') n_{\rm eff}(r') d^2r' \; , \qquad n_{\rm eff}(r) = -n_{\rm LL} - \vec{r} \cdot \vec{\nabla} n \tag{3}$$

For $\mu(n) \to 0$ in (1), *i.e.* without magnetic field, it follows from (1) that $n(r) = -n_{\rm eff}(r)$.

Now, we nondimensionalize the problem by choosing

$$w_0 = \left((\epsilon+1)\hbar\omega_c / 2e^2 |\nabla n| \right)^{1/2} \qquad \text{and} \qquad n_0 = \left((\epsilon+1)\hbar\omega_c |\nabla n| / 2e^2 \right)^{1/2} \tag{4}$$

as the length and density units. Then the only remaining dimensionless parameter is $\gamma = n_{\rm gap}/n_0 = n_{\rm gap} \left(2e^2/(\epsilon+1)\hbar\omega_c|\nabla n|\right)^{1/2}$. The nondimensionalized problem reads:

$$\int \frac{(x' - \delta n(r')) d^2r'}{|r-r'|} = \int_0^{\delta n(r)} F_\gamma(u) du \tag{5}$$

where $\delta n(r) = n(r) - n_{\rm LL}$, and $F_\gamma(u) = \gamma^{-1}$ for $|u| < \gamma/2$, and 0 otherwise.

One can obtain exact results for $\gamma \to 0$ and $\gamma \gg 1$. The strip width at $\gamma = 0$ is $2w_0/\pi$, in accord with [1]. At $\gamma \gg 1$ the deviation from constant density gradient is small, and thus the strip width is $n_{\rm gap}/|\nabla n|$.

We solve the problem numerically for all γ (see Fig. 1). In the whole range of γ the strip width is very accurately given by the formula

$$w \approx (2/\pi + \gamma) w_0 = (2/\pi) w_0 + n_{\rm gap}/|\nabla n| \; . \tag{6}$$

In the experiment [3], at the $m = 2$ plateau, the density of states in the gap $n_{\rm gap} \approx 0.03\, n_{\rm total}$, where $n_{\rm total} = 1.5 \cdot 10^{11}$ cm^{-2}. The density gradient $\nabla n \approx 2 \cdot 10^{10}$ cm$^{-2}/\mu$m. Substituting this in (4), we get $w_0 = 0.3\mu$m, $\gamma \approx 1$. In the fully incompressible case [1], the strip width would be $2w_0/\pi = 0.2\,\mu$m. The observed width $0.5\,\mu$m agrees with Eq.(6) for estimated γ.

The effect of negative compressibility of the compressible edge. For a fully incompressible strip ($n_{\rm gap} = 0$), the density is constant within it and varies outside as a square root of the distance from the strip edge [1]. Here we study how this behavior is modified due to finite compressibility of the Landau level states. The Thomas–Fermi theory recipe

is to use Eq.(1) with $\mu(n) = \delta n/\kappa$, where κ is compressibility. Such a model, however, is inconsistent, because of the *negative* sign of κ in the QH state [7]. The Thomas–Fermi problem with $\kappa < 0$ leads to an unphysical instability.

The difficulty is circumvented by realizing that the exchange interaction in the case of negative compressibility is essentially nonlocal [9]. This motivates using in (1) an effective interaction which is simplest to write in the Fourier representation:

$$V_{\rm eff}(k) = \frac{4\pi e^2}{(\epsilon+1)|k|}\Lambda(k)\ , \qquad \Lambda(k) > 0, \qquad \Lambda(0) = 1, \qquad \Lambda'(0) = \frac{(\epsilon+1)}{4\pi e^2\kappa} = -a\ , \quad (7)$$

where $a > 0$ is the screening length. The interaction (7) with listed restrictions on $\Lambda(k)$ ensures stability as well as correct Hartree interaction and compressibility. Otherwise, one can make a reasonable choice of $\Lambda(k)$ at $ka > 1$.

The problem (1) near the strip edge (with $V_{\rm eff}$ from (7) and $\mu = 0$) can be solved by the Wiener–Hopf method. We write $\delta n(x) = n^+(x)\theta(x) + n^-(x)\theta(-x)$, where $x > 0$ is the compressible region, and Fourier transform Eq.(1): $V_{\rm eff}(k)n_k^+ = -(U_{\rm ext}^+(k) + U_{\rm ext}^-(k))$, where $n_k^\pm$ and $U_{\rm ext}^\pm(k)$ are analytic in the upper and lower complex k half-planes. The Wiener–Hopf trick requires factoring $V_{\rm eff}(k) = A_k^+/A_k^-$, where $\pm$ indicates the analyticity half-plane. Then, $A_k^- U_{\rm ext}^+(k) = \left[A_k^- U_{\rm ext}^+(k)\right]^+ + \left[A_k^- U_{\rm ext}^+(k)\right]^-$ which yields $n_k^+ = -[A_k^- U_{\rm ext}^+(k)]^+/A_k^+$.

We use $V_{\rm eff}(k)$ of the form (7) with

$$\Lambda(k) = \exp\left[-ak(1 - (2/\pi)\tan^{-1}(k/\lambda))\right]\ , \quad (8)$$

and obtain a Wiener–Hopf solution in a closed form. Here the parameter λ regularizes the interaction at large k (and small r): $V_{\rm eff}(r \ll \lambda^{-1}) = e^{-2\lambda a/\pi}V(r)$. Factoring this $V_{\rm eff}(k)$ gives

$$A_k^+ = \frac{4\pi e^2}{(k-i\delta)^{1/2}}\left(\frac{\delta + ik}{\lambda + ik}\right)^{ik/\pi}\ , \quad A_k^- = (k+i\delta)^{1/2}\left(\frac{\delta - ik}{\lambda - ik}\right)^{ik/\pi}\ , \quad (9)$$

where $\delta = +0$. Near the edge $U_{\rm ext}(x) = Ex + c$, and thus

$$n_k^+ = \frac{(\epsilon+1)E}{4\pi e^2}\frac{(i\delta^*)^{1/2}}{(k-i\delta)^{3/2}}\left(\frac{k-i\lambda}{k-i\delta}\right)^{ik/\pi}\ , \quad (10)$$

where $\delta^* \sim w_0^{-1}$. The inverse Fourier transform of n_k^+ gives the charge distribution near the strip edge. Note the asymptotic behavior of $\delta n(x)$: $\delta n(x \gg \lambda^{-1}) = 2n_0(x/\pi w_0)^{1/2}$, $\delta n(x \ll \lambda^{-1}) = 2n_0(x/\pi w_0)^{1/2}e^{\lambda a/\pi}$. Here we expressed E and δ^* in terms of w_0 and n_0.

At large screening length a there is a significant departure of the density near the edge from the square root profile of [1]. The density profile becomes *nonmonotonic* at $a\lambda \gg 1$.

We studied numerically the effect of exchange on the strip width. As the exchange interaction parameter increases, the strip becomes wider (see Fig.2). In the simulation, a model $V_{\rm eff}(r) = \alpha/|r| + (1-\alpha)/(r^2+\tilde{a}^2)^{1/2}$ was used, which is very close to (8) provided the values $\alpha = e^{-2\lambda a/\pi}$ and $\tilde{a} = a/(1-\alpha)$ are chosen. Note that our density functional, being quadratic in $n(r)$, obeys an exact particle–hole symmetry. Hence the density profiles on the upper and lower sides of the plateau in Fig.2 are identical up to a sign change.

In conclusion, we find that finite density of localized states and electron exchange interaction both have similar effect on the width of the incompressible strip. The strip width increases as a function of the localized states density, and as a function of electron exchange parameter. However, the density profile in these two problems evolves differently. For a high density of localized states the density gradient becomes nearly uniform, whereas at large exchange the step in the density distribution becomes sharper and wider. At very high exchange, the density profile even becomes nonmonotonic.

L.L. is grateful to R. Ashoori, G. Finkelstein, T. D. Fulton, and A. Yacoby for useful discussions of their data. Research at MIT is supported by NSF Award 6743000 IRG.

References

1. D. B. Chklovskii, B. I. Shklovskii, and L. I. Glazman, Phys. Rev. B **46**, 4026 (1992).
2. S. H. Tessmer, P. I. Glicofridis, R. C. Ashoori, L. S. Levitov, M. R. Melloch, Nature, **392**, No.6671, 51 (1998);
G. Finkelstein, P. I. Glicofridis, S. H. Tessmer, R. C. Ashoori, M. R. Melloch, preprint
3. A. Yacoby, H. F. Hess, T.A. Fulton, L. N. Pfeiffer and K. W. West, Solid State Communications, **111**, 1-13 (1999)
4. K. L. McCormick, M. T. Woodside, M. Huang, M. S. Wu, P. L. McEuen, C. Duruoz, J. S. Harris, Phys. Rev. B, **59**, 4654 (1999)
5. Y. Y. Wei, J. Weis, K. v. Klitzing, K. Eberl, Phys. Rev. Lett., **81**, 1674 (1999)
6. I. A. Larkin, J. H. Davies, Phys. Rev. B, **52**, R5535 (1995)
7. J. P. Eisenstein, L. N. Pfeiffer, and K. W. West, Phys. Rev. Lett. **68**, 674 (1992);
B. Tanatar, D. M. Ceperley, Phys. Rev. B **39**, 5005 (1989)
8. A. L. Efros, cond-mat/9905368
9. I. A. Larkin, L. S. Levitov, to be published

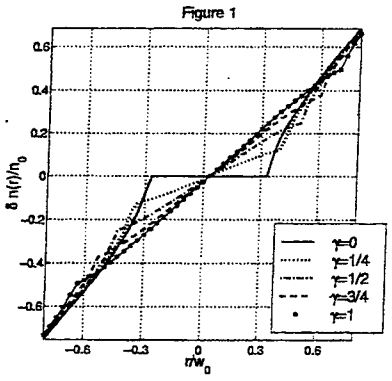

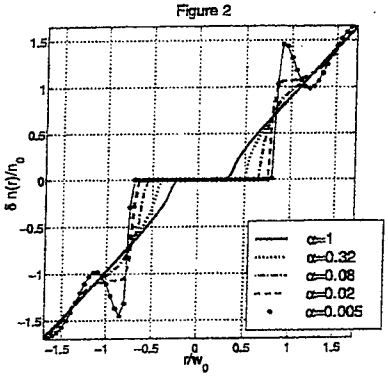

Figure 1. The effect of localized states on $n(r)$ for 5 values of $\gamma = n_{\rm gap}/n_0$. (The units used are $w_0 = ((\epsilon+1)\hbar\omega_c/2e^2|\nabla n|)^{1/2}$ and $n_0 = ((\epsilon+1)\hbar\omega_c|\nabla n|/2e^2)^{1/2}$.)
Figure 2. Incompressible strip density distribution created by effective interaction (see text) shown for 5 values of the exchange parameter α, with $\tilde{a} = 0.5w_0$.

PB.22

Edge state propagation direction in the fractional quantum hall regime: Multi-terminal magnetocapacitance experiment.

J. S. Moon[a], J. A. Simmons[a], B. L. Johnson[b], J. L. Reno[a]

[a]Sandia National Laboratories, Albuquerque, NM 87185 USA

[b]Department of Physics, Western Washington University, Bellingham, Washington 98225 USA

The propagation direction of fractional quantum Hall effect (FQHE) edge states has been investigated experimentally via the symmetry properties of the multi-terminal capacitances of two dimensional electron gases. Although strong asymmetries with respect to zero magnetic field appear, no asymmetries with respect to even denominator Landau level filling factor ν are seen. This indicates that current-carrying FQHE edge states propagate in the same direction as integer QHE edge states. Anomalous capacitance features has been observed, indicative of enhanced bulk conduction at ν = 1/2 and 3/2.

For a two dimensional electron gas (2DEG) in the integer quantum Hall effect (IQHE) regime, the concept of edge states has provide a unified description of transport phenomena. [1] A number of experiments such as capacitance measurements [2-4], inductive probing [5], and local imaging techniques [6] have provided clear evidence of edge states in the IQHE regime.

In the fractional quantum Hall effect (FQHE) regime where the single particle picture is no longer valid, the composite fermion (CF) [7] approach has been strongly supported by experimental results, including measurements of the FQHE energy gaps [8] and Fermi surface effects at even denominator Landau level filling factor ν, where the effective magnetic field B_{eff} = 0 [9,10]. Recently, the CF approach has been extended to edge states in the FQHE regime [11, 12], which are all expected to propagate in the same direction as for the IQHE. To date few experiments have addressed the propagation direction of edge states. Ashoori et al., studied the propagation direction of edge magnetoplasmons and found the same propagation direction for ν = 1 and ν= 2/3. [13] However, the relevance of this result to the propagation direction of FQHE edge states *per se* is unclear. Later, Chen et al. [3] used a magnetocapacitance measurement with multiple 2DEG contacts to determine the propagation direction of IQHE edge states.

In this paper, we extend the multiterminal magnetocapacitance technique of Chen et al. to a high mobility 2DEG to study the propagation direction of the edge states in the integer and fractional QHE regime. [4] Unlike conventional two-terminal capacitance measurements, here the capacitance is measured between a single gate and 3 separated, grounded ohmic contacts to the 2DEG. (See inset to Fig. 1.) Thus, in this multi-terminal configuration, capacitive coupling to each ohmic contact is strongly influenced by *the propagation direction* of the current carrying channels, rather than simply the total density of states (DOS). The resulting capacitance becomes a tensor quantity $C_{G,k}(\omega)$, given by the current $I_k(\omega)$ measured at contact k, divided by the voltage modulation at the gate $V(\omega)$. Therefore $C_{G,1}$ and $C_{G,3}$ are sensitive to the edge state direction, while $C_{G,2}$ becomes significant only when the bulk is compressible and current can flow through it. By studying the symmetry properties of the magnetocapacitance tensor, we found that (1) for the soft-wall boundaries of our sample, the current-carrying FQHE edge states on either side of 3/2 and 1/2 all propagate in the same direction as the IQHE edge states. (2) Near ν = 1/2 and 3/2 (B_{eff} [a] 0) the average motion of CFs is also strongly chiral with the sign of chirality determined by B rather than B_{eff}. These observations are consistent with recent theoretical predictions.

Table 1. Sample parameters.

Sample	n (10^{11} cm^{-2})	μ(cm^2/Vs)
EMC715 (dark)	2.6	1.1x10^6
EA65 (dark)	1.2	1.3x10^6
EA100 (dark)	1.3	1.2x10^6
EA100 (LED)	2.1	3.0x10^6

[11, 12] (3) Finally, we observe anomalous broad flat-topped peaks at filling factors ν = 1/2 and 3/2, in the capacitance between the gate and a 2DEG contact directly connected to it only by paths through the bulk.

Characteristics of the three high-mobility GaAs/AlGaAs heterostructures investigated are listed in Table 1. The sample geometry is shown schematically in the inset to Fig. 1. An AC modulation voltage $Ve^{i\omega t}$ (typically 1 mV) is applied to gate G, a semi-transparent metallic surface gate composed of ~300 Å of Cr, which covers the edge of the 2DEG mesa and much of the bulk. The out-of-phase current $I_k(\omega)$ (of order 10 pA) is then simultaneously measured at the three diffused metallic 2DEG contacts k = 1, 2, 3, using phase-sensitive current-preamplifiers with impedance to ground $\leq 5\ \Omega$. The capacitance tensor elements $C_{G,k}$ are obtained directly by $I_k(\omega)/(\omega V(\omega))$. The in-phase current is negligible with sufficiently low ω (typically 200 Hz). The gate and contact dimensions and separations were typically of order 1 mm.

Fig. 1(a)-(c) shows $C_{G,k}$ of sample EA100 for T = 0.3 K. Fig. 1(d) shows ρ_{xx}, along with the two terminal capacitance C_{2T}, obtained by allowing two of the 2DEG contacts to float. The two-terminal capacitance shows dips at the quantum Hall plateau, reflecting the incompressible nature of the 2DEG bulk regions. The reversal of B field doesn't change the magnitude of the two-terminal capacitance, which remains completely symmetric with B. In contrast, both the 'edge-connected' capacitances $C_{G,1}$ and $C_{G,3}$ exhibit a striking asymmetry upon reversal of B. For positive B, $C_{G,1}$ exhibits a large background with superimposed dips associated with the formation of incompressible states in the bulk. At negative B however, $C_{G,1}$ drops nearly to zero. $C_{G,3}$ exhibits similar behavior, only in reverse. The 'bulk-connected' capacitance $C_{G,2}$, on the other hand, exhibits a large peak at B = 0, but falls off rapidly and symmetrically as B deviates from zero. Qualitatively similar results are obtained for the other samples.

Our results in the IQHE regime are conceptually simplest to understand when ν = integer. Here the bulk is incompressible (σ_{xx} = 0) and an induced current is carried only in the edge channels. For positive B, when the gate voltage changes, current injected from

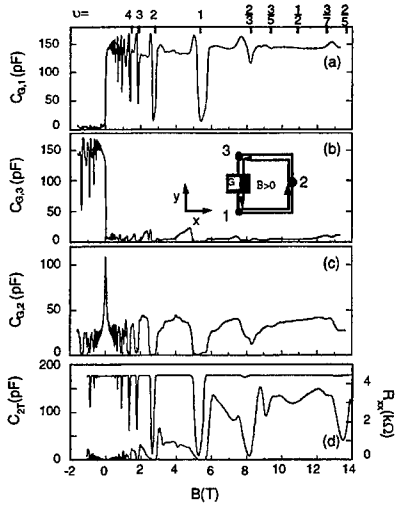

FIG. 1. Sample EA100 multi-terminal capacitance elements for (a) $C_{G,1}$, (b) $C_{G,3}$, and (c) $C_{G,2}$. (d) Two-terminal capacitance C_{2T}, and simultaneously measured ρ_{xx}. Inset shows sample geometry. Arrows indicate propagation direction of edge states for B>0.

contact 3—the 'edge-state sourcing contact'—remains unchanged, since it is determined only by the chemical potential in the ungated regions. (See Fig. 1 inset.) However, current flowing into contact 1—the 'edge-state sinking contact'—*is* changed, since charge is accumulating under the gate. This results in a net, non-zero current appearing at contact 1, proportional to the area of the conducting edge states. When B is negative, the roles of contacts 1 and 3 are interchanged as the edge-state propagation direction reverses. This results in the observed asymmetry between $C_{G,1}$ and $C_{G,3}$. On the other hand, $C_{G,2}$, symmetric with respect to B = 0 T, drops to zero since it is directly connected to the gate only by incompressible states in the bulk.

Outside of the quantum Hall plateaus where the bulk is compressible, the asymmetry is also present except for a slight residual capacitance. Indeed, the asymmetry is almost completely developed at $B \approx \pm 0.05$ T, even at high temperatures. [3, 4] This indicates that the asymmetry is classical in origin, appearing when B is large enough to

change the transport from an isotropically diffusive regime to one in which the Lorentz force is relevant. We have developed a quantitative model based on the bulk transmission probabilities between various contacts in the *ungated* region, where the capacitive coupling is determined by both σ_{xx} and σ_{xy}. [4] Excellent qualitative agreement with the data has been found.

We now discuss our data in the FQHE regime. In the CF picture, the FQHE is viewed as the IQHE of CFs in the presence of an effective magnetic field $B_{eff} = B - B_g$, where for instance B_{eff} is zero at $\nu = 1/2$, positive for $\nu < 1/2$ and negative for $\nu > 1/2$. Geometric resonance experiments [10] have shown that CFs move semiclassically in the presence of small B_{eff}, similar to electrons near B = 0 T. [14] Naively, one would then expect the appearance of assymetrical features in $C_{G,k}$ near $B_{eff} = 0$, analagous to those seen near B=0, and indicating a reversal a reversal in the FQHE edge state propagation direction. However, as is apparent in Fig. 1, at $\nu = 1/2$ no sudden transition nor clear signature of an asymmetry is present in $C_{G,1}$ nor $C_{G,3}$. While nearby features associated with the fractions 4/3 and 5/3 make the situation less clear, at $\nu = 3/2$ no asymmetry is apparent either. All three samples behaved similarly.

To verify the absence of any asymmetries with respect to $B_{eff} = 0$, dependence of the capacitance signal on gate excitation voltage was varied from 0.5 mV to 5 mV and no

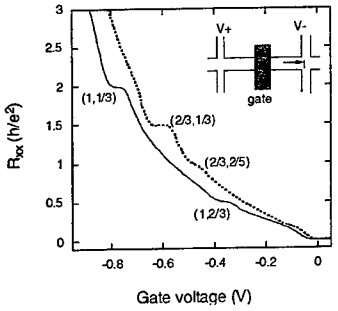

FIG. 2. The four-terminal resistance measured across the gate region vs. gate voltage at T = 0.3 K from sample EA100. See the inset for the sample configuration. The labels denote (ν_b, ν_g), the filling factors in the bulk and the gated regions.

difference found. Assuming an effective CF mass of ~ 0.67 m_e, [8] the quasiparticle energy gap at $\nu = 1/3$ (B = 16.2 T) is estimated as 0.93 meV, much larger than the gate-induced Fermi energy modulation of a few μeV. Frequency dependence was also from 10 Hz to several kHz and no significant quadrature component due to σ_{xx} was observed.

In addition, we studied independently the gate-induced reflection of individual FQHE edge states from the same wafers, using a four-terminal configuration. [17] As shown in Fig. 2, several fractionally quantized plateaus in R_{xx} are clearly observed whenever the filling factor underneath the gate changes. The quantized values of R_{xx} excellently agree with the Landauer-Buttiker formalism [16], $R_{xx} = (1/\nu_g - 1/\nu_b)(h/e^2)$, where ν_b and ν_g are the filling factors in the bulk and underneath the gate. Our results clearly indicate well-defined FQHE edge states in these wafers.

The lack of the magneotcapacitance asymmetries found in the FQHE indicates strongly that the current carrying FQHE edge states all propagate in the same direction as electrons in IQHE edge states, determined by B rather than B_{eff}. This is consistent with recent theories. Theoretical studies [11] indicate that the average (drift) motion of CFs is associated with the drift of the attached magnetic flux, and hence generates a fictitous electric field $E_g = -\langle J \times B \rangle mn/e$. E_g turns out to be equal to $e\langle v \rangle \times B_g$, which exactly cancels the average force due to the fictitious magnetic field. As a result, the *average* force seen by CFs is the same as for electrons, yielding a CF edge state propagation direction which is the same as for electrons. In the ballistic regime, the *individual* CF moves at the Fermi velocity and the average drift force $-e\langle v \rangle \times B_{eff}$ has no effect on the semiclassical motion of CFs near B_{eff}, consistent with experiments [10].

A striking feature of the CF theory is the implication that at $B_{eff} = 0$ there exists a Fermi surface with a well-defined Fermi wavevector $k_F = (4\pi n)^{1/2}$. Since the measured $C_{G,k}$ depend strongly on the bulk transport properties of the ungated regions, one might expect that they would exhibit a CF Fermi surface signature near $B_{eff} = 0$. In Fig. 3(a) we show $C_{G,2}$ for sample EMC715 at 0.3 K.

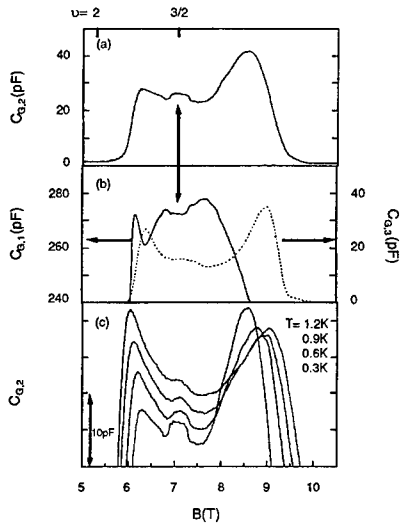

FIG. 3. EMC715 multi-terminal capacitance elements (a) $C_{G,2}$ and (b) $C_{G,1}$ and $C_{G,3}$, near $\nu = 3/2$. An anomalous capacitance peak centered at $\nu = 3/2$ appears in $C_{G,2}$. (c) Same as (a), but for different temperatures, with curves vertically offset for clarity.

A distinct broad flat-topped peak, centered about $\nu = 3/2$, is apparent. The peak has a sharp turn-on at $B - B_{3/2} = \Delta B_{3/2} \approx \pm 0.26$T, yielding a normalized half-width of $\Delta B_{3/2}/B_{3/2} \approx 0.036$. A smaller 'copy' of the peak [Fig. 3(b)] is apparent in $C_{G,3}$, while an inverted peak (or broad flat-bottomed dip) is visible in $C_{G,1}$. The inverted peak in $C_{G,1}$ is expected from current conservation: an increase in bulk current must be compensated by a decrease in current along the edge. As temperature T is increased [Fig. 3(c)], the peak becomes smaller and rounded, nearly disappearing by 1.2 K. Qualitatively similar features are observed in $C_{G,2}$ for sample EA100 and EA65 near $\nu = 1/2$, with the normalized width of $\Delta B_{1/2}/B_{1/2} \approx 0.16$. As temperature is increased the peak diminishes, becoming nearly absent by 0.8 K. By contrast, ρ_{xx} shows no sharp features around 1/2, exhibiting instead a gentle, temperature insensitive minimum.

These anomalous features at even denominator ν *cannot* be attributed to changes in the DOS of the gated 2DEG region, since in that case a peak near 1/2 would appear for C_{2T} and for all $C_{G,k}$, contrary to what we observe. Rather, we speculate that the observed anomalous capacitance features are due to an *enhancement in the bulk conductivity* near $B_{eff} = 0$ *outside* the gate, which, as we have seen, can strongly influence the multi-terminal capacitance. Finally, we note that the capacitance features' characteristic temperature of order 1 K is similar to that predicted for the flux-binding energy of CFs. [18]

Work supported by U.S. Dept of Energy under Contract DE-AC04-94AL85000.

References

[1] B. I. Halperin, Phys. Rev. B **25**, 2185 (1982).
[2] S. Takaoka et al., Phys. Rev. Lett. **72**, 3080 (1994).
[3] W. Chen et al., Phys. Rev. Lett. **73**, 146 (1994).
[4] J. S. Moon et al., Phys. Rev. Lett. **79**, 4457 (1997)
[5] E. Yahel et al., Phys. Rev. Lett. **81**, 5201 (1998).
[6] P. F. Fontein et al., Phys. Rev. B **43**, 12090 (1991); S. H. Tessmer et al., Nature (London) **392**, 51 (1998); K. L. McCormick et al., Phys. Rev. B **59**, 4654 (1999).
[7] J. K. Jain, Phys. Rev. Lett. **63**, 199 (1989); B. I. Halperin, P. A. Lee, and N. Read, Phys. Rev. B **47**, 7312 (1993).
[8] R. R. Du et al., Phys. Rev. Lett. **70**, 2944 (1993).
[9] R. L. Willet et al., Phys. Rev. Lett. **71**, 3846 (1993).
[10] W. Kang et al., Phys. Rev. Lett. **71**, 3850 (1993); V. J. Goldman et al., *ibid.* **72**, 2065 (1994); J. H. Smet et al., *ibid.* **77**, 2272 (1996).
[11] G. Kirczenow and B. L. Johnson, Phys. Rev. B **51**, 17579 (1995); G. Kirczenow, Phys. Rev. B **58**, 1457 (1998);
[12] H.-S. Kim et al., Phys. Rev. Lett. **82**, 596 (1999).
[13] R. C. Ashoori et al., Phys. Rev. B **45**, 3894 (1992).
[14] H. van Houten et. al., Phys. Rev. B **39**, 8556 (1989); J. S. Moon et. al., Appl. Phys. Lett., **71**, 656 (1997).
[15] R. K. Goodall et al., Phys. Rev. B **31**, 6597 (1985); A. M. C. Valkering et. al., Phy. Rev. Lett. **81**, 5398 (1998).
[16] M. Büttiker, Phys. Rev. Lett. **57**, 1761 (1986).
[17] A. M. Chang and J. E. Cunningham, Solid State Commun. 72, 651 (1989); L. P. Kouwenhoven et al., Phys. Rev. Lett. **64**, 685 (1990).
[18] R. Morf and N. d'Ambrumenil, Phys. Rev. Lett. **74**, 5116 (1995).

PB.23

Potential screening in the Integer Quantum Hall Effect: Evidence for Bulk Currents

E. Yahel [1], A. Tsukernik[2], A. Palevski[2], H. Shtrikman[3]
[1]Physics Department NRCN, P.O.B. 9001, Beer-Sheva 84190, Israel
[2]School of Physics and Astronomy, Tel Aviv University, Tel Aviv 69978, Israel
[3]Department of Condensed Matter, The Weizmann Institute of Science, Rehovot 76100, Israel

Abstract

The current distribution in the integer quantum Hall regime was studied by inductive coupling technique and transport measurements. Using an inductive coupling method we were able to study the screening properties of a two-dimensional electron gas (2DEG). We found that having gates in the vicinity of the 2DEG influence the distribution of the non-equilibrium Hall current injected into the sample. From the inductive measurements we proved that the non-equilibrium Hall current is carried by bulk states. We also demonstrated the role of externally applied electric fields. 2DEG V-grooved samples allowed us to realize a configuration at which the normal component of the magnetic field to the plane of the 2DEG alternates in sign. We showed that for such a magnetic field configuration, the quantum Hall effect survives although the number of the grooves multiplies the magnitude of the quantized Hall coefficient. This observation can easily be explained by the alternation of the current direction in each subsequent sidewall of the groove, and therefore implies that the current flow in the bulk of the sample.

PACS: 72.20.My, 73.20.Dx, 73.40.Hm, 85.30.Vw

Introduction

The spatial distribution of current across a Hall bar sample in the Integer Quantum Hall Effect (IQHE) was an open question since the discovery of the effect. Over the years, people tried to describe the current distribution by two models. The first one is a model, which considers the edges of 2DEG samples to be of no importance. According to this model the current distribution is not confined to the edges of the sample. This is known as the bulk-state picture [1,2]. In contrast, the edge-state picture, [3-7] suggested that the Hall voltage (and therefore the current density) drop over a narrow region in the vicinity of the physical boundaries of the sample. During the last decade, experiments aimed to probe the current distribution and the electrostatic potential profile of a 2DEG in the IQHE used various measuring techniques [8-14].

In the presence of an external applied magnetic field, the current in the sample contains two parts. The first part is a diamagnetic current, i.e., equilibrium current, which exists, in a closed Hall bar sample. The second part is a Hall current that is generated or injected into the sample. This is a non-equilibrium component and its spatial distribution could be very different from the distribution of the equilibrium part. The spatial distribution of the non-equilibrium component of the current is the debated subject.

In the following paper we discuss the problem of current distribution in the IQHE by means of two experimental techniques. The first one, the inductive coupling technique, was proposed by the authors recently. This method, which couples a tiny pick-up coil to a 2DEG, was aimed to probe the spatial current distribution at the IQHE conditions [15]. The second technique uses magnetotransport measurements on a V-grooved 2DEG.

Results

Fig. 1 shows a schematic view of the experimental setup. It includes a pick-up coil and a 2DEG sample. The 2DEG samples were fabricated from $GaAs_x/Al_1xGaAs$ heterostructure, and had the typical dimensions of $10X5mm^2$. The current Ohmic contacts were alloyed along edge

opposite to the coil, in order to increase the experimental sensitivity of the pick-up coil signal to changes in the spatial current distribution.

An alternating current at frequency, driven between the Ohmic contacts, produced a time-depended alternating magnetic flux at the pick-up coil. The latter, induced an electro-motive force (emf) at the pick-up coil circuit. The calibration constant was 180±10nV/μA at 26kHz, when the total injected current flows underneath the pick-up coil.

At first, we measured the current distribution in a back gated Hall bar sample. The sample had carrier concentration of $1.8X10^{11}cm^{-2}$ and mobility of $2X10^{6}cm^{2}/Vs$. The amplitude of the injected current was 0.5μA at a frequency of 26kHz at all experiments.

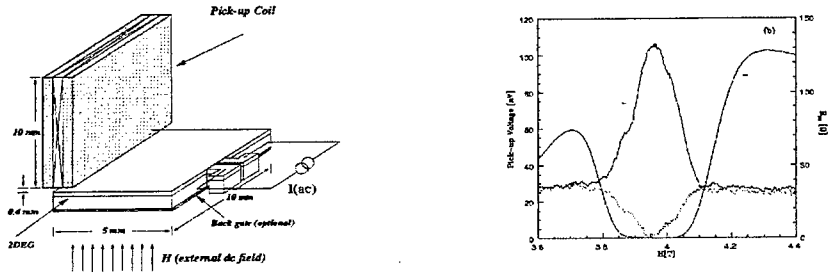

Fig. 1 (left figure): Setup of the inductive coupling experiment.
Fig. 2 (right figure): The pick-up voltage (left axis) and longitudinal resistance (right axis) versus external magnetic field. Solid line: +H, +V. Short dashed line: +H, -V. The traces correspond to ν=2.

Fig. 2 shows traces of the pick-up coil voltage (left axis) and the longitudinal resistance (right axis) versus the external magnetic field, for a fixed direction of the magnetic field and two polarities of the applied voltage. The trace for (+H, +V) give the maximum signal at the pick-up coil according to our calibration constant. It means that the entire Hall current flows along the edge underneath the pick-up coil. The measurement was done at 2.17K. The curve corresponding to (+H, -V) in Fig. 2 shows zero pick-up signals, within our experimental resolution. It means that the entire Hall current flows along the short edge opposite to the coil (c.f. Fig 1). According to the edge-state picture, half of the injected current should flow along each edge. This in turn means that the voltage across the coil should have been about 45nV, which is half of full signal expected for the injected current.

The explanation for the observed signal is based on the screening properties of the 2DEG. In the IQHE, the edges are conducting and are at source (±V) and drain (ground) potentials correspondingly [15]. The potential at a given point in the bulk 2DEG approaches the ground potential of the back gate, as the distance between this point and the edge becomes larger than the distance between this point and the back gate. Therefore, the Hall voltage drops over a region

(~350μm) at one edge, which is biased by the source voltage. Since both the bulk and the second edge are at ground potential, the electrical field is zero at this edge. Therefore, the entire Hall current flows only along one edge. This Hall current, flowing at the edge in a gated 2DEG Hall bar sample, should not be confused with the so-called ``edge" currents, discussed above.

In order to study the spatial current distribution, it is necessary to reduce undesired gating effects of the 2DEG. The same kind of inductive measurements were carried on a sample without a back gate, and the results are presented in Fig. 3. From the figure, it can be concluded that the pick-up signal remains constant at the value corresponding to the current distribution at the dissipative regime ($\rho_{xx}\neq 0$), which is a bulk current. This experiment proves that the non-equilibrium Hall current in a Hall bar geometry sample is carried by bulk states.

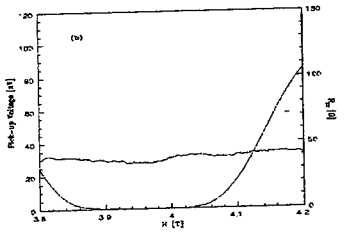

Fig 3: The pick-up voltage and longitudinal resistance versus external magnetic field at ν=2. The sample was attached to the holder by an insulating paste, which prevented gating by the back gate.

Transport experiments on standard Hall bar geometry samples at uniform magnetic field can not provide any information on the spatial distribution of the Hall current. In this part of the paper we presents a magnetotransport experiment, which gives an additional evidence for the validity of the bulk current picture in the IQH regime. This experiment is done on a 2DEG at periodic in space magnetic field resulting in a redistribution of the Hall current through the bulk of the sample. The sample studied in this experiment is a 2DEG grown on a V-grooved prepatterned GaAs substrates, which is usually used for producing one-dimensional wires [16].

An application of a uniform magnetic field parallel to the substrate and perpendicular to the V-grooved 2DEG allows us to realize a configuration at which the normal component of the magnetic field to the sidewalls of V-grooves alternates in sign. Fig. 4 shows this configuration and experimental setup (a), and its analogy for a planner 2DEG (b). The results of two-terminal magnetoresistance measurements at 4.2K are presented in Fig. 5. The wide curve corresponds to 60 grooves (120 sidewalls) and the narrow one corresponds to 30 grooves (60 walls). The figure shows that the quantum Hall effect in a periodic in sign magnetic field survives although exactly the number of sidewalls (twice the number of grooves) multiplies the magnitude of the Hall resistance. This observation can easily be explained by the alternation of current direction in each subsequent sidewall of the groove, implying bulk current distribution. This is schematically shown in Fig. 4(b).

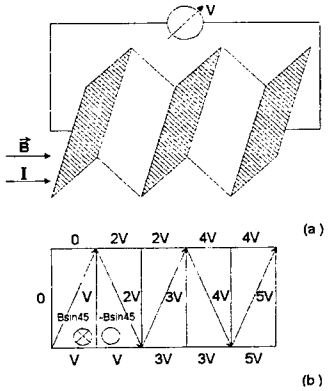

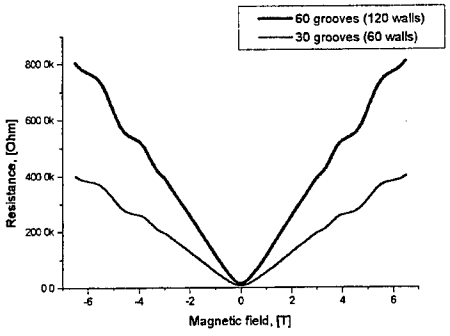

Fig. 4 (left figure): (a) Experimental setup for the V-grooved 2DEG; (b) The analogy for a planner 2DEG. A Potential and schematic current flow is displayed.
Fig.5 (right figure): Two-terminal magnetoresistance measurements on V-grooves.

The edge current approach fails to explain the observed experimental results, unless one assumes that the tops and bottoms of the grooves could be regarded as electronic reservoirs at zero magnetic field. It is hardly plausible assumption since the width of the bottom, where the normal component of the field reverses it's sign, is of order of 100Å which is much smaller than the magnetic length even for the highest field in the experiment.

Conclusions

We performed inductive coupling measurements on a planner 2DEG Hall bar samples and magnetotransport studies on a V-grooved 2DEG. We found that under the conditions, where the surrounding of the 2DEG contained no gate, the current distribution in the IQHE plateaus remained the same as in the dissipative regime. These measurements prove that the Hall current at the IQHE plateaus is carried mostly by extended bulk states, located below the Fermi level. The results of magnetotransport measurements provide a valuable complementary proof for the existence of bulk current carrying states.

References

1. R. B. Laughlin, Phys. Rev. B {\bf 23}, 5632 (1981).
2. J. Avron and R. Seiler, Phys. Rev. Lett. {\bf 54}, 259 (1985).
3. B. I. Halperin, Phys. Rev. B {\bf 25}, 2185 (1982).
4. A. H. MacDonald, Phys. Rev. B {\bf 29}, 6563 (1984).
5. J. K. Jain and S. A. Kivelson, Phys. Rev. Lett. {\bf 60}, 1542 (1988).
6. M. B${\ddot{\rm u}}$ttiker, Phys. Rev. B {\bf 38}, 9375 (1988).
7. K. Shizuya, Phys. Rev. Lett. {\bf 73}, 2907 (1994).
8. P. F. Fontein *et al.*, Surf. Sci. {\bf 263}, 91 (1992).
9. N. Q. Balaban *et al.*, Phys. Rev. Lett. {\bf 71}, 1443 (1993).
10. S. Takaoka *et al.*, Phys. Rev. Lett. {\bf 72}, 3083 (1994).
11. R. G. Mani, Europhys. Lett. {\bf 36}, 203 (1996).
12. S. H. Tessmer *et al.*, Nature (London) {\bf 392}, 51 (1998).
13. K. L. McCormick *et al.*, Phys. Rev. B {\bf 59}, 4654 (1999).
14. J. J. Mare\u{s}, J. Kri\u{s}tofik and P. Hub\'{\i}k, Phys. Rev. Lett. {\bf 82}, 4699 (1999).
15. E. Yahel, D. Orgad, A. Palevski and H. Shtrikman, Phys. Rev. Lett. {\bf 76}, 2149 (1996).
16. E. Kapon, M. C. Tamargo and D. M. Hwang, Appl. Phys. Lett. {\bf 50}, 347 (1987).

PB.24

Novel Umklapp Scattering at Reconstructed Quantum-Hall Edges

U. Zülicke,[1,2] A. H. MacDonald[2]

[1]*Institut für Theoretische Festkörperphysik, Universität Karlsruhe, D-76128 Karlsruhe, Germany**

[2]*Department of Physics, Indiana University, Bloomington, IN 47405, U.S.A.*

We study the low-lying excitations of a quantum-Hall sample that has undergone *edge reconstruction* such that there exist three branches of chiral edge excitations. Among the interaction processes that involve electrons close to the three Fermi points is a novel *Umklapp*-scattering process which has not been discussed before. Using bosonization and a refermionization technique, we obtain exact results for electronic correlation functions and discuss the effect Umklapp scattering has on the Luttinger-liquid properties of quantum-Hall edges.

PACS: 71.10.Pm, 73.40.Hm

Keywords: quantum Hall effect, edge reconstruction, Umklapp scattering

Introduction. The electronic structure at the edge of quantum-Hall (QH) systems depends sensitively on the interplay between the external potential confining the electrons to the finite sample, electrostatic repulsion, as well as exchange and correlation effects. For an ultimately sharp edge [1], a single branch of chiral one-dimensional (1D) excitations is predicted to exist when the filling factor $\nu = 1/m$ where m is an odd integer [2]. In that case, the dynamics of edge excitations can be described [3] using a Tomonaga-Luttinger (TL) model [4] with only the right-moving [5] degrees of freedom present. However, for a confining potential that is just not sharp enough to stabilize a single-branch edge, a different configuration is realized where a lump of electron charge is separated from the bulk of the QH sample [6,7]. Such a *reconstructed* edge supports three branches of chiral 1D edge excitations, two right-moving and one left-moving. For even weaker confining potential, further reconstructions occur, leading to a proliferation of edge-excitation modes [8]. The microscopic structure of a very smooth edge is dominantly determined by electrostatics, which favors a phase separation of the 2D electron system at the edge into a series of alternating compressible and incompressible strips [9].

Effective TL theories [3] describing single-branch and multi-branch QH edges predict Luttinger-liquid behavior, i.e., power laws governing the energy dependence of electronic correlation functions. The characteristic exponents of these power laws depend, in general, on details of the microscopic edge structure. However, in the absence of coupling between different chiral edge branches or, in some cases, due to disorder effects [10], power-law exponents turn out to be universally dependent on the bulk filling factor. At present, microscopic details of the edge structure that is realized in experiment [11] are not fully known. To facilitate a realistic comparison between theory and experiment, it is necessary to study the low-lying edge excitations of reconstructed and smooth edges and investigate interaction effects on the Luttinger-liquid power-law exponents when more than one branch of edge excitations is present.

Derivation of the effective 1D edge theory. We focus on the edge of a spin-polarized [12] QH sample at $\nu = 1$ that has undergone reconstruction such that three branches of edge excitations are present. To be specific, we choose the Landau gauge where lowest-Landau-level (LLL) basis states $\chi_k(x,y) = \Phi_k(y)\exp\{ikx\}/\sqrt{L}$ are labeled by a 1D wave vector k. Here, $\ell = \sqrt{\hbar c/|eB|}$ denotes the

magnetic length, L is the edge perimeter, and $\Phi_k(y) = \exp\{-(y - k\ell^2)^2/(2\ell^2)\}/\sqrt{\pi^{1/2}\ell}$. In the absence of interactions between different edge branches, the ground state would be a generalized Fermi-sea state that is a Slater determinant of LLL basis states whose wave-vector label satisfies $k \leq k_{\rm F}^{(\rm R)}$ or $k_{\rm F}^{(\rm W)} \leq k \leq k_{\rm F}^{(\rm B)}$. The Fermi 'surface' consists of three (Fermi) points $k_{\rm F}^{(\rm R)} < k_{\rm F}^{(\rm W)} < k_{\rm F}^{(\rm B)}$. As in Tomonaga's approach to interacting 1D electron systems [4], long-wave-length electronic excitations at the reconstructed edge can be identified according to which Fermi point they belong to. This makes it possible to rewrite the long-wave-length part of the electron operator as follows:

$$\psi(\vec{r}) = \Phi_{k_{\rm F}^{(\rm R)}}(y)\, e^{ik_{\rm F}^{(\rm R)}x}\, \psi^{(\rm R)}(x) + \Phi_{k_{\rm F}^{(\rm W)}}(y)\, e^{ik_{\rm F}^{(\rm W)}x}\, \psi^{(\rm W)}(x) + \Phi_{k_{\rm F}^{(\rm B)}}(y)\, e^{ik_{\rm F}^{(\rm B)}x}\, \psi^{(\rm B)}(x) \quad . \quad (1)$$

Here, $\vec{r} = (x, y)$ denotes the coordinate vector in the 2D plane, and the operator $\psi^{(\rm R,W,B)}(x)$ creates an electron belonging to the chiral 1D edge branch labeled R, W, B, respectively. The interaction part of the 2D Hamiltonian for electrons in the LLL is

$$H_{\rm int} = \frac{1}{2}\iint d^2r\, d^2r'\, V(\vec{r} - \vec{r}')\, \varrho(\vec{r})\, \varrho(\vec{r}') \quad (2)$$

where $\varrho(\vec{r}) = \psi^\dagger(\vec{r})\psi(\vec{r})$ is the electron density. We consider the case when electrons interact via unscreened Coulomb interaction,

$$V(\vec{r} - \vec{r}') = \frac{e^2/\epsilon}{\sqrt{(x - x')^2 + (y - y')^2}} \quad . \quad (3)$$

We obtain the low-energy part of $H_{\rm int}$ by inserting Eq. (1) into Eq. (2); it is effectively 1D and comprises various scattering processes of electrons that are close to one of the three Fermi points. Terms corresponding to forward scattering and backscattering [13] have been discussed before [7]. Together with the one-body part of the original 2D Hamiltonian, they can be rewritten in terms of a TL model Hamiltonian, $H_{\rm TL}$, which is quadratic in the Fourier components $\varrho_q^{(\alpha)}$ of the chiral 1D densities $[\psi^{(\alpha)}(x)]^\dagger\psi^{(\alpha)}(x)$ (here, $\alpha \in \{\rm R,W,B\}$). In the long-wave-length limit, with Coulomb interaction present, the three normal modes of $H_{\rm TL}$ are [7] a) the edge-magnetoplasmon mode, $\varrho^{(\rm emp)} = \varrho^{(\rm B)} + \varrho^{(\rm R)} + \varrho^{(\rm W)}$, which is right-moving, and b) two linearly dispersing neutral modes, a right-moving one given by $\varrho^{(\rm rn)} = (\varrho^{(\rm B)} - \varrho^{(\rm R)})/\sqrt{2}$, and the left-moving neutral mode $\varrho^{(\rm ln)} = (\varrho^{(\rm B)} + \varrho^{(\rm R)} + 2\varrho^{(\rm W)})/\sqrt{2}$.

Novel Umklapp scattering. In addition to forward and backscattering, the following term occurs in the effective 1D Hamiltonian describing the low-energy excitations of a reconstructed QH edge:

$$H_{\rm U} = \iint dx\, dx'\, V_{\rm U}(x - x') \times \Big\{[\psi^{(\rm R)}(x)]^\dagger[\psi^{(\rm B)}(x')]^\dagger\psi^{(\rm W)}(x')\,\psi^{(\rm W)}(x) \times \exp\Big[iD\frac{x - x'}{2} - i\delta\frac{x + x'}{2}\Big] + \text{H.c.}\Big\}. \quad (4)$$

Here we introduced the parameters $\delta = k_{\rm F}^{(\rm B)} + k_{\rm F}^{(\rm R)} - 2k_{\rm F}^{(\rm W)}$ and $D = k_{\rm F}^{(\rm B)} - k_{\rm F}^{(\rm R)}$. The distance $D\ell^2$ corresponds to the width of the edge. Note that $H_{\rm U}$ represents interaction processes (and their time-reversed version) where two electrons from the left-moving W-branch are scattering off each other such that one of them ends up in the right-moving R-branch and the other one in the right-moving B-branch. (See Fig. 1.) Interaction processes converting two left-movers into two right-movers (and *vice versa*) are familiar from lattice models for conventional interacting 1D electron systems; there they are called *Umklapp* processes [14]. Based on that analogy, we adopt the term *Umklapp scattering* for the interaction processes given by

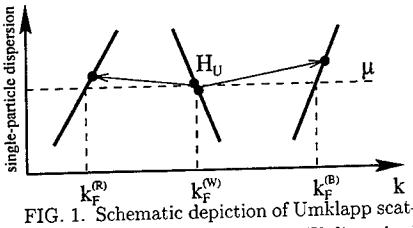

FIG. 1. Schematic depiction of Umklapp scattering at a reconstructed QH edge. We linearized the single-particle dispersion close to the three Fermi points. Shown is one interaction process represented by H_U where two left-moving electrons from the W-branch are scattered into the R and B-branches.

H_U. Momentum conservation sets a momentum scale (and, therefore, a corresponding energy scale) above which Umklapp scattering affects electronic properties. In the 1D Hubbard model, e.g., this momentum scale is expressed in terms of the distance to half-filling [15], whereas it is given by the parameter δ in the case of a reconstructed QH edge. This can easily be seen within a perturbative treatment of Umklapp scattering where momentum conservation implies a finite energy denominator unless $\delta = 0$. The matrix element $V_U(x-x')$ gets small rapidly with increasing D and δ; it is given by

$$V_U(x-x') = \frac{e^2}{\epsilon\ell}\,\frac{\exp\left\{-\frac{\ell^2}{8}\left[\delta^2+D^2\right]\right\}}{\sqrt{2\pi}} \times \int d\kappa\,\frac{\exp\left\{-\frac{1}{2}\left[\kappa-\ell D/2\right]^2\right\}}{\sqrt{(x-x')^2/\ell^2+\kappa^2}} \quad . \quad (5)$$

Bosonization. The new Umklapp process does not conserve particle number in each edge branch separately. Therefore, H_U cannot be written in terms of a Tomonaga-Luttinger model. However, using the bosonization identity [16] for the 1D fermionic operators,

$$\psi^{(R)}(x) = 1/\sqrt{L}\ :\exp[i\,\phi^{(R)}(x)]:\,, \quad (6a)$$

$$\psi^{(W)}(x) = 1/\sqrt{L}\ :\exp[-i\,\phi^{(W)}(x)]:\,, \quad (6b)$$

$$\psi^{(B)}(x) = 1/\sqrt{L}\ :\exp[i\,\phi^{(B)}(x)]:\,, \quad (6c)$$

where $:\ldots:$ symbolizes normal ordering, and

$$\phi^{(\alpha)}(x) = i\,\frac{2\pi}{L}\sum_{q\neq 0}\frac{e^{-iqx}}{q}\,\varrho_q^{(\alpha)} \quad , \quad (7)$$

it is possible to rewrite H_U entirely in terms of bosonic degrees of freedom:

$$H_U = 2\Lambda^2 g_U \int dx\,\cos\left[\phi^{(ln)}(x)+\delta x\right], \quad (8a)$$

$$\phi^{(ln)}(x) = \phi^{(R)}(x)+\phi^{(B)}(x)+2\phi^{(W)}(x)\,. \quad (8b)$$

Expressions of the form (8a) are routinely obtained within the bosonized description of Umklapp scattering in conventional 1D electron systems [14,15]. The parameter Λ is an ultraviolet cut-off; for the situation considered in this work, we have $\Lambda \lesssim (D\ell^2)^{-1}$. The effective Umklapp coupling constant, g_U, is derived from the original Coulomb interaction between the electrons. It is given by

$$g_U = \frac{e^2}{\epsilon}\,\frac{\exp\left\{-\frac{\ell^2[\delta^2+D^2]}{8}\right\}}{\sqrt{2\pi}}\int_\infty^\infty d\kappa\,e^{-\frac{1}{2}\left[\kappa-\ell\frac{D}{2}\right]^2} \times 2\int_0^\infty d\eta\,\frac{\sin\left[\ell D\eta/2\right]}{\sqrt{\eta^2+\kappa^2}} \quad . \quad (9)$$

Note that $\phi^{(ln)}(x)$ is a chiral boson field given in terms of the Fourier components $\varrho_q^{(ln)}$ as expressed in Eq. (7). The Umklapp part of the Hamiltonian, H_U, introduces a self-interaction of the left-moving neutral normal mode of H_{TL}. The edge-magnetoplasmon mode and the right-moving neutral mode are unaffected by Umklapp scattering and remain free.

Exact solution: Summary of results. We have been able to solve the theory including Umklapp *exactly* for arbitrary δ and g_U using a refermionization technique [17] whereby the Hamiltonian for the chiral 1D bosonic field $\phi^{(ln)}(x)$ with interaction H_U is mapped onto

that of a chiral 1D pseudo-spin-1/2 fermion in an external magnetic field that is perpendicular to the pseudo-spin quantization axis. In addition to the characteristic energy scale for Umklapp scattering, given by $\Delta_0 = 2\Lambda g_U$, the parameter $\xi = \hbar v_{ln}|\delta|/(2\Lambda g_U)$ emerges from the calculation that measures the ineffectiveness of Umklapp scattering due to deviation from perfect commensuration. We obtain the spectral functions for tunneling into the chiral R,W,B edge branches. Due to Umklapp scattering, a crossover occurs in their energy dependence between different power laws. With $\alpha \in \{R,W,B\}$, we find

$$\mathcal{A}^{(\alpha)}(\varepsilon) \propto \begin{cases} \varepsilon^{[\lambda^{(\alpha)}_{emp}]^2+[\lambda^{(\alpha)}_{rn}]^2-1} & \text{for } \varepsilon < \Delta \\ \varepsilon^{[\lambda^{(\alpha)}_{emp}]^2+[\lambda^{(\alpha)}_{rn}]^2+[\lambda^{(\alpha)}_{ln}]^2-1} & \text{for } \varepsilon > \Delta \end{cases} \tag{10}$$

where the crossover energy scale is $\Delta = \Delta_0[\sqrt{1+\xi^2}-\xi]$, and the $\lambda^{(\alpha)}_\beta$ are the Bogoliubov coefficients relating the chiral density fluctuations localized at the R,W,B branches to the normal modes of H_{TL}. As the central result of our study, we find that Umklapp scattering *diminishes* the value of the power-law exponent in the tunneling density of states below the energy scale Δ.

---

* Present address.

[1] The sharpness/smoothness of the edge can be quantified by the slope of the bare confining potential at the sample boundary.

[2] A. H. MacDonald, Phys. Rev. Lett. **64**, 220 (1990); X. G. Wen, Phys. Rev. B **41**, 12838 (1990).

[3] X. G. Wen, Int. J. Mod. Phys. B **6**, 1711 (1992); Adv. Phys. **44**, 405 (1995).

[4] S. Tomonaga, Prog. Theor. Phys. **5**, 544 (1950); J. M. Luttinger, J. Math. Phys. **4**, 1154 (1963).

[5] Specifying the chirality of edge excitations fixes the direction of the perpendicular magnetic field.

[6] A. H. MacDonald, S. R. Yang, and M. D. Johnson, Aust. J. Phys. **46**, 345 (1993).

[7] C. de C. Chamon and X. G. Wen, Phys. Rev. B **49**, 8227 (1994).

[8] I. L. Aleiner and L. I. Glazman, Phys. Rev. Lett. **72**, 2935 (1994); S. Conti and G. Vignale, Phys. Rev. B **54**, R14309 (1996); J. H. Han and D. J. Thouless, Phys. Rev. B **55**, R1926 (1997).

[9] See, e.g., C. W. J. Beenakker, Phys. Rev. Lett. **64**, 216 (1990); A. M. Chang, Solid State Commun. **74**, 871 (1990); D. B. Chklovskii, B. I. Shklovskii, and L. I. Glazman, Phys. Rev. B **46**, 4026 (1992).

[10] C. L. Kane and M. P. A. Fisher, Phys. Rev. B **51**, 13449 (1995).

[11] A. M. Chang, L. N. Pfeiffer, and K. W. West, Phys. Rev. Lett. **77**, 2538 (1996); M. Grayson *et al.*, Phys. Rev. Lett. **80**, 1062 (1998).

[12] We only consider the case when the spin-degree of freedom is frozen out such that it is appropriate to assume electrons to be spinless.

[13] For spinless electrons, backscattering terms can be accounted for within a TL model because they only renormalize forward-scattering amplitudes

[14] V. J. Emery, in *Highly Conducting One-Dimensional Solids*, edited by J. T. Devreese *et al.* (Plenum Press, New York, 1979), pp. 247–303; R. Shankar, Int. J. Mod. Phys. B **4**, 2371 (1990); H. J. Schulz, in *Strongly Correlated Electronic Materials*, edited by K. S. Bedell *et al.* (Addison Wesley, Reading, MA, 1994), pp. 187–232.

[15] T. Giamarchi, Phys. Rev. B **44**, 2905 (1991); *ibid.* **46**, 342 (1992); Physica B **230-232**, 975 (1997).

[16] R. Shankar, Acta Phys. Pol. B **26**, 1835 (1995); J. von Delft and H. Schoeller, Ann. Phys. (Leipzig) **7**, 225 (1998).

[17] U. Zülicke and A. H. MacDonald, to be submitted.

PB.25

A direct measurement of the effects of Fermi energy oscillations in quasi-1D systems

L. D. Macks*, C. H. W. Barnes, J. T. Nicholls, W. R. Tribe, D. A. Ritchie, P. D. Rose, E. H. Linfield and M. Pepper
Cavendish Laboratory, Madingley Road, Cambridge CB3 0HE, United Kingdom

We use equilibrium magnetotunneling spectroscopy to probe the Fermi surface of a quasi-one-dimensional electron system, providing a direct measurement of the one-dimensional subband energies and wave-functions. At low electron densities, we observe a distinct pinning of all subband energies whenever a single subband depopulates, and a smooth reduction in the width of the density distribution with increasingly negative front-gate voltage. By comparison with a theoretical model, we show that these effects are related to the distinctive peaked front-gate voltage dependence of the one-dimensional Fermi energy.

PACS numbers: 73.23.-b, 71.10.-w, 73.40.Gk
Keywords: Fermi energy oscillations, one-dimensional, tunneling

It has been shown, both experimentally [1] and theoretically [2], that the confinement potential of a quasi-one-dimensional electron system (Q1DES) is parabolic in shape at low carrier densities, and that self-consistent effects lead to a more square shaped potential at higher densities. These facts have been used extensively in the analysis of Q1DESs. There are, however, other self-consistent effects which arise from modulations in the one-dimensional density of states and the associated oscillations of the Fermi energy, which can dominate the behaviour of Q1DESs at low densities. Signatures of such effects have previously been observed in capacitance measurements of Q1DESs [3]. In this paper, we present the first direct measurements of such effects on the wave-functions and subband energies of Q1DESs. We use equilibrium magnetotunneling spectroscopy to probe the Q1D Fermi surface for a range of confinement potentials, and present the results of measurements throughout the regime where fewer than five 1D subbands are occupied, and effects resulting from density of states modulations and associated Fermi energy oscillations are strongest.

The device we discuss here was fabricated from a modulation doped heterostructure grown by molecular beam epitaxy. The active region of the device comprises two 18 nm wide GaAs quantum wells separated by a 12.5 nm wide $Al_{0.33}Ga_{0.67}As$ barrier. Doping is provided by Si donors incorporated in layers above and below the double quantum well region. Low temperature measurements give an electron density and mobility of 1.8×10^{11} cm^{-2} and 8.5×10^{5} cm^{2}V^{-1}s^{-1} for the two-dimensional electropn gas (2DEG) formed in the upper well, and 2.2×10^{11} cm^{-2} and 5.6×10^{5} cm^{2}V^{-1}s^{-1} for the 2DEG formed in the lower well. An additional, more deeply buried, Si-doped layer was patterned into back-gates *in situ* using focused ion beam lithography [4]. Subsequent fabrication of the structure employed standard photolithography, wet chemical etching, metal evaporation and annealing to define an 80 μm wide mesa, make ohmic contacts to both 2DEGs and each back-gate, and form macroscopic front-gates. Electron beam lithography was used to define a front-gate with fine features: a 250 nm period array of 200 gate fingers of width 100 nm and length 45 μm, connected by a bar of width 5 μm. A schematic representation of the device is shown in Figure 1.

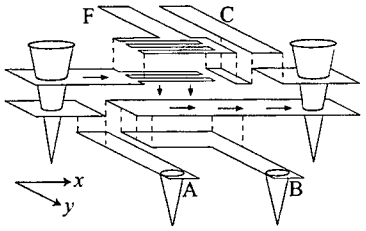

Figure 1: Schematic representation of the device. Front-gates are marked F, C, back-gates A, B. The current path is marked with arrows.

Selective depletion of the upper and lower 2DEGs using front- and back-gates C and A (as labelled in Fig. 1) allows independent contact to be made to each 2DEG, and defines the current path marked with arrows in Fig.1. The patterned front-gate (labelled F) is used to electrostatically define an array of identical Q1D wires in the upper tunneling area. An additional back-gate (labelled B) allows variation of the lower 2DEG density. The tunneling conductance was measured using ac lock-in techniques in two separate experimental configurations: with a 100 μV, 79 Hz excitation signal at 280 mK (in a ^{3}He cryostat), and with a 50 μV, 5 Hz excitation signal at 30 mK (in a dilution refrigerator).

All measurements reported in this paper are in equilibrium, such that only electrons at the Fermi surfaces of the two electron systems contribute to the tunneling conductance. Furthermore, conservation of in-plane momentum restricts tunneling to k-vectors where the Fermi surfaces of the two electron systems overlap. Equilibrium magnetotunneling spectroscopy relies on the relative k-vector shift of $eBd/\hbar$ (where d is the distance between well centres) between the two Fermi surfaces when a magnetic field, B, is applied in the 2D plane. As the 2D Fermi surface is simply a ring in k-space, the equilibrium tunneling conductance measured as a function of in-plane magnetic field maps out the more intricate structure of the Q1D Fermi surface. In the x–direction, parallel to the wires, the Q1D Fermi surface comprises points at k_x values given by:

$$k_x^n = \pm\sqrt{\frac{2m^*(E_F - E_n)}{\hbar^2}} \qquad (1)$$

where E_F is the Fermi energy, E_n are the 1D subband energies (both measured relative to the confinement potential minimum) and $n = 0, 1, 2...$ is the subband index. In the y–direction, perpendicular to the wires, these points form lines which are modulated by the modulus squared of the Fourier transform of the associated wave-function (i.e., the probability density in k-space). The equilibrium tunneling conductance measured as the 2D Fermi ring is swept across the Q1D Fermi surface in an applied magnetic field thus provides a direct measurement of fundamental quantum properties of the Q1DES.

Figure 2 shows the tunneling conductance measured as a function of magnetic field applied in the y–direction for a range of front-gate voltages V_F. A background 2D-2D tunneling component which remained relatively unchanged as a function of V_F has been subtracted from each of the traces. In this magnetic field orientation, the tunneling conduct-

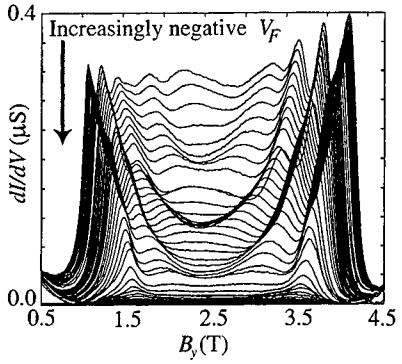

Figure 2: Tunneling conductance measured as a function of in-plane magnetic field applied perpendicular to the 1D wires at 30 mK for front-gate voltages from $V_F = -0.395$ V (top trace) to $V_F = -0.665$ V in 0.005 V steps.

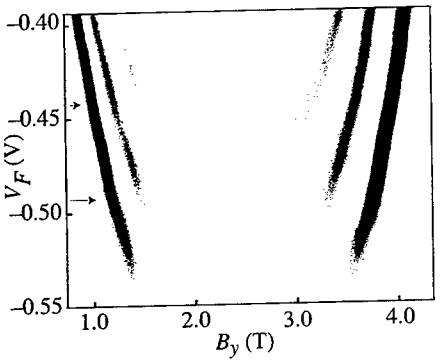

Figure 3: Greyscale representation of the data of Fig. 2 with dark regions indicating conductance peaks. A smoothly varying background has been removed from each trace. Arrows mark the voltages at which the third and fourth sub-bands depopulate.

ance contains peaks at magnetic fields where the 2D Fermi ring overlaps maximally with the points k_x^n. The peaks resolved at $V_F = -0.395$ V thus identify five occupied 1D subbands (the $\pm k$-vector contributions from the fifth subband are resolved as a single peak at 2.15 T). With increasingly negative V_F, the depopulation of 1D subbands is clearly observed, with a strongly modulated signal persisting well into the regime where a single 1D subband is occupied. These measurements were performed with V_B=0 V to maximise the diameter of the 2D Fermi ring, however distortions due to the non-linearity of the 2D probing arc remain, as evidenced by the asymmetry of the observed 1D-2D structure about 2.15 T.

Figure 3 shows a greyscale image of the traces in Fig. 2, with dark regions indicating conductance peaks. A smooth background has been subtracted from each trace. The front-gate voltages at which the fourth and third 1D subbands depopulate are marked with arrows. We note a distinct bowing of each conductance peak trajectory between sudden changes of slope at voltages which appear to be correlated with subband depopulation. This behaviour is particularly clear for the second 1D subband trajectory between the arrows marked on Fig. 3. We interpret these features as resulting from the pinning of each 1D subband as it depopulates.

Figure 4 shows the theoretical energies of the five lowest 1D subbands (labelled $n = 0, 1, 2, 3, 4$) and the confinement potential minimum (dark, lower trace) calculated as a function of front-gate voltage using the Hartree approximation for a model Q1DES with similar parameters to our experimental system. The chemical potential is marked with a horizontal dashed line at E=0 in Fig. 4. Characteristic pinning and jumping of all subband energies is clearly observed in Fig. 4 as a function of front-gate voltage whenever a single subband depopulates . This functional dependence is transferred to the magnetotunneling conductance peak trajectories via equation (1) and accurately accounts for the experimentally observed modulations of the conductance peak trajectories in Fig. 3.

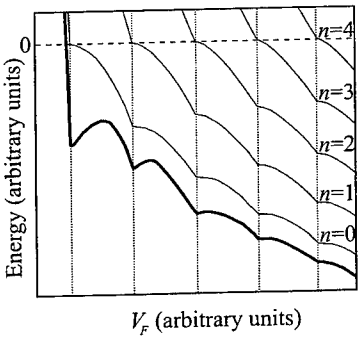

Figure 4: Hartree model of the energies of the lowest five 1D subbands (labelled $n = 0, 1, 2, 3, 4$) and the confinement potential minimum (in bold) as a function of front-gate voltage V_F.

Figure 5 shows the tunneling conductance measured as a function of magnetic field applied in the x–direction for a range of front-gate voltages V_F. A background 2D-2D tunneling component has been subtracted from these traces. In this magnetic field orientation, the

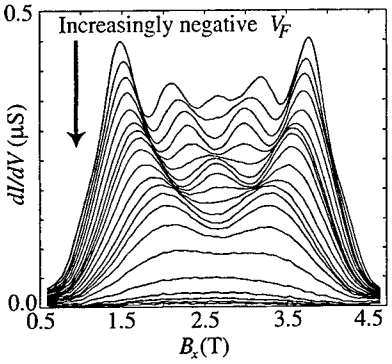

Figure 5: Tunneling conductance measured as a function of in-plane magnetic field applied parallel to the 1D wires at 280 mK for front-gate voltages from $V_F = -0.41$ V (top trace) to $V_F = -0.7$ V in 0.01 V steps.

tunneling conductance is most strongly modulated by the modulus squared of the Fourier transform of the highest occupied 1D subband. The five peaks resolved at $V_F = -0.41$ V correspond to the fifth occupied subband. With increasingly negative V_F, the depopulation of 1D subbands is clearly observed.

The effective diameter of the Q1D Fermi surface decreases monotonically with increasingly negative front-gate voltage [1]. The variation of the width of the traces in Fig. 5 therefore gives an indication of the variation of the width of the Q1DES density distribution with front-gate voltage. It can thus be deduced from Fig. 5 that the width of the experimental density distribution decreases quite smoothly with increasingly negative front-gate voltage, with only small deviations from a linear dependence when more than one 1D subband is occupied. This behaviour agrees well with our theoretical model and, combined with the front-gate voltage dependence of subband energies, indicates that the dependence of the experimental 1D Fermi energy on front-gate voltage should be qualitatively similar to that predicted by our theoretical model. The front-gate voltage dependence of the 1D Fermi energy predicted by our theoretical model can be inferred directly from Fig. 4: as the chemical potential has been set to zero, the Fermi energy is the negative of the confinement potential minimum given by the dark, lower line. The oscillations in E_F in Fig. 4 are directly related to the two effects we have observed experimentally: the pinning of 1D subbands; and the approximately linear decrease of the width of the density distribution. The basic process is that when a subband is pinned at the chemical potential, a reduction in the width of the density distribution is achieved by an increase in both the Fermi energy and the confinement energy.

In conclusion we have experimentally demonstrated two effects related to the oscillation of the Fermi energy in a Q1DES: the pinning of all 1D subbands whenever a single subband depopulates; and the approximately linear reduction of the width of the Q1DES density distribution with increasingly negative front-gate voltage.

CHWB and JTN acknowledge EPSRC advanced fellowships, DAR acknowledges Toshiba Research Europe Limited and EHL the Isaac Newton Trust. This work was funded by the EPSRC.

*Corresponding author: tel.:44-1223-337469, fax:44-1223-337271, email:ldm25@cam.ac.uk

[1] B. Kardynal, C. H. W. Barnes, E. H. Linfield, D. A. Ritchie, J. T. Nicholls, K. M. Brown, G. A. C. Jones and M. Pepper, Phys. Rev. B **55** (1997) R1966.
[2] S. E. Laux, D. J. Frank and F. Stern, Surf. Sci. **196** (1986) 101.
[3] T. P. Smith III, H. Arnot, J. M. Hong, C. M. Knoedler, S. E. Laux and H. Schmid, Phys. Rev. Lett. **59** (1987) 2802; H. Drexler, W. Hansen, S. Manus, J. P. Kotthaus, M. Holland and S. P. Beaumont, Phys. Rev. B **49** (1994) 14074.
[4] E. H. Linfield, G. A. C. Jones, D. A. Ritchie and J. H. Thompson, Semicond. Sci. Technol. **9** (1993) 415.

PB.26

PROBING THE ELECTRONIC DENSITY OF STATES IN SEMICONDUCTOR QUANTUM WIRES USING NONEQUILIBRIUM ACOUSTIC PHONONS

P Hawker, I A Pentland, A J Kent, A J Naylor and M Henini

School of Physics and Astronomy, University of Nottingham, Nottingham NG7 2RD UK.

Abstract

We have used nonequilibrium phonon-induced conductivity (phonoconductivity) measurements to probe the electronic states in semiconductor quantum wire devices. The devices were based on high mobility two-dimensional electron systems (2DESs) in $GaAs/Al_{0.3}Ga_{0.7}As$ heterostructures and quantum wires formed using the well-known split-gate technique. Short (20 ns-long) pulses of nonequilibrium acoustic phonons were generated by heating a metal film on the back surface of the substrate. These phonons propagated ballistically across the substrate and were incident on the quantum wire. The electron-phonon interaction was detected via the phonon-induced change in electrical conductance of the device. We observed giant oscillations of the phonoconductivity with increasing (negative) gate bias. Maxima occurred when the Fermi energy was coincident with the bottom of any one-dimensional electronic subband. In this paper we argue that the phonoconductance is due to phonon-induced backscattering of the electrons in the quantum wire and present evidence that the strength of the phonon signal is proportional to the density of electronic states in the quantum wire.

1. Introduction

Much of the scientific and technological interest in quantum wires stems from the particular nature of the one-dimensional (1D) electronic density of states, $D(E)$, which, in an ideal wire, is singular at the 1D band edge. This may result in lower threshold currents and better spectral characteristics in quantum wire laser structures. Because the strength of the electron-phonon interaction is proportional to $D(E)$, electron-phonon scattering measurements should be a more direct probe of $D(E)$ in quantum wires than are conventional electronic transport measurements. The latter depend on the integral of $D(E)$ and are also very sensitive to disorder related effects such as weak localization.

In an earlier paper [1] we reported phonon-induced conductance measurements on a split-gate short quantum wire (point-contact). A negative correction to the conductance was measured and this was attributed to backscattering of electrons. Giant oscillations in the phonoconductivity were observed, with the peaks occurring close to the steps in DC conductance, i.e. when the Fermi energy (E_F) was coincident with the bottom of a 1D subband. At that time, theoretical calculations of the phonoconductivity [2, 3] predicted that the response due to direct backscattering of electrons in the short channel would be one or two orders of magnitude smaller than measured. It was therefore concluded that the conductance changes had to be due to heating of the electrons in the 2D contacts by the absorption of nonequilibrium phonons. If this explanation is correct then heating the electrons by a different means, e.g. warming up the entire sample, should have the same effect. However, more recent measurements of the equilibrium temperature dependence of the conductance [4] gave very different results to the nonequilibrium phonon measurement. Apparently, this rules out the heating argument despite the fact that it seemed to account for the magnitude of the phonoconductivity signal.

New theoretical calculations of the electron-phonon interaction in a 2DES including the effects of acoustic anisotropy on the coupling matrix elements have recently been reported [5]. These predicted a large enhancement of the interaction for particular phonon modes and directions of propagation when compared to earlier theories which do not include anisotropy. For, example, the coupling to transverse acoustic (TA) modes propagating close to [001] is at least an order of magnitude stronger than originally thought and this was shown to be consistent with the results of phonon emission measurements. It is reasonable to expect that acoustic anisotropy will have the same effect on the electron-phonon interaction in quantum wire devices and so could account for the

magnitude of the phonoconductivity [6].

If, on the basis of the above arguments, we can now attribute the negative phonoconductivity to *direct* backscattering of the 1D electrons by the incident phonons, then we should expect that the amplitude of the response should follow $D(E)$ at E_F. In this paper we present experimental measurements of the phonoconductivity in an applied magnetic field that support this new interpretation.

2. Experimental details

The samples were based on an GaAs/$Al_{0.3}Ga_{0.7}As$ heterojunction, grown by MBE on a 380 μm-thick semi-insulating GaAs substrate. The 2DES carrier density was 4.4×10^{15} m^{-2} and the mobility 100 $m^2V^{-1}s^{-1}$. A TiAu split gate structure was fabricated on top of the heterostructure by electron-beam lithography. The quantum wire channel was defined by 0.4 μm-wide gap in the gate structure. Two channel lengths were used: 0.2 μm and 2 μm. On the back face of the substrate, directly opposite the channel, a 100 μm × 10 μm CuNi heater was made.

The sample was mounted in a liquid helium cryostat at $T = 1.3$ K and the drain-source contacts connected via a low-capacitance (14 pF) coaxial line to a high-input impedance, wide-bandwidth preamplifier at room temperature. The preamplifier output was fed to a high-speed digitiser and signal averager.

Nonequilibrium phonon pulses were generated by applying 20 ns-long pulses of up to 5 V amplitude to the heater. The phonon pulse had an approximately Planckian energy spectrum characterised by the temperature of the heater, T_h (= 28 K for the maximum 5 V excitation pulse). These phonons propagated ballistically in the GaAs substrate and were incident on the quantum wire which was biased with a current of 100 nA. The transient phonoconductivity was detected via the change in voltage drop across the device. It was necessary to average over about 10^6 pulses to achieve an adequate signal-noise ratio. To minimise the effect of electrical pickup of the heater excitation pulse, the phonoconductivity was measured in a 50 ns-wide gate window starting 90 ns after the pulse, 90 ns being the time of flight of phonons across the substrate

Fig. 1 shows a typical example of the amplitude of the phonoconductivity response as a function of the (negative) gate bias for a 0.2 μm-long wire. The amplitude has been corrected for the RC time constant of the device, coaxial line and pre-amplifier input, and expressed as a change in conductance as a fraction of the conductance quantum $G_0 = 2e^2/h$. Also shown in Fig. 1 is the DC conductance of the device as a function of the gate voltage.

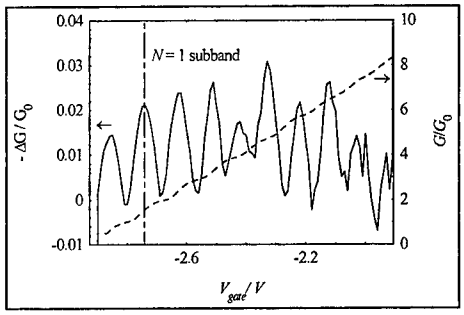

Figure 1 Phonoconductivity of a short quantum wire (point-contact) as a function of split-gate bias. Also shown is a measurement of the DC conductance of the wire.

3. Results and discussion

In Fig. 1 it is seen that the phonoconductivity peaks near a step in the DC conductance (when the steps are resolvable), i.e. when E_F is close to the edge of a 1D subband. This is where the density of states at E_F is a maximum. Compare this with Fig. 2 which shows the difference between the DC conductance at 1.3 K and 4.2 K, i.e. the effect of warming up the sample, and it is clear that the effect of the nonequilibrium phonons is very different. Firstly, the conductance oscillations due to heating pass through zero at steps in the DC conductance. Secondly, the phonoconductance is always negative whereas the heating causes both

positive and negative conductance changes.

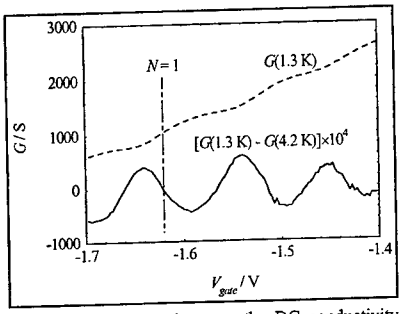

Figure 2 Difference between the DC conductivity measurements at 1.3 K and 4.2 K to show the effects of heating.

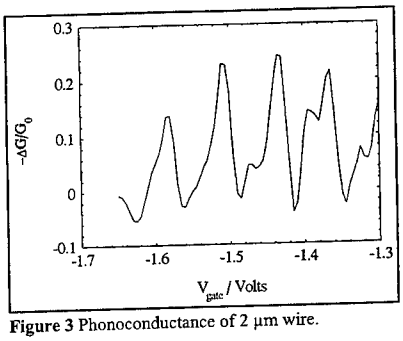

Figure 3 Phonoconductance of 2 μm wire.

Fig. 3 shows the phonoconductivity of the 2 μm-long wire. Again, strong peaks are present, but in this case the DC conductance steps were not seen and warming the sample slightly had no discernable effect on the conductance. The absence of DC conductance steps is probably due to disorder in the longer wire. However, it seems that the phonoconductivity measurement is still able to reveal the nature of the 1D density of states. It is interesting to note the splitting of the peaks in Fig. 3, this is possibly due to fluctuations in width along the channel.

In [2], the change in conductance, ΔG, of a 1D channel of length L_y due to phonon scattering was calculated:

$$\frac{\Delta G}{G_0} = -\frac{L_y m^* C}{(2\pi)^2 \hbar^2} \sum_{MN} \frac{1}{\sqrt{E_F - E_N}} \iint \frac{dq_x dq_z \, q^{\gamma} N(q) |Z(q_z)|^2 |X_{MN}(q_x)|^2}{\sqrt{E_F - E_M + \hbar s q}} .$$

Here q ia the phonon wavevector, s the phonon speed, C is the electron-phonon coupling constant, $\gamma = +1$ for deformation potential coupling and -1 for piezoelectric coupling and $F(q)$ is the Bose distribution function for the phonons. The form-factors $Z(q_z)$ and $X_{MN}(q_x)$ arise from the electron confinement in the heteojunction growth direction and confinement by the gate potential respectively. E_N and E_M are respectively the energies of the $N^{th.}$ and $M^{th.}$ 1D subbands, for intrasubband scattering $N = M$. All the other symbols have their usual meanings. This expression is able to explain the main features of the observed signals: (i) that ΔG is negative, (ii) that ΔG is larger for the longer wire, and (iii) that ΔG is strongly peaked at $E_F \approx E_N$. The latter is due to the term $1/(E_F - E_N)^{1/2}$ which reflects the singularities in the ideal 1D density of states.

Further evidence that the phonoconductivity measurement is sensitive to the 1D density of states is provided by the results obtained in a magnetic field, $B = B_Z$. Fig. 4 shows the phonoconductivity oscillations as a function of gate voltage at 0, 0.34 T and 0.67 T (note that these curves have not been corrected for the RC time constant of the system). Application of the magnetic field has the effect of increasing the amplitude of the oscillations well as broadening and increasing the separation of the peaks. The strong positive phonoconductivity peak at $V_{gate} \approx$ -1.9 V is believed

to be due to phonon-activated conduction when the channel is just pinched-off.

It is well known that the application of a magnetic field perpendicular to the wire axis leads to the formation of hybridized electric-magnetic subbands. Assuming the gate confinement potential is parabolic in profile and the characteristic harmonic oscillator frequency is ω_0, the characteristic frequency of the hybridized state $\omega = (\omega_0^2 + \omega_c^2)^{1/2} > \omega_0$, where ω_c is the cyclotron frequency. The energy of the N^{th} subband is given by $E_N(k) = E_N(B) + \hbar^2k^2/2m^*(B)$, where the magnetic effective mass $m^*(B) = m^*(0)\ \omega^2/\omega_0^2$ accounts for a flattening of the subband dispersion and an increased density of states at the subband edge. In the above formula for $\Delta G/G_0$, we see that the phonoconductivity is proportional to m^*, so by measuring the relative amplitudes of the $N = 0$ peak we can determine the ratio $m^*(B)/m^*(0)$, see inset to Fig. 4, the solid line is given by $m^*(B)/m^*(0) = \omega^2/\omega_0^2$, with $\omega_0 = 2.4 \times 10^{12}$ s^{-1}. This value of ω_0 implies a characteristic width of $l_w = (\hbar/m^*\omega_0)^{1/2} = 26$ nm which seems entirely reasonable.

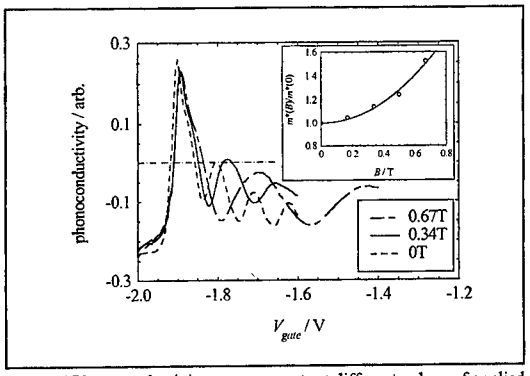

Figure 4 Phonoconductivity measurements at different values of applied magnetic field. The inset shows $m^*(B)/m^*(0)$ deduced from the magnetic field dependence of the amplitude of the $N = 0$ peak.

4. Conclusions

We have described phonoconductivity measurements on quantum wire samples in zero and applied magnetic field. The conductance changes produced by incident nonequilibrium phonon pulses are different to those caused by warming up the sample. The phonoconductivity is attributed to direct phonon-induced backscattering of electrons and the main features of the experimental measurement are in agreement with theoretical predictions. We have shown that the phonoconductivity measurement is able to reveal the form of the density of 1D electronic states in quantum wires, even in samples where the DC conductance fluctuations are smeared out by disorder.

The authors would like to acknowledge the Engineering and Physical Sciences Research Council of the UK for its financial support for this work under grant no. GR/K55561. We also thank Dr M Blencowe, Prof A Shik and Dr D Lehmann for very helpful discussions.

References:

[1] A J Naylor, A J Kent, I A Pentland, P Hawker and M Henini, *Phys. Low-Dim. Strict.*, **1/2** (1998) 167.
[2] M Blencowe and A Shik, *Phys. Rev.*, **B54** (1996) 13899.
[3] M Blencowe, in: P Serena, N Garcia (Eds.), *Nanowires*, Kluwer, Dordrecht, 1997.
[4] A J Naylor, *Ph.D. Thesis*, University of Nottingham (1998).
[5] D Lehmann, Cz Jasiukiewicz and A J Kent, *Physica*, **B249-251** (1998) 718.
[6] D Lehmann, Cz Jasiukiewicz and A J Kent, at this conference.

PB.27

One–dimensional electron transport in devices fabricated by MBE regrowth over a patterned ∂-doped backgate

M. L. Leadbeater†, T. M. Burke*, M. P. Smith*, D. A. Ritchie* and M. Pepper†*

†Toshiba Research Europe Ltd., Cambridge Research Laboratory, 260 Cambridge Science Park, Milton Road, Cambridge, CB4 0WE, UK

*Cavendish Laboratory, University of Cambridge, Madingley Road, Cambridge, CB3 0HE, UK

MBE regrowth and hydrogen radical decontamination of an *ex situ* patterned GaAs wafer have been successfully used to create a one-dimensional constriction which exhibits quantised ballistic conductance. Deviations from exact quantisation are discussed in terms of electron reflection at the entrance to the constriction.

Molecular beam epitaxial (MBE) regrowth on patterned substrates uses the atomic layer precision of MBE in more than one dimension to create highly confined electron structures. [1,2]. A typical regrown structure consists of the initial growth of a series of layers of different doping (or chemical composition) forming a backgate that are exposed by the *ex situ* etching of an angled facet before the wafer is returned to the MBE system for the overgrowth of a two-dimensional electron gas (2DEG). Bias voltages applied to the underlying gate layer(s) control the conduction of electrons in the regrown 2DEG where it intersects the plane of the backgate. The lengthscale of the potential modulation is controlled by the distance from the backgate to the 2DEG and the thickness of the gate layer, which are both defined with atomic precision by the MBE growth. The potential resolution is far smaller than that achievable using conventional lithographic techniques. However, the *ex-situ* wafer patterning introduces contamination at the regrowth interface that seriously degrades device performance. Effective surface contaminant is therefore essential. We have achieved this using *in situ* hydrogen radical (H^*) decontamination [3-7], which enables us to produce high quality material ($>10^6$ cm^2/Vs electron mobility) within a few hundred angstroms of the interface [8].

The structures reported here incorporate a narrow δ-doping plane in the initial growth, which we use to modulate the potential in an overlying 2DEG. The device structure is sketched in Figure 1. A narrow metallic gate was deposited over the wafer surface across the facet and perpendicular to the intersection of the backgate and the regrowth interface. By applying a negative voltage to the front gate and a positive voltage to the backgate, carriers can be depleted in all regions of the 2DEG under the surface gate apart from a narrow area directly overlying the backgate thus forming a narrow constriction between two wide areas of 2DEG. The width and depth of the constriction, and therefore the number of transmitted one-dimensional channels, are controlled by the gate voltages applied.

The initial growth consisted of 1.25 μm of GaAs with a ∂-doping layer of silicon donors 0.5 μm below the surface. Standard optical lithography was used to define a mesa with planar sidewalls that intersected the ∂-doped layer at approximately 20°. The wafers were cleaned then

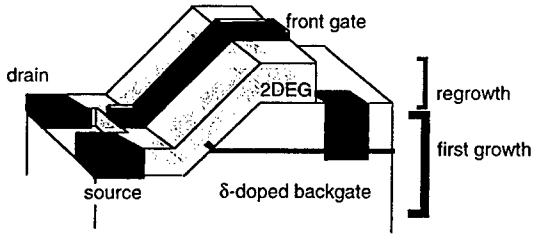

Figure 1 Schematic diagram of a one-dimensional constriction formed by at the intersection of the δ-doped backgate and a narrow surface gate.

loaded back into the UHV system. Here they were heated and exposed to a flux of hydrogen radicals. Following the decontamination, the wafer was transferred (under UHV) to the MBE growth chamber for the regrowth. This consisted of the following layers sequence: 20 Å undoped GaAs, 8 x10^{11} cm^{-2} Si, ∂-doping, 10 Å undoped, GaAs, 270 Å undoped GaAs/AlAs superlattice barrier, 150 Å undoped GaAs quantum well, 200 Å undoped AlGaAs, 400 Å 2x10^{18} cm^{-2} n-type AlGaAs, and 100 Å undoped GaAs. A layer of dopants (8x0^{11} cm^{-2}) was included close to the regrowth interface to counteract the effects of residual carbon contamination. More details of the decontamination process are given in reference 8. The 2DEG was etched to form a mesa and separate NiAuGe ohmic contacts made to the 2DEG and the backgate. The 2DEG had a maximum mobility of 350,000 cm^2/Vs at a carrier concentration of 5.5x10^{11} cm^{-2}, lower than previously achieved [9] indicating remaining contamination or interface roughness following the *ex situ* etch. A narrow (0.5 μm or 1 μm) NiCr/Au surface gate was deposited across the mesa to define the length of the constriction.

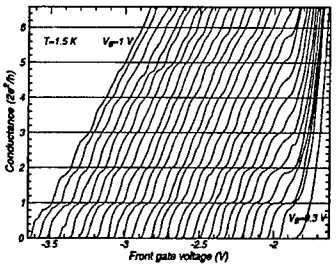

Figure 2. ac conductance of the 1D constriction with a 0.5 μm front gate taken at 1.5 K for V_b between 1.0

Figure 2 plots the four terminal ac conductance as a function of the applied front gate bias for a device with a 0.5 μm front gate. Measurements were taken at 1.5 K with an excitation of 50 μV and backgate biases between +1 and +0.3 V. A series of conductance plateaux develop as the gate bias is swept with values close to multiples of $2e^2/h$, showing ballistic conduction [10] through a one-dimensional channel formed at the intersection of the front and back gates. The quantisation is quite good for the lowest two plateaux, particularly for smaller backgate biases. However the higher index plateaux appear more pronounced at some gate biases than others and are not flat. Although some are close to multiples of $2e^2/h$ this is not true of all the features.

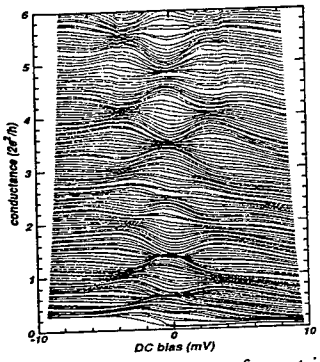

Figure 3 ac conductance of constriction as a function of dc bias for V_b=0.9 V and V_f from -1.25 to -0.875 V.

Figure 3 plots the conductance as a function of the applied dc bias for a range of front gate biases at a backgate bias of +0.9 V for another device with a 0.5 μm front gate. A set of plateaux intermediate between the zero bias levels develop. The traces are skewed which implies a non-symmetric voltage distribution across the constriction. By analysing the voltage spacing between the additional plateaux we derive an energy level spacing of 2.5 meV. Assuming a parabolic confining potential, this corresponds to a channel width of 2000 Å at definition reducing to 400 Å when only one level is occupied. This energy level spacing is consistent with temperature data which show the plateaux are washed out at temperatures above 7 K ($4k_BT=\Delta E$).

Although all samples measured showed similar structure in the conductance, they did not all show the same conductance values. For the device shown in figure 3, the plateaux (even at V=0) are reduced to <80% of the expected values. Since we are performing a four terminal measurement there is no influence from contact resistances and at the low current levels employed (a few nA) the series resistance from the 2DEG regions (approximately 150 Ohms) does not significantly alter the levels of the plateaux. In addition, thermal cycling or illumination can change the detailed characteristics of a single device. Figure 4 shows the conductance for a device with a 1 μm long front gate. The plateaux are not at $2e^2/h$ and depend strongly on the applied gate biases. Plateaux at values other than multiples of $2e^2/h$ have been reported previously and assigned to spin polarisation effects [11,12], electron-electron interaction [13] or back scattering between 2DEG contact regions and the one-dimensional channel [14]. There could also be diffusive scattering in the channel since its length (particularly for the 1 μm gate device) is comparable to the scattering length calculated from the electron mobility (3 μm), however this is not expected to reduce the height of the plateaux. In our device the backgate produces a very sharp potential well whose shape will change with bias and the front gate runs continuously across the constriction producing a barrier to conduction. Therefore it seems likely that there is strong reflection of electrons at the entrance and/or exit of the constriction. This will depend on the exact details of the potential profile, which will differ between devices and change with illumination of the sample if the amount of contamination and therefore the Fermi level pinning at the regrowth interface varies across the wafer.

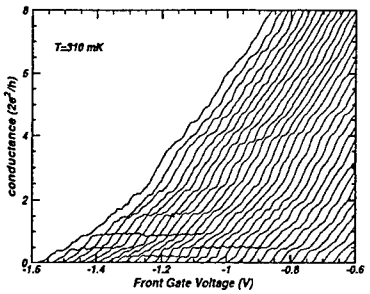

Figure 4 ac conductance of the one-dimensional constriction with a 1 μm front gate taken at 310 mK for backgate voltages between 1.1 and 0.5 V.

To make full use of the atomic resolution of the MBE technique we must produce structures where the variation in the electrical potential is related to a composition variation in the backgate. Therefore we have attempted to optimise the decontamination of a planar AlGaAs surface. The aluminium-rich layers are strongly oxidised when exposed to air and this oxide is more difficult to remove than the gallium oxides. There was no electrical activity in a 2DEG regrown 300 Å from an exposed $Al_{0.3}Ga_{0.7}As$ surface. Depth profile SIMS analysis showed a very high oxygen level throughout the $Al_{0.3}Ga_{0.7}As$ layer (50 nm). For a reduced aluminium concentration of 15% there was a marked improvement in the cleaning efficiency, although still much poorer than the GaAs surfaces. We measure an electron mobility of 370,000 cm^2/Vs at a sheet concentration of $3.7x10^{11}$ cm^{-2} (following illumination) for conduction in a 2DEG regrown 300 Å from the regrowth interface, compared to 620,000 cm^2/Vs and $6.5x10^{11}$ cm^{-2} for a simultaneous growth over GaAs. The different contamination levels on AlGaAs and GaAs surfaces will produce a potential variation that could be used to increase the confinement of the electrons.

In conclusion, we have observed ballistic transport through a one-dimensional constriction fabricated using *in situ* H* cleaning and MBE regrowth where the electrons are confined on a lengthscale of a few hundred angstroms which is defined by the MBE growth process itself.

[1] H. Sakaki 1980 *Jap. J. Appl. Phys.* 19 (1980) L735
[2] J. H. Burroughes et al *Appl. Phys. Lett.* 63 (1993) 2219-2221.
[3] S. Sugata et al *J. Vac. Sci. Technol. B 6* (1988) 1087-1091.
[4] M. Yamada et al *Jap. J. Appl. Phys.* 31 (1992) L1157.
[5] E. J. Petit et al *J. Vac. Sci. Technol. A* 10 (1992) 701.
[6] C. M. Rouleau and J. M. Park *J. Appl. Phys.* 73 (1993) 4610.
[7] T. M. Burke et al, *J. Cryst. Growth* 175/176 (1997) 416-421.
[8] T. M. Burke et al, *Materials Science and Engineering B* 51 (1998) 202-206.
[9] T. M. Burke et al, *J. Cryst. Growth* (1999).
[10] D. A. Wharam, et al *J. Phys. C 21* (1988) L209
[11] K. J. Thomas et al, *Phys. Rev. Lett.* 77 (1996) 135.
[12] P. Ramvall et al, *Appl. Phys. Lett.* 71 (1997) 918-920.
[13] A. Yacoby et al, Phys. *Rev. Lett.* 77 (1996) 4612-4615.
[14] A. Y. Alekseev and V. V. Cheianov, *Phys. Rev. B* 57 (1998) R6834-R6837.

PB.28

Fermi-edge singularities in the photoluminescence and magneto-optical spectra of modulation-doped v-groove quantum wires

A.C. Maciel[1], J. Kim[1], H.D.M. Davies[1], E.D. O'Sullivan[1] and J.F. Ryan[1]
A. Schwarz[2], A.Kaluza[2], H. Hardtdegen[2], Th. Schäpers[2], D.Meertens[3], Ch. Dieker[4] and H. Lüth[2]

[1]Clarendon Laboratory, Department of Physics, University of Oxford, Oxford OX1 3PU, UK
[2]Institut für Schicht- und Ionentechnik (ISI), Forschungszentrum Jülich, 52425 Jülich, Germany
[3]Institut für Festkörperforschung, Forschungszentrum Jülich, 52425 Jülich, Germany
[4]Technische Fakultät, Mikrostrukturanalytik, Universität Kiel, 24143 Kiel, Germany

Abstract

We report the observation of a strong Fermi-edge singularity in the photoluminesecence spectrum of a degenerate one-dimensional electron system in modulation-doped GaAs/GaAlAs v-groove quantum wires. The singularity is pronounced due to 1D subband mixing, which is further enhanced by an applied transverse magnetic field.

Electron-hole correlation effects are predicted to be very pronounced in one-dimensional electron systems (1DES), and many-body effects are expected to dominate their optical response. For example, the excitonic contribution to the interband optical transition rate is strongly enhanced and the free carrier component strongly suppressed near the band edge of an ideal undoped 1D system [1,2]. In a degenerate 1DES strong enhancement of radiative recombination of electrons at the Fermi energy is predicted to arise due to the collective response of the electrons to the Coulomb potential of the valence band hole. This Fermi edge singularity (FES) should be prounounced in 1D due to the strong restriction on hole recoil [3,4]. Observations of FES have been reported in weakly-confined, spatially-indirect quantum wires obtained by ion bombarding GaAs modulation-doped quantum well structures [5], and also in wide InGaAs quantum wire structures which were obtained by chemical etching [6]. In this paper we report measurements of the FES in the optical and magneto-optical spectra of the strongly-confined 1DES in GaAs/GaAlAs modulation-doped v-groove quantum wires (QWR).

Modulation-doped multiple v-groove QWRs were grown by low-pressure metal-organic vapor phase epitaxy on pre-patterned, semi-insulating GaAs substrates [7]. A relatively narrow crescent-shaped quantum wire forms in the bottom of the groove formed by {111}-A facets when a thin quantum well is grown between AlGaAs barriers [8]. TEM and cross-sectional AFM studies revealed the excellent definition of the quantum wires, whose profile could be adjusted by the choice of the gas sources used for the bottom $Al_{0.3}Ga_{0.7}As$ barrier layer and the thickness of the quantum well. The wires studied here have a sidewall quantum well (SQW) width of 2.8nm which is pinched off at the transition between {311}and{111} facets to 1.4nm; the wire thickness in the growth direction in the middle of the v-groove is 7.6nm, and the lateral distance between the pinched-off regions is approximately 40nm. The lateral electron potential barrier is ~150meV, and the 1D level spacing is ~ 40meV. For low barrier doping conditions ($\sim 10^{16} cm^{-3}$) and with a spacer layer of 30nm, we obtain 1D electron densities in the range ~ 10^6 cm^{-1}.

Photoluminescence spectra were obtained using Ar laser excitation at 2.4eV, well above the band gap of the confining barrier material. Relaxation and trapping of photoexcited holes

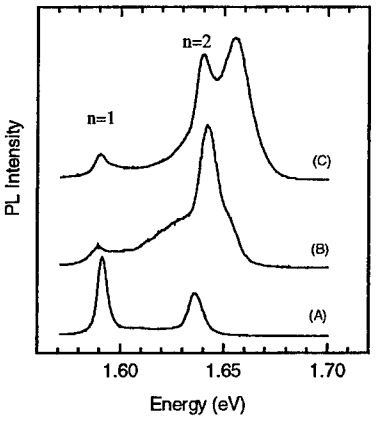

Figure 1 PL spectra of modulation-doped v-groove quantum wires at 10K.

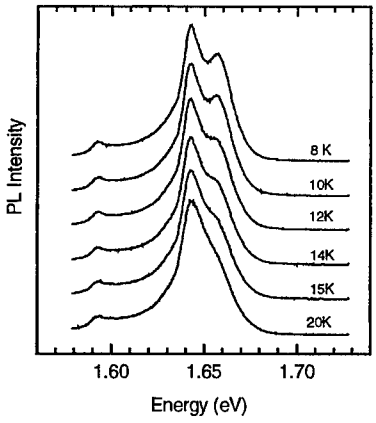

Figure 2 Temperature dependence of the PL spectrum of Sample C

from the barrier into the <111> SQW and the QWR allow the confined quasi-1D states to be measured. Fig. 1 shows photoluminescence (PL) spectra obtained from a series of samples with nominally identical structural parameters but different dopant densities. Sample A is nominally undoped. The sharp lines labelled n=1, 2 are confined quantum wire states whose energies are consistent with band-structure calculations which use a plane wave expansion of the full v-groove confining potential. Samples B and C show the effect of modulation doping on the structure when the Fermi energy lies close to the n=2 level. The relative intensities of n=1 and n=2 change, but their energies remain practically unchanged. For sample B we observe a wing extending to energies below n=2, and a weak but distinct high energy shoulder which is indicative of a Fermi edge. Sample C, with a slightly higher density, shows a distinct peak above n=2 which has the characteristics of a pronounced Fermi edge singularity. The results are similar in outline to those reported by Chen et al [9] who observed strong enhancement of the FES in quantum well structures due to interference between the n=1 and n=2 states. Although we do not have an independent measure of the electron density in these structures, we infer a value of ~$1.5 \times 10^6 cm^{-1}$ from the PL data for sample C.

The temperature dependence of the PL spectrum of sample C is shown in Fig. 2. Whereas the n=1 and 2 lines hardly change, the singularity is rapidly diminished with increasing temperature, and by 20K it is reduced to a shoulder on the n=2 line. At much higher temperatures (not shown in Fig. 2) the line is strongly asymmetric.. This strong sensitivity to temperature is highly characterisitc of a FES which requires a sharp Fermi surface, as well as inhibited hole recoil. In a separate series of measurements we have raised the electron temperature by applying a voltage along the wires, while the lattice temperature remains at approximately 4K. Once again we observe a dramatic reduction in the intensity of the FES [10]. The FES is also strongly dependent on the photoexcited electron-hole pair density: with increasing photoexcited carrier

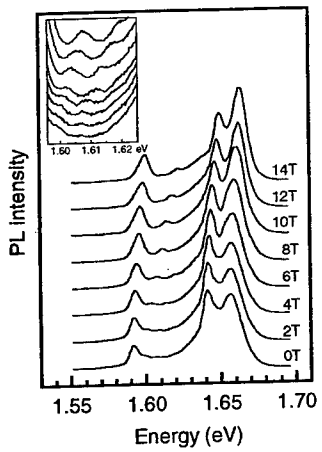

Figure 3 Magneto-PL spectra of sample C measured at 10K. The inset shows the region between n=1 and n=2, in steps of 1T from 0-7T.

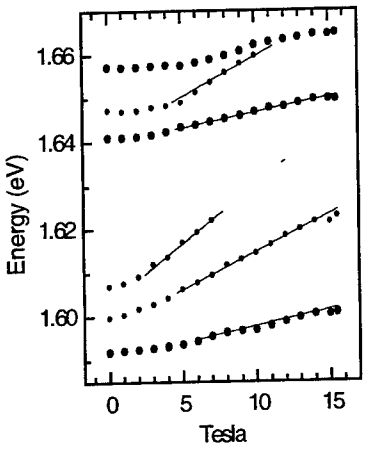

Figure 4 Energy fan diagram showing the B-dependence of the 1D states and the crossover to Landau quantization of hole states.

density the sharp FES rapidly decreases and broadens, the 1D DOS peak at the n=2 subband diminishes, and eventually the spectrum develops at high excitation into a form which we expect to be dominated by electron-hole correlation in a two-component plasma.

The application of a transverse magnetic field gives further information about the form of the 1D confining potential and the origin of the FES. Fig. 3 shows the variation of the PL spectrum for B applied perpendicular to the sample surface. At low fields, the n=1 and n=2 lines shift only slightly. This is expected due to the lateral confining potential: $\omega \sim (\omega_0^2 + \omega_c^2)^{1/2}$ where ω_0 is the effective oscillator frequency and ω_c is the cyclotron frequency, so that only a weak quadratic B-dependence arises at low field. When B is applied in the orthogonal direction, transverse to the wire and in the plane of the sample, so that the lateral confinement is produced by the AlGaAs quantum well barriers, the energy shift is even smaller due to the stronger confining potential. However, in both cases the FES increases significantly in intensity with increasing field. This effect has been predicted theoretically: it arises from field-dependent symmetry breaking which mixes wavefunctions of the n=1 and n=2 states and increases the FES oscillator strength [4]. These results therefore provide supporting evidence that the FES is pronounced in this particular v-groove structure by the effects of subband mixing.

The inset to Fig. 3 shows additional fine structure occurring in the spectral region between the n=1 and n=2 lines. At low fields the features are very weak, and shift only slightly with increasing field. However, for B>5T we see that they begin to shift more rapidly to higher energy. The fan diagram in Fig. 4 summarises the results. It is quite clear that at high fields these lines form a Landau series: i.e. there is a cross-over from 1D confinement to Landau quantization

as the cyclotron energy becomes comparable to the confinement energy. However, the energy scale in this series is clearly not electronic in origin, but in fact is consistent with valence band states. A definitive assignment of the lines will require a detailed calculation of the valence band energy levels and effective masses; however, using accepted vales of m_e and m_{hh} for GaAs, we find that the weak PL features at zero field are consistent with n_e=1, n_h =1,3,5..electron-hole transitions which are weakly allowed due to the complex shape of the confining potential. At intermediate fields the confined hole states transform into Landau states l_h=0,2,4. The heavy-light character of the hole states concerned is quite complex since there is already strong mixing at k=0, B=0 in these v-groove structures. A similar cross-over from 1D electron states to Landau quantization has been observed by Hammersberg et al [11].

The results presented here provide the clearest evidence to date of a Fermi edge singularity in the PL spectrum of a degenerate 1DES, and they raise a number of issues:
(i) We observe little bandgap renormalization on increasing the dopant electron density. This is consistent with expectations of strongly suppressed screening in 1D systems, and is reproduced in the calculations of Rodriguez and Tejedor [4]. The strong bandgap renormalization in 1D systems predicted by Hu and Das Sarma [12] is apparently associated with the filling of low energy localized states.
(ii) The reduction of the n=1 recombination intensity on doping is unexpected. Previous measurements of ion-bombarded GaAs quantum wires ascribed the absence of the n=1 density of states peak in the PL spectrum to the effects of sample disorder: the appearance of sharp peaks in the undoped sample (Fig. 1(A)) indicates low structural disorder, but the effects of the random potential arising from ionized donors in the barrier might be significant.
(iii) The nature of the valence band hole, whether localized or free, is an important issue. Although FES should be more defined in 1D systems for free holes than in 2D or 3D [13], the strong enhancement of the singularity over the n=1 density of states peak is strongly suggestive of hole localization.

References

[1] Tetsuo Ogawa and Toshihide Takagahara, Phys. Rev. B43, 14325 (1991); B44, 8138 (1991)
[2] Fausto Rossi and Elisa Molinari, Phys. Rev. B53, 16462 (1996)
[3] P. Hawrylak, Solid State. Commun. 81, 525 (1992)
[4] F.J. Rodriguez et al, Phys. Rev. B47, 1506 (1993); B49, 16781 (1994)
[5] J.M. Calleja et al., Solid State Commun. 79, 911 (1991)
[6] M. Fritze, A.V. Nurmikko and P. Hawrylak, Phys. Rev. B48, 4960 (1993)
[7] Th. Schäpers, A. Hartmann, A. Schwarz, H. Hardtdegen, M. Bongartz, Ch. Dieker and H. Lüth, App. Surf. Sci. 123/24, 687 (1997)
[8] E. Kapon, D.M. Hwang and R. Bhat, Phys. Rev. Lett. 63, 430 (1989)
[9] W. Chen, M. Fritze, A.V. Nurmikko, D. Ackley, C. Colvard and H. Lee, Phys. Rev. Lett. 64, 2434 (1990)
[10] J. Kim et al., Proceeding MSS-9 (Fukuoka, Japan, 1999), Physica E, to be published
[11] J. Hammersberg, H. Wehman, N. Notomi, T. Lundstrom, T. Tanamura and M. Potemski, Phys. Rev. B54, 4835 (1996)
[12] B. Hu and S. Das Sarma, Phys. Rev. Lett. 68, 1750 (1992)
[13] J.F. Mueller, A.E. Ruckenstein and S. Schmitt-Rink, Phys. Rev. B45, 8902 (1992)

PB.29

Thermopower of One-dimensional Devices - Measurement and Applications

N.J. Appleyard* , J.T. Nicholls, W.R. Tribe, M.Y. Simmons and M. Pepper
Cavendish Laboratory, University of Cambridge,
Madingley Road, Cambridge CB3 0HE, UK

Abstract

We have developed a technique to measure the thermopower of a mesoscopic device. Absolute calibration is possible, and we find that a constriction in a 2D electron gas obeys theoretical predictions sufficiently well that its thermopower can be used for electron thermometry. This has been applied to measure heat loss rates from the 2DEG at zero field, leading to the electron-phonon scattering rate. The same technique can determine the effect of a quantising magnetic field on the coupling, and the electron thermometry also allows a calibrated measurement of the thermal conductance of a mesoscopic device. We discuss how such measurements might be realised.

PACS: 72.20.Pa, 63.20.Kr, 73.23.Ad
Keywords: Point Contact, Thermopower, Thermal Conductance, Hot Electrons

1. Introduction

The thermopower S of a mesoscopic device is the voltage developed in response to a temperature difference across its terminals. The diffusion contribution arises directly from the difference in electron temperature, as opposed to the drag produced by a phonon temperature gradient. It probes the energy derivative of the electron transmission rate at the Fermi energy, and so is usually simply related[1,2] to the derivative of the conductance:

$$S=\left[\frac{\Delta V}{\Delta T}\right]_{I=0} \approx -\frac{\pi^2 k_B^2 T}{3e}\frac{1}{G}\left[\frac{\partial G}{\partial \varepsilon}\right]_{\varepsilon=\mu} \quad . \qquad (1)$$

For a one-dimensional wire, as successive 1D subbands, i, are opened for electron transmission, the conductance rises in steps quantised in units $2e^2/h$, so the diffusion thermopower is expected [3] to show peaks of height

$$\Delta V_{pk} \approx -\frac{\pi^3 k_B^2}{24e\hbar\omega_x}\left(T_1^2-T_2^2\right)\left(i+\frac{1}{2}\right)^{-1} \quad , \qquad (2)$$

where $\hbar\omega_x$ is the characteristic energy width of the transition between conductance steps, determined by the tunnelling rate. Such peaks are indeed observed[4,5], and so with appropriate calibration the peak height allows the electron temperature difference to be measured. We have recently shown [6] how this may be achieved for a short constriction patterned in a 2DEG, and found agreement with Eq.(2) within 50%.

* e-mail: nja11@cam.ac.uk Tel:(+44) 1223 337379 Fax: 337271

2. Calibrated Hot Electron Thermometry

The device geometry and measurement circuit for hot electron thermometry are shown in Fig 1. A 2D electron gas is formed at a GaAs/AlGaAs interface, ~300nm below the surface of a deep HEMT structure grown by molecular beam epitaxy. The electrons in a 100μm wide heating channel, patterned in the 2DEG mesa by etching, are heated to a temperature T_1 by an AC current I_H at frequency f_H.

Voltage probes extend from the mid-point of the heating channel, and a 1D constriction is formed across each of them by depleting the electrons from beneath a pair of split gates, with length L≈0.8μm and gap width W≈0.8μm. Heat is prevented by the constrictions from flowing into the voltage probes, which therefore remain at the lattice temperature, T_2. The temperature drop T_1-T_2 across the constrictions generates a potential difference ΔV, which is recorded as the width of one constriction is swept, whilst the other is kept fixed as a voltage reference. Since ΔV is measured at the harmonic frequency $2f_H$, the signal is sensitive only to thermal effects, which vary as I_H^2.

A simultaneous measurement is made of the four-terminal resistance R of the same constriction using a small current I_R=2nA at a different frequency.

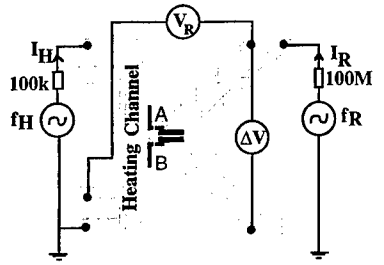

Fig 1 Device geometry and circuitry for the thermopower and resistance measurements. Grey areas are 2DEG mesa and black areas represent gated structures.

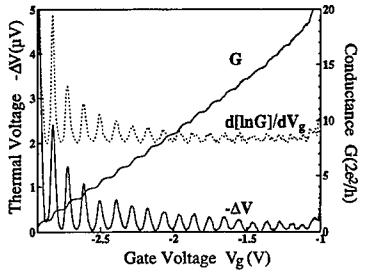

Fig 2 Measured thermopower and conductance of a quantum point contact as its width is varied. The prediction of Eq.(1) is shown for comparison.

Fig 2 shows typical experimental thermopower S and conductance G traces, which are related as described in Eq.(1). As the lattice temperature T_2 and the heating current I_H are varied, the magnitude of ΔV can change over orders of magnitude, but the shape of the traces is unaffected, until thermal broadening sets in, as shown by the data collapse in Fig 3. Comparing this variation of peak height to Eq.(2) allows the heated electron temperature T_1 to be deduced.

This new technique of calibrated electron thermometry has already allowed accurate determination of the energy loss rate from a 2DEG at zero field [6]. A loss rate of $\dot{Q}(T_1,T_2)=61\left(T_1^5-T_2^5\right)\mathrm{eVs}^{-1}$ per electron was measured, together with a small contribution due to heat leaks through the contacts; this provided the first accurate confirmation of the theory of heat loss through acoustic phonon emission in GaAs.[7] The results are shown in Fig 4; the dashed line shows the theoretical predictions, and there are no free parameters.

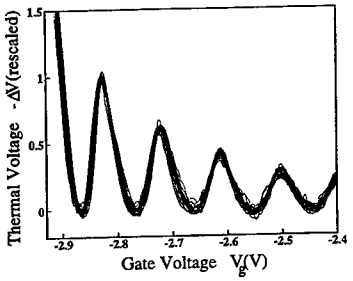

Fig 3 Collapse of thermopower traces taken at different temperatures and heater powers. Each sweep has been rescaled by the i=1 peak height, which varies from 10nV to 10μV.

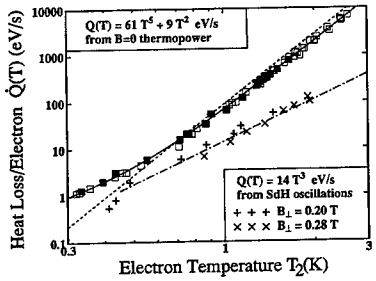

Fig 4 Energy loss rate from a 2DEG, deduced from thermopower measurements (full symbols) and from SdH oscillations (crosses). The zero field prediction is shown as a dashed line.

The commonest established method of hot electron thermometry in a 2DEG relies on a comparison of the amplitude of Shubnikov-de Haas oscillations as a function of lattice temperature and of heating current. This technique yields different behaviour for the heat loss rate $\dot{Q}$, when measured under the same conditions as led to Fig.4. We believe that the discrepancy may be due to a change in electron-phonon coupling in the presence of a magnetic field, as the electrons are no longer plane waves, but are confined within the magnetic length. The Shubnikov-de Haas method therefore probes the electron-phonon coupling at finite field, and a comparison to zero-field theories is inappropriate. The thermopower method can be used to investigate this effect, as long as the constrictions continue to present an effective barrier to heat flow, and the current in the heating channel remains spatially uniform.

3. Mesoscopic Thermal Conductance Measurements

A further application of the electron thermometry technique is to calibrate a thermal conductance measurement, using the device and circuit in figure 5.

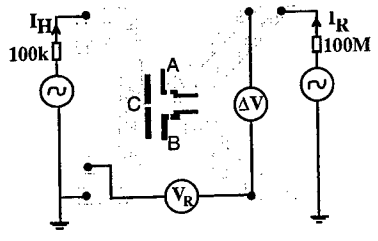

Fig 5 Device design for a thermal conductance measurement.

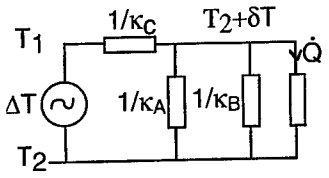

Fig 6 Equivalent circuit for heat flows in the device of Fig.5. The known heat loss through phonon emission provides a reference resistance against which the thermal conductances can be compared.

The thermopower of a pair of constrictions is first calibrated as described above, and used to measure the electron-phonon energy loss rate $\dot{Q}$. A reservoir region of 2DEG is then isolated from the main heating channel by interposing a mesoscopic device with low thermal conductance. The electron temperature in the reservoir is then remeasured.

The temperature $T_2+\delta T$ established in the reservoir region will be determined in a potential divider, for which an equivalent circuit is shown in figure 6. With the heating channel at $T_1=T_2+\Delta T$, a balance between the heat leak $\kappa_C(\Delta T-\delta T)$ through the device under test and the heat flows $\kappa_A\delta T$, $\kappa_B\delta T$ to the voltage probes and $\dot{Q}(T_2+\delta T,T_2)$ to the lattice by phonon emission will heat of the reservoir by an amount

$$\delta T=\Delta T\left(\frac{\kappa_C}{\kappa_C+\kappa_A+\kappa_B+\frac{\partial\dot{Q}}{\partial\delta T}}\right) \quad . \qquad (3)$$

Since the heat loss rate $\dot{Q}(T_1,T_2)$ due to phonon emission is known, it provides a calibrated theermal 'resistance' in the circuit. The proposed measurement therefore allows a direct test of the Wiedemann-Franz law for a mesoscopic device. A similar measurement has been attempted previously [8], and suggested that the thermal conductance for a 1D device might show plateaux, but the reservoir region was unbounded, and the thermometry uncalibrated.

4. Conclusions

Having established that the thermopower of a 1D constriction can be used to measure the electron temperature in a 2DEG, we have measured the energy loss rate through electron-phonon interactions at zero magnetic field. We propose to extend this to finite field to establish the effect of Landau level formation on the coupling. We have also shown how thermopower thermometry could be incorporated into a thermal conductance measurement, to test the Wiedemann-Franz law in mesoscopic devices.

Acknowledgements

We thank the Engineering and Physical Sciences Research Council (UK) for supporting this work, and JTN acknowledges an Advanced EPSRC Fellowship.

References

1. N.F. Mott and H. Jones, The Theory of the Properties of Metals and Alloys, Clarendon, Oxford (1936)
2. U. Sivan and Y. Imry, Phys. Rev. B **33**, 551 (1986)
3. C.R. Proetto, Phys. Rev. B **44**, 9096 (1991)
4. L.W. Molenkamp, H. van Houten, C.W.J. Beenakker, R. Eppenga and C.T. Foxon, Phys. Rev. Lett. **65**, 1052 (1990)
5. A.S. Dzurak, C.G. Smith, L. Martin-Moreno, M. Pepper, D.A. Ritchie, G.A.C. Jones & D.G. Hasko, J.Phys. Cond. Matt. **5**, 8055 (1993)
6. N.J. Appleyard, J.T. Nicholls, M.Y. Simmons, W.R. Tribe & M. Pepper, Phys. Rev. Lett. **81**, 3491 (1998)
7. P.J. Price, J. App. Phys **53**, 6863 (1982)
8. L.W. Molenkamp, Th. Gravier, H. van Houten, O.J.A. Buijk, M.A.A. Mabesoone & C.T. Foxon Phys. Rev. Lett. **68**, 3765 (1992)

PB.31

THE INFLUENCE OF ACOUSTIC ANISOTROPY AND SCREENING ON THE ELECTRON-PHONON COUPLING IN QUANTUM WIRES

D. Lehmann[1], Cz. Jasiukiewicz[2] and A. J. Kent[3]

[1]Institut für Theoret. Physik, Technische Universität Dresden, D-01062 Dresden, Germany
[2]Institute of Theoretical Physics, University of Wroc³aw, PL-50-204 Wroc³aw, Poland
[3]School of Physics and Astronomy, University of Nottingham, Nottingham, NG7 2RD, UK

We have investigated the interaction of nonequilibrium acoustic phonons with quantum wires in semiconductor heterostructures and compared the theoretical results with measurements of the phonoconductivity in short, ballistic GaAs/AlGaAs wires. In these experiments, the change in the conductance caused by a pulsed beam of acoustic phonons, which is generated by a heater on the opposite side of the substrate, is measured. From such angle and time resolved studies, we can obtain more direct information about the phonon wave vector and mode dependence of the electron-phonon interaction. This allows, in connection with corresponding numerical simulations, interesting conclusions about the quasi-one dimensional system itself.

Earlier theoretical studies, which were all based on isotropic models for the electron-phonon matrix elements and, at best, included acoustic anisotropy only in the phonon focusing, predict a decrease in the conductance which is much smaller than measured experimentally [1]. These theories are also unable to account for the observed contributions of the longitudinal and transversal modes. To explain the large discrepancies between theory and experiment, we have concentrated our theoretical work on the influence of the acoustic anisotropy on the electron-phonon coupling and on the effect of screening on the angular dependence of the phonon absorption in quasi-one dimensional systems.

Both effects result in large modifications of the absorption rates both for deformation potential coupling and piezoelectric interaction, particularly for the absorption of phonons propagating in directions close to the normal of the device (heater directly opposite the quantum wire). This is in agreement with the findings of our recent studies of two-dimensional electron systems [2]. In that work we showed that only by inclusion of screening, the details of electron confinement and acoustic anisotropy, can one obtain a satisfactory description of the angular and mode dependence of the phonon emission and absorption process.

[1] M. Blencowe and A.Y. Shik , Phys. Rev. B **54**, 13899 (1996)

[2] Cz. Jasiukiewicz, D. Lehmann, A.J. Kent, A.J. Cross and P. Hawker, Physica B **263-264**, 183 (1999)

PB.32

The influence of contacts and inhomogeneities on the conductivity of nanowires

H. Ruda, A. Shik
Energenius Centre for Advanced Nanotechnology, University of Toronto,
Toronto M5S 3E4, Canada

Abstract

Due to very weak screening in nanowires, their conductivity is very sensitive to contact geometry and any wire inhomogeneities. For different geometry of Ohmic contacts, the current-voltage characteristics and frequency dispersion of wire conductivity are calculated for uniform wires and wires with different kinds of inhomogeneities. The effects of Coulomb blockade in nanowires are also discussed.

1. Introduction

Due to the very weak effectiveness of screening for quasi-one-dimensional electron structures, the conductivity of nanowires is very sensitive to contact geometry and to the presence of any inhomogeneities. The electric fields from contacts or inhomogeneities penetrate very far along the wire and cause long-range redistribution of the carrier concentration $n(z)$, which depends on the applied voltage and results in a nonlinear current-voltage characteristic (IVC). Another related effect not observed in bulk samples, is the frequency dispersion of conductivity occurring when the typical inhomogeneity length becomes comparable with the carrier diffusion length for the period of the a.c. voltage.

In Sections 2, 3 and 4 we analyze these effects for three different models:

(i) uniform wires with three-, two- and one-dimensional Ohmic contacts;
(ii) non-uniformly doped wires;
(iii) wires containing a short high-resistive bottleneck.

Since model (iii) also describes a tunnel contact to wires, results from it are used in Section 5 for discussing the possibility of observing the Coulomb blockade phenomena in nanowires.

2. Uniform wires with low-dimensional contacts

The equation for electric current j in a wire with the account of diffusion and the self-consistent electric field caused by carrier distribution, derived in [1], can be written in the following form:

$$\frac{j}{e\mu} = n(z)\frac{d\phi_0}{dz} - \left[\frac{2e}{\varepsilon}\ln\left(\frac{l_c}{a}\right)n(z) + \frac{kT}{e}\right]\frac{dn}{dz}. \qquad (1)$$

Here μ is the carrier mobility, ε is the ambient dielectric constant, a is the wire radius, l_c is a characteristic length of concentration variations and $\phi_0(z)$ is the potential created by the applied voltage V. For bulk contacts, the electric field between them will be almost uniform, as in a plane capacitor, and n=const(z). Low-dimensional contacts create a strongly non-uniform electric field.

For instance, for two-dimensional contacts[1], $\phi_0=(V/\pi)\arcsin(2z/L)$. That is why continuity of current can be achieved only by redistribution of the electron concentration along the wire.

We calculated the concentration profile $n(z)$ and IVC with the help of (1) using the boundary conditions corresponding to Ohmic contacts: $n(\pm L/2)=n_0$. The resulting IVC is determined by the single parameter $\beta=2e^2n_0\ln(l_c/a)/(\varepsilon kT)$. For 2D contacts at $\beta<<1$

$$j=\frac{2\mu n_0 kT}{L}\tanh v\left(1+\frac{4v^2}{\pi^2}\right); \qquad v=\frac{eV}{2kT}. \tag{2}$$

which means that IVC at large voltages is quadratic, as for space charge limited currents. At $\beta>>1$ the role of charge redistribution decreases and IVC tends to the linear one: $j=e\mu n_0 V/L$. For 1D contacts, non-linearity of IVC is more pronounced:

$$j=\frac{\mu n_0 kT}{L}\frac{\{1-v[\ln(L/a)]^{-1}\}}{[\exp(-v)-a/L]} \tag{3}$$

containing an exponential piece at $1<eV/kT<\ln(L/a)$.

Eq.(1) can be generalized to the case of a.c. voltage oscillating with the frequency ω. The oscillating part of the concentration n_1, linear in V, is described by the equation

$$\frac{d^2n_1}{dz^2}-\frac{n_1}{l^2}=\frac{en_0}{kT(1+\beta)}\frac{d^2\phi_0}{dz^2}, \tag{4}$$

where $l=[ie\omega/\mu kT(1+\beta)]^{-1/2}$ is the complex effective diffusion length introduced in Ref. 2 and describing the distance traveled by non-equilibrium carriers for one period of oscillations under the influence of drift and diffusion. Solution of Eq.(4) with the boundary conditions $n_1(\pm L/2)=0$ allows us to find the a.c. current. For 2D contacts at $|l|<<L$

$$j=\frac{e\mu n_0 V}{\sqrt{\pi L|l|}} \tag{5}$$

which means that for high frequencies the wire conductivity increases $\sim\omega^{1/4}$. Similar approach for 1D contacts gives $j\sim\omega^{1/2}$. The physical meaning of this frequency dispersion is clear: the current is determined by the electric field at a distance $\sim|l|$ from the contact. For low-dimensional contacts with potential singularities near contacts, this field increases for small l as $|l|^{1/2}$ or $|l|$, respectively.

3. Non-uniformly doped wires

Now we consider a non-uniformly doped wire with the equilibrium carrier concentration $n_0(z)$ varying along the wire. To exclude the effects analyzed in the previous section, we restrict ourselves to the case of bulk contacts. Writing the carrier concentration in the form: $n=n_0(z)+n_1(z)$, we can linearize Eq.(1) for a low applied voltage V and solve exactly the resulting linear equation for n_1 (details of solution presented in [3]). The solution contains two unknown parameters: j and one integration constant. Finding them from the condition $n_1(\pm L/2)=0$, we obtain a formula for the current j.

[1] This model corresponds, e.g., to the typical case when wires are fabricated from 2D-electron structures as narrow bridges between two pads of macroscopic size.

The exact answer for $n_1(z)$ and j depends on the parameter β. For $\beta<<1$, the carrier redistribution does not change the electric field noticeably so that the potential along the wire varies linearly. In this case $n_1(z)$ is organized in such a way that the diffusion current exactly compensate the inhomogeneity in the drift current caused by the inhomogeneity in $n_0(z)$. In the opposite limit $\beta>>1$, we can neglect the diffusion current and use the traditional quasi-neutrality approximation where the local electric field is inversely proportional to $n_0(z)$. These two cases are characterized by different distributions of the electric potential and carrier concentration, but result in the same final expression for the current:

$$j = e\mu V\left[\int \frac{dz}{n_0(z)}\right]^{-1}. \tag{6}$$

At very high voltage V, the applied field exceeds the built-in fields of inhomogeneities and carriers become distributed almost uniformly along the wire, independent of their initial distribution. As a result the limiting IVC is again linear:

$$j = e\mu V L^2 \int n_0(z)dz. \tag{7}$$

Since for any $n_0(z)$, Eq.(7) has a larger value than Eq.(6), we may conclude that in the intermediate voltage region the IVC is superlinear.

4. Wires with high-resistance contacts

We consider now another structure: uniformly doped wire separated from a bulk metallic contact by a thin dielectric with a high resistance R_T. The IVC $j(V)$ is determined from the system [3]:

$$\frac{j}{e\mu} = n(z)\frac{V}{L} - \frac{kT}{e}\left[\beta\frac{n(z)}{n_0}+1\right]\frac{dn}{dz} = \frac{\beta kT}{e^2\mu R_T}\left[\frac{n(L/2)}{n_0}-1\right] \tag{8}$$

with the boundary condition $n(-L/2)=n_0$. Eq.(8), being integrated, gives the implicit expression for IVC:

$$jR_T + \frac{kT}{e}\left(1+\frac{\beta jR_0}{V}\right)\ln\left[\frac{V(\beta kT + ejR_T) - jR_0}{\beta kT(V - jR_0)}\right] = V \tag{9}$$

where $R_0=L/(e\mu n_0)$.

Analysis of Eq.(9) reveals the following main features:

1. The system resistance exceeds the classical value R_T+R_0 approaching it only at $\beta>>1$.
2. The linear resistance for a low applied voltage $(dV/dj)_{V\to 0}=R_T(\beta+1)/\beta+R_0$.
3. The IVC for small β is strongly asymmetric with saturation at $j_s= -\beta kT/(eR_T)$ for a negative bias (causing wire depletion).

By analogy with Section 2, the results of the present section can be generalized to a.c. voltage. The main result consists in the calculation of the capacity C between a wire and a bulk electrode considered as a metal plane normal to the wire. In terms of the effective diffusion length l introduced in Section 2, it can be written as

$$C = \frac{e^2 n_0 l}{\beta kT} \frac{[\cosh(L/l) - 1]}{\sinh(L/l)}. \qquad (10)$$

For large enough frequencies when $L \gg |l|$, Eq.(10) gives the dependence $C \sim l \sim \omega^{-1/2}$ already mentioned in Ref. 3.

5. Coulomb blockade in nanowires

The static capacitance C_0 of a nanowire is fairly large, $C_0 = \varepsilon L/(4\ln(L/a))$ [4], which allows us to assume a negligible role of Coulomb blockade in the wire structure. This assumption, however, is not adequate. The effect of single electron tunneling has an essentially dynamic behaviour and can be characterized by some effective frequency $\omega = j/e$ [5]. Due to a considerable frequency dispersion (see Eq.(10)), the corresponding effective wire capacity might be much less than C_0 resulting in noticeable Coulomb blockade effects.

To obtain an analytical expression for the current and analyze the main regularities of the phenomenon, we restrict ourselves to the simplest expression for the IVC: $j = (V - e/2C)/R_T$ adequate at zero temperature and at some additional requirements to the electric circuit discussed in Ref. 5. This is the usual linear IVC of the contact corresponding to large β and R_T in Eq.(9) but shifted by the Coulomb energy $e^2/2C$. Using for C the long-wire ($L \gg |l|$) limit of Eq.(10) and replacing ω by j/e, we obtain the final expression for the IVC:

$$jR_T = V + V_0 - \sqrt{V_0(2V + V_0)}; \qquad V_0 = \frac{2e^2 \ln^2(l/a)}{(\beta + 1)\varepsilon^2 \mu kTR_T}. \qquad (11)$$

At small voltages, $V \le V_0$, the IVC is essentially distorted by the Coulomb blockade effects and has a quadratic, rather than linear, character. These effects will be well pronounced until $kT \ll eV_0$. For $\mu \sim 10^3$ cm^2/V·s and $R_T \sim 10$ kOhm, V_0 can be as large as a hundred millivolts, which means that the Coulomb blockade could be observed at rather high temperatures. This supports the experimental data [6] where peculiarities of the IVC in a system of nanowires were observed even at room temperature and attributed to Coulomb blockade.

References

[1] H. Ruda and A. Shik, *J. Appl. Phys.* **84**, 5867 (1998).
[2] N. S. Averkiev and A. Shik, *Semicond.* **30**, 112 (1996).
[3] H. Ruda and A. Shik (to be published in *J. Appl. Phys.*).
[4] N. S. Averkiev and A. Shik, *Phys. Rev.* **B59**, 3259 (1999).
[5] *Single Charge Tunneling* (Ed. H. Grabert and M. H. Devoret), Plenum Press, N.Y., 1992.

PB.33

Capacitance of Quantum Wires: Simulation Calculations and Experiment

D. Schmerek and W. Hansen,

Institut für Angewandte Physik und Zentrum für Mikrostrukturforschung, Universität Hamburg, Jungiusstraße 11, 20355 Hamburg, Germany

Abstract

Magneto-capacitance spectra of quantum wires clearly reflect the energy quantization of the electronic system in one-dimensional subbands. We present results of simulation calculations of the wire capacitance, in which interaction effects are included by Local Density Approximation. The simulation calculations show that a peak observed in the experiments close to the wire threshold is caused by exchange and correlation effects in the one-dimensional electron system. Spin effects are calculated in the Local Spin Density Approximation. At densities, where the second spin level starts to be occupied, we find effective g-factors similar to values in two-dimensional electron systems at the spin gap.

Electronic properties of quantum wires in the one-dimensional (1d) qantum limit, i.e. only one 1d subband is occupied, are of great interest.[1] We discuss quantum wires that have been realized in special metal insulator semiconductor heterostructures (MIS) optimized for generation of good quality and highly tunable electron wires even in the 1d quantum limit.[2,3] The experiments are performed by capacitance spectroscopy that clearly reflects the occupation of the 1d subbands.[2,5] Here we focus on a pronounced enhancement in the capacitance signal observed at very low electron densities of typical $10^6\,\mathrm{m}^{-1}$, that has not been well understood so far. The results of our simulations strongly augment the assertion that the enhancement is caused by exchange correlation effects.

The quantum wires in the MIS structures are induced beneath a center electrode as sketched in Fig. 1. Side electrodes biased at negative voltages with respect to the center electrode are used to control the confinement potential. The wire is charged with electrons by tunneling from a highly doped back electrode through the unintentionally p-doped GaAs spacer.[2,3] Figure 1(b) shows capacitance spectra recorded on a single, $150\,\mu\mathrm{m}$ long quantum wire. The capacitance is measured with a high sensitivity capacitance bridge by

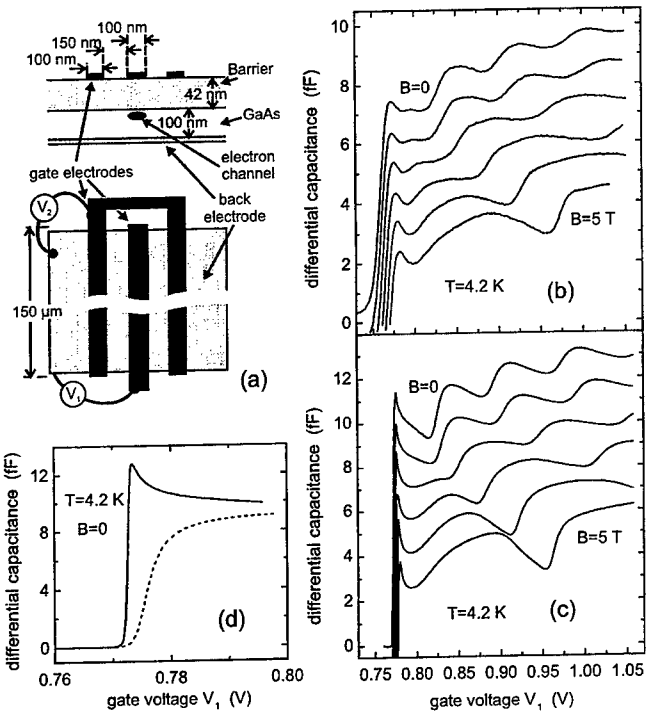

Fig. 1. (a) cross section and top view of a MIS device for investigation of electron quantum wires. The barrier consists of an AlAs/GaAs short period superlattice. Measured (b) and calculated (c) capacitance spectra of a device with geometry as specified in (a). Traces differ by 1 T and are offset by -2 fF for clarity. The side gate voltage has been kept at a fixed bias $V_1 - V_2 = 0.8$ V with respect to the center gate voltage. (d) expanded view of the $B = 0$ trace in (c) close to the onset. The dashed line denotes results obtained in Hartree approximation.

modulating the center gate voltage V_1 by a small excitation of $\Delta V_1 = 2$ mV at a frequency of 100 kHz. Different traces are recorded at magnetic fields between 0 and $B = 5$ T. The strongly increasing capacitance signal at $V_1 = 0.75$ V marks the threshold voltage of the quantum wire. Pronounced steps at higher voltages reflect the occupation of the subsequent 1d subbands. As expected the subband separation increases with the magnetic field. The behavior can be analysed with a simple single-particle model assuming a parabolic effective confinement potential.[2] With this model we derive from the data of Fig. 1(b) a subband spacing of $\hbar\omega_0 = 4.4$ meV, where ω_0 is the characteristic frequency of the parabolic potential.

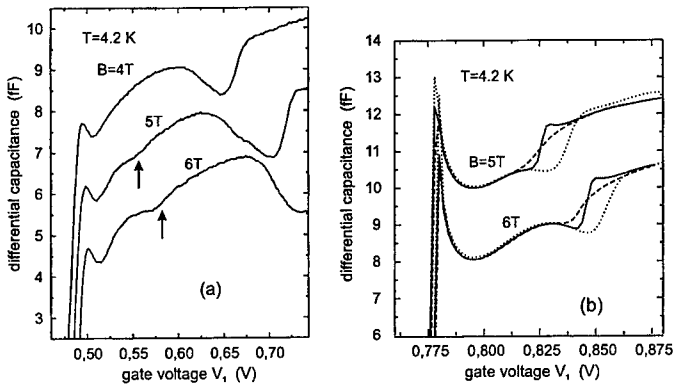

Fig. 2. (a) Capacitance spectra of a MIS device with geometry as specified in Fig. 1 and $V_2 - V_1 = 1.8\,\mathrm{V}$ between side electrodes and center gate. Structure highlighted by arrows is associated to spin splitting of the 1d subband. (b) Capacitance spectra calculated in LSDA with different parametrizations (see text) at magnetic fields of $B = 5$ and $6\,\mathrm{T}$.

A two-dimensional self-consistent Poisson-Schrödinger solver using Local Density Approximation (LDA)[4] has been applied to calculate simulated capacitance spectra as shown in Fig. 1(c).[5] Our results show that for an exact coincidence of the threshold voltages between experimental and calculated data it is essential to assume the presence of an oxide layer at the crystal surface and surface charges between the gate electrodes.[5] Although introducing such additional, not well controlled parameters renders the calculations somewhat arbitrary, the shape of the steps and - most important here - the capacitance enhancement at the onset remain similar with different parameters. The parameters used in Fig. 2(c) are an oxide of dielectric constant of 3.0 and thickness 2.5 nm, a homogeneous surface charge of $-1.8 \cdot 10^{12}\,\mathrm{cm}^{-2}$ and positive line charges aside the gate electrodes that might reflect strain effects.[5] With these values quite good agreement between calculated and measured data is achieved. The calculation yields an energy spacing between the lowest and the first excited subband of almost 6meV at the wire onset.[5] It increases by 0.25 meV when the wire starts to be occupied before it decreases at higher densities. Figure 1(d) gives an expanded view of the calculation at B=0 close to the threshold voltage. The dashed line represents results, where exchange correlation effects have been neglected. It is clearly seen that in this case the capacitance peak at the onset is absent.

Experiments show that the additional structure is not caused by spin effects as can be seen in the data in Fig. 2(a) of a sample, in which spin splitting becomes observable at fields above $B = 4\,\mathrm{T}$. Here an additional structure emerges between the wire threshold and the onset of the second subband that

we associate to the spin polarization of the 1d subbands. In the calculated data of Fig. 2(b) spin splitting is introduced by application of a spin dependent LDA (LSDA). The parametrizations of the exchange correlation potential used for the calculations are taken from (full line) Barth and Hedin,[6] (dotted line) Gunnarsson and Lundqvist[7] and (dashed line) Perdew and Wang.[8] The same geometrical parameters are used as in Fig. 1. No attempt is made to account for the different threshold of the sample in Fig. 2(a) by choice of surface charge and oxide layer.

From the energy separation ΔE between the spin dependent subbands we may determine an effective g-factor g^* according to $\Delta E = g^* \mu_B B$, where μ_B is the Bohr magneton. Depending on the parametrization we find values of the effective g-factor between $g^* = 8$ and 12 at fields $5\,\mathrm{T} \leq B \leq 6\,\mathrm{T}$ and at densities at which the higher spin level just starts to become occupied. These values are similar to values found in two-dimensional electron systems on GaAs and very close to values determined previously with a simple model from experiments.[9]

In summary we present numerically simulated and experimental capacitance spectra of 1d quantum wires. Comparison of the results obtained in LDA and Hartree approximation demonstrates that the capacitance enhancement observed in the experiment close to the wire onset is caused by exchange correlation effects. In high magnetic fields spin splitting of the 1d subbands is observed. The observation are described by LSDA calculations and yield effective g-factors at the onset of the second spin polarized subband close to values found in two-dimensional systems.

We gratefully acknowledge financial support by the DFG via the Graduiertenkolleg "Physik nanostrukturierter Festkörper", and the Sonderforschungsbereich 508 "Quantenmaterialien".

References

[1] J. Voit, Rep. Prog. Physics **58**, 977 (1995).
[2] H. Drexler *et al.*, Phys. Rev. B**49**, 14074 (1994).
[3] D. Schmerek *et al.*, Phys. Rev. B**54**, 13816 (1996).
[4] W. Kohn and L.J. Sham, Phys. Rev. **140**, A1133 (1965).
[5] D. Schmerek and W. Hansen, Phys. Rev. B in press. (1999).
[6] U. von Barth and L. Hedin, J. Phys. C**5**, 1629 (1972).
[7] O. Gunnarsson and B.I. Lundqvist, Phys. Rev. B**13**, 4274 (1976).
[8] J.P. Perdew and Y. Wang, Phys. Rev. B**45**, 13244 (1992).
[9] W. Hansen and H. Drexler in Festkörperprobleme, Advances in Solid State Physics, Vol. **35**, ed. by R. Helbig (Vieweg, Braunschweig/Wiesbaden) p.81.

Evidence of Luttinger Liquid Behavior in GaAs/AlGaAs Quantum Wires

M. Rother[1*], W. Wegscheider[1,2], R. A. Deutschmann[1], M. Bichler[1] and G. Abstreiter[1]

[1]Walter Schottky Institut, Technische Universität München, 85748 Garching, Germany
[2]Universität Regensburg, Universitätsstr. 31, 93040 Regensburg, Germany

Abstract

We present low-temperature measurements of the ballistic transport in high quality quantum wires. As the Fermi energy is varied, the conductance of these wires exhibits quantized plateaus at values lower than integer multiples of $2e^2/h$. We observe Luttinger liquid power laws in the temperature dependence of the plateau conductances as well as in the non-linear current-voltage characteristics. From these power-laws we extract the Luttinger liquid scaling exponent α_N as a function of the Fermi energy and the number of occupied subbands.

Pacs: 73.20.Dx, 73.20.Mf, 73.23.Ad, 73.50.Jt, 73.61 Ey

Keywords: quantum wires, Luttinger liquids, ballistic transport

One of the most important features of ballistic transport in non-interacting one-dimensional electron systems (1DES) is the quantization of the conductance in integer multiples of $G_0 = 2e^2/h$ [1]. In real 1DES electron-electron interaction is expected to lead to a considerable deviation from this exact quantization. These 1DES are theoretically described in the framework of the Luttinger liquid theory. According to this theory the electron-electron interactions show up in the conductance of the quantum wire (QWR) in a twofold manner. First, the interactions lead to a renormalization of the conductance $G = g \cdot G_0$ by an interaction dependent factor g. It has been shown, however, that this renormalization of the conductance does not take place when Fermi liquid contacts are attached to the QWR [2, 3]. Second, in combination with a small amount of disorder, which is inevitably present in real samples, the electron-electron interactions are expected to lead to a characteristic power law dependence of the conductance on the temperature or the applied voltage [4, 5]. The scaling exponent of these power laws is a characteristic fingerprint of the electron-electron interaction in the QWR. While deviations from the exact quantization have been observed in other experiments [6, 7], no systematic search for the predictions of the Luttinger liquid theory has been carried out so far. In this paper we present an experimental determination of the scaling exponent as a function of the Fermi energy and the number of occupied subbands in the QWR both from measurements of the temperature dependence of the conductance and of the non-linear current-voltage characteristics.

We have fabricated high quality QWRs using molecular beam epitaxy (MBE) and the cleaved edge overgrowth technique [8]. This fabrication process has been described in detail in [7]. We start with a modulation doped quantum well of 400 Å thickness on the GaAs [001] surface. This sample is then cleaved *in situ* in the MBE chamber and a modulation doping sequence is grown on the atomically smooth GaAs [110] surface immediately after the

*corresponding author, phone +49 89 28912756, fax +49 89 3206620, email rother@wsi.tum.de

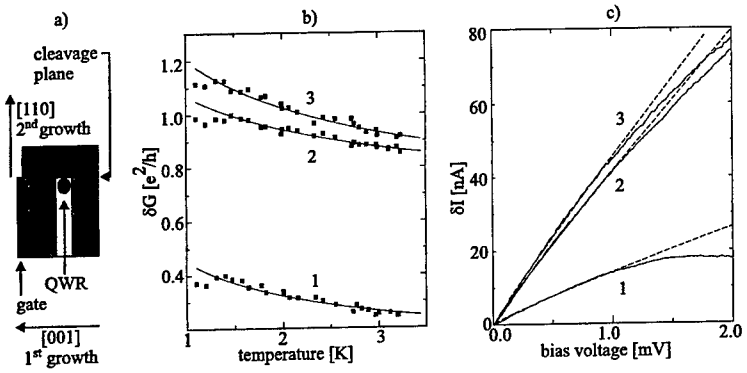

Figure 1: (a) The schematic drawing of the sample structure shows the modulation doped quantum well grown in the first growth step on the GaAs [001] plane and the modulation doping sequence grown in the second growth step on the [110] cleavage plane. Applying a negative bias voltage to a narrow gate on the sample surface separates the two-dimensional electron gas, generated in the quantum well by the modulation doping in the [001] plane, into two sheets. These two-dimensional electron systems then serve as contacts to the QWR whose electron density can be varied by the same gate. The width of the gate thus defines the length of the QWR which was 2 μm in our experiments. (b) The temperature dependent deviation of the conductance from the exact quantization in integer multiples of $2e^2/h$ for the lowest three subbands. The solid lines indicate a fit with the Luttinger liquid power law. (c) The deviation of the current from the current corresponding to exact quantization vs the bias voltage. The curves were taken at the same electron densities in the lowest three subbands as the temperature dependence in plot (b). The dashed lines indicate a fit of the Luttinger liquid power law at voltages less the 1 mV.

cleavage step. A schematic drawing of the sample structure is shown in Fig 1 (a). The QWR is then confined by the quantum well potential and by the triangular potential arising from the modulation doping sequence on the cleavage plane. A gate on the [001] surface allows the continous variation of the electron density within the 2 μm long QWR. As a function of the gate voltage and therefore the 1D electron density our QWRs show quantized plateaus at conductance values significantly smaller than expected for exact quantization.

Fig. 1(b) shows the deviation $\delta G = NG_0 - G$ of the differential conductance from the exact quantization as a function of the temperature measured with standard lock-in techniques at an excitation voltage of 10 μV. These temperature dependencies were measured roughly in the middle of the conductance plateaus of the lowest three subbands. For a QWR subject to slight disorder with Fermi liquid contacts Luttinger liquid theory predicts, that these deviations exhibit a power law behavior as the temperature is changed: $\delta G \propto T^{-\alpha_N}$ [5]. The solid lines indicate a fit of this power law to the experimental data. We now perform this analysis for all gate voltages within the individual conductance plateaus and therefore obtain the scaling exponent α_N as a function of the Fermi energy and the number of occupied

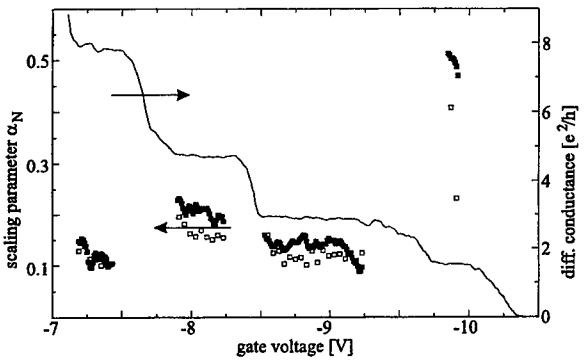

Figure 2: The scaling exponent α_N as a function of the gate voltage and therefore as a function of the Fermi energy and the subband number N in the QWR. The filled squares show the α_N values obtained from the temperature dependence of the conductance, the open squares show α_N obtained from the non-linear current-voltage characteristics. The solid line shows the conductance of the QWR vs the gate voltage.

subbands N. Care must be taken to choose the proper temperature range for the evaluation of the data because the finite length of the QWR leads to a cut-off to Luttinger liquid behavior at temperatures below $T_c = \hbar v_f/(k_B L)$ [4]. Here v_F denotes the Fermi velocity, L the length of the QWR and k_B the Boltzmann constant. This cut-off temperature can be estimated to be less than 1 K for our QWRs. At temperatures higher than approximately 5 K thermal broadening hinders the evaluation, so we use a fitting range 1.5 K $< T <$ 4 K.

Since the scaling exponent α_N is a fundamental parameter of the Luttinger liquid, it also shows up in other quantities of the 1DES which are experimentally accessible. One of these quantities is the current-voltage characteristic. The current is expected to vary non-linearly with the applied bias voltage V, following a power law similar to the power law describing the temperature dependence, i.e. the deviation $\delta I = I_0 - I$ of the current I from the current $I_0 = NG_0V$ corresponding to exact quantization is given by $\delta I \propto V^{1-\alpha_N}$ [4]. Fig. 1(c) shows this deviation vs the bias voltage at a temperature of 0.35 K for the same electron densities in the lowest three subbands, where the temperature dependent measurements of Fig. 1 (b) have been taken. Again we use the appropriate power law to extract the parameter α_N from these non-linear IV-characteristics as a funtion of the Fermi energy and the subband number N. Up to voltages of 1 mV the current can be fitted very well with a power law characteristic whereas at higher bias voltages the current can no longer be described with a power law.

As a result we obtain the Luttinger liquid scaling exponent α_N as a function of the gate voltage as shown in Fig. 2. The solid line represents the conductance of the QWR and is shown to identify the individual subbands. We find, that the α_N obtained from the temperature dependence of the conductance (filled squares) and the α_N obtained from the non-linear current voltage characteristics (open squares) agree very well. The only exception

is the first subband whose width is quite small and thus hampers proper measurement of IV-characteristics. The values of α_N is in the range of 0.1 to 0.5 which indicates repulsive electron-electron interaction. Within the indiviual subbands α_N stays approximately constant. This comes as a surprise, because the electron-electron interaction is expected to depend strongly on the electron density resulting in a Fermi energy dependency of α_N. As the subband number N is increased, α_N shows a slight variation but no clear increase or decrease. The $1/N$-behavior predicted by the theory cannot be observed [9, 10].

In summary we have observed a power law temperature dependence of the quantized conductance plateaus and of the non-linear current-voltage characteristics in high-quality ballistic QWRs. From these power laws we calculate the Luttinger liquid scaling exponent α_N as a function of the Fermi energy and the number of occupied subbands. The values for α_N obtained from both of these independent measurements agree very well. The scaling exponent α_N stays approximately constant within each individual subband and shows no monotonic behavior as the subband number is changed.

We would like to thank W. Häusler, T. Brandes and J. Voit for helpful discussions.

References

[1] C. W. J. Beenakker an H. van Houten, in *Solid State Physics, Semiconductor Heterostructures and Nanostructures*, edited by H. Ehrenreich and D. Turnbull (Academinc Press, New York, 1991).

[2] D. L. Maslov and M. Stone, Phys. Rev. B **52**, R5539 (1995).

[3] I. Safi and H. J. Schulz, Phys. Rev. B **52**, R17040 (1995).

[4] C. L. Kane and M. P. A. Fisher, Phys. Rev. B **46**, 15233 (1992).

[5] D. L. Maslov, Phys. Rev B **52**, R14368 (1995).

[6] S. Tarucha, T. Honda and T. Saku, Solid State Commun. **94**, 413 (1995).

[7] A. Yacoby, H. L. Stormer, N. S. Wingreen, L. N. Pfeiffer, K. W. Baldwin and K. W. West, Phys. Rev. Lett. **77**, 4612 (1996).

[8] L. N. Pfeiffer, H. L. Stormer, K. W. Baldwin, K. W. West, A. R. Goni, A. Pinczuk, R. C. Ashoori, M. M. Dignam and W. Wegscheider, J. Cryst. Growth **849**, 127 (1993).

[9] A. Kawabata and T. Brandes, J. Phys. Soc. Jpn. **65**, 3712 (1996).

[10] N. P. Sandler and D. L. Maslov, Phys. Rev. B **55**, 13808 (1997).

Anomalous anisotropic commensurability oscillations in two-dimensional holes at the GaAs/AlGaAs (311)A interface

J.B. Yau, J.P. Lu, H.C. Manoharan, and M. Shayegan
Department of Electrical Engineering, Princeton University, Princeton, NJ 08544, USA

Abstract

Measurements of commensurability oscillations in GaAs/AlGaAs two-dimensional (2D) hole systems grown on GaAs (311)A substrates reveal a remarkable anisotropy: the amplitude of the measured commensurability oscillations along the $[\bar{2}33]$ direction is about 100 times larger than along $[01\bar{1}]$. For 2D electron systems at similar interfaces, however, we observe nearly isotropic oscillations, suggesting that the anomalous anisotropy is intrinsic to GaAs 2D holes at the GaAs/AlGaAs (311)A interface.

PACS numbers: 73.23.Ad, 73.23.Dx, 73.50.-h, 73.61.Ey
Keyword: Two-dimensional hole systems; Commensurability oscillations; Anisotropy

GaAs/AlGaAs heterojunctions and quantum wells, grown on GaAs (311)A substrates and modulation-doped with Si, are of considerable current interest. These structures can contain very high mobility two-dimensional *hole* systems (2DHSs), and have already shown a number of novel phenomena including signatures of magnetic-field-induced Wigner crystallization [1] and metal-insulator transition at zero magnetic field [2-5]. These systems are also known to exhibit an in-plane transport anisotropy [6-8]; the mobility along the $[\bar{2}33]$ direction is typically larger than along $[01\bar{1}]$ by a factor of 2 to 5. Here we report the observation of commensurability oscillations (COs) revealing a surprisingly large anisotropy in the amplitude of the COs measured along these two directions in this system. We recall that COs refer to the oscillations in the magnetoresistance of a 2D carrier system whose density has a lateral periodic modulation [9,10]. In a simple, semiclassical model [11], the oscillations can be related to the classical cyclotron orbit diameter of the carriers becoming commensurate with a multiple integer of the period a of the potential. The anisotropy of the COs we observe in the 2DHSs is too large to be explained by a simple argument based on mobility anisotropy.

Our samples were grown by molecular-beam epitaxy (MBE) on GaAs (311)A substrates, and have low-temperature mobility in the range of 1.7×10^5 cm^2/Vs to 1.6×10^6 cm^2/Vs. The sample structure is shown schematically in Fig. 1. Arrays of 1000Å–thick PMMA strips were defined perpendicular to the two arms of an L-shaped Hall bar pattern which was made by electron-beam lithography and 5000Å-deep wet etching. The two arms of the Hall bar were aligned along the $[\bar{2}33]$ and $[01\bar{1}]$ directions. The periods of PMMA strips range from 2000Å to 3000Å and their widths equal half of their periods. A front gate was made by evaporating 50Å of Ti and 2000Å of Au. We measured the longitudinal magnetoresistance as a function of perpendicular magnetic field B, at $T \approx 0.5$K using a standard low-frequency lock-in technique.

We studied 2DHSs confined in both triangular and square quantum wells. The low-B magnetoresistances measured along the $[\bar{2}33]$ and $[01\bar{1}]$ directions are represented by $R_{[\bar{2}33]}$ and $R_{[01\bar{1}]}$, respectively. Both $R_{[\bar{2}33]}$ and $R_{[01\bar{1}]}$ are measured with the current running perpendicular

to the direction of the PMMA strips (see Fig. 1a). We find an enormous amplitude anisotropy in the COs measured along the $[\bar{2}33]$ and $[01\bar{1}]$ directions. In the triangular well sample, as shown in Fig. 2, we observe strong COs along $[\bar{2}33]$ while essentially no COs are visible along $[01\bar{1}]$. Significant anisotropy in COs is also observed in the square well sample. As shown in Fig. 3, $R_{[\bar{2}33]}$ exhibits strong COs for $0.1<|B|<1$T while $R_{[01\bar{1}]}$ shows much weaker oscillations. The inset to Fig. 3, where $R_{[\bar{2}33]}$ and $R_{[01\bar{1}]}$ are normalized by $R_{[\bar{2}33]}(B=0)$ and $R_{[01\bar{1}]}(B=0)$, respectively, shows that $R_{[01\bar{1}]}$ does have some oscillating features but their amplitude is about 100 times smaller than along $[\bar{2}33]$.

Surface corrugations, consisting of alternating GaAs and AlGaAs channels along $[\bar{2}33]$, are present in MBE-grown GaAs (311)A surfaces [12,13]. Formation of these channels has previously been reported [6-8] to lead to enhanced interface roughness scattering along $[01\bar{1}]$, causing the mobility along $[01\bar{1}]$ to be smaller than along $[\bar{2}33]$. Previous studies also indicate [6-8] that the mobilities along $[\bar{2}33]$ and $[01\bar{1}]$ differ only by a factor of 2 to 5. This difference is obviously far less than the nearly 100 times difference observed in the amplitudes of COs along $[\bar{2}33]$ and $[01\bar{1}]$ in our square well sample, and cannot explain the dramatic anisotropy observed in COs.

We also studied the COs in a two-dimensional *electron* system (2DES) at the GaAs/AlGaAs (311)A interface. The 2DES was grown under similar MBE growth conditions: The substrate temperature during the growth of the GaAs/AlGaAs interface and the AlGaAs spacer was kept the same as in the 2DHS case and was reduced only when the dopants were introduced [15]. The interface morphology of the 2DES sample should therefore closely resemble that of the 2DHS samples. The mobility measured in this sample along $[\bar{2}33]$ is about 2 times greater than along $[01\bar{1}]$. The COs measured along $[\bar{2}33]$ and $[01\bar{1}]$ in the 2DES are shown in Fig. 4. It is clear that the amplitude of the COs in the 2DES case differ only by a factor of about 2, much less than the nearly 100 times difference observed in the 2DHSs. From the positions of the critical field (marked by the vertical arrows in Fig. 4) for the positive magnetoresistances measured along $[\bar{2}33]$ and $[01\bar{1}]$, we estimate that the magnitude of the potential modulation is about the same along these two directions. These values are reasonably consistent with the amplitude difference of COs observed along $[\bar{2}33]$ and $[01\bar{1}]$ in Fig. 4.

To understand the data more quantitatively, it is useful to examine the strength of the potential modulation along $[\bar{2}33]$ and $[01\bar{1}]$. Beton *et al.* [14] show that 2D carriers subjected to a one-dimensional periodic potential exhibit a low-field positive magnetoresistance. This is because the carriers, affected by the electrical force generated by the periodic potential, stream along the equipotentials (perpendicular to the current flow), and lead to an increase in the resistance. This positive magnetoresistance extends up to a critical B field (marked by the vertical arrows in the inset to Fig. 3) above which the magnetic force is greater than the electrical force and the streaming orbits are suppressed. Therefore, the critical B field can be a measure of the strength of the potential modulation. From this model, we estimate that the strength of the potential modulation along $[\bar{2}33]$ is about twice larger than along $[01\bar{1}]$ fir the 2DHS sample. This is not sufficient to explain the remarkable COs amplitude anisotropy found in the 2DHS. The modulation strength for the 2DES sample is about the same for the two directions.

In summary, we investigated COs in 2DHSs and a 2DES grown on GaAs (311)A substrates under similar MBE growth conditions and found an anomalous anisotropy in the COs'

amplitudes measured along $[\bar{2}33]$ and $[01\bar{1}]$ in the 2DHSs, but not in the 2DES. Our study suggests that the anomalous anisotropy is intrinsic to the 2DHSs grown on GaAs (311)A substrates.

This work was supported by the NSF and the ARO.

References

[1] M.B. Santos et al., Phys. Rev. Lett. 68 (1992) 1188.
[2] Y. Hanein, et al., Phys. Rev. Lett. 80 (1998) 1288.
[3] M.Y. Simmons et al., Phys. Rev. Lett. 80 (1998) 1292.
[4] Jongsoo Yoon, C.C. Li, D. Shahar, D.C. Tsui, M. Shayegan, Phys. Rev. Lett. 82 (1999) 1744.
[5] S.J. Papadakis, E.P. DePoortere, H.C. Manoharan, M. Shayegan, Science 283 (1999) 2056.
[6] A.G. Davies et al., J. Cryst. Growth 111 (1991) 318.
[7] J.J. Heremans et al., Appl. Phys. Lett. 61 (1992) 1652.
[8] J.J. Heremans et al., J. Appl. Phys. 76 (1994) 1980.
[9] D. Weiss, K. von Klitzing, K. Ploog, G. Weimann, Europhys. Lett. 8 (1989) 179.
[10] R.W. Winkler, J.P. Kotthaus, K. Ploog, Phys. Rev. Lett. 62 (1989) 1177.
[11] C.W.J. Beenakker, Phys. Rev. Lett. 62 (1989) 2020.
[12] R. Nötzel, N.N. Ledentsov, K. Ploog, Phys. Rev. B 47 (1993) 1299.
[13] M. Wassermeier et al., Phys. Rev. B 51 (1995) 14721.
[14] P.H. Beton, et al., Phys. Rev. B 43 (1991) 9980.
[15] K. Agawa et al., Appl. Phys. Lett. 65 (1994) 1171.

Figures

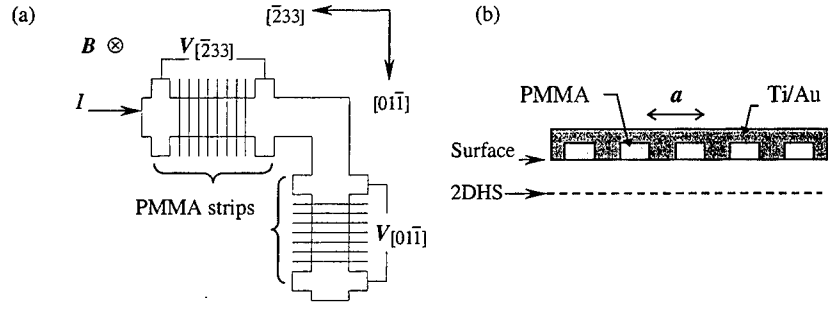

FIG. 1. (a) L-shaped Hall bar pattern for studying COs in a 2DHS on the GaAs (311)A surface. Periodically modulated potentials are realized, by PMMA strips and evaporated gates, along the $[\bar{2}33]$ and $[01\bar{1}]$ directions. (b) Schematic side view of the sample structure. Here a is the period of PMMA strips.

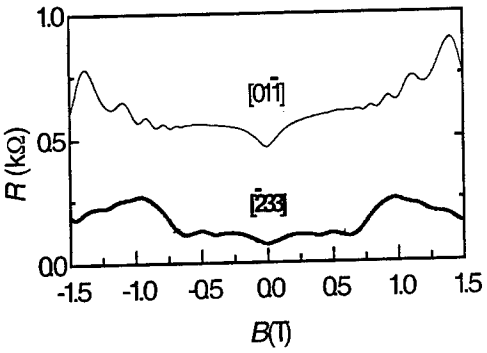

FIG. 2. COs measured in the triangular well 2DHS sample. Strong COs are observed in the [$\bar{2}$33] direction (thick trace), but no COs are observed in the [01$\bar{1}$] direction (thin trace). The high-frequency oscillations observed along [01$\bar{1}$] are the Shubnikov-de Haas oscillations, which appear in both directions starting at $B \sim 1$T.

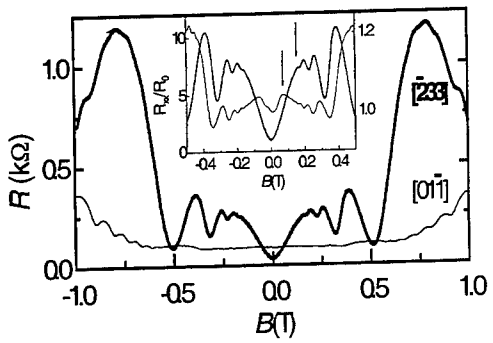

FIG. 3. COs measured in the square well 2DHS sample. We observe strong COs in the [$\bar{2}$33] direction (thick trace), while the [01$\bar{1}$] direction (thin trace) exhibits very weak COs. Inset: The COs along [$\bar{2}$33] and [01$\bar{1}$] are normalized by dividing by R_0, the resistance at B=0, to emphasize the enormous (~100 times) difference in their amplitudes. The vertical arrows mark the critical field below which a positive magnetoresistance is seen.

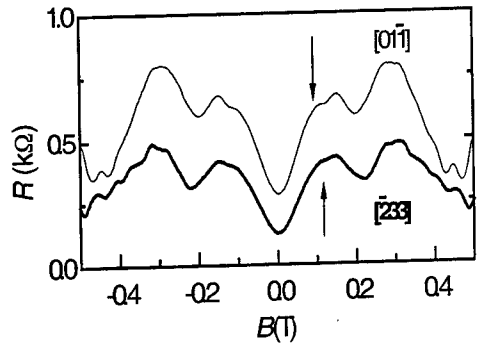

FIG. 4. COs measured in the 2D *electron* sample. The data along both [$\bar{2}$33] and [01$\bar{1}$] directions show similar COs amplitude.

Modulation of Landau levels by a one-dimensional periodic potential

B. Milton, C. J. Emeleus, K. Lister, J. H. Davies, and A. R. Long
Nanoelectronics Research Centre, University of Glasgow, Glasgow G12 8QQ, U. K.

Abstract

We have studied the magnetoresistance of short-period one-dimensional lateral superlattices with strong modulation at low temperatures. Striking interference was seen between commensurability oscillations and the Shubnikov–de Haas effect. This cannot be explained within the usual semiclassical theory and a quantum mechanical explanation is proposed.

The interplay between a magnetic field and a one-dimensional periodic electrostatic potential in a two-dimensional electron gas [1] has attracted considerable interest. Most experiments can be explained in terms of commensurability oscillations (COs) of semiclassical origin [2] at low fields, and the conventional Shubnikov–de Haas (SdH) effect at high fields. Sometimes these regimes overlap but without dramatic mutual interference. Here we report experiments on superlattices with unusually strong potentials and short periods, and find that the magnetoresistance (MR) cannot be explained within this simple semiclassical picture; the effect of the periodic potential must be introduced using quantum mechanics.

The samples were lateral surface superlattices of period 100 nm on a GaAs/AlGaAs heterostructure. The potential was induced by a patterned InGaAs stressor layer [3], overlaid with a blanket metal gate to enable the carrier concentration to be varied. The periodic equipotentials were perpendicular to the direction of current flow. This was chosen to be in the $[01\bar{1}]$ direction on a (100) wafer so that the potentials induced by stress and the patterning of the surface add to produce strong modulation [3]. Two samples were measured at helium temperatures and in a dilution refrigerator at 45 mK. The behaviour of the two samples was identical apart from variations in carrier concentration.

Characteristics with 0.3 V applied to the blanket gate are plotted for low fields in Fig. 1. At low magnetic fields and a temperature of 5 K, we see the usual commensurability oscillations [1] in the longitudinal magnetoresistance, with minima at the predicted fields [2] of 2.75, 1.2, 0.75, 0.55....T. They are obscured below 0.5 T by a strong positive magnetoresistance (PMR). The field at the PMR peak enables us to estimate [4] the magnitude of the periodic potential. The bar on the peak in Fig. 1 corresponds to a potential amplitude of 1.5 meV. This value is confirmed by an direct analysis of the amplitude of the COs, although neither methods is highly accurate.

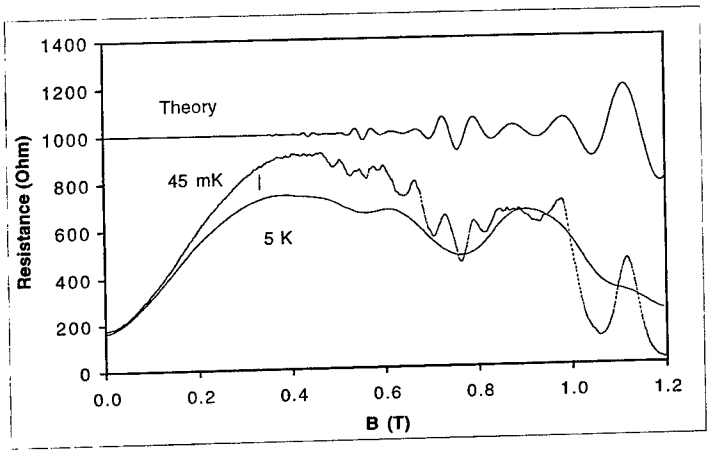

Figure 1. Longitudinal magnetoresistance at low field. Data at 5K show commensurability oscillations with minima at 0.75, 0.55 T; modulated Shubnikov-de Haas oscillations are superimposed at 45 mK. Theory —modulated Shubnikov-de Haas oscillations on the same vertical scale calculated as in the text.

A reduction of the temperature to 45 mK extends the SdH oscillations to lower fields and reveals a new feature, strong interference between the SdH oscillations and the COs. Large SdH oscillations are seen only where the resistance due to the commensurability structure is a minimum. Between these minima, at around 0.6 and 0.9 T, the SdH effect is almost completely suppressed. The SdH oscillations are also displaced from their expected positions by an amount that oscillates with the CO periodicity. At some gate voltages Landau level (LL) peaks near the CO maxima are entirely suppressed. We believe that this is the first observation of such interference in a one-dimensional superlattice.

A quantum-mechanical treatment of the periodic potential is essential to explain these observations. Calculations of the broadening of a Landau level due to a periodic potential [5,6] predict that this should vanish at the minima of the commensurability oscillations. The Landau levels therefore remain relatively sharp there and the usual Shubnikov–de Haas effect, attenuated by the bulk scattering potential, is seen. In contrast, the broadening of the Landau levels due to the periodic potential washes away the structure in the density of states around the commesnsurability maxima, and the Shubnikov–de Haas effect is suppressed.

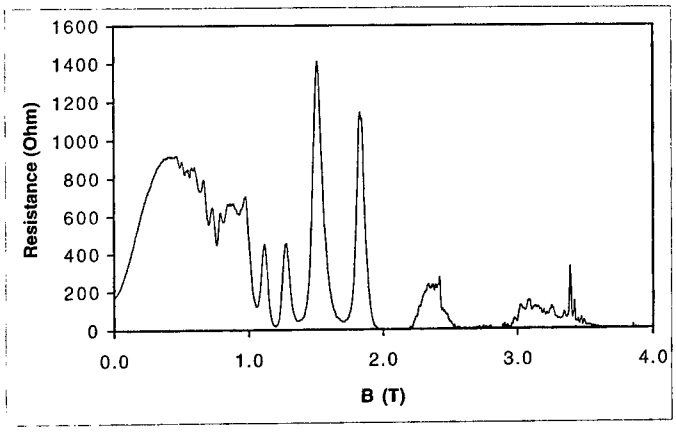

Figure 2. Magnetoresistance at higher field showing isolated Shubnikov–de Haas peaks. There are minima of the commensurability oscillations at 2.8 and 1.2 T. Data taken at 45 mK.

We can make these ideas semiquantitative by performing a calculation based on the theory of Raikh and Shahbazyan [7]. These authors calculate the LL shape to be expected in a standard modulation doped structure at low fields, where the LLs overlap, and predict a Gaussian form with a level width Γ_0 which increases as $\sqrt{B}$, where B is the magnetic induction. When these Gaussian profiles are suitably averaged, the calculation leads to the exponentially damped envelope of SdH oscillations in agreement with experiment and with previous calculations. We introduce the modulation due to the periodic potential by adding the calculated bandwidth Γ_{CO} [5,6] in quadrature to the intrinsic level width according to $\Gamma^2 = \Gamma_0^2 + \Gamma_{CO}^2$ and evaluating the oscillatory density of states as in Ref. 7 with the experimental value of the periodic potential, 1.5 meV. The resultant oscillations (Fig. 1) are in excellent agreement with the data. Moreover an analysis of the positions of the peaks predicts shifts of the same order as those observed. We emphasise that these arise from the strong oscillatory damping of the SdH oscillations, not from intrinsic changes of mean Landau level energy; second-order perturbation theory, using the matrix elements of Ref. 6, predicts shifts that are an order of magnitude smaller than observed. The only disposable parameter in this calculation is the intrinsic damping factor for the LLs. The value we have used translates to a quantum mobility of 1.4 $m^2V^{-1}s^{-1}$. We believe this to be

reasonable because an unpatterned Hall bar of the same material gives a value of 2.5 $m^2V^{-1}s^{-1}$ at a similar carrier density, and a minor increase in the intrinsic scattering due to processing is not unlikely.

At higher fields (Fig. 2) where the Shubnikov–de Haas peaks are fully resolved, the behaviour is different. The widths of the peaks are modulated in the expected manner, but in addition their *heights* vary in accord with the commensurability term. At around 1.2 T and 2.75 T (the CO minima) the LL peaks have low amplitudes, but in between, at around 1.6 T, the peaks are much larger. Normally we expect the SdH peaks to increase monotonically in magnitude and this was seen in an unpatterned Hall bar. Note that this effect has the opposite sign from the behaviour at lower fields where the LLs overlap: the highest peaks occur at the maxima of the CO, whereas at low fields the oscillatory structure is washed out at equivalent points. It may arise from modulation of the velocity of electrons in a Landau level by the periodic potential, in competition with the density of states. It is also possible that tunnelling currents flow between neighbouring LLs and between edge and bulk states when they are strongly perturbed by the periodic potential.

At the highest field commensurability minimum, where Landau levels with indices 3 and 2 pass through the Fermi energy, small highly structured peaks are observed, which are only fully resolved at the lowest temperatures. These are not directly associated with the periodic structure, as they are observed in unpatterned control samples, and we believe that they result from random inhomogeneities in the wafer.

We have observed interference between commensurability oscillations and the Shubnikov–de Hass effect, an influence of a periodic potential that goes beyond the usual semiclassical model. The results at low field have been explained with a quantum-mechanical picture but more work will be required to account fully for the observations at higher fields.

References

1. D. Weiss, K. von Klitzing, K. Ploog and G. Weimann, Europhys. Lett. **8**, 179 (1989).
2. C. J Beenakker, Phys. Rev. Lett. **62**, 2020 (1989).
3. C. J. Emeleus, B. Milton, A. R. Long, J. H. Davies, D. E. Petticrew and M. C. Holland, Appl. Phys. Lett. **73**, 1412 (1998).
4. P. Beton, E. S. Alves, P. C. Main, L. Eaves, M. W. Dellow, M. Henini, O. H. Hughes, S. P. Beaumont and C. D. W. Wilkinson, Phys. Rev. B **42**, 9229 (1990).
5. P. Vasilopoulos and F. M. Peeters, Phys. Rev. Lett. **63**, 2120 (1989); Phys. Rev. B **46**, 4667 (1992).
6. C. Zhang and R. R. Gerhardts, Phys. Rev. B **41**, 12850 (1990).
7. M. E. Raikh and T. V. Shahbazyan, Phys. Rev. B **47**, 1522 (1993)

Anomalous conductance quantization in a novel quantum point contact with periodic(Λ~16nm) potential modulation

Ken'ichi Tanaka[a] *, Yusui Nakamura[b], and Hiroyuki Sakaki
Institute of Industrial Science (IIS), University of Tokyo, and
Quantum Transition Project (QTP), Japan Science and Technolgy Corporation (JST),
7-22-1 Roppongi, Minato-ku, Tokyo 106-8558, Japan

We report on the electron transports in a novel quantum point contact (QPC) structure, in which the heterointerface is corrugated with 16 nm in periodicity and 1.8 nm in height. The conductance in this QPC has distinct step structures, which are equal to be $2e^2/h$ multiplied by 0.3, 0.7, 1.3, 1.8, 2.5, and 3.1. Moreover the first step ($0.3(2e^2/h)$) was accompanied by a quasi-plateau. The several features such as its temperature dependence of this QPC resemble those of conventional QPC. The anomalous conductance quantization may be related to interacton effects enhanced by periodic potential modulation in one dimensional system.

Keywords: Quantum point contact, Periodic potential, Conductance quantization

73.23.-b, 73.23.Ad, 73.61.Ey

The ballistic transport of electrons through ideal quantum point contacts (QPC) or short quantum wires (QWR) is known to yield the quantized conductance $Gq(n)=(2e^2/h)n$, where n is the number of transmitting modes. When a new mode is added by raising gate voltage Vg, a step-like increase of conductance G is anticipated. In G-vs-Vg study of actual QPCs, however, this simple behavior is not always observed.

For example, a quasi-plateau corresponding to G(n=0.7) often appears just below the first step and is ascribed to the spontaneous spin polarization induced by the exchange interactions[1]. It is also pointed out that electron-electron interactions in one dimensional systems (1D) may lead to a unique behavior of electrons not seen in the framework of Fermi liquid behavior. Indeed, Tarucha *et al.* observed the lowering of the first step G(n=1) in long QWRs and ascribe it to Tomonaga-Luttinger state.[2]

In addition, the deviation or lowering from universal conductance quantization was seen by Yacoby *et al.* in long QWRs prepared by cleaved edge over growth technique, the lowering being 20(±5%) of $(2e^2/h)n$.[3] The cause is suggested to be linked with the electron scattering (reflection) at the boundary of the QWR and the electrode.

Moreover, the presence of impurities and any other extra potentials in QPC structures induces quantum-dot like states and brings forth extra conductance peaks via the resonant transmission[4] and/or the charging effects.[5] In addition, the influence of periodic potential modulation in ballistic transport regime has been theoreticaly discussed.[6]

In this paper, we report on our study in a novel QPC device, in which the electron channel is laterally modulated by the heterointerface corrugation with the period of about 16 nm. The conductance in this QPC was found to be quantized but at anomalously low values.

An AlGaAs/GaAs heterojunction was prepared on a vicinal (111)B substrate with the off-angle of 8.5° by molecular beem epitaxy. After growing a 767 nm-thick undoped GaAs layer, we deposited a 22.5 nm undoped $Al_{0.33}Ga_{0.67}As$ spacer layer, a δ-doping layer of Si (5×10^{12} cm^{-2}), an 80 nm undoped $Al_{0.33}Ga_{0.67}As$ layer, and a 20 nm undoped GaAs cap layer. Figure 1 (a) shows the schematic drawing of this QPC. As reported earlier[7], the heterointerface of this wafer is corrugated with period of 16 nm and height of 1.8 nm as illustrate in Fig. 1 (a). ¿From the Shubnikov-de haas oscillation at T=0.3 K, the electron concentration Ns of this wafer with no gate was found to be 3.1×10^{11} cm^{-2} and the mobility across the steps was 9 m^2/Vs. Our earlier work[7] has shown that this corrugation, resulting from the bunched atomic steps on (111)B substrate, reduces the mobility across the steps, especially at high Ns ($\sim 5\times10^{11}cm^{-2}$), while the mobility along the steps remains high. Our novel QPC device was formed across the steps with this wafers by defining a 240 nm-wide mesa constriction on which a metal gate (NiCr/Au) was deposited. Figure 1 (b) illustarate the cross section of constriction part. The measurement was carried out in a pumped ^{3}He cryostat. Four terminal probe method was utilized by standard phase-locked technique using an excitation voltage of 10 μV at a frequency of 625 Hz.

*Corresponding author : Fax:+81-824-22-7195, E-mail: ketanak@ipc.hiroshima-u.ac.jp

Figure 2 shows the conductance G as a function of gate voltage Vg in this QPC measured at T=0.3 K. A series resistance Rs of the device was estimated by measuring the similar sample without the constriction and determined to be 2 kΩ. By subtracting Rs from the measured resistance, G-Vg characteristics was obtained. Figure 2 shows clearly six plateaus for Vg between 120 and 700 mV. Most surprisingly, the heights of steps (in units of $2e^2/h$) were far lower than expected, being 0.3, 0.7, 1.3, 1.8, 2.5, and 3.1. The step structure in this QPC remained visible until T=30 K. The height of the steps was little affected even if the temperature increased.

Next we examined the conductance around the first step (n=0.3). As seen in Fig. 2, we found also a shoulder-like quasi-plateau with n=0.2 just below the first step. Figure 3 is an expanded plot of the first step (n=0.3) at three temperatures, T=0.3 K, 4.6 K, 10 K. Dotted line is marked at first step and the quasi-plateaus are marked by horizontal arrows in Fig.3. Although the quasi-plateau was smeared as the temperature was raised, this remained visible up to 10 K. Note here that the ratio of the quasi-plateau for the first step was revealed to be 0.7 approximately. The first step (n=0.3) was quite sensitive to the increasing temperature, whereas the quasi-plateau (n=0.2) is less sensitive to the rise of temperature. Furthermore its ratio was independent of the temperature. These dependences are very similar to those of the first step (n=1) accompanied by the quasi-plateau (n=0.7), which is usually seen in conventional QWR structures. This structure has been studied in datail by Thomas *et al.* and is identified to originate from the first mode in conventional QWR, whose spin degeneracy is lifted by the exchange interaction[1]. Thus, our data suggests that some unknown mechanisms exist in our QPC structure, which reduces the conductance by a factor of 2-3.

One possible origin of anomalous conductance quantization may be due to the step-induced reduction of transmission in our QPC. Nakamura *et al.* pointed out that the barrier height by bunched steps depends on the gate voltage and is evaluated to be more than ~8 meV.[7] The electrons in the constriction pass through these barriers. Hence the transmission can be reduced, depending on the Fermi energy and the mode index of 1D states. The further investigation is needed for the understanding. Possibility of enhanced coulmb interactions in laterally modulated 1D system has been described theoretically by Ogata *et al.*[6] The importance of such effect in our system should be further investigated.

In summary, we have studied electron transports in a novel point contact, where the interface is corrugated with 16 nm in periodicity and 1.8 nm in height. The steps of quantized conductance are far smaller than $2e^2/h$. This anomalous quantization may be attributed to the change of transmission probability by periodic potential modulation.

One (K.Tanaka) of the authors thanks Profs.M.Yamanishi, Y.Kadoya, T.Ishihara, H.Akiyama, T.Osada, I.Tanaka for their constant encouragement and critical comments on this work.

[a] Present address:Department of Physical Electronics, Faculty of Engineering, Hiroshima University, 1-4-1 Kagamiyama, Higashihiroshima 739-8527, Japan
[b] Present address:Max-Plank-Institut fuer Festkoerperforschung Heisenbergstrasse 1, 70569 Stuttgart, Germany

[1] K. J. Thomas, J. T. Nicholls, N. J. Appleyard, M. Y. Simmons, M. Pepper, D. R. Mace, W. R. Tribe and D. A. Ritchie, Phys. Rev. **B**, 58 4846 (1998).
[2] S. Tarucha, T. Honda and T. Saku, Solid State Commun. **94**, 413 (1995).
[3] A. Yacoby, H. L. Stormer, Ned S. Wingreen, L. N. Pfeiffer, K. W. Baldwin, and K. W. West, Phys. Rev. Lett. **77**, 4612 (1996).
[4] J. C. Wu, M. N. Wybourne, W. Yindeepol, A. Wisshaar, and S. M. Goodnick, Appl. Phys. Lett. **59**, 102 (1991).
[5] C.-T. Liang, M. Y. Simmons, C. G. Smith, G. H. Kim, D. A. Ritchie, and M. Pepper, Phys. Rev. Lett. **81**, 3507 (1998).
[6] Masao Ogata and Hidetoshi Fukuyama, Jpn. J. Appl. Phys., Vol.34 4284 (1995).
[7] Y. Nakamura, S. Koshiba and H. Sakaki J. Crystal Growth 175/176, 1092 (1997).

FIG. 1. (a)Illustration of our QPC with a built-in periodic potentials fabricated by etching technique and a Schottky gate. 2DES is formed at the heterointerface AlGaAs/GaAs. (b)Schematic of cross section diagram of QWR structure. 1DES is formed at the heterointerface AlGaAs/GaAs under the constriction.

FIG. 2. Conductance of our novel point contact device measured at T=0.3 K as a function of gate voltage Vg. A series resistance was estimated to be 2 kΩ.

FIG. 3. (a)The temperature dependence of the first and second plateau together with the quasi-plateau, similar to the 0.7 structure.

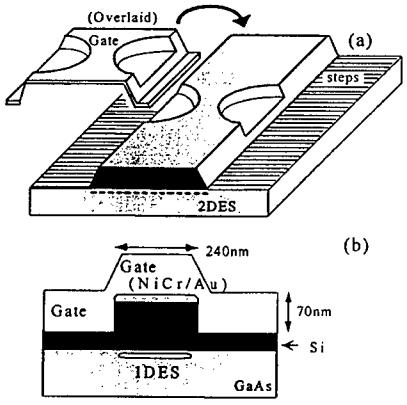

Fig. 1 K.Tanaka et al.

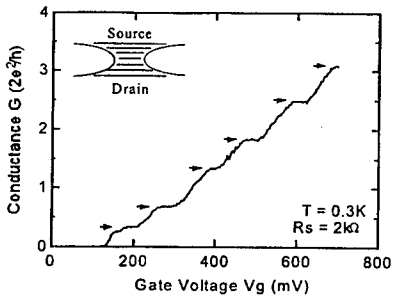

Fig. 2 K.Tanaka et al.

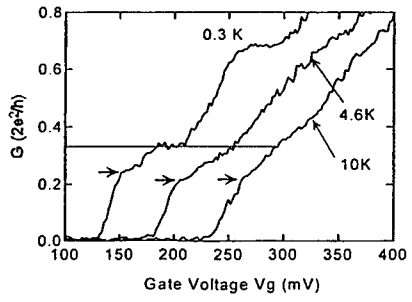

Fig. 3 K.Tanaka et al.

PB.38

Breakdown of SdH Oscillations in a Short Period 1D Lateral Superlattice

R. A. Deutschmann*[1], A. Lorke[2], W. Wegscheider[1,3], M. Bichler[1] and G. Abstreiter[1]

[1]Walter Schottky Institut, Technische Universität München, 85748 Garching, Germany
[2]Sektion Physik and CENS, LMU, Geschwister Scholl Platz 1, 80539 Munich, Germany
[3]Universität Regensburg, Universitätsstr. 31, 93040 Regensburg, Germany

Abstract

Magnetic breakdown is observed in a two dimensional electron system subject to a strong, atomically precise, one dimensional potential with a period of 15 nm. The transition from closed to open electron orbits is studied in magnetotransport experiments by continuously changing the Fermi energy of the superlattice within and above the first miniband. Shubnikov- de Haas oscillations quench for Fermi energies close to the miniband gap but recover at higher magnetic fields. The density of states is clearly altered from a conventional 2D system which manifests itself in aperiodic magnetooscillations when sweeping the Fermi energy at fixed magnetic fields.

Pacs: 73.20.Dx, 73.40.Hm, 73.50.Jt, 73.61.Ey

Keywords: Superlattice, Magnetic Breakdown

Introduction

Man made periodic potentials have long been of great interest for fundamental research and in view of applications. On the one hand epitaxially grown semiconductor superlattices have revealed a large variety of effects in electronic transport, but so far research has mainly concentrated on systems with Fermi energy close to the miniband minimum. Additionally for a given sample the Fermi energy is usually fixed [1]. On the other hand in surface lateral superlattices the Fermi energy is adjustable, but at the price of a rather large periodicity and shallow potential modulation which leads to a large number of occupied bands [2]. We have extended a sample structure developed by Störmer et. al. [3] to combine attractive features of both: A two dimensional electron system (2DES) resides in an atomically precise superlattice, the Fermi energy of which can continuously be adjusted over a wide range by a gate, and the bandstructure of which can be engineered by heterostructure MBE growth. This sample design allows us to study superlattice DC transport as well as magnetotransport properties of a single partially or fully filled band. Results of magnetotransport experiments are the topic of the present paper.

Sample design

Our sample consists of an MBE grown undoped 100 × (119 Å GaAs/31 Å $Al_xGa_{1-x}As$) superlattice (x=0.32) sandwiched between two highly doped n+ GaAs contacts grown on semi-insulating (001) GaAs substrate, as shown in Figure 1a. After *in situ* cleaving the sample an $Al_xGa_{1-x}As$ spacer layer is grown on the freshly exposed (110) plane, followed by a highly doped n+ GaAs gate. By applying a positive gate voltage with respect to the

*corresponding author, phone +49 89 28912756, fax +49 89 3206620, email deutschmann@wsi.tum.de

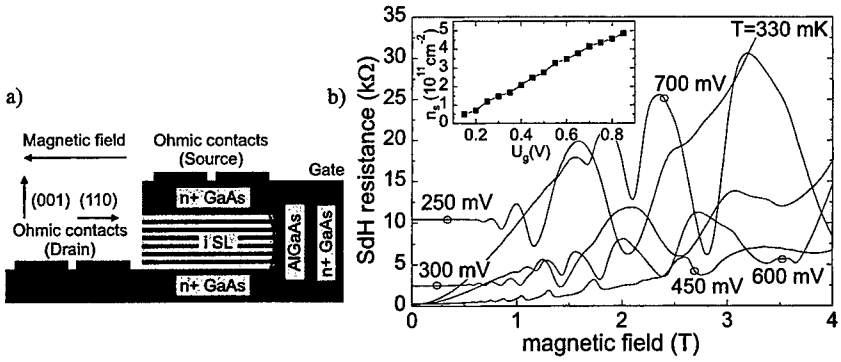

Figure 1: a) Sample structure b) Shubnikov-de Haas measurement. The inset shows the dependence of the electron density n_s on the gate voltage U_g as found by evaluation of the SdH oscillations.

superlattice contacts a 2DES can thus be induced which resides at the interface between the superlattice and the $Al_xGa_{1-x}As$ barrier. A simple Kronig-Penney calculation yields a width for the first miniband of 3.8 meV, separated from the second miniband by a 60 meV one dimensional minigap. The first excited level of the triangular field effect potential is expected at about 15 meV above the first miniband.

Experimental Results

Our measurements are performed in a quasi four probe geometry between the superlattice contacts with standard lock-in technique at liquid Helium temperatures, while magnetic fields up to 14 T are applied perpendicular to the 2DES. First we discuss the Shubnikov- de Haas (SdH) oscillations in the longitudinal magnetoresistance obtained when sweeping the magnetic field strength at fixed gate voltage, i.e. at fixed electron density, see Figure 1b. For gate voltages > 150 mV SdH oscillations are observed. The zero field resistance decreases for increasing gate voltages due to an increasing carrier density, and the magnetic field B_0, where SdH oscillations become visible, decreases, indicating an increasing effective mobility. At a gate voltage of 375 mV the field B_0 has a minimum of 250 mT. From this value we can estimate a lower bound for the electron mobility of 40 000 cm^2/Vs. For larger gate voltages the field B_0 increases again. A drastic change of the magnetoresistance is observed starting at a gate voltage of 450 mV. SdH oscillations at low magnetic fields are quenched in a region of strong positive magnetoresistance which is proportional to the square of the magnetic field. At high magnetic fields, SdH oscillations are recovered.

We now proceed to the analysis of these results. We find that the positions of the minima of the SdH oscillations are periodic if plotted against the inverse magnetic field for *all* gate voltages above 150 mV. By the usual evaluation of the obtained Landau plot or by Fourier transformation we find an almost linear apparent electron density dependence on the gate voltage of $(6.4\pm0.1)\times10^{11}\mathrm{cm}^{-2}\mathrm{V}^{-1}$, as shown in the inset of Figure 1b. This value compares nicely to the capacity per area and charge of $6.7\times10^{11}\mathrm{cm}^{-2}\mathrm{V}^{-1}$ obtained by

taking the sample as a simple capacitor with appropriate dielectric constant. Note that a linear dependence of the electron density on the gate voltage does not imply that the density of states is constant. It may seem surprising that in our evaluation of the SdH oscillations so far no sign of the artificial band structure came into play. The artificial band structure and the presence of a minigap, though, manifest themselves most strikingly in two ways. First in the appearance of a strong, quadratic, positive magnetoresistance for gate voltages above 450 mV, which is exactly what is expected when open orbits become present [4]. This means that at a gate voltage of 450 mV the Fermi energy is raised above the first miniband into the one dimensional minigap. Second, the minigap manifests itself in the quenching of the SdH oscillations in that regime, which is because of the absence of closed orbits in k-space, so that at low magnetic fields SdH oscillations are quenched. However, at higher magnetic fields, SdH oscillations are recovered due to magnetic breakdown [5]. In this regime, Bragg reflections are suppressed due to Lorentz force induced by magnetic fields and electrons tunnel in k-space such that closed orbits are recovered. Magnetic breakdown has been observed in metals [6], in 'bulk' superlattices [7], in density modulated 2DES [2] and in double quantum wells [8]. To our knowledge we show the first example of magnetic breakdown in the first miniband of a modulated 2DES.

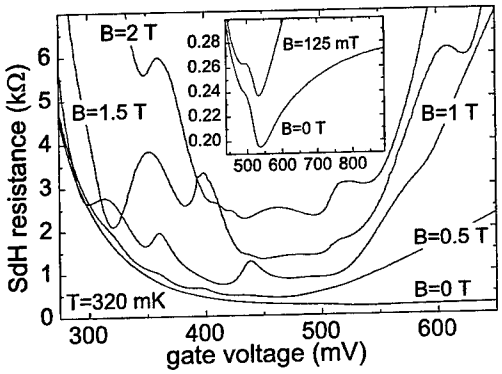

Figure 2: Magnetooscillations for fixed magnetic fields and variable Fermi energy. The inset shows the increase of the zero field resistance when the Fermi energy is raised above the miniband.

Second we discuss the magnetooscillations observed when sweeping the Fermi energy from within the miniband into the minigap through the Landau levels while keeping the magnetic field strength constant. A selection of traces of our experimental results are displayed in Figure 2. For zero magnetic field and for increasing gate voltages up to 500 mV, the longitudinal resistance sharply drops to a minimum of 195 Ω due to an increasing electron density. At 500 mV, though, a W-shaped structure is observed in the resistance, and for larger gate voltages the resistance subsequently increases (see inset). When a magnetic field larger than 500 mT is applied, magnetooscillations are observed. These are quenched for gate voltages larger than 450 mV while the magnetoresistance increases again for increasing gate voltages. For larger magnetic fields magnetooscillations are again observed for gate voltages above

450 mV. Most importantly, the spacing of the magnetooscillations is far from regular.

We now try to give an explanation for the W-shaped longitudinal resistance at zero magnetic field. For a conventional 2DES of free Bloch electrons the longitudinal resistance continuously decreases with increasing electron density. In our system, though, as the Fermi energy approaches the top of the first miniband, the density of states becomes very large and then decreases when the Fermi energy is in the minigap. Therefore close to the minigap electron scattering and thus the longitudinal resistance are enhanced. As the Fermi energy is raised into the minigap, the electron density further increases, but the Fermi surface extends beyond the first Brillouin zone such that the mean electron velocity decreases. The increasing longitudinal resistance at zero magnetic field can again be taken as direct evidence for the existence of a minigap.

When a sufficiently large magnetic field is present, for a 2DES Landau levels are resolved in the magnetoresistance with a constant energy spacing of $\hbar\omega_c$ where ω_c is the cyclotron frequency. In contrast we find magnetooscillations which are not equally spaced in gate voltage, although the electron density in our sample linearly depends on the gate voltage. For a given magnetic field the spacing in gate voltage is larger when measured close to the minigap. Again this observation can be explained by a density of states which becomes large in the vicinity of the miniband edge. A detailed analysis of the density of states per Landau level, taking into account a non constant electron mass, the non trivial shape of the orbits in k-space and the spin splitting of the Landau levels is beyond the scope of the present paper.

In summary we have presented a novel electronic system which bridges the gap between conventional 'bulk' semiconductor superlattices and density modulated two dimensional electron systems. Bandstructure parameters in our sample are entirely known and can be tailored to atomic precision through MBE growth. Additionally the Fermi energy can continuously be controlled by a gate. In magnetotransport experiments the calculated Kronig-Penney bandstructure is directly evidenced. Aperiodic magnetoresistance oscillations for fixed magnetic fields are observed when sweeping the gate voltage. SdH oscillations are found for electron densities below $2.5\times10^{11}\mathrm{cm}^2\mathrm{V}^{-1}\mathrm{s}^{-1}$ as in a conventional high electron mobility 2DES. For higher electron densities SdH oscillations are quenched within a region of strong positive magnetoresistance. SdH oscillations are recovered for high magnetic fields, which we attribute to magnetic breakdown in the minigap. The minigap also becomes visible in the longitudinal resistance when sweeping the Fermi energy above the first miniband at zero magnetic field.

References

[1] *Semiconductor Superlattices, Growth and Electronic Properties*, edited by H. Grahn (World Scientific, Singapore, 1995)

[2] R. R. Gerhardts, D. Weiss and K. V. Klitzing, Phys. Rev. Lett. **62**, 1173 (1989)

[3] H. L. Störmer et. al. Appl. Phys. Lett. **58**, 726 (1991)

[4] C. Kittel *Quantum Theory of Solids*, John Wiley & Sons Inc. (1987)

[5] M. H. Cohen and L. M. Falikov, Phys. Rev. Lett. **7**, 231 (1961)

[6] R. W. Stark and L. M. Falikov, Prog. in Low Temp. Phys. **5**, 235 (1967)

[7] A. B. Henriques et. al. Phys. Rev. B **49**, 11248 (1994)

[8] N. E. Harff et. al. Phys. Rev. B **55**, R13405 (1997)

PB.39

Minibands, magnetic breakdown, and novel magnetoresistance oscillations in short-period lateral superlattices

M. Langenbuch[a], R. Hennig[a], M. Suhrke[a], U. Rössler[1a], C. Albrecht[b], J. H. Smet[b], and D. Weiss[c]

[a]*Institut für Theoretische Physik, Universität Regensburg, 93040 Regensburg, Germany*

[b]*Max-Planck-Institut für Festkörperforschung, 70569 Stuttgart, Germany*

[c]*Institut für Experimentelle und Angewandte Physik, Universität Regensburg, 93040 Regensburg, Germany*

Abstract: Novel $1/B$-periodic low-field oscillations observed in the magnetoresistance of short-period lateral superlattices with weak electrostatic modulation are analyzed as being due to the formation of minibands. The energy gaps caused by the weak superlattice potential distort the Fermi circle of the unmodulated two-dimensional electron system (2DES) at the Brillouin-zone boundaries and form smaller closed Fermi contours giving rise to the novel oscillations. We discuss the periodicity of these novel oscillations for one-dimensional (1D) and two-dimensional (2D) lateral modulation and compare their dependence on the electron density with the well-known classical commensurability oscillations.

PACS: 73.20.Dx, 73.23.Ad, 73.61.-b
Key words: miniband, superlattice, magnetoresistance oscillation

Apart from Shubnikov-de Haas (SdH) oscillations the magnetoresistance of lateral superlattices with weak electrostatic modulation shows $1/B$-periodic oscillations which have been explained classically with the commensurability between cyclotron diameter and lattice constant [1]. On the other hand, 1D minibands have been observed in 2DESs on a high-index surface which influence the period of the SdH oscillations, too [2]. Here we extend the investigations to lateral superlattices with 2D electrostatic modulation. Recently the observation of a novel type of oscillations with a $1/B$-periodicity depending on the superlattice period has been reported [3, 4]. As shown below these oscillations originate from the modification of the energy dispersion of free electrons by the periodic potential and are thus a consequence of the formation of 2D minibands [4]. We discuss 2D and 1D modulations and compare the novel oscillations to the classical commensurability oscillations.

The novel magnetoresistance oscillations [3] were observed at low temperatures ($T = 50\,\mathrm{mK}$) in short-period lateral superlattices with weak electrostatic modulation ($a \approx 100\,\mathrm{nm}$) made from high-mobility GaAs-AlGaAs heterojunctions. They show up at low magnetic fields between a region of positive magnetoresistance and the region where commensurate orbits exist. Both their temperature dependence and the $1/B$-periodicity differ from those of the classical commensurability oscillations.

[1]Corresponding author. tel: +49 941 943 2028; fax: +49 941 943 4382; email: ulrich.roessler@physik.uni-regensburg.de

We model the lateral superlattice by a single-particle Hamiltonian in effective-mass approximation using a phenomenological periodic potential with modulation amplitude V_0 and lattice constant a. For the calculation of the energy spectrum we expand the Hamiltonian in plane waves and use a Fourier expansion of the potential $V(x,y) = \sum_{\mathbf{G}} V_{\mathbf{G}} e^{i\mathbf{G}\cdot\mathbf{r}}$, where $\mathbf{G}$ is a reciprocal superlattice vector.

Fig. 1 shows the calculated miniband structure for a GaAs system (effective mass $m^* = 0.0665\, m_e$). The weak potential only results in a small distortion of the free-electron energy dispersion with gaps determined by the Fourier coefficients $V_{\mathbf{G}}$ of the modulation potential. At the Fermi energy this opens two main energy gaps corresponding to the reciprocal lattice vectors $\mathbf{G} = 2\pi/a(1,0)$ and $(1,1)$, respectively.

The repeated zone scheme at the Fermi energy in Fig. 2 is derived from the calculated

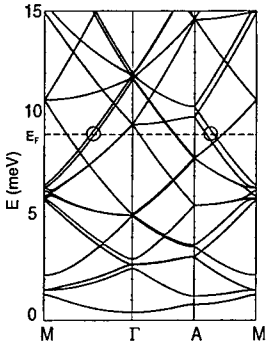

Fig. 1. Miniband structure of a 2DES in GaAs in the presence of a weak 2D modulation $V(x,y) = V_0 \cos^2(\pi x/a) \cdot \cos^2(\pi y/a)$ with $V_0 = 2\,\mathrm{meV}$ and lattice constant $a = 100\,\mathrm{nm}$. The dashed line marks the position of the Fermi energy corresponding to the contours of constant energy in Fig. 4. Circles emphasize the main gaps which break up the Fermi contours of the homogeneous 2DES.

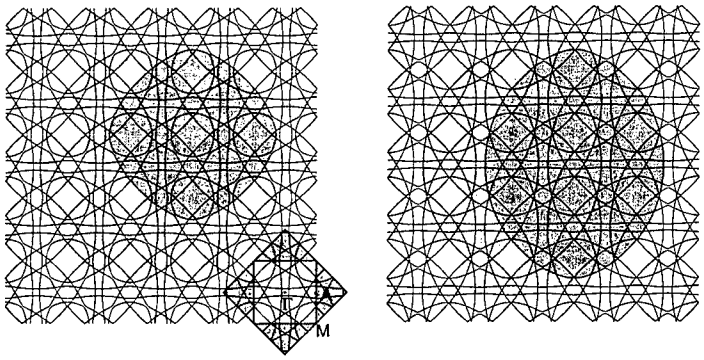

Fig. 2. Fermi contours at $E_F = 9.0\,\mathrm{meV}$ in the repeated zone scheme for 2D (left) and 1D modulation (right). The dark and light shaded areas determine via Eq. 3 the periodicity of the novel oscillations and the SdH oscillations, respectively. The first and second Brillouin zones of the superlattice are depicted by the light and dark shaded boxes in the corner.

miniband structure. It exhibits a slightly distorted Fermi circle due to these gaps which open at the Brillouin-zone boundaries. For the same reason smaller closed contours in k-space become possible for the electrons.

The area of the most pronounced of these contours can be calculated analytically to be

$$A_{\mathrm{F2D}} = \pi k_{\mathrm{F}}^2 + 4\left(\frac{\pi}{a}\right)^2 - 4\left(\frac{\pi}{a}\right)\sqrt{k_{\mathrm{F}}^2 - \left(\frac{\pi}{a}\right)^2} - 4k_{\mathrm{F}}^2 \arcsin\frac{\pi}{ak_{\mathrm{F}}} \tag{1}$$

if the distortion of the curvature of the circle is neglected. For the case of 1D modulation gaps open up only in one direction and new Fermi contours with areas

$$A_{\mathrm{F1D}} = \pi k_{\mathrm{F}}^2 - 2\left(\frac{\pi}{a}\right)\sqrt{k_{\mathrm{F}}^2 - \left(\frac{\pi}{a}\right)^2} - 2k_{\mathrm{F}}^2 \arcsin\frac{\pi}{ak_{\mathrm{F}}} \tag{2}$$

are formed. The areas enclosed by the electron trajectories determine the period of magnetoresistance oscillations within the standard semi-classical approach according to

$$\Delta\left(\frac{1}{B}\right) = \frac{2\pi e}{\hbar}\frac{1}{A_{\mathrm{F}}}. \tag{3}$$

This period and its dependence on the Fermi energy agree favorably with the experimental data [3, 4] as shown in Fig. 3 for two different periods of the 2D lattice.

The magnetic field region where the novel oscillations are observed is determined by magnetic breakdown due to tunneling through the gaps [4, 5]. This breakdown occurs if the cyclotron energy becomes comparable to the corresponding gap energy. Accordingly the novel oscillations appear at magnetic fields where the electrons start to tunnel through the smaller gap (of about 0.25 meV) and disappear once tunneling through the larger gap (of about 0.5 meV) gets possible. Then, the usual SdH oscillations appear. Similar oscillations due to modified contours of constant energy should be observable in systems with weak 1D modulation (see right hand side of Fig. 2 and Eq. 2).

In Fig. 4 we compare the $1/B$-periodicity of the different types of magnetoresistance oscillations in modulated systems. We show the $\Delta(1/B)$ - E_{F} dependence for quantum oscillations due to miniband formation for 1D and 2D modulations, for Weiss oscillations, $\Delta(1/B) = ea/2\hbar k_{\mathrm{F}}$, and for SdH oscillations. According to Fig. 4, the density dependence of the period of the novel oscillations differs significantly from the one of the Weiss oscillations. Moreover it is affected by the dimensionality of the modulation. The agreement with the experimental data found in Fig. 3 thus confirms the novel oscillations as being due to the 2D miniband structure.

There is an optimum range of Fermi energies for the observation of the novel oscillations: E_{F} should be small enough to have periods which differ significantly from those of SdH oscillations but E_{F} should not be too small to avoid large $1/B$-periods which cannot be detected experimentally. This means that several minibands should be occupied as $A_{\mathrm{F}} \to \pi k_{\mathrm{F}}^2$ for $k_{\mathrm{F}} \gg \pi/a$ and $A_{\mathrm{F}} \to 0$ for $k_{\mathrm{F}} \to \pi/a$ according to Eqs. 1 and 2.

In conclusion, we describe the origin of the novel $1/B$-periodic oscillations observed in the magnetoresistance of lateral superlattices with 2D electrostatic modulation. The

oscillations can successfully be explained by formation of a 2D miniband structure due to the modulation. The magnetic breakdown of the gaps in the band structure determines the field range for their appearance. Moreover, we have discussed the characteristic differences between 2D and 1D modulation with respect to the novel oscillations.

The work was supported by the Deutsche Forschungsgemeinschaft (SFB 348 and GRK 176).

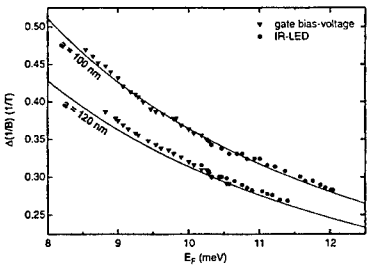

Fig. 3. $1/B$-periodicity of the novel oscillations as a function of the Fermi energy E_F for two lattice constants a. Experimental data (triangles, dots) of [3, 4] are compared with calculations (full lines) for the smaller orbit in $\mathbf{k}$-space (cf. Fig. 2, left).

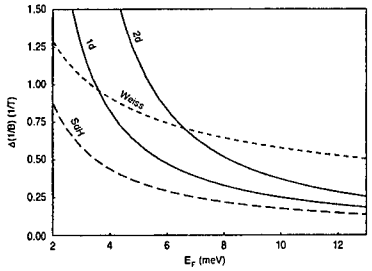

Fig. 4. Dependence of the $1/B$-periodicity of the novel magnetoresistance oscillations for 1D and 2D, of the classical commensurability oscillations (Weiss oscillations) and of the SdH oscillations on the Fermi energy. The lattice constant is $a = 100\,\mathrm{nm}$.

References

[1] D. Weiss *et al.*, Europhys. Lett. **8**, (1989) 179; R.R. Gerhardts, D. Weiss, and K. von Klitzing, Phys. Rev. Lett. **62**, (1989) 1173; R.W. Winkler, J.P. Kotthaus, and K. Ploog, Phys. Rev. Lett. **62**, (1989) 1177; C.B.J. Beenakker, Phys. Rev. Lett. **62**, (1989) 2020

[2] T. Cole, A.A. Lakhani, and P.J. Stiles, Phys. Rev. Lett. **38**, (1977) 722; T. Evelbauer, A. Wixforth, and J.P. Kotthaus, Z. Phys. B **64**,(1986) 69; L.J. Sham, S.J. Allen, Jr., A. Kamgar, and D.C. Tsui, Phys. Rev. Lett. **40**, (1987) 472

[3] C. Albrecht, J.H. Smet, D. Weiss, K. von Klitzing, V. Umansky, and H. Schweizer, Physika B **249-251**, (1998) 914

[4] C. Albrecht, J.H. Smet, D. Weiss, K. von Klitzing, R. Hennig, M. Langenbuch, M. Suhrke, U. Rössler, V. Umansky, and H. Schweizer, submitted to Phys. Rev. Lett.

[5] P. Středa and A.H. MacDonald, Phys. Rev. B **41**, (1990) 11892

PB.40

Effect of a periodic modulation on edge magnetoplasmons in the quantum Hall regime

O. G. Balev [a,b], Nelson Studart [a,1], P. Vasilopoulos [c]

[a] *Departamento de Fí sica, Universidade Federal de São Carlos, 13565-905 São Carlos. São Paulo, Brazil*
[b] *Institute of Physics of Semiconductors, National Academy of Sciences, Kiev 25260, Ukraine*
[c] *Concordia University, Department of Physics, Montreal, Canada, H3G 1M8*

Abstract

A random-phase approximation treatment of edge magnetoplasmons (EMP's) in the quantum Hall regime is presented when a weak periodic potential is imposed along the Hall bar length. We show that the unidirectional periodic potential reshapes essentially the spatial structure of the fundamental EMP, normal and parallel to the edge, and leads to the appearance of a novel fundamental EMP. We find a strong renormalization of the usual fundamental EMP, which depends on the modulation parameters. The novel mode has an acoustical dispersion relation with phase velocity almost equal to the group velocity of the edge states.

Keywords: Quantum Hall effect; edge magnetoplasmons; superlattices; transport

1. Introduction

Recently the role of EMP's in the quantum Hall effect (QHE) has attracted considerable attention with the advent of time-resolved transport experiments [1]. On the other hand, many interesting phenomena have been observed when a periodic spatial modulation is applied to a two-dimensional electron gas (2DEG) in a magnetic field B, in particular the appearance of Weiss oscillations in the magnetoresistance at weak fields B, which reflect the commensurability between the modulation period and the cyclotron diameter [2]. Many works have been devoted to studying the influence of the modulation potential on the transport properties of the 2DEG [3].

From a theoretical point of view, EMP's were first studied only within essentially classical models [4] that imply an edge-wave mechanism in which the charge density profile at the edge of the 2DEG varies but the edge position does not. More recently, different fully quantum mechanical EMP models were provided [5] in which typically only the edge position of the 2DEG varies and the density profile is given as that of the undisturbed 2DEG. A quasimicroscopic model was proposed that incorporates both edge-wave mechanisms mentioned above in the QHE regime [6].

In this work we extend the approach of Ref. [6] to investigate the fundamental EMP's when a relatively weak modulation potential $V_s(x)$ of period a

[1] Corresponding author. E-mail: studart@power.ufscar.br

is imposed along the Hall bar length. We consider the filling factors $\nu = 1$ (2) and low temperatures, $k_BT \ll \hbar v_g/\ell_0$, where v_g is the group velocity of edge states and ℓ_0 is the magnetic length.

2. Integral equations for EMP's

With a self-consistent potential

$$V(x,y,t) = e^{-i(\omega_0 t - q_x x)} \sum_{l=-\infty}^{\infty} V_l(\omega_0, q_x, y) e^{iGlx} + \text{c.c.}, \quad (1)$$

the one-electron Hamiltonian $\hat{H}(t) = \hat{H}_0 + V(x,y,t)$ with $\hat{H}_0 = \hat{h}^0 + V_s(x)$, where $\hat{h}^0$ describes electrons near the edge and $V_s(x) = V_s \cos(Gx)$ is a *weak*, periodic potential with $G = 2\pi/a$. Both $\hat{H}_0$ and the sum $\sum_{l=-\infty}^{\infty} V_l(\omega_0, q_x, y)\exp(iGlx)$ are periodic along x with period a. The corresponding equation of motion for the one-electron density $\hat{\rho}$ is solved together with the Poisson's equation for the self-consistent potential [7]. The Fourier components of the electron charge density are given by

$$\rho_m(\omega, q_x, y) = \frac{2e^2}{\epsilon L} \sum_{n_\alpha=0}^{\bar{n}} \sum_{k_{x\alpha}} \sum_{k_{x\beta}} \sum_{l=-\infty}^{\infty} \int_0^L dx\, e^{-i(q_x+Gm)x} \psi^*_{n_\alpha k_{x\beta}}(\mathbf{r}) \psi_{n_\alpha k_{x\alpha}}(\mathbf{r}) \times \frac{f_{n_\alpha k_{x\beta}} - f_{n_\alpha k_{x\alpha}}}{E_{n_\alpha k_{x\beta}} - E_{n_\alpha k_{x\alpha}} + \hbar\omega + i\hbar/\tau} \int d\tilde{\mathbf{r}}\, e^{i(q_x+Gl)\tilde{x}} \psi^*_{n_\alpha k_{x\alpha}}(\tilde{\mathbf{r}}) \psi_{n_\alpha k_{x\beta}}(\tilde{\mathbf{r}}) \int_{-\infty}^{\infty} dy'\, K_0(|q_x + Gl||\tilde{y} - y'|)\, \rho_l(\omega, q_x, y'). \quad (2)$$

Here $f_{n_\alpha k_{x\beta}}$ is the Fermi-Dirac function, $\bar{n}$ denotes the highest occupied Landau level (LL), and $K_0(x)$ is the modified Bessel function. Since $V_s(x)$ is assumed *weak* the eigenfunctions $\psi_{n_\alpha k_{x\beta}}$ and eigenvalues $E_{n_\alpha k_{x\beta}}$ of $\hat{H}_0$ are obtained by second-order perturbation theory from their unperturbed counterparts $\psi^{(0)}_\alpha = \exp(ik_x x)\Psi_n(y - y_0)/\sqrt{L}$, where Ψ_n is the harmonic oscillator function, and $E^{(0)}_\alpha \approx (n + 1/2)\hbar\omega_c + m^*\Omega^2(y_0 - y_r)^2/2$, respectively, where $y_0 = k_x\ell_0^2$. Equation (2), for $m = 0, \pm1, \pm2, ...$, gives the system of integral equations.

3. Fundamental EMP's for $\nu = 1(2)$

We first consider the case $\nu = 1$ and then indicate how the results change for $\nu = 2$. For $\nu = 1$ we have $\bar{n} = 0$ in Eq. (2). We will look for gapless edge modes, with $\omega \to 0$ for $q_x \to 0$, and assume that $2\pi\ell_0/a \gg 1$. The general solution of the integral equation for $\rho_0(\omega, q_x, y)$ can be written as

$$\rho_0(\omega, q_x, y) = \rho_0^{(0)}(\omega, q_x)\Psi_0^2(\bar{y}) + \rho_0^{(1)}(\omega, q_x) \times [\Psi_0^2(\bar{y} + G\ell_0^2) + \Psi_0^2(\bar{y} - G\ell_0^2)] \quad (3)$$

where $\bar{y} = y - y_{r0}$ and y_{r0} is the edge position at the $n = 0$ LL. This leads to two linear homogeneous equations for $\rho_0^{(i)}(\omega, q_x), i = 0, 1$. The dimensionless frequency branches $\omega'_\pm = \tilde{\omega}/(e^2 q_x/\pi\hbar\epsilon)$, where $\tilde{\omega} = \omega - q_x v_{g0} + i/\tau$, resulting from its determinantal solution are given by

$$\omega'_\pm = \frac{1}{2}a_{00}(q_x) + 2\tilde{V}_{s0}^2\, a_{00}^{00}(q_x, G\ell_0^2) \pm \frac{1}{2}a_{00}(q_x) \times \{1 + 8\tilde{V}_{s0}^2\, a_{00}^{-1}(q_x)[a_{00}^{00}(q_x, G\ell_0^2) + \tilde{V}_{s0}^2\, (a_{00}(q_x) + a_{00}^{00}(q_x, 2G\ell_0^2))]\}^{1/2}, \quad (4)$$

where the coefficients a_{nn}^{mm} are given in Ref. [7], and $\tilde{V}_{s0} = (V_s/2G\hbar v_{g0})\exp(-G^2\ell_0^2/4)$.

From Eq. (4) it follows that the effect of the modulation potential on the fundamental EMP is so strong that it leads, besides to renormalized fundamental EMP of $n = 0$ LL, ω'_+, to the appearance of a completely novel fundamental EMP of the $n = 0$ LL, the ω'_- branch. For a GaAs-based 2DEG, we find that the dispersion relation (DR) of the novel EMP is

$$\omega_- \approx q_x v_{g0} - i/\tau, \quad (5)$$

for both $\nu = 1$ (2). From Eq. (4), we obtain the DR of the renormalized fundamental EMP as

$$\omega_+ \approx q_x v_{g0} + \frac{2}{\epsilon}\sigma^0_{yx} q_x \{\ln(1/q_x\ell_0) + \frac{3}{4} + 4\tilde{V}^2_{s0}\ \ln(1/(Gq_x\ell_0^2))\} - i/\tau, \qquad (6)$$

where $\sigma^0_{yx} = e^2\nu/2\pi\hbar$ for $\nu = 1$ (2). The term $\propto \tilde{V}^2_{s0}$ shows a strong renormalization of the fundamental EMP that depends on the strength and period of the periodic potential.

For a GaAs-based 2DEG and negligible dissipation ($\tau \to \infty$), the DR's given by Eqs. (6) and (5) for the renormalized fundamental EMP, due to the periodic potential and intra-LL Coulomb coupling, and for the novel fundamental EMP, appearing due to the effect of modulation potential, are indicated in Fig. 1. The top and the bottom solid curves show, respectively, the fundamental renormalized and novel fundamental EMP. For comparison, the dashed curve presents the fundamental EMP of $n = 0$ LL without modulation. The material parameters used are the same as those of Ref. [6] and we took $\tilde{V}_{s0} = e^{-2} \ll 1$, $a = \pi\ell_0/\sqrt{2}$, $\omega^* = e^2/\pi\hbar\epsilon\ell_0 \approx 0.3\omega_c$, $\nu = 1$, and $B = 9$ Tesla.

We have also determined the spatial structure of the novel and renormalized fundamental EMP's. For the latter we obtained a small distortion of the edge charge at $\bar{y} = \pm G\ell_0^2$, in comparison with the usual one at $\bar{y} = 0$ because $\rho_0^{(1)}(\omega_+, q_x)/\rho_0^{(0)}(\omega_+, q_x) \approx \tilde{V}^2_{s0}$. On the other hand, for the novel mode, we found that the amplitudes of the charge density of the edge charges localized at $\bar{y} = \pm G\ell_0^2$ have opposite signs and are approximately twice smaller than that of the charge distortion localized at $\bar{y} = 0$. Same results hold for $\nu = 2$. So, the spatial structure of the novel EMP is quite different both from the spatial structure of the fundamental EMP with or without modulation.

The components $\rho_{\pm 1}(\omega, q_x, y)$ induced by $\rho_0(\omega, q_x, y)$ were also calculated. The renormalized charge densities $\rho_\pm(x,y) = \sqrt{\pi}\ell_0 \exp(-iq_x x)$ $\rho(\omega_\pm, x, y)/\rho_0^{(0)}(\omega_\pm, q_x)$ are given, with ($\bar{y}_\pm = \bar{y} \pm G\ell_0^2$), by

$$\rho_+(x,y) = \sqrt{\pi}\ell_0\{\Psi_0^2(\bar{y}) + \tilde{V}^2_{s0}[\Psi_0^2(\bar{y}_+) + \Psi_0^2(\bar{y}_-)] + 2\tilde{V}_{s0}\ \cos(Gx)\Psi_0(\bar{y})$$

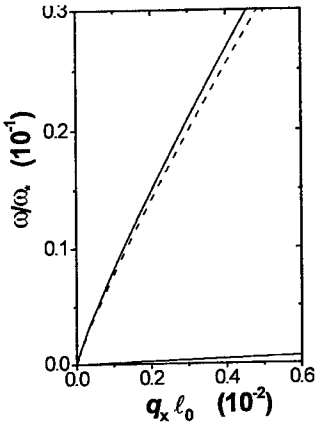

Fig. 1. Dispersion relation for $\nu = 1$ and $B = 9$ Tesla. The upper lower solid curve is for the renormalized fundamental EMP of the $n = 0$ LL and the lower one for the novel fundamental EMP *in the presence* of a periodic potential. The dashed curve is the DR for the fundamental EMP of the $n = 0$ LL *in the absence* of the periodic potential

$$\times[\Psi_0(\bar{y}_+) - \Psi_0(\bar{y}_-)]\}, \qquad (7)$$

for the renormalized fundamental mode and by

$$\rho_-(x,y) = \sqrt{\pi}\ell_0\{\Psi_0^2(\bar{y}) - \frac{1}{2}[\Psi_0^2(\bar{y}_+) + \Psi_0^2(\bar{y}_-)] - \tilde{V}_{s0}^{-1}\cos(Gx)\Psi_0(\bar{y}) \times[\Psi_0(\bar{y}_+) - \Psi_0(\bar{y}_-)]\}, \qquad (8)$$

for the novel fundamental mode. These amplitudes are plotted in Fig. 2 and the parameters are the same as in Fig. 1. $\rho_+(x,y)$ is represented by solid and dotted curves for $x_1^{(m)} = ma$ and $x_0^{(m)} = a(m + 1/2)/2$ respectively, as a function of $Y = \bar{y}/\ell_0$. Notice that the dotted curve is exactly symmetrical with respect to $Y = 0$ and the solid curve deviates from the latter curve due to contributions to the amplitude that commensurate with the modulation potential. We also show $\rho_-(x,y)$, by dot-dashed and dashed curves for $x_1^{(m)}$ and $x_0^{(m)}$, respectively. Observe that the dashed curve is sym-

metric while the dot-dashed curve is clearly asymmetric.

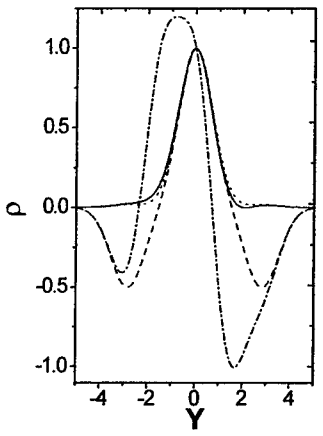

Fig. 2. The form factors as a function of $Y = \bar{y}/\ell_0$. The solid curve and the dotted curve are for the renormalized fundamental EMP and the dot-dashed for the novel fundamental EMP with $x_1^{(m)} = ma$ and $x_0^{(m)} = a(m + 1/2)/2$, with $m = 0, \pm 1, \pm 2, ...$

4. Concluding remarks

The main results of the present work are as follows: **i)** The modulation potential, when V_s is not too small, reshapes noticeably the spatial structure of the usual fundamental EMP of $n = 0$ LL [7], normal and parallel to the edge, and substantially modifies its DR thus renormalizing the fundamental EMP. This renormalization depends on V_s and a. In time-resolved experiments, modulation of the propagation time of a signal by the renormalized fundamental EMP can be obtained by varying V_s. **ii)** The periodic potential, even if V_s is very weak, leads to the appearance of the *novel* fundamental EMP with an acoustical DR and phase velocity typically equal to the group velocity of the edge states v_{g0}, irrespective of V_s and a. Furthermore, the measurement of the velocity of the novel EMP, due to its independence of the modulation parameters, may provide an useful tool to obtain directly such the group velocity v_{g0} of edge states.

Acknowledgments: This work was supported by the Brazilian FAPESP, grants no. 98/10192 and no. 95/0789-3, and by Canadian NSERC grant no. OGP0121756. O. G. B. thanks partial support by the Ukrainian SFFI grant no. 2.4/665 and N. S. is grateful to CNPq for a research fellowship.

References

[1] R. C. Ashoori *et al.*, PRB **45**, 3894 (1992); G. Ernst *et al.*, PRL **77**, 4245 (1996).

[2] D. Weiss *et al.*, Europhys. Lett. **8**, 179 (1989).

[3] 3. R.R. Gerhardts *et al.*, PRL 62, 1173 (1989); R.W. Winkler, *et al.* PRL **62**, 1177 (1989); C.W.J. Beenaker, PRL **62**, 2020 (1989); P. Vasilopoulos and F.M. Peeters, PRL **63**, 2120 (1989); D. Pfannkuche and A. H. MacDonald, PRB 56, R7100 (1997).

[4] V. A. Volkov and S. A. Mikhailov, Sov. Phys. JETP **67**, 1639 (1988); I. L. Aleiner and L. I. Glazman, PRL **72**, 2935 (1994).

[5] X. G. Wen, Phys. Rev. B **43**, 11025 (1991); M. Stone, Ann. Phys. (NY) **207**, 38 (1991); C. de Chamon and X. G. Wen, PRB **49**, 8227 (1994).

[6] O. G. Balev and P. Vasilopoulos, PRB **56**, 13252 (1997); O. G. Balev and P. Vasilopoulos, PRL **81**, 1481 (1998); O. G. Balev, N. Studart and P. Vasilopoulos, J. Phys.: CM **11** (1999).

[7] O. G. Balev and P. Vasilopoulos, PRB **59**, 2807 (1999).

PB.41

Finite size effects in the magnetization of periodic mesoscopic systems

Sigurdur I. Erlingsson[1], Andrei Manolescu[2], and Vidar Gudmundsson[1]
[1]*Science Institute, University of Iceland, Dunhaga 3, IS-107 Reykjavik, Iceland.*
[2]*Institutul Național de Fizica Materialelor, C.P. MG-7 București-Măgurele, România*

We calculate the orbital magnetization of a confined 2DEG as a function of the number of electrons in the system. Size effects are investigated by systematically increasing the area of the confining region. The results for the finite system are compared to an infinite one, where the magnetization is calculated in the thermodynamic limit. In all calculations the electron-electron interaction is included in the Hartree approximation.

I. INTRODUCTION

Magnetization measurements offer a way to directly probe the equilibrium ground state properties of 2DEGs in the quantum Hall regime. Such information is not directly accessible in magnetotransport or optical spectroscopy, in which non-equilibrium behavior of the system is measured. Many years ago the de Haas-van Alphen oscillations of the magnetization were observed and used to characterize the DOS of the 2DEG[1]. In recent years many-body effects, including those related to the FQHE and skyrmions, have also been observed in experiments[2,3]. Two different experimental setups are used: one method uses sensitive mechanical, torque magnetometers[1,2], and a more recent one uses a low noise, superconducting quantum interference device (SQUID)[3,4].

Various thermodynamic quantities, including the magnetization, have been calculated both for a disordered homogeneous 2DEG within the Hartree-Fock approximation (HFA)[5] and a statistical model for inhomogeneities corresponding to the Hartree approximation (HA)[6]. These calculations show many-body effects reflecting screening and, in addition, the HFA produces exchange enhancement at odd filling factors due to spin splitting, and at even filling factors an enhancement, explored to lesser extent in experiments.

For finite systems Kotlyar *et al.* calculated the persistent current in an array of quantum dots using Mott-Hubbard model for the intra-dot and inter-dot electron interaction[7,8]. For two spin split levels per dot oscillations in the persistent current, which is equivalent to magnetization density, were observed as a function of the number of flux quanta penetrating the system.

In the present work we calculate the magnetization of a two dimensional electron system confined to a rectangular box, subjected to a finite one-dimensional periodic potential. Starting from a single unit cell we progressively increase the number of cells until we find convergence of the magnetization to the saw-tooth profile expected from the thermodynamic results. We discuss the edge and the bulk contribution to the orbital magnetization and the effects of the potential.We calculate separately the effects of the periodic potential in the infinite system, and compare the results. The electron-electron interaction is calculated in the HA for both the finite and the extended system.

II. MODELS

The model for a finite system consists of a laterally confined 2DEG. A hard wall potential ensures that the electrons stay in the rectangular region

$$\Sigma = \{(x,y)|0 < x < L_x, 0 < y < L_y\}. \tag{1}$$

A perpendicular magnetic field and an external modulating potential are applied to the system. The potential, which is of the form

$$V_{mod}(x) = V_0 \cos\left(\frac{2n_x\pi x}{L_x}\right), \tag{2}$$

models n_x (n_x integer) parallel quantum wires of width $\ell_x = L_x/n_x$ and length L_y. The length is chosen to be $L_y = n_y\ell_x$ so the geometry of system is controlled by the parameters n_x and n_y. By defining a unit cell of area ℓ_x^2, the parameters n_x and n_y count the number of cells in the x and y direction, respectively. The total number of cells is $N_{xy} = n_x n_y$. The wave functions of the finite systems are expanded in sine Fourier series, since they are required to vanish at the boundary and the Schrödinger equation is solved in the HA. The orbital magnetization in the finite system is calculated according to the definition[9]

$$M = \frac{1}{2L_xL_y}\int_\Sigma d^2\mathbf{r}(\mathbf{r}\times\langle\mathbf{J}(\mathbf{r})\rangle)\cdot\hat{\mathbf{e}}_z. \tag{3}$$

In the extended system the ground state is calculated in the HA, by diagonalizing the Hamiltonian in the Landau basis, and by expanding the matrix elements as Fourier series. Therefore we can evaluate directly the magnetization by the thermodynamic formula appropriate for the canonical ensemble,

$$M = -\frac{1}{L_xL_y}\frac{d}{dB}(E - TS), \tag{4}$$

where E is the total energy, and S the entropy. We shall assume that the temperature is sufficiently low to neglect the entropy term.

III. RESULTS

We use GaAs parameters, $m^* = 0.067m_0$, $\kappa = 12.4$. The magnetic field is $B = 1.5\,\mathrm{T}$, resulting in a magnetic length $\ell_c = 21\,\mathrm{nm}$. The width of the wires is $\ell_x = 75\,\mathrm{nm}$, modulation amplitude $V_0 = 10\,\mathrm{meV}$, and the temperature $T = 1\,\mathrm{K}$. In order to compare the results for the finite system to the infinite one we define the quantity $\bar{\nu} = N_s/N_{LB}$, where N_s is the number of electrons and $N_{LB} = L_x L_y/2\pi\ell_c^2$ is the Landau level degeneracy. When $\ell_c^2 \ll L_x L_y$ we can interprete $\bar{\nu}$ as the filling factor ν.

Since the modulation potential is anisotropic the system will behave differently depending on whether n_x or n_y is increased. Here we consider the cases of one, two , and three parallel wires, $n_x = 1$, 2 and 3, of varying length. We calculate for lengths, $L_y = n_y\ell_x$, corresponding to $n_y = 1$, 2, 3, and 4. The magnetization for the finite system is shown in figure 1. It is plotted in units of $N_{xy}M_0$, where $M_0 = \mu_B^*/\ell_x^2$ and μ_B^* is the Bohr magneton containing the effective electron mass. The top panel shows the magnetization of a single wire, $n_x = 1$. For few electrons, $\bar{\nu} < 2$, the current density circulates clockwise around the maximum density of the wire but for $\bar{\nu}$ between 2 and 3, depending on n_y, the direction of the current reverses and the magnetization decreases again. Around $\bar{\nu} = 4$ a single, dominant current loop splits into two smaller ones for $n_y¿1$ (the current simply reverses for $n_y = 1$) and the magnetization increases. The magnetization of two parallel wires, $n_x = 2$, is shown in the center panel in figure 1. More pronounced jumps around $\bar{\nu} = 2$ and 4 are due to denser energy levels because of the increased system size.

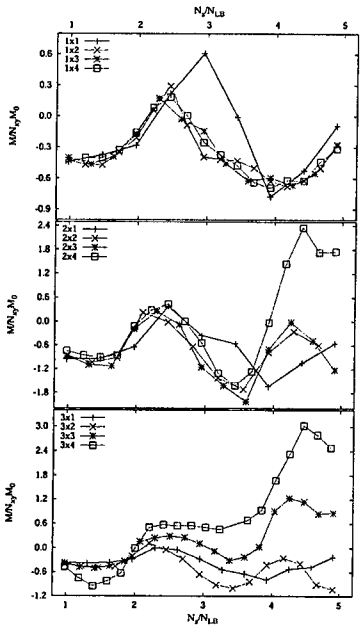

FIG. 1. The magnetization for different $n_x \times n_y$. In the top panel the magnetization for a single wire, $n_x = 1$, of length $1\times$ through $4 \times \ell_x$ is plotted. The center and bottom panel show similarly the magnetization for $n_x = 2$ and $n_x = 3$, respectively.

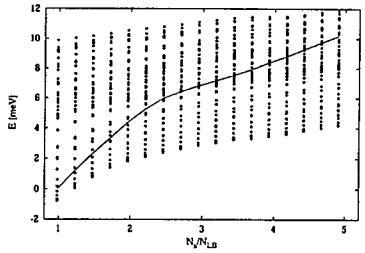

FIG. 2. Energy spectrum as a function of N_s/N_{LB} for two wires $n_x = 2$ of length $n_y = 4$. The solid line denotes the chemical potential.

In figure 2 the energy levels of the system and the chemical potential, shown as a solid line, are plotted as a function of the number of electrons. Below $\bar{\nu} \approx 2.5$ the chemical potential traverses through relatively sparse (longitudinal) energy levels until it enters an energy interval corresponding to the second transverse energy band, with a lower slope. Around $\bar{\nu} = 4$ it grows again. A more complex situation occurs for three wires, $n_x = 3$, since there is a wire in the center of the system which is weaker coupled to the edges than the other two. At the boundary of the system there is a minimum in the Hartree potential due to the positive background charges[10]. As the wire length is increased, more states get localized around this minima and their contribution to the magnetization becomes more important. An interplay of this effect and contribution from the center wire causes the magnetization minimum preceeding the jump at $\bar{\nu} = 4$ to be shifted upwards, and for $n_y = 4$ the region between $\bar{\nu} = 2$ and 4 is relatively flat. In order to estimate the bulk contribution to the magnetization we use equation (3), but instead of integrating over the whole system we define a bulk area which is intergrated over. We choose this area to cover the center wire where we have taken 40 nm of its ends. The bulk magnetization, using the previous definition, is shown in figure 3.

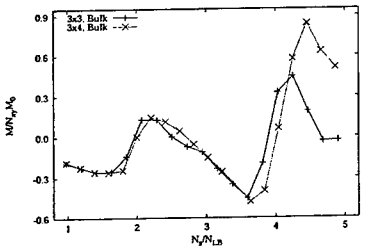

FIG. 3. The bulk magnetization for tree parallel wires of length $n_y = 3$ and $n_y = 4$. See text for the definition of the bulk contribution.

This can be compared with the magnetization calculated for an infinite system of parallel wires ($n_x = \infty$, $n_y = \infty$) also defined by the potential (2), shown in figure 4. In this case the energy spectrum consists of periodic Landau bands. The deviations from the sawtooth profile, corresponding to the homogeneous system ($V_{mod} = 0$) are determined both by the reduced energy gaps, i. e. the reduced jumps, and also by the energy dispersion, i. e. the nonlinear behavior in between even-integer ν-values.

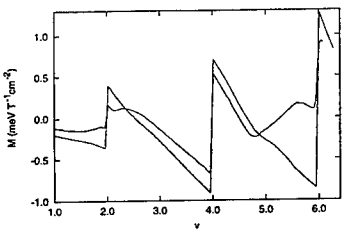

FIG. 4. Thermodynamic magnetization for a modulation with $\ell_x = 75$ nm, in the HA. The solid line is $V_0 = 10$ meV and dashed line $V_0 = 5$ meV.

In summary, the wire modulation used here shows that magnetization due to edge states is nontrivial and large in mircroscopic systems. At the same time the bulk contribution to the magnetization for the system assumes very early the form known for an infinite 2DEG when the system size is increased. This might suggest experiments with a SQUID loop placed inside the system boundaries in order to verify the different contributions to the magnetization. The measurements of magnetization seem to provide a more direct access to the intrinsic equilibrium quantum many-electron structure of the system than transport and far-infrared experiments.

This research was supported in part by the Icelandic Natural Science Foundation, the University of Iceland Research Fund, and NATO Science Fellowship.

[1] J. P. Eisenstein *et al.*, Physical Review Letters **55**, 875 (1985).
[2] S. A. J. Wiegers *et al.*, Physical Review Letters **79**, 3238 (1997).
[3] I. Meinel, T. Hengstmann, D. Grundler, and D. Heitmann, Physical Review Letters **82**, 819 (1999).
[4] I. Meinel *et al.*, Appl. Phys. Lett. **60**, 3305 (1997).
[5] A. H. MacDonald, H. C. A. Oji, and K. L. Liu, Phys. Rev. B **34**, 2681 (1986).
[6] V. Gudmundsson and R. Gerhardts, Phys. Rev. B **35**, 8005 (1987).
[7] R. Kotlyar and S. Das Sarma, Phys. Rev. B **55**, R10205 (1997).
[8] R. Kotlyar, C. A. Stafford, and S. Das Sarma, Phys. Rev. B **58**, 3989 (1998).
[9] J. Desbois, S. Ouvry, and C. Texier, Persistent Currents and Magnetization, cond-mat/9801106, 1998.
[10] U. Wulf, V. Gudmundsson, and R. Gerhardts, Phys. Rev. B **38**, 4218 (1988).

Observation of the Zero-field Spin Splitting of the Second Subband in an Inverted $In_{0.53}Ga_{0.47}As/In_{0.52}Al_{0.48}As$ Heterostructure

C.M Hu, J. Nitta, T. Akazaki, H. Takayanagi, J. Osaka[a], P. Pfeffer[b], and W. Zawadzki[b]

NTT Basic Research Labs, 3-1 Wakamiya, Morinosato, Atsugi-shi, Kanagawa 243-0198, Japan

[a]NTT System Electronics Laboratories Labs, 3-1 Wakamiya, Morinosato, Atsugi-shi, Kanagawa 243-0198, Japan

[b]Institute of Physics, Polish Academy of Sciences, Al. Lotnikow 32/46, 02-668 Warsaw, Poland

A gated inverted $In_{0.52}Al_{0.48}As$ /$In_{0.53}Ga_{0.47}As$/$In_{0.52}Al_{0.48}As$ quantum well is studied via magneto transport. By analysing the gate voltage dependent beating pattern observed in the Shubnikov-de Haas oscillation, we determine the gate voltage (or electron concentration) dependence of the spin-orbit coupling parameter α. Our experimental data and its analysis show that the band nonparbolicity effect can not be neglected. For electron concentrations above 2×10^{12} cm^{-2}, it causes a reduction of α up to 25 %. We report for the first time the α value for the second subband.

Spin degeneracy in the single-electron energy spectra of solid is the combined effect of inversion symmetry in space and time. In semiconductor quantum wells both the bulk inversion asymmetry (BIA) and the structure inversion asymmetry (SIA) break the spatial inversion symmetry and lift the spin degeneracy. The later (known as Bychkov-Rashba spin splitting) can be formulised as spin-orbit interaction of the electron (or hole) moving in the asymmetric confining potential [1]. It causes both macroscopic effects like a beating pattern in the Shubnikov-de Haas (SdH) oscillation [2,3] and mesoscopic effects such as antilocalization [4] and spin-orbit Berry Phase [5,6]. Recently it was found that a surface gate could control the spin-orbit coupling parameter α [7-9]. This is the first step to realise a spin-transistor proposed by Datta and Das [10].

However, the understanding of this subject is still controversial. For example, a contribution of the average electric field to the spin splitting is estimated very differently in different theoretical models [8,11,12]. Experiments on InGaAs/InAlAs [7,8] and InAs/AlSb [13] quantum wells, respectively, found rather different behaviour of the gate voltage (or electron concentration) dependence of α. More precise and comprehensive experimental data are required. In addition, except for a general discussion given by Das *et al* [3], the band nonparabolicity effect was often neglected both in the evaluation of the spin splitting from SdH data and in the self-consistent band structure calculation. While earlier work on Bychkov-Rashba spin splitting focused on mostly GaAs/AlGaAs heterostructures [1,11], recently there is growing interest of using InGaAs or InAs quantum wells [2-8,12,13] where the band nonparabolicity effect is not negligible due to their smaller energy gap.

In this paper, we report on an investigation of the gate voltage V_g dependent SdH oscillations in an inverted $In_{0.52}Al_{0.48}As$ /$In_{0.53}Ga_{0.47}As$/$In_{0.52}Al_{0.48}As$ quantum well. Fourier analysing the SdH oscillations as functions of 1/B confirms for the first time the existence of the

zero-field spin splitting of the second electron subband. The gate voltage dependence of the spin-orbit coupling parameter α of both the first and second subband is determined. We find that taking into account the correction from band nonparbolicity leads to a reduction of α up to 25 % at high concentrations. This effect was not reported in previous studies.

Our device is a gated Hall bar structure fabricated on an inverted modulation doped $In_{0.52}Al_{0.48}As$ /$In_{0.53}Ga_{0.47}As$/$In_{0.52}Al_{0.48}As$ quantum well sample [7]. The SdH measurement is performed in lock-in technique with an excitation current of 73 nA at a temperature of 0.4 K. Fig. 1a) shows the typical results obtained under different gate voltage bias. Beating patterns are observed at the low magnetic field region, in accordance with a previous study on a different sample from the same wafer [7]. The origin of the beating pattern is known to be the zero-field spin splitting, which results in two closely spaced SdH oscillation frequency components with similar amplitudes. At positive gate voltage, a different low SdH oscillation frequency component appears which becomes clearly visible for $V_g > 0.5$ V. It indicates the occupation of the second subband with small carrier density.

In Fig. 1b), we show the correspondent fast Fourier transform (FFT) results performed on the SdH oscillations as functions of 1/B. The (horizontal) frequency axis is normalised to give the unit in the spin-dependent carrier concentration. With increasing gate voltage, carrier concentration of the first subband is found to linearly increase till reaching a saturation value of about 2.8 x 10^{12} cm^{-2} for $V_g > 0.1$ V. Further increase of the gate voltage can only increase the carrier concentration of the second subband. The clearly resolved double-peak structures allow us to determine the concentration of carriers on the same subband but of different spin orientations. Of particular interests is the double-peak structure of the second subband observed for high positive gate voltage. Although it is difficult to identify beating patterns related with the second subband, the FFT analysis shows that the second subband also splits into two spin resolved sublevels.

By analysing the spin-dependent density of state taking into account both the spin-orbit interaction and band nonparabolicity effect [14], α_i of the i-th subband could be determined from the total (n_i) and the difference (Δn_i) of the concentrations of the spin-resolved sublevels by the form

$$\alpha_i = \sqrt{\frac{\pi}{2}}\frac{\hbar^2}{m_0^*}\left(\sqrt{n_i + \Delta n_i} - \sqrt{n_i - \Delta n_i}\right)\left(1 - \xi_i\right), \qquad (1)$$

where $\xi_i = \left(2\pi\hbar^2/m_0^* E_g\right)n_i$ is the normalised modification factor arising from the band nonparabolicity. Here $m_0^* \approx 0.042\ m_e$ and E_g = 0.81 eV are the bandedge effective mass and the energy gap for $In_{0.53}Ga_{0.47}As$, respectively. For large E_g or small n_i where $\xi_i \approx 0$, α_i deduced from Eq. (1) is approximately equal to a form deduced recently from a parabolic band [8,15].

The reason why band nonparabolicity should be considered is straightforward. In the $In_{0.53}Ga_{0.47}As/In_{0.52}Al_{0.48}As$ quantum well structure studied here with a typical total electron concentration of about 2 x 10^{12} cm^{-2}, the nonparabolicity induced energy correction at the Fermi level can be estimated to be $E_F^2/E_g \approx 10\ meV$. Here E_F is the Fermi energy measured from the subband edge. As found in this work this energy correction is larger than the Bychkov-Rashba spin splitting energy at the Fermi level (of about 5 meV). Therefore one has to take into account the modification of the density of states by the band nonparabolicity to get the correct value of α from the measured electron concentrations.

In Fig. 2a) and 2b) we plot the carrier concentration of the spin resolved subbands and the spin-orbit coupling parameter α as a function of the gate voltage, respectively. In Fig. 1a) up- and down-wards triangular marks represent the concentration of electrons on different spin-resolved sublevels. For the gate voltage below 1 V, the spin splitting for the second subband was not resolved. In Fig. 1b) we comparatively plot the value of α determined with (solid marks) and without (open marks) band nonparabolicity correction, respectively. Circles and squares represent the spin-orbit coupling constant of the first and second subband, respectively. Clearly, the band nonparabolicity effect is not negligible when the subband is highly populated. With the saturation density of about 2.8 x 10^{12} cm^{-2} for the first subband, the modification of α_1 due to the band nonparabolicity effect reaches about 25%. We therefore confirm that in our structure α_1 of the first subband could be modulated from a value of 10 x 10^{-12} eVm at –1 V to about 5 x 10^{-12} eVm at + 1.5 V. Such a 100 % changing of the value of α could be applied to modulate the spin precession angle from π to 2 π, which is required to get the maximum current modulation in the field effect spin transistor [10].

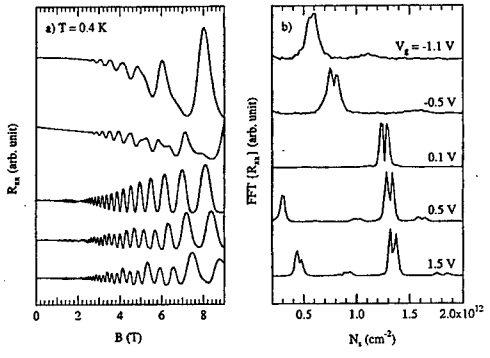

Fig. 1. (a) Shubnikov-de Haas oscillations measured at T = 0.4 K with different gate voltage applied. (b) The correspondent Fourier power spectra of traces in (a). The horizontal axis is normalised to give the unit in the spin-dependent carrier concentration. Traces are shifted vertically for clarity.

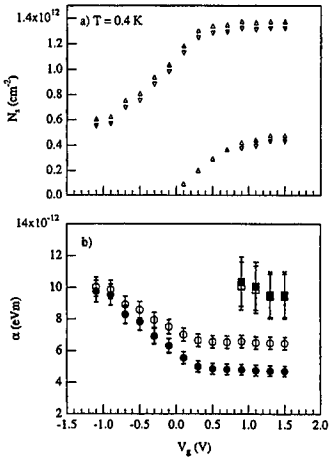

Fig. 2. (a) Up (Δ) and down (∇) spin electron concentrations obtained from experiment as a function of the gate voltage. (b) Spin-orbit coupling parameter α of the first (circle) and second (square) subband obtained with (solid) and without (open) band nonparabolicity correction as a function of the gate voltage.

Another commonly used method to determine α is to fit the measured beating pattern in SdH oscillations with the use of Landau fan chat [2,7,8,13]. Instead of using the slight difference of the density of states of the two spin-resolved sublevels, this method relies on the slight difference in the spin-dependent modification of the otherwise equally spaced Landau-levels. Similar to the above discussion, if the modification of the electron kinetic energy due to the band

nonparabolicity is comparable or larger than that due to the spin-orbit coupling, both effects have to be treated on the same level to get the correct value of α. We emphasise that the correction to α due to the band nonparabolicity depends on both the band gap energy and the electron concentration. The recent study of a gated InAs/AlSb quantum well [13], where the spin-orbit coupling constant was found to be gate voltage independent, need probably be revised since InAs has a small band gap energy.

Finally, we would like to discuss the different value of α found for the first and second subband, respectively. Recent theories [12,16] showed that in a square quantum well α should be determined by the penetration of the wavefunction into the barriers and its asymmetry at both interfaces. Since the wave function for the second (higher) subband penetrates more into the barriers than that of the first subband, Andrada e Silva *et al* [16] predicts $\alpha_2 > \alpha_1$, if the asymmetry of both wavefunctions is similar. That is what we observe. An estimation based on the theory of Pfeffer and Zawadzki[12] found that α_1 can be either smaller or larger than α_2, depending on the detail of the potential shape of the quantum well. A quantitative evaluation of both α values would require a detailed knowledge of electric field distribution in the well, which is at present unknown.

In conclusion, the Rashba spin-orbit coupling of the conduction band electrons in an inverted $In_{0.53}Ga_{0.47}As/In_{0.52}Al_{0.48}As$ heterostructure with different surface gate voltage bias was investigated. Both the concentration and the subband dependence of the spin-orbit coupling parameter α is determined. The band nonparabolicity effect is quantitatively analysed which is found to be not negligible at high density or in heterostructures with small energy gap.

References

[1] Y. A. Bychkov and E. I. Rashba, J. Phys. C **17**, 6039 (1984).

[2] J. Luo, H. Munekata, F.F. Fang, and P.J. Stiles, Phys. Rev. B **38**, 10 142 (1988); Phys. Rev. B **41**, 7685 (1990).

[3] B. Das, D. C. Miller, S. Datta, R. Reifenberger, W. P. Hong, P. K. Bhattacharya, J. Singh, and M. Jaffe, Phys. Rev. B **39**, 1411 (1989); Phys. Rev. B **41**, 8278 (1990).

[4] W. Knap et al., Phys. Rev. B **53**, 3912 (1996).

[5] A. G. Aronov and Y. B. Lyanda-Geller, Phys. Rev. Lett. **70**, 343 (1993).

[6] A.F. Morpurgo, J.P. Heida, T.M. Klapwijk, and B.J. van Wees, Phys. Rev. Lett. **80**, 1050 (1998).

[7] J. Nitta, T. Akazaki, H. Takayanagi, and T. Enoki, Phys. Rev. Lett. **78**, 1335 (1997).

[8] G. Engels, J. Lange, Th. Schäpers, and H. Lüth, Phys. Rev. B **55**, 1958 (1997); J. Appl. Phys. **83**, 4324 (1998).

[9] J. P. Lu, J. B. Yau, S. P. Shukla, M. Shayegan, L. Wissinger, U. Rössler, and R. Winkler, Phys. Rev. Lett. **81**, 1282 (1998).

[10] S. Datta and B. Das, Appl. Phys. Lett. **56**, 665 (1990).

[11] F. Malcher, G. Lommer, and U. Rössler, Superlattices and Microstructures, **2**, 267 (1986).

[12] P. Pfeffer and W. Zawadzki, Phys. Rev. B **59**, R5312 (1999); Phys. Rev. B **52**, R14332 (1995).

[13] J. P. Heida, B. J. van Wees, J. J. Kuipers, and T. M. Klapwijk, Phys. Rev. B **57**, 11911 (1998).

[14] C.M. Hu, J. Nitta, T. Akazaki, H. Takayanagi, J. Osaka, P. Pfeffer, and W. Zawadzki, to be published.

[15] The small difference is caused by an approximation in the integration used in ref. [8], which is not used in this work.

[16] E.A. de Andrada e Silva, G.C. La Rocca, and F. Bassani, Phys. Rev. **B 55**, 16293 (1997).

PB.43

Possible Large Zero-Field Spin-Splittings in $In_xGa_{1-x}As/In_yAl_{1-y}As$ (x, y=0.75) Heterojunctions

S.Yamada*, Y.Sato, S.Gozu and T.Kikutani
School of Materials Science, JAIST Hokuriku,
1-1, Asahidai, Tatsunokuchi, Ishikawa, 923-1292 Japan
*corresponding author, e-mail: shooji@jaist.ac.jp

Abstract

Zero-field spin-splittings are estimated from low-temperature magnetoresistances in two-dimensional electron gas (2DEG) in $In_xGa_{1-x}As/In_yAl_{1-y}As$ (x, y=0.75) van der Pauw, Hall-bar and quantum wire field effect transistor (QWR-FET) samples. Maximum spin-orbit coupling constant α_{zero} of 78 ($x10^{-12}$eVm) was obtained in the Hall bar sample with <-110> direction, which has a sheet electron density and a mobility at 1.5 K of $1.1x10^{12}/cm^2$ and $5.54x10^5$ $cm^2/Vsec$. In-plane anisotropies of mobility as well as of α_{zero} are confirmed in QWR-FET samples with <-110> and <110> directions. If those results are considered together with the fact that a part of α_{zero} was able to be changed by the gate-voltage, interface effect contributing to the zero-field splitting might play an important role in this heterojunction.

1. Introduction

In a past few years, problems related to zero-field spin-splitting in compound semiconductor heterojunctions are re-focused. Gated control of zero-field spin-orbit coupling constant, α_{zero} by Nitta et al. [1] and Engels et al. [2] has triggered the movement and the idea of spin-field effect-transistor (S-FET) [3] is becoming a realistic target with a lot of interests. We recently proposed a new heterojunction, $In_xGa_{1-x}As/In_yAl_{1-y}As$ (x=y=0.75), consisted of two narrow gap materials [4]. This is a new candidate for S-FET [3] or Josepson-FET [5] due to its narrow gap nature with low temperature high 2DEG mobilitiy of up to $5.5x10^5$ $cm^2/Vsec$. In this work, we study zero-field spin-splitting of the 2DEG from low temperature magnetoresistances and report a possible very large spin-orbit coupling constant of α_{zero} ~78 ($x10^{-12}$eV/m) at.1.5K. We also confirmed in-plane anisotropy and gate voltage dependence of α_{zero} in QWR-FETs. The QWR-FET structures are important, since, to inject and collect spin-polarized electrons in future S-FET, we will probably need ferromagnetic electrodes with single magnetic domain, the size of which is within a order of microns.

2. Sample Preparation

The schematic layer structure of our heterojunction is shown in Fig. 1, which is grown by molecular beam epitaxy (MBE) [4]. Sheet electron density, n_s, and mobility, μ_e, at 4.2 K are typically ~$1x10^{12}/cm^2$ and 2-$5x10^5 cm^2/Vsec$, respectively. We prepared van der Pauw ($5x5mm^2$), Hall-bar ($40x400$ μm^2) and QWR-FET samples with SiO_2 gate insulator. The distance between source and drain and the gate length are 60 and 40 μ m, respectively. The wire

widths are 1, 2, 4 and 6 μ m. To determine the coupling constant α, we measured low-temperature (1.5 or 0.3 K) magnetoresistances (MRs) in ac lock-in technique and used Fast Fourier transformation (FFT) for the SdHoscillations and nodes Landau plot [6] for the beats appeared in the low-fields.

3.Results and Discussions

In almost all van der Pauw samples, α_{zero}s of 20-30 (x10^{-12}eVm) were obtained. Figure 2(a) is an example of R_{XX} and its FFT result. Two main peaks around 10(T) denoted as " b" and " c" correspond to sheet electron densities, n(-) and n(+), of the two splitting bands. " a" and " d" are the difference and the sum of them, respectively. In this case, beat nodes plot was poosible and α_{zero} is determined to be 27(x10-12eVm) via the equation [6],

$$\alpha_{zero} = (he/2\pi m^* k_f)(\Delta i/\Delta B^{-1}) \qquad (1),$$

where $(\Delta i/\Delta B^{-1})$ is an inclination of the beat node plot. In Fig.2(b), also R_{XX} and FFT result are shown for <-110> directed Hall bar sample. In the FFT spectrum, peak notations, a', b', c' and d' have the same meanings as those in (a). From the peaks indicated by b' and c' in the spectrum, the difference of n_s between the splitted bands is found to be very large (2.5x10^{11}/cm^2) and α_{zero}= 78(x10-12eVm) was attained by substituting the difference to the beat node period in Eq.(1). Those peak identifications seems reasonable for the following two reasons: 1) Due to the large band bowing of $In_{0.75}Ga_{0.25}As$, conduction band discontinuity at the heterointerface reaches to almost 300 meV, therefore the n_s criterion to occupy the first excited subband is almost 7-8x10^{11}/cm^2, which is larger than the total n_s value (<6x10^{11}/cm^2) of the sample. There could then appear no oscillation due to the upper subband occupation. 2) Since n_ss and μ_es were almost equal for the samples in Figs. 2(a) and (b) (This is confirmed from the van der Pauw Hall measurements and the peak fields of d and d' give the almost equal total n_s) and there seems no upper band occupation in (a). It supports no upper band occupation also in (b) and only the distribution of the total n_s to the splitted subbands is very much different.

This big difference of α_{zero} between the van der Pauw and Hall bar was rather suggesting an in-plane anisotropy for the spin-splitting effect. We then prepared QWR-FET samples made on the identical wafer, the source-drain directions of which are <-110> and <110>. Figure 3(a) and (b) show the FFT results for the derivatives of R_{XX} oscillations at 1.5 K of <-110> and <110> samples, respectively. Again, a, b, c and d denote the peaks for the difference, n(-), n(+) and the sum. As expected and seen in the figures, peak splitting between b and c is much larger in (a) than that in (b), each giving 65 and 27 as α_{zero}(x10-12eVm) values, respectively.

Gate voltage dependence of α_{zero} was also confirmed. In QWR FETs with widths less than 2 μ m, conductance fluctuations often appeared superimposing on the beating oscillation. But the determination of α_{zero} was possible and Fig. 4 is an example of dependences of n(-) and n(+) of two-splitted subbands upon appllied gate voltage, Vg , in a 2 μ m wide wire. By varying Vg from 0 to -3(V), we observed a change of α_{zero}(x10-12eVm) value from 24 to 18, which is about 25 % of the total value. Note here that the Vg dependence of α_{zero} in our FET has a reverse nature to those in former works [2,3]. This is due to the fact that they have used inverted

heterojunction structure, while we utilized the normal one. So that we observed the decrease of α_{zero} by decreasing Vg from zero to certain minus voltage, which brings more flat well bottom potential in our case.

Origin of such big α_{zero} as above is not entirely clear at present. But, as Schapers et al [6] and Pfeffer et al [7] discussed, there are two contributions in the Rashba term, namely, field and interface contributions and the latter is field independent. Although a part of α_{zero} was able to be changed by the gate voltage also in our case, there could be a large contribution from the interface, since our heterojunction is somewhat special in the sense that both materials making a junction have narrow gaps. This interface contribution might be a main origin of the largeness and the in-plane anisotropy of α_{zero}. This hypothesis is plausible, since we also confirmed mobility anisotropy [8] of up to 40 % between <-110> and <110> directions in this material. Some anisotropic ordering or direction dependent interface structure were possively introduced in the growth procedure by MBE and would be resposible to the results obtained here.

4. Summary

To summarize, we have obtained a very large α zero value < 78 ($x10^{-12}$eVm) together with an in-plane anisotropy of almost twice in 2DEGs in $In_xGa_{1-x}As$ / $In_yAl_{1-y}As$ (x=y=0.75) heterojunctions. Their origins are at present considered to be a interface contribution to the zero-field spin-splitting, which might be enhanced in our unique heterostructures.

Very large α_{zero}s observed in this work correspond to the Fermi level spin-splittings of about 30 mV, which might gurantee the forthcoming S-FET operation at room temperature.

Acknowledgements

We are very much indebted to Dr. J.Nitte of NTT laboratories for his stimulating discussions about our results.

References

[1] J.Nitta et al., Phys.Rev.Lett.,78,1335(1997).

[2] G.Engels et al., Phys.Rev.B55,R1958(1997).

[3] S.Datta et al., Appl.Phys.Lett., 56,665(1989).

[4] S.Gozu et al., Jap.J.Appl.Phys., 37,L1501 (1998).

[5] H.Takayanagi et al., Proc.IEDM, 98 (IEEE,New York,1985).

[6] Th.Schapers et al., J.Appl.Phys., 83,4324(1998).

[7] P.Pfeffer et al., Phys.Rev. B59,R5312(1998).

[8] Recently mobility anisotropy of 15 % in $In_{0.75}Ga_{0.25}As$/InP heterojunction was reported by Ramvall et al., Appl.Phys.Lett., 68,1111(1996).

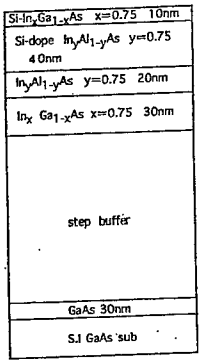

Fig. 1 Layer structure of $In_xGa_{1-x}As$ / $In_yAl_{1-y}As$ (x=y=0.75) heterojunction.

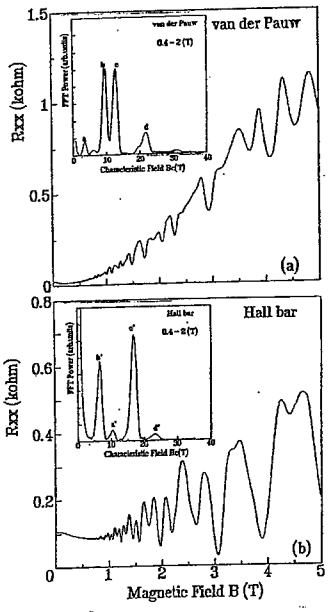

Fig. 2 Low temperature magnetoresistances (R_{XX}s) and their FFT results for (a) vander Pauw and (b)Hall bar sample.

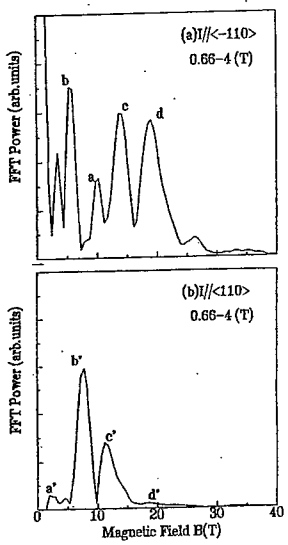

Fig. 3 FFT results of derivatives of R_{XX} for (a) <-110> and (b) <110> directed QWR-FETs. The width of the wire is 4 μ m.

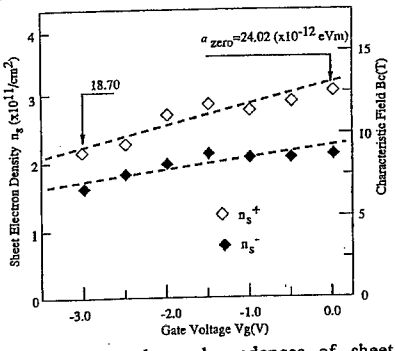

Fig. 4 Gate voltage dependences of sheet electron densities, n(-) and n(+), of the splitted bands and α_{zero}s in 2 μ m wide QWR-FETs.

PB.44

TWO-DIMENSIONAL ELECTRON GAS COUPLED TO Mn^{2+} IONS: A MAGNETO-OPTICAL STUDY OF CdMnTe/CdMgTe MDQWs

F.J. Teran, M.L. Sadowski, M. Potemski, and D.K. Maude
Grenoble High Magnetic Field Laboratory, MPI/FKF and CNRS, 38042 Grenoble, France
G. Karczewski, S. Mackowski, and J. Jaroszynski,
Institute of Physics, Polish Academy of Sciences, 02668 Warszawa, Poland

Abstract

We report the results of magneto-optical experiments on two $Cd_{1-x}Mn_xTe$/CdMgTe modulation doped single quantum well (QW) structures, with x=0.5% and electron sheet concentrations n=3 and $5.65x10^{11}$ cm^{-2}. Experiments have been performed in magnetic fields up to 23T and at low temperatures down to 75mK. The results obtained in the range of low magnetic fields (B<2T) and at temperatures 1K<T<4.2K are relatively well understood in terms of a standard mean field approach adapted for a 2D electronic system coupled to the magnetic environment. Pronounced deviations from the isolated paramagnetic Mn^{2+} behaviour are observed when lowering the temperature in the low field limit as well as in the range of high magnetic fields in the vicinities of integer filling factors.

Keywords: Mn^{2+} local moment– carrier coupling, Magnetic ordering, e-e interaction.
Francisco J. Teran
Grenoble High Magnetic Field Laboratory
MPI/FKF and CNRS
BP 166, F-38042 Grenoble Cedex 9, France
Teleph: + (33) 476887856 fax : +(33) 476855610, e-mail fjteran@labs.polycnrs-gre.fr

The incorporation of local magnetic moments, such as those of Mn^{2+} ions, into a layered II-VI semiconductor structure offers an interesting possibility to study the interactions between local moments [1] and the modifications produced by these ions on the electronic states of the host structure [2]. Advances in the fabrication of diluted magnetic semiconductor nanostructures have lead to increased interest in carrier-mediated spin effects in low dimensional systems. The magnetic interaction between Mn^{2+} ions is short range and antiferromagnetic. However, if Mn^{2+} ions are distributed over a fcc sublattice (such as in CdTe), not all the exchanges energies can be minimised simultaneously (frustration) leading to a spin glass phase above a critical Mn concentration [3]. Studies of $Cd_{1-x}Mn_xTe$ monocrystals have shown that many phases can be triggered by tuning the Mn^{2+} concentration or the temperature: isolated ion, clustering or magnetic ordering (spin glass or antiferromagnetic phase) [4]. Recently, ferromagnetic transitions have also been observed for p-type modulation doped $Cd_{1-x}Mn_xTe$ quantum wells using photoluminescence magneto-spectroscopy, demonstrating that a ferromagnetic coupling between Mn^{2+} spins can be induced by the presence of carriers [5]. Under such conditions, the main magnetic features observed will not longer depend only on the temperature and Mn^{2+} concentration phase diagram.

Due to the relatively large effective masses in II-VI compounds [6], the Landau quantization can be neglected in the low field range. The band realignment induced by exchange interaction between electronic states and local moments leads to a PL spectrum whose energy and intensity are very sensitive to changes in the external magnetic field at low temperatures, mostly driven by the spin polarisation of the magnetic subsystem (see Fig.1). Once the magnetic spin polarisation saturates, further changes in the PL line position and its intensity are determined by the properties of the electronic subsystems. In this way, we can

investigate the magnetic system following the spectral evolution of the two σ+ and σ- PL components of the 2DEG ground state transition as a function of the magnetic field and temperature.

We have performed magneto-optical experiments (luminescence, cyclotron resonance) on two $Cd_{1-x}Mn_xTe/Cd_{1-y}Mg_yTe$ modulation doped, single, 10nm-thick quantum well (QW) structures with x =0.5% and corresponding electron sheet concentrations of n_e=5.65x10^{11} cm^{-2} (sample A) and n_e =3 x10^{11} cm^{-2} (sample B)

In order to have a strong overlap of the wave-functions between the confined states and the magnetic ions, minimising inhomogeneous broadening, the local moments were introduced digitally in few monolayers: the Mn^{2+} distribution in the well is hence a short period superlattice of $CdTe/Cd_{1-x}Mn_xTe$ where, the latter are separated by 2 to 3 nm.

Here, we concentrate on some particular features of luminescence spectra. A detailed investigation of the photoluminescence (PL) as a function of both temperature and weak external field has been carried out in a dilution refrigerator mounted in a superconducting coil. A series of measurement have been performed from 0 up to 3 T in the Faraday configuration, exciting and collecting luminescence using a 600-μm-diameter optical fibre. The QW luminescence was excited above the barrier by the green line (514.5 nm) of an Ar^+ laser and pumped with a laser power below 80μW per cm^2 in order to avoid the effects of laser heating. The analysis of the polarised circular light was performed by a combination of a quarter-wave plate followed by a linear polariser (not active for wavelength of excitation) inserted between the sample and the tip of the fibre. After cooling the samples in a 15mT-external magnetic field from room temperature, the PL experiments were carried out at fixed temperatures between 0.075 and 4.2K. The luminescence spectra were taken using a CCD camera, while slowly sweeping the magnetic field. The PL obtained are independent of the direction of the magnetic field sweep.

The 2DEG luminescence, attributed to recombination processes between electrons occupying states at the bottom of the e1 subband and photogenerated holes thermalised on the top of hh1 valence band state, immediately splits when magnetic field is applied (see Fig.1). The σ+ (σ-) emission line moves to lower (higher) energy whereas the transition intensity dramatically increases (decreases). The energy positions of σ+ and σ- PL components has been followed by means of calculating the center of gravity ($< E > = \Sigma I_i \cdot E_i / \Sigma I_i$) of the corresponding spectra. Such a procedure was found to be very accurate allowing us to measure the spin splitting of the 2DEG recombination line down to a few microelectronovolts.

The σ+/σ- splitting of the recombination line is plotted in Fig. 2a as a function of magnetic field for different temperatures. As shown in this figure, the spin splitting of the luminescence line progressively increases as a function of temperature, reflecting the variation with temperature of the Mn^{2+} magnetisation.

The derivative of the observed spin splitting (Δ) with respect to the magnetic field, measured at H=0 can be related to zero-field magnetic field susceptibility (χ) of manganese ions through the following relation [5]:

$$\chi(T) = \left(\frac{\partial M}{\partial H}\right) = \left(\frac{g\mu B}{|\alpha - \beta|}\right)\left(\frac{\partial \Delta}{\partial H}\right) \quad (1)$$

where g =2.0 is the Landé factor of the Mn spins; α and β are s-d and s-p exchange integrals, respectively, whose values are well known for bulk $Cd_{1-x}Mn_xTe$ [2]. The susceptibility of the manganese ions obtained using to the above formula is shown in Fig. 2b. It can be seen in this figure that for temperatures above 1K, χ(T) follows the Curie law ($1/\chi \sim T$) of an ideal paramagnetic system. In contrast, a clear deviation from this simple law is observed at low temperatures. The susceptibility of the investigated system is found to be finite in the limit of

zero temperature. The observed effect is not sensitive to laser excitation power and we think it is due to the ordering of the $Mn2^{+}$ spins at low temperatures. Such effects can be expected for higher Mn^{2+} concentrations (e.g. formation of the spin glass phase [7]) but in the very diluted systems investigated here it is quite surprising. The observed low temperature saturation of the susceptibility needs to be further investigated. The role of digital doping on the interaction between manganese ions and of the possible coupling between the 2DEG and the magnetic system need to be clarified. We note, however, that both of our samples with significantly different electron concentration show similar behaviour.

As already mentioned above, the spin splitting of the main luminescence peak can be well described by a Brillouin function in the range of moderate temperatures $1K<T<4K$ and low magnetic fields $B<3T$. At higher fields, when we clearly observe the effects of the pronounced Landau quantization (weak emission lines related to higher Landau levels), the dominant $\sigma+$ emission line show a striking behaviour in the vicinity of integer filling factors. The luminescence spectra of a 2DEG are known to show singular behaviour at integer filling factors even in the absence of magnetic ions[8-10]. In our case , however, the effects related to odd filling factors are very much amplified [10]. Figure 3 shows the magnetic field dependence of the energy difference between peak positions of the dominant $\sigma+$ and $\sigma-$ luminescence lines. As can be seen in this figure, a clear enhancement of the spin splitting is observed on the low field side of the filling factor $\nu=3$. Similar, but weaker effects are seen at $\nu=5$, but surprisingly enough no singularities are observed in the vicinity of filling factor $\nu=1$. The enhanced spin splitting of the luminescence line at even filling factors can be related to the exchange interaction between two-dimensional electrons but the absence of the spin-splitting enhancement at $\nu=1$ is very surprising and one may speculate about possible modifications in the spin wave dispersion relations, induced by the magnetic environment. Other effects which need to be taken into account are the decrease of the bare electronic g-factor of CdMnTe and the possible localization of 2D electrons at high magnetic fields. The later effect might be quite important since all our samples show quite distinct excitonic-like behaviour at high magnetic fields, above filling factors $\nu=2$ [8]. The localised character of the 2D electrons in our samples is also indicated by cyclotron resonance measurements.

In conclusion, our measurements indicate the possibility that the low temperature magnetism in very diluted CdMnTe modulation doped quantum wells shows deviations from purely paramagnetic behaviour and that the spin density spectrum of a two dimensional electron gas confined in this structures is not pronounced in the vicinity of filling factor one.

References

1- Crooker et al. Phys.Rev.Lett., 75, 505 (1995)
2- Gaj et al. Solid State Comm. 29, 435 (1979); IPCS, n°43, 1113 (1979); Phys. Stat. Sol. (b) Vol.89, 655 (1978)
3- De Seze, J. Phys. C 10 (1977) L353-356
4-Galazka et al. Phys. Rev. B , 22, 3344 (1980)
5- Haury et al. Phys. Rev. Lett. 79, 511 (1997)
6- Sadowski et al. 24th ICPS Jerusalem 1998 to published.
7- Novak et al. Phys. B 107 (1981) 313
8- Gravier et al. Phys. Rev. Lett. Vol.80, 3344 (1998), Dolpogov et al. Phys. Rev. Lett. Vol.79, 729 (1997)
9- Takeyama et al. Phys. Rev. B Vol.59, 7327 (1999)
10- Teran et al. Physica B 256-258 (1998) 577

Figure captions

Fig.1. Photoluminescence spectra for selected values of the external magnetic field H taken in Faraday configuration at 1.8K. Wavelength excitation as well the power excitation are indicated. The rearrangement of the band structure in an external magnetic field H is sketched in the inset.

Fig.2. (a) Magnetic field dependence of the splitting between the σ^+ and σ^- luminescence components, identified as the energy difference between the centres of gravity of the σ^+ and σ^- emission spectra, measured at different bath temperatures. The data are shown for sample A with $n=5.65\times10^{11}$ cm^{-2} electron sheet concentration. (b) Temperature dependence of the zero-field magnetic susceptibility calculated in accordance to Eq. 1, from the results of spin splitting measurements. Open and closed circles denote the data obtained for sample A and B, respectively.

Fig. 3. Magnetic field dependence (filling factor dependence in the inset) of the splitting between the main (ground state) $\sigma+$ and $\sigma-$ components of the luminescence peaks for bath temperature of 2K and for two samples A (open circles) and B (closed circles)

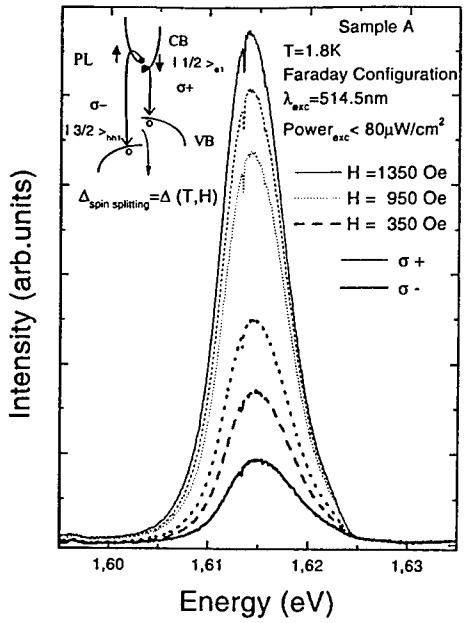

Teran et al. Figure 1

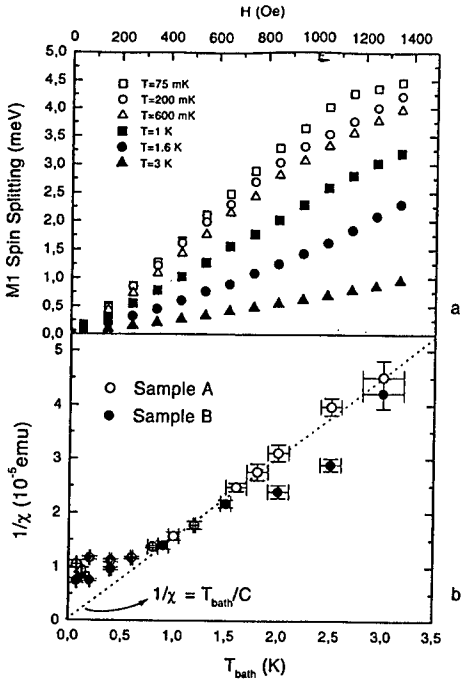

Teran et al. Figure 2

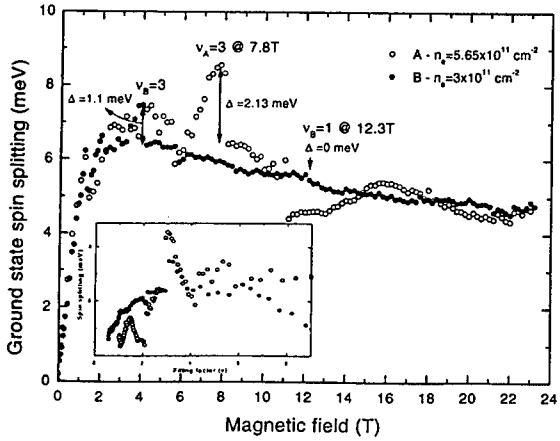

Teran et al. Figure 3

PB.45

Magnetic-field-induced suppression of spontaneous spin splitting of hole subbands

O. Mauritz and U. Ekenberg
Theoretical Physics, Royal Institute of Technology, S-100 44 Stockholm, Sweden

Abstract

The spin splitting in the valence band in an $In_xGa_{1-x}As/\ In_xGa_{1-x}As_yP_{1-y}$ quantum well is investigated theoretically using a 6×6 Luttinger-Kohn Hamiltonian. We compare the Landau levels in a perpendicular magnetic field with the corresponding results for the subband dispersions. It is shown that the asymmetry of the quantum well has a very small impact on the Landau level splitting for $B > 1$ T in sharp contrast to the subbands in the absence of a magnetic field. The significance of our findings on the interpretation of Shubnikov-de Haas experiments is discussed.

1. Introduction

In a two-dimensional system with an asymmetric potential the spin degeneracy is lifted even in the absence of a magnetic field (spontaneous spin splitting). This spin splitting is much larger for hole subbands than for electron subbands and has been investigated both experimentally [1-2] and theoretically [3-5]. Strain can be utilized to shift the heavy-hole (HH) and light-hole (LH) band edges. In an earlier work [5] we found that biaxial compressive strain reduces the spin splitting of the uppermost hole subband by an order of magnitude, whereas for large tensile strain it increases with strain.

Another means of lifting the spin degeneracy is to apply a magnetic field. The direct coupling between the spin of the hole and the magnetic field (Zeeman coupling) gives rise to a spin splitting of the same order of magnitude. One essential issue is if the magnetic field also influences the spontaneous spin splitting. In this paper we therefore investigate the combined effect on the spin splitting of broken inversion asymmetry and a magnetic field perpendicular to the quantum well. We compare the results for a symmetrically and an asymmetrically doped quantum well of the same width. We consider two types of inversion asymmetry. The bulk inversion asymmetry [6] is caused by the different valencies of the III and V ions. The term structure inversion asymmetry [6] refers to an asymmetric potential on the scale of several atomic layers.

2. Method

The valence band structure is calculated in the multiband envelope-function approximation using the Luttinger-Kohn 6×6 Hamiltonian [7]. It incorporates the heavy-hole (HH), light-hole (LH) and spin-orbit split-off (SO) band. The potential, which is calculated self-consistently for $B = 0$, is added along the diagonal. The Hamiltonian in a magnetic field along the z-axis is found by replacing k with $\mathbf{k} + e\mathbf{A}/\hbar$ and introducing the ladder operators

$$a = \sqrt{\hbar/eB}\,(k_x - ik_y) \qquad \text{and} \qquad a^\dagger = \sqrt{\hbar/eB}\,(k_x + ik_y) \tag{1}$$

with the commutation relation $\left[a, a^\dagger\right] = 1$. One also has to add terms proportional to $\kappa J_z B$ which correspond to the direct Zeeman coupling between the spin of the hole and the magnetic field. The Hamiltonian can be written $H = H_0 + \delta H_{\epsilon k} + \delta H_k$, where the two latter

terms result from bulk inversion asymmetry and are absent in the diamond crystal structure. The explicit expressions for the matrices are given in Ref. [8]. The Landau level calculations become simpler and the results more transparent if we make the axial approximation. Then it is clear by inspection of H_0 that the envelope function vector for Landau level n must be in the form

$$\Psi_n = \begin{pmatrix} \phi_{n-1}(\boldsymbol{\rho})f_1(z) \\ \phi_n(\boldsymbol{\rho})f_2(z) \\ \phi_{n+1}(\boldsymbol{\rho})f_3(z) \\ \phi_{n+2}(\boldsymbol{\rho})f_4(z) \\ \phi_n(\boldsymbol{\rho})f_5(z) \\ \phi_{n+1}(\boldsymbol{\rho})f_6(z) \end{pmatrix} \begin{matrix} |3/2,3/2\rangle \\ |3/2,1/2\rangle \\ |3/2,-1/2\rangle \\ |3/2,-3/2\rangle \\ |1/2,1/2\rangle \\ |1/2,-1/2\rangle \end{matrix} \tag{2}$$

where $\boldsymbol{\rho} = (x, y)$ and ϕ_ν is the harmonic oscillator function: $a^\dagger a\phi_\nu = \nu\phi_\nu$. For each component the quantum numbers J and m_J are given. For small values of B every eigenstate, Ψ_n, will be dominated by one component. As B increases the off-diagonal elements in H_0 will increase and other components are admixed, however, n is still a good quantum number. If one leaves the axial approximation or takes δH_k or $\delta H_{\epsilon k}$ into account, n is no longer a good quantum number. In many cases the solution is dominated by one value of n, though.

3. Results

The QW structure studied in this paper is an $In_{0.25}Ga_{0.75}As$ well with lattice-matched $In_{0.38}Ga_{0.62}As_{0.73}P_{0.27}$ barriers. The barrier height is 100 meV. By varying the composition of the $In_xGa_{1-x}As_yP_{1-y}$ substrate through the values of x and y the strain in the well can be changed without changing the barrier height. The effect of a variation of x and y is essentially the same as that of applying external stress but we can easily obtain both biaxial tension and biaxial compression.

As a reference, we consider a symmetric 100 Å well with p-type doped barriers ($N_A = 3 \times 10^{18}\,\mathrm{cm}^{-3}$) and equal spacer layers in the barriers. The carrier concentration N_s is $3 \times 10^{11}\,\mathrm{cm}^{-2}$ in all the cases.

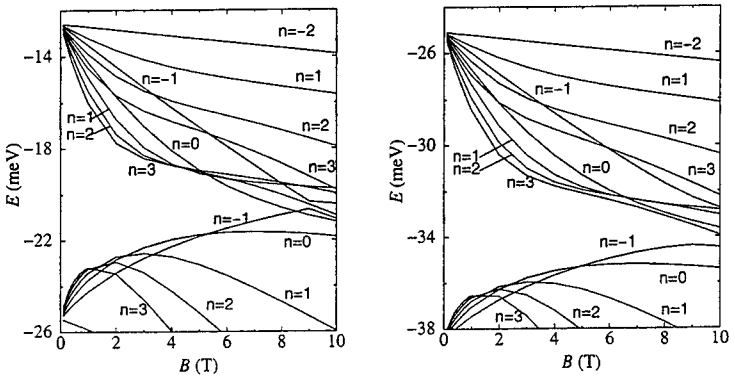

Fig. 1. Fan diagrams with Landau levels for the symmetric well (left) and the asymmetric well (right). Note the similarity between the two diagrams.

We introduce asymmetry of the quantum well by having the same doping as above on one side only. The other side is n-type due to background doping and the result is a built-in electric field over the well.

The fan diagrams for the symmetric and asymmetric wells are presented in Fig. 1. It is remarkable that without a magnetic field there is a significant difference between the subband structures [5], whereas the Landau levels are very similar and one expects the results of Shubnikov-de Haas experiments to be similar.

The Landau level splitting is much more difficult to analyze than the subband splitting. There is in general an interaction between different wavefunction components, but when $n = -2$ only the fourth component, i.e., heavy holes with $m_J = -3/2$, enters Ψ_n, Eq. (2), and H_0 becomes a scalar operator. The eigenstate becomes the simple product

$$\Psi_{-2}(\mathbf{r}) = \phi_0(\rho) f_4(z) \ |3/2, -3/2\rangle \ . \tag{3}$$

Only when $n = 1$ or more all hole components enter the solution. There is no eigenstate with $n < 1$ that contains the $\left|\frac{3}{2}, \frac{3}{2}\right\rangle$ component. We should therefore calculate the Landau level splitting using an eigenstate with the same in-plane wavefunction, in this case ϕ_0, and with $m_J = 3/2$. This implies that its spin partner is a state with $n = 1$ which is dominated by the $\left|\frac{3}{2}, \frac{3}{2}\right\rangle$ component. In general we compare the eigenenergies of the two HH or LH-like states with the same dominant in-plane part $\phi_\nu(\rho)$ of the wavefunction.

In a previous article [8] the Landau level splitting at the highest level ($\nu = 0$) was calculated for the symmetric and asymmetric wells and it was shown that the Landau level splitting differed by no more than 0.1 meV. This should be relevant for large B-values. In this paper we choose to calculate the splitting near the Fermi energy. The two states compared should not both be above or below the Fermi energy. In general several pairs of Landau levels fulfil these conditions. This choice of levels is better related to what can be measured experimentally.

In Fig. 2 we display the spin splitting as a function of magnetic field for the symmetric and the asymmetric wells. The strain is here taken to be zero. For relatively large magnetic fields one first notes the strong oscillations of the spin splitting. The (negative) spin splitting between a given pair of Landau levels increases with B but there are jumps at integral filling factors when transitions between new Landau level pairs become possible.

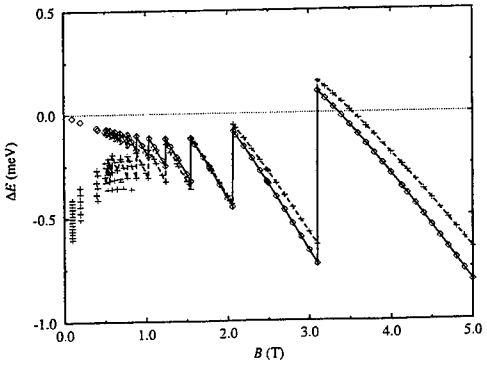

Fig. 2. Landau level splitting between the corresponding levels (see text) in the different wells as a function of B. The strain is taken to be zero. The lines refer to the most intense transitions and the symbols to all possible transitions. The transitions in the symmetric reference well are shown with diamonds and a solid line, the transitions in the asymmetrically doped well are shown with plus signs and a dashed line.

For B >1 T there is virtually no difference between the symmetric and the asymmetric well. For the symmetric well the spin splitting tends to zero in the limit $B \to 0$ while it tends to a finite value in the asymmetric well.

We have investigated the effect of strain and found that the effect of bulk inversion asymmetry, which is dominated by δH_{ck} and becomes important under biaxial tension, is largely retained in a magnetic field, in contrast to that of structure inversion symmetry. In the region of moderate tensile strain where the valence band mixing is at maximum [5], the transition energies can differ considerably between the possible transitions and we also see a difference between the two wells.

In several experiments [1-2, 9] the number of carriers in each spin subband were deduced from the periodicities of the Shubnikov-de Haas oscillations. Our findings that the Landau fans for $B > 1$ T are quite insensitive to structure inversion asymmetry, which is the main contribution to the subband splitting, indicate that a closer analysis is worth pursuing.

To give a tentative semiclassical explanation to this remarkable result we consider the expression

$$\mathbf{B}' = \mathbf{B} \cdot \hat{\mathbf{e}}_\mathbf{v} + \gamma \left(\mathbf{B} - \mathbf{B} \cdot \hat{\mathbf{e}}_\mathbf{v} - \mathbf{v} \times \mathbf{E}/c^2 \right) \tag{4}$$

Here $\mathbf{B}$ and $\mathbf{E}$ are the magnetic and electric fields, respectively, in the laboratory frame and $\mathbf{B}'$ is the magnetic field in the frame of a hole moving with the velocity $\mathbf{v}$. In our case $\mathbf{E}$ is in the z-direction. With a strong magnetic field in the z-direction the hole is forced to move in the xy-plane. If $\mathbf{v}$ at one moment is in the y-direction, $\mathbf{v} \times \mathbf{E}$ is in the x-direction. As the hole moves along an orbit in the xy-plane, the contribution of this term should average to zero.

4. Conclusion

We have shown that spatial asymmetry usually has a small influence on the spin splitting in a p-type quantum well in a magnetic field, in strong contrast to the spin splitting of the subbands at $B = 0$. Only for $B < 1$ T there is a significant effect of structure inversion asymmetry. A tentative semiclassical explanation of the origin of this effect is given.

We are grateful to R. Winkler, U. Rössler, E. Sherman, P. Pfeffer, B. Foreman, A. Hamilton and E. Hauge for valuable discussions. The Swedish Natural Science Research Council is gratefully acknowledged for financial support.

References

[1] J. P. Eisenstein, H. L. Störmer, V. Narayanamurti, A. C. Gossard, and W. Wiegmann, Phys. Rev. Lett. **53,** 2579 (1984).
[2] H. L. Störmer, Z. Schlesinger, A. Chang, D. C. Tsui, A. C. Gossard, and W. Wiegmann, Phys. Rev. Lett. **51,** 126 (1983).
[3] M. Silver, W. Batty, A. Ghiti, and E. P. O'Reilly, Phys. Rev. B**46,** 6781 (1992).
[4] B.-F. Zhu and Y.-C. Chang, Phys. Rev. B**50,** 11 932 (1994).
[5] O. Mauritz and U. Ekenberg, Phys. Rev. B**55,** 10729 (1997).
[6] P. Pfeffer, Phys. Rev. B**55,** R7359 (1997).
[7] J. M. Luttinger and W. Kohn, Phys. Rev. **97,** 869 (1955).
[8] O. Mauritz and U. Ekenberg, Physica Scripta **T79,** 116 (1999).
[9] J. P. Lu, J. B. Yau, S. P. Shukla, M. Shayegan, L. Wissinger, U. Rössler, and R. Winkler, Phys. Rev. Lett. **81,** 1282 (1998).

PB.46

Spin-orbit anomaly in the dielectric function of 2D electron gas

M. E. Raikh [1] and Guang-Hong Chen

Department of Physics, University of Utah
Salt Lake City, UT 84112, U.S.A.

Abstract

We demonstrate that the static dielectric function $\varepsilon(q)$ of 2D electron system with spin-orbit (SO) coupling exhibits an anomaly at small $q = q_0$, where q_0 is the distance between two SO-splitted Fermi surfaces. In contrast to the conventional Kohn anomaly, the SO anomaly is *not* smeared out with increasing temperature. In addition to conventional Friedel oscillations of the screening potential the anomaly leads to the long-period high-temperature oscillations $\delta V(\rho) \propto \cos(q_0\rho)/\rho^2$.

PACS number(s): 71.45. Gm,73.20-r, 73.20.Dx
Keywords: Anomaly, Chirality, Friedel oscillations

1 Introduction

The dielectric function of a two-dimentional electron system was first evaluated by F. Stern [1] within the random phase approximation (RPA). In the static case, Stern obtained the following expression for $\varepsilon(q)$

$$\varepsilon(q) = \varepsilon_0[1 - v(q)F(q)], \tag{1}$$

where q is the wave vector and $v(q) = 2\pi e^2/\varepsilon_0 q$ is the Fourier component of the Coulomb interaction, ε_0 is the dielectric constant of the medium. The response function $F(q)$ is given by

$$F(q) = -\nu \qquad (q \le 2k_F) \tag{2}$$

$$F(q) = -\frac{\nu}{q}(q - \sqrt{q^2 - 4k_F^2}) \qquad (q > 2k_F), \tag{3}$$

where $\nu = m^*/\pi\hbar^2$ is the 2D density of states; m^* is the effective mass. It is well-kown that the singularity in $F(q)$ at $q = 2k_F$ leads to the Friedel oscillations of the screening potential. For a point charge at a distance d from a 2D plane the oscillatory part of the potential has the form

$$V_{osc}(\rho) = -\left(\frac{2e^2}{\varepsilon_0 a_B}\right)\frac{\sin(2k_F\rho)}{(2k_F\rho)^2}e^{-2k_F d}, \tag{4}$$

[1] Corresponding author.
Phone number:001-(801)-585-5017.
Fax:001-(801)-581-4701.
Email:raikh@mail.physics.utah.edu

where $a_B = \hbar^2\varepsilon_0/m^*e^2$ is the effective Bohr radius. Eq. (4) applies at large distances, $k_F\rho \gg 1$. The result (4) is derived for zero temperature $T = 0$. Obviously, the oscillations are smeared out as T increases. This effect amounts to an additional factor $A(u) = u/\sinh(u)$ with $u = \pi k_F \rho T/E_F$.

In the present paper, we study the effect of SO coupling in 2D electron gas on the dielectric function. We demonstrate that, in addition to $2k_F$ anomaly, the SO coupling gives rise to additional anomaly at $k = q_0 \ll k_F$.

To account for SO coupling, we choose the simplest form of the SO interaction for 2D electron system [2]

$$\hat{H}_{SO} = \alpha \mathbf{k} \cdot (\sigma \times \mathbf{n}), \tag{5}$$

where $\mathbf{k}$ is the momentum, $\mathbf{n}$ is the unit vector normal to the 2D plane, $\sigma = (\sigma_1, \sigma_2, \sigma_3)$ are the Pauli matrices, and α is the SO coupling constant. With SO term Eq. (5) the splitted Fermi surfaces represent two circles with radii

$$k_F^{(1,2)} = \mp\frac{q_0}{2} + \sqrt{\frac{q_0^2}{4} + \frac{2m^*E_F}{\hbar^2}} = k_F \mp \frac{q_0}{2} \tag{6}$$

where k_F is related to the Fermi energy as

$$k_F = \sqrt{\frac{q_0^2}{4} + \frac{2m^*E_F}{\hbar^2}}, \tag{7}$$

and $q_0 = k_F^{(2)} - k_F^{(1)}$ is expressed through the SO coupling constant as follows

$$q_0 = \frac{2m^*\alpha}{\hbar^2}. \tag{8}$$

It is important that the difference $k_F^{(2)} - k_F^{(1)}$ does not depend on the position of the Fermi level.

2 Dielectric Function with SO coupling

The Hamiltonian of a free electron with SO term Eq. (5) has the form

$$H = \frac{\hbar^2 k^2}{2m} + \alpha \mathbf{k} \cdot (\sigma \times \mathbf{n}). \tag{9}$$

The energy spectrum and the wave functions are given by

$$E_\mu(k) = \frac{\hbar^2 k^2}{2m} - \mu\alpha k \tag{10}$$

$$\chi_{\mathbf{k}\mu} = \frac{1}{\sqrt{2}}\begin{bmatrix} i\mu e^{-i\phi_{\mathbf{k}}} \\ 1 \end{bmatrix}, \qquad \Psi_{\mathbf{k},\mu}(\rho) = \frac{1}{\sqrt{A}} e^{i\mathbf{k}\cdot\rho}\chi_{\mathbf{k}\mu}. \tag{11}$$

Here $\mu = \pm 1$ is the chirality, A is the normalization area, and $\phi_{\mathbf{k}}$ is the azimuthal angle of the vector $\mathbf{k}$.

The formula for $\varepsilon(q)$ applied to the case when free electron wave functions are the eigenfuctions of the Hamiltonian Eq. (9) has the form [3]

$$\frac{\varepsilon(q)}{\varepsilon_0} = 1 - v(q) \sum_{\mathbf{k},\mu,\mu'} |\chi^{\dagger}_{\mathbf{k},\mu}\chi_{\mathbf{k}+\mathbf{q},\mu'}|^2 \frac{n(E_\mu(k)) - n(E_{\mu'}(|\mathbf{k}+\mathbf{q}|))}{E_\mu(k) - E_{\mu'}(|\mathbf{k}+\mathbf{q}|)}, \tag{12}$$

where $n(E_\mu(k))$ is the Fermi-Dirac distribution function, and

$$|\chi^{\dagger}_{\mathbf{k},\mu}\chi_{\mathbf{k}+\mathbf{q},\mu'}|^2 = \frac{1}{2}(1 + \mu\mu' \cos(\phi_{\mathbf{k}+\mathbf{q}} - \phi_{\mathbf{k}})), \tag{13}$$

are the overlap integrals. It is important to note that the virtual transitions between different chiralities are *allowed*. This contrasts to the case of two size-quantization subbands, where the overlap integral would *reduce to the Kronecker symbol*, so that $\varepsilon(q)$ would represent a sum of contributions from each subband. In the case under the consideration the overlap integral vanishes for $\mu \neq \mu'$ *only* if $\mathbf{k} \parallel \mathbf{q}$.

The algebraic computation give the following form for the dielectric function

$$\frac{\varepsilon(q)}{\varepsilon_0} = 1 - v(q) \sum_{\mu,\mu'} F_{\mu\mu'}(q), \tag{14}$$

where we introduced the following notation [3]

$$F_{\mu\mu'}(q) = \frac{1}{4\pi^2} \int dk \int dp \frac{n(E_\mu(k)) - n(E_{\mu'}(p))}{E_\mu(k) - E_{\mu'}(p)} \left(\frac{q^2 - (k-p)^2}{(k+p)^2 - q^2}\right)^{-\frac{\mu\mu'}{2}}. \tag{15}$$

The small-q anomaly results from the intersubband transitions described by $F_{1,-1} = F_{-1,1}$. The origin of this anomaly is that $E_{+1}(k) = E_{-1}(p)$ when $k - p = q_0$. Straightforward calculations lead to

$$F_{1,-1}(q,T) = -\frac{\nu q_0}{8k_F^2}\left[q_0 - \sqrt{q_0^2 - q^2}\theta(q_0 - q)\right]\left[1 + \frac{\pi^2}{6}\left(\frac{T}{E_F}\right)^2\right]. \tag{16}$$

We see that the response function exibits a square root singularity at $q = q_0$. Since q_0 is determined by the parameters of electron spectrum and does not depend on the Fermi level position, the temperature dependence gets decoupled from this small-q singularity.

3 oscillations of the screening potentail

Consider a point charge e at distance d from the 2D plane. The potential created by this charge within the plane is given by [1]

$$V(\rho) = e\int_0^\infty dq \frac{e^{-qd} J_0(q\rho)}{\varepsilon(q)}. \tag{17}$$

The general approach for extracting the oscillating behavior of $V(\rho)$ is as follows. Suppose that $\varepsilon(q)$ has an anomally at some $q = q_c$. Then the integrand in Eq. (17) should be expanded with respect to $\delta\mathcal{F}$ defined as

$$\delta\mathcal{F}(\kappa) = F(q_c + \kappa) - F(q_c), \tag{18}$$

and the Bessel function should be replaced by its large-ρ asymptotics. This leads to the following general formula for the oscillating part of $V(\rho)$

$$V(\rho) = \frac{ev(q_c)}{\varepsilon_0}\sqrt{\frac{2}{\pi q_c \rho}}e^{-q_c d}\int d\kappa \delta\mathcal{F}(\kappa)\cos[(\kappa+q_c)\rho - \frac{\pi}{4}]. \tag{19}$$

For anomaly at $q_c = q_0$, it follows from Eq. (16) that

$$\delta\mathcal{F}(\kappa) \approx \frac{\sqrt{2}\nu}{8}\frac{q_0^{3/2}}{k_F^2}\sqrt{-\kappa} \tag{20}$$

and $\varepsilon(q_c) \approx \varepsilon_0$. This leads to the SO induced oscillations

$$V_{SO}(\rho) = -\Big(\frac{2e^2}{\varepsilon_0 a_B}\Big)\Big(\frac{q_0}{2k_F}\Big)^2\frac{\cos(q_0\rho)}{(q_0\rho)^2}. \tag{21}$$

4 Conclusion

Let us discuss some consequences of the SO anomaly. Suppose that two localized magnetic moments are located within the 2D plane. In the absence of SO coupling their interaction is governed by the contact (RKKY) mechanism. It can be shown that in the presence of SO coupling, due to the small-q anomaly this interaction acquires a high-temperature component, which falls off with distance slower than conventional RKKY.

It is well known that impurities located within (or close to) the 2D gas cause an inhomogeneity in the electron density around them. At large distances the perturbation of the density oscillates rapidly (as $\sin(2k_F\rho)$). SO coupling introduces a slow-changing component of the density modulation $\propto \cos(q_0\rho)$. This component persists as the temperature is elevated.

References

[1] F. Stern, Phys. Rev. Lett, **18**, 546 (1967).

[2] Yu. A. Bychkov and E. I. Rashba, Pis'ma Zh. Eksp. Teor. Fiz. **39**, 64 (1984) [JETP Lett. **39**, 78 (1984)].

[3] Guang-Hong Chen and M. E. Raikh, Phys. Rev. B **59**, 5090 (1999).

PB.47

Spin-polarized Quantum Transport and Magnetic-field Dependent Carrier Density in Magnetic Two Dimensional Electron Gases

R. Knobel,[a] N. Samarth,[a] S. A. Crooker [b] and D.D. Awschalom[c]

(a) Deptartment of Physics, The Pennsylvania State University, University Park PA 16802.
(b) National High Magnetic Field Lab, MS E536, Los Alamos, NM 86545.
(c) Department of Physics, University of California, Santa Barbara CA 93106.

Abstract

Low temperature magneto-transport and magneto-photoluminescence measurements are reported in magnetic two dimensional electron gas samples formed by modulation doping shallow (Zn,Cd,Mn)Se single quantum wells. The small Fermi energy (~1-2 meV) and large exchange-induced spin splitting (~10 meV) results in a completely spin-polarized electron gas at filling factors as high as $\nu = 12$. Further, the spin splitting significantly perturbs the confinement potential, resulting in a magnetic field dependent carrier density.

Magnetic semiconductor quantum structures, in which confined carriers interact via exchange with magnetic ions (such as Mn^{2+}), exhibit a rich variety of phenomena such as spin-dependent quantum confinement, enhanced magneto-optical effects and carrier-induced ferromagnetism [1,2]. In "magnetic" two dimensional electron gases (M2DEGs) derived by modulation doping magnetic semiconductor quantum wells [3-6], the s-d exchange interaction greatly amplifies the spin splitting (ΔE_S) which easily exceeds the cyclotron energy $(\hbar\omega_C)_e$. Depending on the relative values of ΔE_S, $(\hbar\omega_C)_e$ and the Fermi energy (E_F), a M2DEG can be highly spin polarized gas, with consecutive Landau levels (LLs) separated by a cyclotron gap rather than a spin gap. Such M2DEGs effectively acts as "spinless" fermion gases in which to study phenomena such as insulator-quantum Hall liquid transitions and plateau-to-plateau transitions [5,6].

Although the initial samples based on ZnSe/(Zn,Cd,Mn)Se SQWs have provided important insights into spin-dependent transport and localization in M2DEGs, their low mobility (~3000 $cm^2/V.s$) obscures detailed explorations of any new underlying physics [7]. Here, we describe magneto-transport and magneto-optical studies of higher mobility M2DEG samples (~14,000 $cm^2/V.s$ for a sheet density ~ 10^{11} cm^{-2}) obtained by optimizing both the sample growth and design. The increased mobility is produced in part by employing a smaller Cd concentration in the (Zn,Cd,Mn)Se SQW, hence reducing both alloy disorder and strain. We find that quantum transport in these M2DEGs may be studied at carrier densities as low as 6.5×10^{10} cm^{-2} where $E_F << \Delta E_S$, resulting in complete spin polarization at filling factors as high as $\nu = 12$. In addition, the shallow depth of the SQW (~50 meV) has the unusual consequence that the spin splitting (~10 meV) itself creates a sizeable perturbation on the confinement potential, resulting in a magnetic field dependent carrier density.

We focus on two modulation doped SQWs of (Zn,Cd,Mn)Se, fabricated by molecular beam epitaxy on (100) GaAs substrates after the growth of a ~1.5 μm ZnSe buffer layer. The n-type dopant (Cl) is introduced in two 20 nm thick regions of the ZnSe barrier, located symmetrically on each side of the SQW with a 12 nm undoped spacer of ZnSe. The samples are capped by an 80 nm undoped ZnSe layer followed by a thin (~10 nm) region of highly doped n-ZnSe ($N \sim 10^{18}$ cm^{-3}). The SQW is 10.5 nm thick and is grown "digitally" as a short-period superlattice of

$(Zn_{0.95}Cd_{0.05}Se)_{m-f}(MnSe)_f$, where m is an integer and f is a fraction. Sample A has m = 5, f = 1/8, while sample B has m = 5, f = 1/16. Magneto-transport measurements are carried out using dc Hall bar techniques down to temperatures of ~320 mK and magnetic fields up to 5 T. Contacts are made by annealing In dots in a forming gas atmosphere for 15 minutes. Magneto-photoluminescence (magneto-PL) measurements are carried out in the Faraday geometry in magnetic fields up to 40 T and temperatures down to 2.2 K.

The exchange-enhanced spin splitting ΔE_S in our samples is estimated from the Zeeman shift ΔE_{PL} in the magneto-PL spectrum that arises from electric-dipole allowed transitions between the lowest spin-split electron and heavy hole LLs [8]. The Zeeman shift of the PL peak from its value at zero field is related to ΔE_S as follows:

$$\Delta E_{PL} = 2.63(\Delta E_S) + 1/2[(\hbar\omega_C)_e + (\hbar\omega_C)_{hh} + g_e\mu_B B + g_{hh}\mu_B B], \qquad (1)$$

where $(\hbar\omega_C)_e$ and $(\hbar\omega_C)_{hh}$ are the cyclotron energies for electrons and heavy holes respectively; the last two terms in the equation are the respective intrinsic Zeeman terms and are typically negligible compared to ΔE_S. The prefactor multiplying ΔE_S arises from the known ratio of the s-d and p-d exchange interactions [9]. The spin splitting ΔE_S is proportional to the sample magnetization, so that $\Delta E_S = (\Delta E_S)_{MAX}\, B_{5/2}\, (5\mu_B B/kT_{eff})$, where the Brillouin function is empirically modified by an effective temperature ($T_{eff} = T + T_0$) to account for Mn-Mn interactions [1]. The magneto-PL shift can hence be fit to the sum of a modified Brillouin function and a term linear in magnetic field. The respective fitting parameters for samples A and B are: $(\Delta E_S)_{MAX}$ = 11 meV, 8.3 meV and T_0 = 1.3 K , 0.63 K.

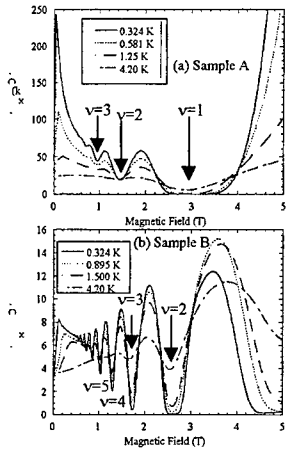

Figure 1: Sheet resistance ρ_{xx} as a function of temperature and magnetic field. Sample A has carrier concentration $N_S = 6.35 \times 10^{10}$ cm^{-2} and mobility 4210 $cm^2/V{\cdot}s$ at 4.2K. Sample B has carrier concentration $N_S = 1.3 \times 10^{11}$ cm^{-2} and mobility 13700 $cm^2/V{\cdot}s$ at 4.2K, both extracted from low field measurements.

The large spin splitting of conduction band states has important implications for the sheet density in the M2DEG since, in the presence of a magnetic field, the conduction band offset ΔE_{CB} is modified to $\Delta E_{CB} = (\Delta E_{CB})_0 + (\Delta E_S)/2$ for spin-down electrons. Hence, the depth of the spin-dependent confinement potential increases with increasing magnetic field and decreasing temperature, leading to an increased transfer of carriers, whether localized or free, from the barrier regions into the SQW. A detailed modeling of this picture requires a self-consistent calculation of the Schrodinger and Poisson equations, taking into account the change in the confinement potential with temperature and magnetic field, as well as the sample preparation-dependent surface states. However, the essential physics can be verified by measuring the temperature- and field-dependence of the sheet density $N_S(B,T)$ deduced from magneto-transport measurements, and correlating this with the measured ΔE_S.

In Figure 1, we show the field- and temperature-dependence of the sheet resistance (ρ_{xx}) in both samples. In sample A, the zero field sheet resistance decreases exponentially with increasing temperature, indicating a strongly localized 2DEG characterized by hopping transport between

localized states. On the other hand, the weak temperature dependence of the zero field resistivity in sample B indicates diffusive transport in a weakly localized electron gas. At low magnetic fields, both samples display the striking positive magneto-resistance characteristic of these M2DEGs and attributed to changes in the diffusive and hopping transport caused by the large spin splitting of electronic states [4,5]. At higher fields, the quantum transport in both samples distinctly shows LLs corresponding to all integer values (ν=1-5 in sample A and ν=1-12 in sample B), again a consequence of the large spin splitting in the samples. A careful analysis of the quantum oscillations in both samples indicates that $N_S(B,T)$ -- as deduced from the location of the minima in ρ_{xx} -- increases with field. In addition, at fixed field we find that $N_S(B,T)$ decreases with increasing temperature. A detailed study of $N_S(B,T)$ in sample B (Figure 2) shows a clear correlation with ΔE_S, providing strong support for the postulate that the exchange-enhanced splitting is responsible for the variation in sheet density. We note further that low field (<0.5 T) Hall measurements clearly indicate a carrier concentration that is lower than that deduced from the Shubnikov-de Haas oscillations. Surprisingly, this low field value of N_S is higher than that extrapolated to zero spin splitting in Fig. 2.

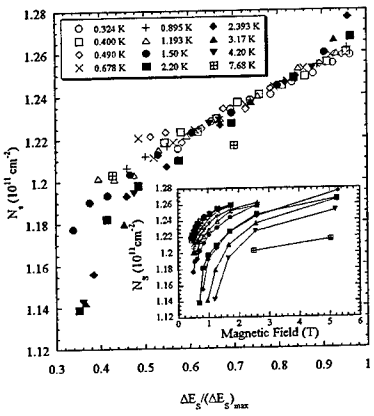

Figure 2: The carrier concentration N_S in sample B (calculated from Shubnikov-de Haas minima) as a function of spin splitting at different temperatures. The inset shows N_S as a function of magnetic field at various temperatures.

The measured spin splitting can be also used to examine the LL structure in the M2DEG samples and to hence gain insights into the observed quantum transport. Since the s-d exchange by itself does not mix LLs of different spin, the relevant LL diagrams may be constructed by adding the experimentally determined spin splitting ΔE_S to the cyclotron energy $(\hbar\omega_C)_e$. We note that we do not account for possible "floating" of the extended states at low field [10]. The resulting LL level diagrams for samples A and B (Figs. 3(a) and 3(b), respectively) indicate complete spin polarization even at large filling factors (for instance, up to ν = 12 in sample B). We note further that sample A undergoes transitions between insulator and quantum hall liquid states at both $\nu = 2$ and ν = 1 (Fig. 1(a)). As usual, we define the insulating regime as one in which ρ_{xx} decreases with increasing temperature, while in the quantum Hall liquid, ρ_{xx} increases with increasing temperature. Even though the varying sheet density precludes systematic studies around the critical points of these phase transitions, we can make two important observations. First, the transition from an insulator to an incipient $\nu = 2$ state occurs even in a completely spin-polarized 2DEG. Second, the $\nu = 2$ and $\nu = 1$ states are separated by an insulating region. Both these features clearly contradict the theoretically proposed global phase diagram for spinless fermions [11], and support earlier experimental findings that direct transitions can occur from the insulating state to integer filling factors other than ν = 1 [12]. We stress that the data presented here are the first to show a transition from insulator to $\nu = 2$ for a system that best represents the "spinless" gas envisaged in theory.

In summary, we have demonstrated that modulation doped ZnSe/(Zn,Cd,Mn)Se SQWs can be designed with high enough quality to permit quantum transport studies at low carrier densities. The shallow confinement required for an enhanced mobility leads to an unusual field- and temperature-dependent carrier density. Nonetheless, we are able to study the generic aspects of quantum transport in M2DEGs that are completely spin polarized right from the onset of quantum transport. Attempts at gating such samples are underway in order to map out the phase diagram in these model spinless fermion gases.

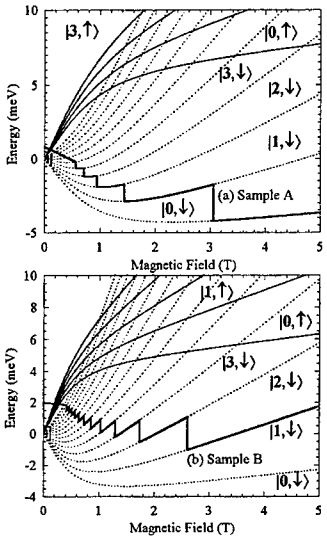

Figure 3: Landau level fan diagrams at 0.32 K calculated using the measured spin splitting. The calculation uses an effective mass $m_e^* = 0.145m_0$, obtained from cyclotron resonance. Dashed lines are spin down and solid lines spin up, while the heavy solid line is the Fermi energy calculated from Shubnikov-de Haas minima in Fig. 2.

This work was supported by grants ONR N00014-99-1-0077 and -0071, and NSF DMR 97-01072 and -01484.

References

[1] D. D. Awschalom and N. Samarth, J. Mag. Magn. Mater. (in press, 1999).
[2] H. Ohno, Science **281**, 951 (1998).
[3] N. Samarth, Current Opinions in Solid State Mater. Sci. **3,** 198 (1998).
[4] I.P. Smorchkova, N. Samarth, J.M. Kikkawa, D.D. Awschalom, Phys. Rev. Lett., **77**, 2814 (1997); I. P. Smorchkova *et al.*, Physica B **249-251** , 676 (1998).
[5] I.P. Smorchkova, N. Samarth, J.M. Kikkawa, D.D. Awschalom, Phys. Rev. B **58**, 4238 (1998).
[6] J. Jaroszinsky *et al.*, Proceedings of the International Conference On the Physics of Semiconductors, World Scientific Press (1998).
[7] In contrast to these quartenary quantum well samples, M2DEGs derived from the dilute ternary (Cd,Mn)Te have significantly higher mobilities (up to 40,000 $cm^2/V.s$) (Ref.6).
[8] In the presence of a magnetic field, the PL spectrum consists of two peaks, only one of which survives beyond $\nu = 1$. We attribute this higher energy peak to the band-edge emission.
[9] S. A. Crooker *et al.* , Phys. Rev. Lett. **77**, 2814 (1996).
[10] R. B. Laughlin, Phys. Rev. Lett. **52**, 2304 (1984).
[11] S. Kivelson, D. H. Lee and S. C. Zhang, Phys. Rev. B **46**, 2223 (1992).
[12] S. H. Song *et al.*, Phys. Rev. Lett. **78**, 2200 (1997).

PB.48

Temperature and size scaling of the QHE resistance: the case of spin-polarized electron gas

J. Jaroszyński,[a] G. Karczewski,[a] J. Wróbel,[a] T. Andrearczyk,[a] A. Strycharczuk,[b] T. Wojtowicz,[a] G. Grabecki,[a] E. Papis,[c] E. Kamińska,[c] A. Piotrowska,[c] T. Dietl[a]

[a]Institute of Physics, Polish Academy of Sciences, al. Lotników 32/46, PL 02–668 Warsaw Poland

[b]College of Science, Polish Academy of Sciences, al. Lotników 32/46, PL 02–668 Warsaw Poland

[c]Institute of Electron Technology, al. Lotników 32/46, PL 02–668 Warsaw Poland

Abstract

We report on transport study in modulation-doped CdMnTe/CdMgTe:I heterostructures. This novel quantum Hall system due to giant *s-d* exchange energy is highly spin-polarized even at large filling-factors. In spite of the high polarization we observe a standard temperature and size scaling of QHE. Low temperature saturation of the QHE scaling, observed in wires, allows us to evaluate the coherence length in our structures.

Recent works demonstrate a strong influence of Mn spins on electron transport of 1D [1, 2] and 2D [3] structures of diluted magnetic semiconductors (DMS)[4]. In particular, the giant *s-d* spin-splitting of the electronic band constitutes a novel mechanism by which the universal conductance fluctuations (UCF) are generated as a function of the magnetic field and temperature [1]. Furthermore, the recent observation $1/f$ quantum noise in DMS wires and its spectral analysis have provided important information on the nature of spin-glass dynamics [2]. Another important consequence of a large ratio of the Zeeman to Landau splittings is the possibility to examine the quantum Hall effect (QHE) in the case of spin-polarized electron gas [3]. Under such conditions the dependence of the localization length on the distance to the center of the Landau level is not obscured by the two overlapping densities of states originating from the adjacent spin subbands. This worthwhile possibility is explored in the present study, which concerns with the problem of temperature and size scaling of the resistance in the QHE regime in nanostructures containing a substantial concentration of localized spins.

As the temperature T is lowered, the widths of both the resistance peak and the transition region between two adjacent quantum Hall plateaus are known to shrink. Such a behavior is thought to reflect a metal-insulator transition, and a corresponding divergence of the localization length at a single energy near the center of each Landau level (LL) [5, 6, 7]. This divergence is characterized by an exponent α: $\xi \propto |E - E_c|^{-\alpha}$. According to this picture the conductance remains non-zero as long ξ exceeds either phase coherence length $L_\varphi(T)$ or the sample size W.

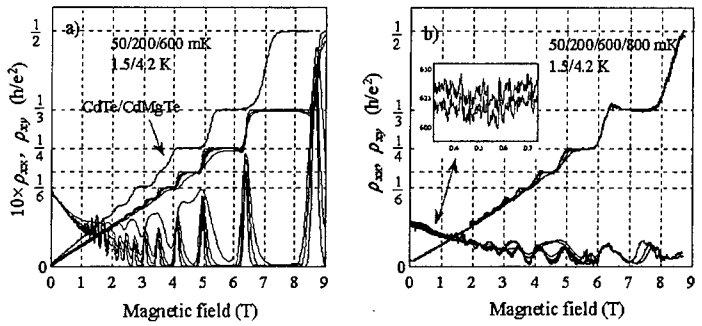

Fig. 1. Longitudinal ρ_{xx} and Hall ρ_{xy} resistances as a function of the magnetic field perpendicular to 2DEG at various temperatures for wide (a) $W = 0.5$ mm and narrow (b) $W = 2$ μm channels (structure C). For comparison, ρ_{xy} of control nonmagnetic structure A is also presented. Inset shows universal conductance fluctuations.

It has experimentally been found that the half width ΔB of the ρ_{xx} peak between adjacent Hall plateaus and the maximum slope $d\rho_{xy}/dB$ of the Hall resistance show a power-low behavior $\Delta B \propto T^{-\kappa}$ and $d\rho_{xy}/dB \propto T^{\kappa}$. The scaling exponent κ is related to the localization exponent p, according to $\kappa = p/\alpha$. The exponent p describes divergence of the phase coherence length $L_\varphi \propto T^{-p/2}$ as $T \to 0$. While some experimental works [8, 9, 10] find κ as universal and equal ≈ 0.4, independent of material and Landau level, in other reports the universality of κ is questioned [11, 12, 13].

The $(CdTe)_{m-f}(Cd_{1-x}Mn_xTe)_f$/ $Cd_{1-y}Mg_yTe$ modulation-doped heterostructures were grown by a molecular beam epitaxy (MBE) on semi-insulating (001) GaAs substrate followed by ~ 10 Å ZnTe layer and thick ~ 3 μm undoped CdTe buffer. Magnetic ions were introduced to the quantum well (QW) either uniformly or by a digital alloy technique. The results presented here were obtained for samples of three structures A, B, and C, in which QW was either nonmagnetic ($x = 0$), uniformly doped by Mn ($m = f$, $x = 0.02$), or consisted of a digital alloy ($f = 1$, $m = 8$, $x = 0.1$). The 10 nm QW is buried in $Cd_{1-y}Mg_yTe$:I ($y \simeq 0.17$) barriers and separated from the Iodine doped CdMgTe layer by an undoped 10 nm thick spacer. The structure is capped by a 150 Å slightly doped CdTe layer. The electron mobilities in such structures, between 5×10^4 and 10^5 cm^2/Vs [14], are the highest that have been reported for the II-VI wide-gap materials.

Millikelvin magnetotransport studies were carried out on mesa etched Hall bars having dimensions ranging from 1×5 μm^2 to 0.5×1 mm^2, patterned by means of electron-beam lithography and chemical etching in 0.05 % solution of Br_2 in ethylene glycol. Samples have indium soldered contacts.

Figure 1 shows longitudinal ρ_{xx} and Hall resistance ρ_{xy} in 2D and 1D samples of magnetic structure C at various temperatures. For comparison, ρ_{xy} of control nonmagnetic structure A is also shown. In the magnetic structure, sharp quantum Hall steps are clearly seen for

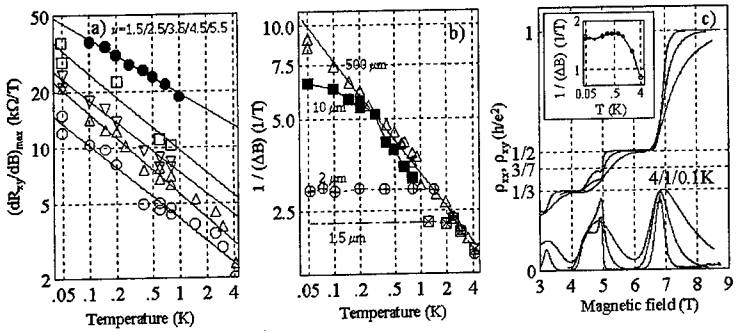

Fig. 2. (a) Temperature scaling of the slope of the Hall resistance in-between the plateaus in structure B (full symbols) and C (open symbols). (b) Temperature scaling of longitudinal resistivity ρ_{xx} for different widths of wires made of structure A (full symbols) and C (open symbols) (c) Hall ρ_{xx} and ρ_{xy} for the structure B with uniformly introduced Mn ions. Inset shows a breakdown of scaling for ρ_{xx} maximum at fractional occupation $\nu \approx 7/3$.

both even and odd filling factors up to $\nu \geq 11$. (at $T = 1.5$ K). At the same time, in the case of the nonmagnetic heterostructure, odd plateaus are resolved only up to $\nu = 3$. This indicates a strong spin polarization of 2D electron gas in the magnetic sample due to the *s-d* exchange interaction with the Mn spins. Thus, the Mn spins influence electron transport, despite their non-uniform distribution in the QW.

As it is shown in Fig. 2a, in the case of large 2D samples, the inverse width of the resistance peaks and the slope of the Hall resistance in between the plateaus, $1/\Delta B$, $\partial\rho_{xy}/\partial B$, respectively, obey the characteristic power law $T^{-\kappa}$, with $\kappa = 0.39^{+0.03}_{-0.06}$ for $7.5 \geq \nu \geq 1.5$ in the temperature range 4.2 K $\geq T \geq$ 50 mK. Our data demonstrate, therefore, that (i) κ is independent of ν and (ii) scaling is not affected by the presence of the magnetic ions. Indeed, in the magnetic field $g\mu_B B > k_B T$ the localized spins are expected to enhance the spin-splitting of the electronic states but not to contribute to their dephasing.

In Fig. 2b, the inverse width ΔB of the resistance peaks as determined at several temperatures for a wide $W = 0.5$ mm and narrow $W \approx 2$ μm, $W \approx 1.5$ μm channels, made of magnetic structure C, as well as for nonmagnetic $W \approx 10$ μm wide channel (structure A) are presented. It is seen that in the case of $W \approx 1.5$, 1, and 10 μm wires, Hall and longitudinal resistance becomes independent of temperature below $T \simeq 2$ K, $T \simeq 1$ K and $T \simeq 0.3$ K, respectively, as it is expected for small QHE samples. At the same time, as shown in the inset to Fig. 1b, the magnetoresitance reveals the presence of random but reproducible universal conductance fluctuations (UCF). Their amplitude increases with decreasing temperature down to the lowest temperature we have achieved without any indication of a saturation. Such a behavior of UCF demonstrates that the observed saturation in the temperature scaling of QHE is indeed a consequence of the size effect, not simply an effect of sample heating by the excitation current or external noise. This makes it possible to determine the

temperature dependence of L_φ from which we evaluate $p = 1.1 \pm 0.2$. This value, together with κ quoted above, leads to $\alpha = 2.5^{+0.3}_{-0.2}$. The latter is to be compared with the theoretical value $\alpha = 7/3 \approx 2.3(3)$ [15] as well as with $\alpha = 2.3 \div 3.3$ and, which result from previous size-scaling [13] and frequency studies [9, 10] of the QHE resistatances in GaAs/AlGaAs heterostructures. Our determination of α constitutes, therefore, an independent confirmation of the theoretical value.

In structure B that consists of an uniform $Cd_{0.98}Mn_{0.02}Te$ quantum well, an additional structure is observed at a fractional occupation $\nu \approx 7/3$, as shown in Fig. 2c. In the vicinity of this surprising feature, the scaling saturates below $T > 500$ mK, as is commonly [13] observed for overlapping Landau levels. The origin of this novel phenomenon, particularly whether it results from FQHE or from the formation of charged strips [16, 17], is under study now.

The work was supported by KBN Grants 2-P03B-6411 and -11914 and PBZ-28.11.

References

[1] J. Jaroszyński *et al.*, *Phys. Rev. Lett.* **75**, 3170 (1995).

[2] J. Jaroszyński *et al.*, *Phys. Rev. Lett.* **80**, 5635 (1998).

[3] I.P. Smorchkova *et al.*, *Phys. Rev. Lett.* **78**, 3571 (1997).

[4] For a review on DMS, see, *e.g.*, T. Dietl, in Handbook on Semiconductors, eds. T.S. Moss, (North-Holland, Amsterdam, 1994) vol. 3b, p. 1251; J.K. Furdyna, *J. Appl. Phys.* **64** R29 (1988).

[5] D.E. Khmielnitskii, *JETP Lett.* **38**, 552 (1983).

[6] A.M.M. Pruisken, *Phys. Rev. Lett.* **61**, 1297 (1988).

[7] B. Huckestein, *Rev. Mod. Phys.* **67**, 357 (1995).

[8] H.P. Wei *et al.*, *Phys. Rev. Lett.* **61**, 1294 (1988).

[9] L.W. Engel *et al.*, *Phys. Rev. Lett.* **71**, 2638 (1993).

[10] W. Belitsch et al., *Physica B* **249-251**, 119 (1998).

[11] N.Q. Balaban, U. Meirav, and I. Bar-Joseph, *Phys. Rev. Lett.* **81**, 4967 (1998).

[12] J. Wakabayashi, M. Yamane, and S. Kawaji, *J. Phys. Soc. Jpn.* **58**, 1903 (1989).

[13] S. Koch *et al.*, *Phys. Rev. Lett.* **67**, 883 (1991); *Phys. Rev.* B**43**, 6828 (1991).

[14] G. Karczewski et al., *J. Crystal Growth* **184/185** 814 (1998).

[15] G.V. Milnikov and I.M. Sokolov, *JETP Lett.* **48**, 536 (1988).

[16] J.P. Eisenstein *et al.*, *Phys. Rev. Lett.* **68**, 1383 (1992).

[17] H.C. Manoharan *et al.*, *Phys. Rev. Lett.* **79**, 2722 (1997).

PB.49

Theory of Carrier Induced Ferromagnetism in $Mn_xGa_{1-x}As/GaAs$ Superlattices

T. Jungwirth[1,2], W.A. Atkinson[1], B.H. Lee[1], and A. H. MacDonald[1]

[1] Department of Physics, Indiana University, Bloomington, Indiana 47405
[2]Institute of Physics ASCR, Cukrovarnická 10, 162 00 Praha 6, Czech Republic

Abstract

We present a mean-field theory of free-carrier induced ferromagnetism in semiconductors. Our approach allows spatial patterning, free-carrier spin polarization, finite temperature, and free-carrier exchange and correlation to be accounted for self-consistently. The model is applied on a $Mn_xGa_{1-x}As/GaAs$ superlattice with alternating ferromagnetic and paramagnetic layers and we demonstrate the possibility of semiconductor magnetoresistance systems with designed properties.

The challenge of exploiting synergies between semiconductors and ferromagnetic materials has led to interest in fabricating hybrid systems. Recent advances [1]-[6] in growth and control of diluted magnetic semiconductors open up a plethora of intriguing possibilities for engineered electronic properties. Since these will generally involve spatial patterning of dopant and magnetic ion densities, their description requires a theory of free-carrier induced ferromagnetism in semiconductors appropriate to inhomogeneous systems. We present such a theory and apply it to the case of layered structures which mimic metallic giant-magnetoresistance multilayers [7].

The systems in which we are interested are described by Hamiltonians of the form

$$\mathcal{H} = \mathcal{H}_m + \mathcal{H}_f - J_{pd}\sum_{i,I}\vec{S}_I \cdot \vec{s}_i\delta(\vec{r}_i - \vec{R}_I). \tag{1}$$

Here $\mathcal{H}_m$ is the Hamiltonian of localized spins $\vec{S}_I$, located at positions $\vec{R}_I$, $\mathcal{H}_f$ is the Hamiltonian of a semiconductor free-carrier system described using an envelope function language and including interactions of carriers with a random disorder potential and with other carriers. We assume here that the semiconductor of interest has a single parabolic band; the formalism is readily generalized to multi-band situations which will often be of practical interest. The last term on the right-hand side of Eq. (1) represents the exchange interaction [8] between $\vec{S}_I$ and free-carrier spins $\vec{s}_i$ which is responsible for the novel physics.

In spin-density functional theory practical self-consistent field calculations for inhomogeneous interacting fermions are made possible by the Kohn-Sham separation of the electronic free energy into single-particle, electrostatic and exchange-correlation pieces. The development here is standard apart from the introduction of an additional spin-dependent effective potential corresponding to the interaction between free-carrier and localized spins. We find that the equilibrium free-carrier spin densities and the mean value of the localized spin quantum numbers on each site can be determined by solving self-consistently a free-carrier single-particle Schrödinger equation

$$\left[-\frac{\nabla^2}{2m^*} + V_\sigma(\vec{r})\right]\psi_{k,\sigma}(\vec{r}) = \varepsilon_{k,\sigma}\psi_{k,\sigma}(\vec{r}) \tag{2}$$

with a spin-dependent potential

$$V_\sigma(\vec{r}) = v_{conf}(\vec{r}) - \frac{\sigma}{2} h_{pd}(\vec{r}) \ , \quad h_{pd}(\vec{r}) = J_{pd} \sum_I \delta(\vec{r} - \vec{R}_I) \langle m_I \rangle \ , \tag{3}$$

where $v_{conf}(\vec{r})$ is the envelope function external potential [9, 10] including band edge and ionized impurity contributions, and the free-carrier Hartree and spin-dependent exchange-correlation potentials. $h_{pd}(\vec{r})$ is the exchange-coupling field with the mean-field localized-spin moment $\langle m_I \rangle = S B_S(b_I S)$ and S is the spin quantum number of each localized moment. The argument of the Brillouin function B_S [11] represents an effective field which is proportional to the free-carrier magnetization $m(\vec{r})$: $b_I = J_{pd} m(\vec{R}_I)/2k_BT$.

Once the band edge and ionized and magnetic impurity profiles have been specified, Eqs. (2) and (3) can be used to solve for the sytem's equilibrium properties. As an illustration of our approach, we consider a $Mn_xGa_{1-x}As/GaAs$ superlattice with magnetic impurities in alternate layers. We look for two different self-consistent solutions of Eqs. (2) and (3), a ferromagnetic (F) one with parallel ordered moments in all Mn-doped regions, and a solution with an antiferromagnetic (AF) alignment of adjacent magnetic layers. The interlayer exchange coupling E_c, is defined as the difference in energy between AF and F-states per area per $Mn_xGa_{1-x}As$ layer and is expected [12] to oscillate with GaAs spacer width. In Fig. 1 we present numerical results for E_c as a function of a dimensionless parameter $2d\overline{k}_F$ where $\overline{k}_F$ is the Fermi wavevector corresponding to the average 3D density of free carriers in the superlattice with a period d. The system we consider has 2 nm thick p-type $Mn_xGa_{1-x}As$ layers with Mn concentration 10^{21} cm^{-3}, homogeneously distributed ionized impurities that neutralize free-carrier charge, $S = 5/2$, $J_{pd} = 0.15$ eV nm^3, and hole mass $m^* = 0.5m_e$. The temperature was set to $k_BT = 1$ meV which corresponds to approximately one tenth of the Curie-Weiss temperature. Oscillations in the self-consistent exchange coupling are qualitatively consistent with simple RKKY model estimates [10, 12]; differences exist primarily because of the proximity induced spin-polarization in the nominally paramagnetic GaAs layers mentioned below. The amplitude of oscillations in E_c is $\sim 10\times$ smaller than in metallic systems [13] measured in absolute units and $\sim 10\times$ larger if energy is measured relative to the Fermi energy of free carriers. In order to achieve substantial exchange coupling in experimental systems it will be important to limit disorder scattering in the GaAs layers.

Our mean-field calculation also yields information on the localized and free-carrier spin magnetization densities and on the spin-split bands of the free-carrier system. This information provides a starting point for building a theory of electronic transport. Numerical results for the above $Mn_xGa_{1-x}As$ superlattice with $d = 3.5$ nm and $\overline{k}_F = 1.4$ nm^{-1} (corresponding to average density 10^{20} cm^{-3}) are summarized in Figs. 2 and 3. In the top panels of Fig. 2, the chemical potential and the effective potentials for spin-up and spin-down free carriers (see Eq. (2)) are plotted as a function of z over a AF configuration unit cell. All energies here and below are measured from the spatial average of the electrostatic potential. The potentials V_σ have similar shapes in F and AF cases, except for the reversed order for up and down spins in the right Mn-doped layer. Note that in this example, confinement of carriers in the magnetic layers is due entirely to the exchange potential produced by magnetic order. The localized (middle panels) and itinerant (lower panels) spin systems reach 100 % polarization in the Mn-doped layers at the temperature and carrier density for which these

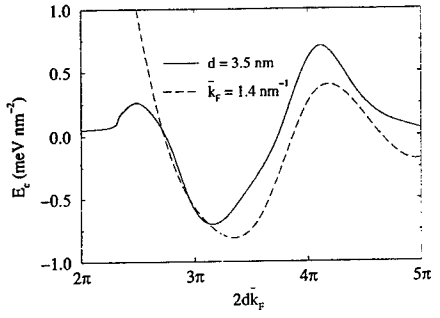

Fig. 1: Interlayer exchange coupling at fixed Mn-undoped GaAs spacer thickness (solid line) and at fixed average density of free-carriers (dashed line). Results are plotted as a function of dimensionless parameter $2d\bar{k}_F$.

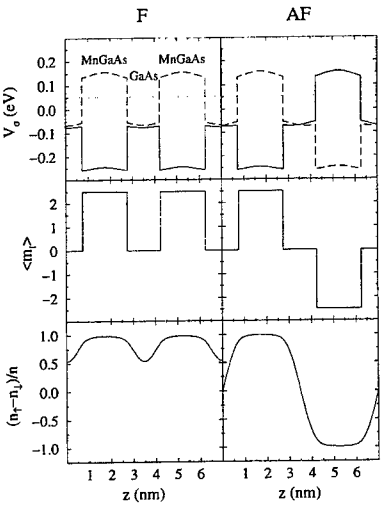

Fig. 2: Self-consistent results plotted within the unit cell of the $Mn_zGa_{1-z}As/GaAs$ superlattice. From top to bottom: i) effective potentials from Eq. 2 for up (solid lines) and down (dashed lines) spin free-carriers (the dotted line here indicates the chemical potential); ii) mean-field localized spin moment; iii) free-carrier relative spin-polarization.

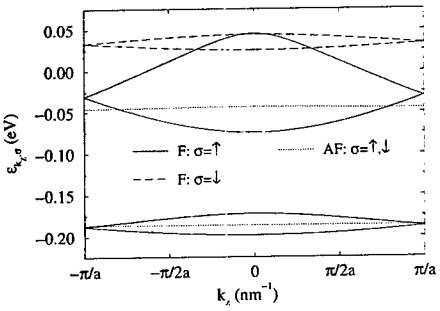

Fig. 3: Partially occupied energy minibands in F-state for spin-up (solid line) and spin-down (dashed line). In the AF-state both spins (dotted line) have the same minibands. The chemical potential is 0.053 eV and a=7 nm is the unit cell length.

calculations were performed. The itinerant system spin-polarization is large in the layers free of magnetic impurities, especially so in the F-state case.

Fig. 3 shows occupied minibands in the superlattice Brillouin zone. In the F-state spin-up and spin-down minibands are split by about 0.25 eV. There is no spin-splitting in the AF-state since the effective potentials $V_\uparrow$ and $V_\downarrow$ differ by a rigid shift in the $\hat{z}$ direction.

The miniband dispersion is much weaker in the AF case because the barriers separating two adjacent minima in the effective potential are twice as thick and high as in the F case. Since the conductance is approximately proportional to the square of the largest miniband width in either coherent or incoherent transport limits, the minibands can be used to estimate the size of the current-perpendicular-to-plane (CPP) magnetoresistance effect. For the case illustrated, the AF state CPP conductance will be three orders of magnitude smaller than the F state CPP conductance. The large difference is expected since the bulk $Mn_xGa_{1-x}As$ bands are half-metallic for these parameters. In general we predict strong CPP magnetoresistance in $Mn_xGa_{1-x}As/GaAs$ multilayer systems if the AF state can be realized.

The authors acknowledge helpful interactions with D.D. Awaschalom, J.K. Furdyna. and E. Miranda. This work was supported by the National Science Foundation under grants DMR-9623511, DMR-9714055 and INT-9602140, by the Ministry of Education of the Czech Republic under grant ME-104 and by the Grant Agency of the Czech Republic under grant 202/98/0085.

References

[1] H. Ohno, Science **281**, 951 (1998); H. Matsukura *et al.*, Phys. Rev. B **57**, R2037 (1998); H. Ohno *et al.*, Appl. Phys. Lett. **69**, 363 (1996); H. Ohno *et al.*, Phys. Rev. Lett. **68**, 2664 (1992).

[2] S. Koshihare *et al.*, Phys. Rev. Lett. **78**, 4617 (1997).

[3] A. Van Esch *et al.*, Phys. Rev. B bf 56, 13103 (1997).

[4] T. Story *et al.*, Phys. Rev. Lett. **56**, 777 (1986).

[5] A. Haury *et al.*, Phys. Rev. Lett. **79**, 511 (1997); I.P. Smorchkova *et al.* Phys. Rev. Lett. **78**, 3571 (1997).

[6] T. Dietl, A. Haury, and Y. Merle d'Aubigné, Phys. Rev. B **55**, R3347 (1997).

[7] B. Heinrich and J.A.C. Bland, *Ultrathin Magnetic Structures*, Vol. 2 (Springer, Berlin, 1994).

[8] J.K. Furdyna, J. Appl. Phys. **64**, R29 (1988); *Semimagnetic Semiconductors and Diluted Magnetic Semiconductors*, edited by M. Averous and M. Balkanski (Plenum, New York, 1991); T. Dietl in *Handbook on Semiconductors*, Chap. 17 (Elsevier, Amsterdam, 1994).

[9] G. Bastard, *Wave Mechanics Applied to Semiconductor Heterostructures* (Les Éditions de Physique, Paris, 1990).

[10] T. Jungwirth *et al.*, Phys. Rev. B **59**, 9818 (1999).

[11] A. Aharoni, *Introduction to the theory of ferromagnetism* (Clarendon Press, Oxford, 1996).

[12] A. Yfet, Phys. Rev. B **36**, 3948 (1987).

[13] Discrepancies exist between experimental and ideal theoretical values of E_c in metallic systems, partly because of interface roughness effects (J. Kudrnovsky *et al.*, Phys. Rev. B **53**, 5125 (1996)). This comparison with metallic systems is based on E_c values for Fe/Au/Fe triplelayers where good agreement is found between theory and experiment: J. Ugrundis *et al.*, Phys. Rev. Lett. **79**, 2734 (1997).

PB.50

An Experimental and Theoretical Study of the Electron Spin Resonance Mechanism in AlGaAs/GaAs

R.Meisels[1], F.Kuchar[1], M.Kriechbaum[2]

[1] Department of Physics, University of Leoben, A-8700 Leoben, Austria
FAX: +43 3842 402 760, Email: meisels@unileoben.ac.at
[2] Institute for Theoretical Physics, University of Graz, A-8010 Graz, Austria

Abstract

The electron spin resonance of the 2DES in AlGaAs/GaAs is investigated at millimeterwave frequencies and is shown to be dominantly a magnetic dipole transition. Strain induced contributions to the electric dipole transition rate can be neglected. The origin of the change of the resistance due to the ESR (millimeterwave photo-conductivity) is found to be a redistribution of the electrons in the lower spin level. From a line shape analysis and a comparison with spin-flip experiments we conclude that the ESR line width is determined by the life time in the upper spin level.

Introduction

In the past, the electron spin resonance (ESR) has been used to investigate spin related properties of conduction electron systems of different dimensionality from 3D to quasi-0D [1, 2, 3, 4, 5, 6]. Spectral ranges to be used extend from microwaves for GaAs with the effective g-factor $g^* \approx -0.4$ to the far-infrared for InSb with $g^* \approx -50$. In this paper we report on an experimental and theoretical study of the ESR of the two-dimensional electron system in AlGaAs/GaAs at millimeterwave (mmw) frequencies. Our new results presented here concern the ESR oscillator strength, the detection mechanism, and the ESR line width.

Experimental

The experiments have been performed on the two-dimensional electron system (2DES) of a $Al_{0.35}Ga_{0.65}As/GaAs$ heterostructure with [001] growth direction at $T = 1.6$K ($n_s = 1.4 \times 10^{11}\text{cm}^{-2}$, $\mu = 0.8 \times 10^6\text{cm}^2/\text{Vs}$). The magnetic field range of 7 - 10.7 T corresponds to filling factors of the lowest Landau level between 0.8 and 0.55. The ESR is observed by a photo-conductivity technique [5, 8]. The longitudinal resistance component R_{xx} and its change ΔR_{xx} caused by the mmw radiation are measured using a double lock-in technique. The sample is placed in a rectangular waveguide (U-band, 40 - 60 GHz). A typical ESR photo-conductivity result is shown in Fig.1. The signal increases linearly with the mmw power ($\leq$ 5mW incident) without a change of the shape within the noise. The ESR signal sits on a background signal. Both have the same polarity regardless if positive or negative (depending on magnetic field). The polarity ΔR_{xx} corresponds to the change of R_{xx} with lattice temperature. The half width of the ESR signal is about 0.05 T with no significant dependence on magnetic field.

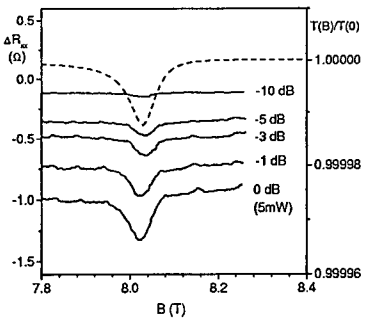

Figure 1: Photo-conductivity signal vs magnetic field B measured at different incident power levels (solid curves). $f = 43$GHz. For comparison of the line shapes a calculated transmission curve is also shown (dashed).

Theory

A $\mathbf{k}\cdot\mathbf{p}$ perturbation calculation is performed using 8 conduction and valence bands[9]. The contributions of higher bands (k^2-terms) are neglected for the electromagnetic transition matrix elements while taken into account for the calculated energies.The confinement of the 2DES is approximated by a triangular potential $V(z) = eFz$. For the consideration of effects specific for conduction band electrons, the 8×8 Hamiltonian is reduced to a 2×2 Hamiltonian perturbatively.

To investigate the processes responsible for the ESR we consider the single-electron Hamiltonian: $\mathbf{H_0} + \mathbf{H_{EDT}} + \mathbf{H_{MDT}}$. $\mathbf{H_0}$ is the unperturbed single-electron Hamiltonian. $\mathbf{H_{EDT}} = \mathbf{A}\cdot\mathbf{j}$ describes the interaction with the electromagnetic field for electric dipole transitions and $\mathbf{H_{MDT}} = g_0\mu_B\sigma\cdot\mathbf{B}/2$ for magnetic dipole transitions. $\mathbf{A}$ is the vector potential of the exciting electromagnetic wave and $\mathbf{B} = \nabla\times\mathbf{A}$ its magnetic field. μ_B is the Bohr magneton and g_0 the free electron Landé factor (=2).

The ESR transition amplitudes are defined by the matrix elements of $\mathbf{H_{EDT}}$ and $\mathbf{H_{MDT}}$. Both EDT and MDT require a CRI polarization (opposite to that of the cyclotron resonance) for the spin-up ($i\uparrow$) to spin-down ($f\downarrow$) transition (notation for electrons in GaAs, i ... initial, f ... final state). This yields for the EDT:

$$
\begin{aligned}
&< f\downarrow|\mathbf{j}\cdot\mathbf{A}_{CRI} \;|\; i\uparrow> /eA_0 = \\
&\frac{P^2}{3\hbar}\left\{ \int \phi_f^*\frac{1}{i}\frac{\partial}{\partial z}\phi_i dz\left(-\frac{1}{E_i+E_g}+\frac{1}{E_i+\Delta+E_g}\right)\right. \\
&\qquad \left. +\int\left(\frac{1}{i}\frac{\partial}{\partial z}\phi_f\right)^*\phi_i dz\left(\frac{1}{E_f+E_g}-\frac{1}{E_f+\Delta+E_g}\right)\right\} \\
&+\frac{\sqrt{6}PiC_2\epsilon_{xy}}{9\hbar}\left\{ \int \phi_f^*\phi_i dz\left(\frac{1}{E_i+E_g}-\frac{1}{E_i+\Delta+E_g}\right.\right.
\end{aligned}
$$

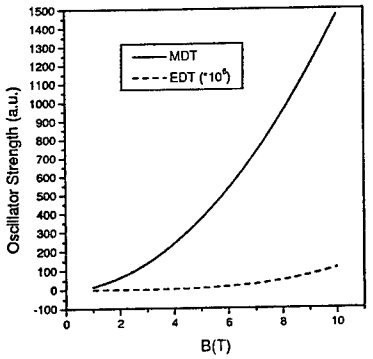

Figure 2: Calculated oscillator strengths for the MDT and EDT. F = 14kV/cm, E_g = 1.519eV, P = 10.493eVÅ, Δ = 0.171eV, ϵ =13.1.

$$-\frac{1}{E_f+E_g}+\frac{1}{E_f+\Delta+E_g}\Big)\Big\} \tag{1}$$

and for the MDT:

$$< f\downarrow|g_0\frac{\mu_B}{2}\sigma\cdot \mathrm{B}_{CRI}|i\uparrow> /eA_0 = \frac{g_0\hbar}{4m_0}\frac{\sqrt{\epsilon}\,\omega_{ESR}}{c}\int \phi_f^*\phi_i dz \tag{2}$$

The first term in Eq. (1) is caused by nonparabolicity. It vanishes for negligible spin-orbit splitting Δ. The second term is induced by strain (ϵ_{xy}) and appears in crystals without inversion symmetry. E_g is the energy gap, E_i and E_f are the energies of the initial and final states relative to the conduction band edge. m_0 is the free electron mass and ϵ the dielectric constant. ϕ_f (=$\phi_\downarrow$) and ϕ_i (=$\phi_\uparrow$) are the envelope functions in the triangular potential [10].

Discussion

Previous experiments [7, 8] have shown that the ESR of electrons in AlGaAs/GaAs is a single-electron transition with the transition energies exactly described within the theory presented above. As regards the oscillator strength there are magnetic and electric dipole contributions. The latter one can be enhanced by strain caused by the lattice mismatch of the layers in a heterostructure. In AlGaAs/GaAs, however, this mismatch is very small (about 0.04%). Furthermore, for the [001] growth direction of our sample there are no off-diagonal strain components ($\epsilon_{xy} = \epsilon_{yz} = \epsilon_{zx} = 0$). Therefore, the contribution containing ϵ_{xy} in Eq. (1) can be neglected. The results of the calculation are displayed in Fig.2. The large ratio of the oscillator strengths MDT/EDT (e.g. 2×10^7 at 8 T) shows that the ESR is predominantly a magnetic dipole transition in accordance with experimental observations [8]. In [8] we have shown that the strength of the ESR is correlated with the magnetic field strength of the electromagnetic wave.

Until now, the ESR of electrons in AlGaAs/GaAs could be observed in photo-conductivity experiments only. For a discussion of the observability we compare the oscillator strength of the ESR with that of the cyclotron resonance (CR). Using Eq. (2) for the ESR (with $\int \phi_f^* \phi_i dz = 1$) and $\hbar n_r / l_c m_0$ for the CR oscillator strength, the ESR/CR ratio is given by: $g_0 l_c \omega_{ESR}/4c$. $\omega_{ESR} = g^* \mu_B B$ is the resonance frequency, $n_r = \sqrt{\epsilon}$ is the refractive index, l_c is the magnetic length. For electrons in AlGaAs/GaAs the ratio is as low as 4×10^{-6} at $B = 8$ T. This is most likely the reason that the ESR could not be observed in a transmission or cavity experiment.

When calculating the transmission [11] and trying to reproduce the line width of our photoconductivity signal (Fig.1) we have to use a value of 1 ns for the relaxation time. This value agrees with the spin-flip time deduced from the scattering rate of hot electrons [12]. In that experiment quantum point contacts were used to inject hot electrons into the upper spin level and to detect the scattering into the lower one. This relaxation mechanism is equivalent to the mechanism determining the lifetime in the upper spin level of the ESR experiment and therefore the width of the resonance transition.

We finally discuss the mechanism producing the photo-conductivity signal ΔR_{xx}. Under our experimental conditions we estimate that about 2×10^6 spins are redistributed, i.e. a relative change of about 4×10^{-5}. However, $\Delta R_{xx} \approx 10^{-4} - 10^{-3}$ in the experiment. Even a strong difference in the electron mobilities of the spin-split levels (localized and delocalized states, resp.) would cause a change of the conductivity much smaller than observed. We therefore consider a change of the electron distribution within the ground state of the 2DES which can be assumed to be the mechanism for the non-resonant background signal. It can also explain the resonant ESR signal where after the resonant absorption relaxing electrons transfer energy and produce an increase of the average energy of the 2DES. This increase of the average energy is expected to have a similar effect on the resistance for resonant as well as non-resonant absorption, including the sign of ΔR_{xx}. This expectation agrees with the experimental observations, viz. the same sign of ΔR_{xx} for the resonant and for the non-resonant signal near the resonance. The interpretation is also supported by the observation that ΔR_{xx} has the same sign when the increase of the average energy is achieved by an increase of the lattice temperature.

Acknowledgments

This work has been supported by the European Union (TMR FMRX-CT98- 0180) and the "Fonds zur Förderung der wissenschaftlichen Forschung", Austria (P12024-PHY). The MBE-AlGaAs/GaAs samples were supplied by the Deutsche Telekom, Darmstadt.

*

References

[1] B.D.McCombe, R.J.Wagner, Adv. in Electronics and Electron Phys. **37**, 1; **38**, 1 (1975).

[2] F.Kuchar et al., Springer Lecture Notes in Physics **177**, 309 (1983).

[3] M.Seck, M.Potemski, and P.Wyder, Phys. Rev. B **56**, 7422 (1997).

[4] M.Dobers, K.v.Klitzing, G.Weimann, Phys. Rev. B **38**, 5453 (1988).

[5] R.Meisels et al., Surf. Sci. **361/362**, 55 (1996).

[6] R.H.Blick et al., Phys. Rev. B **57**, R12685 (1998).

[7] R.Meisels et al., Proc. 23th ICPS, Berlin, 1996, p.2487.

[8] R.Meisels, F.Kuchar, M.Kriechbaum, Phys. Rev. B (submitted).

[9] G.Lommer, F.Malcher, U.Rössler, Phys. Rev. **B 32**, 6965 (1985).

[10] T.Ando, A.B.Fowler, F.Stern, Rev. Mod. Phys.**54**, 437 (1982).

[11] A.Kennedy et al., Sol. St. Comm. **18**, 275 (1976). For a correction see [8].

[12] B.W.Alphenaar, H.O.Müller, and K.Tsukagoshi, Phys. Rev. Lett. **81**, 5628 (1998).

PB.51

Coherence in real space: the transition range from bulk to confined states studied by the Franz-Keldysh effect

H.J. Kolbe, C.Agert, W. Stolz and G. Weiser
Department of Physics and Material Sciences Center, Philipps-Universität, Renthof 5, 35032 Marburg, Germany

Abstract

The reduction of the thickness of samples to less than the mean free path in bulk material leads to confinement effects which can be resolved as deviation of field modulated spectra from the Franz-Keldysh effect of bulk samples. We demonstrate such changes in a 100nm thick GaInAs layer by using differential electroabsorption spectroscopy. The confinement effects are best seen at small fields and lead to reduction of the range of Franz-Keldysh oscillations, the appearance of oscillations related to the Quantum Confined Stark Effect at higher energy and finestructure of Franz-Keldysh oscillations near the gap. These features are reproduced by model calculations based on envelope functions.

PACS:: 78.20.Jq, 78.66-w, 73.20.Fz
Keywords: Modulation spectroscopy, coherence length, Quantum Well, electrooptical effects

The transition from the continuum of bandstates to discrete states of quantum wells occurs when the thickness of a sample becomes less than the coherence length which is equivalent to the mean free path of electron hole pairs. This critical length has been derived for GaInAsP alloys from the range of Franz-Keldysh oscillations in electroabsorption spectra and is as large as 150nm in ternary samples at low temperatures [1]. By comparing samples of different thickness it has recently been shown that deviation from the Franz-Keldysh effect is evident in 100nm thick layers while 200nm thick samples show spectra which agree perfectly with those of much thicker samples [2]. We investigate the relationship of the quantum confined Stark effect (QCSE) and the Franz-Keldysh effect (FKE) by comparing experimental spectra at 20K at different fields with calculations based on the envelope approximation.

The sample, 100nm $Ga_{0.47}In_{0.53}As$ with 450nm thick undoped InP barriers, was grown by MOVPE on the n-doped InP substrate using the compounds TBAS (tertiary butyl As) and TBP (tertiary butyl P) which are less hazardous than arsine and phosphine [3]. The sample was placed in a He flow cryostat and a dc voltage applied between substrate and a semitransparent Pt contact on top sets the field in the sample which was modulated by a small square voltage of ±0.1V. Such differential electroabsorption spectroscopy resembles the widely used photomodulation, however, it provides better control of the field than partial screening of a built-in field by photoexcited carriers. The change $\Delta\alpha$ of the absorption constant is derived from the relative change of the transmitted intensity and the sample thickness d.

Eigenstates are calculated by the tunneling resonance method [4]. The absorption is proportional to the spatial overlap of electron and hole envelope functions and the resulting spectrum is broadened by a Gaussian of 4meV width. The modulated spectra are derived as difference of absorption spectra at the respective fields. Coulomb interaction is ignored because for the fields considered bound exciton states have vanished while the small field modulation has no effect on the Coulomb enhancement [5].

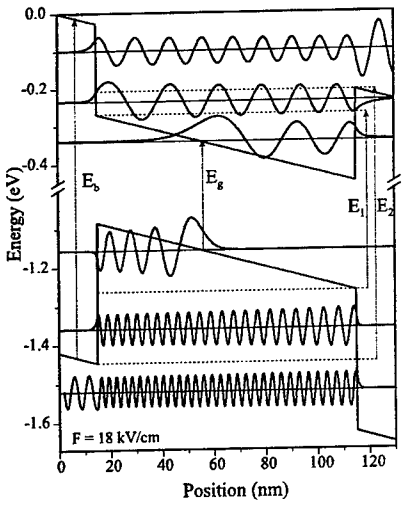

Fig.1: Envelope functions of electrons and heavy holes in a field of 18kV/cm. The quantum number of the corresponding state corresponds to the number of peaks.

Fig. 1 shows envelope functions in a field of 18kV/cm. The 64 confined states of heavy holes and the 17 electron states in the 100nm thick well are mixed by the field F to states of three distinctly different types. The spectrum above the gap of the well material, E_g, and below $E_1=E_g+eFd$ is dominated by transitions between electron and hole states which start at the bottom of the respective well. The wavefunctions are Airy functions, the eigenstate of a free particle state in a constant field. In bulk material an infinite number of such states exist which differ only by their starting point in real space. Confinement by the barrier limits their number and the eigenstates differ by a finite displacement x with respect to each other which results in an energy splitting eFx in the external field. Except for a finite number of states the absorption and $\Delta\alpha$ spectra below E_1 are determined by Airy functions as in bulk material. If energy levels are closely spaced as in wide wells, the discreteness of the spectrum is smeared out and the electroabsorption spectrum should reproduce all features of the Franz-Keldysh effect [6].

In the region between E_1 and $E_2=E_b$-eFd a second type of wavefunctions dominates. They are quantum confined states of high quantum number which extend to both barriers and respond to the field by the QCSE. For fields larger than 30kV/cm for this particular sample the QCSE should disappear because E_1 exceeds E_2. The transition between the two effects, FKE and QCSE, occurs not sharply at E_1 because near that energy transitions between Airy functions and quantum confined states contribute to absorption too but this contribution decreases with the smaller size of the Airy functions deeper in the well. Above E_2 the absorption is dominated by states which are no longer confined to the well. Transitions involving these states are omitted in modeling because of difficulties in appropriate normalization.

Experimental spectra are shown in fig.2. For the highest field, 46.4kV/cm, E_1 exceeds E_2 and all confined states are Airy functions. This spectrum shows many Franz-Keldysh oscillations with beat due to interference of heavy and light hole transitions [5]. Peak positions E_n and peak numbers n obey eq.1 which is unique to overlapping Airy functions and thus identifies Franz-Keldysh oscillations and yields the field in the sample for $m^*/m_0=0.038$.

$$\left(E_n - E_g\right)^{3/2} = \frac{3ehF}{8\sqrt{m^*}}n \qquad (1)$$

This relation is valid at the highest field for most of the spectral range as shown in fig.3a. Small deviations occur near peak number 30, about 450meV above E_g. The range $\delta E=eFL$ of Franz-Keldysh oscillations corresponds to the energy which an electron hole pair gains in the field F before a collision destroys the coherence of the pair state. The value $\delta E=450$meV yields a

coherence length L=97nm in agreement with the limitation of pair states by the width of the well. The discrete electronic structure is washed out by the strong field and the reduction of the coherence length is the only hint to carrier confinement.

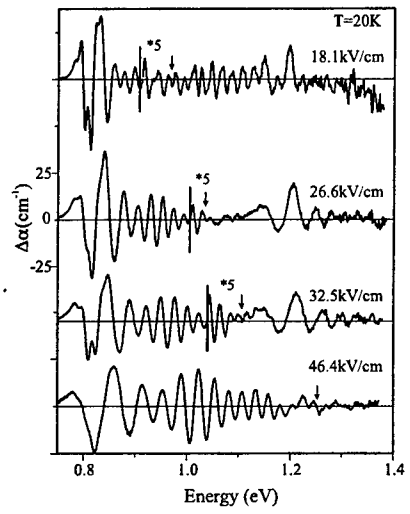

Fig. 2: Experimental spectra for different fields. The arrows mark the begin of deviations from the scaling law of Franz-Keldysh oscillations. Part of the spectra is enlarged by the given factors.

Spectra at lower fields confirm the reduced coherence length by their smaller range of Franz-Keldysh oscillations. Above 1.2eV the FKE of the split-off band is observed which at high field is hidden under the series of the fundamental gap. A new feature is the splitting of the first oscillations near the gap which is also observed in some photomodulated spectra [7]. We attributed this finestructure to the lowest electron and hole states confined by the field to the corner of their well [2]. However, inspection of the envelope functions reveals that not only such interface states but all electron Airy functions contribute to the finestructure. Due to the small influence of the barrier most transitions between pairs of electron and hole Airy functions, like the one shown in fig.1 at E_g, are near degenerate. Since due to their larger mass heavy holes states are less displaced with respect to each other than electron states. Each electron Airy function overlaps with several hole states at the top of the valence band. It is the splitting between these hole states, eFx, which causes the finestructure of the Franz-Keldysh peaks near the gap and reveals the discrete electronic structure. The finestructure is best resolved in weaker fields when mixing of the discrete states by the field is reduced.

For the lowest field numerous oscillations appear beyond E_1, the limit for Franz-Keldysh oscillations. These peaks do not obey eq.1 and are attributed to the quantum confined states higher up in the well in agreement with the model calculations. They again are better resolved when mixing by the field is not too strong. Fig.3b shows the calculated peak positions. The first peaks involve states at the bottom of the well and obey the scaling of Franz-Keldysh oscillations. Consistent with the experimental data deviations occur near E_1 when the absorption is no longer dominated by the Airy functions but by wavefunctions which reach both barriers.

The calculated spectra in fig.4 identify each excited pair in the spectrum and reproduce all details of the experimental spectra: the finestructure near the gap, the oscillations due to the FKE of states at the bottom of the well and, if the field is sufficiently small, also oscillations due to the QCSE of states high up in the well. Since light holes are not included the beating in the experimental spectra is not reproduced. The calculated spectra include only eigenstates confined to the well and do not include their spatial overlap with resonant states above the barrier. The calculated states therefore end at E_2 at low field and at E_1 when E_1 is larger.

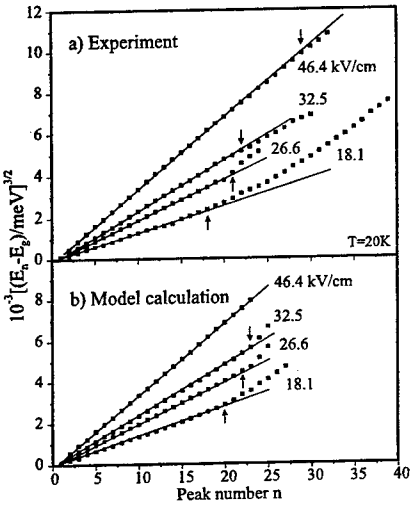

Fig.3: Peak position versus peak number to identify the range of the Franz-Keldysh effect.

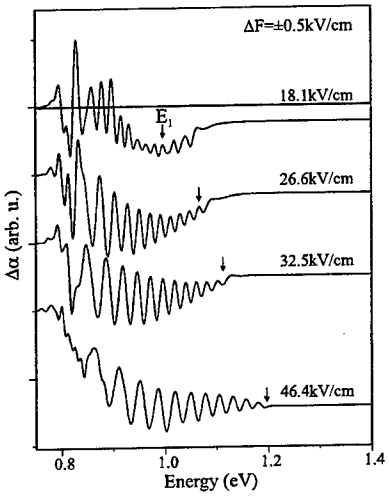

Fig.4: Electroabsorption spectra calculated from the spatial overlap of confined states.

Since the field mixes quantum confined states the optical selection rule which requires the same quantum number for electron and hole envelope function is no longer valid and oscillator strength is transferred from allowed to forbidden transitions. This redistribution includes also the resonant states above the barrier. The neglect of coupling to these resonant states which increases with field strength causes loss of oscillator strength of confined states in the calculation which shifts the baseline down in contrast to the experimental spectra.

In summary we have shown that 100nm thick ternary layers show clear confinement effects and are in fact broad quantum wells. The discreteness of the electronic structure is best seen at low field and is washed out in high fields.

This work has been supported by the Deutsche Forschungsgemeinschaft (SFB 383)

References

1. A. Jaeger, G. Weiser, P. Wiedemann, I. Gyuro, and E. Zielinski, J.Phys. Condens. Mater. **8**, 6779 (1996)
2. H.J. Kolbe, C. Agert, W. Stolz, and G. Weiser, to be published in Phys. Rev. B
3. H. Protzmann, F. Höhnsdorf, Z. Spika, W. Stolz, E.O. Göbel, M. Müller, and J. Lorberth, J. Crystal Growth **170**, 155 (1997)
4. D.C. Hutchings, Appl. Phys. Lett. **55**, 1082 (1989)
5. A. Jaeger and G. Weiser Phys. Rev. B **58** (1998), 10674
6. D.A.B. Miller, D.S. Chemla and S. Schmitt-Rink, Phys. Rev. B **33**, 6976 (1986)
7. B.T. Jonker, O.J. Glembocki, R.T. Holm, and R.J. Wagner, Phys. Rev. Lett. **79**, 4886 (1997)

Ultrafast Coherent Spectroscopy of the Fermi Edge Singularity

Diego Porras, J. Fernández-Rossier and C. Tejedor
Departamento de Física Teórica de la Materia Condensada. Universidad Autónoma de Madrid. Cantoblanco, 28049 Madrid. Spain

Abstract

In this work we present a theoretical description of the transient response of the Fermi Edge Singularity (FES). We study the linear and the nonlinear response of an n-doped QW to laser pulses in the Coherent Control (CC) and Four Wave Mixing (FWM) Configurations. By means of a bosonization formalism we calculate the FWM signal emitted by the sample when it is excited by pulses spectrally peaked around the FES and we show that the long time behavior of the nonlinear signal is very similar to the linear case.

Keywords: Fermi Edge Singularity, Coherent Control, Four Wave Mixing, Bosonization, GaAs Quantum Wells.

1 Motivation

The promotion of an electron from a localized state in a valence band (VB) to an empty state in a partially filled conduction band (CB) is accompanied by a dynamical response of the Fermi gas. The enhancement of the absorption probability when the new electron is promoted just above the Fermi energy is known as the Fermi Edge Singularity (FES)[1]. This phenomena has been experimentally observed, by means of continuous wave (CW) spectroscopy, both in metals[1] and doped semiconductors[2]. FES is understood as a consequence of the appearance of a *coherent* gas of low energy collective excitations of the Fermi gas due to both the sudden appearance of the localized hole and the new electron. It has been shown [3] that these collective excitations can be considered as Tomonaga bosons which are in a Glauber coherent state.

In this paper we propose two types of transient coherent experiments, Coherent Control (CC) and Four Wave Mixing (FWM) in doped Quantum Wells, in order to address the following questions: *i)* Can be these Tomonaga bosons coherently controlled? *ii)* How is the decay of the Tomonaga bosons coherence? and *iii)* What is the nonlinear response of the FES ? In this context, pump and probe experiments have been suggested for the transient spectroscopy of the FES [4]. The experience acquired in the case of undoped samples shows that both CC [5] and FWM [6] are precise and conceptually simple tools to probe excitonic coherence and nonlinearity. We propose to excite an n-doped QW with laser pulses which promote electrons from localized states in the VB to the Fermi level in the CB. The spectral width of the laser pulses ($1/\Delta t$) must be much smaller than the Fermi energy ϵ_F so that the only intraband excitations are the Tomonaga bosons. Therefore, our theoretical approach is not valid to address the FWM experiment of Kim *et al.* [7].

2 Hamiltonian and Linear Response: Coherent Control

The problem of the linear response function of the FES was solved long time ago in a particularly simple way by a description of the Fermi Sea excitations in terms of bosonic operators[3]. If we consider that the photoexcited hole creates a spherical localized potential then the Hamiltonian is:

$$H = E_0\ d^\dagger d + \sum_{k=0}^{k_D} \epsilon_k a_k^\dagger a_k + \frac{V}{N} \sum_{k,k'=0}^{k_D} a_k^\dagger a_{k'} d^\dagger d \tag{1}$$

where E_0, $d^\dagger$ are the energy and creation operator of the localized hole, $a_k^\dagger$ are the creation operators of the electrons in the conduction band and k_D is the bandwidth [3]. Here we will only consider s-wave scattering, and reduce the initial problem to a 1-D one, so that the index k corresponds to the radial wave function index. The polarization induced in the sample by an electric field is described by the operator $P(t) = \mu\ a^\dagger d^\dagger + h.c.$, where $a = \sum_{k=0}^{k_D} a_k$ and μ is the dipole matrix element. The mean value of P(t) in the absence of dephasing can be calculated by means of the linear response function. For zero temperature ($T = 0$) we have:

$$\chi^{(1)}(t) \propto -i\ \mu^2 \theta(t) (i\epsilon_F t)^\alpha e^{-i\epsilon t} + h.c. \tag{2}$$

where ϵ is the FES resonance energy and $\alpha = (1 + V\rho)^2$ is the exponent of the singularity, with $\rho =$ the density of states at the Fermi surface. Let us consider now the CC of the linear response of the sample. The signal emitted is proportional to the polarization created by the incident laser. We will work in the Rotating Wave Approximation (RWA). If the laser pulse has the form $E(t) = E_A(t) + E_B(t) + h.c.$, with $E_A(t) = \mathcal{E}_A(t) e^{-i\epsilon t}$, $E_B(t) = E_A(t - \tau)$, and we approximate $\mathcal{E}_A(t)$ by a delta function, then this signal is, assuming $t >> \tau$:

$$F^{(1)} \propto -i(i\epsilon_F t)^\alpha (1 + e^{i\epsilon\tau}) + h.c \tag{3}$$

This quantity can be measured by means of the time integrated luminescence, as in the undoped case[5], and it turns out to be $I \propto |F^{(1)}|^2 \propto 1 + Cos(\epsilon\tau)$. Therefore, CC of the FES is possible. This can be understood as the interference of the electric dipole induced by the first pulse with that induced by the second pulse. Microscopically, Tomonaga bosons are being coherently controlled in much the same way than the CC of optical phonons[9].

3 Four Wave Mixing signal

In FWM experiments, the system is excited by two phase locked pulses having momenta $\mathbf{k_A}$ and $\mathbf{k_B}$ with $|\mathbf{k_A}| = |\mathbf{k_B}|$ and a relative delay τ. The excitation of electrons near the Fermi surface can be achieved by choosing pulses spectrally peaked around the FES resonance. For the FWM signal to be nonzero the polarization created by the first pulse has to survive the delay time τ until the arrival of the second pulse. This means that dephasing would result in an exponential decay of the FWM signal with a characteristic time T_2. In this paper we are interested in the behavior of the FWM signal when we excite around the FES in the absence of dephasing. We will show that this signal has an intrinsic potential decay, as in the case of the linear response function, something to be taken into account in the interpretation of the experiments.

We need to calculate the third-order contribution to the polarization induced in the sample, which is proportional to the FWM signal emitted in the $2\mathbf{k_B} - \mathbf{k_A}$ direction. We consider two pulses $E_{A,B}(t) = \mathcal{E}_{A,B}(t)e^{-i\epsilon t}$, where $\mathcal{E}_{A,B}(t)$ are the amplitudes of the pulses in the directions $\mathbf{k_A}$, $\mathbf{k_B}$ and $\epsilon = E_g + \epsilon_F$ is the FES resonance energy, E_g being the semiconductor gap. The FWM signal can be written in terms of the third-order response function:

$$F(t) = \int_{-\infty}^{t} dt_1 dt_2 dt_3 \; \chi^{(3)}(t-t_1, t-t_2, t-t_3) \; E_A^*(t_2) E_B(t_1) E_B(t_3) \tag{4}$$

By extending up to third order the usual perturbation scheme developed for obtaining the Kubo formula, one gets:

$$\begin{aligned} \chi^{(3)}(t) \;=\; -i \; [\; & \theta(t-t_1)\theta(t_1-t_2)\theta(t_2-t_3) \; \langle P(t)P(t_1)P(t_2)P(t_3)\rangle \\ & + \; \theta(t-t_1)\theta(t_1-t_2)\theta(t_2-t_3) \; \langle P(t_2)P(t_1)P(t)P(t_3)\rangle \;] + h.c. \end{aligned} \tag{5}$$

where the brackets $\langle\rangle$ mean thermal averages. Equation (5) has been obtained within the RWA in which the width Δt of each pulse is much larger than the period $\propto \epsilon^{-1}$ of the exciting light. Here we will also consider, for simplicity, delta pulses: $E_A(t) = E_A\delta(t)e^{-i\epsilon t}$, $E_B(t) = E_B\delta(t-\tau)e^{-i\epsilon(t-\tau)}$. This assumption does not imply a contradiction with the RWA: it is justified if the variations of the correlation functions are slow enough in a time interval Δt. In (5) only the second term takes a non-vanishing value. Our main task now is the calculation of the correlation function, for which the bosonization formalism is extremely useful. If we define H_i, H_f as the Hamiltonian without and with hole, respectively, then:

$$\langle P(t_2)P(t_1)P(t)P(t_3)\rangle = \mu^4 \langle e^{iH_i t_2} a e^{-iH_f(t_2-t_1)} a^\dagger e^{-iH_i(t_1-t)} a e^{-iH_f(t-t_3)} a^\dagger e^{-iH_i t_3}\rangle \tag{6}$$

If we assume that $\Delta t >> (\epsilon_F)^{-1}$, only excitations near the Fermi Edge will be relevant and we can use the Schotte[3] approach to reexpress this correlation function in the bosonization formalism:

$$\langle P(t_2)P(t_1)P(t)P(t_3)\rangle \propto \langle B^\dagger(t)B(t_1)B^\dagger(t_2)B(t_3)\rangle e^{-i\epsilon t} e^{i\epsilon(t_1-t_2+t_3)} \tag{7}$$

where $B^\dagger$ are operators that create a coherent state of Tomonaga bosons $b_k^\dagger$:

$$B(t) = exp\left[\sum_{k=0}^{k_F} \frac{(1+V\rho)}{\sqrt{kN}} \left(b_k^\dagger e^{i\frac{k}{\rho}t} - b_k e^{-i\frac{k}{\rho}t}\right)\right] \tag{8}$$

After integration with the pulses we arrive at:

$$F^{(3)}(t) \propto -i\mu^4 e^{-i\epsilon(t-2\tau)} \theta(t-\tau)\theta(\tau)\langle B^\dagger(0)B(\tau)B^\dagger(t)B(\tau)\rangle \tag{9}$$

We consider a bath of bosons in equilibrium at temperature T (with $k_B T < \epsilon_F$) for the thermal average:

$$\begin{aligned} F^{(3)}(t) \propto -i \; \mu^4 \; \theta(t-\tau)\theta(\tau) \; e^{-i\epsilon(t-2\tau)} \; exp\left(\alpha \sum_{k=0}^{k_F} (\frac{1}{2} + N_B)\frac{1}{kN} |1 - 2e^{i\frac{k}{\rho}\tau} + e^{i\frac{k}{\rho}t}|^2\right) \\ \times exp\left(i\alpha \sum_{k=0}^{k_F} \frac{1}{kN}\left(-2sin\frac{k}{\rho}\tau + sin\frac{k}{\rho}t\right)\right) \end{aligned} \tag{10}$$

where $N_B = (e^{\frac{k/\rho}{k_B T}} - 1)^{-1}$. We can express the sum in momentum space as an integral: $\sum_{k=0}^{k_F} = \int_0^{k_F} dk$. If we consider the limit $t >> \tau$ we obtain a very simple expression for the complete FWM signal:

$$F^{(3)}(t,T) \propto -i\ \mu^4\ \theta(t-\tau)\theta(\tau)\ e^{-i\epsilon(t-2\tau)}\ \left[\left(\frac{i\epsilon_F}{\pi k_B T}\right)^3\ sinh^2(\pi k_B T\tau)\ sinh(\pi k_B T t)\right]^\alpha \quad (11)$$

This signal has the zero temperature limit:

$$F^{(3)}(t,T=0) \propto -i\ \mu^4\ \theta(t-\tau)\theta(\tau)\ e^{-i\epsilon(t-2\tau)}\ (i\epsilon_F\tau)^{2\alpha}(i\epsilon_F t)^\alpha \quad (12)$$

4 Conclusions

In this paper we have shown that temporal CC of the Tomonaga bosons can be achieved. We have also shown that the bosonization formalism is a simple tool to calculate the nonlinear susceptibility $\chi^{(3)}$, for both zero and nonzero temperature. We have calculated the FWM signal, for the case of Delta pulses, and we have shown that $F^{(1)}$ and $F^{(3)}$ have an *identical* dependence on the detection time t for both $T = 0$ and $T \neq 0$ [8] In absence of any inelastic mechanism, both the $F^{(1)}$ and $F^{(3)}$ have an intrinsic *potential* decay as a function of τ. It must be pointed out that this potential decay will be superimposed, in real experiments, to an exponential decay produced by electron-electron and electron-phonon interactions.

5 Acknowledgements

Work supported in part by MEC of Spain under contract PB96-0085, Fundacion Ramón Areces and CAM under contract 07N/0026/1998. Diego Porras thanks Spanish Education Ministry for its FPU grant.

References

1. G.D. Mahan, *Many-Particle Physics*, Ed. Plenum, New York, 1981
2. M. S. Skolnik *et al.*, Phys. Rev. Lett **58**, 2130 (1987)
3. K. D. Schotte and U. Schotte, Phys. Rev., **182**, 479 (1969).
4. I. Brener, W.H. Knox and W. Schaefer, Phys. Rev. B **51**, 2005 (1995), I.Perakis *et al.*, J. Optc. Soc. Am. **B13** 1313 (1996)
5. A.P. Heberle, J.J. Baumberg, K. Köhler, , Phys. Rev. Lett. **75**, 2598 (1995). X. Marie *et al.*, Phys. Rev. Lett. **79**, 3222, (1997). J.Fernandez-Rossier, C. Tejedor and R. Merlin, J. of Phys.Cond. Mat., *in press.*
6. S. Weiss *et al.*, Phys. Rev. Lett. **69**, 2685 (1992)
7. D. S. Kim *et al.*, Phys. Rev. Lett., **68**, 2838 (1992).
8. See, for instance, K. Ohtaka and Y. Tanabe, Rev. Mod. Phys., **62**, 929 (1990).
9. M. U. Wehner, Phys. Rev. Lett., **80**, 1992 (1998)

CHARGE-SPIN COUPLED EXCITATIONS OF SEMICONDUCTOR QUANTUM DEVICES WITH BROKEN SPIN SYMMETRY

S. P. Hong[1], K. S. Yi[1*] and J. J. Quinn[2]
[1] *Pusan National University, Pusan 609-735, Korea*
[2] *Oak Ridge National Laboratory, Oak Ridge, Tennessee 37831*

It is possible to conceive of two dimensional electron gas systems in which the spin symmetry can be controlled by the application of an external magnetic field. Such systems with broken spin symmery would offer an interesting testing ground for the study of the effects of exchange and correlation on the dynamic response to an external disturbance. One example is a modulation doped dilute magnetic semiconductor quantum wells in which the large effective g-value leads to a spin splitting that is very large compared to the cyclotron energy. Another example is the GaAs quantum well in which the applied magnetic field is along the 2D layer. The spin polarization ζ is defined by $\zeta = (n_\sigma - n_{\bar{\sigma}})/(n_\sigma + n_{\bar{\sigma}})$, where $n_\sigma(n_{\bar{\sigma}})$ is the number of majority(minority) electrons of spin $\sigma(\bar{\sigma})$ per unit area. Arbitrary degrees of spin polarization could be achieved in the presence of an effective strong magnetic field. In this paper we prersent the generalized charge–spin responses and collective excitations of magnetic semiconductor quantum wells with arbitrary spin polarizations. The spin polarized quantum well(SPQW) is described in terms of two different spin subband ladders with eigenvalues $\varepsilon_{ns}(\vec{k})$ and eigenfunctions $|ns\vec{k}>$. Here n is the subband level index, s the spin index, and $\vec{k}$ the wavevector parallel to the layer. The effects of spin polarization and the interaction effects among electrons of spin σ and σ' are included by using a spin-polarization dependent generalized local fields. We evaluate the charge response, and the longitudinal and transverse spin response to a most general external disturbance. The fluctuations in charge and spin density δn, δm_z, and $\delta m_\pm$ can then be expressed, formally, in terms of a generalized susceptibility matrix $\underline{\chi}$ as $\chi_L = \begin{pmatrix} \chi^{ee} & \chi^{em} \\ \chi^{me} & \chi_{\|}{}^{mm} \end{pmatrix}$ and $\chi_T = \begin{pmatrix} \chi_+{}^{mm} & 0 \\ 0 & \chi_-{}^{mm} \end{pmatrix}$. The superscripts e and m on $\underline{\chi}$ designate charge and spin response (or electric and magnetic disturbance), respectively. The χ^{em} and χ^{me} are responsible for the coupling of the dielectric and magnetic responses. The susceptibilities $\chi_\pm{}^{mm}$ become indistinguishable in the case of spin–unpolarized system. Because the condition for the collective modes of the system is that self–sustaining oscillations in the charge and spin densities occur in the absence of the external disturbances φ_{ext} and b_{ext}, these modes are given by the zeros of the 2×2 determinants χ_L and χ_T given above. Both the spin–nonflip longitudinal and spin–flip transverse spin and charge density excitations are examined. The self–consistent spin-subband structures obtained in the dilute magnetic semiconductor quantum wells are used in order to obtain numerical results. Numerical results for the dispersion curves of the modes for both the intra and inter spin split subbands are given for various degrees of spin polarization. As an example, the figure shows the longitudinal intra and inter spin–split subband modes as a function of wavenumbers for $\zeta = 0.5$. The hatched area denotes the single–particle transition continuum. Coupling of spin–charge excitations introduced through the mixing of charge and spin responses of the system shows additional structures in the spectum.

0* Corresponding author. Fax: +82 51 513 7664; e-mail: ksyi@hyowon.cc.pusan.ac.kr

PB.54

Hysteresis and first-order phase transition in the two-dimensional electron gas

Vincenzo Piazza[1], Vittorio Pellegrini, Fabio Beltram,
Scuola Normale Superiore and Instituto Nazionale per la Fisica della Materia, Pisa, Italy
Werner Wegscheider[(a,b)], M. Bichler[(a)]
(a) Walter Schottky Institute, Munich, Germany
(b) Universität Regensburg, Regensburg, Germany
Tomas Jungwirth[(c,d)], and Allan H. MacDonald[(c)]
(c) Department of Physics, Indiana University, Bloomington, Indiana 47405
(d) Institute of Physics ASCR, Cukrovarnicka 10, 162 00 Praha 6, Czech Republic

Abstract

We report experimental evidence of first-order phase transitions in the two-dimensional electron gas formed in a gated wide GaAs/AlGaAs quantum well at even-integer quantum-Hall states. At the filling factor values of $\nu = 2,4$ and low temperatures, crossing of Landau levels through the application of the gate bias yields a suppression of the quantum-Hall-state excitation gap and hysteretical behaviour of the diagonal resistivity in up and down sweeps of the magnetic field. Detailed many-body calculations indicate the occurrence of a first-order phase transition and allow the determination of the exact properties of the electron ground states involved in the transition.

PACS: 75.60.-d; 75.30.Gw. Keywords: quantum Hall effect; ferromagnetism; hysteresis.

The discovery of the integer[1] and fractional [2] quantum Hall effects offered new, invaluable tools to study many-particle effects in electronic systems[3]. In multilayer systems the additional degree of freedom associated with layer index, also creates remarkable correlation effects that can lead to novel ordered ground states[4,5,6,7]. By appropriate choices of system parameters, ordered ground states with several different properties can be achieved, and transitions between them can be driven by external fields. The microscopic understanding of ferromagnetism has particularly benefited from quantum-Hall studies. Ordered ferromagnetic ground states with tunable anisotropies can now be obtained in laboratory thanks to the high-quality of available semiconductor heterostructures[8]. The possibility of realising quantum Hall ferromagnets with the easy-axis (Ising) anisotropy common of familiar magnetic systems, was also proposed[9,10,11]. The close analogy between the ground states of a quantum Hall system and those of two-dimensional ferromagnets is often emphasised by using a pseudospin language[12] to describe the layer-index degree-of-freedom. Ferromagnetic states are thus described by two-component many-particle states whose pseudospin polarisation remains finite even when the splitting between the two Landau levels is zero.

We investigated the effects of Landau level crossings in a wide quantum well with two subbands occupied. The main result of this work is the observation a first-order phase transition at the even-integer filling factors $\nu = 2,4$ between two electronic ground states of an Ising ferromagnet. The sample used consists of a 60 nm wide GaAs

[1] Lab. "G. Polvani", via della Faggiola, 19 Italy. Tel.: +39 050509415; fax.: +39 050509417; e-mail: piazza@sns.it

quantum well positioned 75 nm below the surface and embedded between two hard-wall $Al_{0.25}Ga_{0.75}As$ barriers (see the Fig. 1a). Peculiar to this system is the presence of a barrier originating from the electron-electron Coulomb repulsion. This barrier separates the electron system into two well-defined strongly-coupled two-dimensional electron gases (2DEGs). The resulting tunnelling gap depends on the electron distribution in the subbands. We shall show that the *softness* of this barrier is the source of the anisotropy field leading to Ising ferromagnetism.

At low temperature, the two lowest subbands are occupied by electrons. A gate contact evaporated on the surface of the sample allowed us to apply an electric field across the quantum well. The external electric field changes the two-dimensional electronic density in the well and, more importantly, the separation between the two lowest subbands (see Figs. 1b and 1c). As shown in Fig. 1b the energy separation can be tuned in a wide range of energies and the two subbands can be brought into resonance at $V_g \approx 0.04$ V, where the tunnelling gap is ≈1.2 meV. In our experiments, we use the external bias potential to line up Landau levels originating in a perpendicular magnetic field from these two subbands.

Crossing of Landau levels leads to weakening of quantum-Hall states at several filling factors[13]. For particular gate values and at $\nu = 2,4$, however, a collapse of the quantum Hall gap is observed in agreement with previous experiments in tilted magnetic fields[14,10]. More importantly, we find that at temperatures below 1 K this collapse correlates with hysteretical behaviour in up and down sweeps of the magnetic fields. It is important to note that at these particular values two Landau levels with opposite spin and pseudospin are found to be resonant. Hysteresis are not found at odd values of ν.

The evolution of the $\nu = 4$ state as the gate voltage is swept from $V_g = -0.06\,\mathrm{V}$ to $V_g = -0.19\,\mathrm{V}$ is shown in Fig. 2a. The disappearance of the quantum-Hall minimum at $V_g \approx -0.16\,\mathrm{V}$, correlates with the emergence of hysteresis in ρ_{xx} in up and down sweeps of the magnetic field. A representative curve is shown in Fig. 3c for $V_g = -0.152\,\mathrm{V}$ and $T = 330\,\mathrm{mK}$. The inset of Fig. 3c shows the temperature evolution of the area enclosed in the loop, confirming that the characteristic energy scale involved in this phenomenon is that of the electron-electron interaction with $T_C \approx 1\,\mathrm{K}$.

We also found that the detailed shape and position of the hysteresis changed in different measurement sessions in concert with changes in electron density produced by thermally cycling the sample. This effect, shown in Fig. 3d, suggests an intriguing, not yet explained, correlation with the 2DEG density. A similar scenario applied at $\nu = 2$. As in the $\nu = 4$ case, the onset of hysteresis correlates with the disappearance of the quantum-Hall minimum (see Fig. 2b).

A quantitative estimate for the critical bias potentials V_c at which resonances between two opposite spin and pseudospin levels are driven was obtained by means of numerical self-consistent local-density-approximation (LDA) calculations. For the $\nu = 2$ case we found two resonant conditions at -0.05 V and 0.02 V. The same procedure applied to the $\nu = 4$ case yielded -0.16 V and -0.14 V. These results are in good agreement with the experimental values of the critical gate bias.

The hysteresis and anomalous temperature dependence of the ρ_{xx} traces presented above, indicates the occurrence of easy-axis ferromagnetism with domain structure. Within the LDA model we found that this property is linked to the softness of the barrier. At sufficiently high electron densities, consistent with the experimental density at which the $\nu = 2$ transition occurs, the tunnelling barrier is increased when the $n = 0,\uparrow$ Landau levels from both ladders are occupied compared to the case of occupied $n = 0,\uparrow$ and $n = 0,\downarrow$ of the same ladder. A bigger total barrier leads to a smaller tunneling gap Δ_t, so that in our sample Δ_t depends on the pseudospin orientation. Translated into the pseudospin language, the softness of the barrier leads to the increase of the gap between the occupied lower-energy pseudospin level and the empty higher-energy pseudospin level in either up or down pseudospin polarisations. This anisotropy energy term at the critical gate bias favours the pseudospin orientation up or down, i. e., the system behaves like an Ising ferromagnet. In our LDA calculations this occurs because the exchange energy, that is larger in the fully spin-polarized case, dominates the electrostatic energy associated to the different wavefunction profiles in the two subbands. The resulting coercitivity field gives rise to the observed hysterical behaviour. Similar arguments lead to easy-axis anisotropy at filling factor $\nu = 4$.

These novel observations represent one particular manifestation of a broad class of phenomena that can be associated with crossing of Landau levels and demonstrates that the phenomenology of easy-axis systems, dominated by the hysteretic effects and domain morphology issues familiar in common magnetic systems, is particularly rich. This suggest further studies in the two-dimensional electron gas.

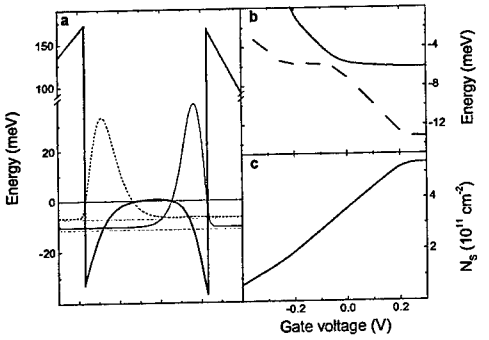

Fig.1 (a) Self-consistent local-density-approximation calculations of the subband energy levels (thin dotted lines), quantum-well profile (thick solid line) and wavefunctions (thin solid and dashed lines) at low temperatures. (b) Energy levels of the two occupied subbands as a function of the gate bias. A crossing between the two subbands occurs at $V_g \approx$ -0.04 V. The zero of energy is chosen at the Fermi level. (c) Total electron concentration in the well as a function of the gate bias. Data in Panels b and c were obtained by Shubnikov-de Haas measurements at 4.2 K by standard lock-in techniques.

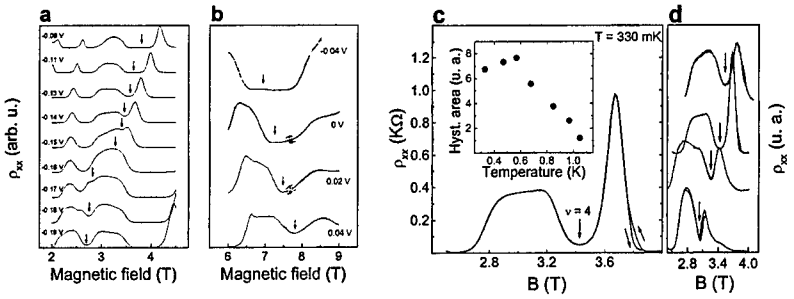

Fig.2 Set of resistivity-versus-magnetic-field curves recorded at different gate voltages showing the disappearance of the $\nu = 4$ (panel a) and 2 (panel b) quantum-Hall states (marked with arrows). The suppression of the excitation gap correlates with the emergence of hysteresis in up and down sweeps of the magnetic field (shown in panel b at $\nu = 2$). The curves are offset for clarity and each curve is labelled with the gate voltage. (c) Diagonal-resistivity curve at 330 mK near filling factor $\nu = 4$ in up and down sweeps of the magnetic field at $V_g = -0.152$ V. The curves are offset for clarity. The inset shows the temperature evolution of the hysteresis area at $V_g = -0.152$ V. (d) Different hysteresis shapes obtained after thermally-cycling the sample. The arrows mark the position of the $\nu = 4$ minima. Measurements were performed at 330 mK with lock-in techniques at a frequency of 12.5 Hz; the AC excitation current was chosen of 100 nA to avoid electron heating.

[1] K. von Klitzing, G. Dorda, and M. Pepper, Phys. Rev. Lett. **45**, 494 (1980)
[2] D. C. Tsui, H. L. Stormer, and A. C. Gossard, Phys. Rev. Lett. **48**, 1559 (1982)
[3] S. Das Sarma, and A. Pinczuk, (eds) Perspectives in Quantum Hall Effects (Wiley, New York, 1996)
[4] S.M. Girvin and A.H. MacDonald in (3) pp. 161-224.
[5] L. Zheng, R.J. Radtke, and S. Das Sarma , Phys. Rev. Lett. **78**, 2453 (1997); S. Das Sarma, S. Sachdev, and L. Zheng, Phys. Rev. Lett. **79**, 917 (1997)
[6] A.H. MacDonald, R. Rajaraman, and T. Jungwirth, preprint [cond-mat/9903318].
[7] S.Q. Murphy, J.P. Eisenstein, G.S. Bobinger, L.N. Pfeiffer, and K.W. West, Phys. Rev. Lett. **72**, 728 (1994)
[8] V. Pellegrini, et al., Science **281**, 799 (1998); V. Pellegrini, et al., Phys. Rev. Lett. **78**, 310 (1997); A. Sawada, et al., Phys. Rev. Lett. **80**, 4534 (1998).
[9] G.F. Giuliani, and J.J. Quinn, Phys. Rev. B **31**, 6228 (1985).
[10] T. Jungwirth, et al., Phys. Rev. Lett. **81**, 2328 (1998).
[11] H. Cho, et al., Phys. Rev. Lett. **81**, 2522 (1998).
[12] A.H. MacDonald, P.M. Platzman, and G.S. Boebinger, Phys. Rev. Lett. **65**, 775 (1990).
[13] V. Piazza, et al., to be published.
[14] A.J, Daneshvar, et al., Phys. Rev. Lett. **79**, 4449 (1997).

PB.55

MAGNETOOSCILLATIONS OF ELECTRONS IN NONPARABOLIC CONFINING POTENTIAL

G.M.Gusev[a], J.R.Leite[a], E.B.Olshanetskii[b], D.K.Maude[b], M.Cassé[b,c], J.C.Portal [b,c], N.T.Moshegov[d], A.I.Toropov[d]

[a]Instituto de Fisica da Universidade de São Paulo, São Paulo, SP, Brazil
[b]CNRS-LCMI, F-38042, Grenoble, France
[c]INSA-Toulouse, 31077, France
[d]Institute of Semiconductor Physics, Novosibirsk, Russia

Abstract

Shubnikov de Haas (SdH) oscillations induced by the small additional perpendicular field are investigated in overfilled parabolic quantum well in the presence of the parallel magnetic field. The dispersion relation of the in-plane electron motion has a double minimum in contrast to the harmonic-oscillator model. Landau levels belonging to the additional subband minima are responsible for the observed behaviour of the SdH oscillations.

Introduction

The parabolic confining potential is realized and investigated in a many semiconductor low-dimensional devices such as quantum wells, wires and quantum dots. Theoretically, parabolic potential has attracted very much attention, since the energy spectrum can be calculated exactly within the harmonic-oscillator model. One of the example is the energy spectrum of the two-dimensional electrons, which are confined in the z direction by the parabolic potential in the presence of the in-plane magnetic field, and energy levels of the quasi-one dimensional electrons in quantum wires subjected to perpendicular B. In this case the energy spacing can be solved explicitly, and each level is the hybrid electric-Landau subband [1]. Magnetoresistance reveals oscillations with B, which are due to the depopulation of subbands by the magnetic field and therefore, they resembles the conventional Shubnikov de Haas oscillations. Depopulation of the subbands in a wide parabolic quantum well under in-plane magnetic field has been studied in [2]. Depopulation of levels in quantum wire in perpendicular magnetic field has been observed in [3]. However, we should note, that an overfilled parabolic well should resemble a partially filled square well, and therefore harmonic-oscillator model is not valid more for realistic wide parabolic well. The calculation of the fully self-consistent electronic structure of a overfilled parabolic quantum well and symmetric and asymmetric square quantum wells in the presence of the in-plane magnetic field has been done in [4,5]. It has been shown that the electron subband possesses the two local minima at finite Fermi vector on the dispersion curve. Fig.1 shows schematically subband energies of a parabolic quantum well as a function of Fermi vector in the presence of the in-plane magnetic field. So when the Fermi level passes through this subband bottom one expects to observe two peaks in the magnetoresistance instead of the single peak for the pure parabolic confining potential case. Anomalous dispersion law with two local minima can be

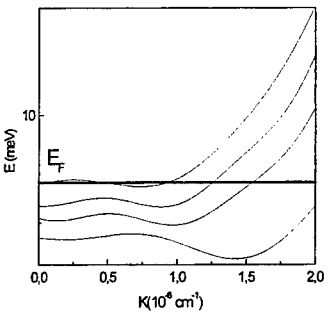

Fig.1 Schematic representation of the subband energies of a parabolic quantum well as a function of the Femi vector in the presence of the in-plane magnetic field.

analyzed from Shubnikov de Haas oscillations induced by sufficiently small additional perpendicular field. For ordinary parabolic dispersion law the electronic states become a series of discrete Landau levels (LL) of energy $E_N = \hbar\omega_c(N + ½)$, with the cyclotron frequency ω_c given by eB/mc. For dispersion curves shown in fig.1 Landau levels demonstrate more complicated behaviour. For example at definite interval of magnetic fields levels with smaller quantum number N move downwards and intersect levels with larger N.

Here we report the measurements of the Shubnikov de Haas oscillations in a quasi-parallel magnetic field. The behavior of the SdH oscillations cannot be explained in terms of a simple Landau fan chart. It is important to take into account additional local minima on the dispersion curve.

Experimental detail and results.

The samples used are the GaAs-Al_x Ga_{1-x} As parabolic quantum well grown by molecular – beam epitaxy. After growth substrate with PQW was processed into Hall bar. Four –terminal resistance and Hall measurements were made down to 30 mK in magnetic field up to 17 T. The measurements were performed with an ac current not exceeding 10^{-8} A. Resistance was measured for different angles between the field and substrate plane in magnetic field using an in situ rotation of the sample. The mobility of the electron gas in the well is 65×10^3 cm^2/Vs, and concentration n_s in the dark is 3.9×10^{11} cm^{-2}. Three dimensional pseudocharge n_{3D} is 2.1×10^{16} cm^{-3} which corresponds the classical width of the 3D electron gas $w_e = n_s/n_{3D} = 190$ nm . This value is close to the geometrical width of the well, therefore the energy spectrum of a parabolic well can be roughly approximated by spectrum of a square well.

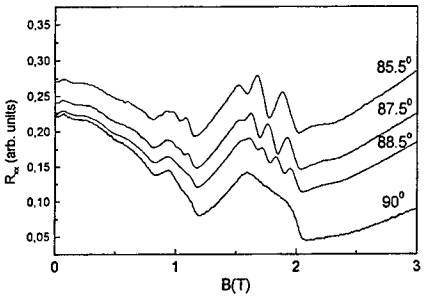

Fig.2 Magnetoresistivity traces in parallel and tilted magnetic field.

Fig.2 shows the magnetoresistivity traces in parallel and quasiparallel magnetic field. We see 4 peaks due to the depopulation of the electric subbands. Oscillations at strong magnetic fields split into two peaks, which we attribute to the two local minima of the subband structure. A small additional perpendicular field induces conventional Shubnikov de Haas (SdH) oscillations. Surprisingly, the SdH oscillations are observed only on the top of the depopulation peaks in the interval of magnetic field, when Fermi level passes "pockets" in the dispersion law (fig.1). We did not find any SdH oscillations in stronger magnetic field.

This observation disagrees with the conventional picture of the Shubnikov de Haas oscillations, which requires an exponential growth of the oscillation amplitude with magnetic field. Assuming that from the 1/B periodicity of the anomalous SdH oscillations we can determine the electron density, we obtain $n_s = 1.3\ 10^{12}\ cm^{-2}$, which is 40 times larger, then the expected value for such angle $n_s/\cos\theta$, where n_s is the total electron density determined from the Hall measurements in the perpendicular field. To explain this value we should take the angle $\theta = 63^0$ instead of 88.5^0. This difference is much larger than precision of the angle measurements $\sim 1^0$.

Theory and discussions

In the following we calculate the energy spectrum of the two-dimensional electron in wide square well subjected to an in-plane magnetic field. We take into account first -order perturbation theory. Treating the terms in Hamiltonian due to the in-plane magnetic field as a small perturbation we can obtain the first-order corrections to the energy of the each subband [6]: $E = \hbar^2(k_x-k_0)^2/2m + e^2B_{II}(\langle z^2\rangle - \langle z\rangle^2)/2m + \hbar^2k_y^2/2m + E_n$ (1)
where $\langle..\rangle$ denotes the quantum-mechanical expectation of length z and z^2 for the corresponding subband with energy E_n, and $k_0 = eB_{II}\langle z\rangle/\hbar$. We can see from equation (1) that the symmetry $E(k_x)=E(-k_x)$ is broken for the asymmetric quantum well [5,6]. For the symmetric quantum well one should expect that $\langle z\rangle = 0$. However, it is necessary to consider self consistent solution of the Poisson equation for the electrostatic potential and the Schrodinger equation for the wave function $\phi(k_x)$. In this case the strong parallel magnetic field leads to the bending of the bottom of the square well, and, consequently, shifting of the wave function from the center of the well. The physical reason for the appearance of the nonzero $\langle z\rangle$ is following. Consider electron moving parallel to the surface with velocity v_x . In the field directed along the surface it experiences a force $F = ev_xB_{II}$, binding it to the surface. In the symmetric quantum well wave function $\phi(k_x)$ is shifted to the left side of the well, therefore $\langle z\rangle > 0$, and $\phi(-k_x)$ is shifted to another side, and $\langle z\rangle < 0$. In this case for the symmetric square quantum well: $E(k_x, k_y) = E(-k_x, k_y) = \hbar^2k_x^2/2m - \alpha^{\pm}k_x + \hbar^2k_y^2/2m + e^2B_{II}\langle z^2\rangle/2m + E_n$ (2), where $\alpha^+ > 0$ for $k_x > 0$, and $\alpha^- = -\alpha^+ < 0$ for $k_x < 0$. We also see that the effect of B_{II} is to make $E(k_x, k_y)$ anisotropic. We should note that for more realistic model $\langle z\rangle$ is not constant and increases with wave vector k_x, because the

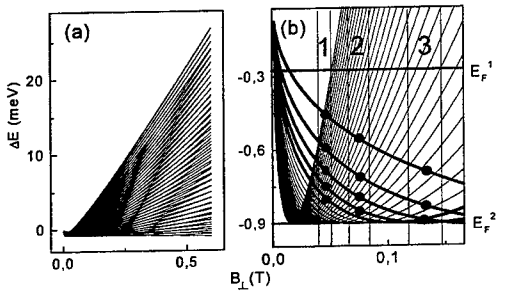

Fig.3 (a) Landau levels as a function of the $B_\perp$. (b) Low field part of the Landau fan chart. Vertical lines indicate intervals of $B_\perp$, when SdH oscillations are observed for different tilt angles : 1-88.5°, 2-87.5°, 3-85.5° . Relative positions of the Fermi level during subband depopulation are indicated.

magnetic force increases with electron velocity, therefore the equation (2) is not valid at small k_x.

Now we discuss the effect of a small perpendicular field on the one hybrid subband. For the sake of the simplicity we consider isotropic energy dispersion. The energy levels in small perpendicular B are determined by the following equation [7]: $E_N=\hbar\omega_c[N-(\gamma/2+\gamma^2N)^{1/2}]$ (3) where $\gamma=2(\Delta/\hbar\omega_c)^{1/2}$, $\Delta=\alpha^2m/2\hbar^2$ - energy minima in the center of the pocket of the dispersion curve (2). From the self consistent calculations it is found that Δ~1-2 meV [4] at B ~ 2-3 T. Fig.3 a shows the dependence of the energy levels (3) on the perpendicular magnetic field. We see that at high magnetic field the dependence E(B) resembles the conventional Landau fan chart, however at small field it is different. Low field dependence of the Landau levels is shown in fig.3b. The levels at low field move downwards, pass minimum, and then move upwards. The Landau levels with small quantum number N move downwards at higher field, and therefore intersect LL with larger N, which already pass the minimum on the dispersion curve. We believe that this behaviour can explain quantitatively our results. We can not vary parallel and perpendicular components of the magnetic field independently. Parallel component of the magnetic field leads to the rise of the all subband levels due to the diamagnetic energy. Fig.3b shows the relative position of the Fermi level during this diamagnetic shift. At the same time perpendicular component of the magnetic field increases too. Vertical lines in the fig.3b shows the intervals of $B_\perp$, when the SdH oscillations appear in quasi-parallel field. Fermi level intersects LL which are moving downwards during the depopulation of the subband (the points of these intersections are marked by the circles in fig.3b). Landau levels moving upwards are not resolved due to the broadening and can be seen as a background with constant density of states. In experiments (fig.2) we find 5 oscillations in interval 1, 4 in 2 and 3 in interval 3, which is roughly consistent with number of circles in fig.3b. At larger tilt angles the levels moving upward become well resolved, and we start to observe SdH oscillations in all interval of B.

In conclusion we have observed anomalous magnetooscillations in quasi-parallel B, which appear in the narrow interval of magnetic field. Effect is due to the Landau quantization of the states in the additional local minima of the dispersion curve.

Acknowledgements
This work was supported by FAPESP and CNPq (Brazilian agencies) and USP/COFECUB.

References

1. J.C.Maan, in Two Dimensional Systems, Heterostructures and Superlattices, eds. G.Bauer et al (Springer, Berlin, 1984), p.183.
2. E.G.Gwinn, R.M.Westervelt, P.F.Hopkins, A J.Rimberg, M.Sundaram, A C.Gossard, Phys. Rev.B, 39, 6260 (1989).
3. K.F.Berggren, T.J.Thornton, D.J.Newson, M.Pepper, Phys. Rev.Lett., 57, 1769 (1986).
4. M.P.Stopa, S.Das Sarma, Phys. Rev.B, 40, 10048 (1989).
5. G.M.G.Oliveira, V.M.S.Gomes, A S.Chaves, J.R.Leite, J.M.Worklock, Phys. Rev. B, 35, 2896 (1987).
6. T.Ando, J.Phys. Soc.Japan, 39, 2 (1975).
7. E.I.Rashba, Fiz.Tv.Tela, 2 1224 (1960) (Sov.Phys.-Solid State, 2, 1109 1960).

PB.56

VARIATION OF MANY-BODY EFFECTS FOR IMPURITY STATES UNDER PRESSURE IN GaAs/AlGaAs MULTIPLE QUANTUM WELLS

J. G. Tischler, H. A. Nickel, B. D. McCombe, B. A. Weinstein
Department of Physics, SUNY at Buffalo, Buffalo, NY 14260, USA
A. B. Dzyubenko
Institut für Theoretische Physik, J. W. Goethe-Universität, 60054 Frankfurt, Germany
General Physics Institute, RAS, Moscow 117942, Russia
A.Yu. Sivachenko
The Weizmann Institute of Science, Rehovot 76100, Israel

Abstract

Applied hydrostatic pressure modifies the Coulomb bound states of a quasi-two dimensional electron gas in quantum wells by *increasing the effective mass* and by *tuning the free electron density*. Here, we explore these mechanisms by measuring the effects of pressure on the cyclotron resonance, the D^0 $1s \rightarrow 2p^+$ transition, and the D^--singlet and singlet-like transitions in low-density and high-density, modulation-doped GaAs quantum wells. For low doping-density, detailed calculations employing a pressure dependent electron mass agree well with the observed magnetic field and pressure dependencies. For high doping-density and low fields, the blue-shift of the D^- singlet-like transition at fields below 8T decreases with applied pressure as anticipated, due to loss of free electrons via the Γ-X crossover. However, near ~7.5T, this singlet-like transition exhibits an anomalous branching for pressures above 4kbar, which indicates the presence of a resonant level and obscures the blue-shift at high fields.

Electrons in low-dimensional semiconductor structures and high magnetic fields are strongly correlated, giving rise to a number of interesting phenomena such as the Fractional Quantum Hall Effect, the Wigner Solid, and Skyrmion excitations. [1] Previous work [2], in which *excess* electrons were introduced into a series of Si modulation-doped multiple quantum wells (MDQWs), demonstrated that for GaAs/AlGaAs structures with a controlled density of randomly distributed impurities in the wells, many-electron interactions of a quasi-two-dimensional electron gas (2DEG) are rendered visible in the far infrared (FIR) magneto-optical spectrum. For example, with increasing excess electron density, the two-electron D^- singlet [3-5] transition evolves continuously into a blue-shifted many-electron ***D^- singlet-like*** bound magnetoplasmon excitation, which exhibits interesting behavior as a function of filling factor.

Earlier studies [6] showed that applied hydrostatic pressure modifies the Coulomb bound states of a 2DEG in MDQWs by *increasing the electron effective mass* and by *tuning the free electron density*. The former mechanism alters the single particle wavefunctions and energies, and the latter mechanism affects the many electron states and their interactions. In the present work the influence of these mechanisms on neutral/negatively-charged donors (D^0/D^-) and on the cyclotron resonance (CR) of free electrons is studied by high-pressure FIR magnetospectroscopy in GaAs/AlGaAs structures.

FIR magneto-transmission experiments were carried out under applied hydrostatic pressure with a diamond-anvil cell (DAC), in which pressure, magnetic field and temperature are varied independently (maximum operating ranges: 0 to 150 kbar, 0 to 9T, and 2 to 300 K). [7] Spectra were recorded up to 35kbar at 4.2K with a Fourier transform infrared spectrometer, in conjunction with a 9T superconducting magnet. A Ge:Ga photoconductive detector measured the FIR signal in the range 80 to 240 cm^{-1}. (See [7] for details.) We studied a series of epitaxially grown $GaAs/Al_{0.3}Ga_{0.7}As$ QWs that were Si δ-doped [2,3] in both the 20nm wells (at 2.0×10^{10}

cm^{-2}) and in the 60nm barriers [in the range $(3.5 - 28)x10^{10}$ cm^{-2}]. We present data recorded in the Faraday geometry for the lowest concentration sample ($3.5x10^{10}$ cm^{-2} – Sample 1) and the highest concentration sample ($28x10^{10}$ cm^{-2} – Sample 2), which were cleaved into specimens of ~150x150x30 μm^3 size (substrate thinned) and suspended in a ^{4}He pressure medium. [7] Any pressure-induced DX centers were deactivated by intermittent exposure to visible (514nm) laser light during ruby pressure calibration.

In Sample 1 (low doping) we observed the pressure and magnetic-field dependencies of the D^0 1s→$2p^+$, the D^- singlet, and the electron CR transitions. For this specimen the free electron concentration changes very little up to ~25 kbar, the onset of the Γ-X crossover between the well and barrier conduction band edges (see Ref. [6]). Hence, in Sample 1 we probe principally the effects of the pressure-induced increase in the effective mass. Figure 1 shows the magnetic field dependencies observed for this sample, at 1atm *and* at the highest pressure at which the different features could be observed – CR (22kbar), D^- singlet transition (25kbar), and D^0 1s→$2p^+$ transition (28kbar). Above 30kbar, no absorption features could be measured within our signal-to-noise level, due to the complete transfer of the QW electrons to the X-associated states in the barrier.

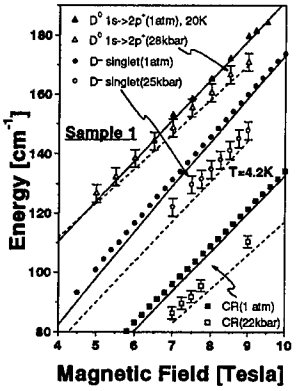

Figure 1. Summary plot for Sample 1, showing the pressure and magnetic field dependencies of the CR, D^- singlet and D^0 1s→$2p^+$ transitions. The 1 atm points are from Ref. [4]. The solid (dashed) curves are calculated results for 1 atm (the same high pressures as the experimental data).

As expected, due to confinement the energy of the D^0 1s-$2p^+$ transition is higher at all pressures in Sample 1 than observed in prior experiments on Si-doped bulk GaAs. [8] A similar comparison is not possible for the D^- singlet transition, since this was not seen in the data of Ref. [8]. The field-slopes of the three observed features in Fig.1 all decrease with applied pressure. The increase of the electron mass with pressure is the principal cause for this decrease in all cases. For the CR and the D^0 1s-$2p^+$ transitions, the rate of decrease in slope agrees, within experimental error, with the prior findings in bulk GaAs. [8] For these transitions, and for the *D^- singlet* QW feature, we explore the effects of changes in the electron mass in more detail by theoretical calculations.

In these calculations, the D^0 1s→$2p^+$, D^- singlet, and CR transitions are computed by numerical diagonalization (with a basis of 3000 Landau-oscillator and size-quantization wavefunctions) of the appropriate one- or two-electron Hamiltonians for a positive charge at the QW-center. Results were obtained for B≥4T with *pressure-dependent* effective mass and dielectric constant [4,9] incorporating the effects of conduction band non-parabolicity, assumed to be pressure-independent and equivalent to that in GaAs at 1atm. The dependence of the effective mass with applied pressure $m_{eff}(P)$ was taken from previous experiments [8], $m_{eff}(P) = m_{eff}(0)$ x $[1+6.08x10^{-3}$ P-$1.3x10^{-5}$ $P^2]$, where P is the pressure in kbar and $m_{eff}(0)$ is the bottom-of- the-conduction-band effective mass at 1atm ($0.067m_e$). The dielectric constant as a function of pressure $\varepsilon(P)$ was obtained by combining this result for $m_{eff}(P)$ with other measurements [10] of the pressure dependent Rydberg constant, $Ry(P) = Ry(0)$ x $[1+9.61x10^{-3}$ P+$1.51x10^{-5}$ $P^2] \equiv [m_{eff}(P)\, e^4]/[2\, \varepsilon^2(P)\, \hbar^2]$. The solid (dashed) curve in Fig. 1 gives the calculated results for the

CR, D^- singlet, and D^0 $1s \rightarrow 2p^+$ transitions at 1atm (22kbar, 25kbar and 28 kbar, respectively). The qualitative behavior is well reproduced, although the calculated transition energies are in all cases somewhat smaller than the measured ones. This discrepancy could arise from an overestimate of the non-parabolicity in the calculation.

Notice in Fig. 1 that the 1atm *and* elevated-pressure curves cross at different B-fields for the D^0 $1s \rightarrow 2p^+$ transition and the D^- singlet transition. Both the theoretical and the experimental results find that this crossing occurs at a higher field for the D^0 $1s \rightarrow 2p^+$ case (at ~ 5T) than for the D^- singlet case (at a field below our measurement range). The overall agreement between theory and experiment is reasonable.

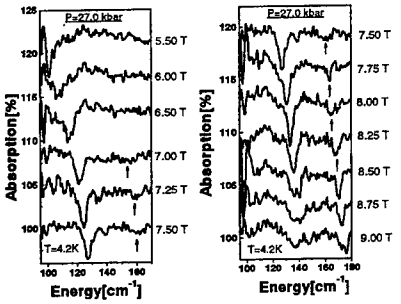

Figure 2. FIR magneto-transmission spectra at 27 kbar for Sample 2, showing the complicated branching of the D^- singlet-like transition.

In Sample 2 (highly doped) we studied the D^- singlet-like transition and the CR over similar magnetic-field and pressure ranges. Typical experimental spectra are shown for 27kbar in Fig. 2. Within the experimental uncertainty, the CR energy position as functions of magnetic field and pressure is found to be the same as in Sample 1. However, the width of the CR evolves with applied pressure from a broad (overabsorbed) feature [2,3] to a much sharper peak. This behavior is a signature of the pressure-induced decrease in electron density caused by the Γ-X crossover.

The D^- singlet-like transition is blue-shifted relative to the isolated D^--singlet energy as expected, because of many electron effects. [3-5] This blue-shift is manifest in Figure 3 by the energy difference between the data points (recorded for Sample 2) and the theoretical curves (calculated for Sample 1 as described). Although the anticipated trend is simply a decrease in the blue-shift due to the pressure-induced reduction in QW electron density, we find much more complicated behavior. The 1atm and 4kbar data in Fig. 3 show essentially the same blue-shift relative to the calculated D^--singlet transition at 1atm (solid curve). This is understandable, since a pressure of 4kbar is too low to cause a decrease in the electron density via the Γ-X crossover. [6] However, at all pressures above 4kbar, the D^- singlet-like data for Sample 2 show an anomalous (*anti-crossing-like*) branching around ~7.5T. With increasing pressure, the magnitude of the splitting between the two branches increases. The upper branch appears to evolve into the D^0 $1s \rightarrow 2p^+$ transition, while the lower branch

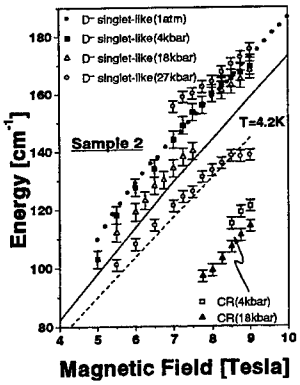

Figure 3. Summary plot for Sample 2, showing the pressure and magnetic field dependencies of both D^- singlet-like branches, and the CR. The 1 atm data is from Ref. [4]. The solid and dashed curves show the theoretical *isolated* D^- singlet transition at 1 atm and 25 kbar, respectively (also in fig. 1).

approaches the isolated D^- singlet position (at the given pressure, dashed line). This behavior is most clear at 27kbar in Fig. 2, where two absorption features are seen simultaneously between 7 and 9T. We also find that the intensity of the higher energy peak increases with magnetic field, while the lower energy peak decreases in strength and broadens. As in the low-density sample, no absorption features were observed in Sample 2 for pressures above the Γ-X crossover.

At fields below the onset of the anomalous D^- branching, the blue-shift of the singlet-like transition with respect to that of an isolated D^- singlet ion behaves as expected. At 18kbar the blue-shift is still the same, within experimental error, as that observed at 1atm. (~13cm^{-1} relative to the *calculated* D^- singlet position). Over this pressure range the excess electron density remains essentially unchanged, and the shifts in energy and slope of the D^- singlet-like transition are related to the mass changes described above. For the highest pressure in Fig. 3 (27kbar), at which the sample's excess QW electron density has now decreased substantially, the blue-shift in the low-field D^- branch is concomitantly smaller (~5 cm^{-1} relative to the calculation).

In contrast, for higher fields (>7.5T) the complicated branching of the D^- singlet-like transition in Sample 2 is currently not well understood. However, it is interesting to speculate on the origin of this branching. One possibility is misalignment of the sample's QW plane with respect to the magnetic field due to twisting of the specimen in the DAC. In this case, the magnetic field component in the QW plane couples free-carrier Landau states and impurity states associated with the first and second sub-bands. However, this possibility is ruled out because the large separation of these sub-bands (~220 cm^{-1}, calculated via the pressure dependent self-consistent model in Ref. [6]) should cause the branching to occur ~75 cm^{-1} above the frequency where it is observed in Fig. 3. In addition, the branch splitting is unreasonably large for the estimated maximum tilt angle of the sample in the DAC.

A more realistic possibility is that the branching arises from the presence of a resonant level, which communicates with the free electrons in the quantum well for this field-pressure regime. If so, the experimental results suggest that the coupling of this level to the shallow donor and free carrier states in the well increases with applied pressure, and that for fields above ~7.5T, carriers are removed from the well into this level. This interesting, and previously unobserved phenomenon, merits further experimental and theoretical investigations.

Acknowledgements

This work was supported by NSF DMR-9624029. ABD is grateful to the Department of Physics at the University at Buffalo, where part of this work was performed, and to the Humboldt Foundation for financial support. We thank W. Schaff for the samples.

References

1. L. Brey, H. A. Fertig, R Côte and A. H. MacDonald, Phys. Rev. Lett. **75**, (1995) 2562.
2. J-P. Cheng, Y. J. Wang, B. D. McCombe and W. Schaff, Phys. Rev. Lett. **70**, (1993) 489.
3. e.g., S. Huant, S. P. Najda and B. Etienne, Phys. Rev. Lett. **65**, (1991) 1486; and E. R. Mueller, D. M. Larsen, J. Waldman, and W. D. Goodhue, Phys. Rev. Lett. **68**, (1992) 2204; S. Holmes, J-P. Cheng, B. D. McCombe and W. Schaff, Phys. Rev. Lett. **69**, (1992) 2571.
4. A. B. Dzyubenko and A. Yu. Sivachenko, JETP Lett. **57**, (1993) 507.
5. Z. X. Jiang, B. D. McCombe and P. Hawrylak, Phys. Rev. Lett. **81**, (1998) 3499.
6. J. G. Tischler, S. K. Singh, H. A. Nickel, G. S. Herold, Z. X. Jiang, B. D. McCombe and B. A. Weinstein, phys. stat. sol. (b) **211**, (1999) 131.
7. R. J. Chen and B. A. Weinstein, Rev. Sci. Instrum. **67**, (1996) 2883.
8. Z. X. Jiang, R. J. Chen, J. G. Tischler, B. A. Weinstein and B. D. McCombe, phys. stat. sol. (b) **198**, (1996) 41.
9. A. B. Dzyubenko and A. Yu. Sivachenko, Phys. Rev. B **48**, (1993) 14690; A. B. Dzyubenko A. Mandray, S. Huant, A. Yu. Sivachenko and B. Etienne , Phys. Rev. B **50**, (1994) 4687.
10. Z. Wasilewski and R. A. Stradling, Semicond. Sci. Technol. **1**, (1986) 264.

PB.57

Magnetic Phase Diagram of a Semiconductor Superlattice at $\nu = 2$

D. C. Marinescu
Solid State Division, Oak Ridge National Laboratory, Oak Ridge, Tennessee 37831
J. J. Quinn
Department of Physics, University of Tennessee, Knoxville, TN 37996 and Solid State Division, Oak Ridge National Laboratory, Oak Ridge, Tennessee 37831
Gabriele F. Giuliani
Department of Physics, Purdue University, West Lafayette, Indiana 47907

Abstract

The magnetic phase diagram of a periodic system of identical quantum wells subject to a strong magnetic field is investigated within the Hartree-Fock approximation. Weak tunneling between the wells accounts for the broadening of the individual energy levels of a single well into minibands of bandwidth Δ. For small tunneling probability, the quasi-two dimensional system undergoes a ferromagnetic to paramagnetic transition as in the case of a single electron gas layer. For larger tunneling probability a critical value of Δ_c is reached for which spin flip excitations between minibands can become soft and lead to a spin density wave coupling between the bands with $Q = \frac{\pi}{a}$, with a the superlattice period.

Electron-electron interactions make possible the existence of spin polarized phases in a single quantum well in the presence of a strong magnetic field, at integer, even values of the filling factor ν and finite Landau and Zeman energies. In this problem the crucial ingredients are the magnitude of the energy scale $\epsilon = \hbar(\omega_c - \omega_s)$ and the predominance of the exchange energy over the correlation energy[1]. In the case of $\nu = 2$ this phenomenon can be understood by noticing transfering electrons from the $n = 0$ spin up Landau level, $|0 \uparrow>$, to the $n = 1$ spin down Landau level $|1 \downarrow>$ can lower the total energy of the system thereby leading, in single component cases, to a ferromagnetic ground state. This prediction has been verified experimentally, as shown in Reference [2].

Inspired by the results obtained in a single two dimensional layer, we study here the magnetic properties of an infinite array of identical quantum wells, in a strong magnetic field at filling factor $\nu = 2$, as a model for a quasi three dimensional system. A different discussion of the same model is presented elsewhere[3], while a study of a similar system can be found in Ref. [4]. Assuming a small, but finite tunneling probability between the wells, the energy spectrum of this system consists of a sequence of minibands whose energy is determined by the wavenumber k_z along the direction of the superlattice axis. The miniband width Δ, which is proportional to the tunneling probability, becomes then

a crucial parameter of the problem.

In a simple approximation, the superlattice is described as a periodic array of attractive δ-function potentials, i.e. $V(z) = -\lambda \sum_l \delta(z-la)$, with l an integer. The single bound state of an isolated quantum well with potential is widened into a miniband described, in a tight binding approximation, by $\epsilon(k_z) = \epsilon_0(1 + 4e^{-\kappa a}\cos k_z a)$. Here, $\epsilon_0 = -\frac{\hbar^2\kappa^2}{2m}$, where $\kappa = m\lambda/\hbar^2$. The corresponding single electron wave function is given by

$$|n, k_y, k_z, \sigma >= e^{ik_z z} u(k_z, z)\phi_{nk_y}(x, y)\eta_\sigma \ . \tag{1}$$

Here $\phi_{nk_y}(x,y) = L^{-\frac{1}{2}}e^{ik_y y}H_n(x + k_y\ell)$, where $\ell = \sqrt{\frac{\hbar c}{eB}}$ is the magnetic length, $H_n(x)$ is the n-th simple harmonic oscillator function, and η_σ represents the spin eigenfunction. $u(k_z, z)$ is the appropriate periodic wave function. As usual the allowed values of k_y and k_z are determined by the periodic boundary conditions.

The nature of the ground state can be analyzed by introducing the Hamiltonian of the interacting system,

$$H = \sum_n \sum_{k_z} \epsilon_{n,k_z,\sigma} c^\dagger_{n,k_z,\sigma} c_{n,k_z,\sigma} + \frac{1}{2}\sum_{n,m} \sum_{\vec{k},\vec{q},\vec{Q},\sigma,\sigma'} v_{nm}(\vec{k},\vec{q},\vec{Q}) c^\dagger_{n,\vec{k}+\vec{Q}+\vec{q},\sigma} c^\dagger_{m,\vec{k},\sigma'} c_{m,\vec{k}+\vec{q},\sigma'} c_{n,\vec{k}+\vec{q},\sigma} \ , \tag{2}$$

where n and m take only the values 0 and 1. between electrons in miniband $|n, \vec{k}+\vec{Q}, \sigma >$ and $|m, \vec{k}, \sigma' >$. The matrix elements $v_{nm}(k_z, \vec{q}, \vec{Q})$ of the Coulomb interaction between electrons in miniband $|n, \vec{k} + \vec{Q}, \sigma >$ and $|m, \vec{k}', \sigma' >$, differ from its 2D counterpart, calculated in Ref.[1], by a form factor $F(k_z, q_z, Q_z)$, which describes the exchange of momentum along the z direction. Assuming small tunneling probability, an approximate expression for $F(k_z, q_z, Q_z)$, is readily obtained within the present model:

$$F(k_z, q_z, Q_z)/\frac{2\pi}{a^2}\left(\frac{4\kappa^2}{4\kappa^2 + q_z^2}\right)^2 =$$
$$\left\{1 - 2\kappa a e^{-\kappa a}\sin\left(\frac{q_z a}{2}\right)\cos\left[\left(k_z + \frac{q_z + Q_z}{2}\right)a\right]\left[\sin\left(\frac{Q_z a}{2}\right) - \frac{2\kappa}{q_z}\cos\left(\frac{Q_z a}{2}\right)\right]\right\} \tag{3}$$

Following an established procedure, we search for a possible Hartree-Fock ground state by coherently mixing the states of opposite spins from the $|0, \vec{k}, \uparrow>$ and $|1, \vec{k}+\vec{Q}, \downarrow>$ minibands. The $|0, \vec{k}, \downarrow>$ miniband is considered fully occupied (and remains such) and does not enter the dynamics of the problem.

Linear independent operators describing such a state are obtained through a standard canonical transformation,[1] $c_{0,\vec{k},\uparrow} = \cos\theta_{\vec{k}} a_{\vec{k}} + \sin\theta_{\vec{k}} b_{\vec{k}}$, $c_{1,\vec{k}+\vec{Q},\downarrow} = -\sin\theta_{\vec{k}} a_{\vec{k}} + \cos\theta_{\vec{k}} b_{\vec{k}}$. The spin inclination angle $\theta_{\vec{k}}$ of each pair of states, is determined by minimizing the total Hartree-Fock energy of the system. By defining the quantity $g_{\vec{k}}$ as $g_{\vec{k}} = \sum_{\vec{q}} v_{01}(\vec{k},\vec{q},\vec{Q})\sin 2\theta_{\vec{k}+\vec{q}}$, $\theta_{\vec{k}}$ is obtained by solving the self-consistent equation

$$\tan 2\theta_{\vec{k}} = \frac{g_{\vec{k}}}{(\tilde{\epsilon}_{1,\vec{k}+\vec{Q},\downarrow} - \tilde{\epsilon}_{0,\vec{k},\uparrow})} \ , \tag{4}$$

where $\tilde{\epsilon}_{n,k_z}$ is the single particle energy with inclusion of exchange.

The trivial solutions of this equation are $\theta = 0$ and $\theta = \frac{\pi}{2}$, for paramagnetic and ferromagnetic occupancy of the ground state, respectively. Values of θ_k that satisfy Eq. (4) for finite g_k correspond to a state characterized by a spatially varying local magnetic moment, a SDW.[5] The existence of such solutions for the self-consistent equation, Eq. (4), is analyzed below.

In the vicinity of a transition point, the order parameter g_k varies continuously from zero to a small, finite value, bound from above by $\sum_{\vec{q}} v_{10}(\vec{k}, \vec{q}, \vec{Q})$. This corresponds to small deviations of the angle θ_k^* from its value $\theta_k = 0$ in the paramagnetic state (or $\theta_k = \frac{\pi}{2}$ in the ferromagnetic case). One can then approximate $\tan 2\theta \approx \sin 2\theta$. This leads to

$$\left| \sum_{q_y, q_z} v_{10}(\vec{k}, \vec{q}, \vec{Q}) / (\tilde{\epsilon}_{1,\vec{k}+\vec{Q},\downarrow} - \tilde{\epsilon}_{0,\vec{k},\uparrow}) \right| \leq 1 \, , \tag{5}$$

as the necessary and sufficient condition for the existence of non-trivial solutions of the self-consistent equation. The denominator in the right hand side of the above equation is estimated for $\theta_k = 0$, if the transition occurs from the paramagnetic state, or at $\theta_k = \frac{\pi}{2}$ if the transition occurs from the ferromagnetic state.

The most relevant electronic states for an instability from the paramagnetic state have $k_z \simeq \frac{\pi}{a}$ (corresponding to the maximum value for the energy in the lower band) and $k_z = 0$ (corresponding to the minimum in the upper band), so that $Q_z = \frac{\pi}{a}$. In this case, the kinetic energy difference is simply $\epsilon - \Delta$. Using these values for k_z and Q_z, and by setting $\ell Q_y = \ell Q_{yc} = 1.25$ (the value for which the corresponding 2D instability would occur) we plot, from Eq. (5), $\epsilon(\Delta)$ in Fig. 1. There, for illustration purposes, we have also chosen $a = 0.5\ell$. Below this curve, the paramagnetic occupancy (of $|0\downarrow>$ and $|0\uparrow>$) is a locally stable Hartree-Fock solution for the interacting system. Above this curve, the Hartree-Fock solution for our model is a SDW.

The transition from a ferromagnetic state involves small deviations from $\theta_k = \frac{\pi}{2}$. As before, the instability first occurs for values of the momentum at the edges of the Brillouin zone, $k_z = \frac{\pi}{a}$ and for a momentum transfer $Q_z = \frac{\pi}{a}$, which are separated by a kinetic energy difference, $-\epsilon - \Delta$. In Fig.1, the curve $\epsilon(\Delta)$, as determined by Eq. (5), delimits the region above which the ferromagnetic occupancy (of $|0\downarrow>$ and $|1\downarrow>$) is a stable Hartree-Fock solution. The two dashed curves cross at $\Delta = \Delta_c$. The paramagnetic to ferromagnetic transition occurs for values of ϵ between the two curves, just as it does for a 2D system[1]. Just as in the single layer case, which of these possible solutions is more stable is determined by a direct comparison of the corresponding total Hartree-Fock energies. This leads to the solid line separating paramagnetic and ferromagnetic states in Fig.1. For higher tunneling values, when $\Delta \geq \Delta_c$, the miniband broadening determines the appearance of an intermediate ground state characterized by a spatially varying local magnetic moment. The SDW solution describes a lower energy state of the interacting system. This can be surmised either from Overhauser original paper [5] or from the result of Reference [6], where it was shown that, for a three dimensional electron

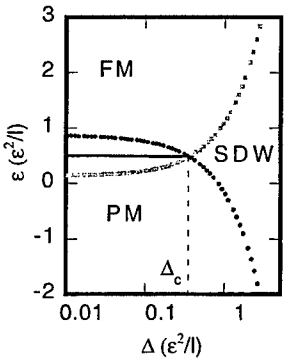

Figure 1: Hartree-Fock phase diagram of the superlattice in the presence of a quantizing magnetic field. The nature of the ground state depends critically on the magnitude of the bandwidth Δ. At small Δ the system undergoes a paramagnetic to ferromagnetic transition. For values of Δ exceeding a critical value Δ_c a SDW type of ground state becomes possible.

gas in the presence of a magnetic field, a linear SDW solution has lower energy than the paramagnetic state (when many Landau levels are assumed to be occupied) independently of the specific form of the repulsion potential. This would correspond in our case to an independence of our results on the exact form of $v_{10}(\vec{k}-\vec{k'})$ in Eq. (4). The magnetic moment associated with the SDW will be proportional to $(\hat{x}\cos Q_z z + \hat{y}\sin Q_z z)\sin 2\theta_{\vec{k}}$. This oscillatory magnetization must be added to the uniform magnetization associated with the fully occupied $|0\downarrow>$ Landau level, which is parallel to the direction of the applied magnetic field (considered for simplicity to be parallel to the superlattice axis).

References

[1] G. F. Giuliani and J. J. Quinn, Phys. Rev. B **31**, 6228 (1985).

[2] S. Koch, R. J. Haug, K. v. Klitzing, and M. Razeghi, Phys. Rev. B **47**, 4048 (1993).

[3] D. C. Marinescu, J. J. Quinn and G. F. Giuliani, to be published.

[4] L. Brey, Phys. Rev. Lett. **81**, 4692 (1998);

[5] A. W. Overhauser, Phys. Rev. Lett. **4**, 462 (1960); Phys. Rev. **128**, 1437 (1962).

[6] V. Celli and D. Mermin, Phys. Rev. **140**, A 839 (1965).

PB.58

EXACT RELATIONS FOR 2-DIMENSIONAL ELECTRON GAS SPIN CORRELATION FUNCTIONS

K. Takiuchi, M. Okada, H. Koizumi, K. Ito and T. Toyoda

Department of Physics, Tokai University
1117 Kitakaname, Hiratsuka, Kanagawa, Japan

Abstract

Using the non-perturbative method we discuss the virial theorem with a spin correlation term, the translational invariance of the spin correlation function and the f-sum rule for the spin response function.

1. Introduction

The aim of this work is to illustrate the power of the non-perturbative canonical field theory (NPCFT) of quantum many-body systems at finite temperatures [1-6] by applying it to an interacting two-dimensional electron gas and deriving some exact relations for the electron spin correlation functions. It has been shown the NPCFT plays an essential role in understanding a number of important quantum many-body effects [1-6], particularly quantum transport and spontaneous symmetry breaking, in various systems. The NPCFT gives a natural extension of Baym-Kadanoff's conserving approximation [2,3] and a finite temperature generalization of Nambu-Goldstone theorem [1]. Therefore, in view of the fact that quantum many-body effect is one of the most attractive features in the physics of a two-dimensional electron gas, it seems worthwhile to exploit the potential applicability of the NPCFT to the 2DEG. In the following we shall discuss the virial theorem with a spin correlation term, the translational invariance of the spin correlation function and the f-sum rule for the spin response function.

2. Scale transformation and the virial theorem

We first consider an interacting two-dimensional electron gas whose hamiltonian contains an effective spin-dependent interaction term,

$$H_{\rm int} = \frac{1}{2}\sum_{\alpha\beta\mu\nu} \int d^2\mathbf{x}\int d^2\mathbf{x}'\psi^\dagger_\alpha(\mathbf{x})\psi^\dagger_\mu(\mathbf{x}')V_{\alpha\beta;\mu\nu}(\mathbf{x}-\mathbf{x}')\psi_\nu(\mathbf{x}')\psi_\beta(\mathbf{x}) \ , \qquad (2.1)$$

where we have defined the potential

$$V_{\alpha\beta;\mu\nu}(\mathbf{x}-\mathbf{x}') = V_0(\mathbf{x}-\mathbf{x}')\delta_{\alpha\beta}\delta_{\mu\nu} + V_1(\mathbf{x}-\mathbf{x}')\sum_{i=1}^{3} s^i_{\alpha\beta}s^i_{\mu\nu} \quad . \tag{2.2}$$

In order to derive the virial theorem we introduce an external potential barrier that confines the two-dimensional electrons inside a finite spatial domain. That is, we add

$$H_{\text{ext}} = \sum_{\alpha} \int d^2\mathbf{x} U_{\text{ext}}(\mathbf{x})\psi^{\dagger}_{\alpha}(\mathbf{x})\psi_{\alpha}(\mathbf{x}) \ , \tag{2.3}$$

to the hamiltonian. By varying the shape of the confining potential, we can change the area of the electron gas. Since the spatial integration is defined over the entire two-dimensional space, the variation can be realized by the scale transformation of the electron field variables. We consider a scale transformation with respect to the spatial coordinate and assume that the number of the electrons are kept unchanged under the transformation. Then the corresponding canonical generator is

$$G = \frac{1}{2}\sum_{\alpha} \int d^2\mathbf{x}\, \mathbf{x}\cdot\left\{\psi^{\dagger}_{\alpha}(\mathbf{x})\left(\nabla - \bar{\nabla}\right)\psi_{\alpha}(\mathbf{x})\right\} \tag{2.4}$$

This is a special case of the generator for the general coordinate transformation [4,10].Hence, by virtue of the canonical generator for the scale transformation, the definition of the surface tension P yields

$$PA = -\left\langle\left[G, H_0 + H_{\text{int}}\right]\right\rangle \ . \tag{2.5}$$

Using the equal time canonical commutation relations for the field operators and the explicit form of the hamiltonian, we obtain

$$\begin{aligned} PA = \sum_{\alpha} & \int d^2\mathbf{x}\left\langle\psi^{\dagger}_{\alpha}(\mathbf{x})\left(\frac{-\hbar^2}{2m}\nabla^2\right)\psi_{\alpha}(\mathbf{x})\right\rangle \\ & -\frac{1}{4}\int d^2\mathbf{x}\int d^2\mathbf{x}'\left\{(\mathbf{x}-\mathbf{x}')\cdot\nabla V_0(\mathbf{x}-\mathbf{x}')\right\}\left\langle\rho(\mathbf{x})\rho(\mathbf{x}')\right\rangle \\ & -\frac{1}{4}\int d^2\mathbf{x}\int d^2\mathbf{x}'\left\{(\mathbf{x}-\mathbf{x}')\cdot\nabla V_1(\mathbf{x}-\mathbf{x}')\right\}\sum_{i=1}^{3}\left\langle S^i(\mathbf{x})S^i(\mathbf{x}')\right\rangle. \end{aligned} \tag{2.6}$$

This is the virial theorem for the 2-dimensional electron gas with a spin-dependent interaction. The last term on the right-hand side is our new result [10].

3. Translational invariance of correlation functions

The spin-spin correlation function for the 2-dimensional electrons under a uniform magnetic field is of particular importance for both theoretical and experimental analysis. From a physical point of view, because the magnetic field is homogenous, the correlation function must be translationally invariant. However, the proof is not trivial because the hamiltonian does not commute with the total momentum operator. Here we shall prove the invariance on the basis of the NPCFT.

As a model hamiltonian for the electrons placed in a uniform magnetic field we assume

$$H = H_{\mathrm{A}} + H_{\mathrm{S}} + H_{\mathrm{int}} \,. \tag{3.1}$$

The first term on the right-hand side is the kinetic energy of the electrons in the magnetic field and the second term is the coupling between the electron spin and the magnetic field. The last term is the electron-electron interaction. In terms of the spin density operator

$$S^i(\mathbf{x},\tau) = \sum_{\alpha\beta} \psi^{\dagger}_{\alpha}(\mathbf{x},\tau)\sigma^i_{\alpha\beta}\psi_{\beta}(\mathbf{x},\tau)\,, \tag{3.2}$$

we define the spin correlation function

$$\Lambda_{ij}(\mathbf{x}',\tau';\mathbf{x}'',\tau'') = -\left\langle T_{\tau}\left\{S^i(\mathbf{x}',\tau')S^j(\mathbf{x}'',\tau'')\right\}\right\rangle \,, \tag{3.3}$$

where $\langle.....\rangle$ denotes the grand canonical ensemble average. The total hamiltonian is obviously not commutative with the total momentum operator

$$P_k(\tau) = -i\hbar\sum_{\alpha} \int d^2\mathbf{x}\,\psi^{\dagger}_{\alpha}(\mathbf{x},\tau)\partial_k\psi_{\alpha}(\mathbf{x},\tau) \tag{3.4}$$

for $k = 2$, because the vector potential has an explicit x_2-dependence in the hamiltonian. Following the general procedure of the non-perturbative canonical formalism [1,5], we obtain

$$\begin{aligned} &-i\hbar\left(\partial'_k + \partial''_k\right)\left\langle T_{\tau}\left\{S^i(\mathbf{x}',\tau')S^j(\mathbf{x}'',\tau'')\right\}\right\rangle \\ &\qquad = \int_0^{\beta\hbar} d\tau\left\langle \frac{\partial P_k(\tau)}{\partial\tau} S^i(\mathbf{x}',\tau')S^j(\mathbf{x}'',\tau'')\right\rangle. \end{aligned} \tag{3.5}$$

The τ-derivative in the integral on the right-hand side can be rewritten using the canonical "equation of motions". Calculations with the help of the equal-time canonical commutation relations yield [7]

$$-i\hbar\left(\partial'_k + \partial''_k\right)\left\langle T_{\tau}\left\{S^i(\mathbf{x}',\tau')S^j(\mathbf{x}'',\tau'')\right\}\right\rangle = 0 \,, \tag{3.6}$$

which shows the spin correlation function $\Lambda_{ij}(\mathbf{x}',\tau';\mathbf{x}'',\tau'')$ is indeed a function of $\mathbf{x}'-\mathbf{x}''$.

4. The f-sum rule

We now consider a 2-DEG in an arbitrary magnetic field. The hamiltonian is same as that given in (3.1) except that the magnetic field is an arbitrary function of the space coordinates. In terms of the spin-density operators, the spin-spin retarded response function and its Fourier transform with respect to the time variables can be defined as [2,3,4]

$$\Lambda^R_{ij}(\mathbf{x},t;\mathbf{x}',t') \equiv -i\theta(t-t')\left\langle\left[S^i(\mathbf{x},t),S^j(\mathbf{x}',t')\right]\right\rangle \tag{4.1}$$

and

$$\Lambda^R_{ij}(\mathbf{x},t;\mathbf{x}',t') = \frac{1}{2\pi}\int_{-\infty}^{\infty} \Lambda^R_{ij}(\mathbf{x},\mathbf{x}';\omega)e^{-i(t-t')\omega}\,d\omega \,. \tag{4.2}$$

Within the framework of the NPCFT we have derived the *f*-sum rule:

$$\frac{1}{2\pi}\int_{-\infty}^{\infty}\omega\Lambda^{R}{}_{u}(\mathbf{x},\mathbf{x}';\omega)d\omega$$

$$=\frac{i\hbar}{2m}\langle\rho(\mathbf{x})\rangle\nabla^{2}\delta(\mathbf{x}-\mathbf{x}')+\frac{i\hbar}{2m}\nabla\delta(\mathbf{x}-\mathbf{x}')\cdot\nabla\langle\rho(\mathbf{x})\rangle \tag{4.3}$$

$$+\frac{ig\mu_{B}}{\hbar}\delta(\mathbf{x}-\mathbf{x}')\left\{\mathbf{B}(\mathbf{x})\cdot\langle\mathbf{S}(\mathbf{x})\rangle-B_{i}(\mathbf{x})\langle S^{i}(\mathbf{x})\rangle\right\}.$$

This is the new f-sum rule for the spin-spin retarded response function for the interacting electron gas in an arbitrary magnetic field.

References

[1] T. Toyoda, *Ann. Phys.* (N.Y.) **173** (1987) 226.

[2] T. Toyoda, *Phys. Rev.* **A39** (1989) 2659.

[3] M. Revzen, T. Toyoda, Y. Takahashi, F. Khanna, *Phys. Rev.* **B40** (1989) 769.

[4] T. Toyoda, *Phys. Rev.* **A48** (1993) 3492.

[5] T. Toyoda, Y. Takahashi and C. Zhang, *Phys. Rev.* **B50** (1994) 18640.

[6] T. Toyoda, *Physica* **A253** (1998) 498.

[7] K. Ito, M. Fukuda and T. Toyoda, *Phys. Rev.* **B56** (1997) 10161.

[8] T. Toyoda, H. Koizumi, *J. Phys.* **A31** (1998) 6209.

[9] T. Toyoda, M. Okada, *Phys. Rev.* **B58** (1998) 1210.

[10] T. Toyoda, K. Takiuchi, *Physica* **A261** (1998) 471.

PB.59

Molecular dynamics study of a classical two-dimensional electron system: Positional and orientational orders

Satoru Muto and Hideo Aoki

Department of Physics, University of Tokyo, Hongo, Tokyo 113-0033, Japan

Molecular dynamics simulation is used to investigate the crystallization of a classical two-dimensional electron system, in which electrons interact with the Coulomb repulsion. From the positional and the orientational correlation functions, we have found an indication that the solid phase has a quasi-long-range (power-law correlated) positional order and a long-range orientational order. This implies that the long-range $1/r$ system shares the absence of the true long-range crystalline order at finite temperatures with short-range ones for which Mermin's theorem applies. We also discuss the existence of the "hexatic" phase predicted by the Kosterlitz-Thouless-Halperin-Nelson-Young theory.

I. INTRODUCTION

More than 60 years ago, Wigner pointed out that an electron system will crystallize due to the Coulomb repulsion for low enough densities (Wigner crystallization) [1]. Although quantum effects play an essential role in a degenerate electron system, the concept of Wigner crystallization can be generalized to a classical case where the Fermi energy is much smaller than the thermal energy. A classical two-dimensional (2D) electron system is wholly specified by the dimensionless coupling constant Γ, the ratio of the Coulomb energy to the kinetic energy. Here $\Gamma \equiv (e^2/4\pi\epsilon a)/k_B T$, where e is the charge of an electron, ϵ the dielectric constant of the substrate, a the mean distance between electrons and T the temperature. For $\Gamma \ll 1$ the system will behave as a gas while for $\Gamma \gg 1$ as a solid. Experimentally, Grimes and Adams [2] succeeded in observing a transition from a liquid to a triangular lattice in a classical 2D electron system on a liquid-helium surface around $\Gamma_c = 137 \pm 15$, which is in good agreement with numerical simulations [4–6].

On the theoretical side, two conspicuous points have been known for 2D systems: (i) Mermin's theorem dictates that no true long-range crystalline order is possible at finite T in the thermodynamic limit [7]. To be precise, the $1/r$ Coulomb interaction is too long ranged to apply Mermin's arguments directly. Although there have been some theoretical attempts [8,9] to extend the theorem to the Coulomb case, no rigorous proof has been attained. (ii) A theory due to Kosterlitz, Thouless, Halperin, Nelson, and Young (KTHNY) predicts that a "hexatic" phase, characterized by a short-range positional order and a quasi-long-range orientational order, exists between a liquid phase and a solid phase [10]. Because the KTHNY theory is based on various assumptions and approximations, its validity should be tested by numerical methods such as a molecular dynamics (MD) simulation. Several authors have in fact applied MD methods to classical 2D electron systems, but they arrived at different conclusions on the KTHNY prediction [5,6].

In order to address both of the above problems, the most direct way is to calculate the positional and the orientational correlation functions, which is exactly the motiva-

tion of the present study.

II. NUMERICAL METHOD

A detailed description of the simulation is given elsewhere [15], so we only recapitulate it. We consider a rectangular area with a rigid uniform neutralizing positive background in periodic boundary conditions. The aspect ratio of the rectangle is taken to be $L_y/L_x = 2/\sqrt{3}$, which can accommodate a perfect triangular lattice [3]. The Ewald summation method is used to take care of the long-range nature of the $1/r$ interaction. We have employed Nosé-Hoover's canonical MD method [11,12] to incorporate temperature accurately.

The system is cooled or heated across the transition with a simulated annealing method. The results presented here are for $N = 900$ electrons with MD runs with 30,000–110,000 time-steps for each value of Γ. The correlation functions and other quantities are calculated for the last ~20,000 time-steps of each run.

Following Cha and Fertig [13], we define the positional and the orientational correlation functions from which we identify the ordering in each phase. The positional correlation function is defined by

$$C(r) \equiv \langle \rho_{\mathbf{G}}^*(\mathbf{r})\rho_{\mathbf{G}}(\mathbf{0})\rangle, = \left\langle \frac{\sum_{i,j}\delta(r-|\mathbf{r}_i-\mathbf{r}_j|)\frac{1}{6}\sum_{\mathbf{G}} e^{i\mathbf{G}\cdot(\mathbf{r}_i-\mathbf{r}_j)}}{\sum_{i,j}\delta(r-|\mathbf{r}_i-\mathbf{r}_j|)}\right\rangle,$$

where $\mathbf{G}$ is a reciprocal vector of the triangular lattice with the summation taken over the six $\mathbf{G}$'s that give the first peaks of the structure factor [inset (a) of Fig. 1]. The orientational correlation function is defined by

$$C_6(r) \equiv \langle \psi_6^*(\mathbf{r})\psi_6(\mathbf{0})\rangle, = \left\langle \frac{\sum_{i,j}\delta(r-|\mathbf{r}_i-\mathbf{r}_j|)\psi_6^*(\mathbf{r}_i)\psi_6(\mathbf{r}_j)}{\sum_{i,j}\delta(r-|\mathbf{r}_i-\mathbf{r}_j|)}\right\rangle,$$

where $\psi_6(\mathbf{r}) \equiv \frac{1}{n_c}\sum_{\alpha}^{\text{n.n.}} e^{6i\theta_\alpha(\mathbf{r})}$ with $\theta_\alpha(\mathbf{r})$ being the angle of the vector connecting an electron at $\mathbf{r}$ and the α-th nearest neighbor with respect to a fixed axis. The summation is taken over n_c nearest neighbors that are determined by the Voronoi construction [14].

III. RESULTS AND DISCUSSIONS

Let us first look at the positional and the orientational correlation functions in Fig. 1 for $\Gamma = 200$ and $\Gamma = 160$, for which the system is well in the solid phase. The positional correlation is seen to decay slowly, indicative of an algebraic (power-law) decay at large distances. The round-off in the correlation function around half of the system size should be an effect of the periodic boundary conditions. The algebraic decay of the positional correlation indicates that the 2D electron solid has only a *quasi-long-range* positional order. Thus we have obtained a numerical indication that Mermin's theorem [7] remains applicable to the $1/r$ Coulomb interaction, which is consistent with the analytical but approximate results obtained in [8,9].

On the other hand, the orientational correlation rapidly approaches a constant, indicating a long-range orientational order. Therefore, while the 2D electron solid has no true long-range crystalline order, we can say that it has a *topological* order. From a snapshot of the configuration [see inset (b) in Fig. 1], we can see that a long-range orientational order is preserved since defects (5- or 7-fold disclinations, etc) tend to appear as dislocation (5-7 combination of disclinations) pairs, i.e., 5-7-5-7 disclination quartets that

only disturbs the orientational correlation locally. Here the coordination number is again determined from the Voronoi construction.

Now we move on to the orientational correlation function (inset of Fig. 2) around the crystallization, which is obtained by cooling the system from a liquid to a solid. In between a short-range orientational order for $\Gamma = 120$ and a long-range one for $\Gamma = 140$, the correlation appears to decay algebraically at $\Gamma = 130$ with a power approximately equal to unity, which deviates from the upper bound of 1/4 predicted by KTHNY. However, numerical difficulties arising from finite-size and finite-time effects prevent us from drawing any definite conclusion on the existence of the hexatic phase. Namely, we cannot rule out the possibility that the power-law behavior is an artifact of insufficient equilibration. In fact, the solid phase persists down to $\Gamma = 130$ when the system is heated from a solid, which is not understandable unless the solid-hexatic and the hexatic-liquid transitions are of first- and second-order, respectively.

The KTHNY theory is based on a picture that the hexatic-liquid transition occurs through unbinding of disclination pairs. To examine if this is the case, we have calculated a defect-defect correlation function (Fig. 2), which we define as a distribution of 7-fold coordinated electrons with respect to a 5-fold coordinated electron. The correlation function exhibits no qualitative difference between $\Gamma = 120$ and $\Gamma = 130$, for which the disclinations are not tightly bound as compared with $\Gamma = 140$. If we look at a snapshot for $\Gamma = 130$ (Fig. 3), we see some domain structure as far as the present numerical simulation with finite-size and finite-time restrictions are concerned.

We have also looked at a dynamical property, i.e., the power spectral density of the velocity (Fig. 4), which is related to the vibrational density of states and is obtained as the Fourier transform of the velocity autocorrelation function via Wiener-Khinchin's theorem. The value at zero frequency, which is proportional to the diffusion constant, is non-zero (vanishingly small) in the liquid (solid) phase. In addition, we find a peak around the typical phonon frequency, which, curiously enough, persists even in the liquid phase, indicating well-defined local configurations.

[1] E. Wigner, Phys. Rev. **46**, 1002 (1934).

[2] C. C. Grimes and G. Adams, Phys. Rev. Lett. **42**, 795 (1979).

[3] L. Bonsall and A. A. Maradudin, Phys. Rev. B**15**, 1959 (1977).

[4] R. C. Gann, S. Chakravarty, and G. V. Chester, Phys. Rev. B**20**, 326 (1979).

[5] R. H. Morf, Phys. Rev. Lett. **43**, 931 (1979).

[6] R. K. Kalia, P. Vashishta, and S. W. de Leeuw, Phys. Rev. B**23**, 4794 (1981).

[7] N. D. Mermin, Phys. Rev. **176**, 250 (1968).

[8] S. Chakravarty and C. Dasgupta, Phys. Rev. B**22**, 369 (1980).

[9] A. Alastuey and B. Jancovici, J. Stat. Phys. **24**, 443 (1981).

[10] D. R. Nelson and B. I. Halperin, Phys. Rev. B**19**, 2457 (1979).

[11] S. Nosé, J. Chem. Phys. **81**, 511 (1984).

[12] W. G. Hoover, Phys. Rev. A**31**, 1695 (1985).

[13] M.-C. Cha and H. A. Fertig, Phys. Rev. B**50**, 14368 (1994).

[14] M. P. Allen, D. Frenkel, W. Gignac, and J. P. McTague, J. Chem. Phys. **78**, 4206 (1983).

[15] S. Muto and H. Aoki, Phys. Rev. B**59**, 14911 (1999).

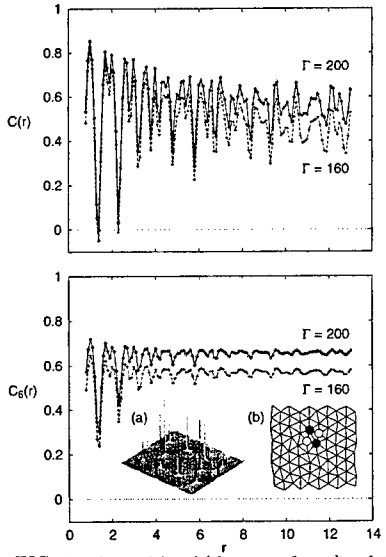

FIG. 1. The positional (the upper frame) and the orientational (the lower frame) correlation functions for $\Gamma = 200$ and $\Gamma = 160$. The horizontal scale is in units of the lattice constant of the triangular lattice. The structure factor for $\Gamma = 200$ is shown in inset (a), and a defect structure that is found for $\Gamma = 160$ is shown in inset (b), where 5-fold (7-fold) coordinated electrons are marked with empty (solid) circles.

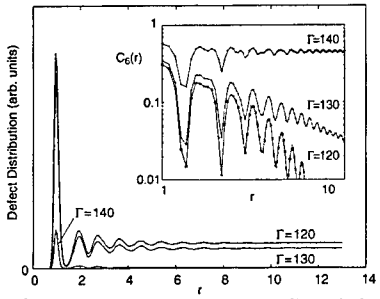

FIG. 2. Distribution of 7-fold coordinated electrons with respect to a 5-fold coordinated electron near the crystallization. The orientational correlation function is also shown in the inset.

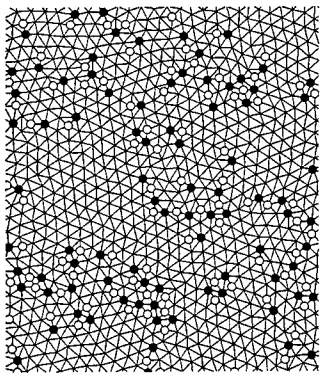

FIG. 3. A snapshot of the electron configuration for $\Gamma = 130$. 5-fold (7-fold) coordinated electrons are marked with empty (solid) circles.

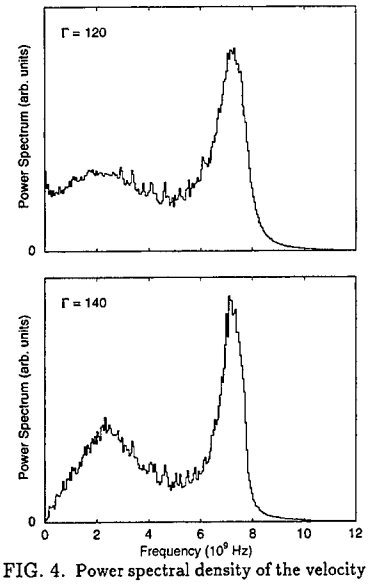

FIG. 4. Power spectral density of the velocity for $\Gamma = 120$ and $\Gamma = 140$. The plot for $\Gamma = 130$ is similar to that of $\Gamma = 120$.

WA.1

Presentation by:

H. Stormer, *Bell Labs, Murray Hill, NJ, USA*
"The Fractional Quantum Hall Effect"

WA.2

Presentation by:

R. Laughlin, *Stanford University, Stanford, CA, USA*
"Theory of the Fractional Quantum Hall Effect"

WA.3

Presentation by:

B.I. Halperin, *Harvard University, Cambridge, MA, USA*
"Outstanding Problems in Quantum Hall Systems"

Composite Fermions and the Fractional Quantum Hall Effect: Essential Role of the Pseudopotential

J. J. Quinn and A. Wójs
University of Tennessee, Knoxville, Tennessee 37996, USA

The mean field (MF) composite Fermion (CF) picture successfully predicts the band of low lying angular momentum multiplets of fractional quantum Hall systems for any value of the magnetic field. This success cannot be attributed to a cancellation between Coulomb and Chern–Simons interactions between fluctuations beyond the mean field. It results instead from the short range behavior of the Coulomb pseudopotential in the lowest Landau level (LL). The class of pseudopotentials for which the MFCF picture is successful can be defined, and used to explain the success or failure of the picture in different cases (e.g. excited LL's, charged magneto-excitons, and Laughlin quasiparticles in a CF hierarchy picture).

Introduction. The MFCF picture [1,2] does remarkably well in predicting the band of angular momentum (L) multiplets that form the low energy sector of a 2D electron system in a strong magnetic field B. A Laughlin [3] incompressible $L = 0$ ground state of an N electron system occurs when the magnetic monopole (which produces the radial magnetic field at the surface of the Haldane [4] sphere) has strength $2S_m = m(N-1)$, where m in an odd integer. For $2S$ different from $2S_m$ there will be $|2S - 2S_m|$ quasiparticles (QP's). This is illustrated in Fig. 1, which displays the energy spectra of ten electrons on a Haldane sphere at monopole strength $25 \leq 2S \leq 29$. Frame (a) shows the Laughlin incompressible ground state at $L = 0$. Frames (b) and (c) show states containing a single quasielectron QE (a) and quasihole QH (b) at $L = 5$. In frames (d) and (e) the two QP states form the low energy bands. In the MFCF picture, the effective monopole strength $2S^*$ is given by $2S^* = 2S - 2p(N-1)$, where p is an integer. S^* is the angular momentum l_0^* of a MF CF in the lowest CF Landau level. At $2S = 27$ (with $p = 1$), $l_0^* = 9/2$ and the lowest shell accommodates $2l_0^* + 1 = 10$ CF's, so that the shell is filled giving $L = 0$. At $2S = 27 \pm 1$ there will be one CF QHwith $l_{QH} = 5$ or one CF QE with $l_{QE} = 5$, giving $L = 5$. At $2S = 27 \pm 2$ there will be two CF QH each with $l_{QH} = 11/2$ giving $L = 0$, 2, 4, 6, 8, 10, or two CF QE each with $l_{QE} = 9/2$ giving $L = 0$, 2, 4, 6, 8.

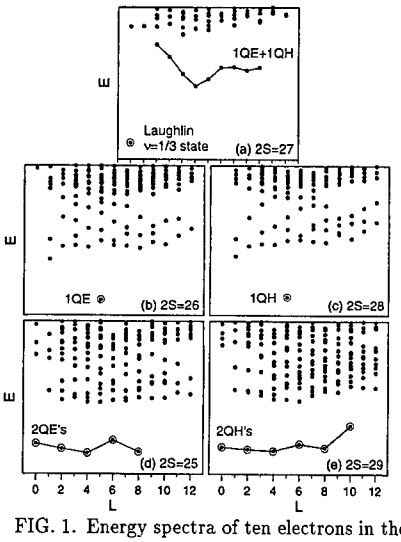

FIG. 1. Energy spectra of ten electrons in the lowest LL at $25 \leq 2S \leq 29$. Open circles mark lowest energy bands with fewest CF QP's.

It is quite remarkable that the MFCF picture works so well since its energy scale is $\hbar\omega_c^* = (2p+1)^{-1}\hbar\omega_c \propto B$, in contrast to the scale of the Coulomb interaction $e^2/\lambda \propto \sqrt{B}$, where λ is the magnetic length. The energy

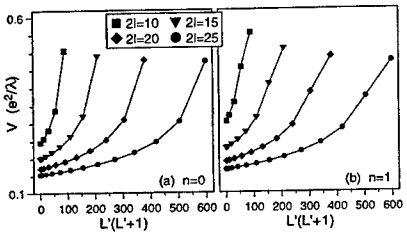

FIG. 2. Pseudopotentials V of the Coulomb interaction in the lowest (a), and first excited LL (b) as a function of squared pair angular momentum $L'(L'+1)$ for different values of $l = S + n$.

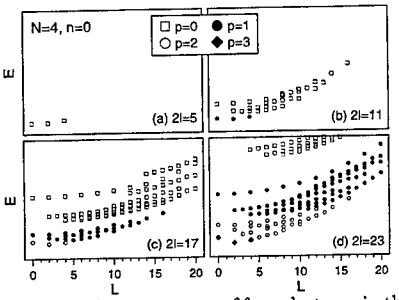

FIG. 3. Energy spectra of four electrons in the lowest LL. Different symbols mark subspaces $\mathcal{H}_p$ for $p = 0$, 1, 2, and 3.

values obtained in the MFCF picture are totally incorrect, but the structure of the low energy spectrum (which multiplets form the lowest lying band) is correct. As first suggested by Haldane [5], this is a result of the behavior of the pseudopotential $V(L')$ (interaction energy of a pair of electrons vs. pair angular momentum) in the lowest LL.

Pseudopotential. In Fig. 2 we plot $V(L')$ vs. $L'(L'+1)$ for the lowest ($n = 0$) and first excited ($n = 1$) LL for different values of $2l$ [6]. Note that for $n = 0$ $V(L')$ rises more steeply than linearly with increasing L' at all values of L', but for $n = 1$ this is not true at the highest allowed values of L'.

A useful operator identity [7] relates the total angular momentum $\hat{L} = \sum_i \hat{l}_i$ to the sum over all pairs of the pair angular momentum $\hat{L}_{ij} = \hat{l}_i + \hat{l}_j$,

$$\sum_{i<j} \hat{L}_{ij}^2 = \hat{L}^2 + N(N-2)\,\hat{l}^2. \qquad (1)$$

Here, each Fermion has angular momentum l, so that $\hat{l}^2$ has the eigenvalue $l(l+1)$. From Eq. (1) it is not difficult to show that for a "harmonic" pseudopotential defined by $V_H(L') = A + B\,L'(L'+1)$, the energy $E_\alpha(L)$ of the αth multiplet with total angular momentum L would be independent of α, and that $E(L)$ would be of the form $a + b\,L(L+1)$ [7]. Because the actual pseudopotential is different from $V_H(L')$, the degeneracy of the multiplets α of the same L is lifted.

For a pseudopotential (which we will refer to as a short range, SR, potential) that rises more quickly with L' than $V_H(L')$, the lowest energy multiplets must, to the extent that it is possible, avoid having pair amplitude (or coefficient of fractional parentage [8]) from the largest values of L'. For $V_H(L')$ the lowest angular momentum states have the lowest energy. However, the difference $\Delta V(L') = V(L') - V_H(L')$ lifts the degeneracy of multiplets having the same value of L. If some low value of L has a very large number N_L of multiplets, $\Delta V(L')$ can push the lowest multiplet at that L value to a lower energy than any multiplet of a neighboring smaller L value for which N_L is much smaller.

Energy Spectra of SR Pseudopotential. Fig. 3 displays some very informative results [7] for a simple four particle system at different values of the single particle angular momentum l (which differs by $\Delta l = p(N-1)$, $p = 1, 2, \ldots$). Note that the set of multiplets at $l - p(N-1)$ is always the subset of the multiplets at l. The SR pseudopotential appears to have the property that its Hilbert space $\mathcal{H}$ splits into subspaces $\mathcal{H}_p$ containing states

with no parentage from pair angular momentum $L' = 2(l-p)-1$. $\mathcal{H}_0$ is the entire space, $\mathcal{H}_1$ is the subspace that avoids $L'_{\rm MAX} = 2l-1$, $\mathcal{H}_2$ avoids $L = 2l-1$ and $2l-3$, etc. Since the interaction energy in each subspace $\mathcal{H}_p$ is measured on the scale $V(L' = 2(l-p)-1)$, the spectrum splits into bands with gaps between bands associated with the differences in appropriate pseudopotential coefficients. The largest gap is always between the zeroth and first band, the next largest between the first and second, etc. Note that the subset of multiplets at $l' = l - p(N-1)$ is exactly the subset chosen by the MFCF picture. In addition, at the Jain values $\nu = n(1+2pn)^{-1}$, where $n = 1, 2, \ldots$, there is only a single multiplet at $L = 0$ in the "lowest subset" for an appropriate value of p.

These ideas can be made more formal by using the algebra of angular momentum addition and the "coefficients of fractional parentage" familiar to atomic and nuclear physicists. The conclusions are quite clear. There is really only one energy scale, that of the Coulomb interaction e^2/λ. Laughlin states occur when the fractional parentage for electrons (or holes) allows avoidance of the pseudopotential $V(2(l-p)-1)$ for $p = 0, 1, \ldots$. Jain states occur when the fractional parentage of the appropriate $V(2(l-p)-1)$ is much smaller (but not zero) for $L = 0$ than for other allowed multiplets. The MFCF picture works only if $V(L')$ is a SR potential that rises like $[L'(L'+1)]^\beta$ with $\beta > 1$ [7].

Other Pseudopotentials. For the $n = 1$ and higher LL's, $V(L')$ is not SR for all values of L'. For $n = 1$, $V(L')$ is essentially harmonic at $L' = L'_{\rm MAX}$, and for $n > 1$ it is subharmonic at the largest values of L'. Therefore, even if ground states at filling factors like $\nu = 2 + 1/3$ have $L = 0$, they are not Laughlin type incompressible states which avoid pair angular momentum $L'_{\rm MAX} = 2l-1$.

A CF hierarchy scheme was proposed by Sitko et al. [9] in which the CF transformation was reapplied to QP's in partially filled shells. The application of the MFCF approximation was found to work in some cases but not in others. Some idea of when the MFCF approximation is valid can be obtained from looking at the 2QE and 2QH states in Fig. 1. The QH pseudopotential is SR at $L = 10$, but not at $L = 8$. The QE pseudopotential is certainly not SR at $L = 8$, but at $L = 6$ it might be. This suggests that Laughlin states will be formed by QH's of the $\nu = 1/3$ state at $\nu_{\rm QH} = 1/3$ and by QE's of the $\nu = 1/3$ state at $\nu_{\rm QE} = 1$, explaining the strong FQHE of the underlying electron system at the Jain $\nu = 2/7$ and $2/5$ filling factors. In contrast, no FQHE at $\nu_{\rm QH} = 1/5$ ($\nu = 4/13$ electron filling) or $\nu_{\rm QE} = 1/3$ ($\nu = 4/11$) would be expected because the QP pseudopotentials are not SR at these values.

A final interesting example is that of a multi-component plasma of electrons and one or more negatively charged excitonic ions X_k^- (a bound state of k neutral excitons and an electron) formed in an electron-hole system. These excitonic ions are long lived Fermions with LL structure [10]. The angular momentum of an X_k^- on a Haldane sphere is $l_k = S - k$. The pseudopotentials describing the interactions of X_k^- ions with electrons and with one another can be shown to be SR. In fact, $V_{AB}(L')$, where A or B or both are composite particles has a "hard core" for which one or more of the largest values of $V_{AB}(L')$ are effectively infinite.

The following configurations of ions have low energy in the twelve electron–six hole system at $2S = 17$. The $6X^-$ configuration (i) has the maximum total binding energy $\varepsilon_{\rm i}$. Other expected low lying bands are: (ii) $e^- + 5X^- + X^0$ with $\varepsilon_{\rm ii}$ and (iii) $e^- + 4X^- + X_2^-$ with $\varepsilon_{\rm iii}$. Here, $\varepsilon_{\rm i} > \varepsilon_{\rm ii} > \varepsilon_{\rm iii}$ are all known. Although we are unable to perform an exact diagonalization for this system in terms indi-

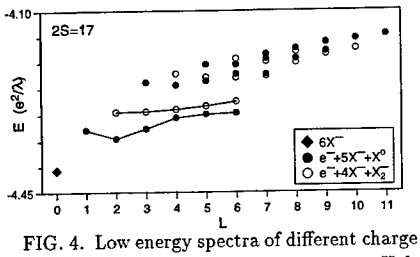

FIG. 4. Low energy spectra of different charge configurations of the $12e + 6h$ system on a Haldane sphere at $2S = 17$.

vidual electrons and holes, we can use appropriate pseudopotentials and binding energies to obtain the low lying states in the spectrum. The results are presented in Fig. 4. There is only one $6X^-$ state (the $L = 0$ Laughlin $\nu_{X^-} = 1/3$ state [3]) and two bands of states in each of groupings (ii) and (iii). A gap of $0.0626\ e^2/\lambda$ separates the $L = 0$ ground state from the lowest excited state.

Generalized Composite Fermion Picture. In order to understand the numerical results obtained in Fig. 4, it is useful to introduce a generalized CF picture by attaching to each particle fictitious flux tubes carrying an integral number of flux quanta ϕ_0. In the multi-component system [11], each a-particle carries flux $(m_{aa} - 1)\phi_0$ that couples only to charges on all other a-particles and fluxes $m_{ab}\phi_0$ that couple only to charges on all b-particles, where a and b are any of the types of Fermions. The effective monopole strength seen by a CF of type a (CF-a) is $2S_a^* = 2S - \sum_b (m_{ab} - \delta_{ab})(N_b - \delta_{ab})$. For different multi-component systems we expect generalized Laughlin incompressible states when all the hard core pseudopotentials are avoided and CF's of each kind fill completely an integral number of their CF shells (e.g. $N_a = 2l_a^* + 1$ for the lowest shell). In other cases, the low lying multiplets are expected to contain different kinds of quasiparticles (QP-A, QP-B, ...) or quasiholes (QH-A, QH-B, ...) in neighboring filled shells. Our multi-component CF picture can be applied to the $12e+6h$ spectrum given in Fig. 4. The agreement is really quite remarkable and strongly indicates that our multi-component CF picture is correct.

In this work we have emphasized that the success of the MFCF picture is critically dependent on the nature of the pseudopotential. We have presented several examples of SR pseudopotentials for which the CF picture works well, and several subharmonic pseudopotentials for which it does not.

We gratefully acknowledge partial support from the Materials Research Program of Basic Energy Sciences, US Department of Energy.

[1] J. Jain, Phys. Rev. Lett. **63**, 199 (1989).
[2] X. M. Chen and J. J. Quinn, Solid State Commun. **92**, 865 (1996).
[3] R. Laughlin, Phys. Rev. Lett. **50**, 1395 (1983).
[4] F. D. M. Haldane, Phys. Rev. Lett. **51**, 605 (1983).
[5] F. D. M. Haldane, in *The Quantum Hall Effect*, edited by R. E. Prange and S. M. Girvin, Springer-Verlag, New York 1987.
[6] A. Wójs and J. J. Quinn, Solid State Commun. **108**, 493 (1998).
[7] A. Wójs and J. J. Quinn, Solid State Commun. **110**, 45 (1999).
[8] A. de Shalit and I. Talmi, *Nuclear Shell Theory*, Academic Press, New York and London 1963.
[9] P. Sitko, K.-S. Yi, and J. J. Quinn, Phys. Rev. B **56**, 12417 (1997).
[10] A. Wójs, P. Hawrylak, and J. J. Quinn, Physica B **256-258**, 490 (1998); Phys. Rev. Lett. (submitted, cond-mat/9810082).
[11] A. Wójs, I. Szlufarska, K.-S. Yi, and J. J. Quinn, Phys. Rev. Lett. (submitted, cond-mat/9904395).

Ten Years of Composite Fermion

J.K. Jain
Physics Department, 104 Davey Laboratory, Pennsylvania State University, University Park, Pennsylvania, 16802
(June 14, 1999)

A single principle, namely the existence of a particle called composite fermion, has not only brought about a synthesis of the rich and non-trivial phenomenology of the two-dimensional electron liquid in high magnetic fields, but also provided an extremely accurate, zero-parameter quantitative theory. A brief perspective is given of what is firmly established and what remains to be understood.

71.10.Pm

I have been asked by the organizers to express my personal views on the present status of our understanding of the fractional quantum Hall effect,[1] and on the promising future directions, which I will do briefly from the perspective of the composite fermion (CF)[2] physics.

The prediction of existence of composite fermion was motivated by the complex phenomenology of the fractional quantum Hall effect (FQHE), where the multitude of fractions observed over the years following the initial discovery[1] and theory[3] of the 1/3 state strongly hinted at a deeper underlying structure. The world of composite fermion has seen a tremendous expansion during the last ten years, with extensions into several directions and repeated successes in explaining and predicting dramatic phenomena[4,5]. Even though the original clue came from the FQHE, which is an observation of quantized CF Landau levels (CF-LLs), composite fermions are now known to be more general than the FQHE. They also make a Fermi sea (composite Fermi sea),[6] execute semiclassical cyclotron orbits,[7] show Shubnikov-de Haas oscillations,[8] have been investigated in mesoscopic experiments,[7,9] and may even form a paired state.[10]

Defining properties of composite fermion:

Composite fermions are electrons that have captured an even number of vortices of the many particle wave function (sometimes conveniently viewed as electrons carrying an even number of flux quanta). They are created because this is how electrons best screen the repulsive inter-electron interaction. Composite fermions are simply screened electrons, with the bound vortices creating a correlation hole aroud each electron.

To a good first approximation, composite fermions can be treated as ordinary, weakly interacting fermions. The vortices bound to composite fermions produce their own phase factors as they move about, partly canceling the Aharonov-Bohm phases due to the external magnetic field. As a result, composite fermions experience a much reduced effective magnetic field. They form their own Landau levels (CF-LLs) in this reduced magnetic field, with their filling factor ν^* related to the electron filling factor ν by $\nu = \nu^*/(2p\nu^* \pm 1)$. This remarkable feature distinguishes composite fermions from electrons, and is responsible for the exotic properties of the lowest LL liquid.

Composite fermions obey fermionic statistics. The charge of a composite fermion is obviously $-e$, since each electron produces a composite fermion. However, when a composite fermion is added to a filled CF-LL state, its charge is partly screened, and the charge of the screened composite fermion ($-e$ plus the charge of the correlation hole) is a sharply defined fraction of the electron charge, given by $-e/(2pn \pm 1)$. It is called the "local charge" of composite fermion;[11] its value depends on the screening properties of the background CF state. It should be stressed that the existence of fractionally charged excitations can be derived from general arguments assuming incompressibility at fractional filling factors, and was known prior to the CF theory.[3] The CF theory, however, provides a microscopic understanding, clarifying that these fractionally charged objects are in fact simply screened electrons!

The wave functions for composite fermions are constructed from the known wave functions of non-interacting electrons at the effective filling factor by attaching $2p$ vortices to each electron, which amounts to a multiplication by the Jastrow factor $\prod_{j<k}(z_j - z_k)^{2p}$. The CF wave functions contain no adjustable parameters for filled CF-LL states and their low-energy excitations.

What we know:

There is a vast body of core knowledge in the field of composite fermion that is securely established, from a combination of real and computer experiments,[4] and provides the basis for further investigation. Here is a partial account.

The FQHE is the IQHE of composite fermions. Perhaps the most compelling evidence for this is simply to plot the FQHE resistance trace as a function of the effective magnetic field and then notice that it is practically indistinguishable from the resistance trace in the IQHE regime. The integer ($\nu^* = n$) sequence of composite fermions produces the observed fractions $\nu = n/(2pn+1)$. Exact numerical studies further confirm this interpretation; the parameter-free CF wave functions with n filled CF-LLs are extraordinarily good representations of the true ground state wave functions

at $\nu = n/(2pn+1)$.

The low-energy branch of excitations seen in exact diagonalization studies is the CF-exciton, in which a single composite fermion is promoted from the topmost filled CF-LL to the lowest unoccupied CF-LL, creating a CF particle-hole pair. An isolated CF-particle (CF-hole) in an otherwise empty (filled) CF-LL is a charged excitation, with a fractional local charge of magnitude $e/(2pn+1)$. The low-energy physics at a filling factor away from $\nu = n/(2pn \pm 1)$ is described in terms of a system in which the topmost CF-LL is only partially occupied. All this is exhaustively verified in exact numerical studies.[4] The observed energy gaps can be characterized phenomenologically in terms of an effective cyclotron energy of composite fermions, which yields an effective mass for composite fermion.[6,12]

The compressible state at the half filled electronic Landau level is the Fermi sea of composite fermions.[6] The radius of the cyclotron orbit of the charge carriers has been measured in several experiments in the vicinity of $\nu = 1/2$,[7] and yields a Fermi wave vector consistent with $k_F = \sqrt{4\pi\rho}$, ρ being the density, as expected for a fully polarized Fermi sea. An observation of the composite Fermi sea is a direct confirmation of the Fermi statistics of composite fermions. The weak oscillations around the CF sea are Shubnikov-de Haas oscillations of composite fermions.[8]

The FQHE at small Zeeman energies is explained in terms of spinful composite fermions.[13] The observed polarizations and the phase diagram as a function of the Zeeman energy are in good agreement with the CF theory.[14]

At $\nu \leq 1/9$, the CF exciton has lower energy than the filled CF-LL state at a finite wave vector,[15] signaling an instability of the CF liquid toward a charge-density-wave state. This is consistent with the fact that no FQHE has been observed at $\nu \leq 1/9$, and also with earlier calculations[16] indicating that a transition to a Wigner crystal takes place at around $\nu = 1/7$.

Unresolved issues:

Some of the interesting open questions that come to mind are as follows.

The puzzle of the 5/2 FQHE[17] still remains. There is a growing consensus that it is a paired state of composite fermions.[10] The theoretical support for this state is not yet as clean and convincing as for the lowest LL FQHE states, but that may be a generic feature of FQHE in higher LLs.

Our understanding of excited states is in general far from satisfactory. Numerical studies show that a model in which composite fermions are taken as completely non-interacting produces spurious states, which are annihilated upon imposing the lowest Landau level constraint.[18] A proper understanding of the energy level counting is crucial for the thermodynamics of the CF state, especially for the CF sea for which there is no gap to excitations. The issue of treating the residual interaction between composite fermions also becomes important here.

For an ideal disorder-free system, will there be FQHE at arbitrary large n along the sequence $\nu = n/(2n+1)$? If not, what is the nature of the instability? What states other than the principal ones are possible?

More work will be needed for a better understanding of the role of disorder, issue of localization of composite fermions, non-uniform systems of composite fermions, edge states, etc. Even though the CF theory gives an excellent quantitative account of the exact numerical experiments, features like non-zero thickness, Landau level mixing, disorder will need to be incorporated reliably for a more accurate comparison with experiment.

Numerical studies have made a convincing case that two-dimensional quantum dots exposed to strong magnetic fields are artificial atoms of composite fermions.[15] It would be worth pursuing if the chemistry of composite fermions can provide further insight into their properties.

If the past is any guide, it is a safe bet that the field of two-dimensional electrons in high magnetic fields will continue to be a fertile source of unpredictable discoveries. The theoretical understanding of the field of 2D electrons in high magnetic fields is now sufficiently mature that it can serve as a playground for testing new and old ideas. Concepts and mathematical techniques formulated in other contexts, e.g. Jastrow wave functions and the Chern-Simons field theory,[19,6] have been useful here. It will be interesting to see what ideas developed in the course of the composite fermion theory will turn out to be relevant elsewhere in physics.

Financial support from National Science Foundation under grant no. DMR-9615005 is gratefully acknowledged.

[1] D.C. Tsui, H.L. Stormer, and A.C. Gossard, Phys. Rev. Lett. **48**, 1559 (1982).
[2] J.K. Jain, Phys. Rev. Lett. **63**, 199 (1989).
[3] R.B. Laughlin, Phys. Rev. Lett. **50**, 1395 (1983).
[4] *Composite Fermions*, edited by Olle Heinonen, (World Scientific, New York, 1998).
[5] *Perspectives in Quantum Hall Effects*, edited by S. Das Sarma and A. Pinczuk (Wiley, New York, 1997).
[6] B.I. Halperin, P.A. Lee, and N. Read, Phys. Rev. B **47**, 7312 (1993).

[7] R.L. Willett *et al.*, Phys. Rev. Lett. **71**, 3846 (1993); W. Kang *et al.*, *ibid.* **71**, 3850 (1993); V.J. Goldman *et al.*, *ibid.* **72**, 2065 (1994); J.H. Smet *et al.*, *ibid.* **77**, 2272 (1996); Semiconductor Sci. Tech. **11**, 1482 (1996).
[8] D.R. Leadley *et al.*, Phys. Rev. Lett. **72**, 1906 (1994); R.R. Du *et al.*, Solid State Commun. **90**, 71 (1994).
[9] J. Herfort *et al.*, J. Phys. Cond. Matter **7**, 9563 (1995); C.-T. Liang *et al.*, Phys. Rev. B **53**, R7596 (1996).
[10] G. Moore and N. Read, Nucl. Phys. B **360**, 362 (1991); M. Greiter, X.G. Wen, and F. Wilczek, Phys. Rev. Lett. **66**, 3205 (1991); K. Park *et al.*, Phys. Rev. B **58**, R10167 (1998); E.H. Rezayi and F.D.M. Haldane, unpublished.
[11] A.S. Goldhaber and J.K. Jain, Phys. Lett. A **199**, 267 (1995).
[12] R.R. Du *et al.*, Phys. Rev. Lett. **70**, 2944 (1993).
[13] R.R. Du *et al.*, *ibid.* **75**, 3926 (1995); R.J.Nicholas *et al.* Semicond.Sci.Technol. **11**, 1477 (1996); I.V. Kukushkin, K. v. Klitzing, and K. Eberl, Phys. Rev. Lett. **82**, 3665 (1999).
[14] K. Park and J.K. Jain, Phys. Rev. Lett. **80**, 4237 (1998); X.G. Wu, G. Dev, and J.K. Jain, *ibid.* **71**, 153 (1993).
[15] J.K. Jain and R.K. Kamilla, Int. J. Mod. Phys. **11**, 2621 (1997).
[16] P.K. Lam and S.M. Girvin, Phys. Rev. B **30**, 473 (1984).
[17] R.L. Willett, *et al.*, Phys. Rev. Lett. **59**, 1776 (1987).
[18] X.G. Wu and J.K. Jain, Phys. Rev. B **51**, 1752 (1995).
[19] A. Lopez and E. Fradkin, Phys. Rev. B **44**, 5246 (1991). For recent developments, see the articles of G. Murthy and R. Shankar, and of S. Simon in Ref. 4.

WB.1

Huge Longitudinal Resistance Maxima at Fractional Filling Factors

S. Kronmüller and W. Dietsche

Max-Planck-Institut für Festkörperforschung, Heisenbergstraße 1, D-70569 Stuttgart, Germany
email: skron@klizix.mpi-stuttgart.mpg.de Fax: 0711-685 1572

Abstract

Very large resistance maxima can be observed in the longitudinal magneto-resistance of a narrow single quantum well. They exist only at certain fractional filling factors and are clearly related to the coupling of the electron to the nuclear spin-system. In resistively detected NMR experiments, which are possible in this system, a very unusual fine structure of the resonance lines is observed, which hints towards an unusual coupling between the electron and nuclear system.

Key words: FQHE, spin transition, nuclear spins PACS: 73.40.Hm, 73.20.Dx

1 Introduction

Two dimensional electron gases (2DEG), that are subjected to a perpendicular magnetic field, show the integer (IQHE) [1] and the fractional (FQHE) [2] quantum Hall effects. The origin of the IQHE is the quantization of the single electron energies in a magnetic field and the resulting energy gaps in the energy spectrum. The FQHE is also caused by energy gaps, but in this case they are a result of the Coulomb interaction between the electrons. This was first suggested by Laughlin [3] who proposed a wave function which allowed the theoretical description of fractions of the type $\nu = 1/q$ with q = 3, 5, 7, .. . The importance of the electron spin for the FQHE states and excitations was first realized by Halperin [4]. Calculations of Chakraborty and Pietiläinen [5] showed that the spin polarization of the ground states and the excited states of the FQHE depend on the absolute magnetic field. The reason for this is the relatively small effective g-factor in GaAs. The transition between the different spin polarized ground states has been experimentally observed for several filling fractions [6,7]. That discussion showed the importance of the Zeeman energy and Coulomb energy for the ground states of the FQHE. It is therefore conceivable that even slightly modified energies, for instance due to a different thickness of the 2DEG, can have a substantial effect on the development of the FQHE states and the measured longitudinal resistivity.

As the FQHE is best developed in the very high mobility samples, one uses usually either interface heterostructures or wide quantum wells to investigate the FQHE regime. Recently, experiments on samples with narrow quantum wells (15 nm), which still have relatively high mobilities ($10^6 cm^2/Vs$), have

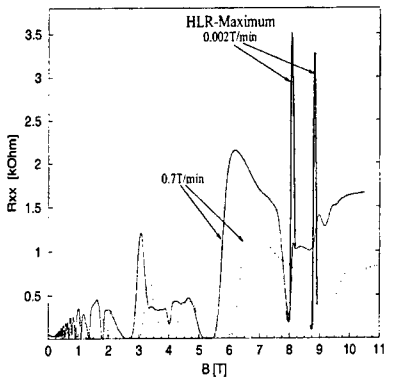

Fig. 1. Longitudinal magneto resistance of a 2DEG at two different densities. If the sweep rate is very slow then one observes a very sharp and huge resistance peak at filling factor $\frac{2}{3}$.

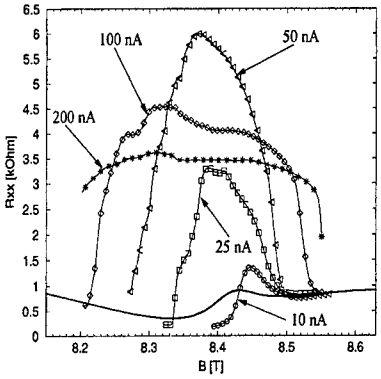

Fig. 2. Current dependence of the huge longitudinal resistance maximum at T=0.4 K. The sweep rate is 0.7 T/min for the bold trace. All other curves are measured with 0.002T/min.

been performed by our group [8]. They show a rather unusual behavior of the longitudinal magneto-resistance in the vicinity of certain fractional filling factors. These effects will be discussed in this contribution.

2 The Huge Longitudinal Resistance

The experiment is performed on a modulation doped AlGaAs/GaAs structure with a GaAs quantum well of 15 nm thickness; the spacer thickness is 120 nm. The carrier density can be varied by illuminating the sample with a LED. Typical carrier densites are between $1.1{\cdot}10^{11}$and $1.4{\cdot}10^{11}$ cm^{-2} after illumination. The mobility of the sample is about $1.8{\cdot}10^{6}$ cm^2/Vs. The samples are shaped as a standard Hall-bar. Measurements are performed on two different Hall-bars having different widths (80 μm and 800 μm). Figure 1 shows typical traces of the longitudinal resistance of the 80 μm wide sample measured at 0.4 K for two slightly different electron densities. As long as the magnetic field is swept with 0.7 T/min, which is a standard sweep rate of the magnetic field, the longitudinal magneto resistance R_{xx} corresponds closely to the traces expected for QHE samples. Integer filling factors ν show a vanishing R_{xx} and the fractional effects start to develop, especially at $\nu = \frac{2}{3}$ a clear minimum can be observed. If the sweep rate is substantially reduced to 0.002 T/min, however, then very prominent resistance maxima are observed at this filling factor (Figure 1). One can see from the figure, that this maximum remains at $\nu = \frac{2}{3}$ if the density of the 2DEG is changed, which means that it is correlated with the FQHE at $\nu = \frac{2}{3}$. This resistance maximum was termed the huge longitudinal resistance (HLR) in the previous publication [8].

The time needed for the maximum to develop is measured by keeping the magnetic field constant and measuring the resistance versus time. The time constant till the max-

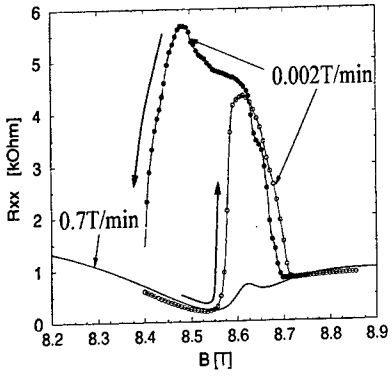

Fig. 3. The hysteresis of a HLR-Maximum measured during both up and down sweeps at 0.4 K.

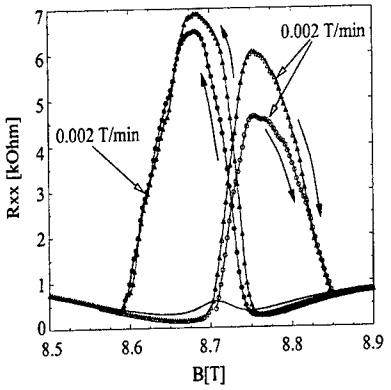

Fig. 4. The hysteresis of a HLR-Maximum for a slightly different carrier density compared with figure 3. Both, up and down sweeps are showed.

imum saturates is about 10 min for a 80 μm wide Hall-bar and about 50 min for a 800 μm wide one, i.e. the time constant scales with the size of the sample [8]. Another surprising property of this HLR-Maximum is its dependence on current. Examples are shown in Fig. 2 which shows the resistance as function of the magnetic field near filling factor $\frac{2}{3}$. At very small currents the maximum is very small and with increasing current it increases until it is optimally developed which means the peak value of the maximum is largest. Exceeding this optimal current the HLR-Maximum becomes very broad and the peak value decreases again. The latter is possibly due to heating because the HLR-Maximum vanishes above 0.6 K. An important observation is, that the HLR-Maximum does not depend on absolute current values but on the current density. For the 800 μm wide Hall-bar an approximately ten times higher current is needed to observe the fully developed HLR-Maximum as compared to the 80 μm wide one.

In view of the significant size and time dependence it is not surprising that the HLR-Maximum shows also very hysteretic effects. These effects can be observed at temperatures of 0.4 K but are more pronounced at lower temperatures. An example is shown as Fig. 3. The experimental parameters correspond closely to the measurement shown in Fig. 1 (T = 0.4 K, I = 100 nA and 80 μm Hall-bar width). If the magnetic field is swept up, then the position of the maximum is at slightly higher fields and it is rather narrow. If the field is swept down, the maximum is much wider and more symmetric around filling factor $\frac{2}{3}$. Using a sample with a slightly different carrier density but otherwise similar experimental parameters one finds that the resistance maximum of the down sweep of the magnetic field is shifted compared to the resistance maximum observed in the up sweep of the magnetic field (Fig. 4).

Figure 5 shows the slow up and slow down sweep of the magnetic field at 40 mK. The sample is a 800 μm wide Hall-bar and the

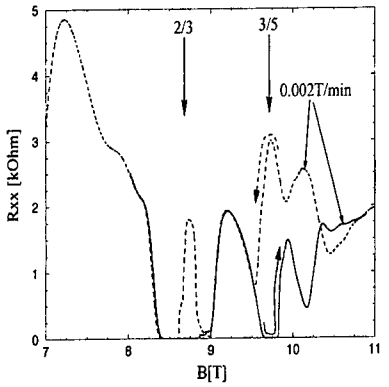

Fig. 5. The hysteresis of a HLR-Maximum measured during both up and down sweeps at 40 mK.

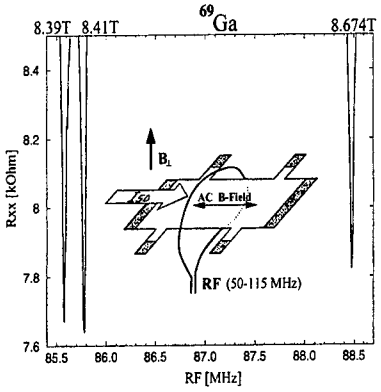

Fig. 6. Resistively detected NMR lines observed at the HLR-Maximum of a 800 μm wide Hall-bar sample at three different electron densities.

applied current is 400 nA. For the up-sweep of the magnetic field, the longitudinal resistance vanishes at fractional filling factors, and for the down sweep, maxima are observed at the affected fractions. At 40 mK this strong hysteresis between the up and the down sweep of the magnetic field can already be observed in measurement with "normal" magnetic field sweep rates of 0.7 T/min [8].

3 Nuclear Magnetic Resonance

The long time constants of the order of minutes and hours are typical for effects involving the nuclear magnetic moments although in most electronic systems interaction with the nuclear spins is too weak to lead to a sizeable change in the electric resistance. Nevertheless it has already been shown in [8] that the relaxation of the HLR-Maximum corresponds to the one expected from the Korringa relaxation of nuclear spins via conduction electrons. A more direct way to study the interaction with the nuclear spins is a nuclear magnetic resonance (NMR) experiment [9]. The used setup is shown in the insert of Fig. 6. An AC magnetic field, which is perpendicular to the static magnetic field, is created by applying radio frequency (RF) to a wire loop around the sample. In the experiment the sample is first put in the HLR state then the RF is applied and its frequency varied with 1 kHz/20 sec.

Figure 6 shows the value of the HLR-Maximum as a function of the RF frequency. If the RF frequency coincides with the nuclear spin splitting of the ^{69}Ga nucleus the resistance drops. In figure 6 three resonance lines are shown each one corresponding to a different electron density of the 2DEG which means a different magnetic field value of the HLR-Maximum and therefore a different nuclear spin splitting. In all three cases the minimum occurs exactly when the frequency coincides with the respective nuclear splitting. The same behavior is observed for ^{71}Ga and ^{75}As at the respective resonance frequencies. The fact that the NMR

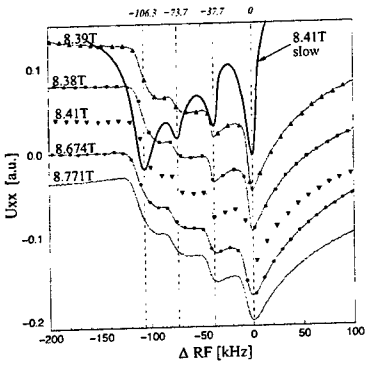

Fig. 7. The nuclear resonance lines of the As nuclei observed at different electron densities. The bold trace was swept with 1 kHz/20sec while the sweep rate of the other ones is 1 kHz/3 sec.

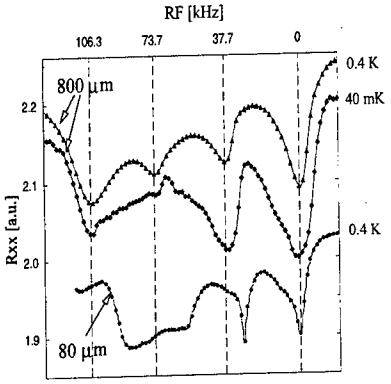

Fig. 8. The nuclear resonance lines of the As nuclei for two different sample widths and different temperatures. For the 80 μm wide sample the splitting is about 30 kHz and for the 800 μm wide sample it is about 35 kHz. At lower temperatures it is more difficult to observe all four lines.

resonances can be observed directly in the resistance means that the HLR-Maximum can be influenced by a change of the nuclear spin polarization and therefore it is closely related to the nuclear spin system.

In Figure 7 the resonance lines of the As nuclei are shown. The top trace (bold line) was taken with the frequency being swept very slowly 1 kHz/20 sec. Surprisingly four different lines are observed, which are nearly equally spaced. The splitting is about 35 kHz. At faster sweep rates the resistance drops in a step-like fashion and does not find time to recover until the frequency hits the next resonance. Leaving the resonance region the HLR needs about the same time to recover which it takes to develop in the first place. The different traces are measured at different magnetic fields, i.e. different carrier densities. They are shifted in such a way that it is possible to compare the field dependence of the splitting. No significant dependence is found in the studied field range.

It is noteworthy, however, that the splitting of the As resonance line into four sub lines is different for the two different sample widths (Fig. 8). The 80 μm wide sample has a smaller splitting of approximately 30 kHz compared with the splitting of about 35 kHz of the 800 μm wide sample. At this time it is not clear if this difference in the splitting is due to different sample sizes or due to growth inhomogeneities in the wafer.

The As nuclei have a nuclear spin of 3/2 and four equidistant energy levels of the nuclear ground state are expected in an external magnetic field. This means that in a NMR experiment only one resonance line is expected. Therefore the existence of four sub lines of the As resonance which we observe in our experiment is very surprising. Even with an electric quadrupole perturbation one can only expect three different transitions, which are indeed observed in more

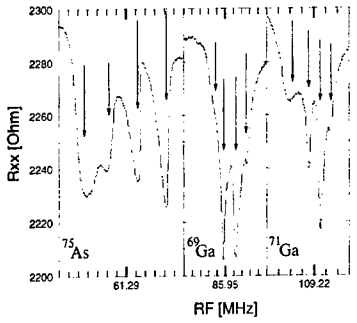

Fig. 9. NMR of the three nuclei of the quantum well measured with a 80 μm wide quantum well (lines mark 10 kHz steps).

conventional resonance experiments [10,11]. As the two Ga isotopes have also a nuclear spin of 3/2, their resonance lines should as well show the four sub lines observed in the As resonance. It turns out, that the Ga isotope shows the fourfold splitting if the homogeneity of the magnetic field is improved. This is the case with the 80 μm wide sample, because the field inhomogeneity is better than with the 800 μm wide one of Fig. 6. Now the same fourfold splitting is indeed observed for all three nuclei of the quantum well, see Fig. 9. The origin of the different line-shapes for the three nuclei is not clear. They can possibly be related to the different nuclear environments or slightly different relaxation mechanisms for the three nuclei.

4 Conclusion

The NMR experiments show clearly, that a change of the nuclear spin polarization, caused by the RF, leads to a change of the resistance in the HLR situation. Therefore, a close relation between the nuclear spins and the HLR-Maximum exists. In the experiment the RF is irradiated continuously, which leads to an near equilibration of the nuclear spin levels and therefore to a reduction of the nuclear spin polarization. The polarization of the nuclei can only be caused by the current which leads to a dynamic nuclear polarization (DNP). With increasing DNP the resistance increases until a saturation value is reached. A DNP by current has only rarely been observed. One example is the tunneling between different spin levels at a point-contact structure [12]. Another case is the tunneling between edge channels with different spin polarization [13].

The situation studied here is clearly different from these two. We suspect that it is connected with the possibility to form two different ground states of the fractional QHE with different spin polarization. Let us assume that the two states are very close in energy in our sample, then it is conceivable that domains of the two different ground states form. This might be favored by the reduction of the g-factor due to the reduced well thickness [14]. If current flows through the sample then electrons must cross from one domain to the other and flip their spins in the process. This electron spin flip is accompanied by a polarization of the nuclei. In this picture the nuclear spin polarization would take place only along the domain walls.

This model does however not explain why the NMR lines consist of four sub lines. The fourfold splitting of the NMR resonances could be caused by an interaction with other spins of 3/2. This splits each nuclear spin level into four levels and therefore leads to four resonance lines. The other nuclei have spin 3/2 but the strength of nuclear dipole-dipole interaction is only of the order of 1 kHz, i.e. it is much too weak and further-

more, there should be rather a broadening of the resonances because the interacting nuclear dipoles have varying distances and orientation. On the other hand, since the fourfold splitting has not been observed in other NMR experiments in related 2DEG systems one must conclude that it is not a purely nuclear effect but must be related to the electronic system in the HLR state. This is also supported by the size of the splitting which is comparable to the size expected for the hyperfine interaction. In delocalised systems the hyperfine interaction should however only lead to a shift and not to a splitting of the resonance [11]. Another important point is, that the ratio of the splittings observed for the two Ga isotopes in Fig. 9 does not scale with the gyromagnetic ratio of the two Ga nuclei. This should however be the case for plain dipole-dipole interaction as well as for hyperfine interaction. The gyromagnetic ratio lets us predict a splitting of ^{71}Ga which is a factor of 1.27 larger than the one of ^{69}Ga. In this experiment, however, it is found to be smaller by a factor of about 0.7. This means that the fourfold splitting can neither be described by a standard dipole-dipole interaction nor by hyperfine interaction. To explain the four lines and the size of the splitting it must probably be a dipole-dipole interaction which is enhanced by the interaction with the electrons in a still unexplained way.

5 Acknowledgments

This work is the result of a collaboration with K. v. Klitzing and J. Weis from the MPI für Festkörperforschung and with G. Denninger from the Universität Stuttgart. The samples are grown by M. Bichler and W. Wegscheider from the Walter-Schottky-Institut in München.

References

[1] K. von Klitzing, G. Dorda and M. Pepper, Phys. Rev. Lett.**45**, 494 (1980).

[2] D.C. Tsui, H.L. Stormer and A.C. Gossard, Phys. Rev. Lett. **48**, 1559 (1982).

[3] R.B. Laughlin, Phys. Rev. Lett. **50**, 1395 (1983).

[4] B.I. Halperin, Helv. Phys. Acta. **56**, 75 (1983).

[5] T. Chakraborty and P. Pietiläinen, *The Quantum Hall Effects*, (Springer, Berlin, 1995).

[6] R.G. Clark, S.R. Haynes, J.V. Branch, A.M Suckling, P.A. Wright and P.M.W. Oswald, Surf. Sci. **229**, 25 (1990).

[7] J.P. Eisenstein, H.L. Stormer, L.N. Pfeiffer and K.W. West, Phys. Rev. B **41**, 7910 (1990).

[8] S. Kronmüller, W. Dietsche, J. Weis, K. von Klitzing, W. Wegscheider and M. Bichler, Phys. Rev. Lett. **81**, 2526 (1998).

[9] S. Kronmüller, W. Dietsche, K. von Klitzing, G. Denninger, W. Wegscheider and M. Bichler, Phys. Rev. Lett. **82**, 4070 (1999).

[10] M. Krapf, G. Denninger, H. Pascher, G. Weimann and W. Schlapp, Solid. State. Comm. **78**, 459 (1991).

[11] S.E. Barrett, R. Tycko, L.N. Pfeiffer and K.W. West, Phys. Rev. Lett. **72**, 1368 (1994).

[12] B.E. Kane, L.N. Pfeiffer and K.W. West, Phys. Rev. B **46**, 7264 (1992).

[13] K.R. Wald, L.P. Kouwenhoven, P.L. McEuen, N.C. van der Vaart and C.T. Foxon, Phys. Rev. Lett. **73**, 1011 (1994).

[14] G.P. Flinn, R.T. Harley, M.J. Snelling, A.C. Tropper and T.M. Kerr, Semicond. Sci. Technol. **5**, 533 (1990).

ULTRA-LOW TEMPERATURE STUDY OF THE ν = 5/2 EVEN-DENOMINATOR FQHE STATE

W. Pan [1,2], J-S. Xia [3,2], V. Shvarts [3,2], E.D. Adams [3,2], R.R. Du [4,2], H.L. Stormer [5,6], D.C. Tsui [1], L.N. Pfeiffer [5], K.W. Baldwin [5], K.W. West [5]

[1] Princeton University, Princeton, NJ 08544, USA
[2] NHMFL, Tallahassee, FL 32310, USA
[3] University of Florida, Gainesville, FL 32611, USA
[4] University of Utah, Salt Lake City, UT 84112, USA
[5] Bell Labs, Lucent Technologies, Murray Hill, NJ 07974, USA
[6] Columbia University, New York, NY 10027, USA

Abstract

We present experimental data showing unambiguously an even-denominator fractional quantum Hall effect (FQHE) state at ν=5/2. At a bath temperature T_b=8mK, we observe a Hall plateau quantized to a value of $2h/5e^2$ with an uncertainty smaller than 2 parts in 10^6 and a vanishing R_{xx} (R_{xx}=1.7±1.7 Ω). The thermal activation energy gaps Δ_ν at Landau level filling factors ν=5/2, 7/3, and 8/3 are 0.11, 0.10, and 0.055 K, respectively. Adding a disorder broadening (typically ~ 2K) to these values, we deduce that all three FQHE states have probably very similar energy gaps. The electron heating experiment shows that the 2D electrons are efficiently cooled to the bath temperature for $T_b \geq$ 8mK. We also explore the density dependence of the activation gap at ν=5/2. Preliminary results at $T_b \geq$ 25mK show that the 5/2 state is very sensitive to disorder.

1. Introduction

Over one decade ago, Willett *et al* [1] reported an apparently even-denominator fractional quantum Hall effect (FQHE) in a two-dimensional electron system (2DES). A deep minimum was observed in the diagonal resistance (R_{xx}) and a change of slope in the Hall trace close to ν=5/2. The origin of the 5/2 FQHE state has remained unclear, ever since. On one hand, this fraction escapes the odd-denominator rule of theory [2]. On the other hand, it has the beginning features of a FQHE state, such as a resistance minimum and a beginning Hall plateau. Initially, a so-called hollow-core model [3] was proposed, whose spin-singlet was supported by experiment [4]. However, in detail, numerical calculations [5] showed this state to be an unlikely candidate for the ν=5/2 FQHE. With the forthcoming of the composite fermion (CF) theory [6], it is now conjectured that the 5/2 state is due to the condensation of p-wave composite fermion pairs [7], not unlike the BCS condensation of electron Cooper pairs in a normal low-temperature superconductor. In this report, we show for the first time a fully developed even-denominator FQHE state at ν=5/2, featuring a highly accurate quantization of R_{xy} and vanishing R_{xx}.

2. Experiment

The sample is a GaAs/Al_xGa_{1-x}As single heterostructure with density $n=2.3\times10^{11}/cm^2$ and mobility $\mu=17\times10^6 cm^2/Vs$. The size of the sample is about 4mm×4mm with eight indium

contacts placed symmetrically around the edges --- four at the corners and four in the centers of the four edges. The sample, with contacts soldered separately to eight specially designed sintered silver powder heat exchangers, was immersed in liquid ^{3}He, which was cooled by in a 5mol $PrNi_5$ nuclear demagnetization refrigerator. A standard low frequency (~ 5Hz) lock-in technique was employed to measure the transport coefficients. All measurements were performed in an ultra-quite environment shielding from the electron-magnetic noise.

3. Results and Discussions

Fig.1 shows the Hall resistance R_{xy} and the diagonal resistance R_{xx} between Landau level filling factors ν=2 and ν=3 at a bath temperature, T_b=8mK. For the first time, we observed a wide and flat Hall plateau at ν=5/2, as well as at ν=7/3 and 8/3. In a separate measurement at lower temperature (T_b=2mK), we determined the uncertainty in the R_{xy} quantization to be less than 2 parts in 10^6 at ν=5/2, limited by the experimental instrumentation. The R_{xy} trace in Fig.1 was measured in two opposite B-field directions to average out the mixing of R_{xx} into R_{xy}, since our sample was not patterned into a Hall bar. While most of the peaks between Hall plateaus in Fig.1 reversed direction under field reversal, the deep R_{xy} minimum at B~3.53 T hardly changed on reversing the B field. It is also puzzling, that its resistance is close to R_{xy} at ν=3. Presently it is not clear whether the existence of this anomaly is related to a new electronic phase [8].

At T_b=8mK, R_{xx} shows several interesting features, such as vanishing resistance minima at ν=5/2, 7/3, and 8/3. For example, the resistance at ν=5/2 drops to $R_{5/2}$=1.7±1.7 Ω. In addition, R_{xx} also shows strong minima at ν=12/5 and 13/5. The progression of the FQHE sequences from ν=7/3 (2+1/3), 12/5 (2+2/5), ... and from ν=8/2 (2+2/3), 13/5 (2+3/5), ... towards ν = 5/2 (2+½) can be described by one formula ν=2+p/(2p+1) with p=±1, 2, ... This sequence of FQHE fillings resembles the one around ν=½, ν=p/(2p+1), which currently is understood as the integer QHE states of composite fermions which form at ν=1/2.

Fig.2 shows the temperature dependence of R_{xx} around ν=5/2 between T_b = 8mK and 50mK. We show data from four different temperature ramps to demonstrate the reproducibility of our data The activation energy gap Δ_ν, defined by $R_{xx} \propto \exp(-\Delta_\nu/2k_BT)$, is obtained from an Arrhenius plot in which $\log(R_{xx})$ is plotted against 1/T. We obtained $\Delta_{5/2}$=0.11K, $\Delta_{7/3}$=0.10K, and $\Delta_{8/3}$= 0.055K. However, if we add the disordering broadening, typically ~2K measured from other fillings [9], all three states have very similar energy gaps. Of course, accepting a gap reduction of ~2K for FQHE gaps due to remnant disorder, which is much larger than the experimental activation gap, only establishes the existence of a true gap of ~2K. Comparison between actually measured activation energies of different fraction becomes less meaningful, although it should remain an acceptable indicator for whether a specific gap increases or decreases in response to a perturbation.

In order to determine the true electron temperature, we conducted an electron heating experiment. R_{xx} was measured at an excitation current (I) from 0.5nA to 100nA at T_b=8mK. Using the resistance of the peak at B=3.75 T as a thermometer, we were able to determine T_e at each I by comparing the current dependence and the temperature dependence of peak resistance. Fig.3 shows the plot of $\ln(I^2)$ against $\ln(T_e^5-T_b^5)$, where I is in units of nA, T_e and T_b in units of mK. Assuming a "two-bath" model for the thermal relaxation of electrons [10], we should obtain $I^2 \propto (T_e^5-T_b^5)$. Indeed, all the data points can be well fitted by $\ln(I^2)$ = constant + $\ln(T_e^5-T_b^5)$, where constant = -7.5. From this linear dependence, we conclude that there is no apparent

electron heating when $T_b \geq 8$mK with 1 nA excitation current. The constant in the above fitting is similar to that obtained by Gammel et al [10]. In the same sample cool down, we measured the R_{xx} at T_b=2mK with 1nA of current. The resistance peaks in R_{xx} continue to increase with decreasing bath temperature from T_b=8mK to 2mK. This indicates, that the electrons were cooled below 8mK. Indeed, if we assume that the equation $\ln(I^2) = -7.5 + \ln(T_e^5 - T_b^5)$ continues to hold to T_b=2mK, we obtain an electron temperature T_e=4mK. In fact, the efficient additional cooling of the electron system via the cold contacts probably reduced its temperature below 4mK.

4. Conclusion

In summary, we have conducted an ultra-low temperature study on the 5/2 even-denominator FQHE state. R_{xx} becomes vanishingly small at T_b=8mK and, for the first time, a Hall plateau quantized to $2h/5e^2$ is observed. The uncertainty of the quantization is less than 2×10^{-6}, limited by the experimental instrumentation. Our data also show fully developed FQHE state at ν=7/3 and 8/3. The energy gaps at all three fillings are very similar after adding a usually encountered broadening of ~2K to the measured values. The electron heating results suggest that there is no apparent electron heating when $T_b \geq 8$mK with an excitation current of 1nA.

5. HIGFET experiments

We have fabricated a variable-density 2DES in a so-called HIGFET (Heterojunction Insulated Gate Field-Effect Transistor) [11] in order to pursue the 5/2-state over a wide range of B field. From such experiments, we should be able to deduce the density-dependence of the energy gap, which may provide some insights as to the origin of the 5/2 state, or, at least, to rule out some of the competing models. At this point, we are able to tune the 2DES density in a typical HIGFET continuously from very low levels up to $7.5\times10^{11}/cm^2$. We have observed a strong minimum at 5/2 at B-fields as high as 12.5T. Preliminary results at $T_b \geq 25$mK show that the resistance minimum and the energy gap at ν=5/2 have a strong dependence on the 2DES mobility and density. However, since R_{xx} at ν=5/2 does not vanish in our HIGFET sample, either because of insufficiently low bath temperature or insufficiently high mobility, we can only obtain the quasi-energy gap at ν=5/2. This is determined from the temperature dependence of the depth of the 5/2 minimum with respect to the height of the two adjacent peaks [4]. In Fig.4, the quasi-energy gap at ν=5/2 and the electron mobility are plotted against the electron density n. Since the quasi-energy gap and the mobility show a very similar dependence on density, we may conclude that the 5/2 state is very sensitive to the disorder.

Acknowledgements

We would like to thank N. Bonesteel for useful discussions. A portion of this work was performed at the NHMFL which is supported by NSF Cooperative Agreement No. DMR-9527035 and by the state of Florida. D.C.T. and W.P. are supported by NSF and the DOE.

References:

[1] R.L. Willett, J.P. Eisenstein, H.L.. Stormer, D.C. Tsui, A.C. Gossard, and J.H. English, Phys. Rev. Lett. 59 (1987) 1779.

[2] See, for a review, The Quantum Hall Effect edited by R.E. Pranger and S.M. Girvin (Springer-Verlag, New York, 1990).

[3] F.D.M. Haldane and E.H. Rezayi, Phys. Rev. Lett. 60 (1988) 956; 60 (1988) 1886.
[4] J.P. Einsenstein, R.L. Willett, H.L. Stormer, D.C. Tsui, A.C. Gossard, and J.H. English, Phys. Rev. Lett. 61 (1988) 997; J.P. Eisenstein, R.L. Willett, H.L. Stormer, L.N. Pfeiffer, and K.W. West, Surface Science 229 (1990) 31.
[5] A. H. MacDonald, D. Yoshika, and S.M. Girvin, Phys. Rev. B 39 (1989) 8044; R. Morf, Phys. Rev. Lett. 80 (1998) 1505.
[6] See, for a review, Perspectives in Quantum Hall Effect, edited by S. Das Sarma and A. Pinczuk (Wiely, New York, 1996).
[7] M. Greiter, X.G. Wen, and F. Wilczek, Phys. Rev. Lett. 66 (1991) 3205; G. Moore and N. Read, Nucl. Phys. B 360 (1991) 362; K. Park, V. Melik-Alaverdian, N.E. Bonesteel, and J.K. Jain, Phys. Rev. B 58 (1998) 10167; N.E. Bonesteel, Phys. Rev. Lett. 82 (1999) 984.
[8] Recently, a similar behavior in R_{xy} has been observed at $\nu \sim 4 + 1/4$ and $4 + 3/4$ around $\nu = 9/2$ by M.P. Lilly, K.B. Cooper, J.P. Eisenstein, L.N. Pfeiffer, and K.W. West, Phys. Rev. Lett. 82 (1999) 394 and R.R. Du, D.C. Tsui, H.L. Stormer, L.N. Pfeiffer, K.W. Baldwin, and K.W. West, Solid State Communications 109 (1999) 389.
[9] R.R. Du, H.L. Stormer, D.C. Tsui, A.S. Yeh, L.N. Pfeiffer, and K.W. West, Phys. Rev. Lett. 73 (1994) 3274.
[10] P.L. Gammel, D.J. Bishop, J.P. Eisenstein, J.H. English, A.C. Gossard, R.Ruel, and H.L. Stormer, Phys. Rev. B 38 (1988) 10128; A.M. Wennberg, S.N. Ytterboe, C.M. Goild, H.M. Bozler, J. Klem, and H. Morkoc, Phys. Rev. B 34 (1989) 4409.
[11] B.E. Kane, L.N. Pfeiffer, K.W. West, and C.K. Harnett, Appl. Phys. Lett. 63 (1993) 2132.

Figure captions:

Fig.1. Overview of R_{xx} and R_{xy} at a bath temperature T_b=8mK. Vertical lines mark the Landau level filling factors. R_{xy} is measured in two opposite B-field directions.

Fig.2. Temperature dependence of R_{xx} around ν=5/2 at three temperatures.

Fig.3. Electron heating plot $\ln(I^2)$ vs. $\ln(T_e^5-T_b^5)$. I is current in nA, T_e is electron temperature, and T_b bath temperature, in mK. The inset shows R_{xx} at I = 5, 50nA.

Fig.4. Density dependence of quasi-energy gap Δ (solid squares) and electron mobility μ (open circles) for a HIGFET sample.

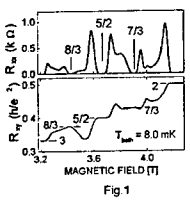

Fig.1

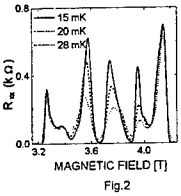

Fig.2

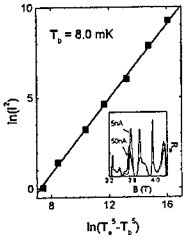

Fig.3

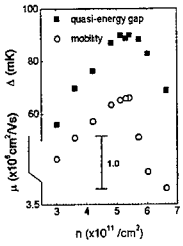

Fig.4

Hysteresis, Spin Transitions, and Magnetic Ordering in the Fractional Quantum Hall Effect

H. Cho[1#], W. Kang[1], K.L. Campman[2], A.C. Gossard[2], M. Bichler [3], and W. Wegscheider[3]
[1]James Franck Institute and Department of Physics, University of Chicago, Chicago, Illinois 60637
[2]Department of Electrical Engineering, University of California at Santa Barbara, Santa Barbara, California 93106
[3]Walter Schottky Institut, Technische Universität München, Am Coulombwall, D-85748 Garching, Germany

Abstract

We have studied the development of metastable properties associated with a nearly spin-degenerate two-dimensional electron system. Application of large hydrostatic pressure significantly reduces the g-factor experienced by electrons in GaAs/AlGaAs heterostructure, and various fractional quantum Hall effect (FQHE) states are found to undergo transition to a spin-unpolarized ground state. In case of even numerator FQHE states, the spin transitions are accompanied by hysteresis and nonlinearity in the magneto-transport. These results strongly support a recent theory of quantum Hall magnetism in which competition between spin-polarized and spin-unpolarized ground states leads to an ordered phase that exhibits ferromagnetic correlation.
PACS numbers: 73.40.Hm

Introduction

Driven by strong electron-electron interaction and quantum fluctuations, the two-dimensional electron system (2DES) is known to undergo transitions to liquid and crystalline ground states[1]. These transitions between various quantum Hall states occur in the limit of zero temperature and are well-known examples of quantum phase transitions[2]. Another type of quantum phase transition involves changes in the spin polarization of the fractional quantum Hall effect (FQHE) states. These spin transitions are made possible by the smallness of the Lande g-factor in GaAs/AlGaAs heterostructure (g = -0.44) that opens the possibility of the FQHE states with non-trivial spin configurations[3,4]. In this paper, we present our study of the spin transitions induced by application of large hydrostatic pressure. Significant reduction in the magnitude of the g-factor in GaAs/AlGaAs heterostructures under pressure favors formation of spin-unpolarized FQHE states. These spin transitions are accompanied by strong hysteresis over a range of pressures above and below the critical pressure at which a spin transition is found. Results of our experiment are consistent with the presence of an easy-axis ferromagnetically ordered state in vicinity of the spin transitions[5].

Experimental

The experiment was performed on a high quality GaAs/AlGaAs heterostructure and a 250 Å-wide quantum well of densities n = 3.5 and 2.0 $\times 10^{11} cm^{-2}$ and mobilities μ = 2.4 and 4.0 $\times 10^{6} cm^{2}/Vsec$, respectively. Eight symmetrically placed indium contacts were diffused around the edges of the sample. Hydrostatic pressure was generated using a miniature pressure clamp made of beryllium-copper. A small LED chip placed inside the pressure cell was used to illuminate the sample at low temperatures.

Results

In Fig. 1a we present the magnetoresistance around filling fraction ν = 2/5 in the range of pressure from 11.2 to 13.8 kbar. The reentrant behavior of the ν = 2/5 FQHE state obtained

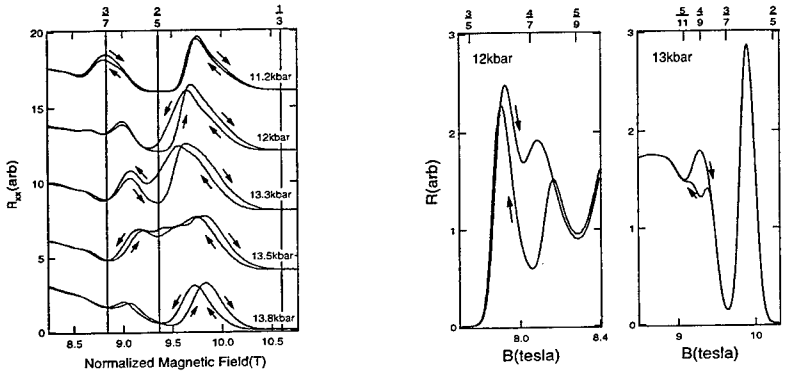

Figure 1: (a) Magnetoresistance of a high quality GaAs/AlGaAs heterostructure under pressure near filling fraction $\nu = 2/5$. The data was taken at 40 mK. Arrows indicate the sweep direction. Magnetic field scale has been normalized to the highest pressure shown in the figure for the sake of comparison. (b) Magnetoresistance of a 250Å wide quantum well sample under 12 (left) and 13 (right) kbar of pressure at 60 mK.

under pressure is accompanied by striking hysteresis between up and down sweeps of magnetic field over a wide range of pressure[6]. At pressure below 11.2 kbar, the $\nu = 2/5$ FQHE state is well-developed and no hysteresis is found. As the $\nu = 2/5$ FQHE state becomes weaker under increasing pressure, the hysteresis between up and down sweeps begins to appear. The hysteretic behavior is also evident at 13.8 kbar even though a strong magnetoresistance resistance has reappeared. Pressure and tilted magnetic field studies suggest that the $\nu = 2/5$ FQHE state above the critical pressure of ~13.5 kbar is spin-unpolarized while it is polarized at lower pressures[7]. Our experiment shows that the observed hysteretic behavior is intimately related to the spin transitions.

In addition to the $\nu = 2/5$ FQHE state, hysteresis in magnetotransport can be observed in conjunction with the spin transitions of other FQHE states. Fig. 1b illustrates the hysteretic behavior observed in vicinity of the $\nu = 4/7$ and $\nu = 4/9$ FQHE states in a 250Å-wide quantum well. Under 12 kbar of pressure a strong hysteresis is centered about the $\nu = 4/7$ FQHE state. Up sweep data shows a magnetoresistance minimum that is weaker than the neighboring $\nu = 5/9$ FQHE. In subsequent down sweeps, a much deeper magnetoresistance minimum is recovered. The overall behavior is qualitatively similar to that observed in the $\nu = 2/5$ FQHE. A spin transition found in the $\nu = 4/9$ FQHE under 13 kbar of pressure results in a even more dramatic discrepancy between up and down sweeps. During up sweeps, a resistance maximum, instead of a usual minimum, is obtained at $\nu = 4/9$. In down sweeps the peak seen during up sweeps reverts back to a minimum, creating a distinct bubble loop between up and down sweeps.

In Fig. 2a, we present a temperature evolution of the hysteresis around $\nu = 2/5$ for a 2DES under 13 kbar of pressure. At 80mK, strong hysteresis between up and down sweeps generates a complicated resistance loop about $\nu = 2/5$. The hysteresis loop gradually is reduced under increasing temperature and no hysteresis can be detected above 300mK. The temperature dependence of the hysteresis largely mirrors the strength of the $\nu = 2/5$ FQHE state. As the $\nu = 2/5$ FQHE state becomes weaker at higher temperatures, the hysteretic behavior becomes weaker. There is no

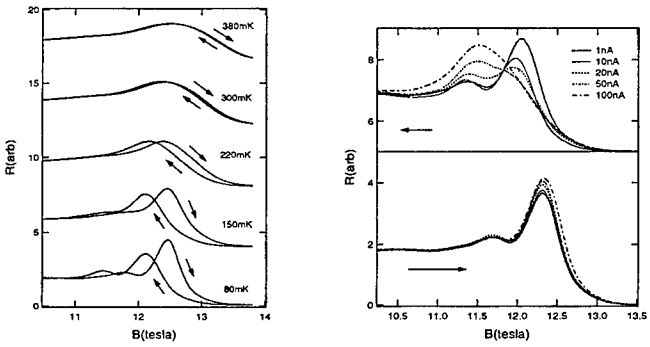

Figure 2: (a). Temperature dependence of magnetoresistance around $\nu = 2/5$ for a heterostructure sample under 13 kbar of pressure. Arrows indicate the sweep direction. (b). Magnetoresistance for various excitation currents. Lower (upper): up (down) sweeps of magnetic field.

signature of the $\nu = 2/5$ FQHE state and hysteresis at higher temperatures.

In addition to the temperature dependence, the hysteretic behavior is accompanied by an intriguing non-ohmic behavior. In Fig. 2b we present a series of magnetoresistance traces for various excitation currents. At low excitation currents, the hysteresis largely appears as clearly defined shift in the transport features about $\nu = 2/5$. At higher currents, the transport features remain essentially unchanged in the up sweeps. However, various transport features near $\nu = 2/5$ become distinctively smooth as the doublet of resistance peaks around $\nu = 2/5$ coalesce into a single peak. Such behavior is not observed in other FQHE states.

Discussion

The bizarre hysteretic behavior associated with various fractional Hall states necessitates a new look at the spin transitions in the FQHE. Since hysteresis often accompanies a first order phase transition over the coexistence region of the phase space, it is necessary to consider whether the spin transitions in the FQHE occurs as a first order phase transition. In particular, the width of the coexistence region between polarized and unpolarized states needs be compared with the size of the hysteretic region. According to Fig. 1a, the coexistence region is rather narrow with only the data at 13.5 kbar exhibiting a weak doublet of resistance minima at $\nu = 2/5$. Slight increase or decrease of pressure removes the doublet and a strong resistance minimum is found. In contrast, the hysteretic behavior can be observed over a greater range of pressures, far above and below the critical pressure. Hysteresis occurs even though there exists a well-defined resistance minimum at $\nu = 2/5$. Appearance of hysteresis in the polarized and unpolarized region of the phase space suggests that the hysteretic behavior is not related to a possible first order phase transition.

This view is reinforced by the occurrence of strong hysteretic behavior associated with the even numerator FQHE states at $\nu = 2/5$, $4/7$, and $4/9$[6]. Surprisingly no strong hysteresis is observed in the in the odd numerator FQHE states. This intriguing difference between the spin transitions of even and odd numerator FQHE states, plus the persistence of the hysteretic behavior over a wide range of pressures, cannot be easily reconciled in terms of first order phase transitions.

For a 2DES system at an even integral filling factor, coincidence of two Landau levels with

different spin polarization has been mapped to a two-dimensional ferromagnet[5]. In vicinity of the spin transitions, spin-polarized and spin-unpolarized ground states are nearly degenerate in energy. Ensuing competition between the two ground states lead to a spontaneous symmetry breaking to a ferromagnetically correlated state with each state representing an Ising-like psuedospin. In this picture, the dynamics of FQHE states resemble a two-dimensional Ising ferromagnet. Local fluctuations can produce domains with different spin orientations and magnetic field sweeps lead to hysteresis in the magnetization. Coupling between the transport and the order parameter of the ferromagnetically correlated state produces the observed hysteresis in the magnetoresistance. Interfacial resistance and domain wall dynamics is expected to produce nonlinearity in transport, in qualitative agreement with our data.

Conclusion

In summary, striking hysteresis associated with the spin transitions of even numerator FQHE has been observed. The hysteretic behavior is found to persist over an extended range of parameters. Competition between nearly degenerate spin-polarized and unpolarized ground states appears to be essential in the origin of hysteresis. Our results are consistent with a presence of a novel, ferromagnetically correlated ground state in vicinity of the spin transitions.

Acknowledgment

We would like to thank A.H. MacDonald for fruitful discussions. The work at the University of Chicago was supported in part by the MRSEC Program of the National Science Foundation under Award No. DMR-9808595 and the David and Lucille Packard Foundation.

References

-Current address: Jet Propulsion Laboratory, Pasadena, California 91109.

[1] S. Das Sarma and A. Pinczuk, *Perspectives on Quantum Hall Effects* (Wiley, New York, 1997).

[2] S.L. Sondhi, S.M. Girvin, J.P. Carini, and D Shahar, Rev. Mod. Phys. **69**, 315 (1997).

[3] B.I. Halperin, Helv. Phys. Acta **56**, 75 (1983);T. Chakraborty and F.C. Zhang, Phys. Rev. **B 29**, 7032 (1984); F.C. Zhang and T. Chakraborty, Phys. Rev. **B 30**, 7320 (1984);E. Rezayi, Phys. Rev. **B 36**, 5454 (1987); X.C. Xie, Y. Guo, and F.C. Zhang, Phys. Rev. B **40**, 3487 (1989); T. Chakraborty and P. Pietilainen, Phys. Rev. B **41**, 10862 (1990); A.H. MacDonald, Surface Science **229**, 1 (1990); X.G. Wu, G. Dev, and J.K. Jain, Phys. Rev. Lett. **71**, 151 (1993).

[4] J.P. Eisenstein, H.L. Stormer, L.N. Pfeiffer, and K.W. West, Phys. Rev. Lett. **62**, 1540 (1989); R.G. Clark, S.R. Haynes, A.M. Suckling, J.R. Mallett, P.A. Wright, J.J. Harris, and C.T. Foxon, Phys. Rev. Lett. **62**, 1356 (1989); J.P. Eisenstein, H.L. Stormer, L.N. Pfeiffer, and K.W. West, Phys. Rev. **B 41**, 7910 (1990); L.W. Engel, S.W. Hwang, T. Sajoto, D.C. Tsui, and M. Shayegan, Phys. Rev. **B45**, 3418 (1992); R.R. Du, A.S. Yeh, H.L. Stormer, D.C. Tsui, L.N. Pfeiffer, and K.W. West, Phys. Rev. Lett. **75**, 3926 (1995).

[5] T. Jungwirth, S. Shukla, L. Smrcka, M. Shayegan, and A. H. MacDonald, Phys. Rev. Lett. **81**, 2328 (1998).

[6] H. Cho, J.B. Young, W. Kang, K.L. Campman, A.C. Gossard, M. Bichler, and W. Wegscheider, Phys. Rev. Lett. **81**, 2522 (1998).

[7] W. Kang, J.B. Young, S.T. Hannahs, E. Palm, K.L. Campman A.C. Gossard, Phys. Rev. B **56**, R12776 (1997).

HALF-FILLED LANDAU LEVEL AS A FERMI LIQUID OF DIPOLAR QUASIPARTICLES*

Ady Stern[a], Bertrand I. Halperin[b], Felix von Oppen[c], and Steven H. Simon[d]
[a]Department of Condensed Matter Physics, The Weizmann Institute of Science, Rehovot 76100, Israel
[b]Physics Department, Harvard University, Cambridge, Massachusetts 02138
[c]Institut für Theoretische Physik, Universität zu Köln, Zölpicher Str. 77, 50937 Köln, Germany
[d]Lucent Technologies Bell Labs, Murray Hill, NJ 07974

In this work we study the relation between the conventional Fermion-Chern-Simons (FCS) theory of the half-filled Landau level ($\nu = ½$), and alternate descriptions that are based on the notion of neutral quasi-particles that carry electric dipole moments. We have previously argued that these two approaches are equivalent, and that e.g., the finite compressibility obtained in the FCS approach is also obtained from the alternate approach, provided that one properly takes into account a peculiar symmetry of the dipolar quasiparticles – the invariance of their energy to a shift of their center of mass momentum. Here, we demonstrate the equivalence of these two approaches in detail. We first study a model where the charge and flux of each fermion is smeared over a radius Q^{-1} where results can be calculated to leading order in the small parameter Q/k_F. We study two dipolar-quasiparticle descriptions of the $\nu = ½$ state in the small-Q model and confirm that they yield the same density response function as in the FCS approach. We also study the single-particle Green's function and the effective mass, for one form of dipolar quasiparticles, and find the effective mass to be infra-red divergent, exactly as in the FCS approach. Finally, we propose a form for a Fermi-liquid theory for the dipolar quasiparticles, which should be valid in the physical case where Q is infinite.

*A. Stern, B. I. Halperin, F. von Oppen, and S. H. Simon, Phys. Rev. B, in press; preprint cond-mat/9812135.

THA.1

Presentation by:

I. Kukushkin, *Russian Academy of Sciences, Chernogolovka, Russia*
"Magneto-optical Probes of Electron Interactions in 2DEG's"

Ballistic Phonon Studies in the Lowest Landau Level

A.M. Devitt, S.H. Roshko*, U. Zeitler**, C.J. Mellor, A.J. Kent, K.A. Benedict,
T. Cheng and M. Henini
School of Physics and Astronomy, University of Nottingham, Nottingham, NG7 2RD, UK.
*Present address: School of Physics, University of Exeter, Exeter, EX4 4QL, UK.
**Present address: Institut fur Festkorperphysik, Universitat Hannover, Appelstrasse 2, D-30167
Hannover, Germany.

Abstract

We report time-resolved studies of ballistic phonon absorption in the fractional quantum Hall regime at Landau level filling factors of ν=1/3, 2/5 and 1/2. The technique used can resolve the interaction of the two dimensional electron system with LA and TA phonons and has been used to measure the temperature variation of the heat capacity of a single layer of electrons at ν=1/3. The energy gaps at ν=1/3 have also been measured and found to be in good agreement with theory. The roles of compressible and incompressible regions in the phonon absorption process are discussed. Angle resolved measurements at ν=2/5 are also in good agreement with theory.

Introduction

The fractional quantum Hall effect (FQHE) occurs due to the formation of a quantum liquid when the Landau level filling factor, $\nu = r/s$, where r and s are integers and s is odd. When ν=1/s the wavefunction is accurately described by Laughlin's variational wavefunction [1] and the low-lying collective excitations of the system, by the theory of Girvin, MacDonald and Platzman [2]. More generally, the collective excitation dispersion has been calculated by Kamilla, Wu and Jain [3]. The most significant features of the excitations are the existence of a finite energy gap at low wavevectors, due to the incompressibility of the FQHE state, and a deep minimum in the energy, Δ^*, of the excitations known as magnetorotons, close to the wavevector where the static structure factor of the liquid is a maximum. The experiments described here probe the interaction of acoustic phonons with these excitations and use the results to determine the temperature variation of the heat capacity of the 2DES at ν=1/3. The interaction between longitudinal acoustic (LA) and transverse acoustic (TA) phonons and the two dimensional electron system (2DES) have been resolved.

Experimental Method

The detailed description of the experimental technique has been given elsewhere [4]. The samples used are single GaAs/AlGaAs heterojunctions grown on a 2mm thick substrate. The 2DES (n_s=1.1 $\times$ 10^{15} m^{-2}, mobility = 150 $m^2V^{-1}s^{-1}$) is patterned into a meandering hall bar with a length to width ratio of around 260. This maximises the sensitivity to changes in longitudinal resistance. On sample A, the meander covers an area of 5mm $\times$ 5 mm, whilst on sample B the area of the meander is 1mm $\times$ 1mm to decrease the solid angle of the device as seen from the other side of the wafer. On the reverse of the wafer, thin film constantan heaters have been evaporated directly opposite the meander and at 45° to it.

A voltage pulse (5-50ns) is applied to the thin film heater causing it to emit a black body spectrum of phonons of known temperature [5]. The emitted phonons travel ballistically across the wafer and a small fraction are absorbed by the 2DES. This absorption process heats the 2DES causing a change in the longitudinal resistance of the device. This resistance change is

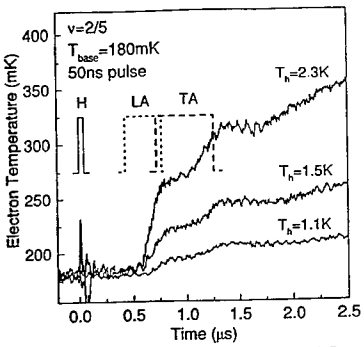

Fig. 1: Phonon absorption signal at v=2/5, heater is at an angle to the meander.

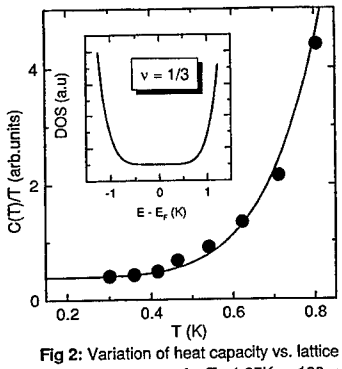

Fig 2: Variation of heat capacity vs. lattice temperature for T_h=1.95K, τ=100ns

measured with a time resolution of approximately 30ns by a signal averaging technique. By calibrating the meander resistance against substrate temperature in the absence of ballistic phonons, the transient electron temperature during the absorption of ballistic phonons can be found. A typical trace for the case of a heater at a 45° to the meander in the [110] direction is shown in Fig. 1.

Ballistic phonon absorption at $\nu=1/2$

Previously, we have shown that at $\nu=1/2$, the fraction of incident phonon flux absorbed is reduced above a heater temperature of 1.4K for the case when the heater is directly under the meander [4]. Along with other measurements, this suggests that the strength of the phonon interaction is limited by the finite thickness, a_0, of the 2DES which can be determined to be around 5 +/- 1 nm from the phonon measurements. This is in agreement with the behaviour of two dimensional systems at zero magnetic field [6] and suggests a broad spectrum frequency absorption due to the creation of particle hole pairs until the perpendicular component of the phonon wavevector, $q_\perp$ exceeds $1/a_0$.

Ballistic phonon absorption at $\nu=1/3$

The fraction of acoustic phonons absorbed, r_0, at the magnetoroton energy, Δ^*, will be approximately constant as long as $exp(-\Delta^*/k_BT) << 1$. This means that the energy absorbed by the FQHE liquid from a pulse of non-equilibrium phonons,

$$dE = C(T)dT = r_0 P_h \tau$$

where P_h is the heater power, τ, the pulse length, C the 2DES heat capacity and dT, the temperature change of the 2DES. Keeping the heater temperature and pulse length constant, we vary the lattice temperature and as long as the temperature variation $dT << T$, a good estimate of the temperature variation of the heat capacity can be determined. Whilst a Schottky heat capacity is predicted [7], the heat capacity is found to vary as $C(T) = AT + BT^7$ (see Fig. 2). A density of states can be constructed from the heat capacity using the Sommerfeld construction (see Fig. 2). A possible explanation of the data is that the linear term in the heat capacity at low temperatures

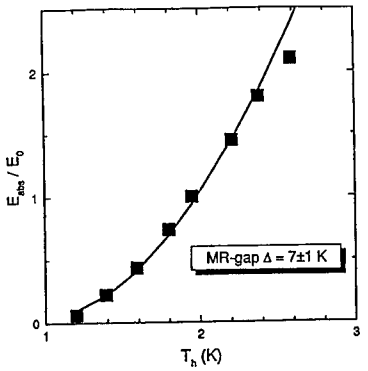

Fig 3: Energy absorbed by 2DES as a function of heater temperature at v=1/3.

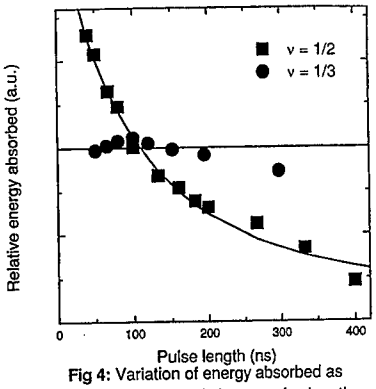

Fig 4: Variation of energy absorbed as a function of phonon pulse length.

is due to compressible localised states whilst the higher power is the low temperature tail of a Schottky-like heat capacity due to the incompressible FQHE liquid.

Initially the 2DES is at a low base temperature $T_0(0)$ whilst the phonons are characterized by an effective temperature, T_h. The 2DES is not uniform but consists of compressible islands within a percolating sea of incompressible electron liquid. Within the incompressible regions screening is very inefficient and the lowest lying excitations are the magnetorotons. In the compressible regions, the screening is metallic and relatively more efficient while the low lying density excitations (to which the phonons couple directly) are particle-hole pairs as in a normal metal. When the phonon pulse comes into contact with the 2DES particle hole pairs are created in the compressible regions and magnetorotons in the incompressible regions. The relative efficiency of the screening in the compressible regions leads us to suppose that the coupling to the phonons will be relatively weak and that, for a sufficiently small coverage of compressible regions, the energy transfer will be dominated by magnetoroton creation in the incompressible regions. The expectation is that the excitations created by the absorption processes will then rapidly (on the timescale of the experiment) equilibrate leading to an increased electron temperature. The heat capacity of the compressible regions will be metallic ($\sim a_c T_e$) while that of the incompressible regions will be activated ($\sim a_i \exp(-\Delta^*/ kT_e)$ so that the latter is negligible at a sufficiently low electron temperature. In other words, the rare high energy phonons create magnetorotons in the incompressible fluid, these deposit their energy into the compressible regions which act as heat baths establishing a well-defined electron temperature. The longitudinal conductance is activated, $\sigma_{xx} \sim \sigma_0 \exp(-\Delta_\infty / T_e(t))$, where Δ_∞ is the energy gap for the creation of unbound Laughlin quasiparticles, so its measurement gives the electron temperature.

If the intial temperature of the lattice is maintained and the heater temperature varied for constant pulse length, the energy absorbed as a function of heater temperature can be calculated (Fig. 3). The results are consistent with phonon absorption across a well-defined energy gap. The energy gap obtained from the measurements is in good agreement with theoretical estimates of the magnetoroton gap [2] and is unaffected by disorder in the sample. The energy gap obtained from magnetotransport measurements is much lower than the phonon-determined gap.

It is possible to imagine a process whereby the creation of magnetorotons by the absorption of phonons from the high energy tail of the non-equilibrium Bose distribution leads directly to the formation of unbound charged quasiparticles. However a careful analysis shows that it is not possible for magnetorotons to sizes in excess of a few times the magnetic length, l_0. Collisions between magnetorotons are therefore the most likely mechanism by which the magnetorotons decay to charged quasiparticles that can contribute to the resistance.

Experimental evidence in support of the above hypothesis can be found in the fraction of energy absorbed from the phonon pulse as the length of the pulse is varied. The results are shown in Fig. 4. At $\nu=1/2$, as the proportion of energy absorbed by the 2DES decreases as the pulse length is increased. All phonon energies up to the cut-off can be absorbed but also emitted by the 2DES. This leads to a saturation of the total energy absorbed as a function of the pulse length. At long times the 2DES emits as much energy in phonon emission as it absorbs. The curve in Fig. 4 is the expected saturation behaviour with a saturation time of 70ns. At $\nu=1/3$, no saturation is observed even at times as high as 300ns. This strongly suggests that the 2DES loses energy by internal processes rather than by the direct emission of acoustic phonons.

Angle-resolved experiments at $\nu=2/5$

At $\nu=2/5$, we have observed ballistic phonon absorption in which the in-phonon wavevectors lie in a small range close to the wavevector at which the magnetoroton minimum is predicted (Fig. 1). The geometric range of angles subtended by the heater was from 30° to 60°. Experimentally, both absorption of both LA and TA phonons are observed. To calculate the range of in-plane wavevectors the effect of phonon anisotropy needs to be taken into account in the interaction, therefore here we present the results for the LA phonons only, as LA phonons are only weakly focussed. For $\nu=2/5$ we find that the magnetoroton energy gap for phonons with in-plane momenta, q, in the range $0.4<ql_0<0.75$ is $0.025(3)e^2/4\pi\varepsilon\varepsilon_0 l_0$. This is in reasonable agreement ($0.032(3)e^2/4\pi\varepsilon\varepsilon_0 l_0$) with theoretical estimates [3] corrected for finite thickness effects [8].

Conclusion

In summary, the use of ballistic phonons provides unique information on the excitations of the fractional quantum Hall effect. The results support the magnetoroton theory and have provided the first measurements of the temperature variation of the heat capacity of a single layer 2DES at a fractional filling factor. At $\nu=2/5$, the magnetoroton gap has been probed at large, in-plane wavevectors.

We would like to thank Dr Dietmar Lehmann for useful discussions and the EPSRC for funding the research.

References

1. R. Laughlin, *Phys. Rev. Lett.* **50**, 1395 (1984)
2. S.M. Girvin, A.H. MacDonald, and P.M. Platzman, *Phys. Rev. Lett.* **54**, 581 (1985); *Phys. Rev.* **B33**, 2481 (1986).
3. R.K. Kamilla, X.G. Wu and J.K. Jain, *Phys. Rev. Lett.* **76**, 1332 (1996).
4. U. Zeitler et al. *Physica B* **249-251**, 49 (1998) and *Phys. Rev. Lett.* (in press).
5. F. Rosch and O. Weiss, *Z. Phys.* **B27**, 33 (1977).
6. A.J. Kent, R.E. Strickland, K.R. Strickland and M. Henini, *Phys. Rev.* B **54** 2019 (1996).
7. T. Chakraborty and P. Pietilainen, *Phys. Rev.* **B55**, 1954 (1997).
8. F.C. Zhang and S. Das Sarma, *Phys. Rev.* **B33**, 2903 (1986).

The Effect of Zeeman Energy on Heat Capacity of GaAs/AlGaAs Heterostructures near $\nu = 1$

S. Melinte [a], E. Grivei [a], J.-M. Beuken [a], G. Mariage [a], L. Malcorps [a], C. Gustin [a], V. Bayot [a] and M. Shayegan [b]

[a]Université Catholique de Louvain, B-1348 Louvain-la-Neuve, Belgium

[b]Department of Electrical Engineering, Princeton University, Princeton, New Jersey 08544

Abstract

By controlling the ratio η between the Zeeman and Coulomb energies, the heat capacity of a multilayer two-dimensional electron system (2DES) is measured near Landau level filling ν=1 at 60 mK. The data reveal the disappearance of the nuclear spin contribution of GaAs quantum wells to the heat capacity as η exceeds a critical value η_C≈0.04. This result is interpreted as the effect of the transition from Skyrmions to single electron spin flips at large Zeeman energy. Our experimental η_C is 25% lower than the calculated η_C=0.054 for an ideal 2DES.

Introduction

The spin configuration of the ground state of a two-dimensional electron system (2DES) near Landau level filling ν=1 have attracted much experimental and theoretical interest [1-9]. At this filling, the lowest energy charged excitations of the 2DES are expected to be spin textures known as *Skyrmions* [2]. Optically pumped nuclear magnetic resonance [3], magnetotransport [6,7] and magneto-optical [8] data provided strong evidence for the existence of quantum Hall effect (QHE) Skyrmions.

Near ν=1, the low temperature (T) heat capacity (C) of GaAs/AlGaAs heterostructures containing 2DESs is dominated by the Schottky nuclear heat capacity [10,11] of Ga and As atoms in the quantum wells (QWs). Of many remarkable features exhibited by the heat capacity data, the disappearance of the QWs' nuclei contribution to the heat capacity at fillings where Skyrmions are no longer relevant (ν<3/4 and ν>4/3) is of particular interest. This observation suggests that heat capacity is a sensitive probe of the presence or the absence of Skyrmions in 2DESs.

Early experimental work on QHE Skyrmions was largely confined to the range of small ratio $\eta=|g^*|\mu_B B/(e^2/\varepsilon l_B)$ between the Zeeman and Coulomb energies [3,7,8,10], where $|g^*|\mu_B$=0.3 K/T, ε≈13, $l_B=(\hbar/eB_\perp)^{1/2}$ is the magnetic length, and B and $B_\perp$ are the total and perpendicular components of the magnetic field, respectively. According to the theory, a transition from Skyrmions to single spin-flip excitations is expected above a critical η_C [2,9]. In this report, evidence for η_C in the range 0.7<ν<1.3 in a low-density (8.5×10^{10} cm^{-2}) 2DES is given.

Experimental technique

The sample is a multiple-quantum-well heterostructure that consists of one hundred 300 Å-thick GaAs QWs, separated by 2500 Å-thick $Al_{0.1}Ga_{0.9}As$ barriers which are δ-doped with donors (Si) near their centers. The heat capacity near ν=1 and the QHE excitation gap (Δ) at ν=1 were measured [10,11] as the Zeeman energy was tuned by tilting *in situ* the sample in the magnetic field so that an angle $0°\le\theta\le77°$ forms between B and the normal to the electron layers.

Results and discussion

We first briefly present our transport data which highlight the difficulty of determining an accurate η_c from such measurements. The value of the excitation gap at ν=1 was determined from the T-dependence of the longitudinal resistivity (R_{xx}) in the thermally activated regime where $R_{xx} \propto \exp(-\Delta/2T)$. The evolution of Δ with θ is presented in Fig. 1. Similar to previous results for single QWs and heterostructures [6], there is an overall qualitative agreement between the measured and calculated gaps in Fig. 1 [13]. In particular, assuming that the slope $K=\partial\Delta/\partial(|g^*|\mu_B B)$ gives the number of flipped electron spins within a single, charged quasiparticle excitation at ν=1, both theory and experiment give $K\cong1$ in the limit of large η [14]. However, the rather large experimental uncertainty in measured gaps and the fact that Δ is expected to slowly approach the single spin-flip dependence (K=1) prohibit an accurate determination of η_c based on transport measurements.

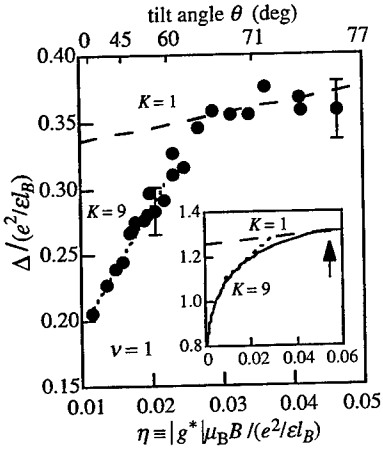

Fig. 1. Δ vs Zeeman energy, both in units of $e^2/\varepsilon l_B$. The corresponding tilt angles are indicated on the top axis. Inset: The energy gap to create a Skyrmion/Antiskyrmion pair (in units of $e^2/\varepsilon l_B$) as a function of η from Hartree-Fock calculations for an *ideal* 2DES [12]. The vertical arrow points to $\eta_c \approx 0.054$ above which a transition from Skyrmions to single spin-flip excitations is predicted. The dotted and dashed lines in the main figure and in the inset correspond to K=9 and K=1, respectively.

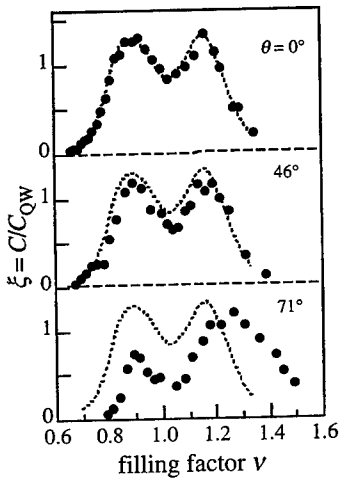

Fig. 2. $\xi=C/C_{QW}$ vs ν at T=60 mK at the indicated tilt angles. The ξ envelope for θ=0° (dotted line), is reproduced for comparison. [Adapted from Ref. 11]

We now discuss heat capacity experiments, which reveal a dramatic and rather abrupt dependence on η and provide evidence for the disappearance of Skyrmions. In the investigated range of T and B, the results can be understood by using the Schottky nuclear heat capacity model developed in Ref. [10]. In the present sample, the Schottky nuclear heat capacity of Ga and As atoms in the QWs is estimated at: $C_{QW} = 3.3\times10^{-11}\, B^2\, T^{-2}$ (J/K) [10,11]. The ratio (ξ) between the measured C and calculated C_{QW} provides us with an estimate of the number of nuclei which *strongly couple* to the lattice. This strong coupling signals the presence of low-energy spin excitations in the 2DES attributed to Skyrmions [2,5]. Figs. 2 and 3 capture the evolution of the heat capacity, represented by the parameter $\xi \equiv C/C_{QW}$ with tilt angle, at T=60 mK. At θ=0° (Fig. 2), the data are qualitatively similar to those reported for a 100-period $GaAs/Al_{0.3}Ga_{0.7}As$ heterostructure with a density of 1.4×10^{11} cm^{-2} per layer [10]. As shown in Fig. 2, ξ vs ν at θ=46°, is nearly identical to the θ=0° data. On the other hand, at θ=71°, the data show a significant asymmetry with respect to the ν=1 position. Most remarkable, however, is that the magnitude of ξ at the ν>1 peak is comparable to the θ=0° data, implying a still strong coupling of the nuclei to the lattice. This is a particularly noteworthy observation as it highlights that the heat capacity is a very sensitive probe for Skyrmions, in a regime where the transport data and calculations both reveal a small Skyrmion size (K<3) and a very weak dependence of Δ on η [see Fig. 1 and its inset near $\eta\approx0.035$ (θ=71°)]. When θ is further increased above 71° only by few degrees (Fig. 3), the nuclear heat capacity decreases dramatically for all ν. For θ>74°, the nuclear heat capacity is no longer measurable up to the highest investigated tilt-angle (77°). To bring into focus the evolution of the coupling between the nuclear spin system and the lattice with θ and η, we plot ξ at ν>1 and ν<1 maxima vs η (Fig. 4). The coupling due to low-energy spin excitations is progressively suppressed for $\eta\geq0.035$ and vanishes in the range $0.037\leq\eta\leq0.043$. We believe that this behavior provides evidence for the *transition from Skyrmions to single spin-flip excitations* at $\eta_c\approx0.04$ in our sample. This η_c is smaller than the theoretical η_c=0.054 calculated for the Skyrmion to single spin-flip transition for an *ideal* 2DES [2,9]. Several factors, however, are expected to reduce η_c for a *real* 2DES. This includes the finite thickness of the electron layer [9], Laudau-level mixing, and disorder. Indeed, calculations by Cooper [9,12] reveal that taking into account the finite z-extent of the 2DES *alone* leads to η_c=0.047, closer to our experimental value. We mention here another interesting and novel possibility to explain the observed $\eta_c\approx0.04$. Self-consistent calculations [15] performed for our sample predict that a crossing between the first spin-down Landau level and the second spin-up Landau level occurs precisely at θ=72°. This Landau level crossing would certainly affect the spin energy spectrum of the 2DES and may explain the disappearance of the Skyrmions, and hence the observed suppression of the nuclear heat capacity near θ=72°.

Summary

In conclusion, the heat capacity experiments reveal the subtle and critical influence of tilted magnetic fields on the ground and excited states of 2DESs near ν=1 in GaAs/AlGaAs heterostructures. The data indicate the disappearance of low-energy spin excitations in the 2DES, which we interpret as evidence for the suppression of Skyrmions above a critical Zeeman energy ($\eta_c\approx0.04$ in our sample).

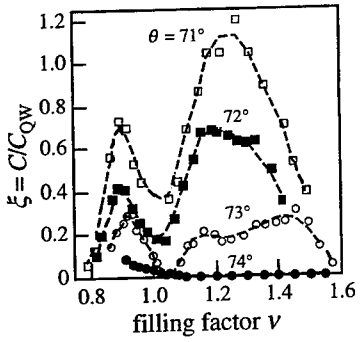

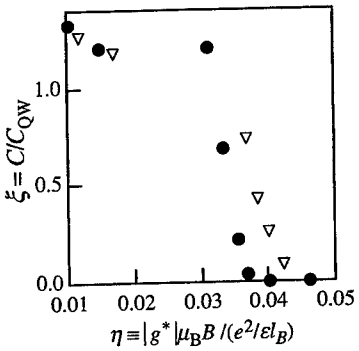

Fig. 3. $\xi = C/C_{QW}$ vs ν at T=60 mK for 71°≤θ≤74°. Fig. 4. $\xi = C/C_{QW}$ at ν>1 (•) and ν<1 (▽) maxima is plotted vs η at θ=0°, θ=46° and θ≥71°. [Adapted from Ref. 11] The dashed lines are guides to the eye. [Adapted from Ref. 11]

Acknowledgments

The authors are much indebted to N.R. Cooper, T. Jungwirth and S.P. Shukla for numerical calculations. This work has been supported by NATO grant CRG 950328 and the NSF MRSEC grant DMR-9400362. The work performed in Louvain-la-Neuve was carried out under financial support of the programme "PAI" sponsored by the "Communauté Française de Belgique".

References

[1] R.J. Nicholas et al., Phys. Rev. B 37 (1988) 1294.
[2] S.L. Sondhi et al., Phys. Rev. B 47 (1993) 16419.
[3] S.E. Barrett et al., Phys. Rev. Lett. 74 (1995) 5112.
[4] L. Brey et al., Phys. Rev. Lett. 75 (1995) 2562.
[5] R. Côté et al., Phys. Rev. Lett. 78 (1997) 4825.
[6] A. Schmeller et al., Phys. Rev. Lett. 75 (1995) 4290.
[7] D.K. Maude et al., Phys. Rev. Lett. 77 (1996) 4604.
[8] E.H. Aifer et al., Phys. Rev. Lett. 76 (1996) 680.
[9] N.R. Cooper, Phys. Rev. B 55 (1997) R1934.
[10] V. Bayot et al., Phys. Rev. Lett. 76 (1996) 4584.
[11] S. Melinte et al., Phys. Rev. Lett. 82 (1999) 2764.
[12] N.R. Cooper, private communication.
[13] As in Ref. [6], our measured Δ is about 30% of the theoretical value for an *ideal* 2DES.
[14] For η=0.012 the experiment gives K≅9. An excellent agreement between this experimental value and the theoretical prediction is found when calculations take into account the finite-thickness of the electron layer [12].
[15] T. Jungwirth and A.H. MacDonald, private communication.

Low-energy electronic spin excitations between filling factors $\nu = 1$ and $\nu = 1/2$ studied by optically detected nuclear magnetic resonance

H.D.M. Davies, R.L. Brockbank, J.F. Ryan, M.A. Thomson and A.J. Turberfield

Department of Physics, University of Oxford, Clarendon Laboratory, Parks Road, Oxford OX1 3PU, United Kingdom.

Abstract

We report measurements of the spin relaxation time (T_{1n}) for nuclei in the potential well confining a high-mobility two-dimensional electron system at a single GaAs - GaAlAs heterojunction. At low temperatures nuclear spin relaxation is dominated by electron-nuclear spin scattering: we find that T_{1n} displays sharp maxima at incompressible states throughout the $\nu = 2/3$ hierarchy of the fractional quantum Hall effect. This behaviour is consistent with the existence of low-energy spin excitations only where the electron system is compressible. Our measurements also provide evidence for a gap in the spin excitation spectrum at $\nu = 1/2$.

Key words: NMR; Fractional quantum Hall effect; Skyrmion.

There is substantial experimental evidence[1-3] that the low-lying charged excitations of a two-dimensional electron system (2DES) in a perpendicular magnetic field near Landau level filling factor $\nu = 1$ are charged spin texture excitations or skyrmions[4,5]. The ground state at $\nu = 1$ is believed to be completely spin polarized[4]. Skyrmions minimise the exchange energy associated with the addition of a reversed-spin electron or a spin hole to this state, at the expense of an increased Zeeman energy, by reversing more than one electron spin per added charge in such a way that spins rotate gradually away from a central reversed spin. Nuclear magnetic resonance of nuclei in the potential well confining the 2DES has proved to be a powerful tool for investigating the electronic spin polarization of these systems: NMR measurements provided the first and most conclusive proof of the existence of skyrmions around $\nu = 1$[1] by demonstrating that the electron spin polarization, determined from Knight shift measurements, falls off abruptly on either side of $\nu = 1$. Similar measurements around $\nu = 1/3$ at 12 T show a much slower change in polarization corresponding to ~ 0.1 spin flips per quasi-particle[6]. Activated transport measurements performed at $\nu = 1/3$ reveal that, as the electronic g-factor is tuned towards zero by the application of hydrostatic pressure, charged excitations involve three spin reversals[7]. Recent calculations suggest that skyrmions may be stable near a spin polarized $\nu = 2/3$ state for fields less than ~ 30 T[8].

Measurements of the nuclear spin-lattice relaxation time (T_{1n}) have also provided information about spin excitations of the 2DES near $\nu = 1$.

T_{1n} has been measured directly by NMR[1,9] and indirectly via heat capacity measurements[10] and is strongly dependent on filling factor. Rapid nuclear spin relaxation is interpreted as evidence for the presence of low-energy electronic spin excitations consistent with the presence of skyrmions[11]. We report measurements of the T_{1n} at a single high-mobility heterojunction throughout the entire $\nu = 2/3$ hierarchy.

The spins of conduction-band electrons in GaAs are magnetically coupled to those of the Ga and As nuclei via the contact hyperfine interaction; at low temperatures this provides the dominant nuclear spin relaxation mechanism. By driving the electron spin system out of equilibrium by resonant inter-band optical excitation of the 2DES we are able to use electron - nuclear spin coupling to produce up to 80% dynamic nuclear polarization[13]. Hyperfine interaction with oriented nuclei causes a change in the Zeeman energy of an electron: this *Overhauser shift* may be considered as being due to an effective magnetic field which is proportional to the mean nuclear polarization. By using light scattering to measure the electronic Zeeman energy, and thus the Overhauser shift, we are able to deduce the nuclear polarization[13]. This measurement is extremely sensitive: only nuclei within ~100 Å of the heterojunction, which occupy the same volume as the 2DES, are directly polarized by optical excitation of the 2DES, and the light scattering signal depends only on the polarization of the same nuclei.

A high-mobility 2DES ($n = 9.5 \times 10^{10}$ cm^{-2}, $\mu \sim 10^7$ cm^{2}V^{-1}s^{-1}) is confined at the interface of a GaAs - $Al_{0.33}Ga_{0.66}As$ single heterojunction. The sample is attached to the cold finger of a dilution refrigerator, whose temperature can be adjusted between 50 mK and 4 K, in a 16 T superconducting magnet. Light from an etalon-tuned titanium:sapphire laser enters the dilution refrigerator through bottom windows and is focused onto the sample. Inelastically scattered light is collected with optical fibres and dispersed by a quadruple grating spectrometer onto a liquid nitrogen cooled CCD camera. A pair of single-turn coils are mounted next to the sample to allow for the application of RF irradiation. The experimental details have been described elsewhere[12,13].

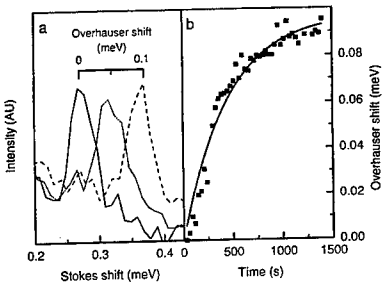

Fig. 1. a) Resonant inelastic light scattering spectra from $k \sim 0$ spin-wave excitations of the 2DES. The solid spectrum was recorded after the sample had been in the dark for 12 hours; the dashed spectrum followed 10 minutes of illumination; the dotted spectrum was recorded after 10 minutes illumination followed by resonant RF irradiation of the ^{75}As nuclei. b) The time dependence of the buildup of dynamic nuclear polarization during continuous resonant inter-band optical excitation. The solid line is an exponential fit to the data. All data were measured at 11.35 T and ~ 50 mK.

Figure 1a shows inelastic light scattering from spin excitations of the 2DES. The Stokes shift of the scattering peak is equal to the energy of small-wavevector spin-wave excitations which, by Larmor's theorem, is equal to the single-particle Zeeman energy. The solid line is a spectrum taken after the sample has been left in the dark for 12 hours to allow the nuclear polarization to attain thermal equilibrium ($\lesssim$ 5% at 100 mK, 11.35 T). The spectrum shown with the dashed line was taken after 10 minutes of resonant optical illumination: this is sufficient to polarize the nuclei to a saturated value of 80%, producing an Overhauser shift of the electron Zeeman energy of 0.093 meV[13]. GaAs contains three nuclear species: ^{69}Ga(60%), ^{71}Ga(40%) and ^{75}As (all have nuclear spin quantum number $I = 3/2$). Before the dotted spectrum of Figure 1a was recorded the nuclei were optically polarized, then ^{75}As nuclei were selectively depolarized by applying a transverse RF field at the ^{75}As NMR frequency. Resonant RF depolarization of all three nuclear species has been measured; the FWHM

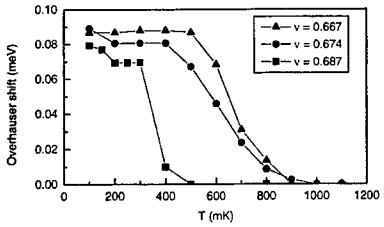

Fig. 2. Temperature dependence of dynamic nuclear polarization induced by resonant interband optical excitation at $\nu \geq 2/3$.

of the resonances is $\sim$ 75 ppm[13]. Figure 1b shows the time dependence of dynamic nuclear polarization at a typical illumination intensity; here with the nuclei initially unpolarized the sample was illuminated and spectra were taken every 30 seconds. The solid line is an exponential fit to the data yielding a time constant of 446 s.

Figure 2 shows the temperature dependence of the dynamic nuclear polarization achieved at filling factors $\nu \geq 2/3$. The sample was illuminated continuously for 30 minutes at each temperature to allow the nuclear spins to reach dynamic equilibrium before the nuclear polarization was measured. The data show a rapid loss of nuclear polarization in a narrow temperature range similar to that observed at $\nu = 1/3$[13]. The temperature at which the polarization falls to 50% of its low-temperature value is maximal at $\nu = 2/3$ and falls off sharply to higher filling factors. For filling factors much above $\nu = 0.690$ we are unable to produce detectable dynamic polarization even at 100 mK. This contrasts with the behaviour near $\nu = 1/3$ where dynamic nuclear polarization is only weakly dependent on filling factor (with a weak *minimum* at $\nu = 1/3$)[12,13]. We expect the magnitude of dynamic nuclear polarization to be independent of the strength of electron-nuclear spin coupling (as long as this remains the dominant spin relaxation mechanism) and to increase with the ratio between the electron and nuclear Zeeman energies[13]. Our observations are consistent with the interpretation that the electron spin excitation gap shrinks rapidly as the filling

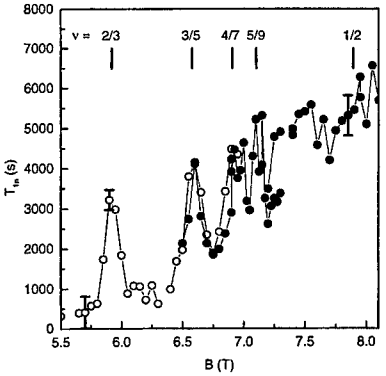

Fig. 3. Spin-lattice relaxation time T_{1n} for nuclei in the potential well confining the 2DES. Nuclei were polarized under standard conditions at a fixed magnetic field (11.35 T) by resonant optical excitation of the 2DES, then allowed to depolarize in the dark during a dwell time of 1 hour (•) or 30 minutes (○) at a lower field at 70 mK.

factor moves away from $\nu = 2/3$.

The degree of dynamic nuclear polarization achieved in these experiments depends not only on the spectrum of electronic spin excitations but also on the population of such excitations generated by optical excitation. A simpler measure of the coupling between electron and nuclear spins is the nuclear spin relaxation time T_{1n} measured in the dark, whose filling-factor dependence is shown in Figure 3. For each measurement the sample was illuminated for 15 minutes at 11.35 T at 70 mK (with an intensity three times larger than that used to measure the polarization time in Figure 1b) to produce a large, reproducible, nuclear polarization. The illumination was switched off and the field was swept down quickly (in $\lesssim$ 5 minutes) to the filling factor of interest. With the sample still in the dark the field was held constant for a certain dwell time and then swept back up to 11.35 T where the sample was re-exposed to the light for the purpose of recording a short-exposure (30 s) inelastic light scattering spectrum from which the residual nuclear polarization could be deduced. Figure 3

shows T_{1n} calculated by assuming an exponential decay of polarization with time after dwell times of one hour (•) or 30 minutes (○) at filling factors between $\nu = 1$ and $\nu = 1/2$. The figure clearly shows that T_{1n} is significantly reduced at filling factors on either side of the incompressible $\nu = 2/3$, $\nu = 3/5$, $\nu = 4/7$ and $\nu = 5/9$ states of the 2/3 hierarchy. In fact repeating the same experiment with no dwell time reveals that T_{1n} falls to < 30 s (too fast to measure with this technique) between $\nu = 1$ and $\nu = 2/3$, compared with ~ 1 hour at $\nu = 2/3$.

Nuclear spin scattering by lattice vibrations is strongly suppressed at low temperatures[15]. Scattering by the 2DES is also suppressed when there is a gap in the electronic spin excitation spectrum[9]. The oscillations of T_{1n} for $\nu > 1/2$ indicate a strongly filling-factor dependent coupling between electron and nuclear spins. The relatively long T_{1n} at incompressible states of the 2/3 hierarchy is consistent with the presence of a gap in the spectrum of spin excitations of the 2DES at these filling factors. Shorter T_{1n}s suggest the existence of low-energy electronic spin excitations at intermediate filling factors. Côté and coworkers[11] have pointed to zero-energy spin excitations of a Skyrme crystal as a possible cause of strong electron-nuclear spin coupling near $\nu = 1$; our results suggest that a similar mechanism may operate at filling factors between the incompressible states of the 2/3 hierarchy.

No such variation of T_{1n} with filling factor is observed in the 1/3 hierarchy in this sample; the long T_{1n} observed at filling factors $\nu < 1/2$ is consistent with a spin-polarized ground state. At $\nu = 1/2$ the excitation spectrum of the 2DES is expected to be gapless[14,16]. Nevertheless, Figure 3 shows that T_{1n} is relatively long at $\nu = 1/2$, indicating the absence of low-lying electronic spin excitations. We infer that the low-energy excitations responsible for the compressibility of the 2DES at $\nu = 1/2$ in this sample are pure charge density excitations. It is interesting to note that transport measurements cannot detect the presence a spin gap when the 2DES is compressible.

We have shown that the nuclear spin lattice relaxation time T_{1n} is strongly reduced at filling factors between the incompressible states of the 2/3 hierarchy. This is consistent with the presence of low-energy spin modes, which may be associated with charged spin texture excitations, in the excitation spectrum of the 2DES at these filling factors. T_{1n} is relatively long, consistent with the presence of a gap in the spectrum of spin excitations of the 2DES, at $\nu = 1/2$ and throughout the 1/3 hierarchy.

References

[1] S.E. Barrett, G. Dabbagh, L.N. Pfeiffer, K.W. West and Z. Tycko, Phys. Rev. Lett. **74** (1995) 5112.

[2] A. Schmeller, J.P. Eisenstein, L.N. Pfeiffer and K.W. West, Phys. Rev. Lett. **75** (1995) 4290.

[3] E.H. Aifer, B.B. Goldberg and D.A. Broido, Phys. Rev. Lett. **76** (1996) 680.

[4] S.L. Sondhi, A. Karlhede, S.A. Kivelson and E.H. Rezayi, Phys. Rev. B **47** (1993) 16419.

[5] H.A. Fertig, L. Brey, R. Côté and A.H. MacDonald, Phys. Rev. B **50** (1994) 11018.

[6] P. Khandelwal, N.N. Kuzma, S.E. Barrett, L.N. Pfeiffer and K.W. West, Phys. Rev. Lett. **81** (1998) 673.

[7] D.R. Leadley, R.J. Nicholas, D.K. Maude, A.N. Utjuzh, J.C. Portal, J.J. Harris and C.T. Foxon, Phys. Rev. Lett. **79** (1997) 4246.

[8] Kang-Hun Ahn and K.J. Chang, Phys. Rev. B **55** (1997) 6735.

[9] R. Tycko, S.E. Barrett, G. Dabbagh, L.N. Pfeiffer and K.W. West, Science **268** (1995) 1460.

[10] V. Bayot, E. Grivei, S. Melinte, M.B. Santos and M. Shayegan, Phys. Rev. Lett. **76** (1996) 4584; V. Bayot, E. Grivei, J.-M. Beuken, S. Melinte and M. Shayegan, Phys. Rev. Lett. **79** (1997) 1718; S. Melinte, E. Grivei, V. Bayot and M. Shayegan, Phys. Rev. Lett. **82** (1999) 2764.

[11] R. Côté, A.H. MacDonald, Luis Brey, H.A. Fertig, S.M. Girvin and H.T.C. Stoof, Phys. Rev. Lett. **78** (1997) 4825.

[12] H.D.M. Davies, J.C. Harris, J.F. Ryan and A.J. Turberfield, Phys. Rev. Lett. **78** (1997) 4095.

[13] H.D.M. Davies, R.L. Brockbank, J.F. Ryan and A.J. Turberfield, Physica B **256** (1998) 104.

[14] B.I. Halperin, P.A. Lee and N. Read, Phys. Rev. B **47** (1993) 7312.

[15] A. Abragam, The Principles of Nuclear Magnetism, O.U.P., Oxford, 1961.

[16] A. Stern, B.I. Halperin, F. von Oppen and S.H. Simon, Phys. Rev. B **59** (1999) 12547.

Composite Fermion Picture for Multi-Component Plasmas in 2D Electron-Hole Systems in a Strong Magnetic Field

A. Wójs[1,2], I. Szlufarska[1,2], K.-S. Yi[1,3], P. Hawrylak[4], J. J. Quinn[1]

[1]*Department of Physics, University of Tennessee, Knoxville, Tennessee 37996, USA*

[2]*Institute of Physics, Wroclaw University of Technology, Wroclaw 50-370, Poland*

[3]*Physics Department, Pusan National University, Pusan 609-735, Korea*

[4]*Institute for Microstructural Sciences, National Research Council, Ottawa, Canada K1A 0R6*

Low lying states of a 2D electron-hole system contain electrons and one or more types of charged excitonic complexes. Binding energies and angular momenta of these excitonic ions, and the pseudopotentials describing their interactions with electrons and with one another are obtained from numerical studies of small systems. Incompressible fluid ground states of such multi-component plasmas are found in exact numerical diagonalizations. A generalized composite Fermion (CF) picture involving Chern–Simons charges and fluxes of different types is proposed and shown to predict the low lying states at any value of the magnetic field.

PACS: 71.10.Pm, 73.20.Dx, 73.40.Hm, 71.35.Ji

Keywords: Composite Fermion, Quantum Hall Effect, Charged Exciton

Introduction. In a 2D electron-hole system in a strong magnetic field, the only bound complexes are neutral excitons X^0 and spin-polarized charged excitonic ions X_k^- (k excitons bound to an electron) [1–4]. Other complexes found at lower fields [5] unbind due to a hidden symmetry [6]. The X_k^- ions are long lived Fermions whose energy spectra contain Landau level structure [2–4]. By numerical diagonalization of small systems we can determine binding energies and angular momenta of the excitonic ions, and pseudopotentials which describe their interactions with electrons and with one another [4]. We show that a gas of X_k^-'s can form Laughlin [7] incompressible fluid states [4], but only for filling factors $\nu_k \leq (2k+1)^{-1}$ (in the following, subscript k denotes X_k^-). Multi-component plasmas containing electrons and X_k^- ions of one or more different types can also form incompressible fluid states. A generalized composite Fermion (CF) picture [8] is proposed to describe such a plasma [9]. It requires the introduction of Chern–Simons [10] charges and fluxes of different types (colors) in order to mimic generalized Laughlin type correlations [11]. The predictions of this CF picture agree well with numerical results for systems containing up to eighteen particles.

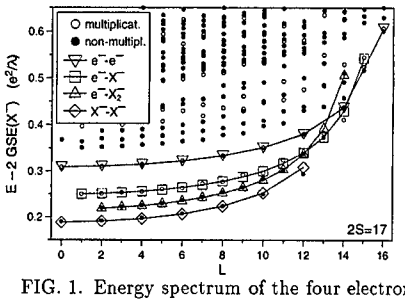

FIG. 1. Energy spectrum of the four electron and two hole system at $2S = 17$.

Four Electron–Two Hole System. Understanding of the energy spectrum of this simple system is essential for our considerations. Result of the numerical diagonalization in Haldane spherical geometry [12], for the magnetic monopole strength $2S = 17$, is shown in Fig. 1. Open and solid circles mark multiplicative and non-multiplicative states [6], respectively. For $L < 12$ there are four low lying bands, which we have identified, in order of increasing energy, as two X^-'s, an electron and an X_2^-, an electron and an X^-

and a decoupled X^0, and finally two electrons and two decoupled X^0's. We find that the X_k^- has an angular momentum $l_k = S - k$ in contrast to an electron which has $l_0 = S$. All relevant binding energies and pseudopotentials are also determined. An important observation is that the pseudopotential of composite particles ($k > 0$) is effectively infinite (hard core) if L exceeds a particular value. This is due to unbinding of ions at too small separation. Once the maximum allowed L's for all pairings are established, the four bands in Fig. 1 can be approximated by the pseudopotentials of electrons (point charges) with angular momenta l_A and l_B, shifted by the appropriate binding energies (large symbols).

Larger Systems We know from exact calculations for up to eleven electrons [13] that the CF picture correctly predicts the low lying states of the fractional quantum Hall systems. The reason for this success is [13] the ability of the electrons in states of low L to avoid large fractional parentage (FP) [13] from pair states associated with large values of the Coulomb pseudopotential. In particular, for the Laughlin $\nu_0 = 1/3$ state, the FP from pair states with maximum pair angular momentum $L = 2l_0 - 1$ vanishes. We hypothesize that the same effect should occur for an X^- system when $l_0 = S$ is replaced by $l_1 = S - 1$. We define an effective X^- filling factor as $\nu_1(N, S) = \nu_0(N, S - 1)$ and expect the incompressible X^- states at all Laughlin and Jain fractions for $\nu_1 \leq 1/3$. States with $\nu_1 > 1/3$ cannot be constructed because they would have some FP from pair states forbidden by the hard core repulsion [4].

Fig. 2 shows energy spectra of the $6e + 3h$ system at $2S = 8$ and 11. Both multiplicative (open circles) and non-multiplicative (solid circles) states are shown in frames (a) and (c). In frames (b) and (d) only the non-multiplicative states are plotted, together with the approximate spectra (large symbols)

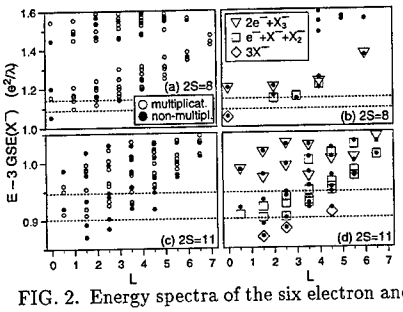

FIG. 2. Energy spectra of the six electron and three hole system at $2S = 8$ and 11.

obtained by diagonalizing the system of three ions with the actual pseudopotentials appropriate to the three possible charge configurations: $3X^-$ (diamonds), $e^- + X^- + X_2^-$ (squares), and $2e^- + X_3^-$ (triangles).

Good agreement between the exact and approximate spectra in Figs. 2b and 2d allows identification of the three ion states and confirms our conjecture about incompressible states of a X^- gas. States corresponding to different charge configurations form bands At low L, the bands are separated by gaps, predominantly due to different total binding energies of different configurations. The lowest state in each band corresponds to the three ions moving as far from each other as possible. If the ion–ion repulsion energies were equal for all configurations (a good approximation for dilute systems), the two higher bands would lie above dashed lines, marking the ground state energy plus the appropriate difference in binding energies. The low lying multiplicative states can also be identified as $3e^- + 3X^0$, $2e^- + X^- + 2X^0$, $2e^- + X_2^- + X^0$, and $e^- + 2X^- + X^0$. The bands of three ion states are separated by a rather large gap from all other states, which involve excitation and breakup of composite particles.

The largest systems for which we performed exact calculations are the $6e + 3h$ and

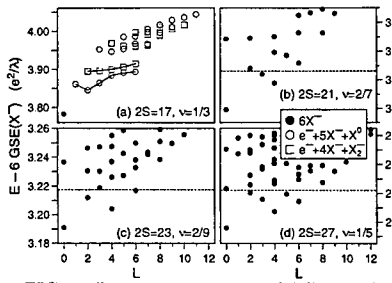

FIG. 3. Low energy spectra of different charge configurations of the twelve electron and six hole system at $2S = 17$, 21, 23, and 27.

$8e + 4h$ systems at $2S$ up to 12 (Laughlin $\nu_1 = 1/5$ state of three X^-'s and one quasi-X^--hole in the $\nu_1 = 1/3$ state of four X^-'s). In each case the CF picture applied to the X^- particles works well. For larger systems the exact diagonalization becomes difficult. For example, for the $12e + 6h$ system we expect the $\nu_1 = 1/3$, 2/7, 2/9, and 1/5 incompressible states to occur at $2S = 17$, 21, 23, and 27, respectively. We managed to extrapolate the involved pseudopotentials making use of their regular dependence on $2S$, and use them, together with the binding energies, to determine approximate low lying bands in the energy spectra, as shown in Fig. 3. At $2S = 17$, the only state of the $6X^-$ configuration is the $L = 0$ ground state (filled circle); other $6X^-$ states are forbidden by the hard core. The low lying states of other low energy configurations, $e^- + 5X^- + X^0$ (open circles) and $e^- + 4X^- + X_2^-$ (open squares) are separated from the $6X^-$ ground state by a gap. At $2S = 21$, 23, and 27, all features predicted by the CF picture occur for the $6X^-$ states.

Generalized Composite Fermion Picture In order to understand all of the numerical results presented in Fig. 3a, we introduce a generalized CF picture by attaching to each particle fictitious flux tubes carrying an integral number of flux quanta ϕ_0. In the multi-component system, each a-particle carries flux $(m_{aa} - 1)\phi_0$ that couples only to charges on all other a-particles and fluxes $m_{ab}\phi_0$ that couple only to charges on all b-particles, where a and b are any of the types of Fermions. The effective monopole strength [8,13] seen by a CF of type a (CF-a) is $2S_a^* = 2S - \sum_b (m_{ab} - \delta_{ab})(N_b - \delta_{ab})$. For different multi-component systems we expect generalized Laughlin incompressible states when all the hard cores are avoided and CF's of each type fill completely an integral number of their CF shells. In other cases, the low lying multiplets will contain different types of quasiparticles (QP-a, QP-b, ...) or quasiholes (QH-a, QH-b, ...) in the neighboring incompressible state.

Our multi-component CF picture can be applied to the system of excitonic ions, where the CF angular momenta are given by $l_k^* = |S_k^*| - k$. As an example, let us consider Fig. 3a and make the following CF predictions. For six X^-'s we obtain the Laughlin $\nu_1 = 1/3$ state at $L = 0$. Because of the X^--X^- hard core, it is the only state of this configuration. For the $e^- + 5X^- + X^0$ configuration we set $m_{11} = 3$ and $m_{01} = 1$, 2, and 3. For $m_{01} = 1$ we obtain $L = 1$, 2, 3^2, 4^2, 5^3, 6^3, 7^3, 8^2, 9^2, 10, and 11; for $m_{01} = 2$ we obtain $L = 1$, 2, 3, 4, 5, and 6; and for $m_{01} = 3$ we obtain $L = 1$. For the $e^- + 4X^- + X_2^-$ configuration we set $m_{11} = 3$, $m_{02} = 1$, $m_{12} = 3$, and $m_{01} = 1$, 2, or 3. For $m_{01} = 1$ we obtain $L = 2$, 3, 4^2, 5^2, 6^3, 7^2, 8^2, 9, and 10; for $m_{01} = 2$ we obtain $L = 2$, 3, 4, 5, and 6; and for $m_{01} = 3$ we obtain $L = 2$. Note that the sets of multiplets obtained for higher values of m_{01} are subsets of the sets obtained for lower values; we would expect them to form lower energy bands since they avoid additional large values of e^--X^- pseudopotential. As marked with lines in Fig. 3a, this is indeed true for the states predicted for

$m_{01} = 2$. However, the states predicted for $m_{01} = 3$ do not form separate bands. This is because e^--X^- pseudopotential increases more slowly than linearly as a function of $L(L+1)$ in the vicinity of $L = l_0 + l_1 - m_{01}$; in such case the CF picture fails [13].

The agreement of our CF predictions with the exact spectra of different systems, as in Figs. 2 and 3, is really quite remarkable and strongly indicates that our multi-component CF picture is correct. We are actually able to confirm predicted Laughlin type correlations [11] in the low lying states by calculating their FP coefficients [13]. In view of the results obtained for many different systems that we were able to treat numerically, we conclude that if exponents m_{ab} are chosen correctly, the CF picture works well in all cases.

Summary Low lying states of electron-hole systems in a strong magnetic field contain charged excitonic ions X_k^- interacting with one another and with electrons. For different combinations of ions occurring at low energy, we introduced general Laughlin type correlations into the wavefunctions and demonstrated formation of incompressible fluid states of such multi-component plasmas at particular values of the magnetic field. We also proposed a generalized multi-component CF picture and successfully predicted lowest bands of multiplets for various charge configurations at any value of the magnetic field. It is noteworthy that the fictitious Chern-Simons fluxes and charges of different types or colors are needed in the generalized CF model. This strongly suggests that the effective magnetic field seen by the CF's does not physically exist and that the CF picture should be regarded as a mathematical convenience rather than physical reality. Our model also suggests an explanation of some perplexing observations found in photoluminescence, but this topic will be addressed in a separate publication.

We thank M. Potemski for helpful discussions. AW and JJQ acknowledge partial support from the Materials Research Program of Basic Energy Sciences, US Department of Energy. KSY acknowledges support from Korea Research Foundation.

[1] A. J. Shields, M. Pepper, M. Y. Simmons, and D. A. Ritchie, Phys. Rev. B **52**, 7841 (1995); G. Finkelstein, H. Shtrikman, and I. Bar-Joseph, Phys. Rev. B **53** 1709, (1996).

[2] A. Wójs and P. Hawrylak, Phys. Rev. B **51** 10 880, (1995).

[3] J. J. Palacios, D. Yoshioka, and A. H. MacDonald, Phys. Rev. B **54**, 2296 (1996).

[4] A. Wójs, P. Hawrylak, and J. J. Quinn, Physica B **256–258**, 490 (1998); Phys. Rev. Lett. (submitted, cond-mat/9810082).

[5] K. Kheng, R. T. Cox, Y. Merle d'Aubigne, F. Bassani, K. Saminadayar, and S. Tatarenko, Phys. Rev. Lett. **71**, 1752 (1993); H. Buhmann, L. Mansouri, J. Wang, P. H. Beton, N. Mori, M. Heini, and M. Potemski, Phys. Rev. B **51**, 7969 (1995).

[6] I. V. Lerner and Yu. E. Lozovik, Sov. Phys. JETP **53**, 763 (1981); A. H. MacDonald and E. H. Rezayi, Phys. Rev. B **42**, 3224 (1990).

[7] R. B. Laughlin, Phys. Rev. Lett. **50**, 1395 (1983).

[8] J. K. Jain, Phys. Rev. Lett. **63**, 199 (1989).

[9] A. Wójs, I. Szlufarska, K.-S. Yi, and J. J. Quinn, Phys. Rev. Lett. (submitted, cond-mat/9904395).

[10] A. Lopez and E. Fradkin, Phys. Rev. B **44**, 5246 (1991).

[11] B. I. Halperin, Helv. Phys. Acta **56**, 75 (1983).

[12] F. D. M. Haldane, Phys. Rev. Lett. **51**, 605 (1983); T. T. Wu and C. N. Yang, Nucl. Phys. B **107**, 365 (1976).

[13] A. Wójs and J. J. Quinn, Solid State Commun. **108**, 493 (1998); ibid. **110**, 45 (1999); Phys. Rev. B (submitted, cond-mat/9903145).

Ferromagnetism and Heterostructures of III-V Magnetic Semiconductors

Hideo Ohno

Laboratory for Electronic Intelligent Systems
Research Institute of Electrical Communication, Tohoku University
Katahira 2-1-1, Aoba-ku, Sendai 980-8577, Japan
e-mail ohno@riec.tohoku.ac.jp

Abstract

Ferromagnetism in III-V based magnetic semiconductors introduced a new degree of freedom associated with the magnetic cooperative phenomena to the low dimensional heterostructures. This article reviews the preparation and the structure, magnetic, and transport properties of ferromagnetic III-V semiconductor (Ga,Mn)As, which can be grown pseudomorphically on GaAs heterostructures, and heterostructures related to the ferromagnetic semiconductor.

1. Introduction

III-V based heterostructures have been used not only in practical devices such as semiconductor lasers and high electron mobility transistors but they also have been the test bench for new ideas and rich soil of new physics. This is because one can tailor the electronic states to extreme precision and control them by external fields in virtually impurity free environment. Magnetism, especially ferromagnetism, however, has not been a part of it because of the lack of material technologies that allow us to introduce such magnetic cooperative phenomena into III-V based heterostructures. The discovery of ferromagnetism in (In,Mn)As, an alloy between III-V non-magnetic semiconductor InAs and magnetic ion Mn [1], and subsequent synthesis of GaAs based ferromagnetic semiconductor, (Ga,Mn)As [2], changed the situation. We now have in our hands a new degree of freedom associated with ferromagnetism together with all the freedoms we have been enjoying working with, because ferromagnetic (Ga,Mn)As can be pseudomoriphically grown on GaAs substrates, thus can be incorporated into III-V heterostructures. Mn in (Ga,Mn)As provides both localized spins and holes, due to its magnetic and acceptor nature. High concentration of holes introduced by Mn is believed to mediate the magnetic interaction among Mn, leading to the appearance of ferromagnetism. This paper reviews the current status of the new III-V based ferromagnetic semiconductor (Ga,Mn)As and heterostructures based on it.

2. Preparation of (Ga,Mn)As and its heterostructures

To observe pronounced magnetic cooperative phenomena, one needs to introduce a sizable amount of magnetic ions into the host non-magnetic GaAs, which requires high doping of magnetic ions that exceeds its solubility limit. It was shown by the combination of InAs and Mn that low temperature molecular beam epitaxy (LT-MBE, growth temperature < 300 ℃) could suppress Mn segregation at the growth front and produce epitaxial layers of (In,Mn)As with Mn concentration far beyond its solubility limit [3]. (Ga,Mn)As layers are prepared by the same method, LT-MBE, to overcome the solubility limit of Mn in GaAs, i.e. they are in their non-equilibrium state. A high temperature anneal results in phase separation of (Ga,Mn)As to GaAs and NiAs-structure MnAs, which has been investigated as a method to incorporate ferromagnetic inclusions (MnAs) in the GaAs host [4]. When the growth temperature and/of Mn concentration are too high, formation of MnAs phase at the growth front occurs, which can be detected *in situ* by reflection high energy electron diffraction, allowing one to optimize the growth conditions.

In spite of the low growth temperatures, high structural quality of (Ga,Mn)As epitaxial layers and (Ga,Mn)As/GaAs superlattices on (001) GaAs substrates has been confirmed by X-ray diffraction studies [5, 6]; the half width at full maximum of (Ga,Mn)As diffraction peaks was as low as 37.5 arc seconds. The lattice constant of strain free (Ga,Mn)As increases with increasing its Mn composition x as $a = 0.566\ (1\text{-}x) + 0.598\ x$ (nm) [2]. Extended X-ray absorption fine structure (EXAFS) study showed that Mn atoms occupy the group III sites [7]. (Al,Ga)As/(Ga,Mn)As as well as (In,Ga)As/(Ga,Mn)As heterostructures have already been demonstrated [8, 9, 10]. The low temperature growth currently limits the two dimensional growth of (Al,Ga)As to Al composition $x_{Al} < 0.4$ or $x \approx 1$ (AlAs); $0.4 < x < 1$ leads to three-dimensional growth.

3. Properties of (Ga,Mn)As

Magnetization measurements revealed sharp, square hysteresis loops in magnetization (M) versus magnetic field (B) curves at low temperatures, showing the presence of ferromagnetism in the (Ga,Mn)As films. Ferromagnetic transition temperature T_C increases with increasing x as 2000 $x \pm 10$ K ($x < 0.05$); below $x = 0.005$, however, no ferromagnetism could be detected. The highest T_C so far obtained is 110 K [11]. Magnetic easy axis was in plane due to compressive strain from GaAs substrate; the easy axis can be made perpendicular with the reversal of the strain direction [12]. The low temperature saturation magnetization M_S of (Ga,Mn)As was consistent with the spin of Mn $S = 5/2$. Susceptibility χ follows the Curie-Weiss form $\chi = C/(T-\theta)$, where C is the Curie constant and θ the paramagnetic Curie temperature. In fully compensated (Ga,Mn)As samples, however, θ becomes negative (-2 K) [13], showing that the direct exchange among Mn is antiferromagnetic and the ferromagnetic interaction observed in these films are carrier (hole) induced.

Resistivity as well as Hall resistivity measurements as a function of temperature T as well as B have revealed rich information about the properties of (Ga,Mn)As. The Hall effect is dominated by the anomalous Hall effect in (Ga,Mn)As, which made it possible to determine the magnetic properties from the magnetotransport measurements alone. The sheet Hall resistivity R_{Hall} in (Ga,Mn)As can be expressed as,

$$R_{Hall} = \frac{R_0}{d}B + \frac{R_S}{d}M \qquad (1),$$

where R_0 is the ordinary (normal) Hall coefficient, R_S the anomalous Hall coefficient, and d the sample thickness. Separate measurements indicated that R_S is proportional to R_{sheet} in the present samples (skew scattering [14]) and thus $R_S/d = c\ R_{sheet}$, where c is a temperature independent constant. The anomalous Hall term is dominant often up to room temperature. This allows one to determine M of the sample from R_{Hall} ($M \sim (1/c)\ R_{Hall}/R_{sheet}$). One can determine T_C by the use of the Arrott plots [11, 12], in which $(R_{Hall}/R_{sheet})^2$ is plotted against $(B/(R_{Hall}/R_{sheet}))$ at each temperature to obtain a quantity proportional to M_S from the extrapolated intercept (M_S is zero when intercept is at the origin). Note that R_{Hall}/R_{sheet} is proportional to M. This way the T dependence of M_S and T_C can be determined from the transport results. Figure 1 summarizes the x dependence of T_C for 200 nm (Ga,Mn)As grown on (Al,Ga)As buffer layers ($x_{Al} = 0.9$). Since the anomalous Hall effect is dominant even at room temperature, and hence $\chi \approx (1/c)(R_{Hall}\mu_0 / R_{sheet}B)$ holds for a wide temperature range, one can determine θ by plotting $1/\chi$ (determined from transport measurements) as a function of T [5].

The ordinary Hall coefficient can be measured as the slope of the R_{Hall}-B curve at low temperature under high magnetic field, where M saturates, although the procedure is not as straightforward as it sounds because of the presence of negative magnetoresistance that

extends to high fields. One needs to go to low temperature (< 2 K) and high fields (> 20 T) to saturate M and the negative magnetoresistance, where one can unambiguously determine R_0. Such measurements on a metallic sample (x = 0.053) shows that p = 3.5 x 10^{20} cm^{-3}, 30 % of nominal concentration of Mn [15].

Temperature T (2 - 300 K) dependence of R_{sheet} of six 200 nm thick (Ga,Mn)As epitaxial films grown on $Al_{0.9}Ga_{0.1}As$ buffer layer shows that the samples with intermediate Mn composition (x = 0.035, 0.043 and 0.053) are on the metal side of the metal-insulator transition, whereas low and high x samples are on the insulator side (x = 0.015, 0.022, and 0.071). At T_C, all the samples showed a hump in R_{sheet}-T curves. This temperature dependence, especially in the metallic samples, is most probably due to the critical scattering. Resistivity ρ due to critical scattering by fluctuations of magnetic spins is given by [16],

$$\rho = 6\pi^2 \frac{k_F}{pe^2} \frac{m^2\beta^2}{h^3} \frac{k_B T}{g^2 \mu_B{}^2} \chi(T,B) \qquad (2),$$

where k_F is Fermi wave number, m effective mass (we assume the heavy hole mass in GaAs, $m = 0.5m_0$, m_0: free electron mass), β the exchange between the carriers and the magnetic spins, k_B the Boltzmann constant, e elementary charge, h the Plank constant, g Landé-factor of the Mn spins, and μ_B the Bohr magneton. The temperature dependence of ρ in the high temperature region of metallic samples can be reproduced well by eq. (2) as shown in Fig. 2; the measured data can be fitted by χT, characteristic temperature dependence of critical scattering. Deviation of χT fit from experiment as T_C approaches occurs because the q = 0 value of χ is used in the place of wavevector (q) dependent χ, which is responsible for the scattering. Ordinarily, $\chi(q)$ is a decreasing function of q in ferromagnetic materials and thus the fit overestimates the scattering near T_C, where $\chi(q = 0)$ diverges.

Negative magnetoresistance was observed in all the samples at low temperatures. Negative magnetoresistance of the metallic samples first increases as T decreases and peaks at T_C, whereas that of the insulating samples continues to increase as T decreases further below T_C and it becomes quite pronounced at low temperatures. The negative magnetoresistance of metallic samples can also be understood as the reduction of spin-dependent scattering by aligning the spins by B described by eq. (2).

The fit of eq. (2) to T and B dependence of ρ yields $|N_0\beta|$ in the range of about 1.5 ± 0.2 eV (N_0: the density of cation sites). Previous estimate of $|N_0\beta|$ using the expression for the high temperature limit of eq. (2) gave the upper limit of the interaction [11]. There is, however, a number of factors one needs to take into account to properly understand $|N_0\beta|$ obtained from transport. One example is the effect of localization induced by disorder, which enhances the ferromagnetic interaction through hole-hole interaction. Large p-d exchange (2.5 eV, positive) was deduced from the magneto-optical study of GaAs doped with Mn [17]. Smaller exchange of 1.0-1.2 eV (negative) was inferred from the photoemission experiments on (Ga,Mn)As [18]. Typical p-d exchange ($N_0\beta$) in II-VI DMS's is about -1 eV.

Very large negative magnetoresistance has been observed in "reentrant" insulating samples at high x [19, 20]. This large negative magnetoresistance may be understood by considering either (or both) formation of bound magnetic polarons as was suggested in an earlier work on (In,Mn)As [1] or increase of Fermi energy in a spin split band which reduces the localization length by reducing the energy difference between the mobility edge and the Fermi level [20].

4. Origin of Ferromagnetism

Since the magnetic interaction between Mn has been shown to be antiferromagnetic in semi-insulating fully carrier-compensated (Ga,Mn)As using Sn as a donor [13], the ferromagnetic interaction in magnetic III-V's is most likely hole induced. One approach to the

understanding of the carrier-induced ferromagnetic interaction starts from approximating the interaction as between the conduction carrier Fermi sea and the localized magnetic moments. This approach has been employed to understand various optical and magnetic phenomena observed in II-VI based paramagnetic semiconductors. The nature of exchange is expressed in terms of exchange integrals $N_0\alpha$ and $N_0\beta$ for the conduction band and for the valence band, respectively. A mean field theory has been developed by Dietl et al. [21] taking into account the feedback mechanism between the magnetization polarization and the carrier polarization; magnetization polarization produces carrier polarization and it in turn produces magnetization polarization. This mean field theory results in the same expression of T_C as that of the well-known Ruderman-Kittel-Kasuya-Yosida (RKKY) interaction. The RKKY interaction is carrier-induced, sufficiently long ranged to account for the magnetic interaction in dilute systems, and has been put forward to explain the carrier (hole) induced ferromagnetism as well as spin-glass phase observed in a IV-VI compound (Pb,Sn,Mn)Te [22].

T_C calculated from the hole free energy in the framework of the mean field theory [23] by solving a 6 x 6 Luttinger Hamiltonian taking into account the presence of the p-d interaction, shows that $|N_0\beta| = 1.3$ eV to obtain $T_C = 110$ K for $p = 3.5 \times 10^{20}$ cm^{-3}, in rather good agreement with the range of $N_0\beta$ and p inferred from transport. The mean field approach can also explain the absence of ferromagnetism in n-type materials; in n-type materials, the small effective mass together with the small $N_0\alpha$ (about 0.2 eV) makes it difficult for the ferromagnetic interaction to overcome the direct antiferromagnetic coupling among Mn. The mean field picture was used to explain the hole-induced ferromagnetism observed about 2 K in II-VI magnetic quantum wells [24].

Ferromagnetism in insulating samples can be understood along the same line, if one considers the difference between the length-scales involved in the transport and the magnetism. In insulating samples, the localization length is smaller than the sample size (millimeters) but may still be significantly larger than the length scale of magnetic interactions (nanometers), thus making the mean field approach a good starting point, although localization phenomena would be increasingly important.

Another approach emphasizes the role of the d-band formed by transition metal impurities. Based on a first principle calculation of the ground state energy of (In,Mn)As, Akai stressed the partial d-character of the holes and invoked a double-exchange picture for the observed ferromagnetism [25]. The energy gain of the ferromagnetic phase is proportional to the carrier concentration and therefore the calculation showed that compensating the holes results in destabilization of the ferromagnetic state. It is also interesting to point out that the calculation indicates that (In,Mn)As is half metallic, as was pointed out for (Ga,Mn)As using hypothetical ordered alloy and local spin density approximation [26].

Whether the two approaches are different or not probably depends on the physical properties under discussion, because the partial d-character of the holes is the source of enhancement of the hole-localized spin exchange $|N_0\beta|$ over the electron-localized spin exchange $N_0\alpha$.

5. Heterostructures

New physics such as fractional quantum Hall effect have emerged from the non-magnetic III-V semiconductor heterostructures. There is a number of new possibilities one can explore with the added degree of freedom associated with ferromagnetic semiconductor compatible with the III-V heterostructures. We may use the ferromagnetic semiconductor as a spin polarized carrier source to achieve spin-injection into semiconductors. Or one may be able to demonstrate field-controlled ferromagnetic phase transition by changing the density of carriers that mediates the magnetic interaction. Although these two are yet to be demonstrated, following are some of the examples of what has been done using the ferromagnetic III-V

semiconductor heterostructures.

5.1 Ferromagnetic/Non-magnetic/Ferromagnetic Trilayers

(a) Interlayer Coupling

A study was carried out to look into the magnetic interactions between two ferromagnetic (Ga,Mn)As layers separated by a non-magnetic semiconducting layer. In order to examine the presence and nature of the magnetic interaction, two series of structures with a 30 nm (Ga,Mn)As (x = 0.04) layer and a 30 nm (Ga,Mn)As (x = 0.02) layer separated by a nonmagnetic (Al,Ga)As layer were grown on $(Al_{0.9}Ga_{0.1})As$ buffer layers on (001) GaAs substrates [27]; one with GaAs as the nonmagnetic layer with thickness d_{GaAs} ranging from 0 to 106 monolayers (ML) and the other with 10 ML (Al,Ga)As with two different Al composition (x_{Al} = 0.16 and 0.29).

Magnetotransport measurements of these layers done by applying B perpendicular to the sample plane indicated that, as the thickness of the GaAs layer decreases (from n = 106 to 0), B_{sat} (at which $R_{Hall}/R_{sheet} \propto M$ saturates) of the top x = 0.04 layer decreases. The reduction of B_{sat} shows the presence of stronger coupling between the two magnetic layers, because the bottom (Ga,Mn)As layer (x_{Mn} = 0.02) has lower B_{sat} than that of the top layer (confirmed by separate measurements on reference samples). In the case of the (Al,Ga)As intermediary layer, the results indicated that B_{sat} of x_{Al} = 0.29 is higher than that of x_{Al} = 0.16, showing weakening of coupling with increasing the barrier height in the valence band. These experiments delineated the critical role of the hole density in the intermediary layer in the interlayer coupling; the higher the hole concentration, the stronger the interaction. The results suggest that the magnetic interaction is mediated by holes in the non-magnetic intermediary layer. Recent calculation shows that the magnetic interaction should oscillate as a function of the hole density and thickness [28].

(b) Spin-dependent transport

Figure 3 shows the result of magnetotransport measurements on a trilayer structure, where clear increase in resistance is observed when M of the two layers becomes anti-parallel [29]. Current flow is along the plane, i.e. the measurement configuration is current-in-plane (CIP). R_{Hall} in this case shows clear hysteresis reflecting M of the two layers because (1) tensile strain is built into the trilayer to make the easy axis perpendicular to the plane by usnig a (In,Ga)As buffer layer whose lattice constant is greater than the (Ga,Mn)As layers used, and (2) x of the two layers (0.03 and 0.05) were chosen in such a way that conductance of both layers are comparable at low temperature.

5.2 Resonant Tunneling Structures

When a semiconductor becomes ferromagnetic, spin splitting of the conduction as well as the valence bands is expected to occur due to s-d and p-d exchange interactions. Because (Ga,Mn)As can be grown pseudomorphically on nonmagnetic GaAs-based heterostructures, one can fabricate resonant tunneling diodes (RTD) to investigate the spontaneous band splitting in (Ga,Mn)As. Temperature and magnetic field dependence of current-voltage (I-V) characteristics of p-type AlAs/GaAs/AlAs double barrier RTD's having (Ga,Mn)As as an emitter material were studied [30, 31]. Spontaneous splitting of resonant peaks in the absence of magnetic fields was observed upon lowering the measurement temperature below T_C, which was interpreted as the spin splitting of the valence band of ferromagnetic (Ga,Mn)As observed in tunneling spectra.

6. Conclusion

Properties of ferromagnetic III-V semiconductor (Ga,Mn)As and its heterostructures

were reviewed. Ferromagnetic (Ga,Mn)As prepared by LT-MBE exhibits ferromagnetism with T_C as high as 110 K. Magnetic and magnetotransport properties of (Ga,Mn)As and its heterostructures showed the critical role played by holes and its exchange interaction with Mn local spins in ferromagnetism. Heterostructures based on (Ga,Mn)As, such as trilayer structures and RTD's, were shown to exhibit a number of new properties not present in nonmagnetic structures. Although not covered here, I should note that a number of optical studies on (Ga,Mn)As [32, 33, 34] have been carried out as well as studies on magnetic III-V's other than (Ga,Mn)As and (In,Mn)As [35, 36]. I believe ferromagnetic III-V's are an excellent tool to explore a new field of semiconductor physics and technology, where both semiconductor-heterostructure properties and magnetic/spin-dependent properties play critical roles.

Acknowledgements

I thank F. Matsukura, N. Akiba, T. Omiya, T. Dietl, D. Chiba, Y. Ohno, B. Beschoten, P. Crowell, D. D. Awschalom, and A. Twardowski for valuable discussion. The work at Tohoku University was partly supported by the "Research for the Future" Program (# JSPS-RFTF97P00202) from the Japan Society for the Promotion of Science and partly by Grant-in-Aid on Priority Area "Spin Controlled Semiconductor Nanostructures" (# 09244103) from the Ministry of Education, Japan.

References

1. H. Ohno, H. Munekata, T. Penney, S. von Molnár, and L. L. Chang, Phys. Rev. Lett., **68**, 2664 (1992).
2. H. Ohno, A. Shen, F. Matsukura, A. Oiwa, A. Endo, S. Katsumoto, Y. Iye, Appl. Phys. Lett. 69, 363 (1996). See also H. Ohno, Science, 281, 951 (1998).
3. H. Munekata, H. Ohno, S. von Molnár, A. Segmüller, L. L. Chang, and L. Esaki, Phys. Rev. Lett., 63, 1849 (1989).
4. J. De Boeck, R. Oesterholt, A. Van Esch, H. Bender, C. Bruynseraede, C. Van Hoof, and G. Borghs, Appl. Phys. Lett. 68 2744 (1996).
5. A. Shen, H. Ohno, F. Matsukura, Y. Sugawara, Y. Ohno, N. Akiba, and T. Kuroiwa, Jpn. J. Appl. Phys. 36 L73 (1997).
6. A. Shen, F. Matsukura, S. P. Guo, Y. Sugawara, H. Ohno, M. Tani, H. Abe, and H. C. Liu, J. Crystal Growth, 201/202, 679 (1999).
7. R. Shioda, K. Ando, T. Hayashi, and M. Tanaka, Phys. Rev. B58, 1100 (1998).
8. A. Shen, H. Ohno, F. Matsukura, Y. Sugawara, N. Akiba, T. Kuroiwa, A. Oiwa, A. Endo, S. Katsumoto, and Y. Iye, J. Crystal Growth 175/176, 1073 (1997).
9. T. Hayashi, M. Tanaka, K. Seto, T. Nishinaga, and K. Ando, Appl. Phys. Lett., 71 1825 (1997).
10. A. Shen, H. Ohno, F. Matsukura, H. C. Liu, N. Akiba, Y. Sugawara T. Kuroiwa, and Y. Ohno, Physica B, 249-251, 809 (1998).
11. F. Matsukura, H. Ohno, A. Shen, and Y. Sugawara, Phys. Rev. B57, R2037 (1998).
12. H. Ohno, F. Matsukura, A. Shen, Y. Sugawara, A. Oiwa, A. Endo, S. Katsumoto, and Y. Iye, Proc. of the 23rd Intl. Conf. on Physics of Semiconductors (Eds., M. Scheffler and R. Zimmermann, World Scientific, Singapore. 1996) , pp.405-408.
13. Y. Satoh, N. Inoue, Y. Nishikawa, and J. Yoshino, Proceedings of the 3rd. Symp. on Physics and Application of Spin Related Phenomena in Semiconductors (eds. H. Ohno, J. Yoshino, and Y. Oka, Nov. 17-18, 1997, Sendai, Japan), p. 23.
14. See, e.g. The Hall Effect and Its Applications, ed. by C.L. Chien and C.R. Westgate (Plenum, New York, 1980).
15. T. Omiya, F. Matsukura, T. Dietl, Y. Ohno, T. Sakon, M. Motokawa, and H. Ohno, presented at the 9th International Conference on Modulated Semiconductor Structures, Fukuoka, Japan, July 11-16, 1999. Proceedings will be published in Physica E.
16. T. Dietl, in Handbook on Semiconductors Vol. 3b, Ed. T. S. Moss (North-Holland, 1994) pp.1282-1287.
17. J. Szczytko, W. Mac, A. Stachow, A. Twardowski, P. Becla, and J. Tworzydlo, Solid State Commun., 99, 927, (1996).
18. J. Okabayashi, A. Kimura, O. Rader, T. Mizokawa, A. Fujimori, T. Hayashi, and M. Tanaka, Phys. Rev. B58, R4211 (1998).
19. A. Oiwa, S. Katsumoto, A. Endo, M. Hirasawa, Y. Iye, H. Ohno, F. Matsukura, A. Shen and Y. Sugawara,

phys. status solidi (b), 205, 167 (1998).
20. S. Katsumoto, A. Oiwa, Y. Iye, H. Ohno, F. Matsukura, A. Shen, and Y. Sugawara, phys. status solidi (b), 205, 115 (1998).
21. T. Dietl, A. Haury, and Y. Merle d'Aubigne´, Phys. Rev. B55, R3347 (1997).
22. T. Story, R. R. Galazka, R. B. Frankel, and P.A. Wolff, Phys. Rev. Lett. 56, 777 (1986).
23. T. Dietl, unpublished.
24. A. Haury, A. Wasiela, A. Arnoult, J. Cibert, S. Tatarenko, T. Dietl, and Y. Merle d'Aubigné, Phys. Rev. Lett., 79, 511 (1997).
25. H. Akai, Phys. Rev. Lett., 81, 3002 (1998).
26. M. Shirai, T. Ogawa, I. Kitagawa, and N. Suzuki, J. Magn. Magn. Mater., 177-181, 1383 (1998).
27. N. Akiba, F. Matsukura, A. Shen, Y. Ohno, H. Ohno, A. Oiwa, S. Katsumoto, and Y. Iye, Appl. Phys. Lett., 73, 2122 (1998).
28. T. Jungwirth, W. A. Atkinson, B. H. Lee, and A. H. MacDonald, Phys. Rev. B, 59, 9818 (1999).
29. N. Akiba, D. Chiba, K. Nakata, F. Matsukura, and H. Ohno, unpublished results.
30. H. Ohno, N. Akiba, F. Matsukura, A. Shen, K. Ohtani, and Y. Ohno, Appl. Phys. Lett., 73, 363 (1998).
31. N. Akiba, F. Matsukura, Y. Ohno, A. Shen, K. Ohtani, T. Sakon, M. Motokawa, and H. Ohno, Physica B, 256-258, 561 (1998).
32. K. Ando, T. Hayashi, M. Tanaka, and A. Twardowski, J. Appl. Phys., 83, 6548 (1998).
33. B. Beschoten, P. A. Crowell, I. Malajovich, S. J. Allen, D. D. Awschalom, F. Matsukura, A. Shen, and H. Ohno, presented at the 24th Int. Conf. Physics of Semiconductors, Jerusalem, Israel, August 2-7, 1998.
34. J. Szczytko, W. Mac, A. Twardowski, F. Matsukura, and H. Ohno, Phys. Rev. B, 59, 12935 (1999).
35. (Ga,Mn)Sb: E. Abe, F. Matsukura, H. Yasuda, Y. Ohno, and H. Ohno, the 9th International Conference on Modulated Semiconductor Structures, Fukuoka, Japan, July 11-16, 1999.
36. (Ga,Fe)As: M. Yamaura, S. Haneda , K. Hara, S. Hirose, Y. Takatani, S. Harigae, and H. Munekata, Materials Research Society 1999 Spring Meeting (San Francisco, USA, April 5-9, 1999), and J. Yoshino, private communication.

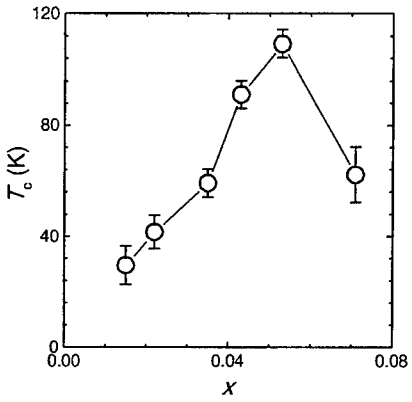

Figure 1. Mn composition (x) dependence of ferromagnetic transition temperature T_C for 200 nm (Ga,Mn)As grown on (Al,Ga)As buffer layers (x_{Al}=0.9). All layers were grown on (001) GaAs substrates.

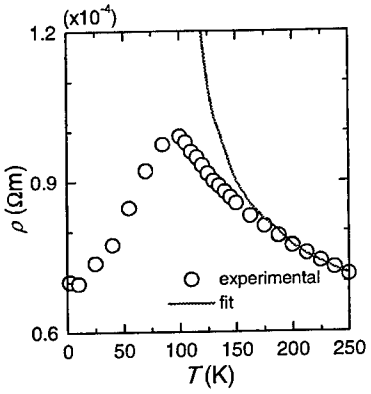

Figure 2. Temperature dependence of resistivity ρ of a 200 nm sample with x=0.053 (Open circles). Solid line is a fit of $\rho = a\ \chi\ T + b$ (a, b constants) to the high-temperature part; χ is susceptibility determined experimentally from the anomalous Hall effect measurements.

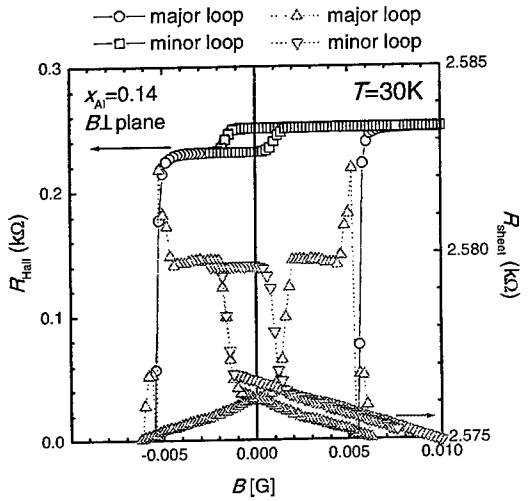

Figure 3. Magnetic field dependence of R_{Hall} and R_{sheet} of a 30 nm (Ga,Mn)As (x=0.05) /10 ML (Al,Ga)As (x_{Al}=0.14)/ 30 nm (Ga,Mn)As (x=0.03) trilayer structure. A lattice relaxed (In,Ga)As buffer layer was used to tensiley strain the trilayer structure so that the easy axis becomes perpendicular to the sample plane. Step structure seen in R_{Hall} ($\propto M$) at B = 0.001-0.005 T shows that M of the two ferromagnetic layers are antiparallel in that magnetic field range. R_{sheet} also shows a marked increase at the step region indicating the presence of spin-dependent scattering in the structure; the first of this kind in a semiconductor structure. A minor loop experiment shown also in the figure supports this interpretation. The skewed minor loop with respect to B = 0 is an evidence of ferromagnetic coupling between the two magnetic semiconductor layers.

ORDERED MAGNETIC PHASE IN $Cd_{1-x}Mn_xTe/Cd_{1-y-z}Mg_yZn_zTe$:N HETEROSTRUCTURES: MAGNETOOPTICAL STUDIES

P. Kossacki,[a-c] D. Ferrand,[a] A. Arnoult,[a] J. Cibert,[a] S. Tatarenko,[a] A. Wasiela,[a] Y. Merle d'Aubigné,[a] J-L. Staehli[b], J-D. Ganiere[b], W. Bardyszewski,[c] K. Świątek,[d] M. Sawicki,[d] J. Wróbel,[d] and T. Dietl [d-e]

a) Laboratoire de Spectrométrie Physique, Université Joseph Fourier Grenoble 1 CNRS (UMR 55 88), B.P. 87, F-38402 Saint Martin d'Hères Cedex, France
b) Department of Physics, Federal Inst. of Technology, CH-1015, Lausanne, Switzerland
c) Faculty of Physics, Warsaw University, ul. Hoża 69, PL-00681 Warszawa, Poland
d) Institute of Physics, PAS, al. Lotników 32/46, PL-02668 Warszawa, Poland
e) Research Institute of Electrical Communication, Tohoku University, 2-1-1 Katahira, Aoba-ku, Sendai 980, Japan

Photoluminescence magnetospectroscopy is employed to examine the low temperature magnetic phase that is induced by the carrier-mediated ferromagnetic exchange interaction in modulation-doped $Cd_{1-x}Mn_xTe$ quantum well. Unusual properties of the domain structure are linked to tendency towards spin-density wave formation in this low dimensional magnetic system.

Two recent developments have considerably renewed the interest into mechanisms underlining carrier-mediated ferromagnetic couplings in semiconductor material systems. First, low-temperature epitaxy of $Ga_{1-x}Mn_xAs$ results in a material, in which the critical temperature T_c of a ferromagnetic phase transition attains values as high as 110 K for x as low as 0.05. [1] Second, it was experimentally confirmed [2] that, according to theoretical prediction, [3] free holes in low-dimensional structures of II-VI diluted magnetic semiconductors (DMS) can induce a ferromagnetic order, demonstrating that the well-established methods of modulation of the carrier concentration in semiconductor quantum structures can be applied for a tailoring of magnetic properties.

In this Communication, we present new results of investigations, which aim at determining the dependence of the critical temperature T_c in p-doped $Cd_{1-x}Mn_xTe$ quantum well (QW) on the Mn content x and the hole concentration p, as well as at establishing the nature of the magnetic order. Due to the excellent structural characteristics of MBE-grown II-VI layered structures, their properties near the ferromagnetic phase transition can be examined by magnetooptical effects [2]. In particular, a Moss-Burstein shift obtained by comparing photoluminescence (PL) and its excitation spectra (PLE) permits the determination of the carrier concentration. The energy distance between the emission lines observed for the two complementary circular polarizations gives, in turn, direct information on the magnitude of the band spin-splitting, and thus on the magnetization inside the domains. At the same time the difference between the integrated intensities of the lines shows how the degree of domain alignment depends on the magnetic field and temperature.

The PL experiments were carried out in Faraday geometry. The photon energy of the excitation beam was tuned below the energy gap of the barrier material. Additional illumination by above-barrier light resulted in a trapping of the photoholes in the barrier, and a partial neutralization of the holes in the QW by the photoelectrons under stationary conditions, allowing

us to precisely tune the hole density p. The Zeeman splitting of the excitonic features observed in reflectivity between 10 and 50 kOe, together with the well-known values of the band, [4] exchange, [5] and magnetic [5,6] parameters of $Cd_{1-x}Mn_xTe$, served to obtain an exact value of x.

Two types of cryogenic systems were employed: A pumped liquid ^{4}He cryostat [2] and a dilution refrigerator. In the dilution refrigerator, a fiber-optic system was used to guide the light to and out of the sample mounted on a cold finger; the temperature was monitored by a calibrated resistor located in close proximity of the sample. Considering the strong temperature dependence of the PL splitting, the actual temperature of the spin-subsystem at a given excitation power was thoroughly evaluated: Such an analysis indicated that measurements down to 0.6 K were possible with a reasonable signal to noise ratio. Time resolved PL was measured using a streak camera and excitation light pulses (<3ps) from a mode-locked Ti-saphire laser.

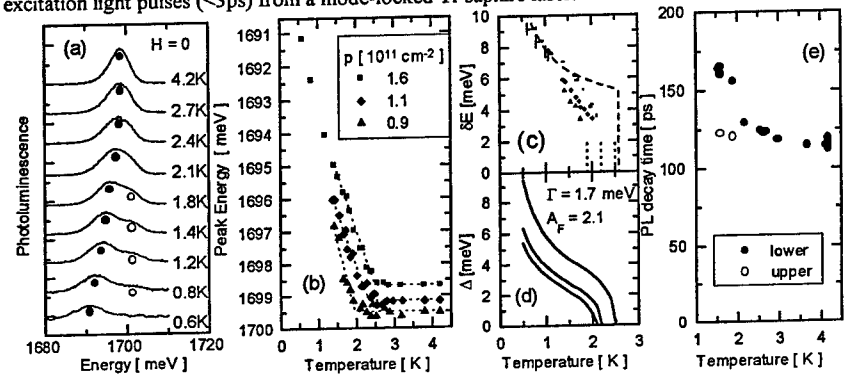

Fig. I PL spectra at selected temperatures (a). Peak positions of the low- and high-energy lines are marked by full and empty points, respectively. Temperature dependence of the low-energy peak positions and the line splitting are shown for selected values of the hole concentrations in (b) and (c), respectively. Dashed and solid lines in (c) and (d) are calculated neglecting and taking disorder into account, respectively. Vertical lines in (c) show critical temperatures T_c corresponding to slope changes of the points in (b). PL decay times for upper (empty points) and lower (full symbols) split lines versus temperature are shown in (e).

Our findings in the absence of external magnetic field are summarized for one of the structures in Fig. 1. The PL line which corresponds to the energy gap in the QW region, below a characteristic temperature T_C, features a splitting and a shift of its spectral position. Furthermore there is a significant increase of the PL decay time below T_C. These observations, together with the observed critical behavior of the field-induced splitting at $T \to T_C^+$ (i.e., a diverging susceptibility), [2] constitute the experimental evidences for the presence of a ferromagnetic transition in the modulation-doped p-$Cd_{1-x}Mn_xTe$ QW. As shown in Fig. 2, the dependence $T_C(x)$ is well described by the mean-field model [3] with an enhancement factor A_F=2.1 resulting from the carrier-carrier correlations [3,2].

Figures 1(b) and 1(c) show how the energy of the PL peak and its splitting δE vary with the temperature and hole concentration. According to the simple model,[3] whose predictions are

shown by a dashed line in Fig. 1(c), the band spin-splitting Δ, and thus δE, are expected to attain rather abruptly the value corresponding to the full polarization of the hole liquid. We see that the experimental values of δE reaches the theoretically calculated splitting at the lowest temperatures, a result supporting strongly the general consistency of our interpretation. However, δE decreases with rising temperature faster than expected theoretically. Furthermore, T_C is predicted to be independent of p in 2D systems, [3] a supposition at variance with the results of Fig. 1(b) and 2(b). We assign these discrepancies to the effect of static disorder upon the energy dependence of the density-of-states (DOS). To check this conjecture, we insert into the self-consistent procedure[3] the hole polarization, $p_\downarrow - p_\uparrow$, calculated from the expression,

$$p_{\uparrow\downarrow}(\Delta) = \frac{A_F m_{hh}}{4\pi\hbar^2}\int_{-\infty}^{+\infty} d\varepsilon \frac{1+erf[(\varepsilon \pm \Delta/2)/\gamma]}{1+\exp[(\varepsilon-\varepsilon_F)/k_BT]},$$ in which the step-like DOS of clean 2D systems with the dispersion $\varepsilon_k = \hbar^2k^2/2m_{hh}$ is broadened by disorder. This broadening is characterized by the parameter $\Gamma = \sqrt{2}\gamma$, the FWHM of the Gaussian distribution of the energy levels which contribute to DOS. As shown in Figs.1(d) and 2(b), such a model with Γ = 1.7 meV explains qualitatively the essential features of our data.

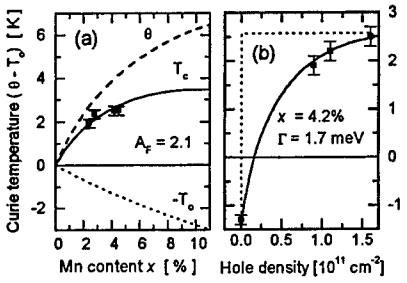

Fig. 2. Critical temperature $T_c = \Theta - T_o$ of the ferromagnetic transition as a function of Mn (a) and hole (b) concentrations. Solid lines are theoretical taking the enhancement factor due to the Coulomb interactions between the holes (a) and also disorder (b) into account. The values of temperature Θ and T_o corresponding to the ferromagnetic and super-exchange antiferromagnetic interactions are shown in (a) by dashed and dotted line, respectively. The dashed line in (b) is theoretical neglecting disorder (Γ=0).

Turning to the properties of the ferromagnetic phase we note that the easy axis is expected to be oriented along the growth direction as a result of the interaction between the hole spin and the strain and confinement potential [3],[7]. The spectra in Faraday geometry give, therefore, information about the relative concentration of domains with the two relevant orientations, as shown schematically in Fig. 3(a). The difference in the integrated intensities of the two circularly polarized components contributing to the PL line, normalized to their values at H=0, is depicted as a function of the magnetic field at 1.53 K in Fig. 3(c).

A number of conclusions emerge from this plot. First, we see that the domains become aligned in a magnetic field of the order of 100 0e. Second, since we know the magnitude of the spin-splitting, and thus the corresponding magnetization, we are in position to evaluate the contribution of the Mn spins to the macroscopic magnetic induction from the system of aligned domains, $B_S = 4\pi M_S = 14 \pm 1 Gs$ at 1.5K. Such a small value of B_S makes the dipole interaction weak, and substantiates *a posteriori* our assumption that the spontaneous magnetization is oriented perpendicularly to the surface. Finally, the data point to small coercive force, $H_C < 4$ *0e*.

The virtual absence of hysteresis in the studied ferromagnet is further supported by the observation that the spectra for the two polarizations, that is the concentrations of the two kinds of the domains, are identical at $H=0$, even after cooling the sample from above T_C down to 1.5K in the magnetic field of 500Oe or after 15 min of illumination by circularly polarized light.

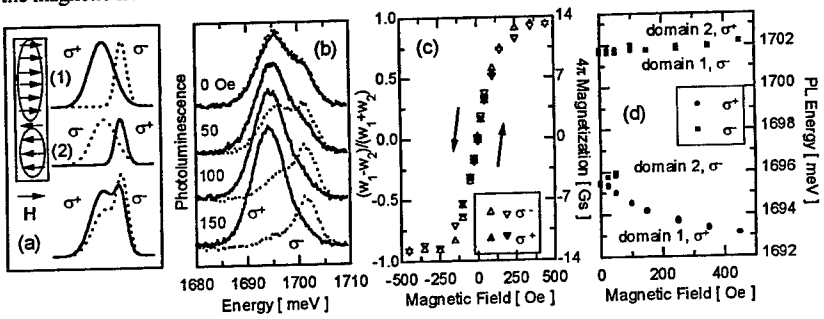

Fig. 3 Schematic (a) and experimental results on domain structure studied by polarization-resolved luminescence spectroscopy of modulation-doped p-$Cd_{0.957}Mn_{0.043}Te$ at 1.53 K. Peak positions are shown in (d), while (c) presents the difference $(w_1 - w_2)/(w_1+w_2)$, where $w_i = I_i(H)/I_i(0)$, are the normalized integrated intensities I of the two contributions to the line at each polarization for the field swept up and down.

We suggest that these unusual domain properties result from the proximity to the spin-density-wave instability in this low-dimensional magnetic system. Indeed, following the procedure developed previously [3] (see also [8]), the characteristic temperature $T_{SDW}(q)$ of the spin wave instability corresponding to the wavevector q is given by $T_{SDW}(q) = \Theta_F(q)$, where F(q) is the static Lindhard function of the carrier magnetic response function. According to our numerical evaluation, F(q) =1 for q =< $2k_F$, even if the complex structure of the relevant hole subband is taken into account. This means that the ground state may involve SDW with various q values. This is supported by our calculation of the magnetic response function, which is virtually q-independent (from q=0 to $2k_F$) even if the complex structure of the relevant hole subband is taken into account.

References

1. See, H. Ohno, Science **281**, 951 (1998), and references therein.
2. A. Haury *et al.*, Phys. Rev. Lett. **79**, 511 (1997).
3. T. Dietl, A. Haury, and Y. Merle d'Aubigné, Phys. Rev. B **55**, R3347 (1997).
4. G. Fishman, Phys. Rev. B **52**, 11 132 (1995).
5. J.A.Gaj, W.Grieshaber, C.Bodin-Deshayes, J.Cibert, G.Feuillet, Y.Merle d'Aubigné, A.Wasiela Phys. Rev. B **50**, 5512 (1994)
6. M.A. Novak, O.G. Symko, D.J. Zheng, and S. Oseroff, J. Appl. Phys. **57**, 3418 (1985)
7. P. Peyla, A. Wasiela, Y. Merle d'Aubigné, D.E. Ashenford, and B. Lunn, Phys. Rev. B **47** (1993) 3783; B. Kuhn-Heinrich, W. Ossau, E. Bangert, A. Waag, and G. Landwehr, Solid . State Commun. **91** (1994) 413.
8. T. Jungwirth et al., Phys. Rev. B **59** (1999) 9818.

Quantum Transport in n-type and p-type Modulation Doped Mercury Telluride Quantum Wells

G. Landwehr, J. Gerschütz, S. Oehling, A. Pfeuffer-Jeschke,
V. Latussek, and C. R. Becker
Physikalisches Institut der Universität Würzburg, Am Hubland,
97074 Würzburg, Germany

Abstract

Asymmetrically modulation doped HgTe quantum wells of (001) orientation were produced by molecular beam epitaxy. N-type doping was achieved with iodine and p-type doping by the incorporation of nitrogen. At 4.2 K the n-type samples have electron mobilities up to $10^5 cm^2/Vs$, the maximum Hall mobility of the p-type specimens is around $2 \times 10^4 cm^2/Vs$. Very pronounced Shubnikov–de Haas oscillations were observed in both n-type and p-type samples. In the n-type specimens the quantum oscillations persisted up to temperatures of 60 K. The Shubnikov–de Haas oscillations in the p-type samples were highly irregular. Because the data can not be explained without detailed theoretical calculations of Landau levels for the heterostructure self consistent Hartree calculations were performed using a 8×8 $\mathbf{k} \cdot \mathbf{p}$ model. The magnetic field dependent density of states was calculated. More regular oscillations are predicted at higher magnetic fields approaching 30 T.

In the past quantum transport experiments on n-type modulation doped HgTe heterostructures in the past have been performed primarily on superlattices and multiple quantum wells (MQW). Shubnikov-de Haas (SdH) oscillations and quantum Hall effect have been observed in those samples [1,2]. Quantum transport effects in modulation doped n-type HgTe single quantum wells (SQW) grown by molecular beam epitaxy were initially reported by Goschenhofer et al. [3]. These samples show very pronounced Shubnikov–de Haas (SdH) oscillations in a temperature range between 1.6 K and 60 K together with well pronounced quantum Hall plateaus at low temperatures. Fig. 1 shows the temperature dependence of the magnetoresistance and the Hall effect for one sample with a mobility of $68.2 \times 10^3 cm^2/Vs$ and a carrier concentration of $5.16 \times 10^{11} cm^{-2}$. The existence of SdH oscillations up to 60 K is the consequence of the small effective mass of about $0.02\ m_0$ [4]. At low temperatures spin splitting is observed for magnetic fields above 2 T. Quantum Hall plateaus at all integer filling factors are observed in this regime. For specimens with a small carrier concentration of about $1.6 \times 10^{11} cm^{-2}$ the plateau with occupation number of 1 at 25.813 kΩ was achieved at a field strength of about 4 T.

In this article we shall concentrate on p-type modulation doped HgTe SQWs. Quantum transport experiments on intrinsic p-type HgTe/HgCdTe superlattices and intrinsic p-type HgTe/HgCdTe SQWs have been reported in the literature before [5,6]. Whereas the superlattices showed Hall mobilities up to $30 \times 10^3 cm^2/Vs$ the mobility of the SQWs was only about $1 \times 10^3 cm^2/Vs$. SdH oscillations and quantum Hall effect were evident in the SQWs, but

the SdH oscillations were not pronounced. A weakly developed Hall plateau at filling factor 2 was observed and a very wide one at filling factor 1 ranging from a magnetic field of 4 T to a magnetic field of 15 T. To our knowledge no quantum transport results on p-type modulation doped HgTe SQWs have been reported in the past.

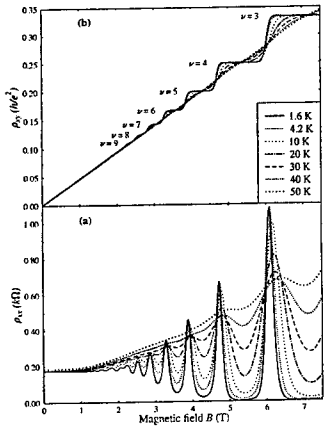

Fig. 1: Temperature dependence of the SdH oscillations (a) and the quantum Hall effect (b) for a n-type HgTe QW.

We have produced asymmetrically modulation doped (001) HgTe QWs with $Hg_{0.3}Cd_{0.7}Te$ barriers by molecular beam epitaxy (MBE) in which a CdTe layer was doped with nitrogen on top of the structure. All samples were grown on $Cd_{0.96}Zn_{0.04}Te(001)$ substrates. A $Hg_{0.3}Cd_{0.7}Te$ barrier with thickness of 26 nm was grown on top of 10 nm thick CdTe buffer.The thicknesses of the subsequently grown HgTe QWs varied from 12 nm to 20 nm. The upper barrier consisted of a 2 nm $Hg_{0.3}Cd_{0.7}Te$ layer. This QW structure was separated from the doped layer by a spacer. The spacer consisted of a 2 nm thick graded gap transition from HgCdTe to CdTe and a 2.5 nm thick CdTe layer. The CdTe layers with a typical thickness of 12 nm were doped with nitrogen at growth temperatures between 220°C and 230°C. All samples are fully strained as was confirmed by high resolution X-ray diffraction.

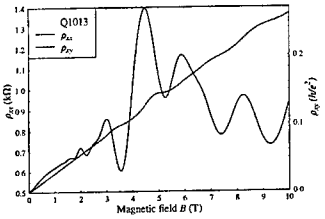

Fig. 2: SdH oscillations and Hall effect of a p-type sample at 1.6 K.

Magnetotransport measurements have been performed up to magnetic fields of 10 T and for temperatures between 1.6 K and 4.2 K. All samples showed a high degree of homogenity as confirmed by measurements in different magnetic field orientations and with redundant contact combinations. The hole densities deduced from the classical Hall effect varied between 4.7×10^{11} and $8.65 \times 10^{11}\mathrm{cm}^{-2}$ at 1.6 K and the mobility varied between 14.3×10^3 and $35.8 \times 10^3 \mathrm{cm}^2/\mathrm{Vs}$. At 1.6 K the samples showed well pronounced SdH oscillations and the quantum Hall effect was evident, even though the plateaus were not well developed. In contrast to the n-type samples mentioned above the oscillations died out very fast with increasing temperature as a consequence of the large mass of the holes. Fig. 2 shows the magnetoresistance and the Hall effect of a typical sample with a well width of 15 nm, a carrier concentration of $8.65 \times 10^{11}\mathrm{cm}^{-2}$ and a Hall mobility of $14.3 \times 10^3 \mathrm{cm}^2/\mathrm{Vs}$ at 1.6 K. Weakly developed Hall plateaus at filling factors of 10, 7, 5 and 4 can be observed and the SdH oscillations are highly irregular. If one takes the Hall plateaus seriously the sequence of minima in the SdH oscillations cannot be associated with a regular sequence of filling factors. Nevertheless the information about the filling factor is useful in determining a hole concentration which can be compared to that of the Hall effect. For a carrier

concentration of $p = 8.65 \times 10^{11}\mathrm{cm}^{-2}$ we expect minimia in the SdH oscillations according to the formula $B = hp/e\nu$ for filling factors of $\nu = 10$, 7, 5 and 4 at magnetic fields of about 3.6 T, 5.1 T, 7.1 T and 8.9 T respectively. These values coincide quite well with the position of the minima in the magnetoresistance.

Irregular patterns in the SdH oscillations are well known from heterostructures with two or more occupied subbands [7]. In order to understand main features of the data we have performed self consistent Hartree calculations of the band structure based on a 8×8 $\mathbf{k} \cdot \mathbf{p}$ model. The model includes all second-order terms representing the remote-band contributions, but neglects the intrinsic inversion asymmetry of the material, which is known to be extremely small. The envelope function approximation is used to calculate the subbands of the heterostructure. We have calculated the band structure of a HgTe QW embedded in $Hg_{0.3}Cd_{0.7}Te$ barriers taking the anisotropy of the inplane band structure (warping) into account. This anisotropy is known to be negligible for the conduction bands but is important for the valence bands, for the band parameters see reference [4].

In the following the results for a 150 Å wide HgTe SQW with a hole density of $8.0 \times 10^{11}\mathrm{cm}^{-2}$ are discussed. HgTe QWs of this thickness are in the so called inverted semiconducting regime, where the conduction band is the first heavy hole subband (H1) and the valence band is the second heavy hole subband (H2). Fig. 3 shows the self consistently calculated band structure. The subband dispersion for $\mathbf{k} = (k_x, k_y)$ in (0,1) and (1,1) directions is shown. Whereas the H1 subband is nearly axialy symmetric, the importance of the axial asymmetry (warping) of the H2 subband is obvious. Due to the asymmetric doping of the heterostructure the Hartree potential itself is asymmetric which results in a lifting of the spin degeneracy for each subband for a given k-vector. The band structure demonstrates that the QW is an indirect semiconductor because the maximum of the valence band is not located at the center of the Brillouin zone but at a finite $\mathbf{k}$.

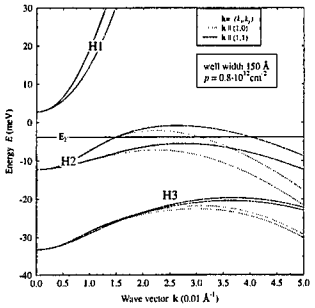

Fig. 3: Self consistently calculated band structure of a HgTe QW with $p = 8.0 \times 10^{11}\mathrm{cm}^{-2}$

Only one spin component of the H2 subband is occupied with holes above the Fermi energy. This band structure shown in Fig. 3 results in two Fermi contours for the holes. This is also shown in Fig. 4 where lines of constant energy for the occupied subband have been plotted.

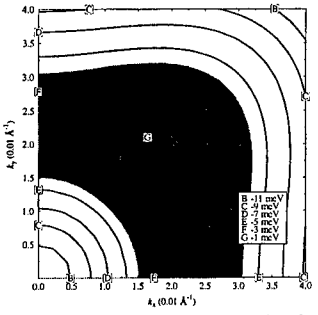

Fig. 4: Contour plot of the first valence band with the occupied states (grey area) of the example discussed in the text.

Only the first quadrant of the Brillouin zone is shown. The grey area is a ring-like region that is occupied by the holes. In contrast to the inner Fermi contour which is nearly a circle the outer one shows clearly the fourfold symmetry of the band structure.

Using the Hartree potential from the self consistent band structure calculation we have calculated the Landau level spectrum from 2 T up to 30 T. The Landau levels corresponding to the band structure discussed above have been plotted in the lower part of Fig. 5. Again we have taken the fourfold symmetry of the QW into account. This results in four sets of Landau levels with the same symmetry. Landau levels with different symmetry may cross in contrast to Landau levels with the same symmetry.

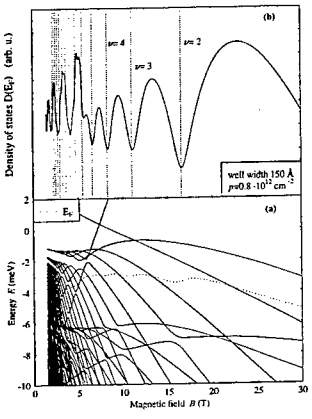

Fig. 5: Landau levels (a) and density of states (b) of a HgTe QW with $p = 8.0 \times 10^{11}\,\mathrm{cm}^{-2}$.

This anticrossing behaviour is well known from p-type systems where the axial asymmetry of the band structure is important [7]. But due to the complex band structure of the H2 subband this anticrossing behaviour is more pronounced here. It is noteworthy that to our knowledge this is the first Hartree calculation for p-type HgTe QWs and the first calculation of Landau levels in which warping has been taken into account in this system. The Landau level structure is very complicated for small magnetic fields where there is a quasicontinuum. For fields above 7 T we obtain a more regular structure. This can also be seen in the upper part of Fig. 5 where we have plotted the density of states (DOS) at the Fermi energy. Assuming a Gaussian broadening of the Landau levels the DOS has been calculated according to

$$D(E) = \frac{1}{2\pi l_c^2} \sum_n \frac{1}{\sqrt{\pi\Gamma^2}} \exp\left(-\frac{(E-E_n)^2}{\Gamma^2}\right),$$

where $l_c = \sqrt{\hbar/eB}$ is the magnetic length and the sum is over all Landau levels. For the broadening parameter we assumed $\Gamma = \Gamma_0\sqrt{B/\mathrm{Tesla}}$ with $\Gamma_0 = 0.2$ meV. The oscillations in the DOS below 6 T are highly irregular and the minima in the DOS cannot be associated with integer filling factors (vertical dotted lines in Fig. 5). Above 6 T the oscillations become more regular and the minima can be found at integer filling factors.

In conclusion our calculations have shown that only one subband is occupied in our samples. Due to the fact that the holes are located at finite $\mathbf{k}$, irregular oscillations in the DOS arise at lower magnetic fields. More regular SdH oscillations are predicted for higher magnetic fields up to 30 T.

Support of the Deutsche Forschunggemeinschaft (SFB 410) is gratefully acknowledged.

References:

1. C. A. Hoffman, J. R. Meyer, F. J. Bartoli, Y. Lansari, J. W. Cook, Jr. , and J. F. Schetzina, Phys. Rev. B 44, 8376 (1991)
2. C. A. Hoffman, J. R. Meyer, and F. J. Bartoli, Semicond. Sci. Technol. 8, S48 (1993)
3. F. Goschenhofer, J. Gerschütz, A. Pfeuffer-Jeschke, R. Hellmig, C. R. Becker, and G. Landwehr, J. Elec. Mat. 27, 532 (1998)
4. A. Pfeuffer-Jeschke, F. Goschenhofer, S. J. Cheng, V. Latussek, J. Gerschütz, C. R. Becker, R. R. Gerhardts, and G. Landwehr, Physica B 256-258, 486 (1998)
5. K. C. Woo, S. Rafol, and J. P. Faurie, Phys. Rev. B 34, 5996 (1986)
6. K. C. Woo, S. Rafol, and J. P. Faurie, Surf. Sci. 196, 665 (1988)
7. V. Latussek, E. Bangert, and G. Landwehr, Annalen der Physik 48, 394 (1991)

Spin-valve Effects in a Two-Dimensional Electron Gas System

S. Gardelis, C.G. Smith, W.Y. Lee, C.H.W. Barnes, E.H. Linfield, D. A. Ritchie, J.A.C. Bland

Cavendish Laboratory, Madingley Road, Cambridge CB3 0HE, United Kingdom

Abstract

We present results on spin-polarized electron transport from a ferromagnet to a two-dimensional electron gas system (2DEG). The investigated device consists of an injector and a collector contact made from ferromagnetic permalloy thin films with different coercive fields. That allows parallel or antiparallel magnetization of the contacts in different applied magnetic fields. The conducting medium is a 2DEG formed in an AlSb/InAs quantum well. Data from this device suggest that its resistance is controlled by two different types of spin-valve effect: the first is due to the ferromagnet-semiconductor contact resistance, determined by the zero-field spin-splitting in InAs, and the second is due to the propagation of electrons with a spin imbalance through the 2DEG without spin-scattering.

An electron carries not only a charge but also a spin. The two components of its nature open new prospects for the implementation of a new class of devices in which electron spins store and transport information, referred to as 'spintronic' devices, such as spin transistors and spin-based memories.

In this article, we present results from a spintronic semiconductor device based on the *theoretical* ideas of Datta and Das [1]. In their proposed device, resistance modulation is achieved through the spin-valve effect by varying the degree of spin precession which occurs in a two dimensional electron gas (2DEG) between identical ferromagnetic contacts. In our device, resistance modulation is also achieved through the spin-valve effect but by having ferromagnetic contacts with different coercivities and varying an applied magnetic field. We show that the low field magnetoresistance of the device results from two types of spin-valve effect: the first is due to a ferromagnet-semiconductor contact resistance; and the second due to the direct propagation of the electrons without spin-scattering through the 2DEG between the magnetic contacts [2].

Our sample contained a two dimensional electron gas (2DEG) formed in a 15nm wide InAs well. The well was sandwiched between two AlSb barriers, the top one being 15nm thick. A 5nm thick cap layer of GaSb was used to prevent oxidation of AlSb. Two parallel ferromagnetic permalloy ($Ni_{80}Fe_{20}$) contacts, one 5μm wide and the other 1μm wide, were defined using electron beam lithography. The contacts were 1μm apart and stretched across a 25μm wide Hall bar which was produced by optical lithography techniques (see inset of figure 1b). To ensure a good ohmic contact to the InAs layer the top GaSb and AlSb layers were etched away selectively in the area of the contacts using Microposit MF319 developer [3]. Any oxide on the InAs surface, which can act as spin scatterer, was removed by dipping the sample in $(NH_4)_2S$. This is known to passivate the InAs surface with sulfur and decelerate the oxidation process. Moreover, it has been shown to improve the tunneling properties in Scanning Tunneling Microscopy (STM) studies of InAs [4]. It is also expected to remove any Sb residue which is known to be present after etching of AlSb with the MF319 developer [3].

Within 5 minutes of passivation the sample was inserted in an evaporator. A film of 50nm of permalloy was evaporated followed by 20nm of Au in order to protect permalloy

from oxidation. A network of extended NiCr/Au contacts (shown as 1-8 in figure 1b, inset), patterned by optical lithography, was used in order to connect the contacts A and B with the external circuitry. An identical Hall bar without magnetic contacts was prepared on the same wafer for basic non-magnetic characterization. A reduction in mobility of the device 2DEG from μ=4.9 to 0.09m^{2}s^{-1}V^{-1} (at 0.3K) was observed after removal of the AlSb barrier in the regions of contacts A and B and subsequent dipping of the device in $(NH_4)_2S$. A reduction in mobility (from 3.6 to 0.5m^{2}s^{-1}V^{-1} at 0.3K) was observed in a reference sample, having no magnetic contacts, after removal of the AlSb barrier above the InAs well over the whole surface of the Hall bar. We believe that the reduction in mobility in the device is partly due to lateral etching of the AlSb barrier layer located between the magnetic contacts after dipping in $(NH_4)_2S$. It is known that $(NH_4)_2S$ attacks GaSb and AlSb chemically [5]. It is also possible that inhomogeneous band bending at the sulfur-passivated surface produces greater charge scattering than an oxide surface.

The spin transport properties of the 2DEG are important to the operation of the device. There are two parts to this: a 2DEG in an InAs quantum well is diamagnetic [6]; and has strong spin precession [7,8]. This spin precession results from the Rashba [7] term in the spin-orbit interaction. In transport, the combination of multiple elastic scattering from non-magnetic impurities and spin-precession results in a randomisation of spin orientation and can give rise to weak antilocalization [8]. This effect was observed in our characterization Hall bar enabling us to estimate the spin dephasing length, ℓ_{sd}, and the related zero-field spin-splitting energy, ΔE, of the device 2DEG. These measurements were made in a magnetic field applied perpendicular to the 2DEG. By fitting the weak antilocalization peak as in ref. [8] we estimated a spin dephasing length, ℓ_{sd}. This was calculated to be 1.8 μm. ΔE was estimated to be 0.4 meV.

The coercive fields of the magnetic contacts A and B were determined by four-terminal magnetoresistance measurements and micron-scale magneto-optic Kerr effect (MOKE) measurements [9]. The magnetic field was applied along the wires which is an easy axis for magnetization. The coercive fields are estimated to be Hc_A=35 Oe for contact A and Hc_B=85 Oe for contact B. These measurements are shown in figures 1a and 1b.

Magnetoresistance measurements were carried out in magnetic fields applied parallel to the plane of the 2DEG and along the easy axis of the contacts A and B at temperatures ranging from 0.3K to 10K. A constant ac current of 1μA was applied between positions 1 and 4 (see inset in figure 1b) of the magnetic contacts and the voltage drop between positions 5 and 8 was recorded. Figure 1c shows these measurements, plotted as the change in the magnetoresistance, ΔR:

$$\Delta R = R(H) - R(H = 0), \tag{1}$$

from its zero field value $R(H = 0) = 588\Omega$. H is the applied magnetic field. At 0.3 K figure 1c shows both an up sweep (solid line) and a down sweep (dashed line). The principal features in these sweeps are a peak in magnetoresistance between the two coercive fields H_{C_A} and H_{C_B} and a dip on either side of this peak. The dip on the low-field side is deeper than the one on the high-field side. This structure is repeated symmetrically on opposite sides of zero field for the up and down sweeps.

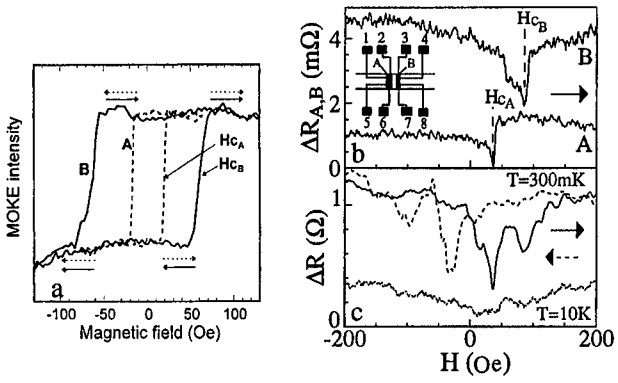

FIG. 1. (a) MOKE hysterisis loops of contacts A and B. (b) Magnetoresistance change ΔR_A and ΔR_B of contacts A and B, respectively. Inset: schematic of the device. (c) Magnetoresistance change, ΔR, measured between contacts A and B at 300mK and 10K.

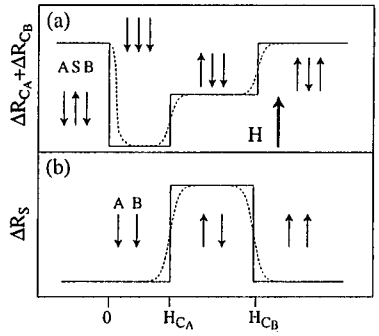

FIG. 2. (a) Schematic of the interface spin-valve effect: ΔRc_A+ΔRc_B. Arrows indicate magnetization direction in A and B and 2DEG S. H is the external field which is being swept up from negative value. (b) Schematic of direct spin-valve effect: ΔR_s. Dashed lines in (a), (b) indicate averaging over the local switching of different magnetic domains in A and B.

We can model the magnetoresistance change measured in our sample, ΔR, as:

$$\Delta R = \Delta R_A + \Delta R_B + \Delta Rc_A + \Delta Rc_B + \Delta R_s \qquad (2)$$

where ΔR_A and ΔR_B are the magnetoresistance changes of the magnetic contacts A and B respectively, ΔRc_A and ΔRc_B are those of the interface between the semiconductor and the magnetic contacts A and B respectively, and ΔR_s results from electrons propagating from the first ferromagnetic contact to the second without spin scattering.

ΔR_A and ΔR_B ($\simeq 2\text{m}\Omega$) are much smaller compared to ΔR ($\simeq 1\Omega$) as can be seen in figures 1b and 1c. Therefore these contributions can be ignored in our model. Taking into account the zero-spin splitting in InAs and the fact that it is diamagnetic, we can model the contribution from the interface contacts, $\Delta Rc_A + \Delta Rc_B$, as in figure 2a. In this model this contribution is maximum when the magnetization in both magnetic contacts is antiparallel to the spin orientation in the InAs 2DEG and minimum when the magnetization in the two ferromagnetic contacts is parallel to the spin orientation in InAs. On the other hand ΔR_s, as shown in figure 2b, is minimum when both ferromagnetic contacts are magnetized parallel to each other and maximum between the two coercive fields where the magnetization of the two contacts is antiparallel to each other. The peak observed in figure 1c, corresponds well with the switching fields deduced from the magnetoresistance measurements of contacts A and B.

The small amplitude of the device resistance modulation ΔR/R(H=0)$\approx$0.2% shown in figure 1b is consistent with the above picture. Electrons contributing to the direct spin-valve effect shown in figure 2b have to take fairly direct paths between contacts A and B. Those which take paths involving multiple scattering pick up random angles of spin orientation and therefore on average will cancel with each other and not contribute to the effect. The temperature dependence of the magnetoresistance is also consistent with our picture. The peak between the two coercive fields decreases in amplitude with increasing temperature and almost disappears at 10K (see figure 1c). At this temperature k_BT (= 0.8meV) is greater than the zero-field spin splitting and therefore thermal activation has sufficient energy to destroy both spin-valve effects shown in figure 2.

In conclusion, we have provided evidence that we observed experimentally two kinds of spin-valve effect in our spintronic device. The first effect results from the ferromagnet-2DEG interface resistance and the second effect results from spins propagating from one ferromagnetic contact to the other. The combination of these effects produces a resistance maximum between the coercive fields of the two contacts and dips in resistance on either side. Both effects are suppressed with increasing temperature as the thermal smearing becomes comparable to the zero field spin splitting.

We thank M. Pepper and C. J. B Ford for invaluable discussions. This work was funded under EPSRC grant GR/K89344, and the Paul Instrument Fund. CHWB,EHL and DAR acknowledge support from the EPSRC the Isaac Newton Trust, and Toshiba Cambridge Research Centre.

References

1. Datta and B. Das, Appl. Phys. Lett. **56**, 665 (1990).
2. S. Gardelis et al, cond-mat/9902057; also to be published in Phys. Rev. B
3. C. Gatzke et al, Semic. Sci. Techn. **13**, 399 (1998).
4. L. Canali et al, Proceedings of the 9th International conference on scanning tunneling microscopy/spectroscopy and related topics (STM'97). Submitted to Appl. Phys. A - Material Science and Processing.
5. I.A. Andreev et al, Sov. Phys. Semicond. **31**, 556 (1997).
6. T. Sahu, Phys. Rev. B **43**, 2415 (1991).
7. E.I. Rashba, Sov. Phys. Solid State **2**, 1109 (1960).
8. G.L. Chen et al, Phys. Rev. B **47**, 4084 (1993).
9. A.O. Adeveve et al, J. App. Phys. **79**, 6120 (1996).

Spin coherent transport in a ferromagnetically contacted carbon nanotube

B.W. Alphenaar*, K. Tsukagoshi* and H. Ago†
* Hitachi Cambridge Laboratory, Madingley Road, Cambridge CB3 0HE, UK
† Cavendish Laboratory, Madingley Road, Cambridge CB3 0HE, UK

Abstract

We use ferromagnetic contacts to inject and detect spin polarized electrons in multi-walled carbon nanotubes. The small diameter of the nanotube allows us to probe individual magnetic domains. As the alignment of the magnetizations within a pair of contacts switches from parallel to antiparallel, the nanotube resistance switches from a low to a high resistance state. This result is a first step towards the possibilty of carbon nanotube based spin electronics.

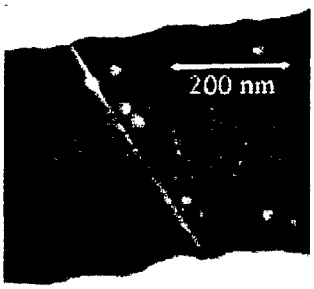

FIG. 1: Electron micrograph of a typical Co contacted MWNT.

Spin polarized electrons can be injected from a ferromagnet into non-ferromagnetic materials[1–3], and also through oxide tunnel barriers[2, 4, 5]. Here, we investigate spin injection into carbon nanotubes, and observe direct evidence for spin coherent transport. We measure a hysteretic magnetoresistance in a number of ferromagnetically contacted multi-walled carbon nanotubes, with a maximum resistance change of 9 %. From this we estimate the nanotube spin-flip scattering length to be at least 130 nm.

Figure 1 is an electron micrograph of one of our ferromagnetically contacted nanotube devices. We use crude multi-wall carbon nanotubes (MWNTs) synthesised from graphite rods by the arc discharge evaporation method[6]. The nanotubes are dispersed onto a SiO_2/Si substrate, and subsequently located with respect to Pt/Au alignment marks using a scanning electron microscope. Ferromagnetic cobalt (Co) contacts are thermally evaporated at a pressure of $4x10^{-7}$ Torr. Magnetoresistance measurements are performed at 4.2 K with B directed in the plane of the substrate. Figure 2 shows the two-terminal differential resistance of a Co contacted nanotube as a function of magnetic field. The field is swept

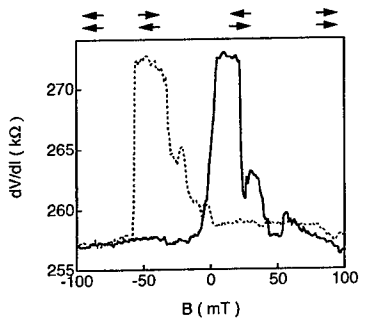

FIG. 2: Magnetoresistance of a cobalt contacted MWNT. The solid (dashed) line corresponds to the up (down) sweep direction.

first from -100 mT to 100 mT (solid line) and then back to -100 mT (dashed line). A resistance peak appears as the magnetic field moves through 0 T. The width of the resistance peak is approximately 50 mT, which is commensurate with the coercive field strength for a thin Co film[7]. There is also a large hysteresis in the peak position ($\approx \pm 50$ mT) between positive and negative sweep directions, indicating the probable influence of the contact magnetization.

Similar hysteretic magnetoresistance has been observed in magnetic tunnel junctions, and has been attributed to spin-polarized electron tunneling[4, 5, 8]. The conduction electrons within a ferromagnet such as Co have a preferred spin direction, which is determined by the local magnetization. In the absence of spin-scattering, the tunnel resistance between two ferromagnetic contacts depends on their relative spin orientation. In the anti-parallel state the majority spin states are out of alignment and the junction resistance is higher than in the parallel state in which the majority spin states are aligned.

The observed peak in the nanotube resistance in Fig. 2 suggests that the contact magnetizations, which are aligned parallel with the magnetic field at $B = \pm 100$ mT, become misaligned as the field is swept through $B = 0$ T. The misalignment may be caused by magnetization fluctuations that occur locally, on the scale of the nanotube diameter (30 nm). The average Co domain size (50 nm)[7] is on the order of the width of the nanotube so that the nanotube contacts only a small number of magnetic domains. The coercivity of each domain varies, and depends on its geometry and the local energy conditions.

Any change in the nanotube magnetoresistance due to spin-injection requires that a sufficiently small amount of spin scattering occurs both within the nanotube, and at the interfaces between the nanotube and the contacts. The difference between the tunnel resistance in the parallel (R_p) and antiparallel (R_a) states[4] is given by:

$$\Delta R/R_a = (R_a - R_p)/R_a = 2P_1P_2/(1 + P_1P_2).$$

Here, P_1 and P_2 are the percentage of conduction electrons polarized in the majority spin band in the ferromagnetic contacts 1 and 2. For Co, the polariza-

tion has been determined to be 34 %[9] giving a maximum resistance change of 21 %. In Fig. 2, $\Delta R/R_a$ is 9 % (Fig. 2(b)) so that approximately 14 % of the spin-polarized electrons travel the 250 nm through the nanotube without spin-flipping. The spin-scattering length, l_s, can then be estimated by assuming that the spin polarization drops off as $\exp(-l/l_s)$ within the nanotube. This gives l_s = 130 nm. Although fairly long, this is probably an underestimation, because we do not take into account spin-scattering at the ferromagnet/nanotube interfaces.

Figure 3 shows the high field magnetoresistance of a second Co contacted nanotube device, measured between ± 1 T. A hysteretic magnetoresistance peak is again observed around zero field (see inset for detail). The resistance drops substantially as the magnetic field increase to higher values. A similar decrease in the high field resistance has been observed in non-magnetically contacted nanotube devices, and attributed to the quenching of weak localization among current pathways through the nanotube[10]. What is unusual in our device, however, is that the magnetoresistance is assymetric in B ($R(B) \neq R(-B)$). This is in conflict with the reciprocity theorem for a two-terminal resistance measurement[11]. It is possible that the local domain configuration is different in the two field directions, thus altering the contact resistances. Further work is necessary to understand this effect.

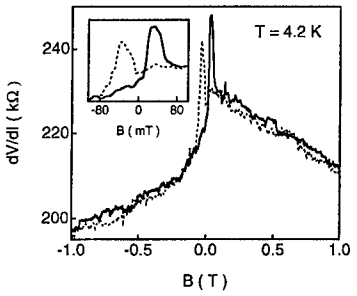

FIG. 3: High field magnetoresistance of a second cobalt contacted MWNT. The solid (dashed) line corresponds to the up (down) sweep direction. The inset details the region near zero field.

In Fig. 4 we show the magnetoresistance of a MWNT fabricated using a shadow evaporation technique, which allows the two contacts to be made from different magnetic materials. NiFe is evaporated from one side of the substrate, followed by Co evaporation from the other side. A gold capping layer is then evaporated from directly above the substrate to protect the magnetic surface. Figure 4 shows the magnetoresistance of a NiFe/MWNT/Co device. Hysteretic magnetoresistance is again observed; however, the absolute resistance and the resistance change are smaller than in the Co contacted samples. The exact reason for this difference is unknown—perhaps the shadow evaporation technique improves the continuity of the magnetic film and reduces the contact resistance in comparison with the single layer Co devices.

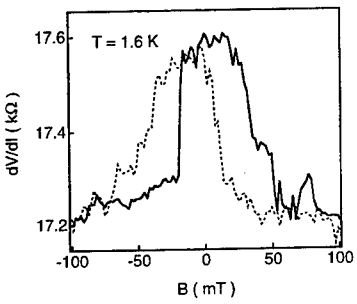

FIG. 4: Magnetoresistance of a MWNT contacted with two different ferromagnetic materials: Co and NiFe. The solid (dashed) line corresponds to the up (down) sweep direction.

Our results are consistent with recent experiments that show that the electron path lengths within MWNTs are extremely long. The phase coherence length is found to be 250 nm and the elastic scattering length 60 nm[10]. Further work indicates that MWNTs behave as ballistic conductors, even at room temperature [12]. We expect the spin-flip scattering in the nanotubes should also be highly suppressed. Consider for example that the spin scattering length in a metal[3] or a semiconductor[13] is typically much longer than the phase coherence length or the elastic scattering length. Carbon nanotubes have already been considered as potentially useful electronic devices because of their low-dimensionality and relatively high conductivity[14, 15]. Our observations of clear spin-dependent phenomena show that the nanotube is also a strong candidate to form the basis of new spin-electronic devices.

[1] P.M. Tedrow and R. Meservey, Phys. Rev. Lett. **26**, 192 (1971).
[2] A.G. Aronov, Pis'ma Zh. Eksp. Teor. Fiz. **24**, 37 (1976) [JETP Lett. **24**, 32 (1976)].
[3] M. Johnson and R.H. Silsbee, Phys. Rev. Lett. **55**, 1790 (1985).
[4] M. Julliere, Phys. Lett. **54A**, 225 (1975).
[5] J.S. Moodera *et al.*, Phys. Rev. Lett. **74**, 3273 (1995).
[6] T.W. Ebbesen and P.M. Ajayan, Nature **358**, 220 (1992).
[7] U. Rüdiger *et al.*, Phys. Rev. B **59**, 11914 (1999).
[8] G.A. Prinz, Science **282**, 1660 (1998).
[9] R. Meservey and P.M. Tedrow, Physics Reports **238**, 173 (1994).
[10] C. Schönenberger *et al.*, preprint cond mat/9905144.
[11] M. Büttiker IBM J. Res. Dev. **32**, 317 (1988).
[12] S. Frank *et al.*, Science **280**, 1744 (1998).
[13] J.M. Kikkawa and D.D. Awschalom, Phys. Rev. Lett. **80**, 4313 (1998).
[14] J.T. Tans, A.R.M. Verschueren, and C. Dekker, Nature **393**, 49 (1998).
[15] R. Martel *et al.*, Appl. Phys. Lett. **73**, 2447 (1998).

Quantum phases of electron double layers: soft collective modes and finite-temperature phase transitions

Vittorio Pellegrini
Scuola Normale Superiore and INFM, Pisa, Italy
Aron Pinczuk
Depts. of Physics and of Applied Physics, Columbia University, New York (NY); and Bell Laboratories, Lucent Technologies, Murray Hill (NJ)
Brian S. Dennis, Loren N. Pfeiffer, and Ken W. West
Bell Laboratories, Lucent Technologies, Murray Hill (NJ)

Abstract

The extreme softening of spin-excitations in electron double-layers is studied by resonant inelastic light scattering. At even integer quantum Hall states we find evidence of three distinct configurations of spin. Transformations among these spin states appear as quantum phase transitions tuned by interlayer interactions and Zeeman energies. A broken-symmetry phase emerges when a long wavelength spin-excitation across the tunneling gap goes soft. Spectra measured in this phase offer remarkable evidence of a finite-temperature phase transitions. Critical temperatures determined from spectra display significant dependence on magnetic field.

The two-dimensional electron gas (2DEG) in quantum Hall states exhibits a diverse group of quantum phase transformations that are driven by fundamental interactions(for recent reviews see Refs.[1,2]. Strong electron interactions are here easily tuned by density, sample design, etc.. The additional degree of freedom associated with layer or subband index in a double or wide quantum well structure creates new venues for quantum phase transitions. Evidence of such trasformations were found as magnetotransport anomalies in electron double-layers in the quantum Hall state with Landau level filling factor $\nu = 1$ [3]. These anomalies have been interpreted theoretically in terms of magnetoroton modes that soften to vanishing energies and trigger the phase transitions[4,5]. Soft roton excitations also play key roles in theoretical constructions that predict instabilities and quantum phase transitions in the 2DEG.

Recently, we discovered soft spin-excitations in electron double-layers at even integer quantum Hall states [6]. These modes are observed by inelastic light scattering(ILS) experiments, and are associated with intersubband transitions across the symmetric-antisymmetric tunneling gap Δ_{SAS} of coupled GaAs double quantum wells(DQW). The softening occurs at the small wavevectors ($q \sim 0$) accessible by ILS experiments. It results from excitonic bindings, also known as vertex-corrections, in the neutral particle-hole pairs of the excitations. The strengths of such vertex-corrections, which depend on the difference n_S-n_{AS} in the occupations of symmetric and antisymmetric states, are tuned by the perpendicular magnetic field and reach a maximum at $\nu = 2$ when all the electrons occupy the lowest spin-split symmetric states. Light scattering intensities by the soft spin-excitations display anomalous temperature dependence as they soften to the Zeeman energy. This anomalous behavior has been interpreted as evidence of a finite temperature transition. In this paper we review our previous work [6,7] and describe the results on the magnetic field dependence of the finite temperature phase transition.

Figure 1 displays typical measurements of the magnetic field dependence of spin-density excitations energy (ω_{SDE}) across the tunneling gap at T=0.2K (solid circles) in a GaAs/$Al_{0.1}Ga_{0.9}As$ DQW with 18 nm-thick quantum wells and 7.9nm thick barrier. This sample

(with Δ_{SAS}} = 0.7 meV, electron density n=9.4x10^{10} cm^{-2}, and mobility $\mu \sim 10^6$ cm^2/Vs) was mounted in a $^3He/^4He$ dilution refrigerator with optical windows. Resonant ILS was performed using a laser diode tuned near the fundamental optical transition of the GaAs DQW (~ 812 nm). Incident power densities were kept below 10^{-4} W/cm^2 in order to avoid electron heating.

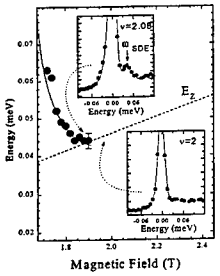

Fig.1 Energy evolution of the q=0 δS_z=0 spin-density excitation (SDE) as a function of magnetic field at tilt angle θ=0 and T=0.2K. Solid line is a guide for the eyes. Dashed line corresponds to the measured Zeeman energy. The insets show the resonant inelastic light scattering spectra with orthogonal linearly polarized incident and scattered photons at T=02.K and two values of the filling factors. The peak corresponds to the SDE at energy close to the Zeeman splitting.

The results in Fig. 1 demonstrate that ω_{SDE} reaches its lowest value at $\nu \sim 2.08$. For lower values of ν the spin-density excitation (SDE) peak disappears from the ILS spectra. Within the experimental errors the minimum of ω_{SDE} occurs when it is close to the Zeeman splitting E_Z shown by the dotted line in Fig. 1. This striking behavior seen in ILS spectra is displayed in the two insets to Fig.1, at $\nu = 2.08$ and $\nu = 2$. The SDE excitation dissappears from the spectra when it reaches the Zeeman energy. This occurs at the *critical* value of $\nu = 2.08$.
To interpret these results, we recall that intersubband spin-excitations in the conduction band of a GaAs semiconductor are triplets classified by changes in total angular momentum $\delta S_z = 0$ (SDE) and +-1 (spin-flip excitations). While at zero magnetic field (B= 0) the excitations are degenerate, at B>0 the excitations are expected to have energies $\omega = \omega_{SDE} - E_Z \delta S_z$ [6]. Within this conceptual framework for spin-excitations at $\nu = 2$, the collapse of ω_{SDE} to the Zeeman energy implies the emergence of spin-flip excitations with $\delta S_z = 1$ at vanishingly small energy ω_{SDE}-E_Z.
The evolution of spin-configurations of the bilayers was studied in ILS measurements as a function of a tilted total magnetic field B_T [7]. The results revealed three distict phases of spin at the even-integer filling factors ν =2,6 as a function of the total magnetic field B_T and Δ_{SAS}. To that effect the tilt angle between B_T and the bilayers was changed while the perpendicular component of the magnetic field was kept at the chosen value of ν thus allowing to tune the value of the Zeeman splitting.
Figure 2 shows the diagram obtained from data measured in four DQW samples that differ in density and Δ_{SAS}. The diagram indicates that at large magnetic field and relatively small Δ_{SAS} the bilayers are in the spin-polarized phase P. In the ILS measurements, such a phase is

characterized by spin-wave excitation across the Zeeman gap set to the Zeeman energy by Larmour's theorem. The energy of this excitation thus shows a (quasi) linear dependence versus total magnetic field [7]. At smaller magnetic fields such that $\Delta_{SAS} >> E_Z$ the bilayers are in the spin-unpolarized phase U where well-defined SDE with the characteristic magnetic field dependece shown in Fig.1 are observed. A new phase (called phase D) occurs at intermediate Δ_{SAS} and E_Z, when the q ~ 0 tunneling spin excitation goes soft and disappears from the spectra. The pronounced sensitivity of phase D on B_T and Δ_{SAS} , however, implies that it has to be regarded as a distict phase of spin. We note that the phase diagram in Fig. 2 is consistent with the predictions of Ref. [8]. The fact that the soft-mode has $\delta S_z = +1$ suggests an order-parameter associated with the operator $\delta S^+ = \delta(S_x - i S_y)$\$. Such broken-symmetry creates a canted

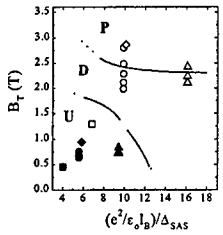

antiferromagnet, as proposed in Refs.[8,9].

Fig.2. *Phase diagram for electron bilayers at even-integer values of filling factors and T=0.2K. Solid lines indicate the positions of phase boundaries determined from experiment. Dotted lines are introduced to give continuity to the boundaries. The total magnetic field B_T is plotted here against the reciprocal tunneling gap in units of the Coulomb interaction energy ($e^2\backslash\varepsilon_o l_B$). The samples are GaAs quantum wells of different densities. Squares: $n=6.2x10^{10}$ cm^{-2}; circles: $n=9.9x10^{10}$ cm^{-2}; triangles: $n=1.05x10^{11}$ cm^{-2} and diamonds: $n=1.44x10^{11}$ cm^{-2}. Open symbols are for $\nu = 2$ and full symbols for $\nu = 6$.*

The absence of SDE and/or spin-flip excitations in ILS spectra obtained when the bilayers are in phase D is a remarkable result. We have proposed that the broken-symmetry phase is disordered at the finite temperatures of the ILS experiments [6,7]. Recent evaluations in the framework of an effective spin theory predict that in the presence of finite disorder the broken-symmetry state is a novel Bose-glass phase [10]. This disordered phase is characterized by domains of canted antiferromagnetic order, but no average antiferromagnetic order. Given that only short range correlations exist in the Bose-glass, the long wavelength Goldstone mode associated with the broken-symmetry disappears. This scenario is consistent with the absence of spin-excitations in the ILS spectra from phase D.

The connection between phase D and the broken-symmetry state with canted antiferromagnet order suggests novel intriguing effects as a function of temperature. The ordering of the canted phase, in fact, breakes the U(1) spin-rotational symmetry. In the disorder-free limit it is expected that the symmetry will be restored at $T=T_{KT}$ by a finite-temperature phase transition of the Kosterlitz-Thouless (KT) type. For sufficiently low magnetic fields, it has been predicted that T_{KT} scales linearly with magnetic field following the relation $T_{KT}=\kappa B_T$ where κ is an universal constant[11]. Corrections at larger magnetic fields yield a departure from the linear behavior that

also depends on the strength of the tunneling gap [11,8]. The increased stability of the broken-symmetry phase at larger magnetic fields can be explained in terms of a larger spin-stiffness i.e. energy cost of rotation of the order parameter by a slowly varying angle.
Evidence of the finite-temperature phase transition corresponding to a reversal D->U transformation is displayed in Fig.3 for a tilt angle $\theta = 30^{\circ}$ ($B_T = 2.28$ at $\nu = 2$). The measured critical temperatures (solid circles) correspond to the lowest values of the temperature at which the SDE modes reappear in the spectra. The inset of Fig.3 shows the dependence of the critical temperature on B_T at three different filling factors.

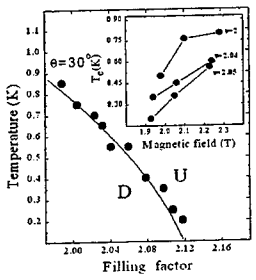

Fig.3 Dependence of the critical temperature T_c on filling factors at tilt angle $\theta = 30^{\circ}$ (T_c is the lowest value of the temperature at which the spin-density excitation modes reappear in the spectra of phase D). The inset shows the values of T_c at three different total magnetic fields and for different filling factors.

The behavior shown in the inset of Fig.3 and the measured values of the critical temperatures are both consistent with the prediction of Refs. [8,11] thus suggesting the intriguing correlation between the finite-temperature phase transition here observed and the KT phase transitions predicted theoretically. Future ILS experiments at different tilt angles and lower temperatures should lead to the definitive identification of the mechanism responsible for the D->U transition and should provide a valid test for current theories.

[1] S.M. Girvin, and A.H. MacDonald, in Perspectives in Quantum-Hall effects, S. Das Sarma, and A. Pinczuk Eds. (Wiley, New York, 1996).
[2] S.L. Shondi, S.M. Girvin, J.P. Carini, and D. Shahar, Rev. of Mod. Phys. **69**, 315 (1997).
[3] G.S. Boebinger, et al., Phys. Rev. Lett. **64**, 1793 (1990); S.Q. Murphy, et al., Phys. Rev. Lett. **72**, 728 (1994).
[4] L. Brey, Phys. Rev. Lett. **65**, 903 (1990).
[5] A.H. Macdonald, P.M. Platzman, and G.S. Boebinger, ibid. p.775
[6] V. Pellegrini, et al., Phys. Rev. Lett. **78**, 310 (1997).
[7] V. Pellegrini, et al., Science **281**, 799 (1998).
[8] S. Das Sarma, S. Sachdev, and L. Zheng, Phys. Rev. Lett. **79**, 917 (1997).
[9] L. Zheng, R.J. Radtke, and S. Das Sarma, Phys. Rev. Lett. **78**, 2453 (1997).
[10] E. Demler and S. Das Sarma, Phys. Rev. Lett. **82**, 3895 (1999).
[11] M. Troyer, and S. Sachdev, Phys. Rev. Lett. **81**, 5418 (1998).

The spin structure of two vertically coupled quantum dots

B. Partoens and F. M. Peeters

Departement Natuurkunde, Universiteit Antwerpen (UIA), B-2610 Antwerpen

Abstract

The electronic states of a pair of vertically coupled quantum dots are calculated using spin density functional theory, where the tunneling between the dots is included. For small and large interdot distances Hund's rule determines the groundstate, while for intermediate distances new phases are predicted. The number of intermediate phases increases with the total number of electrons in the coupled dots. These phases are expected to be observable in the addition energies.

Key words: quantum dots, artificial molecules, spin density functional theory

Quantum dots, or *artificial atoms*, have been a subject of intense theoretical and experimental research over the last few years [1]. A more recent development is the study of vertically coupled dots [2] or *artificial molecules*. These atoms and molecules are ideal systems for the investigation of the fundamental properties caused by the electron-electron interactions. Tarucha *et al.* [3] reported the fabrication of single quantum dots and found that they show atomic like properties. At zero magnetic field Hund's rule determines the filling of the electron levels. More recently, they fabricated vertically coupled dots with different interdot distances and performed single-electron tunneling experiments on these artificial molecules [4]. For these coupled quantum dots: 1) the interdot distance can be varied which controls the interdot interaction, and 2) the electrons can tunnel between both dots. As we will show, the combination of these two features is responsible for the appearance of new phases. Such a double dot system was recently studied by Rontani *et al.* [5] who calculated the groundstate energies for different interdot distances through a general Hubbard approach and an exact diagonalization scheme. Asano [6] studied the correlation effects in a double dot molecule. However in the latter paper one restricted themselves to the situation where the confinement energy is much larger than the typical Coulomb interaction energy. This condition is not fulfilled in typical GaAs quantum dots. As such exact diagonalisation techniques are limited to small particle numbers, mean-field

methods are needed to simplify the complicated many-body problem. In the present paper we apply the spin density functional formalism which was succesfully applied before to describe single quantum dots [7] and which does not have the above restrictions.

We solve the following Kohn-Sham equations numerically

$$\left[\frac{-\hbar^2}{2m}\left(\nabla_{\vec{r}}^2+\nabla_z^2\right)+\frac{m\omega_0^2 r^2}{2}+V(z)+V_{eff}^{\sigma}(\vec{r})\right]\psi_i^{\sigma}(\vec{r})\,Z_i^{\sigma}(z) = \epsilon_i^{\sigma}\psi_i^{\sigma}(\vec{r})\,Z_i^{\sigma}(z), \qquad (1)$$

where the electrons in both dots are confined by the potential $m\omega_0^2 r^2/2$ in the plane and by the potential $V(z)$ in the z-direction and σ refers to the spin state of the electron. We assume that the wavefunction in the plane is decoupled from the z-wavefunction. The total density is obtained as $\rho(\vec{r}) = \sum_\sigma \rho^\sigma(\vec{r}) = \sum_{\sigma,i}|\psi_i^\sigma(\vec{r})|$, where we approximated the wavefunctions in the z-direction by delta functions. The effective potential consists of three terms: the intradot Hartree potential, the interdot Hartree potential and the exchange-correlation potential. Because both dots are identical the density in each dot is half the total density. The exchange-correlation potential is obtained by taking the functional derivative of the local exchange-correlation energy $E_{xc} = \int \rho(\vec{r})\,\epsilon_{xc}\left(\rho^\uparrow(\vec{r}),\rho^\downarrow(\vec{r})\right)$, where the Tanatar-Ceperley [8] functional for $\epsilon_{xc}\left(\rho^\uparrow,\rho^\downarrow\right)$ was used. Our results were applied for the material GaAs which has the effective mass $m^* = 0.067\ m_e$, and the dielectric constant $\varepsilon = 12.4$. The strength of the external confinement is set to $\hbar\omega_0 = 5.78\ N^{-1/4}$ meV, which assures that the average electron density in the droplet is kept approximately constant: $n_e = 1.28\times10^{15}$ m^{-2}. The motion in the z-direction is decoupled from the in plane motion in the Kohn-Sham Eq. (1) and is determined by $V(z)$ which consists of two coupled quantum wells with: $W = 120$ Å for the width of both dots, $V_0 = 250$ meV for the heigth of the barrier between the dots, and d is the interdot distance. The lowest energy level splits in a bonding and an antibonding level, which are included in our calculation and neglect the contribution from excited states because the confinement in the z-direction is much stronger than in the plane. The energy splitting Δ between the lowest bonding and antibonding levels could be fitted to an exponential decaying function $\Delta = 22.86\exp(-d/13.455)$ meV, with d expressed in Å. In our results we label the groundstate with three quantum numbers: spin S_z, angular momentum M_z, and an isospin quantum number I, which is the difference between the electrons in the bonding level and those in the antibonding level. As an example we show in Fig. 1(a) the energies as a function of the interdot distance for $N = 6$. As the Kohn-Sham scheme is a single particle picture it is natural to try to interpret the results in terms of Hund's rule. For small interdot distances, i.e. $\Delta \gg \hbar\omega_0$, all electrons are in the bonding levels, i.e. $I = 6$. In this case the electronic states are not localized in the single wells, and the molecule resembles a single artificial atom. As shown by the schematic picture of the single particle energy levels in Fig. 1(a) Hund's rule predicts that the groundstate is given by $S_z = 0, M_z = 0$. For large interdot distances Δ goes to zero which results in $I = 0$. The bonding and antibonding lev-

els are now degenerate and thus the electronic states in the system are now localized. In this case Hund's rule predicts that the groundstate is given by $S_z = 1, M_z = 0$. But as shown in Fig. 1(a) for intermediate interdot distances a new phase exists. This transition occurs when an electron in a bonding level jumps to an antibonding level, although the lowest antibonding level has still a higher energy than the highest filled bonding level. It is the exchange energy gain due to the spin flip that induces this transition. The groundstate energies for $N = 7$ are shown in Fig. 1(b). Here Hund's rule predicts that the groundstate is given by $S_z = 1/2, M_z = 2$ for small interdot distances. For large interdot distances the groundstate is given by $S_z = 3/2, M_z = 1$. But as shown in Fig. 1(b) in between these two phases exist two new phases. In the single particle scheme, as shown by the schematic pictures of the energy levels in Fig. 1(b), each phase transition occurs when an electron in a bonding level jumps to an antibonding level. We investigated molecules with $N = 3-8$ electrons and found that for $N = 3-6$ there is only one intermediate phase, while for $N = 7-8$ electrons two intermediate phases exist.

These new phases should be observable in single electron tunneling experiments. From these experiments one can obtain the addition energies. This is the energy needed to add one more electron in the double quantum dot, i.e. $\mu(N+1) - \mu(N)$, with $\mu(N) = E_{N+1} - E_N$. In Fig. 2 the addition energies are shown for two interdot distances. For small interdot distance $d = 15$ Å the two dots are very strongly coupled and the addition energies correspond to the single dot case, namely large peaks for 2, 6 and 12 electrons corresponding to closed shells, and smaller peaks for 4 and 9 electrons corresponding with half-filled shells. The peak structure changes with increasing d, i.e. for $d = 35$ Å $N = 6$ and 12 are no longer magic numbers, while $N = 5$ becomes a magic number, which reflects the modification of the shell structure due to the appearance of new phases. To see the continuous evolution of these peaks we show in Fig.3 the addition energies as a function of the interdot distance

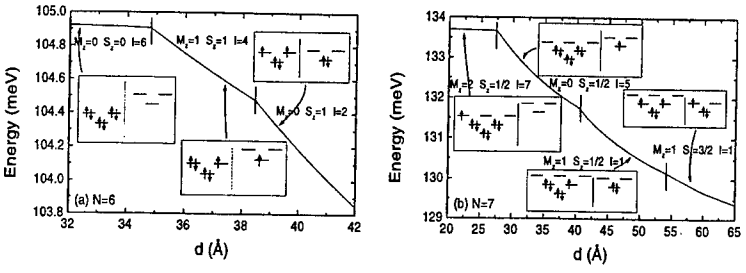

Fig. 1. The groundstate energies for (a) N=6 and (b) N=7, labeled with the spin (S_z), angular momentum (M_z) and isospin (I) quantum numbers. The insets show a schematic picture of the single particle energy levels ($\hbar\omega_0(1 + 2k + |l|)$ with k the radial and l the angular quantum number) for each phase.

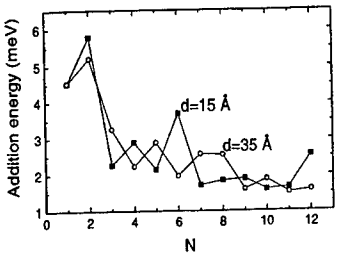

Fig. 2. The addition energies for two interdot distances $d = 15$ Å and $d = 35$ Å as a function of the number of electrons in the coupled dots.

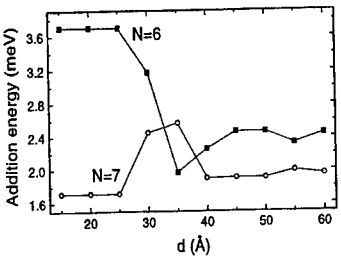

Fig. 3. The addition energies as a function of the interdot distance for six and seven electrons in the two vertically coupeld dots.

for six and seven electrons in the system. The decrease of the addition energy for $N = 6$ together with the increase for $N = 7$ around $d = 35$ Å can be understood from the existence of the intermediate phase for $N = 6$.

Acknowledgments: BP is a Research Assistant and FMP a Research Director with the Fund for Scientific Research - Flanders (FWO-Vlaanderen).

References

[1] L. Jacak, P. Hawrylak, and A. Wójs, *Quantum dots* (Springer-Verlag Berlin Heidelberg, 1998).

[2] J.J. Palacios and P. Hawrylak, Phys. Rev. B **51**, 1769 (1995); H. Imamura, P. A. Maksym, and H. Aoki, Phys. Rev. B **53**, 12613 (1996); *ibid.*, **59**, 5817 (1999); S. C. Benjamin and N. F. Johnson, Phys. Rev. B **51**, 14733 (1995); J. H. Oh, K. J. Chang, G. Ihm, and S. J. Lee, Phys. Rev. B **53**, R13264 (1996).

[3] S. Tarucha, D. G. Austing, T. Honda, R. J. van der Hage, and L. P. Kouwenhoven, Phys. Rev. Lett. **77**, 3613 (1996).

[4] D. G. Austing, T. Honda, K. Muraki, Y. Tokura, and S. Tarucha, Physica B **249**, 206 (1998).

[5] M. Rontani, F. Rossi, F. Manghi, and E. Molinari, preprint (1999).

[6] Y. Asano, Phys. Rev. B **58**, 1414 (1998).

[7] M. Koskinen, M. Manninen, and S. M. Reimann, Phys. Rev. Lett. **79**, 1389 (1997); K. Hirose and N. S. Wingreen, Phys. Rev. B **59**, 4604 (1999).

[8] B. Tanatar and D. M. Ceperley, Phys. Rev. B **39**, 5005 (1989).

BONDING AND ANTIBONDING STATES IN STRONGLY COUPLED BALLISTIC ONE-DIMENSIONAL WIRES

K. J. Thomas, J. T. Nicholls, W. R. Tribe, M. Y. Simmons, A. G. Davies, D. A. Ritchie, and M. Pepper
Cavendish Laboratory, Madingley Road, Cambridge CB3 0HE, United Kingdom
(June 16, 1999)

Low temperature conductance measurements of strongly coupled ballistic one-dimensional (1D) wires show the formation of bonding and antibonding 1D states. Two parallel 1D wires are defined by a split-gate structure deposited on a GaAs/AlGaAs double quantum well with a 25 Å AlGaAs barrier. A midline gate positioned at the centre of the split-gate allows both the widths and electron densities of the two wires to be tuned. At resonance when the wires are matched, symmetric and antisymmetric 1D energy levels are formed separated by an energy gap Δ_{SAS}. The overlap integral that describes the mixing of the 1D wavefunctions of different index in the two wires can be altered with a small in-plane magnetic field B. We also present preliminary measurements of the mixing of edge states in the quantum Hall regime.

Keywords: ballistic, strongly-coupled, one-dimensional, wavefunction mixing.

The two-dimensional electron gas (2DEG) has been well studied over the past 20 years, and the understanding of its basic properties has been enhanced by investigations of double 2DEGs (2×2DEG). In such systems, two GaAs quantum wells have been grown in close proximity to each other, and the degree of wavefunction overlap is controlled by the width of the AlGaAs tunnel barrier separating the two layers. In systems where the wavefunctions weakly overlap, tunneling from one layer to another allows the spectral properties of the 2D electron gas to be measured. [1] In more strongly coupled electron gases a new energy scale, Δ_{SAS}, the energy gap between the symmetric and antisymmetric 2D energy levels, has enriched studies of the quantum Hall regime.

A one-dimensional (1D) electron gas is formed when a 2DEG is electrostatically squeezed by application of a negative voltage to a split-gate. [2] Transport properties of the 1D electron gas crucially depend on the purity of the 2DEGs from which they are formed. In high mobility samples the electrons can pass through the 1D device ballistically, leading to the key result that the 1D wire exhibits conductance plateaus quantised in units of $2e^2/h$ - in accordance with a model of transmission via 1D modes, as put forward by Landauer. [3] The placing of one 1D wire in close proximity to another was first carried out in a lateral device, [4] where tunneling from one wire to the other revealed the sharpness of the 1D density of states. Vertical tunnelling from one single wire to another, where the width of the tunnel barrier is controlled using the precision of MBE growth, was measured in an etched resonant tunnelling diode structures. [5] In this paper we present results for two parallel wires fabricated using a modified split-gate pattern, [6] and which are strongly coupled in the growth (z) direction.

The energy levels of a two-level system described by a Hamiltonian $H(a)$ may cross at some particular value of the parameter a. A perturbation applied to the system will couple the two levels, which will repel each other in accordance with the "no-crossing" theorem [7]. When the energy levels in the individual wires become nearly degenerate (as controlled by gate voltages) they may interact with each other.

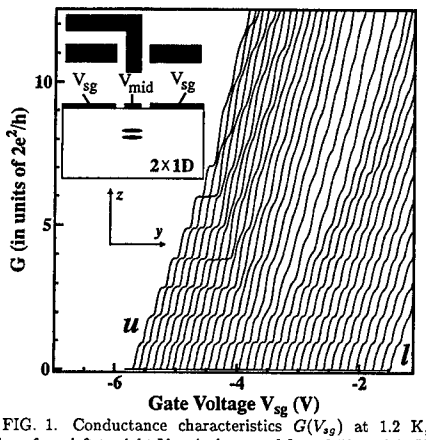

FIG. 1. Conductance characteristics $G(V_{sg})$ at 1.2 K, where from left to right V_{mid} is decreased from 0.59 to -0.85 V in steps of 40 mV. In the region to the left (right), only the upper (lower) wire is occupied. Inset: Schematic plan and side view of the device. The 2×1D electron gases are formed 2800 Å below the sample surface. They lie parallel to the x-axis (out of the page), coupled in the z-direction, with lateral confinement in the y-direction provided by the split-gate.

We show that at zero magnetic field there is mixing between 1D subbands of the same index, forming bonding and antibonding states, where the gate voltages control-

ling the device play the role of the parameter a. In an in-plane magnetic field there can be mixing of the wavefunctions of different subband index.

The starting material for our sample is a 2×2DEG wafer (T210) grown by molecular beam epitaxy, and comprises two 150 Å-wide GaAs quantum wells separated by a 25 Å $Al_{0.33}Ga_{0.67}As$ barrier, with a center-to-center distance of d = 175 Å. The double quantum well is doped both above and below using 2000 Å of Si-doped (1.2×10^{17} cm^{-3}) AlGaAs, offset by 600 Å and 800 Å AlGaAs spacer layers, respectively. The carrier density in each layer is 1.3×10^{11} cm^{-2}, with an average mobility of 1.45×10^6 cm^2/Vs. The 2D symmetric-antisymmetric (SAS) energy gap at resonance was measured [8] to be Δ_{SAS} = 1.4 meV. The wafer was processed into a Hall bar, and the gate pattern shown in the Fig. 1 inset was defined by electron beam lithography. The split-gate has a width of 1.2 μm and a length of 0.4 μm, and to add further control, a midline gate of width 0.4 μm was deposited along the centre of the split-gate.

The two-terminal conductance $G = dI/dV$ of the parallel wires was measured using conventional techniques. Conductance traces $G(V_{sg})$ of the 2×1D device at 1.2 K are shown in Fig. 1, as the midline voltage V_{mid} was changed from 0.59 to -0.85 V in 40 mV steps. In the measurements of strongly coupled 2DEGs it is not possible to make separate contact to the upper (u) and lower (l) layers, and so the measured conductance is that of the two wires in parallel. After correcting for a series resistance, R_s = 570 Ω, the plateaus in the conductance are quantized in units of $2e^2/h$. The split-gate voltage V_{sg} defines both the u and l wires; however, as V_{sg} becomes more negative the subbands in the l wire are depopulated first, and when V_{mid} is made more negative the u wire is depopulated first. [6] Therefore, by varying V_{sg} and V_{mid}, the fraction of the current passing through the u and l wires can be tuned. The clean conductance steps on the left-hand and right-hand sides of Fig. 1 originate from just the u and l wires, respectively, and the more complicated structure in between occurs where 1D subbands of the two wires become nearly degenerate.

A clearer picture of the mixed states is obtained by differentiating the $G(V_{sg})$ characteristics with respect to V_{sg} to generate the grey scale plot in Fig. 2(a). [9] The dark lines correspond to the transconductance (dG/dV_{sg}) maxima between plateaus, indicating where a 1D subband edge passes through the chemical potential. The Fig. 2(a) inset shows the subband positions redrawn with new axes a and b. Using the quantised conductance plateaus we are able to count the number of the subbands passing through the coupled wires at any gate voltage and this helps us to work out how the subbands mix. The subbands in the inset are indexed by n and n^*, which we shall show are the bonding and antibonding states formed by mixing the n^{th} wavefunctions of the u and l wires.

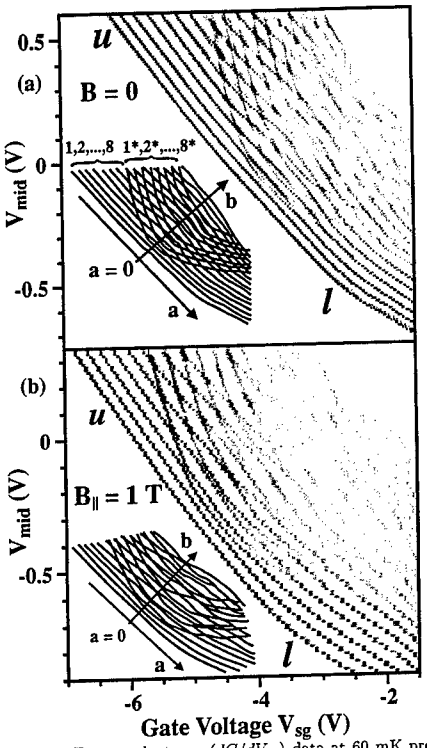

FIG. 2. Transconductance (dG/dV_{sg}) data at 60 mK presented as a grey scale plot at (a) B = 0, and (b) $B_{\|}$ = 1 T. The inset to (a) show the indexed subbands plotted with new axes a and b.

In a recent paper [10] we assume that the unperturbed wavefunctions in each wire are separable:

$$\Psi_j(x,y,z) = e^{ik_z x}\ \phi_{j,m}(y)\ Z_{j,m}(z), \qquad (0.1)$$

where $m = p$ for $j = u$, and $m = q$ for $j = l$; $\phi_{j,m}(y)$ is the m^{th} 1D subband wavefunction due to confinement in the y direction. The coupling between the two wavefunctions at the joint saddle point is determined by the integral

$$I = \int \phi_{u,p}(y)\ \phi^*_{l,q}(y)\ \ dy. \qquad (0.2)$$

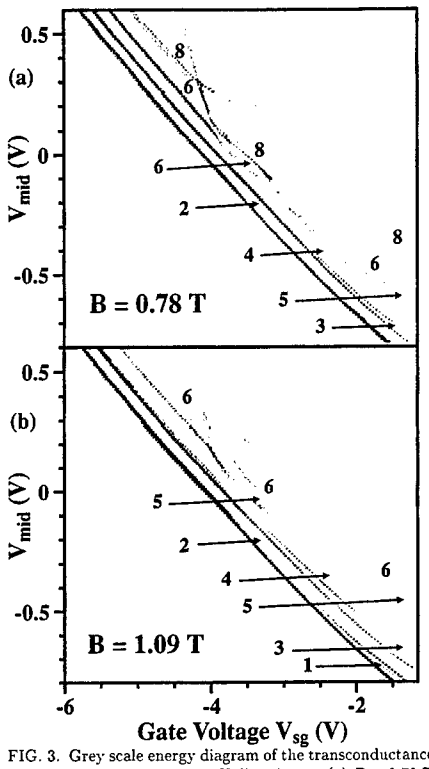

FIG. 3. Grey scale energy diagram of the transconductance data measured in the quantum Hall regime at (a) $B = 0.78$ T and (b) $B = 1.09$ T.

If the two wires are aligned and have approximately equal widths, $I = \delta_{p,q}$, in which case the y and z components of the unperturbed wavefunctions mix when $p = q = n$ to give the bonding

$$F_n(y,z) = [\phi_{l,n}(y)Z_{l,n}(z) + \beta\phi_{u,n}(y)Z_{u,n}(z)]/\sqrt{1+\beta^2}, \tag{0.3}$$

and antibonding wavefunction

$$F_{n^*}(y,z) = [\beta\phi_{l,n}(y)Z_{l,n}(z) - \phi_{u,n}(y)Z_{u,n}(z)]/\sqrt{1+\beta^2}. \tag{0.4}$$

The number β describes how much of the wavefunction is in each wire and is determined by the position along the a-axis, which is itself a linear combination of V_{sg} and V_{mid}. For example, the state labeled $n = 1$ in Fig. 2(a) has the wavefunction $F_1(y)$. When a is large and negative, $\beta \to \infty$, and conduction is through the u wire.

When a magnetic field is applied parallel to the 2×2DEG, mixing depends on whether B is aligned parallel or perpendicular to the double-wire axis. When the in-plane field is aligned perpendicular to the wire, the energy diagram $E_b(a)$ at $B_\perp = 2$ T shows mixing between subbands of the same index, similar to that shown in Fig. 2(a) at $B = 0$. In the parallel field configuration, $B_\parallel$ introduces a relative shift of the two wire wavefunctions in k_y-space by an amount $\Delta k_y = eB_\parallel d/\hbar$, where d is the tunneling distance between the two layers in the z-direction. The overlap integral is now determined by [10]

$$I(B_\parallel) = \int \tilde{\phi}_{u,p}(k_y - eB_\parallel d/\hbar)\ \tilde{\phi}^*_{l,q}(k_y)\ dk_y, \tag{0.5}$$

where $\tilde{\phi}_{j,p}(k_y)$ is the Fourier transform of $\phi_{j,p}(y)$. The condition $I = \delta_{p,q}$ that holds for aligned wires at $B = 0$ is relaxed, and in a $B_\parallel$ field there are overlaps (and hence anticrossings) between subbands of different index. In Fig. 2(b) we show the diagram obtained at $B_\parallel = 1$ T; this should be compared with previous measurements [10] at $B_\parallel = 2$ T. The overall characteristics look similar, but the detailed crossings and anticrossings (as determined by Eq. 0.5) are completely different at the two magnetic fields. At high in-plane fields, the two Fermi circles are completely decoupled, $\Delta k > k_{F,u} + k_{F,l}$, the mixing is destroyed.

When the magnetic field is applied perpendicular to the 2D electron layers, Landau levels are formed in the individual 2DEGs, and there is mixing of edge states at the joint saddle point. Preliminary conductance experiments in this regime are shown in Figs. 3 at (a) $B = 0.78$ T and (b) $B = 1.09$ T, where the total filling factors in the 2×2DEG are $\nu = 14$ and $\nu = 10$, respectively, with roughly equal filling factors in each 2D layer. The coupled wire data is presented in the form of a grey scale plot of the transconductance, and the indexing of the subbands takes into account spin splitting. In the quantum Hall (QH) regime the relevant energy scales are the Landau level spacing $\hbar\omega_c$, the Zeeman splitting $2g\mu_B BS$, and the symmetric/antisymmetric gap Δ_{SAS}. The data in Figs. 3(a) and (b) suggest that the energies are ordered as $\hbar\sqrt{(\omega_c^2\omega_0^2)} > \Delta_{SAS} > 2g\mu_B BS$, where $\hbar\omega_0$ is the 1D confinement energy at $B = 0$. At higher magnetic fields, $B > 3$ T (not shown), when only a few Landau levels are occupied, the subbands passing through the 2×1D device are bonding states, which have flat $E_b(a)$ diagrams (the subbands edges lie parallel to the a-axis). In the bottom right hand region where only the lower wire is populated, the energy levels show much greater spin splitting than when only the upper wire is populated (top left hand corner); this may be due to weaker confinement that is experienced in the lower wire. It appears that spin-splitting is greater for the antisymmetric states than the symmetric states; however, more quantitative measurements are needed to confirm this result.

In conclusion, we have shown that in a 2×1D device the wavefunctions of the 1D subbands are mixed at one point. The behaviour of the subbands in a parallel field can be qualitatively explained by a model which assumes the wavefunctions are separable. The preliminary measurements in the QH regime show that similar wavefunction mixing occurs at low magnetic fields.

[1] J. T. Nicholls, N. P. R. Hill, B. Kardynal, N. Turner, E. H. Linfield, D. A. Ritchie, C. H. W. Barnes, G. A. C. Jones, and M. Pepper, Physica E **3**, 52 (1998).

[2] T. J. Thornton, M. Pepper, H. Ahmed, D. Andrews, and G. J. Davies, Phys. Rev. Lett. **56**, 1198 (1986).

[3] R. Landauer, IBM J. Res. Dev. **1**, 223 (1957).

[4] C. C. Eugster and J. A. Delalamo, Phys. Rev. Lett. **67**, 3586 (1991).

[5] N. Mori, P. H. Beton, J. Wang, and L. Eaves, Phys. Rev. B **51**, 1735 (1995).

[6] I. M. Castleton, A. G. Davies, A. R. Hamilton, J. E. F. Frost, M. Y. Simmons, D. A. Ritchie, and M. Pepper, Physica B **249-251**, 157 (1998).

[7] E. Merzbacher, in *Quantum Mechanics*, 2nd ed. (Wiley, NY, 1970), pp. 428–429.

[8] A. G. Davies, C. H. W. Barnes, K. R. Zolleis, J. T. Nicholls, M. Y. Simmons, and D. A. Ritchie, Phys. Rev. B **54**, R17331 (1997).

[9] The data shown in Figs. 1, 2(a) and 2(b) were taken on different cooldowns, whereas those in Figs. 3(a) and 3(b) were taken on the same cooldown.

[10] K. J. Thomas, J. T. Nicholls, M. Y. Simmons, W. R. Tribe, A. G. Davies, and M. Pepper, Phys. Rev. B **59**, 12252 (1999).

Drag-Effect Between 2D-Electron-Gases; Composite Fermion and Screening Effects

C. Jörger[1], W. Dietsche[1], W. Wegscheider[2], and K. v. Klitzing[1]

[1] *Max-Planck-Institut für Festkörperforschung, Stuttgart, Germany*
[2] *Walter-Schottky-Institut, TU München, München, Germany*

Abstract

We report on experimental data of the drag-effect between 2D-electron-gases confined to two separate layers in a strong perpendicular magnetic field. We investigate the coupling at Landau level filling factor $\nu = 1/2$ as a function of temperature, carrier-densities of the two layers and distance between them. A good agreement is found with a recent theory based on Coulomb interaction. Furthermore we investigate the coupling at higher filling-factors as function of temperature and parallel magnetic field.

The coupling between two charge-systems can be studied in the non-tunneling regime via the drag-effect. When a current I_{drive} is driven through one of the two layers, the electrons of the nearby one are dragged along due to a frictional force, resulting in a measurable voltage drop V_{drag} along the nearby layer. The coupling strength is usually stated as the transresistivity

$$\rho_T = (W/L)(V_{drag}/I_{drive}) \qquad (1)$$

where (W/L) is the width to length ratio of the sample. The transresitivity has also been derived theoretically [1]. It depends on the product of the imaginary parts of the electric susceptibilities χ of each layer. In two-dimensional (2D) systems χ changes drastically in a perpendicular magnetic field and so does ρ_T.

The samples consist of modulation doped MBE-grown GaAs/AlGaAs-heterostructures. Two-dimensional-electron-gases (2DEGs) are located in 20 nm thick GaAs-quantum-wells each, separated by an $Al_{0.3}Ga_{0.7}As$ barrier. The as-grown carrier-density of each 2DEG is $2 \cdot 10^{11}$ cm^{-2} and the electron mobilities are between 1 and $2 \cdot 10^6$ cm^2/Vs at $T = 4.2$ K. Separate contacts to the 2DEGs are achieved by a selective depletion-technique using overgrown buried n^+-back-gates and evaporated metal-front-gates[2]. The carrier-density in each 2DEG can be controlled by a front- and a back-gate. The 2DEG is shaped as a 80 μm wide and 800 μm long Hall-bar.

In order to measure the drag-effect a current of 50 nA with a frequency of 1.1 Hz is applied to one 2DEG while the voltage drop is measured in the nearby 2DEG. We avoid parasitic signal caused by RF-noise, reported earlier [3,4], by low-pass-filtering each lead close to the sample inside the ^{3}He-insert.

First, we investigate the transresistance ρ_T

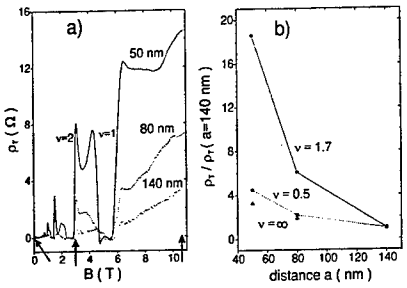

Fig. 1. a) The transresistivity ρ_T as a function of a perpendicular magnetic field B for three samples with different distances between the 2DEGs (a = 50 nm, 80 nm, 140 nm) at T = 1.6 K. The carrier-density of the 2DEGs are $1.3 \cdot 10^{11}$ cm^{-2} each. b) The transresistance normalized by its value at a = 140 nm as function of the distance a between the 2DEGs for three different filling-factors ($\nu = 1/2, 1.7, \infty$), which are indicated by an arrow in (a).

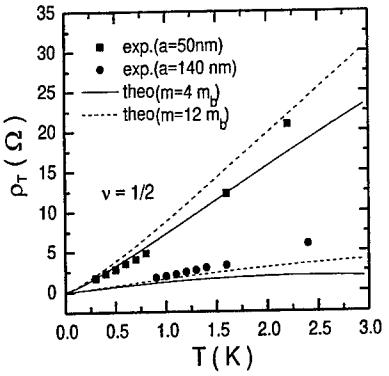

Fig. 2. The transresistivity as function of temperature at $\nu = 1/2$ for samples with layer separation a = 50 nm and a = 140 nm. Full (dashed) lines correspond to calculation of ρ_T at $\nu = 1/2$ with an effective mass of the composite-fermions of $4m_b$ ($12m_b$) [5]. The band-mass of GaAs is $m_b = 0.067m_e$.

as function of a perpendicular magnetic field up to 10.5 T for three samples with different distances a between the wavefunctions of the 2DEGs (a = 50 nm, 80 nm, 140 nm), which is approximately the barrier-thickness d plus 20 nm at T = 1.6 K (Fig. 1a). The carrier-density in each 2DEG is $1.3 \cdot 10^{11}$ cm^{-2}. Shubnikov-de Haas (SdH)-oscillations are clearly observed for the sample with a = 50 nm. Furthermore, ρ_T decreases with increasing barrier-thickness. For the samples with a = 80 nm and 140 nm SdH-oscillations are not detected below 2 T. In Fig. 1b ρ_T, extracted from (a), is plotted as function of distance, a, for three different Landau level filling factors, ($\nu = 1/2, 1.7, \infty$ (positions indicated by arrows in (a)). The data of $\nu = \infty$ are taken at 4.5 K, where phonon-coupling is present. The dependence of ρ_T at $\nu = 1/2$ and $B = 0$ on distance is rather weak, whereas at $\nu = 1.7$ (in the case of strong quantisation) a strong decay is observed. We obtained similar dependences of ρ_T on distance also for $1.3 < \nu < 1.7$. These data indicate a similarity of the coupling at $B = 0$ and $\nu = 1/2$ as function of distance. Filling factor $\nu = 1/2$ can be assigned to the existence of quasi-particles (composite fermions) in a vanishing effective magnetic field ($B_{eff} = 0$).

Next we investigate the coupling at $\nu = 1/2$ as function of temperature. The carrier-densities are still $1.3 \cdot 10^{11}$ cm^{-2} in each 2DEG. In Fig. 2 ρ_T is shown as function of temperature for the samples with a = 50 nm and a = 140 nm. A monotonic increase with T is observed. For T = 1.6 K the signal at $\nu = 1/2$ ($B_{eff} = 0$) is about 1000 times larger than the one at $B = 0$. The data are compared with recent calculations [5], which are shown for both samples as a full line ($m = 4m_b$) and dashed a line ($m = 12m_b$),

where m is the mass of the composite fermions and $m_b = 0.067m_e$ is the bandmass of GaAs. A very good agreement between the data of the sample with $a = 50$ nm is found for $m = 4m_b$ and $T < 1$ K. However, the calculation with $m = 12m_b$ does not differ strongly from the experimental data also, because the theoretical drag-effect is not much different for $4m_b < m < 12m_b$. For the sample with $a = 140$ nm the experimental values are slightly larger than the calculated ones. The good overall agreement is surprising, since the calculation includes only a Coulomb-coupling between the composite fermions. Similar calculations for 2DEGs at $B = 0$ result in a ρ_T which is far too small. In the case of $B = 0$ phononic coupling has to be taken into account to explain the experimental data. Therefore we conclude that Coulomb-coupling is enhanced at $\nu = 1/2$ ($B_{eff} = 0$) compared to the case of $B = 0$. The remaining deviations between theory and experiment are possibly still to phonon-coupling.

Third, we investigate ρ_T as function of filling factor between $\nu = 0.35$ and $\nu = 0.6$ in both 2DEGs at $T = 1.4$ K. The magnetic field is fixed at 10.5 T. This is shown as a combined grey tone-contour plot in Fig. 3. The line of matched densities is identified as axis of symmetry for ρ_T which is also observed at $B = 0$ in ρ_T as function of the upper and lower carrier-density. At $B = 0$ evidence for phonon-coupling is given by a maximum in ρ_T when both carrier-densities are equal [6,7]. This maximum is not visible at matched filling-factors around $\nu = 1/2$. Instead, ρ_T increases monotonically with decreasing filling-factor. From these data one cannot prove that phonon-coupling is present between the 2DEGs at $\nu = 1/2$.

At last ρ_T and the longitudinal resistance ρ_{xx} are investigated for filling-factors $\nu > 1$

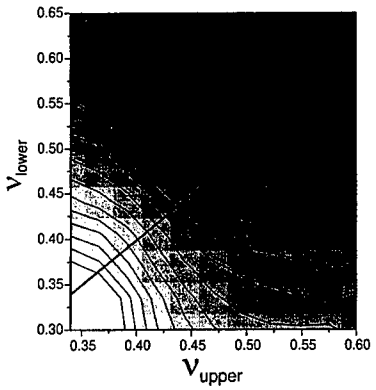

Fig. 3. Contour plot of the transresistivity as function of filling-factors in the upper (ν_{upper}) and the lower (ν_{lower}) 2DEG at $T = 1.4$ K and $B = 10.5$ T. The barrier-thickness is 120 nm. White areas indicate the strongest (5 Ω), the black ones the weakest coupling (0.5 Ω). The solid line runs along equal filling factor.

as function of a perpendicular magnetic field for different temperatures. This is shown in Fig. 4. The carrier-densities are matched at $1.4 \cdot 10^{11}$ cm^{-2}. As reported in former work [3,4] a double-peak-structure in ρ_T is observed which is not present in ρ_{xx} of a single 2DEG at the same temperature (e.g. the curve for $T < 1.6$ K and $B < 1.5$ T). Its origin is still in discussion. By lowering the temperature we focus on the maximum between $\nu = 4$ and $\nu = 3$. This spin-polarised maximum does not split into two for 0.3 K$< T <$ 1.6 K neither in ρ_{xx} nor in ρ_T. Therefore the minimum at $\nu = 3$ is due to spin-splitting and not to screening-effects as in [4,8].

The transresistance ρ_T was further investigated in an additional parallel magnetic field to study the effect of spin-splitting on the drag-effect. An increase of the maximum in ρ_T between $\nu = 4$ and $\nu = 3$ or between

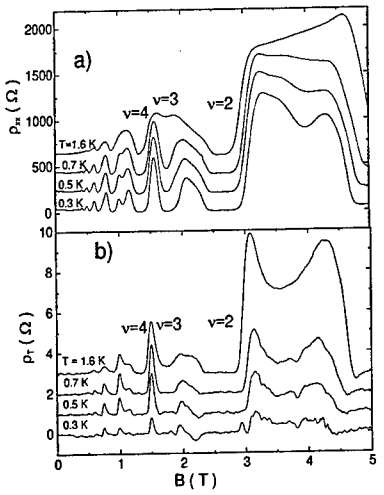

Fig. 4. The longitudinal resistance ρ_{xx} (a) and the transresisistivity ρ_T (b) as function of perpendicular magnetic field for different temperatures. The carrier densities of both 2DEGs are $1.4 \cdot 10^{11}$ cm^{-2} each. Lines are offsetted for clarity.

$\nu = 3$ and $\nu = 2$ up to 100% was found by tilting the magnetic field from 0° (only perpendicular field) up to 82°. The value of ρ_T at odd filling-factors did not change whereas a decrease of ρ_{xx} at same filling-factors is observed. Qualitatively one can understand the data by assuming that the drag-effect is sensitive to the entire 2DEG whereas in a normal tranport experiment edge effects are more important. Therefore the drag-effect probes mainly the properties of the bulk which results in pronounced SdH-oscillations compared to ρ_{xx}.

In conclusion we showed measurements of the drag-effect between high-mobility 2DEGs in strong perpendicular magnetic field. We found a similarity of the coupling at $\nu = 1/2$ ($B_{eff} = 0$) and $B = 0$, but at $\nu = 1/2$ Coulomb-coupling is the dominant process compared to phonon-coupling in good agreement with [5]. At higher filling-factors we investigated in detail the double-peak-structure and found that it is not caused by screening effects.

References

[1] A.-P. Jauho, H. Smith, Phys. Rev.B **47**, 4420 (1993).

[2] H. Rubel, A. Fischer, W. Dietsche, K. v. Klitzing and K. Eberl, Materials Science & Engineering B **51**, 207 (1998).

[3] N.P.R. Hill, J.T. Nicholls, E.H. Linfield, M. Pepper, D.A. Ritchie, A.R. Hamilton und G.A.C. Jones, J.Phys.:Condens.Matter **8**, L557 (1996)

[4] H. Rubel, A. Fischer, W. Dietsche, C. Jörger, K. v. Klitzing and K. Eberl, Physica E **1**, 160 (1997); H. Rubel, A. Fischer, W. Dietsche, K. von Klitzing, K. Eberl, Phys.Rev.Lett. **78**, 1763 (1997).

[5] I. Ussishkin and A. Stern, Phys.Rev.B **56**, 4013 (1997).

[6] T.J. Gramila, J.P. Eisenstein, A.H. MacDonald, L.N. Pfeiffer, and K.W. West, Phys. Rev. B **47**, 12957 (1993); H. Rubel, E.H. Linfield, D.A. Ritchie, K.M. Brown, M. Pepper and G.A.C. Jones, Semicond. Sci. Technol. **10**, 1229 (1995).

[7] C. Jörger, S.J. Cheng, H. Rubel. W. Dietsche, R. Gerhardts, P. Specht, K. Eberl, K. v. Klitzing, Proceedings EP2DS 1999 Ottawa.

[8] M.C. Bønsager, K. Flensberg, B. Yu-Kuang Hu, A.-P. Jauho, Phys.Rev.Lett. **77**, 1366 (1996) and Phys.Rev.B **56**, 10314 (1997)

Absorption Spectroscopy in Electron Double Layers: Evidence for Broken Symmetry States

M. J. Manfra,[1,2] B. B. Goldberg,[1] J. C. Pniower,[1] A. Pinczuk,[2,3] V. Pellegrini,[4] L. N Pfeiffer,[2] and K. W. West[2]

[1]Department of Physics, Boston University, Boston, Massachusetts 02215
[2]Bell Laboratories, Lucent Technologies, Murray Hill, New Jersey 07974
[3]Physics Department, Columbia University, New York, NY, 10027
[4]Scuola Normale Superiore and INFM, Piazza dei Cavalieri 7, I-56126, Pisa, Italy

Abstract

Optical absorption spectroscopy has been used to explore the phase diagram of the double layer electron system at $\nu=1$. Absorption spectroscopy is shown to be sensitive to the evolution of the electron system from a regime in which a gap in the single-particle tunneling spectrum accounts for the quantized Hall state to a regime of weak tunneling in which inter-layer Coulomb interactions determine the nature of the excitation gap. Qualitative differences in magnetic field and temperature dependence of spectra are observed depending on the relative size of the single-particle tunneling gap. Most intriguingly, our measurements of samples in the regime of weak tunneling do not display a quenching of absorption intensity at $\nu=1$ characteristic of the quantum Hall effect.

PACS numbers: 73.20.Dx, 73.20Mf, 78.30.Fs

Introduction.

A new degree of freedom, the layer index, is created when two 2D electron layers are formed in close proximity. In direct analogy with the spin-1/2 system, the layer index is associated with the eigenvalues of a double-valued pseudospin operator, S_z. In the presence of inter-layer tunneling, symmetric and antisymmetric combinations of the eigenstates of S_z can be constructed which are eigenstates of S_x and are separated by a single-particle tunneling energy gap, Δ_{SAS} (B=0). In the quantum Hall regime at $\nu=1$, the non-interacting ground state would be a fully populated symmetric state of the spin-up branch of the lowest Landau level (LLL). In reality, the interplay of collective electron interactions and single-particle tunneling gives rise to a rich phase diagram of incompressible and compressible states for charge transport at $\nu=1$ [1].

Murphy, *et al.*, [1] determined the phase boundary between gapped and compressible ground states at $\nu=1$ in double layer electron systems, and surprisingly, found that the gap in the incompressible sector survives in the limit of zero tunneling. While the ground state must evolve as the tunneling strength is reduced relative to the inter-layer Coulomb interactions, transport cannot clearly distinguish between the two regimes nor directly probe the spin or pseudospin configuration of the ground state. Presently little is experimentally known about the evolution of the ground state as the ratio of intra- to inter-layer Coulomb interactions and single particle tunneling are modified.

In this work we describe the first measurements of optical absorption in the double layer system in the quantum Hall regime. As absorption can only occur into unoccupied levels, magneto-absorption spectroscopy can discriminate between occupied and unoccupied states in the vicinity of the Fermi level. This technique has been used previously to probe the spin configuration in the single layer system at $\nu=1$ [2]. Our preliminary experiments in the double layer system have yielded unexpected results. In the limit of strong tunneling we observe a strong quenching of the absorption intensity of left circularly polarized light. This observation is consistent with previous

studies of the single layer system and is interpreted as an optical signature of the quantum Hall effect at ν=1. In sharp contrast, in weakly tunneling samples near the phase boundary no such quenching is observed and the absorption remains finite to the lowest accessible temperatures. We emphasize that all samples discussed here exhibit strong ν=1 quantum Hall states in transport.

Experiment and Discussion.

Direct transmission spectroscopy concentrated on two samples: Sample A consists of two identical 180A GaAs quantum wells separated by a 79A $Al_{0.1}Ga_{0.9}As$ undoped barrier layer. The electron density is $6.3x10^{10}$ cm^{-2}, the mobility is $10^6 cm^2/Vs$, and Δ_{SAS}=0.7 meV at B=0. Sample B consists of two identical 180A GaAs quantum wells separated by a 31A undoped $Al_{0.3}Ga_{0.7}As$ barrier. Its density is $1.3x10^{11}$ cm^{-2}, the mobility $10^6 cm^2/Vs$, and the tunneling gap is Δ_{SAS}=0.4 meV. We have also performed simultaneous transport and transmission spectroscopy, confirming not only the carrier density, but also the presence of a gap in the charged excitations at ν=1.

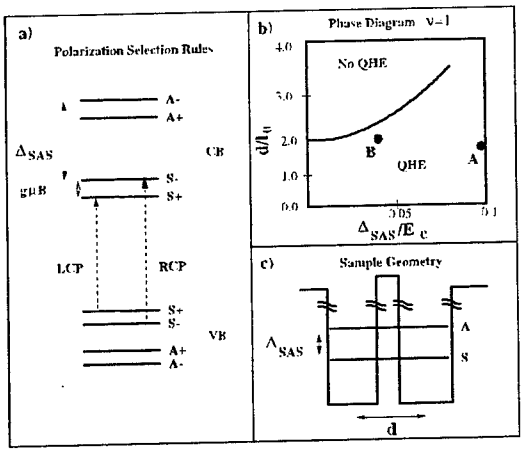

FIG 1: (a) Polarization selection rules for inter-band absorption at ν=1. The dashed lines correspond to the two lowest-energy transitions in the left- and right-circular polarization (LCP and RCP). (b) Phase diagram of in the DQW structure constructed by Murphy. The *x* axis measures the tunneling gap Δ_{SAS} in units of the Coulomb energy, and the *y* axis scale measures the ratio of intra-layer to inter-layer Coulomb interactions. (c) Schematic of DQW structure used in these studies with the symmetric-antisymmetric gap.

Polarization selection rules for inter-band absorption at ν=1 are shown in Fig. 1a. In a single particle picture, the lowest energy transition in LCP has its final state as the symmetric spin-up state of the LLL. Similarly in RCP, the final state is the symmetric spin-down state of the LLL. Fig. 1 also shows an approximate energy level configuration for our samples as well as their positions on the ν=1 QHE phase diagram. Figure 2 displays the absorption in LCP into the LLL in sample A, whose tunneling gap of Δ_{SAS}=0.7 meV puts it deep into the single-particle regime and so should form a nearly fully pseudospin polarized ground state at ν=1. In the optical transmission data, the lowest-energy transition is strongly quenched as E_F passes through ν=1. This quenching is interpreted as the optical signature of a ferromagnetically aligned ground state and is reminiscent of the quenching seen in the single layer system where the ground state is fully spin polarized at ν=1 [2]. The absorption minimum shows that the lowest-energy transition in LCP is sensitive to the ground state occupation of the symmetric spin-up level at ν=1.

Fig. 3 shows a set of spectra of the absorption for sample B in LCP at T=0.53K. Sample B has a much smaller tunneling gap (Δ_{SAS}=0.4meV, see fig. 1) and so should be in the regime where

interaction effects dominate. In striking contrast to sample A, the absorption at ν=1 for sample B shows no quenching of the lowest energy transition, implying the existence of a finite density of available states in the spin-up electron level at ν=1.

Similarly intriguing behavior is seen in the temperature dependence of the absorption in sample B. The observation of non-zero absorption persists to the lowest accessible temperature of T=0.5K, illustrated in Fig. 4. The absorption changes dramatically as the temperature is reduced below T=1K, anomalously increasing at low temperatures, precluding a simple interpretation based on the thermal population of single-particle excitations. Large temperature dependent changes in the absorption are quite unusual, as previous measurements on many single [2] and double well samples have shown no significant changes below 1K. Again we emphasize that at these temperatures, sample B displays a well-developed quantum Hall state in transport.

Current theoretical work in the double layer system has focused on incomplete pseudospin polarization of the ground state at ν=1, attributed to the reduction in symmetry caused by the inter-layer Coulomb interactions [3-6]. To our knowledge, little work has been done exploring the combined roles of pseudospin and real spin at ν=1. Our data would seem to imply some unanticipated behavior in the spin degree of freedom for samples close to the ν=1 bi-layer QHE phase boundary yet within the quantum Hall regime. In lieu of a more complete theoretical understanding of our data, we note that sample B is close to the boundary of a quantum phase transition between compressible and incompressible states. Quite generally, a quantum phase transition is associated with long time scale fluctuations of the ground state configuration. Given sample B's proximity to the boundary, it is possible that the fluctuations at ν=1 are long on the time scale of our optical probe and thus absorption may be sensitive to these excursions from full polarization.

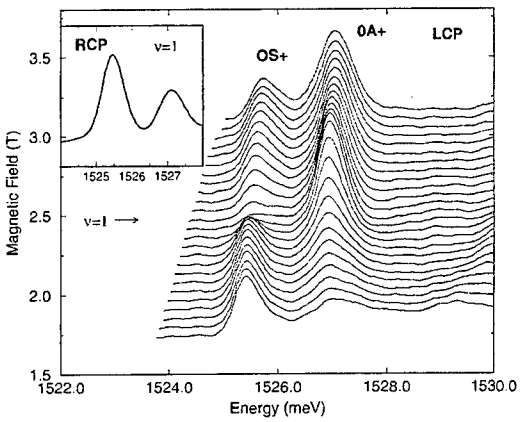

FIG. 2. Low-energy absorption in LCP at T=0.53K of sample *A*. The transition labeled 0A+ corresponds to absorption into the antisymmetric, spin-up state. Note the strong quenching of the lowest energy transition exactly at ν=1. The inset displays the absorption in RCP at ν=1 and highlights the distinctly different behavior observed in the two polarizations. The ratio of 20:1 in absorption between RCP and LCP at 1525.5 meV indicates that the optical selection rules shown in Fig. 1 are active.

We speculate that the observed lack of quenching of absorption exhibited in sample B may be associated with an impending phase transition to the compressible state. Of course, further experimental and theoretical justification is needed, not least of all a mechanism for the loss of spin polarization. Presently experiments are underway to explore samples in the compressible phase.

Conclusions

Absorption spectroscopy has been shown to be a powerful tool for the investigation of the double layer electron system at $\nu=1$. For the first time we have been able to experimentally distinguish between regimes in which single particle effects are paramount and those in which many-body interactions dominate. Our data in a weakly tunneling sample, while intriguing, remain unexplained. It suggests that correlations may be playing an unanticipated role in the formation of the quantum Hall ground state at $\nu=1$.

Acknowledgements: This work was supported by the National Science Foundation under DMR-9701958. We acknowledge helpful discussions with Allan MacDonald, and David Broido.

References

1. S. Q. Murphy, J. Eisenstein, L. Pfeiffer, and K. West, Phys. Rev. Lett. **72**, 728 (1994).
2. M. Manfra, *et al*, *Phys. Rev. B* **54**, R17327 (1996).
3. *Perspectives in Quantum Hall Effects*, eds. S. Das Sarma and A. Pinczuk (Wiley Interscince, New York, 1997).
4. A. H. MacDonald, P. M. Platzman, and G. S. Boebinger, Phys. Rev. Lett. 65, 775 (1990).
5. K. Yang, Phys. Rev. Lett. 72, 732 (1994).
6. K. Moon, *et al.*, Phy. Rev. B. 51, 5138 (1995).

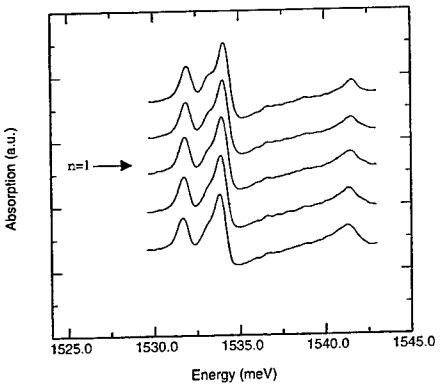

FIG. 3. Absorption in LCP for sample B at T=0.53K. The spectra are at the filling factor $\nu=1$ with field steps of 0.05T. Note, in sharp contrast to sample A, the lack of quenching of the lowest-energy transition at $\nu=1$.

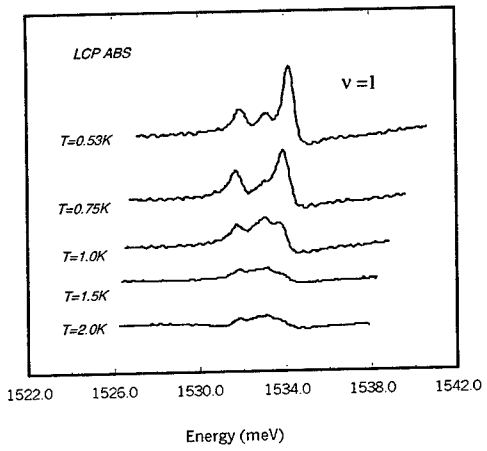

FIG. 4. Individual absorption spectra in LCP at $\nu=1$ for sample B taken at various temperatures. The spectra change dramatically between 2K and 1K, suggesting a rapidly evolving ground-state. Below T=0.8K the lowest energy transitions appear activated.

Temperature Dependence of Interlayer Surface Transport in Multilayer Quantum Hall System

M. Kuraguchi and T. Osada
Institute for Solid State Physics, University of Tokyo,
5-1-5, Kashiwanoha, Kashiwa, Chiba 277-8581, Japan.

Abstract

We have studied interlayer surface transport in GaAs/AlGaAs multilayer quantum Hall systems. By canceling bulk conductance between different shaped samples, we have successfully extracted only the conductivity of surface transport over wide temperature range. At low temperatures, the surface conductivity in an integer quantum Hall state is much smaller than e^2/h and independent of temperature. These are the theoretically predicted natures of the chiral surface state. As the temperature is increased, the surface transport is enhanced by mixing with bulk states, and finally the surface transport vanishes reflecting the disappearance of the quantum Hall effect.

It is well accepted that two-dimensional (2D) electron gases with the conductivity less than e^2/h are always localized due to quantum interference effects in the absence of magnetic field. However, recent theoretical studies discuss that a novel 2D system at the surface of multilayer quantum Hall system [1] remains metallic transport. The edge state of each layer couples by interlayer tunneling and forms the "chiral surface state". In this 2D system, the localization effects are suppressed by its chirality [2-4]. Since bulk states are localized in the quantum Hall state, the chiral surface states are well-separated from bulk states due to the short bulk localization length. So, we can consider the surface transport and the bulk transport independently. In the low temperature limit, the surface transport dominates the interlayer transport because the bulk transport freezes out due to localization. Recent experimental studies have demonstrated the existence of the surface transport below 200mK where the bulk transport can be neglected [5,6]. The conductivity of the surface transport in the integer quantum Hall state was nearly constant and well below e^2/h. These features have been predicted theoretically as those of chiral surface states.

However, the temperature dependence of surface conductivity has not been studied, because the transport through the bulk cannot be neglected at high temperatures. In order to overcome this difficulty, we prepared different mesa-shaped samples with the same sectional area but different perimeters, and have extracted only the conductivity of surface transport by canceling their bulk conductance. This technique is very useful to study wide-range temperature dependence of interlayer surface transport due to the chiral surface state.

The GaAs/AlGaAs superlattices were grown by molecular-beam epitaxy on non-doped GaAs and n^+-GaAs substrates. The superlattice part was common for each wafer, and consisted of 50 periods of 150 Å GaAs wells and 150 Å $Al_{0.1}Ga_{0.9}As$ barriers where Si was δ-doped at the center. Employing the Kronig-Penny model, the first

miniband width was estimated as 0.12meV. The in-plane mobility and the sheet carrier density per layer at 4.2K were estimated as 15000cm^2/Vs and 4.9 $\times$ 10^{11}cm^{-2}, respectively. The wafers with insulating substrates were used for studies of in-plane transport in order to check whether the electron system was in the quantum Hall state or not. They were pattered into a standard Hall bar shape. The wafers with conducting substrates were used for measurements of interlayer transport. Three mesas with different shapes were fabricated close to each other on them. Ohmic contacts of all samples were achieved with alloyed AuGe.

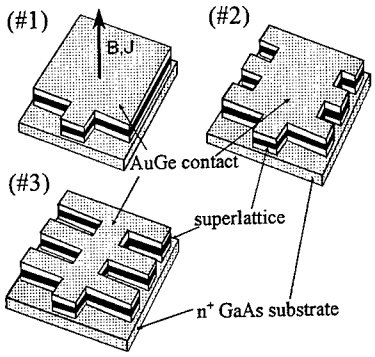

Figure 1
Schematic bird's-eye view of mesa-shaped samples for interlayer transport. All samples have the same sectional area 11500μm^2 but different perimeters: 460μm (#1), 780μm (#2), and 1100μm (#3).

Figure 1 shows the schematic view of three types of mesa-shaped samples. These samples have the same sectional area but different perimeters. Therefore, these samples should have the same interlayer conductance through bulk states, but different ones through surface states if it would exist. The difference of interlayer magnetoresistance between the samples means the existence of surface transport. The common bulk conductance can be cancelled by subtracting the measured conductance of one sample from that of another. Regardless of the existence of bulk transport, we can extract only the contribution of surface transport up to high temperatures.

Figure 2(a) shows the in-plane magnetoresistance R_{xx} and interlayer one R_{zz} for each samples at T=4.2K. R_{xx} shows Shubnikov-de Haas (SdH) oscillations, but the quantum Hall states, *i.e.* zero-resistance states, are not realized in this field range. R_{zz} also shows SdH oscillations, but their peaks appear where R_{xx} shows local minima. Three R_{zz} traces for three mesa-shaped samples coincide almost perfectly. This fact means that the surface conduction proportional to the sample perimeter is almost zero at this temperature.

Figure 2(b) shows R_{xx} and R_{zz} at a lower temperature T=0.5K. Around B=10T, R_{xx} shows zero-resistance, and the in-plane Hall resistance R_{xy} exhibited a well-defined plateau (i=2). Therefore, a quantum Hall state is realized in this field region. It is remarkable that three R_{zz} traces show clear difference only in the quantum Hall state. In other words, the interlayer transport has strong perimeter dependence there. This means that the surface transport exists only in the quantum Hall state. As mentioned above, this surface transport almost vanishes at a higher temperature T=4.2K where the quantum Hall effect disappears.

Figure 2(c) shows the interlayer surface conductivity $\sigma_{zz}^{(surface)}$ obtained by subtracting the interlayer conductance (G_{zz}=1/R_{zz}) of the sample #1 from that of the sample #3 at T=0.5K. Although the data below 7.5T have rather large ambiguity because of so small difference of R_{zz}, we can somehow see that the surface transport vanishes except at the quantum Hall region. We also notice that the surface transport is

strongly enhanced not at the center field (A) of the quantum Hall region, but at both sides of this region. As shown by arrows, $\sigma_{zz}^{(surface)}$ shows double peaks around the borders of quantum Hall region.

Next, we investigate the temperature dependence of surface conductivity at several magnetic fields indicated in Fig.2. Figure 3(a) shows the temperature dependence of interlayer surface conductivity $\sigma_{zz}^{(surface)}$ at the center field (A) B=10.2T of the i=2 quantum Hall state. Only the surface contribution is well extracted although the bulk contribution cannot be neglected over this wide temperature range. This dependence can be divided into three temperature regions. In the low temperature region (T<750mK), the surface conductivity $\sigma_{zz}^{(surface)}$ is nearly constant (~$10^{-3}e^2/h$) and well below e^2/h. This feature is consistent with the theoretical prediction for the chiral surface state in a multilayer integer quantum Hall state [2-4]. Here, the interlayer conduction is considered to be diffusive. In the high temperature region (T>1.5K), $\sigma_{zz}^{(surface)}$ monotonously decreases with increasing temperature. This feature corresponds to disappearance of the quantum Hall effect. The thermal excitation to bulk extended states kills individual surface transport.

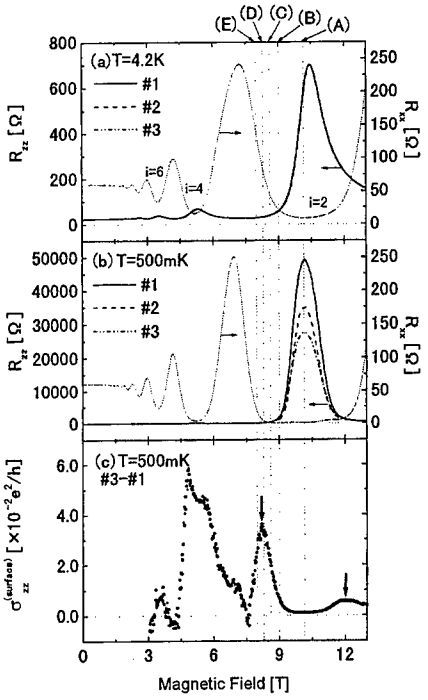

Figure 2
(a) In-plane and interlayer magnetoresistance at 4.2K. (b) In-plane and interlayer magnetoresistance at 0.5K. (c) Extracted interlayer surface conductivity at 0.5K.

In the intermediate temperature region (750mK<T<1.5K), $\sigma_{zz}^{(surface)}$ increases as a function of temperature: $d\sigma_{zz}^{(surface)}/dT$>0. In other words, the surface transport shows an "insulating" behavior.

Figure 3(b) shows the temperature dependence at several off-center fields: (B)B=9.0T, (C)B=8.7T, (D)B=8.4T, and (E)B=8.0T. These fields are located in the low-field side of the center field (A) in the i=2 quantum Hall state. As the field approaches to the border of the quantum Hall state, the "breakdown" temperature, above which the surface conduction decreases monotonously, becomes lower. This feature is consistent with the fact that the excitation energy to the extended states becomes smaller at the off-center fields.

As mentioned above, the behaviors of surface conduction in low and high temperature regions are understood as the nature of the chiral surface state and as thermal excitation to bulk extended states, respectively. In what follows, we will discuss the origin of the insulating temperature dependence in the intermediate region. In

addition, we must explain the enhancement of surface conduction around the borders of the quantum Hall state in the field dependence. We see that these features are qualitatively explained by the mixing of the surface states and bulk localized state.

In the quantum Hall state, the localization length of bulk localized states is much shorter than the sample size, so that the surface states are well separated from bulk states. But, a small number of bulk localized states, whose distance from the surface is less than the localization length, reach to the surface, and can mix with surface states. This causes the increase of conduction channels contributing to the surface transport. The localization length takes a minimum at the edge of the Landau subband (the center of the quantum Hall region) and increases rapidly as the energy becomes close to the Landau subband center. Therefore, the surface conductivity $\sigma_{zz}^{(surface)}$ is enhanced around the border of the quantum Hall region where the localization length becomes very large. In the case that the temperature is increased at the center field of the quantum Hall region, the thermal excitation to the surface mixing states enhances the surface transport, so that the insulating behavior $d\sigma_{zz}^{(surface)}/dT>0$ is observed.

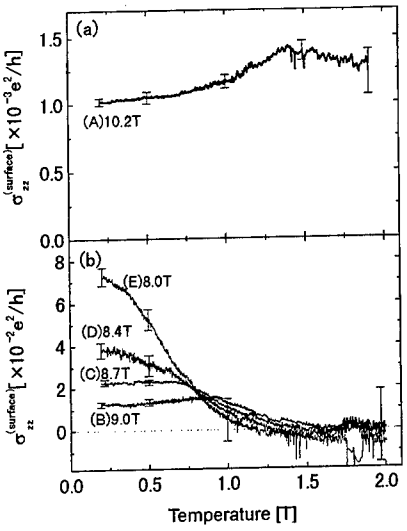

Figure 3
Temperature dependence of interlayer surface conductivity at various magnetic fields shown in Fig.2.

In conclusion, we have extracted the interlayer surface transport and studied its temperature dependence over wide temperature range. The temperature dependent features are explained by the diffusive conduction due to the chiral surface states, the thermal excitation to the mixing states between the surface and bulk states, the thermal excitation to the extended states. This work is supported by the Torey Science Foundation.

References

[1] H.L. Stormer, J.P. Eisenstein, A.C. Gossard, W. Wiegmann, and K. Baldwin, *Phys. Rev. Lett.* **56**, 85 (1986).
[2] L. Balents and M.P.A. Fisher, *Phys. Rev. Lett.* **76**, 2782 (1996).
[3] J.T. Chalker and A. Dohmen, *Phys. Rev. Lett.* **75**, 4496 (1995).
[4] S. Cho, L. Balents, and M.P.A. Fisher, *Phys. Rev.* **B56**, 15814 (1997).
[5] D.P. Druist, P.J. Turley, K.D. Maranowski, E.G. Gwinn, and A.C. Gossard, *Phys. Rev. Lett.* **80**, 365 (1998).
[6] B. Zhang, J.S. Brooks, Z. Wang, J.A.A.J. Perenboom, J. Simmons, J. Reno, N. Lumpkin, J. O'Brien, and R. Clark, *Physica* **B256**, 279 (1998).

Frictional Drag Between Coupled 2D Hole Gases in GaAs/AlGaAs Heterostructures

C. Jörger, S.J. Cheng, W. Dietsche, R. Gerhardts, P. Specht, K. Eberl and K. v. Klitzing

Max-Planck-Institut für Festkörperforschung, Stuttgart, Germany

Abstract

We report on the first measurements of the drag effect between coupled 2D-hole gases. The coupling is investigated by changing the temperature, the carrier densities in the quantum wells and the widths of the barriers between the gases. From the data we are able to attribute the frictional drag to phonon coupling because the non-parabolicity allows the separate tuning of the Fermi wavevector and of the Fermi velocity allowing to distinguish between phonon- and plasmon-dominated coupling.

Two closely spaced two-dimensional charge systems are still subject of strong interest, owing to the diversity of coupling mechanisms between the layers. If the layer separation is large enough that tunneling between them is negligable, coupling is dominated by interlayer scattering processes. This is called the frictional drag. A drive current I_{drive} is passed through one layer leading to a drag voltage V_{drag} in the other one. The size of the coupling is usually stated as the transresistivity

$$\rho_T = (W/L)(V_{drag}/I_{drive}) \qquad (1)$$

where (W/L) is the width to length ratio of the sample. The case of two coupled two dimensional electron gases (2DEGs) in GaAs/AlGaAs heterostructures has been studied both experimentally and theoretically by several authors (e.g. [1,2]). No work has been published on the drag between 2d hole gases (2DHGs). In this contribution we report, to the best of our knowledge, the first measurements of the drag between two 2DHGs.

The coupled 2DHGs are defined via two 20 nm thick quantum wells in GaAs/AlGaAs-heterostructures. Remote doping was achieved using carbon with a spacer layer thickness of typically 20 nm. Six samples are produced with GaAs/$Al_{.3}Ga_{.7}As$ barriers with thicknesses varying from 30 to 190 nm between the quantum wells. In some samples the doping of one well is placed inside the barrier leading to a strong asymmetry between the layers. The samples are shaped as a Hall bar geometry with 80 μm width and 800 μm length. Ohmic contacts to both layers are made by diffusion of Au and Zn. Separate contacts to the two layers are achieved by using the standard selective depletion technique. In our case, metallic front gates and p-doped buried backgates are used [3]. Two more gates cover the main part of the Hall bar and allow the independent variation of the carrier densities. Typical hole mobilities

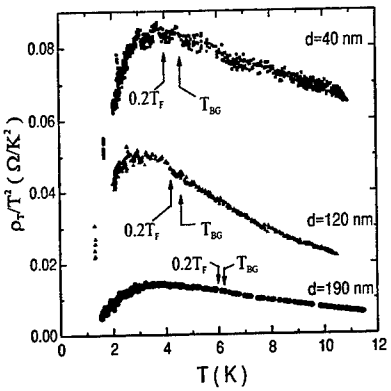

Fig. 1. The transresistivity ρ_T normalized by T^2 as a function of temperature for three samples of different barrier-thickness (d = 40 nm, 120 nm, 190 nm). Positions of 0.2 times the Fermi-velocity T_F and the Bloch-Grueneisen-temperature T_{BG} are indicated.

at 4 K of the upper 2DHG are $8 \cdot 10^4$ cm^2/Vs and $4 \cdot 10^4$ cm^2/Vs for the lower one which are reasonably good values for hole gases on (001) surfaces. The hole concentration can be varied typically from zero to about $5 \cdot 10^{11}$ cm^{-2}. The drag measurements were done by passing drive currents of 100 nA at a frequency of 1.1 Hz through one of the layers and using lock-in technique to measure the resulting drag voltage in the other layer.

First, we present data on the dependence of the transresistivity ρ_T on the temperature T. In Fig. 1 we show ρ_T normalized by T^2 as function of temperature for three samples with different barrier-thickness d. For all three samples a deviation from the behaviour $\rho_T \propto T^2$ is observed which is expected simply from the broadening of the two Fermi-surfaces. Furthermore a maximum in ρ_T/T^2 is visible between 2 und 4 K. It can result either from coupling mediated by acoustic phonons [2] or from coupling mediated by interlayer plasmon modes [4,5]. In the case of phonon-coupling the peak is expected to be close to $T = T_{BG}$ with $T_{BG} = 2\hbar c_S k_F/k_B$ the Bloch-Grueneisen-temperature. c_S is the velocity of sound in GaAs. In the case of plasmon-coupling a maximum in ρ_T/T^2 is expected at the temperature of most efficient coupling ($0.2 - 0.5T_F$) [4]. T_F is the Fermitemperature. Both quantities, T_{BG} and $0.2T_F$, are indicated in Fig. 1. The dispersion of the coupled plasmon modes relative to the single -particle-excitation-spectrum is sensitive to the barrier-thickness, which should strongly influence the position of the maximum in ρ_T/T^2. This is not observed in the experiment which supports a phonon-coupling between the 2DHGs.

Second, we present data on the dependence of the transresistivity ρ_T on the hole concentrations. The respective densities are determined by Shubnikov-de Haas measurements at 1.5 K. In Fig. 2 we show ρ_T as a combined grey tone-contour plot at 2.8 K as a function of the upper and lower hole densities for a coupled 2DHG sample with d = 40 nm. In comparison to coupled 2DEG structures we find a rather broad dependence of ρ_T on the densities in the two layers because of the higher effective mass. We do not observe a peak in ρ_T as a function of only one carrier-density. But if ρ_T is measured as a function of constant total density (dashed line in Fig. 2) the coupling is maximal at matched densities (solid line). This is in agreement with results on coupled 2DEGs. In Fig. 3 we show ρ_T again as function of both carrier densities, but this time for the sample with d = 140 nm. Particularly remarkable is the fact that there is no symmetry in the data if the two densities p_{upper} and p_{lower} are interchanged. At small densities in both layers ($\leq 3 \cdot 10^{11} cm^{-2}$) the maximal coupling strength is found along a "ridge"

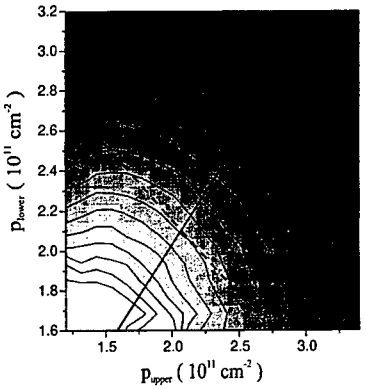

Fig. 2. Contour plot of the transresistivity as function of the carrier-densities in the upper (p_{upper}) and the lower (p_{lower}) 2DHG at $T = 2.8$ K. The barrier-thickness is 40 nm. White areas indicate the strongest (1.5 Ω), the black ones the weakest coupling (450 $m\Omega$). The heavy line runs along equal density $p_{upper} = p_{lower}$. The dashed line runs along constant total density $p_{tot} = p_{upper} + p_{lower}$.

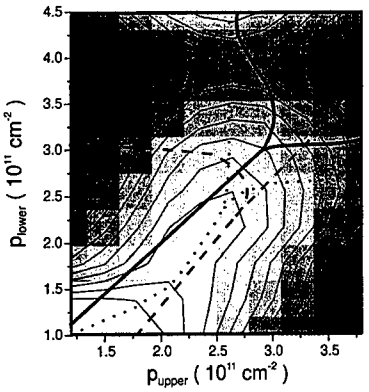

Fig. 3. Contour plot of the transresistivity as function of the carrier-densities in the upper (p_{upper}) and the lower (p_{lower}) 2DHG at $T = 2.8$ K. The barrier-thickness is 140 nm. White areas indicate the strongest (550 $m\Omega$), the black ones the weakest coupling (230 $m\Omega$). The dotted lines run along the "ridges" of maximal ρ_T. The heavy (dashed) lines show the locus of coinciding k_F (v_F) values in equivalent subbands in the two layers.

(marked by heavy dots) running just below the condition of equal densities in the two layers. At higher densities, however, this ridge splits into two which run nearly vertically and horizontally in the figure (also marked by dots). This asymmetry with respect to the densities in the two layer must be a consequence of the asymmetric doping of the two wells because it is also seen in the other asymmetrically doped samples but not in the symetrically doped ones like that of Fig. 2. The asymmetric doping leads to an effective electric field in the respective quantum wells which causes the splitting of the highest hole subband into two. This effect has recently been studied in detail in just one hole layer [6]. The splitting of the subbands automatically leads to different values in the two bands and v_F is no longer proportional to k_F because of the strong nonparabolicity of the dispersion curves. Both quantities are available from the dispersion curves which we calculate using a self-consistent $4 \times 4\,k * p$-method. In Fig. 3 the locus of equal k_F values (full line) and the locus of equal v_F values (dashed line) in the [110]-direction is indicated. We consider only coupling between bands of equal total angular momentum. No agreement with the data is obtained if coupling between bands having different angular momenta is considered, neither for phonons nor for plasmon coupling. If a similar analysis is made for the [100]-direction one finds that the loci for coinciding k_F and v_F values do not differ significantly from those shown in Fig.3. Comparison of the calculations with the data gives a

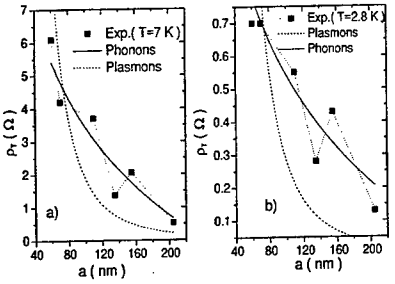

Fig. 4. The transresisistivity ρ_T as a function of distance between two 2DHGs for $T = 7.0$ K (a) and 2.8 K (b), respectively. The carrier density is $3 \cdot 10^{11}$ cm^{-2}. The full line corresponds to the logarhithmic dependence expected for phonon coupling. The dashed line is expected for plasmonic coupling.

better agreement with phonon-coupling, because the locus of equal k_F shows a similar splitting as the experimental maxima.

The coupling between two 2d charge gases depends on the distance between the two layers. Theoretical studies of the interaction via plasmons predict a strong decrease of the transresistivity with distance $\rho_T \propto d_{eff}^{-3}$ [4]. Here d_{eff} is the distance between the wave functions of the respective charge layers. On the other hand, a recent calculation based on the formation of coupled plasmon-phonon modes predicts a weaker decrease according to $\rho_T \propto \ln(l_{ph}/d_{eff})$ with l_{ph} being the mean free path of the phonons propagating in the crystal parallel to the 2d layers [7]. In Fig. 4 we show data of ρ_T for six coupled 2DHG systems for $T = 2.8$ K (Fig. 4a) and $T = 7.0$ K (Fig. 4b) as function of d_{eff} at matched densities of $3 \cdot 10^{11} cm^{-2}$. The fits to the data using the two predicted thickness dependencies show clearly that the logarithmic dependence is a better description.

In conclusion we report the first data of the frictional drag between coupled 2d hole gases. By variation of doping profiles and the application of gate voltages we vary k_F and v_F independently from each other and establish that the coupling mechanism is dominated by phonon coupling at wavevectors $\simeq 2k_F$. We find a logarithmic dependence of the coupling on the distance between the layers which agrees with a theoretical prediction of coupled phonon-plasmon modes.

This work was supported by the German government under the grant BM621/4.

References

[1] A.-P. Jauho, H. Smith, Phys. Rev. B**47**, 4420 (1993).

[2] T.J. Gramila, J.P. Eisenstein, A.H. MacDonald, L.N. Pfeiffer, and K.W. West, Phys. Rev. B **47**, 12957 (1993); H. Rubel, E.H. Linfield, D.A. Ritchie, K.M. Brown, M. Pepper and G.A.C. Jones, Semicond. Sci. Technol. **10**, 1229 (1995).

[3] H. Rubel, A. Fischer, W. Dietsche, K. von Klitzing and K. Eberl, Materials Science & Engineering B **51**, 207 (1998).

[4] K. Flensberg and B.Y.-K. Hu, Phys. Rev. B**52**, 14796 (1995).

[5] N.P.R. Hill, J.T. Nicholls, E.H. Linfield, M. Pepper, D.A. Ritchie, A.R. Hamilton und G.A.C. Jones, Phys.Rev.Lett. **78**, 2204 (1997).

[6] J.P. Lu et al., Phys. Rev. Lett. **81**, 1282 (1998).

[7] M.C. Bønsager, K. Flensberg, B.Y.-K. Hu, and A.H. MacDonald, Phys. Rev. B**57**, 7085 (1998).

Magnetic Field Variation of Tunneling Gap between Disordered Two-Dimensional Electron Systems

Yu.N. Khanin[1], Yu.V. Dubrovskii[1], E.E. Vdovin[1], D.K. Maude[2], J.C. Portal[2,6,7], L.Eaves[3], P.C. Main[3], M. Henini[3], A.K. Geim[4], J.C. Maan[4], and G. Hill[5]
[1] Institute of Microelectronics Technology RAS, 142432 Chernogolovka, Russia
[2] GHMFL, MPI-CNRS, BP166 38042 Grenoble Cedex 9, France
[3] The School of Physics and Astronomy, University of Nottingham, Nottingham NG7 2RD, UK
[4] High Field Magnet Laboratory, Research Institute for Materials, University of Nijmegen, 6525 ED Nijmegen, The Netherlands
[5] Department of Electronic & Electrical Engineering, University of Sheffield, Sheffield S3 3JD, UK
[6] Institut Universitaire de France
[7] INSA, F31077 Toulouse Cedex 4, France

Abstract

We have investigated tunneling between disordered two-dimensional electron systems in a magnetic field parallel to the current. At liquid helium temperatures, the high magnetic field creates a gap in the tunneling density of states that depends linearly on magnetic field. The temperature dependence of the magnetic field variation of the equilibrium tunneling conductance reveals features which could be interpreted as a manifestation of the insulator-quantum Hall-insulator transition.

It was discovered recently that a high magnetic field suppresses equilibrium tunneling between two-dimensional electron systems [1-3] and between 2D and 3D electron systems [4]. These studies were performed on samples with low [2-4] or very low disorder in the 2D electron gas [1]. There is general agreement that the observed suppression is related to in-plane Coulomb correlations between 2D electrons in a high magnetic field. Equilibrium tunneling between strongly disordered electron systems has been studied only for the case of 3D electron systems [5], where a gap in the tunneling density of states in zero magnetic field was reported.

In this work we present tunnel current measurements between two strongly disordered two-dimensional electron systems (2DES) in a magnetic field B parallel to the current. We find that high B suppresses tunneling near zero bias. To form the 2DES we used Si donors sheets (δ-doped layers) with the donor concentration corresponding to insulator behaviour [6,7], i.e. slightly below the metal-insulator transition at zero magnetic field. The typical electron mobility in this kind of 2DES is about $\mu \approx 1000 cm^2 V^{-1} s^{-1}$ at 4.2 K. In our experiments, electron transport along the layers does not contribute to the measured current which flows perpendicular to the plane of the barrier. This allows us to measure the zero-bias conductance which is proportional to the tunneling density of states of the strongly localised 2D electron systems.

The MBE-grown sample was a single barrier GaAs/$Al_{0.4}Ga_{0.6}$As/GaAs heterostructure with a 12 nm thick barrier. The barrier was separated from the highly-doped, bulk contact regions

by 50 nm thick, undoped GaAs spacer layers. Si donors sheets with concentration of $3*10^{11}$ cm^{-2} were located 5 nm from each side of the barrier. The tunneling transparency of the main barrier was much lower than that of the spacer regions, so that most of the applied voltage is dropped across the barrier. Measurements of the Shubnikov-de-Haas (SdH) like oscillations in the tunnel current gave electron sheet concentrations approximately equal to the donor doping levels. Samples were fabricated into mesas of diameter 400 μm. The schematic band diagram of the structure at zero bias is shown in the insert to Fig.1.

Figure 1 shows the differential tunnel conductance G, at 4.2 K, measured using standard lock-in techniques, versus external voltage V_b at various magnetic fields up to 15 T. In zero magnetic field the differential conductance has a peak at zero bias and two pronounced shoulders at higher voltages of both polarities. We argue that the zero voltage peak reflects resonant tunneling between the ground states of the 2DESs, and that the shoulders are due to resonant tunneling between the emitter ground state and extended states in the collector. The observation of a pronounced maximum at zero bias in zero magnetic field indicates that, despite the relatively large number of scattering centres in the 2D layers, the conservation of in-plane momentum is important for the tunnelling process. The evolving structure in the curves with increasing magnetic field reflects resonant tunneling between different Landau levels.

In this work, we concentrate on the equilibrium tunneling processes around zero bias. The tunneling differential conductance at low voltage reflects the joint density of states at the Fermi levels in the 2D electron layers. Around B=6 T, which is close to ν=2 for our sample, experimental $G(V_b)$ curves show (see Fig.1) a pronounced minimum at zero voltage. With a further increase of the magnetic field, the minimum of the differential conductance at zero bias gradually becomes a maximum. For B higher than 8T, a dip at zero bias appears within this maximum, reflecting the gap in the tunneling density of states around the Fermi level of the 2D electron systems. The dip disappears with increasing temperature, as can be seen in Figure 2.

We define the gap parameter Δ_1 as the voltage difference between the maxima of differential conductance (Fig.1b). This choice of gap parameter was also used to characterise suppression of the tunneling current between slightly disordered 2D electron systems [2,3]. We find that Δ_1 is proportional to magnetic field $\Delta_1 = (0.30 \pm 0.01)\hbar\omega_c$ at 4.2 K, where ω_c is the cyclotron frequency.

The temperature variation of G at constant magnetic field (Fig.2) allows an alternative definition of the gap parameter Δ_2. At certain biases, V_1* and V_2*, G is independent of temperature for all magnetic fields from 11 T to 15 T. Similar behaviour of the differential tunneling conductance between 2DESs was reported in reference [2], where the existence of the voltage biases V_1* and V_2* was justified by numerical calculations. The gap parameter Δ_2=V_2*-V_1* is also proportional to magnetic field $\Delta_2 \approx (0.10 \pm 0.01)\hbar\omega_c$. It is difficult to compare values of the gap parameters with current theories because, as far as we know, there are no calculations of the gap dependence on the magnetic field for strongly localised systems. We would like only to emphasise that, perhaps surprisingly, the measured dependence coincides with that found for tunneling between slightly disordered ($\mu \approx 30{,}000 cm^2V^{-1}s^{-1}$) 2D electron systems, $\Delta_1 \approx (0.28 \pm 0.02)\hbar\omega_c$ at 4.2 K [3], and is weaker than that found for 2DES with higher mobility ($\mu \approx 100{,}000 cm^2V^{-1}s^{-1}$), $\Delta_1 \approx (0.44 \pm 0.01)\hbar\omega_c$ [2].

Figure 3 shows the zero-bias (V_b=0) differential conductance G_0 versus magnetic field at different temperatures. The variation of G_0 with temperature, $\partial G_0/\partial T$, had obvious local minima

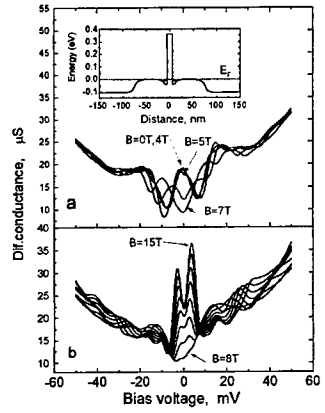

Figure 1. Tunneling differential conductance at 4.2 K as a function of external voltage in different magnetic fields: a) for 0T, 4T, 5T, 6T, and 7T; b) from 8T up to 15T with 1T magnetic field step between the curves. The insert shows a schematic band diagram of the structure at zero bias.

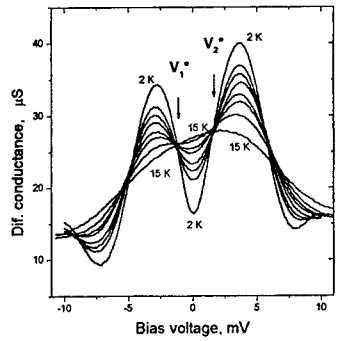

Figure 2. The tunneling differential conductance at B = 15 T as a function of external voltage at different temperatures:2.0K; 4.2K; 5.2K; 6.1K;7.2K; 8.3K; 10.3K; 15K. The differential tunneling conductance G does not depend on temperature at bias voltages V_1* and V_2*.

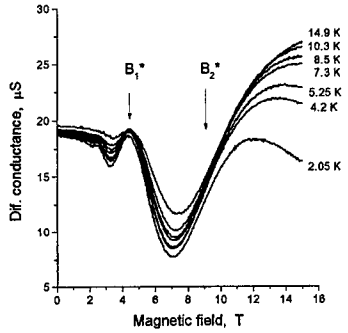

Figure 3. Equilibrium tunneling conductance G_0 as a function of magnetic field at different temperatures. Arrows indicate magnetic fields at which G_0 has weakest temperature dependence.

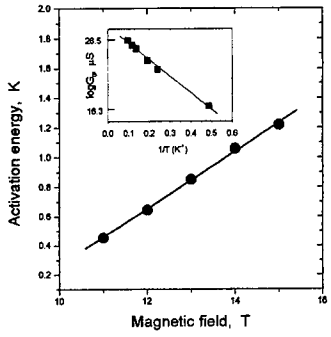

Figure 4. Activation energy E_a as a function of magnetic field. Insert shows Arrhenius plot for magnetic field B=15T.

at B_1* and B_2* marked in Figure 3. We were not able to perform in-plane transport measurements on our samples. However, magnetotransport measurements [7] on 2DES formed by δ-doping with electron concentration $4*10^{11}$ cm^{-2}, slightly above that used in our work, indicate that the 2DES undergoes an insulator quantum Hall (ν=2) state-insulator transition as the magnetic field is increased. The measured dependence of σ_{xx} on magnetic field is similar to that of the equilibrium tunneling conductance dependence $G_0(B)$ measured in this work. Two local minima in $\partial\sigma_{xx}/\partial T$ separate different quantum phases in the 2DES [7]. It is reasonable to assume that the local minima of $\partial G_0/\partial T$ at B_1* and B_2* in Figure 3 also reflect critical points of the insulator - quantum Hall - insulator transition revealed in the tunneling measurements. The dip near zero bias in the $G(V_b)$ curves appears close to B_2* (see Figure 1b). It should be noted here that local currents in the plane of the 2DES might be present, due to the microscopic inhomogeneities in the structure, and these could influence the measured tunneling conductance.

By assuming an activated G_0 we were able to evaluate the corresponding activation energy E_a in magnetic fields from 11T to 15T. The Arrhenius plot at 15T is shown in the insert to Figure 4. The measured conductance variation is not sufficient to establish unambiguously the activated behaviour or to obtain reliable data for E_a. Nevertheless, the magnitude of E_a is linear in magnetic field to a high degree of accuracy. It was found that $E_a(K) = (-1.68 \pm 0.06) + (0.194 \pm 0.005)B(T)$. Unlike the gap parameters Δ_1 and Δ_2, the energy E_a falls to zero at B=8.6 T which is very close to B_2*. At B=13 T we found that $E_a/\Delta_1 \approx 0.011$ and $E_a/\Delta_2 \approx 0.033$. For slightly disordered 2DESs [2] it was found that $E_a/\Delta_1 \approx 0.047$ at B=13 T. We would like to note here only that Δ_1 and Δ_2 are the same order of magnitude as the Coulomb interaction energy in the 2D layers, and that E_a/k_B is comparable to the Mott or Sklovskii-Efros temperatures found from transport studies of strongly localised 2DES in zero magnetic field [8]. We are not aware of any theory which explains the difference between the value of the gap parameters determined from G measurements and the value of the activation energy.

In summary, we have investigated equilibrium tunneling between strongly localised 2D electron systems in a high magnetic field in a structure with pure vertical transport. High magnetic field suppresses equilibrium tunneling, creating a gap in the tunneling density of states which depends linearly on magnetic field.

This work was partly supported by the INTAS (grant 97-11475), RFBR (98-02-17642, 98-02-22008), PICS-CNRS (628), and national program "Physics of the solid state nanostructures" (97-1057).

References

1. J.P.Eisenstein, L.N.Pfeiffer, and K.W.West, Phys.Rev.Lett. 69, 3804 (1992)
2. N.Turner, J.T.Nicholls, E.H.Linfield, et al., Phys. Rev. B 54, 10614 (1996)
3. Yu.V.Dubrovskii, E.E.Vdovin, Yu.N.Khanin, et al., JETP Letters 69, 255 (1999)
4. R.C.Ashoori, J.A.Lebens, N.PBigelov, et al., Phys.Rev. B 48, 4616 (1993)
5. E.L.Wolf, D.L.Losee, D.E. Cullen, et al., Phys.Rev.Lett. 26, 438 (1971)
6. Qiu-Yi Ye, A.Zrenner, F.Koch, and K.Ploog, Semicond. Sci. Technol. 4, 500 (1989)
7. R.J.F.Hughes, J.T.Nicholls, J.E.F.Frost, et al., J.Phys.: Condens. Matter 6, 4763 (1994)
8. S.I.Khondaker, I.S.Shlimak, J.T.Nicholls, et al., Phys. Rev B 59, 4580 (1999)

Intersubband transitions in coupled wells with disorder

C. Metzner, C. Steen, R. Winkler*, M. Hofmann*, M. Hackenberg and G.H. Döhler
Institut für Technische Physik I (III), Universität Erlangen,*
Erwin-Rommel-Str. 1, 91058 Erlangen, Germany,
Tel: +49 9131 852 7282, Fax: +49 9131 852 7293, email: metzner@physik.uni-erlangen.de

Disorder due to doping or interface roughness in quasi-twodimensional systems causes in-plane localization of the electrons and strongly affects their optical properties. We present numerical calculations of intersubband (IS) emission spectra for the case of a doped double-quantum-well, including disorder localization by an exact diagonalization method. It is demonstrated that the inhomogeneous line broadening of the IS peak is then determined by an interplay of correlation-effects in the single-particle spectrum and the spatially indirect nature of the IS inter-well transitions. The resulting line width is larger than in the case of intra-well transitions, but still considerably smaller than the typical fluctuations of the effective random potential. We further show how the energy selective tunneling injection of electrons into the upper subband of a coupled-well structure and the observation of the IS luminescence spectrum can yield valuable information about the physics of localization in multi-subband systems.

PACS: 78.20.Bh, 78.20.-e, 71.23.An
Keywords: Coupled wells, Disorder, Intersubband.

I. INTRODUCTION

Many promising device applications are based on optical IS transitions [1,2]. For functional reasons, most of these structures are (modulation) doped or contain rather narrow wells in their optically active part. Thus they are subject to more or less pronounced disorder effects, which tend to broaden their optical spectra and are thus critical for the device performance.

It has been shown that the IS peak becomes narrower, when dopands are removed from the active part [3,4], or in systems with thicker quantum wells (weaker sensitivity for interface fluctuations) [5]. The remaining line width of about 3-4 meV is often attributed to homogeneous lifetime broadening (determined mainly by optical phonons), which seems to be supported by the Lorentzian shape of the IS line in such high quality samples.

On the other hand, recent theoretical investigations on modulation doped single quantum wells with thin spacer layers (of 2-5 nm) have shown that IS correlation effects (i.e. the subbands fluctuating "in parallel") can lead to narrow IS absorption spectra of only a few meV width, although random potential fluctuations in the 100 meV range prevail in the system [6]. In such a case the electrons become in-plane localized by the disorder and the usual picture of free electron motion parallel to the layers is no longer appropriate. Instead of the k-conserving IS transitions characteristic for the ideal system, the localized electrons are optically excited to specific, "correlated final states" in the higher subband, with a similar lateral structure of the wavefunction. The energy separation between a pair of correlated (i.e. optically coupled) states is usually very close to the subband spacing of the corresponding ideal system without disorder.

However, some important IS devices, especially the quantum cascade laser, use a multi-quantum-well as the active part. When electrons in the ground- and excited subband are localized in different spatial regions (with respect to the growth-direction z), the above mentioned IS correlation effect is expected to be much less important. Therefore, in such systems the disorder should be (to a higher degree) visible in the IS spectrum and lead to a considerably stronger broadening.

To clarify this point, we have investigated theoretically IS emission spectra for the case of a disordered double-well structure, which closely resembles a typical quantum cascade laser. We have acounted for the lateral localization of electron states in the random disorder potential by an exact numerical solution of the quasi-2D multi-subband Schrödinger equation. The optical, spatially indirect tunneling (IS) transitions have then been calculated with Fermi's Golden Rule on the basis of the disordered single-particle states. After describing our model system in the following chapter II, the results of our calculations are reported and discussed in section III of this paper.

II. MODEL SYSTEM

For reasons of clarity, we have chosen a simplified model system, which however containes the physically essential features of a quantum cascade laser. It consists of a "tunneling injector", an asymmetric double-quantum-well (ADW) as the optically active part and a "collector" (compare Fig.1).

Without refering to a specific practical realization of the injector, we assume that it provides a narrow band (width ΔE_i) of electrons, centered around some tunable injection energy E_i. If the tunneling rate to the ADW region is much faster than the typical IS transition rate, we can assume that each localized quantum state, which has some minimum wavefunction overlap with the injector region and which lies within the injection energy intervall, becomes occupied with probability one and is immediately refilled after each 1-0-transition. (Note that elec-

trons are usually injected into the 1-subband only, but due to disorder-induced subband-mixing, such a distinction is not strictly possible any longer.)

The ADW consists of a narrow well (width a_1), providing the upper subband 1 (level ϵ_1), a tunneling barrier (thickness b) and a wider well (width a_0), in which the lower subband 0 (level ϵ_0) is located. The individual transition rate for a given pair of initial- and final states (which will typically descent from the 1- and 0-subband, respectively), depends on the lateral overlap of the localized in-plane wavefunctions.

The collector is assumed to remove the electrons after their 1-0 transition efficiently from the active part, so that in the emission mode the ground subband 0 can be considered un-occupied.

In our simple model system, impurity disorder is simulated by a compensated "co-doping" δ-layer, i.e. charged donors (positive) and acceptors (negative) of equal sheet concentration $N_D^{(2)}$, which are distributed randomly within a single monolayer at z-position z_D. Such a macroscopically neutral co-doping layer produces potential fluctuations with a statistics similar to ordinary δ–layers, but it is free of band-bending effects in the average conduction band z-profile (Fig.1). Thus, for theoretical investigations, this concept is advantageous, because the co-doping layer can be placed at different z–positions in the structure, without changing the fundamental subband quantization of the system.

Since in practical situations the narrow 1-well is subject to the strongest disorder, we have placed the co-doping-layer either in the center of this well ("center doped" case *C* below), or further to it's left side with a spacer layer thickness d ("modulation doped" case *M*).

In addition, we have assumed that the average electron density in the ADW region is small enough to neglect electron-electron interactions (Note that an accurate modelling of the electron density distribution would be non-trivial for the non-equilibrium system in the stationary emission mode). This allowed us to compute the subband-structure of the ideal system (for a given electrical field strength F) once and for all. The localized quantum states in the corresponding disordered system have then been expanded with respect to these subband states in the z-direction and in terms of plane waves in the lateral directions. The details of the method have already been published [6,7] and will not be repeated here.

III. RESULTS AND DISCUSSION

In our calculations we used an effective electron mass of $m_w^* = 0.041\, m_0$ (well) and $m_b^* = 0.075\, m_0$ (barrier) and a barrier height of $V_b = 492.5$ meV. The design parameters of the simulated structure were as follows: Well widths $a_1 = 1.1$ nm, $a_0 = 3.7$ nm and tunneling barrier $b = 3.7$ nm. The electric field was fixed to $F = 45$ kV/cm.

In the ideal system (without co-doping), this would yield subband egdes at $\epsilon_0 = 179.9$ meV and $\epsilon_1 = 433.5$ meV (using the energy axis defined in Fig.1), i.e. a transition energy of $\hbar\omega_{id} = \epsilon_1 - \epsilon_0 = 253.6$ meV.

For simulating disorder we used a co-doping density of $N_D^{(2)} = 2.0{\cdot}10^{12}$ cm^{-2}. In the modulation doped case, the spacer layer thickness was set to $d = 5$ nm (comp. Fig.1). The band width of the tunneling-injected electrons was assumed as $\Delta E_i = 5$ meV.

Fig.2 shows the density of states (DOS) of the ideal (I), the modulation doped (M) and the center doped (C) system in the natural units of $m^*/\pi\hbar^2$. The arrows indicate the three injection energies at $E_a = \epsilon_1 - 30$ meV, $E_b = \epsilon_1$ and $E_c = \epsilon_1 + 30$ meV. Without disorder (I), one obtaines of course a step-like DOS with the two subband edges located at energies ϵ_0 and ϵ_1. The modulation doped system shows already a strong (and asymmetric) DOS broadening of about 40 meV and 90 meV, for the 0- and 1-subband, respectively (Here, the broadening was defined as the energy intervall, in which the DOS rises from 0.1 to 0.9 of its final value). As could have been expected, the 1-electrons experience stronger disorder effects due to their closer proximity to the doping layer. In the case C, the DOS-broadening, which is a direct measure of the potential fluctuations, increases to 80 meV and 180 meV, respectively.

We now turn to the emission spectra as a function of the electron injection energy (three cases a,b,c), shown in Fig.3 and Fig.4 for the M- and C-system, respectively. In the ideal system one would obtain here a δ–peak at $\hbar\omega_{id}$, independent from the injection energy and band width, as far as nonparabolicity effects and the homogeneous linewidth are neglected. Including the potential fluctuations we obtain IS emission peaks with widths in the range of 10 meV (M-system, weak disorder) and 25 meV (C-system, strong disorder), which has to be compared with the 1-subband DOS broadening of 90 meV (M-system) and 180 meV (C-system). This demonstrates again the importance of the IS correlation effects. On the other hand, for single quantum wells of similar width and spacer layer thickness, we obtained considerably narrower lines of less than 5 meV width. We attribute the increased peak width in our ADW to the suppression of the correlation effects due to the spatialy indirect transition. It should also be noted that our calculated IS spectra are asymmetric with a pronounced low energy tail and fit neither to a Lorentzian, nor a Gaussian. The most striking feature is, however, the dependence on the injection energy.

For both the weakly (M) and strongly (C) disordered system, the peak photon energy of the emission spectrum is clearly red shifted with respect to the IS line position $\hbar\omega_{id}$ of the ideal system. With increasing injection energy, this red shift becomes smaller, with the peak finally approaching the ideal value.

Insight into this effect can be gained by following the continuous transformation of the energy spectrum of electron states as a function of disorder strength, assuming

(for easier explanantion) perfect IS correlations (each 0-state being optically coupled to only one specific 1-state) during the whole process. Let us consider the evolution of some specific energy intervall of 0-subband states, together with the correlated intervall in the 1-subband. For zero disorder (plane wave states, $\vec{k}$-conservation rule), the two correlated intervalls have the same width and a separation of exactely $\epsilon_1 - \epsilon_0$. When the disorder is now gradually "turned on", the DOS of the system will become increasingly broadened. Embedded into the flow of energy levels, our two intervalls of interest will be displaced and deformed to a certain degree, depending on their original position on the energy axis. There will be an overall flow of levels from the high energy region of the DOS to the tail states, most pronounced in the energetic vicinity of the original subband edges ϵ_m and becoming smaller with increasing kinetic energy. Thus, our "marked" intervalls will also become red shifted and streched during the transformation from the ideal to the strongly disordered system.

If the disorder would act on both subbands in exactely the same way, the correlated intervalls would evolve "in parallel", leaving the transition photon energies $\hbar\omega = \hbar\omega_{id}$ invariant. In our ADW model structure, however, the 1-subband is influenced much stronger by the potential fluctuations. Correspondingly, the red shift and streching of the 1-intervall is faster than that of the 0-subband. This leads to a red shift of the 1-0-transition photon energies compared to the ideal value $\hbar\omega_{id}$ and a broadening of the IS line. In the final state of the transformation (corresponding to the true situation), the red shift of the emitted photons will be most pronounced, if the electron is injected into the tail region of the 1-subband. This is actually the behaviour we find in our simulation. We have confirmed this explanation by placing the doping-layer on the right side of the ADW structure. In this case, the 0-subband is stronger broadened and the observed IS peak is then indeed blue shifted relative to $\hbar\omega_{id}$.

It is interesting to note that in the experiments published for similar systems in Ref. [4], some of the above mentioned effects have been observed at least qualitatively, as for example the red shift of the IS peak with increasing disorder, or the slightly more pronounced low energy tail of the spectrum. In the measured sample, the amount of additional broadening due to charged donors was (with about 20 meV) comparable to our model system, although the distribution of dopands was different (3D volume doping with setback).

We thus conclude that the detailed, spatial distribution of potential fluctuations plays a crucial role in the physics of IS linebroadening. The investigation of IS emission spectra in disordered ADW structures could strongly contribute to an understanding of the broadening mechanism. Especially, the possibility of energy selective injection of electrons into the upper subband would yield direct information about the correlation effects in the single particle spectrum. For a practical realization of such an experiment, it may be favourable to inject the electrons not by tunneling, but optically via interband excitation from the valence band.

IV. ACKNOWLEDGEMENTS

One of the authors (C.M.) would like to thank the Deutsche Forschungsgemeinschaft DFG for financial support.

[1] B. Levine, K. Choi, C. Bethea, J. Walker and R. Malik, Appl. Phys. Lett. **50**, 1092 (1987).
[2] J. Faist, F. Capasso, L. Sivco, C. Sirtori, A. Hutchinson and A. Cho, Science **264**, 553 (1994).
[3] E.B. Dupont, D. Delacourt, D. Papillon, J.P. Schnell and M. Papuchon, Appl. Phys. Lett. **60**(17), 2121 (1992).
[4] J. Faist, C. Sirtori, F. Capasso, L. Pfeiffer and K.W. West, Appl. Phys. Lett. **64**(7), 872 (1994).
[5] K.L. Campman, H. Schmidt, A. Imamoglu and A.C. Gossard, Appl. Phys. Lett. **69**(17), 2554 (1996).
[6] C. Metzner, M. Hofmann and G.H. Döhler, Phys. Rev. B **58**, 7188 (1998).
[7] C. Metzner, M. Hofmann and G.H. Döhler, Superlattices and Microstructures **25**, 239 (1999).

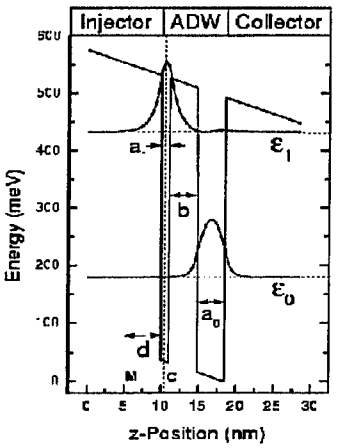

FIG. 1. Conduction band edge diagram and subband states of our model system.

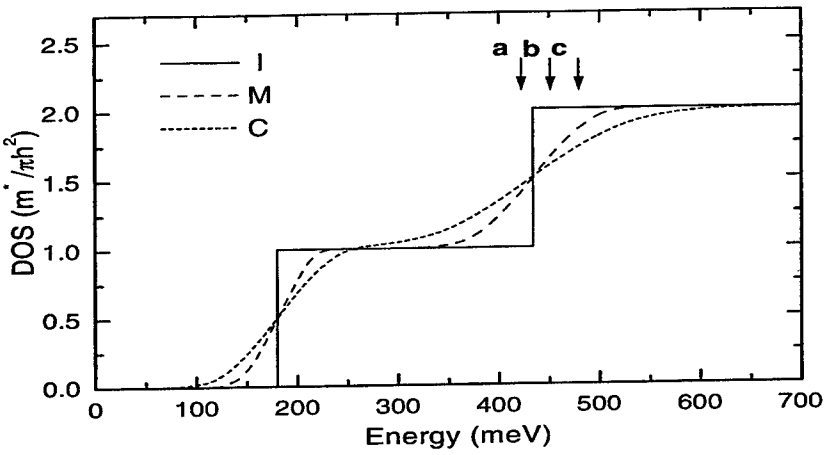

FIG.2. Density of states (DOS) of the ideal (I), the modulation doped (M) and the center doped (C) system. The arrows denote the injection energies of the electrons in the upper subband (three cases a,b,c).

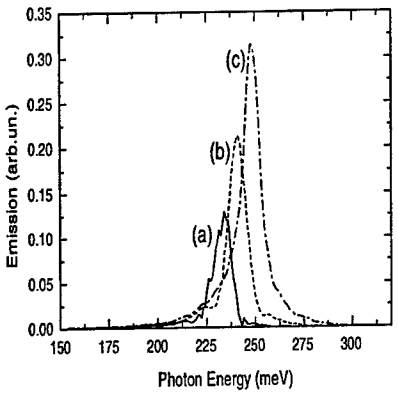

FIG.3. IS-emission spectra of the modulation doped system (M), for the three different injection energies a,b,c.

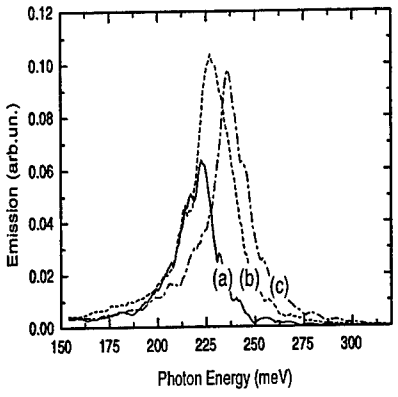

FIG.4. IS-emission spectra of the center doped system (C), for the three different injection energies a,b,c.

Interlayer Correlation Effects in Frictional Drag of Carriers in Coupled Quantum Wells

Ben Yu-Kuang Hu
Department of Physics, University of Akron, Akron, OH 44325-4001, U.S.A.

Abstract

Interlayer correlations can significantly affect the Coulomb drag signal in coupled quantum wells. Using the T-matrix approximation, I consider the Maki-Thompson interlayer correlation effects on the drag rate. The strong interlayer coupling modifies the temperature behavior of the drag rate from the standard weak-coupling T^2 result to a more complicated and non-monotonic temperature dependence.

Pacs: 72.20.-i, 74.10.+v
Keywords: Coulomb drag, double quantum well, electron–hole condensation

Recently, experimentalists studying the physical properties of two-dimensional electronic systems have added yet another technique to their arsenal; *i.e.*, frictional drag in coupled quantum wells [1]. In these drag experiments, a pair of doped quantum wells are placed in close together (typically tens of nanometers apart), separated by a potential barrier wide enough to prevent significant tunneling between the wells yet thin enough to permit substantial interlayer interaction. Contacts are attached to each well separately, resulting in two independently contacted two-dimensional electron gases (2DEGs) which interact strongly with each other. Current is then drawn through one of the layers. The interlayer interactions produce a net momentum transfer from one layer to the other, resulting in a friction-like force which opposes the relative motion of the electrons in the separated layers; *i.e.*, the electrons on one layer appear to drag those in the other. The magnitude and direction of this frictional drag force provide vital clues about the properties of the 2DEGs and the effective interlayer forces.

The drag rate is quantified by the transresistivity ρ_{21}, defined by $\rho_{21} = J_1/E_2$ where $\mathbf{J}_1$ is the current density in the driven layer (hereafter designated layer 1) and $\mathbf{E}_2$ is the electric field which is built up in the neighboring layer (layer 2) when it is kept as an open circuit. (In this paper, I assume the isotropic systems in the absence of magnetic fields, where J_1 and E_2 are parallel by symmetry.) Experimental activity in this area has been and continues to be vigorous [2–4].

In the earlier drag experiments (*e.g.*, Refs. [2]) the interlayer coupling between the electrons in neighboring wells was weak, and hence theories which treated interlayer interaction at the Born approximation level were adequate. One incontrovertible consequence of this weak-coupling theory is that $\rho_{21} \to 0$ as the temperature $T \to 0$, due to vanishing scattering phase space. Recently, however, one experiment [4] reported a ρ_{21} which seemed not to vanish as $T \to 0$. If these experimental results are accurate, then the weak interlayer coupling theory is clearly insufficient, and an extension to the strong-coupling regime is necessary. In

this paper, I outline the formalism of drag in the strong-coupling regime within the T-matrix approximation, and address possible experimental consequences of this theory.

The model Hamiltonian I use to describe the system is

$$\hat{H} = \sum_{i=1,2} \sum_{\mathbf{k}\sigma} \epsilon_i(\mathbf{k})\, \hat{c}^{\dagger}_{i,\mathbf{k}\sigma}\, \hat{c}_{i,\mathbf{k}\sigma} + \sum_{\mathbf{q}} \hat{\rho}_1(\mathbf{q})\, \hat{\rho}_2(-\mathbf{q})\, U(\mathbf{q}) + \hat{H}_{\rm imp}, \tag{1}$$

where $\hat{c}^{(\dagger)}_i$ are the field operators of layer i, $\mathbf{k}$ is the momentum, $\epsilon_i(\mathbf{k})$ is the kinetic energy, σ is the spin index, $\hat{\rho}_i(\mathbf{q})$ is the the density operator, $U(\mathbf{q})$ is the interlayer interaction, and $\hat{H}_{\rm imp}$ is the disorder term. The disorder is assumed to be caused by non-correlated δ-function static impurities. To calculate ρ_{21}, I utilize the Kubo formalism using thermal Matsubara Green functions. This formalism gives a formal expression for the *transconductivity* $\sigma_{21} = J_2/E_1$ in terms of the current–current correlation function [5,6]

$$\sigma_{21}(\omega) = -\frac{i}{\mathcal{A}\omega}\left[\lim_{i\Omega_n \to \omega + i0^+} \int_0^{1/T} d\tau\ \exp(i\Omega_n \tau)\, \langle \hat{j}_{2,x}(-i\tau)\, \hat{j}_{1,x}(0)\rangle\right]. \tag{2}$$

Here, $\hat{j}_i(t)$, e_i, m_i are the i-th layer Heisenberg current operator, charge and effective mass, respectively, $\mathcal{A}$ is the area of the system, Ω_n is a Matsubara boson frequency, and $\langle \cdots \rangle$ denotes thermal averaging. Note $\hbar, k_B = 1$ in this paper. Under normal circumstances $|\sigma_{12}| \ll \sigma_{11}, \sigma_{22}$; then the transresistivity is given by $\rho_{21} \approx -\sigma_{21}/(\sigma_{11}\sigma_{22})$.

The current–current correlation in Eq. (2) can be evaluated by standard techniques. When the interlayer coupling is weak, σ_{21} is adequately described by expanding the correlation function in powers of the interlayer coupling and evaluating the lowest non-vanishing (*i.e.*, second) order term [6,7]. The physics described at this order is the Born approximation scattering of excitations in the neighboring layers; interlayer correlations are completely neglected. Since the number of excitations goes to zero as the temperature goes to zero, the lowest order approximation invariably leads to $\rho_{21} = 0$ at $T = 0$.

The experiment [4] which contradicted this weak-coupling result was done at very high magnetic fields, where the occupation of the lowest spin-split Landau level was $\nu = 1/2$. There are two flux quanta per electron at this filling fraction, and it is widely believed that the magnetic flux lines bind to the electrons and make them behave like "composite fermions" with a renormalized mass [8]. The non-zero ρ_{21} as $T \to 0$ suggests that the composite fermions in the neighboring layers are correlated, and that the theoretical description must go beyond the Born approximation.

Ussishkin and Stern [9] theoretically investigated composite fermion drag by considering the so-called Asmalazov-Larkin diagrams. These terms correspond physically to the drag enhancement due to pairing fluctuations occurring above the predicted (but still not observed) critical temperature T_c at which there is a phase transition to a paired state [10]. Maki and Thompson [11] found that in clean superconducting systems a different set of terms gave a bigger fluctuation contribution to the conductance when $T > T_c$. In the context of drag, a clean system would correspond to an ultra-pure high mobility coupled electron–hole system. It has been postulated that at low enough temperatures, a transition to a superfluid or exciton-condensate state develops [12]. While the drag signature below the transition temperature has been studied theoretically [13], the effect of pairing fluctuations on ρ_{21} above the transition temperature has not yet been examined. In the case of drag transconductivity,

the Feynman diagrams corresponding to the Maki-Thompson diagrams are shown in Fig. 1. The interlayer correlations are contained within the T-matrix, as it describes the pairing which ultimately leads to a phase transition at low enough temperatures. The T_{pp} and T_{ph} correspond to the particle–particle (pp) and and particle-hole (ph) channels, respectively. In this work, T_{pp} and T_{ph} are evaluated using the Bethe-Salpeter equation.

The current–current correlation function Eq. (2) can be evaluated using standard diagrammatic rules. The resulting general expression is rather unwieldy. It can be simplified by (1) using the assumption that the scattering in the individual layers is small, so only terms which contain the lifetime τ_i of the particles in layer i are kept; (2) utilizing the generalized optical theorem [14] to rewrite $\mathrm{Im}[T_{pp}]$ and $\mathrm{Im}[T_{ph}]$ in terms of $\mathbf{q}$-integrals over $|T_{pp}|^2$ and $|T_{ph}|^2$. The final result, after simplification, is

$$\rho_{21} = \frac{32\pi^3 m_1 m_2}{e_1 e_2 k_{F,1}^2 k_{F,2}^2 T} \int \frac{d\mathbf{k}_1}{(2\pi)^2} \int \frac{d\mathbf{k}_2}{(2\pi)^2} \int \frac{d\mathbf{q}}{(2\pi)^2} v_{1,x}(\mathbf{k}_1)\, v_{2,x}(\mathbf{k}_2)$$
$$\Big\{ n_F(\xi_{\mathbf{k}_1})\, n_F(\xi_{\mathbf{k}_2})\, n_F(-\xi_{\mathbf{k}_1+\mathbf{q}})\, n_F(-\xi_{\mathbf{k}_2-\mathbf{q}}) |\langle \mathbf{k}_{pp}|T_{pp}(\mathbf{P}_{pp};\xi_{\mathbf{k}_1}+\xi_{\mathbf{k}_2})|\mathbf{k}_{pp}+\mathbf{q}\rangle|^2$$
$$\delta\Big(\xi_{\mathbf{k}_1}+\xi_{\mathbf{k}_2}-\xi_{\mathbf{k}_1+\mathbf{q}}-\xi_{\mathbf{k}_2-\mathbf{q}}\Big) - n_F(\xi_{\mathbf{k}_1})\, n_F(-\xi_{\mathbf{k}_2})\, n_F(-\xi_{\mathbf{k}_1+\mathbf{q}})\, n_F(\xi_{\mathbf{k}_2+\mathbf{q}})$$
$$|\langle \mathbf{k}_{ph}|T_{ph}(\mathbf{P}_{ph};\xi_{\mathbf{k}_1}-\xi_{\mathbf{k}_2})|\mathbf{k}_{ph}+\mathbf{q}\rangle|^2\, \delta\Big(\xi_{\mathbf{k}_1}-\xi_{\mathbf{k}_2}-\{\xi_{\mathbf{k}_1+\mathbf{q}}-\xi_{\mathbf{k}_2+\mathbf{q}}\}\Big)\Big\}, \qquad (3)$$

where v_x is the x-component of the velocity, n_F is the Fermi distribution function $\xi_{i,\mathbf{k}}$ is the energy relative to the chemical potential in layer i, $\mathbf{P}_{\substack{pp\\ph}} = \mathbf{k}_1 \pm \mathbf{k}_2$ and $\mathbf{k}_{\substack{pp\\ph}} = (m_2\mathbf{k}_1 \mp m_1\mathbf{k}_2)/(m_1+m_2)$.

The above result can be interpreted to some extent within the semiclassical Boltzmann picture. The integral over $\mathbf{q}$ corresponds to the sum of all possible momentum transfers between carriers in layer 1 and 2. The term containing $|T_{pp}|^2$ ($|T_{ph}|^2$) can be interpreted as the contribution of momentum exchange from a particle in state $\mathbf{k}_1$ scattering off a particle (hole) in state $\mathbf{k}_2$. In the limit where the interlayer coupling is weak, the T-matrices approach the Born approximation result, $\langle \mathbf{k}_{pp}|T_{pp}(\mathbf{P}_{pp};\omega)|\mathbf{k}_{pp}+\mathbf{q}\rangle = \langle \mathbf{k}_{ph}|T_{ph}(\mathbf{P}_{ph};\omega)|\mathbf{k}_{ph}+\mathbf{q}\rangle = U(q,\omega)$, and the standard weak-coupling result [6,7] is regained.

Eq. (3) shows that the low-temperature transresistivity depends crucially on the temperature dependence of the T-matrix. If either T_{pp} or T_{ph} develops a precursor of a singularity as the temperature $T \to T_c^+$, the magnitude of ρ_{21} would increase with decreasing temperature, in contrast with the standard weak-coupling result. In a conventional superconductor $|T_{pp}(\mathbf{P}_{pp}=0)|$ diverges as $T \to T_c^+$ due to the attractive phonon-mediated interaction. In coupled electron-hole bilayers with coinciding Fermi surfaces, the attractive Coulomb interaction could lead to an analogous exciton or a superfluid transition [12]. However, no experimental signature of this transition has ever been observed. This suggests the interesting possibility that drag can be used to seek out this phase transition in coupled electron–hole systems. An increasing ρ_{21} with decreasing T indicates the possibility that a phase transition occurs when the temperature is further lowered.

This work was initiated at Mikroelektronik Centret in Danmarks Tekniske Universitet. I thank K. Flensberg and A.-P. Jauho for useful discussions.

REFERENCES

[1] For a review, see A. G. Rojo, J. Phys.: Condens. Matter **11**, R31, 1999.

[2] T. J. Gramila *et al.*, Phys. Rev. Lett. **66**, 1216 (1991); U. Sivan, P. M. slomon, and H. Shtrikman, Phys. Rev. Lett. **68**, 1196 (1992).

[3] A partial list includes H. Rubel *et al.*, Phys. Rev. Lett **78**, 1763 (1997); N. P. R. Hill *et al.*, Phys. Rev. Lett. **78**, 2204 (1997); N. K. Patel *et al.*, Semicond. Sci. Technol. **12**, 309 (1997); X. G. Feng *et al.*, Phys. Rev. Lett. **81**, 3219 (1998); H. Noh *et al.*, Phys. Rev. B **58**, 12621 (1998).

[4] M. P. Lilly *et al.*, Phys. Rev. Lett. **80**, 1714 (1998);

[5] See, *e.g.*, Gerald D. Mahan, *Many-Particle Physics*, 2nd ed. (Plenum, New York, 1990).

[6] K. Flensberg *et al.*, Phys. Rev. B **52**, 14761 (1995); L. Zheng and A. H. MacDonald, Phys. Rev. B **48**, 8203 (1993); A. Kamanev and Y. Oreg, Phys. Rev. B **52**, 7516 (1995).

[7] A.-P. Jauho and H. Smith, Phys. Rev. B **47**, 4420 (1993); K. Flensberg, B. Y.-K. Hu, Phys. Rev. B **52**, 14796 (1995); M. C. Bønsager *et al.*, Phys. Rev. B **56**, 10316 (1997).

[8] For a review of composite fermions, see *e.g.*, *Perspectives in Quantum Hall Effects*, edited by S. Das Sarma and A. Pinczuk (Wiley, New York, 1997).

[9] I. Ussishkin and A. Stern, Phys. Rev. Lett **81**, 3932 (1998).

[10] N. E. Bonesteel, I. A. McDonald, and C. Nayak, Phys. Rev. Lett. **77**, 3009 (1996).

[11] K. Maki, Prog. Theor. Phys. (Kyoto) **39**, 897 (1968); **40**, 193 (1968); R. S. Thompson, Phys. Rev. B **1**, 327 (1970).

[12] See *e.g.*, X. Zhu *et al.*, Phys. Rev. Lett. **74**, 1633 (1995), and references therein.

[13] G. Vignale and A. H. MacDonald, Phys. Rev. Lett. **76**, 2786 (1996).

[14] L. Kadanoff and G. Baym, *Quantum Statistical Mechanics* (Benjamin, New York, 1962).

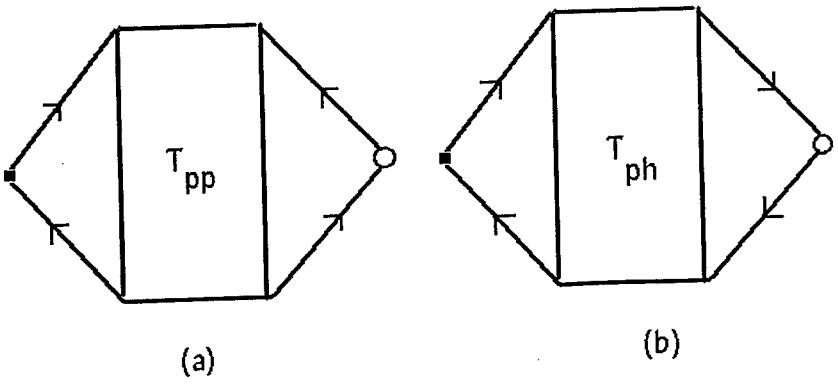

FIG. 1. Feynman diagrams corresponding to the Maki-Thompson contribution to the transconductivity: (a) particle–particle and (b) particle–hole scattering channels. The arrowed lines are the particle Green functions. The black square and the open circle indicate the current vertices in the first and second layers, respectively.

BILAYER $\nu = 2$ QUANTUM HALL STATE IN PARALLEL HIGH MAGNETIC FIELD

A. Sawada[a], Z.F. Ezawa[a], H. Ohno[b], Y. Horikoshi[b], N. Kumada[a], Y. Ohno[b], S. Kishimoto[b], F. Matsukura[b], and S. Nagahama[a]

[a] *Department of Physics, Tohoku University, Sendai 980-8578, Japan*
[b] *Research Institute of Electrical Communication, Tohoku University, Sendai 980-8577, Japan*
[b] *School of Science and Engineering, Waseda University , Tokyo 169-8555, Japan*

Received

Abstract

By tilting the sample as well as by varying density difference between the two layers, we have measured the activation energy of a bilayer quantum Hall state as a function of the total magnetic field. Let Θ be the tilt angle. When the densities are balanced, the activation energy begins to increase linearly beyond a certain critical angle Θ^* as the total magnetic field increases. The slope of the curve is $5.6|g^*|\mu_B$, from which we conclude that a skyrmion pair with spin 5.6 is excited. On the other hand, as the density difference increases, the activation energy decreases rapidly and eventually disappeares. These results imply that the bilayer QH state is not a coherent state but rather a compound state beyond the critical angle ($\Theta > \Theta^*$).

PACS: 73.40.Hm, 73.20.Dx, 73.40.Kp, 72.20.My

Keywords: Quantum Hall effect, Activation energy, Skyrmion, Zeeman energy

1. Introduction

The quantum Hall effect in double quantum wells has attracted much attention, where the structure introduces an additional degree of freedom in the third direction. Various bilayer quantum Hall (BLQH) states are realized [1, 2] by controlling system parameters such as the strengths of the interlayer and intralayer Coulomb interactions, the tunneling interaction and the Zeeman effect. It is an intriguing problem whether an interlayer coherence develops spontaneously in BLQH systems [3, 4]. Such a coherence is known to develop in the $\nu = 1$ BLQH state [5]. The $\nu = 2$ BLQH state is by far interesting, since it has been revealed experimentally to possess a richer phase diagram [6, 7, 8, 9]. See also Ref.[10].

In this paper we make a further study of the $\nu = 2$ BLQH state. In a previous work [6] we have discovered experimentally the compound state made of two isolated monolayer $\nu = 1$ states and the interlayer coherent state made of interacting electrons between the layers. Furthermore, as the sample is tilted in the magnetic field, we have

found [7] that the coherent state yields a phase transition at a certain critical angle Θ^*, which looks very much like the commensurate-incommensurate phase transition [11] originally discovered at $\nu = 1$ [5]. Based on this similarity we have suggensted a possibility that the phase transion at $\nu = 2$ has the same origin. However, a difference is readily noticed between the $\nu = 1$ state and the $\nu = 2$ state with respect to the behaviors of the Hall-plateau width as a function of Θ for its large value (Fig. 1). In this paper we have measured the activation energy carefully in the region $\Theta > \Theta^*$ to elucidate the nature of the phase transition at Θ^* in the $\nu = 2$ BLQH state.

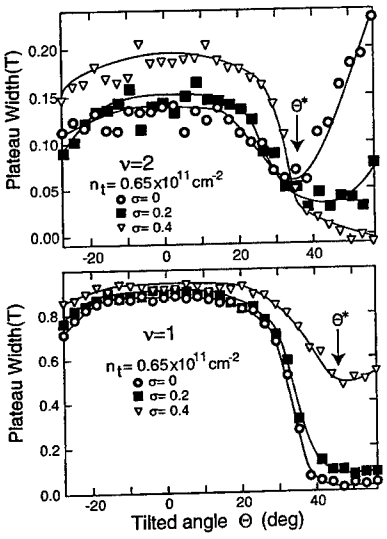

Fig. 1. The Hall-plateau width of the $\nu = 1$ and $\nu = 2$ state at 50 mK and $n_t = 0.65 \times 10\,\mathrm{cm}^{-2}$ as a function of Θ at various density difference σ. The plateau width is defined [12] with respect to the perpendicular field $B_\perp$.

2. Experimental results

The sample was grown by molecular beam epitaxy on a (100)-oriented GaAs substrate, and consists of two modulation doped GaAs quantum wells of width $W = 200$ Å, separated by an $Al_{0.3}Ga_{0.7}$-As barrier of thickness $d_B = 31$ Å. The total electron density n_t of this sample was 2.3×10^{11} cm^{-2} at zero gate voltage, the mobility was 3.0×10^5 cm^2-/Vs at temperature $T = 30$ mK, and the tunneling-energy gap Δ_{SAS} was 6.8 K. The Schottky gate electrodes were fabricated on both front and back surfaces of the sample so that the front-layer (n_f) and the back-layer electron density (n_b) can be independently controlled by adjusting the front (V_{fg}) and the back gate voltage (V_{bg}).

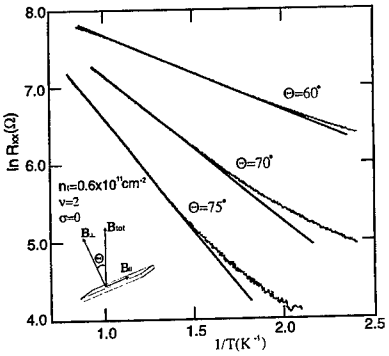

Fig. 2. Arrhenius plots of the longitudinal resistance R_{xx} at filling factor $\nu = 2$ ($B_\perp = 1.2$ T). The data sets are recorded for tilt angles $\Theta = 60°$, $\Theta = 70°$ and $\Theta = 75°$. The experimental geometry is shown in the inset.

Measurements were performed with the sample mounted in a mixing chamber of a dilution refrigerator. The magnetic field with maximum 13.5 T was applied to the sample. Standard low-frequency ac lock-in techniques were used with currents less than 100 nA to avoid heating effects.

The sample mounted on a goniometer with the superconducting stepper motor [13] can be rotated into any direction in the magnetic field.

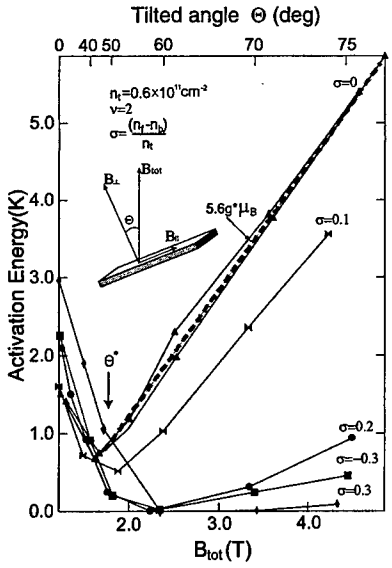

Fig. 3. Results of tilted-field experiments on the $\nu = 2$ QHE. The activation energy gaps Δ at fixed $B_\perp$ are plotted vs the total magnetic field. Each data set starts with $\Theta = 0$ and $B_{tot} = B_\perp$ at the lower left. From top to bottom density differences σ are 0, 0.1, 0.2, $\pm$0.3, respectivly. The data points of the density diference $\sigma = 0$ between first-run to second-run are consistent, whose sloop is $5.6|g^*|\mu_B$.

We have measured the activation energy of the $\nu = 2$ BLQH state as a function of the total magnetic field B_{tot} by tilting the sample and by varying the density difference. Figure 2 shows typical temperature dependences of the longitudinal resistance R_{xx} in the balanced configuration ($\sigma = 0$) at various tilt angles with the perpendicular field $B_\perp$ fixed. The $\sigma = (n_f - n_b)/n_t$ is normalized density difference.

The activation energy Δ is derived from the temperature dependence of the longitudinal resistance; $R_{xx} = R_0 \exp(-\Delta/2T)$. In Fig. 3 we give the activation energy as a function of the total magnetic field B_{tot} by tilting the sample, where the filling factor of the state is fixed ($\nu = 2$). At any density difference the activation energy has a peak at $\Theta = 0$, and drops rapidly to a certain critical angle Θ^*. This rapid decrease, found originally [5] at $\nu = 1$ and found previously [6] at $\nu = 2$, may be regarded as a proof of the interlayer coherence.

A prominent feature revealed in Fig.3 is that, when the densities are balanced ($\sigma = 0$), the activation energy begins to increase linearly beyond the critical point Θ^* as the total field increases. This increase will be due to the increase of the Zeeman energy of a quasipariclе pair. Then, the activation energy is written as:

$$\Delta = \Delta_{0,s}(B_\perp) + 2N_{spin}|g^*|\mu_B B_{tot}, \qquad (1)$$

with N_{spin} the spin of one quasiparticle. Here, $\Delta_{0,s}$ is the contribution to the gap arising from all non-Zeeman sources and depends only upon the perpendicular magnetic field $B_\perp$; g^* and μ_B are the gyromagnetic ratio and the Bohr magneton, respectively, with $g^* = -0.46$ in GaAs[14]. The slope of the curve is $5.6|g^*|\mu_B$, from which we obtain $N_{spin} = 2.8$. This is the spin of one skyrmion, though it is slightly smaller than the spin of a skyrmion excitation in the monolayer $\nu = 1$ state [15].

Another important feasure found in Fig.3 is that the activation energy decreases rapidly as the density difference (σn_t) increases and eventually disappeares beyond $\sigma = 0.3$. This is a typical signal that that there is no interlayer coherence in the state for $\Theta > \Theta^*$. The state must be a compound state.

Our experimental results are summarized as follows. Provided the total density is small enough, the interlayer coherence may develop in the $\nu = 2$ BLQH state, but it is lost beyond the critical angle Θ^* when the sample is tilted. The phase transition is presumably from the commensurate coherent phase to the compound phase. Such a transition is induced because the one-body tun-

neling interaction decreases as the sample is tilted. However, it is an open question why the spin of a skyrmion is relatively small, $N_{\rm spin} = 2.8$ around $B = 3$ Tesla.

Acknowledgement

We thank T. Saku (NTT) for growing the sample used in the present work. Part of this work was done at Laboratory for Electronic Intelligent Systems, RIEC, Tohoku University. The research was supported in part by Grant-in-Aids for the Scientific Research from the Ministry of Education, Science, Sports and Culture (11304019, 09244103, 10138203), and by the Asahi Glass Foundation.

References

[1] G.S. Boebinger, H.W. Jiang, L.N. Pfeiffer and K.W. West, Phys. Rev. Lett. **64**, 1793 (1990).

[2] Y.W. Suen, L.W. Engel, M.B. Santos, M.Shayegan, and D.C. Tsui, Phys. Rev. Lett. **68**, 1379 (1992); J.P. Eisenstein, G.S. Boebinger, L.N. Pfeiffer, K.W. West and Song He, Phys. Rev. Lett. **68**, 1383 (1992).

[3] Z. F. Ezawa and A. Iwazaki, Int. J. Mod. Phys. B **6**, 3205 (1992); *ibid.* **8**, 2111 (1994); Phys. Rev. B **47**, 7295 (1993); *ibid.* **48**, 15189 (1993).

[4] Z. F. Ezawa, Phys. Rev. B **51**, 11152 (1995); *ibid.* **55**, 7771 (1997).

[5] S.Q. Murphy, J.P. Eisenstein, G.S. Boebinger, L.N. Pfeiffer and K.W. West, Phys. Rev. Lett. **72**, 728 (1994).

[6] A. Sawada, Z.F. Ezawa, H. Ohno, Y. Horikoshi, Y. Ohno, S. Kishimoto, F. Matsukura, M. Yasumoto, and A. Urayama, Phys. Rev. Lett. **80**, 4534 (1998).

[7] A. Sawada, Z.F. Ezawa, H. Ohno, Y. Horikoshi, A. Urayama, Y. Ohno, S. Kishimoto, F. Matsukura, and N. Kumada, Phys. Rev. **B59** (1999) 14888.

[8] V. Pellegrini, A. Pinczuk, B.S. Dennis, A.S. Plaut, L.N. Pfeiffer and K.W. West, Phys. Rev. Lett. **78**, (1997) 310.

[9] V. Pellegrini, A. Pinczuk, B.S. Dennis, A.S. Plaut, L.N. Pfeiffer and K.W. West, Science **281**, (1998) 799.

[10] L. Zheng, R.J. Radtke and S. Das Sarma, Phys. Rev. Lett. **78**, (1997) 2453.

[11] K. Yang, K. Moon, L. Zheng, A.H. MacDonald, S.M. Girvin, D. Yoshioka and S.C. Zhang, Phys. Rev. Lett. **72**, (1994) 732; K. Moon, H. Mori, K. Yang, S.M. Girvin, A.H. MacDonald, L. Zheng, D. Yoshioka and S.C. Zhang, Phys. Rev. B **51**, (1995) 5138.

[12] A. Sawada, Z.F. Ezawa, H. Ohno, Y. Horikoshi, O. Sugie, S. Kishimoto, F. Matsukura, Y. Ohno and M. Yasumoto, Solid State Commun. **103**, 447 (1997).

[13] M. Suzuki, A. Sawada, A. Ishiguro and K. Maruya, Cryogenics **37**, (1997) 275.

[14] M. Seck, M. Potemski and P. Wyder Phys. Rev. **B56**, (1997) 7422.

[15] A. Schmeller, J.P. Eisenstein, L.N. Pfeiffer and K.W. West Phys. Rev. Lett. **75**, (1995) 4290.

Magnetoresistance of Chiral Surface States in the Integer Quantum Hall Effect

D. P. Druist[1], E.G. Gwinn[1], K.D. Maranowski[2], and A.C. Gossard[2]

[1]*Physics Department, University of California, Santa Barbara, CA 93106*
[2]*Materials Department, University of California, Santa Barbara, CA 93106*

We study the conductance of the edge state sheath that forms in the integer quantum Hall effect from the coupled edge states of a GaAs/$Al_{0.1}Ga_{0.9}As$ multilayer, as the magnetic field is tilted away from the direction perpendicular to the layers. As the tilt angle, and hence the total magnetic field, increases, the conductance perpendicular to the layers decreases. The effect is not strongly dependent on whether the sample surface is perpendicular or parallel to the in-plane component of the magnetic field. This result is inconsistent with theoretical predictions for a smooth surface and suggests that the edge state sheath may be rough.

Two dimensional (2D) electronic systems often exhibit interesting behavior when penetrated by magnetic fields, e.g., weak localization and the quantum Hall effect. A relatively new type of 2D electronic system is the chiral metal that forms at the surface of a 3D multilayered sample in the integer quantum Hall (QH) effect, from the edge states in each layer[1,2]. Previous experiments have shown that when the in-plane Hall resistance is well quantized, the vertical transport current flows perpendicular to the layers on the edge state sheath[1]. We thread this 2D system with magnetic flux by tilting the multilayer in a large magnetic field. The magnetic field perpendicular to the layers creates the edge state sheath and the in-plane magnetic field either penetrates or is along the surface.

To investigate the effects of a magnetic field along the layer planes, we use a GaAs/$Al_{0.1}Ga_{0.9}As$ multilayer structure that was grown by molecular-beam epitaxy. The structure contains 50 periods of 150Å GaAs quantum wells that alternate with 150 Å $Al_{0.1}Ga_{0.9}As$ barriers (Si delta-doped at their centers)so that the period of the multilayer is 300 Å, and the total height of the multilayer is 1.5 μm. A simple Kronig-Penney analysis of the structure yields a width t = 0.12 meV for the lowest subband. (The Fermi energy of 10 meV is well below the second subband). The wafer has degenerately doped ($2x10^{18}$) n+ GaAs layers above and below the multilayer, and 50 Å n+ GaAs ($2.5x10^{17}$) immediately above and below the outermost $Al_{0.1}Ga_{0.9}As$ layers to reduce overfilling of the outer wells. Alloyed NiAuGe contacts these top and bottom n+ layers. We patterned the wafer into two mesas, each 150 μm x 3 mm, oriented at 90 degrees from one another(Fig 1). The two mesas were dry etched via to have nearly vertical sidewalls. The samples are mounted in good thermal contact with the mixing chamber of a dilution refrigerator, and care was taken to exclude noise and keep excitation currents small to avoid electron heating.

We measured the vertical conductance of the two mesas in tilted magnetic fields at a temperature of 110 mK. We have shown previously for samples fabricated from the same wafer that this temperature is low enough that the edge state sheath dominates the vertical transport along the device[1]. The samples were oriented so that for one device, sample A, the component of the magnetic field in the planes of the superlattice is along the long axis of the device(see Figure 1). Thus the in-plane field only penetrates the surface only on the small end of the mesa. The second sample, sample B, then, has the in-plane field through the portion of the edge state sheath on the long faces of the device. Thus for sample A, the in-plane field penetrates 5% of the edge state sheath, while for sample B, the in-plane field penetrates 95 % of the edge state sheath(assuming that the sheath is flat). If the magnetic field going through the sheath strongly affects the dynamics of electrons on the coupled edge states, one expects to see a qualitative difference in the transport

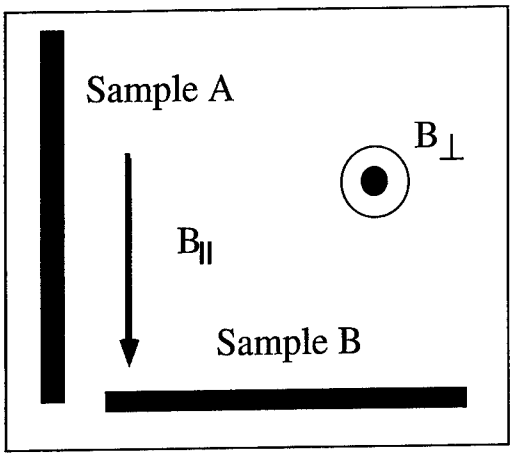

Figure 1: Schematic top view of sample. The two long rectangles are the two mesas.The in-plane magnetic field, $B_{||}$,is along the surface for most of Sample A, and through the surface for most of the Sample B.

properties of the two mesas.

A recent theoretical paper[3] discussed the effects of magnetic flux that penetrates the edge state sheath. Using a simple hamiltonian model that assumes continuous tunnelling all along the edge states, the theory predicts a Drude-like form for the effect of the field B_{surf} that penetrates the surface

$$\sigma = \frac{\sigma(B_{surf}=0)}{1+(\frac{B_{surf}}{B_0})^2} \tag{1}$$

with $B_0 = \Phi_0/al_{el}$. Here Φ_0 is the flux quantum, a is the multilayer period, and l_{el} is an elastic scattering length. Thus the characteristic field scale for the suppression of the conductance is the field needed to thread one flux quantum through an area equal to the layer spacing times the elastic scattering length. In addition to the above effect, one would also expect the in-plane magnetic field to reduce the tunnelling by reducing the overlap of the wavefunctions in neighboring wells. This second type of effect has been considered for the case of a two layer system [4]. In a quantum mechanical calculation for the tunnelling between two layers in a tilted magnetic field, the authors of [4] find

$$T_n = -t_0 e^{-\alpha^2} L_n(2\alpha^2) \tag{2}$$

where T_n is the tunnelling matrix element for electrons in the nth Landau level, t_0 is the zero field tunnelling matrix element, L_n is the n_{th} Laguerre polynomial, and $\alpha = B_{||}a/B_\perp l_\perp$, with $B_{||}$ the magnetic field in the planes, $B_\perp$ the magnetic field perpendicular to the layer planes, and $l_\perp$ the magnetic length corresponding to the perpendicular field. The theory is for a system that is translationally invariant in the planes, and ignores interactions between the electrons. Although the calculation is for two wells, the treatment is in principle applicable to a weakly coupled many layer system. In the case of the quantum Hall effect in multilayers, however, it is not clear that this calculation for tunnelling in the bulk will quantitatively describe transport, which is dominated by the edge state sheath.

Figure 2 shows the conductance of the samples versus the magnetic field perpendicular to

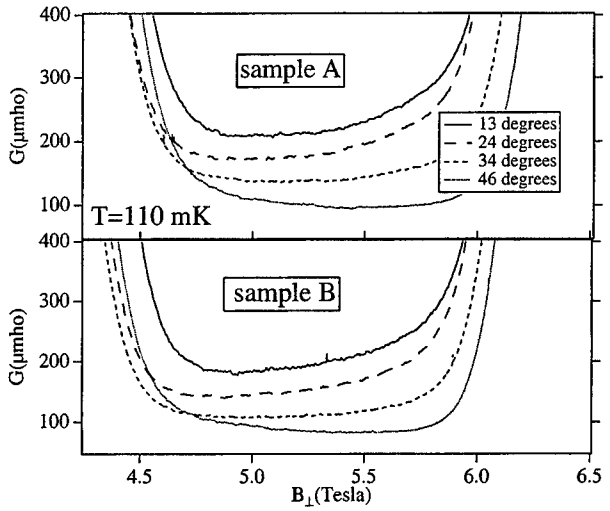

Figure 2:Conductance of the two devices versus magnetic field perpendicular to the layers for four tilt angles. The conductance decreases as the tilt angle and hence the overall magnetic field increases.

the superlattice planes, for four tilt angles of 13, 24, 34, and 46 degrees. The broad plateau in the conductance around a perpendicular field of 5 Tesla corresponds to the ν=2 quantum Hall plateau(previous studies[1] have shown that the in-plane transport is non dissipative at these temperatures, fields, and tilt angles). As the tilt angle and hence the total magnetic field is increased, the conductance of the two mesas drops. In addition, the slope of the conductance versus magnetic field within the quantum Hall states changes sign from positive to negative for the highest tilt angles. The magnetic length $l_{||}$ for the in-plane magnetic field is equal to the layer spacing when the tilt angle is 30.2 degrees for a perpendicular field of 5.0 Tesla. It is possible that the effect of increasing $B_{||}$ decreases the conductance within the Hall plateaus once the magnetic length is significantly smaller than the spacing between the layers. The data show the slope being near zero for the trace at 35 degrees, but negative for the 46 degree trace.

To obtain the 'magnetoresistance' of the edge state sheath, we plot the conductance of the two mesas versus the in-plane magnetic field, for a fixed perpendicular field of 5.5 Tesla(Figure 3). The data for other values of fixed perpendicular field are similar. The overall decrease in conductance for the two devices is about a factor of three as the in-plane field is increased from 1 to 6 Tesla. The conductance of the two devices differs by about 15 percent. The two devices also differ at zero magnetic field by the same factor. Since the two devices are rather large, the difference may be due to gradients in the multilayer properties across the wafer. Another possibility for the discrepancy is the fact that the two devices have their long axes lined up along different crystal axes.

Further examination of the data reveals that the shapes of the curves for the two devices are quite similar. This indicates that the effect of the in-plane field is not strongly dependent on whether it penetrates or is along the surface of the sample. This result is inconsistent with eq.(1). The 'magnetoresistance' we see is possibly due to reduction of tunneling due to the presence of the in-plane magnetic field, which increases the confinement of the electrons in the individual quantum

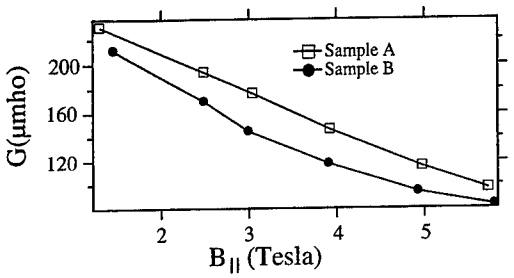

Figure 3. Conductance of the two mesas versus in plane magnetic field at a fixed perpendicular field of 5.5 Tesla. The two curves have similar shape, and the overall decrease in conductance with increasing in-plane magnetic field is about the same.

wells. This enhanced confinement has been demonstrated in semiconductor superlattices in parallel fields($B_\perp = 0$) using C-V profiling techniques[5]. The reduction of the tunnelling between successive layers in the superlattice in the presence of a tilted magnetic field has been calculated in [4]. The theory gives two different forms for the reduction in tunnelling strengths T_1 and T_2 for the first and second Landau levels(Eq.2). In our experiments there are two filled Landau levels, which will give two sets of coupled edge states in parallel. Assuming that the conductivity of the n^{th}edge state sheath $\sigma \propto T_n^2$[6], we have attempted to fit to a form $G = AT_1^2 + BT_2^2$ No satisfactory fits were obtained, however. It is perhaps not surprising that this translationally invariant model, which would not predict the existence of the QHE, does not quantitatively describe the reduction in tunnelling at the surface of the quantum Hall multilayer.

The theoretical model[3] for the edge state system is appropriate to the case of a smooth edge, with tunneling continuously along the edge states. Our data are consistent with the edge state sheath being rough on the scale of the layer spacing. Indeed, the Fermi Thomas screening length for a 3D GaAs sample of equivalent doping density is about 100 Å, much shorter than in 2D samples. The dry etch used to define the mesas is known to introduce a large number of charge trap states on the surface, and probably leaves the surface quite rough on the atomic scale. Since the screening length in these 3D samples is fairly short, the edge state sheath(which should lie ~ 1 screening length from the etched surface) may also be quite rough.

REFERENCES

[1] D.P. Druist, P.J. Turley, E.G.Gwinn, K.D Maranowski and A.C. Gossard, Phys Rev Lett **80**, 365 (1998).
[2] B. Zhang, et.al., Physica B **258**, 279 (1998) .
[3] J.T. Chalker and S.L. Sondhi,Phys. Rev. B **59**, 4999(1999).
[4] J.Hu and A.H. Macdonald, Phys Rev. B **46**, 12554(1992).
[5] P. Denk, M. Hartung, M. Streibl, A. Wixforth, K. L. Campman and A.C. Gossard Phys Rev. B **57**, 13094(1998).
[6] L. Balents and M.P.A. Fisher, Phys Rev. Lett. **76**, 2782(1996).

Far-Infrared Magneto-Absorption of Double-Layer Two-Dimensional Electron System in Tilted Magnetic Fields

S. Takaoka[a,*], A. Kuriyama[a], K. Oto[a], K. Murase[a,b], S. Shimomura[c], S. Hiyamizu[b,c]
M. Cukr[d], T. Jungwirth[d], and L. Smrcka[d]

[a]Graduate School of Science, [b]Research Center for Materials Science at Extreme Conditions and [c]Graduate School of Engineering Science, Osaka University,
1-1 Machikaneyama, Toyonaka, 560-0043, Japan

[d]Institute of Physics, Academy of Science of the Czech Republic,
Cukrovarnická, 10, 160 00, Praha 6, Czech Republic

Abstract

Far-infrared magneto-absorption of double-layer two-dimensional electron system has been measured by Fourier transform spectrometer in tilted magnetic fields. We have measured the dependence of cyclotron mass (m_C) on the parallel ($B_{//}$) and perpendicular ($B_{\perp}$) magnetic field systematically. The obtained $B_{//}$ dependence of m_C is complicated and varies with $B_{\perp}$, which can not be explained by semiclassical theory.

PACS: 78.66.-w; 71.70.Di
Keywords: double-layer two-dimensional electron system; cyclotron resonance

1. Introduction

When a magnetic field is applied in parallel to the double-layer two-dimensional electron system of GaAs/AlGaAs heterostructure, the "Fermi loop" of each subband is distorted from the originally isotropic one in the following way[1,2]. The subbands split into a pair of quasi-symmetric states (SS) and quasi-antisymmetic states (AS) caused by the coupling between two layers. The "Fermi loop" of the SS is distorted to "peanut" at first and then splits into two parts with increasing $B_{//}$. On the other hands, the "Fermi loop" of the AS becomes small and vanishes above the critical magnetic fields. Until now, the distortions have been investigated mainly by the Shubnikov-de Haas oscillations in tilted magnetic fields[2,3]. Such distortions of the "Fermi loop" also induce the variation of the cyclotron mass (m_C) of each subband. However there are few cyclotron resonance studies on this subject[4]. In this study, we have measured the dependence of m_C on the parallel ($B_{//}$) and perpendicular ($B_{\perp}$) magnetic field systematically[5,6].

* Corresponding author: Tel.: +81 6 6850 5374 ; fax: +81 6 6850 5376 ;
e-mail: takaoka@phys.sci.osaka-u.ac.jp

2. Experiments

Two types of samples are used in this study: one with the asymmetric double-layer structure (sample A) formed by inserting the 2.3 nm AlGaAs barrier layer in the normal two-dimensional electron system of GaAs/AlGaAs heterostructure as shown in Fig.1(a), the other with the symmetric structure (sample B) formed in the wide GaAs quantum well (40 nm) as shown in Fig.1(b). The electron concentrations in the SS and AS (n_S and n_A) determined from the Shubnikov-de Haas oscillations and the average mobility (μ) obtained from the Hall measurement at 2 K are listed in Table 1. It is noted that only the SS is occupied in sample B. The far-infrared magneto-absorption of the samples was measured by means of the Fourier spectrometer and the horizontal field split pair superconducting magnet up to 12 T as shown schematically in Fig.2. In this measurement, the sample can be rotated with respect to magnetic field direction and the $B_{//}$ and $B_{\perp}$ are changed independently by adjusting the magnetic field direction and strength.

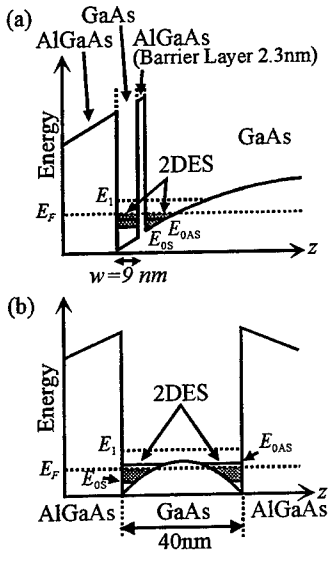

Fig.1. Schematic view of energy structures of (a) sample A and (b) sample B.

Table 1. Electronic properties of samples.

Sample	n_S (10^{11}cm^{-2})	n_A (10^{11}cm^{-2})	μ (10^4cm^2/Vs)
A	2.8	0.7	25
B	1.7	—	11

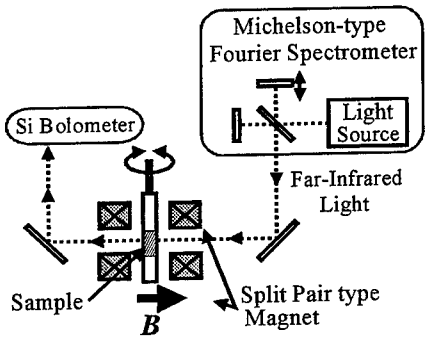

Fig.2. Schematic geometry of Fourier spectrometer (right), superconducting magnet (center), and detector (left).

3. Results and Discussion

From the dip positions of far-infrared absorption spectra, we determined the dependence of $m_C = e B_\perp/\omega_C$ on $B_{//}$ (0~8 T) at various $B_\perp$ (2~8 T) systematically, where ω_C is the cyclotron resonance frequency. Typical $B_{//}$ dependence of m_C at low and high $B_\perp$ is shown in Fig.3. The obtained $B_{//}$ dependence of m_C is complicated and varies with $B_\perp$. It is expected from the semiclasscial calculation, in which $B_\perp$ is a weak perturbation, that the m_C of the SS increases and that of the AS decreases with $B_{//}$ as shown in Fig.4. There are the increasing m_C and decreasing m_C with $B_{//}$ as denoted by SS and AS, respectively in Fig.3. We can qualitatively regard these m_C as m_C from the SS and AS, respectively. The result that a

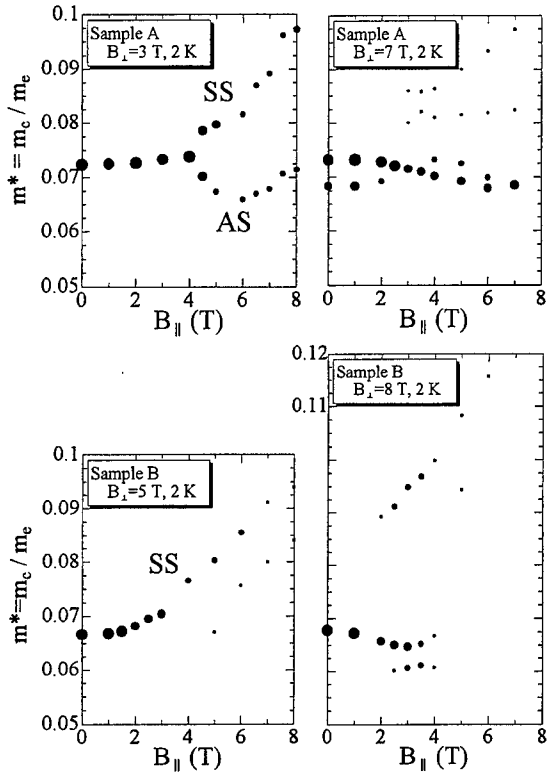

Fig.3. Typical $B_{//}$ dependence of m_C at high $B_\perp$ and low $B_\perp$ for sample A and B. The size of plot denotes the absorption intensity of each dip in the transmission spectrum.

decreasing m_C with $B_{//}$ at low $B_\perp$ in the sample B is not observed can be also explained by absence of electrons in the AS. However, the observed rates of change of m_C with $B_{//}$ are considerably smaller than the calculated ones. At high $B_\perp$, the dominant signal of the decreasing m_C with $B_{//}$ is observed in both samples. This decreasing m_C can not be regarded as m_C from the AS, because the AS is empty in sample B. We have to consider the existence of unknown mechanism at strong $B_\perp$, after the AS becomes empty. The observed $B_{//}$ dependence of m_C can not be explained by the semiclassical calculation in zero $B_\perp$ limit. In this experiment, $B_\perp$ is so strong that we have to calculate Landau levels quantum mechanically. Furthermore, more than two cyclotron masses are observed in the strong $B_{//}$ region. The optical transition between the Landau levels is allowed only in the same subband at zero $B_{//}$. The transition between the Landau levels from different subbands becomes to be allowed by the strong $B_{//}$[4]. We also need to take into account such a transition. The quantum level (the Landau level) calculation taking into account of the finite $B_{//}$ and $B_\perp$ and such a $B_{//}$-induced transition between different subbands would be necessary in order to explain the complicated experimental results.

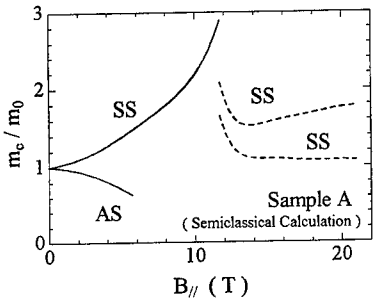

Fig.4. Calculated $B_{//}$ dependence of m_C for sample A semiclassically. The cyclotron mass (m_C) is normalized by m_C at zero $B_{//}$ (m_0).

Acknowledgements

We thank H. Aikawa for his help in the experiment. This work is supported in part by a Grand-in-Aid for COE Research (10CE2004) from the Ministry of Education, Science and Culture (Japan) and GACR under contracts 202/98/0085 and 102/99/0415 (Czech Republic).

References

[1] L. Smrcka and T. Jungwirth, J. Phys. Condens. Matter 7 (1995) 3721.
[2] N.E. Harff et al. , Phys. Rev. B 55 (1997) R13405.
[3] J.A. Simmoms, N.E. Harff and J.F. Klein, Phys. Rev. B 51 (1995) 11156.
[4] D.D. Arnone et al., Phys. Rev. B 56 (1997) R4340.
[5] S. Takaoka et al., Microelectronic Engineering in press.
[6] A. Kuriyama et al., Solid State Commun. in press.

Order Parameter Suppression in Double Layer Quantum Hall Ferromagnets

Yogesh N. Joglekar * †, Allan H. MacDonald
Department of Physics,
Indiana University,
Bloomington IN 47405

Abstract

Double-layer quantum Hall systems at Landau level filling factor $\nu = 1$ have a broken symmetry ground state with spontaneous interlayer phase coherence and a gap between symmetric and antisymmetric subbands in the absence of interlayer tunneling. We examine the influence of quantum fluctuations on the spectral function of the symmetric Green's function, probed in optical absorption experiments. We find that as the maximum layer separation at which the $\nu = 1$ quantum Hall effect occurs is approached, absorption in the lowest Landau level grows in strength. Detailed line shapes for this absorption are evaluated and related to features in the system's collective excitation spectrum.

Introduction During recent years double quantum wells in the quantum Hall regime have been a subject of intensive study. These systems consist of two 2-dimensional electron layers in a perpendicular magnetic field with a distance d ($d \approx 100$ Å) between layers comparable to the typical distance between electrons in the same layer. When the magnetic field is strong enough to accommodate all electrons in the lowest Landau level (LLL), interactions between the electrons largely determine the properties of the system. Even when the spin degree of freedom can be ignored because of complete spin alignment, the system exhibits a rich variety of phases [1] associated with the layer index degree-of-freedom and dependent on the difference between interlayer and the intralayer Coulomb interactions. These states are referred to as quantum Hall ferromagnets. In particular, even in the absence of a finite tunneling amplitude, there is *spontaneous* interlayer phase coherence, which lifts the degeneracy between single-particle symmetric states which are occupied and antisymmetric states which are empty [1]. In a mean-field theory this splitting blocks optical absorption in the lowest Landau level at T=0. Absorption is permitted only because of quantum fluctuations, making this probe particularly important. In this paper we present a theory of quantum fluctuations and optical absorption in double-layer quantum Hall ferromagnets.

†Ph: 1-812-855-7359, Fax: 1-812-855-5533

*Email: yojoglek@indiana.edu

Formalism In the following, we discuss the nature of the many-body ground state wavefunction for such a system in a mean field approximation and systematically improve upon it by including the effect of quantum fluctuations. We present some numerical results and briefly discuss their experimental implications. Let us consider a system at filling factor ν=1, neglect the spin dynamics and use the lowest Landau level approximation. It is convenient to describe the layer index degree-of-freedom by a 'pseudospin', where the symmetric state corresponds to 'pseudospin up' ($|\uparrow\rangle$) and the antisymmetric state is 'pseudospin down' ($|\downarrow\rangle$). Then the interaction between the electrons is a sum of two potentials: a term $V_0 = (V_A + V_E)/2$, which conserves pseudospin and a term $V_x = (V_A - V_E)/2$, which reverses the pseudospins of the interacting electrons. (V_A and V_E are the intralayer and interlayer Coulomb interactions respectively.) We expect the mean-field ground state to be fully pseudospin polarized, with all electrons occupying the symmetric single-particle orbitals. Since the V_x term flips pseudospins, however, it is clear that the *exact* ground state must have an indefinite pseudospin polarization. Hence *even at zero temperature*, there must be some mixing of reversed pseudospins in the true ground state. We calculate this mixing by considering the scattering of electrons off of virtually excited collective excitations, pseudospin-waves. The finite temperature expression for the symmetric-state self energy is given by [2]

$$\Sigma_S(i\omega_n) = -\frac{1}{\beta}\sum_{i\Omega}\sum_{a=S,AS} \mathcal{G}_a^{MF}(i\omega_n - i\Omega) M^{-1}_{Sa,sS}(i\Omega), \tag{1}$$

where $\mathcal{G}_a^{MF}(i\omega_n) = (-i\omega_n + \xi_a)^{-1}$ is the mean-field Matsubara Green's function and M^{-1} is the pseudospin-wave propagator matrix. At zero temperature the symmetric-state self energy becomes

$$\Sigma_S(i\omega_n) = \frac{2\pi l^2}{A}\sum_{\vec{q}} \frac{(E_{sw}(\vec{q}) + \Delta)^2}{2E_{sw}(\vec{q})} \frac{\epsilon(\vec{q}) - E_{sw}(\vec{q})}{i\omega_n - \xi_{AS} - E_{sw}(\vec{q})}. \tag{2}$$

Here $E_{sw}(\vec{q})$ is the pseudospin-wave energy [3], $\xi_{AS} = -\xi_S > 0$ is the mean-field energy of the antisymmetric state and $\Delta = 2\xi_{AS}$ is the interaction enhanced quasiparticle level splitting between the symmetric and the antisymmetric state energies.

For models with delta-function electron-electron interactions, like the Hubbard model which is frequently used for theories of itinerant electron magnetism, self-energy expressions of this form are most efficiently done by using the Hubbard-Stratonovich transformation [4] after formally expresssing the electron-electron interaction as an exchange interaction favoring parallel spin alignment. For double layer systems, however, this transformation is not possible and both Hartree and exchange fluctuations are important in the collective excitation spectrum and the fluctuation physics. To make progress we have derived the above results using a modified version of the Hubbard-Stratonovich transformation [5] designed to cope with this difficulty, which is almost always present in realistic models.

In magnetic systems, spin wave energies usually increase monotonically with momentum so that low-energy physics is long-wavelength physics, which in turn can be described by a continuum (effective) field theory. In contrast, for a double layer system, the pseudospin collective mode energies usually have a minimum at $pl \approx 1$ where l is the magnetic length [3] and so an effective field theory discription is not useful. (See fig. 1). We also note that when the distance between the layers vanishes, the pseudospin flipping interaction vanishes,

and then the mean-field approximation for the ground state is exact. This is reflected in the vanishing zero temperature self energy expression (2) when $d = 0$.

We analytically continue the above self-energy expression to real frequencies and solve the Dyson's equation, $\omega - \xi_S = \Sigma_S(\omega + i\eta)$, numerically to obtain the spectral function for the symmetric state. In the absence of the fluctuation self-energy correction, the thermal Green's function is given by $\mathcal{G}_S(i\omega_n) = \mathcal{G}_S^{MF}(i\omega_n)$. This corresponds to a spectral function $A_S(\omega) = \delta(\omega - \xi_S)$; all the spectral weight is in the delta function at the negative energy (occupied) symmetric state quasiparticle pole. When the self energy correction is included, the spectral weight at the symmetric state quasiparticle pole reduces to $z_S = (1 - \partial\Sigma_S/\partial\omega|_{\omega^*})^{-1}$ where ω^* satisfies the Dyson's equation. The remaining spectral weight is distributed in a continuum piece at positive (unoccupied) energies where the self-energy (2) has a branch cut, *i.e.* in the interval $\xi_{AS} + E_{sw}^{min} \leq \omega \leq \xi_{AS} + \Delta$. If excitonic interactions can be neglected the lowest-Landau-level contribution to the optical absorption spectrum is given by the positive energy part of $A_S(\omega)$. One index of the amount of spectral weight at positive frequencies is the suppression of the ground-state pseudospin polarization,

$$m(T = 0) = z_S = \int_{-\infty}^{\infty} \frac{d\omega}{2\pi} n_F(\omega) \left[A_S(\omega) - A_{AS}(\omega) \right], \tag{3}$$

from it's mean-field value.

Results We have calculated the pseudospin polarization for various values of the two experimentally controlable parameters in these systems, namely the distance between the layers d and the tunneling amplitude Δ_{SAS}. (We have neglected the finite thickness of the electron layers to simplify the calculations). A phase diagram showing curves of equal polarization is plotted in fig. 3. The line corresponding to $z_S = 0$ is the same as the phase boundary between QHE/NO-QHE regions [6,7]. As we approach the phase boundary, the minimum of the pseudospin-wave energy, E_{sw}^{min} (occuring at a finite wavevector) approaches zero, leading to the instability which destroys the pseudospin polarized state and also the quantum Hall effect. The polarization drops to zero rather sharply as a function of d for a given Δ_{SAS} (see fig. 2) since E_{sw}^{min} vanishes rapidly with layer separation. The spectral function for $d = 1.4$ and $\Delta_{SAS} = .10$ is shown in fig. 4. We see that in this case, the pseudospin polarization is reduced by 10% from its maximum value of 1. The nonvanishing spectral function at positive energies reflects the possibility of adding a symmetric electron as an antisymmetric state quasiparticle by destroying a pseudospin-wave present in the ground state.

We stress the important role of special properties of the lowest Landau level single-particle states and the absence of band structure in simplifying the calculation described here. The presence, at $\nu = 1$ and low temperatures, of positive energy symmetric state spectral weight has been detected recently by Manfra and Goldberg [8] in a sample which is close to the quantum Hall boundary. Extending the above numerical calculations to take into account the finite thickness of the layers is possible without much difficulty. It will be interesting to see if the predictions for positive energy spectral weight made by this theory are in agreement with experiments as they are refined and as the theory is refined by accounting for excitonic effects.

Acknowledgement This work was supported by NSF grant no. DMR9714055.

REFERENCES

[1] K. Moon *et al.*, Phys. Rev. B **51**, 5138 (1995).
[2] Y. N. Joglekar and A. H. MacDonald, in preparation (1999).
[3] H. A. Fertig, Phys. Rev. B **40**, 1087 (1989).
[4] J. Negele and H. Orland, *Quantum Many-Particle Systems* (Addison-Wesley NY, 1988).
[5] A. K. Kerman, S. Levit and T. Troudet, Ann. Phys. **148**, 436 (1983).
[6] A.H. MacDonald, P.M. Platzman, and G.S. Boebinger, Phys. Rev. Lett. **65**, 775 (1990).
[7] S. Q. Murphy *et al.*, Phys. Rev. Lett. **72**, 728 (1994).
[8] M. J. Manfra *et al.*, cond-mat/9809373.

FIGURES

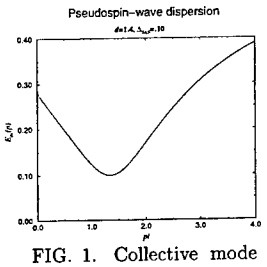

FIG. 1. Collective mode dispersion for $d = 1.4l$ and single-particle tunneling gap $\Delta_{SAS} = 0.1e^2/\epsilon l$. Note the minimum at finite wavevector.

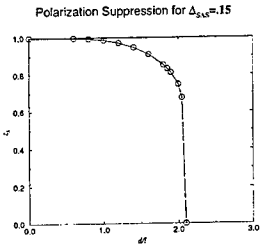

FIG. 2. Pseudospin polarization *vs.* layer separation for $\Delta_{SAS} = 0.15e^2/\epsilon l$.

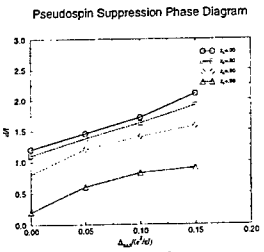

FIG. 3. Ground state pseudospin polarization contours. In this theory, the $z_S = 0$ line is coincident with the stability boundary of the quantum Hall state. Polarization suppression and positive energy symmetric spectral weight grow rapidly as the stability boundary is approached.

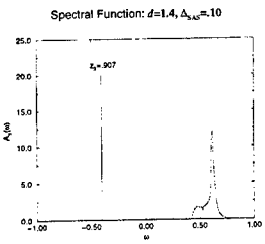

FIG. 4. Symmetric spectral function for $d = 1.4l$ and $\Delta_{SAS} = 0.1e^2/\epsilon l$. The zero of the energy is at the chemical potential. The positive energy spectral function is proportional to the lowest Landau level contribution to the optical absorption spectrum, neglecting excitonic corrections.

Edge State Transport of Separately Contacted Bilayer Systems in the Fractional Quantum Hall Regime

Daijiro YOSHIOKA and Kentaro NOMURA
Department of Basic Science, The University of Tokyo
3-8-1 Komaba, Meguro, Tokyo 153-8902, Japan

Hall and diagonal resistances of bilayer fractional quantum Hall systems are discussed theoretically. The bilayers have electrodes attached separately to each layer. They are assumed to be coupled weakly by interlayer tunneling, while the interlayer Coulomb interaction is negligibly small. It is shown that source-drain voltage dependence of the resistances reflects the Luttinger liquid parameter of the edge state.

Recently it has become possible to fabricate bilayer systems where electrodes are attached separately to each layers[1]. Most experimental and theoretical investigations have been done for the phenomenon called as Coulomb drag in these systems, which occurs only when the system is in the compressible phase. However, even in the incompressible states non-trivial transport phenomena are expected to occur if the two-layers are coupled through tunneling. Actually, in the integer quantum Hall regime deviation from the quantized Hall value and finite dissipation have been observed experimentally[2], and analyzed theoretically[3, 4]. The purpose of the present paper is to investigate the consequences of the tunneling for weakly coupled bilayer systems in the fractional quantum Hall regime.

For the bilayer system, where current is supplied to only one of the layer, the two layers are out of equilibrium, especially at the edges. The tunneling cause the two layers to approach to the equilibrium. It is known that the tunneling in the bulk is suppressed as long as the voltage difference between the two-layers is small[5]. Therefore we assume that the tunneling occurs only between the chiral Luttinger liquids realized at the sample edge.

However, even at the edges, it has been shown that for the principal quantum Hall states realized at filling factor $1/q$ ($q > 1$) the tunneling is irrelevant and suppressed in contrast to the integer quantum Hall (IQH) case, where it is relevant[6]. For the case of FQH, The irrelevancy of the tunneling gives power law dependence of the tunneling current on the voltage difference or on the temperature[7]. The power is given by the Luttinger liquid parameter, which is nothing but the filling factor of the system. This theory suggests new experiment to investigate the Luttinger liquid property of the fractional quantum Hall edges.

Following ref.3 we introduce local effective chemical potential $\mu_\sigma(x)$ to describe the current flowing in the σ-layer at coordinate x along the edge, where $\sigma = \pm$ is the layer index. The introduction of the effective chemical potential does not necessarily mean that each layer is in thermal equilibrium[8]. The current in each layer is given by

$$I_\sigma(x) = \frac{\nu e}{h}[\mu_\sigma(x) - \epsilon_0], \tag{1}$$

where ϵ_0 is a common origin to measure energy and defines the edge current. Due to the chirality of the edges the sum of the current $I_+(x)+I_-(x)$ is conserved along the edges both from source to drain and from drain to source. However, the tunneling current causes the change in the current in each layers. Since the electrons flow at a constant velocity along the edges, the temporal evolution of the difference in the chemical potential is projected to the spatial evolution of the chemical potential. The spatial evolution should be described by Boltzman type differential equation as follows

$$\frac{\mathrm{d}\mu_\sigma(x)}{\mathrm{d}x} = -\frac{1}{\xi}[\mu_\sigma(x) - \mu_{-\sigma}(x)]^\lambda. \tag{2}$$

In this equation λ is given by the Luttinger parameter of the edge state. For the standard theory of the edge state in the principal FQH state at $\nu = 1/q$, $\lambda = 2q-1$ [9]. However, we can consider λ as a parameter to be determined experimentally. The parameter ξ, which has the meaning of the relaxation length for the IQH, is inversely proportional to the tunneling probability. We solve this equation under the condition that the total current through the sample is I, and only the minus layer is connected to the source and drain electrodes. We assume that the current is injected ideally without reflection into the upper edge of the minus layer from the source at $x = 0$, and drained at $x = L$, namely L is the sample length. Thus the boundary condition for the minus layer is $\mu_-(0+) = \mu_S$, and $\mu_-(L-) = \mu_D + (h/\nu e)I$. Similarly boundary condition for the lower edge of the minus layer is $\mu_-(L+) = \mu_D$, and $\mu_-(2L-) = \mu_S - (h/\nu e)I$, where neglecting the width of the electrodes, the edge state extends from the drain at $x = L$ to the source at $x = 2L \equiv 0$. On the other hand, since the upper layer is not connected to the current electrodes, the condition for $\mu_+(x)$ is $\mu_+(0-) = \mu_+(0+)$ and $\mu_+(L-) = \mu_+(L+)$.

To solve the equations we introduce an auxiliary variable ζ such that

$$\begin{aligned}(\mu_S - \mu_D)\zeta &= \mu_-(0+) - \mu_-(L-) = -[\mu_+(0) - \mu_+(L)] \\ &= \mu_-(L+) - \mu_-(0-).\end{aligned} \tag{3}$$

This ζ is determined by the following transcendental equation:

$$(1-3\zeta)^{1-\lambda} - (1+\zeta)^{1-\lambda} = 2(\lambda-1)\frac{L}{\xi}[\frac{1}{2}(\mu_S - \mu_D)]^{\lambda-1}. \tag{4}$$

Once ζ is determined, $\mu_\pm(x)$ is given: Namely for $0 < x < L$,

$$\begin{aligned}\mu_\pm(x) = &\frac{1}{4}[(3-\zeta)\mu_S + (1+\zeta)\mu_D] \\ &\mp \frac{1}{2}[\{\frac{1+\zeta}{2}(\mu_S - \mu_D)\}^{1-\lambda} + \frac{2(\lambda-1)}{\xi}x]^{1/(1-\lambda)},\end{aligned} \tag{5}$$

and for $L < x < 2L$,

$$\begin{aligned}\mu_\pm(x) = &\frac{1}{4}[(1+\zeta)\mu_S + (3-\zeta)\mu_D] \\ &\pm \frac{1}{2}[\{\frac{1+\zeta}{2}(\mu_S - \mu_D)\}^{1-\lambda} + \frac{2(\lambda-1)}{\xi}(x-L)]^{1/(1-\lambda)}.\end{aligned} \tag{6}$$

It is easily verified that $\mu_\pm(x)$ satisfies the differential equation with the proper boundary conditions.

Now, the current through the sample is given as follows:

$$I = \nu\frac{e}{h}(1-\zeta)(\mu_S - \mu_D). \tag{7}$$

Therefore the source-drain conductance is given by

$$G = \frac{\nu e^2}{h}(1-\zeta). \tag{8}$$

Hall and diagonal resistances when the probe electrodes are attached to the minus layer at $x = a$, $x = L - a$, and $x = 2L - a$ are calculated from Eq.(5) and Eq.(6):

$$\begin{aligned} R_{\rm H} &\equiv \frac{\mu_-(a) - \mu_-(2L-a)}{eI} \\ &= (\frac{h}{\nu e^2})\{\frac{1}{2} + \frac{1}{4(1-\zeta)}[\frac{L-a}{L}(1+\zeta)^{1-\lambda} + \frac{a}{L}(1-3\zeta)^{1-\lambda}]^{1/(1-\lambda)} \\ &+ \frac{1}{4(1-\zeta)}[\frac{a}{L}(1+\zeta)^{1-\lambda} + \frac{L-a}{L}(1-3\zeta)^{1-\lambda}]^{1/(1-\lambda)}\}, \end{aligned} \tag{9}$$

and

$$\begin{aligned} R_{xx} &\equiv \frac{\mu_-(a) - \mu_-(L-a)}{eI} \\ &= (\frac{h}{\nu e^2})\frac{1}{4(1-\zeta)}\{[\frac{L-a}{L}(1+\zeta)^{1-\lambda} + \frac{a}{L}(1-3\zeta)^{1-\lambda}]^{1/(1-\lambda)} \\ &- [\frac{a}{L}(1+\zeta)^{1-\lambda} + \frac{L-a}{L}(1-3\zeta)^{1-\lambda}]^{1/(1-\lambda)}\}. \end{aligned} \tag{10}$$

These results are shown in Figs. 1 and 2. First in Fig.1 the normalized conductance $G/(\nu e^2/h) = (1-\zeta)$ is plotted as a function of $(L/\xi)[(\mu_{\rm S} - \mu_{\rm D})/2]^{\lambda-1}$. As the tunneling current increases either as the length L or $(\mu_{\rm S} - \mu_{\rm D})$ increase or ξ decreases, the source-drain conductance decreases. This is due to the increase of the back-scattered current through the plus layer. A peculiarity of the FQH case is that it depends on $(\mu_{\rm S} - \mu_{\rm D})$. The conductance tends to $(2/3)(\nu e^2/h)$ as the tunneling current increases.

In Fig.2 the Hall and longitudinal resistances, which are normalized by $h/\nu e^2$, are plotted for the choice of $a = 0.2L$. Effect on the longitudinal resistance is smaller in the fractional case. The Hall resistance tends to 1/2 of the isolated layer case in the large tunneling current limit, while R_{xx} tends to zero similarly to the IQH case.

The results in this paper show that if $(\mu_{\rm S} - \mu_{\rm D})$-dependence of the various quantity is measured for tunnel-coupled bilayer systems, we can deduce the parameter λ, or the Luttinger parameter of the edge state. Of course such an experiment should be done at low temperature and for small source-drain voltage, since tunneling in the bulk must be negligible. We hope such an experiment will be done in the near future. This work is supported by Grant-in-Aid for Scientific Research (C) 10640301.

REFERENCES

1) J.P. Eisenstein, L.N. Pfeiffer and K.W. West: Appl. Phys. Lett. **57** (1990) 2324.
2) Y. Ohno, M. Foley and H. Sakaki: Phys. Rev. B **54** (1996) R2319.
3) D. Yoshioka and A.H. MacDonald: Phys. Rev. B **53** (1996) R16168.
4) D. Yoshioka and A.H. MacDonald: Physica E **1** (1997) 167.
5) J.P. Eisenstein, L.N. Pfeiffer and K.W. West: Phys. Rev. Lett. **69** (1992) 3804
6) K. Nomura and D. Yoshioka: to be published in J. Phys. Soc. Jpn., cond-mat/9904192.
7) M. Grayson, D.C. Tsui, L.N. Pfeiffer, K.W. West and A.M. Chang: Phys. Rev. Lett. **80** (1998) 1062.
8) If the interlayer relaxation is faster than the intralayer relaxation, each edge will be in thermal equilibrium, and the effective chemical potential is nothing but the true chemical potential.
9) X.G. Wen: Phys. Rev. B **44** (1991) 5708.

FIGURES

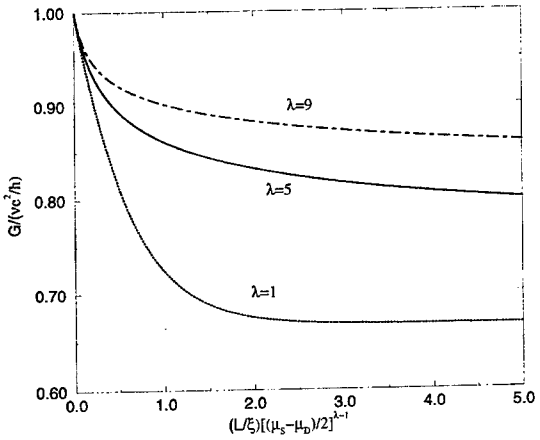

FIG. 1. Two terminal conductance G scaled by $\nu e^2/h$ is shown as a function of tunneling strength $(L/\xi)[(\mu_S - \mu_D)/2]^{\lambda-1}$ for $\lambda = 1$, 5, and 9 by dotted, solid and dot-dashed lines, respectively.

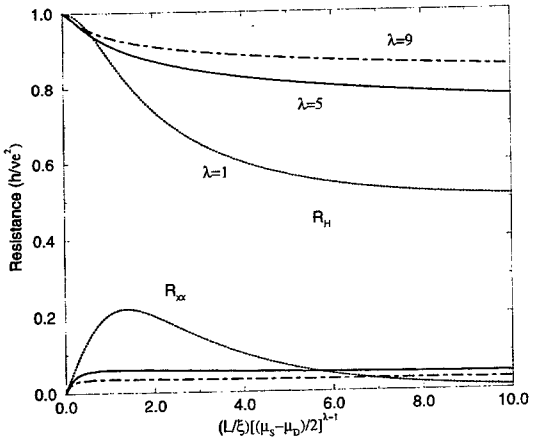

FIG. 2. The diagonal and Hall resistances R_{xx} and R_H scaled by $h/\nu e^2$ are shown as a function of tunneling strength $(L/\xi)[(\mu_S - \mu_D)/2]^{\lambda-1}$ for $\lambda = 1$, 5, and 9 by dotted, solid and dot-dashed lines, respectively. The length of the sample is L and voltage probes are attached at $0.2L$ from the source and drain.

TWO-COMPONENT CYCLOTRON RESONANCE IN BILAYER QUANTUM HALL SYSTEMS

Kenichi ASANO* and Tsuneya ANDO

Institute for Solid State Physics, University of Tokyo
7-22-1 Roppongi, Minato-ku, Tokyo 106-8666, Japan

Effects of electron-electron interaction on two-component cyclotron resonance is studied in bilayer quantum Hall systems at absolute zero temperature. At high filling factors $\nu \gtrsim 3/2$, the low frequency peak is pushed away to the low frequency side with the increase of the interaction. This negative mode repulsion is opposite to a positive mode repulsion occurring at low filling factors $\nu \lesssim 1$.

1. Introduction

Kohn's theorem [1] is no longer applicable to multi-component systems, which consist of more than two kinds of electrons with different cyclotron frequencies. In such systems, cyclotron resonance (CR) is generally modified by electron-electron interaction in its positions and lineshapes. In this paper, interaction effects on two-component CR is studied in asymmetric double quantum well (QW) systems in quantum Hall regime by means of a numerical diagonalization method.

Interesting behaviors were observed in CR in Si (100) inversion layers, in which there are two kinds of electrons with different masses because of multi-valley structure of conduction band [2]. A Fermi-liquid theory approach predicted that electron-electron interaction gives rise to a mode repulsion with intensity transfer [3]. A Boltzmann equation approach showed that electron-electron scattering important at high temperatures leads to merging of two peaks, i.e., a motional narrowing [4]. In GaAs/AlGaAs heterostructures, an up-spin electron has slightly larger cyclotron frequency than a down-spin electron. In the extreme quantum limit, an interesting mode repulsion behavior was observed experimentally [5] and analyzed theoretically [6].

In previous papers [7,8] interaction effects on spin-split CR were studied in a quantum Hall regime. It was shown that spectra are categorized into three types of behaviors, a positive mode repulsion, a negative mode repulsion, and a motional narrowing, depending sensitively both on the filling factor of up- and down-spin electrons and on temperature. In this paper, we shall consider two-component CR in bilayer systems where the strength of intralayer and interlayer interactions can be controlled independently. Some experiments have been performed in such systems and shown intriguing results [9].

2. Model and Method

An asymmetric bilayer system is illustrated in Fig. 1. The cyclotron frequency $\omega_{\rm n}$ in the narrow QW is slightly smaller than frequency $\omega_{\rm w}$ in the wide QW because of a nonparabolicity of the conduction band, i.e., $\Delta = \omega_{\rm w} - \omega_{\rm n} > 0$. We consider a rectangular system with a finite area $ab = 2\pi\ell^2 N_\phi$ under periodic boundary conditions, where the integer N_ϕ denotes the number of flux quanta passing through the system and a and b are its linear dimension. The filling factor of the layer i $(= {\rm w}, {\rm n})$ is defined by $\nu_i = N_i/N_\phi$, where N_i denotes the number of electrons in the corresponding layer. The total filling

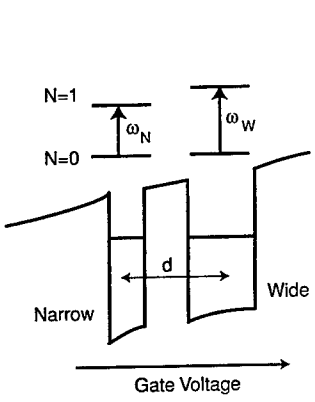

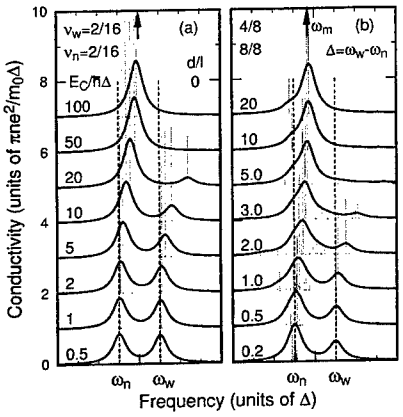

Fig. 1 (left) Schematic figure of bilayer system.

Fig. 2 (right) Some examples of calculated CR spectra for $d/\ell=0$. (a) $\nu_w=\nu_n=1/8$ and (b) $(\nu_w,\nu_n)=(1/2,1)$.

factor is defined by $\nu=\nu_w+\nu_n=N_e/N_\phi$ with the total electron number $N_e=N_w+N_n$. The spin of electrons is completely neglected.

The potential energy between two electrons located in layers i and j is given as

$$v(r)=\frac{e^2}{4\pi\epsilon\sqrt{r^2+d^2(1-\delta_{ij})}},$$

where r is the distance between two electrons projected onto a two-dimensional plane, d is the distance between the layers, $-e$ is the electron charge, and ϵ is the background dielectric constant. Thus, intra- and inter-layer coupling of CR modes are characterized by $\alpha_{\rm intra}=E_C/\hbar\Delta$ and $\alpha_{\rm inter}=\alpha_{\rm intra}\ell/\sqrt{\ell^2+d^2}$ with $E_C=e^2/4\pi\epsilon\ell$, respectively. The case of vanishing d is exactly same as that of spin-split CR considered previously [7,8].

We shall consider the case that both $\hbar\Delta$ and E_C are much smaller than the averaged cyclotron energy $\hbar(\omega_w+\omega_n)/2$. All possible initial and final states and their energies are obtained by numerical diagonalization and the dynamical conductivity is calculated with use of the Kubo formula. Because of the moment sum rule, the first moment of spectra is independent of interaction and given by $\omega_m=(\nu_w\omega_w+\nu_n\omega_n)/\nu$.

3. Results

The dynamical conductivity is calculated under the condition $4\le N_0\le 8$ and $a/b=N_0/4$, where $N_0=\mathrm{Max}(N_e,2N_\phi-N_e)$ and a/b is the aspect ratio. The results are weakly dependent on N_0 and a/b as long as $N_0\gtrsim 4$ and $a/b\sim 1$. The spectra are shown by histograms with width $\Delta/100$ (gray spikes) and a convolution with a Lorentzian with width $\Delta/5$ (solid lines).

Figure 2 shows some examples of spectra at $(\nu_w,\nu_n)=(1/8,1/8)$ and $(1/2,1)$ for $d/\ell=0$. The results are same as those of spin-split CR if ν_w and ν_n are replaced by $\nu_\uparrow$

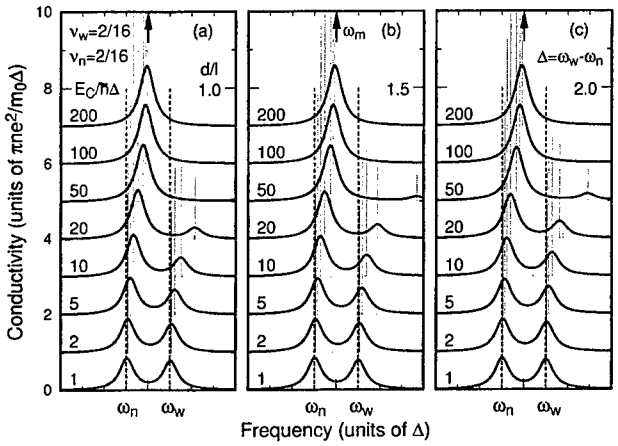

Fig. 3 CR spectra calculated at $\nu_w = \nu_n = 1/8$ when (a) $d/\ell = 1$, (b) 1.5, and (c) 2.

and $\nu_\downarrow$, respectively, and exhibit a positive mode repulsion. In fact, both peaks are shifted to the high-frequency side with the increase of the interaction, the frequency shift of the high-frequency peak is much larger than that of the low-frequency peak, and the intensity is transferred to the low-frequency peak.

Resulting spectra at $(\nu_w, \nu_n) = (2/16, 2/16)$ for $d/\ell > 0$ are shown in Fig. 3. In this case, CR exhibits a positive mode repulsion same as that for $d/\ell = 0$. The coupling strength between two CR modes is mainly determined by the inter-layer interaction decreasing slowly with the increase of inter-layer distance d. In this regime, electrons are separated from each other and CR transition can be approximated as excitations localized around a minimum point of an effective potential formed by electrons in the other layer. As a result, the effective cyclotron frequencies of both two CR modes are enhanced.

Figure 4 shows results at a high filling factor $(\nu_w, \nu_n) = (4/8, 8/8)$. CR spectra tend to show a negative mode repulsion behavior, i.e., both peaks are shifted to the low-frequency side and the low-frequency peak is pushed away to the low-frequency side with the increase of the interaction. This behavior is quite opposite to the positive mode repulsion exhibited by the corresponding spin-split CR spectra at $(\nu_\uparrow, \nu_\downarrow) = (4/8, 8/8)$ as shown in Fig. 2 (b). The correlation between two CR modes rapidly decreases with the increase of inter-layer distance and the spectra at $d/\ell = 2$ show only a slight effect of interaction even when $E_C/\hbar\Delta \sim 100$.

In the case of spin-split CR, there is a wide region in the filling-factor space where CR exhibits a motional narrowing behavior and such a negative mode repulsion appears only in special cases [8]. In the bilayer system with $d/\ell \gtrsim 1$, the intra-layer correlation of electrons is much larger than the inter-layer correlation and inter-layer overlapping has to be increased to reduce large overlapping of the cyclotron orbits in the same layer. As a result, CR transition is likely to occur at a "maximum" point of the effective potential formed by electrons in the other layer. This presumably enhances the negative mode repulsion behavior.

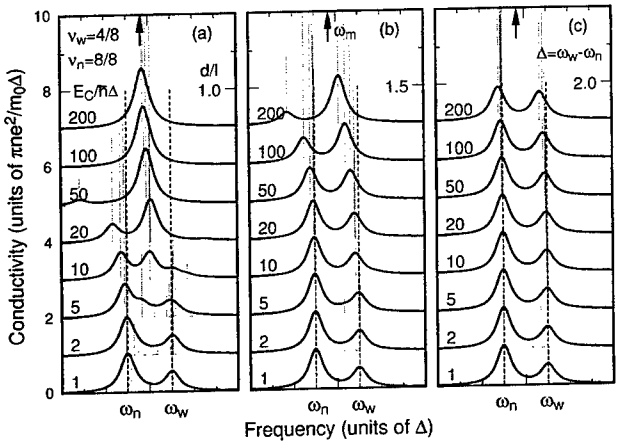

Fig. 4 CR spectra calculated at $(\nu_w, \nu_n) = (1/2, 1)$ for (a) $d/\ell = 1$, (b) 1.5, and (c) 2.

4. Conclusion

Two-component CR has been studied in bilayer quantum Hall systems at absolute zero temperature. At low filling factors $\nu \lesssim 1$, spectra show a positive mode repulsion, while they are inclined to show a negative mode repulsion at high filling factors $\nu \gtrsim 3/2$. More extensive calculations covering the whole filling-factor space and temperature are now underway and will be presented elsewhere.

Acknowledgments

This work is supported in part by the Japan Society for the Promotion of Science ("Research for the Future" Program JSPS-RFTF96P00103). One of authors (KA) is supported by Research Fellowships of the Japan Society for the Promotion of Science for Young Scientists. Numerical calculations were performed in part on FACOM VPP500 in Supercomputer Center, Institute for Solid State Physics, University of Tokyo.

References

* Present address: Department of Physics, University of Tokyo, 7–3–1 Hongo, Bunkyo-ku, Tokyo 113-0033, Japan.

1. W. Kohn, Phys. Rev. **123**, 1242 (1961).
2. See, for example, H. Küblbeck and J. P. Kotthaus, Phys. Rev. Lett. **35**, 1019 (1975).
3. Y. Takada and T. Ando, J. Phys. Soc. Jpn. **44**, 905 (1978).
4. J. Appel and A. W. Overhauser, Phys. Rev. B **18**, 758 (1978).
5. See, for example, G. M. Summers, R. J. Warburton, J. G. Michels, R. J. Nicholas, J. J. Harris, and C. T. Foxon Phys. Rev. Lett. **70**, 2150 (1993).
6. N. R. Cooper and J. T. Chalker, Phys. Rev. Lett. **72**, 2057 (1994).
7. K. Asano and T. Ando, J. Phys. Soc. Jpn. **65**, 1191 (1996).
8. K. Asano and T.Ando, Phys. Rev. B **58**, 1485 (1998).
9. See, for example, K. Ensslin, D. Heitmann, M. Dobers, K. von Klitzing, and K. Ploog, Phys. Rev. B **39**, 11179 (1989).

Quantum Coherence and Skyrmion Textures in Bilayer Quantum Hall Systems

Z.F. Ezawa[a], A. Sawada[a], K. Muraki[b] and Y. Hirayama[b]

[a]*Department of Physics, Tohoku University, Sendai 980-8578, Japan*
[b]*NTT Basic Research Laboratories, Atsugi, Kanagawa 243-0198, Japan*

Quantum coherence develops spontaneously in bilayer quantum Hall systems when the Coulomb exchange energy is dominant. We argue that there exists a distinctive transition between the coherent phase and the resonant phase because different types of skyrmions are excited in these two phases.

Keywords: Quantum Hall Effect, Skyrmion, Macroscopic Coherence, Bilayer System

The quantum Hall (QH) effect is a remarkable macroscopic quantum phenomenon in the two-dimensional electron system. Attention has recently been paid to quantum coherence driven by the Coulomb exchange energy. A specific feature is that quasiparticles are skyrmions [1]. The bilayer system allows a rich family of QH states, where different types of skyrmions are excited. They are SU(2) spin skyrmions, SU(2) pseudospin skyrmions and SU(4) spin-pseudospin skyrmions [2]. In this paper we characterize bilayer QH states by the properties distinguishable by magnetotransport experiments ditecting skyrmion excitations.

We label the two layers by the index $\alpha = \mathrm{f}, \mathrm{b}$. We call the layer $\alpha = \mathrm{f}$ the front layer and the layer $\alpha = \mathrm{b}$ the back layer. There are four types of electrons associated with the two spin states and the two layers, which are described by the field operators $\psi^{\mathrm{f}\uparrow}$, $\psi^{\mathrm{f}\downarrow}$, $\psi^{\mathrm{b}\uparrow}$ and $\psi^{\mathrm{b}\downarrow}$. We restrict our concern to the lowest Landau level, which contains four one-body energy levels. The spin-pseudospin SU(4) symmetry underlies bilayer QH systems.

The Hamiltonian consists of the kinetic term (H_K), the SU(4)-invariant Coulomb term (H_C^+), the capacitance term (H_C^-), the tunneling term (H_T), the Zeeman term (H_Z) and the bias-voltage term (H_{bias}). We rewrite it as $H = H_0 + \Delta H$ by grouping them into the SU(4)-invariant part H_0 and the SU(4)-breaking part ΔH, with

$$H_0 = H_K + H_C^+,$$
$$\Delta H = H_C^- + H_T + H_Z + H_{\mathrm{bias}}. \qquad (1)$$

The total Hamiltonian H commutes with the SU(4)-breaking term ΔH and the Zeeman term H_Z. The Zeeman gap is $g^*\mu_B B$, which we assume to be small enough so that the spin coherence develops spontaneously. The tunneling gap Δ_{SAS} may or may not be small.

We start our analysis when the SU(4)-breaking term ΔH is large, where one-body eigenstates of ΔH determine energy levels. An integer QH state is realized when each level is filled up. Fractional QH states are generated when it is partially filled at $\nu = n/m$ with odd m. An exact analysis is very difficult, however, since the capacitance term H_C^- and the tunneling term H_T do not commute. We investigate two simple cases where either the capacitance term or the tunneling term is dominant. They correspond physically to the following two cases.

(A) When the two layers are separated sufficiently apart ($d \to \infty$), we expect to have a *compound state* made of two monolayer QH states. Indeed, in the limit $d \to \infty$, the capacitance term becomes largest ($H_C^- = H_C^+$) while the tunneling interaction is negligible, $\Delta H \simeq H_C^- + H_Z$. The QH state is an eigenstate of the capacitance term H_C^-.

(B) When the interlayer separation d becomes small, we expect to have a *resonant state* stabilized by the tunneling term. Indeed, in the limit $d \to 0$, since the capacitance term becomes negligible ($H_C^- = 0$), the tunneling interaction may be dominant, $\Delta H \simeq H_T + H_Z$. The QH state is an eigenstate of the tunneling term H_T.

There exists a prominent feature distinguishing the resonant state from the compound state. When a bias voltage is applied ($V_{\mathrm{bias}} \neq 0$), electrons are transferred smoothly from one layer to the other in the resonant state but not in the

compound state. To elucidate the resonant state it is convenient to define the bond and antibond field operators [2],

$$\psi^{\rm B}(x) = \sqrt{\frac{1+\sigma_0}{2}}\psi^{\rm f}(x) + \sqrt{\frac{1-\sigma_0}{2}}\psi^{\rm b}(x),$$
$$\psi^{\rm A}(x) = \sqrt{\frac{1-\sigma_0}{2}}\psi^{\rm f}(x) - \sqrt{\frac{1+\sigma_0}{2}}\psi^{\rm b}(x), \quad (2)$$

for each spin component, where σ_0 is a parameter to be fixed later. The bond state $|g_{\rm B}\rangle$ and the antibond state $|g_{\rm A}\rangle$ are created by operating these operators on the vacuum. By neglecting the capacitance term and the Zeeman term, we diagonalize the symmetry-breaking Hamiltonian,

$$\Delta H \simeq -\frac{1}{2}\int d^2x(\psi^{\rm f\dagger}\psi^{\rm b\dagger})\begin{pmatrix} -eV_{\rm bias} & \Delta_{\rm SAS} \\ \Delta_{\rm SAS} & eV_{\rm bias}\end{pmatrix}\begin{pmatrix}\psi^{\rm f}\\ \psi^{\rm b}\end{pmatrix}$$
$$= -\frac{1}{2}\Delta_{\rm BAB}\int d^2x\{\rho^{\rm B}(x) - \rho^{\rm A}(x)\}, \quad (3)$$

with $\Delta_{\rm BAB} \equiv \sqrt{\Delta_{\rm SAS}^2 + (eV_{\rm bias})^2}$, where $\rho^{\rm B}(x) = \psi^{\rm B\dagger}(x)\psi^{\rm B}(x)$ and $\rho^{\rm A}(x) = \psi^{\rm A\dagger}(x)\psi^{\rm A}(x)$ are electron densities in the bond and antibond states. The diagonalization requires

$$\sigma_0 = \frac{eV_{\rm bias}}{\sqrt{\Delta_{\rm SAS}^2 + (eV_{\rm bias})^2}}. \quad (4)$$

Hence, the ground state is the bond state with the one-particle gap energy $\Delta_{\rm BAB}$.

We mention some specific properties of the resonant state. First, the number density in each layer is given by

$$\langle g_{\rm B}|\rho^{\rm f}(x)|g_{\rm B}\rangle = \frac{1}{2}\rho_0(1+\sigma_0),$$
$$\langle g_{\rm B}|\rho^{\rm b}(x)|g_{\rm B}\rangle = \frac{1}{2}\rho_0(1-\sigma_0). \quad (5)$$

The physical meaning of the parameter σ_0 is the normalized density difference. However, there exists a large uncertainty in number densities $\rho^{\rm f}$ and $\rho^{\rm b}$ in each layers except at $\sigma_0 \simeq \pm 1$. Density operators $\rho^{\rm B}$ and $\rho^{\rm A}$ are good quantum operators but $\rho^{\rm f}$ and $\rho^{\rm b}$ are not in the resonant state. Second, the charge transfer is possible only at $\nu = 1, 2$ and 3 when $\Delta_{\rm SAS} > g^*\mu_B B$, and at $\nu = 1$ and 3 when $\Delta_{\rm SAS} < g^*\mu_B B$, because it occurs by mixing the symmetric and antisymmetric states [Fig.1].

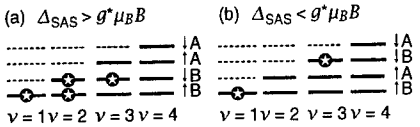

Figure 1: One Landau level is split into four energy levels, the up-spin bond state (↑B), the down-spin bond state (↓B), the up-spin antibond state (↑A) and the down-spin antibond state (↓A). A heavy line indicates a filled level. A heavy line with symbol ✪ indicates that it is a charge-transferable level. A charge-transferable state is either a *resonant state* or a *coherent state*. Compound states are stabler than resonant states at $\nu = 2$ for $\Delta_{\rm SAS} < g^*\mu_B B$.

We proceed to analyze the case when the symmetry-breaking term ΔH is small. In this case the Coulomb exchange energy arising from the SU(4)-invariant Coulomb interaction term $H_C^{\pm}$ becomes essential. It drives the SU(4) spin-pseudospin coherence to develop [2]. The ground state is a coherent state, representing a homogeneous configuration of electrons, upon which the exchange energy vanishes and the total Hamiltonian reads

$$\langle\mathcal{H}\rangle = \frac{Q^2}{2C} - \frac{1}{2}\Delta_{\rm SAS}\rho_0\sqrt{1-\sigma_0^2} - V_{\rm bias}Q, \quad (6)$$

except for the Zeeman energy, which is a constant depending on the filling factor. Here, $Q = \frac{1}{2}e\rho_0\sigma_0$ is the charge imbalance induced by the voltage $V_{\rm bias}$, while C is the capacitance ($C \simeq \varepsilon/d$). The imbalance parameter σ_0 is determined by minimizing (6), or by solving

$$\frac{e^2\rho_0\sigma_0}{2C} + \frac{\Delta_{\rm SAS}\sigma_0}{\sqrt{1-\sigma_0^2}} = eV_{\rm bias}. \quad (7)$$

The solution is given by (4) when $C \to \infty$ or $d \to 0$. By controlling the voltage $V_{\rm bias}$, the density difference $\rho_0\sigma_0$ can be smoothly varied without breaking the interlayer coherence. It is clear that the coherence develops only on charge-transferable states [Fig.1]. It is to be emphasized that the number densities $\rho^{\rm f}$ and $\rho^{\rm b}$ are good quantum numbers in coherent states, as makes a clear contrast to resonant states, though both of them are charge-transferable states. At $\nu = 1$ pseudoparticles

are spin skyrmions for $\Delta_{SAS} > g^*\mu_B B$ and pseudospin skyrmion for $\Delta_{SAS} < g^*\mu_B B$, while at $\nu = 2$ they are spin-pseudospin skyrmions [2].

We give a rough sketch of phase diagrams in Fig.2 by assuming that only compound states, resonant states and coherent states are possible.

Let us consider the QH state at $\nu = 1$, where spins are spontaneously polarized and there exists no compound state. Resonant states are realized when Δ_{SAS} is large, while coherent states develop when both d and Δ_{SAS} are reasonably small [4, 5]. Consequently, we expect the phase diagram as in Fig.2(a). Related phase diagrams are found in literature [3]. We also mention a speculation that no clear distinction exists between the coherent state and the resonant state.

Let us next consider the QH state at $\nu = 2$, where all three states are possible. The spin degree of freedom plays a nontrivial role. Compound states are spin polarized. Resonant states exist only when $\Delta_{SAS} > g^*\mu_B B$, and they are spin unpolarized [Fig.1]. This is a result of a competition between the tunneling energy and the Zeeman energy. The boundary of the two phases is given by the condition $g^*\mu_B B = \Delta_{SAS}$ at $d = 0$. Finally, resonant states are replaced by coherent states when both d and Δ_{SAS} are reasonably small [2]. Consequently, we expect the phase diagram as in Fig.2(b). A related phase diagram is found in literature [6].

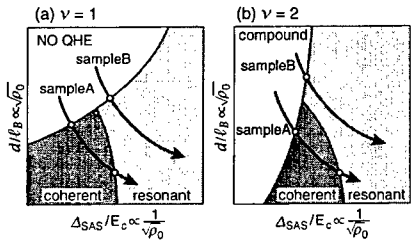

Figure 2: Phase diagrams are sketched for $\nu = 1$ and $\nu = 2$ at the balance point ($\sigma_0 = 0$). An arrow on the figure is a flow of a QH state as the total density ρ_0 decreases in one sample.

In the rest of this paper we address the problem how to distinguish these three states experimentally. There are three standard techniques to elucidate bilayer QH states in magnetotransport experiments: (I) First, the total electron density ρ_0 is varied. (II) Second, the imbalance parameter σ_0 is varied between the two layers. (III) Third, the sample is tilted in the external magnetic field. By changing ρ_0 the interlayer separation d is effectively changed with respect to the magnetic length, $d/\ell_B \propto \sqrt{\rho_0}$, while the tunneling energy is effectively changed with respect to the Coulomb energy E_C, $\Delta_{SAS}/E_C \propto 1/\sqrt{\rho_0}$. The key observation is that the QH state moves along a line in a single sample as indicated in Fig.2. In a high-density limit ($\rho_0 \to \infty$) there exists no bilayer QH state at $\nu = 1$, but there exists a compound state at $\nu = 2$ at the balance point.

We first consider the case where $d\Delta_{SAS}$ is reasonably small [sampleA in Fig.2]. As the total density ρ_0 decreases an interlayer coherence will develop spontaneously, which has been argued at $\nu = 1$ in Refs.[4, 5, 7] and at $\nu = 2$ in Ref.[2]. We expect a phase transition at $\nu = 2$ between the compound state and the coherent state but not at $\nu = 1$. These two states are clearly distinguishable by using the second technique, i.e. by applying gate bias voltage, because the compound state is unstable. Furthermore, the activation energy increases as σ_0 increases in the coherent state due to the increase of the capacitance energy $\langle H_C^- \rangle$ of skyrmion excitations [2]. To confirm that it is a coherent state, we may use the third technique. As the sample is tilted, the activation energy exhibits an anomalous decrease [8] in the coherent state, but if $\Delta_{SAS} > g^*\mu_B B$ it exhibits a smooth increase due to the Zeeman energy in the compound state where spin-skyrmions are excited. All these features have been experimentally confirmed in recent works [9, 10] at $\nu = 1$ and 2.

As ρ_0 decreases further, the QH state will be turned into a resonant state [Fig.2]. It is essentially a monolayer state to be realized when the up-spin bond state is filled at $\nu = 1$, and the down-spin bond state at $\nu = 2$ [Fig.1]. At $\nu = 1$ pseudoparticles are spin skyrmions, while at $\nu = 2$ they are vortices whose excitations decreases the Zeeman energy but increases the tunneling energy. The capacitance term is suppressed since it is an eigenstate of the tunnel-

ing interaction. Consequently, the activation energy will remain constant as the bias voltage is increased (the second technique), as makes a clear contrast to the coherent state. We may also examine the activation energy by tilting the sample (the third technique). It will increase due to the increase of the Zeeman energy of spin skyrmions at $\nu = 1$, as makes also a clear contrast to the coherent state. On the other hand, it will decreases slowly at $\nu = 2$ because both the Zeeman energy and the one-particle tunneling energy decrease. This decrease in the resonant state will be distinguishable from the anomalous decrease in the coherent state.

Coherent states are absent in samples where $d\Delta_{SAS}$ is large [sampleB in Fig.2]. We have only the resonant state at $\nu = 1$, and the compound state and the resonant state at $\nu = 2$. They are distinguishable by the criterion we have given in the above.

In Table1 we summarize the expected behaviors of the stability of the bilayer QH states when the total density (ρ_0), the density difference (σ_0) and the tilted angle (Θ) are increased ($\nearrow$) or decreased ($\searrow$) at the balanced point, independently.

The characteristic feature of the resonant state is yet to be confirmed experimentally. In the sample used in Ref.[9, 10], as the density is decreased sufficiently, the QH state becomes unstable and disappear before the resonant state is reached. We hope to verify these predictions on the resonant state experimentally in a near future.

	ν	$\rho_0\nearrow$	$\rho_0\searrow$	$\sigma_0\nearrow$	$\Theta\nearrow$
resonant	1	$\searrow$	$\nearrow$	$\rightarrow$	$\nearrow$
coherent	1	$\searrow$	$\searrow$	$\nearrow$	$\searrow$
compound	2	$\nearrow$	$\searrow$	$\searrow$	$\nearrow$
resonant	2	$\searrow$	$\nearrow$	$\rightarrow$	$\searrow$
coherent	2	$\searrow$	$\searrow$	$\nearrow$	$\searrow$

Table 1: It is summarized how the stability of typical bilayer QH states changes at the balance point when the total density (ρ_0), the density difference (σ_0) and the tilted angle (Θ) are changed in samples with $\Delta_{SAS} > g^*\mu_B B$. The symbol $\nearrow$, $\searrow$and $\rightarrow$indicate that the stability increases, decreases and remains unchanged, respectively.

We have characterized the compound state, the coherent state and the resonant state in the lowest Landau level of the bilayer QH system. In passing, we remark a prediction of the canted state [6], which might be relevant when the tunneling energy and the capacitance energy are both important. We also remark that there exists a rich family of bilayer QH states in higher Landau levels, about which we wish to discuss elsewhere [11].

References

[1] S.L. Sondhi, A. Karlhede, S. Kivelson and E.H. Rezayi, Phys. Rev. B **47**, (1993) 16419; D.H. Lee and C.L. Kane, Phys. Rev. Lett. **64**, (1990) 1313.

[2] Z.F. Ezawa Phys. Rev. Lett. **82**, (1999) 3512.

[3] A.H. MacDonald, P.M. Platzmann and G.S. Boebinger, Phys. Rev. Lett. **65**, (1990) 775; S. He, S.D. Sarma and X.C. Xie, Phys. Rev. B **47**, (1993) 4394.

[4] Z.F. Ezawa and A. Iwazaki, Int. J. Mod. Phys. B **6**, (1992) 3205; Phys. Rev. B **47**, (1993) 7295; Phys. Rev. B **48**, (1993) 15189.

[5] Z.F. Ezawa, Phys. Lett. A **229**, (1997) 392; Phys. Rev. B **55**, (1997) 7771.

[6] L. Zheng, R.J. Radtke and S. Das Sarma, Phys. Rev. Lett. **12**, (1997) 2453.

[7] K. Moon, H. Mori, K. Yang, S.M. Girvin, A.H. MacDonald, L. Zheng, D. Yoshioka and S.C. Zhang, Phys. Rev. B **51**, (1995) 5138.

[8] S.Q. Murphy, J.P. Eisenstein, G.S. Boebinger, L.N. Pfeiffer and K.W. West, Phys. Rev. Lett. **72**, (1994) 728.

[9] A. Sawada, Z.F. Ezawa, H. Ohno, Y. Horikoshi, Y. Ohno, S. Kishimoto, F. Matsukura, M. Yasumoto, and A. Urayama, Phys. Rev. Lett. **80**, (1998) 4534.

[10] A. Sawada, Z.F. Ezawa, H. Ohno, Y. Horikoshi, A. Urayama, Y. Ohno, S. Kishimoto, F. Matsukura, N. Kumada Phys. Rev. B **59**, (1999) 14888.

[11] K. Muraki, N. Kumada, T. Saku, Z.F. Ezawa, A. Sawada and Y. Hirayama , (in preparation) .

TEMPERATURE DEPENDENCE OF THE RESISTANCE RESONANCE IN WEAKLY COUPLED QUANTUM WELLS

S. Charlebois*, J. Beerens, R. Côté,
Centre de recherche en physique du solide and Département de physique,
Université de Sherbrooke, Sherbrooke, Québec, Canada J1K 2R1

E. Lavallée, J. Beauvais,
Centre de recherche en physique du solide and
Département de génie électrique et de génie informatique,
Université de Sherbrooke, Sherbrooke, Québec, Canada J1 K 2R1

and Z. R. Wasilewski,
Institute for Microstructural Sciences, National Research Council, Ottawa, Canada K1A 0R6

ASTRACT

We report on measurements of the resistance of a double quantum well structure (DQW) with weakly coupled wells (tunneling gap Δ=0.29 meV) as a function of temperature and in-plane magnetic field. Our data clearly show the expected enhancement of the resistance when the DQW is placed in its balanced conditions (using an electrostatic gating technique). Although most features of this "resistance resonance" (RR) can be explained in the framework of a theory put forward by Berk et al. [Phys. Rev. B **50**, 15420 (1994)], the amplitude of the RR observed in our sample cannot be quantitatively explained by this theory. We attribute this discrepancy to the weak tunneling conditions in our case, which lead to a situation where the inter-well transfer time is larger (by a factor of 2) than the electron scattering time.

When electrons are localized in separate wells in a double quantum well (DQW) structure, the resulting resistance can be calculated with the usual classical rule for two conductors connected in parallel. If the mobility is different in the two wells, the clean well shunts the dirty one and the total resistance is that of the higher-mobility well. At resonance, when energy levels of both wells coincide, electrons are delocalized and no shunting occurs. The total resistance then approaches that of the well with poor mobility. When the band profile of the structure is modified by the application of an external bias on a surface gate, the total resistance of the DQW exhibits a maximum when resonance is achieved. This phenomenon called *resistance resonance* (RR) has been reported and studied in a number of papers.[1-3, 5, 7]

Fig. 1 shows the RR observed in our sample when the gate voltage V_G is swept. The sample consists of a symmetric $GaAs/Al_{0.3}Ga_{0.7}As$ DQW structure with 18 nm well width and 3.4 nm barrier. Electrons are supplied by two Si δ-doping layers located 120 nm above and below the DQW. Standard Hall bar shaped samples were lithographically defined. A front gate, made by evaporating a gold layer on top of a ~600 nm thick SiO_2 layer deposited on the sample, covers the whole Hall bar, enabling us to control the balance between the wells. Measurements were performed with the current flowing perpendicular to the magnetic field, using a standard 4-point low frequency lock-in technique at temperatures down to 300 mK. Shubnikov-de Haas oscillations measurements were performed to determine the electron densities in both quantized levels, n_{E1} and n_{E2}, at any given gate bias. From these results, a tunneling gap value of Δ=0.29 meV was obtained. The mobility in both wells as a function of V_G was deduced from the analysis of the $R(V_G)$ curve.[4] In the balanced conditions, the electron mobility of the top and bottom wells were 46.5 $m^2/V{\cdot}s$ and 2.9 $m^2/V{\cdot}s$, respectively, for an electron concentration of $1.8{\times}10^{11}$ cm^{-2} in each well. We assume the mobility difference between the wells to be caused mainly by diffusion of Si from the lower δ-doping layer during the growth.

Using a two-parameter theory based on the quantum and transport scattering times,[2] the total resistance as a function of a gate bias is given, if all relevant energies are much less than the Fermi energy, by (we put $\hbar = 1$):

$$R = R_{off}\left\{1 + A\frac{\overline{\Delta^2}}{W^2}\cdot\frac{1}{1+(E_1-E_2)^2/W^2}\right\},\ \text{where}\ \overline{\Delta^2} = \Delta^2\frac{\tau^{tr}}{\tau}\ \text{and}\ W^2 = \overline{\Delta^2} + \frac{1}{\tau^{tr}\tau},\quad (1)$$

with $1/\tau = (1/2\tau_1) + (1/2\tau_2)$ and $1/\tau^{tr} = (1/2\tau_1^{tr}) + (1/2\tau_2^{tr})$. R_{off} is the resistance in off-resonance conditions, and τ^{tr} and τ are the transport and quantum scattering times, respectively. In Eq. (1), A is an asymmetry coefficient given by $A = \left(\tau_1^{tr} - \tau_2^{tr}\right)^2 / 4\tau_1^{tr}\tau_2^{tr}$. The other parameters are defined in Ref. [2]. This theory predicts that when an in-plane magnetic field is applied, at resonance, in a direction perpendicular to the current, the RR amplitude should decrease according to:[3]

$$R(B)^{-1} - R_{off}^{-1} = \left[R(0)^{-1} - R_{off}^{-1}\right] f(B/B_c)\ \text{where}\ f(x) = \frac{2\left(\sqrt{1+x^2}-1\right)}{x^2\sqrt{1+x^2}} \qquad (2)$$

$$B_c = \frac{1}{ev_f\tau b}\sqrt{1+\Delta^2\frac{\tau_1^{tr}+\tau_2^{tr}}{2}\tau}$$

Since the critical field B_c is the only fitting parameter, a study of the decrease of the RR in a parallel magnetic field allows one to extract the quantum scattering time τ.

The amplitude of the RR is given by $C = A\overline{\Delta^2}/W^2$. For our sample, this coefficient takes a value of 0.95. However, our measurement of the RR amplitude gives 2.11, which is twice larger than the theoretical prediction. We find that a good fit to the data can be obtained by making $C \to \beta C$ where β is some *ad hoc* coefficient, equal to 2.2 in our case. This is shown in Fig. 1b. We note that this renormalization of C does not change the FWHM of the Lorentzian which corresponds to a quantum scattering time of $\tau^{-1} \sim 0.69$ meV. This value of τ^{-1} is identical to the one we obtain by fitting the in-plane magnetic field dependence of the resistance using Eq. (2), and is also in a very good agreement with the value (0.67 meV) deduced from a Dingle plot analysis adapted to a two-band situation. [6] Therefore, the theory leading to Eqs (1) and (2) seems adequate to fit the shape of the RR, but not the observed amplitude. These results suggest that the discrepancy between theory and experiment arises from an underestimation of the C factor for our sample. This could be related to the fact that our sample lies deeply in the "dirty" limit $\overline{\Delta^2}/W^2 \ll 0.5$.

Fig. 2 shows the temperature dependence (below 7K) of the quantum scattering time obtained by fitting the magnetoresistance under in-plane field using Eq. (2). The temperature dependence is well approximated by a $T^{3/2}$ law. As done in previous studies (e.g. [2]), the total quantum scattering can be divided into two contributions : one from diffusion on the impurities which, in the range of temperature studied, is expected to be temperature independent, and another one which is temperature dependent: $\frac{1}{\tau(T)} = \frac{1}{\tau(0)} + \frac{1}{\tau(T)}$. In our case (see Fig. 2), the temperature dependent scattering cannot be attributed completely to electron-electron scattering alone which should show a T^2 dependence with logarithmic corrections [3] (approximated by a $T^{1.77}$ power law in Fig. 2). This is expected for weak tunneling samples (see [7]). For comparison, we also plot in Fig. 2 the *transport* scattering rates, τ_σ, extracted from the high temperature conductivity (valid from 2K to more than 100K).

At resonance the temperature and in-plane magnetic field dependence of the RR should be given by

$$R(B,T) = R_{off}(T)\left\{1 + C(\tau^*)\cdot\frac{f(B/B_c(\tau))}{1+C(\tau^*)\left[1-f(B/B_c(\tau))\right]}\right\} \qquad (4)$$

where $\tau^*(T)$ will be discussed below. In these fits, $R_{off}(T)$ was chosen in such a way that the calculation of $R(B,T)$ equals the experimental value at B= 6 T. At such field, the resonance has

almost completely vanished ($f(x) \approx 0.01$). We first tried to reproduce the experimental data using $\tau^*(T) = \tau(T)$, but this causes the resistance resonance to vanish much too fast (at T~20 K; see Fig. 3). We therefore had to introduce a scattering rate that includes electron-electron scattering mechanism:

$$\frac{1}{\tau^*(T)} = \frac{1}{\tau(0)} + \gamma \frac{1}{\tau_{ee}(T)} \qquad (3)$$

where $1/\tau_{ee}$ is defined in [3], and the factor $\gamma \approx 0.17$ to fit our data. In Ref. [3], authors found that a factor $\gamma > 1$, taking into account interband processes, was needed to provide an agreement with the experiment. A more detailed analysis is necessary to confirm if such interband processes can account for the value of γ in our context (i.e. "dirty" limit). We also point out that the small bumps seen in $R(B,T)$ are not caused by our choice of $R_{off}(T)$ but are inherent to Eq. (3).

In summary, our study shows that the amplitude of the RR in our sample cannot be described by the model of Ref. [2], even though the magnetoresistance is in very good agreement with the experimental curves and the extracted quantum scattering rate τ^{-1} is consistent with the width of the RR. In our structure, the quantum scattering time is close to the transport time, suggesting that additional scattering mechanisms need to be considered in the analysis.

REFERENCES

*e-mail : scharleb@physique.usherb.ca, phone : (819)-821-8000 ext 3042, fax (819)-821-8046

[1] A. Palevski et al., Phys. Rev. Lett. **65**, 1929 (1990).
[2] Y. Berk et al. Phys. Rev. B **50,** 15420 (1994).
[3] Y. Berk et al. Phys. Rev. B **51,** 2604 (1995).
[4] The V_G<-1.5V part of the R(V_G) curve provided $\mu_1(V_G)$ – bottom well - as the top well was depleted and $\mu_2(V_G)$ was evaluated using the assumption that, far from resonance, the total mobility is that of two uncoupled wells connected in parallel $\mu = \mu_1 + \mu_2$.
[5] Y. Berk et al. Surf. Sci. **361,** 126 (1996).
[6] P. T. Coleridge, Semicond. Sci. Technol. **5,** 961 (1990).
[7] M. Slutzky et al. Phys. Rev. B **53,** 4065 (1996).

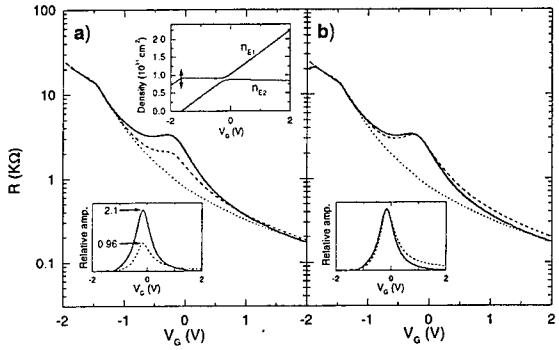

Figure 1 a) Resistance as a function of the gate bias V_G showing the resonance centered around V_G = -0.2V (solid line). Calculations (dashed line) made using the uncorrected model clearly cannot account for the amplitude of the resonance. The dotted line corresponds to the resistance of the two wells connected in parallel assuming no tunneling ($\Delta = 0$). The top inset gives the electron densities of the two subbands, as obtained by a Fourier analysis of the Shubnikov-

de Haas oscillations. The double arrow indicates the onset gate voltage at which the upper well becomes totally depleted. The bottom inset shows the relative amplitude of the experimental and theoretical resonance. b) Experimental $R(V_G)$ curve (solid line) and theoretical curve (dashed line) using a phenomenological amplitude factor $\beta = 2.21$. The inset shows that the width of the experimental resonance is adequately represented by the model using $\tau^{-1} = 0.694$ meV, as in a).

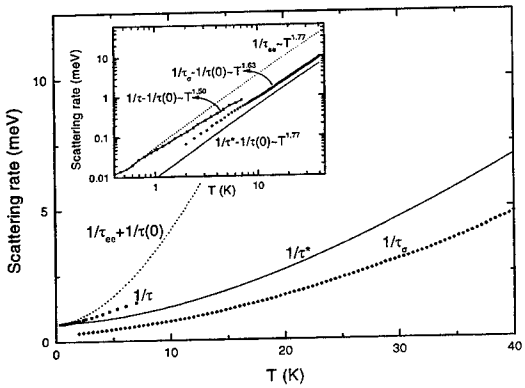

Figure 2 Temperature variation of i) the small-angle scattering rate τ obtained from magnetoresistance (squares and extended by the dashed line), ii) the transport scattering rate τ_σ extracted from the high temperature conductivity (diamonds), iii) the theoretical electron-electron scattering rate τ_{ee} (dotted line), and iv) the scattering rate τ^* used in the $R(T, B)$ calculation of Fig. 1b (solid line). The inset shows an equivalent representation of the same data on a log-log scale.

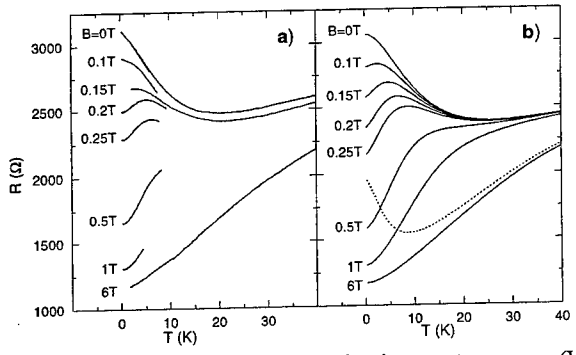

Figure 3 a) Temperature dependence of the measured resistance at resonance (V_G = -0.2V) for various in-plane magnetic field values. b) Theoretical dependence of the resistance at resonance, calculated using Eq. 3. The dotted line shows the R(T, B=0 T) calculation without the phenomenological amplitude factor and using the theoretical electron-electron scattering rate in $C(\tau^* = \tau_{ee})$.

HYSTERETIC MICROWAVE CYCLOTRON RESONANCE OF A LATERALLY CONFINED 2DEG

B. M. Ashkinadze and V. I. Yudson*)
Solid State Institute, Technion- Israel Institute of Technology, Haifa 32000, Israel

Abstract

A hysteretic cyclotron resonance (CR) is discovered in a laterally confined high mobility two-dimensional electron gas (2DEG) in GaAs/AlGaAs heterostructures. The hysteresis and switching phenomena are observed in microwave radiation (36GHz) transmission at temperature 1.8-25K. It is found that the hysteresis is accompanied by long-lived, microwave-induced changes of the 2DEG density. These density changes is attributed to a modification of electron vertical transport processes in heterostructures under the microwave heating of the 2DEG. A phenomenological model based on the 2DEG density-dependent CR, describes reasonably the main experimental findings.

Introduction

A cyclotron resonance (CR) is extensively used in study of high mobility 2D-electrons in modulation-doped GaAs-AlGaAs heterostructures [1-3]. For a laterally confined 2DEG the CR is modified by a depolarization effect. This leads to the CR resonance frequency shift [4], and the resonance is considered as a dimensional magnetoplasma resonance (DMPR). The DMPR lineshape for a linearly polarized mw radiation is described by

$$P_{mwa}(B) = C\sigma_0 P_{in} \frac{1+(\omega_L^2+\omega_R^2)\tau_m{}^2}{(1+(\omega_L^2-\omega_R^2)\tau_m{}^2)^2+4\omega_R^2\tau_m{}^2} \qquad (1)$$

Here P_{mwa} and P_{in} are absorbed and input mw powers, respectively; C is a factor which takes into account the waveguide and sample geometry; σ_0 is a dc conductivity; τ_m is an electron momentum relaxation time; $\omega_R = \omega - \omega_p^2(n_{2D})/\omega$; $\omega_p(n_{2D}) = [3\pi^2 e^2 n_{2D}/(2a\varepsilon m^*)]^{1/2}$ is the plasmon frequency for the 2DEG confined within the mesa of the diameter a (a is smaller than the mw wavelength); ε is an averaged value of the dielectric constant of free space and GaAs [5]. At a given mw frequency $\omega=2\pi f$, the DMPR occurs at the magnetic field $B_R = B_{CR} - 3\pi^2 e c n_{2D}/2\varepsilon\omega a$ which depends on a 2DEG density n_{2D}., on a and differs from B_{CR} taken from the CR condition: $\omega = \omega_L^{CR} = eB_{CR}/(m^* c)$.

The CR experiments are usually performed at low temperatures and under low intensity far-infrared (FIR) or microwave (mw) irradiation that does not affect the 2DEG parameters. Increasing FIR/mw radiation intensity leads to the electron heating that becomes more efficient at the CR (DMPR). This gives rise to a resonant mw/FIR modulation of the photoluminescence (PL) (optically detected resonances - ODR) [6-9], as well as to the resonant mw/FIR photoconductivity (PC) and photovoltage [10-12]. These effects, in particular the resonant electron heating of the laterally confined 2DEG, are used to study the spectra of dynamic excitations of the 2DEG [11, 12]. However, physical processes accompanying the electron heating as well as physical mechanisms underlying the PL and PC modulations under intense FIR/mw irradiation, are not well understood. We report the electron density decrease under 2DEG heating by mw radiation, and as a result of this, an appearance of a hysteretic cyclotron resonance (CR) for the laterally confined 2DEG.

Experiment

A mw radiation) f=36GHz) transmission in a wide range of mw powers, P_{in} = 10^{-3}mW-5mW, have been studied on high quality modulation-doped GaAs/$Al_{0.3}Ga_{0.7}As$ heterostructures (quantum wells and heterojunctions (HJ) grown by molecular beam epitaxy). The sample was inserted in 8-mm waveguide which was short-circuited at one end, and it was immersed in liquid He or in cold He gas so that the temperature can be varied in the range of T=1.8-25K. An external magnetic field B is applied perpendicularly to the heterointerface, and it is slowly scanned back and forth in the range of 0-0.2 T. Here we discuss the results obtained on the HJ characterized by the dark 2DEG density n_{2D}^0 =$1.6\cdot10^{11}$ cm^{-2} and a dc-measured mobility μ of 2 10^6 cm^2/Vs. Electrons were supplied by a Si-doped layer separated from the interface by a 30nm $Al_{0.3}Ga_{0.7}As$ spacer. The lateral dimension of the sample was reduced by fabricating mesa with the diameter a =0.7 mm. The small sample size ensures the linearity of the mw absorption at low mw power.

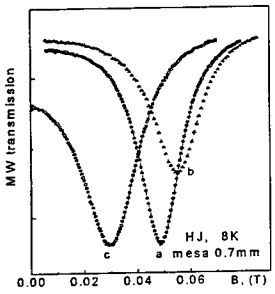

FIG. 1.The mw transmission vs B measured at low mw power (see text).

Fig. 1 shows the mw transmission (MWT) traces at lowest P_{in} . The traces are obtained under various experimental conditions affected the 2DEG at 2K: a. after cooling the sample in the dark, b. under He-Ne light illumination and c. after the illumination is turned off. Each MWT trace exhibits the DMPR resonance at B_R values that are lower than the resonant value B_{CR} = 0.086 T expected for a free electron CR in GaAs at f=36 GHz [13]. The DMPR shifts and the DMPR linewidth changes when the 2DEG density and the 2DEG mobility is modified either due to optical depletion under light illumination [9] or due to persistent photoconductivity.

The MWT is strongly affected by increased P_{in} at 2K as well as 8K (see Fig. 2a, b). One can see that the resonance line shifts to higher B_R values as P_{in} increases. Above a certain threshold magnitude of P_{in} , a hysteresis occurs: there appears a difference between the MWT traces obtained at increasing and at decreasing

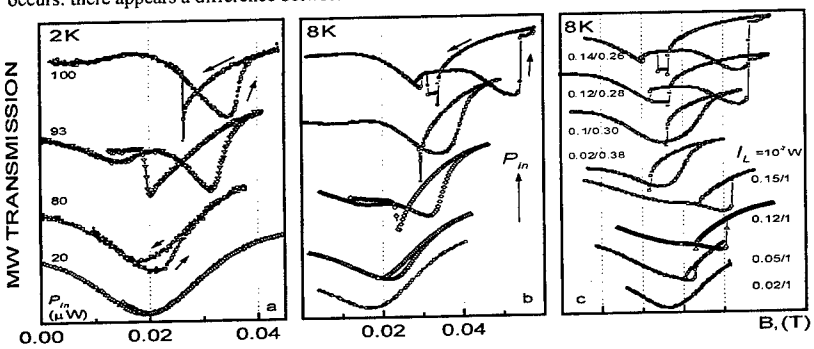

FIG. 2. MWT vs B as a function of P_{in} values, shown near the traces. The traces are shifted vertically for clarity . Continuos mw radiation: a). T_L=2K; b) T_L=8K. (c): Pulse-modulated mw radiation T_L=8K, P_{in} =100μW. Duty-cycle ratios. t_p/T_p (t, $10^{-3}s$) are given near the curves. Four upper traces are obtained in dark, four bottom ones are measured under weak (10^{-7}W) He-Ne laser illumination. Arrows indicate the scanning direction of the magnetic field.

magnetic field. At still higher P_{in} a sudden MWT switching is observed.

Surprisingly, the CR hysteresis persists also under modulated mw irradiation (Fig. 2c). The microwave power is applied by pulses. A pulse duration t_p and a time-interval Tp between the pulses are varied. We find that the hysteresis loop depends only slightly on Tp as far as $Tp < 10^{-3}$ s and $tp > 10^{-5}$ s. Since the hysteresis exists even for small duty cycle ratios t_p/Tp, it means that the intense mw irradiation induces a long-lived modification in the 2DEG state. This modification lasts after the mw pulse, and the 2DEG reaches its new steady-state after a certain number of mw pulses. The 2DEG changes recover with the characteristic time of 10^{-2} s at 1.8K.

Discussion

An intense mw field heats up the 2DEG. Due to fast electron-electron scattering, this results in an increased 2DEG temperature T_e. The electron heating experiments carried out in dc, FIR and mw electric field [14, 15], allow to estimate T_e for a given mw power absorbed per electron. Measuring the total mw power absorbed by the mesa, we deduce that T_e does not exceed 30K in our experiments. In this regime the electron energy losses occur via an emission of low-energy acoustic phonons with the energies of sk_f (s is the sound velocity, k_f is the 2DEG Fermi wavevector). At low temperature these phonons are ballistically propagated over whole sample [16].

To interpret the nonlinear and hysteretic CR we assume that an intense mw irradiation induces a long-lived reduction of the DEG density. This is consistent with the observation of the DMPR shift to higher B_R with increasing P_{in} (see Fig.2) as well as with the observed the long-lived (of 10^{-2} s) modification of the 2DEG parameters. The only proper 2DEG parameter that can be characterized by such long relaxation times, is the 2DEG density determined by slow vertical electron transport (tunneling) processes. It should be noted that the long memory effect excludes any explanation based on the sample heating, since the transfer time of the ballistically propagated phonons into liquid He does not exceed 10^{-6}s. Therefore, the mw-induced 2DEG density decrease should be associated with the increase of the electron temperature and, perhaps, with a flux of the nonequilibrium acoustic phonons. We assume that the 2DEG heating modifies the rates of electron transport into and out of the 2DEG so that the 2DEG density reduces. At present we do not specify mechanisms of the mw-induced vertical electron transport and the role of the phonon wind.

As a simple phenomenological model, we suppose that the rate of electron escape from the 2DEG increases linearly with the mw power absorbed per electron , $P_{mwa}(B)/n_{2D}$, while the electron return rate τ^{-1} is un affected by mw radiation. Then, from the steady state solution of the balance equation, we get $n_{2D} = n^0_{2D}(1-\beta\, P_{mwa}/n^0_{2D})$, where β is a coefficient of mw-induced nonlinearity. Thus, the resonant frequency ω_R in Eq. (1) depends on P_{mwa}, and Eq. (1) becomes a nonlinear equation which determines the nonlinear CR absorption in the steady-state regime. A numerical solution of Eq. (1) demonstrates the hysteretic phenomena (Fig. 3).

For a circularly (electron CR-active) polarized mw field, conditions for the hysteresis were analytically found [17]. Comparison of the experimental results (Fig.2) with the calculated curves shows that our model explains the main features of the nonlinear hysteretic CR found in the laterally confined 2DEG systems.

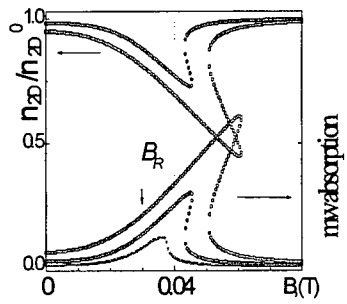

FIG. 3. Calculated mw absorption vs B for the nonlinear coefficient β=0.05; μ=1.4.10 ^{6} cm^2 /Vs; dimensionless input mw power are 5, 15, 50. The 2DEG density vs. B is presented for input mw power of 15 and 50. The DMPR position B_R is marked by arrow.

The time-resolved mw experiments allow to measure the phenomenologically introduced time (τ) of the electron transport from adjacent layers (spacer) into the 2DEG. We have found that τ varies from sample to sample and depends on the ambient temperature and light illumination. At illumination, τ decreases, the hysteresis becomes sharper. At high illumination (when there is strong optical depletion), the hysteresis disappears.

The revealed 2DEG density decrease caused by the electron heating, is likely to be responsible for the optically or photoelectrically detected resonances observed in the heterostructures with the 2DEG [7-12]. The long relaxation time of the CR-induced photoconductivity [10], the resonant photo-electrical response due to the chemical potential shift of the bulk 2DEG states (or of the edge states) under CR heating [12], the strong saturation of the FIR intersubband absorption under high intense FIR [12], can be explained by fast transfer of the excited electrons to the spacer layer. It should be noted, an important role of the phonon wind emitted by the hot 2DEG, on vertical electron transport [15]. This was revealed on high quality heterojunctions by studying the modulation of the bulk free exciton PL by the spatially separated 2DEG heated at DMPR [15, 18].

In conclusion, a novel hot-electron nonlinear phenomenon - the hysteretic cyclotron resonance under intense microwave irradiation - is observed for the 2DEG in laterally confined GaAs/AlGaAs heterostructures. We assign the nonlinearity to 2DEG density changes caused by a modification of electron vertical transport processes under intense mw irradiation. A simple phenomenological model based on the 2DEG density-dependent CR, describes reasonably the experimental findings. Further research is required for understanding the microscopic mechanisms of the revealed fast vertical electron transport.

Acknowledgments

We are grateful to L. Pfeiffer and V. Umansky for the sample growth and to E. Buchstab for the sample processing. We thank E. Cohen and Arza Ron for useful discussions. The research at Technion was done in the Barbara and Norman Seiden Center for Advanced Opto-electronics and was supported by US-Israel BSF grant. V.Y. acknowledges the hospitality at the Technion.

References

[1]Institute of Spectroscopy, Russian Academy of Sciences, Troitsk, Moscow r-n, 142092 Russia

1. G. Abstreiter , J. Kotthaus, J. F. Koch, G. Dorda, Phys. Rev.**B14**, 2480, (1976)
2. M. J. Chou, D. C. Tsui, G. Weimann, Phys. Rev .**B37**, 848, (1988)
3. J. P. Cheng, B. D. McCombe, Phys. Rev ..**B44**, 3070, (1991)
4. S. J. Allen, H. L. Stormer, J. C. M. Hwang, Phys.Rev. **B28**, 4875 (1983)
5. W. Hansen *et al.*., in Semicond&Semimetals, Ed. M. Reed, vol.35, 279, (1992)
6. M. Godlevskii *et al* ..Crit. Rev. Solid State Mater. Sci 19, 241(1994)
7. R. J. Warburton, J. G. Michels, R. J. Nicholas *et. al.*, **B46**, 13394, (1992)
8. G. S. Herold, H. A. Nickel *et. al* ..Physica E, 2, 39 (1998(
9. B. M. Ashkinadze *et al.* Proc. 23rd ICPS, 2327, (1996); Phys.Stat Sol. (a), 164, 523 (1997)
10. J. C. Maan *et al.*, Appl.Phys.Lett, 40, 609 (1982).
11. B. Meurer *et al.*, Phys. Rev. B49, 16813 (1994).
12. S. Tsujino *et al.*, Physica B249, 571, (1998); Phys. Stat.Sol. (b), 204, 162 (1997)
13. M. Kozhevnikov, B. M. Ashkinadze *et al.*, Phys. Rev. **B52**, 17165 (1995)
14. B. K. Ridley, Rep. Prog. Phys. 54, 169 (1991)
15. B. M. Ashkinadze *et al.*, Proc. 24rd ICPS, Ed. D. Gershoni, Jerusalem, (1998)
16. A .J. Kent *et al.*, Phys. Stat. Sol. (b), 204, 230 (1997)
17. B. M. Ashkinadze, V. Yudson will be published in PRL (1999)
18. J. X. Shen *et al.* Phys. Rev., **B59**, 8093, (1999)

Interacting Separately Confined Two-Dimensional Electron and Hole Gases: Magnetic Field Dependence of the Circularly Polarized Photoluminescence

A. Nazimov, E. Cohen, Arza Ron, E. Linder, H. Shtrikman[1)] and L. N. Pfeiffer[2)]
Solid State Institute, Technion - Israel Institute of Technology, Haifa 32000, Israel
[1)]Weizmann Institute of Science, Rehovot 76100, Israel
[2)]Bell Laboratories, Lucent Technologies, Murray Hill, NJ 07974, USA

Abstract

We present a study of interacting, separately confined electron and hole layers that are photoexcited in undoped GaAs/AlAs mixed type I - type II quantum wells. The low temperature interband photoluminescence spectra and circularly polarized integrated intensity were studied as a function of a perpendicularly applied magnetic field ($B \leq 7T$) and 2DEG density ($n_e \leq 8 \times 10^{11}$ cm^{-2}). The observed rich structure of the lowest Landau index magnetoexcitons and the strong intensity oscillations at integral filling factors are interpreted as due to cooperative 2DEG-2DHG transitions and, possibly, to the formation of weakly bound inter-layer excitons.

1. Introduction

The first theoretical treatment of the double layered electron-hole system indicated that it might show a transition into a superfluid and superconducting state [1]. In recent years both e-e and e-h double layer systems were experimentally studied in semiconductor quantum structures. Generally, these systems are distinguished by the interlayer interaction strength that is determined by their separation: 1. Double coupled quantum wells (QW) [2-4] that are undoped but optically excited. Typical reported well and barrier widths were 2-5 nm. The e and h subbands are split by the interlayer interaction and both direct and indirect excitons are formed. 2. Electron and hole 2D gases are induced in a GaAs/AlGaAs/GaAs structure on the opposite sides of a thin (20nm) AlGaAs barrier by means of an electric bias [5]. 3. Modulation doped double e-e or e-h layers with a large separation (30-200 nm) that are studied by magnetotransport measured separately for each layer [6]. The coupling mechanisms between either the double 2DEG's or the 2DEG-2DHG were studied as a function of magnetic field and layer separation by analyzing the magnetoresistance of each layer. For thin spacers (30 and 60nm), a transition was observed from a phonon induced coupling at zero magnetic field to a Coulomb dominated one at quantizing magnetic fields. In the case of 2DEG-2DHG, only systems with large separations (190nm and more) were studied [6] and the coupling mechanism was phonon induced at all values of magnetic field.

In this work we study the intermediate case of interacting 2DEG and 2DHG that are separated by a distance of 10 nm, about the QW exciton Bohr radius. For this we use a mixed type I - type II GaAs/AlAs structure (MTQW) in which separate 2DEG and 2DHG are photoexcited and their (equal) density is varied by the excitation intensity. This structure is schematically shown in Fig.1 and the mechanism of photoexciting the (separate) 2DEG and 2DHG is detailed in [7].

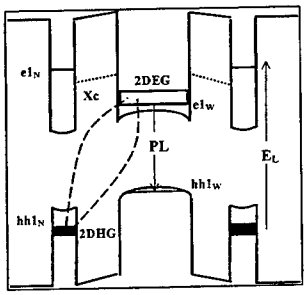

Fig.1. Schematic description of the mixed type I - type II structure. Only the subbands involved in the optical transitions are shown.

We measured the electron cyclotron resonance by photomodulated microwave absorption of the MTQW and found that the 2DEG (with $n_e \geq 2x10^{11}$ cm^{-2}) has an electron mobility value of 10^5 cm^2/V sec. This mobility is an order of magnitude smaller than measured in MDQW's with a similar n_e [8]. Hole cyclotron resonance was not observed, probably due to the high degree of hole localization in the narrow QW's, resulting in a very low mobility. A study of the $e1_W$-$e2_W$ and $hh1_N$-$hh2_N$ intersubband transitions in several MTQW structures [9] demonstrated the existence of separate, long-lived ($\tau \sim 10^{-6}$ sec at T=80K) 2DEG and 2DHG in the wide and narrow wells, respectively. Therefore, under photoexcitation the following types of particles exist in the MTQW structure (Fig.1): (1) electrons in the $e1_W$ subband that form the 2DEG and recombine with (2) minority $hh1_W$ holes in the same wide well; (3) holes in the $hh1_N$ subband that form the 2DHG. Both the in-plane and interlayer Coulomb interaction are screened by the high density 2DEG and 2DHG. However, the interlayer e_W - h_N interaction is sufficiently strong due to the very small spatial separation (the average distance between particles in the wells is twice the barrier width, at the maximum attainable carrier density $n_e=n_h \sim 8x10^{11}$ cm^{-2}). A perpendicularly applied magnetic field decreases the interlayer screening and increases the in-plane particle localization [10]. This has a pronounced effect on the $e1_W$ - $h1_W$ recombination observed in PL spectra under an applied magnetic field. In order to identify the effects that are due to the interlayer 2DEG-2DHG interaction, similar spectroscopic studies were done on MDQW's with $n_e \geq 2x10^{11}$ cm^{-2}. The main finding of this research is that the coupling between the two gases is sufficiently strong to induce cooperative interband transitions and, possibly, even weakly bound inter-layer excitons.

2. Experimental Results

Undoped, mixed type I - type II GaAs/AlAs multiple QW's with 5 to 25 periods were studied. Their narrow well, barrier and wide well widths are L_N=2.6nm, L_B=10nm and L_W=20nm, respectively. 2DEG and 2DHG densities are zero at I_L=0 and can be gradually increased up to ~$8x10^{11}$ cm^{-2} at $I_L \sim 5W/cm^2$. For comparison, single, one-sided modulation doped QW samples (MDQW's) with densities $n_e \sim 1\text{-}3x10^{11}$ cm^{-2} and well width of 25 nm were studied. The MTQW's were excited by a He-Ne laser (E_L=1.96eV>E_{gN}) and MDQW's with a titanium-sapphire laser ($E'_L \sim 1.6$ eV). The magnetic field was applied perpendicularly to the QW plane and varied in the range B=0-7T. The samples were either immersed in liquid helium (T=2K) or in helium gas (T<15K).

Under excitation at $E_L > E_{gN}$ the PL spectrum of the wide QW is determined by I_L. For $I_L \geq 5$ mW/cm^2 the PL lineshape becomes typical of a 2DEG - hole recombination spectrum (as observed in MDQW's [11]) and, for B=0 it is determined by n_e and the effective temperature of the recombining carriers.

A perpendicularly applied magnetic field splits the continuum of electron and hole states into isolated Landau levels. Fig.2a shows σ^+ circularly polarized PL spectra of the MTQW at several B values and excitation intensity of ~0.1 W/cm^2. Each spectrum observed at B>0 is decomposed into a number of Lorentzian components, as shown in Fig.2a. The fan diagrams (Fig.2b) show the peak energies of the Landau transitions observed in σ^+(dots) and σ^- (circles)

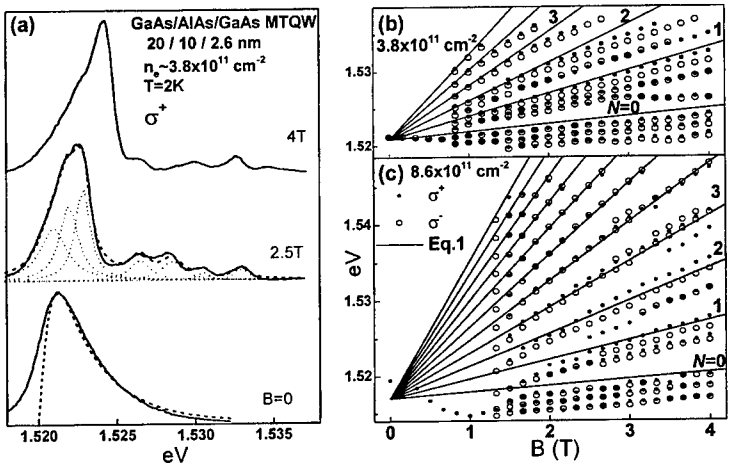

Fig.2. (a) Typical PL spectra. Solid lines: experimental, dashed lines: fitted, dotted lines: components of a decomposed spectrum. (b) and (c) Fan diagrams obtained for two n_e values.

circularly polarized PL. The solid lines represent Landau transition energies E_{LL} computed with Eq.(1) (the spin splitting is excluded):

$$E_N = E_{gW} + \left(N + \frac{1}{2}\right)\frac{\hbar e}{c}\left(\frac{1}{m_e} + \frac{1}{m_h}\right)B \qquad (1)$$

Here E_{gW} =E(e1$_W$-hh1$_W$), m_e and m_h are effective electron and hole masses in the wide well, taken to be $0.067m_0$ and $0.34m_0$, respectively. The slopes of the N=0 Landau transitions are lower than that expected for free e-h pairs (becoming negative with increasing I_L, Fig.2c). The calculated $E_N(B)$ fit better the N>3 transitions. The N=0-2 Landau transitions consist of several components at all excitation intensities and for both polarizations. Their integrated intensity (not shown) oscillates with increasing B. The MDQW Landau transitions show a set of lines corresponding to N=0,1... with slopes that are very close to the calculated dE_N/dB, as given by Eq.1.

The circularly polarized integrated PL intensity of the MTQW's was measured as a function of magnetic field by focusing the total emission onto a Si photodiode. The measured PL intensity is essentially that coming from the wide wells, because higher transitions (direct recombination in the narrow wells and indirect recombination of barrier electrons with well holes) are several orders of magnitude weaker. The total polarized PL intensity shows magneto-oscillations. Their amplitude increases with increasing excitation intensity. The oscillations observed for positive and negative circular polarizations are almost exactly in antiphase. The sum of the two polarized components $\sigma^+ + \sigma^-$ shows no oscillations (Fig.3a). The polarization, defined as $P(B)=|\sigma^+ - \sigma^-|/(\sigma^+ + \sigma^-)$, oscillates strongly with B. The minima of the oscillations correspond to the integer filling factors $\nu = hn_e/(eB)$ assuming $n_e = 8\times10^{11}$ cm^{-2} (Fig.3b). The amplitude of the oscillations decreases with increasing T. The oscillations are completely washed out at 12K (Fig.3c). The MDQW (with $n_e = 2\times10^{11}$ cm^{-2}) total PL polarization does not oscillate with B.

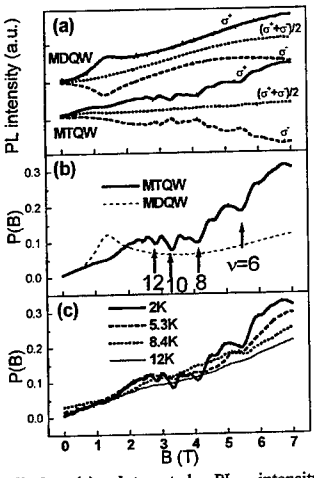

Fig.3. (a) Integrated PL intensity dependence on magnetic field for the MTQW and MDQW. (b) Polarization oscillations with magnetic field in the MTQW. (c) Temperature dependence of the polarization oscillations.

3. Discussion

The multiple components of the N=0-3 transitions (Fig.2) and the polarization oscillations (Fig.3) are observed only in a MTQW that contain photoexcited 2DEG and 2DHG. This leads to the conclusion that they originate in the coupling between the electron and hole layers. The Landau transitions (observed in the spectra of Fig.2a) are due to the recombination of the 2DEG and $hh1_W$ holes, all in the wide QW's. The multiple components of the N=0-3 transitions and their reduced slopes (relative to those expected for free electrons and holes) are attributed to the 2DEG interaction with the 2DHG in the narrow QW's. The multiple components can be explained as shake-up transitions of the 2DHG that reduce the recombination energy of ($e1_W$-$hh1_W$) due to the coupling between the layers. The analogous transitions of a 2DEG in MDQW's are very weak (about 0.01 of the N=0 transition intensity [12]). In the present case, they all have similar intensities. The oscillatory dependence on B of the total PL polarization observed in the MTQW's (and not in the MDQW) can be attributed to the existence of complexes formed by the (weak) binding of electrons in the 2DEG layer and holes in the separate 2DHG. First we note that the intensity of the individual Landau transitions (N=0-3) oscillates with B and, thus, the entire 2DEG must contribute to P(B), rather than just the particles near the Fermi energy. Secondly, the P(B) oscillations disappear at T~12K indicating that the polarized states are separated by an energy ~1 meV. We propose that in addition to the 2DEG, there are polarizable complexes that give rise to the observed P(B).

Acknowledgments

The work at the Technion was done in the Barbara and Norman Seiden Center for Advanced Optoelectronics. It was supported by the Israel Science Foundation (founded by the Israel Academy of Sciences and Humanities).

References

1. Yu. E. Lozovik and V. I. Yudson, *Sov. Phys. JETP* **44**, 389 (1976)
2. T. Fukuzawa *et al.*, *Phys. Rev. Lett.* **64**, 3066 (1990)
3. J. A. Kash *et al.*, *Phys. Rev. Lett.* **66**, 2247 (1991)
4. L. V. Butov *et al.*, *Phys. Rev.* **B52**, 12153 (1995)
5. U. Sivan *et al.*, *Phys. Rev. Lett.* **68**, 1196 (1992)
6. H. Rubel, *et al.*, *Physica* **E 1**, 160 (1997)
7. I. Galbraith *et al.*, *Phys. Rev.* **B45**, 13499 (1992)
8. L. Pfeiffer *et al.*, *Appl. Phys. Lett.* **58**, 2258 (1991)
9. Y. Garini *et al.*, Proceedings of the 22nd ICPS, **vol. 2**, 1153 (1995)
10. T. Ando *et al.*, *Rev. Mod. Phys.* **54**, 437 (1982)
11. B. M. Ashkinadze *et al.*, *Phys. Stat. Solidi* **A164**, 231 (1997)
12. M. S. Skolnick *et al.*, *Phys. Rev.* **B50**, 11771 (1994)

Magneto-optics of the spatially separated electron and hole layers in GaAs/AlGaAs coupled quantum wells

L. V. Butov [1,2], A. Imamoglu [2], A. A. Shashkin [1], V. T. Dolgopolov [1], A. V. Mintsev [1], S. G. Feklisov [1], K. L. Campman [2], and A. C. Gossard [2]

[1] Institute of Solid State Physics, Russian Academy of Sciences, 142432 Chernogolovka, Russia
[2] Department of Electrical and Computer Engineering and Center for Quantized Electronic Structures (QUEST), University of California, Santa Barbara, CA 93106

We report on the photoluminescence (PL) study of the spatially separated electron and hole layers in GaAs/AlGaAs coupled quantum wells at low temperatures T≥50 mK. At high magnetic fields cusps are observed in the energy and intensity of the indirect (interwell) exciton PL. We tentatively attribute these to the commensurability effects of the magnetoexciton with island structures in the sample. Strong nonlinearities in the indirect exciton PL kinetics are observed: right after the excitation is switched off, the indirect exciton PL intensity jumps up, and the consequent PL intensity decay rate increases strongly with excitation density. The effects can be attributed to stimulated exciton scattering to the optically active exciton states (the boser effect) and exciton superradiance.

The system of spatially separated electron (*e*) and hole (*h*) layers in coupled quantum wells (CQWs) is remarkable by the fact that because of much longer *e-h* recombination time compared to single-layer *e-h* systems one can reach lower *e-h* temperatures that are close to the lattice temperature. Therefore, CQWs provide a unique opportunity for studying low temperature 2D neutral *e-h* systems.

We report on the cw and time resolved photoluminescence (PL) study of the spatially separated *e* and *h* layers in GaAs/AlGaAs CQW at low temperatures T≥50 mK and high magnetic fields B≤16 T. The electric-field-tunable n^+ - i - n^+ GaAs/AlGaAs CQW structure was grown by MBE. The i-region consists of two 8 nm GaAs QWs separated by a 4 nm $Al_{0.33}Ga_{0.67}As$ barrier and surrounded by two 200 nm $Al_{0.33}Ga_{0.67}As$ barrier layers. The n^+ - layers are Si-doped GaAs with $N_{Si} = 5 \cdot 10^{17}$ cm^{-3}. The electric field in the z-direction is monitored by the external gate voltage V_g applied between n^+ - layers. The small disorder in the CQW is indicated by the indirect exciton PL linewidth of about 1 meV. Carriers were photoexcited by either a HeNe laser ($\hbar\omega$ =1.96 eV) or a pulsed semiconductor laser ($\hbar\omega$ =1.85 eV, the pulse duration was about 50 ns, the edge sharpness including the system resolution was ≈0.2 ns, and the repetition frequency was 1 MHz). The PL measurements were performed in a He^3/He^4 dilution refrigerator by means of an optical fiber with diameter 0.2 or 0.6 mm positioned 0.3 to 0.6 mm above the mesa.

A typical V_g dependence of the ground state PL line positions at low excitation densities is shown in the inset to Fig. 1. The crossover between the direct to indirect ground state proceeds from the V_g behaviour of the direct $\mathcal{E}_D = E_g + \hbar\omega_c/2 - E_D$ and indirect $\mathcal{E}_I = E_g + \hbar\omega_c/2 - E_I - eFd$ exciton energies, where E_g is the energy gap including the *e* and *h* confinement energies in the CQW, E_D and E_I are the direct and indirect exciton binding energies, d is the separation between *e* and *h* layers, $F = V_g/d_0$ is the electric field in the z-direction, d_0 is the i-layer width, $\hbar\omega_c$ is the sum of the *e* and *h* cyclotron energies. The direct-to-indirect ground state crossover field, F_{D-I}, given by $eF_{D-I}d = E_D - E_I$, increases with magnetic field; also, the indirect line shifts with B to higher energies stronger than the direct line (inset to Fig. 1). This corresponds to the stronger enhancement of E_D compared to that of E_I with magnetic field [1,2]; particularly, in the high magnetic field limit these energies are evaluated as $E_D \sim 1/l_B$ and $E_I \sim 1/(l_B^2 + d^2)^{1/2}$, where $l_B = (\hbar c/eB)^{1/2}$ is the magnetic length.

Figure 1 shows that, unlike the direct exciton, the indirect exciton energy increases with excitation density. This observation is consistent with the theoretically predicted enhancement of the indirect exciton energy with *e-h* density: it can be understood in terms of the net repulsive interaction

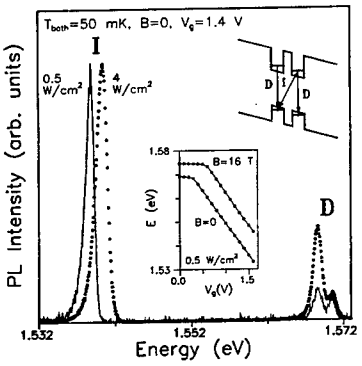

FIG. 1. PL spectra in the indirect regime. Top inset: band diagram of the GaAs/AlGaAs CQW structure under applied gate voltage; the direct (D) and indirect (I) exciton transitions are indicated. Bottom inset: the ground state PL line energy as a function of gate voltage.

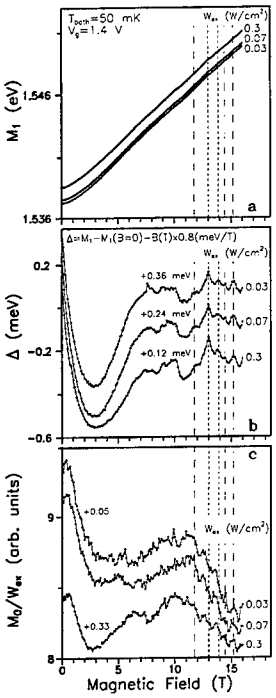

FIG. 2. Magnetic field dependences of the indirect exciton PL line position M_1 (a), its deviation from the linear shift $\Delta = M_1 - M_1(B=0) - B(T)\cdot 0.8(meV/T)$ (b), and the integrated indirect exciton PL intensity M_0 normalized by the excitation density (c) vs excitation density. Some of the curves are shifted vertically for clarity, the shift magnitudes are indicated.

between indirect excitons caused by the dipole-dipole repulsion for low exciton densities, and in terms of the energy shift originated from the electric field between the separated electron and hole layers for high *e-h* densities [3,4]. In the latter case the energy shift can be roughly estimated using the plate capacitor formula $\delta E = 4\pi n_{eh} e^2 d/\varepsilon$, which allows the estimation of the exciton density $\approx 9\cdot 10^9$ cm^{-2} at $W_{ex} = 4$ W/cm^2 for the data of Fig. 1.

We analyze both the integrated indirect exciton PL intensity $M_0 = \int I(E)dE$ and the PL line position given by the line gravity center $M_1 = M_0^{-1} \int EI(E)dE$ as a function of magnetic field. The energy shift of the indirect exciton PL line with magnetic field reflects the excitonic recombination: a quadratic shift at low fields changes to an approximately linear shift at high fields (Fig. 2(a)) [5,6]. The magnitude of the linear shift 0.8 meV/T corresponds to the zero Landau level energy $\hbar eB/2mc$ with $m=0.072m_0$ which is higher compared to the reduced *e-h* mass because of the magnetic field dependence of E_I discussed above. For visualization purpose this shift is subtracted from the dependences $M_1(B)$ to obtain $\Delta(B)$. As seen from Fig. 2(b), pronounced well-reproducible cusps in energy occur at high fields B>7 T. Also, the integrated indirect exciton PL intensity exhibits a similar oscillating behavior that is correlated to a certain extent with the energy variations (Fig. 3(c)): some of the energy maxima coincide with the maxima of M_0 (dashed lines in Fig. 3), whereas the others coincide with the minima of M_0 (dotted lines in Fig. 3). The cusp position is insensitive to both excitation density and V_g, and their amplitude drops with temperature [7].

Since the position of the cusps in the energy and intensity of indirect exciton PL is independent of the excitation-controlled exciton density (Fig. 2(b)), the cusps are not related to either filling-factor-

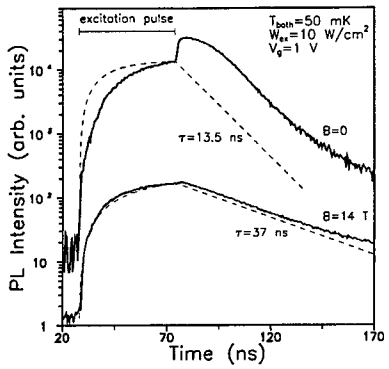

FIG. 3. Kinetics of the indirect exciton PL. The dashed lines represent the monoexponential PL rise/decay with time constants corresponding to the fastest PL decay rate.

sensitive collective states (contrary to cusps in the energy and intensity of 2DEG or 2DHG PL observed at fractional filling factors [8]) or magnetic-field-dependent screening and are likely to be of one-magnetoexciton origin. At the same time no cusps in energy and intensity are expected for both the indirect and direct one-magnetoexciton PL in ideal single- or double-layer *e-h* systems [2,5,6,9,10]. Therefore, we tentatively attribute the observed cusps to the commensurability effects of the magnetoexciton with island structures in the sample. The cusp presence may reveal the potential correlations in the CQW.

The indirect exciton PL kinetics is shown in Fig. 3. At high excitation densities, low temperatures, and low magnetic fields the indirect exciton PL kinetics strongly differs from monoexponential PL rise/decay: right after the excitation is switched off, the indirect exciton PL intensity first jumps up and then decays with a rate that changes non monotonously with time. On the contrary, at low excitation densities [11], high magnetic fields (Fig. 3), and high temperatures [11] the indirect exciton PL kinetics are close to monoexponential with long time constants.

The integrated exciton PL intensity remains almost constant with V_g variation while the decay time varies by several orders of magnitude [11]. Hence, the radiative recombination is dominant in the CQW studied. For delocalized 2D excitons only the states with small center-of-mass momenta k $\leq k_0 \approx E_g/\hbar c$ (where c is the speed of light in the medium) can decay radiatively [12]. The exciton PL kinetics is determined by the kinetics of occupation of the optically active exciton states with $E \leq E_0 = \hbar^2 k_0^2/2m \approx 1$ K. The occupation of these states is increased through the energy relaxation of photoexcited high energy excitons and decreased as a result of exciton recombination. The PL-jump

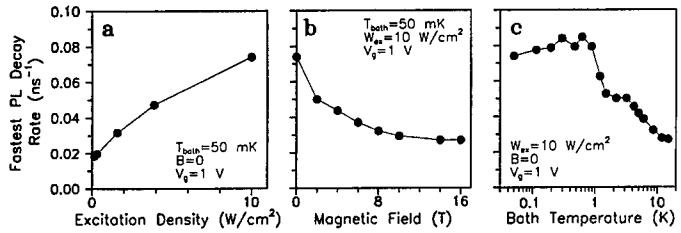

FIG. 4. The fastest PL decay rate vs excitation density, magnetic field and temperature.

denotes a sharp increase of the occupation of the optically active exciton states just after the excitation is switched off [11].

We emphasize that the fastest PL decay rate is increased with excitation density (Fig. 4a) and discuss this below. The exciton radiative decay rate is proportional to the dipole matrix element connecting Bloch states in the valence and conduction bands, the overlap between the *e* and *h* wave functions describing *e-h* relative motion, the lateral size of the exciton center-of-mass wave function (so-called exciton coherent area as determined by the exciton localization length and scattering length), and the occupation of the optically active exciton states [12]. The observed increase of the fastest PL decay rate can be attributed to two distinct effects. The first is related to the increase of the exciton coherent area (the exciton superradiance effect) [13]. The increase of the exciton coherent area with increasing exciton density is due to the enhanced exciton screening of random potential fluctuations and filling of low energy strongly localized states. The second is related to the superlinear increase of the occupancy of the optically active exciton states with excitation density caused by stimulated exciton scattering (the boser effect) [14]: it occurs when the occupation numbers of the states approach and exceed unity. The exciton accumulation is promoted by the long lifetime of indirect excitons [11].

The fastest radiative decay rate is reduced with increasing magnetic field (Fig. 4b). We note that this is qualitatively different from the case of AlAs/GaAs CQWs where the indirect exciton radiative and nonradiative decay rates were observed to increase abruptly at low temperatures and high magnetic fields which was related to the exciton condensation [15]. In the studied GaAs/AlGaAs CQW, where no exciton condensate is expected at high magnetic fields because of large separation between *e* and *h* layers ($d>l_B$ at B>4 T) [3,16], no such increase of the decay rate is observed. The observed reduction of the indirect exciton radiative decay rate with magnetic field (Fig. 4b) can be explained by reduction of the exciton coherent area and of the occupation numbers of optically active exciton states. The origin for both effects is an order of magnitude increase at the highest magnetic fields of the magnetoexciton mass for the interwell excitons with large $d \approx 12$ nm, as calculated in Ref. [10]. The competitive increase of the magnetoexciton radiative decay rate due to the shrinkage of the in-plane exciton radius (given by l_B at high fields [9]) is, apparently, weaker effect.

With increasing bath temperature the occupation of the low energy optically active states reduces, which results in the observed reduction of the PL decay rate (Fig. 4c).

We would like to thank G.E.W. Bauer, N.A. Gippius, and S.G. Tikhodeev for useful discussions, W. Zhao, J. Kono, S. Crooker, D. Druist, E. Gwinn, and D.D. Awschalom for their help with this research, Yu. Akulova for help in processing the sample. We acknowledge support for this project from NSF grant DMR-9413708, NSF Center for Quantized Electronic Structures (QUEST), the Russian Foundation for Basic Research, and the Programme "Physics of Solid State Nanostructures" from the Russian Ministry of Sciences.

References

1. L.V. Butov, A. Zrenner, G. Abstreiter, A.V. Petinova, and K. Eberl, Phys. Rev. B **52**, 12153 (1995).
2. A.B. Dzyubenko, and A.L. Yablonskii, Phys. Rev. B **53**, 16355 (1996).
3. D. Yoshioka, and A.H. MacDonald, J. Phys. Soc. Jpn. **59**, 4211 (1990).
4. X. Zhu, P.B. Littlewood, M.S. Hybersten, and T.M. Rice, Phys. Rev. Lett. **74**, 1633 (1995).
5. O. Akimoto, and H. Hasegawa, J. Phys. Soc. Jpn. **22**, 181 (1967).
6. G.E.W. Bauer, and T. Ando, Phys. Rev. B **38**, 6017 (1988).
7. L.V. Butov, A.A. Shashkin, V.T. Dolgopolov, K.L. Campman, and A.C. Gossard, unpublished.
8. for review see I.V. Kukushkin and V.B. Timofeev, Adv. Phys. **45**, 147 (1996).
9. I.V.Lerner and Yu.E.Lozovik, Zh.Eksp.Teor.Fiz. **78**, 1167 (1980) [Sov.Phys.JETP **51**, 588 (1980)].
10. Yu.E. Lozovik, and A.M. Ruvinskii, Zh. Eksp. Teor. Fiz. **112**, 1791 (1997) [JETP **85**, 979 (1997)].
11. L.V.Butov, A.Imamoglu, A.V.Mintsev, K.L.Campman, A.C.Gossard, Phys. Rev. B **59**, 1625 (1999).
12. J. Feldmann, G. Peter, E.O. Göbel, P. Dawson, K. Moore, C. Foxon, R.J. Elliott, Phys. Rev. Lett. **59**, 233 (1987).
13. G. Björk, S. Pau, J. Jacobson, and Y. Yamamoto, Phys. Rev. B 50, 17336 (1994).
14. A. Imamoglu and R.J. Ram, Physics Letters A **214**, 193 (1996).
15. L.V. Butov, and A.I. Filin, Phys. Rev. B **58**, 1980 (1998).
16. X.M. Chen, and J.J. Quinn, Phys. Rev. Lett. **67**, 895 (1991).

CYCLOTRON RESONANCE IN AN ASYMMETRIC ELECTRON-HOLE INAS/GASB DHET STRUCTURE

C Petchsingh[1], R J Nicholas[1], A J L Poulter[2], V J Hales[1], N J Mason[1] and P J Walker[1]
[1]*Clarendon Laboratory, Department of Physics, University of Oxford, Park Road, Oxford OX1 3PU, United Kingdom*
[2]*Grenoble High Magnetic Field Laboratory, MPI-FKF and CNRS, BP 166, F-38042 Grenoble CEDEX 9, France*

The influence of the interface states on the Cyclotron Resonance (CR) of the broken-gap two carrier InAs/GaSb DHET system has been investigated. Enhanced coupling between electron and hole levels is observed in the samples with a monolayer of the InSb formed on one of the interfaces, leading to evidence of strong interband transitions close to that of the electron CR. This is believed to be the result of the asymmetry introduced into the structure, which increases the interband transition probability due to the increase of the band offset. The results are consistent with the theoretical analysis from self-consistent **k.p** calculations.

There is much still to be understood about the InAs/GaSb broken-gap system where the bottom of the conduction band (CB) in InAs lies below the top of the valence band (VB) in GaSb. In this regime electrons transfer from the GaSb VB to the InAs CB, resulting in band bending and an overlap of the electron and hole states. As a consequence, a semi-metallic 2 dimensional electron-hole system is formed. Many investigators [1-3] have utilised AlSb barriers to spatially separate electron and hole gases enabling studies of the electron-hole interaction which is influenced by resonant tunnelling. CR amplitude and linewidth oscillations in such a system have been observed to be dependent on the thickness of the barrier. An intense investigation has been carried out to explain this observation by proposing Coulomb mediated electron hole coupling as a possible mechanism for Bose-Einstein condensation of excitons [1]. However it has been recently shown that the oscillation of the CR lines is a consequence of the crossing of the electron and hole levels, consistent with the theoretical predictions of single particle hybridisation of the states [2,4]. The interpretation of this precursor has been confirmed experimentally with a variety of electron and hole densities at different temperatures and magnetic fields [3], which otherwise cannot be explained via the interexcitonic Coulomb interaction.

It is also important to note that the device properties are significantly influenced by the band alignment of the DHET structure. In fact great attention has been focussed on the interface states of the component compounds as they play a vital role in determining the band offset between the two materials. A number of theoretical studies have predicted that the InAs/GaSb valence band offset should depend on the growth order of the materials forming the junction and on the nature of the interface between them [5,6]. In general a monolayer of an InSb-like or GaAs-like junction can be grown by controlling the gas sequence at the interface [5]. A monolayer at the interface is believed to introduce crucial variations in the confinement energy of the carriers. Previous investigations have demonstrated that when such a system experiences a magnetic environment, a redistribution of the interface dipoles results, due to the different bond lengths between the monolayer and the InAs/GaSb quantum well layer. The strains consequently introduced at the interface alters the band offset between the InAs and GaSb materials [7]. Several experiments have confirmed that for ideal InSb-like interfaces the band overlap is 30-40 meV higher than for GaAs-like interfaces [8]. Mile et al. have found higher absorption for an InSb-like interface, consistent to a smaller energy gap [9]. Moreover,

recent discoveries indicate the tendency that as the width of the interface increases, the interfacial composition affects the properties of the heterostructure more strongly [10].

We have studied the influence of interface states on the CR of a single InAs well sandwiched by GaSb barrier layers and have observed not only oscillations in the width and amplitude of the electron CR absorption line, but also enhanced coupling between the electron and hole levels. The experiments were carried out on single InAs/GaSb Quantum Well structures grown by Metal Organic Vapour Phase Epitaxy (MOVPE). A thick GaSb buffer layer (~2μm) was grown on top of the GaAs substrate to accommodate strain, followed by a 300Å InAs layer and then a 700Å GaSb capping layer. These growth parameters apply to all samples: A, B and C with the exception that samples B and C were grown with a deliberate bias by introducing a monolayer of InSb on the first and second interfaces respectively. As a consequence, an asymmetric structure was formed in samples B and C whereas sample A remained an unbiased structure. The insets of Figure 2 illustrate schematically the band structure of all the samples. The samples were mounted in the centre of a 14 T superconducting magnet in the Faraday configuration at a temperature of 2.2 K. The CR spectra were obtained using a rapid scan Fourier Transform Spectrometer and were normalised to the spectrum obtained at zero magnetic field. Radiation from the FIR source was incident perpendicular to the plane of the sample and the transmission was detected by a Si bolometer placed 10 cm below field centre. The resonance positions, widths, and intensities were obtained from fitting Lorentzian lineshapes to the data.

The results reveal strong oscillations of the width and the amplitude of the absorption peak, similar to previous observations [2]. Figure 1 shows an extract of such oscillations obtained from sample A in the low magnetic field range. The amplitude of the CR line decreases as the width increases, suggesting coupling of the states. The figure shows that the coupling resonance enters from the low-energy side while the original resonance curls away and disappears to the high-energy region. The pattern repeats at higher fields and the oscillations in linewidth and amplitude are periodic with 1/B. The energies of the resolved cyclotron absorption peaks for sample A are plotted versus magnetic field as illustrated in figure 2(a). Figures 2(b) and 2(c) represent the data taken for samples B and C respectively. All the samples exhibit clear electron cyclotron resonance as indicated by the dotted line, which corresponds to an effective electron cyclotron mass, $m^* \sim 0.04m_0$. In the sample with unbiased interfaces, the absorption amplitude oscillates with magnetic field and breaks up into a series of resonances, which are confined to a narrow energy range centred on the classical CR condition $\hbar\omega = \hbar\omega_c$. For the samples with a biased interface, in addition to the oscillations in the intensity as in the previous sample, a strong high-energy broadening of the resonances is also present as a sequence of long-tailed traces rising rapidly in energy with increasing magnetic field. These traces separate from the main CR line at the points where the Landau energy levels of the electrons and holes anticross. The splitting energies range from 3.5-10 meV which corresponds well with the theoretical prediction for the

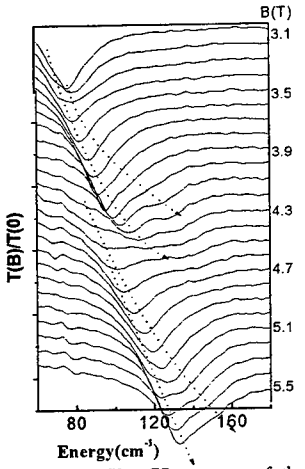

Figure 1. The CR spectra of the transmission T(B) at magnetic field B. The oscillations of the width and the amplitude are evident. Dotted lines guide the eye for the CR traces.

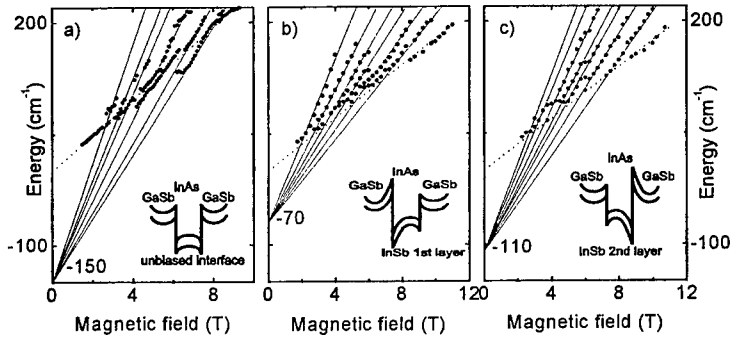

Figure 2. The peak positions of the CR resonances are plotted against field for the three different samples. The interband transitions are evidenced by the resonances breaking up from the main CR line (dotted line) as a high-energy shoulder. The insets illustrate schematically the band structure of each sample.

hybridisation gap [11]. We postulate that strong high-energy shoulder of the main CR line is attributed to interband transitions between the Landau levels of hole-like states below the Fermi level to electron-like Landau levels above the Fermi level. The lines drawn through the data are correlated with the theoretical predictions from self-consistent **k.p** calculations, as demonstrated in Figure 3. The calculations account for all possible transitions between the electron and hole states. The transitions which break away from the e-CR line correspond to the electron-hole transitions. The inset of figure 3 illustrates schematically the possible interband transitions close to an anticrossing between the electron and hole states. The comparison between the theoretical calculations and the experimental results confirms our reasoning for the high-energy CR broadening.

The extrapolated negative energy gap of each sample is deduced from the energy-intercept of the interband transition lines. It is revealed that sample A has a larger band gap (-18.5 meV) than the other samples which have a single InSb interface. Moreover, we observed a smaller band gap (-8.6 meV) in sample B in comparison to that (-13.5 meV) obtained from sample C. The band gap results are in general much lower than previously determined [12].

The dynamics of the CR spectra in the unbiased and biased samples can be interpreted by considering the effects of the interface biasing on the band offset

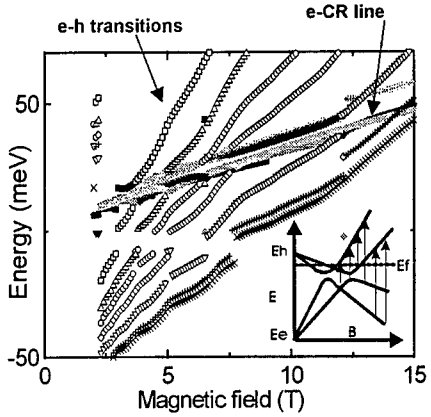

Figure 3. The results from k.p calculations of the transition energies between electron and hole Landau levels. The inset shows schematically the anticrossing of the levels. The arrows refer to the possible interband transitions that can be accounted for the observed CR traces.

of the device. The results for the samples with a single InSb biased interface exhibit electron CR with a strong high-energy shoulder, which is thought to arise from the excitation of electron-hole transitions. The results thus indicate that the monolayer of InSb enhances the electron-hole coupling in the device. There are two main reasons to support a singly biased interface as a candidate for the enhancement of the interband transition of the device. The first effect arises from the presence of an additional interface that gives rise to additional mixing. A monolayer forms two interfaces, one to the barrier and the other to the well. The wave functions overlap twice, so the possibility of more mixing between states taking place is naturally increased. The second reason comes from the asymmetric structure. The schematic diagrams of the band structure of the individual samples are illustrated in the insets of Figure 2. An asymmetric structure causes electrons and holes to shift towards the same interface and hence the overlap of their wave function is enhanced. Intriguingly, our observation reveals a higher degree of electron-hole transitions in the sample with InSb in the first interface layer. It can be realised that the asymmetry is already present in an unbiased structure due to the strain between the substrate surface and the barrier layer. This phenomena accounts for the initial band offset which is intensified by an addition of a monolayer at the first interface. On the other hand, the experimental results suggest that the asymmetric feature is compensated by the existence of InSb in the second layer. However the fact that the interband couplings are less prominent in the symmetric sample shows that the mixing of states is a greater influence than that of the band offset.

We have demonstrated that an interface layer, which lies at one of the interfaces of the DHET InAs/GaSb structure, influences the strength of the electron hole coupling in the system. The observations have confirmed that the asymmetry of the structure caused by the biased interface increases the e-h coupling leading to the enhancement of the interband transitions close to the e-CR energy. We have also observed that the existence of the interface state causes a decrease in the negative band gap due to enhanced e-h coupling.

Acknowledgements

One of the authors (C.P.) would like to acknowledge the Development and Promotion of Science and Technology (DPST) of Thailand for the financial support of this work.

References

[1] Kono J et al., Phys. Rev. B **55**, 1617 (1997)
[2] Vasilvey Yu B et al., JETP Lett. **69**, 343 (1999)
[3] Marlow T P et al., Phys. Rev. Lett. **82**, 2362 (1999)
[4] Suchalkin S D et al., JETP Lett. **68**, 792 (1998)
[5] Symons D M et al, Semicond Sci. Technol. **9**, 118 (1994)
[6] Hemstreet L A et al, J Vac Sci. Technol. B **11**, 1693 (1993)
[7] Wagner J et al, Physica E **2**, 320 (1998)
[8] Daly M S et al., Semicond. Sci Technol. **11**, 833 (1996)
[9] Miles R H et al, Semicond. Sci. Technol. **8**, 102 (1993)
[10] Kim G, Superlattices and Microstructures **21**, 575 (1997)
[11] Altarelli M, Phys. Rev. B **28**, 842 (1983)
[12] Bruelemans P et al, Solid State Commun. **105**, 513 (1998)

A New Approach to Current and Noise in Double Quantum Dot Systems

H. B. Sun and G. J. Milburn
Department of Physics, University of Queensland,
St Lucia, QLD 4067, Australia
sun@physics.uq.edu.au; Tel: (+61 7) 33652816; Fax: (+61 7) 33651242

We use a quantum master equation to describe transport in double-dot devices. The coherent dot-to-dot coupling affects the noise spectra strongly. For phonon assisted tunneling, the calculated current spectra are consistent with those of experiments. The model shows that quantum stochastic theory may be applied to some advantage in mesoscopic electronic systems.
PACSnumbers:73.23-b,73.50.Td, Keywords:quantum dot, transport, coupling

Quantum transport of electrons through coupled quantum dot systems has attracted the interest of both theoretical [1] and experimental [2–4] researchers. In such structures, the coupling between adjacent dots leads to strong superposition of the electron states. In that case, charge transport through the system cannot be described purely by population-rate equations. We have developed a new approach [5] for the calculation of current and noise in coupled-dot systems. For coherently coupled devices, current-noise spectra show either Lorentzian or non-zero frequency spectral peaks, depending on the relative strength of coherent coupling versus elastic scattering. At very high coupling rates the spectrum shows dips at a frequency double the coupling rate. For systems with inelastic tunneling, the calculated current spectra are comparable with experimental results [2].

The system studied consists of two dots, which are isolated from each other and from the source and the drain by three potential barriers. The charging effects are tuned away by means of the gate voltages [3], and are not included in the model. There is only one energy state in each dot. Under normal bias both dot states are well below the Fermi energy of the source and above the Fermi energy of the drain. The tunneling between two dot states, controlled by the gate voltages in the experiments, can be coherent, or sequential. First we consider a coherently coupled dot device with elastic scattering. The quantum master equation for the density operator representing the system state in interaction picture is expressed as [5]

$$\frac{d\rho}{dt} = \frac{\gamma_L}{2}\left(2c_1^\dagger \rho c_1 - c_1 c_1^\dagger \rho - \rho c_1 c_1^\dagger\right) + \frac{\gamma_R}{2}\left(2c_2 \rho c_2^\dagger - c_2^\dagger c_2 \rho - \rho c_2^\dagger c_2\right) - \eta_1\left[c_1^\dagger c_1, \left[c_1^\dagger c_1, \rho\right]\right] - \eta_2\left[c_2^\dagger c_2, \left[c_2^\dagger c_2, \rho\right]\right] - i\Omega\left[(c_1^\dagger c_2 + c_2^\dagger c_1), \rho\right] \quad (1)$$

where $c_1(c_1^\dagger)$ and $c_2(c_2^\dagger)$ are annihilation (creation) operator of electron in the left and right quantum dot respectively, γ_L and γ_R are constants determining the transmission rate of electrons from source into the left dot and from the right dot into the drain respectively, η_i is the rate of elastic scattering in the *ith* dot, and Ω is the coherent coupling rate between the two dot states. The first two terms represent electrons entering and leaving the device. The third and fourth terms describe the elastic scattering in left and right dot respectively. The last term is for the coherent coupling between two dots. We assume that the temperature

of the bath is high enough that the bath states are well away from the ground states. The steady state current is calculated as

$$i_\infty = \frac{4e\Omega^2\gamma_L\gamma_R}{\gamma_L\gamma_R(\gamma+2\eta)+4\gamma\Omega^2} \tag{2}$$

where $\gamma \equiv \gamma_L + \gamma_R$ and $\eta \equiv \eta_1 + \eta_2$. Applying the theory of quantum open systems [6] we have the current noise spectrum in a symmetric structure ($\gamma_L = \gamma_R \equiv \gamma_e$, $\eta_1 = \eta_2 \equiv \eta_e$):

$$S(\omega) = 2ei_\infty\left\{\frac{1}{2} + \frac{\gamma_e}{4d}\left[\frac{(\eta_e+d)(\gamma_e-\eta_e+d)}{(-\gamma_e-\eta_e+d)^2+\omega^2} + \frac{(-\eta_e+d)(\gamma_e-\eta_e-d)}{(-\gamma_e-\eta_e-d)^2+\omega^2}\right]\right\} \tag{3}$$

where $d \equiv \sqrt{\eta_e - 4\Omega^2}$. The current noise (normalized by the full shot noise $2ei_\infty$) spectra for various parameter combinations are plotted in Fig.1. It is shown that the coherent coupling

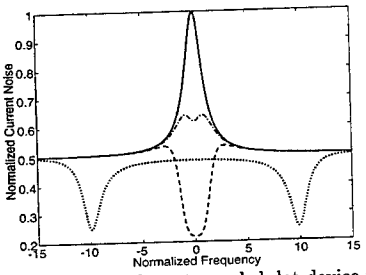

FIG. 1. Normalized current noise of a coherent coupled dot device versus normalized frequency (ω/γ_e) for various parameters (η_e/γ_e, Ω/γ_e): solid:(0.2, 0.0); dot-dash:(0.2, 0.3); dash:(0.0, 0.5); dotted: (0.0, 5.0)

introduces correlations between the two dots and reduces the noise while the scattering makes the device noisier. The non-zero frequency spectral peaks appear when the coherent coupling is stronger than elastic scattering. When the coherent coupling dominates, the periodic return of the electron to the first dot excludes another electron from entering the dot and causes the strong noise suppression (dips) at a frequency double the coupling rate in the spectrum. Secondly we study phonon assisted tunneling in a double quantum dot device (elastic scattering is excluded this time). The relevant Hamiltonian for this type of devices is:

$$H = \hbar\Delta(c_1^\dagger c_1 - c_2^\dagger c_2) + \hbar\Omega(c_1^\dagger c_2 + c_1 c_2^\dagger) + \sum_k g_k c_1 c_2^\dagger b_k^\dagger + h.c. \tag{4}$$

where $\Delta = (\varepsilon_L - \varepsilon_R)/\hbar$ is the energy mis-match of two dot states, and $b_k^\dagger$ is the phonon operator with momentum k and g_k is the electron-phonon coupling strength. The first two terms describe the transition between two dot states due to inelastic coupling and coherent coupling respectively. The last two terms are for the coupling to the phonon-bath. The Hamiltonian for the source and drain, and the tunneling between the dots and the leads are

not listed. Using the technique expounded in reference 5, the master equation describing the double-dot system with phonon interaction can be derived as

$$\begin{aligned}\frac{d\rho}{dt} &= -i\Delta[c_1^\dagger c_1 - c_2^\dagger c_2, \rho] - i\Omega[c_1^\dagger c_2 + c_1 c_2^\dagger, \rho] \\ &+\frac{\chi}{2}(\overline{n}+1)(2c_1 c_2^\dagger \rho c_1^\dagger c_2 - c_1^\dagger c_1 c_2 c_2^\dagger \rho - \rho c_1^\dagger c_1 c_2 c_2^\dagger) \\ &+\frac{\chi}{2}\overline{n}(2c_1^\dagger c_2 \rho c_1 c_2^\dagger - c_1 c_1^\dagger c_2^\dagger c_2 \rho - \rho c_1 c_1^\dagger c_2^\dagger c_2) \\ &+\frac{\gamma_L}{2}(2c_1^\dagger \rho c_1 - c_1 c_1^\dagger \rho - \rho c_1 c_1^\dagger) + \frac{\gamma_R}{2}(2c_2 \rho c_2^\dagger - c_2^\dagger c_2 \rho - \rho c_2^\dagger c_2) \end{aligned} \tag{5}$$

where χ is the phonon coupling rate for bore process ($T = 0$) depending on g_k; $\overline{n}$ is the average phonon occupation number; The first and the second terms describe the inelastic and elastic tunnelling between two dot states respectively. The third and fourth terms correspond to the phonon absorption and emission processes in the dots. For simplicity of calculation we assume $\gamma_L = \gamma_R \equiv \gamma_e$. The steady state current is calculated analytically to be:

$$i_\infty = 2e\gamma_e \frac{\chi(1+\overline{n})(AB + 16\Delta^2) + 4A\Omega^2}{16\Delta^2 B + A(AB + 16\Omega^2)} \tag{6}$$

with

$$A \equiv 2\gamma_e + \chi(1+\overline{n}); B \equiv 2\gamma_e + \chi(3+4\overline{n}). \tag{7}$$

The currents versus energy mis-match between two dot states are plotted in Fig. 2a for various coherent coupling rates at a fixed phonon coupling rate. The horizontal axis variable Δ is normalized by the transmission rate γ_e, and the vertical axis variable current uses arbitrary units (proportional to $4e\gamma_e$). All other parameters are normalized by γ_e.

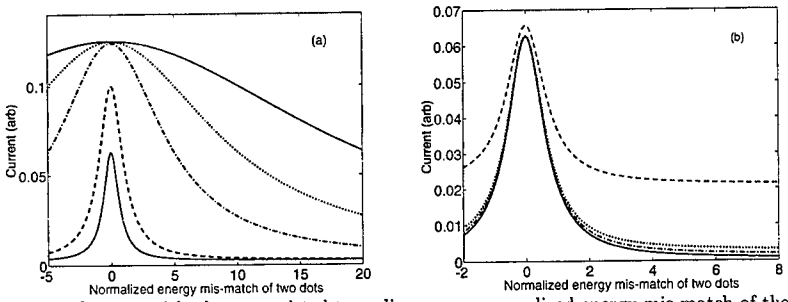

FIG. 2. Current with phonon assisted tunneling versus normalized energy mis-match of the two dots for (a) fixed inelastic transmission rate $\chi/\gamma_e = 0.001$, average phonon occupation number $\overline{n} = 10$, and various coherent coupling rates: $\Omega/\gamma_e = 20$ (top solid), 10 (dotted), 5.0 (dot-dash), 1.0 (dash), 0.5 (bottom solid), (b) fixed inelastic transmission rate $\chi/\gamma_e = 0.001$, coherent coupling rate $\Omega/\gamma_e = 0.5$, and various phonon occupation number: $\overline{n} = 100$ (dash), 10 (dotted), 5 (dot-dash), 1 (solid).

One can see from the plots that (i) the current decreases as the energy difference between two dot-states Δ increases and the maximum current occurs at $\Delta = 0$; (ii) as the coherent coupling rate increases the current increases and gets flatter. These characteristics are consistent with those of Fig. 3 (A) in reference [2], and may be interpreted as follows. When $\Delta = 0$, the device is at resonance and the total current reaches a maximum; when $\Delta \neq 0$, only inelastic transitions occur involving energy exchange with the phonon bath. Emission ($\Delta > 0$) and absorption ($\Delta < 0$) probabilities decrease exponentially as Δ increases, and hence so does the inelastic current. With the coherent coupling between the two dot states, the electron in the right dot may tunnel back to the left dot instead of tunnelling to the drain stopping further electron tunnelling from the source into the state of the left dot and reducing the current. The stronger the coherent coupling, the faster the process. The resonant peak feature is therefore less prominent and the curves are flatter. Fig. 2b shows the current as function of the energy difference between the two dot states for various phonon occupation numbers (proportional to the temperature) at a fixed coherent coupling rate. This shows the same trend (the total current increases as the temperature increases) as those in Fig. 2 (A) & (B) in reference [2]. When the coherent coupling rate is unchanged the elastic current does not change, but the inelastic current and therefore the total current increases as $\overline{n}$ increases. In summary, we have applied quantum stochastic theory to calculate the current and noise spectrum in double quantum dot devices including both elastic and inelastic tunneling processes. The results show that new transport features arise from the coupling between two dots. The comparability between theoretical and experimental results illustrates that the new approach is useful in transport characterization of quantum electronic devices.

[1] J.M. Golden and B.I. Halperin, Phys. Rev. B **56**, 4716 (1997); A. Kaminski and L.I. Glazman, Cond-mat/9810237; G. Klimeck, G. Chen and S. Datta, Phys. Rev. B, **50**, 2316 (1994); T. Pohjola, J. Kkonig, M.M. Salomaa, J. Schmid, H. Schoeller and G. Schon, Europhys. Lett., **40**, 189 (1997); C.A. Stafford and N.S. Wingreen, Phys. Rev. Lett. **76**, 1916 (1996); P. Pals and A. MacKinnon, J.Phys.: Condens. Matter. **8**, 3177 (1996); *ibid.* **8**, 5401(1996); T.H. Stoof and Y.V. Nazarov, Phys. Rev. B **53**, 1050 (1996).

[2] T. Fujisawa, T.H. Oosterkamp, W.G. van der Wiel, B.W. Broer, R. Aguado, S. Tarucha, L.P. Kouwenhoven, Science, October, 282, 932, (1998).

[3] T. Fujisawa and S. Tarucha, Superlattices and Microstructures, **21**, 247 (1997).

[4] R.H. Blick, D. Pfannkuche, R.J. Haug, K. v. Klitzing and K. Eberl, Phys. Rev. Letts, 80, 4032, (1998); G. Schedelbeck et al. Science, **278**, 1792 (1997); C. Livermore et al., Science **274**, 1332 (1996); N.C. van der Vaart et al. Phys. Rev. Lett. **74**, 4702, (1995); F. Hofmann, et al. Phys. Rev. B **51**, 13872, (1995).

[5] H.B. Sun and G.J. Milburn, Phys. Rev. B, 59, 10748, (1999).

[6] H. Carmicael, An Open Systems Approach to Quantum Optics, Springer- Verlag (1993); H. M. Wiseman and G.J . Milburn, Phys. Rev. A **47** , 1652 (1993).

PC.20

Strongly Electrostatically Coupled Quantum Dots with Separate Leads

U. Wilhelm and J. Weis

Max-Planck-Institut für Festkörperforschung, Heisenbergstraße 1, D-70569 Stuttgart, Germany
email: wilhelm@klizix.mpi-stuttgart.mpg.de, Fax: +49-711-689 1572

Abstract

Two strongly electrostatically coupled quantum dots have been realized in a double-quantum-well GaAs/AlGaAs heterostructure by reactive ion etching. The vertically stacked dots are separated by a 40 nm thin AlGaAs barrier with a diameter of less than 0.5 μm. By contacting the quantum wells separately, each quantum dot has its own two leads allowing to monitor the current through each of the quantum dots. Transport measurements show a strong electrostatic interaction between the dots. This arrangement should allow the investigation of energy transfer between the quantum dots and Kondo physics.

Key words: Quantum Dot, Coulomb Blockade, Single Electron Tunneling, Electrostatic Interaction, Kondo Effect
PACS: 73.23.Hk,75.20.Hr

1 Motivation

The electron-electron interaction on a quantum dot (QD) leads to Coulomb blockade and single-electron charging effects in electrical transport through the QD [1]. The electrostatic interaction also determines transport properties of multi-dot setups arranged in series [2–6] or in parallel [7,8]. The electrostatic coupling between electronic islands was already studied and used in a variety of devices – namely the turnstile [9], the single-electron pump [10], the single-electron trap [11,12].

In strongly electrostatically coupled QD systems the interaction could furthermore be exploited to learn more about the structure of excited states in QDs. Transport spectroscopy measurements [13] and theoretical investigations [14,15] indicate that the transport through excited states of a QD of few electrons is governed by (quasi-) selection rules if the electron-electron interaction leads to correlation effects. More information about the individual excitations of a QD should be accessible by studying selection rules for transferring the excitation energy between two strongly electrostatically coupled QDs. To detect such a transition one quantum dot would be kept in a Coulomb-blockade state. In this situation electron transport is possible whenever the energy of the excited, neighboring QD is transferred to this dot.

A strongly electrostatically coupled dou-

ble QD structure should also reveal Kondo physics as observed in single QD devices [16–18]. In the case of a single QD, the spin degeneracy on the quantum dot – occurring under certain circumstances – allows for a class of virtual tunneling processes between the leads and the dot which flip the spin on the QD. The use of this internal degree of freedom leads to a high conductance through the QD around zero bias *within* the Coulomb blockade regime. Two strongly electrostatically coupled QDs – both with its own leads – deliver under certain conditions a degeneracy between the two charge states (N_1+1, N_2) and (N_1, N_2+1). By identifying these two states with the two orientations of an iso-spin, the analogy to a QD with spin degeneracy becomes obvious [19].

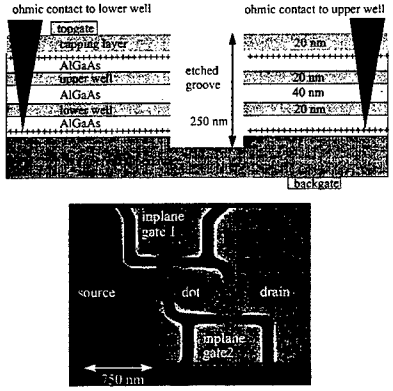

Fig. 1. Schematic cross-section through structure and top-view of etch defined device geometry. Etched grooves appear black.

2 Device Requirements and Realization

To realize the proposed experiments the following requirements need to be met: (1) High electrostatic coupling between the QDs without much screening from surrounding gates. (2) Each dot has its own two leads. (3) Tunable tunnel coupling of each dot to its leads. (4) The dots should have a similar confinement potential leading to a well-developed discrete energy spectrum.

Very strong electrostatically interacting dots can be obtained in pillars etched out of vertically stacked GaAs/AlGaAs layers defined by molecular beam epitaxy [5,6]. In electrical transport, they have been studied in series, not in parallel as needed by our experiment proposal. A planar arrangement of QDs is feasible by using split-gate defined devices [2]. They have the advantage of an adjustable tunnel coupling strength between the dot and the leads. The electrostatic coupling between the QDs is however weaker in comparison to stacking the two QDs on top of each other. Since metallic split–gates are very close and even situated between the dots, screening of the interaction between the QDs should also be considerable.

By using a technique [20] that makes it possible to contact two closely-spaced two-dimensional electron systems (2DES) in a double-quantum-well GaAs/AlGaAs heterostructure (the layer sequence is shown in Fig. 1), we are able to exploit the best for our experiment from the above described device designs. Separate contacts to the 2DESs are realized by buried back-gates and evaporated top-gates depleting the lower and upper 2DES in certain areas (Fig. 1). The strong electrostatic coupling between the QDs is realized by the 40 nm thin AlGaAs layer between the quantum wells. The dot regions are defined by electron-beam lithography, followed by reactive-ion etching (RIE) through both quantum wells, leaving two small ridges towards the leads. Since RIE provides very steep edge profiles, the geometric symmetry of the QDs is very high. The tunnel barriers are defined by the

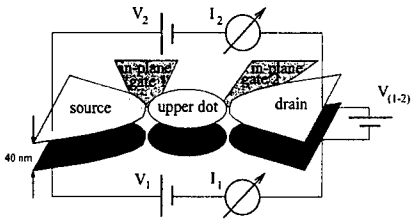

Fig. 2. Device schematics

depletion effect of the etched surfaces and can be electrostatically fine-tuned by nearby in-plane gates. Due to the arrangement, these in-plane-gates should show almost no screening on the QD-QD interaction. The geometric cross-section of the disk-shaped dot-regions is about 800 nm. The device size is essentially reduced by the depletion width, which is about 250 nm.

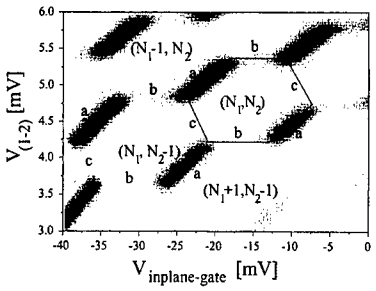

Fig. 3. Current through upper dot versus $V_{\text{inplane-gate}}$ and V_{1-2}. White regions represent low current, dark indicates high current.

3 Experimental Results

For estimating the coupling strength between the QDs, transport measurements of this double dot system as a function of two gate voltages have been performed. The experimental setup is shown in Fig. 2. For metallic systems, the regions of stable charge configuration (N_1, N_2) versus two gate voltages can be described by capacitances, leading to a honey-comb-like structure as depicted in Fig. 3 [10]. The gray scale plot shows the conductance through dot 1 depending on two gate voltages. The white regions represent states of stable charge configuration for both dots. Lines surrounding such a region of zero conductance are referred to by letters a,b, and c as depicted in Fig. 3 in the following discussion. Transport through dot 1 occurs whenever the energy for the N_1-state is degenerate with the $(N_1 + 1)$-state. This process takes place along a-lines interrupted by b-lines of much lower conductance. Along these intermediate b-lines both dots conduct simultaneously since the $(N_1 + 1, N_2)$-state is degenerate with the $(N_1, N_2 + 1)$-state. For such a process to occur the number of electrons of dot 1 has to change simultaneously with dot 2. This kind of "co-tunneling" is comparatively unlikely and exhibits therefore a much lower conductance than the dominant process of transport along a-lines. C-lines are not visible in this plot, since they are due to charge transport through dot 2. Though in principle accessible the current through dot 2 could not be resolved due to high tunnel barriers within the range of gate voltages presented in Fig. 3.

The full honey-comb-structure is only visible when at least one of the gates couples selectively stronger to one of the dots than to the other. This condition was fulfilled by using the inter-well-voltage $V_{(1-2)}$ (Fig. 2) as the sweep-parameter. The leads of the upper 2DES therefore act as a strongly coupled gate to the upper dot, whereas the coupling

4 Conclusion

Low temperature transport measurements show indeed that separately contacted quantum dot systems have been realized. The coupling strength of the dots amount to $C_{12}/C_{\Sigma 1} \approx C_{12}/C_{\Sigma 2} = 0.8 \pm 0.1$ for both dots. At gate voltages, where the energies of the (N_1+1, N_2) and the (N_1, N_2+1) states are degenerate, electrical transport through both QDs is possible due to co-tunneling. The above suggested Kondo anomalies should be visible in this regime.

5 Acknowledgment

The authors like to thank A.Fischer, H. Rubel, C. Joerger, M. Riek, T. Reindl and U. Waizmann for technical support. Thanks also to J. Schmid, D. Pfannkuche and G. Philipp for valuable discussions. This work has been supported by the Bundesministerium für Bildung und Forschung (BMBF) under the Grant No. 01 BM 624/7.

References

[1] J. Weis, R.J. Haug, K.v. Klitzing, and K. Ploog, Semicond. Sci. Technol. **9**, 1890 (1994).

[2] F.R. Waugh, M.J. Berry, C.H. Crouch, C. Livermore, D.J. Mar, and R.M. Westervelt, Phys. Rev. B **53**, 1413 (1996).

[3] R.H. Blick, R.J. Haug, J. Weis, D. Pfannkuche, K.v. Klitzing, and K. Eberl, Phys. Rev. B **53**, 7899 (1996).

[4] D. Pfannkuche, R.H. Blick, R.J. Haug, K.v. Klitzing, and K. Eberl, Superlattices and Microstructures **23**, 1255 (1998).

[5] S. Tarucha, D.G. Austing, T. Honda, R.J. van der Hage, and L.P. Kouwenhoven, Phys. Rev. Lett. **77**, 3613 (1996).

[6] T. Schmidt, R.J. Haug, K.v. Klitzing, A. Förster, and H. Lüth, Phys. Rev. Lett. **78**, 1544 (1997).

[7] F. Hofmann, T. Heinzel, D.A. Wharam, and J.P. Kotthaus, Phys. Rev. B **51**, 13872 (1995).

[8] Alexei O. Orlov, Islamashah Amlani, Geza Toth, Craig S. Lent, Gary H. Bernstein, and Gregory L. Snider, Appl. Phys. Lett. **73**, 2787 (1998).

[9] L.J. Geerligs, V.F. Anderegg, P.A.M. Holweg, and J.E. Mooij, Phys. Rev. Lett. **64**, 2691 (1990).

[10] H. Pothier, P. Lafarge, C. Urbina, D. Esteve, and M.H. Devoret, Europhys. Lett. **17**, 249 (1992).

[11] P. Lafarge, P. Joyez, H. Pothier, A. Cleland, T. Holst, D. Esteve, C. Urbina, and M. Devoret, C.R. Acad. Sci. Paris **314**, 883 (1992).

[12] P.D. Dresselhaus, L.Ji, Siyuan Han, J.E. Lukens, and K.K. Likharev, Phys. Rev. Lett. **72**, 3226 (1994).

[13] J. Weis, R.J. Haug, K.v. Klitzing, and K. Ploog, Phys. Rev. Lett. **71**, 4019 (1993).

[14] D. Pfannkuche and S. Ulloa, Phys. Rev. Lett. **74**, 1194 (1995).

[15] D. Weinmann, W. Häusler, and B. Kramer, Phys. Rev. Lett. **74**, 984 (1995).

[16] D. Goldhaber-Gordon, H. Shtrikman, D. Mhalu, D. Abusch-Maggder, U. Meirav, and M.A. Kastner, Nature **391**, 156 (1998).

[17] S.M. Cronenwett, T.H. Oesterkamp, and L.P. Kouwenhoven, Science **281**, 540 (1998).

[18] J. Schmid, J. Weis, K. Eberl, and K.v. Klitzing, Physica B **182**, 256 (1998).

[19] J. Schmid, H. Schoeller, and T. Pohjola, private communication .

[20] H. Rubel, A. Fischer, W. Dietsche, C. Jörger, K.v. Klitzing, and K. Eberl, Physica E **1**, 160 (1997).

Phase Coherence and Size Effects in Double Quantum Well Mesoscopic Wires

S.T. Stoddart, R.J.A. Hill, A.C. Neumann, P.C. Main, A. Nogaret*,
L. Eaves, M. Henini, and S.P. Beaumont†
School of Physics and Astronomy, University of Nottingham, Nottingham NG7 2RD, UK
†Dept. of Electronics and Electrical Engineering, University of Glasgow, Glasgow G12 8QQ, UK

Conductance fluctuations (CF) have been observed when an *in-plane* magnetic field is applied to 800 nm-wide mesoscopic wires fabricated from GaAs/(AlGa)As double quantum well structures. This shows that the inter-well tunnelling transition preserves electron phase coherence. The CF disappear when the magnetic field becomes large enough to suppress tunnelling between the quantum wells. The CF amplitude is smaller when the tunnelling rate is reduced either by unbalancing the double well potential, or by increasing the thickness of the tunnel barriers. The wires display strong magnetoresistance features that have been seen in macroscopic Hall bars, but are modified due to diffuse edge scattering in the wires.

Conductance fluctuations (CF) in the magnetoresistance of a mesoscopic system are caused by changing conditions for electron interference and imply the existence of phase-coherent electron trajectories enclosing a variable magnetic flux. Considering a two-dimensional electron system confined at a semiconductor heterojunction or in a quantum well [1], we can observe CF if there is a magnetic field component perpendicular to the 2D layer, but not if the magnetic field lies entirely in the plane containing the 2D electrons. In this work, we investigate mesoscopic wires containing two coupled 2D electron gases, and find CF on application of an in-plane magnetic field in the presence of inter-well tunnelling. The amplitude of the CF depends on the degree of tunnel coupling, which is controlled by the in-plane magnetic field as well as an external gate voltage and the thickness of the tunnel barrier. In addition, magnetoresistance features seen in macroscopic Hall bars are reproduced, but with modifications due to size effects.

A set of four samples (A - D) was grown by molecular beam epitaxy, each sample comprising two 14.3 nm-wide GaAs quantum wells separated by a thin $Al_{0.33}Ga_{0.67}As$ barrier. The barrier thickness is different for each sample, varying from 2.2 nm to 4.9 nm (see Table 1). The quantum wells are embedded in modulation-doped $Al_{0.33}Ga_{0.67}As$ barriers, and are separated from the doped layers by 40 nm-thick spacers.

Mesoscopic wires were fabricated with a width of 800 nm, and with voltage probes separated by 0.5μm, 1μm and 3μm lengths of wire. The side walls of the wires were defined by reactive ion etching. Electrical connections were made simultaneously to both quantum wells with diffused ohmic contacts. A dot of conducting silver epoxy was placed on top of some wires, providing a Schottky gate. Macroscopic gated Hall bars were also fabricated for characterisation measurements. These displayed behaviour typical of coupled quantum wells with two occupied subbands for magnetic fields applied perpendicular to ($B \perp DQW$) [2] or parallel to the quantum well plane ($B \| DQW$) [3-5].

With $B \perp DQW$ and at temperatures less than ~4 K, the wires displayed conductance fluctuations at low magnetic fields, followed by Shubnikov-de Haas oscillations which

confirmed that both subbands remained occupied. By applying a small voltage (<0.1 V) to the epoxy gate, the double quantum wells were easily brought into balance. Here we will concentrate on sample A which has the thinnest barrier, but all samples display qualitatively the same behaviour. We have already established for these samples that there is diffuse edge scattering and that edge depletion reduces the electrical width of the wires to ~600 nm [6]. Measurement of the correlation field of the CF gives the phase coherence length $l_\phi \approx 3$ μm [6].

The sample was then rotated so that $B \| DQW$. In Figure 1(a), for sample A in the balanced condition ($V_g = 0$ V), we see reproducible CF with an amplitude $\sim e^2/h$ that persist up to a magnetic field $B_{high} = 8.6$ T and then disappear at higher fields. The presence of CF demonstrates that electrons occupying the wells maintain phase coherence over a path comprised of free particle motion in the wells coupled by phase-coherent inter-well tunnelling transitions. The CF disappear when tunnelling is suppressed by the in-plane magnetic field. The in-plane field introduces a relative shift in k-space of $\Delta k = eBz_o/\hbar$ [7] between the centres of the Fermi discs associated with the two subbands. (z_0 is the separation of the peak electron density in the two quantum wells.) For sample A, given the total electron concentration $n_{2D} = 4.5\times10^{11}$ cm^{-2} and $z_o = 19$ nm from a self-consistent calculation, we expect the Fermi discs to decouple at $B = 8.3$ T, close to the observed value of B_{high}. For $B > B_{high}$, the Fermi discs have separated, and electrons can no longer tunnel between the quantum wells.

For the in-plane field orientation, we take the correlation field of the CF to be $\Delta B_c \approx h/e \cdot 1/A$ [8] and the characteristic area $A = z_0 l_\phi$, assuming z_0 to be the extent of the electron trajectory in the direction normal to the quantum well plane. We find $\Delta B_c = 70$ mT and using the value for l_ϕ obtained previously, $z_0 = 18$ nm in good agreement with the value of 19 nm given above.

There are two additional features in the magnetoresistance that may be seen in Figure 1. The first is a low field resistance resonance, previously seen in macroscopic Hall bars [3], and ascribed to the rapid reduction in tunnelling as the Fermi discs start moving from concentricity. The second feature, an increase in resistance around B_{high}, is qualitatively different to that observed in macroscopic Hall bars [4,5], where the resistance first decreases and then increases as the Fermi discs decouple and the Fermi level moves through a partial energy gap [9]. The behaviour in the wires can be explained qualitatively by considering the shape of the Fermi surface close to B_{high}, shown as an inset to Figure 1. Because of the diffuse electron scattering at the wire edges, electrons travelling along the axis of the wire will make a greater contribution to the conductivity. These electrons occupy states indicated by shading on the Fermi surface. In the macroscopic case, states all around the Fermi surface are important. As the Fermi discs uncross, there are shaded states that lie at a saddle point in k-space where the electron group velocity is low and there is also a logarithmic singularity in the density of states. These states are also directed towards the wire edges. Hence there is increased resistance as the Fermi discs decouple. This behaviour is reproduced by a semi-classical calculation of the conductivity, as is the anisotropy observed when the magnetic field is applied parallel to the current [10].

If the double well potential is unbalanced by an external gate voltage, the magnitude of the conductance fluctuations steadily decreases. The magnetoresistance trace in Figure 1(b) was

recorded with a gate voltage $V_g = -0.7\,\mathrm{V}$. The total electron concentration is reduced from 4.5×10^{11} cm^{-2} at balance to 3.4×10^{11} cm^{-2} in the unbalanced state. The effect of the applied electric field is to reduce the tunnel coupling, and the wavefunctions of the two subbands become progressively more localised, each in a different well. More of the electrons will remain in one well or the other, with a greater probability of scattering inelastically and losing phase coherence before traversing the closed trajectories that contribute to the CF. The correlation field does not depend on gate voltage, so there are no changes in l_ϕ which could affect the CF amplitude.

In Figure 2 conductance fluctuations are plotted for samples A - D over two ranges of in-plane field, $B < B_{high}$ and $B > B_{high}$. In all cases, the suppression of CF can be seen in the high field range. In the low field range, the CF amplitude decreases rapidly with increasing tunnel barrier thickness d_B. The correlation field ΔB_c shows no systematic dependence on barrier thickness, with $\Delta B_c = 70 \pm 10$ mT for all samples. This is reasonable because d_B changes by ~2 nm, which is much smaller than the separation of the two electron sheets. Note that the changes in barrier thickness are tiny in comparison with any other length scale in the system, but because of the exponential sensitivity of the tunnelling interaction, changes in the barrier have a strong influence on CF amplitude. A thicker barrier means a much-reduced tunnelling rate, so that within the dephasing time, fewer electrons will tunnel from one well to the other and back again completing a closed trajectory before a phase-breaking inelastic scattering event. Thus the CF amplitude is determined by the interplay between the tunnelling rate and the rate of intra-well inelastic scattering.

To conclude, we have observed CF in mesoscopic double quantum well wires on application of an in-plane magnetic field. This shows directly that electrons maintain phase coherence over a path comprised of free particle motion in the wells coupled by phase-coherent inter-well tunnelling transitions. The CF depend on the strength of the tunnel coupling between the wells and their amplitude decreases rapidly with increasing tunnel barrier thickness or as the double well potential is unbalanced by a gate voltage. The CF are suppressed completely when the wells are decoupled by a sufficiently large in-plane magnetic field B_{high}. The wires also show a resistance anomaly at B_{high} which is qualitatively different to that observed in macroscopic systems, and which is explained as a classical size effect.

This work was supported by the EPSRC (UK) and L.E. is supported by an EPSRC senior fellowship. *Present address of A.N. is Dept. of Physics, University of Bath, Bath BA2 7AY.

References

1. S.B. Kaplan and A. Hartstein, Phys. Rev. Lett. **56** (1986) 2403
2. G.S. Boebinger, Physica Scripta T**39** (1991) 230
3. Y. Berk *et al.*, Phys. Rev. B **51** (1995) 2604
4. J.A. Simmons, S.K. Lyo, N.E. Harff, and J.F. Klem, Phys. Rev. Lett. **73** (1994) 2256
5. A. Kurobe *et al.*, Phys. Rev. B **50** (1994) 4889
6. S.T. Stoddart *et al.*, Physica B **258** (1998) 413
7. F. Stern, Phys. Rev. Lett. **18** (1968) 1687
8. P.A. Lee, A.D. Stone, and H. Fukuyama, Phys. Rev. B **35** (1987) 1039
9. S.K. Lyo, Phys. Rev. B **50** (1994) 4965
10. S.T. Stoddart *et al.*, Proc. 24th Int. Conf. on the Physics of Semiconductors (1998)

Sample	n_{2D} ($\times 10^{11}$ cm^{-2})	Δ_{SAS} (meV)	d_B (nm)
A	4.5	1.6±0.05	2.2
B	4.2	0.74	3.2
C	3.2	0.48	3.8
D	4.1	0.21	4.9

Table 1 Total electron concentration n_{2D} and symmetric-antisymmetric splitting Δ_{SAS} of balanced double quantum well samples obtained from measurements on macroscopic Hall bars. The tunnel barrier thickness d_B is derived from Δ_{SAS} via a self-consistent solution of the Schrödinger and Poisson equations and differs by 10-30% from the nominal barrier thickness.

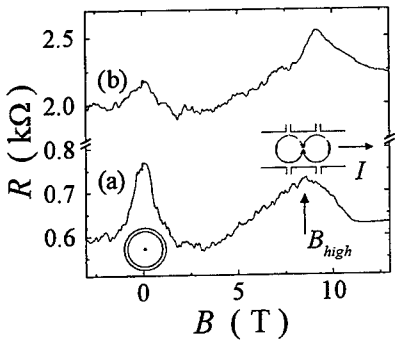

Figure 1 Resistance at $T = 0.3$ K of sample A as a function of magnetic field B applied in the quantum well plane and perpendicular to the current direction. The double quantum well potential is (a) balanced with $V_g = 0$ V and (b) unbalanced with $V_g = -0.7$ V. The insets show the Fermi discs of the two subbands at $B = 0$ (concentric circles) and close to $B = B_{high}$.

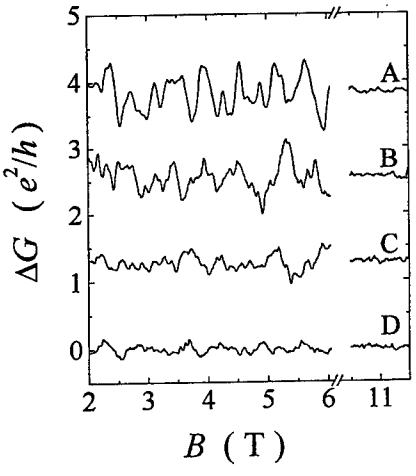

Figure 2 Conductance fluctuations at $T = 0.3$ K plotted as a function of in-plane magnetic field $B \perp I$ for samples A to D. The smoothly varying background conductance has been removed and the curves are offset for clarity. The x-axis is broken into two regions : $B < B_{high}$ and $B > B_{high}$. The thickness of the tunnel barrier increases from top (sample A) to bottom (sample D). Each trace is recorded over a segment of wire of the same length (0.5 μm), and in samples with similar phase coherence lengths ($l_\phi \sim 3$ μm).

PC.22

SINGLE ELECTRON TUNNELING THROUGH TWO VERTICALLY COUPLED QUANTUM DOTS

Y.Tokura [a,b] S. Sasaki [b] D. G. Austing [b] and S. Tarucha [b,c]

[a] *Delft Institute of Microelectronics and Submicrontechnology (DIMES), Delft University of Technology, 2628 CJ Delft, The Netherlands*

[b] *NTT Basic Research Laboratories, 3-1 Morinosato Atsugi, 243-0198 Japan*

[c] *University of Tokyo, 7-3-1 Hongo, Bunkyo-ku, Tokyo, 113-0033 Japan*

Abstract

Electron states and tunneling properties of two vertically coupled quantum dots are analyzed. The energy mismatch of the dots affects the phase diagram as a function of the quantum mechanical coupling and magnetic field normal to the plane. A magnetic field parallel to the barrier mixes the single particle states and also induces a singlet-triplet transition.

Key words: Quantum dot; Coulomb blockade; Correlation 73.23 73.61 85.30

1 Introduction

Quantum dots confined by a cylindrical potential in a double barrier heterostructure have been studied intensively since the dots have a high degree of cylindrical symmetry and the electron number can be precisely controlled from zero with a gate electrode. Recently, the electron states and Coulomb oscillations (COs) of two such quantum dots coupled vertically had been analyzed. [1,2] We predict a parameter region where the tunneling current is strongly suppressed because of the orthogonality of the quantum states. Here we discuss three effects, namely, energy mismatch in the two dots, magnetic field perpendicular to the current, and the coupling to the electrodes.

[1] Corresponding author. E-mail:tokura@duttnto.tn.tudelft.nl Fax: +31 15278 1203.
This work was partly supported by NEDO joint research program (NTDP-98) and by the "Stichting voor Fundamenteel Onderzoek der Materie" (FOM).

For both dots the lateral confining potential is parabolic with a frequency ω_0, and the vertical ($z-$direction) confining potential is formed by a triple-barrier hetero-structure. [1] The rectangular wells of thickness W are separated by a central barrier of thickness d. The states of the isolated two dots (U and L) are characterized by quantum numbers $[n,m]$ which are the radial and the angular quantum numbers ($n = 0, 1, 2, \ldots$, and $m = 0, \pm 1, \pm 2, \ldots$). A magnetic field B_n is applied along the $z-$direction and the energy of the $[n,m]$ Darwin-Fock state is $(2n + |m| + 1)\hbar\Omega - m\hbar\omega_{cn}/2$ where $\omega_{cn} = eB_n/m^*$ and $\Omega = \sqrt{\omega_0^2 + \omega_{cn}^2/4}$. The confinement energy and the wave function in the $z-$ direction are E_{zU}, E_{zL} and $\zeta_{U/L}(z)$. Coupled single-electron states split into symmetric (S) states and antisymmetric (A) states with an energy difference $\Delta_{SAS} = \sqrt{\Delta_0^2 + \delta^2}$, which consists of the energy difference between the isolated levels, $\delta = E_{zU} - E_{zL}$, and the quantum mechanical coupling energy, Δ_0. The wave functions are given by $\zeta_S(z) = \zeta_L \cos\Theta + \zeta_U \sin\Theta$ and $\zeta_A(z) = \zeta_L \sin\Theta - \zeta_U \cos\Theta$, where the angle, $\theta = \arccos(\Delta_0/\Delta_{SAS})$, characterizes the degree of mismatch between the dots. $\theta = 0$ is for the symmetric case and $\theta = \pi/2 - 2\Theta$. Nonzero Coulomb matrix elements are $V_{DA} = \langle SS|V|SS\rangle = \langle AA|V|AA\rangle$, $V_{DB} = \langle SA|V|AS\rangle = \langle AS|V|SA\rangle$, $V_{XA} = \langle AA|V|AS\rangle = -\langle SS|V|SA\rangle$, $V_{XB} = \langle SS|V|AA\rangle = \langle SA|V|SA\rangle$, which are functions of θ, $V_{intra} = \langle LL|V|LL\rangle = \langle UU|V|UU\rangle$ and $V_{inter} = \langle LU|V|UL\rangle = \langle UL|V|LU\rangle$. [2] We employ an exact diagonalization method with single electron basis sets as far as the fourth shell to find the N electron eigen-energies $E_{N,j}$ and the eigen-states of total spin **S**, and total angular momentum **M**, represented by a pair **(M,S)**. We restricted the values of (Δ_0, d) to experimentally accessible values with $\hbar\omega_0 \sim 4$ meV and 12 nm thick InGaAs wells.

2 Energy mismatch

If $B_n = 0$T, the two electron ground state in the coupled dots is spin singlet, **(0,0)**, for any θ, which is asymptotically degenerate with the spin triplet state **(0,1)**, in the limit of $\Delta_{SAS} = 0$. If we restrict the configuration space to $[n,m] = [0,0]$ and $\theta = 0$, the energy of **(0,0)** state is $\Delta_{SAS} + V_{inter} + V_{XB} - \sqrt{\Delta_{SAS}^2 + V_{XB}^2}$, and that of **(0,1)** is $\Delta_{SAS} + V_{inter}$. For $B_n > 0$T, the ground state eventually evolves into the spin triplet state, **(0,1)** favored by Zeeman energy or **(1,1)** favored by exchange energy, depending on the value of Δ_{SAS} [*singlet-triplet transition*]. [3] The **(0,1)** state becomes stable for more mismatch between the two dots.

The CO peak corresponding to the transition from an N to $N+1$ electron system is suppressed at low temperatures if the change of spin $|\Delta\mathbf{S}| \neq \frac{1}{2}$. This Spin selection rule has been predicted for coupled dots in the transition from $N = 2$ to $N = 3$. [4] We find it here for a transition from $N = 3$ to $N = 4$ for

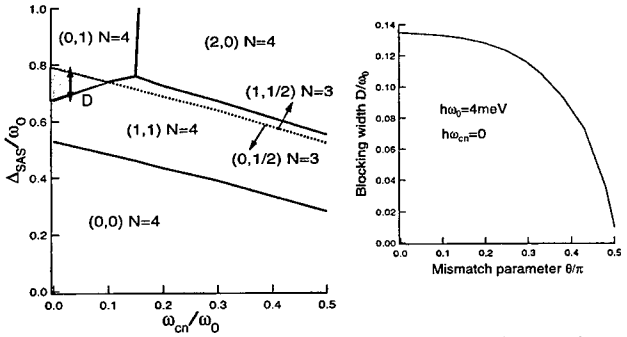

Fig. 1. Phase diagram for $N = 3$ and $N = 4$ as a function of Δ_{SAS} and ω_{cn}. In the shaded region, the CO current is suppressed at low temperature. Inset: the width D of the current suppressed region as a function of mismatch parameter θ.

the region of $\Delta_{SAS} < 0.1\hbar\omega_0$ and $\omega_c \sim 1.5\omega_0$. ($|\Delta S| = \frac{3}{2}$), which persists even for the mismatched case. By evaluating the spectral weight between possible N and $N+1$ electron eigen functions we predict that the CO peak for the transition between $\mathbf{(0,\frac{1}{2})}$ for $N = 3$ and $\mathbf{(0,1)}$ for $N = 4$ is almost completely suppressed near zero field, because of the wave-function orthogonality (Fig. 1). The region of this suppression in the phase diagram becomes smaller when mismatch of the dots is introduced as shown in the inset of Fig. 1.

3 In-plane magnetic field

Since the wave functions confined in the two quantum wells have finite spreading in the $z-$direction, the energy levels are modified by in-plane magnetic field B_{ip} by mixing different wave functions. The lowest order correction for the energy difference of the two lowest single electron levels is $\frac{\delta\Delta_{SAS}}{\Delta_{SAS}} = \frac{-(\hbar\omega_{cip})^2}{(\hbar\omega_0)^2-\Delta_{SAS}^2}(\frac{d+W}{2l_0})^2$, where $l_0 = \sqrt{\hbar/(m^*\omega_0)}, \omega_{cip} = eB_{ip}/m^*$. We have neglected very small positive diamagnetic term. This originates from the mixing of levels (so-call Van Vleck paramagnetic term) and is valid for Δ_{SAS} not very close to $\hbar\omega_0$ ($B_n = 0$T). Therefore, the energy separation reduces with increasing B_{ip} if $\hbar\omega_0 > \Delta_{SAS}$. The boundary between the $\mathbf{(0,0)}$ and $\mathbf{(0,1)}$ two-electron phase is determined by Δ_{SAS}, V_{XB} and the Zeeman energy. Since B_{ip} reduces Δ_{SAS} while maintaining the same Zeeman energy, the phase boundary is shifted to larger (bare) Δ_{SAS} from the case for B_n as shown in Fig. 2(a). B_{ip} also modifies V_{XB} and the phase boundary moves towards smaller B_{ip}. The singlet-triplet transition by B_{ip} has recently been observed in tunneling experiments, [5] which confirms our predictions. Numerical results with a tight binding method for a two-dimensional $(y-z)$ mesh are shown in Fig. 2(b). Since B_{ip} breaks the

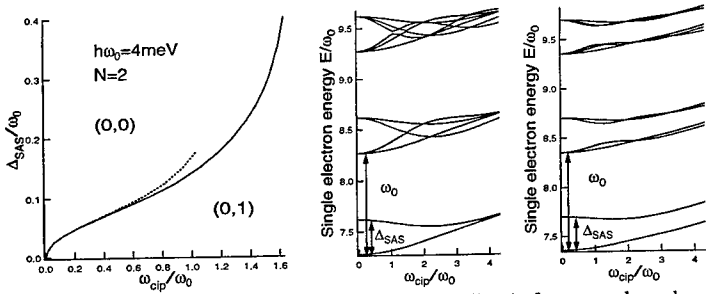

Fig. 2. (a) left: Two electron phase diagram. Solid line is for case when change of Coulomb matrix element is neglected. Dashed line is for case when corrections using perturbation (up to $\omega_{cip} \sim \omega_0$) are included. (b) right: Single electron energy spectrum as a function of ω_{cip}. Left and right panels are for matched dots, and mismatched dots ($\theta = \pi/4$), respectively.

cylindrical symmetry of the system, the degeneracy in the second and third shells is lifted and a complicated dependence on B_{ip} can be seen, although intriguingly, the shell structure is roughly preserved.

4 Coupling to electrodes

If $\Delta_0 < \Gamma$ (level broadening), we cannot treat the coupled dot as a whole and quantum mechanical correlations between symmetric and antisymmetric modes become important. [6] The $d = 75$nm dot in ref. [1] has $\Delta_0 \sim 0.1$meV which is comparable to Γ. Moreover, in such a situation the electron is apt to occupy a localized state in one of the dots because of intrinsic (finite δ) or extrinsic energy mismatch (applied electric field), and the tunneling probability to the contacts varies substantially for different N electron states.

References

[1] D. G. Austing, T. Honda, K. Muraki, Y. Tokura, and S. Tarucha, Physica B 249-251, 206 (1998).

[2] Y. Tokura, D. G. Austing, and S. Tarucha, unpublished.

[3] J. H. Oh, K.J. Chang, G. Ihm, and S. J. Lee, Phys. Rev. B **53**, R13264 (1996).

[4] H. Imamura, H. Aoki, and P. A. Maksym, Phys. Rev. B **57**, R4257 (1998).

[5] S. Sasaki, Y. Tokura, D. G. Austing, K. Muraki, and S. Tarucha, to be published.

[6] M. R. Wegewijs and Y. Nazarov, unpublished.

PC.23

Delocalization in a Double Quantum Dot System

M. Brodsky [1], N.B. Zhitenev[1,2], R.C. Ashoori[1], L. N. Pfeiffer[2], K.W. West[2]
[1] *Massachusetts Institute of Technology, Cambridge, MA 02139.*
[2] *Bell Laboratories, Lucent Technologies, Murray Hill, NJ 07974.*

We study the delocalization process in a double dot system by merging two quantum dots of different densities. The addition of each electron to the system is detected by a capacitive technique, allowing us to monitor the evolution of the addition spectrum over a very broad range of electron densities. The data indicate that delocalization can occur in different fashions depending on the merging density. While the magnetic field has no effect on the merging of two high-density dots ($n \geq 2\times10^{11}$ cm^{-2}), it dramatically affects the merging of two dots of lower density ($n \sim 1\text{-}2\times10^{11}$ cm^{-2}).

For a metallic island weakly coupled to its surroundings the number of electrons on the island is quantized. Due to the Coulomb repulsion between electrons the energy required to add an additional electron onto the island increases by an amount E_c for each successive electron. At sufficiently low temperatures ($kT<E_c$), the number of electrons on the island is well determined. An external gate capacitively coupled to the island can then be used to change the electron number. The electron additions occur periodically in the gate voltage with a period e/C_g, where C_g is the capacitance between the gate and the island.

We study electron additions in quantum dots using single electron capacitance spectroscopy (SECS) [1]. This method is unique in allowing us to probe electron additions into localized states. It thereby enables us to study the addition spectrum over a broad range of electron densities. Previous SECS studies [1,2] have demonstrated that at certain densities the electron addition spectrum of an individual dot is highly nonperiodic and, strikingly, contains bunches: two successive electrons can enter the dot at almost the same energy. A more recent experiment has demonstrated that the bunches appear at densities just below the *localization – delocalization transition* in the dot, when electrons in the dot separate into distinct regions, an inner core and a periphery [3]. The periodic bunches are associated with the existence of the localized peripheral state; one electron in the bunch tunnels to the periphery, and the other to the core. While the mechanism for pairing remains unknown, localization of electrons into separated regions within the dot appears to be a precondition for production of bunches in addition spectrum [2]. The reproducible periodicity of the paired electron additions leads us to believe that such separation is an intrinsic property of a low-density electron droplet.

In the present experiment we employ a novel approach to study the localization-delocalization transition (LDT). We create a barrier between two regions of a dot and study the LDT across this barrier in a broad range of electron densities. The simplest such arrangement is the double dot system described below. The presence of electrons in the dot modifies the confinement potential by screening. Even though the bare confinement potential associated with an empty dot has a fixed barrier defined lithographically, the actual barrier seen by electrons at finite density is very different due to screening. Therefore, the actual barrier is expected to be density dependent. Unexpectedly, the data indicate that for low enough electron densities $n \sim 1\text{-}2\times10^{11}$ cm^{-2} the barrier strength is enhanced by the magnetic field.

The dots were fabricated within an AlGaAs/GaAs heterostructure as described in previous work [1,2]. The essential layers (from bottom to top) are a conducting sheet of GaAs serving as the only contact to the dots, a shallow AlGaAs tunnel barrier, a GaAs active layer where electrons are accumulated, and an AlGaAs blocking layer. On the top surface a small AuCr top gate was formed with electron beam lithography. This top gate was used as a mask for reactive ion etching, which completely depletes the active GaAs layer outside the covered region and therefore produces a quantum dot below the top gate.

To realize a barrier within a dot we pattern a top gate in a dumbbell shape. That creates two small vertical dots laterally separated by a very small distance (a schematic of our samples is shown on the Fig.1). The top gate controls the electron density of the entire system. This geometry results in a double potential well with two valleys separated by a saddle. By changing the top gate bias V_g, we are able to gradually fill the double dot system with electrons. At first electrons accumulate in two independent electron puddles, one localized in each dot. The puddles grow laterally with increasing electron number and eventually couple to each other. The coupling mixes states of one dot with those of the other, and electrons start traversing the saddle point. When finally two puddles merge into a single large dot, the electron wave functions spread over the entire area of the resulting large dot.

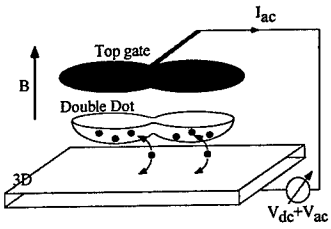

FIG. 1. Schematic of our samples

By varying lithographic dimensions, we control the height of the saddle and therefore the individual dot electron density at which merging occurs. We examine a number of samples to investigate a broad range of such densities: from two dots each containing a few localized electrons up to densities $n=2.5\text{-}3.5\times10^{11}cm^{-2}$ in each dot.

The measurements are carried out using on-chip bridge circuit described in [1]. At first we repel all electrons from the dot by applying a large negative potential to the top gate. Then, the top gate potential V_g is made more positive drawing the electrons back into the double dot one by one. To register electron additions, we monitor the a.c. capacitive response to a small ($<80\mu V$) a.c. excitation applied between the top gate and the contact layer. At V_g values corresponding to electron additions, an electron oscillates between the double dot and the contact, increasing the measured capacitance. Since one top gate covers both individual dots, an electron addition to either of the dots results in a peak in capacitance.

To distinguish electrons added to one dot from those added to the other we follow the evolution of the addition spectrum with perpendicular magnetic field. The general behavior of dot addition spectra in magnetic field is well known both for case of few-electron droplets [1,4] and for larger dots [5,6]. Addition energies oscillate with the field as an electron added to a dot occupies different angular momentum states. The exact pattern of those oscillations is very sensitive to the details of the confinement potential, and serves as a "signature" of a particular dot. Though in our sample two small dots are made to be nominally identical, the particular shapes of the confinement potential of the two dots are slightly different due to disorder and imperfections in the lithography process. Therefore, the respective addition energies for the two

FIG. 2. Gray scale image of the measured capacitance as a function of gate voltage (vertical axis) and magnetic field (horizontal axis). Black denotes capacitance peaks. T=0.3K. The diagonal line points to the boundary discussed in the text.

dots depend differently on the perpendicularly applied magnetic field. This permits us to associate each electron addition with a particular dot.

The capacitance traces taken at different values of the magnetic field are plotted together on the greyscale panel in Fig. 2. Black denotes high capacitance. Each successive trace corresponds to the energy for adding an electron to the double dot system. There are no electrons in the dot for the V_g<-290mV. The lowest trace shown represents the first electron added to the system. The low-density part of the spectrum (-290mV<V_g<-135mV) can be viewed as a simple superposition of two different sets of traces. Each set has its own periodicity in energy, as is typical for Coulomb blockade. Traces belonging to each set exhibit identical oscillations with field. We interpret each set as the addition spectrum of an individual dot. Because such separation of the entire spectrum is possible, we conclude that up to V_g=-135mV our system consists of two independent dots. Incidental alignment of the ground states of two dots for some particular values of the gate bias and the magnetic field may cause simultaneous but independent electron additions to each individual dot. Indeed, multiple level crossings can be seen on the plot. At each crossing point the peak in the capacitance signal has double height, indicating an addition of two electrons to the system. At much higher densities (V_g>-45mV) there is only one periodic Coulomb ladder. This indicates that initially separate electron puddles have merged into a single one. The transition between the two limits occurs over gate biases -135mV<V_g<-45mV. At zero field the merging occurs in the interval $\Delta V_g \cong 25$mV centered around V_g=-125mV. The gate bias V_g=-125mV corresponds to densities in the two dots of: 1.2×10^{11}cm^{-2} and 1.7×10^{11}cm^{-2}, respectively. Each dot contains about 30 electrons. For higher densities at zero field there is one combined dot under the gate. However, magnetic field higher then 4T dramatically affects the spectrum.

The most prominent feature of the spectrum is a clearly visible boundary, which separates the spectrum in two parts. It is marked by a line on Fig.2. The boundary extends up to densities in the two dots of 1.8×10^{11}cm^{-2} and 2.3×10^{11}cm^{-2}, respectively (over 60 electron additions), and can be approximated by the relation $n_{tr}\sim0.13\times B(T)\times10^{11}$cm^{-2}. To the left of the boundary (the

low field side) all electron addition traces are undistinguishable. To the right of the boundary (the high field side) the addition traces group in two sets as in the low-density case. Traces from each set exhibit the oscillatory pattern intrinsic to the individual dot. We conclude that the boundary separates two regimes in V_g-B space. In one regime, electrons are spread over the entire area of the double well and in the other each electron dwells in one of two wells.

In the latter regime the two dots are not completely independent, because the barrier between them is small and the interdot tunneling is possible [7]. When ground states of individual wells are aligned with each other a finite tunnel coupling exists between electrons in those states. This coupling splits two aligned levels as described in references [8,9]. We can estimate the coupling strength from our data [10]. Since both set of traces have roughly the same slope in field up to 8T, if two states are aligned they keep the alignment up to fields of 8T. Surprisingly we find that for two aligned levels the coupling strength does not depend on the field. In this case of such alignment a molecular hybrid state is formed, which appears as a bunch in the spectrum.

Though constant in field, this coupling increases with density, and becomes comparable to $E_c=e/C$ at densities $2\text{-}2.3\times10^{11}cm^{-2}$. The boundary ceases to exist at these densities. In fact, the boundary is altogether absent is samples for which the individual dot densities at the merging point are higher than $2.3\times10^{11}cm^{-2}$. Magnetic field has no effect on the merging of two high-density dots.

To conclude, we study localization-delocalization transition (LDT) over the barrier created within a dot. In our geometry the transition happens in a narrow interval of electron density (density change is about 10%). Thus we can define a density of the transition n_{tr}. We find that the transition occurs in a different fashion depending on the electron density. For high densities $n_{tr}>2\times10^{11}cm^{-2}$ the transition does not depend on magnetic field. Remarkably, the magnetic field strongly affects the transition when it happens in the density range $n_{tr}=1\text{-}2\times10^{11}cm^{-2}$. We determine the field dependence of the transition density: $n_{tr}\sim0.13\times B(T)\times10^{11}cm^{-2}$. We estimate the coupling strength between two localized stated for the densities just below the transition. To our surprise the condition for the the LDT in a double dot precisely coincides with the condition for existence of periodic bunches in the addition spectrum of a single dot[2].

We would like to acknowledge useful discussions with H.B.Chan, C.deC.Chamon, D.Goldhaber-Gordon, G.Finkelstein, L.S.Levitov, K.A.Matveev and M.A.Kastner. Expert etching of samples was performed by S.J.Pearton. This work is supported by the ONR, JSEP-DAAH04-95-1-0038, the Packard Foundation, NSF DMR-9357226 and DMR-9311825.

References:

[1] R.C.Ashoori et al., PRL **68**, 3088 (1992); R.C.Ashoori, Nature **379**, 413 (1996)
[2] N.B.Zhitenev et al., PRL **79**, 2308 (1997); R.C.Ashoori et al., Physica E **3**, 15 (1998)
[3] N.B.Zhitenev et al., to appear in Science
[4] S.Tarucha et al., PRL **77**, 3613 (1996); R.C.Ashoori et al., PRL **71**, 613 (1993)
[5] P.L.McEuen et al., PRB **45**, 11419 (1992)
[6] O.Klein et al., PRL **74**, 785 (1995)
[7] C.Livermore et al., Science, **274**, 1332 (1996) and references therein
[8] K.A.Matveev et al., PRB **53**, 1034 (1996); PRB **54**, 5637 (1996)
[9] J.M.Golden at al., PRB **53**, 3893 (1996); PRB **54**, 16757 (1996)
[10] M.Brodsky, to be published

QUANTUM PHASES IN ARTIFICIAL MOLECULES: THE ROLE OF INTER- VS. INTRA-DOT ELECTRON COUPLING

M. Rontani[1,2], F. Rossi[1-3], F. Manghi[1,2], and E. Molinari[1,2,*]

[1] Istituto Nazionale per la Fisica della Materia (INFM), Italy

[2] Dipartimento di Fisica, Università di Modena e Reggio Emilia, Italy

[3] Dipartimento di Fisica, Politecnico di Torino, Italy

We present a theoretical study of vertically coupled double quantum dots [1] through a generalized Hubbard approach where intra- and inter-dot Coulomb correlation and tunneling effects are described on the basis of realistic three-dimensional electron wavefunctions [2]. We study the addition spectra of these artificial molecules as a function of the inter-dot separation, which here can be varied far out of the regimes known in natural molecules where the ground-state interatomic distance is dictated by the nature of chemical bonding.

We find that the ground-state configuration undergoes transitions between different quantum phases: a 'coherent phase' dominated by tunneling effects, that is stable at the smallest interdot distances (phase I), and a phase where the inter-dot coupling is purely electrostatic, that occurs at the largest inter-dot distances (phase II). In addition, when the number of electrons is N 3 we predict an unexpected intermediate phase (phase III) whose range of stability is controlled by the relative importance of inter- and intra-dot interactions.

The peculiar properties of these phases are discussed in terms of the energies of their ground and excited states and the corresponding electronic pair correlation functions. The calculated magnetic-field dependent addition spectra present clear signatures of the phase transitions described above. Moreover, the changes in the magnetization induced by the addition of one electron are expected to follow a pattern characteristic of each phase.

Some evidence for phases I and II is already present in the experimental literature. We obtain quantitative predictions of the conditions that should lead to observation of the novel phase III.

* molinari@unimo.it

[1] S. Tarucha et al, Phys. Rev. Lett. 77, 3613 (1996); D.G. Austing et al., Jpn. J. Appl. Phys. 36, 1667 (1997).

[2] M. Rontani, F. Rossi, F. Manghi, and E. Molinari, Appl. Phys. Lett. 72, 957 (1998); Phys. Rev.B (1999), in press.

PC.25

Resistance and Transresistance of Two Coulomb- and Tunnel-coupled Quantum Wires

P. Vasilopoulos† and O. Raichev*

†*Concordia University, Department of Physics, Montréal, Québec, Canada, H3G 1M8*
Tel. (514) 848-3290, Fax (514) 848-2828, E-mail: takis@boltzmann.concordia.ca

**Institute of Semiconductor Physics, NAS, 45 Prospekt Nauki, Kiev 252650, Ukraine*

A linear-response theory of electron transport is developed for a system of two identical quantum wires, coupled by Coulomb interaction and tunneling. The interaction of electrons with acoustical phonons is taken into account but that with impurities is neglected. The transport is formulated in terms of the splitting energy Δ between the lowest states in each wire and of the lengths l_P, l_D, l_T, and l_C that describe, respectively, electron-phonon interaction, drag coupling, tunneling, and phase-breaking ($l_C \ll l_P, l_D, l_T$). The results are valid for wire lengths L ranging from the ballistic ($L < l_C$) to the diffusive ($L \gg l_P$) regime. In short wires, $L \ll l_P$, both tunneling and drag lead to a **negative** transresistance R_{TR}, while in long wires, $L \gg l_P$, the tunneling opposes the drag and leads to a **positive** R_{TR} with a non-monotonic dependence on L. For $L < l_C$ the tunneling leads to *interference oscillations* of R_{TR} and of the direct resistance as Δ is changed.

PACS 73.40.Gk. 73.23.-b, 73.23.Ad
Keywords: Coulomb coupling, tunneling, transresistance

Introduction

In submicrometer-long quantum wires and at low temperatures the electron transport is mainly ballistic[1] and the wire conductance reaches its fundamental value of $G_0 = e^2/\pi\hbar$. In contrast, for sufficiently long wires this transport is limited by scattering processes. The tunneling of electrons between parallel quantum wires and/or interlayer electron-electron (e-e) interaction are essential as demonstrated, e.g., by experimental and theoretical works on electron transport[2-11] along the layers in coupled double-wire systems. These works are mostly devoted to studying interlayer tunneling in the purely ballistic regime[2-9] or momentum transfer between the wires (Coulomb drag) in the diffusive[10] and ballistic[11] transport regimes.

Despite this progress, the description of electron transport in in coupled quantum wires is substantially insufficient and two important questions arise. The first one is how to describe transport when tunneling, the interactions of electrons with each other, and that with impurities or phonons are essential. The second question is how to bridge the gap between the ballistic and diffusive regimes in such a description. Here we present a linear-response theory of electron transport in coupled quantum wires that gives a reasonable answer to both questions and the results mentioned in the abstract.

Formalism

We consider two parallel, tunnel-coupled 1D layers of degenerate electrons adiabatically contacted to equilibrium reservoirs (leads) as shown and labelled in Fig. 1. We start from the quantum kinetic equation $\partial\hat{\rho}/\partial t + (i/\hbar)[\hat{H}_0 + \hat{H}_C + \hat{H}_{e-ph}, \hat{\rho}] = 0$ for the density matrix $\hat{\rho}$ and assume that electrons interact with the Coulomb field ($\hat{H}_C$) and with acoustical phonons($\hat{H}_{e-ph}$). Elastic scattering is neglected.

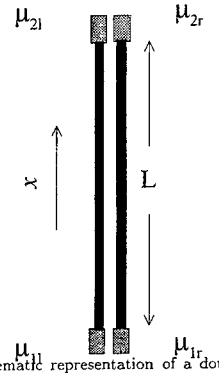

FIG. 1. Schematic representation of a double quantum wire system.

We employ a tight-binding description with basis that of the isolated left (l) and right (r) layer states in which the potential energy matrix is $\hat{h} =$

$(\Delta/2)\hat{\sigma}_z + T\hat{\sigma}_x$ when only the lowest subband is occupied in either layer. Here $\hat{\sigma}_i$ are the Pauli matrices, Δ is the level splitting energy, and T the tunneling matrix element.

The kinetic equation can be written as one for the Keldysh's Green's function $\hat{G}^{-+}$. Below we consider the case when the characteristic spatial scale of the electronic distribution is large in comparison with the Fermi wavelength $\pi\hbar/p_F$ and use the Keldysh's matrix Green's function in the Wigner representation $\hat{G}^{-+}_{\varepsilon,t}(p,x)$, where p and ε are the momentum and energy. In the steady-state regime the time-averaged Green's functions are linearized in the manner $\hat{G}^{\alpha\beta}_{\varepsilon}(p,x) = \hat{G}^{(0)\alpha\beta}_{\varepsilon}(p) + \delta\hat{G}^{\alpha\beta}_{\varepsilon}(p,x)$, where α and β stand for $+$ or $-$. The unperturbed part $\hat{G}^{(0)\alpha\beta}_{\varepsilon}(p)$ is expressed through the retarded and advanced matrix Green's functions and the equilibrium Fermi-Dirac function $f(\varepsilon) = 1/[1 + e^{(\varepsilon-\mu)/T_e}]$. The linearized kinetic equation reads

$$\frac{\hbar}{2}\{\hat{v}_p, \frac{\partial}{\partial x}\delta\hat{G}^{-+}_{\varepsilon}(p,x)\} - \frac{\hbar}{2}\{\frac{\partial}{\partial x}\hat{\varphi}, \frac{\partial}{\partial p}\hat{G}^{(0)-+}_{\varepsilon}(p)\}$$
$$+i[\hat{\varphi}, \hat{G}^{(0)-+}_{\varepsilon}(p)] + i[\hat{h}, \delta\hat{G}^{-+}_{\varepsilon}(p,x)] = i\delta\hat{\mathcal{I}}(\varepsilon,p,x) \quad (1)$$

Here $\{...\}$ denotes anticommutators, $\hat{v}_p = \hat{P}_l v_{lp} + \hat{P}_r v_{rp}$ is the diagonal matrix of the group velocities, and $\hat{P}_l$ and $\hat{P}_r$ are the projection matrices. We consider only the case of equal group velocities in the layers, when $v_{lp} = v_{rp} = v_p = p/m$. Further, $\hat{\varphi}$ is the matrix of the self-consistent electrostatic potential resulting from the perturbation of the electron density. The generalized collision integral is given as $\hat{\mathcal{I}} = -[\hat{\Sigma}^{-+}\hat{G}^{++} + \hat{\Sigma}^{--}\hat{G}^{-+} + \hat{G}^{-+}\hat{\Sigma}^{++} + \hat{G}^{--}\hat{\Sigma}^{-+}]$, where $\hat{\Sigma}^{\alpha\beta}$ is the self-energy due to Coulomb and electron-phonon interactions, and where the arguments of all functions are ε, p, and x. This corresponds to a quasiclassical description of the scattering. Despite the approximations made, Eq. (1), due to its matrix structure, is not reduced to a classical Boltzmann equation.

We assume that the Fermi energy is large in comparison with both T and Δ. We sum up Eq. (1) over the electron momentum p in the regions of forward (+) and backward (−) group velocities and introduce the non-equilibrium part of the energy distribution function $\hat{g}^{\pm}_{\varepsilon}(x) = (1/2\pi i)\int_{\pm} dp|v_p|\delta\hat{G}^{-+}_{\varepsilon}(p,x)$. Since $\delta\hat{G}^{-+}$ is essentially nonzero only in narrow intervals of energy and momentum near the chemical potential μ and Fermi momentum, we can replace $|v_p|$ by the Fermi velocity v_F common to both layers. The result is

$$\pm v_F(\partial\hat{g}^{\pm}_{\varepsilon}(x)/\partial x) + i[\hat{h}, \hat{g}^{\pm}_{\varepsilon}(x)]/\hbar = \delta\hat{I}_{\pm}(\varepsilon,x) \quad (2)$$

where $\delta\hat{I}_{\pm}(\varepsilon,x) = (1/2\pi\hbar)\int_{\pm}|v_p|dp\ \delta\hat{\mathcal{I}}(\varepsilon,p,x)$ depends on both $\hat{g}^{+}$ and $\hat{g}^{-}$.

The matrix kinetic equation (2) is equivalent to eight scalar equations for the four components of $\hat{g}^{+}$ and those (four) of $\hat{g}^{-}$. The boundary conditions for them are determined, in the Landauer-Büttiker-Imry approach, by the distribution functions of the leads described by the four chemical potentials μ_{1l}, μ_{1r}, μ_{2l}, and μ_{2r}, so that $\hat{g}^{+}_{\varepsilon}(0) = -(\partial f(\varepsilon)/\partial\varepsilon)[\hat{P}_l\delta\mu_{1l} + \hat{P}_r\delta\mu_{1r}]$, and $\hat{g}^{-}_{\varepsilon}(L) = -(\partial f(\varepsilon)/\partial\varepsilon)[\hat{P}_l\delta\mu_{2l} + \hat{P}_r\delta\mu_{2r}]$. The nondiagonal components vanish at the contacts since the tunneling is absent beyond the region $x = [0, L]$.

We now introduce the local chemical potential matrix $\delta\hat{\mu}^{\pm}(x) = \hat{P}_l\delta\mu^{\pm}_l(x) + \hat{P}_r\delta\mu^{\pm}_r(x) + \hat{\sigma}_x\delta\mu^{\pm}_x(x) + \hat{\sigma}_y\delta\mu^{\pm}_y(x)$ according to $\delta\hat{\mu}^{\pm}(x) = \int d\varepsilon\ \hat{g}^{\pm}_{\varepsilon}(x)$. Assuming that backscattering occurs much less frequently than forward-scattering, which is the case when the e-e scattering dominates over the electron-phonon one, and that tunneling also occurs much less frequently than forward-scattering, we can write $[\hat{g}^{\pm}_{\varepsilon}(x)]_{ll,rr} = -(\partial f(\varepsilon)/\partial\varepsilon)\delta\mu^{\pm}_{l,r}(x)$. Below we omit the symbol "δ" in $\delta\hat{\mu}^{\pm}(x)$ and in the potentials of the leads since all potentials are measured from the same equilibrium value μ. Then integrating Eq. (2) over the energy we obtain eight coupled, first-order differential equations:

$$\pm d\mu^{\pm}_l/dx + (\mu^{\pm}_l - \mu^{\mp}_l)(1/l_P + 1/l_D)$$
$$-(\mu^{\pm}_r - \mu^{\mp}_r)/l_D - 2l_F\mu^{\pm}_y = 0, \quad (3)$$

$$\pm d\mu^{\pm}_r/dx + (\mu^{\pm}_r - \mu^{\mp}_r)(1/l_P + 1/l_D)$$
$$-(\mu^{\pm}_l - \mu^{\mp}_l)/l_D + 2t_F\mu^{\pm}_y = 0, \quad (4)$$

$$\pm d\mu^{\pm}_x/dx + \delta_F\mu^{\pm}_y + \mu^{\pm}_x/l_C = 0, \quad (5)$$
$$\pm d\mu^{\pm}_y/dx - \delta_F\mu^{\pm}_x + \mu^{\pm}_y/l_C + t_F(\mu^{\pm}_l - \mu^{\pm}_r) = 0. \quad (6)$$

Here $t_F = T/\hbar v_F, \delta_F = \Delta/\hbar v_F$. The evaluation of $\delta\hat{I}$ was carried out assuming a weak tunnel coupling, when T is small in comparison to the imaginary part of the self-energies. The characteristic lengths l_P, l_D and l_C, coming from the collision integral $\delta\hat{I}_{\pm}(\varepsilon,x)$, are expressed, respectively, through the phonon-assisted 1D transport time τ_P, the 1D Coulomb drag time[10] τ_D, and the phase-breaking time τ_C (which describes the suppression of tunnel coherence) as $l_P = 2v_F\tau_P$, $l_D = 2v_F\tau_D$, and $l_C = v_F\tau_C$. Accounting only for the lowest-order Coulomb contributions τ_C is given by

$$\frac{1}{\tau_C} \simeq [e^4\ln^2(w/a)\Delta/2\pi\hbar^3\epsilon^2 v_F^2]\tanh^{-1}\frac{\Delta}{4T_e}, \quad (7)$$

where ϵ is the dielectric constant, w is the distance between the wires and a the wire width. Estimating the characteristic lengths for typical parameters, we find $l_C \ll l_P, l_D$ since the electron-phonon coupling and the e-e backscattering are weak.

Equations (3)-(6) with the boundary conditions $\mu_l^+(0) = \mu_{1l}$, $\mu_l^-(L) = \mu_{2l}$, $\mu_r^+(0) = \mu_{1r}$, $\mu_r^-(L) = \mu_{2r}$ and $\mu_{x,y}^+(0) = \mu_{x,y}^-(L) = 0$ give a complete description of electron transport in double quantum wire systems in a wide range of regimes starting from the purely ballistic regime, for $L \ll l_C$, to the diffusive regime, for $L \gg l_P, l_D$. The local currents flowing in the layers $j = l, r$ are given by

$$J_j(x) = G_0[\mu_j^+(x) - \mu_j^-(x)]/e. \qquad (8)$$

Below, to characterize the effects of drag and tunneling, we calculate the transresistance $R_{TR} = [\mu_{1l} - \mu_{2l}]/eJ_r$, where J_r is the current injected in the wire r when no current is allowed to flow into wire l. This is the typical setup for the drag experiments. In this case $J_r(0) = J_r(L) = J_r$ and $J_l(0) = J_l(L) = 0$. We also calculate the direct resistance $R = [\mu_{1r} - \mu_{2r}]/eJ_r$.

Results.

The relation $l_C \ll l_P, l_D$ allows us to simplify Eqs. (3)-(6) and distinguish two important physical cases.

Long wires, $L \gg l_C$. One can neglect derivatives $d\mu_{x,y}^{\pm}/dx$ in comparison to $\mu_{x,y}^{\pm}/l_C$ in Eqs. (5) and (6). Equations (3)-(6) are transformed to a set of four coupled balance equations presented as

$$\pm d\mu_j^{\pm}/dx + (\mu_j^{\pm} - \mu_j^{\mp})(1/l_P + 1/l_D)$$
$$-(\mu_{j'}^{\pm} - \mu_{j'}^{\mp})/l_D + (\mu_j^{\pm} - \mu_{j'}^{\pm})/l_T = 0, \qquad (9)$$

where $j = l, r$ and $j' \neq j$. The tunneling length is expressed as $1/l_T = (1/v_F\tau_C)2T^2/(\Delta^2 + \hbar^2/\tau_C^2)$. Solwing Eq. (9), we find

$$R = (\pi\hbar/2e^2)[2 + L/l_P + \sqrt{1 + l_T/l_1}\tanh K], \quad (10)$$
$$R_{TR} = (\pi\hbar/2e^2)[L/l_P - \sqrt{1 + l_T/l_1}\tanh K]. \quad (11)$$

where $K = L(1/l_T^2 + 1/l_T l_1)^{1/2}$ and $1/l_1 = 1/l_P + 2/l_D$. In the ballistic regime ($L \ll l_P, l_T$) we obtain $R \simeq \pi\hbar/e^2 = G_0^{-1}$, while the transresistance is given by $R_{TR} = -(\pi\hbar/e^2)L[1/l_D + 1/2l_T]$. As seen, R_{TR} is small, always *negative*, and proportional to L. If we neglect tunneling, the resulting R_{TR} describes the Coulomb drag in the ballistic regime[11]. When L increases and the electron transport becomes diffusive ($L \gg l_P$), we obtain, for $K \ll 1$, $R \simeq (\pi\hbar/e^2)L[1/l_P + 1/l_D]$. This resistance, if one omits the drag contribution, is expressed in terms of the Drude conductivity $\sigma = L/R = e^2 l_P/\pi\hbar = e^2 n\tau_P/m$, where n is the 1D electron density in layer r. Then $R_{TR} = -(\pi\hbar/e^2)(L/l_D)[1 - (L/L_0)^2]$ where $L_0 = (6l_P^2 l_T/l_D)^{1/2}$. Introducing the drag transresistivity $\pi\hbar/e^2 l_D$ and the 1D-1D tunneling conductance $e^2\rho_{1D}/\tau_T = 2e^2/\pi\hbar l_T$, where ρ_{1D} is the 1D density of states at the Fermi level, we formally obtain the result of Ref. 12, where a competition of drag and tunneling effects was investigated for double quantum well systems. As follows from Eq. (11), in the diffusive regime the tunneling opposes the drag and the resistance increases, changing its sign from negative to positive. If $K \sim 1$, R_{TR} is large and comparable to R, because a large fraction of the current penetrates in the l layer due to tunneling.

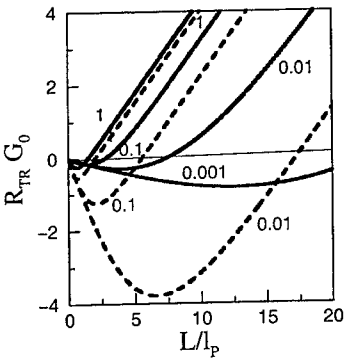

FIG. 2. Transresistance R_{TR} as a function of the wire length L. The solid curves correspond to $l_P/l_D = 0.1$ (weaker drag) and the dashed ones to $l_P/l_D = 1$ (stronger drag). The value of l_P/l_T marks all curves.

In Fig. 2 we show the length dependence of R_{TR} given by Eq. (11) for different relative contributions of the Coulomb drag and tunneling. R_{TR} is *negative* for small L but it always changes sign and becomes *positive* as L increases. This occurs at smaller L when the tunneling is stronger (larger l_P/l_T) or the drag is weaker (smaller l_P/l_D).

A peculiar transport regime, without backscattering, can be realized in tunnel-coupled magnetic edge states[13]. Assuming $1/l_P = 1/l_D = 0$, we transform Eq. (9) to the balance equations of Ref. 13 and obtain $R = (\pi\hbar/e^2)[1 + (1/2)\tanh(L/l_T)]$ and $R_{TR} = -(\pi\hbar/2e^2)\tanh(L/l_T)$.

Short wires $L \sim l_C \ll l_P, l_D$. Since the electrons pass through the wires almost without backscattering, one can solve Eqs. (3)-(6) by iteration, using $\mu_{l,r}^+ = \mu_{1l,r}$, $\mu_{l,r}^- = \mu_{2l,r}$, and $\mu_{x,y}^{\pm} = 0$ as an initial approximation. The calculation gives

$$R = \frac{\pi\hbar}{e^2}[1 + \frac{L}{l_P} + \frac{L}{l_D} + \frac{L}{2l_T} - \frac{l_C}{2l_T}\Phi(L)], \qquad (12)$$

$$R_{TR} = \frac{\pi\hbar}{e^2}[-\frac{L}{l_D} - \frac{L}{2l_T} + \frac{l_C}{2l_T}\Phi(L)]. \qquad (13)$$

The term proportional to $\Phi(L) = (l_C^{-2} + \delta_F^2)^{-1}[2(\delta_F/l_C)e^{-L/l_C}\sin(\delta_F L) + (l_C^{-2} - \delta_F^2)(1 -$

$e^{-L/l_C}\cos(\delta_F L))\}$. describes oscillations of the resistance damped due to the factor $\exp(-L/l_C)$. Its contribution to R_{TR} is not small at $L \sim l_C$, when the electrons tunneling between the layers partly conserve their phase memory. The periodic behavior results from tunneling-assisted interference of l and r electron waves along the length L.

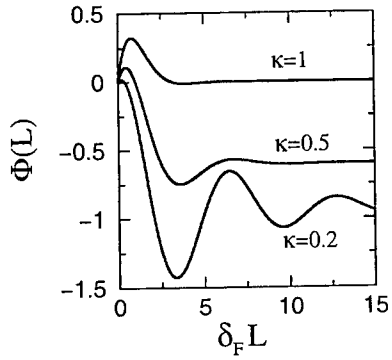

FIG. 3. The factor $\Phi(L)$ as a function of $\Delta L/\hbar v_F$.

Figure 3 shows the dependence of $\Phi(L)$ on $\delta_F L = \Delta L/\hbar v_F$; we used Eq. (7) at zero temperature so that $1/l_C = \kappa|\delta_F|$, where κ is a dimensionless parameter.

The level splitting Δ can be changed not only by a transverse voltage, but also by a magnetic field[8] H perpendicular to the plane of the quantum wires. For sufficiently weak H the results presented so far still hold with the phase $2\pi\phi/\phi_0$ added to $\delta_F L$. Here $\phi_0 = h/e$ is the magnetic flux quantum and $\phi = HwL$ the flux enclosed by the area between the wires. Though the two wires do not form a closed current loop, this should lead to Aharonov-Bohm-type oscillations in R and R_{TR}.

Finally, we apply Eq. (2) to the *purely ballistic* regime in which we can neglect the collision integral and need not make the assumption of weak tunnel coupling. Then we obtain Eqs. (3)-(6) without the terms containing l_P, l_D and l_C; they describe oscillations of the wave packets between the layers due to coherent tunneling. Solving them, we obtain

$$R = (\pi\hbar/e^2)[1 - r\sin^2\psi][1 - 2r\sin^2\psi]^{-1}, \quad (14)$$

$$R_{TR} = -(\pi\hbar/e^2)r\sin^2\psi[1 - 2r\sin^2\psi]^{-1}. \quad (15)$$

where $r = 2T^2/\Delta_T^2$, $\Delta_T = (\Delta^2 + 4T^2)^{1/2}$ and $\psi = \Delta_T L/2\hbar v_F$. The periodicity of the oscillations becomes the same as in Eqs. (12) and (13) if one replaces Δ by Δ_T. However, since the tunnel coupling is not weak, the oscillations described by Eqs. (14) and (15) have large amplitudes. The experimentally observed[6] resistance oscillations in tunnel-coupled ballistic quantum wires were of small ($\sim$ 0.5 KΩ) amplitude. This is not surprising because there are many factors, e.g., long-scale inhomogeneities, inelastic and elastic scattering, which compete against the tunnel coherence. Previous theoretical studies of the ballistic transport regime[2–5,7,8] were based on a quantum-mechanical calculation of the electronic wave transmission, while we recover the essential results from a quantum-kinetic analysis.

Conclusions.

We developed a linear-response, steady-state theory of electron transport in parallel one-dimensional layers coupled by tunneling and Coulomb interaction. The quantum-kinetic description of the problem leads to linear differential equations describing the distribution of local chemical potentials of the forward- and backward-moving electrons. The results for the direct resistance R and the transresistance R_{TR} are valid in the whole range from the pure ballistic to the diffusive regime. R_{TR} always depends nonmonotonically on the length L: in the *ballistic* regime tunneling and drag lead to a *negative* transresistance R_{TR}, while in the *diffusive* regime the tunneling opposes the drag and leads to a *positive* R_{TR}. If L is smaller than the phase-breaking length, the tunneling leads to oscillations of the resistance damped exponentially with L.

Acknowledgements. This work was supported by the Canadian NSERC Grant No. OGP0121756.

[1] S. Datta, *Electronic Transport in Mesoscopic Systems*, Cambridge Univ. Pr. (1997).
[2] J. A. del Alamo *et al.*, Appl. Phys. Lett. **56**, 78 (1990).
[3] N. Tsukada *et al.*, Appl. Phys. Lett. **56**, 2527 (1990).
[4] R. Q. Yang *et al.*, Rev. B **43**, 1699 (1991).
[5] P. Zhao, Phys. Rev. B **45**, 4301 (1992).
[6] M. Okuda *et al.*, Phys. Rev. B **47**, 4103 (1993).
[7] J.-Q. Wang *et al.*, Phys. Rev. B **47**, 13442 (1993).
[8] J.-R. Shi *et al.*, Phys. Rev. B **55**, 9941 (1997).
[9] I. M. Castleton *et al.*, Physica B, **245**, 157 (1998).
[10] Yu. M. Sirenko *et al.*, Phys. Rev. B **46**, 1611 (1992); H. C. Tso *et al.*, ibid **45**, 1333 (1992).
[11] V. I. Gurevich *et al.*, J. Phys.: Cond. Matter **10**, 2551 (1998).
[12] O. E. Raichev, J. Appl. Phys. **81**, 1302 (1997).
[13] Y. Ohno *et al.*, Phys. Rev. B **54**, R2319 (1996); D. Yoshioka *et al.*, Phys. Rev. B **53**, R16168 (1996).

PC.26

Magnetoconductance of independently tunable tunnel-coupled double quantum wires

M. A. Blount[1,2], J. S. Moon[1], J. A. Simmons[1,2], S. K. Lyo[1], J. R. Wendt[1], J. L. Reno[1]
[1]*Sandia National Laboratories, Albuquerque, New Mexico, 87185, USA*
[2]*University of New Mexico, Department of Physics and Astronomy, NM 87131, USA*

We report on our recent experimental studies of vertically-coupled quantum point contacts subject to in-plane magnetic fields. Using a novel flip-chip technique, mutually aligned split gates on both sides of a sub micron thick double quantum well heterostructure define a closely-coupled pair of ballistic one-dimensional (1D) constrictions. We observe quantized conductance steps due to each quantum well and demonstrate independent control of each 1D constriction width. In addition, a novel magnetoconductance feature at ~6 T is observed when a magnetic field is applied perpendicular to both the current and growth directions. This conductance dip is observed only when 1D subbands are populated in both the top and bottom constrictions. This data is consistent with a counting model whereby the number of subbands crossing the Fermi level changes with field due to the formation of an anticrossing in each pair of 1D subbands.

Coupled low dimensional electronic systems have become of increasing interest recently due to advances in fabrication technology. While much attention has been focused on closely coupled two-dimensional electron systems and coupled quantum dots, little work has been done on coupled quantum wires. Early work focused on tunneling between wires defined laterally by planar lithography, in which case the lateral tunneling is weak and the barrier profile poorly characterized. [1] Recently, vertically coupled quantum wires were fabricated in a double quantum well (DQW) heterostructure by mesa etching. [2] This system has a narrow tunnel barrier, yet lacks the control over constriction width that split gates can provide.

To overcome these difficulties, we have fabricated a pair of vertically coupled quantum point contacts (VCQPCs) using mutually aligned top and back split gates in a closely coupled $GaAs/Al_{0.3}Ga_{0.7}As$ DQW. The DQW had 200 Å wells separated by an 11 Å barrier. The two occupied subbands of the DQW had densities of 2.5 and 1.2 x 10^{11} cm^{-2}, and had a total mobility of 5.8 x 10^5 cm^2/Vs, yielding a mean free path of ~10 μm. A symmetric-antisymmetric energy gap Δ_{SAS} = 1.7 meV was measured, corresponding to the minimum density difference between the two lowest energy subbands when the QWs are balanced. We used the epoxy-bond-and-stop-etch (EBASE) technique, described elsewhere [3], to define a pair of vertically aligned split

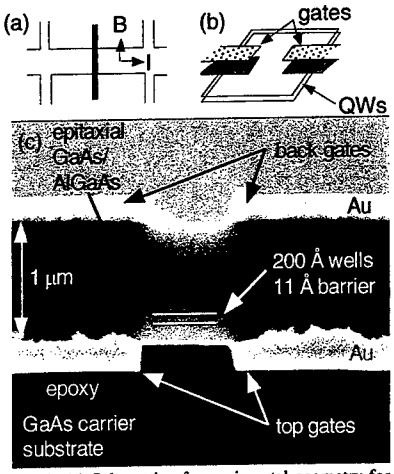

Fig. 1 (a) Schematic of experimental geometry for magnetoconductance measurement. (b) Split gate geometry. (c) Scanning electron micrograph of a test structure. The actual sample was only 3000 Å thick, so that the front and back split gates were equally distant from the electron layers.

gates by electron beam lithography *on each side* of the DQW heterostructure, whose thickness is only 3000 Å. Not only does this process allow sub-tenth-micron alignment of top and back gates, but has no deleterious effect on sample mobility. The resulting sample has both top and back split gates, each placed only ~1500 Å from the DQW. Fig. 1(a) and (b) show schematics of the sample, and Fig. 1(c) shows a scanning electron micrograph of a cross sectioned dual split-gate test structure of similar geometry, but a thickness of ~1 μm.

By controlling the relative values of top and back split-gate voltages V_T and V_B, the sample can be tuned into five different regimes depending on the widths of the individual QWs. These regimes are (i) 2D-2D; (ii) 2D-1D; (iii) 1D-1D; (iv) 1D-pinched-off; and (v) both pinched-off. Fig. 2 shows the sample resistance as a function of V_T, with $V_B = 0$. A number of features appear which correspond to transitions between the different regimes. At $V_T = 0$, both channels are 2D. As V_T is made increasingly negative, the channel resistance shows a clear shoulder at –0.3 V followed by a sharp increase at –0.7 V. These two features are due to the sequential depletion of first the top and then the bottom QW, *in the regions directly beneath* the top split gate. Thus, at $V_T \approx -0.7$ V, where electrons beneath the top split gate become completely depleted from *both* QWs, coupled 1D channels are formed in both QWs. Hence this marks the transition from regime (ii), the 1D-2D case, to regime (iii), the 1D-1D case. A simple capacitance calculation predicts the complete depletion of electrons beneath the split gates at $V_T = -0.9$ V, close to the experimental value.

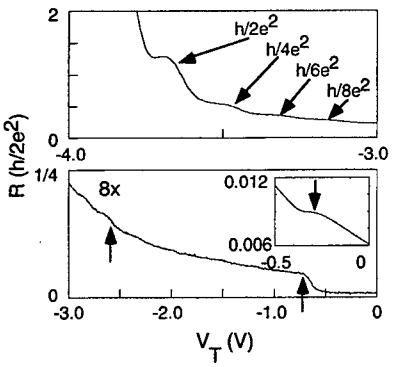

Fig. 2 Resistance of device as V_T is swept with V_B grounded. Inset at bottom shows transition from regime (i) to (ii) at $V_T = -0.3$ V. Transition from (ii) to (iii) can be seen at $V_T = -0.7$ V while distinct increase in slope at $V_T = -2.6$ V marks transition from (iii) to (iv). Bottom figure is magnified 8x to illustrate detail.

As V_T is swept further, we expect the QPC widths to narrow. Due to the fact that the split gate separation is comparable to the electron layer depth, the top channel width narrows more rapidly than the bottom width. At $V_T = -2.6$ V, the top QPC completely pinches off, leaving only the bottom QPC, corresponding to the transition between regimes (iii) and (iv). A weak plateau is observed at this point, as well as a change in the slope of the resistance. As V_T is made yet more negative, the familiar steps in resistance occurring at $h/2ne^2$ ($n = 1, 2, \ldots$) are observed due to the narrowing of the bottom QPC. Finally, at $V_T = -3.8$ V, after the last step at $R = h/2e^2$ occurs, both channels are completely pinched off. Similar results are obtained when instead $V_T = 0$ and V_B is swept negative.

These different regimes are evident in a waterfall plot of the conductance G of the device as a function of both V_T and V_B, shown in Fig. 3. Regimes (iii) and (iv) are now easily identified by their markedly different behavior. When only one wire is occupied (regime iv), uniform steps in the conductance quantized in units of $2e^2/h$ appear. This can be seen clearly at the base of the plot, near $V_T = -1.0$ V, $V_B = -2.0$ V, and $V_T = -3.0$ V, $V_B = -1.0$ V. However, when both wires are occupied (regime iii), quantized steps are again present, but form a complicated interference pattern as V_T and V_B are varied. By tracking the position of individual conductance steps as a function of both V_T and V_B, each step can be assigned to one quantum wire or the other. As expected, the total conductance of the VCQPC throughout regime (iii) and (iv) agrees with a count of the total number of quantized steps multiplied by $2e^2/h$, indicating that the transport is ballistic. Clearly, each QPC width--and thus the number of occupied

subbands--can be independently controlled by the action of V_T and V_B.

We now turn to the behavior of the conductance under an applied magnetic field B perpendicular to both the current and growth directions. Figure 4 shows a contour plot of $\partial[\ln(R)]/\partial V_T$, the logarithmic derivative of the resistance with respect to V_T, as a function of V_T and V_B, easing identification of the different regimes. Insets (a) – (e) show G vs. B taken at several different values of V_T and V_B, as indicated on the main figure by labels. Inset (a) was taken at V_T = -0.25 V and V_B = 0.0 V. The familiar 2D-2D anticrossing features, a conductance peak followed by a shallow dip, are observed centered around B = 6.5 T. This is consistent with the sample being in regime (i). As the sample is biased into regime (ii), the 2D-2D conductance features begin to change. This is evident in inset (b), taken at V_T = -0.50 V and V_B = 0.0 V. Here the 2D-2D conductance features now appear to be superimposed upon a broad conductance dip. For V_B= 0 and values of V_T greater than –0.7 V, the 2D-2D conductance features *disappear completely* and are replaced by a *broad conductance minimum* around 6.5 T. This feature is evident in insets (c) and (d), and is a hallmark of conductance behavior in regime (iii). Note that inset (d) is for V_T = -1.75 V and V_B = -1.25 V, showing that this conductance dip occurs over a wide range of V_T and V_B, so long as the sample is biased into regime (iii). Eventually, at high enough negative gate bias, the sample moves into regime (iv) where only one QPC remains occupied, and the conductance dip almost completely disappears. This can clearly be seen in inset (e). This phenomenon has been observed in several similar samples, indicating that this broad magnetoconductance dip is a characteristic feature of closely coupled ballistic 1D wires.

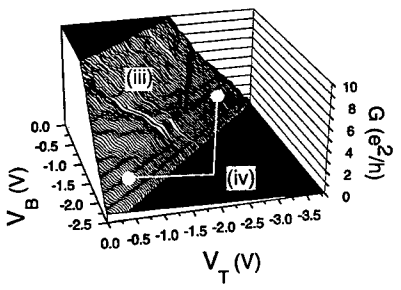

Fig. 3 Waterfall plot of G vs. V_T and V_B shows quantized conductance steps for regime (iv). Beating between steps is evident in regime (iii).

To discuss the origin of this 1D-1D magnetoconductance feature, it is useful to first consider previous work on the 2D-2D case. [4] The 2D-2D magnetoconductance features, exemplified in Fig. 4 inset (a), were shown to arise due to an in-plane magnetic field displacing the two 2D QW dispersion curves relative to each other in k-space by $\Delta k = eBd/\hbar$, where d is the distance between the two electron layers. At sufficiently high B the 2D dispersion curves anticross, forming a partial energy gap. Singularities in the 2D density of states and Fermi velocity occur at the upper and lower gap edges. As B is increased the gap edges cross the Fermi level, producing first a maximum in the conductance, followed by a minimum. These two magnetoconductance anticrossing features are centered about a point $B = [(2\pi n_1)^{1/2} + (2\pi n_2)^{1/2}]h/edB$. Using the measured density values for our sample, we obtain $B \approx 6.5$ T, in agreement with the data of Fig. 4 inset (a).

A similar analysis based on the **k**-space offset of the 1D-1D dispersion curves, combined with the ballistic transport through the sample, explains the 1D-1D data. Due to tunnel coupling, at sufficiently high B the 1D dispersion curves from one wire will anticross with their counterparts from the other wire, opening a quasi gap of Δ_{SAS}, similar to the 2D case. The resulting dispersion curve thus consists of several anticrossed pairs of 1D subbands, as sketched in Fig. 4 inset (f). In our model, we assume that the transport is ballistic and hence the conductance is given simply by the number of 1D subbands crossing the Fermi level. The application of B thus changes the conductance in two ways: (1) Whenever the Fermi level falls within a 1D anticrossing gap, the conductance is reduced by $2e^2/h$ from the uncoupled double quantum wire case. (2) Because for each pair of anticrossed 1D subbands there is a large increase in the density of states at the

edges of the anticrossing gap, each anticrossed pair of subbands can accommodate many more electrons than if no anticrossing occurred. Since particle number is constant, as B is increased and the anticrossings are formed, the Fermi level *drops substantially* and intersects fewer 1D subbands. This results in a large drop in conductance. Eventually B becomes large enough that all the anticrossings in the 1D subbands (and the associated singularities in the DOS) rise above the Fermi level. The number of electrons accommodated by each subband thus correspondingly decreases. As a result, the Fermi level rises again and many more subbands must then become occupied to accommodate all of the electrons, causing the conductance to rise again. While mechanism (1) will only be significant in QPCs with few occupied subbands, mechanism (2) will still be significant for relatively wide QPCs with dozens of occupied subbands.

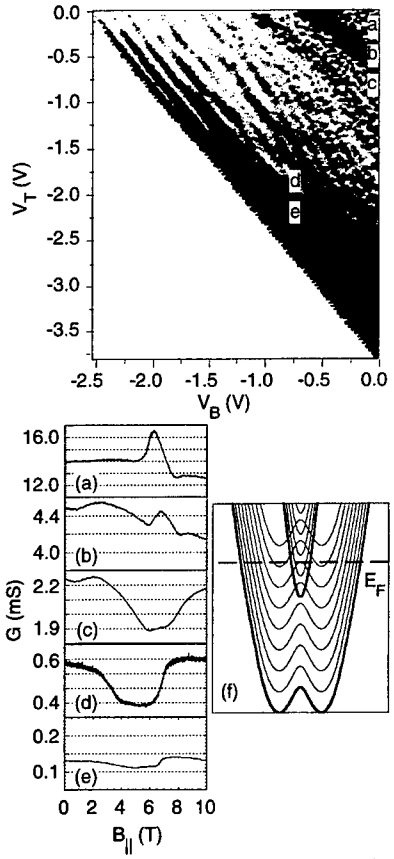

Fig. 4 Contour plot of the logarithmic derivative shows conductance steps in different regimes. Inset s (a) – (e) are magnetoconductance features for the primary regimes of interest. Inset (f) illustrates action of magnetic field on 1-D dispersion curves of VCQPC.

This behavior is consistent with that observed in the data of Fig. 4. The broad magnetoconductance dip appears only when the sample is biased into the 1D-1D regime. Biasing the sample far enough so that only one QPC is occupied extinguishes the magnetoconductance dip, due to the fact that there are no anticrossings present for a single QW. This clearly illustrates that the magnetoconductance dip is present *only when the coupled 1D-1D wires are defined,* i. e. only in regime (iii). This magnetoconductance feature, which is so qualitatively different from that observed in the 2D-2D case, can thus be considered to be an intrinsic property of ballistic transport through closely-coupled QPCs. Our data is consistent with recent theoretical calculations by Lyo. [5]. We note that a similar magnetoconductance dip has been observed by the Nottingham group in a mesa-etched double quantum wire, but was explained using an argument based on diffusive boundary scattering at the wire edges. [2]

Sandia is a multiprogram laboratory operated for the Department of Energy under contract DE-AC04-94AL85000.

[1] Tsukada, *et. al.* Appl. Phys. Lett **56**, 2527 (1990).
[2] Gompertz, *et. al.* Physica B **249**, 162 (1998).
[3] Weckwerth, *et. al.* Superlattices and Microstructures **20**, 561 (1996).
[4] Simmons, *et. al.* Phys. Rev. Lett. **73**, 2256 (1994).
[5] Lyo, to be published.

PC.27

Experimental Observation of Coulomb Drag in Parallel Ballistic Quantum Wires

P. Debray[1,2], P. Vasilopoulos[3], O. Raichev[4], R. Perrin[1], M. Rahman[5], and W. C. Mitchel[1]

[1] Air Force Research Laboratory (AFRL/MLPO), Dayton, Ohio, USA
[2] Corresponding author. Permanent address : Service de Physique de l' Etat Condensé, CEA de Saclay, F-91191 Gif-sur-Yvette Cedex, France. Tel. 33-1-6908-7449, Fax 33-1-6908-8786, E-mail: debray@spec.saclay.cea.fr
[3] Concordia University, Department of Physics, Montreal, Canada
[4] Institute of Semiconductor Physics, National Academy of Sciences, Kiev, Ukraine
[5] University of Glasgow, Department of Physics, Glasgow, UK

Abstract

We report the experimental observation of Coulomb drag in two parallel, ballistic quantum wires fabricated from a high-mobility 2DEG at the interface of a AlGaAs/GaAs heterostructure. The Coulomb drag resistance R_D in wire 1 due to a drive current in wire 2 was measured at 1.3 K and in a magnetic field of 1 tesla, applied to completely suppress tunneling between the wires when their separation was small. As the widths of the wires are changed by appropriately biasing the Schottky gates, R_D shows a structure with peaks whose magnitudes decrease rapidly with the distance d between the centers of the wires. These results can be understood qualitatively in the framework of recent theoretical treatments, which predict peaks in R_D when the level splitting between the 1D subbands of the wires and the Fermi momentum k_F are small.

Introduction

Momentum transfer, or Coulomb drag, between spatially separated electron layers has been studied experimentally [1] and theoretically [2] mostly between 2D layers. Theoretically, this drag has also been studied between very long quantum wires in which the wire length L is much longer than the electron mean free path l_i (*diffusive* regime) [3] and recently between quantum wires of length $L << l_i$ (*ballistic* regime) in which the electron motion along the wire at low temperatures is ballistic [4, 5]. It has been predicted that the drag resistance should attain its maximum value when the subbands in the two wires line up precisely and the Fermi wavevector is small. Motivated by these results and the absence, to our knowledge, of any experimental results on the 1D Coulomb drag, we undertook to study it experimentally in the ballistic regime.

Experimental Setup and Measurements

The coupled quantum-wire devices, shown schematically in Fig. 1, were fabricated from a high-mobility 2DEG (μ = 100 m^2/Vs, E_F = 10 meV, electron mean free path of 9 μm) at the interface of a AlGaAs/GaAs heterostructure and lithographically defined by three independent surface Schottky gates T, M, and B in order to have two identical, parallel quantum wires of lithographic length L = 0.4 μm. By appropriately voltage biasing the gates, it was possible to create two parallel quantum wires of variable width and separation. Measurements of the conductance of the individual wires at 1.3 K showed nearly quantized conductance plateaus indicating ballistic transport. All measurements were carried out at 1.3 K using a standard low-

bias (80 μV), low-frequency (33Hz), ac measurement technique. In all cases we chose the bottom wire as the *drive* wire and the top wire as the *drag* wire. Measurements were done in a perpendicular magnetic field B = 1 tesla. This field was chosen to suppress tunneling while at the same time having a reasonable separation d between the wires for which the drag effect could be observed. The Coulomb drag voltage was measured in two different ways at values of the middle gate voltage V_{MG} for which no tunneling was observed between the drive and the drag wire. In the first case, the voltage of the middle gate was kept at a fixed value and the voltages of the top and bottom gates were swept together. The drive current I and the drag voltage V_D were measured simultaneously as a function of the sweep voltage. The measurements were repeated for different values of the middle gate voltage. These measurements were designed to study the effect of wire separation on the drag voltage or equivalently the drag resistance $R_D = V_D/I$. In the second case, the voltage of the middle gate was kept at -0.550 V for all the measurements. A voltage of the top gate was chosen to be at the middle of the conductance step of the drag wire. V_D and I were then measured simultaneously as the voltage of the bottom gate was swept. The measurements were repeated for different fixed values of the top gate voltage. These measurements were geared to study the effect of wire width on the drag voltage. Figures 2 and 3 show typical representative results for the two different ways of measuring the Coulomb drag effect.

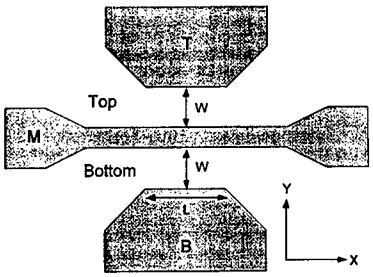

Fig. 1. Schematic diagram of a coupled quantum-wire device. Lithographic dimensions : L=0.4 μm and W=0.25 μm. Middle gate width is 50 nm.

Results and Discussion

Figure 2 shows the measured drive current I and the drag resistance R_D as a function of the top and bottom gate voltage V_{TB} changing simultaneously ($V_T = V_B = V_{T,B}$). In Fig. 3, I and R_D are plotted as a function of the bottom gate voltage V_B. The parameters used are indicated in the figures. In both cases, I shows the usual conductance plateaus characteristic of ballistic transport. In Fig. 2, R_D shows a prominent peak at $V_{B,T}$ = -1.07 V, followed by a much smaller peak at -0.78 V. The peaks are thus centered at voltages just beyond the right ends of the respective conductance plateaus where the conductance rises into steps. In Fig. 3, I and R_D show a behavior similar to that in Fig. 2. R_D has a strong peak at -1.01 V, and a weaker one at -0.71 V. The observed experimental results can be understood qualitatively in the framework of theories presented in Refs. 4 and 5 which dealt with Coulomb drag in the *ballistic* regime and considered only the interwire electron-electron coupling and neglected all other interactions. More appropriate for the present results is the theory of Ref. 5, valid at finite magnetic fields B,

whereas that of Ref. 4 is for B=0. With parabolic confinement (along y-direction) of the same

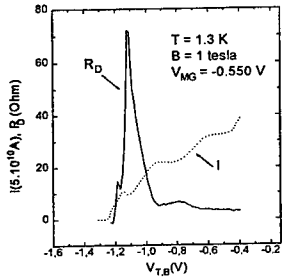

Fig. 2. Drag resistance R_D and drive current I as a function of the top and bottom gate voltage changing simultaneously ($V_T = V_B = V_{T,B}$).

frequency for both the wires and transport along the lengths (x-direction) of the wires, the drag resistance is given by

$$R_D = C_1 \frac{LT\Omega^3}{\kappa^2\omega^3 k_F^3}\frac{z^2}{\sinh^2 z}\exp\left(-C_2\frac{\omega_c^2 k_F^2}{\Omega\omega^2}\right)\times\left[\int_{-\infty}^{\infty} du\exp(-u^2/2)\times K_0\left(\sqrt{\frac{C_2\Omega k_F^2}{\omega^2}}\left|C_3\Omega^{1/2}d+u\right|\right)\right]^2 \quad (1)$$

The above expression corresponds to the case when only the lowest subbands, displaced in energy by Δ (splitting energy), are occupied in each wire. C_1, C_2, C_3, are constants, and u is a dimensionless variable. K_0 is the modified Bessel function, $z = \Delta/2k_BT$, ω the frequency of the confining potentials, $\Omega^2 = \omega^2 + \omega_c^2$, and $\omega_c = eB/m^*$. d is the distance between the centers of the wires, κ the dielectric constant of the wire material. The constant C's are: $C_1 = e^2 k_B m^3/\pi\hbar^5$, $C_2 = 4\hbar/m$, $C_3 = \sqrt{m^*/\hbar}$, and $m = m^*\Omega^2/\omega^2$. Eq. (1) is valid when both Δ and k_BT are small compared to the Fermi energy ε_F, defined as $\varepsilon_F = \hbar^2 k_F^2/2m$, where k_F is the x-component of the Fermi wave vector. This condition entails that the wavevectors of the electrons participating in Coulomb collisions in both the wires are close to k_F. Eq. (1) shows that R_D increases as z and k_F decrease. Peaks in R_D should therefore result when the highest occupied 1D subband bottoms of the drive and drag wire line up and sweep across the Fermi level. This dependence of R_D on z and k_F is also valid when the two wires are different and higher subbands are occupied [4]. Since K_0 is a rapidly decreasing function of its argument , R_D is expected to diminish rapidly as d increases. An increase in wire width correponds to a decrease in ω and an increase in d. The combination of these two effects as the wires widen should result in a significant suppression of the drag effect. Eq. (1) demonstrates that the influence of the magnetic field is to significantly reduce R_D, due to the exponential factor and due to the increase with B of the argument of K_0.

In the light of the above discussion we conclude that the observed peaks in R_D shown in Figs. 2 and 3 result when the 1D quantized transverse energy levels of the drive and the drag wire

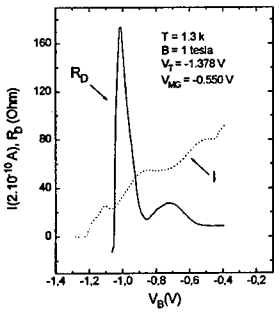

Fig. 3. Drag resistance R_D and drive current I as a function of the bottom gate voltage V_B.

nearly line up and sweep across the Fermi level. Under these conditions Δ and the Fermi momentum k_F are small ; the smallness of Δ and k_F results in a high R_D and in a peak as the gate voltage is swept. Assuming parabolic confinement for the wires, the confining frequency ω decreases for the higher subbands since the wire width increases. The wire separation d increases at the same time. Both these changes should lower the drag effect significantly. This explains why the second R_D peaks in Figs. 2 and 3 are much weaker compared to the first ones. The applied magnetic field enhances this weakening effect. We have estimated the confinement strength of the wires for gate voltages at which the first R_D peaks occur : $\hbar\omega_1 = 6.94$ meV. R_D was computed using Eq. (1) with the following values for the wire parameters : L = 0.4 μm, $\hbar\omega = 6.94$ meV, $\varepsilon_F = 1$ meV, $\Delta = 0$, B = 1 tesla, T = 1.3 K, and d = 50 nm. We obtained a value of 423 Ohm for R_D. Considering the uncertainties involved, we believe this value is in reasonable agreement with experimental results.

References

[1] N. P. R. Hill, J. T. Nichols, E. H. Linfeld, K. M. Brown, M. Pepper, D. A. Ritchie, G. A. C. Jones, B. Y. Hu , and K. Flensberg, Phys. Rev. Lett. **78**, 2204 (1997); H. Rubel, A. Fisher, W. Dietche, K. von Klitzing, and K. Eberl, *ibid*, **78**, 1763 (1997);U. Sivan, P. M. Solomon, and H. Shtrikmann, *ibid*, **68**, 1196 (1992).

[2] H. C. Tso, P. Vasilopoulos, and F. M. Peeters, Phys. Rev. Lett. **68**, 2516 (1992) ; *ibid* **70**, 2146 (1993) ; K. Flensberg, and B. Y. Hu, *ibid* **73**, 3572 (1994) ; M. Bonsager, K. Flensberg, B. Y. Hu, and A. Jauho, *ibid* **77**, 1366 (1996) ; Vignale and A. H. MacDonald, *ibid* **76**, 2786 (1996); O. E. Raichev, J. Appl. Phys. **81**, 1302 (1997) and references therein.

[3] H. C. Tso and P. Vasilopoulos, Phys. Rev. B **45**, 1333 (1992); Yu. M. Sirenko and P. Vasilopoulos, *ibid* **46**, 1611 (1992).

[4] V. I. Gurevich, V. B. Pevzner, and E. W. Fenton, J. Phys.: Cond. Matter **10**, 2551 (1998).

[5] O. E. Raichev and P. Vasilopoulos, Nano-99 Symposium, St. Petersburg, 1999.

PC.28

Direct Observation of Single Electron Decay from an Artificial Nuclei

J. Cooper, C. G. Smith, D. A Ritchie, E. H. Linfield
Semiconductor Physics Group, Cavendish Laboratory, Madingley Road, Cambridge CB3 OHE, UK
Y. Lin, H. Launois
CNRS/L2M 196, Avenue Henri Rivera, F-92220 Bagneaux, Paris

Abstract

We describe the behaviour of an isolated quantum dot charged up with an excess of 30 electrons over its equilibrium value. A non-invasive voltage probe with a charge resolution of e/10 is fabricated next to the dot and used to measure the electron decay rate. The system behaves like an artificial nucleus with the electron escape rate following a Poisson distribution. We observe times for tunnelling of electrons out of the dot in excess of 1000 seconds.

In this paper we will show how strongly isolated quantum dots can be made to trap non-equilibrium electrons for over a thousand seconds. We show how a non-invasive voltage probe can be used to measure the escape time for these electrons, and discuss how this mimics alpha decay from a nucleus.

Early zero dimensional measurements of semiconductor quantum dots [1] consisted of ballistic 1-D channels with two fine barriers defined across them. These measurements showed that there were two regimes, one for open quantum dots where the barrier conductances were greater than $2e^2/h$ and one for closed quantum dots were the values were less than this figure. The early result showed that the barriers caused quantum mechanical reflections which modified the transmission probability through the channel in the open case. The closed quantum dot showed sharp resonances which were interpreted [2] as being caused by single electron charging (SET) as had been seen for many years in small metal islands [3]. The resonances are due to single electron charging or Coulomb blockade (CB) and have been extensively studied [4,5]. More recently investigations of open quantum dots have revealed that, surprisingly, single electron charging can also be observed in open quantum dots [6]. Specific open quantum cavities have also revealed self-similarity [7] and wave function scarring [8].

Work on isolated quantum dots has mostly concentrated on the regime where $G<2e^2/h$, but is still measurable. With a current of 1pA this corresponds to 10^7 electrons passing through the dot per second. To measure the charging processes occurring in isolated quantum dots on longer time scales non-invasive voltage probes were developed capable of measuring single electron processes [9]. This system involved fabricating a 1-D ballistic detector channel in a separate circuit next to the quantum dot. The charging on the dot alters the 1-D channel resistance when it is in the tunnelling regime close to pinchoff. In this work we have returned to look at this device geometry in more detail.

The insert of figure 1 shows the dimensions and geometry of the device. Metal gates were fabricated using electron beam lithography on the top surface of an MBE grown GaAs/AlGaAs heterstructure in which a two dimensional electron gas (2DEG) layer is approximately 70 nm beneath the surface. A negative electric potential is applied to each of the gates, depleting the area of 2DEG directly beneath and so defining the dot and detector structure. All measurements were made in a dilution refrigerator with a base temperature of 100 mK. Modulated bias voltages of 50 μV and 300 μV were applied to the QD and the detector simultaneously and the output current from each passed to Lock-in amplifiers. The dot and detector circuits were kept electrically isolated and the bias voltages were modulated at well separated frequencies of 22.3 Hz and 77.1 Hz respectively. The gates of the QD were biased with a computer controlled voltage source. The extreme sensitivity required of the detector however meant that the gates were controlled from a battery source.

The system was initially set up showing CB oscillations as the voltage on the plunger gate V_{PL} was swept. From measurements with an applied magnetic field we where able to obtain the sheet density and effective dot size and so estimate that there were around 300 electrons in the dot with the gates just at pinch off. The charging energy was found from summing up the total

capacitances of all the gates to be 0.5 meV. The 1-D detector was biased so as to be close to pinch off with resistance of around 100 KOhms. With it in this state, it became sensitive enough to variations in the electric potential of the QD that it effectively acted as an electrometer with a resolution of at least e/10, allowing the detection of a change in charge of a single electron from the adjacent quantum dot.

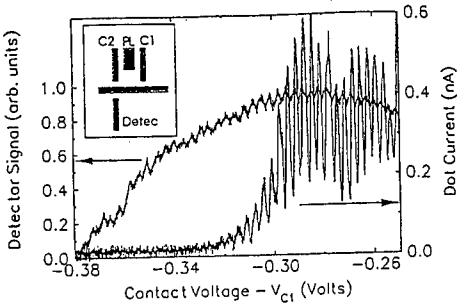

Figure 1. Current through the dot and detector signals measured simultaneously. The Coulomb Blockade Oscillations can be detected with the detector even when the SET current is too small to measure. The voltages are V_{PL} = -0.4V, V_{QP1} = -0.7 V. The inset shows a schematic of the gate structure.

The tuning of the gates was found to be very critical. In common with other similar devices, we often observed random telegraph switching (RTS) due to a single nearby impurity. The RTS noise was found to increase dramatically once a critical value of gate voltage (V_c) is exceeded. The value of V_c is unique for each gate and effectively sets a voltage limit beyond which these gates could not be taken.

Since the resolution and sensitivity of the detector was so critical, a wide range of conditions were tested. It was found that the optimum detector signal was obtained with the resistance in the range of 50 KOhms - 100 KOhms and a relatively large current flow of about 10 nA. This current gave a good signal to noise with no obvious loss of base temperature or sharpness of CB oscillations in the adjacent QD.

The data presented in this paper is from two sets of measurements, both carried out on the same device but cooled down twice. Each of the two measurement sets were carried out over the space of a few months.

Fixing the QD's plunger voltage and one of the contact voltages whilst sweeping the other contact, leads to CB oscillations in which the SET current (shown by the peak heights) rapidly reduces below a level that was measurable, as can be seen in figure 1. Inherent and external (instrument) noise means that it is in practice very difficult to measure currents less than 1 pA on this type of system. Even once the SET current is so small that it was no longer possible to observe CB oscillations, the detector signal continues to show clear oscillations and so give information about the state of the system. The limit to which these can be measured is determined by the gate voltage at which onset of RTS noise occurs.

The curves in figure. 2 show the detector signal as the plunger is swept up (more negative) and down (more positive) for a progressively more isolated dot. For each trace the dot is first 'filled' by reducing the two barrier voltages V_c to -0.2 V, then they are rapidly increased to the value shown and the gradual plunger sweep begins. With V_c = -0.28 V both the up and down sweeps are essentially identical, where each cycle of the sawtooth represents an electron entering or leaving depending on the sweep direction.

At V_c= -0.36 V the up sweep still show signs of electrons leaving the dot (although they are now less regular), however the down trace in the region between -0.8 V and -0.4 V is smoother, indicating that here no electrons are leaving. In the V_c= -0.44 V trace we see a similar process except that it appears that no electrons leave on the down sweep, indicating that the dot is effectively sealed off. This comes about as a result of the increasing gate voltages not only sealing the dot, but also raising its potential far above that of the surrounding 2DEG as is shown

diagrammatically in the inset of figure 3. Electrons may be expelled by the sweeping plunger but cannot subsequently re-enter.

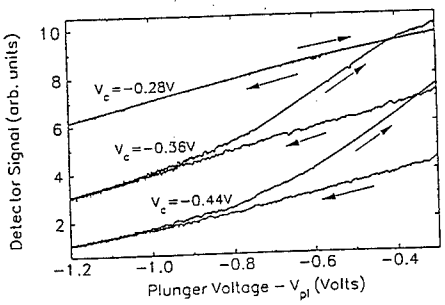

Figure 2. The detector signal as the plunger is swept between -0.3 V and -1.2 V. Between each trace the QPC voltages are reduced to -0.3 V so as to bring the system back to equilibrium.

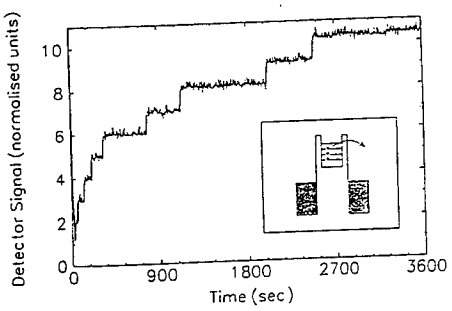

Figure 3. Time dependent detector signal response. The dot has been 'filled' by reducing the 1-D channel and Plunger gate voltages, sealed off by rapidly increasing the QPC voltage. The large kink at the start is the system settling, and then the steps that are seen each indicate one electron tunnelling out of the dot as shown in the inset.

In figure 3 the following cycle has been carried out prior to the start of measurement at t=0: The plunger gate and contact gates have been reduced to -0.20 and -0.21 Volts respectively, the contact gates are rapidly (within less than 1 second) ramped to -0.44 V and then the plunger gates ramped to -0.4V. From then on the gates are unaltered, and the detector signal is measured for over an hour. From figure 2 we can estimate that the dot will initially contain about 30 excess electrons. Each of the steps seen on this staircase like trace represents the change in detector signal due to one single electron leaving the dot. The left hand scale has been normalised to show electron number, but the relative values are unchanged. The step heights are relatively small compared to the working range of the detector, so making its response effectively linear and giving step heights that are approximately equal over the range of about 10 electrons.

The gradual drift upwards of the signal over the hour long period is due to the changing detector sensitivity and may have a variety of causes including the continuous shifting of charges in the impurity layer and a drift of the external battery driven bias voltage. Occasionally there is a switching event caused by electrons interacting with a nearby impurity, but these can be distinguished from an electron emission since the height of the step is not the same.

Normally, from one hour-long trace to the next, the total drift is less than the step size of one electron decay. This means that it is possible to go from one trace to the next and apply a normalisation to each which allows the decays times of equivalent electrons to be measured. This may be sequentially extended to a whole series of traces giving a sample of decay times.

In these measurements, about 150 time sweeps were carried out, and the decay times, measured from the gate definition time, for each particular electron energy collected. In figure 4 this data has been collated into a single plot where each dot represents the time of a decay event of particular electron state. The decay time for a given electron number fits well to a Poisson distribution with times starting from the initial gate sweep, rather than the last electron emission. In the upper inset the electron lifetime (as obtained from the peak of the frequency curve) has been plotted against electron number.

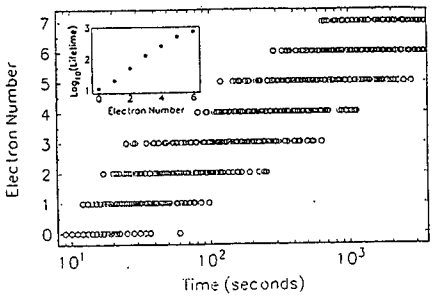

Figure 4. Approximately 150 traces similar to that seen in fig 3 were collected and the lifetimes of electrons at each particular energy determined. Here a frequency plot of the lifetimes is shown.

Although there has been much discussion recently of QDs as artificial atoms [10] the physical structure of the dot, i.e. a group of electrons confined by the surrounding negative potential of the gates, matches much more closely to that of the combined effect of the strong and electromagnetic forces of the atomic nucleus. This nuclear model was successfully used to demonstrate why the lifetimes of alpha particles ranged over twenty four orders of magnitude whilst the emitted energy varied by a factor of just over two [11].

This paper has shown that a 1-D chanel biased close to pinch can act as an extremely sensitive electrometer with a resolution greater than the electronic charge e. If this is positioned close to a quantum dot it can be used to derive information about the state of that dot even when the system is effectively sealed of from the external environment. The long lifetimes for electrons trapped in isolated quantum dots is very encouraging for their use as capacitance standards.

Proposals for advanced electronic technologies, such as Cellular Automata [12] will rely on a detector such as this to allow logic elements to be based upon the positioning of electrons within multi-QD cells.

This work was funded by an EC (QUADRANT grant No: 23362) and by UK EPSRC funds. We would also like to acknowledge support form Toshiba Research Europe Limited and the Newton trust.

References

1. C. G. Smith *et al.*, J. Phys. C **21**, L893 (1988)
2. L. I. Glazman and R. I. Shekhter., J. Phys. Condens. Matter, **1**, 581 (1989)
3. R. Lambier, *et al* Physica **XVI**, 907 (1950) and C. J. Gorter Physica **XVII,**, 777, (1951)
4. U. Meirav, M. A. Kastner, and S. J. Wind, Phys. Rev. Lett. **65**, 771 (1990)
5. P. L. McEuen *et al.*, Phys Rev. Lett. **66**, 1926 (1991)
6. C. -T. Liang*et al* ., Phys. Rev. Lett. **81**, 3507 (1998)
7. A. P. Micolich *et al.*, Semicond. Sci. Technol. **13** A41 (1998)
8. J. P. Bird *et al.*, Phys. Rev. Lett. (To be published)
9. M. Field *et al.*, Phys. Rev. Lett. **70,** 1311 (1993)
10. R. C. Ashoori *et al.*, Nature **379**, 413 (1996).
11. R. W. Gurney and E. Condon, Nature **122,** 439 (1928).
12. C. S. Lent, P. D. Tougaw, and W. Porod, Appl. Phys. Lett. **65**, 771 (1990)

PC.29

Correlations Effects in Few-electron Quantum Dots between ν=2 and ν=1

C. Gould[1,2], P. Hawrylak[1], A.Sachrajda[1], Y. Feng[1], P. Zawadzki[1], and Z. Wasilewski[1]

[1]Institute for Microstructural Sciences,National Research Council of Canada, Ottawa, Canada , K1A 0R6.
[2]Département de Physique and CRPS, Université de Sherbrooke, Sherbrooke, Québec, Canada, J1K 2R1.

Abstract

We investigate correlation effects in few-electron lateral quantum dots between filling factor ν=2 and ν=1. The correlations are the non-trivial spin depolarization events associated with the evolution of the total spin of the droplet with increasing magnetic field. We monitor the spin evolution by measurements of coulomb blockade (CB) peaks on lateral quantum dot devices containing from 5 to 20 electrons. Measurements are made as a function of the magnetic field, temperature, and source-drain bias. The temperature and high source-drain bias dependence of the CB peaks in the vicinity of the spin flip are consistent with spin depolarization events due to electronic correlations.

Introduction

In lateral quantum dots the lateral motion of quasi-two-dimensional (2DEG) electrons is confined by a smooth confining potential. A reasonably general model of a quantum dot[1-7] corresponds to the system of N quasi-two dimensional electrons in a strong perpendicular magnetic field B and lateral parabolic confining potential with characteristic frequency ω [1,2]. In a strong magnetic field the single-particle Hamiltonian corresponds to a single harmonic oscillator with magnetic field tunable energy[1,2]. The harmonic oscillator energy levels $E(m,\sigma)$ are similar to the angular momentum states $|m\rangle$ of the lowest degenerate Landau level with two spin components σ . In a sufficiently strong magnetic field we expect all electrons to occupy the spin split lowest angular momentum states $m=0,1,\ldots,N/2$. This defines the filling factor ν=2 droplet, as shown in Fig.1a. Increasing magnetic field reduces the kinetic energy of each spin component, increases the Zeeman energy, and leads to the redistribution of electrons among the spin-up and spin-down energy levels, as illustrated in Figs.1 b,c. Eventually, half of the electrons flip their spin and we end up with a spin polarized droplet at filling factor ν=1. Hence magnetic field implies monotonic reduction of the number of spin up N_u electrons through spin flip events. The number of spin flip events in the evolution of the droplet from ν=2 to ν=1 equals

half of the number of electrons N. An ability to count spin flips allows us to know exactly the number of electrons in the dot. These processes are an important characterization tool for quantum dots. The picture described here has been investigated extensively [2-7]. We address here how electronic correlations modify this picture[2] in analogy with correlation effects and spin textures in Quantum Hall ferromagnets[8].

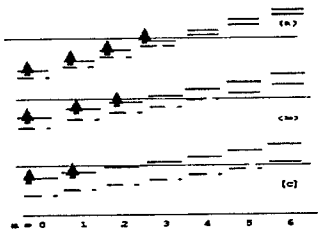

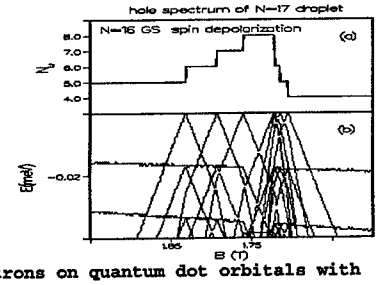

Figure 1 (left): Redistribution of electrons on quantum dot orbitals with increasing magnetic field.
Figure 2 (right): Top: the magnetic field dependence of the number of spin up electrons N_u in the ground state of the N=16 electron droplet. Bottom: all possible energy levels of a particle removed from the N=17 droplet.

We include interactions via exact diagonalization techniques using a fully interacting Hamiltonian of electrons confined in a quantum dot [2]. For a fixed N, the number of spin-up electrons N_u and the total angular momentum R are good quantum numbers. We construct many-particle configurations and diagonalize the Hamiltonian numerically in each Hilbert space (N_u,R). The number of configurations i.e. the amount of correlations, increases rapidly with increasing number of N_u electrons. Details of calculations were reported in Refs.[2,7]. We illustrate results of calculations by considering the spin flip process N_u =5 $\rightarrow$ N_u =4 in N=16 droplet. Fig.2 shows the magnetic field dependence of the number of spin up electrons N_u in the ground state of the droplet. We see that the spin flip i.e. the reduction of the number of N_u electrons, is interrupted by a rapid increase of the number of N_u electrons [2,7]. Hence the increase of spin polarization of the droplet is interrupted by completely spin-depolarized states. The spin depolarization event in the ground state implies many level crossings. Level crossings imply no gap in the excitation spectrum. Hence spin depolarizations are equivalent to a collapse of the Zeeman gap in the excitation spectrum of the quantum dot. This is illustrated by plotting all possible energy levels of a particle removed from the N+1=17 electron droplet i.e. "hole". The "hole" spectra can be measured

by tunneling through quantum dots with finite source-drain bias. The most characteristic feature of these "excited" states is

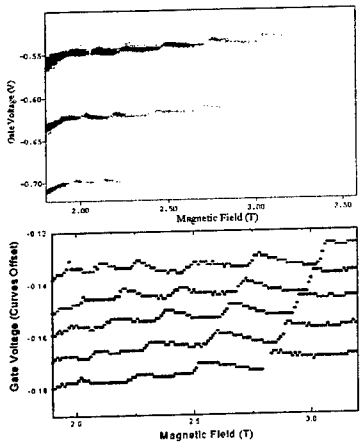

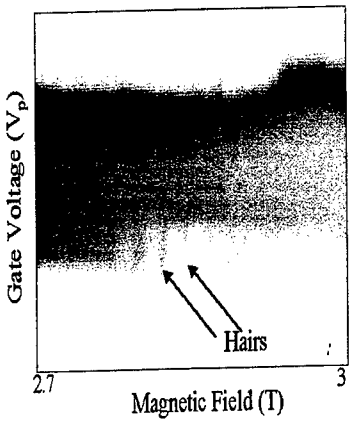

Figure 3 (left): Top; Succesive CB peaks as a function of the magnetic field between V=2 and V=1. Bottom; Position of the CB peaks with the charging energy removed.
Figure 4 (right): Last spin flip for a source-drain voltage of .5mV.

their magnetic field dependence. The spin depolarization during the spin flip event is accompanied by many excited states "running into" chemical potential.

To investigate these correlation effects we have fabricated lateral quantum dots defined by electrostatic gates on a AlGaAs/GaAs wafer containing a high mobility 2DEG. A plunger electrode is used to control the number of electrons in the dot. In the experiment a source-drain bias is applied across the dot and the current is measured as a function of the plunger voltage V_p. The experiments were carried out in a magnetic field perpendicular to the plane of the 2DEG on a dilution refrigerator. The amplitude of the CB peaks still varied as a function of temperature at temperatures below 100mK. In Fig.3 we show the current-plunger voltage spectrum for a fixed source drain voltage of 10μV in magnetic fields from 1.7- 3.0T. The bright regions correspond to high current and represent Coulomb blockade (CB) peaks. The CB peaks are separated by the charging energy. Their position and amplitude change with magnetic field. These changes are clearly visible by removing the charging energy and replotting the position of successive CB peaks as a function of the magnetic field. We clearly see oscillations of the position of the CB peaks. Each oscillation of position is

accompanied by a significant decrease in the amplitude of CB peak. We identify these decreases of the CB amplitude with spin flip events. The spin flip events start from the filling factor ν=2 droplet at B~1.7T and continue to a filling factor ν=1 droplet at B~3T. The three CB peaks shown here correspond to three different numbers of electrons on the dot. From the number of spin flip events we conclude to have from N=10 to N=12 electrons on the droplet. We have previously reported an unusual sensitivity to temperature of the CB minima in the spin flip regime. This puzzling behavior could have been understood in terms of the collapse of the Zeeman gap, or, equivalently, an existence of many very low energy excited states which become available for tunneling as the temperature increases[3]. Here we report a finite source-drain spectroscopy of the spin-flip event. In Fig.4 we show the finite SD spectra of the last spin flip in the N=16 electron associated with the spin flip event is accompanied by a number of "excited states" ("hairs") running into the CB line. The comparison with Fig.2 leads us to interpret the excited states as direct evidence of spin depolarization in the electronic droplet.

In conclusion, we present results of "lateral" magneto-tunneling experiments on small quantum dots in the few electron regime. The lateral nature of the dot allows additional spectroscopic information related to the amplitude modulation. Detail spectroscopic studies of the amplitude and position modulation of the tunneling current suggest the existence of nontrivial spin depolarization events due to electronic correlations.

References

[1] For reviews and references see L. Jacak, P. Hawrylak, A. Wojs, "Quantum Dots", Springer Verlag (1998).
[2] P. Hawrylak, C. Gould, A. Sachrajda, Y. Feng, and Z. Wasilewski, Phys. Rev. B59, 2801 (1999).
[3] L. Kouwenhoven, T.H. Oosterkamp, M.W. Danoesastro, M. Eto, D.G. Austing, T. Honda, S. Tarucha, Science. 278, 1788 (1997).
[4] P.L. McEuen, E.B. Foxman, J.M. Kinaret, U. Meirav, M.A. Kastner, N.S. Wingreen, S.J. Wind, Phys.Rev.B45, 11419 (1992).
[5] O. Klein, S. de Chamon, D. Tang, D.M. Abusch-Magder,U. Meirav, X.-G. Wen, M.A. Kastner, and S.J. Wind, Phys. Rev. Lett. 74, 785 (1995)
[6] S. R. Eric Yang, A. H. MacDonald, and M. D. Johnson, Phys. Rev. Lett. 71, 3194 (1993); J.H. Oaknin, L. Martin-Moreno, C. Tejedor, Phys. Rev. B54, 16 850 (1996); Hiroshi Imamura, Hideo Aoki, Peter A Maksym, Phys.Rev. B57, R4257 (1998).
[7] Arkadiusz Wojs, Pawel Hawrylak, Phys. Rev. B56, 13227 (1997).
[8] A.H. MacDonald, NATO ASI Series E Applied Sciences,v.326, 63 (1996).

PC.30

What is the Hall resistance of a Quantum Dot?

P. Grousset, D.C. Glattli, Y. Jin and B. Etienne**

Service de Physique de l'Etat Condensé, CEA Saclay,
F-91191 Gif-sur-Yvette, France

*Laboratoire de Microelectronique et Microstructures,
CNRS, F-9225-Bagneux, France.

In macroscopic samples, the Hall resistance is known to gives a determination of the 2D density of the homogeneous electron fluid which carry the current. This is a very fundamental quantity robust again many microscopic and geometric factors. In the case of a Quantum Dot where Coulomb Blockade and energy level quantization occurs, is not obvious that this quantity will survive as now the current is no longer transported by an continuous flow of electrons but is due to random temporal motion of single charges crossing theDot.

We have realized a four terminal Quantum Dot where the four contacts are in the tunnel regime. By passing the current between two opposite contacts and measuring the transverse voltage using the two remaining contacts we have been able to do four-point measurements. Our analysis of the Coulomb blockade transport using fisrt and second order perturbation theory in the tunnel coupling show that 1) Coulomb blockade is essentially a contact resistance effect and is the dominant information that we can get from simple two-point mesurements 2) coherent tunneling process are the only process measured in four-point measurements which more generally are shown to give information on the transport inside the dot. 3) the Hall resistance has no definite sign at low field. 4) at high field in the edge state regime the Hall resistance keep always the conventional sign but remains lower that the expected quantized Hall resistance. We show that this is due to the finite and long dwell time of electrons in the Dot and this provides a measure of this time. The measurements presented here have been performed in both low field and high field regimes, giving for the first time a measure of the Hall resistance in a Quantum Dot. At low field we observe a dominant Coulomb Blockade contribution in the 2-point resistance with weak surimposed variations reflecting a coherent transport contribution, while the 4-point resistance show only coherent transport contributions in agreement with 1) and 2). Also the sign of the Hall resistance fluctuates with field. At high field we find a positive Hall resistance (sign reversed when field reversed) but weaker by a factor ten compared to the quantized Hall resistance, giving a measure of the electron dwell time in this regime.

Far Infrared Response OF InAs-GaSb Type II Quantum Dots

D. A. Broido [a], K. Kempa [a], and U. Rössler [b]

[a] Department of Physics, Boston College,
Chestnut Hill,MA 02167, USA
[b]Institut für Theoretische Physik,Universität Regensburg
D-93040 Regensburg, Germany

July 5, 1999

Abstract

We have investigated theoretically the ground state and electromagnetic response of InAs-GaSb type II quantum dots in the presence of a vertical magnetic field. The ground state is calculated within the Hartree approximation using a 2-band $\mathbf{k}\cdot\mathbf{p}$ effective mass Hamiltonian to represent the coupling between the two spin-split sets of dot levels deriving from the lowest InAs electron subband and the highest GaSb heavy hole subband. The FIR response is calculated within the RPA. We show that the interlayer Coulomb interaction between electrons and holes combined with the $\mathbf{k}\cdot\mathbf{p}$ mixing breaks the generalized Kohn's theorem leading to a complex FIR spectrum.

Introduction

InAs-GaSb quantum well systems are characterized by unusual band structure associated with the type II band alignment. By varying the InAs and GaSb layer thicknessesΓ the electron and hole subbands can be intermixed A charge redistribution then takes place between the layers creating an interacting electron-hole gas [1Γ2Γ3]Γ where the electrons (holes) are confined primarily in the InAs (GaSb) layer. In this paperΓ we study the effect of lateral confinementΓwhich gives rise to quantum dotsΓon the corresponding ground state and FIR response of this electron-hole system.

For this investigationΓwe take the InAs and GaSb layers to be sandwiched between two AlSb barrier layers. We assume the barrier potential at the AlSb-InAs and GaSb-AlSb interfaces to be infiniteΓbut we include the finite potential offset of 0.962eV (0.568eV) between the InAs and Gasb conduction (valence) band. We envision a scenario in which teh dots are formed by etching of the AlSb-InAs-GaSb-AlSb composite quantum well so as to produce lateral parabolic confining potentials that localize electrons and holes about the same dot center.

Ground State

We will be focusing on the 150 meV energy range between the bottom of the conduction band in InAs and the top of the valence band in the GaSbΓwhich characterizes the type II band alignment. Our calculations will refer to a system with a 140 Å InAs layer and a 45 Å GaSb layer. The strong confinement due to: (i) the narrow GaSb layerΓand (ii) the light conduction band effective mass in InAsΓallows us to restrict our consideration to the lowest InAs electron subbandΓand the topmost GaSb heavy hole subband. The effective mass Hamiltonian for the coupled $\mid 1/2, +1/2 >$ InAs conduction band state and the $\mid 3/2, +3/2 >$ GaSb valence band state is described through the 2×2 $\mathbf{k}\cdot\mathbf{p}$:

$$H_+ = \begin{pmatrix} \epsilon_{1e} + H_e + V_H(\rho) & \frac{s_{11}}{\sqrt{2}} P\hat{k}_+ \\ \frac{s_{11}}{\sqrt{2}} P\hat{k}_- & \epsilon_{1hh} - H_{hh} + V_H(\rho) \end{pmatrix} \tag{1}$$

$$H_\alpha = (a^\dagger_{+\alpha} a_{+\alpha} + \frac{1}{2})\hbar\omega_{\alpha+} + (a^\dagger_{-\alpha} a_{-\alpha} + \frac{1}{2})\hbar\omega_{\alpha-} + \frac{1}{2} g_\alpha \mu_B B$$

$$\omega_{\alpha\pm} = \sqrt{\omega_{0\alpha}^2 + \frac{\omega_{c\alpha}^2}{4}} \pm \frac{\omega_{c\alpha}}{2} .$$

HereΓ $\alpha = e, hh$ stands for electrons or heavy holesΓ H_e and H_{hh} are the in-plane Hamiltonians for uncoupled electrons and holesΓwhich yield the Fock-Darwin statesΓ and $V_H(\rho)$ is the Hartree potential. The operatorsΓ$a_{\pm\alpha}$ and $a^\dagger_{\pm\alpha}$Γare defined in terms of the uncoupled electron and hole dot states. $\omega_{0\alpha}$ is the frequency associated with the lateral parabolic confining potentialΓ$\omega_{c\alpha}$ is the cyclotron frequencyΓand g_α is the effective g-factor for the InAs conduction band and GaSb valence band ($g_{hh} = 3/2\kappa$Γ where κ is the associated Luttinger parameter). s_{11} is the overlap integral of the electron and hole subband functions and is typically quite small ($s_{11} \sim 0.1$) due to the large conduction and valence band offsets between the InAs and GaSb. P is the Kane momentum matrix elementΓwhich we take to be the average of that for InAs and GaSb. ϵ_{1e} and ϵ_{1hh} are the electron and hole ground subband energies obtained under flat-band conditions by numerical solution of the Schrödinger equation. Their relative position is defined by the choice of InAs and GaSb layer thicknesses. The coupling between $\mid 1/2, -1/2 >$ and $\mid 3/2, -3/2 >$ states is described through a similar 2×2 HamiltonianΓH_-Γobtained from H_+ through the substitutionΓ$\hat{k}_\pm \rightarrow \hat{k}_\mp$ and a change in sign of the Zeeman term in H_α.

As a result of the assumed isotropy in the plane of the InAs and GaSb layers the total z-component of angular momentumΓ$l = M_j + m_\alpha$ is a good quantum numberΓ where $M_j = \frac{1}{2}$ or $\frac{3}{2}$ ($-\frac{1}{2}$ or $-\frac{3}{2}$) for quasi-spin indexΓ$s = +$ ($s = -$)Γand m_α is the quantum number corresponding to the operator $L_z \sim a^\dagger_{+\alpha} a_{+\alpha} - a^\dagger_{-\alpha} a_{-\alpha}$. We exploit this symmetry by expanding the in-plane envelope function components as $\mid \lambda m_\alpha M_j s >= \sum_n A_{n m_\alpha M_j s} \mid n m_\alpha M_j s >$. For given m_αΓM_jΓand sΓV_H couples states with different n. The off-diagonal matrix elements couple states for which $m_e = m_{hh} \pm 1$: $< n_e, m_e, \pm\frac{1}{2} \mid \hat{k}_\pm \mid n_h, m_h, \pm\frac{3}{2} > \sim \delta_{m_e, m_{hh} \pm 1}$. This leads to anti-crossings in the dot level spectrum.

The Hartree potentialΓ$V_H(\rho)$Γis given from the solution of Poisson's equation for the coupled dot density:

$$n(\rho, z) = -e \sum_\gamma f(\epsilon_\gamma) |\Psi^e_\gamma(\mathbf{r})|^2 + e \sum_\gamma (1 - f(\epsilon_\gamma)) |\Psi^h_\gamma(\mathbf{r})|^2 \tag{2}$$

HereΓfis the Fermi functionΓand $\Psi^{\alpha}_{\gamma}(\mathbf{r})$ is the α^{th} component of the eigenfunction of H_s with quantum numbers $\gamma \rightarrow (\lambda, l, s)$.

FIR Response

We consider an EM wave propagating in the z-direction and polarized in the x-y plane: $V^{ext}(\rho)e^{i\omega t}$. The FIR response is obtained by solving the RPA formula for the induced density [4Γ5]:

$$\delta n(\mathbf{r},\omega) = \int d\mathbf{r}'\chi(\mathbf{r},\mathbf{r}',\omega)[V^{ext}(\rho) + \frac{e^2}{\epsilon}\int d\mathbf{r}''\frac{\delta n(\mathbf{r}'')}{|\mathbf{r}'-\mathbf{r}''|}] \tag{3}$$

where the susceptibility is

$$\chi(\mathbf{r},\mathbf{r}',\omega) = \sum_{\gamma,\gamma'}\frac{f(\epsilon_\gamma)-f(\epsilon'_\gamma)}{\hbar\omega+\epsilon_\gamma-\epsilon'_\gamma+i\Gamma}\Psi^*_\gamma(\mathbf{r})\Psi_{\gamma'}(\mathbf{r})\Psi^*_{\gamma'}(\mathbf{r}')\Psi_\gamma(\mathbf{r}') \tag{4}$$

The axial symmetry is exploited by expanding $V^{ext}\Gamma\chi$ and δn in angular momentum componentsΓl. This leads to a $2D$ integral equation for $\delta n_l(\rho,z,\omega)$ for each l. The induced density is taken to be composed of separated electron and hole densities located at the centers of the respective layers:

$$\delta n_l(\rho,z\omega) = \delta n^e_l(\rho,\omega)\delta(z+a/2) + \delta n^h_l(\rho,\omega)\delta(z-b/2) \tag{5}$$

This reflects the fact that the z confinement is much stronger than the lateral confinement. After integrating over zΓthe resulting 1D integral equation is solved by direct matrix inversion for $l = \pm 1$Γwhich give the two circular polarization directions.

The polarizability is obtained from $\delta n_l(\mathbf{r},\omega)$ as:

$$\alpha_\pm(\omega) = \frac{1}{E^{ext}}\int dr\delta n_l(\mathbf{r})\mathbf{r} \tag{6}$$

and the crossection for photon absorption is:

$$\sigma_\pm(\omega) = 4\pi\frac{\omega}{c}Im[\alpha_\pm(\omega)] \tag{7}$$

Results

We take the lateral confinement such that $\omega_{0e} = 10meV$Γwhich gives $\omega_{0h} = (\frac{m_e}{m_h})^{1/2}\omega_{0e} \simeq 6meV$. Other parameters used in the calculation are: TemperatureΓ$T = 1K$Γbroadeningℾ$\Gamma = 0.4meV$Γstatic dielectric constantΓ$\epsilon = 13.75$ (average of InAs and GaSb).

We consider first the case of a distinct electron-hole system in which the electrons in the InAs layer do not interact with the holes in the GaSb layer. ThusΓthe each carrier species is confined by its respective $2D$ parabolic bare potential. The FIR response calculated for this case is illustrated in Fig. 1a for several values of magnetic field and for the two circular polarizationsΓ$l = \pm 1$. The spectra shown reproduce the values expected from the generalized Kohn's theorem [6]Γin which the absorption peaks follow : $\omega^\alpha_\pm = (\omega^2_{0\alpha} + (\omega_{c\alpha}/2)^2)^{1/2} \pm (\omega_{c\alpha}/2$. This result is independent of the number of electrons and holes. It reflects the fact that for strictly parabolic confinementΓ

the center-of-mass and relative motion are completely decoupled. Long wavelength EM radiation couples only to the center-of-mass motion leading to the simple Kohn resonance spectrum.

The actual InAs-GaSb dot system can be viewed as spatially separated but interacting electrons and holesΓwhich arise through the Coulomb interaction between charges and from the $\mathbf{k} \cdot \mathbf{p}$ mixing. Both of these interactions introduce coupling between the center-of mass and relative motion thereby breaking Kohn's theorem and leading to a much more complex spectrumΓas illustrated in fig. 1b. For each value of magnetic field and polarizationΓthe spectra shown consist of many peaksΓeach associated with single particle inter-level transitions. Within the mean field approach used hereΓthe collective nature of this many particle system manifests itself through small depolarization shifts of the absorption peaks from respective inter-level spacings.

Another interesting aspect of this system is that with increasing magnetic fieldΓlevels from the InAs conduction band and GaSb valence band move in opposite directions causing electron charge to shift back to the GaSb layer. At high fieldΓ$B > 10T$ (not shown here)Γeach layer becomes intrinsicΓand the FIR absorption intensity drops to zero.

References

[1] M. AltarelliΓPhys. Rev. B 28Γ842 (1983).

[2] M. J. YangΓC. H. YangΓB. R. BennettΓand B. V. ShanabrookΓPhys. Rev. Lett. 78Γ4613 (1997).

[3] Y. Naveh and B. LaikhtmanΓAppl. Phys. Lett. 66Γ1980 (1995).

[4] D. A. BroidoΓK. KempaΓand P. BakshiΓPhys. Rev. B 42Γ11400 (1990).

[5] T. DarnhoferΓU. RösslerΓand D. A. BroidoΓPhys. Rev. B 53Γ13631 (1996).

[6] P. A. Maksym and T. ChakrabortyΓPhys. Rev. Lett. 65Γ108 (199).

Figure Captions

Figure 1a. FIR spectrum .vs. frequency for the electron-hole system without interlayer Coulomb and $\mathbf{k}\cdot\mathbf{p}$ coupling. described in the text. The solid (dashed) lines for each value of magnetic field are for the $l=+1$ ($l=-1$) circular polarizations.

Figure 1b. FIR spectrum .vs. frequency for the actual electron-hole system including the $\mathbf{k}\cdot\mathbf{p}$ and interlayer coulomb couplings. The solid (dashed) lines for each value of magnetic field are for the $l=+1$ ($l=-1$) circular polarizations.

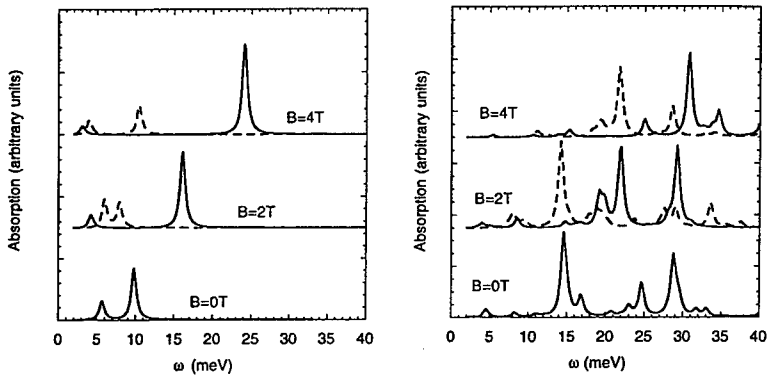

PC.32

SPIN-DEPHASING PROCESSES IN SEMICONDUCTOR QUANTUM DOTS

A.V.Khaetskii, Yu.V. Nazarov

Faculty of Applied Sciences and DIMES, Delft University of Technology,
Lorentzweg 1, 2628 CJ Delft, The Netherlands

Abstract

We have studied the physical processes responsible for the spin -flip in GaAs quantum dots. We have calculated the rates for different mechanisms which are related to spin-orbit coupling and cause a spin-flip during the inelastic relaxation of the electron both with and without a magnetic field. It is generally observed that the corresponding spin-flip rates are by several orders of magnitude lower than those for the spin-flip processes for free 2D electrons (i.e. in the case when there is no confinement in the plane). We have shown that it is due to the zero-dimensional character of the problem (electron wave functions are localized in all directions) which leads to freezing out of the most effective spin-flip mechanisms related to the absence of the inversion centers in the elementary crystal cell and on the heterointerface.

PACS codes: 73.23.Hk; 73.40.Gk; Keywords: spin relaxation; quantum dots; phonons.

As it is known, quantum dots (QD) are considered as possible candidates for building a quantum computer. In this respect, there is a great demand in a theoretical estimation of the typical dephasing (especially spin dephasing) time of the electron in the QD.

We have calculated the rates for different spin-orbit related mechanisms which cause a spin-flip during the inelastic relaxation of the electron in the dot both with and without a magnetic field. The corresponding spin-flip rates are by several orders of magnitude lower than for any (elastic and inelastic) spin-flip processes for free 2D electrons. In the latter case the absence of an inversion centre either in the elementary crystal cell or on the heterointerface [1,2] brings about terms in the Hamiltonian [1] which are linear in the two-dimensional electron momentum and proportional to the first power of the small parameter $\Delta/E_g \ll 1$, where Δ is the spin-orbit splitting of the valence band and E_g is the energy gap. This leads to the quadratic dependence of the spin-flip rate on this parameter in the 2D case [1]. In this paper we show that in the case of the quantum dot the zero-dimensional character of the problem (the localized electron wave functions) leads to the drastic suppression of the spin-flip rate. Linear in spin-orbit parameter Δ terms in the matrix elements are absent in true two-dimensional case and the spin-flip rate is proportional to the power of the parameter Δ which is higher than the second one. The contribution to the spin-flip rate which is quadratic with respect to Δ exists only if we take into account the small admixture of the electron wave functions of the higher levels of the size quantization in the z-direction.

We start with the effective- mass Hamiltonian which is derived from the Kane model (see [3]) and describes the electron in the conduction band in the presence of an arbitrary confining potential $U(\mathbf{r})$ (both vertical and lateral) and takes into account the spin-orbit interaction:

$$\hat{\mathcal{H}} = \hat{\mathcal{H}}_0 + \hat{\mathcal{H}}_1; \hat{\mathcal{H}}_0 = \frac{\hat{\mathbf{p}}^2}{2m} + U(\mathbf{r}); \hat{\mathcal{H}}_1 = i\frac{\Delta}{3}\hat{\sigma}_\gamma \epsilon_{\gamma\mu\mu'}\{-\frac{\hbar^2}{mE_g^2}(\nabla_\mu U)\nabla_{\mu'}$$
$$+\frac{\hbar^3}{\sqrt{2mE_g}m_{cv}E_g}\cdot[\delta_{\mu,\alpha\beta}\nabla_{\mu'}\nabla_\alpha\nabla_\beta - \delta_{\mu',\alpha\beta}\nabla_\mu\nabla_\alpha\nabla_\beta]\} + \frac{1}{2}V_0\boldsymbol{\sigma}\cdot\boldsymbol{\varphi} \qquad (1)$$

Here $\hat{\mathbf{p}} = -i\hbar\nabla$ is the electron momentum operator, m the effective mass, $\hat{\sigma}$ the Pauli matrices, m_{cv} the parameter of the Kane model with the dimensionality of mass, $\epsilon_{\gamma\mu\mu'}$ the fully antisymmetric unit tensor, $\delta_{\mu,\alpha\beta}$ the unit symmetric tensor of rank three which in the cubic crystal of class T_d (without an inversion center) has only components in which all the three indices differ from each other and all components are equal; $\gamma, \mu, \mu', \alpha, \beta = x, y, z$ and x, y, z are directed along the main crystallographic axes. The first term in $\hat{\mathcal{H}}_1$ is due to the relativistic interaction with the electric field caused by the confinement. An impurity potential should be also added to U. The second term in $\hat{\mathcal{H}}_1$ is related to the absence of an inversion centre in the elementary cell of the GaAs crystal. In the true 2D case the related spin splitting strongly depends on the orientation of the vector of the normal to the 2D plane with respect to the main crystal axes. We consider only the case when the normal is parallel to the [100] direction (the most frequently used orientation).

The last term in Eq.(1) describes the spin-orbit splitting of the electron spectrum due to the strain produced by the phonon. There $\varphi_x = u_{xy}\hat{p}_y - u_{xz}\hat{p}_z$ and φ_y, φ_z are obtained by cyclic permutations, u_{ij} is the lattice strain tensor, V_0 is the characteristic velocity whose value is well known for GaAs, $V_0 = 8 \times 10^7 cm/s$ [4].

Specifically, we have considered the following mechanisms of the spin-flip.

1). The spin-flip event caused by the spin-orbit relativistic coupling to the electric field produced by the emitted phonon (the last term in Eq.(1)). We investigate only the relaxation of the spin component perpendicular to the 2D plane (s_z component). Then, using the standard expression for the strain tensor due to the acoustic deformation, we get for the matrix element, describing the electron spin-flip transition between spacial states Ψ_1 and Ψ_2 with emission of the phonon:

$$M_{1,\downarrow} = \frac{V_0}{4}\left(\frac{\hbar}{2\rho\omega_Q}\right)^{1/2}[q_x d_y + q_y d_x]\left\langle \Psi_1 \mid \frac{1}{2}\{(\hat{p}_x + i\hat{p}_y), \exp(i\mathbf{Q}\mathbf{r})\}_+ \mid \Psi_2 \right\rangle, \qquad (2)$$

where ρ is the crystal mass density, $\mathbf{d}$ the phonon unit polarization vector, $\mathbf{Q} = (\mathbf{q}, q_z)$ the phonon wave vector, $\{,\}_+$ means anticommutator. We consider transition between the neighbouring discrete energy levels, so that the energy transfer $\epsilon = \hbar s Q \approx \hbar^2/m\lambda^2$, where λ is the dot size in the lateral directions. On the other hand, the perturbation theory used (the one-phonon processes) is only valid if $\epsilon \gg ms^2$, s being the sound velocity. From this we obtain the condition $q_z \gg q \approx 1/\lambda$, i.e. the phonon is emitted almost perpendicular to the 2D plane. We obtain finally for the spin decay rate:

$$\Gamma_{1,\downarrow} = \frac{I}{32}\frac{m^3 V_0^2 \epsilon^2}{\rho s \hbar^4}, \qquad (3)$$

where dimensionless quantity I is of the order of unity. The corresponding relaxation time is very long ($1 \div 10^{-2}$ s) for the typical energy transfer of the order of $1 \div 10$ K.

2). The spin-flip event caused by the spin-orbit admixture of different spin states. This means that in the presence of the spin-orbit term in the Hamiltonian the electron "spin-up" state contains actually a small admixture of the "spin-down" state. The electron transition with phonon emission between two states with "opposite" spins leads to the spin-flip event.

We take into account only the interaction with piezo-phonons which is known to be the most effective in the polar crystal. We obtain for the transition rate with the phonon

emission between two states 1 and 2 (which can have either the same spins or the "opposite" ones):

$$\Gamma_{12} = \frac{2\pi}{\hbar} 2 \frac{\hbar (e h_{14})^2}{2\rho s} \int \frac{d^3Q}{(2\pi)^3} \frac{A_t(Q)}{Q} \mid \int d^2r \exp(iqr) \hat{\Phi}_1^{\dagger}(\mathbf{r}) \hat{\Phi}_2(\mathbf{r}) \mid^2 \delta(\hbar s Q - \epsilon), \qquad (4)$$

where h_{14} is the peizomodulus ($eh_{14} = 1.2 \times 10^7 eV/cm$ for GaAs). Since the phonon is emitted almost perpendicular to the 2D electron plane, the transition rate strongly depends on the orientation of the normal with respect to the main crystal axes. The rate is strongly suppressed when the normal is parallel to the [100] axis and this is taken into account in Eq.(4) by the multiplier $A_t(Q) \approx 2q^2/q_z^2 \ll 1$. The difference in the rates between the [100] and [111] orientations of the heterostructure reaches more than an order of magnitude. Here for reference we give the expression for the transition rate *without* spin-flip which follows from Eq.(4):

$$\Gamma_0 \simeq \frac{(eh_{14})^2 m^2 s}{\rho \hbar^2 \epsilon} \qquad (5)$$

which for the transfer energy of 1K has the value $\approx 5 \times 10^8 s^{-1}$. In the true 2D case for the [100] orientation we have from Eq.(1) :

$$\hat{\mathcal{H}}_1 = \beta(-\hat{\sigma}_x \hat{p}_x + \hat{\sigma}_y \hat{p}_y); \beta = \frac{2}{3} \eta \langle p_z^2 \rangle \frac{1}{(2mE_g)^{1/2} m_{cv}} \qquad (6)$$

Constant β is expressed in terms of the mean value of the $\hat{p}_z^2$ operator in the state described by the wave function $\chi_0(z)$ of the lowest quantized level and takes values $(1 \div 3) \cdot 10^5 cm/s$ ($\eta = \Delta/(E_g + \Delta) \approx 0.2$ for GaAs). In Eq.(6) we have dropped the so-called Rashba term which is believed to be much smaller for GaAs heterostructures (and in any case its presence does not influence our conclusions because it has a similar structure). The presence of term $\hat{\mathcal{H}}_1$ leads to a nonzero value of the spin-flip transition matrix element. At first sight, the scalar product of the spinors $\hat{\Phi}$ corresponding to the initial spin-up and the final spin-down states should be proportional to the first power of β. However, in contrast to the delocalized 2D states, in our case we can remove the terms linear in β from the Hamiltonian making the following spin-dependent unitary transformation:

$$\hat{\Phi} = [1 + \frac{im\beta}{\hbar}(x\hat{\sigma}_x - y\hat{\sigma}_y)]\hat{\Phi}'. \qquad (7)$$

We stress that the boundedness of the electron wave functions is essential for this procedure. Then we obtain the Hamiltonian which besides the terms with a unit spin matrix contains only the following spin-dependent term: $(m\beta^2/\hbar)\hat{L}_z\hat{\sigma}_z$, where $\hat{L}_z = -i\hbar\partial/\partial\varphi$ is the angular momentum operator. Therefore, in this approximation the correct spin functions are the eigenfunctions of the $\hat{\sigma}_z$ operator and there are no spin-flip processes. The scalar product of the spinors corresponding to "opposite" spin directions is proportional to the third power of β. The corresponding spin-flip rate $\propto \beta^6$ is very low ($\Gamma^{-1} \simeq 10^{-4} s$ for the energy transfer of the order of 1K). We note, however, that account of these terms may happen to be beyond the applicability of the initial Hamiltonian (1), so the above value should be considered only as an estimation. Contributions to the spin-flip rate proportional to β^2 are either related

to the virtual transitions to the higher quantized energy levels in the z-direction or to the presence of the impurity potential which leads to the nonseparability of the transverse (z) and longitudinal variables in the Hamiltonian (1). However, it can be easily checked that both effects give actually the small contributions to the spin-flip rate. For example, in the first case we get the rate $\Gamma \simeq \Gamma_0(m\beta^2\epsilon/E_z^2)$,E_z is the distance between the quantized levels in the z-direction. For the second case we get $\Gamma \simeq \Gamma_0(m\beta^2/\hbar\omega)(z_0/r_c)^4$, where z_0 is the thickness of the 2D layer in the z-direction, r_c is the correlation radius of the donor potential and ω is the confining frequency for a paraboloc dot. This rate can reach the value of $10^5 s^{-1}$ at the most. Finally, in the presence of magnetic field B directed along the z-axis there is also a contribution to the spin-flip rate proportional to β^2. It reads: $\Gamma \simeq \Gamma_0(m\beta^2/\hbar\omega)(g\mu_B B/\hbar\omega)^2$ and is also low.

Thus, for the energy transfer value of the order of 1K the spin-flip time related to the admixture mechanism cannot be shorter than $10^{-5}s$.

3). In the presence of magnetic field $\mathbf{B}$ parallel to the z-axis the Zeeman term should be added to the Hamiltonian (1): $\hat{\mathcal{H}}_z = (g/2)\mu_B\hat{\sigma}_z B$, where μ_B is the Bohr magneton. In the GaAs crystal the electron g-factor differs strongly from the free electron value $g_0 = 2$ which is due to the spin-orbit interaction [5]. We found that it leads to a new mechanism of spin-flip in GaAs in the presence of an external magnetic field. Namely, the strain produced by the emitted phonon is coupled directly to the electron spin through the variation of the effective g-factor: $\simeq g\mu_B u_{iz}\hat{\sigma}_i B_z$.

To describe this effect we need to extend the calculations presented in [5] for the case of the presence of the deformation. As a result, we obtain:

$$\Gamma_{\uparrow,\downarrow} \simeq \left(\frac{\eta}{(1-\eta/3)}\right)^2 \left(\frac{m_0\mu_B B}{mE_g}\right)^2 \frac{md^2\epsilon^2}{\rho s^3\hbar^4}, \tag{8}$$

where m_0 is the bare electron mass and d one of three deformation constants which describe the interaction of holes with phonons [3] (it is of the order of several eV). The rate given by Eq.(8) has the same order of magnitude as that given by Eq.(3) and is very low.

The results described above are concerned with inelastic transitions between the neighbouring quantized energy levels in the dot. In the case of the spin-flip processes between the Zeeman sublevels of the same orbital level the correct treatment of the problem is more complicated. This is due to the fact that the Zeeman splitting is small and comparable to ms^2 , s is the sound velocity. To treat this polaron state we need the non-perturbative methods which describe the spin-dependent interaction with the bosonic environment. On the other hand, we do not expect high spin-flip rate for small energy transfer because of the adiabaticity of the electron interaction with the phonons under these conditions.

Acknowledgements. This work is part of the research program of the "Stichting voor Fundamenteel Onderzoek der Materie (FOM)". We are thankful to L. Kouwenhoven, T.H. Oosterkamp and G.E.W. Bauer for useful discussions.

1. M.I. D'yakonov, V.Yu.Kachorovskii, Sov.Phys.Semicond.,**20**, 110 (1986).
2. Yu.A.Bychkov, E.I.Rashba, JETP Lett.,**39**, 78 (1984).
3. G.E. Pikus, A.N. Titkov, in *Optical Orientation*, North-Holland, Amsterdam, p.73 (1984).
4. M.I. D'yakonov et al., Zh.Eksp.Teor.Fiz. **90**, 1123 (1986)[Sov.Phys.JETP **63**, 655 (1986)].
5. C. Kittel, Quantum Theory of Solids, J.Wiley and Sons, Inc., New York, London, CH. 14 (1967).

PC.33

Broken Symmetries in the Reconstruction of $\nu = 1$ Quantum Hall Edges

S.M. Reimann, M. Koskinen, S. Viefers(*), M. Manninen and B. Mottelson(*)

University of Jyväskylä, PO Box 35, FIN-40351 Jyväskylä
(*) NORDITA, Blegdamsvej 17, DK-2100 Copenhagen

Abstract

Spin-polarized reconstruction of the $\nu = 1$ quantum Hall edge is accompanied by a spatial modulation of the charge density along the edge. We find that this is also the case for *finite* quantum Hall droplets: current spin density functional calculations show that the so-called Chamon-Wen edge forms a ring of apparently localized electrons around the maximum density droplet (MDD). The boundaries of these different phases qualitatively agree with recent experiments. For very soft confinement, Chern-Simons Ginzburg-Landau theory indicates formation of a non-translational invariant edge with vortices (holes) trapped in the edge region.

PACS 73.20.Dx, 73.61.-r, 85.30.Vw, 73.40.Hm

Introduction

Edge states in the quantum Hall regime have been subject to extensive study in recent years. In particular, much interest has focused on how the edge may reconstruct as the confining potential strength is varied (see [1] and Refs. therein). Various theoretical approaches, including Hartree-Fock methods, density functional theory, composite fermion models and effective (mean field) theories have been used to examine both small electron droplets (quantum dots) and large quantum Hall systems, with and without spin. In particular, many authors have been interested in edge reconstruction of ferromagnetic quantum Hall states, including $\nu = 1$ and simple fractional (Laughlin) fillings. Softening of the confining edge potential allows charge to move outward, and the edge may reconstruct. How this happens, and whether or not the reconstruction involves spin textures, depends on the relative strength of the electron-electron interactions and the Zeeman energy, and on the steepness of the confining potential. Much work has been based on Hartee-Fock techniques. In 1994, Chamon and Wen found that the sharp $\nu = 1$ edge of large systems or quantum dots may undergo a polarized reconstruction to a "stripe phase" [2], in which a lump of electrons becomes separated at a distance $\sim 2l_B$ away from the original edge ($l_B = \sqrt{\hbar/eB}$). This reconstructed state is translation invariant along the edge. Using an effective sigma model and Hartree-Fock techniques Karlhede *et al.* [3] then showed that Chamon and Wen's polarized reconstruction may be preempted by edge spin textures if the Zeeman gap is sufficiently small. These textures are configurations of the spin field in which the spins tilt away from their bulk direction on going across the edge; on going *along* the edge, they precess about the direction of the external field with some wave vector k. The edge textures posess a topological density which can be shown to be proportional to the electron density. Thus, one may say that tilting spins moves charge, which is why edge spin textures represent a mechanism for edge reconstruction. Later it turned out [1,4], that the Chamon-Wen edge

is, in fact, unstable: a polarized reconstruction with a *modulated charge density* along the edge is always lower in energy than the translation invariant Chamon-Wen edge. Numerical (Hartree-Fock) studies of the ground state, together with an analysis of the softening of low-energy edge modes at weak confining potentials, have resulted in a phase diagram [1,4], giving the following picture of the $\nu = 1$ edge: For very steep confining potentials, the edge is sharp and fully polarized. Upon softening of the confining potential, the edge will *either* reconstruct into a spin textured state with a translation invariant charge density along the edge (for small Zeeman gaps) *or* into a polarized charge density wave edge (for large Zeeman gaps). For even softer confining potentials and sufficiently small Zeeman gaps a combination of charge modulation along the edge and spin textures may occur.

Broken-symmetry edge states in quantum dots

The above mentioned phases of edge reconstruction can also occur in *finite* quantum Hall systems such as quantum dots. The spin-textured edge exists only for sufficiently smooth confinement and small enough Zeeman coupling. We restrict the following discussion to the spin-polarized regime. In a strong enough magnetic field, the electrons fill the lowest Landau level: the so-called maximum density droplet (MDD) [5] is formed, in which the electrons occupy adjacent orbitals with consecutive angular momentum. The MDD is the finite-size analogue to the bulk $\nu = 1$ quantum Hall state with an approximately constant density at its maximum value $(2\pi l_B^2)^{-1}$. Increasing the magnetic field effectively compresses the electron droplet. At a certain field strength, the dense arrangement of electrons costs too much Coulomb energy. The droplet then takes advantage of moving electrons from lower to higher angular momentum states and re-distributes its density [2]. This, however, occurs together with a breaking of the rotational symmetry in the internal coordinates of the many-body wave function [6]. It is an advantageous feature of the mean-field approach that the solution can show this *intrinsic* symmetry breaking. The latter implies the occurence of a rotational band which can be obtained by projection.

For filling factors around $\nu = 1$ we apply current spin density functional theory (CSDFT) [7] to calculate the ground-state densities of N parabolically confined electrons, avoiding any spatial symmetry restrictions of the solutions. For the technical details of the calculations, we refer to [6].

An example for the edge reconstruction in finite quantum Hall droplets is shown in the left of Fig. 1 (see next page) for $N = 42$ electrons. In the ground state the MDD is stable up to a field of about 2.6 T. At about 2.7 T, reconstruction has taken place: at a distance of $\sim 2l_B$ from the remaining inner (smaller) MDD, a ring of separate lumps of charge density is formed, with each lump containing one electron and having a radius somewhat larger than the magnetic length l_B. Goldmann and Renn [8] recently suggested crystallized edge states which appear similar to the reconstructed edges within CSDFT. For still higher fields, the sequential formation of ring-like edges continues until the whole droplet is fully reconstructed [6,9]. The apparent localization at the edge is accompanied by a narrowing of the corresponding band of single-particle energy levels. The existence of the inner MDD surrounded by the broken-symmetry edge opens up the possibility to observe rotational spectra of the edge.

We next study the formation of the MDD and its reconstruction systematically, vary-

ing both particle number N and magnetic field B. For fixed N we keep the average electron density constant. Changing the field B has a similar effect on the reconstruction as varying the softness of the external confinement: a higher field compresses the droplet. At constant strength of the oscillator for fixed particle number, but larger field the confinement then is effectively weaker. We obtain a phase diagram as a function of the number N of confined electrons and the field B, which is schematically shown in Fig. 1. (For more details see [6]). With increasing N, the polarization line which separates the fully polarized MDD states from the unpolarized states approaches the reconstruction line. The latter separates the MDD regime from the Chamon-Wen (CW) edge formation. This is schematically indicated by the dashed lines in Fig. 1. Note that the shapes of these phase boundaries differ from the results of Ferconi and Vignale [10], as they used a fixed confinement strength for different dot sizes. In recent experiments [11] a phase diagram was obtained from addition energy spectra measured as a function of magnetic field. The phase boundaries qualitatively agree with the results obtained from the CSDFT calculations, if the average electron density is kept constant. Its value determines the magnetic field strength at which the phase transitions occur: Increasing the density shifts the phase boundaries to higher B-values.

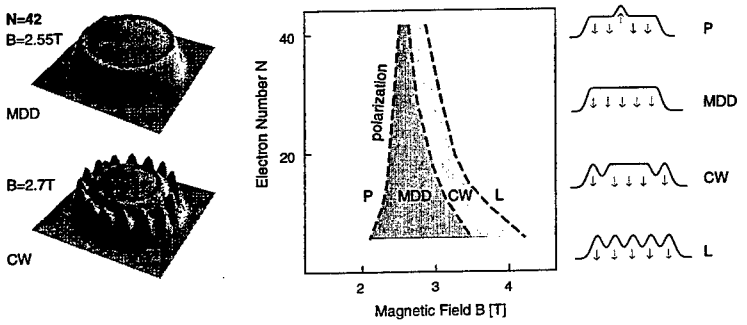

Figure 1: *Left:* Charge density of a spin-polarized MDD before ($B = 2.55$ T) and after ($B = 2.7$ T) edge reconstruction. *Right:* Phase diagram of parabolic quantum dots at a density roughly corresponding to a value $1/(\pi r_s^2)$, where $r_s = 2a_B^*$ and a_B^* is the effective Bohr radius. The schematic density profiles on the right indicate the different phases of polarization (P), formation of the maximum density droplet (MDD), edge reconstruction (CW) and localization (L)

Edge reconstruction within CSGL theory

As an alternative to the above approaches, when turning to filling fractions $\nu \leq 1$, one may study the quantum Hall edge within the framework of Chern-Simons Ginzburg-Landau (CSGL) theory [12]. This is an effective (mean field) model of the FQHE, based on the concept of "statistical transmutation": It models the electrons at $\nu = 1/(2m+1)$ as *bosons*, each carrying $2m+1$ quanta of ("statistical") flux; in the mean field sense, this statistical field is cancelled by the external magnetic field, making the $\nu = 1/(2m+1)$

quantum Hall state equivalent to a system of charged bosons in *zero* magnetic field. This model has proven quite successful in describing bulk properties of the FQHE. The edge can be studied by solving the CSGL field equations in the presence of an external confining potential. Leinaas and Viefers [13] recently showed the existence of edge spin textures in this model for soft enough confining potentials and Zeeman energies smaller than some critical value, in qualitative agreement with the other approaches. Fig. 2 shows such a solution in the limit where the minority spin density is small. As mentioned, the charge density of the spin textured edge is translation invariant along the edge. The CSGL studies [12] further indicate the possibility of another kind of edge reconstruction, at even softer confining potentials, to a non-translation invariant edge with vortices (holes) trapped in the edge region. Several authors have adressed this type of reconstruction (see [4] and references therein).

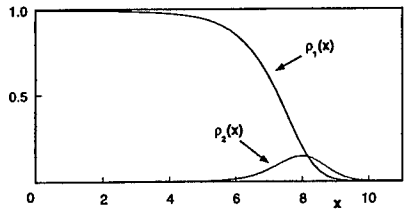

Figure 2: Spin textured edge in CSGL theory: Majority- (ρ_1) and minority (ρ_2) spin density profiles close to the critical Zeeman gap for a harmonic confining potential of the form $V(x) = 0.05\ \theta(x-5)\cdot(x-5)^2$ (with x in units of the magnetic length l_B). The spin unit vector $\hat{n}$ is given by $n_x + in_y = \sqrt{1-n_z(x)^2}\ e^{iky}$ and $n_z(x) = (\rho_1(x) - \rho_2(x))/(\rho_1(x) + \rho_2(x))$. The critical Zeeman gap is approximately $0.06\ \hbar\omega_c$, and the wave vector of spin precession along the edge is $k = 1.0\ l_B^{-1}$. ρ_1 is normalized by its constant bulk value

References

[1] A. Karlhede and K. Lejnell, Physica E **1**, 41 (1997)
[2] C. de C. Chamon and X.G. Wen, Phys. Rev. B**49**, 8227 (1994).
[3] A. Karlhede *et al.*, Phys. Rev. Lett. **77**, 2061 (1996).
[4] M. Franco and L. Brey, Phys. Rev. B**56** 10383 (1997).
[5] A. H. McDonald, S.R.E. Yang, M. D. Johnson, Aust. J. Phys. **46**, 345 (1993).
[6] S.M. Reimann, M. Koskinen, M. Manninen and B. Mottelson, cond-mat/9904067.
[7] G. Vignale and M. Rasolt, Phys. Rev. B**37**, 10685 (1988).
[8] E. Goldmann and S. Renn, to be published
[9] H.-M. Müller and S.E. Koonin, Phys. Rev. B**54**, 14532 (1996).
[10] M. Ferconi and G. Vignale, Phys. Rev. B**56**, 12108 (1997).
[11] T. H. Oosterkamp *et al.*, Phys. Rev. Lett. **82**, 2931 (1999).
[12] S.C. Zhang *et al.*, Phys. Rev. Lett. **62**, 82 (1988); D.H. Lee and C.L. Kane, Phys. Rev. Lett. **64**, 1313 (1990).
[13] J.M. Leinaas and S. Viefers, Nucl. Phys. B**520**, 675 (1998).

PC.34

Accidental degeneracies and fractal structure in the spectrum of quantum dots

B.L.Johnson[1] and G.Kirczenow[2]
1 Dept. of Physics, Western Washington University, Bellingham, WA 98225
2 Dept. of Physics, Simon Fraser University, Burnaby, British Columbia, V5A 1S6

We show that the appearance of 'accidental' degeneracies in the single-particle spectrum of quantum dots in a magnetic field can be understood by analyzing the evolution of the structure of the classical orbits of the system as a function of magnetic field. We demonstrate that these degeneracies are associated with closed orbits, which occur at particular magic ratios of the cyclotron energy to the confinement energy. The spectrum of degenerate energies forms an interesting fractal structure with an associated complete 'devil's staircase.' The degeneracies are not lifted by deviations from parabolicity of the radial confinement potential of the dot and the devil's staircase structure that we predict should be detectable experimentally using available techniques.

The study of quantum dots--quasi-zero dimensional structures created by lateral confinement of two-dimensional electron systems--has yielded many important insights into the physics of mesoscopic phenomena in semiconductor nanostructures[1-4]. Quantum dots can be viewed as 'artificial atoms' whose level structure is controlled by fabrication parameters and applied external fields. Their level structure has been studied primarily via direct conductance experiments analogous to electron affinity measurements on atomic systems, i.e. the energy required to add an electron to the system[1]. Of particular interest is the behavior of the level structure under a transverse external magnetic field. Many interesting features of this problem have been seen experimentally[1-2] and proposed theoretically[3-4]. The level structure has been studied theoretically utilizing models based on a two-dimensional system confined laterally by a parabolic potential.

The (single-particle) parabolic model that applies to quantum dots under a transverse magnetic field was first studied by Fock[5] and by Darwin[6]. One of the main features of the model is the existence of a large number of 'accidental' degeneracies in the quantum-mechanical spectrum as a function of applied magnetic field. Direct evidence of some of these degeneracies has been observed experimentally. [1] In this paper, we suggest an explanation for the occurrence of these degeneracies, based upon a surprising general principle. We also show that the degeneracies form an interesting fractal structure--the locus of degenerate points as a function of magnetic field at constant electron number form a sequence of 'Devil's staircases.' These sequences of ever-narrowing steps should be observable using current experimental techniques; indeed a few steps of the staircase have already been observed[1].

Our explanation of the degeneracies is as follows: There exist classical paths--solutions to the classical equations of motion for a 2D charged particle moving under a transverse magnetic field with parabolic confinement--which are closed. The closed classical paths only occur for specific 'magic' ratios of the cyclotron energy to the confinement energy. Furthermore, these closed classical paths exhibit lower symmetry than the Hamiltonian for the system; i.e. the closed classical paths are invariant only under specific rotations, while the Hamiltonian has full rotational symmetry. The consequences for the quantum system are these: Nondegenerate single-particle eigenstates have the same rotational symmetry as the Hamiltonian. Therefore, if the quantum-mechanical distribution function ($|\psi|^2$) is to have the same (lower) rotational symmetry as the closed classical orbits (at the magic ratios of cyclotron energy to confinement energy), the system must be degenerate to allow for a superposition of single particle states with the proper symmetry. We will demonstrate this principle by explicit calculation.

We begin with a review of the quantum mechanical model of a 2D charged particle in a quantum dot under a magnetic field. The Hamiltonian for this system is

$$H = (\mathbf{p} - Q\mathbf{A})^2 / 2m + m\omega_o^2 r^2 / 2 \qquad (1)$$

where Q is the particle charge, **A** is the vector potential, and ω_o is the confinement frequency. In the symmetric gauge the single particle eigenstates are given (apart from a normalization constant) by

$$\psi = r^{|l|} \exp(-il\theta) L_n^{|l|}(r^2/2\alpha^2) \exp(-r^2/4\alpha^2) \quad (2)$$

where $\alpha^2 = (\hbar/m)(\omega_c^2 + 4\omega_o^2)^{-1/2}$, n is a positive integer, and l is an integer (positive or negative), $L_n^{|l|}$ is a Laguerre polynomial, and $\omega_c = QB/m$ is the cyclotron frequency. Note that the function $|\psi|^2$ is

independent of θ, and that consequently the distribution function is symmetric under all rotations. The eigenvalues corresponding to (2) are

$$E_{nl} = (2n+1+|l|)\hbar\sqrt{\omega_c^2/4+\omega_o^2} - l\hbar\omega_c/2 \quad (3)$$

This is the spectrum of allowed energies for the quantum dot system; a more useful form (for our purposes) is given by a dimensionless version

$$\frac{E_{nl}}{\hbar\omega_o} = (2n+1+|l|)\sqrt{\frac{\omega_c^2}{4\omega_o^2}+1} - \frac{l}{2}\frac{\omega_c}{\omega_o} \quad (4)$$

The ratio ω_c/ω_o will be crucial to our argument. In order to see this, we now turn to the classical model corresponding to the Hamiltonian (1) above.

For clarity and convenience, we write the Hamiltonian in the form

$$H = (\mathbf{p}-Q\mathbf{A})^2/2m + m\omega_o^2((x+\rho)^2+y^2)/2 \quad (5)$$

where we have offset the potential minimum from the origin by a distance ρ. If we assume that the particle is initially at the origin and projected at velocity v_o along the y-axis, the solutions for closed classical orbits are

$$\begin{aligned} x(t) &= a\cos(\omega t) + b\cos(\eta\omega t) - \rho \\ y(t) &= a\sin(\omega t) - b\sin(\eta\omega t) \end{aligned} \quad (6)$$

where η=p/q is a rational fraction (p,q are integers with $p \geq q$), $\omega = \{\sqrt{\omega_c^2+4\omega_o^2} - \omega_c\}/2$, $a = (v_o + \omega\eta\rho)/(\omega(\eta+1))$, and $b = (\omega\rho - v_o)/(\omega(\eta+1))$. The crucial result here is that the closed-orbit criterion forces η to be rational, and this in turn provides a constraint on the ratio of cyclotron energy to confinement energy:

$$\frac{\omega_c}{\omega_o} = (p/q-1)\sqrt{q/p} \quad (7)$$

Whenever the external field on the quantum dot satisfies such a ratio (for fixed confinement energy), the classical orbits will be of the form (6) and the quantum system must exhibit degeneracies to account for the angular symmetries of (6).

In Fig. 1, we show the allowed energies given by (4) as a function of the ratio ω_c/ω_o. The degenerate points are emphasized by open dots to accentuate the fact that the degeneracies lie on vertical lines. At the top of the plot, a few ratios of ω_c/ω_o which satisfy (7) are shown. The lines of degeneracies fall at the ratios given by (7) and at higher energies form a fractal structure.

We will return to a discussion of the pattern of degenerate points in figure 1, but first we shall make the connection between the classical and quantum

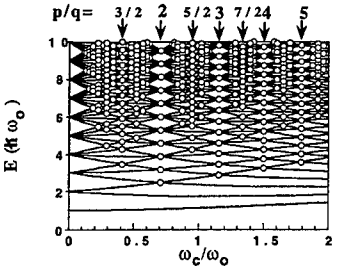

Figure 1. The energy levels of the model Hamiltonian as a function of the ratio of cyclotron energy to confinement energy. The open circles mark the level crossings.

dynamics clear. We shall accomplish this via two illustrations: a path integral calculation and explicit examples of the classical paths/quantum distribution function for a particular degenerate energy.

The connection between the classical and quantum dynamics is most clearly provided by a path-integral picture. For the case at hand, the exact propagator connecting positions $\mathbf{x}_1$ and $\mathbf{x}_2$ in time t is given by $U(\mathbf{x}_1,\mathbf{x}_2,t) = F(t)\exp\{iS_{Cl}/\hbar\}$, where $F(t)$ is a function of the transit time, and S_{Cl} is the classical action connecting the two spacetime points. From this, we can explicitly calculate the phase accumulated by a particle completing a closed orbit and examine the constraints implied by a semi-classical quantization of the closed orbits. Writing the Lagrangian for the system in the convenient form $L = 2T - E + Q(\mathbf{v}\cdot\mathbf{A})$, with E the total energy of the closed orbit, we have the classical action

$$S_{Cl} = \oint m\mathbf{v}\cdot d\mathbf{l} + Q\oint \mathbf{A}\cdot d\mathbf{l} - Et_c \quad (8)$$

where t_c is the orbit time. Inserting this into the propagator then gives two contributions to the phase accumulated for a closed orbit: the ordinary dynamical phase $-iEt_c/\hbar$ associated with a stationary state at energy E, and the phase associated with the spatial transit of the orbit at fixed time. Using the solutions (6) above, we calculate this phase exactly for closed classical orbits:

$$\oint (m\mathbf{v} + Q\mathbf{A}) \cdot d\mathbf{l} = \sqrt{pq}E/\omega_o \qquad (9)$$

In addition, we use the semiclassical quantization conditions prescribed for closed orbits, and find

$$\sqrt{pq}E/\omega_o = \begin{Bmatrix} (k+1/2)2\pi\hbar \\ k2\pi\hbar \end{Bmatrix} \qquad (10)$$

where k is an integer and the upper (lower) condition applies to $p+q$ odd (even). The parity is a result of the number of reflection/turning points of the classical trajectory. We may now use equation (4) above to substitute for E/ω_o in (10), and then using equation (7) we find constraints between the quantum numbers k,n, and l as well as the parameters p and q for closed orbits:

$$k = (p+q)(n+\frac{1}{2}+\frac{|l|}{2}) - (p-q)\frac{l}{2} - \frac{1}{2}$$
$$k = (p+q)(n+\frac{1}{2}+\frac{|l|}{2}) - (p-q)\frac{l}{2} \qquad (11)$$

where, again, the upper (lower) case corresponds to $p+q$ odd (even). The energies, including the degeneracies, are thus accounted for. For a given choice of p and q, the energies are given by $E = (k+1/2)/\sqrt{pq}$ for $p+q$ even and by $E = k/\sqrt{pq}$ for $p+q$ odd. The various energies are then given by integer k, and in turn the degeneracies are given by the number of combinations of n and l which satisfy the relations (11) above. As an example, consider the most prominent fraction in Fig. 1: $p = 2, q = 1$. In this case, $k = 3n+3/2(|l|+1)-1/2(l+1)$, with the corresponding restriction that k be an integer. We find that the allowed energies as well as the degeneracies are accounted for: The ground state energy (again, in units of the confinement energy) is given by $E = 1.061$, for $n = l = 0$ and $k = 1$. The first degenerate level occurs at $E = 2.475$, which has $k = 3$. There are two combinations which give $k = 3$, i.e. $n = 0, l = 2$ and $n = 0, l = -1$. In this way, all of the energies, including degenerate levels, are found. Furthermore, the quantum numbers n and l for the degenerate levels are determined, and the proper superpositions of single particle states are generated.

We now examine specific examples of classical trajectories and quantum distribution functions in order to illustrate the results above. An illustration of some of the allowed paths is given in Fig. 2. In (a) we show the simplest and clearest case, i.e., for the lowest-energy degeneracy in Fig. 1. Here $p = 2$ and $q=1$, with $E = 2.475$, as mentioned above. There is an infinite set of classical paths corresponding this fixed energy, all with different initial conditions. The classes of paths range from the hypocycloid (starting the particle from rest at a distance ρ from the potential center), to starting the particle from the potential center with a kinetic energy equal to E. We depict two paths, the hypocycloid (dashed line) and a path with a relatively large initial kinetic energy. Note the three-fold rotational symmetry exhibited

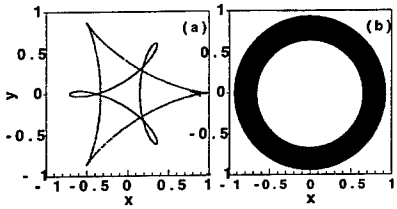

Fig. 2. (a) two classical paths for $p = 2$, $q = 1$. The dashed curve is for zero initial velocity, while the solid curve is for non-zero initial velocity. (b) A path for an irrational p/q.

by the closed paths. This is the lower symmetry alluded to above--the symmetry not contained in the Hamiltonian or the single-particle eigenstates (2). By contrast, Fig. 2 (b) shows a result for irrational p/q; here the classical paths are not closed and the path fills space. The result is full rotational symmetry in the plane, and thus no degeneracy in the quantum spectrum. To connect the classical picture to the quantum picture, we note that semi-classically the quantum distribution should reproduce the features of the classical paths--Since

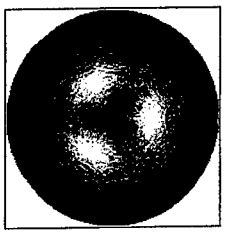

Fig 3. Quantum distribution function $|\psi|^2$ for equal superposition of states at $p = 2$, $q = 1$. Light areas represent high probability.

the semi-classical wavefunction varies inversely with the classical velocity, we expect the quantum distribution to be peaked in those regions where the

particle moves more slowly. In Fig. 3, we show the quantum distribution corresponding to the lowest degeneracy, $p = 2$, $q = 1$, with an equal superposition of the two states given by (2) with the appropriate values of n,l. Note the three-fold rotational symmetry exhibited by the distribution--compare Fig. 2 (a).

We now turn our attention again to the fractal nature of the degenerate points in the spectrum of E vs. ω_c.

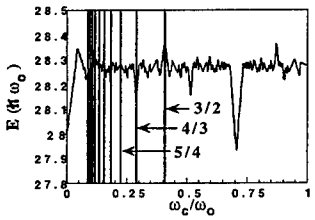

Fig. 4. Highest occupied level in a dot with 800 electrons. The vertical lines mark a series of steps of the Devil's staircase.

The 'devil's staircase' structure mentioned above is predicted to be evident experimentally. To illustrate, we show a trace of the energy of the highest occupied level of the dot vs. the ratio ω_c/ω_o in Fig. 4. The trace represents the highest occupied level in a dot with N = 800 particles. The vertical lines mark the values of ω_c/ω_o corresponding to the sequence p/q = 3/2, 4/3, 5/4, etc. The vertical lines guide the eye. Note that these lines intercept the line of constant particle number at a sequence of discontinuities of its derivative associated with degenerate states. This pattern is a portion of the Devil's staircase which is a result of the underlying structure of degenerate states. Part of this sequence was seen by Tarucha, *et al* [1]

The principle introduced here that the closed classical orbits force the existence of degeneracies in the quantum spectrum is general. The degenracies are robust against changes in the potential function $V(r)$. Since the degeneracies occur for states with different l, and since perturbations in the potential of the form βr^s do not mix states of different l, perturbations of this form cannot lift the degeneracies of Fig. 1. We have performed numerical calculations[7] to confirm this with a quartic correction to the potential: $V' = \beta r^4$. The calculation was performed by diagonalizing the perturbation in a basis of states (2), to obtain the the modified energy spectrum. The results are shown in Fig. 5. The degeneracies are not lifted, but they no longer lie along lines of constant cyclotron energy.

In summary, we have studied the single-particle spectrum of quantum dots in a magnetic field, with an emphasis on the structure of the level crossings in the spectrum. We have shown that these degeneracies occur at specific values of the ratio of cyclotron energy to confinement energy; specifically, at those values where the corresponding classical orbits are closed. The closed classical orbits have a lower rotational symmetry than the Hamiltonian (and the corresponding eigenstates (2)), and in order to account for the lower symmetry, degeneracy must occur, so that the rotational symmetry implied by the classical orbits can be accounted for quantum mechanically.

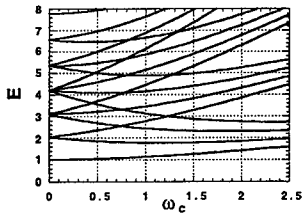

Fig. 5. The lowest energy levels for the quantum dot with a quartic perturbation. Note the level crossings--compare Fig. 1.

The structure of the degenerate points is fractal, exhibiting a unique structure whose signature should be readily accessible experimentally. The degeneracies are robust against perturbations in the radial potential function of the dot.

[1]S.Tarucha, D.G.Austing, T.Honda, R.van der Hage and L.P.Kowenhoven, Phys. Rev. Lett. **77**, 3613 (1996)

[2] R.C.Ashoori, H.Stormer, and J.S.Weiner, Phys. Rev. Lett. **71**, 613 (1993)

[3] N.F.Johnson and M.C.Payne, Phys. Rev. Lett. **67**, 1157 (1991)

[4] B.L.Johnson and G.Kirczenow, Phys. Rev. Lett. **69**, 672 (1992)

[5] V.Fock, Z. Phys. **98**, 446 (1928)

[6] C.G.Darwin, Proc. Cambrige Philos. Soc. **27**, 86 (1930)

[7] B.L.Johnson and G.Kirczenow, unpublished

PC.35

Quantum Transport in Atomic Scale Systems

Jeremy Taylor
Centre for the Physics of Materials, McGill University

Investigations of ultrasmall conductors have revealed several interesting quantum transport phenomena. An exciting new development is the study of wires, dots and tunnel junctions at the *atomic* scale where transport anomalies due to quantum phenomena have been observed at room temperature. These developments hold great promise for future device applications and investigations of fundamental physics in nano-scale systems. In the atomic regime, the transport properties are strongly coupled to the atomic scale structure. It is clear that transport in these systems must be derived from a full quantum mechanical treatment which must include the detailed microscopic degrees of freedom. To this end, we have studied, using first principles methods, the transport properties of several atomic scale wires, dots and tunnel junctions formed by coupling atomic clusters to external metallic leads.

Given the atomic structure of the device and leads, the electronic ground state is obtained by solving the self-consistent Kohn-Sham equations for the entire device including the leads and the atomic cluster. The electrostatic potential is obtained by directly solving the Poisson equation using a multi-grid numerical method. The electronic ground state determines a self-consistent effective potential which describes the interaction of an electron with the device. The quantum transport properties are determined by directly solving the 3-D quantum scattering problem for the effective potential. This gives us the DC conductance, the electro-chemical capacitance, and the AC emittance of the device.

We shall present our methods and results for a number of atomic devices including Al, Si, and C atomic systems: quantized conductance of atomic wires, tunneling through a single atom, conductance and capacitance fluctuations derived from thermal motion of the atoms, quantum characteristics of electro-capacitance to atomic "plates", and the effects of finite external bias voltages.

The work to be reported here are selected from collaborations with Prof. Hong Guo and Dr. C.C. Wan of McGill University; Prof. Jian Wang and Mr. Qingrong Zheng of The University of Hong Kong; Dr. J-L Mozos of the Helsinki University of Technology, Finland; and Gianni Taraschi of MIT.

Special Analytical Solutions of the Schrödinger Equation for 2 and 3 Electrons in a Magnetic Field and *ad hoc* Generalziations to N particles

by M. Taut
University of Technology Dresden, Institute Theoretical Physics
01062 Dresden, Germany
email: mtaut@tmps16.mpg.tu-dresden.de

We found that the two–dimensional Schrödinger equation for 2 electrons in an homogeneous magnetic field (perpendicular to the plane) and a parabolic scalar confinement potential (frequency ω_0) has exact analytical solutions [1]. In the strong correlation limit, where the expectation value of the center of mass is small compared with the average distance between the electrons, the 3 electron system can be replaced by 3 decoupled pair problems, which can be solved exactly as the 2 electron problem. These analytical solutions exist only for certain discrete values of the effective frequency $\tilde{\omega} = \sqrt{\omega_o^2 + (\frac{\omega_c}{2})^2}$. The analytically solvable states are always cusp states in the energy versus total orbital angular momentum curve, and they take the components of higher Landau levels into account. Further, these special analytical solutions for 3 particles and the exact solutions for 2 particles can be written in a unified form. This formula, when *ad hoc* generalized to N coordinates, can be discussed as an ansatz for the wave function of the N–particle system. This ansatz fulfills the following demands: it is exact for two particles and the corresponding solvable fields, it is exact for 3 particles in the limit of small $\mathbf{R}$ and for the corresponding solvable fields, it fulfills the Pauli principle and is an eigenfuncton of the total orbital angular momentum. The Laughlin functions are special cases of this ansatz for infinite solvable fields. The rest of the solutions belong to finite solvable fields.

[1] M. Taut, J. Phys. A**27**, 1045 (1994) and A**27**, 4723 (1994).

PC.38

Enhancement of Coulomb interactions in semiconductor nanostructures by dielectric confinement

G. Goldoni[1,2], F. Rossi[1,3], A. Orlandi[1,2], M. Rontani[1,2], F. Manghi[1,2], E. Molinari[1,2]
[1] *Istituto Nazionale per la Fisica della Materia (INFM)*
[2] *Dipartimento di Fisica, Università di Modena, Via Campi 213/A, I-41100 Modena, Italy*
[3] *Dipartimento di Fisica, Politecnico di Torino, C.so Duca degli Abruzzi 24, I-10129 Torino, Italy*
(June 22, 1999)

We present a theoretical analysis of the effect of dielectric confinement on the Coulomb interaction in dielectrically modulated quantum structures. We discuss the implications of the strong enhancement of the electron-hole and electron-electron coupling for two specific examples: (i) GaAs-based quantum wires with remote oxide barriers, where combined quantum and dielectric confinements are predicted to lead to room temperature exciton binding, and (ii) semiconductor quantum dots in colloidal environments, where the many-body ground states and the addition spectra are predicted to be drastically altered by the dielectric environment.

When a semiconductor nanostructure is embedded in a medium with a smaller dielectric constant, the Coulomb interaction between quantum confined states may be enhanced by virtue of the polarization charges which form at the dielectrically mismatched interfaces[1]. While this effect is relatively small and usually neglected in conventional semiconductor heterostructures (e.g., GaAs/AlAs), we will show that, for hybrid semiconductor nanostructures surrounded by an organic or dielectric medium the enhancement can be large and must be taken into account for a realistic description of Coulomb correlated quantum states. Beside being quantitatively important for the interpretation of experimental spectra, these effects provide an additional degree of freedom for tailoring optical and transport properties of quantum structures.

In this paper we examine two prototype examples relevant to the physics of quantum wires (QWIs) and dots (QDs). We first consider properly designed hybrid semiconductor/insulator QWIs based on GaAs, and show that dielectric confinement (DC) may lead to excitonic states with a binding energy exceeding the room temperature thermal energy kT_{room} (a prerequisite for exploiting excitonic states in electro-optical devices) without degrading the optical efficiency typical of conventional GaAs/AlAs nanostructures. Secondly, we show that the dielectric constant of the environment may strongly affect the addition spectra of QDs by modifying the electronic ground state with respect to the case of good dielectric matching.

Our theoretical scheme[2] moves from the following basic considerations. When the dielectric constant $\epsilon(\mathbf{r})$ is spatially modulated, the Coulomb interaction between, say, two electrons sitting at positions $\mathbf{r}$ and $\mathbf{r}'$, is given by $V(\mathbf{r},\mathbf{r}') = e^2 G(\mathbf{r},\mathbf{r}')$, where $G(\mathbf{r},\mathbf{r}')$ is the Green's function of the Poisson operator, i.e.,

$$\nabla_{\mathbf{r}} \cdot \epsilon(\mathbf{r}) \nabla_{\mathbf{r}} G(\mathbf{r},\mathbf{r}') = -\delta(\mathbf{r}-\mathbf{r}'). \tag{1}$$

Therefore, the space dependence of $\epsilon(\mathbf{r})$ modifies $G(\mathbf{r},\mathbf{r}')$ with respect to the homogeneous case, where $\epsilon(\mathbf{r}) = \epsilon_o$ and $G_o(\mathbf{r},\mathbf{r}') = 1/[4\pi\epsilon_o|\mathbf{r}-\mathbf{r}'|]$. This, in turn, modifies the Coulomb

matrix elements between the quantum states of the structure[3,2] which, in the basis ensuing from the single-particle envelope functions $\Phi^{e(e')}$, can be written as

$$V_{ij} = e^2 \int \Phi_i^{e*}(\mathbf{r}) \Phi_j^{e'*}(\mathbf{r}') G(\mathbf{r},\mathbf{r}') \Phi_i^{e'}(\mathbf{r}') \Phi_j^{e}(\mathbf{r}) d\mathbf{r} d\mathbf{r}'. \quad (2)$$

Here i, j stand for an appropriate set of quantum numbers labelling the states. If the symmetry of the structure is low, as in the realistic quantum wire structures considered below, Eq. (1) must be explicitly solved, and the ensuing potential is then used in (2). In this case it is convenient to cast Eqs. (1) and (2) in Fourier space as described in Ref. 2. In contrast, for particularly simple structures the analytic form of the potential can be directly obtained in real space. This is, e.g., the case for the second prototype structure discussed below, the spherical QD: here two electrons can be shown to interact via the potential[4]

$$V(\mathbf{r}_i,\mathbf{r}_j) = \frac{e^2}{\epsilon_1} \frac{1}{|r_i - r_j|} + \frac{e^2}{\epsilon_1 R_d} \sum_{k=0}^{\infty} \frac{(k+1)(\epsilon-1)}{(k\epsilon+k+1)} \left(\frac{r_i r_j}{R_d^2}\right)^k P_k(\cos\Theta_{ij}), \quad (3)$$

where R_d is the QD radius, $\epsilon = \epsilon_1/\epsilon_2$, and ϵ_1 (ϵ_2) is the dieletric constant of the inner (outer) material. In the following we discuss the basic results and the relevance of these effects for our prototype QWIs and QDs.

(i) QWIs with remote dielectric confinement.
Recently, we have proposed that remote dielectric confinement (RDC)[2] may be used in order to enhance the exciton binding energies E_b. In convential nanostructures E_b is considerably enhanced by quantum confinement; however, for GaAs-based structures, observed values of E_b are still well below kT_{room}[5]. On the other hand, owing to the low optical quality of typical semiconductor/oxide interfaces, oxides cannot be used directly as confining barriers. Our novel approach is based on the idea that *quantum and dielectric confinement can be spatially separated since they are effective over different length scales.* In the proposed structures the enhanced electron-hole overlap induced by quantum confinement in conventional GaAs/AlGaAs structures is combined with the DC provided by polarization charges which form at a *remote interface* with a low-dielectric constant material, typically an insulator; since electron and hole wavefunctions decay exponentially into the barrier, they will not be affected by the presumably disordered remote interface.

As an example of our approach, we discuss quantitative predictions for the case of a conventional V-shaped GaAs/AlAs QWI with two oxide layers added above and below the QWI at a distance L. The cross-section is shown in Fig. 1(a). The additional layers are characterized by a small dielectric constant that we take equal to 2 (see, e.g., Ref. 6). For this structure, we find $E_b = 29.3$ meV, to be compared with $E_b = 13$ meV of the conventional (i.e., with no oxide layers) structure. Fig. 1(a) shows that the origin of this dramatic enhancement is the large polarization of the AlAs/oxide interfaces induced by the excited electron and hole charge densities. A small polarization charge is also induced at the GaAs/AlAs interface, due to the small dielectric mismatch. In Fig. 1(b) we show the calculated E_b for selected values of L. Obviously, E_b is maximum when the oxide layer is at minimum distance[7], $L = 0$, where it is enhanced by more than a factor 3 with respect to E_0, and it is well above kT_{room}. The important point here is that E_b decreases slowly, indeed as L^{-1}, with the distance L, and crosses kT_{room} at L as large as ~ 9 nm, where the effects of the disorder at the Oxide/AlAs interface are very small.

(ii) Quantum dots in dielectric environments.

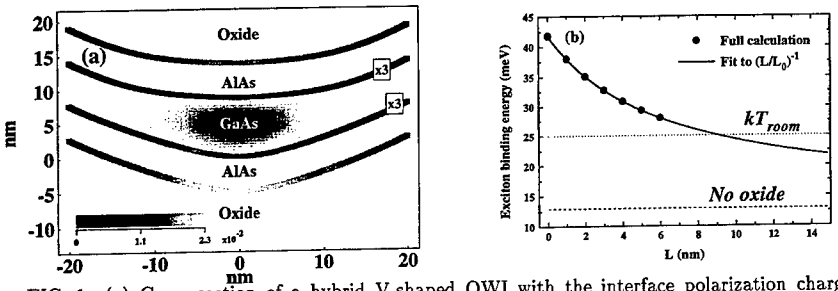

FIG. 1. (a) Cross section of a hybrid V-shaped QWI with the interface polarization charge (units of nm^{-1}) and the lowest-subband hole charge density (arbitrary units). The oxide layers are at $L = 5$ nm from the inner GaAs/AlAs interfaces. The polarization charge at the GaAs/AlAs interfaces is multiplied by 3 for clarity. (b) E_b versus distance of the oxide layers from the inner interfaces. Dots: full calculation. The solid line is a fit to L^{-1}. Dashed line: binding energy E_0 of the corresponding conventional structure (no oxide layers). Dotted line: thermal energy at $T_{\text{room}} = 300$ K.

These structures have become accessible by transport studies only very recently.[8] They are III-V or II-VI nanoparticles embedded in materials with different dielectric properties, such as organic matrices in a colloid. QDs in biological environments are also assuming increasing importance. The addition energies $E_{add}(N)$ (the energy required to add an electron to a QD containing N electrons) have been used used to characterize these systems experimentally, but a theoretical description is still lacking. To obtain it, we must compute the ground state energy, $E_0(N)$, of the QD with N interacting electrons (assumed to be confined in a spherical parabolic potential). The chemical potential of the QD with N electrons is then $\mu(N) = E_0(N) - E_0(N-1)$, from which we obtain

$$E_{add}(N) = \mu(N+1) - \mu(N)$$

The ground state energies $E(N)$, obtained from an Hubbard-like approximation to the many-body hamiltonian[9], give rise to the addition spectra of Fig. 2. For $N \leq 5$, we have also performed the exact diagonalizations of the many-electron hamiltonian, with results that are almost identical.

The solid line in Fig. 2 is the calculated addition spectrum for a dielectrically homogeneuos QD, i.e., $\epsilon = 1$ in Eq. (3). The peaks at $N = 2$ and $N = 8$ correspond to the addition of one electron to a QD with a closed s- and p-shell, respectively; the weaker peaks at $N = 5$ and $N = 13$ correspond to the addition of one electron to a QD with a half-filled outer shell where all spins are parallel, as expected by a filling of the shells according to Hund's rule. When $\epsilon > 1$ the addition spectra of Fig. 2 are affected in several ways. Let us first consider the behaviour for $N \leq 8$. As ϵ is increased, the spectra are shifted to higher energies, since a larger energy is needed to add new electrons to the QD due to the enhanced Coulomb repulsion. Note, however, that this shift is not rigid, and the half-shell peak at $N = 5$ is enhanced with respect to full-shell peaks at $N = 2$ and $N = 8$. This result is quite general and derives from the different combinations of direct and exchange Coulomb terms that enter the ground state energies determining the full and half-shell peaks.

The changes taking place at larger N are more dramatic. As ϵ is increased, the ordering and amplitude of the peaks deviates from the behaviour at $\epsilon = 1$. As can be seen Fig. 2,

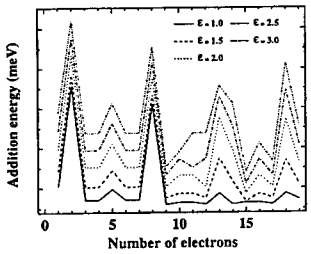

FIG. 2. Addition spectra obtained with the Hubbard approximation for several values of the dielectric mismatch ϵ. The parameters used in the computations are for a CdSe[10] spherical QD of radius of 3 nm, that corresponds to a confinament energy of about 150 meV.

half-shell peaks become comparable with full-shell ones, and additional features appear for the larger values of N. Inspection of the ground state configurations shows that this is due to a shell filling in violation of Hund's rule. Above a critical value N_c, a *reconstruction* of the electronic configuration takes place, i.e., the added electron will not be arranged in the most external shell, leaving the remaining electrons in the previous configuration. Instead, it will cause other electrons in the inner shells to be promoted to shells of higher angular momentum. This reconstruction occuring at large values of the dielectric mismatch is similar to the one predicted in QDs in a strong magnetic field (where a similar enhancement of the Coulomb interaction takes place).

In summary, we have shown that dielectric confinement effects may strongly affect quantum states in dielectrically modulated nanostructures. By modulating the dielectric mismatch between different layers it is possible to tune the Coulomb interaction between the quantum confined states, in analogy to what is done by external magnetic fields and/or doping, thereby modifying substantially the optical and addition spectra of nanostructures.

This paper was supported in part by MURST-40% through grant "Physics of nanostructures" and by INFM through grant PRA-SSQI.

[1] L. V. Keldysh, Pis'ma Zh. Eksp. Teor. Fiz. **29**, 716 (1979) [JETP Lett. **29**, 658 (1979)].

[2] G. Goldoni, F. Rossi, and E. Molinari, Phys. Rev. Lett. **80**, 4995 (1998).

[3] The renormalization of the interaction gives also rise to a self-energy term; in most cases this term is small and will not be discussed in this paper. See also Ref.[2].

[4] L. E. Brus, *J. Chem. Phis.*, **80**, 4403, (1984).

[5] F. Rossi, G. Goldoni, E. Molinari, Phys. Rev. Lett. **78**, 3527 (1997) and Refs. therein.

[6] A. Fiore *et al.*, Nature **391**, 463 (1998).

[7] Our calculations have been extended down to $L = 0$ for completeness, although in this limit they should be taken with caution, due to the neglect of the AlAs/oxide interface effects.

[8] D. L. Klein *et al.*, Nature **389**, 6991 (1997).

[9] M. Rontani, F. Rossi, F. Manghi, and E. Molinari, Appl. Phys. Lett. **72**, 957 (1998); Phys. Rev. B **59**, 10165 (1999).

[10] Landolt-Bornstein, *Numerical Data and Functional Relationships in Science and Technology*, vol 17, Springer-Verlag, (1982).

PC.39

SINGLE ELECTRON TRANSPORT IN SAMPLES CONTAINING InAs SELF-ASSEMBLED DASHES AND DOTS

S. I. Khondaker[$], J. T. Nicholls, W. R. Tribe, D. A. Ritchie, and M. Pepper
Cavendish Laboratory, University of Cambridge, Madingley Road,
Cambridge CB3 0HE, UK.

Abstract

We present measurements of single electron transport in samples where InAs self-assembled dashes and dots are incorporated in a GaAs quantum well in a modulation doped GaAs/AlGaAs heterostructure. The single electron transport is through a dot isolated using a pair of split gates deposited on the sample surface. By application of a source-drain voltage we investigate the energies of a dot that is trapped within the 1D channel defined by the split gates. The measured charging energy of the dots can be as high as 6 meV, and additional structure is observed in the range 0.5-2 meV. We speculate that the dot is formed by strain modulation of the conduction band in the GaAs quantum well.

Self-assembled quantum dots (SADs) have attracted much attention because of their importance in physics and device application. [1] The SADs are naturally formed during epitaxial growth of lattice mismatched materials. For example, 20 nm InAs self-assembled quantum dots can be created on GaAs [2,3] using the Stranski-Krastanow growth mode after depositing a critical thickness of InAs. The formation of the InAs dots depends not only on the critical thickness [4] of InAs layers, but also on the growth temperature and the thickness of GaAs capping. If the growth temperature is high or the capping layer thickness is much less than the dot height, some of the InAs may desorb or segregate to the surface, and the remaining InAs will form cigar shaped dash structures.[5-7]

Recently measurements have concentrated on the electron transport properties of 2DEG containing InAs self-assembled dots [8-12] and self assembled dashes [10]. Sakaki *et al.* [8] showed that the mobility of a two dimensional electron (2DEG) at 77K is drastically reduced when a layer of SAD is grown 15-80 nm away from the electron layer. Horiguchi *et al.* [9] measured the electron transport through a InAs SAD isolated using a split gate, and from the temperature dependence of the I-V characteristics inferred that the charging energy is 14 meV. Kim *et al.* [10,11] showed that the introduction of the dot and dash layer in a 2DEG produces strong potential fluctuations in the 2DEG that localizes electrons - this alters the shape of the phase diagram that describes the quantum Hall liquid - insulator transitions. [10] Ribeiro *et al.* [12] found that the presence of the InAs SADs introduces repulsive scattering that upshifts the magnetic field positions of the quantum Hall plateaus.

In this paper, experimental data are presented on single electron transport studied by split gates in samples containing InAs self-assembled quantum dashes and dots incorporated in a GaAs quantum well (QW) in a modulation doped GaAs/AlGaAs heterostructure. As a function of split gate voltage we observe Coulomb blockade (CB) peaks in the conductance characteristics. The application of a DC source-drain voltage V_{SD} allow us to probe the charging energies, as well as the confinement energies within the dot.

The sample used in this study were grown by MBE on GaAs (100) substrates, with structures that are given elsewhere [10,11]. Fifteen devices from four different wafers were measured, but data from only three samples are presented here. Each sample consists of a 20 nm GaAs QW that is modulation doped with a 40 nm AlGaAs spacer layer. Growth was interrupted at the center of the GaAs QW and 2.15 monolayers (ML) of InAs were grown instead of GaAs.

Subsequent to the deposition of the InAs, either a 5 nm (sample A, B) or 1 nm GaAs capping layer (sample C) as grown and self-assembled dots or dashes were formed. TEM images show that on average the individual circular dots are ~28 nm in diameter and 4 nm in height.[7] The density of the dots is estimated to be ~$3X10^9$ cm^{-2}. A sample similar to the dash sample was characterized using an atomic force microscope during an interruption in the growth, the dashes are typically 500 nm X 60 nm in size and are elongated in the [01 $\bar{1}$] direction. The density of dashes is estimated to be ~$2X10^8$ cm^{-2}.

The wafers were processed into Hall bar samples of dimensions 80 μm X 720 μm, and after definition with electron beam lithography split gates of length 0.1 μm and width 0.3 μm were deposited on the sample surface. These 1D devices are shorter than those normally used to observe 1D ballistic transport; we use the shortest possible length so as to capacitively couple to just one dot. After brief illumination with a red light emitting diode, the samples had the following low temperature properties: samples A and B had a carrier density n=3 X 10^{11} cm^{-2} and mobility μ=3.2 X 10^4 cm^2/Vs. For sample C: n=2.5 X 10^{11} cm^{-2} and μ=3 X 10^4 cm^2/Vs. The two terminal AC conductance G=dI/dV, of the split-gate was measured in a ^{3}He cryostat using an excitation voltage of 20 μV at 31 Hz. The sample used in this study relates to those of Ref.[10,11] in the following way: Samples A and B of the present paper were processed from the same wafer as that of Sample A in Ref.[10] and C1335m in ref.[11], while sample C of the present paper processed from the same wafer as that of sample C of Ref.[10].

By applying a negative gate voltage V_g to the split gates, electrons are depleted from beneath the gates leaving a narrow 1D channel defined in the 2DEG. If a puddle of electrons is formed close to this channel then the charging characteristics of the dot may be investigated as the capacitive coupling between the dot and the split-gate allows the number of electrons in the dot to be varied. Conduction through the dot proceeds when the Fermi level (FL) is aligned with one of the energy levels of the dot. If the FL is not aligned there is Coulomb blockade (CB).

Figure 1(a) shows the conductance characteristics at 0.3 K for sample A as a function of the voltage V_{g1} applied to one arm of the split-gate, while the voltage on the other arm was kept fixed at V_{g2}= -1.67V. Figure 1(b) is a similar plot for sample B. In both cases the resonance peaks can be measured up to 18 K. The peaks were not exactly reproducible on different cooldowns, but are observed at slightly shifted gate voltage positions.

Adding a DC source-drain voltage, V_{SD}, to the AC excitation voltage allows the energies of the dot to be measured[13]. Figure 2(a) shows the differential conductance characteristics $G(V_g)$ for sample A where V_{SD} is incremented from 0 (bottom trace) to 6.9 mV (top trace) in steps of 0.2 mV. Figure 2(b) shows similar characteristics for sample B where V_{SD} is incremented from 0 to 6.0 mV in steps of 0.5 mV; for clarity the traces are offset in the vertical direction. The conductance peaks splits symmetrically into two peaks with increasing V_{SD}, showing that the left and right tunnel barriers are approximately the same. The additional structure measured between the last two linearly split peaks at V_{SD}=2 mV in Fig.2(a) and at V_{SD}=3 mV in Fig.2(b) are associated with electron tunneling through excited states of the dot, and is therefore a measure of the quantum confinement energy within the dot.

Figure 3 shows $G(V_{SD})$ characteristics for sample B over a gate voltage range that spans the last four conductance peaks. The successive sweeps have been displaced vertically as V_g is incremented in steps of 5 mV. Inside the diamond shape structure bounded by the peaks, the conductance is zero and there is Coulomb blockade of the electrical transport. The energy, $U_{n,n+1}$, between the nth and n+1th CB peaks is measured from the centre line to a corner of the

diamond and is $U_{1,2}$=6 meV, $U_{2,3}$=3.5 meV and $U_{3,4}$=3 meV. The measured increases in U towards pinch-

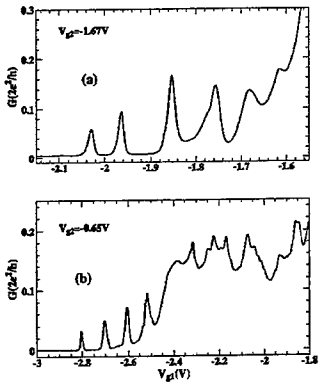

Figure 1: Conductance characteristics $G(V_{g1})$ for (a) sample A and (b) sample B, with V_{g2} kept fixed.

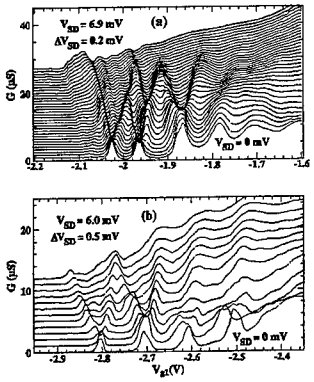

Figure 2: Conductance characteristics $G(V_g)$ at different source-drain voltages V_{SD} for (a) sample A and (b) sample B.

off show that the puddle of electrons within the dot is decreasing in diameter, with an accompanying decrease in its capacitance. Figure 4 show similar $G(V_{SD})$ characteristics for dash sample C at gate voltages around the last few observable CB peaks. The charging energies are measured to be 1.5 to 2.4 meV. The additional structure observed 0.5-1mV outside the CB diamond correspond to electron tunneling through excited states. The overall lower energies for dash sample compared to dot samples suggests that the electron puddle formed in dash sample is larger in than in the dot sample.

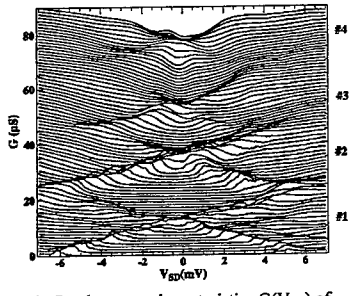

Figure 3: Conductance characteristics $G(V_{SD})$ of sample B for different gate voltages V_g.

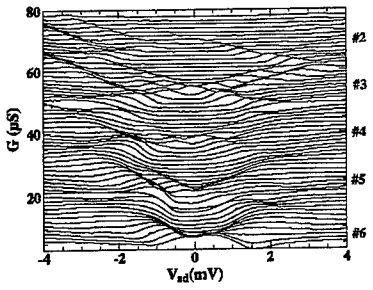

Figure 4: Conductance characteristics $G(V_{SD})$ of sample C for different gate voltages V_g.

Similar charging characteristics have been obtained from many samples, leading us to conclude that the uniform InAs dots and dashes are responsible for the formation of the quantum dots in the 2DEG. Indeed in a control sample where 1ML of InAs was deposited in the GaAS

well no charging effects were observed; at this coverage the InAs layer is uniform, and the strain between the InAs and the GaAs is homogeneous, and hence there is no electron puddling. We speculate that the strain field about the self-assembled InAs dots lift the bottom of the conduction band around the perimeter of the dot, providing the conduction band profile shown in Fig. 5. Such strain modulation of conduction band due to InGaAs in a GaAs QW has been optically studied by Tan et al. [14] where InGaAs were placed at least 20 nm above the GaAs QW layer. In lateral transport we believe we tunnel through the strain induced barriers measuring the properties of the confined GaAs electrons, rather than looking at the more strongly confined electrons in the InAs, which from optical measurements show typical energy spacings of 20 meV. [15] We assume that one or more of the dots is situated near the entrance or exit of the split-gate channel, so that for conductances $G < e^2/h$ the transport properties will be dominated by the zero-dimensional properties of the dot.

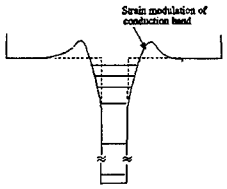

Figure 5: Schematic figure of the conduction band of an isolated InAs dot. There is a deep strongly confined well provided by the InAs, and the barriers are formed by the lifting of the conduction band by the strain field resulting from the 7% lattice mismatch between the InAs and GaAs.

In conclusion, we have demonstrated that using self-assembled InAs dots submicron features can be imprinted into the conduction band profile of the GaAs. We believe that we are observing electron transport through a dot in the GaAs that is created by the strain field emanating from the InAs dots.

REFERENCES:

$ Now at Physics Department, Dhaka University, Dhaka 1000, Bangladesh.
1. S. Raymond *et al.*, Superlattices and Microstructures **21**, 541 (1997)
2. D Leonard *et al.*, Appl. Phys. Lett. **63**, 3203 (1993).
3. J. M. Moison *et al.*, Appl. Phys. Lett. **64**, 196 (1994).
4. D. Leonard, K. Pond, and P. M. Petroff, Phys. Rev. B. **50**, 11687 (1994).
5. K. Tillmann *et al.*, J. Appl. Phys. **78**, 3824 (1995).
6. S. P. Guo *et al.*, Appl. Phys. Lett. **70**, 2738, (1997).
7. G. D. Lian *et al.*, Appl. Phys. Lett. **73**, 49 (1998).
8. H. Sakaki *et al.*, Appl. Phys. Lett. **67**, 3444 (1995)
9. N. Horiguchi *et al.*, Appl. Phys. Lett. **70**, 2294 (1997).
10. G. H. Kim *et al.*, Proceedings of the 24th International Conference of the Physics of Semiconductors, Jerusalem (World Scientific, Singapore) 1998.
11. G. H. Kim *et al.*, Appl. Phys. Lett. **73**, 2468 (1998).
12. E. Ribeiro *et al.*, Phys. Rev. B **58**, 1506 (1998).
13. J. T. Nicholls *et al.*, Phys. Rev. B **48**, 8866 (1993).
14. I. H. Tan *et al.*, Appl. Phys. Lett. **61**, 300 (1992)
15. S. Fafard *et al.*, Appl. Phys. Lett. **65**, 1388 (1994)

PC.40

CONDUCTANCE SPECTROSCOPY OF InAs QUANTUM DOTS BURIED IN GaAs

Kanji Yoh and Hironobu Kazama

Research Center for Interface Quantum Electronics, Hokkaido University
N 13, W 8, Kita-ku, Sapporo, Hokkaido 060-8628 Japan e-mail: yoh@rciqe.hokudai.ac.jp

Abstract

Electron states in self-assembled InAs dots have been studied by a novel approach of conductance spectroscopy in a transistor structure by monitoring the conductance modulation of the δ-doped channel formed in adjacent to the InAs dots. By tracing each current peak, dot confined states were studied and two s-like, and four p-like shell structures were resolved. Charging energy of ≈20meV was consistent with the dot size estimation by atomic force microscope (AFM). From the slope of the s-shell curve on magnetic field, the extent of the electron wavefunction confined in a dot was estimated to be 90Å, which is consistent with the estimation of the dot size. The magnetic depopulation effect of two-dimensional (2-D) δ-doped channl layer was also shown to overlap in the current-voltage characteristics.

PACS 72.20.-i, 73.20.Dx, 73.20.Fz, 73.23.Hk, 73.61.Ey

Introduction

Electron states in self-assembled InAs dots have been measured and reported so far in various methods such as capacitance spectroscopy[1], far-infrared spectroscopy[2,3], and tunneling spectroscopy in split-gate transistor structures[4, 5]. Here, we propose and report for the first time a novel approach of conductance spectroscopy in a transistor structure by monitoring the conductance modulation of the δ-doped channel formed in adjacent to the InAs dots. Electron tunneling into the dots is shown to be monitored by the current modulation where sudden current decrease takes place due to charging of dots in the barrier layer. This method measures the charging effect of the ensemble of dots like capacitance method[1]. Therefore, the present method is complementary to the tunneling spectroscopy method of the 2-D states through single InAs dot[6]. We have investigated the current modulation dependence on magnetic fields. Since the charging condition is met when the Fermi-level of the δ-doped channel and the confined states of the dots, the measurement inevitably associated with the magnetic field dependent shifts of the Fermi level relative to the energy band. We will also discuss this effect associated with the charging effect of the dots under magnetic field.

Experimental

In order to investigate as many energy states as possible in self-assembled InAs dots through adjacent channel current, we have tried to design the device structure so that the confined energy states in InAs dots to be higher and at the same time the Fermi level of the channel to be lower. For these purposes, the InAs dots were buried in thin AlAs barriers and the 2-D channel was made by δ-doped GaAs structure. The δ-doped channel structure was formed in adjacent to the InAs dots, 200Å apart, as shown in Fig.1. The corresponding energy band diagram of the structure is shown in FIg.2. The average size of the InAs dots were 25Å in height and 170Å in diameter. The charging energy of the average sized dot is estimated to be 17meV from the apparent size of the dot by AFM sample whose growth was terminated after the InAs dot formation. Slightly larger charging energy is anticipated in reality because the buried structure are reportedly smaller than the surface dots[4]. The average areal density of the dots was $2.2\times10^{10}cm^{-2}$. From the gate size of 3μm x 10μm, average number of dots under the gate is

estimated to be approximately 6,600. The Hall measurement at 77K revealed that the carrier concentration and the mobility of $8.2 \times 10^{11} cm^{-2}$ and 5,918 $cm^2/V \cdot s$, respectively. Basic process steps were similar to standard GaAs FET fabrication except for the recessed ohmic

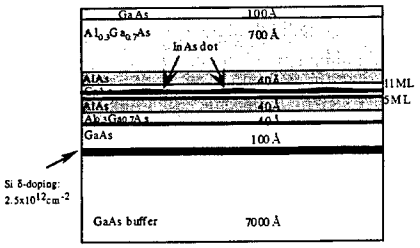

Fig.1 The heterostructure of the δ-doped channel structure. Self-assembled InAs dots were formed 200Å apart in adjacent to the channel.

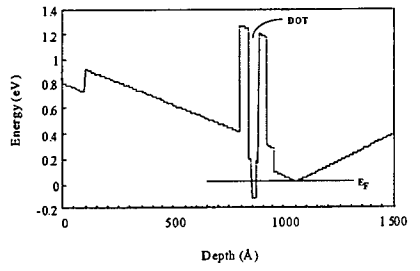

FIg.2 The energy band diagram of the device structure.

contacts to the δ-doped channel. This was to maintain improved ohmic contact characteristics even at liquid helium temperatures. When the channel is off-state except for a single current path, Coulomb oscillation[5] or memory effect[4][7] is expected to occur. In on-state, where nominal geometrical channel region is conductive, charging state of the dots affects current-voltage characteristics through threshold voltage shifts. Whenever the threshold voltage shift occurs, the current peak shows up. Therefore, counting the current peaks and their position shifts depending on external magnetic fields enable us to monitor the electronic states of the average quantum dots.

Results and Discussions

At room temperature, drain current versus gate voltage measurement revealed hysteresis characteristics due to charging of the dots as shown in Fig.3. At liquid helium temperatures, the hysterisis characteristics was also seen at this

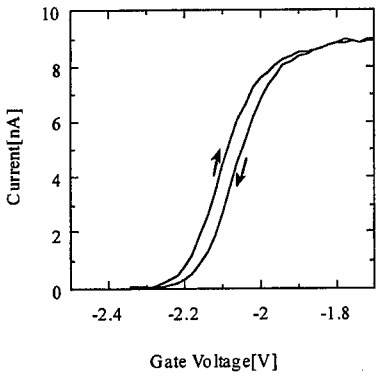

Fig.3 At room temperature, drain current versus gate voltage measurement revealed hysteresis characteristics due to charging of the dots as shown in .

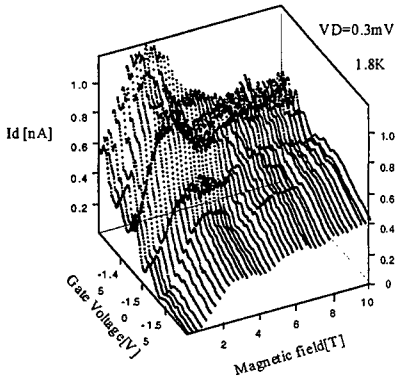

Fig.4 The current-voltage characteristics at low current region. Magnetic field is applied perpendicular to the surface up to 10 Tesla.

temperature after the channel is turned on. Unlike room temperature, the characteristics resolved clear structures which presumably reflects charging of each electronic states of the ensemble of dots when the Fermi level crosses the average dot confined states as illustrated in Fig.2. The threshold voltage shift of ≈20mV corresponds to charging of each InAs dot by a single electron in average. The current-voltage characteristics at low current region is plotted in 3-dimensional plot in Fig.4 where magnetic field is applied perpendicular to the surface and varied from 0 to 10 Tesla. Clearly current peaks show some structures. In order to analyze these current peak shifts more clearly, the gray-scale plot is illustrated in Fig.5 and Fig.6, representing channel current dependence on linear B and B^2, respectively. In these figures, equally spaced three pairs of peak curves are outstanding. The energy separation of the pairs range from 16 to 20meV, which is well accounted for by the charging energy of the dots, 17meV, as predicted in the preceding section. Here, we attribute the total of six lines of the current peak traces as two s-shell states and four p-shell states based on the following arguments. The slope of the "s-shell" peak in B^2 dependence in Fig.6 yields average electron cloud extent, $\langle x^2 \rangle$, in the dot to be 90Å. This result was calculated by taking the lever factor of dot position to the fate to be 5 based on the heterostructure as shown in Fig.1. This is consistent with the expected electron extent, 98Å, confined in the dot with lateral size of 170Å estimated by AFM in the separately grown samples. The slope of the lower "p-shell" pair of peaks gives about 60% of that of "s-shell" slope in Fig.6. Exactly half is expected in the "p-shell" slope against B^2 axis compared to the "s-shell" slope, but the measured slope is thought to be reasonably close. The higher energy pair of "p-shell" peaks seems to have steeper slope than the lower pair of "p-shell" curves. This is also well understood by the p-states splitting argument associated with the opposite angular momentum quantum number. We can even extract effective electron mass from the dependence of the energy split on magnetic fields. The orbital splitting of the p-shell in linear scale yields 2.21meV/T which gives $0.052m_0$ for the effective mass in the InAs dots, where m_0 denotes electron rest mass in the vacuum. This estimation is close to the estimation by capacitance spectroscopy[3]

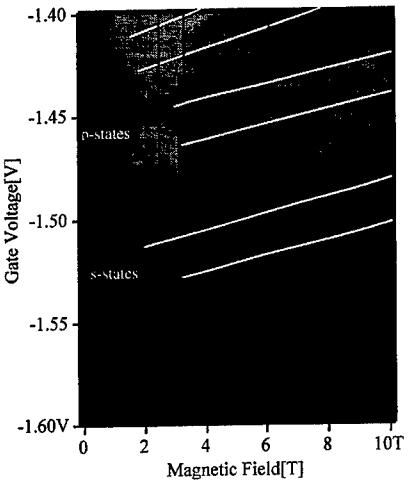

Fig.5 Gray-scale plot of drain currennt chatacteristics of the same sample as in Fig.3. Black solid vertical lines indicate the minimum conductance condition in 2-D channel due to magnetic depopulation of the Landau levels.

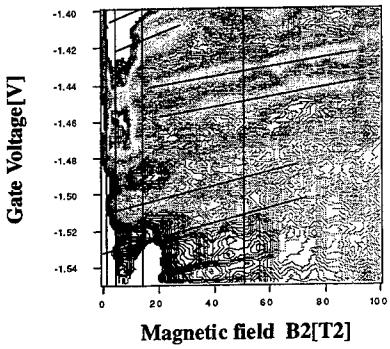

Fig.6 Contour plot of drain currennt of the same sample as in Fig.3. This is a reproduction of Fig.5 with the horizontal axis revised to B^2.

and lower than infrared spectroscopy[2] or RTD spectroscopy[8] by 20% or so. In anycase, all those measurement results show much higher electron effectivemass compared to that of bulk

InAs; $0.023m_0$.

Finally, Fermi-level variation due to magnetic depopulation should be added. The Fermi-level of the δ-doped channel undergoes oscillation whenever the Landau level crosses the Fermi level. This is clearly seen in Fig.4 when data is traced at the gate voltage of -1.6V. Current dips are clearly seen at magnetic fields of ≈3V, ≈ 5V and ≈7V. As a result, the oscillation associated with the magnetic depopulation overlaps the above mentioned current voltage characteristics. In Fig.5, this magnetic depopulation effect is added by black solid vertical lines in addition to the slant current peak lines which represent the shell structure in the dots. The period of these current dips, or equivalently resistance peaks, corresponds to ≈ 1 Tesla-1 which agrees reasonably well with the calculated period of magnetic depopulation using the characteristic numbers of the present δ-doped channel 2-D system such as 2-D density of states in GaAs, sheet carrier concentration of $8.2x10^{11}cm^{-2}$ and Fermi level of 29.2meV.

Present method is complementary to previously reported capacitance spectroscopy[1,3] in a sense that it picks up the average charging by the threshold voltage shift by analyzing DC characteristics. Furhther study would resolve more detailed shell structures in InAs dots as demonstrated by GaAs pillar structure resonant tunneling diode[9].

Conclusions

Electron states in self-assembled InAs dots have been studied by a novel approach of conductance spectroscopy in a transistor structure by monitoring the conductance modulation of the δ-doped channel formed in adjacent to the InAs dots. By tracing each current peak, dot confined states were studied and two s-shell, and four p-shell were suggested. Charging energy of ≈20meV was consistent with the dot size estimation by AFM. From the slope of the s-shell curve on magnetic field, the extent of the electron wavefunction confined in a dot was estimated to be 90Å, which is also consistent with the estimation of the dot size. The magnetic depopulation effect of 2-D δ-doped channel layer was also shown to overlap in the current-voltage characteristics. Present method is complementary to previously reported capacitance spectroscopy[1,3] in a sense that it picks up the average charging of the dots by the DC analysis of a transistor characteristics.

Acknowledgment

This work was partially supported by the Grant-in-Aid for Scientific Research from Japanese Ministry of Education, Science, Sports and Culture.

References

[1] G.Medeiros-Ribeiro, D.Leonard, P.M.Petroff, Appl.Phys.Lett., 66 (1995) 1767

[2] H.Drexler, D.Leonard, W.Hansen, J.P.Kotthaus and P.M.Petroff, Phys.Rev.Lett.73 (1994) 2252

[3] A.Lorke, M.Fricke, B.T.Miller, M.Haslinger, J.P.Kotthaus, G.Medeiros-Ribeiro and P.M.Petroff, Inst.Phys.Ser.No.155:Chapter11 (1997) 803 ; B.T.Miller, W.Hansen, S.Manus, R.J.Ruyken, A.Lorke, P.Kotthaus, S.Huant, G.Medeiros-Ribeiro and P.M.Petroff, Phys.Rev.B 56, 6764 (1997)

[4] K.Yoh and J.Konda, Jpn.J.Appl.Phys. (1997) 4134-4138.

[5] K.Yoh and S.Shiina, In the proceedings of the 23rd International Conference on Physics of Semiconductiors , Jerusalem, 1998 (to be published, World Scientific).

[6] A.S.G.Thornton, T.Ihn, P.C.Main, L.Eaves, K.A.Benedict and M.Henini, Physica B 249-251 (1998) 689-692.

[7] Similar phenomenon is reported in poly-silicon grain FET structure: K.Yano, T.Ishii, T.Hashimoto, T.Kobayashi, F.Murai, and K.Seki, Appl.Phys.Lett., 67 (1995) 828.

[8] Kanji Yoh, Hironobu Kazama and Takaya Nakano, Physica B 249-251 (1998) 243-246.

[9] S.Tarucha, D.G.Austing, T.Honda, R.J.van der Hage and L.P.Kouwenhoven, Phys.Rev.Lett.77 (1996) 3613.

PC.41

Controlled Mechanical AFM Machining of Two-Dimensional Electron Systems: Fabrication of a Single-Electron Transistor

H. W. Schumacher[1], U. F. Keyser[1], U. Zeitler [1], R. J. Haug[1], K. Eberl[2]

[1] *Institut für Festkörperphysik, Universität Hannover, Appelstraße 2, 30167 Hannover, Germany.*
[2] *Max-Planck-Institut für Festkörperforschung, Heisenbergstr. 1, 70569 Stuttgart, Germany.*

By mechanical scratching the surface of GaAs/AlGaAs heterostructure with an atomic force microscope an energetic barrier for the two-dimensional electron gas is formed. The barrier formation is *in-situ* controlled by measuring the room temperature resistance across the barrier. Barrier heights can be tuned from some mV up to more than 100 mV as determined by measurement of the thermally activated current. Low-resistance barriers show typical tunneling behaviour at low temperatures whereas high-resistance lines show GΩ resistances in a bias range up to some ten volts allowing their use as in-plane gates. Transport measurements of a side gated single-electron transistor fabricated this way are presented.

One way of using the atomic force microscope (AFM) as a lithographic tool is the mechanical scratching of surfaces with the AFM tip [1]. The increase of the contact force between tip and surface above a certain threshold leads to the formation of a groove in the surface. Various materials from polymers to metals and semiconductors were patterned this way [2] - [5]. Using this method on an InAs surface quantum well opens a possibility to the direct AFM fabrication of mesoscopic electronic structures as demonstrated by Cortes Rosa et al. [6]. The depletion of the two-dimensional electron gas (2DEG) of a standard GaAs/AlGaAs heterostructure was demonstrated by local anodic oxidation of the GaAs surface [7]. Here, we show how mechanical scratching of the surface of a GaAs/AlGaAs heterostructure can be used for the local depletion of the 2DEG situated about 55 nm below the surface. This way electronic barriers for the 2D electrons can be formed.

Our heterostructures were grown by molecular beam epitaxy and they consist from top to bottom of a 5 nm GaAs cap layer, 40 nm of Si-doped AlGaAs, a 10 nm undoped AlGaAs barrier, a 20 nm GaAs quantum well containing the 2DEG and a 30 nm undoped AlGaAs barrier grown on a GaAs buffer layer. 20 μm wide standard Hall bars were defined by photolithography and wet chemical etching showing a low temperature electron density of 6.1×10^{15} m^{-2} and electron mobilities of 10.9 m^2/Vs.

The influence of scribing the surface on the resistance of the sample is displayed in Fig. 1 with the principle of operation of the controlled mechanical AFM machining depicted in the inset. An electrically contacted Hall bar is mounted in the AFM. The machining process is performed pressing the tip [8] nominally some μm against the surface while multiply scanning along a line over the Hall structure. Contact forces are around 50 to 100 μN with a scan velocity of 100 μm/s. During fabrication the room temperature resistance R of the 2DEG across the written line is controlled. The AFM laser is switched off and the sample is kept in the dark to reduce photoconductivity of the bulk material. In Fig. 1 the measured resistance R of a barrier is plotted against the number of scanlines with a force of 50 μN. The resistance

slowly rises from its starting value of around 20 kΩ. After 75 scans R rises faster and after about 100 scan lines R rapidly grows from 50 kΩ up to 55 MΩ the background resistance of the GaAs whereafter only minor changes occur. This raise of R can be ascribed to a local depletion of the 2DEG due to a local removal of the surface layers of the heterostructure comparable to a shallow etch process [9]. Due to the *in-situ* control of the 2DEG resistance the fabrication of the barriers can be stopped at any predefined value of R opening the possibility of fabricating barriers with tunable characteristics. High resistance grooves ($R \sim$ MΩ) show lateral sizes from around 400 down to less than 100 nm and depths up to 15 nm as measured by AFM and scanning electron microscopy. Lower resistance lines in general show smaller lateral dimensions and lower depths.

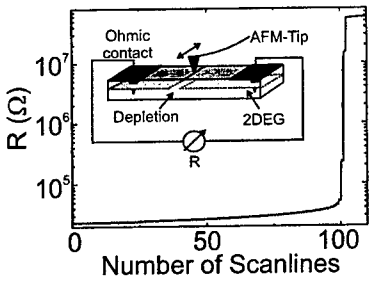

Figure 1: *2DEG resistance R during fabrication against the number of scans with increased force. Inset: Sketch of the controlled mechanical AFM machining.*

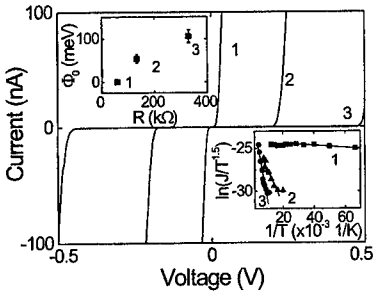

Figure 2: *IV-curves of barriers (1)-(3) taken at 1.5 K. Lower inset: 2D Arrhenius plot of the same barriers. Upper inset: barrier heights Φ_0 plotted against room temperature resistance R.*

In the following the behaviour of three barriers named (1) to (3) having room temperature resistances of $R = 58$, 133, and 330 kΩ respectively will be discussed. At room temperature their current-voltage dependencies do not show strong nonlinearities. In Fig. 2 current-voltage characteristics of the three barriers taken at 1.5 K are displayed. All devices show a suppressed current around zero bias as expected for a tunneling barrier in the 2DEG. With increasing R the onset of the current shifts towards higher bias voltages caused by a rising height of the tunneling barrier. Barrier heights Φ_0 above the Fermi energy E_F can be deduced from thermal activation measurements [10]. Activated currents I were measured at bias voltages between 0.5 and 200 mV in a temperature range from $T = 1.5$ to 200 K in a continous He flow cryostat. In a 2D system the saturation current density J obeys the 2D Richardson law,

$$J = AT^{1.5} exp\left(\frac{-\Phi_0}{k_B T}\right), \tag{1}$$

where $A = e\sqrt{m^*}k_B^{1.5}/\hbar^2(2\pi)^{1.5}$ is the 2D Richardson constant with e, m^* the electrons charge and effective mass [11]. Therefore, Arrhenius plots of the form $ln(I/T^{1.5})$ vs $1/T$ allow the deduction of the barrier heights Φ_0 from the gradient of the plots. Such a plot is shown in the lower inset of Fig. 2 for the three barriers under discussion. The bias voltages of

the displayed data are 1 mV for barrier 1 and 50 mV for barriers 2 and 3. The straight lines mark the gradients used for the determination of Φ_0 at these bias voltages. Values of Φ_0 are calculated from gradients at various bias voltages. Errors are calculated from the standard deviation of these values. The such derived barrier heights are 1 ± 0.4 meV (1), 55 ± 10 meV (2), and 106 ± 16 meV (3). The upper inset of Fig. 2 shows Φ_0 as a function of room temperature resistance R. As can be seen from the plot Φ_0 raises almost linearly with increasing R. In other words measurement of R during the mechanical fabrication provides good control of the height of the barrier in fabrication.

At temperatures of a few Kelvin IV-characteristics of barriers having a room temperature resistance in the MΩ range show a supressed current up to bias voltages of some 10 Volts (not displayed). This speaks for barriers heights Φ_0 much higher than the 100meV measured for device (3). Their leakage resistances greater than 50 GΩ make these high resistance lines ideal candidates for the fabrication of in-plane gates [13]. Mechanical AFM machining therefore provides means of directely writing in-plane gates [12] as well as tunneling barriers which opens the possibility of fabricating a single-electron transistor (SET) [14].

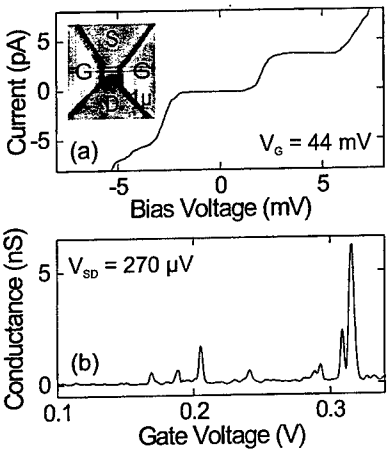

Figure 3: *Mechanically fabricated SET. $T = 350$ mK. (a) Coulomb blockade staircase in the IV-characteristics. Inset: AFM micrograph of a mechanically fabricated SET. (b) Coulomb blockade oscillations under variation of gate voltage.*

A such fabricated SET is shown in the inset of Fig. 3 (a). Source S and drain D are separated from the gates G by high resistance lines forming a conducting channel of about 1 μm width. Two tunneling barriers are added to the channel defining a SET island in the 2DEG. In Fig. 3 (a) current-voltage characteristics taken at 350 mK of such a device are presented. Clear steps caused by Coulomb blockade are observed. A total capacitance

of 110 aF is deduced from the width of the Coulomb blockade. Assuming a simple model of a disk shaped dot a diameter of 250 nm can be calculated which is comparable to the geometrical dimension of the device. Fig. 3 (b) shows the conductance between source and drain at a fixed bias as a function of gate voltage. Peaks in the conductance assigned to single-electron tunneling are separated by regions of supressed transport due to Coulomb blockade. The energy levels of the SET can be effectively shifted applying a voltage to the side gates.

In conclusion mechanical AFM machining was used to create grooves in the surface layers of a GaAs/AlGaAs heterostructure. Using this technique tunneling barriers with variable heights from 1 to more than 100 meV were fabricated in the 2DEG. The room temperature resistance R of the 2DEG across the written grooves was found to be a good measure for the barrier height Φ_0. Therefore measurement of R provides *in-situ* control of the barrier formation process. Additionally to the fabrication of tunneling barriers in-plane gates can be written into the 2DEG by stopping the machining process at higher values of R ($R \sim \mathrm{M}\Omega$). A side-gated single-electron transistor was fabricated proving the feasibility of mechanical AFM machining for the fabrication of mesoscopic electronic devices.

References

[1] See as a review, e. g. : C. R. K Marrian (ed.), Special Issue on Nanometer-Scale Science and Technology, Proceedings of the IEEE, **85**, 481-704 (1997).

[2] X. Jin and W. N. Unertl, Appl. Phys. Lett. **61**, 657 (1992).

[3] T. Sumomogi, T. Endo, K. Kuwahara, R. Kaneko, and T. Miyamoto, J. Vac. Sci. Technol. B **12**, 1876 (1994).

[4] B. Irmer, R. H. Blick, F. Simmel, W. Gödel, H. Lorenz, and J. P. Kotthaus, Appl. Phys. Lett. **73**, 2051 (1998)

[5] R. Magno and B. R. Bennett, Appl. Phys. Lett. **70**, 1855 (1997).

[6] J. Cortes Rosa, M. Wendel, H. Lorenz, J. P. Kotthaus, M. Thomas and H. Kroemer, Appl. Phys. Lett. **73**, 2684 (1998).

[7] M. Ishii and K. Matsumoto, Jpn. J. Appl. Phys. **34**, 1329 (1995); R. Held, T. Vancura, T. Heinzel, K. Ensslin, M. Holland, and W. Wegscheider, Appl. Phys. Lett. **73**, 262 (1998).

[8] Non contact Si AFM tips, Nanosensors.

[9] H. van Houten, B. J. van Wees, M. G. J. Heijman and J. P. André, Appl. Phys. Lett **49**, 1781 (1986).

[10] M. Rossmanith, K. Syassen, E. Böckenhoff, K. Ploog, and K. von Klitzing, Phys. Rev. B **44**, 3168 (1991)

[11] A. J. Peck, S. J. Bending, K. von Klitzing and K. Ploog, Appl. Phys. Lett **62**, 1544 (1993)

[12] H. W. Schumacher, U. F. Keyser, U. Zeitler, R. J. Haug, and K. Eberl, Appl. Phys. Lett., to be published

[13] A. D. Wieck and K. Ploog, Appl. Phys. Lett **56**, 928 (1990).

[14] See as a review, e. g.: U. Meirav and E. B. Foxman, Semicond. Sci. Technol. **10**, 255 (1995).

PC.42

A novel device layout for tunneling spectroscopy of low-dimensional electron systems

G. Ploner, H. Hirner, T. Maier, G. Strasser, J. Smoliner and E. Gornik
Institut für Festkörperelektronik, Mikrostrukturzentrum, TU Wien
Floragasse 7, A-1040 Vienna, Austria

Abstract

We report tunneling spectroscopic investigations on a barrier separated double-electron-layer system using a novel selective depletion scheme based on self-aligned side gates. We show that the side gate technique is also suitable to impose a tunable lateral confinement on a narrow channel. From the study of tunneling processes on a single-wire device we conclude that the energetic spacing of the one-dimensional subbands can be varied from effectively zero to up to 6 meV. A simple electrostatic model confirms the order of magnitude of the measured one-dimensional level spacing.

One of the major technological problems encountered in the fabrication of resonant tunneling devices concerns the ohmic contacts, which have to be established independently to two electron channels that are separated by a tunneling barrier of typically 200 Å. Two successful schemes for selective contact fabrication have been presented so far. The first relies on a series of intricate etching steps leading to the formation of free standing GaAs bridges [1]. The second exploits patterned back-gates, either fabricated on the backside of a wafer thinned to a thickness of a few micrometers or by in-situ implantation followed by overgrowing the back-gate pattern with the active double-layer electron system [2]

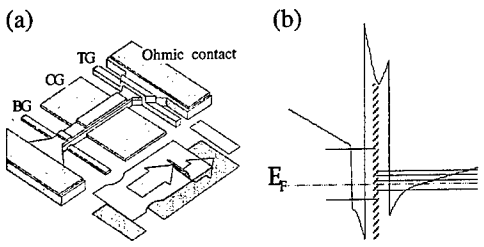

Figure 1 (a) Schematic picture of the device layout (not to scale). The lower part of the figure symbolizes the current path for reverse bias in a situation where the top (TG) and bottom (BG) gates have pinched off the electron gases at their respective positions.
(b) Conduction band profile and self-consistently calculated energy levels of the tunneling structure used to demonstrate the device principle. The shaded region indicates the δ–doping of the barrier.

Recent developments in device technology suggest that resonant tunneling transistors consisting of a double quantum well structure might have promising applications also for room temperature operation in ULSI circuits [3]. It is therefore desirable to have a simple fabrication scheme for tunneling devices that does not require thinning of the wafer and goes without intermediate implantation steps. An attempt to achieve this is provided by using self aligned side gates for the selective formation of Ohmic contacts to the various electron gases. The corresponding device layout is shown in Figure 1. The figure shows a two terminal device, where an approximately 1 μm wide channel, defined by standard optical lithography and wet etching, extends between two large Ohmic contacts. An independent Ohmic contact to the upper electron channel is established in a standard fashion by fabricating a top Schottky gate on the one end of the active region of the

device (in the following referred to as the *top gate* and labeled TG in Fig.1 (a)). At the other end of the device the lower channel is separated from the adjacent Ohmic contact using a side gate in close proximity to the edges of the etched channel (the *bottom gate*, BG in the Figure). A central side gate (CG) can be used to impose a lateral confinement on the active tunneling region. Details of the fabrication process can be found in Ref. [4].

In the following we present some results obtained with this sample layout for a single barrier tunneling structure. Its band profile and energy levels are shown in Fig. 1 (b).

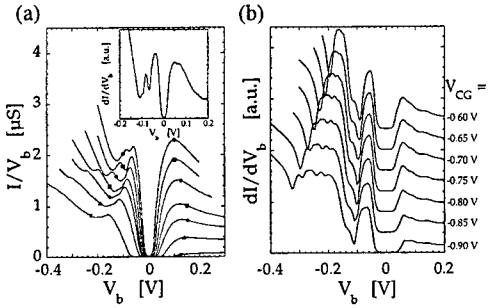

Figure 2 (a) Conductance traces for a typical device, measured at T = 1.9 K and plotted for various central gate voltages. From top to bottom: V_{CG} = 0 V, -0.2 V, -0.4 V, -0.6 V, -0.7 V, -0.8 V and –0.9 V. The inset shows the differential conductance dI/dV_b of the V_{CG} = 0 V trace.
(b) Differential conductance dI/dVb, measured at T = 1.9 K for various values of V_{CG}. Curves are vertically offset.

Figure 2 (a) shows a set of conductance traces for various values of the central gate voltage, revealing a pronounced peak structure. The data were obtained for a device whose electron channel had a lithographic width of 1 μm and a length of 20 μm. For V_{CG} = 0 V, the peaks observed on the negative bias side of the $G(V_b)$ curves can be attributed to resonant tunneling processes starting from the lowest occupied 2D subband of the InGaAs well and ending in one of the 2D subbands of the GaAs-AlGaAs junction [4]. The features due to tunneling into the second excited subband of the junction are too weak to be resolved in $G(V_b)$. They can be discerned, however, as a weak shoulder in the differential conductance dI/dV_b (shown in the inset of Fig. 2 (a)). The broad peak at positive V_b corresponds to tunneling out of the lowest subband of the junction into the first excited subband of the InGaAs well. Increasing the central gate voltage induces a lateral confinement in the upper and lower channel of the active device region. Whereas the quantization into one-dimensional (1D) subbands is not clearly visible in the $G(V_b)$ traces, the differential conductance (dI/dV_b) shown in Figure 2 (b) display a wealth of additional structure. For a proper interpretation of the dI/dV_b traces it is necessary to note that with the device layout shown in Figure 1 (a) tunneling occurs both in a region influenced by the central gate and another region unaffected by this gate. In the gated region the lower channel not only gets increasingly confined but also will be partially depleted as V_{CG} becomes more negative. The first pronounced peak of the dI/dV_b traces around V_b = –0.6 V is seen to remain mainly unchanged with varying V_{CG} .One may therefore attribute this feature to tunneling in the ungated (2D) regions of the device. The broad fine-structured features in the differential conductance traces result from tunneling between the 1D states of the gated region. Due to the depletion of the lower channel the corresponding resonant structure is shifted towards more negative bias voltage.

The fine structure of the dI/dV_b traces can be analyzed in terms of the model of Mori et al. [5]. It is based on the transfer Hamiltonian formalism and describes 1D-1D tunneling processes between laterally confined states, assuming parabolic confinement for the emitter and the collector states of the tunneling process. In order to apply the main results of this model it is

necessary to note the following. First, the bottom gate that is used to separate the lower channel from the adjacent ohmic contact induces a considerable series resistance in the current path (Fig. 1 (a)). Therefore the bias voltage V_b does not directly give the voltage drop across the tunneling barrier. In order to re-scale the voltage axis one can exploit the well-defined energy scale induced for example by the application of a strong magnetic field in the direction of the tunneling current (perpendicular to the sample). The energy levels are then split into Landau levels (LLs) of a definite energy spacing, which is easily determined from the corresponding tunneling spectra. Two typical tunneling characteristics both for $V_{CG} = 0$ V and $V_{CG} = -0.8$ V in a magnetic field of 5 T are shown in Figure 3. In this figure the first peak of the dI/dV_b curve, previously attributed to 2D-2D tunneling in the ungated device regions, is seen to split into a series of peaks due to inter LL tunneling. Comparison of the measured peak spacing with a calculated spectrum allows obtaining a scaling factor for the bias voltage axis for each value of the central gate voltage [6].

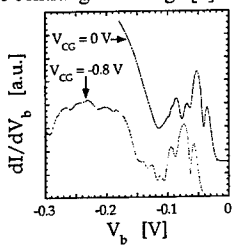

Figure 3 Differential conductance, corresponding to $V_{CG} = 0$ V and –0.8 V, recorded in a magnetic field parallel to the tunneling current with field strength of 5 T.

The other point to be noted here is that the observed resonant structures are rather broad. This is due to the fact that the tunneling barrier of our device is heavily doped. The resulting elastic scattering of the tunneling electrons leads to the observed peak broadening.

And finally we note that the energetic spacing of the 1D subbands will not be equal in the InGaAs well and the GaAs-AlGaAs junction. Due to the geometry of the sample layout and the lower carrier density of the lower channel, the latter will become more strongly confined than the upper one.

As discussed in Refs. [4] and [5], the (re-scaled) peak distance in the dI/dV_b characteristics of Figure 2 (b) approximately equals twice the subband spacing of the lower (collector) GaAs-AlGaAs junction. The smaller subband spacing of the upper InGaAs channel leads to a superimposed fine structure [5], which cannot be resolved in the present experiment due to the large intrinsic width of the single resonances.

The following Figure 4 (a) shows the subband spacing of the lower channel, estimated in this way, as a function of central gate voltage. Solid and open symbols were determined from different pairs of peaks of the 1D-1D tunneling features in Fig. 2 (b). The subband energy is found to be tunable from effectively zero to up to 6 meV. The apparent saturation of the energy values for the highest central gate voltages is due to the fact that in the pinch-off regime ($V_{CG} \geq -1$ V) of the device the bias axis does no longer scale linearly.

We simulated the electrostatics of the confinement using a simple model calculation based on the considerations of Riege et al. [7]. The sidewall depletion of the etched mesa as well as the doped layers and the two 2DEGs can be approximated by two-dimensional sheets of negative or positive charge, respectively. By summing the various contributions to the electrostatic potential of these charge layers it is easy to obtain a model for the confinement potential of the etched channel. It is also possible to include the effect of the metallic side-gate on the lateral

confinement. Some typical results for the confinement of the lower channel are shown in Figure 4 (b) for different values of V_{CG}.

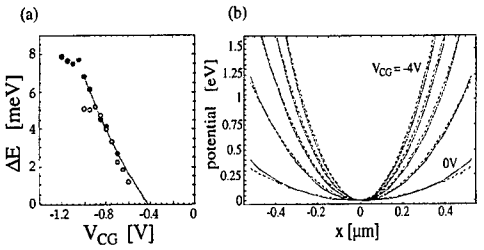

Figure 4 (a) Subband spacing of the lower channel as a function of the central gate voltage. Solid and open symbols were obtained from different pairs of peaks of the 1D-1D tunneling characteristics shown in Figure 2 (b). The solid line is a quadratic fit to the data and serves as a guideline to the eye.
(b) Calculated electrostatic confinement potential (solid lines) together with the best quadratic fit (dashed curves) for various central gate voltages. The calculation is for a device with lithographic width of 1.3 μm of the active region.

Solid curves correspond to the calculated electrostatic confinement for a wire device with a geometrical width of 1.3 μm. Measurements on a device with similar lithographic width gave almost identical results for the tunneling characteristics and the resulting subband spacing as those stated above. Due to the larger width, however, the central gate voltages necessary to achieve a tight confinement of the electron channel, are somewhat higher (pinch-off occurs for the wider device at voltages exceeding V_{CG} = - 4 V). In order to estimate the subband spacing of the calculated confinement potentials we fitted the solid curves of Fig. 4 (b) with a harmonic oscillator potential of the form $V(x) = \frac{1}{2} m^* \omega_0^2 x^2$. The best fits to the calculated potential curves are shown as dashed curves in the figure. The corresponding subband spacings $\hbar\omega_0$ are 3.2 meV at V_{CG} = -1V, 4.1 meV at –2 V, 4.9 meV at – 3 V, 5.5 meV at – 4 V. These values do not take into account self-consistently the presence of the free charge carriers in the two channels (they do take into account, however, the fact that the density of free carriers in the channels is gradually reduced with increasing gate voltage). This means that the calculation overestimates the subband spacing at low central gate voltages, when the carrier density in the channel is not yet considerably reduced. On the other hand the calculated values will represent the correct order of magnitude of the subband energy at the highest gate voltages. In the latter case the carrier density will be sufficiently reduced in order to make self-consistent effects on the true shape of the potential less important. Taking this into account, the calculations are seen to reproduce the observed tuning range of the subband spacing very well. Furthermore, the quadratic fits to the potential curves show that the electrostatic confinement is parabolic to a good approximation, at least for the higher central gate voltages.

[1] J. Wang, P.H. Beton, N .Mori, H. Buhmann, L. Mansouri, L. Eaves, P.C. Main, T.J. Foster and M. Henini, Appl. Phys. Lett. **65**, 1124 (1994)
[2] J.P. Eisenstein, L.N. Pfeiffer and K. West, Appl. Phys. Lett. **57**, 2314 (1990) and Appl. Phys. Lett. **58**, 1497 (1991); K.M. Brown, E.H. Linfield, D.A. Ritchie, G.A.C. Jones, M.P. Grimshaw and M. Pepper, Appl. Phys. Lett. **64**, 1827 (1994)
[3] M.A.Blount, J.A.Simmons, J.S.Moon, W.E.Baca, J.L.Reno and M.J.Hafich, Semicond.Sci.Technol. **13**, A180 (1998); J.S.Moon, J.A.Simmons, M.A.Blount, W.E.Baca, J.L.Reno and M.J.Hafich, Appl.Phys.Lett. **74**, 314 (1999)
[4] G.Ploner, H.Hirner, T.Maier, G.Strasser, J.Smoliner and E.Gornik, Appl. Phys. Lett. **74**, 1758 (1999)
[5] N. Mori, P.H. Beton, J. Wang and L. Eaves, Phys. Rev. B **51**, 1735 (1995)
[6] G.Ploner, PhD thesis, Technische Universität Wien 1998
[7] S.P.Riege, T.Kurth, F.Runkel, D.Heitmann and K.Eberl, Appl. Phys. Lett. **70**, 111 (1997)

PC.43

Huge Magneto-Resistance by Phonon Scattering in Carbon Nanotubes

Hidekatsu SUZUURA and Tsuneya ANDO

Institute for Solid State Physics, University of Tokyo
7-22-1 Roppongi, Minato-ku, Tokyo 106-8666, Japan

The phonon-mediated resistivity in metallic carbon nanotubes is studied based on a continuum model for electrons and phonons. A large magnetoresistance due to the appearance of coupling via a deformation potential is predicted in a high magnetic field.

1. Introduction

Carbon nanotubes (CN's) are quasi-one-dimensional materials made of sp^2-hybridized carbon networks [1] and one third of them become metallic [2]. Transport properties are particularly interesting because of their unique topological structures. The purpose of this paper is to study resistivity of CN's limited by phonons in magnetic fields.

For impurity scattering, it was shown theoretically that there is no backscattering for impurity potentials with a range larger than the lattice spacing in metallic CN's [3,4]. Phonon scattering is another main origin of the resistivity and gives dominant contributions at high temperature. In the absence of a magnetic field, the diagonal energy shift by lattice distortions, usually called the deformation potential, gives no backscattering and the change of local band structure causes a small resistivity.

A magnetic field changes the situation drastically and leads to an appreciable amount of backscattering due to the deformation potential. This leads to increase of the resistivity in a magnetic field, or positive magnetoresistance, in metallic CN's. In this paper, we shall demonstrate this huge positive magnetoresistance by calculating phonon-mediated resistivity using the Boltzmann equation under magnetic fields in the high-temperature limit.

2. Model

Low-energy electronic excitations in CN's are described by a 4×4 matrix $\boldsymbol{k}\cdot\boldsymbol{p}$ equation [5,6] around two Fermi points. In this study, we consider scattering by acoustic phonons with long wavelength and neglect the scattering between the two Fermi points. The $\boldsymbol{k}\cdot\boldsymbol{p}$ equation is reduced to the following 2×2 matrix form in the cylindrical coordinates (r, θ, z),

$$\epsilon \begin{pmatrix} F^A(\theta,z) \\ F^B(\theta,z) \end{pmatrix} = \hbar v_F \begin{pmatrix} 0 & \hat{k}_\theta - i\hat{k}_z \\ \hat{k}_\theta + i\hat{k}_z & 0 \end{pmatrix} \begin{pmatrix} F^A(\theta,z) \\ F^B(\theta,z) \end{pmatrix} \tag{2.1}$$

where $\hat{k}_\theta = -iR^{-1}\partial_\theta + (e/c\hbar)A_\theta$, $\hat{k}_z = -i\partial_z + (e/c\hbar)A_z$, v_F is the Fermi velocity, R is the radius of CN, and $\boldsymbol{A} = (A_\theta, A_z)$ is the vector potential. We use the abbreviation for differential operators as $\partial_\theta = \partial/\partial\theta$, etc. In a magnetic field H perpendicular to the tube axis, electrons on the surface of a CN feel $H_r(\theta) = H\cos\theta$ which is periodic in the circumference direction. This effective magnetic field is given by the vector potential $\boldsymbol{A} = (0, HR\sin\theta)$. The ratio of R and the magnetic length $l = \sqrt{c\hbar/eH}$ characterizes the strength of the magnetic field. A magnetic field parallel to the axis opens the energy gap

in metallic CN's due to the Aharonov-Bohm effect [7], giving rise to a strong modification of transport, but will not be discussed here.

Cylindrical geometry of CN's makes considerable modifications for phonon modes. Here, we introduce the following effective elastic potential for acoustic phonons derived from a microscopic valence-force-field model

$$U[\boldsymbol{u}] = \int R d\theta dz \, \frac{1}{2}\Big[B\big(u_{\theta\theta}+u_{zz}\big)^2 + \mu\big([u_{\theta\theta}-u_{zz}]^2+4u_{\theta z}^2\big)\Big], \tag{2.2}$$

with the displacement vector $\boldsymbol{u} = (u_r(\theta,z), u_\theta(\theta,z), u_z(\theta,z))$ and the strain tensors $u_{\theta\theta} = R^{-1}(\partial_\theta u_\theta + u_r)$, $u_{zz} = \partial_z u_z$, and $2u_{\theta z} = \partial_z u_\theta + R^{-1}\partial_\theta u_z$.

In the infinite R limit, this model describes the zone-folded phonon modes of a two-dimensional isotropic elastic media. Therefore, the parameters B and μ are determined by the sound velocity of transverse and longitudinal acoustic modes in a graphite sheet. It is important that the strain tensors correctly include the coupling between in-plane and out-of-plane deformations for finite R. Two zero modes with regards to translations in the direction perpendicular to the tube axis cannot be reproduced unless the radial displacement is included in a correct manner. Further, a uniform deformation in the radial direction causes in-plane stretching which costs nonzero energy inversely proportional to R corresponding to the appearance of the breathing mode. The present model properly describes such characteristic modes in a cylindrical geometry as well as zone-folded modes of a graphite sheet and shows quite good agreements with the results of a microscopic calculation [8].

In the absence of a magnetic field, only particular phonon modes contribute to the scattering and leads to a resistivity dependent on the chirality of CN at low temperatures [9]. In magnetic fields, various phonons take part in the electron scattering because of nonuniform distribution of the electron wave function along the circumference. Therefore, the correct phonon model is indispensable to the calculation of phonon-mediated magnetoresistance.

Strictly speaking, we should take into account effects of a curvature deformation which gives the k^2 dispersion to the out-of-plane modes in a graphite sheet, where k is the wave vector. Without such effects the model gives many false zero modes corresponding to radial deformation without change in the circumference length of CN. Such effect does not cause any singular effect on the resistivity and gives only a small correction due to the shift of the order of $(a/R)^2$ in the phonon energy, where a is the lattice constant.

Interactions between electrons and acoustic phonons are usually described by a deformation potential appearing as a diagonal energy shift in the $\boldsymbol{k}\cdot\boldsymbol{p}$ equation. There can be an off-diagonal term due to local modification of the band structure caused by acoustic phonons. Within a tight-binding model this can be described by a deformation of a transfer integral between nearest-neighbor sites [10]. The electron-phonon interaction is described by the following matrix Hamiltonian:

$$V_{el-ph} = \begin{pmatrix} g_1\big(u_{\theta\theta}+u_{zz}\big) & g_2 e^{i3\eta}\big(u_{\theta\theta}-u_{zz}+2iu_{\theta z}\big) \\ g_2 e^{-i3\eta}\big(u_{\theta\theta}-u_{zz}-2iu_{\theta z}\big) & g_1\big(u_{\theta\theta}+u_{zz}\big) \end{pmatrix}, \tag{2.3}$$

where η is the chiral angle which is equal to 0 for zigzag nanotubes and $\pi/6$ for armchair nanotubes.

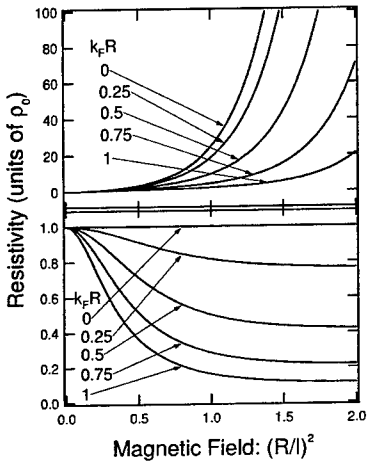

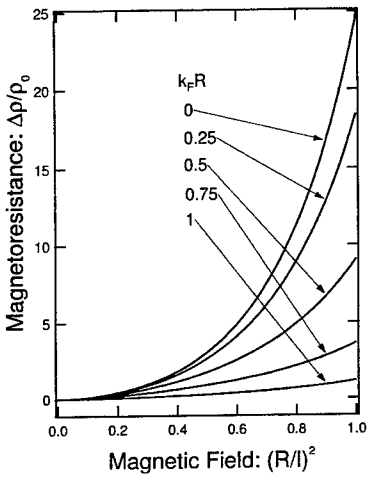

Fig. 1 (left) Resistivity with a fixed electron density in magnetic fields. The upper figure shows contributions from the diagonal deformation potential and the lower shows those from the off-diagonal term for each electron density. The unit ρ_0 is the resistivity at $H=0$.

Fig. 2 (right) Calculated magnetoresistance in a low-magnetic-field region.

We shall calculate the resistivity in the high-temperature regime where phonon scattering is dominant and restrict ourselves to the case that the Fermi level is lower than the bottom of the first excited bands. The electron density is characterized by the Fermi wave number k_F. In the absence of a magnetic field, $k_F=0$ without charge doping and $k_FR=1$ when the Fermi level reaches the first excited bands. In addition, the energy of absorbed or emitted phonons is neglected as it is small compared with that of electrons. Under these conditions, the resistivity limited by phonon scattering is calculated by the Boltzmann transport equation in a similar way for impurity scattering [11].

3. Results

The deformation potential can roughly be estimated to be the Fermi energy in a two-dimensional electron gas [12] and we have $g_1 \simeq 18$ eV from the band width of occupied σ- and π-bands. This value is not different from known values $16 \sim 30$ in graphite [13]. As for g_2, we have $g_2 = (3/4)\gamma_0\beta(\mu/B)$ where $\gamma_0 = 3.03$ eV is a transfer integral and $\beta = \partial \ln \gamma_0 / \partial \ln b$, with b being the bond length. In previous studies [2,12,14], the value of β is located around $2 \sim 3$, which gives $g_1 \simeq 5.4 \sim 8.1$eV. These estimations suggest that g_1/g_2 is at least larger than 2. Therefore, we adopt the ratio $g_1/g_2 = 2$ in the following calculations. The results presented in the following depend only on g_1/g_2 and B/μ. We use $B/\mu = 0.84$ determined by the sound velocity of a graphite sheet.

The upper part of Fig. 1 shows resistivity $\rho(H)/\rho_0$ determined by the diagonal potential g_1, where $\rho_0 = \rho(0)$. Electrons are not backscattered at all in the absence of a magnetic

field but this absence of backscattering disappears in magnetic fields, leading to the huge positive magnetoresistance. This is understood by the analogy with the scattering by the long-range impurity potential [3]. This magnetoresistance decreases with the increase of the charge doping.

On the other hand, the resistivity due to the off-diagonal interaction g_2 is independent of the magnetic field without charge doping ($k_F R = 0$) as shown in the lower part of Fig. 1. With the increase of the charge doping, it starts to exhibit a negative magnetoresistance although its absolute magnitude is smaller than that for the resistivity limited by the diagonal g_1 term. The reduction of scattering in magnetic fields for nonzero k_F for both g_1 and g_2 is caused by the change of the wavefunction at nonzero k_F resulting in the decrease of overlap between the initial and final states [11,15].

Figure 2 shows the total resistance for $g_1/g_2 = 2$ in a low magnetic field regime. The large positive magnetoresistance is apparent particularly for $k_F R = 0$ and decreases gradually with the increase of $k_F R$. The huge positive magnetoresistance predicted here can be observed experimentally in multi-wall CN's. In fact, for CN with $R = 52$ Å, for example, the condition $(R/l)^2 = 1$ is realized in outer shells when $H = 25$ T. For this tube the magnetoresistance reaches about $\Delta\rho/\rho_0 \sim 1.8$ at $H = 10$ T and $\Delta\rho/\rho_0 \sim 25$ at $H = 25$ T.

4. Conclusion

We have studied the resistivity of metallic CN's in a magnetic field. In the absence of charge doping, a huge positive magnetoresistance has been predicted because of the magnetically induced scattering by the diagonal deformation potential. The increase of charge doping reduces the positive magnetoresistance. This phenomena is experimentally observable in large-radius CN's.

Acknowledgments

This work was supported in part by Grants-in-Aid for Scientific Research and for Priority Area, Fullerene Network, from Ministry of Education, Science and Culture, Japan.

References

1. S. Iijima, Nature **354**, 56 (1991).
2. See for example, R. Saito, G. Dresselhaus, and M. S. Dresselhaus, *Physical Properties of Carbon Nanotubes* (Imperial College Press, London, 1998).
3. T. Ando and T. Nakanishi, J. Phys. Soc. Jpn. **67**, 1704 (1998).
4. T. Ando, T. Nakanishi, and R. Saito, J. Phys. Soc. Jpn. **67**, 2857 (1998).
5. H. Ajiki and T. Ando, J. Phys. Soc. Jpn. **62**, 1255 (1993).
6. H. Ajiki and T. Ando, J. Phys. Soc. Jpn. **65**, 505 (1996).
7. H. Ajiki and T. Ando, J. Phys. Soc. Jpn. **62**, 2470 (1993); *ibid.* **63**, 4267 (1994).
8. R. Saito, T. Takeya, T. Kimura, G. Dresselhaus, and M. S. Dresselhaus, Phys. Rev. B **57**, 4145 (1998).
9. H. Suzuura and T. Ando, to be published in the Proceedings of the 10th International Symposium on Intercalation Compounds.
10. L. Pietronero, S. Strässler, H. R. Zeller, and M. J. Rice, Phys. Rev. B **22**, 904 (1980).
11. T. Seri and T. Ando, J. Phys. Soc. Jpn. **66**, 169 (1997).
12. W. A. Harrison, *Electronic Structure and the Properties of Solids* (W. H. Freeman and Company, San Francisco, 1980).
13. B. T. Kelly, *Physics of Graphite* (Applied Science Publishers, Essex, 1981).
14. W. P. Su, J. R. Schrieffer, and A. J. Heeger, Phys. Rev. Lett. **42**, 1698 (1979).
15. T. Ando and T. Seri, J. Phys. Soc. Jpn. **66**, 3558 (1997).

PC.44

Transport through Crossed Nanotubes

M.S. Fuhrer, Andrew K. L. Lim, L. Shih, U. Varadarajan, A. Zettl
and Paul L. McEuen
Department of Physics, University of California at Berkeley and
Materials Sciences Division, Lawrence Berkeley National Laboratory, Berkeley, CA 94720

In order to study the electronic properties of single-walled carbon nanotube junctions we have fabricated several devices consisting of two crossed nanotubes with electrical leads attached to each end of each nanotube. We correlate the properties of the junctions with the properties of the individual nanotubes: metal-metal, metal-semiconductor, and semiconductor-semiconductor junctions are all formed. We find that metal-metal SWNT junctions exhibit surprisingly high conductances of 0.1-0.2 e^2/h. Semiconductor-semiconductor junctions also show significant linear response conductance. Metal-semiconductor junctions behave as p-type Schottky diodes. All the junction types can reliably pass currents of hundreds of nanoamps.

Electron transport experiments have shown that individual single-walled carbon nanotubes (SWNTs) are an ideal system for studying fundamental mesoscopic physics such as single-electron transport[1,2] and Luttinger liquid behavior[3]. Experiments have also demonstrated the utility of SWNTs as nanoscale electronic devices such as field-effect transistors (FETs)[4] and single electron transistors (SETs)[1,2]. Electronic transport measurements on systems of more than one tube could greatly expand upon this base. Multiple-tube devices may prove ideal for constructing experiments to study basic physics such as coupled quantum dots and interacting Luttinger liquids. Moreover, the ability to integrate SWNTs into a device technology may rest upon finding ways to connect them into circuits; the properties of nanotube-nanotube junctions are then essential.

In order to study the properties of SWNT-SWNT junctions we have fabricated devices consisting of two crossed SWNTs with four electrical contacts, one on each end of each SWNT. The devices were fabricated on a backgated substrate consisting of degenerately doped silicon capped with 1μm SiO_2. Cr/Au alignment marks were defined on the SiO_2 surface by electron-beam lithography. The alignment marks consisted of $1\mu m^2$ variously shaped features placed 8μm apart on the substrate, allowing for electrical contacts to be defined in a subsequent lithography with 100nm accuracy over an area of 70μm x 90μm. SWNTs synthesized via laser ablation were ultrasonically suspended in dichloroethane. The suspension was placed on the substrate for approximately 15 seconds, then washed off with isopropanol. An atomic force microscope (AFM) operating in tapping mode was used to locate favorably arranged crossed SWNTs relative to the alignment marks on the substrate. Objects whose height profile was consistent with single SWNTs (≤1.4nm) were preferentially selected, but some devices consisting of small bundles of SWNTs were also fabricated. After locating the desired SWNTs, resist was applied over the substrate, and Cr/Au electrical contacts were fabricated on top of the SWNTs using a standard liftoff electron beam lithography technique. Large bonding pads to

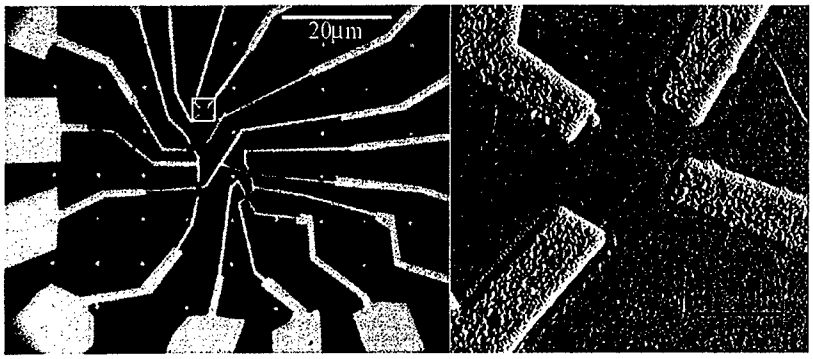

Figure 1. (a) Optical micrograph showing Cr/Au electrical leads to five crossed SWNT devices. (b) Tapping mode AFM image (amplitude signal) of the area indicated by the white box in (a). Two SWNT are evident spanning between the Cr/Au electrodes.

which wires could later be attached were defined in the same lithography step at a lower magnification.

Figure 1 shows a completed device. The optical micrograph (Fig. 1a) shows the Cr/Au metal contacts and leads to five pairs of crossed SWNTs. The original alignment mark pattern can be seen as a regular array of small squares. One pair of crossed SWNTs can be seen in the AFM image (Fig. 1b) of the area denoted by the white box in Fig. 1a.

It is well-known that SWNTs may be metallic or semiconducting depending on their chirality[5-7]. An individual SWNT defined by its circumferential vector (n,m) in terms of graphite lattice units is predicted to be metallic for (n-m)=3i where i is an integer, and semiconducting otherwise. Nominally metallic tubes with n≠m may actually be narrow-gap semiconductors[6], but we will group them here as metals. The two-terminal conductances at room-temperature of individual nanotubes in the devices fall into two general classes of behavior, which have been identified as belonging to metallic and semiconducting SWNTs[4]. Metallic SWNTs have a room temperature linear response conductance which is nearly independent of gate voltage, while semiconducting SWNTs have a room temperature linear response conductance that is strongly gate voltage dependent, becoming conducting at negative gate bias and insulating at positive bias. Figure 2 shows the two-terminal conductances at room temperature as a function of gate voltage of two individual nanotubes making up a crossed-nanotube device. The top trace indicates a conductance which is nearly independent of gate voltage – corresponding

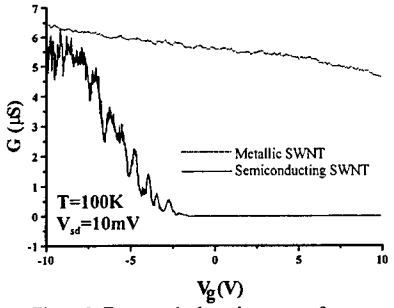

Figure 2. Two-terminal conductances of individual metallic and semiconducting nanotubes as a function of gate voltage.

to a metallic nanotube, while the lower trace shows conduction only for negative gate biases – indicating a semiconducting nanotube. We find we can classify all the individual tubes in our crossed-nanotube devices as metallic or semiconducting according to this scheme. Thus we can divide crossed-SWNT devices into three flavors: metal-metal, metal-semiconductor, and semiconductor-semiconductor. We have observed all three types of crossed-SWNT devices.

With the above technique we have fabricated 10 crossed-tube devices (40 individual electrical contacts to nanotubes) with 38 contacts electrically conducting. The failure of a small percentage of the contacts may represent damage to the devices from electrostatic discharge, or poor alignment during the lithography step. We have also fabricated a number of devices using Ti/Au metal contacts with a lower success rate. Two terminal conductances at room temperature of the metallic SWNT were in the range 400nS to 25 μS; semiconducting SWNT, 1nS to 6μS (at a gate voltage of –10V).

Surprisingly, the two-terminal conductances measured across the junction are often comparable to the two-terminal conductances of the individual SWNT. We use a simple resistor network model (see figure 3) to estimate the junction resistance: the portion of each SWNT (including the contact resistance) on each side of the junction is treated as a single resistor $R_{1\text{-}4}$, and the junction was treated as a single resistor R_J connecting the two SWNT. The six measurable two-terminal conductances of the device can then be used to determine the values of the five resistors in the network. We find junction resistances of metal-metal junctions of 90-360kΩ, corresponding to conductances of 0.07-0.28 e^2/h. This result is surprising, considering that the SWNT-SWNT junction is nearly atomic in size and presumably consists of only weakly (van der Waals) bonded graphite. These conductances are comparable to what is observed for the junctions between the large metal contact pads and the SWNTs, which are a few hundred nanometers in extent. Because of the much larger resistances of the semiconducting tubes, this method was less useful for determining the resistances of semiconductor-semiconductor junctions. However, the largest two-terminal conductance across a semiconductor-semiconductor junction indicates that such junctions may have conductances of greater than 0.02 e^2/h. All three types of SWNT junction are found to reliably pass currents of hundreds of nA.

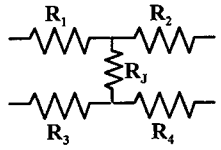

Figure 3. Resistor network model for crossed SWNT devices.

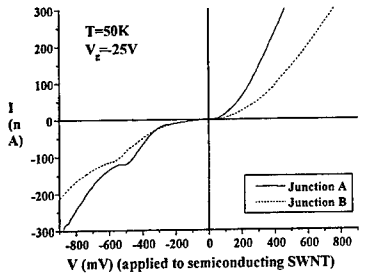

Figure 4. I-V Characteristics of two metal-semiconductor SWNT junctions.

Measured metal-semiconductor junctions show a much smaller linear response conductance of 6-8 x 10^{-4} e^2/h. Beyond linear response, however, the conductance increases, and the current-voltage (I-V) characteristics are asymmetric. Figure 4 shows the I-V curves for two metal-semiconductor junctions measured at 50K. The conductance of each junction is higher for positive bias applied to the semiconducting SWNT, and appears to saturate to a linear behavior with a non-zero x-intercept. This is what is qualitatively expected for a resistor in series with a Schottky diode consisting of a metal in contact with a

p-type semiconductor (semiconducting SWNT are likely doped p-type by contact with the electrodes[4]). The x-intercept of the linear high-bias portion of the curve gives a rough estimate of the Schottky barrier of 150 to 290mV. The reverse-bias conductance of the diode shows a feature at approximately -500 to -600mV. Semiconducting SWNT are observed to have band gaps of 400-900 meV[8-9], so the appearance of this feature ~650-900 mV away from the forward-bias conduction onset may correspond to the alignment of the metal SWNT Fermi level with the conduction band of the semiconducting SWNT.

We have fabricated several devices consisting of a pair of crossed SWNT. We identify metal-metal, metal-semiconductor, and semiconductor-semiconductor junctions. Metal-metal junctions have linear response conductances as large as 0.28 e^2/h. Semiconductor-semiconductor junctions also have significant linear response conductances. Metal-semiconductor junctions act as nanoscale p-type Schottky diodes. The high conductance of SWNT junctions should have bearing on the interpretation of electronic transport in nanotube mats[10-11]. It also suggests that new multiple-SWNT devices may show interesting coherent electron transport effects. In light of the good junction conductances between SWNT, a device technology involving SWNT as devices as well as interconnects is potentially realizable.

References

1. M. Bockrath, D. H. Cobden, P. L. McEuen, N. G. Chopra, A. Zettl, A. Thess and R. E. Smalley, Science **275**, 1922 (1997).
2. S. J. Tans, M. H. Devoret, H. Dai, A. Thess, R. E. Smalley, L. J. Georliga and C. Dekker, Nature **386**, 474 (1997).
3. M. Bockrath, D. H. Cobden, L. Jia, A. G. Rinzler, R. E. Smalley, L. Balents and P. L. McEuen, Nature **397**, 598 (1999).
4. S. J. Tans, R. M. Verschueren and C. Dekker, Nature **393**, 49 (1998).
5. J. W. Mintmire, B. I. Dunlap and C. T. White, Physical Review Letters **68**, 631 (1992).
6. N. Hamada, S. Sawada and A. Oshiyama, Physical Review Letters **68**, 1579 (1992).
7. R. Saito, M. Fujita, G. Dresselhaus and M. S. Dresselhaus, Applied Physics Letters **60**, 2204 (1992).
8. J. W. G. Wildoer, L. C. Venema, A. G. Rinzler, R. E. Smalley and C. Dekker, Nature **391**, 59 (1998).
9. T. W. Odom, J.-L. Huang, P. Kim and C. M. Lieber, Nature **391**, 62 (1998).
10. M. S. Fuhrer, M. L. Cohen, A. Zettl, V. Crespi, Solid State Communications **109**, 105 (1999).
11. G. T. Kim, E. S. Choi, D. C. Kim, D. S. Suh, et al., Physical Review B, **58**, 16064 (1998).

PC.45

Conductance Quantization in the Presence of Huge and Short-Range Potential in Carbon Nanotubes

Takeshi NAKANISHI*, Masatsura IGAMI[1] and Tsuneya ANDO[2]

Institute of Physics and Chemical Research (RIKEN)
2-1 Hirosawa, Wako-shi, Saitama 351-0198, Japan

[1]*Institute of Materials Science, University of Tsukuba*
1-1-1 Tennodai, Tsukuba-shi, Ibaraki 305-8573, Japan

[2]*Institute for Solid State Physics, University of Tokyo*
7-22-1 Roppongi, Minato-ku, Tokyo 106-8666, Japan

Conductance of carbon nanotubes (CN's) with a pair of impurities having a huge and short-range potential is studied within a tight-binding model. When a pair occupies different sublattices, the conductance is given by $2e^2/\pi\hbar$ same as in ideal CN's for a small distance and approaches either $e^2/\pi\hbar$ or 0 with the increase of the distance depending on types of their sites. When a pair occupies same sublattice points, the conductance is either $e^2/\pi\hbar$ or 0 independent of the distance.

* Corresponding author
e-mail: nkns@postman.riken.go.jp, FAX: +81-48-467-5087

1. Introduction

Carbon nanotubes (CN's) are a new kind of quantum wires topologically different from those fabricated at semiconductor heterostructures [1]. They consist of coaxially rolled graphite sheets and their electronic states change critically from metallic to semiconducting depending on their tubular circumferential vector [2-4]. Because of the peculiarity of their geometric and electronic structure, they provide a new kind of quantum wires. The purpose of this work is to study effects of scattering by a pair of vacancies in metallic nanotubes.

Recently, effects of scattering on impurity potential were studied theoretically and it was proved that a Born series for back-scattering vanishes identically for scatters having a potential with a range larger than the lattice constant [5]. This intriguing fact was related to Berry's phase acquired by a rotation in the wave-vector space in the system described by a $\mathbf{k}\cdot\mathbf{p}$ Hamiltonian which is same as Weyl's equation for a neutrino [6]. The conductance was calculated in a tight-binding model by varying the strength of the potential [7].

Effects of scattering by a vacancy in armchair nanotubes in the presence or absence of a magnetic field were also studied [8]. The conductance at the Fermi level (chosen at $\varepsilon = 0$) in the absence of a magnetic field is quantized into zero, one, or two times of $e^2/\pi\hbar$ depending only on the difference between numbers of sites on each sublattice and independent of the shape of the vacancy, when the vacancy is much smaller than the circumference of CN's and closely situated each other.

Some recent experiments suggest the existence of defective nanotubes of carpet-roll or paiermâché forms [9,10]. These systems have many disconnections of the π electron network governing transport of CN's and therefore are expected to exhibit properties different from those in perfect CN's. In fact, effects of topological defects, i.e., five- or seven-member rings, in nanotube junctions were calculated and a universal power-law

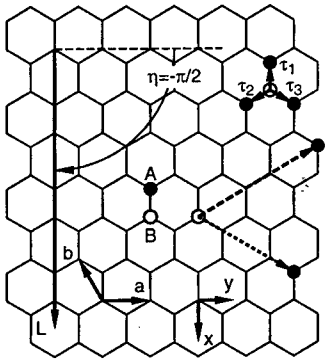

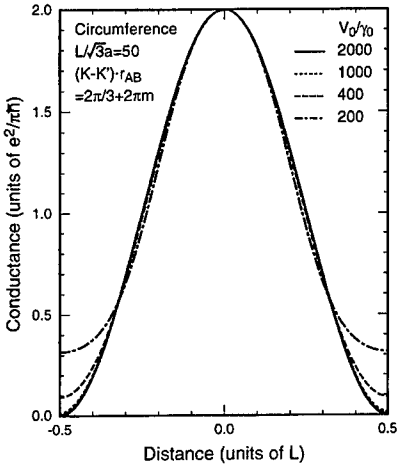

Fig. 1 (left) Lattice structure of two-dimensional graphite sheet.

Fig. 2 (right) Calculated conductance in the presence of a pair of A and B impurity along the circumference direction as a function of their distance d_{AB}.

dependence on the conductance was shown [11-13]. A calculation of the conductance of armchair nanotubes with a single vacancy was also reported [14].

2. Model and Method

Figure 1 shows the structure of a two-dimensional (2D) graphite. A unit cell contains two carbon atoms denoted as A (closed circle) and B (open circle). The coordinate system (x, y) is chosen in such a way that the x axis is in the chiral direction, i.e., the direction along the circumference or the chiral vector $\boldsymbol{L}$, and the y axis in the direction of the axis. In the following, we consider an armchair nanotube with chiral angle $\eta = -\pi/2$. We use a tight-binding model with a nearest-neighbor hopping integral γ_0 and a lattice constant a.

In a 2D graphite, two bands having approximately a linear dispersion cross the Fermi level at K and K' points of the first Brillouin Zone. The wave vectors of the K and K' points are given by $\boldsymbol{K} = (2\pi/a)(1/3, 1/\sqrt{3})$ and $\boldsymbol{K}' = (2\pi/a)(2/3, 0)$. The armchair nanotube is known to be always metallic.

The vacancies are simulated by introducing a large on-site energy V_0 and making $V_0 \to \infty$. This has been shown to be equivalent to actual vacancies where bonds are explicitly disconnected [15]. The method of calculations is same as that in previous studies [7,8,15] and the conductance is calculated by Landauer's formula using a recursive Green's function technique [16]. In the following we shall confine ourselves to the case of $\varepsilon = 0$ and a pair of impurities, which was shown to be most intriguing in a previous study [8].

3. A Pair of Impurities

First, we consider a pair of an A impurity at $\boldsymbol{r}_A$ and a B impurity at $\boldsymbol{r}_B$. Figure 2 shows calculated conductance for impurities located along the circumference direction

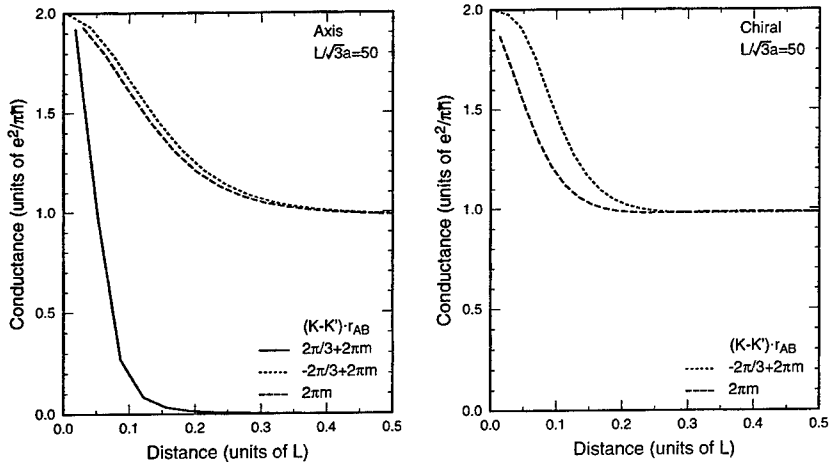

Fig. 3 (left) Calculated conductance in the presence of a pair of A and B vacancy as a function of the distance d_{AB}.

Fig. 4 (right) Calculated conductance in the presence of a pair of A and B vacancy along the chiral direction as a function of the distance d_{AB}.

as a function of their distance $d_{AB} = |\boldsymbol{r}_{AB}|$ with $\boldsymbol{r}_{AB} = \boldsymbol{r}_A - \boldsymbol{r}_B$. The conductance is given by $G \approx 2e^2/\pi\hbar$ close to the ideal value for small d_{AB}, decreases with the increase of d_{AB}, and takes a minimum at $d_{AB} = L/2$ with $L = |\boldsymbol{L}|$. In the limit of a strong scatterer ($V_0/\gamma_0 > 1000$) or a vacancy the minimum value vanishes. The conductance can be fitted to a simple function given by $G \approx [1+\cos(2\pi d_{AB}/L)]e^2/\pi\hbar$ in this case.

Figure 3 shows calculated conductance as a function of d_{AB}, when a pair of A and B vacancies ($V_0/\gamma_0 = 10^8$) is arranged along the axis direction, i.e., $\boldsymbol{r}_{AB} = \tau_3 + n\boldsymbol{a}$ with an integer n. For $n = 3m+1$ (dotted line) and $n = 3m$ (dashed line) with an integer m, the conductance decreases with the increase of d_{AB} and we have $G \approx e^2/\pi\hbar$ for $d_{AB}/L > 0.4$. For $n = 3m-1$ (solid line), the conductance decreases much more rapidly and vanishes for $d_{AB}/L > 0.2$.

Figure 4 shows the conductance as a function of d_{AB} for a pair of A and B vacancies located along helical directions (the dotted and dashed lines in Fig. 1). The conductances decreases with the increase of d_{AB} and approaches a value slightly smaller than $e^2/\pi\hbar$ for $d_{AB}/L > 0.3$. This small deviation from $e^2/\pi\hbar$ decreases rapidly with the increase of the circumference L.

Numerical calculations for various pairs of vacancies show that the conductance is either $\approx e^2/\pi\hbar$ or 0 when the distance becomes of the order of the circumference, depending on the value of the phase factor $\exp[i(\boldsymbol{K}-\boldsymbol{K}')\cdot(\boldsymbol{r}_A - \boldsymbol{r}_B)]$ which is 1, ω, or ω^{-1} with $\omega = \exp(2\pi i/3)$. In fact, we have $G \approx e^2/\pi\hbar$ for pairs satisfying the relation $\exp[i(\boldsymbol{K}-\boldsymbol{K}')\cdot(\boldsymbol{r}_A - \boldsymbol{r}_B)] = 1$ or ω^{-1}. Some examples satisfying the latter and former relation are denoted by the dotted and dashed lines, respectively, in Figs. 3 and 4. We have $G \approx 0$ for pairs with $\exp[i(\boldsymbol{K}-\boldsymbol{K}')\cdot(\boldsymbol{r}_A - \boldsymbol{r}_B)] = \omega$, examples of which are denoted by the solid line in Figs.

2 and 3.

When a pair consists of vacancies located at same type of sublattice points, on the other hand, the conductance is either $e^2/\pi\hbar$ or 0 independent of the distance of vacancies. In fact, for vacancies at $\mathbf{r}_B$ and $\mathbf{r}'_B$ for example, we have $G=e^2/\pi\hbar$ for pairs with $\exp[i(\boldsymbol{K}-\boldsymbol{K}')\cdot(\boldsymbol{r}_B-\boldsymbol{r}'_B)]=1$ and $G=0$ for $\exp[i(\boldsymbol{K}-\boldsymbol{K}')\cdot(\boldsymbol{r}_B-\boldsymbol{r}'_B)]=\omega$ or ω^{-1}.

In contrast to the case of vacancies consisting of different sublattice points, the conductance is exactly given by $e^2/\pi\hbar$ for $\exp[i(\boldsymbol{K}-\boldsymbol{K}')\cdot(\boldsymbol{r}_B-\boldsymbol{r}'_B)]=1$ and there is no deviation depending on the circumference. This is closely related to the fact that the conductance becomes $e^2/\pi\hbar$ for a vacancy consisting of a single A or B atom [8]. The wave function vanishing at a single vacancy $\boldsymbol{r}_B$ is written as $\exp(i\boldsymbol{K}\cdot\boldsymbol{r}_B)-\exp(i\boldsymbol{K}'\cdot\boldsymbol{r}_B)$. This function vanishes also at $\boldsymbol{r}'_B$ when the condition $\exp[i(\boldsymbol{K}-\boldsymbol{K}')\cdot(\boldsymbol{r}_B-\boldsymbol{r}'_B)]=1$ is satisfied. Such a simple interpretation is not possible for a pair of A and B vacancies, however.

4. Summary and Conclusion

We have studied the conductance of CN's with a pair of vacancies. When a pair occupies different sublattices, the conductance is given by $2e^2/\pi\hbar$ same as in ideal CN's for a small distance and approaches either $e^2/\pi\hbar$ or 0 with the increase of the distance depending on types of their sites. When a pair occupies same sublattice points, the conductance is either $e^2/\pi\hbar$ or 0 independent of the distance.

Acknowledgments

This work was supported in part by Grants-in-Aid for Scientific Research and for Priority Area, Fullerene Network, from Ministry of Education, Science and Culture, Japan. One of us (T.N.) thanks the support of a fellowship from Special Postdoctoral Researches Program at RIKEN. One of us (M.I.) thanks the support of a research fellowship of the Japan Society for the Promotion of Science for Young Scientists. Numerical calculations were performed in part at Supercomputer Center, Institute for Solid State Physics, University of Tokyo and at Supercomputer Center, Institute for Molecular Science.

References

1. S. Iijima, Nature (London) **354**, 56 (1991).
2. R. Saito, M. Fujita, G. Dresselhaus, and M.S. Dresselhaus, Phys. Rev. B **46**, 1804 (1992).
3. N. Hamada, S. Sawada, and A. Oshiyama, Phys. Rev. Lett. **68**, 1579 (1992).
4. H. Ajiki and T. Ando, J. Phys. Soc. Jpn. **62**, 1255 (1993).
5. T. Ando and T. Nakanishi, J. Phys. Soc. Jpn. **67**, 1704 (1998).
6. T. Ando, T. Nakanishi, and R. Saito, J. Phys. Soc. Jpn. **67**, 2857 (1998).
7. T. Nakanishi and T. Ando, J. Phys. Soc. Jpn. **68**, 561 (1999).
8. M. Igami, T. Nakanishi, and T. Ando, J. Phys. Soc. Jpn. **68**, 716 (1999).
9. O. Zhou, R. M. Fleming, D. W. Murphy, R. C. Haddon, A. P. Ramirez and S. H. Glarum, Science **263**, 1744 (1994).
10. S. Amelinckx, D. Bernaerts, X. B. Zhang, G. Van Tendeloo, and J. Van Landuyt: Science **267**, 1334 (1995).
11. R. Tamura and M. Tsukada, Phys. Rev. B **55**, 4991 (1997).
12. T. Nakanishi and T. Ando, J. Phys. Soc. Jpn. **66**, 2973 (1997).
13. H. Matsumura and T. Ando, J. Phys. Soc. Jpn. **67**, 3542 (1998).
14. L. Chico, L. X. Benedict, S. G. Louie and M. L. Cohen, Phys. Rev. B **54**, 2600 (1996).
15. M. Igami, T. Nakanishi, and T. Ando, Mol. Cryst. Liq. Cryst. (in press).
16. T. Ando, Phys. Rev. B **44**, 8017 (1991).

PC.46

THEORY OF PLASMA RESONANCE OF 2D WIGNER CRYSTALS ON LIQUID ^{3}He

Hironori MAKABE* and Motohiko SAITOH

Department of Physics, Graduate School of Science, Osaka University
Toyonaka 560-0043, Japan

We report a theoretical analysis of the plasma resonance of quasi-two-dimensional Wigner lattices on liquid ^{3}He by assuming that the ripplon scattering is dominant, and temperature is so low that only a single plasmon is involved in the scattering and the multi-plasmon process is negligible. In our treatment the "modified" Debye-Waller factor of the density-density correlation function which appears in the conductivity formula does not diverge, unlike the ordinary Debye-Waller factor in two dimensions. The calculation shows that the line-width is roughly proportional to the number of the ripplons, or to temperature T, and is in quantitative agreement with the recent experiment by Kirichek *et al.*

1. Introduction

We present here a calculation from first principles of the line-width of the plasmon resonance of two-dimensional Wigner crystals at very low temperature on the basis of the self-consistent harmonic approximation to the Wigner phonon dispersion. It is assummed that the electron scattering is dominated by the ripplons on the surface of liquid ^{3}He.

2. Model and Calculation

We start with the electron-ripplon interaction Hamiltonian given by

$$H_{e-r} = \sum_{\mathbf{R}} \sum_{\mathbf{q}\neq 0} \Gamma_q e^{i\mathbf{q}\cdot(\mathbf{R}+\mathbf{u_R})}(b_{\mathbf{q}} + b^+_{-\mathbf{q}}), \tag{1}$$

where $\mathbf{R}$ and $\mathbf{u_R}$ are the lattice site vector and its deviation from $\mathbf{R}$ of the nth electron, respectively, and Γ_q is the coupling function between electrons and ripplons. The explicit form of the coupling function is given by

$$\Gamma_q^2 = 2\pi\hbar\alpha(q)\Omega_q/Aq^2, \tag{2}$$

where Ω_q the angular frequency of a ripplon with wave vector q, A the surface area of the system, and $\alpha(q)$ is defined as [1,2]

$$\alpha(q) = (eE_\perp + \gamma_q)^2/4\pi\sigma, \tag{3}$$

$$\gamma_q = \frac{\hbar^2 q^2}{2ma_0}\frac{1}{(1-x^2)^{3/2}}\{\ln(\frac{1+\sqrt{1-x^2}}{x}) - \sqrt{1-x^2}\},\ (x = \frac{bq}{2}). \tag{4}$$

Here, $E_\perp$ is the holding electric field perpendcular to the surface, γ_q the polarization field due to bulk liquid ^{3}He, σ the surface tension of liquid ^{3}He, and b is the effective Bohr length

in the presence of the holding field with $a_0(\simeq 8$ nm) the effective Bohr radius at zero holding field.

The dispersion relation of the λth mode of the Wigner phonons can be calculated by minimizing the free energy with respect to the phonon frequencies, which leads to [3]

$$\omega_{\lambda\nu}^2(p) = -\sum_{\mathbf{R}\neq 0}\sum_{\mathbf{q}} V_q e^{i\mathbf{q}\cdot\mathbf{R}}\frac{(\mathbf{q}\cdot\boldsymbol{\epsilon}_\lambda(\mathbf{p}))^2}{m}(1-\cos\mathbf{p}\cdot\mathbf{R})\phi_{\mathbf{q}}(\mathbf{R},0)$$
$$+\sum_{\mathbf{R}}\sum_{\mathbf{q}\neq 0}\Gamma_q^2 e^{i\mathbf{q}\cdot\mathbf{R}}\frac{(\mathbf{q}\cdot\boldsymbol{\epsilon}_\lambda(\mathbf{p}))^2}{m}\int_0^{1/T} d\tau N_q(\tau)(1-\cos\mathbf{p}\cdot\mathbf{R}\cos\nu\tau)\phi_q(\mathbf{R},\tau), \quad (5)$$

where $V_q = (2\pi e^2/Aq)f(q)$ is the Fourier transform of the Coulomb interaction between electrons with $f(q)$ being the form factor subject to the experimental geometry:

$$f(q) = 2\sinh qh\sinh qd/\sinh q(h+d),$$

where h and d are the distances to the anode and to the cathode from the liquid surface, respectively, $\epsilon_\lambda(\mathbf{p})$ the polarization vector of the λth mode phonon with wave vector $\mathbf{p}$, m the electron mass, T the temperature in energy units, $\nu = 2\pi nT$ the Matsubara frequency, $N_q(\tau)$ is the ripplon Green function given by

$$N_q(\tau) = \cosh(\hbar\Omega_q(\tau - 1/2T))/\sinh(\hbar\Omega_q/2T),$$

and $\phi_{\mathbf{q}}(\mathbf{R},\tau)$ is the density-density correlation function defined by

$$\phi_{\mathbf{q}}(\mathbf{R},\tau) = <e^{i\mathbf{q}\cdot\mathbf{u}_{\mathbf{R}}(\tau)}e^{-i\mathbf{q}\cdot\mathbf{u}_0(0)}> = \exp[-\frac{\hbar}{2mN}\sum_{\mathbf{p},\lambda}\frac{(\mathbf{q}\cdot\boldsymbol{\epsilon}_\lambda(\mathbf{p}))^2}{\omega_\lambda(p)\sinh(\hbar\omega_\lambda(p)/2T)}$$
$$\times\{\cosh(\hbar\omega_\lambda(p)/2T) - \cos\mathbf{p}\cdot\mathbf{R}\cosh(\hbar\omega_\lambda(p)(\tau-1/2T))\}], \quad (6)$$

where $\omega_\lambda(p)$ is the angular frequency of the λth mode of the Wigner phonons, N the number of the lattice sites and summation over $\mathbf{p}$ is limited to the first Brillouin zone. The physical meaning of this equation is clear. Namely, the phonon frequency is determined by the product of the second derivative of the sum of the Coulombic and the electron-ripplon interaction potentials, and of the (imaginary) time-dependent density correlation function. Note that the first derivative of the potentials determines the equilibrium positions of the lattice sites. Since the Debye-Waller factor of the density correlation function is a function of the Wigner phonon spectra, the coupled equations (5) and (6) must be solved so that $\omega_\lambda(p)$'s become self-consistent. This scheme is sometimes called the self-consistent harmonic approximation.

To evaluate $\omega_{\lambda\nu}(p)^2$ and $\phi_{\mathbf{q}}(\mathbf{R},\tau)$ the factor $\cos\mathbf{p}\cdot\mathbf{R}$ is approximated to be unity in the integrand of the second integral of (5) and in the exponent of (6), since the wave-vector concerned is very small. The phonon spectrum $\omega_\lambda(p)$ is determined from the solution to $\nu^2 + \omega_{\lambda\nu}(p)^2 = 0$, and is given by

$$\omega_\lambda(p)^2 = \omega_\lambda^{(0)}(p)^2 + N\sum_{\mathbf{G}\neq\mathbf{0}}\frac{\Gamma_G^2}{\hbar\Omega_G}\frac{G^2}{m}\frac{\omega_\lambda^{(0)}(p)^2}{\omega_\lambda^{(0)}(p)^2 - \Omega_G^2}e^{-W(G,T)}, \quad (7)$$

where $\mathbf{G}$ is the reciprocal lattice vector of the Wigner crystal, and $\omega_\lambda^{(0)}(p)$ is the unperturbed phonon frequency of the Wigner crystal:

$$\omega_l^{(0)}(p) = \omega_0 f(p)\sqrt{p/p_0}, \quad \omega_t^{(0)}(p) = \omega_t f(p) p/p_0, \tag{8}$$

Here ω_0 is the longitudinal frequency at the Brillouin zone edge: $\omega_0 = (2\pi e^2 n p_0/m)^{1/2}$ with n the surface density of electrons, $p_0 = (4\pi n)^{1/2}$, and $\omega_t = \xi\omega_0$ with $\xi \simeq \sqrt{2}/4$ [3,4]. The modified Debye-Waller factor is defined by

$$W(G,T) = \frac{\hbar G^2}{4mN} \sum_{\mathbf{p},\lambda} \frac{1}{\omega_\lambda(p)} \tanh \frac{\hbar\omega_\lambda(p)}{4T} \tag{9}$$

where the time-dependent part of $\phi_{\mathbf{q}}(\mathbf{R},\tau)$ has been neglected. The formula (9) is essentially the same as the one obtained by Fisher *et al.* [5], except that they took the form $2W' = (1/2) < (\mathbf{G}\cdot\mathbf{u_0}(0))^2 >$ and needed a cutoff frequency to prevent a divergence. The form (9) does not have such divergence.

3. Resonance width

The line-shape for the plasmon resonance ($\lambda = l$) is expressed in terms of the memory function $M_p(\omega)$ as

$$\sigma(\omega) = \frac{ne^2}{m}\{i\frac{\omega^2 - \omega_l(p)^2}{\omega} + \mathrm{Re}M_p(\omega)\}^{-1}, \tag{10}$$

where $M_p(\omega)$ is an analytic continued function of $(\omega_{\nu\lambda}(p)^2/\nu)$ with $\nu = i(\omega - i\delta)$ [6]. In order to obtain $\mathrm{Re}M_p(\omega)$, the time-dependence of the density-density correlation function is important, and must be incorporated properly. At very low temperature, multi-phonon scattering can be neglected and only a single plasmon scattering process is considered, so that the time-dependent part of $\phi_{\mathbf{G}}(\mathbf{R},\tau = it/\hbar + 1/2T)$ can be expanded to the lowest order in G^2 to obtain

$$\begin{aligned}\mathrm{Re}M_p(\omega) = {} & N\sum_{\mathbf{G}} \frac{\Gamma_G^2}{\hbar\omega}\frac{G^2}{m} \sinh\frac{\hbar\omega}{2T} \mathrm{Re}\int_0^\infty dt e^{-i(\omega - i\delta)t} \frac{\cos\Omega_G t}{\sinh(\hbar\Omega_G/2T)} \\ & \times e^{-W(G,T)}\{1 + \frac{\hbar G^2}{4mN}\sum_{\mathbf{p},\lambda} \frac{\cos\omega_\lambda(p)t}{\omega_\lambda(p)\sinh(\hbar\omega_\lambda(p)/2T)}\}.\end{aligned} \tag{11}$$

After some calculations, the full-width at half-height $\Delta\omega$ is given by

$$\Delta\omega = \mathrm{Re}M_p(\omega_\lambda(p)) = \frac{\pi n T}{4\sigma m^2\omega_t^2\omega} \sum_{\mathbf{G}\neq\mathbf{0}} (eE_\perp + \gamma_G)^2 G^2 e^{-W(G,T)}. \tag{12}$$

4. Comparison with Experiment and Discussion

It is seen from (12) that the collision time $\tau \equiv (\Delta\omega)^{-1}$ is roughly proportional to T^{-1}, since the temperature-dependence of $W(G,T)$ is weak. The factor T comes from the number of ripplons. For ripplons temperatures down to sub mK are still very high, so that the high

temperature approximation is applicable to the Bose factor of ripplons. As for the summation over $\mathbf{G}$, we notice that in ^{3}He the viscosity of ripplon is important [7] and this effectively limits the range of the summation over G up to some cutoff value G_M. Since in our calculation the viscosity or lifetime of ripplons is not explicitly taken into account, G_M is chosen so as to give the best fit to the experiment. Figure 1 shows the comparison between theory and the experiments by Kirichek *et al.* [8], where $M = (G_{\max}/G_0)^2$ for each experiment is taken to be $M = 5, 6$, and 5 for $n = 3.0 \times 10^7, 1.0 \times 10^8$, and 1.4×10^8 cm^{-2}, respectively, with G_0 being the smallest reciprocal lattice vector, $2\pi(2n/\sqrt{3})^{1/2}$. The agreement between theory and experiment is satisfactory and the observed temperature dependence is reproduced over a wide range of T.

Acknowledgement We are grateful to Dr. O.I. Kirichek, Professors K. Shirahama and K. Kono for informative and helpful discussions.

References

* Present Address: Systems Engineering Co., Ltd.
[1] M. Saitoh, J. Phys. Soc. Jpn. **42** (1977) 201.
[2] Yu.P. Monarkha, Sov. J. Low Temp. Phys. **2** (1976) 600.
[3] M. Saitoh, J. Phys. Soc. Jpn. **55** (1986) 1311.
[4] L. Bonsall and A.A. Maradudin, Phys. Rev. **B15** (1977) 1959.
[5] D.S. Fisher, B.I. Halperin and P.M. Platzman, Phys. Rev. Letters **42** (1979) 798.
[6] M. Saitoh, J. Phys. **C15** (1982) 6981.
[7] Yu.P. Monarkha and K. Kono, J. Phys. Soc. Jpn. **66** (1997) 62.
[8] O.I. Kirichek, K. Shirahama and K. Kono, J. Low Temp. Phys. **113** (1998) 1103.

Figure 1. The collision time against temperature for different electron concentrations, and the corresponding theoretical curves, where the cutoff $M = (G_{\max}/G_0)^2$ is taken to be 5, 6, and 5 for $n = 3.0 \times 10^7, 1.0 \times 10^8$, and 1.4×10^8 cm^{-2}, respectively.

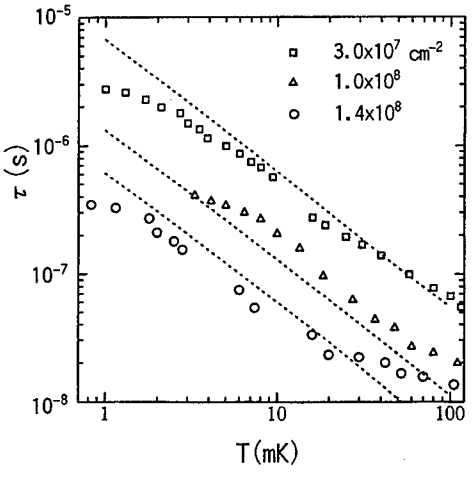

PC.47

Chemical Reaction of Surface State Electrons on Liquid Helium with Atomic Hydrogen

Toshikazu Arai [a,1], Toshiyuki Shiino [a] and Kimitoshi Kono [a]

[a] *Institute for Solid State Physics, University of Tokyo, 7-22-1, Roppongi, Minato-ku, Tokyo, 106-8666, Japan*

Abstract

Chemical reaction in the two dimensional mixture of electrons and atomic hydrogen (H) on the surface of superfluid ^{4}He was observed. With monitoring the conductivity of surface state electrons by Corbino electrode, small amount of H atoms were introduced. Hydrogen destroyed the conductivity signal and we believe it is because of electron capture reaction, $H + e^- \rightarrow H^-$. The reaction rates increased as the temperature decreased and it saturated below 200 mK. This temperature dependence agrees with our analysis which assumes that the chemical process takes place only in the surface state.

Keywords: Surface sate electrons; Atomic hydrogen; Superfluid helium; Electron capture reaction; Negative hydrogen

1. Introduction

A cryogenic atomic hydrogen (H) system shows quantum properties because of its small mass[1]. Since it remains gaseous down to absolute zero temperature, it behaves as a quantum gas. One of the main goals in this field was to achieve Bose-Einstein condensation and it was recently realized in a magnetic trap by MIT group[2]. Another remarkable property is that H atoms are adsorbed on the surface of liquid helium to form a two-dimensional (2D) Bose gas. It forms a 2D quasicondensate at sufficiently high density and low temperature and observation of this state was reported[3].

[1] Corresponding author. E-mail: toshikaz@issa.issp.u-tokyo.ac.jp, Fax: +81-3478-6843, Phone: +81-3478-6811 ex. 5221

Surface state electrons (SSE) also form a 2D system on liquid helium. It provides many interesting properties, such as Wigner solid transition, transport phenomena, etc.[4] Moreover, SSE can serve as a sensitive tool for studying the superfluid helium surface, since the motion of SSE is affected by elementary excitations in underlying liquid[5].

The question we study here is: What occurs when SSE are exposed to H? From the analogy that two H atoms recombine into molecular state at low temperatures[1], we can expect a chemical reaction between H and electron (e^-), $H + e^- \rightarrow H^- + 0.75$ eV, namely, electron capture reaction, on the surface.

The product, negative hydrogen ion H^-, is interesting, because it is very different from other two electron atom/ion, such as He, Li^+, etc. because of the strong repulsive correlation between

two electrons compared to the attractive interaction of electron with the nucleus[6]. H^- has only one bound state[7]. The reaction at low temperature has a purely quantum nature. In addition, it is of great interest whether H^- stays on the surface or penetrate into the bulk liquid. If it floats on the surface, we can obtain a new 2D charge system on liquid helium.

As far as we know, there is no prior work on the mixture of H and e^- or on H^- ion at low temperatures. Since H^- plays important roles in the atmosphere of the Sun or other stars or in accelerators, most of the works have been concentrated on the excited states of H^- and high energy collision between H and e^-[7].

We report here the first experimental study of the 2D H-e^- mixture on the surface of superfluid ^{4}He, at temperatures from 0.1 to 0.4 K. We introduced H atoms to the surface where SSE were prepared. The chemical reaction between H and e^- does take place in the adsorbed phase, we believe it is the electron capture reaction by H.

2. Experimental

In the sample cell, a Corbino electrode is placed to measure the conductivity of the SSE. It is made from copper-coated epoxy plate by etching. The diameters are 25 mm for the outer ring and 17.6 mm for the inner disk. The gap between these two is 0.1 mm. The details and electronics for conductivity measurement are described in ref.[8]. The distance between the upper and lower (Corbino) electrode is 3 mm and the liquid ^{4}He is prepared such that the surface is at 1 mm above the Corbino electrode. SSE are obtained by trapping the thermoelectrons emitted from a tungsten filament. It is important to ignite the filament at about 1.5 K where a certain density of helium vapor exists, in order to reduce the energy of the electrons by collisions with the atoms in the vapor before arriving at the surface. Otherwise, the energetic electrons penetrate into the liquid. A positive DC bias voltage is applied to the Corbino electrode relative to the upper electrode and the guard ring. This voltage creates electric field which holds the SSE at the liquid surface.

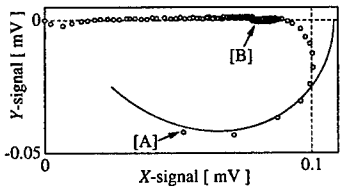

Fig. 1. Argand diagram of the conductivity signal. The open circles represent the measured signal and the solid line shows the calculated curve. The surface was charged at [A] and H atoms were introduced at [B]. The deviation from the solid curve between [A] and [B] is due to the shift of the liquid level in the sample cell during the cooling down process.

H atoms are produced by cryogenic pulsed RF glow discharge, which dissociates H_2 molecules. The dissociator is thermally anchored to the still of the dilution refrigerator, the temperature of which is 0.7 - 0.8 K. A helical resonator tuned at 439 MHz is in the dissociator and its quality factor is $Q = 800$. H atoms are delivered to the sample cell through 0.7 mm i.d. Cu-Ni capillary.

The conductivity signal of Corbino electrode is shown in Fig. 1. The inphase (x) and quadrature (y) output signals of lock-in amplifier are plotted as horizontal and vertical axis, respectively, which is called Argand diagram[8]. The solid line is a calculated curve. As for constant surface charge, the trajectory of the signal moves from the origin (zero conductivity) along the semi-circle to the x axis (large conductivity). A typical signal measured is shown by the open circles. At point [A], the surface is charged at 1.5 K. As the sample cell is cooled down, the trajectory moves along a semi-circle curve toward higher conductivity side. This behavior is interpreted in terms of the scattering of SSE by helium vapor atoms and ripplons[9]. When the sample cell temperature is stabilized at the working temperature, the trajectory stops moving (point [B]). When H atoms are introduced, the sig-

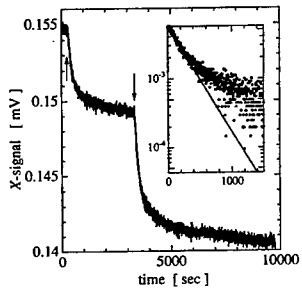

Fig. 2. Decay of SSE signal amplitude due to H atoms. The conductivity signal, which is supposed to be proportional to the number of the SSE, starts to decrease from the time point indicated by arrows when H atoms were supplied into the cell. The inset is the semi-log plot of the signal, which shows that the decay is exponential and the time constant τ is determined from the slope. This data was taken at $T = 0.2$ K.

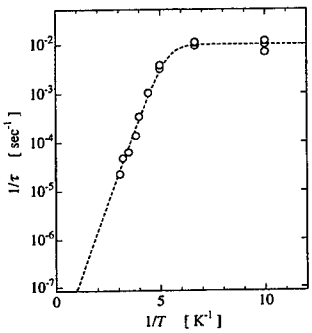

Fig. 3. Arrhenius plot of the decay rate of SSE signal, $1/\tau$. The dashed curve is obtained from the fit to the model described in the text.

nal starts to move along the x-axis toward the origin. If the amount of H is large enough, the signal eventually disappears. This behavior means that the capacitance between the Corbino electrode and the surface charge decreases whereas the conductivity remains high.

We attribute the above behavior to the electron capture reaction which gives rise to the number decay of SSE. We measured the decay rate of SSE after the injection of small amount of H. Fig. 2 is a typical decay curve. The x-signal of the lock-in output is plotted against time. When H atoms are introduced, as pointed by the arrows, the decay starts. By assuming that the x-signal is proportional to the total amount of SSE, we determine the time constant τ from the initial slope of the semi-log plot (the inset of Fig. 2).

The $1/\tau$ is plotted as a function of inverse temperature in Fig. 3, where the open circles represent the measured points. The lower the temperature is, the faster the reaction and it saturates below 0.2 K ($1/T > 5$ K^{-1}). The data can be fitted to the model described in the next section, which is shown by the dashed curve in Fig. 3.

3. Discussions

The model for analysis is the following. First, we will make assumptions: The number decreases of both H and e^- are only induced by electron capture reaction. The recombination of H, $H + H \rightarrow H_2$, is much slower and it can be ignored. The reaction occurs only on the surface. According to these assumptions, we obtain the coupled rate equation for the total number of H (N_H) and e^- (N_e),

$$\frac{dN_H}{dt} = \frac{dN_e}{dt} = -KA_c\sigma_H\sigma_e, \qquad (1)$$

where K is the reaction rate constant, A_c is the surface area of the Corbino electrode, σ_H and σ_e are the surface density of H and e^-, respectively. Since the SSE exist only on the Corbino electrode, the reaction occurs in the area of A_c. It should be noted that the loss rates of H and e^- are equal. Since H atoms in the 3D gas phase are in equilibrium with the adsorbed surface state, the surface and the volume density (n_H) of H are related by the adsorption isotherm,

$$\sigma_H = n_H\lambda_{th}e^{\varepsilon_s/k_BT} \qquad (2)$$

where $\lambda_{th} = \left(2\pi\hbar^2/mk_BT\right)^{1/2}$ is the thermal de Broglie wavelength with atomic hydrogen mass m,

ε_a is the adsorption energy of H on liquid ^{4}He surface and T is the temperature. From equations (1) and (2) with $N_H = Vn_H + A\sigma_H$, where A is the whole surface area of the sample cell and V is the cell volume, the rate equation for H becomes

$$\frac{dN_H}{dt} = -\frac{1}{\tau}N_H, \tag{3}$$

with

$$\frac{1}{\tau} = \frac{KN_e}{(V/\lambda_{th}e^{\varepsilon_a/k_BT}) + A}. \tag{4}$$

Since supplied H is much smaller amount compared to N_e, we can consider N_e in eq.(4) independent of time and it is equal to the initial value determined by the pressing electric field. In this work, $N_e(0) = 1.2 \times 10^8$ electrons. We neglect the temperature dependence of K, which is supposed to be weak compared with the exponential dependence in the denominator in eq.(4). Therefore, the solution of the rate equation for e^- is

$$N_e(t) = N_e(0)\left(1 - e^{-t/\tau}\right). \tag{5}$$

We adjusted K and ε_a so as to fit the data and obtained $K = 4.0 \times 10^{-10}$ cm^2/sec and $\varepsilon_a/k_B = 2.5$ K. The dashed curve in Fig. 3 is calculated from eq.(4) using these values. Our model well explains the measured points. We conclude that the chemical reaction takes place on the surface. However, the measured ε_a is significantly larger than the well established value, $\varepsilon_a/k_B = 1.0$ K for H on pure ^{4}He surface[10]. Because our surface is charged with electrons, the interaction of H with the surface may be modified.

We postpone quantitative discussions until future experiment is done because the assumption that the signal amplitude is proportional to N_e is not well established. We are planning to employ the vibrating capacitor electrometer technique, the signal of which is proportional to the surface charge. Application of a strong magnetic field must be interesting. When the electron spin is aligned, the reaction rate is expected to be suppressed because the bound state of H^- is spin singlet.

4. Summary

The 2D mixture of H and e^- on the surface of superfluid ^{4}He was studied experimentally. As H atoms are introduced, the number of e^- started to decrease. From the analysis of the temperature dependence of the decay rate, we conclude that the chemical reaction of H and e^- takes place on the adsorbed surface phase.

Acknowledgement

We thank P. Leiderer, F. I. B. Williams and A. Würl for valuable discussions, K. Shirahama and H. Suto for many advices. This wok is partly supported by Grant-in-Aid for Scientific Research from Monbusho and JSPS.

References

[1] I. F. Silvera and J. T. M. Walraven, in '*Prog. in Low Temp. Phys. vol. X*', edited by D. Brewer, p. 139, 1980

[2] D. G. Fried, T. C. Killian, L. Willmann, D. Landhuis, S. C. Moss, D. Kleppner and T. J. Greytak, Phys. Rev. Lett. **81**, 3811, 1998

[3] A. I. Safonov, S. A. Vasilyev, I. S. Yasnikov, I. I. Lukashevich and S. Jaakkola, Phys. Rev. Lett. **81**, 4545, 1998

[4] '*TWO-DIMENSIONAL ELECTRON SYSTEMS on Helium and other Cryogenic Substrates*', edited by E. Y. Andrei, Kluwer Academic Publishers, Netherlands, 1997

[5] For example, K. Shirahama, O. I. Kirichek and K. Kono, Phys. Rev. Lett. **79**, 4218, 1997

[6] H. A. Bethe and E. E. Salpeter, '*Quantum mechanics of one- and two- electron atoms*', Springer-Verlag, 1957

[7] A. R. P. Rau, J. Astrophys. Astr. **17**, 113, 1996

[8] K. Shirahama and K. Kono, J. Low Temp. Phys. **104**, 237, 1996

[9] P. Leiderer, J. Low Temp. Phys. **87**, 247, 1992

[10] W. N. Hardy, M. D. Hürlimann and R. W. Cline, Jap. J. App. Phys. **26**, 2065, 1987

PC.48

Oscillator Strength of Excitons and Charged Excitons in ZnSe/ZnMgSSe QWs with a 2DEG of Low Density

W. Ossau[1], D.R. Yakovlev[1,2], G. Astakhov[2], V.P. Kochereshko[2], J. Nürnberger[1], W. Faschinger[1], and G. Landwehr[1]

[1]*Physikalisches Institut der Universität Würzburg, Am Hubland, 97074 Würzburg, Germany*
[2]*A.F.Ioffe Physico-Technical Institute, Russian Academy of Sciences, 194021 St.Petersburg, Russia*

We report on reflectivity studies of negatively charged excitons (trions) and exciton states in ZnSe/(Zn,Mg)(S,Se) quantum wells with a two-dimensional electron gas of low density ($n_e < 2\times10^{11}$ cm^{-2}). The radiative damping (i.e. oscillator strength) of the trion states grows linearly with increasing electron concentration. The exciton radiative damping is weakly sensitive to the electron concentration, but we found a strong contribution of exciton-electron scattering processes to the broadening of the exciton resonance. An optical method to determine the electron concentration of diluted 2DEG is developed.

PACS: 71.35.-y, 73.20.Dx, 78.66.Hf, 78.20.Ls
keywords: negatively charged exciton, exciton oscillator strength

The existence of charged exciton complexes (trions) in semiconductors has been predicted by Lampert in 1958 [1]. In analogy to the charged hydrogen ion H^- a negatively charged exciton (X^-), consisting of two electrons and one hole has been suggested. In 1993. Kheng *et al.* reported the observation of a negatively charged exciton state in CdTe-based quantum well (QW) structures with a two-dimensional electron gas (2DEG) of low density [2]. It follows from the calculation of the charged exciton binding energy that this complex is only weakly bound in bulk materials (about 5% of the exciton Rydberg energy), which hinders its experimental observation in 3D systems. However, reducing the dimensionality of the system down to quasi two strongly favors the trion stability and increases its binding energy up to 20÷45% of the Rydberg energy. Therefore, negatively charged excitons have attracted an increasing [3, 4] in recent years.

Being scaled with the exciton Rydberg energy the trion binding energy can be enhanced considerably by a proper choice of the material system. Consequently after studies on GaAs (with an exciton binding energy of 4.2 meV) and CdTe (10 meV) ZnSe (20 meV) was the next step to investigate semiconductors with further enhanced Coulomb interaction. The technique of molecular-beam epitaxy (MBE) is well developed for the growth of ZnSe-based QW structures due to the work on blue-green emitting laser diodes [5]. However, most of the grown laser structures contain (Zn,Cd)Se ternary alloys as QW and ZnSe as barrier materials. In these structures the exciton resonances are broadened significantly due to alloy fluctuations, which makes highly-resolved optical spectroscopy of exciton and trion states very difficult. We are aware of one report on X^- observation with (Zn,Cd)Se/ZnSe QW only [6]. Very recently we reported on the growth of high-quality lattice-matched ZnSe/(Zn,Mg)(S,Se) QWs with an exciton inhomogeneous broadening smaller than 1 meV [7] and on the observation of positively and negatively charged excitons in these QWs [8,9]. In this contribution we report on reflectivity studies of exciton and trion resonances in QWs with different 2DEG concentrations. Furthermore, we demonstrate an optical method to determine the electron concentration of diluted 2DEG avoiding the problem of ohmic contacts on materials with a low conductivity.

Samples under study were grown by molecular-beam epitaxy on (100)-oriented GaAs substrates. We investigated single 80 Å thick ZnSe/$Zn_{0.89}Mg_{0.11}S_{0.18}Se_{0.82}$ QWs with *n*-type modulation doping by Chlorine in the barrier layer (a 30-Å thick doped layer is separated by an

100 Å spacer from the QW). A set of structures with concentrations of the 2DEG (n_e) varying from below 10^{10} cm^{-2} up to 1.5×10^{11} cm^{-2} was grown. Reflectivity spectra detected at low temperature of 1.6 K and in external magnetic fields up to 7.5 T (Faraday geometry) are analyzed.

Fig. 1 shows reflection spectra taken from QW structures with different 2D electron concentrations. For the nominally undoped sample (upper spectrum) there is one strong reflectivity line only which corresponds to the heavy-hole exciton (X) in the QW. In doped samples a new line attributed to the negatively charged exciton (X^-) appears about 4 meV at the low energy side of the exciton reflectivity line. The amplitude of X^- reflection line grows with increasing electron concentration. Simultaneously the amplitude of the exciton reflection line decreases.

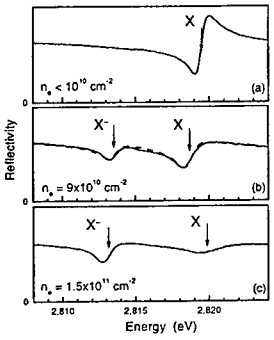

Fig.1 *Reflectivity spectra of 80 Å $ZnSe/Zn_{0.89}Mg_{0.11}S_{0.18}Se_{0.82}$ QWs with different concentrations of the 2DEG. The calculated spectrum is exemplified in (b) by the dashed line. Exciton and trion resonance frequencies are marked by arrows. T = 1.6 K.*

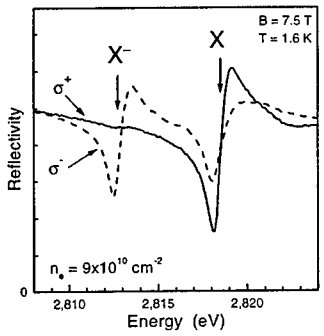

Fig.2 *Reflectivity spectra of an 80 Å $ZnSe/Zn_{0.89}Mg_{0.11}S_{0.18}Se_{0.82}$ QW with $n_e=9\times10^{10}$ cm^{-2} detected for different circular polarizations in a magnetic field of 7.5 T.*

A procedure described in Ref.[10] was used to fit the reflectivity spectra in the frame of the nonlocal dielectric response theory and to deduce excitonic parameters like resonance frequency, radiative damping Γ_0, corresponding to the exciton oscillator strength and the nonradiative damping Γ, which is effected by inhomogeneous broadening and exciton scattering mechanisms. An example of a line fit is shown by the dashed line in Fig.1b.

The strong polarization of the X^- absorption in magnetic fields is a fingerprint of the trion which allows to distinguish clearly the trion resonance from the excitonic one [2]. At 7.5 T the X^- transition in the reflectivity spectra is totally polarized (see Fig.2). Its oscillator strength becomes two times stronger in σ^- polarization, in comparison with the zero field value, and vanishes for σ^+ polarization keeping the integral oscillator strength $\Gamma_0^+(X^-)+\Gamma_0^-(X^-)$=135 μeV constant. The degree of polarization of the trion transition calculated by $P_c=(\Gamma_0^+-\Gamma_0^-)/(\Gamma_0^++\Gamma_0^-)$ is represented in Fig.3 by circles. The equilibrium polarization of a nondegenerate 2DEG, calculated with a Boltzmann distribution for the carriers, $g_e=+1.14$ and T=1.6 K, is traced by the dashed line. The experimental data coincide well with the calculated line at fields above 3.7 T, which evidences that the 2DEG in the QW has a bath temperature of 1.6 K. Deviation from the Boltzmann distribution at low magnetic fields takes place for filling factors $\nu>1$. For these conditions the Fermi-Dirac

statistic is more appropriate to describe the polarization properties of the 2DEG (shown by the solid line). We conclude from Fig.3 that the condition $\nu = 1$ is achieved at a magnetic field strength of 3.7 T. This, in turn, allows us to determine the carrier concentration of the 2DEG $n_e = veB/hc = 9\times10^{10}$ cm^{-2} (details of this optical method of measuring carrier density in QWs will be published elsewhere).

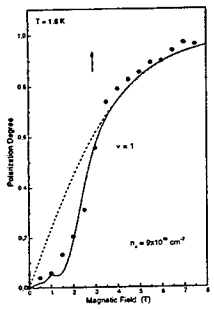

Fig.3 *Polarization degree of the trion resonance in reflectivity as a function of the magnetic field for an 80 Å $ZnSe/Zn_{0.89}Mg_{0.11}S_{0.18}Se_{0.82}$ QW with $n_e = 9\times10^{10}$ cm^{-2}: circles are experimental data and lines represent the calculation based on the Fermi distribution (solid line) and the Boltzmann distribution (dashed) with $g_e = +1.14$ at T=1.6 K.*

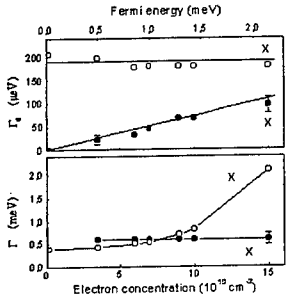

Fig. 4 *Dependence of the radiative (Γ_0) and nonradiative (Γ) damping of exciton and trion transitions on the 2DEG concentration in 80 Å $ZnSe/Zn_{0.89}Mg_{0.11}S_{0.18}Se_{0.82}$ QWs. Lines are guide to the eye. T=1.6 K.*

In contrast to the exciton the radiative damping of the trion depends strongly on the magnetic field strength. The radiative damping increases in σ^- circular polarization and decreases in σ^+. This dependence reflects the fact that the trion ground state is a singlet. Therefore, the polarization of the trion transition should follow the polarization of the electron gas in magnetic fields. Therefore, we can use this polarization to determine the 2D electron concentration. In Fig.4 circles represent the experimental dependence of the polarization degree for the trion line for samples with different electron concentrations. In the case of low electron concentration $n_e = 6\times10^{10}$ cm^{-2} the degree of polarization of the trion line can be described by a Boltzmann distribution for the electrons on Zeeman sublevels at 1.6K with an electron g-factor $g_e = +1.15$ (dotted line). A small disagreement between experimental data and the Brillouin function appears at small magnetic fields only. This disagreement increases with increasing electron concentration. For the highest electron concentration ($n_e = 1.5\times10^{11}$ cm^{-2}) the trion line is found to be completely polarized at magnetic fields B<4 T. In order to correctly describe the polarization of the trion line in a degenerate 2DEG we should use the Fermi-Dirac instead of Boltzmann statistics for the calculation of the electron distribution on the Zeeman sublevels (solid line in Fig.4). The fitting of the experimental data with the calculated circular polarization allows us to determine the 2DEG density.

We can use this method to determine the 2DEG density optically. It is particularly important for weakly doped QWs because of the absence of perfect ohmic contacts for such structures which makes direct transport measurements not reliable. However, this determination of the carrier concentration is not possible for very low electron concentration where the electron gas is nondegenerate. Alternatively for these low density structures we can use the linear concentration

dependence of the trion oscillator strength on the electron concentration to determine the carrier density as shown below.

The dependencies of exciton and trion radiative and nonradiative damping versus 2D electron concentration in the QWs are plotted in Fig.4. In the upper panel of Fig.4 one can see that the trion radiative damping increases linearly with the electron concentration. The exciton radiative damping shows no dependence on the electron concentration (the decrease of the amplitude is caused by the broadening of the exciton resonance). The weak decrease of the exciton oscillator strength with the electron concentration may be reasoned in a weak electrostatic field which is created by the asymmetrical doping applied in our structures.

It is shown in the lower panel of Fig.4 that the exciton nonradiative damping increase superlinearly with the electron concentration of the 2DEG. It is obvious to correlate this increase with exciton-electron scattering which increases strongly for higher 2DEG concentrations. We have shown recently that this scattering mechanism is spin-dependent and can be effectively suppressed by external magnetic fields [9].

The trion nonradiative damping, in contrary to that of the exciton, shows no concentration dependence for the structures under study. Taking into account that the trion is a charged particle and should interact with electrons very actively this fact looks very surprising. This result could imply that the main contribution to the trion oscillator strength is caused by a small momentum which is transferred to the excess electron by the exciton that is created by the absorbed photon. A theoretical support of this suggestion is already discussed in the paper of Stebe et al. [11].

In conclusion, a detailed analysis of the reflectivity spectra has been performed for modulation doped ZnSe/(Zn,Mg)(S,Se) quantum well structures. Excitonic and trionic parameters were determined in dependence of the 2DEG carrier density. A linear dependence of the trion radiative damping on the 2D electron concentration is found. Furthermore, a relation between exciton and trion oscillator strength is established and a contactless optical method to determine the density of very diluted 2DEGs is developed.

Acknowledgements - The authors are thankful to E.L.Ivchenko for useful discussions. This work has been supported by the NATO grant HTECH.LG 974702, the Deutsche Forschungsgemeinschaft through SFB 410 and the Russian Foundation for Basic Research (98-02-18219).

References:

[1] M.A. Lampert, Phys. Rev. Lett. 1, 450 (1958).
[2] K. Kheng, R.T. Cox, Y. Merle d'Aubigne, F. Bassani, K. Saminadayar, and S. Tatarenko, Phys. Rev. Lett. 71, 1752 (1993).
[3] G. Finkelstein, and I. Bar-Joseph, Il Nuovo Cimento 17D, 1239 (1995).
[4] R.T. Cox, V. Huard, K. Kheng, S. Lovisa, R.B. Miller, K. Saminadayar, A. Arnoult, J. Cibert, S. Tatarenko, and M. Potemski, Acta Physica Polonica A 94, 99 (1998).
[5] S. Ivanov, A.Toropov, S.Sorokin, T. Shubina, A. Lebedev, P. Kop'ev, Zh. Alferov, H.-J. Luagauer, G. Reuscher, M.Keim, F.Fischer, A.Waag, G.Landwehr, Appl. Phys. Lett. 73, 2104 (1998).
[6] K. Kheng, R.T. Cox, V.P. Kochereshko, K. Saminadayar, S. Tatarenko, F. Bassani, and A. Franciosi, Superlatt. & Microstruct. 15, 253 (1994).
[7] W.Ossau, D.R.Yakovlev, U.Zehnder, G.V.Astakhov, A.V.Platonov, V.P.Kochereshko, J.Nürnberger, W.Faschinger, M.Keim, A.Waag, G.Landwehr, P.C.M.Christianen, J.C.Maan, N.A.Gippius, and S.G.Tikhodeev, Physica B 256-258, 323 (1998).
[8] G.V.Astakhov, D.R.Yakovlev, V.P.Kochereshko, W.Ossau, J.Nürnberger, W.Faschinger, and G.Landwehr, Phys. Rev. B - *in press* (1999).
[9] D.R.Yakovlev, G.V.Astakhov, V.P.Kochereshko, A.Keller, W.Ossau, and G.Landwehr, Proc. 7th Int. Symposium "Nanostructures: Physics and Technology" St.Petersburg, (1999).
[10] E.L. Ivchenko, A.V. Kavokin, V.P. Kochereshko, G.R. Posina, I.N. Uraltsev, D.R. Yakovlev, R.N. Bicknell-Tassius, A. Waag, G. Landwehr, Phys. Rev. B. 46, 7713 (1992).
[11] B.Stebe, E. Feddi, A.Ainane, and F.Dujardin, Phys.Rev. B 58, 9926, (1998)

PC.50

Electron-Plasmon Resonance in Quantum Wells with Inverted Subband Population

Mikhail Kisin[a], Michael Stroscio[b], Gregory Belenky[a] and Serge Luryi[a]

[a] *Department of Electrical Engineering, SUNY at Stony Brook, New York 11794*
[b] *US Army Research Office, PO Box 12211, Research Triangle Park, NC 27709*

Abstract

The inverted order of subband occupation, $n_2 > n_1$, in quantum-well heterostructures designed for the intersubband lasers results in a novel effective relaxation mechanism for nonequilibrium electrons in the lower subband due to emission of the intersubband plasmons. In contrast to the cascade relaxation by phonons and intrasubband plasmons, this one-step scattering process efficiently fills the final states for light-emitting transitions. Resonant screening, which is influenced by the process of intersubband plasmon excitation, leads to downshift and narrowing of the intersubband optical emission spectra.

At low 2D-electron concentrations, the relaxation processes in A_3B_5 quantum wells are determined basically by polar optical phonons. The optical-phonon spectrum of the heterostructure is significantly modified by the presence of the interfaces and includes interface and confined modes. The antisymmetric interface mode, $\hbar\omega_{ph}^{A}$, dominates the intersubband electron relaxation especially under the condition of electron-phonon resonance, $\Delta_{21} \approx \hbar\omega_{ph}^{A}$, when intersubband 2-1 electron transitions are nearly vertical in the momentum space [1]. At the level of electron concentrations $N_s \geq 10^{11}$ cm^{-2} plasmon branches of the spectrum of collective polar excitations become equally important for the electron relaxation [2]. The plasmon spectrum in a quantum well is also modified and consists of low-energy intrasubband and high-energy intersubband excitations [3]. The intersubband plasmon mode, being characterized by an antisymmetric potential distribution, could participate in the intersubband relaxation causing electron intersubband 2-1 transitions with a small momentum transfer q. However, for the normal ordering of subband filling, when most of electrons occupy the lower subband states, $N_s \approx n_1$, $k_1 \leq k_F$, this kind of transition becomes possible only for high-energy electrons in the second subband $\varepsilon_2 \geq \varepsilon_{th} \approx \varepsilon_F + \delta$ because of the up-shift δ of the energy of the intersubband plasmons [4]:

$$\hbar\omega_{pl}^{A+}(q) \approx \Delta_{21} + \delta \; ; \quad \delta(q << k_F) \approx \frac{e^2 N_s S}{\kappa_0 \kappa}. \tag{1}$$

Here S is the depolarization integral, κ is the dielectric constant, and k_F and ε_F are Fermi wave vector and energy.

In a system with normal subband occupation the intersubband plasmon excitation *raises* the ground state energy E_0 by quantum $\hbar\omega_{pl}^{A+}$. On the contrary, the polarization of

the nonequilibrium system with inverse population, $N_s \approx n_2$, leads to the *lowering* of the energy of the initial state by the quantum $\hbar\omega_{pl}^{A-} \approx \Delta_{21} - \delta$, since the intersubband plasmon potential admixes the lower energy states from the first subband to the occupied second subband states. As a result, the scattering process with intersubband plasmon emission in the inverted system must include the intersubband 1-2 electron transition associated with the absorption of the de-excitation energy $\hbar\omega_{pl}^{A-}$. For this scattering process, the initial and final state energies, $E_i = E_0 + \varepsilon_1(k)$ and $E_f = E_0 + \Delta_{21} + \varepsilon_2(\mathbf{k}-\mathbf{q}) - \hbar\omega_{pl}^{A-}(q)$, are related by the conservation law, which imposes the same threshold for the allowed kinetic energy ε_1 of scattered electrons, viz. $\varepsilon_1 \geq \varepsilon_{th} \approx \varepsilon_F + \delta$. In random phase approximation, the state of the inverted system with one excited intersubband plasmon can be represented as $\left|E_0 - \hbar\omega_{pl}^{A-}(q)\right\rangle = \sum F(k)\hat{c}_{1,\mathbf{k}+\mathbf{q}}^{+}\hat{c}_{2,\mathbf{k}}|E_0\rangle$. The expectation value of the first-subband number operator in this state is then $\left\langle \hat{c}_{1,\mathbf{k}}^{+}\hat{c}_{1,\mathbf{k}} \right\rangle = |F(\mathbf{k}+\mathbf{q})|^2$, where the form-factor $F(k)$ obeys the normalization condition $\sum|F(k)|^2 = 1$. This implies an effective increase of the first subband occupation by one electron. Since $q << k_F$ this process fills the bottom states of the first subband - to a good approximation uniformly.

In Figure 1 we show the spectrum of electron excitation in a two-subband system with normal (a) and inverted (b) ordering of subband occupation. The continuum single-particle excitations of the initial state E_0 is represented by shaded regions and the dispersions of intrasubband (11), (22) and intersubband (12), (21) collective excitations are shown by heavy solid lines. Dashed lines illustrate the scattering of an external electron **e** by an intersubband plasmon. In the insets we show electron-electron scattering events which are analogous to the electron-plasmon processes but are ineffective due to electron wave function orthogonality (a) or large momentum transfer (b).

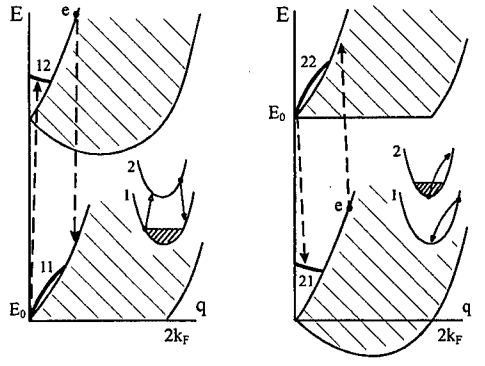

(a) Fig. 1 (b)

Consider now the simplest model of intrasubband relaxation for nonequilibrium high-energy electrons coming to subband 1 from subband 2 after the emission of an optical phonon [5]. We suppose the depopulation time of the first subband, τ_{1out}, be fast enough, so that in a steady state one has $n_1 << n_2$. Then, the electron-plasmon scattering rates are determined essentially by the electron concentration in the second subband, and

the balance equation for the electrons occupying the bottom of the first subband (with partial concentration n_0) can be written in the form

$$\frac{n_0}{\tau_{1out}} = \frac{m}{\pi\hbar^2}\int_{\varepsilon_{th}}^{\Delta-\hbar\omega_{ph}} d\varepsilon_1 \frac{f(\varepsilon_1)}{\tau_{pl}^{(21)}(\varepsilon_1)} \,. \tag{2}$$

Here $f(\varepsilon_1)$ is the electron distribution function in the first subband, normalized as

$$\frac{m}{\pi\hbar^2}\int_{\varepsilon_F}^{\Delta-\hbar\omega_{ph}} d\varepsilon_1 f(\varepsilon_1) = n_1 - n_0; \quad f(\varepsilon_1 < \varepsilon_F) = f_0 \approx \frac{\pi\hbar^2 n_0}{m\varepsilon_F} \,, \tag{3}$$

and $1/\tau_{pl}^{(21)}$ - is the electron scattering rate by intersubband plasmons. In the high-energy region, $\varepsilon_F < \varepsilon_1 < \Delta_{21}$, the distribution function $f(\varepsilon_1)$ is established by optical phonon and intrasubband-plasmon cascade emission and can be approximated by the simple expression:

$$f(\varepsilon_1) \propto \exp\left(-\frac{\Delta_{21} - \hbar\omega_{ph} - \varepsilon_1}{W_{11}\tau_{1out}}\right), \tag{4}$$

where $W_{11} = W_{ph}^{(11)} + W_{pl}^{(11)}$ is the total cascade cooling rate for 1-1 intrasubband relaxation processes. For an exemplary calculation, we consider an infinitely deep quantum well with subband energy separation $\Delta_{21} = 300$ meV and well width $a = 4$ nm. All material parameters correspond to $Ga_{0.47}In_{0.53}As$. The scattering rates, $\tau_{pl,ph}^{-1}$, have been calculated for $T = 0$ K using the dielectric continuum model. Fig. 2 represents the distribution function for the electron population in the first subband calculated for subband depopulation time τ_{1out} = 1 psec and two values of electron concentration n_2: **a** - $1\text{x}10^{11}$ cm^{-2}, **b** - $5\text{x}10^{11}$ cm^{-2}. Two separate groups of electrons are readily seen in the first subband: "cool" electrons in the subband bottom and "hot" electrons in high-energy states characterized by the distribution function (4). The inverted population of the high-energy states is formed by cascade-like emission of optical phonons and intrasubband plasmons, whereas the subband bottom states with $k \le k_F$ are filled mostly due to the one-step events of intersubband plasmon excitation. We would like to emphasize that the latter process effectively fills precisely those states which are

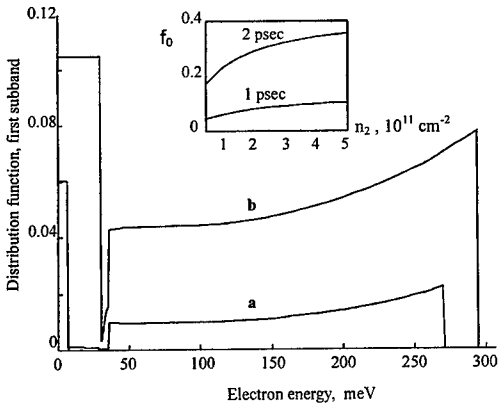

Fig. 2

the final states for light-emitting transitions (states with $k \le k_F$ in the model considered here), restricting to some extent the value of inverted population. This effect becomes more pronounced if the depopulation time increases. The inset in Fig. 2 shows the occupation number f_0 for the bottom states in the first subband as a function of the electron concentration n_2, calculated for two different values of depopulation time τ_{1out}.

The optical characteristics of the quantum well are substantially influenced by the intersubband plasmon spectrum due to the resonant screening of the light-wave field. In a system with normal ordering of the subband occupation this leads to an up-shift in the energy and to substantial narrowing of the intersubband absorption spectrum [6]. Figure 3 shows down-shift and narrowing of the optical gain spectra due to the depolarization effect calculated for the quantum well with inverted subband occupation. Dashed curves represent calculations neglecting the depolarization effect for two values of electron concentration n_2 : **a** - $5\text{x}10^{10}$ cm^{-2}; **b**- $4\text{x}10^{11}$ cm^{-2}. Solid curves labeled with the value of the depopulation time τ_{1out} (in psec) illustrate the influence of the resonance screening and first subband bottom filling on the gain spectrum at $n_2 = 4\text{x}10^{11}$ cm^{-2}. The low-temperature value 1 meV was taken for the polarization dephazing rate in this calculation.

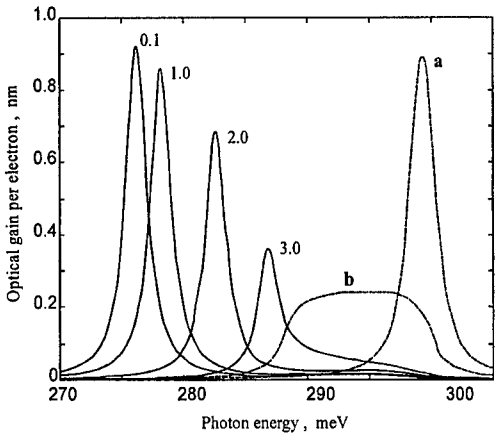

Fig. 3

This work was supported by U.S. Army Research Office under grant DAG55-97-1-0009.

References

1. M.A. Stroscio, G.J. Iafrate, K.W. Kim, M.A. Littlejohn, H. Goronkin, and G.N. Maracas, Appl. Phys. Lett. **59**, 1093 (1991); M. Stroscio, J. Appl. Phys. **80**, 6864 (1996).
2. S. Das Sarma, In *Hot Carriers in Semiconductor Nanostructures*, ed. by J. Shah (Academic, NY), p.53 (1996).
3. L. Wendler and R. Pechstedt, Phys. Status Solidi (b), **141**, 129 (1987).
4. S. J. Allen, D. C. Tsui, and B. Vinter, Solid State Comm. **20**, 425 (1976).
5. V.Gorfinkel, S.Luryi and B.Gelmont, IEEE Journal of Quantum Electronics, **32**, 1995 (1996); M. Kisin, M.A. Stroscio, G. Belenky, S. Luryi, Appl. Phys. Lett. **73**, 2075 (1998).
6. R.J. Warburton, C. Gauer, A. Wixforth, J.P. Kotthaus, B. Brar and H. Kroemer, Superlattices and Microstructures, **19**, 365 (1996).

PC.51

Anomalous hysteretic phenomena in cyclotron resonance spectra of GaAs/AlGaAs quantum well under tilted magnetic fields of short pulse up to 150 T

H. ARIMOTO, N. MIURA
Institute for Solid State Physics, University of Tokyo, 5-1-5, Kashiwanoha, Kashiwa-shi, Chiba 277-8581, Japan

Y. HIRAYAMA, T. SAKU
NTT Basic Research Laboratory, 3-1, Morinosato-Wakamiya, Atsugi-Shi, Kanagawa 243-0198, Japan

We observed a new type of hysteresis in cyclotron resonance spectra of two-dimensional electron gas confined in GaAs/AlGaAs multi quantum wells when we applied high magnetic fields tilted from the growth direction. Pulsed high magnetic fields up to 150 T were generated by the single turn coil technique. We investigated in detail the condition for the occurrence of the hysteresis, that is a disagreement between two traces in up- and down-sweeps of the pulsed magnetic fields. The dependencies of the hysteresis on wavelength, sweep-rate of the fields and temperature has led to a conclusion that the hysteresis is due to inequilibrium states in tilted magnetic fields. The relaxation time from inequilibrium to equilibrium states was revealed to be of the order of microsecond.

In magnetic fields tilted to 2D electrons in quantum wells from the growth direction by an angle θ, the angular dependence of cyclotron resonance (CR) peaks deviates from the so-called $1/\cos\theta$ law, when the Landau level energy spacing $\hbar\omega_c$ is comparable with the subband energy spacing E_{10} [1]. This behavior has been explained by the coupling between the Landau levels belonging to different subbands due to the parallel component of the magnetic field, which is called subband-Landau-level coupling (SLC) [2]. An analytical calculation of the SLC in a parabolic potential well [3] predicts that with increasing θ, a CR peak shifts to higher fields with a θ dependence stronger than the $1/\cos\theta$ law for $E_{10} > \hbar\omega$ (radiation energy), while it shifts to lower fields for $E_{10} < \hbar\omega$. For $E_{10} \approx \hbar\omega$, the SLC occurs resonantly, so we can expect some anomalous behaviors in CR spectra.

In this paper, we report a comprehensive study of hysteretic phenomena in cyclotron resonance (CR) spectra of two-dimensional electron gas under the application of high magnetic fields tilted from the growth direction. As shown in Fig. 1, we observed a reproducible hysteresis for some angles and photon energies. Besides the spin splitting which appears at $\theta = 0°$ or 30° at high magnetic fields, we observed two split peaks in tilted magnetic fields. We will discuss mainly about the stronger absorption peaks. The smaller peaks observed in fields higher than the main peaks will be discussed briefly in the latter part of this paper.

CR experiments were performed in pulsed high magnetic fields up to 150 T generated by the single-turn coil technique [4]. We obtain two traces for up- and down-sweeps of magnetic fields in one shot, and thus can observe a hysteresis between the two traces if any. Wavelengths λ of the radiation were 9.25-10.6 μm (in energy 117-130 meV) by a CO_2

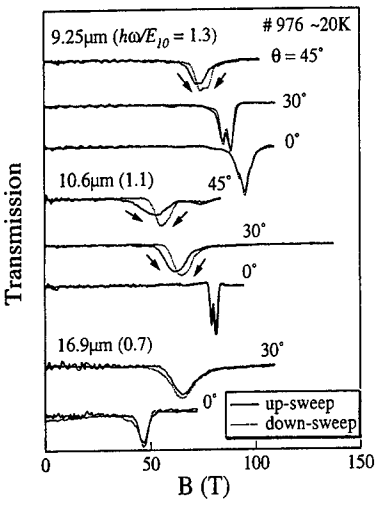

Figure 1: CR traces in ♯976 at λ = 16.9, 10.6 and 9.25 μm at various tilt angles. Temperature is approximately 20 K. The solid lines are traces for the up-sweep and dotted lines are traces for the down-sweep.

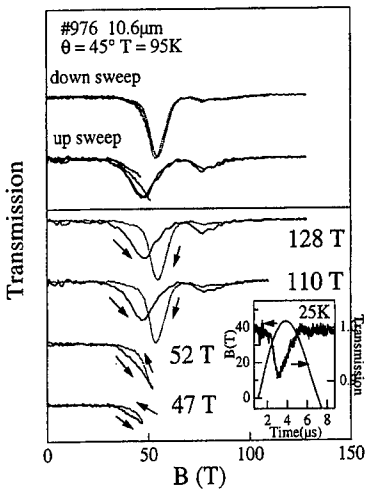

Figure 2: Sweep-rate dependence of CR in ♯976 at λ = 10.6 μm. T $\sim$ 95 K and θ = 45°. In the upper part, spectrum for the up and the down-sweeps are placed at the same offset, respectively. (Inset) Waveforms of magnetic fields and transmission in a maximum field of 43 T at 25 K.

laser and 16.9 μm (74 meV) by an H_2O laser. GaAs/AlGaAs multi quantum wells (40 layers) were grown by molecular beam epitaxy at NTT Basic Research Laboratory. The multi-layer structure was made to gain an absorption intensity and each well is thoroughly independent of each other because of the large barrier width. The well width (nm), Al concentration of barrier layers and electron concentration ($\times 10^{11}$ cm^{-2}) are (10, 0.2, 2.75) for sample ♯972, (10, 0.4, 1.3) for ♯976 and (5, 0.4, 2.3) for ♯981. In this paper, sample ♯976, whose E_{10} is 105 meV and the barrier height is 300 meV from the ground subband, is mainly discussed. The ground and first-excited subbands are completely confined in the well. The barrier height of sample ♯972 is half of that of ♯976. E_{10} is 82 meV and the barrier height is 135 meV from the ground subband. The well width of sample ♯981 is half of that of ♯976 and E_{10} is 156 meV, which is larger than the radiation energy by a CO_2 laser.

Figure 1 shows the angular dependence of CR spectra in ♯976 at λ = 16.9, 10.6 and 9.25 μm. At λ = 16.9 μm, for which $\hbar\omega/E_{10} = 0.7$, the absorption peak shifted to higher fields with no hysteresis. The SLC for a photon energy smaller than E_{10} brings about the shift to higher fields which is stronger than the $1/\cos\theta$ law. At λ = 10.6 μm and 9.25 μm,

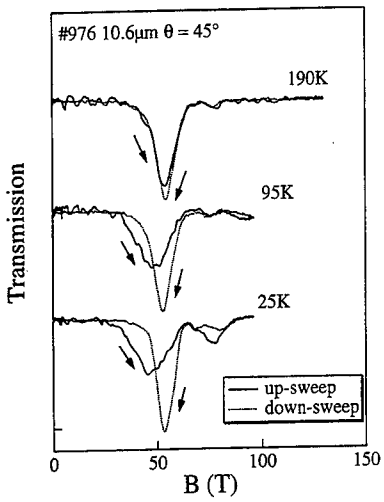

Figure 3: Temperature dependence of CR in ♯976 at 10.6 μm and $\theta = 45°$.

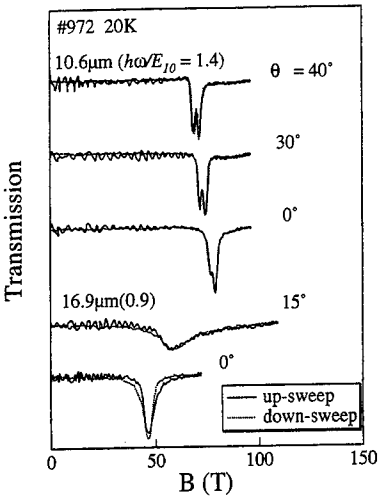

Figure 4: Angular dependence of CR in ♯972 at 10.6 μm and T = 20 K.

a clear disagreement was observed between the two traces for the up- and down-sweeps. The absorption peaks shifted to lower fields and the hysteresis became more prominent with increasing θ. Values of $\hbar\omega/E_{10}$ are 1.1 for $\lambda = 10.6$ μm and 1.3 for $\lambda = 9.25$ μm. The stronger SLC for a photon energy larger than E_{10} brings about the larger shift to lower fields at $\lambda = 10.6$ μm than at 9.25 μm.

The hysteresis is nothing to do with an artifact arising from the detector system or a tilt angular change of the sample by the large Maxwell force. The sharp peaks of spin-split CR at $\lambda = 10.6$ μm and $\theta = 0°$ ensures a sufficiently fast response time of the detector system. A tilt angular change of as large as 15° could make a clear hysteresis. Not shown in this paper, the spin-split CR peak in ♯981 at $\lambda = 10.6$ μm, for which $\hbar\omega/E_{10}$ = 0.7, shifted to higher fields with no hysteresis. This fact excludes the possibility that electrons move to some states outside the barrier, because the Al concentration in the barrier layers is the same and the well width is half in comparison to ♯976. Stronger hysteresis is observed at $\lambda = 10.6$ than at 9.25 μm and the hysteresis is absent at 16.9 μm. This indicates that the resonant SLC at an energy slightly larger than E_{10} is the necessary condition for the hysteresis.

Figure 2 shows the sweep-rate dependence of CR traces at $\lambda = 10.6$ μm, $\theta = 45°$ and T = 95 K in ♯976. All spectra were taken in the same pulse duration ($\sim$5 μs), so the sweep rate is in proportion to the maximum field. No dependence was found in the spectra for the down-sweep, while the absorption intensity decreased with decreasing the sweep rate for the up-sweep. From the above observations, we conclude that the trace

for the down-sweep represents an optical response in equilibrium states, whilst the trace for the up-sweep takes various inequilibrium profiles depending on the sweep rate. This consideration is strongly supported by a good agreement between the absorption peak positions for the down-sweep and the calculation of the CR transition energy in a built-in square well potential. A relaxation process to equilibrium states is clearly observed in the trace of a maximum field of 43 T in the inset of Fig. 2. At the top of the magnetic field, the absorption intensity decreased with a relaxation time of the order of microsecond.

Figure 3 shows the temperature dependence of CR traces at $\lambda = 10.6$ μm and $\theta = 45°$ in ♯976. No dependence was found in the spectra for the down-sweep, while the absorption peak shifted to lower fields with decreasing the temperature for the up-sweep. No hysteresis was observed at 190 K. It seems that with increasing temperature, the relaxation process becomes faster, so the hysteresis disappears at a relatively high temperature of 190 K. These observations exclude a possibility of a temperature rise by the large dB/dt, because the temperature rise should bring a trace for the up-sweep at low temperature close to a trace at a higher temperature.

Figure 4 shows the angular dependence of CR traces at $\lambda = 10.6$ μm and T = 20K in ♯972. As the value of $\hbar\omega/E_{10}$ is 1.4 for 10.6 μm, the spin-split peaks should shift to lower fields as was actually observed. However, we can't observe any hysteresis up to $\theta = 60°$. The large value of $\hbar\omega/E_{10} = 1.4$ may be a reason for the absence of the hysteresis. Another possibility is that the second excited subband, which has a continuous spectrum located about 50 meV above the first excited subband, may suppress the hysteresis.

Concerning the smaller peaks observed in fields higher than the main peaks, we found that the absorption intensity increased with increasing radiation intensity, which indicates that these peaks is due to the absorption of CR excited electrons.

The fact that the long relaxation time of inequilibrium profiles for the up-sweep is in the same order of the pulse duration drives the hysteresis to appear in spectra in pulsed magnetic fields. The origin of inequlibrium profiles in tilted and pulsed high magnetic fields is not clear at this moment. However, such a long relaxation process has not been known in semiconductor quantum wells. The anomalous hysteretic behavior found in the present study should have some relevance to the relaxation phenomena of electrons to the ground state, the change of E_{10} due to the change of the Coulomb potential by electrons, or a formation of a new kind of coupled states.

We thank to Dr. N. Mori of Osaka University for valuable discussions to the theoretical calculation.

References

1. J.H. Crasemann et al., Solid State Commun. **47,** (1983) 917.
2. T. Ando, Phys. Rev. B **19,** (1979) 2106.
3. J.C. Maan, in Two-Dimensional Systems, Heterostructures and Superlattices, Vol. 53 of Springer Series in Solid-State Sciences, ed. G. Bauer, F. Kuchar and H. Heinlich (Springer, Berlin, 1984) pp. 183-191.
4. N. Miura, Physica B **201,** (1994) 40.

PC.52

Strong Resonant Intersubband Magnetopolaron Effect in Heavily Modulation-Doped GaAs/AlGaAs Single Quantum Wells at High Magnetic Fields

Y.J. Wang[1], Y.A. Leem[1], B. D. McCombe[2], X.-G. Wu[3], F.M. Peeters[4], E.D. Jones[5], J.R. Reno[5], X.Y. Lee[6], and H.W. Jiang[6]

[1]National High Magnetic Field Lab at Florida State University, Tallahassee, FL 32310, USA

[2] Department of Physics, State University of New York at Buffalo, Buffalo, NY 14260, USA

[3] National Lab for Superlattices and Microstructures Institute of Semiconductors, Beijing, China

[4] Department Natuurkunde, University of Antwerpen, (UIA), B-2610 Antwerpen, Belgium

[5] Sandia National Laboratories, Albuquerque, NM 87185-0601, USA

[6] Department of Physics and Astronomy, University of California at Los Angels, CA 90095, USA

Electron cyclotron resonance (CR) has been studied in magnetic fields up to 32 T in two heavily modulation-δ-doped GaAs/$Al_{0.3}Ga_{0.7}As$ single-quantum-well samples. Little effect on electron CR is observed in either sample in the region of resonance with the GaAs LO phonons. However, above the LO phonon frequency energy E_{LO} at B > 27 T, electron CR exhibits a strong avoided-level-crossing splitting for both samples at energies close to $E_{LO} + (E_2 - E_1)$, where E_2, and E_1 are the energies of the bottoms of the second and the first subbands, respectively. The energy separation between the two branches is large, reaching a minimum of about 40 cm^{-1} around 30.5 T for both samples. This splitting is due to a three-level resonance between the second LL of the first electron subband and the lowest LL of the second subband plus a LO phonon. The large splitting in the presence of high electron densities is due to the absence of occupation (Pauli-principle) effects in the final states and weak screening for this three level process.

The interaction of electrons with optical phonons in quasi-two dimensional (Q2D) systems has been studied both theoretically [1-5] and experimentally [6-10] for a number of years because of its importance with respect to both device application and fundamental physics of these systems. Recently, due to the availability of sufficient high magnetic fields, new, and interesting phenomena associated with electron-phonon (e-ph) interaction have been observed [11-12]. For polar GaAs/AlGaAs bulk materials, the dominant interaction is between the electrons and longitudinal optical (LO) phonons. For a Q2D system, this interaction (polaron effect) can affect both free electron cyclotron resonance (CR) and intra-band impurity transition. When a pair of unperturbed electron energy levels, e.g., N=0 to N=1 LL, or 1s to 2p+ impurity levels, has energy separation close to E_{LO}, the LO-phonon energy, a two-level resonant magnetopolaron effect occurs. For intra-band impurity transitions, when magnetic field is so high that the energy separation of the $2P^+$ and $2P^-$ states is close to E_{LO}, it has been shown [13] that a three-level magnetopolaron effect occurs. In this case an electron is excited from the ground (1S) state to the $2P^+$ state, which is resonantly coupled to the $2P^+$ state via emission of a LO phonon.

The two-level magnetopolaron effect has been observed in electron CR measurements, but three-level effects in electron CR measurements have not been reported. Recently, our theoretical calculations have predicted that three-level coupling should affect the ECR excitation spectrum greatly at fields high enough to involve the two different subbands in the three-level process. Similar to the impurity system, a three-level resonance should occur when magnetic field is such that the energy difference between a higher LL of the first subband and a lower LL of the second subband is equal to E_{LO} for GaAs. In the electron CR process a free electron is excited from the N=0 LL in the lowest subband (E_1) to the N = 1 LL in the same subband via the electric dipole interaction; the final state of this transition is coupled resonantly via the emission of an LO phonon to the N = 0 LL of the second subband (E_2).

To study this three-level resonant magnetopolaron effect and the effects of a high density of free electrons we have measured electron CR in two heavily modulation-δ-doped GaAs/$Al_{0.3}Ga_{0.7}As$ 240Å single-quantum-well samples in magnetic fields up to 32 T. In the two-level resonant magnetopolaron region ($E_{CR} = E_{LO}$) there is little effect on ECR in either sample. The LL occupation (Pauli-principle) effects and the strong screening of the e-

ph interaction for non-integer filling factors combine to reduce the effective interaction. However, above the GaAs LO phonon frequency at high fields (B > 27 T), electron CR exhibits a very strong avoided-level-crossing splitting for both samples at energies close to $E_{LO} + (E_2 - E_1)$. The splitting between the two branches is large, with a minimum energy separation of about 40 cm^{-1} near 30.5 T for both samples. This splitting is attributed to the three-level resonance discussed above.

Since these two samples are very heavily-doped, occupancy and electron screening effects should be very strong. This is the reason for the absence of an observable direct resonant interaction (two level system) between the electrons and GaAs LO phonons at lower fields and photon energies. For a three-level resonance, the Pauli-principle (occupation effect) plays no role, because the final state is essentially unoccupied - it lies in the next (unoccupied at high fields) subband. In addition, screening is also weak, because the single particle wave functions in the z-direction are orthogonal for the first and second subbands. Therefore the screening of states in the second subband due to electrons in the lowest subband is expected to be weak. This basic physics accounts for the large splitting observed for the three level system and the absence of an observable effect for the two level system.

The far infrared transmission measurements were carried out in the National High Magnetic Field Laboratory at Florida State University. The set-up consists of a Bruker 113v Fourier transform spectrometer in conjunction with a metal light-pipe condensing-cone system (details are given elsewhere [14]), and a 4.2 K silicon bolometer. The temperature of the sample is maintained at 4.2K, and the applied field is up to 32 T. The two GaAs/$Al_{.3}Ga_{.7}As$ single quantum well samples were grown by molecular beam epitaxy at Sandia National Laboratories. The well width for both samples is 240 Å, and both samples are δ-doped with silicon in the barrier with 240 Å set-off distance. The electron densities measured from the quantum Hall effect and longitudinal resistivity are 8.0 x $10^{11}cm^{-2}$, and 8.9 x$10^{11}cm^{-2}$, and the electron mobilities measured at 4.2K are 160,000 cm V sec and 86,000 cm V sec, respectively for samples 1 and 2. The nominal doping concentrations for the two samples are 2 x 10^{12} cm^{-2} and 4 x 10^{12} cm^{-2}, which are very different from the measured electron densities. The possible reason for the discrepancy is that band banding for our samples is very large because of heavily-doping, this can bring the donor level in the barrier down to the chemical potential, leading to some neutral donors in the barrier and causing parallel conduction.

Figure 1 is a plot of the measured electron CR frequency vs magnetic field for the two samples. The solid lines are the calculated single particle electron CR transition frequencies for the N = 0 to N =1 transition (ignoring spin) of the ground subband including non-parabolicity. These calculations do not consider the e-ph interaction. At low magnetic fields, there is no significant deviation from the single particle calculation. At higher

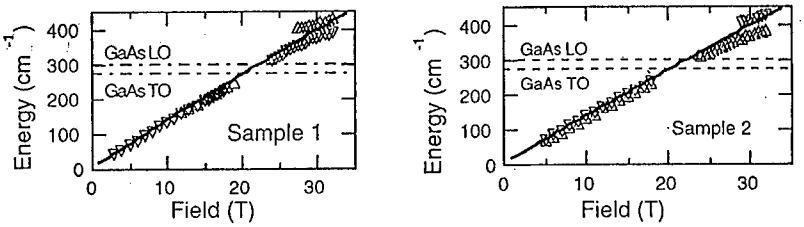

Fig. 1. Summarized experimental CR transition energy vs. field for the two samples. The solid line is the calculated single particle CR transitions including non-parabolicity only.

fields a small splitting is observed, and there is some deviation of one of the two peaks to lower energies when the electron CR energy approaches that of the GaAs LO phonon (e.g. see Fig. 1a) above 10 T. The splitting results from a combination of self-consistent band bending, occupancy of LLs in the second subband in this field region, and non-parabolicity [15]. The deviation of the lower line at fields above 15T may be due to the (two-

level) resonant magnetopolaron effect for a small density of electrons occupying the lowest LL of the second subband in this region. Further detailed analysis is needed to substantiate this assertion. Apart from this effect in the lower density sample, in the region of resonance with the GaAs LO phonons ($E_{CR} = E_{LO}$), little effect on CR is observed in either sample. However, above the GaAs LO phonon frequency at high fields (B > 27 T), electron CR exhibits a very strong avoided-level-crossing splitting for both samples. The pinning frequency is slightly different for the two samples, about 400 cm^{-1} for sample 1, and 395 cm^{-1} for sample 2. The subband separations obtained from our self-consistently calculations are 12.9 mev and 12.2 mev for samples 1 and 2, respectively. The summation of the calculated subband energy and the GaAs LO phonon energy gives rise to a resonant frequency which is almost identical to the pinning frequency observed in the experiment for both samples.

Figure 2 is the raw magnetotransmission spectra for these two samples at 30 T and 32 T. These spectra are normalized magnetotransmission; ratios of a spectrum taken at magnetic field to a spectrum taken at zero field. It is clear that both samples show similar behavior. When the two branches are first observable, the lower

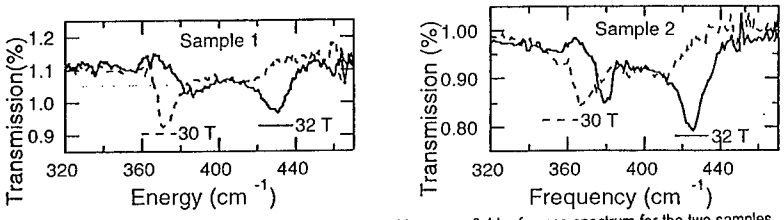

Fig. 2. Transmission spectra at 30 T and 32 T divided by a zero field reference spectrum for the two samples.

energy branch is definitely the dominant one. Above the resonant field, (about 30.5 T) or energy, the upper branch becomes dominant. The lower energy branch loses intensity gradually as the field is increased, while the higher energy branch gains intensity over the same region. This is typical behavior for the resonant magnetopolaron effect.

Several possible origins for this splitting have been considered. Since the resonance region is very close the LO phonon frequency of AlAs, the possibility of this splitting being from the interaction between electron and some kind of AlAs LO-phonon modes has been considered. There are two possible scenarios in which electrons can interact significantly with AlAs LO-phonon modes [11]: 1) electrons in the wells can interact with the AlAs-like slab LO phonons in the barriers via penetration of the electronic envelope function into the barriers, or 2) electrons in the wells can interact with AlAs-like interface phonons which have displacements that exist in the wells. Both scenarios are easily excluded based on arguments similar to those presented in ref. [11] Basically, for such wide well (240 Å) the calculated splittings are very small. As stated previously, we believe that this splitting is due to a three-level resonance between the second LL of the first electron subband and the lowest LL of the second subband plus a LO phonon (at an energy of $E_{LO} + (E_2 - E_1)$). Our self-consistent calculation of electron CR, which includes e-ph interactions and the influence on the e-ph interaction from LL occupancy, electron screening, and band nonparabolicity, has predicted this three-level resonance. However, the large contrast between the substantial energy splitting for the three-level resonance, and the almost non-existent effect in the two-level resonance region was not anticipated. This interesting behavior has been understood based on the fact that electron screening and occupancy effects are very strong in the two level system, and very weak in the three level system. These qualitative arguments account for the large splitting observed for the three level system (with essentially NO splitting observed for the two level system).

To test the above arguments quantitatively, detailed calculations specifically for our two sample structures have been carried out to compare with the experimental results. Details of the general calculation are given in ref. [16]. In the self-consistent subband calculation, the center of the quantum well is taken as the zero of

the Hartree potential, and the δ-doping in the barrier is assumed to be symmetric about the quantum well, each doping spike contributing half of its the electrons to adjacent wells. The conduction band non-parabolicity is taken into account via the simple two-band Kane model. The e-ph interaction and the influence of LL occupancy and screening on it are included in the calculation. The comparison between the calculated results and the

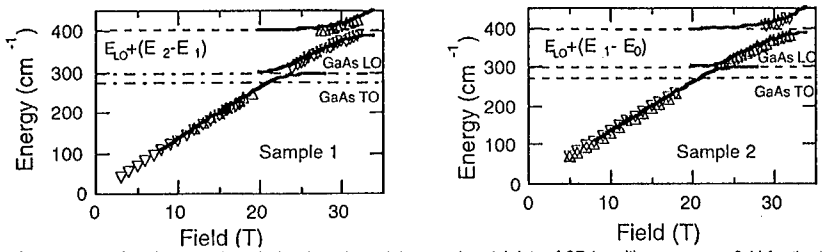

Fig. 3. The comparison between the calculated results and the experimental data of CR transition energy vs. field for the two samples. The calculated solid CR energy curves include non-parabolicity, e-ph interaction, and the influence of LL occupancy and screening effects to the e-ph interaction. The subband energy ($E_2 - E_1$) is calculated self-consistently.

experimental results is shown in Fig. 3. The agreement between the experimental results and theoretical calculations is very good over the entire field region for both samples. This provides quantitative confirmation of the qualitative arguments given above.

We have clearly demonstrated the importance of electron occupation and screening effects for the e-ph interaction. Certain e-ph interaction can be greatly reduced by high electron densities in the system. This effect can be possibly used for making some quantum well devices with high electron densities.

High field measurement was performed at the National High Magnetic Field Laboratory supported by NSF Cooperative Agreement No. DMR-9016241 and by the State of Florida. Sandia is a multiprogram laboratory operated by Sandia Corporation, a Lockheed Martin Company, for the United States Department of Energy under contract DE-AC04-94AL85000. Part of this work is supported by FWO-VI and IUAP (Belgium).

References

[1] S. Das Sarma, Phys. Rev. B **27**, 2590 (1983).
[2] D.M. Larsen, Phys. Rev. B **30**, 4595 (1984).
[3] S. Das Sarma and B.A. Mason, Phys. Rev. B **31**, 5536 (1985).
[4] G.Q. Hai, F.M. Peeters, and J.T. Devreese, Phys. Rev. B **47**, 10358 (1993).
[5] R. Chen, D.L. Lin, and T.F. George, Phys. Rev. B **41**, 1435 (1990).
[6] M. Horst, U. Merkt, and J.P. Kotthaus, Phys. Rev. Lett. **50**, 745 (1983).
[7] W. Seidenbusch, G. Lindemann, R. Lassnig, J. Edlinger, and G. Gornik, Surface Sci. **142**, 375 (1984).
[8] H. Sigg, P. Wyder, and J.A.A.J. Perenboom, Phys. Rev. B **31**, 5253 (1985).
[9] Y.-H. Chang, et al, Phys. Rev. Lett. **61**, 1408 (1988).
[10] M. Ziesmann, D. Heitmann, and L.L. Chang, Phys. Rev. B **35**, 4541 (1987).
[11] Y.J. Wang, et al, Phys. Rev. Lett. **79**, 3226 (1997).
[12] Y.J. Wang, et al, Physica B **256-258**, 292 (1998).
[13] J.P. Cheng, B.D. McCombe, and G. Brozak, Phys. Rev. B **43**, 9324 (1991).
[14] H.K. Ng and Y.J. Wang, Proceedings of the Physics Phenomena at High Magnetic Field – II, edited by Z. Fisk, L. Gor'kov, D. Meltzer, and R. Schrieffer, World Scientific, Singapore, 729 (1995).
[15] S.R. Ryu, et al, Physica B **249-251**, 955 (1998).
[16] F.M. Peeters, et al, Phys. Rev. B **45**, 4296 (1992).

PC.53

Visible light emission from Si/SiO_2 multilayers in planar microcavities

D.J. Lockwood, M.W.C. Dharma-wardana, N. Tit, B.T. Sullivan

Institute for Microstructural Sciences, National Research Council, Ottawa, Canada K1A 0R6

Abstract

Bright quantum-confined photoluminescence (PL) at visible wavelengths can be obtained from ultrathin-layer Si/SiO_2 superlattices. We demonstrate that with the use of an optical resonator the PL peak wavelength and bandwidth can be modified selectively. The strong enhancement and subsequent decrease in the PL intensity in these superlattices with decreasing Si layer thickness has been investigated theoretically. Calculations of the band structure of a Si quantum well separated by crystalline SiO_2 barriers using a tight-binding method reveal that the confined conduction and valence bands along the [001] symmetry direction are essentially dispersionless, are strongly nested, and have a direct band gap character. The enhanced band-edge density of states and the stronger electron-hole interaction across the low-dielectric barriers lead to a competition between several length scales and produce the PL intensity variation with well width observed.

1. Introduction

Efficient light emission from Si-based materials has been sought for some time, as such materials could be incorporated into the devices required by the optoelectronics industry using well-known Si processing technology [1,2]. The fabrication of Si-based light emitting materials has been a very active area of research recently [1,3], stimulated in part by the discovery of intense visible light emission in porous Si (π-Si) formed by the electrochemical etching of Si [4]. Room-temperature photoluminescence (PL) in the visible spectral region was recently observed in thin-layer *amorphous* Si/SiO_2 superlattices (SLs) [5]. The PL peak energy and intensity were found to change rapidly with the disordered Si (d-Si) layer thickness indicating that quantum confinement (QC) was occurring. More recently we have described a method of fabricating such SLs with hundreds of periods using an automated deposition system [6]. The resulting structures have a bright PL at room temperature that is visible to the eye. Here we report on the effect of placing such SLs in a planar optical microcavity. In the theoretical part of this study we use well tested tight-binding methods to determine the electronic structure and optical properties of *crystalline* Si/SiO_2 [001] multilayers and compare the results with experiment.

2. Microcavity photoluminescence

A superlattice was produced (following the method given in Ref. [6]) with 425 periods of Si (~1.6 nm) and SiO_2 (~1 nm) on a cover glass substrate covered with an Al film. A multilayer SiO_2/Nb_2O_5 high-reflectance broad-band coating was later added to part of this sample in the same deposition chamber. The PL of the superlattice was excited with 80 mW of Ar laser light at 457.9 nm.

The PL obtained from the superlattice deposited on the Al-coated glass substrate is shown in Fig. 1. There is a pronounced modulation of the PL intensity with a modulation period of $0.23\pm0.01\ \mu m^{-1}$. The modulation period is consistent with optical interference of the emitted light in the optical cavity formed by the entire d-Si/SiO_2 superlattice. Figure 1 also shows the effect on the PL of adding a multilayer high-reflectance mirror to the superlattice. A number of sharply peaked features are evident at energies that are, in general, different from PL peaks in the uncoated original sample, where clear integral and half-integral wavelength nodes occur. For a superlattice optical thickness of 2000 nm, these nodes are expected at wavelengths of $\lambda=4000/i$ (nm) where $i=1, 2, 3\ldots$, *i.e.,* they occur approximately at λ=800, 670, 570, and 500 nm for i=5, 6, 7, and 8, respectively. The other peaks occur because the mirror stack was very thick (3440/6350 nm metric/optical thickness) compared with the SL, and other optical resonances within the stack and SL together are allowed. By tilting the sample and observing the shifts in the PL peaks with tilt angle, and by comparison with the output mirror transmission, which shows no sharp feature in this wavelength region, it was clear that the 1.8 eV (688 nm) PL peak corresponds to the expected i=6 (3λ) d-Si/SiO_2 cavity resonance. Other PL peaks that can be associated with SL cavity resonances occur at 566 nm ($7\lambda/2$) and 495 nm (4λ) These PL peaks are very sharp, as expected. For example, the 1.8 eV peak has a full width at half maximum of only 17 meV. Furthermore, the red light emitted by this structure is easily seen. In conclusion, these results show that a suitably designed planar microcavity can be used to decrease the bandwidth and selectively tune the peak wavelength of light emission in d-Si/SiO_2 SLs.

3. Theory: Electronic structure and optical properties

The theoretical studies are for the crystalline structure $..AI_{ab}BI_{ba}..$, where A is a layer containing m unit cells of crystalline Si (c-Si) and I_{ab} is an atomically thin interface layer from $A \rightarrow B$. Layer B is made up of n unit cells of c-SiO_2 derived from the β-crystobalite (β-c) structure. The detailed structure of the large-band-gap SiO_2 barrier is not very critical. We have studied a double-bonded oxygen structure, a bridge-bonded structure and a first-principles energy-optimized structure and found very similar results [7,8].

The electronic properties of structures containing many atoms can be conveniently studied via the tight binding (TB) method. Here a minimal basis of atomic functions (*e.g,* s,p^3 functions on each Si atom), which are orthogonalized using Löwdin's method, is used to form linear combinations which diagonalize an effective Hamiltonian. The parameters of the effective Hamiltonian are the TB parameters of the problem. We included nearest-neighbour (NN) as well as next-nearest-neighbour (NNN) interactions within the s,p^3 basis, using the TB parameters of Grosso and Piermarochhi [9] as they reproduce the conduction-band minimum correctly. This is important here since the imposed periodicity along [001] leads to a zone-folding and energy splittings along the ΓX line, which maps to the $Z\Gamma$ line in the tetragonal Brillouin zone. The TB parametrization of LaFemina and Duke is used for β-c, where NN and NNN interactions have been included [10]. In relating the TB parameters of Si-atoms in the Si layers with the Si atoms in the SiO_2 layers, band offsets have to be considered. We use a valence band offset (VBO) of 3.75 eV. If c-Si is replaced by d-Si, the VBO shifts by about 0.25–0.3 eV. The results presented here are unaffected by such shifts of the VBO.

The β-c structure is adopted for the SiO_2 layer because it is cubic and leads to a simple model for the interface. Experiments show that the interface is rather abrupt, contains very few interface states, exhibits a density bulge, and contains all the suboxide charge states Si^{1+}, Si^{2+}, and Si^{3+}. Further, the model must accommodate the large lattice mismatch between c-Si (a_{si}=5.43 Å) and β-c (a_{sio2}=7.14 Å). Following Batra [11], the β-c structure is applied along the *diagonal* of the (001)-surface unit cell of the c-Si layer. In the simplest realistic models of the Si/SiO_2 interface, the atomic arrangement involves one extra oxygen atom that saturates the interface bonds [8]. These models produce a density bulge at the interface and also contain the suboxide charge states Si^{1+} and Si^{2+}, but lack the state Si^{3+}, as is also the case in the energy optimized model [12]. The TB parameters for the Si atom in the interface are the average of the values in c-Si and in β-c. The near-neighbour Si atoms on both sides of the interface feel the presence of the interface. Thus by including, or excluding, the NNN-effects of the interface atoms in the tight-binding calculation, we can effectively obtain two interface models to gauge the robustness of the results to variants of the interface structure. It should be noted that the atoms entirely in the Si layers and in the β-c layers are always treated within the NNN schemes of Refs. [9] and [10].

The energy gap $E_g(m,n)$ as a function of the layer thicknesses m,n for a sequence of $Si_m(SiO_2)_n$ SLs grown along [001] was determined. The layer thicknesses are $L_{si}=ma_{si}$ and $L_{sio2}=na_{sio2}$. As expected, the value of E_g is insensitive to the SiO_2 layer thickness but depends on the thickness of the Si layer. As m increases the QC decreases and E_g tends to that of bulk Si: $E_g(m,1)$ for m=1 to 5 are 2.19±0.61, 1.71±0.34, 1.43±0.18, 1.29±0.13, 1.23±0.10 eV respectively. The E_g variation is $1/L_{si}^2$ for m>4, as was also found experimentally [5]. The confined conduction and valence bands along the ZΓ symmetry direction are essentially dispersonless, show a strongly nested direct band gap character, and contain the minimum energy gap of the system. Thus these SLs have the potential to emit strong PL along the full ZΓ symmetry line. The calculated energy bands are displayed in Fig. 3 of Ref. [7].

The confined Si layers are found to have an increased density of states (DOS) at the band-edges, and the bonding structure at the Si/SiO_2 interfaces seems to enhance their polarizability, as also observed for small semiconductor crystals [13]. A quantity that summarizes the optical properties of a material is the imaginary part of the dielectric constant, $\varepsilon_2(\omega)$. We have calculated $\varepsilon_2(\omega)$ for SLs with (m,n)=(1,1) to (5,1) using our TB approach [8] and the results are shown in Fig. 2. The essential point is that the light-absorption and the emission are shifted to the blue and strongly enhanced when going to thinner and thinner layers. However, the active optical volume in thin layer samples is smaller than in thick layer samples, and hence there is a cross-over in the theoretical optical brightness on going from bulk to thinner and thinner layer samples. This is one of the reasons for the observation of a PL intensity maximum around 1.5–2.0 nm [5]. The oscillator strength of the excitonic recombination process has been calculated for GaAs quantum wells by Brum and Bastard [14] and it shows a similar intensity maximum, but their treatment is not appropriate for ultrathin Si wells. If π-Si contained nanocrystalline Si regions (<3 nm) that incorporated SiO_2 interfaces into some type of self-organized local structure, a mechanism like the one explored here could be operative in the enhanced PL of such Si nanostructures as well.

Acknowledgements

We thank L. Howe, G. Clarke, H.J. Labbé, and J.-M. Baribeau for their help in the fabrication and characterization of the d-Si/SiO_2 superlattices.

References

1. D.J. Lockwood, *Light Emission in Silicon,* Academic Press, Boston, 1997.
2. R.A. Soref, Proc. IEEE 81 (1993) 1687.
3. S.S. Iyer and Y.-H. Xie, Science 260 (1993) 40.
4. A.G. Cullis, L.T. Canham, and P.D.J. Calcott, J. Appl. Phys. 82 (1997) 909.
5. D.J. Lockwood, Z.H. Lu, and J.-M. Baribeau, Phys. Rev. Lett. 76 (1996) 539.
6. B.T. Sullivan, D.J. Lockwood, H.J. Labbé, and Z.H. Lu, Appl. Phys. Lett. 69 (1996) 3149.
7. N. Tit and M.W.C. Dharma-wardana, Solid State Commun. 106 (1998) 121.
8. N. Tit and M.W.C. Dharma-wardana, J. Appl. Phys. 85 (1999) 12059.
9. G. Grosso and C. Piermarochhi, Phys. Rev. B 51 (1995) 16772.
10. J.P. LaFemina and C.B. Duke, J. Vac. Sci. Technol. A 9 (1991) 1847.
11. I. Batra, in *The Physics of SiO_2 and its Interfaces,* edited by T. Pantelides, Pergamon Press, NY, 1978, p. 333.
12. A. Pasquarello, M.S. Hybertsen, and R. Car, Appl. Phys. Lett. 68 (1996) 625.
13. I. Vasiliev, S. Öğüt, and J.R. Chelikowsky, Phys. Rev. Lett. 78 (1997) 4805.
14. J.A. Brum and G. Bastard, J. Phys. C: Solid State Phys. 18 (1995) L789.

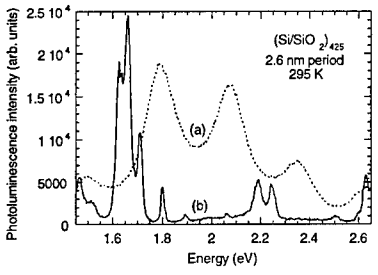

Fig. 1. Comparison of room-temperature PL obtained from the 425-period *d*-Si/SiO_2 superlattice deposited on Al-coated glass (a) before and (b) after addition of a high-reflector multilayer coating.

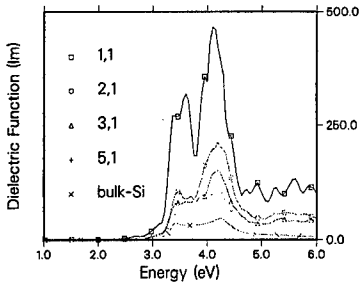

Fig. 2. The imaginary part of the dielectric function for Si slabs containing 1 to 5 unit cells of Si interposed in SiO_2 barriers. The absorption (also, emission) in thin layers is strongly enhanced.

PC.54

SPIN POLARIZATION DEPENDENT OPTICAL TRANSITION RATES OBSERVED IN THE INTEGER QUANTUM HALL REGION

R. Pittini[a,b,*], J.X. Shen[a,b], Y. Oka[a,b], W. Ossau[c], Kai Shum[d]

[a]*RISM, Tohoku University, Katahira 2-1-1, Sendai, 980-8577, Japan and*
[b]*CREST, Japan Science and Technology Corporation, Kawaguchi 332-0012, Japan*
[c]*Physikalisches Institut der Universität Würzburg, Am Hubland, 97074 Würzburg, Germany*
[d]*Electrical Engineering Dep., the City College of the City Univ. of New York, NY 10031, USA*

Abstract

We report on a field dependent photoluminescence (PL) emission rate for the transitions between band states in modulation doped $CdTe/Cd_{1-x}Mg_xTe$ single quantum wells in the integer quantum Hall region. The recombination time observed for the magneto-PL spectra varies in concomitance with the integer quantum Hall plateaus. Furthermore, different PL decay times were observed for the two circular polarizations, i.e. for the transitions between the Zeeman split subbands of the Landau levels. We analyzed the data in comparison with the experimentally determined spin polarization of the conduction electrons and the Zeeman splitting of the valence band. Furthermore, we discuss the relevance of the spin polarization of the conduction electrons, the electron-hole exchange interaction and the spin-flip processes of the hole states for the PL decay time.
Keywords: Modulation doped II-VI heterostructures, time-resolved photoluminescence, quantum Hall effect

1. Introduction

The correlation effects of the electrons and the photo-excited holes are known to affect the photo-luminescence (PL) spectra of a two-dimensional electron gas [1,2]. In particular, oscillations of the PL peak energies and the enhanced Zeeman splittings of the electrons with the magnetic field observed in magneto-PL spectra have been found to be caused by the electron-electron exchange interaction and the Coulomb interaction of the electrons and the photo-excited holes [3]. Furthermore, the effective *g* factor of the electrons in CdTe is four times larger than in GaAs. This condition makes it favorable to find strongly enhanced Zeeman energies of the electrons and the holes in CdTe based materials due to the electron-electron and the electron-hole exchange interactions. Therefore, a giant spin polarization arises whenever the Fermi level is located between the two Zeeman-split states having the same Landau level index. In this work, we focus on the polarization of the PL signal arising from the recombinations of the photo-excited holes with a two-dimensional electron gas and show that the optical interband transition matrix elements depend on the spin. This yields a spin dependent PL recombination time, as can arise in several cases. For example, a spin dependent PL decay time can be observed when (*i*) spin-orbit split states are involved in the optical transitions (for example heavy-hole and light-hole states), or when (*ii*) spin-flip processes deflate the population of a level after the photo-excitation, or when (*iii*) dark excitons (optically inactive) are created, or when (*iv*) special states as skyrmions exist. But here we discuss a situation in which none of these effects is relevant. We discuss a spin-dependent optical interband transition probability from the conduction band to the heavy-hole states in the integer quantum Hall region. In this particular situation, the electronic spin polarization has changed interband transition probability by modifying the Landau orbit of the photo-excited holes through the interband exchange interaction between the conduction and the valence band and by changing the optical weight of the indirect interband transitions for the two spin polarizations of the conduction band.

2. Experimental details

The magneto-PL experiments were performed on modulation doped $CdTe/Cd_{0.74}Mg_{0.26}Te$ single quantum wells (SQWs) with a well width of 60 Å grown by molecular beam epitaxy. A two-dimensional carrier density of 4.5×10^{11} cm^{-2} was achieved in the SQWs by doping the barrier with ZnI_2 [4]. This yields a Fermi energy of 12.1 meV for the two-dimensional electron gas. The mobility of the conduction electrons is 60 000 cm^2/Vs. The sample quality was checked by transport measurements, in which the quantum Hall plateaus could be observed starting from a field of 1 T [5]. All PL experiments were carried out between 1.7 and 2.0 K in fields up to 7.5 T. For the CW

photoluminescence experiments, the sample was excited at 514 nm with the output with an Ar laser with a power below 1 mW/cm^2. For the detection, a 1 m monochromator with a resolution of 0.1 Å was used. For the time-resolved PL experiments, the excitation was carried out at 400 nm with the frequency doubled output of a mode-locked titanium sapphire laser. The pulses were as short as 120-200 fs with a repetition rate of 86 MHz and a pulse energy of 0.13 pJ/cm^2. The PL spectra were detected with 1/4 m spectrometer and time dependence was recorded with a streak camera with a time resolution of 5 ps.

3. Results and discussion

In Fig. 1 we plot the CW magneto-PL spectra taken at 1.7 K in fields of 4.6, 5.2 and 6.4 T for both circular polarizations. For comparison, we show also the PL spectrum taken at zero field. The signal with σ^+ polarization arises from the transition with the selection rule $\Delta m_j = -1$ (m_j is the z-component of the total momentum), while the PL intensity with σ^- polarization arises from the transition with $\Delta m_j = +1$. In zero field, the PL peak is observed at 1.643 eV. This is the average direct band gap in our sample and the band edge fluctuations are as small as 4 meV, as one reads from the low-energy tail of the PL spectrum. On the high-energy side, the PL lineshape shows an additional signal ending with a sharp edge at 1.6525 eV. This is understood to arise from the indirect recombinations from the electronic states up to the Fermi level to the hole states near the center of the Brillouin zone. The enhanced PL intensity at the sharp edge observed at 1.6525 eV indicates the presence of a Mahan exciton at the Fermi level [6]. In a field of 4.6 T, the band edge increases by $(n+1/2)\hbar\omega_{cc} + (m+1/2)\hbar\omega_{cv}$ for the n-th Landau level in the conduction band and the m-th Landau level in the valence band. Here, ω_{cc} and ω_{cv} are the cyclotron frequencies of the conduction and valence bands, respectively. As a consequence, the high-energy side of the PL signal develops into four peaks for both circular light polarizations. We observe the recombinations of the electrons from the first four Landau levels to the holes states of the first Landau level of the heavy-hole valence subband. One shall notice that the Landau level peaks appear only above 1.643 eV (energy of the PL peak observed in zero field), i.e. above the mobility edge of the sample. The different PL spectra observed for the left and right circular light polarizations correspond to the

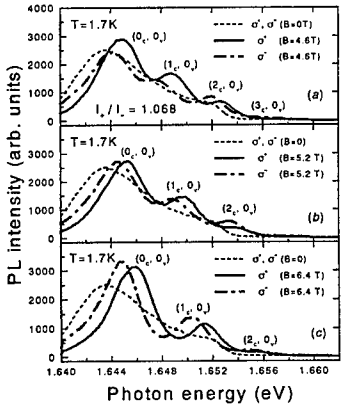

Fig. 1. Magneto-PL spectra of modulation doped CdTe/$Cd_xMg_{1-x}Te$ single quantum wells taken at 1.7 K in zero field and at (*a*) 4.6 T, (*b*) 5.2 T, (*c*) 6.4 T.

recombinations between the same Landau levels of the conduction and valence bands but involve two different Zeeman split subbands of each Landau level. The energy difference between the PL peaks found for the two light polarizations corresponds to the Zeeman splitting of the conduction band states and the heavy-hole states of the valence band plus the difference of the self energies. The energy difference between two adjacent PL peaks observed for each light polarization corresponds to the cyclotron energy of the conduction electrons. The ratio of the integrated PL intensities of the Zeeman split peaks of the same Landau levels (we compare the same Landau level peak measured with the two circular light polarizations) reflects the electronic spin polarization and the hole population of the two Zeeman split heavy-hole subbands.

In Fig. 2 we show the time dependence of the PL signal measured at 2.0 K for 5.25 and 6.5 T. In the inserts, we depict the interband transitions corresponding to the observed polarized PL signal. We found that at 5.25 T both PL polarizations have the same decay time. Instead at 6.5 T the PL signal with σ^- polarization has a 10% slower decay compared to the σ^+ polarization. We have therefore observed a spin dependent decay time of the band states in our material. To achieve a deeper understanding of this phenomenon we evaluated the spin polarization of the conduction electrons (Fig.3.*a*) by taking the experimentally determined

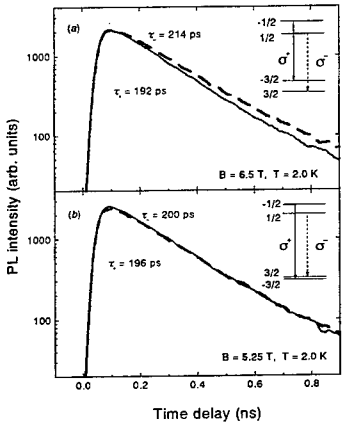

Fig. 2. Time dependence of the PL signal spectrally integrated in the range between 1.63 and 1.66 eV. The experiments were carried out at 2.0 K in (*a*) 6.5 T, (*b*) 5.25 T. The inserts denote the interband transitions between the Zeeman split levels with σ^+ and σ^- polarizations.

position and width of the Landau levels. The occupation of the spin up and down states was then determined by checking the Fermi level crossing of spin split Landau levels. We found that the spin polarization of the conduction band oscillates with the quantum Hall plateaus as does the halfwidth of the Landau levels observed in the PL spectra (Fig. 3.*c*). Furthermore, the Zeeman splitting of the valence band (Fig. 3.*b*) was determined from the polarized PL excitation signal to the Fermi level [7,8]. We observe several zero crossings of the hole Zeeman splitting (one is near 5.2 T) arising from the electron-hole exchange interaction. At 6.5 T, we find a negative hole Zeeman splitting. Therefore, the state $m_j = -3/2$ has higher energy than the state $m_j = 3/2$. In the spin-flip process of the holes, the $m_j = 3/2$ state is deflated. This yields a faster PL decay of the transition with σ^- PL than for the transition with σ^+ polarization. But this is in contrast to our observations (Fig. 2.*a*). We conclude that the spin-flip processes of the holes are not the origin of the observed spin dependent decay time. Instead, we consider other two effects yielding a spin-dependent optical interband transition probability, i.e. *a*) the modification of the Landau orbits by the electron-hole exchange interaction and *b*) the different number of indirect transitions assisted by the emission or absorption of acoustic phonons for the spin-polarized states in the conduction band.

a) The electron-hole exchange interaction modifies the wavefunction of the photo-excited holes and therefore affects the electrical dipole matrix element relevant for the optical interband transition. To estimate the size of this effect, we calculated the hole wavefunction to first order perturbation theory taking the electron-hole exchange interaction as a perturbation acting between the first Landau level of the heavy-hole valence band and up to the first five Landau levels of the conduction band. This modifies the optical transition probability by 5% for both PL polarizations σ^+ and σ^-. But the difference of the σ^+ and σ^- interband transition probabilities is only

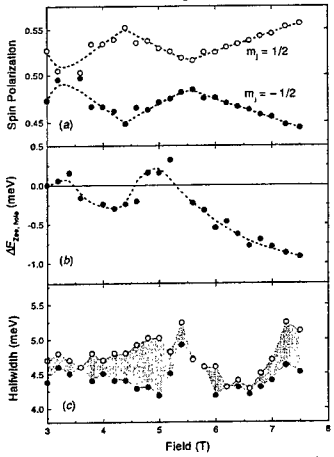

Fig. 3: Field dependences of the (*a*) spin polarization of the conduction band, (*b*) Zeeman splitting of the heavy-hole valence band, (*c*) halfwidth of the Landau levels detetcted from the PL peaks. All values are determined for 2 K. The dashed lines are a guide to the eye.

weakly affected by the electron-hole exchange interaction. Furthermore, we considered the effect of the confinement in the sample growth direction on the electron-hole exchange interaction. In fact, the wavefunction of the lowest level peaks at the center of the quantum well, enhancing the exchange interaction there. This reduces the interband transition probability by only 0.2% and is therefore not relevant for our discussion.

b) The recombination processes accompained by a phonon emission or absorption (indirect optical transitions) yield a much lower PL intensity than the direct transitions. But the transition probability for

the indirect recombinations cannot be neglected when the number of electrons is much larger than the number of holes. In general, the indirect transition rate depends on the momentum of the conduction electrons, in particular when impurity scattering is important [9]. We write the observed transition rate as

$$\left\langle \frac{1}{\tau} \right\rangle_{\mp} = \frac{nM_{\mathrm{dir}}}{N_{\uparrow\downarrow}\tau_{\mathrm{dir}}} + \int_0^{k_{F\uparrow\downarrow}} \frac{(f(k)-n)M_{\mathrm{ind}}}{N_{\uparrow\downarrow}\tau_{\mathrm{ind}}(k)}\,dk$$

for the σ_- and σ_+ polarizations. Here, n is the density of photo-excited holes, $N_{\uparrow\downarrow}$ is the density of up ($\uparrow$) and down ($\downarrow$) spin polarized conduction electrons with Fermi vector $k_{F\uparrow\downarrow}$ and Fermi distribution $f(k)$, M_{dir} and M_{ind} are the probabilities for direct and indirect recombinations, which have the respective transition rates $1/\tau_{\mathrm{dir}}$ and $1/\tau_{\mathrm{ind}}$. For simplicity, we take a k-independent τ_{ind} and we write $M_{\mathrm{dir}} / M_{\mathrm{ind}} = \tau_{\mathrm{ind}} / \tau_{\mathrm{dir}}$ considering the optical transition rate as the transition probability per unit time. From the energy of the excitation pulse we estimate a density of $4\times10^5\mathrm{cm}^{-2}$ for the photo-excited holes and from the data of Fig. 3.*a* we determined $N_\uparrow$ and $N_\downarrow$. With these values, we simulated the field dependence of the relative difference $\Delta\tau/\tau$ for the PL decay times for the σ^- and σ^+ polarizations. The result is shown in Fig. 4.*b* together with the experimental values of $\Delta\tau/\tau$. The difference of the PL decay times has a minimum of nearly zero at the boundary of the filling factor $\nu = 4$ and increases on both sides of this minimum. The model reproduces the experimental data well in spite of the simplifications described above. We remind that the simulated curve contains no fitting parameters. The calculated difference of the PL decay times oscillates with the period of the Landau plateaus and this is also the main trend of the experimental $\Delta\tau/\tau$ data. In addition, the experimental data contain a weaker oscillation, with the half period of the quantum Hall plateaus (Fig. 4). This is believed to originate from the electron-hole exchange interaction.

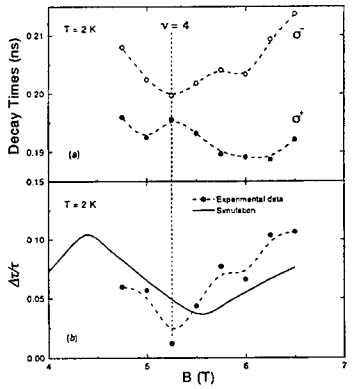

Fig. 4. Field dependence of the (*a*) PL decay times and (*b*) the relative decay time difference for the σ^- and σ^+ polarizations. The solid line is the result of the simulation described in the text.

4. Summary and conclusions

In summary, we observed a spin dependent optical transition probability in modulation doped $CdTe/Cd_{0.74}Mg_{0.26}Te$ SQWs in the integer quantum Hall region. In particular, the PL decay time for the σ^- polarization becomes slower than that of the σ^+ polarization in a field of 6.5 T, while at 5.25 T the PL signal has nearly equal decay times for the two polarizations. This effect cannot be explained by the spin-flip processes of the holes because these would make the decay with the σ^- polarization faster at 6.5 T. Instead, the effect is understood to arise from the spin polarization of the conduction band through the different number of indirect recombinations for the spin up and spin down states. The electron-hole exchange interaction also affects the PL decay times but this effect turns out to have a minor relevance.

References

1. T. Ando, *Series in Solid State Sciences*, vol. 87, Springer, Berlin, 1988, p. 164
2. G.E.W. Bauer and T. Ando, J. Phys. C: Solid State Phys. **19** (1986) 1537
3. S. Katayama and T. Ando, Solid State Comm. **70** (1989) 97
4. A. Waag, F. Fischer, J. Gerschütz, S. Scholl, G. Landwehr, J. Appl. Phys. **75**, 1368 (1994)
5. S. Scholl, J. Gerschütz, F. Fischer, A. Waag, K. Schüll, H. Schaefer, G. Landwehr, Solid State Comm. 94 (1995) 935
6. G.D. Mahan, Phys. Rev. 153 (1967) 882
7. J.X. Shen, W. Ossau, F. Fischer, A. Waag, G. Landwehr, in *23rd Int. Conf. On the Physics of Semiconductors*, vol. 3, Berlin, Germany, 1996, p. 2163
8. J.X. Shen, Y. Oka, W. Ossau, F. Fischer, A. Waag, G. Landwehr, Phys. B **249-251** (1998) 589
9. S.K. Lyo, Phys. Rev. B **40**, 8418 (1989)

PC.55

Coulomb-interaction enhanced dephasing in a two-dimensional electron gas at high magnetic fields

N. Fromer, C. Schüller, and D. S. Chemla
Department of Physics, University of California at Berkeley, and Materials Sciences Division, Lawrence Berkeley National Laboratory, MS 2-300, 1 Cyclotron Road, Berkeley, CA 94720

K. Maranowski and A. C. Gossard
Department of Electrical and Computer Engineering, University of California at Santa Barbara, Santa Barbara, CA 93106

Abstract

We investigate the quantum coherence of two-dimensional electron gases in modulation-doped GaAs-AlGaAs quantum wells in the regime of the integer quantum-Hall effect by means of degenerate four-wave mixing (FWM). We observe oscillations in the decoherence time of the FWM signal dependent on the Landau level filling factor, and we interpret this as evidence for oscillatory screening behavior in the quantum-Hall regime. Furthermore, we observe quantum beats between up to three different Landau level transitions.

Free electrons in modulation-doped semiconductor quantum systems are a field of enormous and still growing research interest since they allow, in specially tailored systems, the investigation of fundamental properties, such as many-particle interactions, of electrons in reduced dimensions. Especially, they show such unique electronic transport properties as the integer and fractional quantum-Hall effects. In addition, linear optical experiments were successfully used to highlight these regimes of a two-dimensional electron gas (2DEG) [1]. Femtosecond time-resolved coherent wave mixing experiments have proved to be a very powerful tool in investigating the dynamic properties of elementary excitations in undoped *intrinsic* semiconductors. For example, experiments at high magnetic field have recently revealed correlation effects beyond the Hartree-Fock approximation [2,3]. Compared to the wealth of experiments on intrinsic systems, rather few investigations of *coherent* dynamics in modulation-doped quantum wells, which contain a *cold* electron gas, have been reported [4-6]. In this paper we investigate the quantum coherence of a 2DEG in modulation-doped GaAs-AlGaAs quantum wells in the regime of the integer quantum-Hall effect.

The samples are modulation-doped multiple quantum wells with carrier densities in the range of 2-5 $\times$ 10^{11} cm^{-2} under illumination, mounted for transmission measurements on a sapphire substrate. The active regions of the samples have thirty periods , each consisting of a 12 nm GaAs well and a 42 nm AlGaAs barrier, where the center 12 nm of the barrier is doped with Si. The samples were immersed in superfluid helium in an optical split-coil cryostat at a temperature of 1.8 K. The experiments were performed with two laser beams of equal intensity which were in resonance with transitions from valence-band to conduction-band Landau levels. The beams were either left (σ^-) or right (σ^+) circularly polarized and separated by a time delay

Δt. For time integrated four wave mixing (TI-FWM) experiments, the total signal intensity is measured by a PMT, while for spectrally resolved (SR-FWM) experiments a spectrometer with 0.75 m focal length and a charge-coupled-device camera were used to record the spectrum of the emitted signal.

In Fig. 1, the linear absorption of σ^- polarized light is shown as a function of magnetic field B for sample A, with $n = 2.6\times10^{11}$ cm^{-2}. At $B = 0$, a Fermi-edge singularity can be seen at $E \sim 1550$ meV very clearly. For $B > 5.1$ T, the filling factor ν is smaller than 2, so that only the lowest Landau level is occupied with electrons. The right panel of Fig. 1 shows a comparison of the absorption of σ^- (white spectrum) and σ^+ (gray spectrum) light at $B = 10$ T. The spin splitting of the lowest Landau level is clearly resolved. The black curves show the spectrum of the 100 fs laser pulses, which were used in the nonlinear experiments described below.

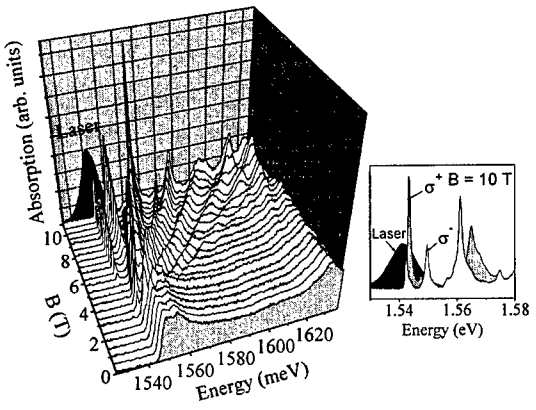

FIG. 1 Linear absorption spectra of σ^- light in dependence on magnetic field. The black-shaded spectrum in the back corresponds to the 100 fs pulses which were used in the nonlinear experiments. The right panel shows absorption spectra for two different circular polarizations at $B = 10$ T.

Typical measurements of TI-FWM in sample A are shown in the inset of Fig. 2, for several values of B using σ^+ polarized light (the σ^- data shows the same behavior). As one can see, the complex many-body interactions create an unusual temporal profile, and clearly require an intensive theoretical treatment to get a full understanding of the results. However, by simply extracting a decay time from these curves we can get a measure of the dephasing of the interband polarization. These results are displayed in Fig. 2 (filled circles). It is striking to note the large increase in decay time just after the system passes through filling factor $\nu = 2$. We have repeated these experiments in sample B with a much higher doping density $n = 4.9\times10^{11}$ cm^{-2} (open circles in Fig. 2). Since the features are nicely reproducible as a *function of filling factor* for samples with different densities, we can say quite clearly that this is evidence of filling factor dependent screening of the cold electron gas [8]. At the quantum-Hall state $\nu = 2$, the system is in an insulating state. This means that the Coulomb interaction is not screened at that point and

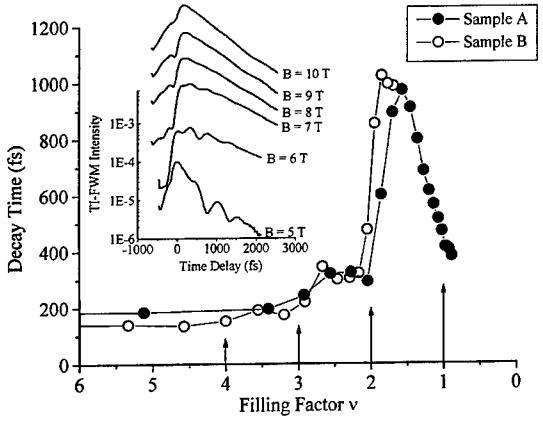

FIG. 2 TI-FWM decay times versus filling factor for samples A and B. The inset shows TI-FWM spectra of sample A for different magnetic fields. Data shown was taken using σ^+ polarized light.

thus the dephasing due to Coulomb scattering has a maximum. At $\nu = 3/2$, the upper spin level of the lowest Landau level is just half filled, which means that the metallic behavior, i.e., the screening effects, should be well pronounced and the Coulomb interaction should be screened. Indeed, we observe the maximum of the decay time, which means the minimum of Coulomb scattering, near $\nu = 3/2$. We can see another maximum between $\nu = 2$ and $\nu = 3$, which is smaller than the first. This can be understood by noting that at $\nu = 3/2$, one-third of the electrons are metallic-like and can screen, while at $\nu = 5/2$, only one-fifth of them contribute to screening.

In addition to the screening effects discussed above, there is dephasing due to Coulomb scattering, which depends on the magnetic field. Considering only Coulomb scattering as a source of dephasing and neglecting screening effects [7], the unexpected increase of dephasing at high magnetic fields can be understood in terms of an increase of the Coulomb matrix elements at high fields and hence stronger scattering. The Coulomb matrix elements scale with e^2/ l_0, where $l_0=[h/(2\pi eB)]^{1/2}$ is the magnetic length. While we expect this effect to contribute to the dephasing as well, it appears from our data that the screening effects are dominant in the magnetic field and density ranges we have measured.

We have also performed SR-FWM experiments, in order to clarify the nature of the oscillations seen in the TI-FWM experiments, for example in the inset of Fig. 2. In Fig. 3 we show a SR-FWM spectrum taken with the laser tuned to overlap with several absorption peaks. The data shows that we have complete oscillations vs. Δt of all the peaks. These oscillations are in phase for all three transitions, and have minima which are nearly zero in intensity, indicating that these are quantum beats between the different transitions, rather than polarization interference. This implies strong Coulomb correlation effects involving the photo-excited

electron-hole pairs as well as the electron Fermi sea, the dynamics of which we are only beginning to investigate.

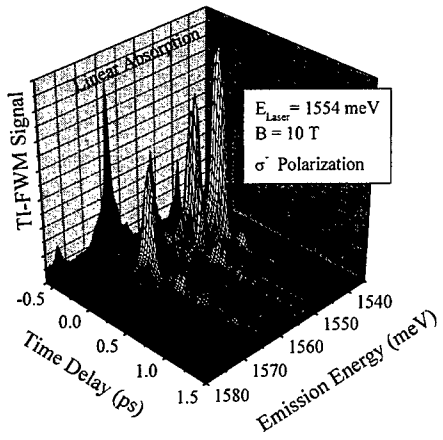

FIG. 3 Spectrally-resolved FWM spectra for sample A for σ^- polarized light and a center frequency of the laser of E = 1554 meV, in resonance with the second Landau level. The absorption spectrum is shown as a black shadow on the back screen.

In conclusion, we have investigated the quantum coherence of 2D electron systems in dependence on a strong magnetic field. We have observed a modulation of the dephasing of the photo-excited electron-hole pairs, as the electron gas went from a metallic state (partially filled Landau levels) to an insulating one (completely filled levels). We explain this as filling factor dependent screening of the Coulomb interaction by the cold electron gas. Furthermore, we have observed quantum beats where up to three different Landau level transitions are coupled. It is clear that these systems exhibit a wealth of complex, many-body interactions, which are to be explored in more detail in future work.

The authors are grateful to Lu Sham and Ming Wei Wu for very helpful discussions. This work was supported by the Alexander von Humboldt-Stiftung (C.S.) and by the Director, Office of Energy Research, Office of Basic Energy Sciences, Division of Material Sciences of the U.S. Department of Energy, under contract No. DE-AC03-76SF00098.

References

1. see, e.g., I. V. Kukushkin et al., Phys. Rev. Lett. **72**, 736 (1994), B. B. Goldberg et al., Phys. Rev. Lett. **65**, 641 (1990), A. J. Turberfield et al., Phys. Rev. Lett. **65**, 637 (1990), E. H. Aifer et al., Phys. Rev. Lett. **76**, 680 (1996).
2. P. Kner et al., Phys. Rev. Lett. **78**, 1319 (1997).
3. P. Kner et al., Phys. Rev. Lett. **81**, 5386 (1998).
4. D. S. Kim et al., Phys. Rev. Lett. **68**, 2838 (1992).
5. P. Hawrylak, J. F. Young, and P. Brockmann, Semicond. Sci. Technol. **9**, 432 (1994)
6. S. Bar-Ad et al., Phys. Rev. Lett. **72**, 776 (1994).
7. M. W. Wu and H. Haug, Phys. Rev. B **58**, 13060 (1998).
8. Lu Sham, private communication.

PC.56

X_X-X_Y Interface Band Mixing in GaAs/AlAs Heterostructures

Hyunsik Im, L. E. Bremme, Y. C. Chung, P. C. Klipstein,
Clarendon Lab, Dept. of Physics, Univ. of Oxford, Parks Road, Oxford, OX1 3PU, U.K.
Fax: 44-1865-272400, Email: p.klipstein@physics.ox.ac.uk.

R. Grey and G. Hill
Dept. of Electrical & Electronic Eng., Univ. of Sheffield, Mappin Street, Sheffield SI 3JD, U.K.

Abstract

The in-plane dispersion of the $X_{X,Y}$ states in a GaAs/AlAs "double barrier structure" is measured by varying the angle of an in-plane magnetic field. When $X_{X,Y}$ (1) states in the emitter AlAs layer tunnel into collector $X_{X,Y}(m>1)$ states, a characteristic dumbbell shape is observed for the bias shift of the resonant tunneling peak vs. magnetic field angle, with the major axis along [110] or [$\bar{1}$10]. This corresponds to an elliptical constant energy surface in the collector AlAs layer which is rotated by 45° with respect to the bulk Fermi surface. We explain the new symmetry by X_X-X_Y interface band mixing which is closely analogous to the widely studied Γ-X_Z mixing. Our results provide new insight into the microscopic origin of both types of mixing.

Introduction

About ten years ago it was predicted that in GaAs/AlAs heterostructures grown along [001] (*z*-direction), it is possible for mixing to occur between the AlAs X_X and X_Y conduction band edge states, located near the four in plane <100> boundaries of the bulk Brillouin zone [1]. In this paper we show that the effect of the mixing on the in-plane dispersion can be dramatic, particularly when an electric field is applied in the *z*-direction to break the four-fold symmetry in the plane. At the band edge, the four ellipses oriented along [100] and [010], which form the X_X and X_Y constant energy surfaces, are then replaced by a single elliptical surface oriented along either [110] or [$\bar{1}$10]. Using resonant magneto-tunneling, we are able to measure the in-plane dispersion which, to the best of our knowledge, constitutes the first observation of X_X-X_Y mixing. We estimate the values of the mixing potentials associated with Bloch states of X_1 and X_3 symmetry respectively. We show that *interference* between these two contributions to the overall mixing potential is directly responsible for the new symmetry of the constant energy surface. Contrary to a recent theory, our results show that the X_1 related potential is finite.

Experimental

We have studied 2D→2D tunnelling between confined states in a GaAs/AlAs structure comprising two 70Å wide AlAs *wells* separated by a 30 Å wide GaAs *barrier*, surrounded by 100Å spacers and doped GaAs contacts. The $Ga_{1-x}Al_xAs$ region before each spacer has been graded linearly over a distance of 1000Å from $x = 0$ to $x = 0.1$ to enable efficient electron transfer from Γ states in the graded region to ground $X_{X,Y}$ states in the emitter well. The conductance characteristic is shown in fig. 1. $X_{X,Y}(1)$→$X_{X,Y}(m)$ processes responsible for the peaks, where *m* is the confinement quantum number, are identified by comparison with a similar ungraded sample, in which the emitter $X_{X,Y}$ states were populated using a pressure of ~9 kbar and which

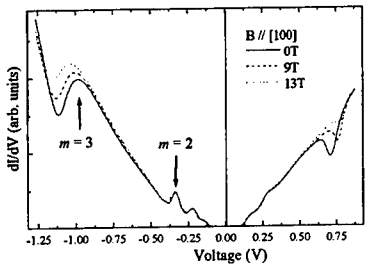

Figure 1: Conductance vs. bias at 4.2K. A magnetic field is applied in the [100] direction

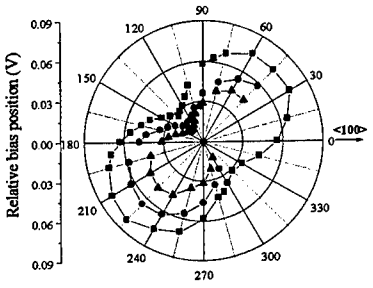

Figure 2: Bias shift of the reverse bias $X_{X,Y}(1) \rightarrow X_{X,Y}(3)$ peak in fig. 1 with angle of the in-plane magnetic field. Triangles, circles and squares are for 12, 13.5 and 15T respectively.

was the subject of detailed fitting to a self consistent Schrödinger-Poisson model [2].

The dispersions of the $X_{X,Y}$ states were studied by applying an in-plane magnetic field which introduces a change in wave-vector during tunneling, $\Delta k_y = -\, eB_x \Delta z/\hbar$, where Δz is the distance between emitter and collector wavefunctions [3]. For the present sample at 15T, $\Delta k_y \sim 0.02 \times 2\pi/a_0$, where a_0 is the cubic lattice constant. The resulting shift in bias allows the dispersion in the collector to be mapped out. Fig. 1 shows the shift for the $X_{X,Y}(1) \rightarrow X_{X,Y}(3)$ peak as the field is increased in the [100] direction. When the shift is plotted in fig. 2 vs. the angle of the in-plane field, a characteristic dumbbell shape is observed corresponding to an elliptical constant energy surface with its principal axes along [110] and $[\bar{1}10]$. We have also observed similar behaviour in a 60-40-60Å sample [4]. For the sample of fig. 2, the dumbbell axis is identical for both bias directions, although in reverse bias the ratio of the shifts for the two <110> magnetic field directions is significantly larger (~2.8) than in forward bias (~1.6).

Discussion

Near the <100> faces of the bulk Brillouin zone, the six X_3 valleys lie $\Delta \sim 0.35$eV above the six X_1 valleys, and ***k.p*** mixing between the $X_{1\sigma}$ and $X_{3\sigma}$ states produces the familiar Camel's back dispersion along k_σ, where $\sigma = x,y$ or z [5, 6]. In a heterostructure, the presence of interfaces can cause mixing between states $\Psi_{X_\sigma} = \left\{\Xi_\sigma(z)\left[b(k_\sigma)u_{X_{1\sigma}} + a(k_\sigma)u_{X_{3\sigma}}\right] + \ldots\right\} \cdot e^{i\,\mathbf{k}_\parallel \cdot \mathbf{r}}$ with σ = X and Y, in which Ξ_σ is the dominant envelope-function in each case [7]. Here $u_{X_{1\sigma}}$ and $u_{X_{3\sigma}}$ are the $\boldsymbol{k}_\parallel = (k_x, k_y) = 0$ Bloch functions associated with the X_1, X_3 manifold of the *average* bulk crystal and the three dots represent the small contribution of the remote bands outside this manifold [7]. The amplitudes of the two Bloch states, $b(k_\sigma)$ and $a(k_\sigma)$, are given explicitly in terms of Δ and the ***k.p*** interaction parameter, R, in refs [4] and [5]. If the origin of k_σ is chosen to be at an X-point, then a takes the sign of k_σ while b is always positive and close to unity, with $a(0) = 0$, $b(0) = 1$.

The mixed state energies are found by diagonalising the Hamiltonian:

$$H_{XY} = \begin{bmatrix} E_X & V \\ V & E_Y \end{bmatrix}, \text{ where } E_X = \frac{\hbar^2}{2}\left[\frac{k_x^2}{m'_Z} + \frac{k_y^2}{m_{X,Y}}\right] - E_{\mathbf{k}.\mathbf{p}}(k_x) \text{ and } E_Y = \frac{\hbar^2}{2}\left[\frac{k_x^2}{m_{X,Y}} + \frac{k_y^2}{m'_Z}\right] - E_{\mathbf{k}.\mathbf{p}}(k_y)$$

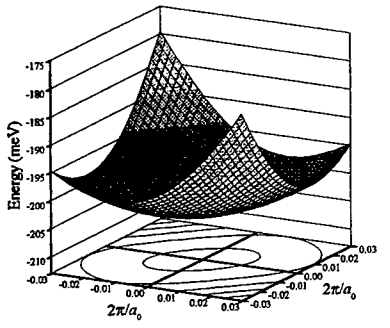

Figure 3: Dispersion and energy contours in the (k_x,k_y) plane of an X_1 quantum well, calculated using $\bar{V}_1^{X-Y}$= 30meV, $\bar{V}_3^{X-Y}$= 850meV. The zero of energy is midway between the bulk X_1 and X_3 edges.

are the bulk dispersions in the (k_x,k_y) plane and $E_{\mathbf{k}\cdot\mathbf{p}}(k_\sigma)=\sqrt{(\Delta/2)^2+R^2k_\sigma^2}$. We take R=1eVÅ, Δ= 0.35eV, $m_Z'/m_0\approx1.56$ and m_{XY}/m_0 = 0.25 [2,5]. The mixing matrix element in H_{XY} was shown to be $V(k_x,k_y)=\Sigma_{z_i}\Xi_X^*(z_i)\Xi_Y(z_i)[b^*(k_x)b(k_y)V_1^{X-Y}$ + $a^*(k_x)a(k_y)V_3^{X-Y}]$ for interfaces at z_i [7]. The two mixing potentials obey the following relations: $V_1^{X-Y}(z_i)=\beta_1\cdot\exp(i2\pi z_i/a_0)$ and $V_3^{X-Y}(z_i)=\beta_3\cdot\exp(i2\pi z_i/a_0)\cdot P(z_i)$, with constants $\beta_1 << \beta_3$ and where $P(z_i)$ = 1 (-1) for AlAs on GaAs (GaAs on AlAs) [5,4,7]. It is convenient to write $V(k_x,k_y)=b^*(k_x)b(k_y)\bar{V}_1^{X-Y}+a^*(k_x)a(k_y)\bar{V}_3^{X-Y}$. The signs and magnitudes of the two potentials $\bar{V}_1^{X-Y}=\beta_1\Sigma_{z_i}\Xi_X^*(z_i)\Xi_Y(z_i)\exp(i2\pi z_i/a_0)$ and $\bar{V}_3^{X-Y}=\beta_3\Sigma_{z_i}\Xi_X^*(z_i)\Xi_Y(z_i)P(z_i)\exp(i2\pi z_i/a_0)$ depend on the z-direction electric field through the envelope functions. They also depend on the precise details of the interface roughness because of the exponential phase factors which change sign with each monolayer. Therefore, when evaluating $\bar{V}_1^{X-Y}$ and $\bar{V}_3^{X-Y}$, the phase factors should be averaged over the effective area of each interface [4].

In fig. 3, we plot the dispersion and constant energy contours in the (k_x, k_y) plane for $\bar{V}_1^{X-Y}$ = 30 meV and $\bar{V}_3^{X-Y}$ = 850 meV. It can be seen that the contours are elliptical with their major axis along [110]. The sub-band kinetic energy in fig. 3 at constant $k_\parallel$ should be proportional to the bias shift plotted in fig. 2 when $k_\parallel$ is at right angles to the magnetic field. In fig. 4, we show kinetic energy plots for $k_\parallel$ =0.02×2π/a_0 with $\bar{V}_1^{X-Y}$ = 6 or 30meV and $\bar{V}_3^{X-Y}$ = 850meV. The value of $\bar{V}_3^{X-Y}$ was chosen by noting that the ratio of kinetic energies for the two <110> directions is very sensitive to $\bar{V}_3^{X-Y}$. Fig. 4 shows that $\bar{V}_1^{X-Y}$ hardly affects this ratio but it does influence the shape of the kinetic energy plot. We find good correspondence between fig. 2 and fig. 4(b) suggesting that $\bar{V}_1^{X-Y}\sim$ 30 meV is a good estimate for the 70-30-70 sample in reverse bias.

The <110> orientation of the elliptical contours in fig. 3 is due to interference between the $\bar{V}_1^{X-Y}$ and $\bar{V}_3^{X-Y}$ terms in the expression for $V(k_x,k_y)$, since $a^*(k_x)a(k_y)>0$ for $k_\parallel$ along [110] but $a^*(k_x)a(k_y)<0$ for $k_\parallel$ along $[\bar{1}10]$. The major axis of the ellipse is along [110] if both $\bar{V}_1^{X-Y}$ and $\bar{V}_3^{X-Y}$ have the same sign, and along $[\bar{1}10]$ if they have opposite signs. The interference shows that both mixing potentials are finite, in contrast to ref. [8] which predicts zero for V_1^{X-Y}. The result $V_1^{X-Y} << V_3^{X-Y}$ is consistent with theory [7,8,9], while the relatively large size of both $\bar{V}_1^{X-Y}$ and $\bar{V}_3^{X-Y}$ is due in part to the large amplitudes of Ξ_X and Ξ_Y at the last interface of the collector quantum well, where each nearly has an antinode [4]. These large interfacial amplitudes are a consequence of the substantial electric field in the sample and the

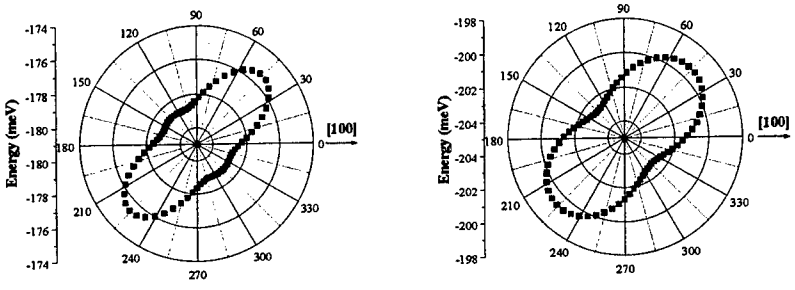

Figure 4: Kinetic energy at $k_{\parallel}$ =0.02× $2\pi/a_0$ for field angles in the (k_x, k_y) plane, calculated with $\bar{V}_3^{X-Y}$ =850meV and (a) $\bar{V}_1^{X-Y}$ =6meV (b) $\bar{V}_1^{X-Y}$ =30meV. Zero angle corresponds to [100].

large confinement energy for m=3. For lower electric fields and lower m, the mixing between X_X and X_Y is expected to be much weaker. We also point out that even though $\bar{V}_3^{X-Y}$ is large so that large splittings could be expected for states confined in AlAs by the X_3 symmetry potential well, these states are unlikely to give strong resonances in the tunnel current because the emitter electrons have predominantly X_1 symmetry. Note that in the emitter quantum well, we require $\bar{V}_1^{X-Y}$ >2meV, in order to ensure that a minimum exists in the dispersion at $k_{\parallel}$ = 0 which is lower in energy than the bulk minima at (0,~0.1) and (~0.1,0) × $2\pi/a_0$ [4]. In view of the large value of $\bar{V}_1^{X-Y}$ in the collector well where the interfacial amplitudes of the envelope functions are about a factor of 2 larger, this is certainly the case [4].

In conclusion we have observed the first clear evidence for mixing between AlAs X_X and X_Y states predicted in ref. [1]. We have shown that the mixing leads to a rotation of the constant energy surface from the two in-plane <100> directions to one of the <110> directions. Which of the <110> directions depends on the details of the interface structure and the bias conditions. The rotation is a consequence of interference between the X_1 and X_3 contributions to the mixing potential. This shows that V_1^{X-Y} cannot be zero, as recently suggested in ref. [8]. We find $\bar{V}_3^{X-Y} >> \bar{V}_1^{X-Y}$ ~30meV in the collector well of our *biased* sample. By considering the microscopic interface potential, a close analogy has been shown to exist between X_X-X_Y and Γ-X_Z mixing [7]. It thus follows that the Γ-X_Z mixing potential associated with the X_1 Bloch state, $V_{\Gamma-X_1}$, must also be finite, contrary to the models presented in refs [5] and [9].

[1] Y-T Lu and L. J. Sham, *Phys. Rev. B* **40**, 5567 (1989)
[2] J. M. Smith et al., *Phys. Rev. B* **57**, 1740 (1998)
[3] J. M. Smith et al., *Phys. Rev. B* **58**, 4708 (1998)
[4] H. Im, P.C. Klipstein, R. Grey and G. Hill, to be published (1999)
[5] Y. Fu et al., *Phys. Rev. B.* **47**, 13498 (1993)
[6] A. A. Kopylov, *Sol. St. Commun.* **56**, 1 (1985)
[7] P. C. Klipstein, 24th *Int. Conf. Phys. Semiconductors* (Jerusalem, August 1998), (1999)
[8] B. A. Foreman, *Phys. Rev. Lett.* **81**, 425 (1998)
[9] T. Ando and H. Akera *Phys. Rev. B.* **40**, 11619 (1989)

PC.57

Electric and Magnetic Field Fluctuations in Modulation Doped Si/Ge Quantum Wells

W. Jantsch[1], Z. Wilamowski[1,2], N. Sandersfeld[1], and F. Schäffler[1]

[1]Institut für Halbleiterphysik, Johannes Kepler Universität, A-4040 Linz, Austria

[2]Institute of Physics, Polish Academy of Sciences, Al. Lotnikow 32746, PL 0668 Warsaw, Poland

The recently observed electron spin resonance (ESR) of conduction electrons in modulation doped Si/Ge quantum wells is utilised to determine the density of states (DOS) of the two-dimensional electron gas (2DEG). Instead of the constant DOS expected for an ideal 2DEG we find tails extending into the energy gap. With increasing carrier density (adjusted by persistent photoconductivity or applied gate voltage in our experiment) these tails become weaker. We attribute them to the screened potential fluctuations caused by fluctuations in the charge distribution of ionised donors in the doping layer. For low carrier concentration we observe a tendency for a divergence of these potential fluctuations, the 2D analogue of the Anderson transition.

Recently the observation of conduction electron spin resonance (CESR) was reported for 2D quantum wells formed by Si_XC_{1-X}[1,2] in-between Si barriers or Si wells defined by Si_XGe_{1-X} [3-5] barriers. The CESR was detected either electrically (measuring conductivity) [5] or directly by microwave absorption [1-4]. The latter method is applicable since the line width of the resonance is outstandingly narrow - values of down to 4 μT have been observed - yielding a sensitivity of better than 10^9 spins in a conventional ESR X-band spectrometer. The spin properties are sensitive to many different kinds of interactions of electronic systems. Therefore we expect to obtain information on the manybody system of the 2DEG in modulation doped quantum well samples.

In particular, as we pointed out in a preliminary report [4], the integral CESR signal is proportional to the density of states, $g(\varepsilon_F)$ at the Fermi level since we are dealing here with a degenerate electron gas that exhibits rather Pauli susceptibility than the usual Curie behaviour of weakly interacting paramagnetic spins of defects. In this paper we make use of this fact to determine $\rho(\varepsilon_F)$ and we find band tails extending below the band edge instead of the sharp step function expected for an ideal 2DEG. We attribute these band tails to potential fluctuations arising from the statistical distribution of charges in the doping layer, screened by correlation effects in the impurity system and by the 2DEG. Assuming a Gaussian distribution of these fluctuation, we determine their amplitude as a function of the 2DEG density. The latter is varied (i) making use of persistent photoconductivity in moderately doped samples or (ii) by use of a Schottky gate. We report here a sudden increase of these fluctuations below some critical carrier density that indicates the 2D analogue of Anderson localisation.

Modulation doped $Si_{0.75}Ge_{0.25}$/Si quantum wells were grown pseudomorphically on top of a linearly graded, relaxed $Si_{0.75}Ge_{0.25}$ buffer by MBE. To achieve n-type conductivity, an Sb-doped layer (25 nm thick) was placed 12 nm above the quantum well. After cooling in darkness, samples with a volume doping concentration of 7.10^{17} cm^{-3} are insulating. Prolonged illumination increases the electron concentration to 3.10^{11} cm^{-2} and a mobility exceeding 10^5 cm^2/Vs at 4.2 K. For the gated samples, a Pd layer was evaporated.

Measurements were performed with a standard Bruker X-band spectrometer and preliminary results were presented in Refs. [3,4]. We observe a strong increase of the integral CESR absorption with increasing illumination dose after cooling in darkness and finally for prolonged illumination, the signal saturates. For a gated sample, we see a rather weak signal for zero bias that increases for accumulation and it saturates also for higher positive bias voltage.

In order to determine the carrier concentration *in situ*, we make use of cyclotron resonance (CR) which causes a broad background signal [4] in the standard ESR experiment. The CR amplitude increases and at the same time the CR width decreases persistently with increasing illumination dose. The latter reflects momentum scattering indicating improved mobility as the Fermi level moves up and away from the tail states. The CR signal can be fitted using the Drude expression for the dielectric function taking both the CR-active and the CR-inactive parts into account as it is necessary since linear polarized microwaves are used in our experiments [4]. The carrier concentration is normalized to its saturation value. The latter was determined independently by investigating Shubnikov - de Haas oscillations.

In order to evaluate the DOS quantitatively we normalized the integral CESR signal to its saturation value and we assigned the unperturbed 2D DOS to that value. Typical results for the DOS at the Fermi level, $g(\varepsilon_F)$, are given in Fig. 1 as a function of the 2D electron density. The results show a smooth increase in the density of states instead of the sharp jump expected for an ideal 2DEG. After prolonged illumination it approaches the ideal constant value asymptotically. For an ideal 2D DOS, the saturation carrier density of $n_{2d} \square 3.10^{11}$ cm^{-2} corresponds to a Fermi energy of about 2 meV above the unperturbed band edge.

The existence of band tails indicates disorder and the improving mobility with increasing n_{2d} shows that the disorder effect looses importance as the Fermi level increases. This rules out *e.g.* alloy scattering or thickness fluctuations as dominant scattering mechanisms and also as the most important source of fluctuations in these samples. It is rather plausible that scattering and band tails have the same origin, namely potential fluctuations stemming from ionized donors in the doping level.

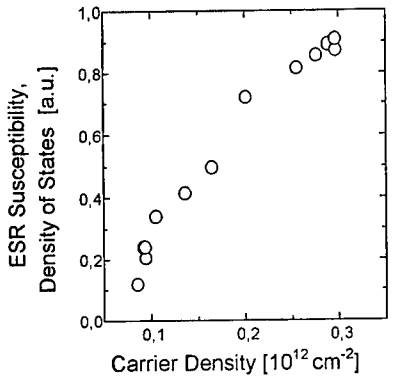

Fig.1: Density of states of the 2DEG at the Fermi level as a function of the carrier density. The former is obtained from the integral CESR absorption, the latter from the integral CR absorption.

In these samples, the doping layer and the 2D channel are in equilibrium, *i.e.*, they have a common Fermi level. Persistent photoconductivity arises from photoionisation of deep states in the bulk and at the surface and the carriers distribute themselves between the doping layer and the 2D channel. Consequently the number of ionised donors in the doping layer is

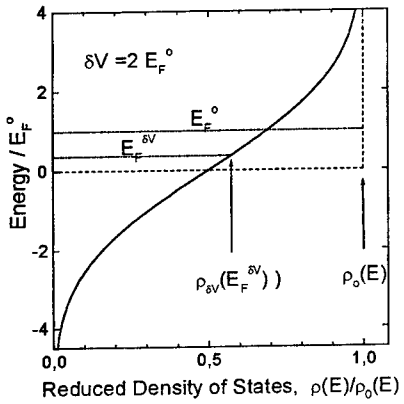

Fig.2: Density of states of an ideal 2DEG (step function) and a real 2D structure with Gaussian broadening assuming an amplitude $\delta V=2\varepsilon_F^0$. Arrows indicate the evaluation of the DOS at the Fermi level for the same carrier density.

Fig. 2. There the DOS, $\rho^0(\varepsilon)$, is plotted *vs.* energy for the ideal 2D case and then also for the assumed case of a Gaussian broadening with an amplitude $\delta V=2\varepsilon_F^0$, where ε_F^0 is the unperturbed Fermi energy. As a consequence of broadening now the Fermi level changes for constant number of carriers and therefore also $\rho_{\delta V}(\varepsilon_F^{\delta V})$. The relation between the density of states at the Fermi level, $\rho_{\delta V}(\varepsilon_F^{\delta V})$, for a given carrier density, and the fluctuation amplitude δV can be calculated thus. The resulting function allows us to derive the fluctuation amplitude as a function of experimental values for the DOS at $\varepsilon_F^{\delta V}$ as obtained from the normalised CESR intensity.

Results for the fluctuation amplitude are given in Fig. 3a as a function of the concentration of carriers in the reduced with increasing illumination dose. Self-consistent numerical estimation shows, however, that the number of charges in the doping layer changes only little in comparison to n_{ed}.

Charged donors in the doping layer cause potential fluctuations in the 2D well. These fluctuations are superimposed on the energy level system of the 2DEG. Consequently the band edge fluctuates in the same way as the potential and thus summing up the states in the plane the overall effect of these fluctuations is a broadening of the distribution of band states. In order to evaluate the amplitude of the potential fluctuations we assume a Gaussian distribution for them. The (Gaussian) broadening of the band edge changes the Fermi level as it is illustrated in

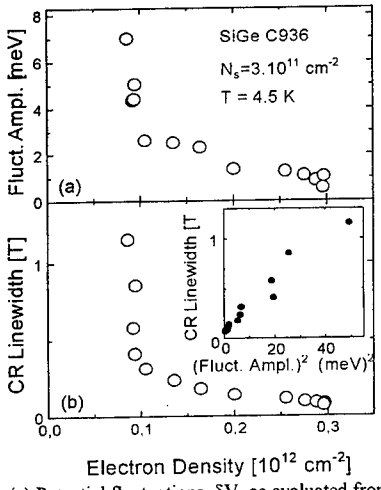

Fig. 3: (a) Potential fluctuations, δV, as evaluated from the data of Fig. 1 and (b) cyclotron resonance line width as a function of the carrier density in the quantum well. In the inset, the CR line width is plotted as a function of the square of the fluctuation amplitude, $(\delta V)^2$.

channel. A rather smooth dependence is seen for $n_{2d} > 10^{11}$ cm^{-2} but below there is a dramatic increase in the fluctuation amplitude. In Fig. 3b we plot the CR line width as a function of n_{2d}, and a similar dependence is seen from an entirely different measurement showing that the momentum scattering increases strongly as the fluctuation amplitude increases. In order to test this relation we plot the CR linewidth in the inset of Fig. 3b as a function of $(\delta V)^2$. The linear dependence obtained in this plot shows that these fluctuations really are the main mechanism for momentum scattering in this regime and other sources of scattering are not important for these high mobility samples.

The main results of this paper are: (i) the experimental determination of the DOS as a function of carrier density, (ii) its interpretation in terms of potential fluctuations and (iii) the tendency for a divergence of the potential fluctuations at low carrier concentration. Obviously a highly non-linear positive feedback mechanism is necessary to explain result (iii). Somehow the system is able to screen the potential fluctuations much more efficiently for high carrier density. This is a consequence of the fact that the screening efficiency is proportional to the DOS at the Fermi level and that increases strongly as the 2D carrier density increases.

The investigation of CESR yields also additional information on the 2DEG contained in the g-factor and the resonance line width. Both of these quantities exhibit 2D symmetry. The g-factor is very close to 2.0000 for perpendicular orientation of the magnetic field but for in-plane field it is smaller by an amount which increases with increasing carrier concentration. We attribute this effect to magnetic dipole fields caused by strong exchange correlation of the free carriers. These fields cancel for a homogeneous distribution of charge. So these results also demonstrate directly the existence of exchange and correlation effects [6]. For perpendicular spin polarisation, the dipole field is reduced because of the demagnetising field of neighbouring electrons whereas for in-plane orientation the dipole fields add up. Consistent with this explanation, inhomogeneous line broadening occurs only for in-plane field and vanishes for perpendicular orientation. The line broadening therefore also reflects the potential fluctuations and its magnitude is consistent with the δV obtained from the CESR amplitude.

Acknowledgements: Work supported in Austria by the *Österreichischer Akademischer Austauschdienst,* and the *Fonds zur Förderung der Wissenschaftlichen Forschung*, Vienna, Austria, and in Poland within the KBN grant 2 P03B 007 16.

References

[1] N. Nestle, G. Denninger, M. Vidal, C. Weinzierl, Phys. Rev. **B56**, R4359 (1997)

[2] H.-J. Kümmerer, K. Hüftle, C. Weinzierl, G. Denninger, N. Nestle, and K. Eberl, Phys Rev **B59**, 12568 (1999)

[3] W. Jantsch, Z. Wilamowski, N. Sandersfeld and F. Schäffler, Proc. Int. Conf. Phys. Semiconductors, Jerusalem 1998, *in print*

[4] W. Jantsch, Z. Wilamowski, N. Sandersfeld and F. Schäffler, Phys.stat.sol (b) **210**, 643 (1998)

[5] C.F.O. Graeff, M.S. Brandt, M. Stutzmann, M. Holzmann, G. Abstreiter, F. Schäffler, Physical Rev. **B59**, 13242 (1999)

[6] Z. Wilamowski, W. Jantsch, N. Sandersfeld and F. Schäffler, Proc. XXII. Int. Conf. Phys. on Low Temperature Physics, Helsinki 1999, *to be published*

PC.58

Optics and Magneto-optics of Coexisting Localized and Free Holes in GaAs Quantum Wells

H.P. van der Meulen, J. Sanchez Páramo and J.M. Calleja
Dept. Física de Materiales, Universidad Autónoma de Madrid, Cantoblanco, E-28049, Madrid, Spain
and
K.J. Friedland, R. Hey and K. Ploog
Paul-Drude-Institut für Festkörperelektronik, Hausvogteiplatz 5-7, D-10117 Berlin, Germany

Abstract

The photoluminescence and photoluminescence excitation spectra have been studied in two twin GaAs quantum wells containing a two-dimensional electron gas with high density and high-mobility. One of the wells includes a few Be acceptors in a δ-layer at the center of the well, which localize part of the photocreated holes. In the other well the holes are free. Comparison of the optical spectra of both samples shows that the Fermi-edge singularity in emission is only observed for localized holes, while in excitation spectra both Be-bound- and free holes display the same singularity. Thus, localization of holes appears to be relevant mainly by its effect on the final-state density. Magneto-optical measurements confirm the presence of the two kinds of holes and provide estimates of their apparent effective masses.

PACS No.: 71.10.Ca; 78.30.Fs; 78.66.-w
keywords: two-dimensional electron gas, Fermi-edge singularity, quantum well

1. Introduction

The Fermi-edge singularity (FES) appears as an enhancement of the absorption or emission intensity in the optical spectra of two-dimensional electron gases (2DEG) with a power-law spectral distribution. It has been extensively studied, both experimentally [1-4] and theoretically [5-8]. The FES is originated by the coherent response of the Fermi sea to the sudden creation or annihilation of the photocreated hole in the absorption or emission process respectively, similarly to the case of the X-ray absorption spectra of metals [9]. In GaAs quantum wells FES has been mainly reported in photoluminescence excitation (PLE) spectra [1], as the lack of holes with the Fermi wavevector (k_F) at low temperatures prevents its observation in photoluminescence (PL) spectra. In contrast in InGaAs/InP wells, due to high hole masses, FES has been observed in PL spectra [2]. Only recently a weak FES has been observed [10] in the PL spectrum of a high quality GaAs QW. Its intensity has been interpreted as due to a non-equilibrium population of holes. Existing theoretical models require either hole localization [7,8], and/or coupling of electrons at the Fermi level to empty conduction subbands [8] for the FES to be observed.

In this paper we present PL and PLE measurements with and without magnetic field on two initially identical GaAs single QW containing a 2DEG with high electron density and mobility. In order to study the effect of hole localization in the characteristics of the FES, a low-density Be δ-doping layer has been included at the well center in one of the samples. Its effect is to localize a fraction of the photogenerated holes [3], so that mobile and localized holes coexist in the Be-doped sample, while holes in the Be-free sample are mobile. Comparison of the spectra of both samples at zero magnetic field indicates that hole localization is needed for the observation of

FES in PL, as a consequence of the final density of states, but it is not needed to observe FES in PLE spectra. PL measurements under magnetic field and the corresponding fan-plots clearly reveal the presence of the two kinds of holes in the Be-doped sample.

2. Experiment

The samples studied are initially identical single GaAs 10 nm QW's with barriers made of AlAs-GaAs short period superlattices grown by solid-source molecular beam epitaxy. In the QW of one of the samples an additional Be-δ doping layer with Be density of about $1.2x10^{10}$ cm^{-2} was grown into the center of the QW in order to localize the photocreated holes. An electron gas with both high density and high mobility has been obtained by remote modulation doping with X-electrons [11]. Shubnikov-de-Haas and Hall measurements in parallel samples give values of: $n=1.6x10^{12}$ cm^{-2} and $\mu= 8x10^5$ cm^2/Vs for the Be-free sample and $n=1.5x10^{12}$ cm^{-2} and $\mu=1.6x10^5$ cm^2/Vs for the Be-doped one. In both cases, the corresponding Fermi energies ϵ_F of about 50 meV coincide with the values obtained from the optical spectra [12], and only the lowest subband is occupied by electrons. PL and PLE measurements at zero magnetic field have been performed at temperatures between 1.7 and 100 K in a Helium bath cryostat. The spectra at fields up to 12 T have been obtained for σ^+ and σ^- circular polarizations in a superconducting magnet. The excitation source was a Ti-sapphire laser with a power density of 10 W/cm^2.

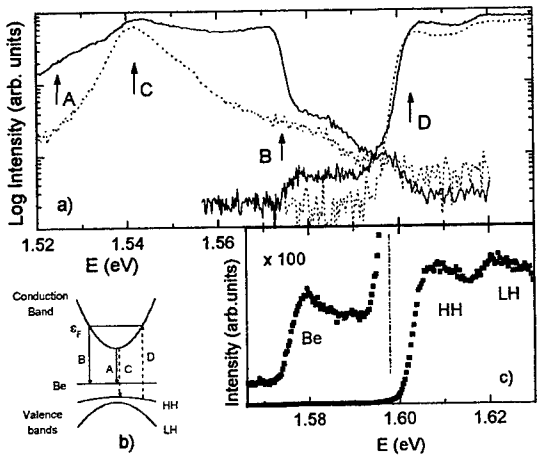

Fig. 1 a) PL and PLE spectra of the Be-free (dashed) and Be-doped (solid) quantum wells on logarithmic intensity scale;
b) diagram of the transitions between the bands, and those between band and acceptor;
c) PLE spectra, measured with higher precision, of the Be-doped QW.

3. Results and discussion

The PL and PLE spectra at 2 K of the two samples studied are shown in Fig. 1a in a logarithmic scale. The PL emission of the Be-free sample (left, dotted line) is most intense at the band edge, corresponding to recombinations with holes relaxed to the highest valence-band edge (the heavy-hole or HH band). The shoulder at 1.554 eV is due to transitions to the light-hole (LH) band edge, whereas the ones at 1.585 and 1.598 reflect transitions from the Fermi level to the HH and LH respectively, as indicated in the diagram. The intensity of these three shoulders is not

consistent with the equilibrium thermal population of holes for 2 K. Consequently, one has to assume either hole localization in this Be-free sample (which we discard further on) or holes out of thermal equilibrium, as reported in ref. [4]. The corresponding PLE spectrum (right, dashed line) also shows the two peaks corresponding to transitions from the HH and LH bands to the Fermi level. They display (even if not clear in the log scale) the typical power law spectral shape and the temperature dependence of the FES [12]. The PL spectrum of the Be-doped sample (left) is indeed composed of two kinds of transitions (see the diagram): one set is the same as in the Be-free sample, while the second set is composed of transitions to Be-bound holes, which do not conserve momentum. The FES occurring for transitions from the Fermi level to the Be-bound holes (1.574 eV) shows up as a maximum in the PL intensity. It also has the expected temperature dependence, disappearing between 20 and 40 K [12]. The PLE spectra of the Be-doped and the Be-free samples are identical, except for the weak step observed in the former at 1.578 eV. This step is the contribution of the Be-bound holes to the QW absorption, and its weakness reflects the very small Be concentration in the QW. Thus, one has to conclude that the holes involved in the FES at the band-to-band PLE onset are not localized. Otherwise they should be observed in PL with an intensity around 100 times larger than that of the peak near 1.574 eV. In Fig. 1c. (in a linear scale) one observes clearly that the FES has a very similar shape and relative intensity for both Be-bound holes and free ones.

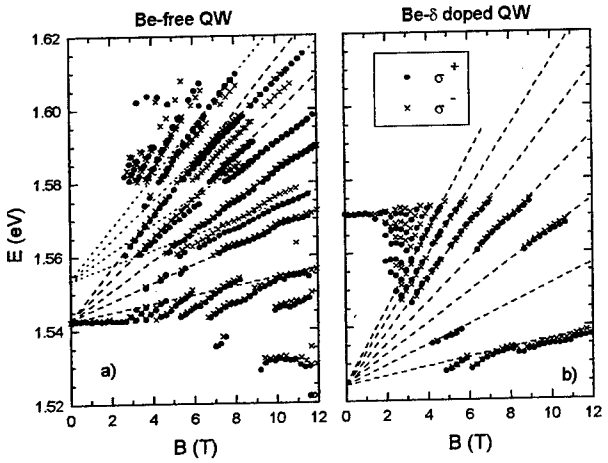

Fig.2 Fanplots for the two samples, at 1.7 K up to 12 T, a) Be-free QW, b) Be-doped QW, after removing the points in common with a); dots and crosses stand for σ^+ and σ^- respectively. The Landau level field dependences are represented by dashed and dotted lines.

Under a magnetic field, the PL spectra display a very rich set of transitions composed of Landau levels, shakeup satellites and phonon replicas [13], which due to the complexity of the valence band and the many crossings of energy levels induced by the field, are often difficult to interpret. In Fig. 2 we present fan plots showing the energy dependence of the magneto-PL peaks of our samples for the two circular polarizations, taken at 2 K. The results for the Be-free sample are displayed in Fig. 2a. One can identify two clear sets of transitions linked to the HH and the LH bands respectively. Their energy spacing at fixed field corresponds to relative effective masses

of 0.075 and 0.069 respectively. Both are close to the conduction mass of GaAs (0.067). The fan plot of the Be-doped sample is shown in Fig.2b after eliminating the datapoints common with the Be-free sample. It therefore contains only magneto-optical transitions associated to Be-bound holes. At zero field they converge indeed to the energy of the transition involving an electron at the conduction band-edge and a Be-bound hole (1.524 eV). Comparison of this number with the corresponding to the Be-free QW gives 18 meV for the Be binding energy in our QW. The energy spacing of the Landau levels yields a relative effective mass of 0.076, practically identical to the Be-free sample. Experimental uncertainty in the determination of the masses from the slopes in the fanplot (~10%) prevent the observation of any difference between localized and free holes.

4. Summary

The use of a two-dimensional electron gas of simultaneously high density and high mobility has allowed us to study the conditions required for the observation of optical FES in PL and PLE spectra. Direct comparison of spectra involving both localized and extended holes in a Be-doped sample indicates that the FES in PL spectra only is observed for localized holes. Instead, localization of holes does not appear to be required in PLE, as FES is clearly observed for valence band holes in high mobility samples. In the spectra in magnetic field the transitions to the Be-bound holes and the valence band holes show separate Landau level fans, confirming the values for the zero field transition energies.

Acknowledgments: This work has been supported by the DGICYT grant No. PB96-0085, the Community of Madrid (grant No. 07N/26/1998) and the Ramon Areces Foundation. The authors are indebted to J. Rubio and C. Tejedor for helpful discussions.

References

[1] for general reference see for instance: J.M.Calleja, J.S.Weiner, A.R. Goñi and A.Pinczuk in *Optics of Semiconductor Nanostructures*, chap. III.2, edited by F. Henneberger, S.Schnitt-Rink and E.O. Göbel, Akademie Verlag, Berlin (1993).

[2] M.S. Skolnick, J.M. Rorison, K.J. Nash, D.J. Mowbray, P.R. Tapster, S.J. Bass, and A.D. Pitt, Phys. Rev. Lett. **58**, 2130 (1987).

[3] I.V. Kukushkin, K. von Klitzing and K. Ploog, Phys. Rev. B **40**, 7788 (1989).

[4] S.A. Brown, Jeff F. Young, J.A. Brum, P. Hawrylak and Z. Wasilewsky, Phys. Rev. B **54**, R11082 (1996).

[5] S. Schmitt-Rink, D.S. Chemla and D.A.B. Miller, Adv.Phys. **38**, 89 (1989).

[6] T. Uenoyama and L. Sham, Phys. Rev. Lett. **65**, 1048 (1990).

[7] P. Hawrylak, Phys. Rev.B **42**, 8986 (1990); *ibid.* **44**, 6262 (1991); *ibid.* **45**, 4237 (1992).

[8] F. Rodriguez and C. Tejedor, Phys. Rev. B **47**, 1506 (1993).

[9] For a review and general references see G. D. Mahan *Many Particle Physics* Plenum, New York (1981).

[10] S.A Brown, J.F. Young, Z. Wasilewsky, and P.T. Coleridge, Phys. Rev. B **56**, 3937 (1997).

[11] K.J. Friedland, R. Hey, H. Kostial, R. Klann and K. Ploog, Phys. Rev. Lett. **77**, 4616 (1996).

[12] H.P. van der Meulen, I. Santa-Olalla, J. Rubio, J.M. Calleja, K.J. Friedland, R. Hey and K. Ploog, Phys. Rev.B (in press).

[13] K.J. Nash, M.S. Skolnick, M.K. Saker and S.J. Bass, Phys. Rev. Lett. **70**, 3115 (1993)

PC.59

Screening effects on the spin-splitting in n-doped GaAs/AlGaAs quantum wells

J. Urdanivia, F. Iikawa, J.A. Brum
Instituto de Física Gleb Wataghin, Universidade Estadual de Campinas, 13083-970 Campinas-SP, Brazil

M.Z. Maialle
DFGA, Universidade São Francisco, 13251-900 Itatiba-SP, Brazil

P. Hawrylak, Z. Wasilewski
National Research Council of Canada, Ottawa, Canada
(June 14, 1999)

The spin dynamics of free carriers is studied by time resolved photoluminescence in n-type GaAs/AlGaAs modulation doped multi-quantum wells. We study a series of samples with different two-dimensional electron densities. The photoluminescence spectra obtained at fixed time delay present energy splitting for the two different circularly polarized configurations. This energy splitting increases with the laser power and decreases as the intrinsic electron density increases. We interpret these results as a combination of two effects: the screening of the Coulomb interaction which decreases the exciton binding energy and the phase-space filling, which enhances the splitting between the two polarized exciton populations.

Keywords: exciton, spin dynamics, time-resolved spectroscopy

78.47.+p, 78.66.-w

I. INTRODUCTION

The excitonic energy spin-splitting has been studied in undoped semiconductor quantum wells (QWs) [1–5]. The short spin relaxation time [1], when compared to the exciton lifetime in GaAs quantum wells, makes the time resolved photoluminescence (TRPL) technique an ideal tool to study the dynamic of excitonic spins.

The TRPL spectra, obtained at a fixed time delay and moderate excitation intensity, for the two components of circular polarization of light present different peak energies [1–4]. They are related to the energies of the two optically active exciton spin states. The energy-splitting is attributed to the exciton-exciton exchange interaction [1–5], which depends on the unbalanced population of the two optically active excitons. Recently, a similar splitting was observed in p-type doped quantum wells [6,7]. In this case, the splitting is explained based on the quasi-equilibrium carrier distributions of the unbalanced populations of the electron-spin states.

In this work, we present experimental results of TRPL in a series of n-type GaAs/AlGaAs modulation-doped multi-quantum wells. An energy splitting is observed in our samples and is dependent on the excitation power and on the intrinsic two-dimensional (2D) electron gas density. This behavior is attributed to a combination of the screening and phase-space filling effects from the intrinsic electron gas and the photocreated plasma.

II. EXPERIMENT

The samples are 50 period of n-type (50 Å) GaAs / (400 Å) $Ga_{0.7}Al_{0.3}As$ modulation doped multi-quantum wells grown on (001) GaAs substrate by molecular beam epitaxy. The 2D electron gas density in the QW, n_e, varies for each sample from zero to 2×10^{11} cm^{-2} [8]. The TRPL experiments were performed using a Ti-Sapphire laser for excitation. The photoluminescence was detected using standard up-conversion method with $\sim$ 3 ps time resolution. The incident light was polarized at the σ^+ configuration and the photoluminescence was detected at σ^+ and σ^- configurations. From now on, they will be assigned by I^+ and I^-, respectively. The sample temperature was kept constant at 7K.

III. RESULTS

The experimental results were obtained with an excitation energy resonant with the absorption threshold for each sample. The heavy- and light-hole states have a typical energy separation of 25 meV. The Fermi energy of the sample with the highest doping is 7 meV. We will neglect, therefore, the ligh-hole

related states in our analysis. Figure 1 shows the typical TRPL spectra, I^+ (solid circles) and the I^- (open circles), of the modulation-doped sample with $n_e = 2.5\times10^{10}$ cm^{-2} obtained at 20 ps after excitation and an excitation power of a) 3 mW and b) 30 mW. The spectra are interrupted at high energy close to the laser line due to experimental limitations. We observe an energy splitting between the two circularly polarized photoluminescences, whereas the I^+ emission band appears at higher energies. The energy splitting increases with the laser power. Figure 2 shows the energy splittings (circles) and the difference of the integrated photoluminescences (squares) for the same sample as in Figure 1 as a function of a) the laser power, for 20 ps time delay, and b) the time delay for a laser power of 10 mW. At lo laser power the energy splitting shows a weak spli ting which rapidly increases as we increase the las power. It decreases as the time delay increases. A ter 200 ps, there is no sizeable splitting between tl two polarizations. This behavior closely follows tl decrease of the difference of the integrated lumine cence due to spin relaxation mechanisms.

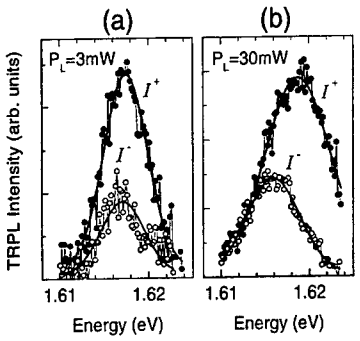

FIG. 1. TRPL spectra, I^+ and I^-, of the sample wi n_e=2.5 $\times$ 10^{10} cm^{-2} measured at an excitation energy 1.626 eV, time delay of 20 ps and for laser powers of (a) 3 mW and (b) 30 mW. The solid lines are fitting Gaussian functions of the experimental data.

These results, clearly, demonstrate the strong correlation between the difference of integrated photoluminescence of the carriers and the energy splitting. Similar results are observed for the other samples with higher two-dimensional electron gas.

The energy splitting at initial times, however, decreases with the intrinsic electron concentration. For higher doped samples (n_e = 1 and 2 $\times$ 10^{11} cm^{-2}) there is practically no initial energy splliting. This is in contrast with the initial polarization in these samples which remains sizeable. The undoped sample shows a higher initial energy splitting when compared to the one shown in Figure 1 but a similar behavior of the energy splitting and the difference in the integrated luminescence as a function of the time delay. Figure 3 shows the energy splitting as a function of the intrinsic electron concentration for different values of the laser power and the time delay. The energy splitting rapidly decreases with the intrinsic electron concentration and practically disappears for electron concentrations $\geq$ 1 $\times$ 10^{11} cm^{-2}.

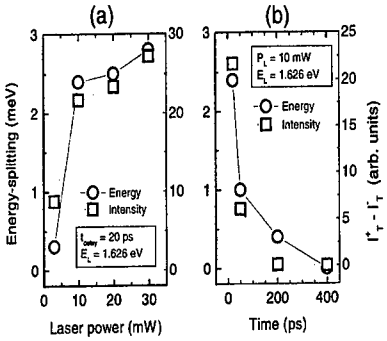

FIG. 2. The energy splittings (circles) and the difference of the integrated photoluminescence intensities, I_T^+ and I_T^-, (squares) of the same sample as in Fig. 1 as a function of (a) the laser power measured with a time delay of 20 ps and (b) the time delay measured at a laser power of 10 mW. The lines are guide for the eyes.

IV. DISCUSSION AND CONCLUSION

For undoped quasi-two-dimensional systems, the influence of the photocreated electron-hole pairs in the low-temperature emission line is dominated by two effects: i) an attractive van der Waals-like interaction between the bound electron-hole pairs and ii) a repulsive contribution due to the Pauli exclusion principle acting on the electrons and holes. The noncompensation of these two contributions gives an excitation power dependence on the emission line. For circularly polarized excitation, at initial times, only one kind of exciton is formed (e.g. with angular momentum +1). Neglecting the initial exciton spin flip,

the repulsive contribution will act only on the emission line associated with the same angular momentum as the photocreated excitons. This gives rise to an energy splitting between the excitonic emissions with angular momentum $+1$ and -1 in the case of unbalanced populations of excitons of spins ± 1. As the excitons relax their spin, balancing the two populations, the energy splitting should disappear. This effect was observed in previous works [1–4] and is in agreement with our results for the undoped sample. The doped samples with low doping levels (n_e=2.5 and 5×10^{10} cm^{-2}) also show a similar behavior, suggesting a common origin for the energy spin splitting as that discussed for undoped samples, namely, an excitonic effect.

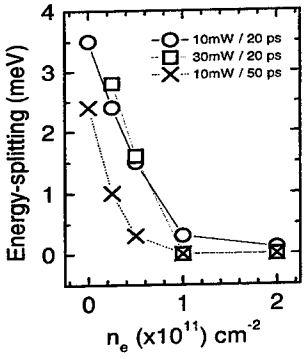

FIG. 3. The energy splitting as a function of the sample intrinsic electron gas density measured at different laser powers and time delays. The lines are guide for the eyes.

For doped samples, at relatively high densities, the intrinsic carrier gas quenches the electron-hole bound pair due to screening and phase-space filling effects. An energy splitting between the two circularly polarized emissions was also observed in p-type doped quantum wells [6,7]. Their results were interpreted on the basis of non-equilibrium distributions of the two spin-polarized electron gases, characterized by the same quasi-temperature but different chemical potential. This results in an energy splitting for the photoluminescence originated from the recombination of unbound electron-hole pairs. Therefore, no excitonic effect is invoked in this interpretation. In contrast, our results for the higher doping concentrations (n_e=1 and 2×10^{11} cm^{-2}) do not show any significant energy splitting although the difference in the integrated photoluminescence from the two different components of circular polarization is significant. The discrepancy between their results [7] and ours may come from the different species of intrinsic carriers. In our case, it is the hole gas that is strongly polarized. As the heavy holes present a high density of states due to their heavy masses, this may prevent the built up of a sizeable difference between the quasi-chemical potentials in the two hole populations.

Our set of samples allows us to study the transition from a quasi-two-dimensional system dominated by the excitonic emission to one dominated by the free carrier emission. As the intrinsic electron concentration increases, the exciton binding energy decreases as a consequence of screening and phase-space filling effects. This leads to a decrease of the energy splitting since it has an excitonic origin. The energy splitting disappears as the exciton bound state is quenched. The screening and phase-space filling reduces the exciton binding energy as well as the oscillator strength. In a first approximation, we neglect these effects in the oscillator strength and assume that the difference of the integrated luminescence is proportional to the difference in the two components of spin populations. This allows us to obtain an estimate of the critical electron carrier concentration, n_C, for which the exciton binding energy is quenched in quantum wells. From our results (Figure 3), we obtain $n_C \sim 1 \times 10^{11}$ cm^{-2}. Theoretical work is in progress in order to obtain a more quantitative analysis of our data. In particular, the regime of low intrinsic electron concentration is of interest since in this case the concept of an electron gas becomes questionable.

Acknowledgments: We are grateful to M. Potemski for helpful discussions and to I. Rasnik and M.J.S.P. Brasil for help with the experimental setup. The work at Unicamp (Brazil) was supported by CNPq, FINEP, CAPES and FAPESP.

[1] T. C. Damen, L. Viña, J. E. Cunningham, J. Shah, L. J. Sham, Phys. Rev. Lett. **67**, 3432 (1991).
[2] L. Viña, L. Muñoz, E. Péres, J. Fernández-Rossier, C. Tejedor, and K. Ploog, Phys. Rev. B**54**, R8317 (1996).
[3] T. Amand, X. Marie, B. Baylac, B. Dareys, J. Barrau, M. Brousseau, R. Planel, and D.J. Dunstan, Physics

Letters A**193**, 105 (1994).
[4] P. Le Jeune, X. Marie, T. Amand, F. Romstad, F. Perez, J. Barrau, and M. Brousseau, Phys. Rev. B**58**, 4853 (1998).
[5] J. Fernández-Rossier, C. Tejedor, L. Muñoz, and L. Viña, Phys. Rev. B**54**, 11582 (1996).
[6] M.D. Martin, E. Pérez, L. Viña, L. Gravier, M. Potemski, K. Ploog, A. Fisher, Physica **E 2**, 186 (1998).
[7] M. Potemski, E. Pérez, M.D. Martin, L. Viña, L. Gravier, A. Fisher, K. Ploog, Solid State Communication **110**, 163 (1999).
[8] J. Urdanivia, F. Iikawa, J.A. Brum, M.Z. Maialle, P. Hawrylak, and Z. Wazilewski, Proc. of 24th International Conference on Physics of Semiconductors, August 2-7, 1998, Jerusalem, Israel. in press.

PC.60

Electron Spin Relaxation Beyond D'yakonov-Perel' Interaction in GaAs/AlGaAs (110) Quantum Wells

Y. Ohno, R. Terauchi, T. Adachi, F. Matsukura, and H. Ohno

Laboratory for Electronic Intelligent Systems, Research Institute of Electrical Communication, Tohoku University

Abstract

Electron spin relaxation time τ_s and the relaxation mechanisms in GaAs/AlGaAs (110) quantum wells (QWs), where a predominant spin scattering mechanism (D'yakonov-Perel') for conventional (100) QWs is substantially suppressed, have been investigated. τ_s in (110) QWs was found nano-second order at room temperature, more than an order of magnitude longer than that of the ordinary (100) QWs. To elucidate the mechanism responsible for the slow spin relaxation, its dependence on the quantized energy, electron mobility, excitation intensity, and temperature was studied. The results suggest that excitonic electron-hole scattering may limit τ_s in a wide temperature range.

Keywords: electron spin relaxation, D'yakonov-Perel' interaction, GaAs/AlGaAs (110) quantum wells

1. Introduction

Electron spin dynamics in semiconductor nanostructures has attracted much attention from both viewpoints of physics and applications, and understanding of the spin dephasing mechanism is of great importance for the practical use of spins as information transfer or storage. So far a number of time-resolved optical experiments have been carried out in order to elucidate the spin relaxation processes in III-V or II-VI bulk semiconductors and their heterostructures. Extremely long (~100 ns) electron spin relaxation time τ_s in n-GaAs at 5 K [1], and τ_s~1.5 ns in n-type ZnCdSe/ZnSe quantum wells (QWs) at 275 K [2] have been reported. Electron-hole exchange has been put forward for the mechanism of the electron spin depolarization, since τ_s becomes longer when electrons and holes are spatially separated by applying external electric fields [3]. In the case of undoped GaAs/AlGaAs (100) quantum wells (QWs), on the other hand, typical τ_s at higher temperature (~ room temperature (RT)) is limited to several tens of picoseconds at most because of the D'yakonov-Perel' (DP) interaction [4]. In the DP mechanism, the lack of inversion symmetry of zinc-blende structure results in spin-splitting of the conduction band via spin-orbit coupling, which is the driving force for precession of spins leading to spin relaxation [5]. In two dimensional systems, this process is expected to have strong dependence on the growth axis, although in most of experiments

only QWs formed on a (100) plane have been investigated. In this paper, we report our study on τ_s in undoped and n-type GaAs/AlGaAs QWs grown on (110) substrates. At room temperature, we observed that τ_s in (110) QWs reaches ~ 4 ns, about 30 times longer than that of similarly prepared (100) QWs. This long spin relaxation time can be explained in terms of anisotropic dependence of the DP mechanism on the growth axis: the contribution from the DP interaction is expected to be suppressed for electron spins polarized in [110] direction.

2. Experimental

For a systematic study, we prepared several GaAs/AlGaAs QW structures grown on semi-insulating (110) GaAs substrates by molecular beam epitaxy. All the samples consist of 60 periods of GaAs QWs separated by $Al_{0.4}Ga_{0.6}As$ barriers. Undoped samples with different well widths were used to study the electron quantized energy (E_1) dependence of τ_s, while Si-doped QW samples (with different doping concentration) were prepared in order to investigate the effect of doping of electrons as well as the mobility (μ) dependence of τ_s.

To evaluate τ_s of the samples, we employed a degenerate circularly-polarized pump-probe transmission technique using an ultrashort optical pulses (~110 fs duration) generated by a mode-locked Ti:Al_2O_3 laser and tuned at heavy hole exciton resonance. τ_s was defined by $\tau_s = 2\tau$ when the decay of the polarization P is fit by a single exponential function $P=P_0\exp(-t/\tau)$. The excitation intensity I_{ex} (~2 mW) was fixed except for the study of I_{ex} dependence of τ_s. The temperature dependence of τ_s was obtained in the range of 5~300 K with the sample set in a liquid He cryostat.

3. Results and Discussions

In Fig. 1, we plot τ_s for the undoped sample

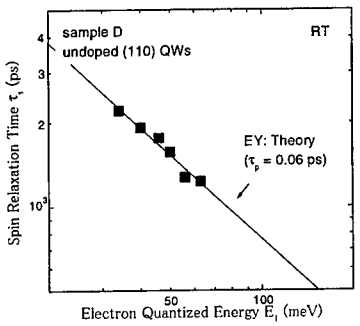

Fig. 1. Symbols are plots of ts as a function of quantized energy E_1 at room temperature.

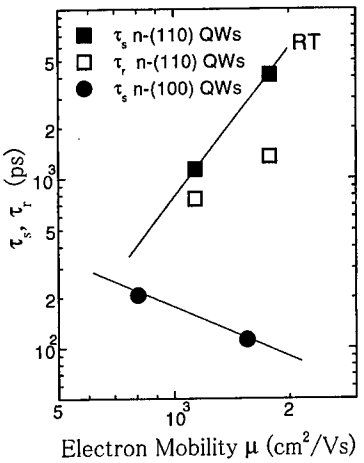

Fig. 2. Electron mobility μ dependence of spin relaxation time τ_s and recombination time τ_r measured at room temperature.

measured at room temperature as a function of E_1. It is seen that for (110) QWs τ_s reaches ~2 ns, while in the case of QW structures with the same well width grown on (100) substrates, τ_s was ~70 ps (not shown). The increase of τ_s can be attributed to the fact that the spin relaxation is quite anisotropic and

substantially suppressed when the growth axis and the spin polarization axis are taken along [110] direction, which is consistent with the DP theory [5]. As indicated by a line, $\tau_s \propto E_1^{-1}$, which qualitatively agrees with that of Elliott-Yafet mechanism [6]; we can fit the data by assuming the momentum relaxation time τ_p = 0.06 ps, the same order of the expected electron mobility in undoped sample. In Fig. 2, τ_s of both n-type (110) (solid squares) and (100) QWs (solid circles) with different doping concentrations are plotted against μ measured at RT. It can be seen that τ_s of (110) QWs increases with μ, while that of (100) QWs decreases as $\tau_s \propto \mu^{-1}$. The latter is in good agreement with the DP prediction [7]. On the other hand, $\tau_s \propto \mu$ is expected if the spin relaxation is governed by the EY mechanism.

Although μ-dependence of τ_s shown in Fig. 2 as well as E_1-dependence supports that the EY mechanism is the most probable mechanism governing the spin relaxation in (110) QWs, it is difficult to explain I_{ex}- and T-dependences of τ_s shown in Figs. 3 and 4 within the framework of the EY mechanism. In Fig. 3, we plot τ_s of (110) and (100) QWs measured at RT as a function of I_{ex}. Clear difference in I_{ex}-τ_s relation between (110) and (100) QWs can be seen. When I_{ex} is increased one order of magnitude, τ_s of (110) QWs decreases by a factor of 3, while τ_s of (100) QWs does not change.

In Fig. 4, we plot the T-dependence of τ_s for undoped sample. One observes two different temperature regimes below and above T = 20 K. A distinct feature is that τ_s increases with T as $\tau_s \propto T^{0.6}$ when T > 20 K. This behavior cannot be explained by neither DP nor EY models: both predict that τ_s increases with T. Another candidate, an exchange interaction between free electrons and holes (Bir-Aronov-Pikus mechanism), can also be ruled out by the same reason [8]. Instead, an excitonic spin relaxation model can qualitatively explain the T dependence of τ_s; thermal ionization of excitons is enhanced with increasing T, resulting in the reduction of the spin scattering rate at higher T [2]. The I_{ex} dependence of τ_s (shown in Fig. 3) can be understood by taking into account the fact that the electron spin scattering is enhanced as the hole concentration is increased.

When T < 20 K, τ_s was saturated at ~ 300 ps. The absolute value of τ_s as well as the feature of saturation of τ_s below 20 ~ 30 K are quite similar to those of undoped (100) QWs

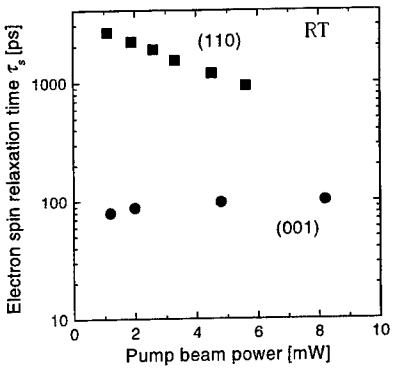

Fig. 3. Excitation intensity dependence of the electron spin relaxation time in (110) and (100) quantum wells

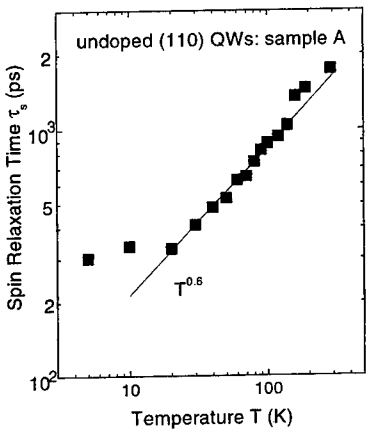

Fig. 4. Temperature dependence of τ_s of undoped (110) QWs. The solid line is guide for eyes.

[9]. This suggests that at low temperatures the spin relaxation mechanism responsible for (100) QWs is also limiting τ_s of (110) QWs.

It should be noted, however, that hole spin relaxation time might be quite different between (100) and (110) QWs. The dominant spin relaxation mechanism for holes at low temperature regime is considered to be the EY interaction [9]. In the case of (100) QWs, the hole spin relaxation time at low temperature limit reaches as long as a few hundreds picoseconds due to separation of heavy and light hole states. On the other hand, mixing between the two valence bands occurs in (110) QWs since the growth axis is not a principal axis [10]. This may result in quite fast spin relaxation of holes even at low temperature limit. Thus further study is still necessary to clarify whether τ_s of $T < 20$ K is determined by excitonic spin relaxation effect or not.

4. Conclusion

In conclusion, we investigated the spin relaxation mechanism of 2DEGs in GaAs/AlGaAs (110) QWs, where the DP interaction is suppressed. The temperature dependence $\tau_s \propto T^{0.6}$ observed in an undoped sample when $T > 20$ K, as well as the excitation intensity dependence, indicate that the excitonic electron-hole exchange interaction is most effective even at higher temperature in the absence of DP interaction.

Acknowledgement

The authors wish to thank T. Dietl for valuable discussion. This work is partly supported by "Research for the Future" Program from the Japan Society for the Promotion of Science, and Grant-in Aid for Scientific Research (No. 09244103 and No. 11650002) from the Ministry of Education, Science, Sports, and Culture, Japan.

References

[1] J.M. Kikkawa and D.D. Awschalom, Phys. Rev. Lett. **80**, 4313 (1998).

[2] J.M. Kikkawa, I.P. Smorchkova, N. Samarth, D.D. Awschalom, Science **277**, 1284 (1997).

[3] D. Hagele et al., Appl. Phys. Lett. **73**, 1580 (1998); J.M. Kikkawa and D.D. Awschalom, Nature **397**, 139 (1999).

[4] A. Tackeuchi *et al.*, Appl. Phys. Lett. **68**, 797 (1996); R.S. Britton *et al.*, Appl. Phys. Lett. **73**, 2140 (1998).

[5] M.I. D'yakonov and V.Yu. Kachorovskii, Sov. Phys. Semicond. **20**, 110 (1986).

[6] R.J. Elliott, Phys. Rev. **96**, 266 (1954); S. Muto and A. Tackeuchi, unpublished.

[7] R. Terauchi et al., Jpn. J. Appl. Phys. **38**, 2549 (1999).

[8] G. Fishman and G. Lampel, Phys. Rev. B **16**, 820 (1977).

[9] S. Adachi et al., J. Lumin., **72-74**, 307 (1997).

[10] Y. Kajikawa, Phys. Rev. B **51**, 16790 (1995).

PC.61

Non-Ohmic Vertical Transport in Multilayered Quantum Hall Systems

Minoru Kawamura Akira Endo, Shingo Katsumoto [1] and Yasuhiro Iye [1]

Institute for Solid State Physics, University of Tokyo
7-22-1, Roppongi, Tokyo 106-8666, Japan

Abstract

The vertical transport in weakly coupled multilayered two-dimensional electron systems has been studied in the integer quantum Hall regime. The current-voltage characteristics show prominent non-Ohmicity in the vertical transport when each layer is in the quantum Hall state. The voltage dependence curves of the differential conductivity scaled by the mesa perimeter collapse onto a single curve at lower voltages, while those scaled by mesa area are on a single curve at higher voltages. This shows that the current flows through the surface of the sample at low voltage region and through the bulk at high voltage region. A crossover from the surface transport to the bulk transport occurs in a fairly narrow range of the bias voltage.

Key words: vertical transport, superlattice, quantum Hall effect, chiral surface state
PACS: 73.40.Hm, 73.20.Dx

Two-dimensional electron gas (2DEG) exhibits the integer quantum Hall effect (QHE) when placed under a strong magnetic field. The issue of the QHE in weakly coupled multilayered 2DEG systems has been addressed theoretically and experimentally since early 1980's [1–4]. Störmer *et al.*[4] first demonstrated experimentally that the quantized Hall resistance and the vanishing diagonal resistance occur in the presence of the interlayer coupling in semiconductor superlattice. Multilayered quantum Hall systems have recently gained renewed interest by the theoretical prediction [5,6] of the existence of a new metallic state at the periphery of the sample, called a chiral surface state. At the edge of an isolated 2D quantum Hall state, edge channels are formed which are free from backscattering because of their chirality. When interlayer transfer is introduced, the edge states in adjacent 2D planes are coupled to form a metallic 2D sheath at the periphery of the sample. The electrons in a chiral surface state are expected to flow ballisticaly in the in-plane direction and diffusively in the out-of-plane direction. Despite of its 2D character, the surface state is free from the localization (interference) effect because of the chirality along the in-plane direction. This enables us to observe metallic 2D sheet conductivity smaller than e^2/h.

The existence of such surface states is confirmed experimentally by Druist *et al.*[7] They have found that the vertical conductivity in the QHE regime scales with the sample perimeter at low enough temperatures. At higher temperatures where the current mainly flows through bulk, the verti-

[1] Also at *CREST, Japan Science and Technology Corporation*

cal conductivity scales with the sample area. In the present work, we have found that the current-voltage characteristics in the QHE regimes exhibits prominent nonlinearity.

Sets of two identical $GaAs/Al_{0.15}Ga_{0.85}As$ superlattice wafers were grown. One wafer for the vertical transport was grown on an n^+ GaAs substrate and capped with a heavily doped n^+ GaAs layer. The other wafer for the lateral transport was grown on a semi-insulating GaAs substrate. The superlattice part consists of 100 units of 10 nm wide GaAs well layer and 15 nm wide AlGaAs barrier layer. The total height of superlattice is $L = 2.5$ μm. Relatively low Al content $x = 0.15$ was chosen to achieve a sufficient large interlayer transfer integral. Si donors were doped only in the central 5nm of the AlGaAs barrier layer to a concentration 1.3×10^{18} cm^{-3}. For the vertical transport, square columnar mesas were fabricated by photolithography and wet chemical etching. Ohmic contact was achieved by standard AuGe alloying technique on the top face of the mesa and the backside of the chip. Four mesas with different crosssections were fabricated on a single chip, 50×50 , 100×100 , 200×200 and 400×400 μm^2. Figure 1 shows the superlattice structure and a schematic picture of the sample for the vertical transport. The samples for the lateral transport was patterned into the Hall bar shape. Magnetotransport measurements was carried out using a dilution refrigerator down to 30 mK in a superconducting solenoid up to 15 T. A standard ac lock-in technique was employed for the resistance measurement.

Magnetic field dependence of the in-plane resistance R_{xx} and the Hall resistance R_{xy} are shown in Fig. 2 (a). From these lateral transport data, we obtain the sheet carrier density $n = 2.3 \times 10^{15}$ m^{-2}/layer and the mobility $\mu = 6300$ cm^2/Vsec. The QHE occurs at filling factors $\nu = 1$ and $\nu = 2$. In Fig. 2(b), the magnetic field dependence of the out-of-plane resistance R_{zz} are plotted for three samples with sizes 50×50 , 100×100 and 200×200 μm^2. The R_{zz} curve takes large maxima at magnetic field values where the lateral transport shows the QHE. The inset of Fig. 2(b) shows the size dependence of the out-of-plane conductance $G_{zz} = 1/R_{zz}$ at a filling factor $\nu = 2$. G_{zz} is almost proportional to the mesa perimeter indicating that the current is carried by the surface channels.

The temperature dependence of the out-

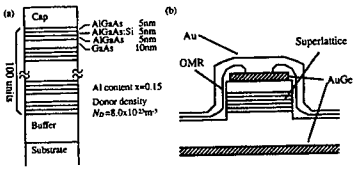

Fig. 1. Schematic picture of the superlattice structure (a) and the sample for the vertical transport (b).

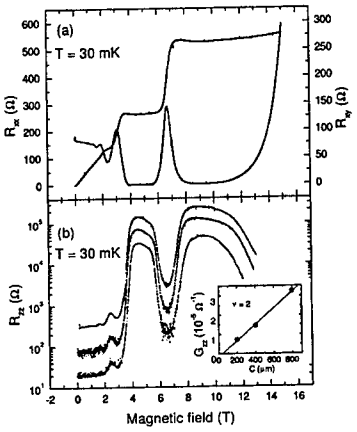

Fig. 2. (a) Magnetic field dependence of the in-plane resistance R_{xx} and the Hall resistance R_{xy}. (b) Magnetic field dependence of the out-of plane resistance R_{zz} in three samples with crosssections, 50×50, 100×100 and 200×200 μm^2 (from top to bottom). The inset shows G_{zz} at $\nu = 2$ versus sample perimeter.

of-plane conductance G_{zz} at $\nu = 2$ is plotted in Fig. 3. The vertical axis is scaled by mesa perimeter in Fig. 3(a) and by mesa area in Fig. 3(b). The out-of-plane conductivity decreases rapidly with decreasing temperature following an Arrhenius type temperature dependence and tends to an almost constant value below 100 mK. Above 100 mK, the out-of-plane conductivity scaled by mesa area is on a single curve indicating that the transport in the high temperature region is through the bulk of the sample. On the other hand, below 100 mK, the almost temperature independent values of the out-of-plane conductivity are scaled by mesa perimeter. This implies that transport is through the surface channels. According to Balents and Fisher[6], the sheet conductivity of the chiral surface states at filling $\nu = N$ is given by

$$\sigma_{zz}^{2D}(\nu = N) = N\frac{e^2t^2\tau a}{2\pi\hbar^3 v}, \qquad (1)$$

where t is the interlayer transfer integral, τ is the elastic scattering time, a is the interlayer spacing and v is the electron velocity of the edge state. This formula contains two unknown parameters τ and v which are difficult to determine independently. This makes it hard to compare the observed sheet conductivity with the theoretical predictions.

Above 100 mK, the measured conductance G_{zz} shows the Arrhenius type temperature dependence, $G_{zz} \propto \exp(-E_a/k_BT)$, with the activation energy $E_a = 0.95 \pm 0.05$ K which is much smaller than $\hbar\omega_c/2 = 4.1$ meV $= 48$ K. Note that there is a band of extended states with the band width $4t$ at the center of each Landau subband. Although it decreases the activation energy to $\hbar\omega_c/2 - 2t$, the band width $4t = 0.12$ meV is too small to explain the experimental data. The observed small activation energy implies that the relevant conduction process is not the excitation to the extended states at the center of Landau subbands but the hopping among the localized states. The activation energy for the latter process might be much smaller

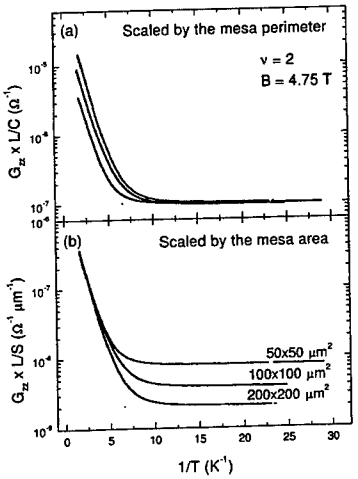

Fig. 3. Temperature dependence of the out-of-plane conductivity G_{zz}. The vertical axis is scaled by mesa area in (a) and by mesa perimeter in (b).

than $\hbar\omega_c/2 - 2t$, although it is hard to estimate since it depends sensitively on the random potential profile.

Now we turn to the current-voltage (I-V) characteristics. We measured the out-of-plane differential resistance by varying the applied dc bias current. In Fig. 4, we plot the inverse of the measured differential resistance (*i.e.* differential conductance) at 30 mK as a function of the voltage across the superlattice part. The vertical axis is scaled by mesa perimeter in Fig. 4(a) and by mesa area in Fig. 4(b) in the same manner as done in Fig. 3. In the low voltage region, the differential conductance curves scaled by mesa perimeter collapse onto a single curve, while those by mesa area are on a single curve at higher voltages. As the voltage is increased, a crossover from the surface transport to the bulk transport occurs in a fairly narrow voltage range. Similar non-Ohmic behavior is observed at a filling factor $\nu = 1$ as shown in

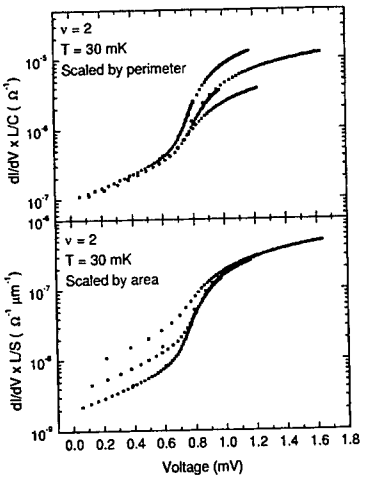

Fig. 4. Voltage dependence of differential conductivity at $\nu = 2$. The vertical axis is scaled (a) by mesa area and (b) by mesa perimeter.

Fig. 5. The voltage for the crossover from the surface transport to the bulk transport for $\nu = 1$ is smaller than that for $\nu = 2$.

It is also noted that the differential conductance exhibits significant voltage dependence even in the region away from the crossover. The non-Ohmicity in the high voltage region, where the current mainly flows through the bulk, is attributed to the non-linearlity in the hopping process among the localized states near the Fermi level[8]. Non-Ohmicity is also observed in the low voltage region. It is noteworthy that the sheet conductance in this region is almost independent of temperature. This non-Ohmicity, together with the sheet conductivity much smaller than e^2/h, reflects the marginally metallic nature of the chiral surface state. According to recent theories[9], provided that the coherence length ξ is much greater than the mesa perimeter C, increasing the ratio of the mesa height to the mesa perimeter L/C leads to a transition from a metallic 2D chiral surface state to a 1D insulator. We speculate that the observed non-Ohmicity in low voltage region may be related to such trend.

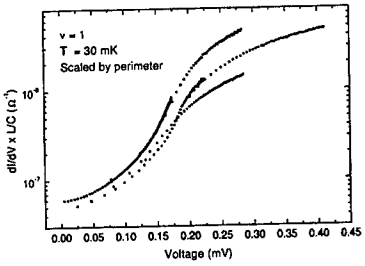

Fig. 5. Voltage dependence of the differential conductivity scaled by mesa perimeter at $\nu = 1$.

References

[1] M. Ya. Azbel, Phys. Rev. B 26 (1982) 3430.

[2] B. I. Halperin, J. J. Appl. Phys. Suppl. 26 (1987) 1913.

[3] T. Ohtsuki, B. Kramer and Y. Ono, J. Phys. Soc. Jpn. 62 (1993) 224.

[4] H. L. Störmer, J. P. Eisenstein, A.C. Gossard, W. Wiegmann and K. Baldwin, Phys. Rev. Lett. 56 (1985) 85.

[5] J. T. Chalker and A. Dohmen, Phys. Rev. Lett 75 (1995) 4496.

[6] L. Balents and M. P. A. Fisher, Phys. Rev. Lett 76 (1996) 2782.

[7] D. P. Druist, P. J. Turley, K. D. Maranowski, E. G. Gwinn and A. C. Gossard, Phys. Rev. Lett. 80 (1998) 365.

[8] M. Kawamura, A. Endo, S. Katsumoto and Y. Iye, J. Phys. Soc. Jpn. in press.

[9] I. A. Grunzberg, N. Read and S. Sachdev, Phys. Rev. B 56 (1997) 13218; S. Cho, L. Balents and M. P. A. Fisher, Phys. Rev. B 56 (1997) 15814; V. Plerou and Z. Wang, Phys. Rev. B 58 (1998) 1967.

PC.62

DISORDER-INDUCED PEAK IN THE LOW-FREQUENCY CONDUCTIVITYOF A 2DEG IN QUANTIZING MAGNETIC FIELD

F. Kuehnel†, M.I. Dykman†, and L. Pryadko*

† Physics Department, Michigan State University, East Lansing, Michigan 48824, USA

* Institute for Advanced Study, Princeton, New Jersey 08540, USA

We investigate the low-frequency magnetoconductivity $\sigma_{xx}(\omega)$ of a nondegenerate 2D electron gas in quantizing magnetic fields. Naively, the conductivity would be expected to have peaks of width $\approx \Gamma$ at $\omega = n\omega_c$, with $n = 0,1,\ldots$ (ω_c is the cyclotron frequency and $\hbar\Gamma$ is the disorder-induced width of the Landau levels). On the other hand, since single-electron states are localized for all energies but one, the single-electron conductivity $\sigma_{xx}(0)$ should be equal to zero for finite temperatures and in the absence of energy relaxation. Then $\sigma_{xx}(\omega)$ should have a peak at a *nonzero* frequency $\omega \approx \Gamma$. We show that this peak indeed emerges, and we analyze it for $\hbar\omega_c > k_BT > \hbar\Gamma$ — the conditions usually met for electrons on helium surface and also achievable in ultra high quality heterostructures. In order to investigate the shape of the low-frequency peak we use the method of moments (MOM) in combination with an appropriately modified method of optimal fluctuations and the scaling arguments. In MOM, $\sigma_{xx}(\omega)$ is restored from the spectral moments of the low-frequency conductivity. By analyzing the convergence of the moment expansion we find that $\sigma_{xx}(\omega) \propto \omega^{\mu}$ for $\omega \to 0$, with the exponent $\mu \approx 0.26$. A power-law behavior is also obtained by the scaling analysis of semiclassical drift of the cyclotron orbit centers, which can be mapped onto a problem of 1D Hamiltonian motion with fractal phase space. We also establish the role of many-electron effects, which determine the low-frequency cutoff of the single electron theory and therefore become substantial even for low electron densities.

Statistics of the Coulomb blockade peak spacings of a silicon quantum dot

David Abusch-Magder[1,2,3], F. Simmel[2], D. A. Wharam[4],
M. A. Kastner[3], and J. P. Kotthaus[2]
(1) Bell Labs, Lucent Technologies, 600 Mountain Ave., Murray Hill NJ, 07974,
(2) Center for NanoScience and Sektion Physik, LMU München,
Geschwister-Scholl-Platz 1, D-80539 München,
(3) Department of Physics, Massachusetts Institute of Technology, Cambridge, MA 02139,
(4) Institut für Angewandte Physik, Universität Tübingen,
Auf der Morgenstelle 10, D-72076 Tübingen

We present an experimental study of the fluctuations of Coulomb blockade peak positions of a quantum dot. The dot is defined by patterning the two-dimensional electron gas of a silicon MOSFET structure using stacked gates. The ratio of charging energy to single particle energy is considerably larger than in comparable GaAs/AlGaAs quantum dots. The statistical distribution of the conductance peak spacings in the Coulomb blockade regime was found to be unimodal and does not follow the Wigner surmise. The fluctuations of the spacings are much larger than the typical single particle level spacing and thus clearly contradict the expectation of random matrix theory. Measurements of the natural line width of a set of several adjacent conductance peaks suggest that all of the peaks in the set are dominated by electrons being transported through a single broad energy level.

The spectral properties of many quantum mechanical systems whose classical behavior is known to be chaotic are remarkably well described by the theory of random matrices (RMT) [1]. This has been experimentally confirmed, for example, in measurements of slow neutron resonances of nuclei [2] and in microwave reflection spectra of billiard shaped cavities [3]. Electron transport experiments performed on semiconductor quantum dots in the Coulomb blockade (CB) regime [4] provide a further possibility to check RMT predictions. The classical motion of electrons in these structures can be assumed to be chaotic due to an irregular potential landscape produced by impurities, an asymmetric confinement potential [5], and/or electron-electron interactions [6]. The transport properties of quantum dots are inherently related to their energy spectra and electronic wavefunctions and thus the connection with RMT is readily made [5,7].

On the other hand, the distribution of the Coulomb blockade peak spacings have been found to deviate from the expectations of RMT [8–11]. The results suggest that the peak spacings are not distributed according to the famous Wigner surmise. Furthermore, there is no indication of spin degeneracy which would result in a bimodal peak spacing distribution [10]. In Refs. [8,9,11] the fluctuations of the peak spacings are considerably larger than expected from RMT, whereas the experiments presented in Ref. [10] yield smaller peak spacing fluctuations, which, however, are still larger than those predicted by RMT.

The deviations from the RMT predictions have been frequently interpreted as fluctuations in the charging energy. As the charging energy reflects the Coulomb interactions both between the electrons on the dot as well as between the dot and its environment, the dependence of the fluctuations on the interaction strength is of fundamental interest. Numerical studies suggest that the fluctuations are proportional to the charging energy rather than to the single particle level spacing [8,12]. Recently, also a non-interacting explanation for the Gaussian shape of the peak spacing distribution has been given in terms of level dynamics due to shape deformation of the quantum dot [13].

Here we present an experimental study of the statistics of Coulomb blockade peak positions of a quantum dot. The dot is defined by patterning the two-dimensional electron gas of a silicon metal oxide semiconductor field effect transistor (MOSFET) structure using stacked gates. These experiments differ significantly in two major ways from prior experiments on quantum dots defined in GaAs/AlGaAs heterostructures: first and foremost, due to the different electron density and material properties of silicon, the ratio of the charging energy, E_C, to the single particle energy level spacing, $\Delta\epsilon$, is considerably larger; likewise the dimensionless parameter r_s, which characterizes the strength of the Coulomb interactions, is larger than in previous studies. Secondly, the number of electrons is varied by the application of a voltage to a top gate instead of by squeezing the quantum dot with a plunger gate. We find that the distribution of the peak spacings is unimodal and roughly Gaussian. The magnitude of the fluctuations is 15 times larger than that predicted by RMT.

Conduction through a small electron island coupled to leads via tunnel barriers is normally suppressed if $k_BT \ll E_C$, where E_C is the charging energy of the island. This effect is known as the Coulomb blockade [4]. The blockade is lifted when the condition $\mu_d < \mu_{dot} < \mu_s$ is satisfied, where μ_s, μ_d, and μ_{dot} are the chemical potentials of the source, drain and dot, respectively. The chemical potential of the dot is defined as $\mu_{dot}(N+1) = E(N+1) - E(N)$ where $E(N)$ is the total energy of the dot occupied by N electrons. In the case where the blockade is lifted an electron can tunnel from the source onto the dot, changing the dot's occupation from N to $N+1$, and sequentially tunnel off the dot to the drain

leaving the dot in its original state. The resulting fluctuation of the electron number on the dot leads to a finite conductance. Experimentally this can be achieved by appropriately tuning μ_{dot} with an external gate.

In the constant interaction (CI) model [4] the energy of the dot is approximated as $E(N) = (Ne)^2/2C_\Sigma + \sum_{i=1}^{N} \epsilon_i$, where the electrostatic interactions are treated using a simple capacitive charging model with a total dot capacitance C_Σ, and the quantum mechanical terms are taken into account as single particle energies ϵ_i. In this model the difference of the chemical potentials for successive occupation numbers, the so called addition energy, is $\Delta\mu_N = \mu(N+1) - \mu(N) = E_C + \Delta\epsilon_N$ with a constant charging energy $E_C = e^2/C_\Sigma$, and the level spacing $\Delta\epsilon_N = \epsilon_{N+1} - \epsilon_N$. This is mapped to gate voltages via $e\frac{C_g}{C_\Sigma}\Delta V_g = E_C + \Delta\epsilon_N$ where C_g is the capacitance of the dot to the gate and ΔV_g the difference between the gate voltages at which adjacent conductance maxima occur.

This final expression motivated the original investigations of the peak spacings in the light of random matrix theory. RMT shows that the normalized spacings S ($\langle S\rangle = 1$) between adjacent eigenvalues of a generic time-reversal invariant Hamiltonian are distributed according to the Wigner surmise

$$P_W(S) = \frac{\pi}{2} S e^{-\frac{\pi}{4}S^2}. \qquad (1)$$

The fluctuations of these spacings are $(\langle S^2\rangle - \langle S\rangle^2)^{1/2} \approx 0.52\,\langle S\rangle$. However, experiments have shown that the combined CI-RMT model is not capable of describing the observed peak spacing distribution correctly [8–11].

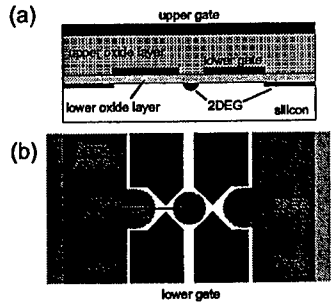

FIG. 1. Schematic representation of the device design. A cross section of the device is shown in (a). Two oxide and two gate layers are formed on top of a silicon substrate. The voltage on the upper gate is used to vary the electron density in the 2DEG induced at the interface of the lower oxide and the silicon. A top view of the device is shown in (b). The pattern in the lower gates defines a quantum dot in the induced electrons; note that the upper gate covers all of the area show in (b) and overlaps the source and drain. The lithographic dimensions of the quantum dot are 250 nm × 270 nm.

The Coulomb blockade measurements on which the following analysis is based have been performed on a quantum dot defined in a silicon MOSFET structure. We have utilized a stacked gate structure to pattern the electron gas as shown in fig. 1. First, a 20 nm thick gate oxide is grown on a p-type silicon substrate (lower oxide), and then a lower metal gate is deposited and patterned using electron beam lithography and lift-off techniques. Above the lower gate a second layer of silicon dioxide is deposited (upper oxide, 80 nm thick), and finally an upper gate is formed; the upper oxide layer serves to insulate the lower gate from the upper gate. Application of positive voltages to the upper gate leads to the formation of a two-dimensional electron gas (2DEG) at the Si/SiO_2 interface; n^+ implanted regions serve as Ohmic contacts to the 2DEG. Further details about this device may be found elsewhere [15,16]. The lower gates locally screen the electric field created by the upper gate, and a quantum dot is formed by applying appropriate negative voltages to the lower gates. The size of the dot is estimated from the capacitance to be $A \approx 200\,\text{nm} \times 200\,\text{nm}$, which agrees well with the lithographic dimensions of 250 nm × 270 nm when electrostatic depletion at the edge is considered. The electron density can be varied by changing the upper gate voltage, whereas the lower gate voltage controls the tunnel barriers and the electrostatic confinement potential of the quantum dot. This technique allows the definition of very small structures which therefore have low capacitances and high charging energies.

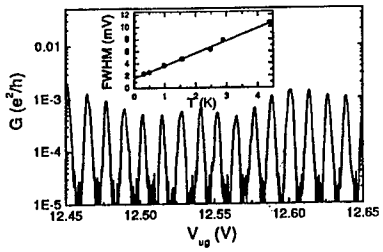

FIG. 2. The conductance as a function of gate voltage at $T = 320\,\text{mK}$. The inset shows the temperature dependence of the full width at half maximum of one of the conductance peaks.

In contrast to previous experiments on quantum dots in GaAs/AlGaAs heterostructures the electron density is considerably higher, $n_s \approx 2.5 \cdot 10^{16}\,\text{m}^{-2}$. The mobility of the two-dimensional electron gas is $\mu = 0.56\,\text{m}^2/\text{Vs}$, and the mean free path $l \approx 100\,\text{nm}$ is comparable to the system size. The single particle energy level spacing can

be obtained from the estimated dot area, A, via Weyl's formula [17] as $\Delta\epsilon = \frac{2\pi\hbar^2}{gm^*A} = 15\,\mu$eV, where g is the degeneracy of electronic states in the two-dimensional electron gas, and m^* is the effective mass of the electrons. In a 2DEG in a silicon MOS system $m^* = 0.2m_e$, and at $B = 0$ both the spin and valley degeneracies must be considered and therefore $g = 4$. While these quantum dots are smaller than many of the GaAs/AlGaAs quantum dots studied [8–10], $\Delta\epsilon$ is of the same order due to the larger effective mass, and to the valley degeneracy.

To determine the value of E_C we measure the temperature dependence of the full width at half maximum ($FWHM$) of several conductance peaks; one such measurement is shown in the inset of fig. 2. From the slope $\frac{d(FWHM)}{dT}$ we determine $\frac{C_\Sigma}{C_2}$, while from the $T = 0$ intercept we determine the natural line width Γ [14]. Four consecutive peaks were measured and all yield $\frac{C_2}{C_\Sigma} = 0.15 \pm .01$, from which we calculate that $C_\Sigma \approx 85$ aF and $E_C = 1.9$ meV.

The measured values of Γ range from $100 - 165\,\mu$eV, are remarkably uniform, and seem to contradict the Thouless criterion [18], $\Gamma < \Delta\epsilon$, believed necessary for charge localization and therefore Coulomb blockade. However, recent theoretical work [19] predicts just such behavior in chaotic quantum dots due to the effects of a single, well coupled energy level. In the model of ref. [19] an electron tunnels into and subsequently out of a single, well coupled energy level on the quantum dot. When the gate voltage is adjusted between conductance peaks the additional electron scatters into another, narrower single particle state leaving the original broad level unoccupied. The next conductance peak is due to transport throught the same broad energy level; this situation may repeat many times allowing one level to dominate the transport through more than 20 conductance peaks. Our data may be explained by this hypothosis, and suggest that further experimental studies are needed to test this model.

The strength of the electronic interactions characterized by the dimensionless parameter $r_s = g/(2\sqrt{\pi n_s}a_B^*) = 2.1$ considerably exceeds the values obtained in recent experiments (where $r_s \approx 1$) [8–10]; here a_B^* is the effective Bohr radius. Similarly, the ratio of charging energy to single particle energy level spacing $E_C/\Delta\epsilon \approx 125$, another measure of the relative importance of electron-electron interactions, is larger than in the experiments performed on GaAs/AlGaAs quantum dots.

The measurements were performed in a ^{3}He refrigerator at a temperature of $T = 320$mK using standard lock-in techniques at low frequencies and bias. The conductance oscillations were measured as a function of the upper gate voltage. Consequently, the electron density was varied without drastically changing other system parameters such as charging energy, single particle energy, and dot shape. This also contrasts with former experiments on the statistics of conductance oscillations where the shape of the quantum dot was distorted by plunger gates [10].

The following analysis is based on a series of more than 100 conductance peaks occurring in the upper gate voltage range from 12.1 V to 13.5 V. In this range the electron density changes from $2.4 \times 10^{16}\,\mathrm{m}^{-2}$ to $2.6 \times 10^{16}\,\mathrm{m}^{-2}$. The quantum point contacts connecting the quantum dot to the leads are tuned into the tunneling regime by applying voltages of -4.5 V and -8.0 V to the left and right pair of lower gates, respectively. The precise position of each peak is obtained by fitting the peak by a thermally broadened line shape. The gate voltage spacings, ΔV_g, are calculated from the peak positions.

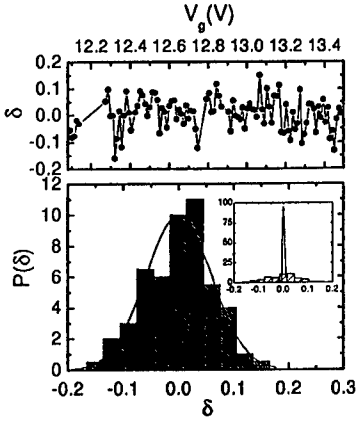

FIG. 3. The top panel shows normalized peak spacings δ obtained from an upper gate voltage sweep. The fluctuations around the mean value 0 are much larger than expected from the CI-RMT model. The bottom panel is an histogram showing the distribution of the normalized peak spacings. The area of the histogram is normalized to unity. A Gaussian fit with standard deviation of $\sigma = 0.06$ is also displayed. The inset shows the same histogram alongside the Wigner surmise, the distribution predicted by CI-RMT, for $\Delta\epsilon = 15\,\mu$eV. The experimental distribution is much broader than expected from CI-RMT.

The mean value $\langle\Delta V_g\rangle$ changes by only 4 parts per thousand in the gate voltage range of the experiment showing that the influence of the upper gate on the capacitance and therefore on the size of the dot is rather weak. Accordingly, the shape deformation which has been postulated to explain the distribution of ΔV_g [13] plays no

significant role in this experiment. The normalized peak spacings

$$\delta = \frac{\Delta V_g - \langle \Delta V_g \rangle}{\langle \Delta V_g \rangle} \qquad (2)$$

are displayed in Fig. 3. The fluctuations of δ are computed to be $\langle \delta^2 \rangle^{1/2} \approx 0.06$. The fluctuations in the addition energy are, therefore, roughly 115μeV, which is 7.5 times the mean level spacing $\Delta\epsilon$, and thus 15 times larger than the fluctuations expected from CI-RMT. This supports the view that the fluctuations of the addition energy scale with the Coulomb energy rather than with the kinetic energy. However, the proportionality factor 0.06 is smaller than that suggested by numerical calculations (0.1 - 0.2) [12]. It should be noted that in these experiments $\Delta\epsilon \approx k_B T$. We expect that the effect of thermal broadening would be to reduce the fluctuations in peak spacing. A simple model [10] predicts that the fluctuations expected within CI-RMT would be reduced by a factor of $2-3$. If we incorporate this correction into CI-RMT then the fluctuations we find in our experiment are $30-45$ times larger than those predicted by CI-RMT.

The distribution of the peak spacings normalized to an area of unity is shown in Fig. 3. The distribution is unimodal and roughly has the shape of a Gaussian. In the inset of Fig. 3 the experimental distribution is depicted together with the Wigner surmise (Eq. 1); for comparison to δ we have rescaled the predictions of CI-RMT taking into account the experimental values of E_C and $\Delta\epsilon$. As in previous experiments there is no evidence of a bimodal addition spectrum as is predicted by the CI-RMT model. This is in agreement with the theoretical prediction that the influence of spin degeneracy on the addition spectrum is washed out for stronger electron-electron interactions ($r_s > 1$) [12].

In conclusion, we have investigated the Coulomb blockade peak spacing distribution of a quantum dot fabricated in the 2DEG of a silicon MOSFET structure. In accordance with experiments on GaAs/AlGaAs quantum dots the distribution differs from the Wigner surmise and is roughly Gaussian. The fluctuations are approximately $0.06 \times E_C$. Due to the large ratio of charging energy E_C to single particle energy $\Delta\epsilon$ this strongly suggests that the fluctuations scale with E_C and not with $\Delta\epsilon$. This clearly contradicts the predictions of CI-RMT and indicates that the fluctuations are dominated by electron-electron interactions in this system.

The authors would like to thank the staff of the Microelectronics Lab at Lincoln Laboratory for their help with device fabrication, and U. Sivan, M. Stopa, H. Baranger for fruitful discussions. This work was supported by the Alexander-von-Humboldt Foundation, the DFG Sonderforschungsbereich 348, and by the Army Research Office under contract DAAH04-94-0199 and contract DAAH04-95-0038. Work at Lincoln Laboratory was sponsored by the U.S. Air Force. DA-M gratefully acknowledges support from the Alexander-von-Humboldt Foundation, and the Bell Labs Foundation.

[1] M. L. Mehta, *Random Matrices*, 2nd ed. (Academic Press, London, 1991).
[2] R. U. Haq, A. Pandey, and O. Bohigas, Phys. Rev. Lett. **48**, 1086 (1982).
[3] H. D. Gräf, H. L. Harney, H. Lengeler, C. H. Lewenkopf, C. Rangacharyulu, A. Richter, P. Schardt, and H. A. Weidenmüller, Phys. Rev. Lett. **69**, 1296 (1992).
[4] For a review of Coulomb blockade phenomenon in semiconductor quantum dots see L. P. Kouwenhoven, C. M. Marcus, P. L. McEuen, S. Tarucha, R. M. Westervelt, and N. S. Wingreen, in *Mesoscopic Electron Transport*, edited by L. L. Sohn, L. P. Kouwenhoven, and G. Schön, NATO ASI Series E (Kluwer, Dordrecht, 1997) and references therein.
[5] R. A. J. Jalabert, A. D. Stone, and Y. Alhassid, Phys. Rev. Lett. **68**, 3468 (1992).
[6] L. Meza-Montes and S. E. Ulloa, Phys. Rev. E **55**, R6319 (1997).
[7] C. W. J. Beenakker, Rev. Mod. Phys. **69**, 731 (1997).
[8] U. Sivan, R. Berkovits, Y. Aloni, O. Prus, A. Auerbach, and G. Ben-Yoseph, Phys. Rev. Lett. **77**, 1123 (1996).
[9] F. Simmel, T. Heinzel, and D. A. Wharam, Europhys. Lett. **38**, 123 (1997).
[10] S. R. Patel, S. M. Cronenwett, D. R. Stewart, A. G. Huibers, C. M. Marcus, C. I. Duruöz, J. S. Harris Jr., K. Champman, and A. C. Gossard, Phys. Rev. Lett. **80**, 4522 (1998).
[11] F. Simmel, David Abusch-Magder, D. A. Wharam, M. A. Kastner, J. P. Kotthaus, Phys. Rev. B **59**, R10441 (1999).
[12] R. Berkovits, Phys. Rev. Lett. **81**, 2128 (1998).
[13] R. O. Vallejos, C. H. Lewenkopf, and E. R. Mucciolo, Phys. Rev. Lett. **80**, 677 (1998).
[14] The determination of $\frac{C_2}{C_\Sigma}$ is discussed in E. B. Foxman *et. al.*, Phys. Rev. B **50**, 14193 (1994), while the determination of $FWHM(T=0) = 0.78\Gamma$ is discussed in D. Goldhaber-Gordon *et. al.*, Phys. Rev. Lett. **81**, 5225 (1998).
[15] David Abusch-Magder, M.A. Kastner, C.L. Dennis, W.F. DiNatale, T.M. Lyszczarz, D.C. Shaver, and P.M. Mankiewich, in *Quantum Transport in Semiconductor Submicron Structures*, edited by B. Kramer, NATO ASI Series E 326 (Kluwer, Dordrecht, 1996), p. 251.
[16] David Abusch-Magder, Ph.D. Thesis, Massachusetts Institute of Technology, 1997.
[17] H. P. Baltes and E. R. Hilf, *Spectra of Finite Systems: A Review of Weyl's Problem*, Bibliographisches Institut, Zürich (1976).
[18] D. J. Thouless, Phys. Rev. Lett. **39** 1167 (1977).
[19] P. G. Silvestrov, and Y. Imry, cond-mat/9903299.

Coulomb Blockade Peak Spacing Fluctuations in Chaotic Quantum Dots

Kang-Hun Ahn and Klaus Richter
Max-Planck-Institut für Physik komplexer Systeme, Nöthnitzer Str. 38, 01187 Dresden, Germany

Abstract

We study ground states of interacting electrons in classically chaotic quantum dots using exact diagonalization and the self-consistent Hartree-Fock (SCHF) method. We find a remarkable validity of SCHF results for energies and charge densities. With increasing interaction the ground states show a crystal-type structure which originates from the interplay between direct and exchange interaction and the confinement. Corresponding capacitive energies exhibit fluctuations which are strongly enhanced with increasing interaction.

Due to the remarkable progress in fabrication and measurement of mesoscopic samples it has become possible to build and study electronic properties of quantum dots with controllable geometry, in particular clean dots with both rotational symmetric and asymmetric, irregular-shaped confining potential. On the one hand, experimental [1] and theoretical studies [2] of symmetric circular quantum dots have shown that they exhibit magic numbers for the occupation of electrons and shell structures similar to atoms. Hence such systems were coined artificial atoms. On the other hand, quantum dots with an asymmetric or irregular confinement [3], which were much less studied, do not obviously allow for such an electronic structure due to the absence of symmetry. Thus, contrary to atoms, such electronic devices open up the new possibility and the challenging program to study quantum interference and interaction effects in systems with tunable geometry. In particular, their shape gives usually rise to chaotic independent-particle dynamics. Hence such systems are ideal tools to investigate the interplay between many-body interactions and *(quantum) chaos* [4], which has evolved to a prominent field in mesoscopic physics.

In this respect new experiments in the Coulomb bloackade regime are of prime interest: recently measured fluctuations of the conductance peaks around their mean spacing, governed by the average charging energy, indicate the breakdown of the simple charging model and point towards a more subtle influence of interactions in confined quantum systems. Corresponding experiments [5–8] show: (i) Gaussian-type peak spacing distributions, which do not fit with the constant interaction model combined with random matrix theory (RMT) predicting a Wigner-Dyson distribution [5]; (ii) widths of the spacing distribution which vary between the different experiments and range from rather small fluctuations [7], comparable to the mean level spacing Δ of the independent-particle eigenstates, up to large fluctuations ($\gg \Delta$) which scale rather with the charging energy [8].

Here we study the inter-relation between many-body effects and chaotic dynamics in ballistic quantum dots by modelling them by quantum billiards. These structures, which have served as prototypes to investigate quantum signatures of chaotic independent-particle dynamics, appear to be appropriate systems to generalize such approaches for interacting particles. Recently, using self-consistent Hartree-Fock (SCHF) within such a billiard model,

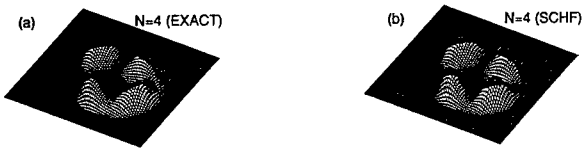

FIG. 1. Total ground state charge densities for $N = 4$ interacting electrons ($R/a_B^* = 15$) in the quantum billiard shown in the inset of Fig. 2(b). Panel (a): exact diagonalization; (b): SCHF method. Note the considerable agreement and the appearence of a crystal-type structure.

As shown in Fig. 1 the electrons in the quantum dot are located close to its boundary in a crystal-type formation. This structure at stronger interaction strength arises from the increasing coupling between Slater-determinant states as is seen by examining $\langle c_i^\dagger c_j \rangle$. The difference between the exact and the SCHF ground state energy is commonly referred to as correlation energy. In the present case it is less than 1% of the total ground state energy showing that real correlation effects are of minor importance. Accordingly, ordered charge density structures in quantum dots as those depicted in Fig. 1 and similar states discussed in Ref. [3] for larger electron numbers are *not* based on a correlation effect, such as e.g., the two dimensional Wigner crystal and fractional quantum Hall states. Instead the *ordered crystal-type structure is well understandable within a mean-field picture* and stems mainly from the direct and exchange interaction between the electrons.

From the precision of the SCHF results for few particles we infer that SCHF is also accurate for larger electron numbers, relevant for the experiments in the Coulomb blockade regime. The spacing between neighboring Coulomb blockade peaks as a function of an applied gate voltage is proportional to the capacitive energy or inverse compressibility [3,9],

$$\chi_N = E_{N+1} - 2E_N + E_{N-1} \,, \tag{3}$$

where E_N denotes the many-body ground state of the quantum dot. In Fig. 2(a,b) χ_N is shown for two different representative billiard geometries (see insets) giving both rise to chaotic independent-particle motion. The lines (guides to the eye) connect data points of equal interaction strength. The different lines depict results for increasing interaction from $R/a^* = 0$ to 20 (from bottom to top, in steps of 1). The following trends are visible:
(i) χ_N shows fluctuations as a function of electron number around mean values which increase with interaction strength. The size of the fluctuations is rather insensitive to N but grows with increasing interaction strength for a given geometry.
(ii) The fluctuations are more pronounced for the dot with a less deformed shape, Fig. 2(a).
(iii) there are regions where χ oscillates rather regularly as a function of N.

A systematic analysis of the statistics of the fluctuations shows that, up to $R/a_B^* \simeq 12$ corresponding to $r_s \sim$ 1–2, the rms of χ_N is approximately of order $\Delta/2$, as predicted by the constant interaction and RMT model. For larger interaction, the rms of χ_N increases roughly linearly with R/a_B^*. Inspection of the ground state charge densities shows that the increasing fluctuations visible in Fig. 2 are related to a rearrangement of charges from

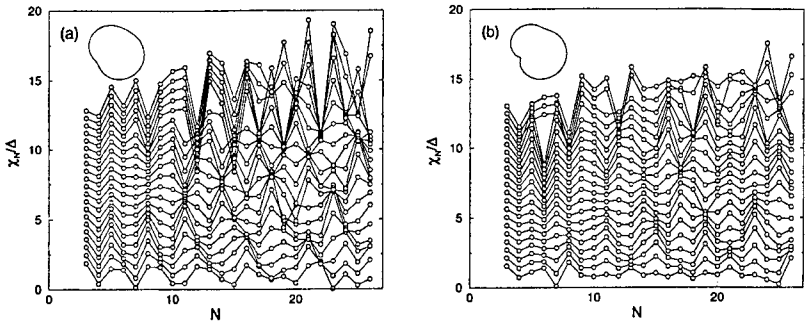

FIG. 2. Fluctuations of capacitive energies $\chi_N = E_{N+1} - 2E_N + E_{N-1}$ as a function of particle number N for interacting electrons in two chaotic billiards of different deformation shown in the upper left insets. The different lines are guides to the eye and connect data points (of equal interaction) for increasing interaction strength $R/a_B^* = 0, 1, 2, 3, \ldots, 20$ (from the bottom to top).

ergodic states extending over the whole chaotic dot at small R/a_B^* into ordered states near the dot edge [3]. The charge density shown in Fig. 1 for few electrons can be regarded as a precursor for this behavior. In dots with strong deformation, as that in Fig. 2(b), the charge reordering and hence the enhancement of fluctuations is less pronounced. The enhancement found in Fig. 2 can be viewed as one possible mechanism to explain the large Coulomb blockade peak spacing fluctuations observed in the recent experiments.

To conclude we have considered interacting electrons in asymmetric, chaotic quantum dots. By comparing with exact diagonalization for few electrons we find that a mean-field (SCHF) treatment is well suited to describe charge ordering along the edge of the dots for strong interaction. Moreover we find with increasing interaction an enhancement of capacitive energy fluctuations which is non-universal and depends on the shape of the dot.

[1] For a recent review, see e.g. L.P. Kouwenhoven et al., *Electron Transport in Quantum Dots*, ed. By L.P. Kouwenhoven, G. Schön, L.L. Sohn (Klewer, 1997).

[2] see, e.g., S. Tarucha *et al.*, Phys. Rev. Lett. **77**, 3613 (1996); O. Steffens, U. Rössler, M. Suhrke, Europhys. Lett. **42**, 529 (1998); K. Hirose and N.S. Wingreen, Phys. Rev. B **59**, 4604 (1999); I.-H. Lee *et al.*, Phys. Rev. B **57**, 9035 (1998), and references therein.

[3] Kang-Hun Ahn, Klaus Richter, and In-Ho Lee, cond-mat/9906046.

[4] M. Stopa, Physica B **251**, 228 (1998) and this volume; D. Ullmo, H.U. Baranger, K. Richter, F. von Oppen, and R.A. Jalabert, Phys. Rev. Lett. **80**, 895 (1998).

[5] U. Sivan *et al.*, Phys. Rev. Lett. **77**, 1123 (1996).

[6] F. Simmel *et al.*, Europhys. Lett. **38**, 123 (1997).

[7] S. R. Patel *et al.*, Phys. Rev. Lett. **80**, 4522 (1998).

[8] F. Simmel *et al.*, Phys. Rev. B **59**, R10441 (1999); D. Abusch-Magder *et al.*, this volume.

[9] Ya. M. Blanter, A. D. Mirlin, and B. A. Muzykanskii, Phys. Rev. Lett. **78**, 2449 (1997).

[10] M. V. Berry and M. Robnik, J. Phys. A **19**, 649 (1986).

we have shown [3] that the widths of Coulomb blockade peak spacing distributions show a clear cross-over from an RPA prediction [9] to a *non-universal* behavior arising from the formation of charge-ordered states near the edge of chaotic quantum dots [3].

Here we investigate the electronic ground state structure of clean dots by comparing SCHF with exact diagonalization results for small electron number and show that the arising charge-ordered states in asymmetric chaotic geometries are indeed well described in the SCHF treatment. Furthermore, we study the related enhancement of capacitive energy fluctuations as a function of particle number, geometry, and interaction strength.

As models for quantum dots with tunable shape a family of billiards proves convenient, which arise from a continuous deformation [10] of a disk with radius R. Details on the conformal mapping which defines the shapes can be found in Ref. [3]. Here we use two represetative geometries shown as insets in Fig. 2. They both give rise to chaotic independent-particle dynamics, e.g. Wigner-Dyson statistics for the quantum single-particle levels.

From the information of single-particle eigenstates and -energies ϵ_i of the non-interacting geometry we construct the many-electron Hamiltonian for spinless fermions,

$$H = \sum_i \epsilon_i c_i^\dagger c_i + \frac{1}{2} \sum_{ijkl} V_{ijkl} c_i^\dagger c_j^\dagger c_l c_k \ , \tag{1}$$

where $c_i^\dagger$ (c_i) creates (annihilates) the i-th eigenstate of the single-particle Hamiltonian. The interaction matrix elements V_{ijkl} are given by integrals of single-particle eigenfunctions ϕ_i,

$$V_{ijkl} = \int d\mathbf{r}_1 d\mathbf{r}_2 \phi_i(\mathbf{r}_1)\phi_j(\mathbf{r}_2)V(\mathbf{r}_1 - \mathbf{r}_2)\phi_k(\mathbf{r}_1)\phi_l(\mathbf{r}_2) \ . \tag{2}$$

Here $V(\mathbf{r}) = e^2/\epsilon r$ is the Coulomb interaction with dielectric constant ϵ of the host material. When scaling the Hamiltonian with $\hbar^2/(2m^*R^2)$, the interaction V_{ijkl} is measured through the dimensionless strength R/a_B^* with $a_B^* = \hbar^2\epsilon/m^*e^2$ the effective Bohr radius. Eqs. (1,2) serve as starting point for both exact diagonalization and SCHF calculations.

Unlike tight-binding models for finite lattices, the dimension of the matrix to be diagonalized is, in principle, infinite for the continuum model used. Hence we calculate eigenstates by truncation of the Hilbert space after checking the convergence of eigenenergies and wavefunctions with increasing Hilbert space dimension. The truncation is performed by considering the total kinetic energy of the system, i.e., by taking into account the single Slater-determinant states, $|\Phi_\alpha\rangle$, which satisfy the condition $\sum_i i\langle\Phi_\alpha|c_i^\dagger c_i|\Phi_\alpha\rangle \leq M_c$, where $M_c\Delta$ is the kinetic energy cut-off value for the sum over single-particle quantum numbers i. A many-body ground state is obtained from exact diagonalization as a linear combination of many single Slater-determinant states. For example, $M_c = 35$ for 4 electrons gives a Hamiltonian matrix of size 1477×1477 which leads to a well converged ground state for intermediate interaction strength $R/a_B^* = 15$.

To study the precision of corresponding SCHF calculations we compare in Fig. 1 the total charge density of the ground state of 4 electrons obtained within SCHF with exact diagonalization. We find considerable agreement which is also reflected in rather precise SCHF ground state energies [3]. The high precision of the SCHF approach may be related to the fact that the asymmetric shapes considered lead to ergodic independent-particle wavefunctions which appear to be a favorable starting point for a mean-field treatment.

Origin of conductance oscillations in square electron billiards: A semi-classical approach.

T. Blomquist and I. V. Zozoulenko
Department of Physics (IFM), Linköping University, S-581 83 Linköping, Sweden

June 5, 1999

We perform semi-classical and quantum mechanical calculations on square billiards and provide a semi-classical interpretation of the conductance oscillations. We outline its relation to the Gutzwiller's picture of periodic orbits. The frequencies of the conductance oscillations are shown to be due to interference of *pairs of long trajectories*, which in the phase space are typically situated near the corresponding periodic orbit. We identify the pair of trajectories causing the pronounced peak in a recent experiment and from this directly extract the phase coherence length.

Keywords: electron billiards, conductance fluctuations, phase-coherence length, semi-classical approach

The conductance oscillations in quantum dots (also called electron billiards), due to interference of electron waves, have been studied extensively both experimentally and theoretically[1, 2]. One interesting question is whether it is possible to explain/predict the spectrum of the conductance oscillations for a quantum dot of a given shape. A common interpretation is that the oscillations are dominated by the density of states which in turn, according to Gutzwiller[3, 4], is given by periodic orbits in the billiard. Each periodic orbit contributes to a specific frequency in the spectrum. Albeit being simple and intuitive, this picture does not provide satisfactory answers to many important questions. For example, it does not explain how *closed* orbits, which may be classically decoupled from the leads, mediate the conductance. In this paper we examine the validity of this approach by performing quantum mechanical (QM) and semi-classical (SC) conductance calculations for a square quantum dot. The choice of this geometry is motivated by a recent experiment[2] where highly periodic oscillations were found as a function of the Fermi wavelength k_F. However, the frequency of these oscillations could neither be reproduced by QM calculations, nor explained within the periodic orbit approach. In this paper we demonstrate that pronounced frequencies of the conductance oscillations are due to interference of *pairs of long trajectories*, which in the phase space are typically situated near the corresponding periodic orbits. Introducing a finite coherence length, we reproduce the observed frequency[2] and thus unambiguously identify the pair of trajectories causing the pronounced peak in the experiment.

For a billiard with two leads, the zero-temperature conductance is given by the Landauer formula $G = (2e^2/h)T$ where the total transmission coefficient $T = \sum_{mn} T_{mn}$ is the sum over all transmission coefficients from all propagating modes m in one lead to the modes n in the other lead[5]. In the absence of a magnetic field the transmission amplitude t_{nm} is given by the projection of the retarded Green's function, $G(y_1, y_2, k_F)$, onto transverse wave functions $\phi_n(y)$ in the incoming and outgoing leads[5]

$$t_{mn}(k_F) = -i\hbar\sqrt{v_n v_m}\int dy_1 \int dy_2 \times \phi_n^*(y_1)\phi_m(y_2)G(y_1, y_2, k_F), \qquad (1)$$

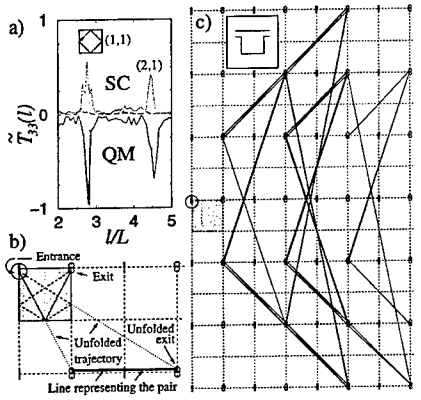

Figure 1: (a) The length spectrum of the quantum-mechanical (QM) and the semi-classical (SC) transmission coefficient T_{33} for a square billiard (see inset in (c)). In SC calculations trajectories with up to 5 and 10 bounces are included, dashed and dotted curves respectively. The dotted vertical line indicates the frequency corresponding to the (1,1) periodic orbit, which is shown as an inset. (b) Illustration of the "unfolding" of two classical trajectories (solid and dashed lines) connecting the entrance (the encircled dash) and the exit (circle). The original square is shaded, the two trajectories are "unfolded" into the dotted lines, continuing into successive mirror-images of the square. The pair of trajectories is represented by a solid line binding the two unfolded exits. (c) The solid lines represent *pairs* of trajectories (as described in (b)) that give the dominant contribution to the peak at $l = 2\sqrt{2}L$ in (a). The length difference in all the pairs is $\Delta l \approx 2\sqrt{2}L$. The inset shows the geometry of the billiard.

where v_n is the longitudinal velocity for the mode n. In QM calculations of the conductance we used a tight-binding Hamiltonian and calculated $G^{qm}(y_1, y_2, k_F)$ using the modified version[6] of the standard recursive Green's function technique based on the Dyson equation[5]. In the semi-classical approach we replaced the Green's function by its semi-classical limit $G^{sc}(y_1, y_2, k_F)$ given by all classical trajectories connecting the entrance and the exit leads of the billiard[7, 3, 4]. Each trajectory carries an amplitude and a phase. For a square billiard with hard-wall leads of width w, Eq. (1) reduces in the semi-classical limit to

$$t^{sc}_{mn}(k_F) = \sum_s a_s h^*_m(k_F, \theta^s_1) h_n(k_F, \theta^s_2) e^{ik_F l_s - i\mu_s \frac{\pi}{2}}, \tag{2}$$

where summation is performed over all classical trajectories s connecting the two leads. Here l_s is the length of the trajectory and $\theta^s_{1(2)}$ is the corresponding entrance (exit) angles; $a_s = -\sqrt{2k_n k_m/2\pi i}/(wk_F l_s)$, k_n is the longitudinal wave vector for n-th mode, μ_s is the Maslov index, the factor $h_n(k_F, \theta)$ is related to the electron diffraction at the lead mouths and describes the angular distribution of the electrons injected from the lead with the angle θ^s (an explicit expression for $h_n(k_F, \theta)$ can be found in[8]).

The functions $h_n(k_F, \theta)$ varies slowly with k_f so the length spectrum, given by the Fourier transform $\tilde{t}(l) = \int dk_F t(k_F) e^{-ik_F l}$, will be strongly peaked at the positions $l = l_s$, that is at the lengths of the classical trajectories. This behavior of $\tilde{t}(l)$ is verified for a large number of billiard[8] and is well understood. However the transmission amplitude is not measurable in experiments. The total transmission coefficient, $T(k_F)$, that is measurable, has not been analyzed as thoroughly. We have performed both SC and QM calculations of $T(k_F)$ for the square billiard with different lead positions where the entrance (exit) leads are placed on opposite sides of the billiard, distances d_1 (d_2) from the upper wall. Both the SC and QM length spectra of the conductance oscillations, $\tilde{T}(l)$, match each other well both in amplitude and position of the peaks. We find that the peak positions do not depend on lead geometry (i.e. on the distances d_1, d_2), although the heights of the peaks do. The most remarkable observation is that the positions of most peaks in the length spectra coincide with the lengths of primitive periodic orbits of a square, (i, j), see Fig. 1(a). This

length is given by $l^{p.o.}_{(i,j)} = 2L\sqrt{i^2+j^2}$ where L is the length of the side of the square, i and j are two integers with largest common divider equal to one[4]. To explain this behaviour let us focus at the semi-classical transmission coefficient $T_{nm} = |t_{nm}|^2$

$$T^{sc}_{mn}(k_F) = \sum_s |a_s|^2 |H_s|^2 + \sum_{s,s'} a_s a^*_{s'} H_s H^*_{s'} e^{ik_F(l_s - l_{s'}) - i(\mu_s - \mu_{s'})\frac{\pi}{2}} \tag{3}$$

where $H_s = h^*_m(k_F, \theta^s_1) h_n(k_F, \theta^s_2)$. The second term is the quantum-mechanical correction to the classical transmission and expresses the interference between trajectories s and s'. It follows from Eq. (3) that the spectrum of $T^{sc}_{mn}(k_F)$ is strongly peaked at the lengths $l = \Delta l = l_s - l_{s'}$. Thus, the frequencies in the spectrum of the transmission coefficients are related to the length differences in *pairs of trajectories*. In order to study the length differences between trajectories in a square billiard, we "unfold" the square in to a plain by reflecting at all its sides. A bouncing trajectory transforms into a straight line by continuing into successive mirror images of the original square (see Fig. 1). A trajectory is characterized by the two integers m and n, which correspond to the number of bounces against the left and lower walls respectively. The length of the trajectory is given by the Pythagoras law as $l^2_{m,n} = L^2(2m+1)^2 + (2nL + d_1 \pm d_2)^2$ where $m \geq 0$ and n are integers. (Note that in the analysis based on the "unfolded" trajectories, the contributions from the trajectories "shadowed" by "unfolded" entrances or exits must obviously be excluded). A simple analysis shows that there exist sets of trajectories for which the successive length differences converges to the lengths of the periodic orbits $l^{p.o.}_{(i,j)}$. These sets typically consist of trajectories which in the phase space are close to the corresponding periodic orbit. An example is the trajectories with $n \approx \pm m$ (i.e. parallel to diagonals of the square), bouncing near the (1,1) orbit in the phase space. The length difference between such trajectories is $l_{m+1,m+i} - l_{m,m+1+i} = 2\sqrt{2}L(1 + O(\frac{i}{m}) + O(\frac{d_1 \pm d_2}{L}\frac{i}{m}))$, where i is an integer. Thus, if the lengths of the trajectories are sufficiently large, $|i| \ll m$, *their length difference* Δl *coincides with the length of the corresponding periodic orbit,* $l^{p.o.}_{(1,1)} = 2\sqrt{2}L$. This explains why the position of the characteristic frequencies of the conductance oscillations is typically peaked at the length of the shortest periodic orbits.

To illustrate this let us consider the transmission coefficient T_{33} for a square billiard with lead geometry $d_1 = d_2 = 0$, see Fig. 1. Let us concentrate at the pronounced peak in the length spectrum at $l \approx 2\sqrt{2}L$. Figure 1(c) shows the pair of trajectories whose contribution to this peak (calculated according to Eq. (3)) is dominant. In accordance to the above analysis, all these trajectories bounce in the vicinity of the periodic orbit (1,1) (i.e. $m \approx n$). It is worth to notice that the two shortest trajectories have the lengths $l_s = \sqrt{5}L$ and $l_s = 5L$, and therefore the semi-classical calculation using only trajectories with up to 5 bounces does not reproduce this frequency, while with 10 bounces it does. It is also worth noting that not all frequencies in the spectrum correspond to periodic orbits. Consider for example a lead geometry when $|d_1 - d_2| = L/2$. Inject electrons in the phase space near the (2,1) orbit ($l^{p.o.}_{(2,1)} = 2\sqrt{5}L$). There are two direction in which the electron can bounce inside the square. One direction along the orbit gives a set of trajectory lengths $l \approx (\frac{1}{4} + n) l^{p.o.}_{2,1}$ while following the other direction gives a set of trajectory lengths $l \approx (\frac{3}{4} + n) l^{p.o.}_{2,1}$, n integer. Therefore, the length difference between such trajectories is $\Delta l \approx \frac{1}{2} l_{2,1}$, that is a half of the length of the corresponding periodic orbit.

Let us apply the above analysis to the experiment[2] where highly periodic oscillations as function of k_F were observed in the conductance of a square billiard. The experimental length spectrum showed only one frequency $l \approx 1.4L$. The experiment was performed in a four terminal geometry (see inset in Fig. 2). According to the Landauer-Büttiker formalism[5], the observed four-terminal resistance can be expressed via only two independent transmission coefficients. These are approximately those given by the two two-terminal set-ups shown to the right in Fig. 2. The calculated

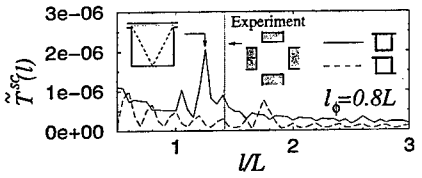

Figure 2: The length spectrum, calculated with phase coherence length $l_\Phi = 0.8L$, of two square quantum dots with the leads positions given to the right. The pair of trajectories responsible for the pronounced peak at $l \approx 1.24L$ is shown to the left. The experimental setup[2] is shown in the inset and the observed frequency is indicated by a dotted line.

spectra for these two geometries are dominated by the two frequencies $l_s = 2L$ and $l_s = 2\sqrt{2}L$. As shown above they are due to interference of relatively long trajectories ($l \gtrsim 5 - 7L$). It is therefore likely that these features are missing in the experiment because the trajectories that give these frequencies are longer than the phase coherence length l_ϕ. The probability for an electron to travel the distance l without loosing its phase coherence is e^{-l/l_ϕ}. Including this probability in Eq. (3) we effectively suppresses the contribution from long trajectories.

Figure 2 shows that for a coherence length $l_\phi \lesssim 0.8L$ only one frequency $l = 1.24L$ survives, which is within 12% of the measured value. This is satisfactory taking into account the uncertainty in the actual size of the billiard. This analysis gives a phase coherence length of $l_\phi \approx 0.8L = 2\mu$m for the dot[2]. This value is consistent with the results[9, 10] but lower than for the structures[11]. However it is worth to stress that different methods for determination of the phase coherence length may vary as much as in order of magnitude, even for the same dot[10]. In contrast, our analysis provides a direct assessment of l_ϕ.

We thank K.-F. Berggren, J. Martorell, K. Ensslin and A. S. Sachrajda for valuable discussions. This work was supported by NGSSC and NFR.

References

[1] C. M. Marcus *et al.*, Phys. Rev. Lett. **69** 506 (1992); M. Persson *et al.*, Phys. Rev. B **52**, 8921 (1995); L. Christensson *et al.*, Phys. Rev. B **57** 12 306 (1998); P. Bøggild *et al.*, Phys. Rev. B **57** 15 408 (1998); I. V. Zozoulenko *et al.*, Phys. Rev. B **558**, 10 597 (1998).

[2] I. V. Zozoulenko *et al.*, Phys. Rev. B **55**, R10209 (1997).

[3] M. Gutzwiller,*Chaos in Classical and Quantum Mechanics*,(Springer-Verlag New York Inc.,1990).

[4] M. Brack and R. K. Bhaduri, *Semiclassical Physics*, (Addison-Wesley, Reading, Mass., 1997).

[5] see, e.g., S. Datta, *Electronic Transport in Mesoscopic Systems* (Cambridge University Press, Cambridge, 1995).

[6] I. V. Zozoulenko, F. A. Maaø and E. H. Hauge, Phys. Rev B **53**, 7975 (1996); ibid. B **53**, 7987 (1996).

[7] W. H. Miller, Adv. Chem. Phys. **25**, 69 (1974); R. A. Jalabert, H. U. Baranger, and A. D. Stone, Phys. Rev. Lett. **65**, 2442 (1990).

[8] L. Wirtz, J.-Z. Tang, and J. Burgdörfer, Phys Rev. B **56**, 7589 (1997).

[9] H. Hiramoto *et al.* Appl. Phys. Lett. **54**,2103 (1989); J. A. Katine *et al.*, Phys. Rev. B **57**, 1698 (1998).

[10] P. Bøggild, Ph. D. thesis, Niels Bohr Institute (Copenhagen), 1998; and unpublished.

[11] A. Yacoby *et al.*, Semicond. Sci. Technol. **9**, 907 (1994); J. P. Bird *et al.*, Phys. Rev. B **51**, 18 037 (1995); R. M. Clarke *et al.*, Phys. Rev. B **52**, 2656 (1995).

Capacitance fluctuations in quantum dots

M. Stopa
Walter Schottky Institute
1 Am Coulombwall
D-85748 Garching, Germany
phone 49-89-289-12198, Fax: 49-89-289-12737
e-mail: stopa@wsi.tum.de

Abstract

We discuss fluctuations of the charging energy E_C and gate voltage spacings between Coulomb oscillation conductance peaks, as computed within spin density functional theory for a realistic $GaAs-AlGaAs$ dot. We explicitly exhibit the fluctuations in the portion of the total free energy which incorporate the interaction between the dot and its surroundings. These variations in the dot *capacitance* show a dispersion which is typically greater than the dispersion of the total dot charging energy.

Numerous efforts have been made to explain the experimentally observed fluctuations in the Coulomb oscillation peak spacings of a quantum dot first described by Sivan *et al.* and later by others [1]. In the the constant interaction plus random matrix theory formulation (CI+RMT) [1] the statistics of the charging energy E_C, defined as the change in the chemical potential as dot electron number N is increased by unity, depend only on the single particle level spacing statistics. For a sufficiently non-integrable dot shape, these latter are given by the Wigner distribution (for the orthogonal ensemble) with a dispersion $\sim 0.52\Delta$, where Δ is the mean level spacing. Further, within CI+RMT, the spacings, ΔV_g, between Coulomb oscillation conductance peaks can be simply related to E_C, so that the statistics of ΔV_g also scale as Δ. The experiments have shown convincingly that these predictions are not borne out. The dispersion of V_g spacings is significantly greater that 0.52Δ and has been argued [1] to scale with E_C itself, rather than with Δ.

The failure of CI+RMT is not surprising in that it is well-known that RMT fails in the ground state problem [2]. The experiments have thus invigorated and provided a framework for the investigation into the statistical properties of the ground state of an interacting assembly of particles subject to varying N by providing accessible ensembles of such systems. Recent theoretical studies [3] have included small system Hubbard model calculations, generalizations of RMT+CI to incorporate the variation to the spectrum produced by the evolving shape of the dot, and treatments of the dot charging energy within the random phase approximation (RPA). While each of these studies have illuminated a salient feature of the problem, specifically: electronic correlation, shape, and capacitance variations respectively; none of the employed methods can hope to make quantitative comparison with experiment insofar as they all employ parameterizations relevant to the feature in question and summarily ignore the other features.

By contrast, spin density functional theory (SDFT), in seeking a realistic model of an interacting system, is well-suited to study of the ground state problem [4,5,6]. While many-body correlations are treated only approximately (via local density approximation, or LDA), these are arguably small in the semiconductor systems under study [7]. Otherwise the calculation requires no parameters, treating shape, disorder, and Coulomb interaction realistically.

In addition to avoiding the parameterizations demanded by the preceding models, SDFT permits the study of a quantum dot interacting with the gates and leads which surround an actual dot. It is this interacting feature on which we concentrate here.

Our calculations for the electronic structure of lateral, semiconductor quantum dots have been described in detail previously [4]. We here employ the device structure, including growth profile, gate pattern, doping density etc., from the quantum dot investigated experimentally by Sivan *et al.* [1]. The calculation proceeds via input of this data as well as gate voltages and dot electron number, temperature and magnetic field if desired (we treat only $B = 0$ in this paper). The self-consistent electronic structure is comprised of a set of Kohn-Sham eigenvalues and eigenfunctions for the electrons confined in the dot, a self-consistent electrostatic potential throughout the simulation region, and electronic densities in the lead regions which are incorporated into the problem via a Thomas-Fermi approximation. From these we can derive the induced charge Q_i on each gate by computing the normal gradient of the potential along the relevant surfaces.

An essential feature of our calculation is the evaluation of the total interacting free energy $F(N, V_g)$ for the *dot-gates-leads system* [6] which can be written as follows:

$$\begin{aligned} F(\{n_p\}, N, V_i) &= \sum_p n_p \varepsilon_p - \frac{1}{2}\int d^3r\, \rho_{dot}(\mathbf{r}) e\phi(\mathbf{r}) \\ &+ \frac{1}{2}\int d^3r\, \rho_{ion}(\mathbf{r}) e\phi(\mathbf{r}) + \int d^3r\, \rho_{dot}(\mathbf{r})[\epsilon_{xc}(\rho(\mathbf{r})) - \mu_{xc}(\rho(\mathbf{r}))] \\ &- \frac{1}{2}\sum_{leads}\int d^3r\, \rho_j(\mathbf{r}) e\phi(\mathbf{r}) - \frac{1}{2}\sum_{gates} Q_i V_i \end{aligned} \tag{1}$$

where n_p is the occupancy of dot level p, ε_p is the eigenvalue, ρ_{dot} is the dot total electron density, ϕ is the electrostatic potential, ρ_{ion} is the density of the background, modulation doped ions, ϵ_{xc} is the exchange-correlation energy per particle and μ_{xc} is the exchange-correlation contribution to the chemical potential. Also, ρ_j is the charge in lead j, Q_i is the induced charge on gate i (see above) and V_i is the voltage applied to gate i. Note that, in SDFT the density is further divided according to spin species, which we have suppressed here for simplicity. Note also that both the energy related to the leads and that related to the gates enters with a minus sign as a consequence of the need to include the work from the power supplies, which is here computed within the "global rule" [7]. The charging energy is $E_C \equiv \frac{\partial^2 F}{\partial N^2}$.

We have noted previously [4,5,6] that the charging energy is only simply related to the gate voltage spacing of Coulomb oscillations in the constant interaction model. That is, $F(N, V_g) - F(N+1, V_g) = 0$ is an implicit equation for that V_g where a conductance peak occurs, and $F(N+1, V_g') - F(N+2, V_g') = 0$ is an implicit equation for the position of the next peak. While these peak positions can be disentangled numerically, there is no simple prescription for determining $\Delta V_g \equiv V_g' - V_g$ analytically. Another way of saying this is that the various terms in the free energy are generally dependent on N and V_g.

In figure 1 we plot calculated results for E_C and ΔV_g as a function of changing N. We have allowed V_g (the "plunger" gate) to vary and N to also "co-vary" by maintaining a constant chemical potential in the dot. In order to compute E_C we actually must solve for several N at each V_g (to compute the second partial of F). We are also able numerically to find the

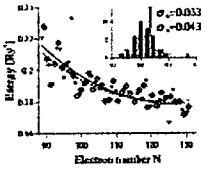

FIG. 1 Charging energy (diamonds, fit with dashed line) and gate voltage spacings (inverted triangle, solid line) as a function of dot electron number from SDFT calculation results. Inset shows histogram of deviations of E_C and ΔV_g from their local average values (i.e. their fits) normalized by the fit. Thus the standard deviations are as a fraction of the charging energy.

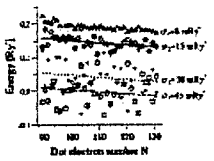

FIG. 2 Components of E_C, due to E_I (hexagons with linear fit dashed line), charge on gates F_C (inverted triangles, fit with dotted line) and self-consistent level sum with double-counting correction removed E_Σ (diamonds, solid line). Total E_C is reproduced from fig. 1 as open triangles.

degeneracy points and, consequently, the gate voltage spacing between oscillations. Thus each point in figure 1 actually comprises the results of several full self-consistent electronic structure calculations.

The average value for E_C is of order 0.18 Ry^*. This value is somewhat larger than that obtained experimentally in reference [1], where a value ~ 0.1 Ry^* was found. We are unsure as to the source of this discrepancy, although the slope of E_C with N is very consistent with experiment. In the inset of Figure 1 the histograms of the fluctuations in E_C and ΔV_g, normalized by the smooth fits (the lines in the main figure) are shown. The standard deviation for ΔV_g (σ_B) is significantly greater than that of E_C (σ_A). Also note that the dispersions are roughly symmetrical and that several points lie far outside of the central area, which is consistent with experiment. These points are related to the gate voltage values at which double filling of strongly "scarred" states occurs [5]. Finally, σ_B (and σ_A) are smaller than that in the experiment by about a factor of two. This is at least partly due to the fact that the N values here are somewhat large than those considered in reference [1]. Considering the results from ref. 1 at the higher end of N only, the results are more satisfactory. Nonetheless, there is apparently some real discrepancy.

In figure 2 we show the various contributions to the charging energy obtained by calculating separately the second partials of the various parts of F with respect to N. We denote E_Σ as the eigenvalue sum minus the double-counting correction (second term RHS) in Eq. 1, E_I as the ionic energy term and F_C as the gates-related energy (final term). We find that the contributions of the exchange-correlation energy and the lead energies to E_C are entirely negligible. The remaining contributions to E_C, however, are all substantial. In particular,

note that $\partial^2 E_\Sigma/\partial N^2$, while the dominant term, gives by no means all of E_C. Furthermore, it is extremely interesting that the fluctuations in all of the various components of E_C *exceed* the fluctuations in E_C itself, that is, they compensate for each other. Thus, the standard deviation from the mean of the charging energy (as derived from the full free energy F), denoted σ_F, is only $\sim 8\ mRy^*$ (milli-effective Rydbergs, $1\ Ry^* \approx 5.8\ meV$).

To discuss these results briefly, we note that in the CI model the total energy is generally written $U = \frac{N^2e^2}{2C} + Ne\alpha V_g + \sum_{i=1}^{N} \epsilon_i$ where C is the dot total capacitance, α is a lever arm related to the capacitance to the plunger gate, and ϵ_i are the non-interacting dot levels. This leads immediately to $E_C = \frac{e^2}{C} + \Delta_N$. If, in contrast to the CI model, we allow C, say, to depend on N (this can be thought of as a fluctuation in the size of the charge puddle due to the incommensurability of the eigenfunctions which does not itself affect the spacing of the eigenvalues significantly) the charging energy becomes

$$E_C = \frac{\partial^2 U}{\partial N^2} \approx \frac{e^2}{C}(1 - 2N\frac{C'}{C}) + \Delta_N \tag{2}$$

plus terms of order C'' where $C' \equiv \partial C/\partial N$ and Δ_N is a level spacing at the Fermi surface. The fact that the fluctuation of the capacitance enters with a factor of $2N$, since it involves the electrostatic energy of all the electrons in the dot, suggests that it can be a substantial part of the fluctuating E_C. Thus, our findings, displayed in figure 2, show that we can speak of the dot capacitance as fluctuating in addition to the fluctuation in the level spacings and that, furthermore, there is an interplay and a compensation between the fluctuation in the different parts of the energy.

In conclusion, we have investigated the fluctuating charging energy and gate voltage spacings of a semiconductor quantum dot via a functional for the total interacting free energy based on the results of SDF calculations. The results show that the dispersions of E_C and ΔV_g, while large enough to rule out RMT, are still smaller than that obtained experimentally. We have shown that portions of the free energy other than the level sum are important both in E_C and its fluctuations. Finally, we have found the fascinating result that the fluctuations of the various elements of E_C are anti-correlated and combine to produce fluctuations in the total E_C which are much smaller than fluctuations in its parts.

[1] U. Sivan *et al.* Phys. Rev. Lett. **77**, (1996) 1123; S. Patel *et al.*, Phys. Rev. Lett. **80**, 4522 (1998); F. Simmel, T. Heinzel and D. A. Wharam, Europhys. Lett. **38**, 123 (1997).

[2] T. A. Brody, J. Flores, J. B. French, P. A. Mello, A. Pandey and S. S. M. Wong, Rev. Mod. Phys. **53**, 385 (1981).

[3] R. Berkovits, Phys. rev. Lett. **81**, 2128 (1998); G. Hackenbroich, W. D. Weiss and H. A. Weidenmüller, Phys. Rev. Lett. **79**, 127 (1997); R. O. Vallejos, C. H. Lewenkopf and E. R. Mucciolo, Phys. Rev. Lett. **81**, 677 (1998); Ya. M. Blanter, A. D. Mirlin and B. A. Murzykanstskii, Phys. Rev. Lett. **78**, 2449 (1997).

[4] M. Stopa , Phys. Rev. B, **54**, (1996) 13767.

[5] M. Stopa, Physica B, **249-251**, 228 (1998); M. Stopa, cond-mat/9709119.

[6] M. Stopa, Semicond. Sci. and Tech., **13**, A55 (1998).

[7] *Electron Correlations in Molecules and Solids*, Peter Fulde (Springer-Verlag, Berlin, 1995).

Thermopower of Quantum Chaos

H. Buhmann and L.W. Molenkamp
Physikalisches Institut, Universtität Würzburg, Am Hubland, 97074 Würzburg, Germany
(June 14, 1999)

The thermopower of a chaotic quantum dot has been studied in the Coulomb and the ballistic transport regime. Theoretical examinations predict distinct features for quantum dots where the electron trajectories are chaotic. Accordingly, we give experimental evidence for a residual effective charging energy in the case of asymmetric ajusted leads ($G \leq 2e^2/h$) and for non-Gaussian thermopower fluctuation distributions in the ballistic regime ($G = 4e^2/h$).

73.20.Dx,05.45.-a,72.20.Pa

Thermopower measurements can often provide the transport physicist with information that is complementary to results obtained from ordinary conductance measurements. Here, we present two examples of thermopower measurements on chaotic transport in quantum dot in two different transport regimes, i.e. the Coulomb blockade, lead conductance $G \leq 2e^2/h$, and the ballistic regime ($G = 4e^2/h$):

First, theoretical investigations of chaotic quantum dots predict deviation [1] from the previously predicted [2] and observed, for deterministic quantum dots [3], power-law scaling of the effective charging energy, E^*, as a function of the coupling leads conductance. In the Coulomb blockade regime the scaling of the effective charging energy is determined from the amplitute and line shape of the thermopower oscillations which depent strongly on the ratio k_BT/E^*. In the ballistic regime ($G_{\text{contacts}} > 2e^2/h$), where the conductance exhibits characteristic random fluctuations as a function of an external parameter (dot shape and magnetic field), thermopower fluctuations are measured accordingly and statistially analysed.

Second, chaos in quantum dots has been investigated [4–6] in conductance measurements but the analysis turns out to be difficult. So-called short trajectories [7] and weak localization effects [4,8] add up to the signature of chaotic motion. Moreover, current heating of the electrons in the dot appears to be unavoidable in conductance measurements. Electron heating effects in the dot smear out the underlying chaotic statistics and therefore the observed fluctuations exhibit mostly a Gaussian distribution, although theory predicts non-Gaussian distributions when a small number of electron modes is admitted to the dot [9]. Also in thermopower experiments non-Gaussian distributions are predicted [10]. As we will show below, our experimental techniques enable us to perform thermopower experiments without complicating electron heating of the electrons in the quantum dot themself.

The sample, schematically shown in Fig. 1, is electrostatically defined by TiAu Schottky-gates in a two-dimensional electron gas (2DEG) in a GaAs-(Al,Ga)As modulation doped heterostructure. The 2DEG has an

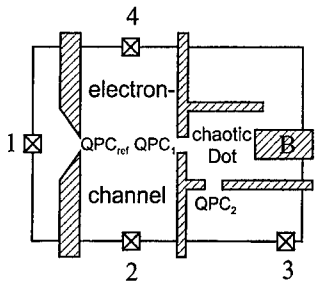

FIG. 1. Schematic top view of the sample structure. The hatched areas show the structure of the Schottky-gates, the crosses denote ohmic contacts. The heating-current is passed between contacts 2 and 4. The thermovoltage V_{Th} is measured between contacts 1 and 3.

electron density $n_s \approx 3.4 \times 10^{11}$ cm^{-2} and an electron mobility $\mu \approx 10^6$ cm^2 (Vs)$^{-1}$. The gates define the main features of the sample: The quantum dot with a lithographical size of 700 nm × 800 nm, coupled to the reservoirs by two adjustable barriers (quantum point-contacts QPC$_1$ and QPC$_2$), a 2 μm wide and 20 μm long channel and a quantum point-contact QPC$_{\text{ref}}$ in the channel boundary. The electrochemical potential and size of the dot can be varied by changing the applied voltage to gate B, V_g^{B}, while the tunnel barriers are kept constant. All experiments were done at $T < 40$ mK, using a dilution refrigerator equiped with a superconducting magnet.

A temperature difference ΔT across the dot is created by current-heating techniques: A low-frequency (13 Hz) current I is passed through the electron channel, increasing the temperature of the electron system in the channel by $\Delta T \propto I^2$ [11]. Measuring the potential difference between the voltage contacts 1 and 3 by phase sensitive lock-in techniques at twice the frequency of the heating current gives a thermovoltage

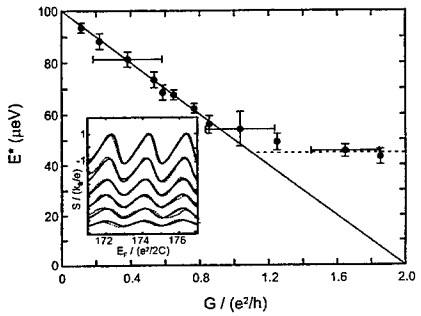

FIG. 2. Plot of the measured ratio E^* as a function of the conductance of QPC_1. Solid line shows the expected linear scaling; Dashed line is a guide to the eye. Inset: Experimental traces of the thermovoltage for a heating current of 40 nA (dotted line). The conductance of QPC_1 was 0.06, 0.19, 0.29, 0.38, 0.43, 0.82 $e^/h$ from top to bottom. Calculated curves of the thermopower of a quantum dot (solid line). The values of k_BT/E^* are 0.22, 0.25, 0.30, 0.33, 0.37 and 0.45 from top to bottom.

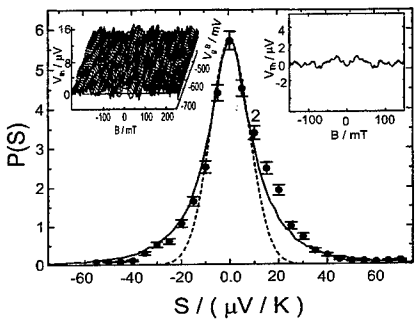

FIG. 3. Thermopower distribution for broken TRS ($|B| \geq 50$ mT). Experimental results (dots), simulation results (solid line) and Gaussian fit (dashed line). Inset, left: thermovoltage of the quantum dot as a function of magnetic field (X-Axis) and of gate voltage on gate B (Y-Axis). $\Delta V_g^B = 10$ mV for each magnetic field sweep. Inset, right: Averaged thermopower measurement.

$$V_{\rm Th} := V_1 - V_2 = (S_{\rm ref} - S_{\rm dot})\Delta T \,. \qquad (1)$$

Thus, assuming a constant thermopower $S_{\rm ref}$ of the reference quantum point contact $QPC_{\rm ref}$ and a constant averaged temperature difference ΔT between the electron channel and the reservoirs, variations of $V_{\rm Th}$ reflect directly changes in the thermopower of the dot.

The scaling behaviour of the charging energy is determined by measuring $V_{\rm Th}$ as a function of $V_g^{\rm B}$ for various values of the conductance of QPC_1. The transmission of QPC_1 is kept constant at a value of $G_1 \approx 0.06e^2/h$. Some of the resulting curves are shown in the inset of Fig. 2 for a gate-voltage range of -938 mV $< V_g^{\rm B} <$ -925 mV and six different transmission probabilities of QPC_1, G = 0.06, 0.19, 0.29, 0.38, 0.43, and 0.82 e^2/h (top to bottom). The thermovoltage oscillations decrease with increasing point-contact conductance and become more symmetric.

The experimental curves are fitted theoretically using the ratio between thermal energy and charging energy, k_BT/E^* as only variable parameter (dashed lines). Using the bare charging energy of the quantum dot, $E_c \approx 100 \pm 20$ μeV, which was determined from thermal activation studies of the conductance in the Coulomb-blockade regime, it is possible to evaluate the effective charging energy quantitatively.

The dependence of E^* on the conductance of QPC_1 is displayed in Fig. 2. A remarkable deviation from the expected scaling behaviour for non-chaotic dots (solid line) is observed. The effective charging energy approches a value of $E* \approx 0.45E_0$ for $G \to 2e^2/h$.

Physically, this plateau is caused by electrons that, after being reflected by the closed contact, are not able to find the open contact on the other side of the dot. This chaos-induced effect strongly reduces the charge fluctuations on the dot. Aleiner and Glazman [1] used RMT in connection with the Tomonaga-Luttinger formalism to compute this behaviour. Using this approach for the actual structure $E*$ can be estimated to

$$E_c^*(t=1) = 0.49 \pm 0.03\, E_c \,, \qquad (2)$$

where a mean level spacing $\Delta E \approx 23$ μeV is assumed, which was estimated from the 2DEG density of states and the size of the quantum dot. The actual position of the plateau in E* is in very good agreement with theoretical predictions.

Additional experiments verifying the fact that the investigated quantum dot is indeed chaotic using conventional transport experiments with open contacts, $G_{\rm contacts} = 4e^2/h$, by analysing the line shape of the weak localization peak have been discussed elsewhere [12].

In addition, with open contacts, $G_{\rm contacts} = 4e^2/h$, we have studied the statistical distribution of the random fluctuations in the thermopower as a function of dot shape and magnetic field. A very fundamental prediction of quantum chaos theory is that these fluctuations should exhibit a characteristic non-Gaussian distribution. In conductance experiments, such non-Gaussian distributions could not be demonstrated, which was attributed to current heating effects. Again, in our thermopower experiments, the current is not passed directly through the dot.

A typical sequence of the magnetic field dependent thermopower for different dot sizes are displayed in left

inset of Fig. 3. The voltage difference between magnetic field sweeps on gate B is $\Delta V_g^B = 10$ mV. In the right inset (Fig. 3) the averaged thermopower is displayed. It can be seen that week localization effects are absent in thermopower measurements. The thermopower amplitude has as well positive as negative values aroung $B = 0$ T. Counting the fluctuation amplitudes we obtain the distribution displayed in Fig. 3. Note, in order compare the experimental data with theory one has to consider the system symmetry. Time reversal symmetry (TRS) is present for magnetic fields around $B = 0$ and broken for high fields. Therefore, experimental data were split into two regime: First, TRS is present, $|B| \leq 40$ mT, and second, TRS is broken, $|B| \geq 50$ mT. Here, only the case for broken TRS is shown. The situation for TRS is discussed elsewhere [13]. In both cases a strong deviation from a Gaussian distribution is obtained (Fig. 3, dotted line). Typical are long tails, i.e. a high probability for large thermopower amplitudes is observed. Monte Carlo simulation techniques have been use to calculate the thermopower fluctuation distribution from

$$S = -\frac{\pi^2}{3}\frac{k_B^2 T}{e}\frac{d}{dE}\ln T(E)\Big|_{E=E_F} \qquad (3)$$

where $T(E) = \sum_{\alpha\in 1,\beta\in 2}|M_{\alpha\beta}|^2$ is the probability for the transmission from QPC_1 to QPC_2. The differentiation is done numerically for each realization of the Hamiltonian. The density of states $\rho(E_F) = 1/2\pi i\,\mathrm{Tr}\,(M^\dagger dM/dE)|_{E=E_F}$ is used as a weight factor to account for a large charging energy [14]. The resulting distributions of the thermopower fluctuations is shown as solid lines in Fig. 3. Evidently, the simulations represent the experimental results much better than a Gaussian distribution function.

In conclusion, we have demonstrated thermopower experiment in order to investigate typical properties of chaotic quantum dots. Theoretical predictions on a residual effective charging energy for an asymmetrically ajusted chaotic quantum dots were verified and the expected non-Gaussian distribution of fluctuations in transport related quantities was demonstrated. These experiments reveal thermopower measurement as a powerful in investigation chaotic systems, where convential transport measurement turn out to have systematic difficulties.

ACKNOWLEDGMENTS

Part of this work was supported by the DFG MO 771/3.

[1] I.L. Aleiner, and L.I. Glazman, Phys. Rev. B **57**, 9608 (1998).
[2] K. Flensberg, Phys. Rev. B **48**, 11156 (1993).
[3] L.W. Molenkamp, K. Flensberg, and M. Kemerink, Phys. Rev. Lett. **75**, 4282 (1995).
[4] C.W.J. Beenakker, Rev. Mod. Phys. **69**, 731 (1997).
[5] C.M. Marcus, A.J. Rimberg, R.M. Westervelt, P.F. Hopkins, and A.C. Gossard, Phys. Rev. Lett. **69**, 506 (1992).
[6] I.H. Chan, R.M. Clarke, C.M. Markus, K. Campman, and A.C. Gossard, Phys. Rev. Lett. **74**, 3876 (1995).
[7] H.U. Baranger and P.A. Mello, Europhys. Lett. **33**, 465 (1996).
[8] Z. Pluhar, H.A. Weidenmüller, J.A. Zuk, and C.H. Lewenkopf, Phys. Rev. Lett. **73**, 2115 (1994); H.U. Baranger, R.A. Jalabert, and A.D. Stone, Phys. Rev. Lett. **70**, 3876 (1993).
[9] K.B. Efetov, Phys. Rev. Lett. **74**, 2299 (1995).
[10] S.A. van Langen, P.G. Silvestrov, and C.W.J. Beenakker, Superlattice Microstruct. **23** 691 (1998).
[11] L.W. Molenkamp, H. van Houten, C.W.J. Beenakker, R. Eppenga, C.T. Foxon, Phys. Rev. Lett. **69**, 731 (1990).
[12] S. Möller, H. Buhmann, S.F. Godijn, and L.W. Molenkamp, Phys. Rev. Lett. 81, 5197 (1998).
[13] S.F. Godijn, S. Möller, H. Buhmann, L.W. Molenkamp, and S.A. van Langen, Phys. Rev. Lett. **82**, 2927 (1999). 82 (1999).
[14] P.W. Brouwer, S.A. van Langen, K.M. Frahm, M. Büttiker, and C.W.J. Beenakker, Phys. Rev. Lett. **79**, 913 (1997).

FA.6

2D CHAOTIC QUANTUM STATES IN SUPERLATTICES

S. Bujkiewicz, C.R. Tench, T.M. Fromhold, M.J. Carter, F.W. Sheard and L. Eaves

School of Physics and Astronomy, University of Nottingham, Nottingham NG7 2RD, UK

Abstract: The semiclassical motion of an electron along the axis of a superlattice may be calculated from the miniband dispersion curve. Under a weak electric field the electron executes Bloch oscillations which confines the motion along the superlattice axis. When a magnetic field, tilted with respect to the superlattice axis, is applied the electron orbits become chaotic. The onset of chaos is characterised by a complex mixed stable-chaotic phase space and an extension of the orbital trajectories along the superlattice axis. This delocalisation of the orbits is also reflected in the quantum eigenstates of the system some of which show well-defined patterns of high probability density whose shapes resemble certain semiclassical orbits. This suggests that the onset of chaos will be manifest in electron transport through a finite superlattice. We also propose that these phenomena may be observable in the motion of trapped ultra-cold atoms in an optically induced superlattice potential and magnetic quadrupole potential whose axis is tilted relative to the superlattice axis.

The correspondence between the classical and quantum descriptions of chaotic dynamics has been recently studied using electronic motion in semiconductor structures [1-3]. For electrons in a two-dimensional electron gas and in the quantum well of a resonant tunnel structure, chaotic electronic states have been observed in a controlled environment. Particularly striking has been the influence of certain classical periodic orbits, both stable and unstable, on the quantum wave functions and electronic conductance of the structures [2,3].

Here we report on a new type of quantum chaotic system; a superlattice in a longitudinal electric field and tilted magnetic field, Fig. 1. In this system the effective Hamiltonian which describes the underlying classical orbits originates from an *intrinsic quantum property* of the system i.e. the miniband dispersion curve. In our calculations we have considered electron motion in the lowest miniband, using a tight binding expression for the dispersion. In a weak electric field F along the superlattice axis, the effective Hamiltonian describing the motion is

$$H = \frac{\Delta}{2}\left(1 - \cos\frac{p_x a}{\hbar}\right) + \frac{(p_y^2 + p_z^2)}{2m^*} - eFx,$$

where p_x, p_y, p_z are the momentum components, Δ is the miniband width, a the superlattice period and m^* the effective mass for motion perpendicular to the superlattice (x) axis. With the applied magnetic field $\boldsymbol{B}$ in the xz plane (see Fig. 1), we take the vector potential to be $\boldsymbol{A} = (0, xB\sin\theta - zB\cos\theta, 0)$ and make the replacement $p_y \rightarrow p_y + eA_y$. We then see that

$p_y = \hbar k_y$ is a constant of the motion and the problem thus reduces to 2D (x, z) motion in the miniband in the presence of an effective potential field

$$V(x,z) = \frac{e^2B^2}{2m*}\{x\sin\theta - (z-z_0)\cos\theta\}^2 - eFx,$$

where $z_0 = \hbar k_y/eB\cos\theta$. This Hamiltonian can be used to calculate the semiclassical electron orbits from the equations of motion, $\dot{\boldsymbol{r}} = \partial H/\partial \boldsymbol{p}$, $\dot{\boldsymbol{p}} = -\partial H/\partial \boldsymbol{r}$, provided the electric and magnetic fields are small enough to preserve the miniband structure.

Fig. 2 shows real-space trajectories for electrons in a GaAs/$Ga_{0.3}Al_{0.7}As$ superlattice with well width w = 9.5 nm, barrier width b =1.25 nm ($a = b + w$), barrier height E_c = 240 meV and Δ = 26 meV. For $\theta = 0^o$ the Hamiltonian is separable and describes cyclotron motion in the z direction and Bloch oscillations, with spatial amplitude $\ell = \Delta/eF$, in the x direction, Fig. 2(a). For nonzero θ the orbits depend on magnetic field strength. For example at $\theta = 40^o$ and for B = 0.6 T, Fig. 2(b), most orbits are stable and qualitatively similar to that in Fig. 2(a). But when B = 1.5 T the orbits become chaotic, Fig. 2(c), and have a much larger spatial extent ($\gg \ell$) along the x axis, because the magnetic field, by transferring momentum between the lateral and longitudinal directions, can shift the locality of the Bloch oscillations.

The transition to chaos in this system is characterised by a rich mixed stable-chaotic phase-space structure. This is illustrated in Fig. (3), which shows Poincaré sections calculated from a range of electron trajectories starting from $x = 0$ with different initial velocities but the same kinetic energy (48 meV). The scattered points are values of transverse velocity components (v_y, v_z) at each turning point when $v_x = 0$. The phase-space structure contains a complex hierarchy of stable islands, Fig. 3(a), which disintegrate to a chaotic sea as the magnetic field is increased, Fig. 3(b).

We have investigated the relation between these classical properties of the one-miniband Hamiltonian and the electronic eigenstates of the system. The eigenstates were calculated using a basis set of Wannier states along the x direction and harmonic oscillator Landau states along the z direction. Fig. 4(a) for $\theta = 0^o$ shows a typical eigenfunction localised within the caustics of the corresponding classical orbit, in which an electron executes a superposition of cyclotron and Bloch oscillations. For $\theta = 40^o$, Fig. 4(b), (c) and (d) show eigenfunctions calculated in the mixed stable-chaotic regime. Some wave functions reveal patterns of high probability density whose shape resembles stable classical orbits, Fig. 4(b), while others, Fig. 4(c) and (d), have more diffuse and irregular patterns which extend across many Bloch oscillation spatial amplitudes. Since the onset of chaos strongly delocalises the electron orbits and wave functions, these results suggest this onset will be

manifest in electron transport experiments, when the Bloch oscillation amplitude is less than or comparable with the superlattice length and also less than the electron mean free path. This places stringent demands on sample purity and quality to reduce electron scattering processes.

However, analogous experiments could also be performed using ultracold atoms in the presence of an optically induced superlattice potential. In this case scattering processes are almost absent. Because the Bloch oscillation frequency of the ultracold atoms is very low (1 kHz) compared with that of electrons in semiconductors (1 THz), it has been possible to directly measure the atomic velocities as a function of elapsed time since injection into the laser field [4]. By using a magnetic quadrupole an additional 2D configurational potential well can be created. When the quadrupole axis is tilted with respect to the superlattice axis, a mixed stable-chaotic phase space is found similar to the case of electrons in the semiconductor superlattice and tilted magnetic field. In principle Poincaré sections could be experimentally measured which has not been possible in previous quantum chaotic systems. Quantized Wannier-Stark states have already been measured for atoms in uniformly accelerating optically induced superlattice potentials [5]. This type of superlattice structure provides a qualitatively new quantum chaotic system for which the classical and quantum properties can both be studied experimentally. Such experiments could therefore provide direct information concerning the links between the classical and quantum pictures of chaotic dynamics.

Acknowledgments: TMF (LE) are supported by EPSRC UK Advanced (Senior) Fellowships

References

[1] C.M. Marcus, A.J. Rimberg, R.M. Westervelt, P.F. Hopkins and A.C. Gossard, *Phys. Rev. Lett.* **69**, 506 (1992).
[2] P.B. Wilkinson, T.M. Fromhold, L. Eaves, F.W. Sheard, N. Miura and T Takamasu, *Nature* **380**, 608 (1996).
[3] T.M. Fromhold, L. Eaves, F.W. Sheard, M.L. Leadbeater, T.J. Foster and P.C. Main, *Phys. Rev. Lett.* **72,** 2608 (1994); T.M. Fromhold, P.B. Wilkinson, F.W. Sheard, L. Eaves, J. Miao and G. Edwards, *Phys. Rev. Lett.* **75,** 1142 (1995).
[4] M. Ben Dahan, E. Peik, Y. Castin and C. Salomon, *Phys. Rev. Lett.* **76,** 4508 (1996).
[5] S.R. Wilkinson, C.F. Barucha, K.N. Madison, Q. Niu and M.G. Raizen, *Phys. Rev. Lett.* **76**, 4512 (1996).

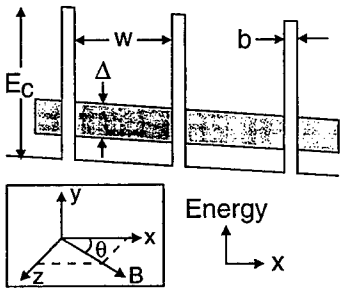

Fig. 1 Variation of band-edge energy of an electron with position x in a superlattice under applied bias, showing width Δ of first miniband (shaded). Inset: orientation of magnetic field $\boldsymbol{B}$ relative to superlattice (x) axis.

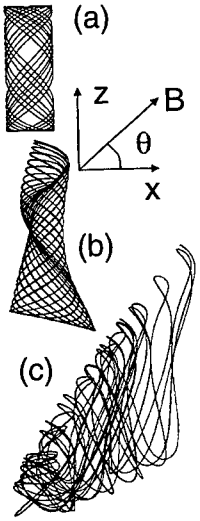

Fig. 2 Semiclassical orbits calculated for $F = 2.44 \times 10^5$ V m^{-1} and (a) $B = 0.6$ T, $\theta = 0^o$, (b) $B = 0.6$ T, $\theta = 40^o$, (c) $B = 1.5$ T, $\theta = 40^o$.

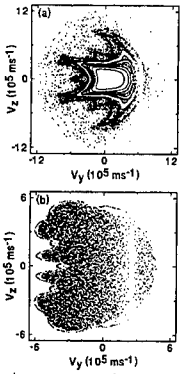

Fig. 3 Poincaré sections of (v_y, v_z) points when $v_x = 0$, calculated for $F = 2.44 \times 10^5$ Vm^{-1} in (a) mixed stable-chaotic regime ($B = 0.6$ T, $\theta = 40^o$), (b) strongly chaotic regime ($B = 1.5$ T, $\theta = 40^o$).

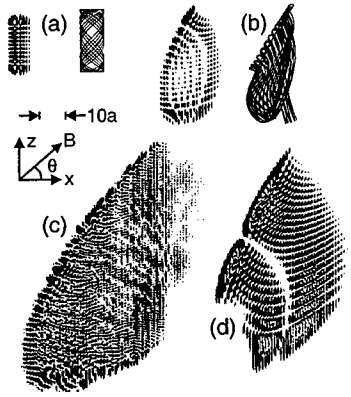

Fig. 4 Probability density plots (white = 0) of electron eigenstates for (a) $F = 2.44 \times 10^5$ V m^{-1}, $B = 0.6$ T, $\theta = 0^o$ (stable regime) showing amplitude of Bloch oscillations $\ell = 10a$, (b) $F = 4.88 \times 10^5$ V m^{-1}, $B = 1.5$ T, $\theta = 40^o$ (mixed stable-chaotic regime) showing eigenfunction and associated stable orbits, (c) and (d) $F = 4.88 \times 10^5$ V m^{-1}, $B = 1.5$ T, $\theta = 40^o$ showing spatially extended states corresponding to chaotic motion.

FB.1

Presentation by:

U. Sivan, *Technion III. Haifa, Israel*
"Self-Assembled of Nanoelectronics by Biotechnology"

FB.2

Presentation by:

S.G. Louie, *University of California, Berkeley, CA, USA*
"Theory of Nanotubes"

FB.3

Photon Assisted Andreev Transport and Sub-Gap Structures

Morten Wildt[1,2], Jonatan Kutchinsky[1], Rafael Taboryski[3], Claus B. Sørensen[2],
Jørn Bindslev Hansen[1], and Poul Erik Lindelof[2].
[1] Depart. of Physics, Technical University of Denmark, Build. 309, DK-2800 Lyngby, Denmark
[2] Niels Bohr Institute, University of Copenhagen, DK-2100 Copenhagen Ø, Denmark
[3] Danish Institute of Fundamental Metrology, Anker Engelundsvej 1, DK-2800 Lyngby, Denmark

Abstract

We report new measurements of microwave induced perturbations of the sub-harmonic energy gap structures in the current-voltage characteristics of superconductor-semiconductor-superconductor junctions. Around the sub-gap bias voltages associated with the enhanced quasi-particle transfer mediated by multiple Andreev reflection processes we observe microwave induced satellites, shifted in voltage by multiples of hf/en, where hf is the photon energy and n is the number of quasi-particle traversals as determined by the Andreev processes. The observed behaviour is the analogue of the socalled photon assisted tunneling but here associated with the multiple Andreev reflections.

Introduction

The electrical properties of junctions formed between a superconducting material, S, and a non-superconducting metallic material, N, which may be a metal or a strongly degenerate semiconductor, are determined by a special boundary condition. If we consider a superconductor-semiconductor (S-N) interface with high transparency, a proximity effect is observed due to the injection of electron pairs (Cooper pairs) from the superconductor into the semiconductor where they decay over a characteristic length, the induced coherence length ξ_N.

Over the last few years, the proximity effect has been re-examined in the context of phase coherence in the normal region, and a new understanding based on the Andreev reflection process at N-S interfaces has emerged. The characteristic length scales which here depend on the phase relaxation have been clarified. For S-N-S junctions the role of Andreev bound states as channels of phase coherent currents have been studied. In this paper we present new data on S-N-S junctions of the Al/n++GaAs/Al type with highly transparent interfaces for which we have observed photon assisted transport in the GHz range.

Theory

The Andreev reflection is a second order quantum mechanical process by which an electron-like particle incident on a superconductor with a quasiparticle excitation energy ε above the Fermi energy, may be transmitted as a Cooper pair in the superconductor, if a hole-like particle with energy $-\varepsilon$ is retroreflected along the path of the incoming electron [1]. For a superconductor/normal-conductor (S-N) interface with low contact resistance (high transparency), e.g. a superconductor-semiconductor interface with a negligible Schottky barrier, the Andreev scattering leads to an increased conductance, which is seen as an excess current at high voltage bias $V > 2\Delta/e$, where Δ is the energy gap in the superconductor [2].

For S-N-S junctions the excess current is also observed and in addition multiple Andreev reflections of particles at the two N-S interfaces give rise to a series of "bumps" in the I-V characteristics at bias voltages $V = \pm 2\Delta/ne$ with $n = 1,2,3....$ This relation simply expresses the

condition for maximum charge transfer for multiple Andreev reflections given the number of traversals of the normal region [3]. The resulting series of conductance maxima in the I-V curve is known as the sub-harmonic energy gap structure, SGS. The SGS was given a semiclassical explanation in Refs.[2] and [3]. The semiclassical model, however, completely neglects scattering and the influence of coherent states in the normal region (mesoscopic phenomena). Recently coherent transport in short S-N-S junctions has been taken into account [4].

As first observed by Dayem and Martin [5] in $Al/Al_2O_3/In$ junctions, an applied microwave field with frequency f induces a series of socalled photon-assisted tunneling steps (PAT steps) in the I-V characteristics of a superconductor-insulator-superconductor (S-I-S) junction. The PAT steps are centered around the gap voltages at $V = \pm 2\Delta/e$ and spaced equidistantly by hf/e along the voltage axis. The PAT steps were explained by Tien and Gordon [6] who calculated the perturbations of the I-V characteristics by assuming that the applied high frequency voltage modulates the energy of the charged particles adiabatically thereby giving rise to a series of hf/e spaced replica (sidebands) of the singularities in the quasi-particle density of states of a superconductor at $\pm\Delta$ around the Fermi energy. For a voltage biased S-I-S junction the result is that the perturbed I-V curve is equal to a weighted sum of unperturbed I-V curves each displaced mhf/e along the V-axis. The weight factors are given by the squares of Bessel functions of the m'th order, $J_m^2(eV_{rf}/hf)$, where the argument is the ratio between the applied microwave voltage, V_{rf}, and hf/e. Later, similar PAT steps were observed in other types of superconducting junctions, point contacts and microbridges (which behave more like S-N-S junctions) and in such junctions a new type of PAT steps spaced by hf/ne were observed centered around the sub-harmonic energy gap structure (SGS) voltages given above [7].

Experimental techniques

The samples were fabricated as follows [8]: a 200 *nm* thick layer of degenerate GaAs was grown in a VARIAN molecular beam epitaxy chamber on an undoped GaAs substrate. The GaAs was doped with Si to $4.4\times10^{18} cm^{-3}$ and capped with five Si monolayers (δ-doping) separated by 2.5 *nm* of GaAs. Each of the δ-doped layers contained 5×10^{13} Si atoms per cm^3 producing an anomalous high electron concentration. These layers reduce the width of the Schottky barrier at the superconductor-semiconductor interface, which was formed by depositing 200 *nm* of Al *in-situ* after the GaAs had cooled down. The result was a highly transparent superconductor-semiconductor interface with a measured contact resistivity between Al and GaAs for the best material of $\rho_c = 8\times10^{-13}\Omega m^2$. From the excess current in devices made from this material we estimate a barrier transmission coefficient of $T_n = 0.5$. The GaAs had a carrier density of $n = 4.8\times10^{18} cm^{-3}$ and a diffusion constant $D = 0.016 m^2/s$. At 0.25 K the coherence length in the GaAs is ξ_N = 0.28 μm.

The devices were made as follows: First, 18 μm wide mesa structures in the Al and GaAs layers were etched with separate current and voltage contacts for four point measurements. Second, the S-N-S structures were fabricated by removing Al in selected areas by the use of electron beam lithography with standard PMMA resist and wet etching [8]. The devices were shaped as simple planar Josephson junctions 18 μm wide and with a length equal to the slit width *L*.

The samples were characterized electrically in a ^{3}He cryostat with a base temperature of $0.235mK$. The measurement leads were pair twisted and filtered. The *I/V* and *dV/dI* vs. *V* characteristics of the devices were measured by applying a low frequency ac modulation current superimposed on a dc bias. The ac voltage was measured with a lock-in amplifier. The ac current

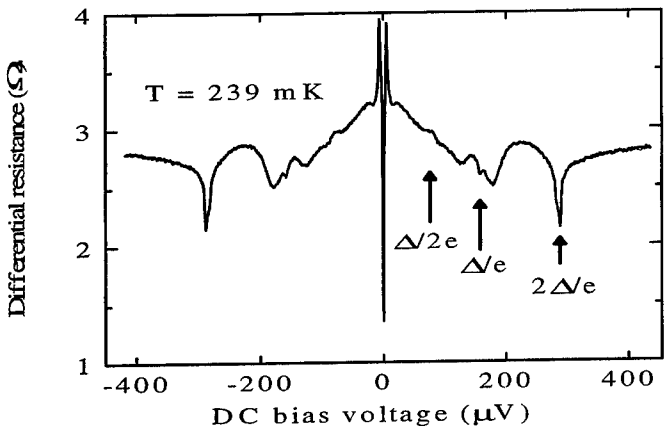

Fig. 1
dV/dI vs. V for superconductor-semiconductor-superconductor (Al/N++GaAs/Al) junction at 239 mK. The sub-harmonic energy gap structure (SGS) is observed at $V = 2\Delta/ne$ ($n = 1,2,4$).

amplitude was kept below 500 nA. A magnetic field was applied from a superconducting solenoid powered by a high resolution current source. The rf (microwave) field was applied through a loosely coupled loop antenna placed approximately 1 cm above the sample.

Experimental results

Fig. 1 shows the differential resistance dV/dI vs. dc bias voltage V for a Al/n++GaAs/Al junction with L = 0.3 μm measured at the base temperature of the cryostat. In this measurement no rf (microwave) voltage was applied. The minimum at V = 0 stems from the (noise-perturbed) supercurrent flowing between the two superconducting aluminium electrodes which have a superconducting transition temperature of 1.2 K (close to the value for bulk aluminium). The superconducting energy gap, Δ, of aluminium is 175 μeV. Minima in the differential resistance are clearly observed at $V = 2\Delta/e$ and at the sub-harmonic voltages $V = \Delta/e$ and $V = \Delta/2e$, the latter two minima exhibit a complex and so far unexplained splitting. In Fig. 2 we present an example of the observation of photon assisted transport along with the best fit based on the Tien-Gordon theory of PAT steps. The curves show dV/dI vs. V around $V = \Delta/e$ at the same temperature as before. The two upper curves are displaced along the dV/dI axis by 0.2 ohm and 0.4 ohm, respectively. The lower curve is a magnified version of the relevant part of the curve of Fig. 1, i.e. the unperturbed dV/dI-V curve (no rf). The middle curve is the experimental curve recorded with a microwave field at 5.975 GHz applied to the junction, the satellites (sidebands) are observed spaced hf/2e from the center Δ/e structure. The upper curve is the curve calculated from the Tien-Gordon theory for S-I-S junctions with a weight factor adjusted to give the best fit.

Conclusion

The good agreement between the measured and the calculated curves leads us to the conclusion that photon assisted transport is observed in S-N-S junctions whose enhanced

conductance at V = 2Δ/ne (here with n = 2) is due to Andreev reflected particles. We have also observed the expected periodic dependence of the strength of the PAT structures with varying microwave amplitude.

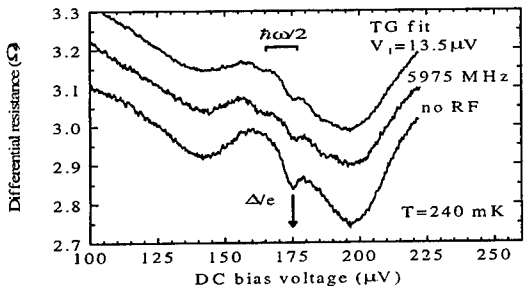

Fig. 2
dV/dI vs. V for the same junction as in Fig. 1 with and without rf (microwave) power applied. The two lower traces are experimental curves,the upper trace is calculated from the Tien-Gordon theory. For clarity the two upper traces have been displaced 0.2 and 0.4 ohm, respectively, along the dV/dI axis.

Acknowledgment

This work was supported by the Danish Technical Research Council, the Velux Foundation, the III-V Nanolab, and the CNAST Center Program.

References

[1] A.F. Andreev, Zh.Eksp.Teor.Fiz. **46**, 1823 (1964) [Sov.Phys.JETP **19**, 1228 (1964)].
[2] T.M.Klapwijk, G.E.Blonder, and M.Tinkham, Physica (Amsterdam) **109-110B+C** 1657 (1982); G.E.Blonder, M.Tinkham, and T.M.Klapwijk. Phys.Rev. B **25**, 4515 (1982).
[3] M.Octavio, M.Tinkham, G.E.Blonder, and T.M.Klapwijk, Phys.Rev. B **27**, 6739 (1983); K.Flensberg, J.Bindslev Hansen, and M.Octavio, Phys.Rev. B **38**, 8707 (1988).
[4] E.Sheer, P.Joyez, D.Esteve, C.Urbina, and M.Devoret, Phys.Rev.Lett. **78**, 3535, (1997).; E.N.Bratus, V.N.Shumeiko, and G.Wendin, Phys.Rev.Lett. **74**, 2110 (1995); J.C.Cuevas, A.Martin-Rodero, and A. Levy-Yeyati, Phys.Rev. B **54**, 7366 (1996); A.V.Zeitsev and D.V.Averin, Phys.Rev.Lett. **80**, 3602 (1998).
[5] A. H. Dayem and R.J. Martin, Phys. Rev. **8**, 246 (1962).
[6] P.K. Tien and J.P. Gordon Phys. Rev. **129**, 647 (1963).
[7] P. E. Gregers-Hansen, E. Hendricks, M.T. Levinsen, and G.R. Pickett, Phys. Rev. Lett. **31**, 524 (1973); O. H. Sørensen, B. Kofoed, N.F. Pedersen and S. Shapiro, Phys. Rev. B **9**, 3746 (1974) and L.-E. Hasselberg, M.T. Levinsen and M.R. Samuelsen, Phys. Rev. B **9**, 3757 (1974).
[8] R.Taboryski, T.Clausen, J.Bindslev Hansen, J.L.Skov, J.Kutchinsky, C.B.Sørensen, and P.E.Lindelof, Appl.Phys.Lett. **69**, 656 (1996); J.Kutchinsky, R.Taboryski, C.B.Sørensen, A.Kristensen, P.E.Lindelof, J.Bindslev Hansen, C. Schelde Jacobsen, and J.L.Skov, Phys.Rev.Lett. **78**, 931 (1997) and R.Taboryski, T.Clausen, J.Kutchinsky, C.B.Sørensen, P.E.Lindelof, J.Bindslev Hansen, and J.L.Skov, IEEE Trans. Appl. Sup. **7**, 2809 (1997).

AUTHOR INDEX

Ottawa 1999

	Monday, August 2	Tuesday, August 3	Wednesday, August 4	Thursday, August 5	Friday, August 6
08:45-09:00	Opening Ceremony				
09:00-10:30	**Session MA** QHE	**Session TA** Coherence and Transport	**Session WA** Special FQHE Session	**Session THA** Spectroscopy of the QHE	**Session FA** Chaos
	Coffee Break				
11:00-12:30	**Session MB** Optics and Imaging	**Session TB** Quantum Dots	**Session WB** FQHE 11:15-12:30	**Session THB** Spin Effects	**Session FB** Non-semiconducting Systems
12:30-14:00	Lunch Break				Closing Ceremony
14:00-15:30	**Session MC** Metal-Insulator Transition	**Session TC** New Systems: Observations and Concepts	Time for Informal Discussions	**Session THC** Double Layers	
	Coffee Break			Coffee Break	
16:00-18:00	Poster Session A	**Session TD** Kondo Effect and Interactions		Poster Session C	
19:30-21:30		Poster Session B (19:30 - 21:30)	Banquet		